Lecture Notes in Electrical Engineering 293

Jengnan Juang
Cheng-Yi Chen
Cheng-Fu Yang
Editors

Proceedings of the 2nd International Conference on Intelligent Technologies and Engineering Systems (ICITES2013)

Springer

Lecture Notes in Electrical Engineering

Volume 293

For further volumes:
http://www.springer.com/series/7818

About this Series

"Lecture Notes in Electrical Engineering (LNEE)" is a book series which reports the latest research and developments in Electrical Engineering, namely:

- Communication, Networks, and Information Theory
- Computer Engineering
- Signal, Image, Speech and Information Processing
- Circuits and Systems
- Bioengineering

LNEE publishes authored monographs and contributed volumes which present cutting edge research information as well as new perspectives on classical fields, while maintaining Springer's high standards of academic excellence. Also considered for publication are lecture materials, proceedings, and other related materials of exceptionally high quality and interest. The subject matter should be original and timely, reporting the latest research and developments in all areas of electrical engineering.

The audience for the books in LNEE consists of advanced level students, researchers, and industry professionals working at the forefront of their fields. Much like Springer's other Lecture Notes series, LNEE will be distributed through Springer's print and electronic publishing channels.

Jengnan Juang · Cheng-Yi Chen
Cheng-Fu Yang
Editors

Proceedings of the 2nd International Conference on Intelligent Technologies and Engineering Systems (ICITES2013)

Springer

Editor
Jengnan Juang
Department of Electrical and Computer Engineering, School of Engineering
Mercer University
Macon, GA
USA

Co-Editors
Cheng-Yi Chen
Department of Electrical Engineering
Cheng Shiu University
Kaohsiung
Taiwan

Cheng-Fu Yang
Department of Chemical and Materials Engineering
National University of Kaohsiung
Kaohsiung
Taiwan

ISSN 1876-1100 ISSN 1876-1119 (electronic)
ISBN 978-3-319-04572-6 ISBN 978-3-319-04573-3 (eBook)
DOI 10.1007/978-3-319-04573-3
Springer Cham Heidelberg New York Dordrecht London

Library of Congress Control Number: 2014934565

Printed on acid-free paper

Springer is part of Springer Science+Business Media (www.springer.com)

Preface

The papers presented at the International Conference on Intelligent Technologies and Engineering Systems (ICITES 2013) held at the Cheng Shiu University in Taiwan during December 12–14, 2013 are compiled in this volume. The primary objective of this conference is to bring together on a common platform, academicians, researchers, application engineers, industry personnel, and the users of emerging intelligent technologies and engineering systems. The conference is intended to encourage and facilitate knowledge sharing, interactions, and discussions on future evolutions of new challenges in the twenty-first century.

Over 200 participants attended the conference, made technical presentations, and discussed about various aspects of intelligent technologies and engineering systems. The number of papers published in this volume and the number of unpublished presentations at the conference indicate the evidence of growing interest in the areas of emerging intelligent technologies and engineering systems.

The papers published in this volume include but not limited to the following areas of interest: intelligent decision models, intelligent computing systems and applications, smart sensor network and applications, networking and signal processing, signal processing and computing technologies, systems control and applications, software engineering, intelligent electronic circuits and systems, innovative motor electronics and computer applications, mechanical and materials engineering, materials and communications, functional materials and radio frequency applications, and applied technology for engineering materials.

We would like to appreciate the efficient work done by Springer-Verlag in publishing this volume.

Jengnan Juang

Contents

Chapter 1
Integrated Taguchi Method with Immune Algorithm for Solving Profit-Base Unit Commitment

Ming-Tang Tsai

Abstract This paper presents a new approach to deal with the Price-Based Unit Commitment (PBUC) problem in day-ahead electricity markets. This new approach hybrids the Taguchi method (TM) and Immune Algorithm (IA), which provides a powerful global exploration capability. TM is embedded in the crossover operations to select the better gene for achieving crossover when the PBUC problem is solved by IA. TM has been widely used in experimental designs for problems with multiple parameters. The proposed approach is applied to a 15 units test system. Results show that the proposed method is feasible, robust, and efficiency.

Keywords Immune algorithm · Price-based unit commitment · Taguchi method

1.1 Introduction

Deregulating the power market creates competition and trading mechanism for market players. It moves from the cost-based unit commitment to price-based Unit Commitment (PBUC) [1, 2]. That means GENCOs had to produce the power to satisfy their customers with a minimizing operating cost of the whole scheduling period. In PBUC, satisfying hourly load and system security is no longer an obligation for GENCOs. GENCOs need to maximize the profit instead of minimize the operating cost. In this new objective, the price including the fuel purchase price, energy sale price, …, etc., will enforce a unit' ON/OFF status. To obtain a better dispatch, efficient tools are needed to solve the PBUC problem.

By considering the maximizing profit, a GENCO offer its energy to market by setting a proper limit on generation. The solution of PBUC can be obtained by a

M.-T. Tsai (✉)
Department of Electrical Engineering, Cheng-Shiu University, Kaohsiung, Taiwan, Republic of China
e-mail: tsaymt@csu.edu.tw

J. Juang et al. (eds.), *Proceedings of the 2nd International Conference on Intelligent Technologies and Engineering Systems (ICITES2013)*, Lecture Notes in Electrical Engineering 293,
DOI: 10.1007/978-3-319-04573-3_1,

complete enumeration of all feasible combinations, which can not be applied to realistic power system because of the prohibitive computational complexity [3]. In the pervious publications, various approaches have been developed to solve this problem [4–6]. The major disadvantages of numerical techniques are the curse of dimensionality, computational time, and local optimality when the number of units and operating constraints increased. Most artificial intelligent techniques have the ability to conquer restrictions, however, it is difficult to get a good performance.

Recently, some hybrid algorithms based on meta-heuristic techniques have been presented to solve the PBUC problem and have shown their effectiveness [7–12]. Richter and Shedble [7] and Yamin and Shahidehpour [8] presents a price/profit-based UC solution based on Genetic Algorithm (GA). For large size unit commitment, the computation time remains a major problem. Attaviriyanupap et al. [9] and Yamin et al. [10] propose a hybrid LR-EP for solving the PBUC problem. However, PBUC involves a high complexity in searching the wide solution space, which manifests itself in the form of complicated constraints imposed on the probable large number of variables in the scheduling process.

The Taguchi Method (TM) [11] uses many concepts derived from statistic experimental design for evaluating and implementing improvements in products, processes, and equipment. The fundamental principles are employed to improve the quality of products by minimizing the effect of the varied factors. Two major functions used in the searching procedure are (1) signal-to-noise ratio (SNR) [12, 13], a technique which measures quality, and (2) orthogonal arrays, which are used to simultaneously study a number of design parameters. TM can be used to find the optimal operating parameters (better chromosomes) for dealing with the local optimality problem. This paper proposes the Taguchi-Immune Algorithm (TIA) as a new approach to solve unit commitment problems. The effectiveness of TIA is demonstrated by performing optimization on study case. Our results show that the proposed method is feasible, robust, and efficiency.

1.2 Problem Formulation

The objective function and associated constraints of the PBUC problem can be formulated as

$$obj\_f = Max\left\{\sum_{t=1}^{H}\sum_{i=1}^{N} LMP(i,t)\times P(i,t) - [C_i(P(i,t)U(i,t) + ST(i,t)U(i,t)(1-U(i,t-1))]\right\} \tag{1.1}$$

where H is the scheduling time and N is the total number of units. $LMP(i,t)$ is the Location Marginal Price of a committed unit i at time t. $P(i,t)$ is the power output of a committed unit i at time t. $C_i(P(i,t)) = a_iP^2(i,t) + b_iP(i,t) + c_i$, approximated by the quadratic function, is the production cost of unit i at time t. a_i, b_i, c_i are the coefficients of the production cost of unit i. $U(i,t)$ is the on/off status of unit i at time

t. $ST(i,t)$ is the start-up cost of unit i at time t, which includes the hot start cost and cold start cost. The start-up cost is dependent upon the operating time that

$$ST(i,t) = \begin{cases} hot\ start\ cost & when\ T_i^{off} \le X_i^{off} \le H_i^{off} \\ cold\ start\ cost & when\ X_i^{off} > H_i^{off} \end{cases} \tag{1.2}$$
$$H_i^{off} = T_i^{off} + csh_i$$

where T_i^{off} is minimal down time of unit i. X_i^{off} is the continued down time of unit i. csh_i is the cold start time of unit t.

The constraints include both the system constraints and the unit's constraints:

(a) load balance:

$$\sum_{i=1}^{N} P(i,t) \times U(i,t) \ = P_d(t) \tag{1.3}$$

(b) spinning reserve:

$$\sum_{i=1}^{N} P_{\max}(i) \times U(i,t) \ \ge \ P_d(t) + R(t) \tag{1.4}$$

(c) unit power generation limitation:

$$P_{\min}(i) \le P(i,t) \le P_{\max}(i) \tag{1.5}$$

(d) minimum up-time constraint:

$$T_{on}(i) \ge T_i^{on} \tag{1.6}$$

(e) minimum down-time constraint:

$$T_{off}(i) \ge T_i^{off} \tag{1.7}$$

$P_d(t)$ and $R(t)$ represent the system demand and the spinning reserve at time t. $P_{\max}(i)$ and $P_{\min}(i)$ are the maximum and minimum generation limits of unit i. $T_{on}(i)$ and $T_{off}(i)$ are the continual up-time and continual down-time of unit i. T_i^{on} is minimal up time.

1.3 The Proposed Methodology

In solving the UC problem, two variables needing to be determined are (i) the integer unit's status $U(i,t)$, and (ii) the continuous power output $P(i,t)$. A feasible

combinatorial solution is first randomly generated while satisfying the system and operational constraints.

1.3.1 Encoding

The initial solution is obtained by assigning a binary digit for the ON/OFF operating status for each unit. The feasibility is assured by the following steps.

(1) The ON/OFF status of a unit is generated at random by:

$$U^j(i,t) = sign[random(-1\ ,\ P)]$$
$$P = 1 + \frac{p_{\max}(t)}{\sum_{i=1}^{N} P_{\max}(i)} \tag{1.8}$$

where

j	the number of population
random (a, b)	uniform distribution between -1 and P
sign [X]	the binary function. $X \geq 0, sign\ [X] = 1$; $X < 0, sign\ [X] = 0$.

(2) If the status of a unit violated the minimal up-time or minimal down-time constraints, it would be reversed. The system constraints are also checked in this process. If the units' status violated the system constraints, step (1) would be performed again.

1.3.2 Affinity and Diversity Evaluation

There are two classes of affinity in TIA. One is the affinity between antigens and antibodies. It represents the combination intensity between antigen and an antibody. The other one is the affinity between two antibodies which shows the similarity between two antibodies. The diversity of the k-th antibody can be computed by

$$E_k^t(M) = -\sum_{m=1, m\neq k}^{M} P_{mk}^t \log_{10} P_{mk}^t \tag{1.9}$$

where M is the number of antibodies, P_{mk}^t is the probability of t-th allele of the m-th antibody coming out of t-th allele of the k-th antibody. Thus the total diversity of the k-th antibody is

$$E_k(M) = \frac{1}{H}\sum_{t=1}^{H} E_k^t(M) \tag{1.10}$$

where H is the number of gene of the k-th antibody.

Two affinity forms must be taken into account in the proposed TIA. $(Aff_b)^{jk}$ is set between zero and one. Another one is applied to investigate the affinity between antibodies and antigens with

$$(Aff_g)^k = (1 + Obj\_f_k)^{-1} \tag{1.11}$$

Obj_f_k is the objective function for the k-th antibody. The affinity score of each antibody is obtained by calculating the objective function.

1.3.3 Antibody Re-composition by TM

The orthogonal arrays of TM are used to find better combinations of decision variables with a small number of experiments. An orthogonal array is a fractional factorial matrix which ensures a balanced comparison of levels of any factor. In this study, a two-level orthogonal array was used.

(i) Define the control factors

The integer matrices C^m will be produced when the status of a unit in the scheduling duration is generated by using the crossover process. The integer matrix is randomly divided into a predetermined F parts which represent the control factors of the orthogonal array. So matrix $C^m = [C^{m1}, C^{m2}, \ldots, C^{mF}]$.

(ii) Generate potential offspring

In this paper, randomly select two chromosomes C^1, C^2 to apply the $L_4(2^3)$ TM for the experiment list to generate the potential offspring. The three factors in chromosomes C^1 and C^2 correspond to the factors 1, 2 and 3, respectively, as defined in Table 1.1.

(iii) Calculate the factor effect

The effects of the factors can be defined as

$$E_{fl} = sum\ of\ SNR_{STB,i}\ for\ factor\ f\ at\ level\ l \tag{1.12}$$

where i is the experiment number, $f = 1, 2$ is the factor name, and $l = 1, 2, 3$ is the level number. The optimal level of each factor was determined by the larger value of either E_{f1} or E_{f2}. This solution will be checked against the constraints to see if it is feasible. Only feasible solutions will be kept.

Table 1.1 Chromosome applied in orthogonal array

Factor	1	2	3
Level 1 (chrom. C^1)	C^{11}	C^{12}	C^{13}
Level 2 (chrom. C^2)	C^{21}	C^{22}	C^{23}

1.3.4 Elitism Selection

The antibodies including parents and offspring are then ranked in ascending order according to their objective function. One half of the antibodies with the best value are kept as the parents for the next generation.

1.3.5 Stopping Rule

The process of generating new antibodies with the best affinity between antibody and antigen will continue until the affinity values are optimized or the maximum generation number is reached. Figure 1.1 shows the flowchart of TIA.

1.4 Test Result

The PBUC procedure was implemented with Matlab 2.4 GHz Pentium IV computer 1 GB RAM. An IEEE 15 Units [14] is chosen to study the proposed algorithm. The spinning reserve is assumed to be 10 % of load demand in this case with a total scheduling period of 24-h. Data for all units are detailed in Table 1.2.

To observe the variations in the performance due to the stochastic nature of the proposed algorithm, a total of 100 runs were taken for each example. In each run, the simulated parameters remained the same. The total cost of all cases for the maximal and minimal runs, and the average cost and average time over 100 runs were recorded, as shown in Table 1.3. Table 1.3 also indicates the number of trials reaching the optimum and the average number of generations to converge. From Table 1.3, it can be seen that the TIA was a good performer in terms of solution quality, number of generations to converge, and the number of trials reaching optimum. Figure 1.2 shows the convergent characteristics of IA and TIA.

To evaluate the reliability of the optimization schemes, the PBUC problem was solved 100 times by TIA and IA. To compare the TIA results with IA in a statistical manner, the number of counts of convergence was provided for each cost range, as shown in Table 1.4. From Table 1.4, it is observed that TIA achieved a higher degree of robustness than did the other evolutionary algorithm.

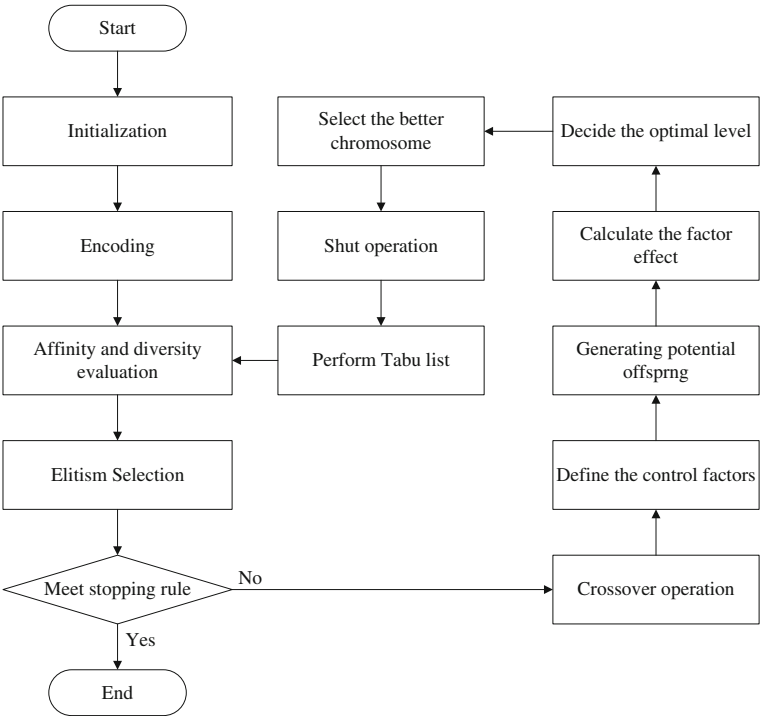

Fig. 1.1 Flowchart of TIA

Table 1.2 Data for all units

Gen	MDT	P_{max}	P_{min}	a	b	c	SCC	SCF	ST
11	2	76	15.2	81.3	13.35	0.009	50	50	3
17	3	155	54.3	142.7	10.69	0.005	150	150	6
18	3	155	54.3	143	10.72	0.005	150	150	6
21	4	197	68.9	259.1	23	0.003	200	200	8
27	5	500	140	210	12	0.001	800	500	4
28	7	500	140	180	12.1	0.001	800	250	4
34	4	250	75	140	12.4	0.001	20	50	3
43	8	440	120	250	7.4	0.001	30	450	4
63	4	185	54.3	143.7	11.69	0.007	160	160	6
64	4	185	54.3	144	11.72	0.006	160	160	6
70	5	360	150	187.1	11.86	0.003	210	210	8
83	2	80	20	210	14.2	0.009	40	50	2
84	4	200	50	150	13.4	0.002	30	60	3
86	5	440	120	80	8.9	0.005	40	500	5
95	9	600	100	170	7.5	0.003	60	410	6

Table 1.3 Simulation results on test systems

	IA	TIA
Minimal	240,388.4905	246,865.2319
Average	243,975.6849	250,521.8856
Maximal	248,289.6649	252,846.2456
Number of trail reaching optimum	5	8
Average number of iterations to converge	85	142
Average execution time(s)	101.4723	130.2981

100 RUNS, 200 Iterations

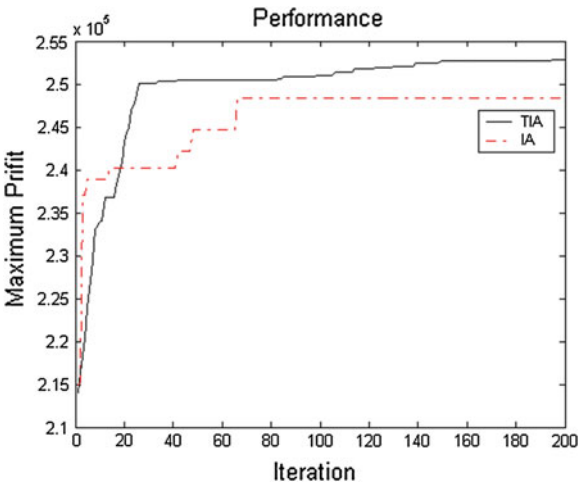

Fig. 1.2 The convergent characteristics of two methods

Table 1.4 Number of convergent cost range for each trial test

	Range of cost (× 1000$)									
	253.0 –251.7	251.7 –250.4	250.4 –249.1	249.1 –247.8	247.8 –246.5	246.5 –245.2	245.2 –243.9	243.9 –242.6	242.6 –241.3	241.3 –240.0
IA	–	–	–	3	4	9	36	29	16	3
TIA	15	65	11	8	1	–	–	–	–	–

1.5 Conclusion

In this paper, we presented a Taguchi-Immune Algorithm (TIA) to deal with unit commitment problems. TIA integrates the TM and the IA to provide a powerful global exploration capability. The TM was incorporated in the crossover operations to select a better gene, consequently enhancing IA. Test results proved the effectiveness of the proposed algorithm in solving PBUC problems under a

reasonable execution time. The proposed algorithm has great potential for further applications to many other mixed integer combinational optimization problems in power system planning and operation.

References

1. Hao, S. (2000). A study basic bidding strategy in clearing pricing auction. *IEEE Transactions on Power Systems, 15*(3), 975–980.
2. Lin, W. M., & Chen, S. J. (2002). Bid-based dynamic economic dispatch with an efficient interior point algorithm. *International Journal of Electrical Power and Energy Systems, 24*(1), 51–57.
3. Wood, A. J., & Wollenberg, B. F. (2003). *Power Generation, Operation and Control*. New York: John Wiley.
4. Granelli, G. P., Marannino, P., Montagna, M., & Zanellini, F. (2006). Monte Carlo based unit commitment procedures for the deregulated market environment. *International Journal of Electrical Power and Energy Systems, 28*, 712–722.
5. Li, T., & Shahidehpour, M. (2005). Price-based unit commitment; a case of Lagrangian relaxation versus mixed integer programming. *IEEE Transactions on Power Systems, 20*(4), 2015–2025.
6. Sebastian, T., Arroyo, J. M., Conejo, A. J., & Contreras, J. (2002). Price maker self-scheduling in a pool-based electricity market: A mixed-integer LP approach. *IEEE Transactions on Power Systems, 17*(4), 1037–1042.
7. Richter, C. W., & Shedble, G. B. (2005). A profit-based unit commitment GA for the competitive environment. *IEEE Transactions on Power Systems, 20*(4), 2015–2025.
8. Yamin, H. Y., & Shahidehpour, S. M. (2004). Unit commitment using a hybrid model between Lagrangian relaxation and genetic algorithm in competitive markets. *Electric Power Systems Research, 68*, 83–92.
9. Attaviriyanupap, P., Kita, H., Tanaka, E., & Hasegawa, J. (2003). A hybrid LR-EP for solving new profit-based UC problem under competitive environment. *IEEE Transactions on Power Systems, 18*(1), 229–236.
10. Yamin, H. Y., El-Dwairi, Q., & Shahidehpour, S. M. (2007). A new approach for GenCos profit based unit commitment in day-ahead competitive electricity markets considering reserve uncertainty. *International Journal of Electrical Power and Energy Systems, 29*, 609–616.
11. Ross, P. J. (1998). *Taguchi techniques for quality engineering*. New York: The McGraw-Hill Companies.
12. Mosca, E. (1995). *Optimal predictive and adaptive control*. Englewood Cliffs, NJ: Prentice-Hall.
13. Astrom, K. J., & Wittenmark, B. (2009). *Adptive control*. Reading, MA: Addison-Wesley.
14. Hobbs, B. F., Rothkopf, M. H., O'neill, R. P., & Chao, H. P. (2001). *The next generation of electric power units commitments models*. Norwell, MA: Kluwer Academic Publishers (Appendix I).

Chapter 2
Optimal Expansion Planning of Distribution Substations Using Loading Gravity with Genetic Algorithm

Hui-Jen Chuang, Wen-Yuan Tsai, Chao-Shun Chen, Chin-Yin Ho, Chia-Chung Lin and Yi-Pin Tsai

Abstract This paper has presented a methodology to solve the optimal substation capacity expansion problem for distribution system by using the genetic algorithm (GA). The S curve with different time constant is used to represent the load growth of each customer class for the load forecasting of each fence area. The load flow analysis is performed to find power demand of each fence area for annual system operation over the study period. The overall costs of power loss and substation investment are included in the objective function, and each feasible solution is expressed as a chromosome in the GA simulation process. The fitness is then enhanced by considering the diversity of chromosomes so that the global optimization during the solution process can be obtained. The proposed approach has been tested on Taipei Distribution System through the utility data. Test results demonstrated the feasibility and effectiveness of the method for the applications.

Keywords Substation planning · Genetic algorithm · Distribution system

2.1 Introduction

Due to Taiwan's economic development in the past decade, more and more air conditioners are used by the commercial and residential customers, which have resulted in dramatic load growth in several metropolitan areas. To meet load

H.-J. Chuang (✉) · W.-Y. Tsai · C.-Y. Ho · Y.-P. Tsai
Department of Electrical Engineering, Kao Yuan University,
Kaohsiung 82151, Taiwan, Republic of China
e-mail: t20006@cc.kyu.edu.tw

C.-S. Chen
Department of Electrical Engineering, I-Shou University,
Kaohsiung 84001, Taiwan, Republic of China

C.-C. Lin
Taiwan Power Company, Kaohsiung, Taiwan, Republic of China

J. Juang et al. (eds.), *Proceedings of the 2nd International Conference on Intelligent Technologies and Engineering Systems (ICITES2013)*, Lecture Notes in Electrical Engineering 293,
DOI: 10.1007/978-3-319-04573-3_2,

demand, and achieve the reliability and efficiency of distribution system operation, substation expansion planning has become a very important issue for Taiwan Power Company (Taipower). To support distribution system planning more effectively, the Outage Management System (OMS) [1] in Taipower, which has stored all of the distribution components with attributes in the Automated Mapping/Facility Management/Geographic Information System (AM/FM/GIS) [2] database, has been applied for load forecasting. Information for all of the customers residing in each fence area is retrieved from the OMS database, and the load demand of the fence area can therefore be derived according to the energy consumption and service types of customers served. The S curve with different time constant is used to represent the load growth of each customer class for the load forecasting of each fence area. The load flow analysis is performed to find power demand of each fence area for annual system operation over the study period. The substation expansion planning has to determine the capacity of substations to meet annual peak demands over the whole planning periods. This becomes a network design problem with a dynamic dimension because of the interaction existing between annual load demands, substations and the different periods to be considered for the global solution.

To solve the problem of optimal substation expansion for distribution systems, the GA is used in this paper to improve the efficiency of simulation process [3–5]. The overall costs of power loss and substation investment are included in the objective function, and all feasible solutions are expressed as chromosomes in the GA. The genetic operators which include crossover and mutation are then processed to produce individual of the population in a feasible space. The fitness is then enhanced by considering the diversity of population so that the global optimization during the solution process can be obtained.

2.2 Problem Description

2.2.1 The Annual Load Forecasting of Each Small Area

According to the historical load demand of different customer classes in Taipower, it will take 7.99, 5.07, 3.8 and 3.2 years for the load demand of the residential area, commercial area, education area and administrative area to reach 63.2 % of the saturated load demand, respectively [6]. The annual load demand of each customer class is then determined by considering the corresponding load growth patterns and the load forecasting of the small area is then obtained by the summation of annual load demands of all customer classes. Figure 2.1 shows load forecasting for each different land use, as well as the whole fence area. It is found that the area load demand becomes saturated after 16 years with load demand of 6590 kVA.

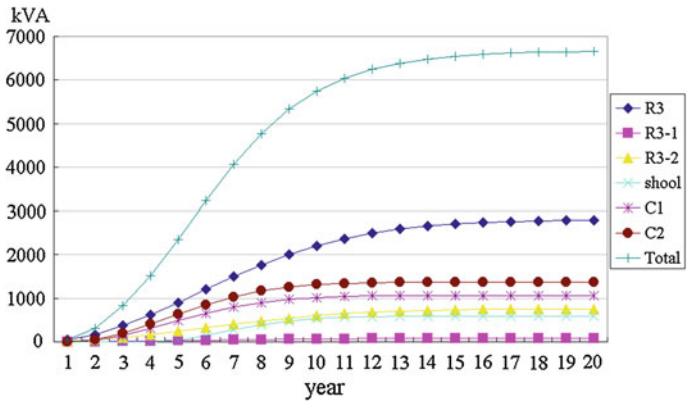

Fig. 2.1 The load forecasting of the fence N6348

2.2.2 Equivalent Loading Gravity Center

With the load demand of customers determined by load forecasting for each land base, the gravity method is applied to find the equivalent location of total load demand within each small area by:

$$u_j = \frac{\sum_{i=1}^{n} x_i \times S_i}{\sum_{i=1}^{n} S_i} \tag{2.1}$$

$$v_j = \frac{\sum_{i=1}^{n} y_i \times S_i}{\sum_{i=1}^{n} S_i}. \tag{2.2}$$

Here, S_i represents the load forecast of land base i at location (x_i, y_i) and the corresponding coordinates of loading center of small area j is calculated as u_j and v_j respectively.

2.2.3 Objective Function

For the study period of y years with m substations candidates, the total cost of power loading loss and the possible substation investment cost are represented in the objective function as:

$$\min C == \sum_{y=1}^{y} \left(\sum_{i=1}^{m} X_{yi} C_{inv,i} + C_{loss,y} \right). \tag{2.3}$$

2.2.3.1 Equivalent Power Loss Cost

The cost of power loading loss for the substations to serve the load is represented by Eq. (2.4).

$$C_{loss,y} = \sum_{k=1}^{m} X_{yk} \sum_{j=1}^{nm} \left(\frac{S_{yj}}{V_{yj}} \right)^2 \times r \times \left[(u_k - u_j)^2 + (v_k - v_j)^2 \right]^{\frac{1}{2}} \times W \times 8760. \tag{2.4}$$

Here, m is the number of substation for the final target year, nm is the number of fence areas (all the load points), and X_{yk} is the variable of commitment for substation k at year y. The integer variables X_{yk} uses values of 1 or 0 to represent whether substation k is to be taken away or remained in the system, respectively.

2.2.3.2 Investment Cost of Substations

To simplify the substation expansion planning of distribution systems, the standard substation with two main transformer of 2*60 MW has been adopted by Taipower. The procurement cost of main transformers linearly depreciates over their lifetime of 20 years and the capital investment cost of state with j units of main transformers for year i is expressed as:

$$C_{inv,i} = \frac{I}{20} \times j. \tag{2.5}$$

2.3 Genetic Algorithm [3–5]

In this paper, the GA is proposed to find the optimal substation capacity expansion problem by minimizing the overall cost of power loading loss and investment cost of substations for distribution systems. With the GA method, the objective function and feasible substation planning strategies are represented as population in the GA. The genetic operators which include crossover and mutation are then processed to produce individual of the population in a feasible space. The fitness is then enhanced by considering the diversity of population so that the global optimization during the solution process can be obtained.

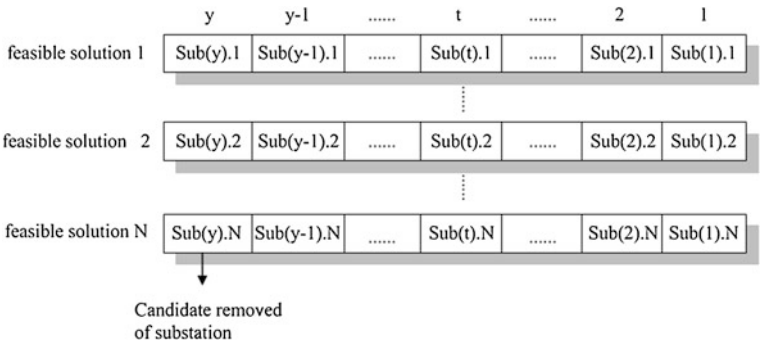

Fig. 2.2 Data structure of GA genes

The data structure of GA genes is depicted in Fig. 2.2, where Sub(y). N represents the candidate number of substations to be removed for year y. For a distribution system with N possible strategies of substation planning over study periods of y years, there will be N feasible solutions with y genes in the pool of genes.

The compusation procedure of GA method is executed as follows:

Step 1: Create an initial population with randomly generated string and set up control parameters of genetic algorithm.
Step 2: Evaluate all of the individuals with the objection function.
Step 3: Select a new population from the old population based on the fitness of the individuals as given by the evaluation function.
Step 4: Apply genetic operations of mutation and crossover to members of the population for creation of new solution.
Step 5: Evaluate the newly created individuals.
Step 6: Check if termination criteria are met. If not, go to Step 3. If yes, output the results.

2.4 Numerical Analysis and Results

To improve the operation efficiency of distribution systems, the unit commitment of main transformers must occur to provide sufficient capacity to meet the loading demand and maintain service reliability for annual power loading over the study years. After that, the GA algorithm is used to solve the optimal expansion planning of substations to achieve the minimization of investment cost. To demonstrate the effectiveness of the proposed methodology, the distribution system of Taipei City District of Taipower is selected for computer simulation.

Figure 2.3 shows the installation locations of standard substations with a capacity of (2*60 MVA) for the target year in Taipei City area. There are 23

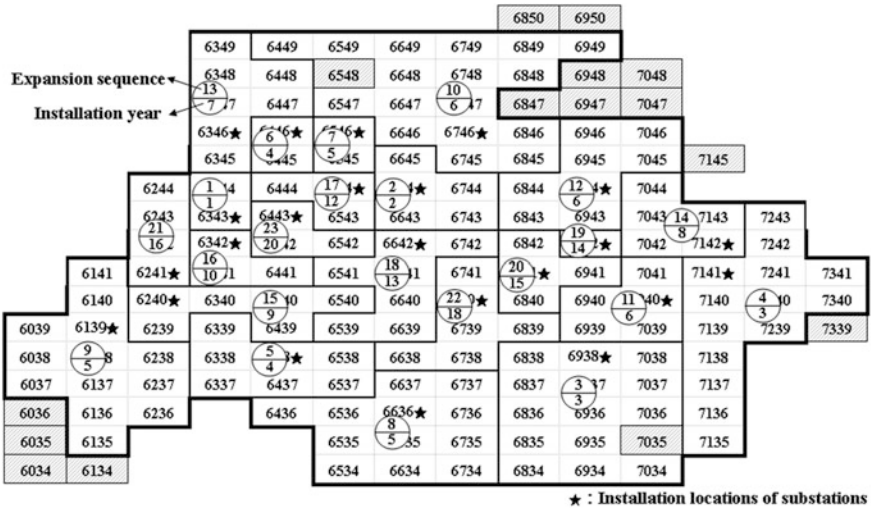

Fig. 2.3 The optimal expansion planning of distribution substations for Taipei City by GA methods

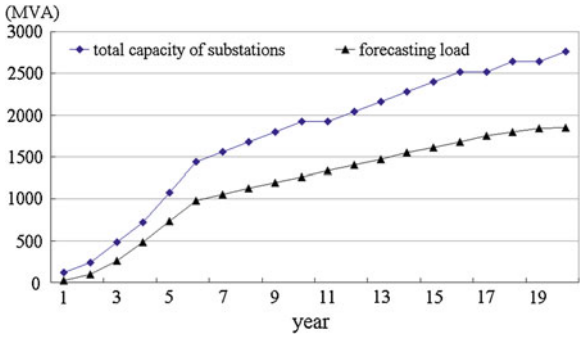

Fig. 2.4 Load forecasting and total capacity of distribution substations to be installed over the study years

substations required to cover the saturated loading of 1894 MVA. Each substation serves several fence areas. For the downtown area with high load density, one substation may serve only two fence areas. For the outskirt area with light load density, one substation may serve more areas.

With the installation of substations to cover the load demand for the final target year, the expansion sequence of substations is derived according to the annual load forecasting of each fence area. After formulating the objective function by considering the investment cost of main transformers and power loading loss of substations to serve the load demand of each fence area, the GA method is then applied to derive the proper year for each substation to be committed. The investment cost of $4.27 M for a main transformer with 60 MVA capacity is used in Eq. (2.3) for the objective function. In this paper, the proposed GA algorithm is implemented with Matlab on a Duo CPU 2.4 GHz personal computer. In the GA

method, the feasible solution pool, the crossover rate, and the mutation rate are 100, 0.8, and 0.1, respectively, based on the simulation of various case studies in this paper. The total system cost has been obtained as $133.3 M by GA methodology, the GA method is converged after 39 generation.  in Fig. 2.3 shows that the substation should be committed in year X with expansion sequence of substation Y. For instance, a new substation should be installed in fence 6642 in year 13. With the annual load growth in each fence area, new substations are installed when the loading factor of existing substation is greater than 70 % of the main transformer capacity and the service areas of each substation are adjusted accordingly to minimize power loading loss. Figure 2.4 shows the annual load forecasting of Taipei City and the capacity of substations over the study years.

2.5 Conclusion

In this paper, the unit commitment of substations to serve the power demand of distribution system in Taipei Taiwan has been proposed. The Genetic Algorithm has been applied to derive the proper expansion planning of substations by minimizing investment cost of substation without violation of operation constraint. The S curves with different time constants are applied to represent load growth for each customer class for the forecasting of annual load within each fence area. The objective function which has been formulated by considering the annual power loading loss and investment cost of main transformers over the study years. By using the GA algorithm, the optimal unit commitment strategy of substations has been solved to achieve best cost effectiveness of expansion planning of substations. With the proposed capacity expansion planning, the minimization of total system loss has been achieved.

Acknowledgments This work was supported in part by the National Science Council of Republic of China under the Contract NSC 102-2221-E-244 -011.

References

1. Lampley, G. C. (2009). Permanent and temporary faults. *IEEE Industry Applications Magazine, 15*(5), 25–31.
2. Chen, T. H., & Cherng, J. T. (1998). Design of a TLM application program based on an AM/FM/GIS system. *IEEE Transactions on Power Systems, 13*(3), 904–909.
3. Naderi, E., Seifi, H., & Sepasian, M. S. (2012). A dynamic approach for distribution system planning considering distributed generation. *IEEE Transactions on Power Delivery, 27*(3), 1313–1322.
4. Najafi, S., Hosseinian, S. H., Abedi, M., Vahidnia, A., & Abachezadeh, S. (2009). A framework for optimal planning in Large distribution networks. *IEEE Transactions on Power Systems, 24*(2), 1019–1028.

5. Chang, G. W., Wang, H. L., & Chu, S. Y. (2004). Strategic placement and sizing of passive filters in a power systems for controlling voltage distortion. *IEEE Transactions on Power Delivery, 19*(3), 1204–1211.
6. Distribution system load forecasting manual, Taiwan Power Company Operations Branch (2010).

Chapter 3
Evaluation of Sensory Nerve Dysfunction by CPT Index in Hemodialysis Patients Based Flexible Fuzzy Classifier

Ming-Jui Wu, Guan-Chun Chen, Hsiu-Hui Lin, Chia-Hung Lin, Yi-Chun Du, Jian-Xing Wu and Pei-Jarn Chen

Abstract Sensory nerve dysfunction is a common symptom in hemodialysis (HD) patients and to have a more objective diagnose is more and more important for clinician recently. The current perception threshold (CPT) is a method for evaluation sensory nerve function via pain feeling and which has been reported better than the conventional methods. In this study, we proposed a system based on Flexible Fuzzy Classifier (FFC) using CPT index to evaluate sensory nerve dysfunction in HD patients. All patients were recruited at Yong-Kang Veterans Hospital including 35 HD patients (20 male/15 female) versus 20 control patients (10 male/10 female) and measured from arm and above the ankles before HD therapy. The results indicated that CPT levels in HD patients were significantly higher than normal aged subjects (control group), and over 7 years of HD patients were appeared to be higher but not significant with other patients. Furthermore, FFC method could classify HD patients and controls group successfully with 100 % accuracy; 82 % accuracy for over 7 years HD patients and others. The FFC method with CPT index has high potential to be an automatic classification system for early stage detection of sensory nerve dysfunction.

M.-J. Wu · H.-H. Lin
Department of Internal Medicine, Kaohsiung Veterans General Hospital Tainan Branch, Tainan, Taiwan, Republic of China

G.-C. Chen · J.-X. Wu
Department of Biomedical Engineering, National Cheng Kung University, Tainan, Taiwan, Republic of China

C.-H. Lin
Department of Electrical Engineering, Kao-Yuan University, Kaohsiung City, Taiwan, Republic of China

Y.-C. Du (✉) · P.-J. Chen
Department of Electrical Engineering, Southern Taiwan University of Science and Technology, Tainan, Taiwan, Republic of China
e-mail: terrydu@mail.stust.edu.tw

J. Juang et al. (eds.), *Proceedings of the 2nd International Conference on Intelligent Technologies and Engineering Systems (ICITES2013)*, Lecture Notes in Electrical Engineering 293,
DOI: 10.1007/978-3-319-04573-3_3,

Keywords Sensory nerve dysfunction · Flexible Fuzzy Classifier (FFC) · Current Perception Threshold (CPT) · Hemodialysis (HD)

3.1 Introduction

Sensory nerve dysfunction refers to nerve damage at peripheral nervous system is a common symptom in HD patients. As it progresses may cause myasthenia gravis, tendon atrophy and limb deformation, moreover, these conditions are irreversible. Therefore, an objective method to diagnose sensory function is more and more important for clinicians in HD patients recently [1]. Early diagnosis of peripheral neuropathy is an important clinical issue which requires an efficient and easy used method non-invasively to evaluation on human body. There are some literatures reported that sensory nerve dysfunction could be evaluated by pain intensity assessment [2] such as the electrical stimulation test using PainVision PS-2100 (Nipro Co, Osaka, Japan) that provided a quantitative measure of pain tolerance to sensory nerve including neuroselective for large (A-beta fibers), small myelinated (A-delta fibers) and unmyelinated (C fibers) nerve fibers [3]. This electrodiagnostic procedure has established normative painless index, called CPT index, for various cutaneous and/or a mucosa site from studies carried out around the world in various branches of medicine [4, 5] and recently emerged in urology [6]. Recently, these reports provided more evidence in significant correlations of CPT index in A-delta and C-fibers with clinical symptoms and indicated that it was better than conventional urodynamic variables, as well as the efficacy of various treatments. It allowed detection in both hyperesthetic and hypoesthetic sensory thresholds [6, 7].

CPT is a good index for evaluation of sensory nerve dysfunction, however, there are still not enough researches have been reported application of CPT in HD patients Moreover, an efficient, non-invasive and easy using method is an important clinical issue for early diagnosis and that could contribute to further understanding severity of sensory nerve dysfunction in pathological condition of HD. Flexible Fuzzy Classifier (FFC) is proven to have an easy design, good generalization, strong tolerance for input noise, and online learning ability. In this study, we proposed a novel FFC method using non-linear regression model which architecture with non-linear or linear consequent functions (curve approximation). Recursive least squares is exploited to update the FFC's parameters [8, 9].

3.2 Methods

There are three parts including CPT index measurement, FFC and Experiment design would express in below sections.

3.2.1 CPT Index Measurement

Afferent nerves are generally comprised of three major subpopulations of fibers with different diameters [10]. The meter of normative painless is a peripheral nerve perception threshold measurement device, capable of calculating the amount of stimulating current at the lowest detectable level in a subject. There are three frequencies 2000, 250 and 5 Hz of standard sinusoidal current waves to stimulate three nerve fibers (A-beta, A-delta and C) specifically. In the cutaneous sensory system, the A-beta fibers conduct touch and pressure sensations; the A-delta fibers conduct temperature, pressure and fast pain; and the C fibers conduct temperature and slow pain sensations which protect the body from serious injury. The perception threshold could calculate as CPT index in applying a neuroselective current to the test sites, determined by the absolute value of the lowest perceptible current in a certain nerve fiber. This enables quantitative evaluation of perception threshold for each type of nerve fiber to measure nerve fiber-specific perceptional functions, such as pain, touch, temperature and deep sensations for evaluation various peripheral nerve diseases.

The device, PainVision PS-2100, utilized in this study could provide CPT index for neuroselectivity researches, which could select a specific stimulating current to depolarize a specific fiber. It is to take advantage of the unique characteristics of each type of nerve fiber. The picture of CPT index measurement is shown in Fig. 3.1.

3.2.2 Flexible Fuzzy Classifier Design

As introduced previously, CPT is an index for evaluation of sensory nerve dysfunction in hemodialysis patients. Refer to previous studies [1, 4], the correlation between CPT and sensory nerve dysfunction is higher. In this study, three groups with the specific ranges of CPT index and the unknown discrete nonlinear system is expressed as followed:

$$y(k-1) = f[\Theta(k-1)] \tag{3.1}$$

where $\Theta(k-1) = [\psi 1(k-1), \psi 2(k-1), \ldots, \psi \mathrm{N}(k-1)] = [y(k-2), \mathrm{y}(k-3), \ldots, \mathrm{y}(k-n-1), \mathrm{u}(k-2), \mathrm{u}(k-3), \ldots, \mathrm{u}(k-m-1)]$, $\Theta(k-1)$ is the input vector, $\mathrm{y}(k-1)$ is the output vector, and f is an unknown non-linear smooth function. A fuzzy classifier is presented as a set of fuzzy rules, the form of the jth rules, $j = 1, 2, 3, \ldots, \mathrm{M}$. $\Theta \in R_N$ ($N = n + m$) could be presented as the following:

$$R_j: \ \text{IF}\, \psi_1 \,\text{is}\, \mathrm{A}_{1,j} \,\text{and}\, \psi_2 \,\text{is}\, \mathrm{A}_{2,j} \,\text{and}\, \ldots \,\text{and}\, \psi_N \,\text{is}\, \mathrm{A}_{N,j} \,\text{Then}\, v \,\text{is}\, B_j \tag{3.2}$$

where ψn, $n = 1, 2, 3, \ldots, N$, is the input variable, M fuzzy rules and N fuzzy sets are used for each rule to map an input linguistic vector to an output linguistic

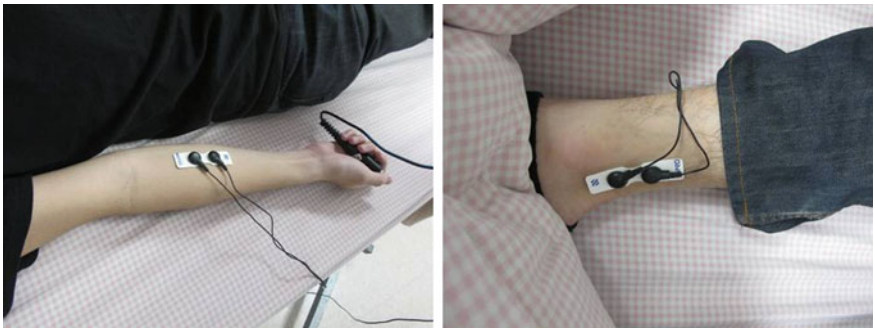

Fig. 3.1 The picture of CPT index measurement from patient's arm (*left*) and just above the ankles (*right*) before HD therapy

scalar v, $A_{n,j}$ and Bj are fuzzy rules. Finally, the equation of flexible fuzzy classifier (FFC) can be modified as Eq. (3.3).

$$\hat{y}(k-1) = \sum_{j=1}^{M} v_j(k-1)R_j(k-1) = V^T(k-1)R^T(k-1) \tag{3.3}$$

where $V(k-1) = [v_1(k-1), v_2(k-1), \ldots, v_M(k-1)]^{\mathrm{T}}$, $R(k-1) = [R_1(k-1), R_2(k-1), \ldots, R_M(k-1)]^{\mathrm{T}}$, and $C(k-1) = [c_1(k-1), c_2(k-1), \ldots, c_M(k-1)]^{\mathrm{T}}$. According to the Stone-Weierstrass theorem, the unknown non-linear function f is approximated as Eq. (3.4).

$$\hat{y}(k-1) = \sum_{j=1}^{M} v_j(k-1)R_j(k-1) + \varepsilon \tag{3.4}$$

where ε is the modeling error. For K input–output paired of training data $[\Theta, C] = [\psi, \Delta\text{Error}]$, $k = 1, 2, 3, \ldots, K$, the optimal parameters, σ_j and v_j, can minimize the modeling error. The least-square algorithm is used to adjust the FFC's structure and parameters as Eqs. (3.5–3.7).

$$R^{*T}(k-1) = R^T(k-1) + \eta\Delta\frac{\partial V^T(k-1)R^T(k-1)}{\partial\sigma_j(k-1)} \tag{3.5}$$

$$V^{*T}(k-1) = V^T(k-1) + \eta\Delta\frac{\partial V^T(k-1)R^T(k-1)}{\partial v_j(k-1)} \tag{3.6}$$

$$\Delta = y(k-1) - \hat{y}(k-1) \tag{3.7}$$

where η, $0 < \eta \leq 1$, is the learning rate. Its mechanism design with the essentials of updating parameters, σ_j and v_j, to minimize the "root mean squared error

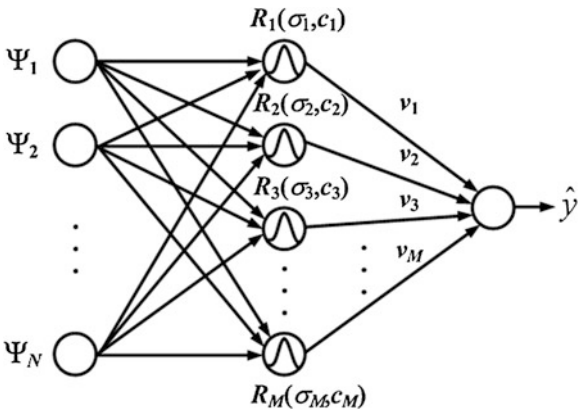

Fig. 3.2 The structure of FFC

(RMSE)", and the convergent condition is as Eq. (3.8). The structure of FFC is shown in Fig. 3.2.

$$RMSE = \sqrt{\frac{1}{K}\sum_{k=1}^{K}\left(\hat{y}(k-1) - y(k-1)\right)^2} \leq \varepsilon \tag{3.8}$$

3.2.3 Experiment Design

We divided all patients into three part, including patients with over 7 years HD, patients under 7 years HD and normal aged subjects (control group). The study enrolled all the subjects from Kaohsiung Veterans General Hospital Tainan Branch. CPT index measured from subjects' arm and above the ankles before HD therapy. This study was performed in accordance with the Declaration of Taiwan health agency and all participants have been provided with written informed consent before enrollment. During the follow-up period, patients were evaluated monthly by nephrologists and nurses at the clinic for data collection, including age, gender, race, cause of end-stage renal disease (ESRD), previous HD, body mass index (kg/m^2), PD indication (medical, patient's option, or only option) and previous nephrology referral.

3.3 Results and Conclusions

The proposed method was developed on a PC AMD Athlon II × 2 245 2.91 GHz with 1.75 GB RAM and Matlab software. The results of CPT index in normal subjects and patients are shown in Table 3.1 that CPT levels in patients were

Table 3.1 CPT index of normal subjects and HD patients

	Normal subjects	HD patients	*p*
Quantity (M/F)	20 (10/10)	35 (20/15)	–
Age	62.5 ± 13.2	69 ± 15.2	NS
CPT index	8.8 ± 3.2	21.1 ± 13.4	<0.0001

Note NS means no significant

Table 3.2 Data arrangement of HD patients and statistical analysis

	HD	HD (male)	HD (female)	*P*
Quantity	35	20	15	–
Diabetes (Y/N)	15/20	9/11	6/9	NS
Cardio disease (Y/N)	15/20	9/11	6/9	NS
High BP (Y/N)	16/19	11/9	5/10	NS
HD Periods	6.5 ± 5.0	5.6 ± 4.1	8.1 ± 6.3	<0.05
Age	69 ± 15.2	71.3 ± 16.0	61.5 ± 13.1	NS
CPT index	21.1 ± 13.4	19.7 ± 10.1	21.9 ± 14.1	<0.0001

Table 3.3 Classification rate based on FFC network for three groups

	Normal aged subjects*	HD under 7 years^{+}	HD over 7 years$^{♀}$
Quantity	20	20	15
HD Periods	–	3.1 ± 1.5	11.4 ± 4.3
Age	62.5 ± 13.2	61.5 ± 13.1	71.3 ± 16.0
CPT index	8.8 ± 3.2	20.0 ± 2.4	22.7 ± 6.8
Classification rate of proposed method	100 % (* vs^{+} and * vs$^{♀}$)		
		82 % ($^{+}$ vs$^{♀}$)	

Note Marker *, + and ♀ meant the group of Normal aged subjects, HD under 7 years and HD over 7 years, respectively

significantly higher than control group. Table 3.2 is shown that statistical analysis of HD patients divided into male and female groups. We could find that the CPT index in female HD patients is significantly higher than in males. However, this result maybe cause by longer HD period in the female group than male group, it is needed to collect more data to verify this issue. Table 3.3 is shown the results that compared between patients with over/under 7 years HD and normal aged subjects. It indicated that CPT index in patients with over/under 7 years HD was higher than normal aged subjects, but not reach significant different between over/under 7 years HD patients. Our results showed that CPI is a suitable index for evaluation of sensory nerve dysfunction in HD patients and it also accorded with other clinical researches [1, 4] that patients with over 7 years HD have higher probability to have sensory nerve dysfunction. Furthermore, the results of classification rate by FFC method between HD patients and normal aged subjects was 100 %, and between HD patients with over/under 7 years was about 82 %. All the process

time of FFC method was within 0.5 s. The FFC method with CPT index has high potential to be an automatic classification system for early stage detection of sensory nerve dysfunction.

Acknowledgments This work was supported by grants from Kaohsiung Veterans General Hospital Tainan Branch (VHYK101-08) and approved by an Institutional Review Board (IRB) of the Kaohsiung Veterans General Hospital Tainan Branch (VGHKS12-CT9-03).

References

1. American Association of Electrodiagnostic Medicine. (1999). Technology review: The Neurometer current perception threshold (CPT). *Muscle and Nerve, 22*, 523–531.
2. Murakawa, K., Moriyama, K., Yanamoto, F., Nakano, S., Fukunaga, T., & Arimura, Y. (2006). Measurement of clinical pain intensity: Quantitative sensory testing. *Masui, 55*(9), 1080–1086.
3. Kato, J. (2011). Pain vision. *Masui, 60*(9), 1059–1063.
4. Katims, J. J. (1998). Electrodiagnostic functional sensory evaluation of the patient with pain: a review of the neuroselective current perception threshold (CPT) and pain tolerance threshold (PTT). *Pain Digest, 8*, 219–230.
5. Oishi, M., Mochizuki, Y., Suzuki, Y., et al. (2002). Current perception threshold and sympathetic skin response in diabetic and alcoholic polyneuropathies. *Internal Medicine, 41*, 819–822.
6. Ukimura, O., Ushijima, S., Honjo, H., et al. (2004). Neuroselective current perception threshold evaluation of bladder mucosal sensory function. *European Urology, 45*, 70–76.
7. Takekuma, K., Ando, F., Niino, N., & Shimokata, H. (2002). Prevalence of hyperesthesia detected by current perception threshold test in subjects with glucose metabolic impairments in a community. *Internal Medicine, 41*, 1124–1129.
8. Angelov, P., Lughofer, E., & Zou, X. (2008). Evolving fuzzy classifiers using different model architectures. *Fuzzy Sets and Systems, 159*(23), 3160–3182.
9. Angelov, P. (2011). Fuzzy connected multimodel system evolving autonomously from data streams. *IEEE Transactions on Systems, Man, and Cybernetics-Part B: Cybernetics, 41*(4), 898–910.
10. Fowler, C. J., Griffiths, D., & de Groat, W. C. (2008). The neural control of micturition. *Nature Reviews Neuroscience, 9*, 453–466.

Chapter 4
High Performance Microelectronic Molding Compounds Cured with Organophosphine Accelerators

Chean-Cheng Su, Chien-Huan Wei, Yin-Shuo Li and Ping-Hsun Yang

Abstract Curing characteristics of microelectronic molding compounds (EMCs) that were accelerated by triphenylphosphine-1,4-benzoquinone (TPP-BQ) and triphenylphosphine (TPP) were studied using a differential scanning calorimeter (DSC). Although an analysis of thermal characteristics revealed that TPP-BQ is inactive at low temperatures, at high temperatures, TPP-BQ increases the curing rate of EMC in dynamic and isothermal curing experiments. Before gelation, EMC containing TPP-BQ had a lower melting viscosity than that of EMC containing TPP, explaining why the former flowed longer in the spiral flow test than the latter. Additionally, the new organophosphine accelerator exhibited excellent thermally latency in the curing of biphenyl-type epoxy molding compounds.

Keywords Thermal latency · Epoxy molding compounds · Molding

4.1 Introduction

In IC design, semiconducting chips have become larger while devices have become smaller. Highly reliable plastic-encapsulated semiconductor packages are needed for advanced electronic devices. New molding compounds for encapsulating microelectronic devices are needed in the near future because halogen-containing flame retardants and antimony oxide flame retardant synergists, which are widely used in present-day molding compounds, may be environmentally hazardous. In typical green molding compounds, flame retardants (e.g., phosphorus-containing compounds, nitrogen-containing compounds, metal hydrate, metal oxide, inorganic

C.-C. Su (✉) · C.-H. Wei · Y.-S. Li · P.-H. Yang
Department of Chemical and Materials Engineering, National University of Kaohsiung, No. 700, Kaohsiung University Rd., Nan-Tzu Dist., Kaohsiung 81148, Taiwan, Republic of China
e-mail: ccsu@nuk.edu.tw

J. Juang et al. (eds.), *Proceedings of the 2nd International Conference on Intelligent Technologies and Engineering Systems (ICITES2013)*, Lecture Notes in Electrical Engineering 293,
DOI: 10.1007/978-3-319-04573-3_4,

filler and resins with high C/H ratios) have generally replaced the conventional halogen-containing flame retardants and antimony oxide flame retardants used in EMCs [1, 2]. Notably, EMC with biphenyl resins and highly loaded fillers can retard flammability and is a green material. To produce reliable packaging materials for microelectronic devices, a highly loaded filter with specific characteristics is needed: high flame retardation, high thermal resistance, high moisture resistance, favorable mechanical properties and a low thermal expansion coefficient of EMC [3, 4].

This work synthesized a new organophosphine thermally latent accelerator, triphenyl phosphine-benzoquino (TPP-BQ), for use in high filler-loaded EMCs based on biphyenyl-type epoxy. The objective of this study was to characterize the reactivity and cure behavior of EMCs cured with thermal latency catalysts. A kinetic model was used to show how a thermal latency catalyst affects curing in an EMC.

4.2 Experimental

4.2.1 Materials and Sample Preparation

Scheme 4.1 shows the chemical structure of the epoxy and the hardener.

The TPP catalyst was obtained from Hooko Co. The TPP-BQ catalyst was synthesized by the authors and was identified using Fourier transform infrared spectroscopy (FTIR) and nuclear magnetic resonance (NMR). The chemical structure of the catalysts is described in Scheme 4.2.

The materials were weighed out and thoroughly kneaded using a two-roll mill with the cold roller operated at 15 °C and the hot roller operated at 120 °C. After mixing, EMC was cooled and pulverized. Each sample was then stored in a refrigerator at 4 °C.

4.2.2 Instruments

Calorimetric measurements were made using a differential scanning calorimeter (DSC) (Perkin-Elmer DSC-7) equipped with an intracooler. Isothermal and dynamic-heating experiments were performed at a 50 ml/min nitrogen flow. In dynamic curing, the sample was heated at a rate of 10 °C/min from 0 to 250 °C. The isothermal curing reaction was performed at five temperatures (130, 150, 165, 175 and 185 °C). The reaction was considered complete when the isothermal DSC thermogram stabilized at the baseline level, which generally required approximately 1 h. At the end of the reaction, the total area under the exotherm calculated according to the extrapolated baseline was used to calculate the isothermal heat of curing, ΔH_{Io} (Jg^{-1}). After the curing reaction was completed in the calorimeter, the

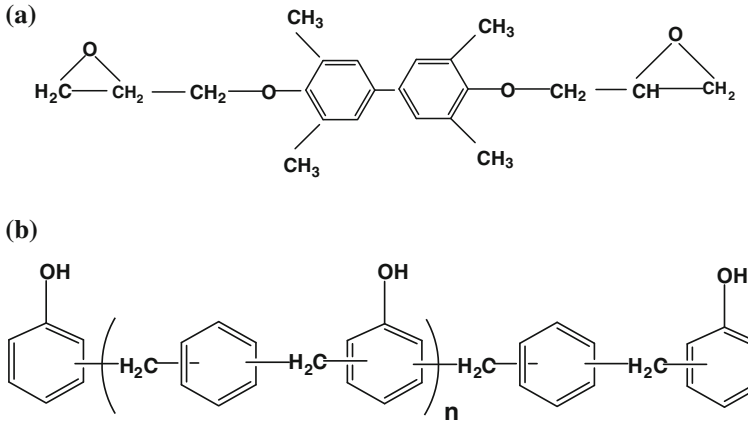

Scheme 4.1 The chemical structure of the **a** 4,4′-diglycidyloxy-3,3′,5,5′-tetramethyl biphenyl epoxy and **b** phenol-aralkyl resin

Scheme 4.2 The chemical structure of the **a** TPP and **b** TPP-BQ

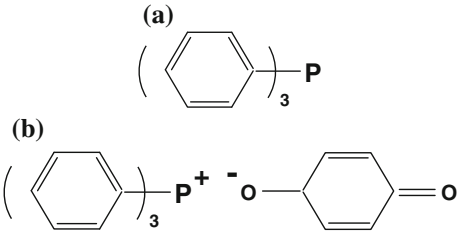

sample was cooled to 40 °C. After curing, the samples were scanned at 10 °C/min from 40 to 250 °C to measure residual heat from the reaction, ΔH_R (Jg^{-1}). The total heat of curing (ΔH_T) was calculated by summing the isothermal heat (ΔH_{Io}) and the residual heat (ΔH_R) from the reactions. The isothermal conversion at time t was defined as $\alpha_I(t) = \Delta H_I(t)/\Delta H_T$. The obtained T_g values were taken as the temperatures of the onset of glass transition (at which the specific heat changed) in the DSC thermograms.

4.2.3 Kinetic Analysis

PA general equation for the autocatalytic cure reactions of many epoxy systems is as follows [5–9]:

$$r = \frac{d\alpha}{dt} = (k_1 + k_2\alpha^m)(1-\alpha)^n \tag{4.1}$$

where α is the extent of conversion, r is the rate of the reaction, k_1 and k_2 are the apparent rate constants, and m and n are the kinetic exponents of the reactions. The cure reactions in most epoxy systems are autocatalytic.

4.3 Result and Discussion

After the EMCs with TPP and TPP-BQ catalysts were cured at isothermal temperatures of 130, 150, 165, 175 and 185 °C, the above models were used for kinetic analysis. Figures 4.1 plot the curing rate curves for EMCs catalyzed by TPP-BQ and TPP, respectively, at five isothermal temperatures. Figure 4.1 shows that the curves are distinctly autocatalytic with the maximum rates occurring 3.0, 1.9, 1.2, 1.0 and 0.8 min after the start of the reaction at isothermal reaction temperatures of 130, 150, 165, 175 and 185 °C, respectively. The result shown in these figures also demonstrate that the presence of TPP-BQ catalyst in the molding compounds does not affect a change in the autocatalytic nature. However, the reaction rate of the biphenyl type epoxy is clearly enhanced at high temperature and restrained at low temperature since the maximum rate increases with reaction temperature in the molding compounds. The epoxy reaction rate revealed a similar effect in the epoxy molding compounds with TPP catalyst. Figure 4.1 clearly shows that these rate curves are autocatalytic. The maximum rates were observed at 3.0, 2.2, 1.9, 1.8 and 1.7 min after the start of the reaction at isothermal reaction temperatures of 130, 150, 165, 175 and 185 °C, respectively.

The molding compound data were then analyzed using the proposed autocatalytic mechanism. The kinetic parameters were determined using the above procedures. For the kinetic constants k_1 and k_2, two activation energies, ΔE_1 and ΔE_2, could be obtained by plotting $\ln k_1$ and $\ln k_2$, respectively, versus 1/T. Figure 4.2 shows the plots for $\ln k_1$ and $\ln k_2$ versus 1/T, from which the activation energies were determined for the EMCs. The rate constants obtained after considerable iteration and graphic procedures. Reaction orders m and n approximated 0.5 and 1.4, respectively, and did not substantially vary among EMCs with different organophosphine accelerators. For the TPP-BQ-catalysis EMCs, the Ea_1 and Ea_2 values obtained in this study were 15.2 and 11.6 kJ mol^{-1}, respectively. In contrast, the Ea_1 and Ea_2 values obtained for the TPP-catalysis EMCs were 11.4 and 9.6 kJ mol^{-1}, respectively. As activation energy increased, the temperature sensitivity of the reaction increased. Restated, for a large activation energy, a temperature increase of only a few degrees significantly increased k, subsequently increasing the reaction rate. In comparison to TPP catalyst-cured EMCs, TPP-BQ catalyst-cured EMCs had higher activation energies. Further, since the difference in ΔEa_1 (3.8 kJ mol^{-1}) between TPP-BQ catalyst-cured EMCs and TPP catalyst-cured EMCs was larger than the difference in ΔEa_2 (2 kJ mol^{-1}) between TPP-BQ catalyst-cured EMCs and TPP catalyst-cured EMCs, the increased reaction rate might be associated with k_1.

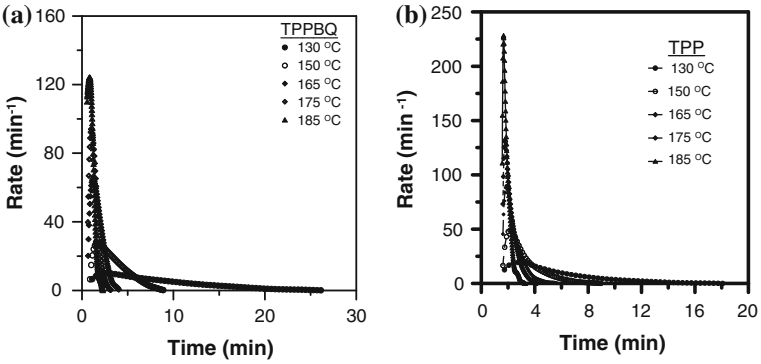

Fig. 4.1 Plots of the reaction rate versus time for accelerators-cured EMCs at isothermal temperatures: **a** TPP-BQ, **b** TPP

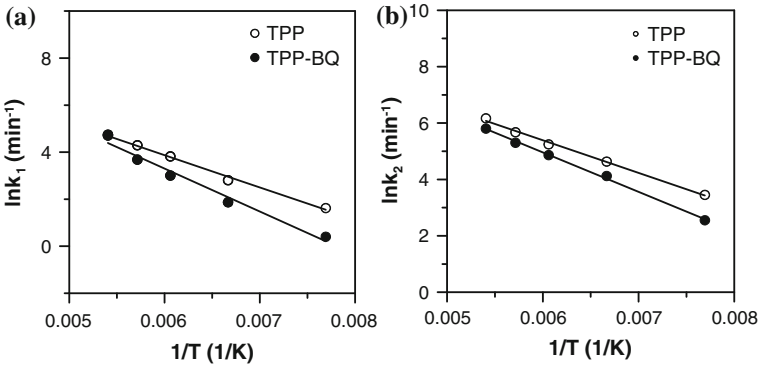

Fig. 4.2 Kinetic analysis for organophosphine accelerators-cured EMCs in an autocatalysed reaction: **a** Plots of lnk1 against 1/T, **b** Plots of lnk2 against 1/T, respectively

Since k_1 governs the early stage-autocatalytic reaction and since k_2 affects the reaction after the initial autocatalytic stage, the rate of increase at high temperatures in EMCs with TPP-BQ catalyst should be expected to accelerate in the initial stage of the reaction.

4.4 Conclusions

During molding, EMCs containing TPP-BQ are less active before molding temperature is reached. Furthermore, in TPP-BQ accelerator-cured biphenyl EMCs, the reaction of the EMC at high conversions remained high as the cure reaction progressed during the EMC transfer molding process. In microelectronic

packaging, the acceleration of the reaction of EMC containing thermal latency TPP-BQ accelerator correlates positively with temperature. This suggests that the TPP-BQ accelerator is an ideal thermal latency accelerator for curing EMCs.

References

1. Su, C. C., Wei, C. H., & Yang, C. C. (2013). Elucidating how advanced organophosphine accelerators affect molding compounds. *Industrial and Engineering Chemistry Research, 52*, 2525–2536.
2. Su, C. C., Wei, C. H., & Li, B. C. (2013). Thermal and cure kinetics of epoxy molding compounds cured with thermal latency accelerators. *Advances in Materials Science and Engineering*, 391267. doi:10.1155/2013/391267
3. Kinjo, N., Ogata, M., Nishi, K., & Kaneda, A. (1998). Epoxy molding compounds as encapsulation materials for microelectronic devices. *Advanced Polymer Science, 88*, 1–48.
4. Nakamura, Y., Yamaguchi, M., Tanaka, A., & Okubo, M. (1993). Thermal shock test of integrated circuit packages sealed with epoxy moulding compounds filled with spherical silica particles. *Polymer, 34*, 3220–3224.
5. Kim, W. G., & Ryu, J. H. (1997). Physical properties of epoxy molding compound for semiconductor encapsulation according to the coupling treatment process change of silica. *Journal of Applied Polymer Science, 65*, 1975–1982.
6. Su, C. C., & Woo, E. M. (1995). Cure kinetics and morphology of amine-curerd tetraglycidyl-4,4′-diaminodiphenylmethane epoxy blends with polyetherimide. *Polymer, 36*, 2883–2894.
7. Su, C. C., Huang, Y. P., & Woo, E. M. (2005). Curing kinetics and reaction-induced homogeneity in networks of poly(4-vinyl phenol) and diglycidylether epoxide cured with amine. *Polymer Engineering and Science, 45*, 1–10.
8. Su, C. C., & Woo, E. M. (1997). Diffusion controlled reaction mechanisms during cure in polymer/epoxy networks. *Journal of Polymer Science Part B: Polymer Physics, 35*, 2141–2150.
9. Cole, K. C., Hechler, J. J., & Noel, D. (1991). A new approach to modeling the cure kinetics of epoxy/amine thermosetting resins. 2. Application to a typical system based on bis[4-(diglycidylamino)phenyl]methane and bis(4-aminophenyl) sulfone. *Macromolecules, 24*, 3098–3110.

Chapter 5
Using an Android Smartphone for Robotic Image Recognition

Tsung-Kai Chao, Bing-Shiun Yang, Wing-Kwong Wong and Sheng-Kai Yin

Abstract In this study, an Android smartphone was used to control a robot of Lego NXT running leJOS by automatically tracking and pushing a ball forward. OpenCV was run on the smartphone for ball recognition. In addition, HCT (Hough Circle Transform) was used to recognize circular objects of particular colors in the environment. Furthermore, the smartphone controlled the robot with Bluetooth wireless communication.

Keywords Android · OpenCV · Hough circle transform · NXT · leJOS

5.1 Introduction

Smartphones are becoming hot consumer products in recent years [1]. In a study, a softcore JOP (Java optimized processor) was downloaded to a DE2-70 development board from Altera [2]. JOP is the embedded real-time system of JVM hardware implementation, whose performance depends on the planning of the CPU and the internal and external memories. Bluetooth was used as a wireless communication protocol in another study [3].

T.-K. Chao (✉)
Graduate School of Engineering Science and Technology, National Yunlin University of Science and Technology, Yunlin 64002, Taiwan, Republic of China
e-mail: g9810815@yuntech.edu.tw

B.-S. Yang · W.-K. Wong
Graduate School of Electronic and Optoelectronic Engineering, National Yunlin University of Science and Technology, Yunlin 64002, Taiwan, Republic of China

S.-K. Yin
Department of Digital Design, Mingdao University, Changhua 52345, Taiwan, Republic of China
e-mail: ysk@mdu.edu.tw

J. Juang et al. (eds.), *Proceedings of the 2nd International Conference on Intelligent Technologies and Engineering Systems (ICITES2013)*, Lecture Notes in Electrical Engineering 293,
DOI: 10.1007/978-3-319-04573-3_5,

In this study, a smartphone is used to detect a ball object and control the motion of a robot built with Lego Mindstorms NXT. The communication between the smartphone and the robot is done with Bluetooth with low power consumption and low cost. This study does image processing on a smartphone.

5.2 Image Processing With OpenCV in Android

Android, an operating system, was unveiled in 2007 [4]. Currently, Android takes the largest market share of operating systems for smartphones. Android SDK is a software development kit specially made for developers of application programs.

Google has published different versions of Android software development platform and adds or modifies APIs according to each version to provide developers with more functions by making full use of the system architecture and components.

Android NDK is a tool to work with Android SDK in compiling native application codes such as C/C ++ for Android applications to run on the Dalvik virtual machine [5]. With this method, native codes can be used repeatedly and the execution speed can be faster. Android NDK provides the native API compiler system and packages the native codes into APKs by integrating JNI with Android SDK.

JNI (java native interface) is an important function in Java programming for Android [6]. If an Android programmer wants to use other languages, such as C/C ++, to develop his app, he can call C/C ++ libraries from Java through JNI, allow native codes to be used in the application (Fig. 5.1).

Cygwin is a Linux-like environment in Windows [7]. In this study, the GNU development kit in Cygwin is used for cross compilation. The cross-platform function is based on a transfer layer for Linux system calls, which are mapped to those of Windows. Android NDK has to work in Cygwin for compilation (Fig. 5.2).

5.2.1 Hough Circle Transform and Color Transform in Android Application

OpenCV, short for Open Source Computer Vision Library, is a cross-platform computer vision library [8]. It is developed by Intel and distributed with the BSD license. Android applications need SurfaceView API to display images in the framework (Fig. 5.3).

The OpenCV Library has to be used by the application as a library with JNI. With the OpenCV Java-API, the native code is compiled and called through JNI by

```
JNIEXPORT void JNICALL Java_ClassName_MethodName
  (JNIEnv *env, jobject obj, jstring javaString)
{
    /*Get the native string from javaString*/
    const char *nativeString = (*env)->GetStringUTFChars(env, javaString, 0);

    /*Do something with the nativeString*/

    /*DON'T FORGET THIS LINE!!!*/
    (*env)->ReleaseStringUTFChars(env, javaString, nativeString);
}
```

Fig. 5.1 JNI programming [6]

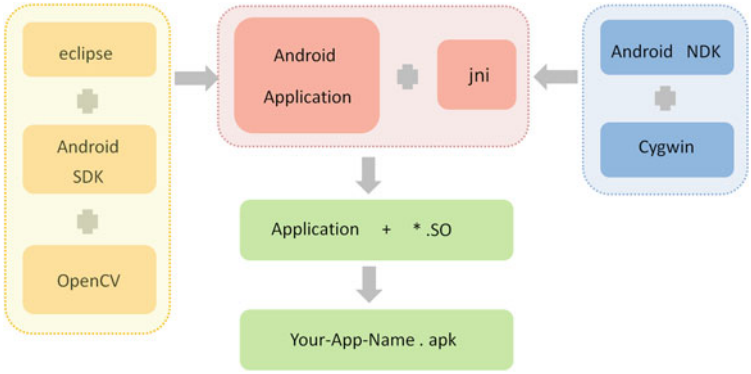

Fig. 5.2 Components of the application for image processing and robotic control

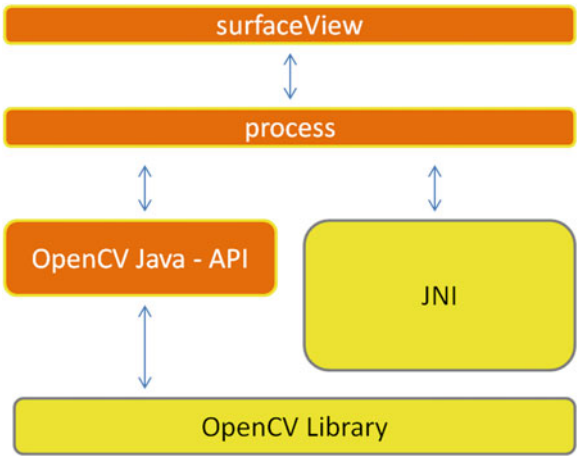

Fig. 5.3 OpenCV application

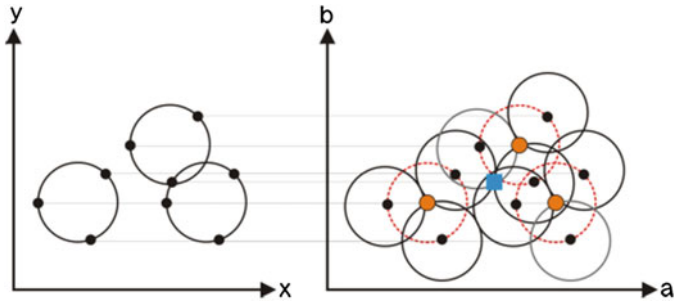

Fig. 5.4 Detecting multiple circles

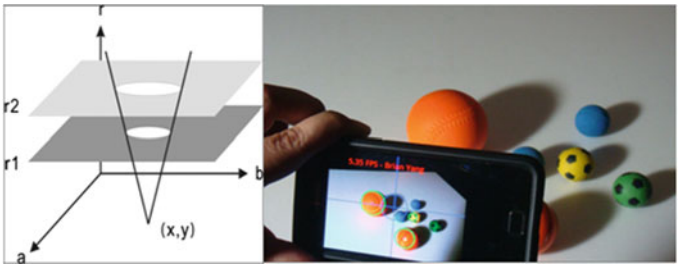

Fig. 5.5 Detecting circles of unknown radii

Java programs. Finally, the results of image processing are displayed on a SurfaceView on the screen of the smartphone.

HSV is the color attribute model used in this study. It indicates the relation between points in an RGB color model and describes a more accurate color relation than RGB but still keeps the calculation simple. A HSV model is usually used in computer graphic applications in which colors are applied to specific graphic elements in various application environments. Hough transform (HT) was patented by P. Hough [9] and was discussed by Duda and Hart [10].

Hough transform can be used to determine the parameters of a circle. Suppose the point (a, b) is the center of a circle in the x and y direction respectively and r is the radius. These parameters can be described with the parametric equations:

$$\begin{aligned} x &= a + r\cos(\theta) \\ y &= b + r\sin(\theta) \end{aligned} \tag{5.1}$$

In two-dimensional parameter space, the radius of each circle is known in the image. Every edge points (x, y) in the parameter space were painted on a circle of radius r centered at (a, b). The true center point will be common to all parametric circles, and can be found with a Hough accumulation array [11].

Multiple circles with the same radius can be found with the same technique. The center points are represented as red cells in a parameter space drawing.

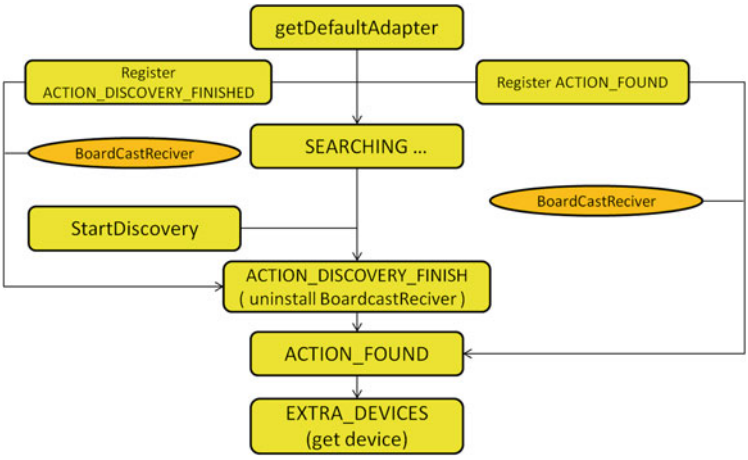

Fig. 5.6 Searching/pairing Bluetooth devices

Overlapping circles can cause spurious centers to be found. Spurious circles can be removed by matching to circles in the original image (Fig. 5.4).

If the radius is unknown, then the edge points in the parameter space will be painted on the surface of a cone. Each point (x, y) on the perimeter of a circle will produce a cone surface in the parameter space. The parameters (a, b, r) will correspond to a three dimensional accumulation matrix and the cone surfaces are the circles on the image (Fig. 5.5).

5.2.2 Bluetooth Application and Lego NXT in Android

Bluetooth technology was first created by Ericsson in its 1994 project [12]. The standard used by Bluetooth is IEEE-802.15.1. In addition, the Bluetooth protocol operates in the unlicensed ISM (Industrial Scientific Medical) band at 2.45 GHz. Android supports Bluetooth since the 2.0 version. Figure 5.6 explains how Bluetooth devices activate and search devices in an Android application, what types of BluetoothDevice should be used to search Bluetooth devices, and how to use the getRemoteDevice approach in BluetoothAdapter to obtain the address specified by BluetoothDevice. In the Bluetooth APIs of Android, BluetoothServerSocket and BluetoothSocket are necessary for a socket connection. A Bluetooth server registers a BluetoothServerSocket with a name and UUID through threads and monitors the requests from the client via BluetoothSocket.

Lego Mindstorms NXT is a robotic kit collectively developed by Lego and MIT, in which Arm7-TDMI-32-bit and LEGO bricks are combined to build robots [13]. leJOS NXJ is a JVM (Java Virtual Machine) which can be executed in Lego NXT-bricks [14]. In this study, a NXT brick with leJOS was used as the Bluetooth

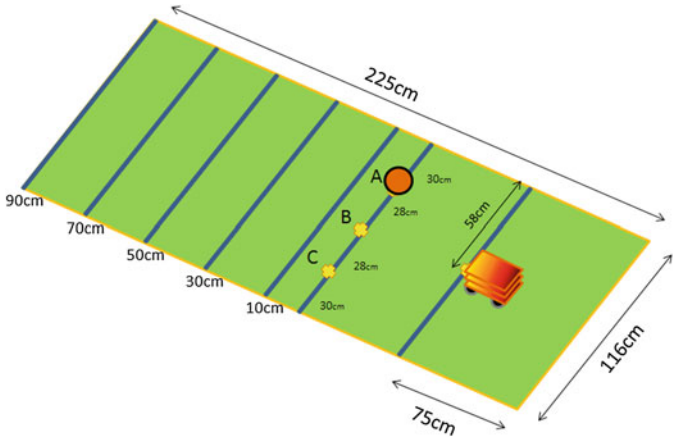

Fig. 5.7 Environment for the robot to push a ball forward

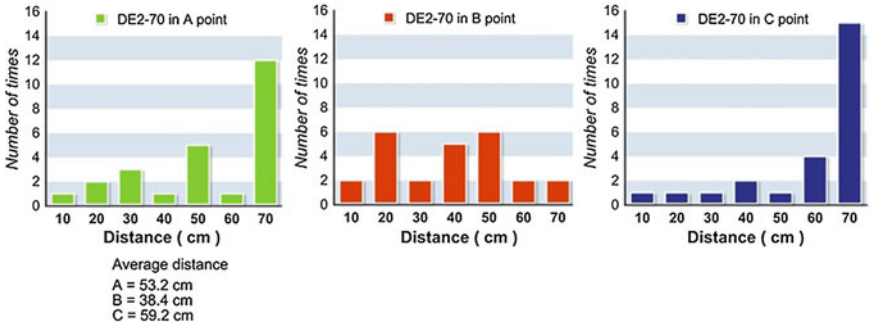

Fig. 5.8 DE2-70

client controlled by a smartphone as the Bluetooth server. Depending on the results of the image recognition, the smartphone sends control codes to the NXT brick, commanding it to go forward or backward, or turn left or right.

5.3 Experiment and Results

We designed an experiment to evaluate the performance of the robot. The environment was a 225 cm*116 cm field, as shown in Fig. 5.7. The robot started in the middle of the starting line. A ball was placed on Points A, B, or C, 60 cm in front of the robot. The robot's task was to find the ball and pushed it forward until the ball touched the wall or reached the end of the field. For each start point of A, B, or C, the experiment was repeated 25 times. The pushed distances were averaged for each start point. The smartphone used was Samsung-i9100.

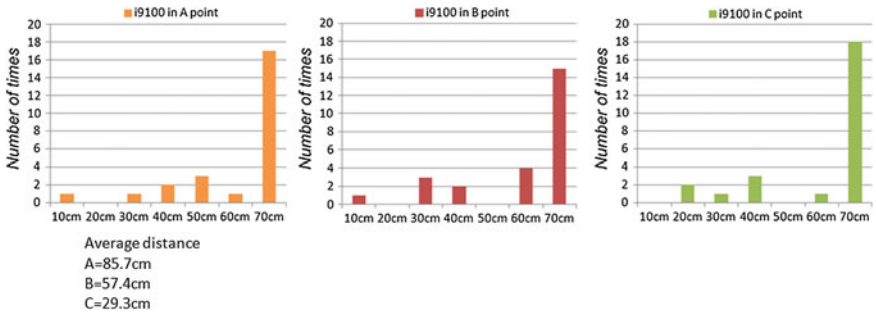

Fig. 5.9 Samsung-i9100

During an experiment, when the target ball was pushed by the robot, the ball sometimes moved sideward and fell out of the vision of the robot. In this case, or generally when the robot did not find any target in its vision, the robot moved backwarduntil an object was found. This strategy worked most of the time. After the experimental results were collected, they were compared with the data of DE2-70 in the analysis (Fig. 5.8).

5.3.1 Results of Experiment

The experimental data were plotted as a histogram in Fig. 5.9. A column refers to the number of times the ball was pushed for a certain distance in cm. These data were compared to those of a similar experiment reported by another study a year ago (Fig. 5.8). In the previous study, the robot was driven by a JVM soft core called JOP running on a FPGA platform DE2-70. By comparing the results, for start points A (on the right of the robot) and C (on the left), the Android-driven robot pushed the ball for a longer distance in general than the JOP-driven one. When the ball was placed straight ahead of the robot in start point B, the performances of both robots were similar.

5.4 Conclusion

A smartphone is capable of doing many amazing things. This study showed that a smartphone can capture the images of the environment and control a robot to respond to the environment. The robot in this study was a Lego Mindstorms NXT and the control commands from the smartphone were sent via a Bluetooth channel. The robot's task was to track a ball and pushed it forward. The image processing was done with an open-source library OpenCV from Intel. The robot performed

better than a robot driven by JOP ported on a DE2-70 FPGA platform. A limitation of the robot was that it did not know where the end field was. It just pushed the ball forward depending on its current direction. This weakness should be addressed in the future.

References

1. http://www.isuppli.com/mobile-and-wirelesscommunica-tions/marketwatch/pages/apple-and-google-clear-win-ners-with-dominant-three-quarters-s-hare-of-smartphone-market.aspx
2. Wong, W. K., Jai, Y. S., & Wei, J. C. (2011). Robotic applications with FPGA implementation of java virtual machine. *International Journal of Intelligent Technologies and Engineering Systems, 1*(1), 32–38.
3. Uichin, L., et al. (2010). P2P content distribution to mobile Bluetooth users. *IEEE Transactions on Vehicular Technology, 59*, 356–367.
4. http://developer.android.com/index.html
5. http://elinux.org/Android_Architecture
6. http://en.wikipedia.org/wiki/Java_Native_Interface
7. http://www.cygwin.com/
8. http://opencv.org/
9. Hough, P. V. C. (1962). Method and means for recognizing complex patterns. US Patent 3,069,654.
10. Duda, R. O., & Hart R. E. (1972). Use of the Hough transform to detect lines and curves in pictures. *CACM, 15*(1), 11–15.
11. Carlson C. F. (2005). *Lecture 10: Hough circle transform*. Rochester Institute of Technology: Lecture Notes, October 11, 2005.
12. http://zh.wikipedia.org/wiki/%E8%93%9D%E7%89%99
13. http://mindstorms.lego.com/en-us/Default.aspx
14. http://lejos.sourceforge.net/

Chapter 6
Comparison of Memristive Behaviors of $HfTiO_4$/Invar-Based Structures at Nanometer Scale

Jing-Jenn Lin, You-Lin Wu, Wei-Wen Wang and Cheng-Fu Yang

Abstract In this paper, we compare the IV behaviors of the memresistive devices with structures of $HfTiO_4$/ITO/Invar and SiO_2/$HfTiO_4$/SiO_2/Invar. The IV measurements are conducted at nanometer scale using a conductive atomic force microscopy (C-AFM). The Invar is used as a back contact during the IV measurement. After repeated set/reset bias scans, it is found that the device with structure of SiO_2/$HfTiO_4$/SiO_2/Invar presents better performance in memresistive characteristics. A minimum forming current of 10 nA is needed to startup the memresistive IV behavior. Both structures are unipolar memristor suggesting that the IV behaviors are strongly correlated with the joule heat induced by the ultra-high current density in the nonoscale measurements.

Keywords Memresistive · $HfTiO_4$ · Invar · Nonometer scale

6.1 Introduction

Leon Chua inferred the existence of a fourth basic circuit element memristor in 1971 [1]. Strakove presented a more complete theory until 2008 [2]. In recent years, the use of oxide material resistive random access memory (RRAM) began to

J.-J. Lin (✉) · W.-W. Wang
Department of Applied Materials and Optoelectronic Engineering, National Chi Nan University, Puli, Nantou, Taiwan, Republic of China
e-mail: cclin@ncnu.edu.tw

Y.-L. Wu
Department of Electrical Engineering, National Chi Nan University, Puli, Nantou, Taiwan, Republic of China

C.-F. Yang
Department of Chemical and Materials Engineering, National University of Kaohsiung, Kaohsiung, Taiwan, Republic of China

J. Juang et al. (eds.), *Proceedings of the 2nd International Conference on Intelligent Technologies and Engineering Systems (ICITES2013)*, Lecture Notes in Electrical Engineering 293,
DOI: 10.1007/978-3-319-04573-3_6,

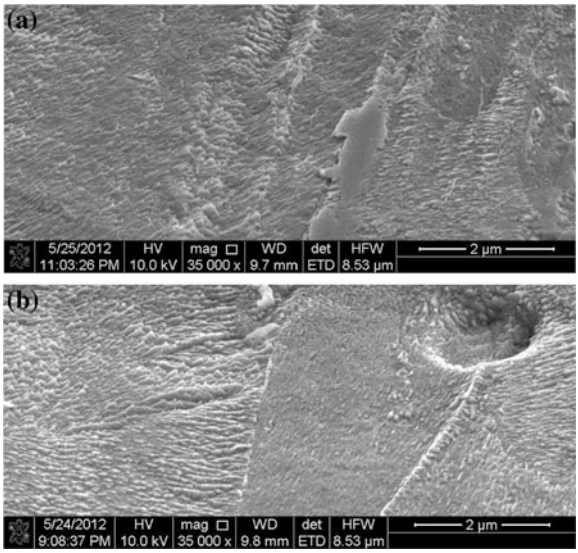

Fig. 6.1 SEM pictures of the sampling points on the Invar surface. The Invar surface exhibits roughness due to the foil-rolling process

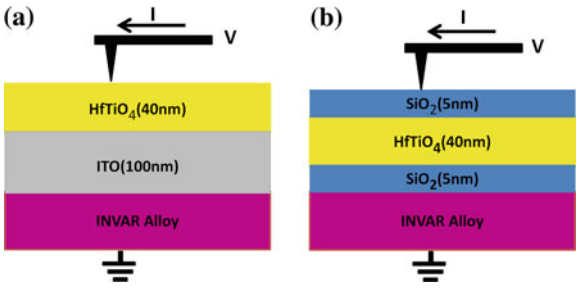

Fig. 6.2 Schematic diagrams of device and nanoscale IV measurement for **a** $HfTiO_4$/ITO/Invar and **b** SiO_2/$HfTiO_4$/SiO_2/Invar

be studied extensively. With its small size, simple structure, low power, high switching speed, and easy compatibility with CMOS devices, providing ultra-high density integrated production elements that make the RRAM has the potential to become the next generation of non-volatile memory device [3].

Invar (Fe–Ni alloy) has a near-zero thermal expansion coefficient, and has been widely used in applications requiring high dimensional stability despite variations in temperature [4]. In this work, we present two type structures of RRAM, using Invar as back contact. The use of Invar can reduce the effects induced by the thermal expansion of the bottom metal in the study of the memristor's temperature-dependent resistance value. C-AFM was used as tool for IV nanometer scale measurement because of the localized nature of the memristor.

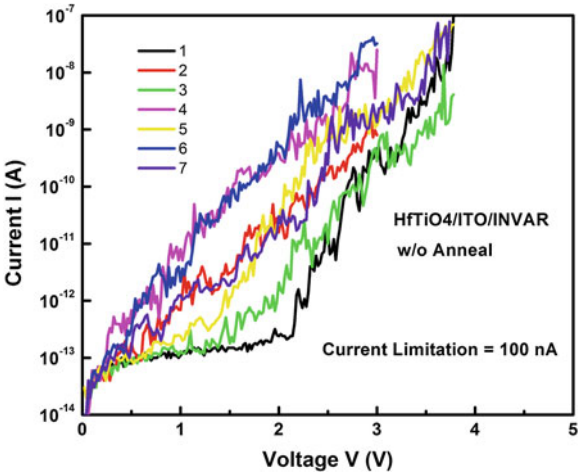

Fig. 6.3 Standard group of unipolar IV curves of the $HfTiO_4$/ITO/Invar memristor during several set/reset cycles. The current limit of the measurement system is set at 100 nA

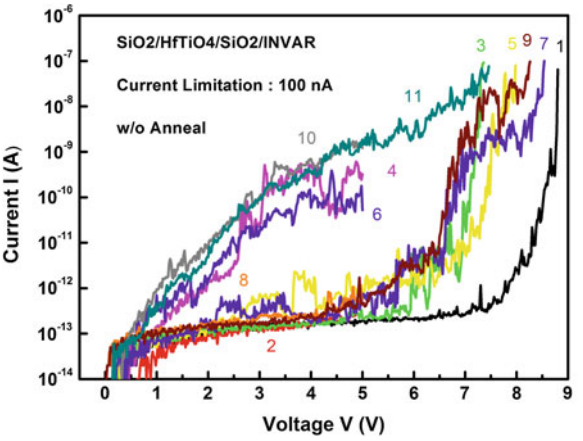

Fig. 6.4 Standard group of unipolar IV curves of the $SiO_2/HfTiO_4/SiO_2$/Invar memristor during several set/reset cycles. The current limit of the measurement system is set at 100 nA

6.2 Experiments

A cold-rolled NAS 36 Invar foil with a thickness of 40 μm is available from TOYO SEIHAKU Corp. Figure 6.1 shows the SEM pictures of the sampling points on the Invar surface. Because of the rolled imprint on the Invar surface, buffer layers of ITO or SiO_2 were sputtered on the Invar surface before the coating of memristor film material. The memristor film material of $HfTiO_4$ was fabricated by sputtering from a target of binary oxide alloy (HfO_2:TiO_2 = 1:1). Two type structures of $HfTiO_4$/ITO/Invar and $SiO_2/HfTiO_4/SiO_2$/Invar RRAMs were fabricated. The IV behaviors were characterized by C-AFM in conjunction of semiconductor analyzer of Agilent 4145B. The AFM tip can characterize the memristor's IV behavior in an extremely localized area of 3×10^{-12} cm^2. Figure 6.2 shows the structures and the nanoscale measurement schematic diagrams of the devices.

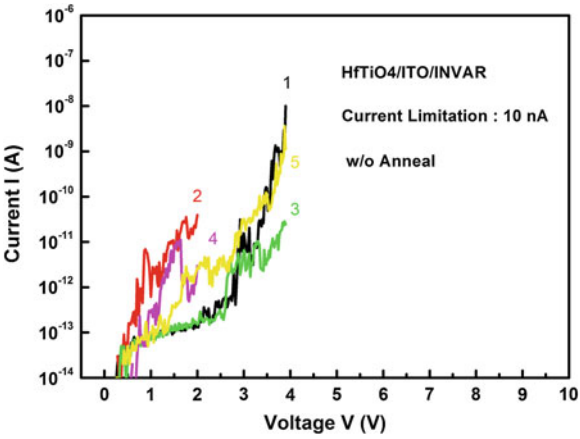

Fig. 6.5 Standard group of unipolar IV curves of the $HfTiO_4$/ITO/Invar memristor during several set/reset cycles. The current limit of the measurement system is set at 10 nA

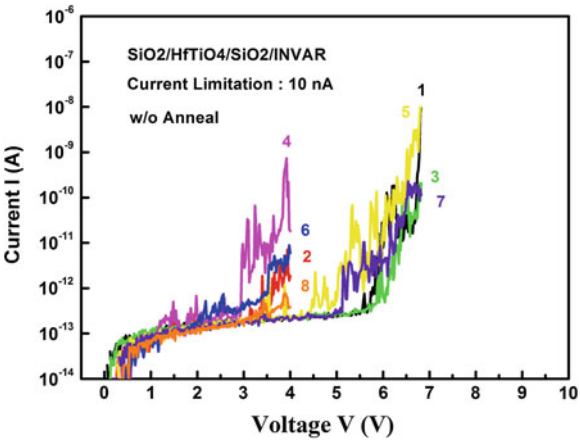

Fig. 6.6 Standard group of unipolar IV curves of the $SiO_2/HfTiO_4/SiO_2$/Invar memristor during several set/reset cycles. The current limit of the measurement system is set at 10 nA

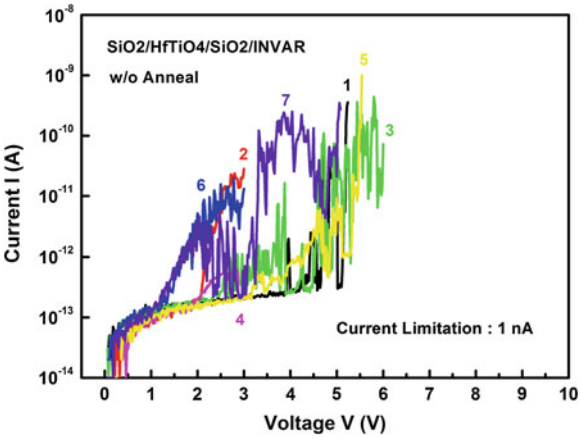

Fig. 6.7 Standard group of unipolar IV curves of the $SiO_2/HfTiO_4/SiO_2$/Invar memristor during several set/reset cycles. The current limit of the measurement system is set at 1 nA

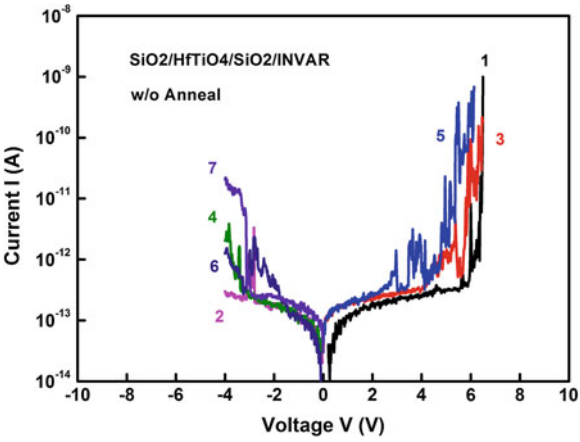

Fig. 6.8 Standard group of bipolar IV curves of the SiO_2/$HfTiO_4$/SiO_2/Invar memristors

6.3 Results and Discussion

Figures 6.3, 6.4, 6.5, 6.6 show the group of unipolar IV curves during several set/reset cycles for $HfTiO_4$/ITO/Invar and SiO_2/$HfTiO_4$/SiO_2/Invar structures under current limits of 100 and 10 nA. The $HfTiO_4$/ITO/Invar device shows unstable set/rest behaviors in the repeated unipolar scans. However, the SiO_2/$HfTiO_4$/SiO_2/Invar device shows more stable set/rest behaviors in the corresponding scans. Figure 6.7 shows the unipolar IV curves of SiO_2/$HfTiO_4$/SiO_2/Invar device with a current limit of 1 nA. The charges trap/detrap has affected the performance of memristor at such low current level. Figure 6.8 shows a standard group of bipolar IV curves of the memristors. No bipolar memristive behaviors are observed. The two structures exhibit the unipolar memristive characteristics in the set/reset bias scans. Due to the extremely small area of the C-AFM tip, the current density is very high at the current limitation value (10–100 nA). Violent Joule heating is expected to induce thermal decomposition of the film material, releasing possible oxygen ions (O^{2-}), which results in unipolar behaviors. The unipolar memristive behavior at the nanometer scale is consistent with the recently proposed theorem of the unified physical mechanism.

6.4 Conclusions

It was found that the memresistive device with structure of SiO_2/$HfTiO_4$/SiO_2/Invar exhibited a more stable unipolar memresistive IV behavior at nanometer scale than $HfTiO_4$/ITO/Invar. Because the C-AFM tip can produce an ultra-high current stress within an extremely localized area, it is believed that the nano-scaled IV evaluation providing a good way for the investigation of Joule-heating related mechanism of the RRAM.

Acknowledgments This work was financially supported by the National Science Council of Taiwan, ROC under contract no. NSC 100-2221-E-260-004-MY3.

References

1. Chua, L. O. (1971). Memristor—the missing circuit element. *IEEE Transactions on Circuit Theory, 18*, 507–519.
2. Strukov, D. B., et al. (2008). The missing memristor found. *Nature Letters, 453*, 80–83.
3. Sun, B., et al. (2009). Highly uniform resistive switching characteristics of TiN/ZrO_2/Pt memory devices. *Journal of Applied Physics, 105*, 061630.
4. Grimmett, D. L., Schwartz, M., & Nobe, K. (1988). Electrodeposition of iron-nickel (Invar) alloys. *Plating and Surface Finishing*, *75*.

Chapter 7
An Intelligent Traffic Regulator Scheme in Multimedia Networks

Ming-Chang Hsiao and Chien-Yuan Liu

Abstract This paper proposed an intelligent and regulative traffic method for solving congestion control problems in multimedia networks. The proposed scheme, which is capable of rate-based predictive control, consists of two subsystems: a long-term policy critic and a short-term rate-selector. Each controller in multimedia networks jointly learns the control policy by real-time interactions without prior knowledge of a network model. In addition, a reward evaluator provides reinforcement signals based on game theory to train controllers to adapt to fluctuant network environment. The well-trained controllers can take actions correctly to regulate source flow to simultaneously meet the requirements of high link utilization, low packet loss rate (PLR) and packet delay. Simulation results show that the proposed approach is effectively in controlling congestion of the multimedia traffic in internet networks.

Keywords Congestion control · Reinforcement signals

7.1 Introduction

Multimedia transmission services in computer networks can be roughly classified into time-sensitive and time-insensitive transmissions. The former is designed for real time applications, e.g., video and audio applications which require strict transmission delay and delay variation guarantees, but some packet losses are

M.-C. Hsiao
Department of Computer Science and Information Engineering, WuFeng University, Chiayi 62153, Taiwan, Republic of China

C.-Y. Liu (✉)
Department of Computer Science and Information Engineering, Cheng Shiu University, Kaohsiung 83347, Taiwan, Republic of China
e-mail: cyliu@csu.edu.tw

J. Juang et al. (eds.), *Proceedings of the 2nd International Conference on Intelligent Technologies and Engineering Systems (ICITES2013)*, Lecture Notes in Electrical Engineering 293,
DOI: 10.1007/978-3-319-04573-3_7,

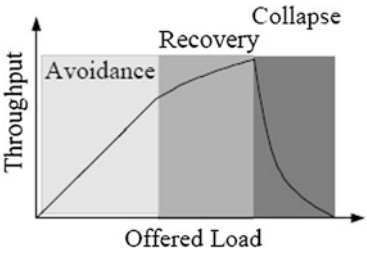

Fig. 7.1 Throughput versus offered load

tolerable. By contrast, the latter is used for non real-time applications, such as best effort services, which request strict packet loss guarantees, e.g., file transfer. To satisfy different services for guaranteeing the quality of services (QoS), computer networks must support a variety of services. However in most networks, there are circumstances in which the externally offered load is large than can be handled. Then, if no measures are taken to restrict the entrance of traffic into the network, the link will be congested. Congestion results from mismatch between network resources available for these connections and traffic capacities admitted for transmission. As a result, as the offered load increases, the actual network throughput decrease and packet loss increase enormously. Therefore, a high-speed network must have an appropriate and regulative traffic scheme not only to guarantee QoS for existing links but also to achieve high system utilization.

Moreover, packet losses in congestion control are inevitable owing to uncertainties and highly time-varying traffic patterns in best effort service model [1] or in conventional end-to-end rate control scheme which uses additive-increase, multiplicative decrease (AIMD) [2]. Congestion problems can cause high packet loss rate (PLR) and long delays, and can even break down the entire system because of congestion collapse as shown in Fig. 7.1. In other word, when the offered load exceeds the network capacity, any increase in the load leads to a decrease in the useful work done by the network. The main task of the traffic regulator methods is to utilize the buffers of the controlled load service as optimally as possible [3]. The data rates of controlled data flows should be kept as high as possible without danger of packet losses the controlled data flows [4].

7.2 System Model

The proposed system model with traffic regulator which we so called reinforcement learning congestion controller (RLCC) as shown in Fig. 7.2. There are several multi-medias sources sending packets to the multiplexer at various rates for some certain duration. The RLCC senses the buffer's states of the multiplexer and makes a decision on which rate should be adopted by sources, and then the control signals made by the congestion controller are fed back to the traffic sources to regulate the sources traffic in order to reduce CLR and increase the utilization of multiplexer's output bandwidth.

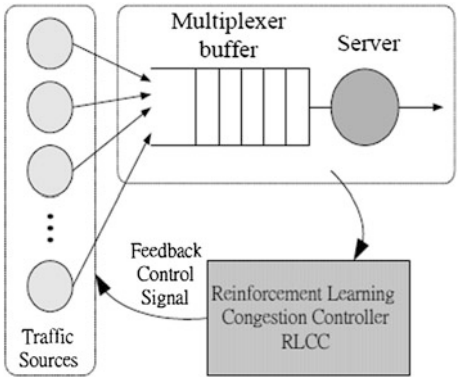

Fig. 7.2 The framework of RLCC

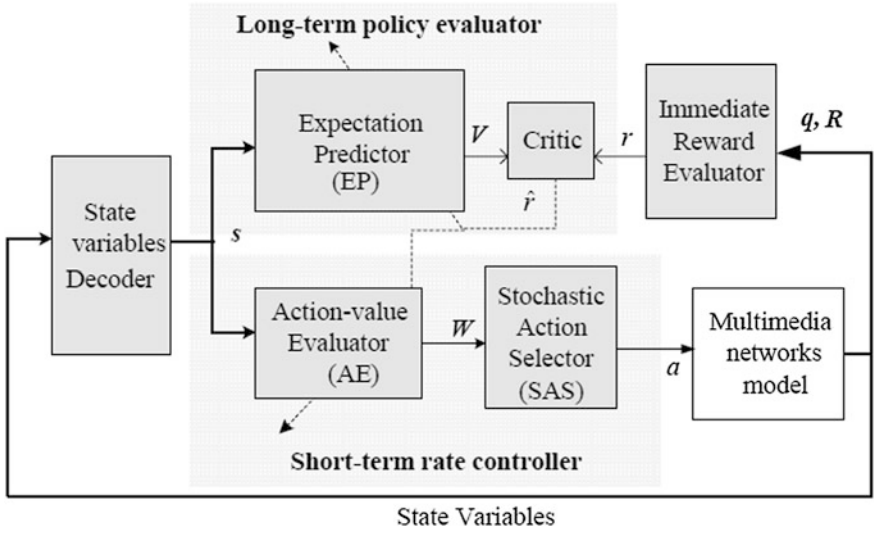

Fig. 7.3 The schematic structure of RLCC

7.2.1 System Implementation

The RLCC consists of two subsystems: the Evaluation-return Predictor (EP), a long-term policy selector and the Action-value Evaluator (AE), which takes charge of making the short-term decision [3]. The RLCC, as shown in Fig. 7.3, persistently receives the state inputs and a scalar signal called the external reinforcement signal from the environment and then accordingly performs a congestion avoidance action to affect the environment. The EP network, by means of the external reinforcement signal, predicts a heuristic reinforcement signal to the AE network,

Table 7.1 The variables of RLCC

q	Queue length in switches
R	Explicit sending rate of sources
s	State vector of the system
V	Output of EP network (the utility index of the state vector s)
V'	Expected utility index of the state vector $s(t)$
W	Output of AE network
a	Feedback control signals generated by SAS network
r	Reinforcement scalar signal provided by Immediate Reward Evaluator
$\hat{r}$	Heuristic reinforcement signal

which not only receives the heuristic reinforcement signal but also receives the external reinforcement signal to criticize the control signal action selected by Stochastic Action Selector (SAS).

The long-term policy selector model the action trend by the predicting a long-term utility index and the short-term decision maker determines which action should be taken by a short-term utility index. Comparatively, the conventional reinforcement learning structure merely learns to maximize immediate reinforcement signal, instead of the long-term utility, such that the optimal performance is not guaranteed [5]. Instead, the proposed RLCC take into account both the short-term reinforcement signal and signal. As well, it uses the long-term utility for training to stabilize the controller. The specification of the variables is depicted in Table 7.1.

7.2.2 Theoretical Framework

Topologically, RLCC consists of two neural networks. The state vector $\boldsymbol{s}$ is only composed of the state vector $\boldsymbol{q}$ and $\boldsymbol{R}$. The EP and the AE networks receive the state vector to produce an optimal control signal a in response to the status of high-speed multimedia networks. In practice, TD methods learn their estimates in part on the basis of other estimates, that is, they learn a guess from previous experience. Since the process generates reinforcement signal r_t at each transition from state s_t to state s_{t+1}, we may want V_t, which is the output of EP at state s_t, to predict the associative discounted cumulative reinforcement cost (or long-term utility index), $Q_t = \sum_{k=0}^{\infty} \gamma^k r_{t+k}$, where γ is the discounted factor, $0 \leq \gamma \leq 1$. If the prediction of V_t should equal Q_t, *i.e.*, the predictions are accurate, then

$$V_t = \sum_{k=0}^{\infty} \gamma^k r_{t+k+1} = r_{t+1} + \gamma \sum_{k=0}^{\infty} \gamma^k r_{t+k+2} = r_{t+1} + \gamma V_{t+1}. \tag{7.1}$$

Based on the above equations, TD error can be defined as the difference between the two sides of this equation, i.e., $(V' - V)$. For better results, we combined TD methods with eligibility trace to obtain a more general method that

may learn more efficiently. An eligibility trace is a temporary record of the occurrence of an event. The trace marks the memory parameters associated with the event as eligible states or actions are assigned credit or blame for the error. The learning rules are written as

$$w_{t+1}(s,a) = w_t(s,a) + \eta\,\hat{r}_t e_t(s,a), \text{ for all } s,\ a, \tag{7.2}$$

$$\hat{r}_t = r_{t+1} + \gamma V_t(s_{t+1}, a_{t+1}) - V_t(s_t, a_t) \tag{7.3}$$

$$e_t(s,a) = \gamma\lambda e_{t-1} + \nabla_{w_t} V_t(s_t, a_t), \tag{7.4}$$

where η is the learning rate; the r_t is a reinforcement signal; the $\hat{r}$ is the TD error; γ is the discount rate and λ is the trace-decay parameter. In the learning process, we define $r = 0$ for award, and $r = -1$ for penalty.

Because reinforcement signals in our system can merely provide some hints as to what right actions should be, consequently no gradient information is available. Whereas, the AE element maintains a separate estimated action-value for each state-action pair (s, a), in order to balance exploration and exploitation in reinforcement learning, the SAS element adopts a Softmax action selection method to choose an action a_i on the tth play for a state s with probability, such as

$$\pi_t = \text{Prob}(a_i) = \frac{\exp(W_t(\text{s},a_i)/T)}{\sum_{b=1}^{n}\exp(W_t(\text{s},b)/T)}, \tag{7.5}$$

where T is a temperature parameter for an annealing process. The action probabilities are varied as a graded function of estimated value. For alleviating the dilemma between exploration and exploitation, the probability of all actions for a specific state behave as a roulette wheel, and a random number generated by uniform distribution is employed as a seed to select a suitable action according to the probability of each action.

7.2.3 Simulations and Comparisons

The input traffic is categorized into two types: real-time (type-I) and non-real-time (type-II) traffic. Video and voice services are of type-I traffic, while data services are of type-II traffic. For voice sources interrupted Bernoulli process (IBP) are used to model its behavior, with the probability for on, $p_{ON} = \lambda_1$ and the probability for off, $p_{OFF} = \lambda_2$. During the ON period the source sends packets to the multiplexer with a constant rate. For video sources a first order autoregressive Markov process $X(k)$ are used to model the sending rate during nth frame. $X(k)$ is defined with:

$$X(k) = mX(k-1) + nG(k), \tag{7.6}$$

where m and n are constants, and $G(k)$ is a sequence of independent Gaussian random variables.

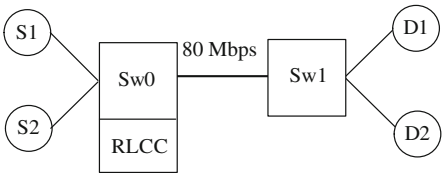

Fig. 7.4 A high-speed multimedia network model with two switches

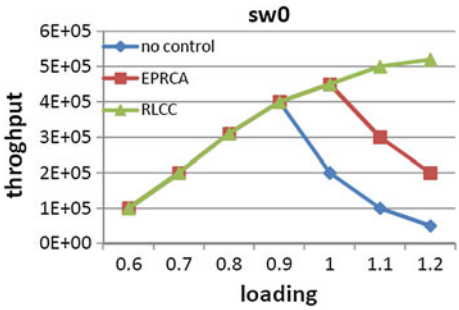

Fig. 7.5 Throughput comparisons

To ensure the performance of RLCC superior to that of best-effort control and the EPRCA method, four measures, throughput, CLR, buffer utilization, and probability mass function (PMF) of sending rate, are used as performance indexes. The status of the input multiplexer buffer reflects the degree of congestion resulting in CLR, and the level of the sending rate of the input sources reflects the quality of the voice/video traffic. Figure 7.4 shows the configuration of one node controller in which two nodes Sw0 and Sw1 are cascaded. In addition, Two sources, S1 and S2, are connected to Sw0, and two destinations, D1 and D2, are connected to Sw1.

Figure 7.5 shows the throughput behavior of three different kinds of control methods. The throughput, which is the amount of received packet at the destination, depends on the fact that the network would cause heavy retransmitted traffic when CLR is over predefined QoS. It is obvious that the throughput of best-effort control and the EPRCA method degrade sharply about at loading of 0.6 and 0.9, respectively. On the contrary, the RLCC still remains a high throughput and meets QoS requirements with low CLR even when the loading is over 1.0. This is because that RLCC possesses the ability to predict the system behavior and to learn a better policy in advance. Furthermore Fig. 7.6 shows the CLR of different control methods. It is no doubt that without the controller CLR is high. Even though adopting EPRCA, CLR is still high. However, using RLCC can decrease CLR enormously. Therefore, the system performance is substantially promoted because of the reduction of packet retransmission. Figure 7.7a, b and c show the PMF of buffer utilization for different methods under various loading. Noticeably, buffer utilization of different methods performs no discrepancy under lower loading. In contrast, as the traffic loading is increasing, the results are totally different. Obviously, most of the buffer utilization of RLCC is lower than that of best-effort control and the EPRCA method, it means that the long queue length in

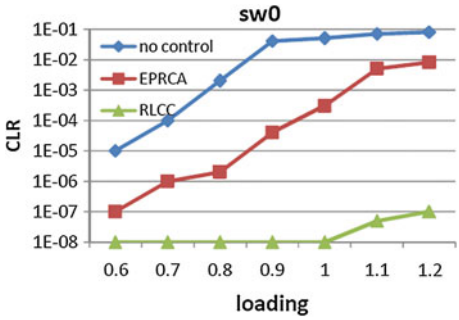

Fig. 7.6 CLR comparisons

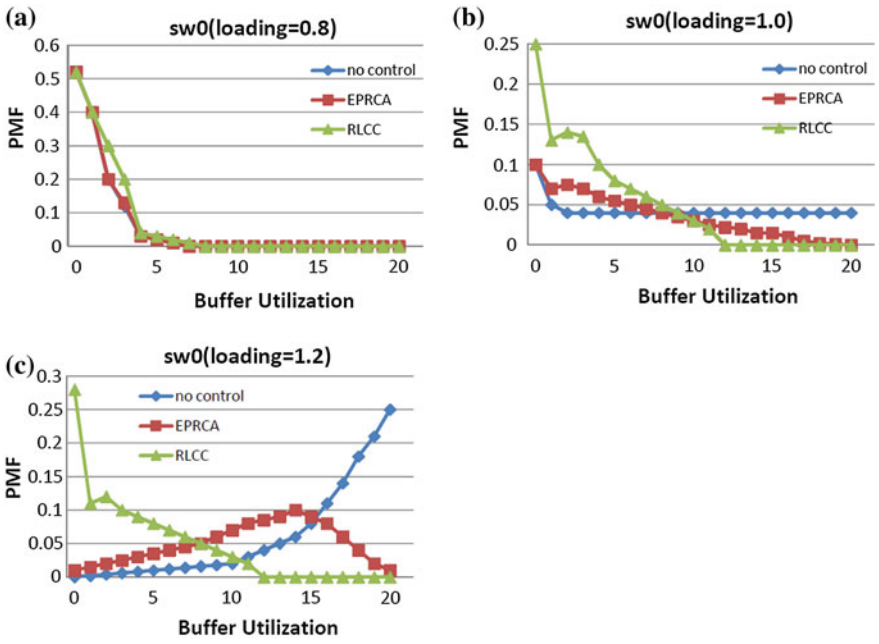

Fig. 7.7 **a** Buffer Utilization at loading 0.8. **b** Buffer Utilization at loading 1.0. **c** Buffer Utilization at loading 1.2

the switch buffer sometimes may lead to unacceptable end-to-end delay and cause high CLR. Figure 7.8 shows the PMF of the distribution of feedback control signal for different methods under various loading. Most of the time RLCC are operating at a speed of the maximal sending rate to transmit packets form sources to various destinations, and only a small amount of low rates are used to accommodate traffic to avoid cell loss, so that the throughput is definitely high. On the other hand, when

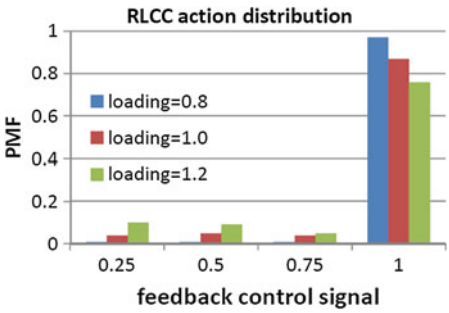

Fig. 7.8 PMF of feedback control signal

the traffic becomes heavier, a more conservative policy is preferred, and the percentage of higher rate action is decreased, whereas that of the lower rate is increased for the purpose of avoiding congestion.

7.3 Conclusions

The performances of best-effort control, EPRCA control, and proposed RLCC approaches to congestion control have been compared. In RLCC, the couple action-value prediction methods and TD with eligibility traces technique was used for policy improvement and action selection. By a proper training process and according to the reward function, TD methods are used to learn empirical without prior information on the environmental dynamics. The RLCC controller maintains an expectation of reward and takes the best action to control source flow. Simulation results have shown that the proposed method can increase the utilization of available bandwidth and decrease packet losses simultaneously. Therefore, RLCC not only guarantees QoS for existing links but also achieves high system utilization with fairness.

Acknowledgments The authors greatly appreciate to the support of the National Science Council, R.O.C., under the Grant no. NSC 101-2632-E-230-001-NY3.

References

1. Gevros, P., Crowcoft, J., Kirstein, P., & Bhatti, S. (2005) Congestion control mechanisms and the best effort service model. *IEEE Network, 15,* 16–26.
2. Chiu, D., & Jain, R. (1989) Analysis of the increase and decrease algorithm for congestion avoidance in computer networks. *Computer Networks and ISDN Systems, 17*, 1–14.
3. Lee, S. J., & Hou, C. L. (2009). A neural-fuzzy system for congestion control in ATM networks. *IEEE Transactions on System, Man and Cybernetics, 30*, 2–9.

4. Cheng, R.-G., Chang, C.-J., & Lin, L.-F. (1999). A QoS-provisioning neural fuzzy connection admission controller for multimedia high-speed networks. *IEEE/ACM Transactions on Networking, 7*, 111–121.
5. Rajkumar, Nigam, M. J., Sharma, S., & Bhavsar, P. (2012). Temporal difference based tuning of fuzzy logic controller through reinforcement learning to control an inverted pendulum. *I.J. Intelligent Systems and Applications, 9*, 15–21.

Chapter 8
CORDIC Algorithm for FPGA Implementation

Sun-Ting Lin, Tzu-Hao Wang, Shou-Sheu Lin and Yan-Bang Li

Abstract For traditional hyperbolic and trigonometric functions calculation algorithms, multiplier and a lookup table are needed to achieve calculation of multiple transcendental functions, which will lead to hardware circuit complexity and lower operation speed. Aim at overcoming the disadvantages of traditional algorithm, a CORDIC algorithm is proposed and implemented by FPGA program. Two types of realization circuits for CORDIC algorithm are implemented into the FPGA and their performances are compared. One is the flatten pipeline and the other is the folded one, while the first performs higher throughput and the last saves more chip area.

Keywords CORDIC · Flatten pipeline · Folded · FPGA

8.1 Introduction

The coordinate rotation digital computer (CORDIC), presented by the J. D. Volder in 1959, is a simple and efficient algorithm to calculate hyperbolic and trigonometric functions [1]. Trigonometric functions such as sine and cosine are fundamental arithmetic operations and widely applied in the field of image processing, communications, and acoustics technology, etc. [2]. When a hardware multiplier is available (e.g., in a DSP microprocessor), table-lookup methods and power series are generally faster than CORDIC algorithm. Although the trigonometric functions

S.-T. Lin (✉) · T.-H. Wang
Department of Electronic Engineering, National Kaohsiung Normal University, Yanchao 824, Kaohsiung, Taiwan, Republic of China
e-mail: stl@nknu.edu.tw

S.-S. Lin · Y.-B. Li
Department of Computer and Communication Engineering,
National Kaohsiung First University of Science and Technology,
Nanzih 811, Kaohsiung, Taiwan, Republic of China

J. Juang et al. (eds.), *Proceedings of the 2nd International Conference on Intelligent Technologies and Engineering Systems (ICITES2013)*, Lecture Notes in Electrical Engineering 293,
DOI: 10.1007/978-3-319-04573-3_8,

can also be implemented by the Taylor series to expand it into a polynomial, it is not suitable for the realization of the hardware design due to the requirement of many multiplications.

The basic idea of the CORDIC algorithm is through a series of the continued deflection angle, fixed and associated with base number of calculate, to approximate the required rotation. Because of its basic operation unit being only shift, add and subtract, which laid a good foundation for the CORDIC algorithm combines with the rapid development of FPGA technology. A significant reduction in FPGA resources makes these algorithms easier to be achieved in hardware, and thus meet the requirements of designer [4, 5].

The rest of this paper is constructed as follows. Section 8.2 shows the system model of the CORDIC algorithm. To show the differences between two types of the circuit structures for the CORDIC algorithm, the function block diagrams and performance in speed and are presented in Sect. 8.3. Section 8.4 concludes this paper.

8.2 CORDIC Algorithm

The basic principle of the CORDIC algorithm is shown in Fig. 8.1. The main idea of the CORDIC algorithm is to realize vector rotation iteratively by calculating the value of some special degrees. The vector converges to the required objective.

It can be seen that if the vector (x_0, y_0) rotates angle θ in counterclockwise direction, a new vector (x_1, y_1) can be got as shown in (8.1).

$$\begin{cases} x_1 = x_0 \cos\theta - y_0 \sin\theta \\ y_1 = y_0 \cos\theta + x_0 \sin\theta \end{cases} \tag{8.1}$$

And Eq. (8.1) can be rearranged as (8.2)

$$\begin{cases} x_1 = \cos\theta(x_0 - y_0 \tan\theta) \\ y_1 = \cos\theta(y_0 + x_0 \tan\theta) \end{cases} \tag{8.2}$$

For easy hardware implementation, we set the nth times of rotation and the rotation angle of every time is α_i and α_i equals to $\tan^{-1}(2^{-i})$. Then, the CORDIC algorithm can be represented as:

$$\alpha_i, 90^\circ \leqq \alpha_i < 90^\circ,$$
$$\alpha_i = \tan^{-1}\left(2^{-i}\right),$$
$$\alpha_0 > \alpha_1 > \ldots > \alpha_{k-1} > \ldots \to 0$$
$$\beta = \sum_{i=0}^{\infty} \delta_i \alpha_i, 0^\circ \leq \theta < 90^\circ, \text{ for } i = 0, 1, 2, \ldots \delta_i = 1 \text{ or } -1$$

Table 8.1 shows the value of α_i corresponding to the value i. From the above table, the calculated value can be obtained by adding or subtracting the above α_i

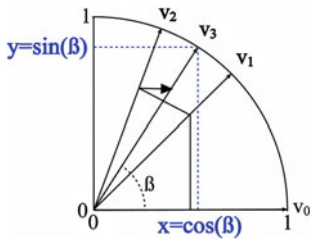

Fig. 8.1 An illustration of the CORDIC algorithm in progress

Table 8.1 The values of θ with correspond to i

i	0	1	2	3	4	5	6	7	8
α_i	45	26.6	14	7.1	3.6	1.8	0.9	0.4	0.2

according to the summation of previous δ_i α_i is smaller or larger than the target value β. For all β, $0° \leqq \beta < 90°$, the sign bit δ_0 of the first item α_0 is set to 1. If the sum of previous $(i - 1)$ item is larger than the target value, the next sign bit δ_i is negative. On the other hand, sign bit δ_i is positive. Generally after 16 times of iterations, i.e., i is equal to 16, the error can be converged to less than $\tan^{-1}(2^{-16}) = 1.53 \times 10^{-5}$. For example, if the input target degree is 30, which is smaller than 45, the δ_1 is set to minus one. The second step to the target value is 45 minus 26.6, which equals to 18.4. The third step to the target value is 18.4 plus 14, which equals to 32.4. The final summation will be closed to the target value if enough iterations of the previous processes are operated.

8.3 FPGA Implementation of CORDIC Algorithm

In this paper, the CORDIC algorithm are realized by using two different architectures, i.e., flatten and the folded, respectively. Both of these two architectures can be implemented into the Altera DE2-70 FPGA platform. The VHDL language are used to realize the above two designs and also used to complete the fixed-point simulation. After the RTL-level coding to complete the circuit describing by VHDL language, Quartus II is used to compile and program the design to the FPGA platform. The structure diagrams of both flatten and folded designs are shown in Fig. 8.2. In addition, the performance comparisons in area and speed of these two designs are listed in Table 8.2.

From the previous analysis of the CORDIC algorithm, after 16 times of iterations, the error can be converged to less than $\tan^{-1}(2^{-16}) = 1.53 \times 10^{-5}$. Therefore, the rotate unit stage should be repeated 16 times to control the final error rate less than 10^{-5}, as shown in Fig. 8.2a. To achieve more accurate results from the CORDIC algorithm, the more rotate unit stages are required. The

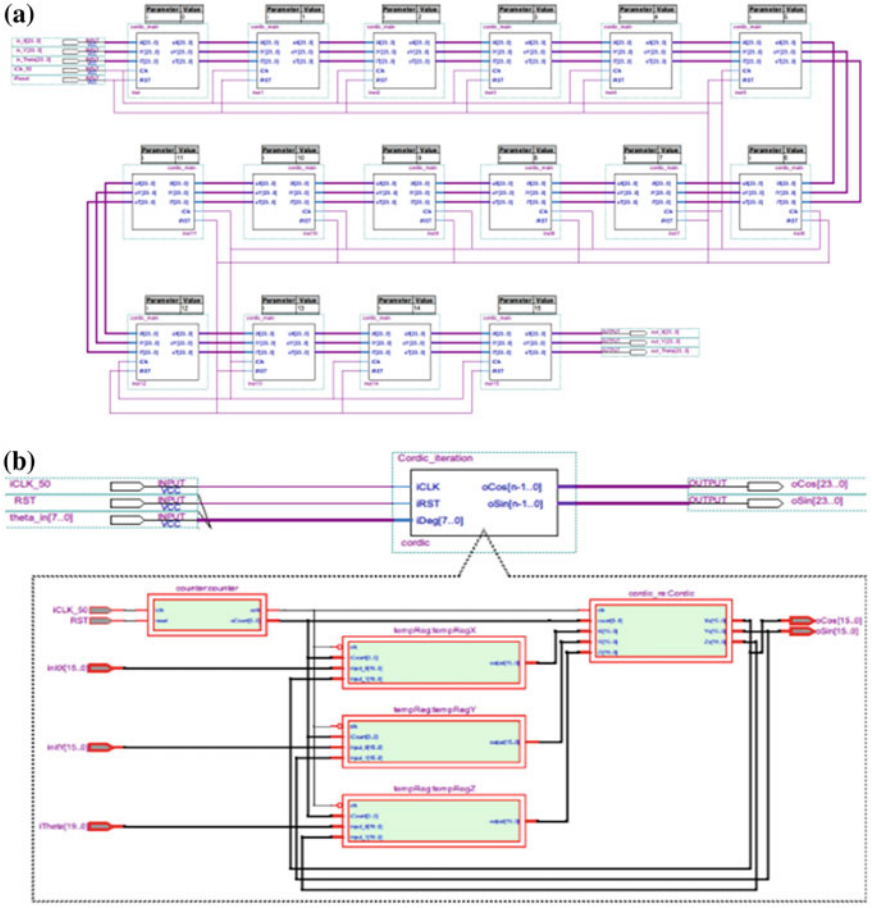

Fig. 8.2 **a** Flatten and **b** folded architecture of the CORDIC algorithm

Table 8.2 Area comparison for two types of CORDIC algorithm implementation

Item	Flatten	Folded	Ratio (%)
Total logic elements	1,848	357	19.3
Logic register	1,152	127	11.0
Total pins	144	58	40.2

architecture of the flatten pipeline CORDIC algorithm realization consume large number of logic elements and registers as shown in Table 8.2. To save the hardware circuit, another CORDIC algorithm implementation architecture called folded structured are shown in Fig. 8.2b. It use only one rotate unit hardware and the results are feedback into the rotate stage N times, where N is the total rotation number. From the measured results, to meet 10^{-7} accuracy requirement, the

Table 8.3 Speed comparison for two types of CORDIC algorithm implementation

Item	Flatten	Folded
Max. freq. (MHz)	215.75	138.64
Clock period (ns)	4.635	7.213

Table 8.4 Results from the CORDIC algorithm and its corresponding theoretical values

	CORDIC algorithm (Theoretical value)		
	sin	cos	Error (%)
0°	0.0 (0.0)	1.0 (1.0)	–
30°	0.50001 (0.5)	0.86602 (0.86603)	0.00002
45°	0.70712 (0.70711)	0.70710 (0.70711)	0.00001

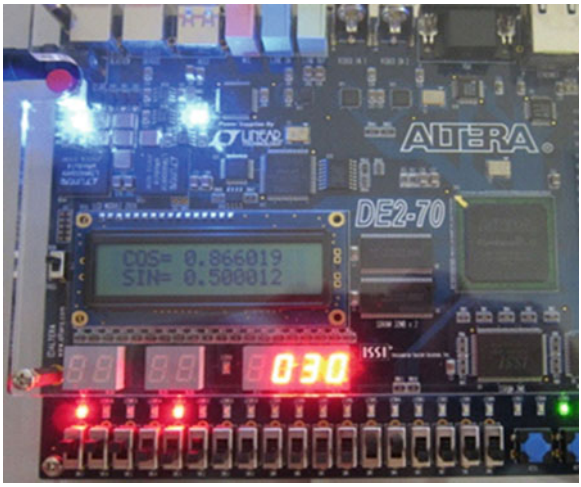

Fig. 8.3 CORDIC algorithm implementation in DEII-70 platform

maximum clock for flatten and folded architectures can reach 215.7 and 138.6 MHz, respectively. While folded structure consumes only 19.3 % of total logic elements of the flatten one.

Although the flatten architecture requires more hardware resources, its speed is higher than the folded one as shown in Table 8.3. The results obtained from the CORDIC algorithm and its corresponding theoretical values are listed in Table 8.4. The CORDIC algorithm can be implemented in DE2-70 platform and the results are shown in the LCD panel, as shown in Fig. 8.3.

8.4 Conclusions

In this paper, the fixed-point CORDIC algorithm is realized into FPGA board. In addition, both the flatten and folded architecture of CORDIC algorithm are also implemented into the FPGA board and their performance are compared. The

correctness of the CORDIC algorithm implemented by the VHDL code are verified by comparing the calculated results to the theoretical values. The accuracy of the method can be close to 10^{-6}. The CORDIC algorithm can give full play to the advantages of hardware. It provides an alternative choice to calculate the trigonometric functions without using complicated multiplier circuits. Therefore, the CORDIC algorithm is suitful for FPGA or ASIC designs.

References

1. Hu, Y. H. (2002). CORDIC-based VLSI architecture for digital signal processing. *IEEE Signal Processing Magazine, 7*, 17–35.
2. Yan, L. (2002). CORDIC algorithm application in the DSP algorithm hardware implement. *Modern Electronic Technology, 6*, 85–89.
3. Volder, J. E. (1959). The CORDIC trigonometric computing technique. *IRE Transactions on Electronic Computers, EC-8*, 330–334.
4. Chakraborty, M. (2011) Multiplier less realization of adaptive filters—A CORDIC based approach. Summer short course, CCM, NKFUST, Jul 2011.
5. Hu, Y. H. (1992). CORDIC-based VLSI architectures for digital signal processing. *IEEE Signal Processing Magazine, 9*(3), 16–35.
6. Meher, P. K., Valls, J., Juang, T., Sridharan, K., & Maharatna, K. (2009). 50 years of CORDIC: Algorithms, architectures, and applications. *IEEE Transactions on Circuits and Systems I, 56*(9), 1893–1906.
7. Andraka, R. (1998) A survey of CORDIC algorithms for FPGA based computers. In *Proceedings of the 6th ACM/SIGDA International Symposium on Field Programmable Gate Arrays (FPGA'98)* (pp. 191–200), Feb 1998.

Chapter 9
Compact Bow-Tie Antenna for WLAN Applications

Chun-Cheng Lin and Chih-Yu Huang

Abstract In this study, a dual-band bow-tie antenna with a self-complementary radiating element, a horn-shaped metallic patch and a rectangular metallic ground patch with a horn-shaped slot is presented. The antenna provides two separate impedance bandwidth of 230 MHz (about 9.4 % centred at 2.45 GHz) and 1190 MHz (about 21.6 % centred at 5.5 GHz). This feature makes it easily to cover the required bandwidths for wireless local area network (WLAN) operation at the 2.45 GHz band and 5.2/5.8 GHz bands. Additionally, the compact size (7×24 mm^2) of the antenna is profitable to be integrated with wireless communication devices on the restricted RF-elements space.

Keywords Bow-tie antenna · Dual-band · WLAN

9.1 Introduction

Recently, the antennas with self-complementary (SC) structure have raised considerable attention attributing to their broad impedance bandwidth characteristics [1, 2]. This feature is promising for wideband or multiband wireless communication systems. In previous studies, Wong et al. [3] reported a T-shaped strip and a rectangular patch loaded with a T-shaped slit to be a quasi-self-complementary (QSC) structure. It had shown that the QSC structure is appropriate for WLAN operation in the 5.2- and 5.8-GHz bands. A few years later, Liu et al. [4] proposed

C.-C. Lin (✉)
Department of Mathematic and Physical Sciences, R.O.C. Air Force Academy, Kaohsiung 820, Taiwan, Republic of China
e-mail: cclincafa@gmail.com

C.-Y. Huang
Department of Electronic Engineering, National Kaohsiung Normal University, Kaohsiung 802, Taiwan, Republic of China

J. Juang et al. (eds.), *Proceedings of the 2nd International Conference on Intelligent Technologies and Engineering Systems (ICITES2013)*, Lecture Notes in Electrical Engineering 293,
DOI: 10.1007/978-3-319-04573-3_9,

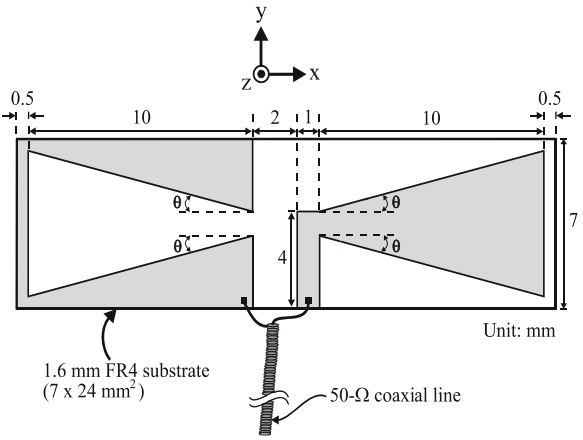

Fig. 9.1 Geometry of proposed dual-band bow-tie antenna for WLAN application

a fractal antenna consisted of a Hilbert-curve and self-complementary configuration with dual-band (2.4/5.2 GHz) and circular polarization characteristics. However, these previous studies still have some drawbacks. For example, the T-shaped SC [3] cannot provide dual-band (2.4 and 5.2/5.8 GHz) WLAN operations. The configuration of the fractal SC [4] is complex, which may diminish the radiating performance, especially the power gains.

Here, we propose a bow-tie antenna with self-complementary structure for wireless local area network (WLAN) operations. The antenna covers the 2.4 GHz (2400–2484 MHz) and 5 GHz (5150–5825 MHz) for IEEE 802.11 b/a standard. Simultaneously, it has a simple geometry and compact size, makes it easy to install narrow locations of wireless devices. Details of the design concepts are described and the experimental results of the constructed prototype are discussed.

9.2 Antenna Design and Experimental Results

Figure 9.1 shows the geometry of the proposed dual-band bow-tie antenna for 2.4/5.2/5.8 GHz WLAN applications. The antenna was printed on an FR4 dielectric substrate with size of 7×24 mm^2, thickness of 1.6 mm and relative permittivity $\varepsilon_r = 4.4$. A 50-Ω coaxial line was introduced for feeding the RF signal. The bow-tie antenna consisted of a self-complementary radiating element: a horn-shaped metallic patch and a rectangular metallic ground patch with a horn-shaped slot.

Figure 9.2 demonstrates the simulated and measured return loss as a function of various θ of the horn-shaped patch and slot versus frequency. In this experiment, the simulations were computed with Ansoft HFSS and the measurements were obtained with an R&S® ZVB 40 vector network analyzer. It can be noticed that the lower band shifts toward lower frequency while the upper band changes slightly as θ varied from 0 to 14°. The measured lower band has an impedance bandwidth of 180 MHz (2360–2590 MHz), which covers the 2.4-GHz band (2400–2484 MHz).

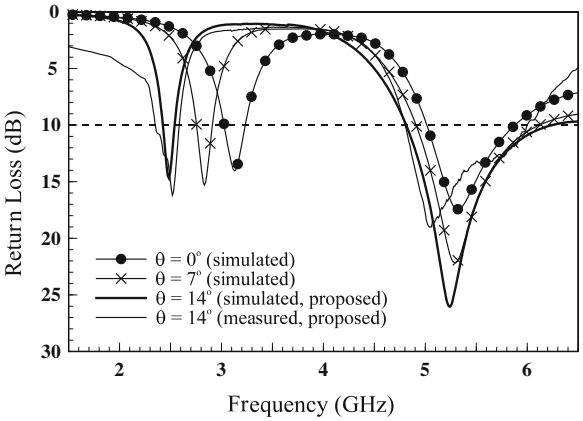

Fig. 9.2 Simulated and measured return loss versus frequency for various θ

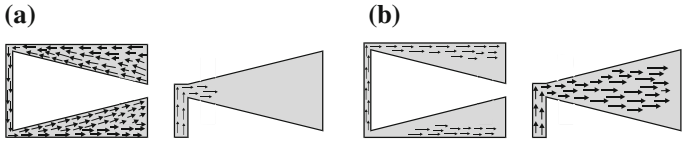

Fig. 9.3 Simulated surface electrical current distributions obtained at **a** 2.45 and **b** 5.5 GHz for proposed antenna

Besides, the measured upper band has an impedance bandwidth of 1190 MHz (4810–6000 MHz), which is sufficient for the 5-GHz (5150–5825 MHz) band. The results exhibit an acceptable agreement between the measurement and the simulation.

The excited surface current distributions simulated from the Ansoft HFSS at 2.45 and 5.5 GHz are illustrated in Fig. 9.3a, b, respectively. For the lower band excitation, the major surface current distribution (=28 mm) is observed around the horn-shaped slot, which is approximate quarter-wavelength corresponding to 2.45 GHz. On the upper bands, the major surface current distribution (=14.5 mm) is noted on the horn-shaped patch, which mainly propagates in x–z direction and near quarter-wavelength corresponding to 5.5 GHz. Consequently, the larger size of the horn-shaped slot procures the longer current path in the lower band while θ increases. This feature clarifies the variable θ principally affect the lower band but not the upper band.

Figure 9.4 describes the measured radiation pattern at 2.45 and 5.5 GHz. A figure-of-eight radiation pattern in the x–z plane and a nearly omni-directional radiation pattern in the y–z plane are obtained. The results in x–z plane indicate that the radiation intensity in $\pm x$ directions is much smaller than in $\pm z$ directions. These characteristic signifies that the radiating performance of the antenna is similar to a conventional dipole antenna. Figure 9.5 plots the measured antenna

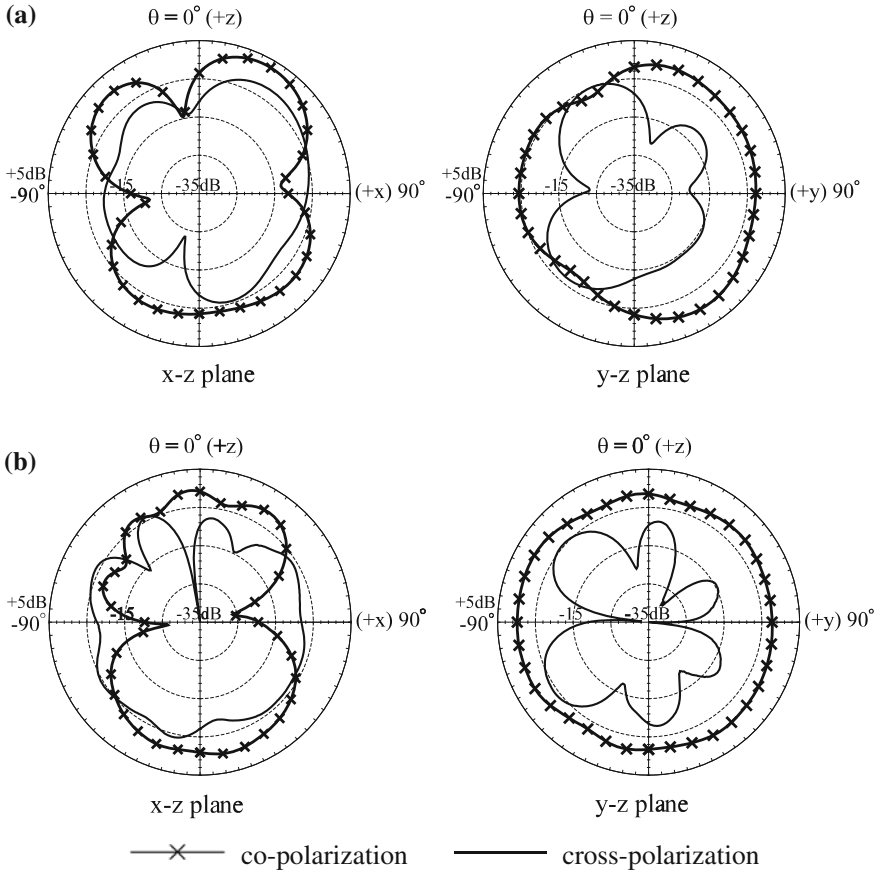

Fig. 9.4 Measured radiation patterns of proposed antenna obtained at **a** 2.45 and **b** 5.5 GHz

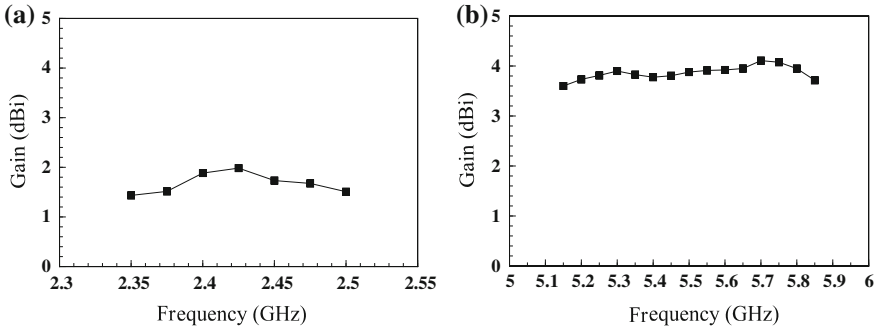

Fig. 9.5 Measured antenna gain versus frequency at **a** 2.35–2.5 and **b** 5.15–5.85 GHz for proposed dual-band crescent slot antenna

gain against frequencies. The gain varies in a range of 1.4–2 dBi at the lower band and 3.6–4 dBi at the upper band. It can be seen that the gain values within the operation bands are generally stable.

9.3 Conclusions

A dual-band bow-tie antenna with self-complementary structure for WLAN application has been successfully designed and implemented. Both the bandwidths of the lower and upper bands of the proposed antenna are satisfied for the required bandwidths of the 2.4 and 5.2/5.8 GHz bands of WLAN operation. Dipole-like antenna radiation performance can also be obtained, which is suitable for the complex wave propagation environment. Furthermore, the antenna has a compact size of 7×24 mm^2, and thus makes it easy to be integrated with the RF terminals of the wireless devices for satisfying miniaturizing tendency.

References

1. Mushiake, Y. (1992). Self-complementary antennas. *IEEE Antennas and Propagation Magazine, 34*, 23–29.
2. Mushiake, Y. (2003). A report on Japanese developments of antennas from Yagi-Uda antenna to self-complementary antennas. *IEEE Antennas and Propagation Society, 3*, 841–844.
3. Wong, K. L., Wu, T. Y., Su, S. W., & Lai, J. W. (2003). Broadband printed quasi-self-complementary antenna for 5.2/5.8 GHz WLAN operation. *Microwave and Optical Technology Letters, 39*, 495–496.
4. Liu, J. C., Zeng, B. H., Chen, H. L., Bor, S. S., & Chang, D. C. (2010). Compact fractal antenna with self-complementary Hilbert-curves for WLAN dual-band and circular polarization applications. *Microwave and Optical Technology Letters, 52*, 2535–2539.

Chapter 10
Compact Bow-Tie Antenna for UWB Applications

Chun-Cheng Lin

Abstract In this paper, a bow-tie quasi-self-complementary antenna (QSCA) for ultra-wideband (UWB) applications is presented and discussed. By a CPW-like matching technique, the proposed antenna provides a broad VSWR $< 2{:}1$ impedance bandwidth from 3.04 to 11.47 GHz. This feature is in favor of covering the required bandwidth from 3.1 to 10.6 GHz UWB operations. Additionally, the compact size (10×35 mm^2) of the antenna is favorable for integrated with wireless communication devices on restricted radio-frequency elements space.

Keywords Bow-tie · Quasi-self-complementary antenna · Ultra-wideband

10.1 Introduction

Recently, the self-complementary antenna (SCA) have raise considerable attention attributing to their broad impedance bandwidth characteristics [1, 2]. Theoretically, the frequency-independent impedance property can be achieved when the configuration of antenna is complementary to itself. This feature is promising for wideband or multiband wireless communication systems. In spite of these beneficial properties of the SCA, the matching network to convert the input impedance from 188.5 to 50 Ω for integrating with the RF terminals is indispensable. In previous studies, a self-complementary folded antenna fed by a two-port self-complementary asymmetric CPW-line and a self-complementary H-shaped antenna fed by a short-circuited microstrip line were investigated to increase the bandwidth of miniaturized antennas [3]. Guo et al. introduced a built-in CPW-like matching section to for impedance matching [4]. Subsequently, they also reported

C.-C. Lin (✉)
Department of Mathematic and Physical Sciences, R.O.C. Air Force Academy, Kaohsiung 820, Taiwan, Republic of China
e-mail: cclincafa@gmail.com

J. Juang et al. (eds.), *Proceedings of the 2nd International Conference on Intelligent Technologies and Engineering Systems (ICITES2013)*, Lecture Notes in Electrical Engineering 293,
DOI: 10.1007/978-3-319-04573-3_10,

a quasi-self-complementary antenna with triangular notch embedded on the microstrip line for wireless universal serial bus (USB) dongle applications [5]. In our earlier work, we rendered an ultra-wideband quasi-self-complementary antenna with a notch on the ground plane for good impedance matching [6]. However, the above-mentioned UWB antennas still had large size, which were 28.5 × 26 mm^2 to 51.5 × 40 mm^2.

Here we propose a bow-tie quasi-self-complementary antenna for ultra-wideband operations. We focus on impedance transforming method and compact design in this paper. With a CPW-like matching technique, the antenna covers 3.1–10.6 GHz bands and has a compact size of 10 × 35 mm^2. We also investigate the mechanism of the CPW-like matching technique in terms of analyzing the simulated surface current distributions. Simultaneously, the antenna has a simple geometry and compact size, making it suitable for wireless devices. Details of the design are given and experimental results of the constructed prototype are discussed.

10.2 Antenna Design and Experimental Results

Figure 10.1 shows the geometry of the proposed bow-tie QSCA for ultra-wideband applications. The antenna was printed on an FR4 dielectric substrate, which had a dimensions of 10 × 35 mm^2, a thickness of 1.6 mm and a relative permittivity $\varepsilon_r = 4.4$. A 50-Ω SMA connector was introduced for feeding the RF signal. The bow-tie QSCA consists of two radiating elements: a horn-shaped conductive patch and a counterpart horn-shaped slot. A CPW-like matching technique comprised a central strip and a triangular piece was used to modulate the impedance matching.

Figure 10.2 demonstrates the simulated return loss versus frequency for impedance matching evolution. The simulations were computed using Ansoft HFSS [7]. Initially, there was only central strip ($\theta_1 = 0$) and a VSWR < 2:1 impedance bandwidth was 6–12 GHz. While the triangular piece was attached and θ_1 reached 50°, a good VSWR < 2:1 impedance bandwidth achieved 3–12 GHz. The original un-matched bands (4–6 GHz) were improved by the CPW-like matching technique. Thus, the proposed QSCA can cover UWB (3.1–10.6 GHz) operation bands.

Figure 10.3 plots the simulated and measured return loss versus frequency for θ_2 values of 18–28°. In our experiment, the measurements were obtained with Rohde & Schwarz ZVB 40 vector network analyzer. As θ_2 was 18°, the cut-in frequency was 3.5 GHz. The cut-in frequency was getting lower gradually as θ_2 increased from 18 to 28°. Furthermore, the results exhibited compatibly for the measurement and the simulation when θ_2 was 23°, which indicated we successfully converted the simulation into the entity.

To clarify the mechanisms of the variation of cut-in frequency and the CPW-like matching technique, the excited surface current distributions simulated from Ansoft HFSS at 3 and 5 GHz are illustrated in Fig. 10.4a–c, respectively. For the excitation in Fig. 10.4a, the major surface current distribution (=45 mm) was

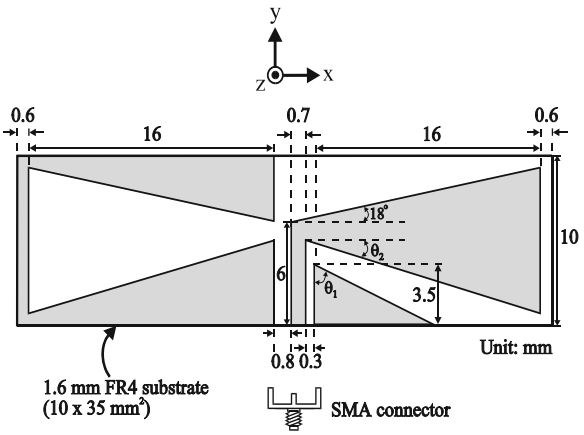

Fig. 10.1 Geometry of proposed bow-tie quasi-self-complementary antenna for UWB applications

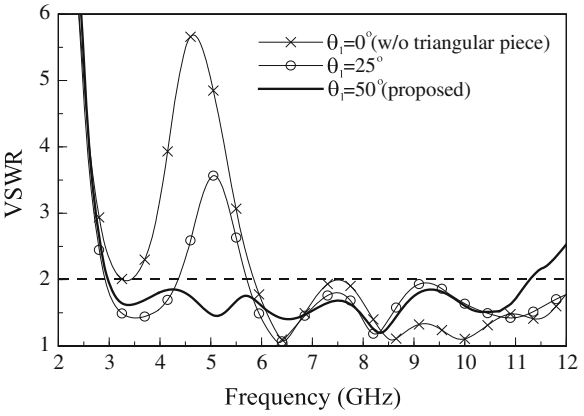

Fig. 10.2 Simulated VSWR versus frequency for various θ_1 values

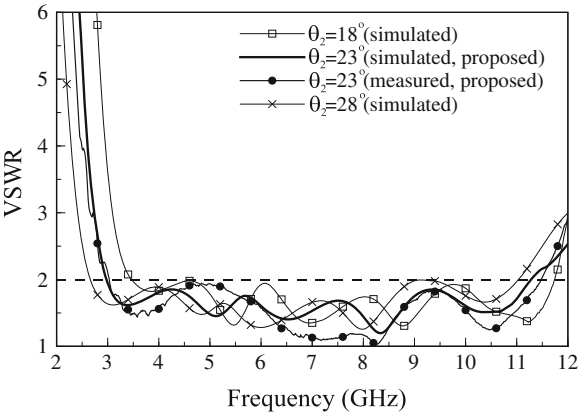

Fig. 10.3 Simulated and measured VSWR versus frequency for various θ_2 values

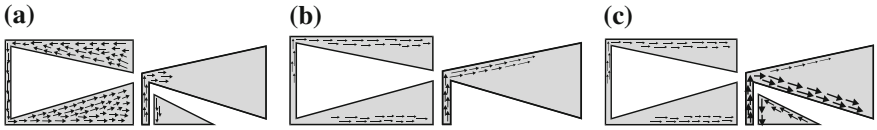

Fig. 10.4 Simulated surface electrical current distributions obtained at **a** 3 GHz, **b** 5 GHz (*only central strip*), and **c** 5 GHz (*with triangular piece*) for proposed antenna

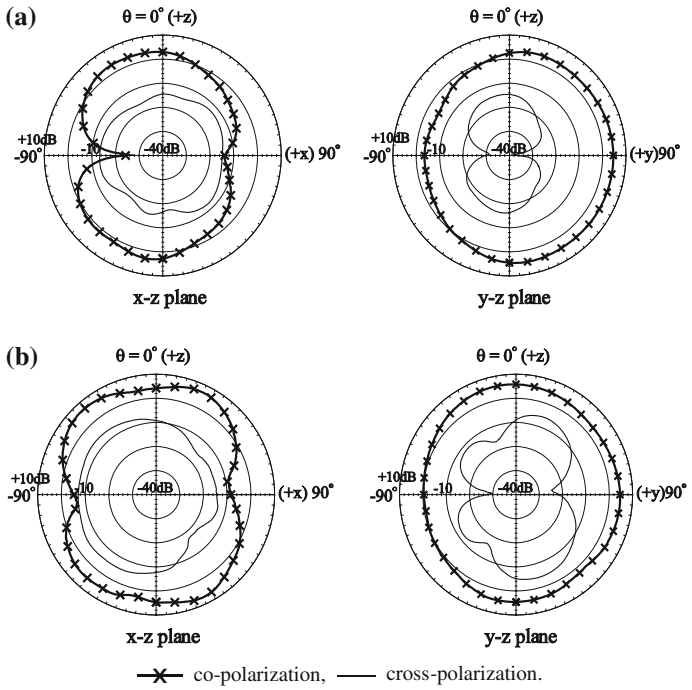

Fig. 10.5 Measured radiation patterns of proposed antenna obtained at **a** 4 and **b** 8 GHz

observed around the horn-shaped slot, which was approximately a half-wavelength corresponding to 3 GHz. A larger horn-shaped slot excited a longer current distribution with increasing θ_2. Accordingly, a lower cut-in frequency was realized. For 5 GHz excitation, we compared two situations, i.e., only central strip and with triangular piece. In Fig. 10.4b, there was handful of current distribution on the central strip. Hence, a week radiation was generated and a poor impedance matching arose was obtained around 5 GHz bands. On the other hand, with the triangular piece added, a large current distribution occurred on it. Meanwhile, a large current distribution on the central strip and the lower edge of the horn-shaped patch was generated, as shown in Fig. 10.4c. This can be attributed to the capacitive coupling effect produced by the triangular piece [8]. Besides, the

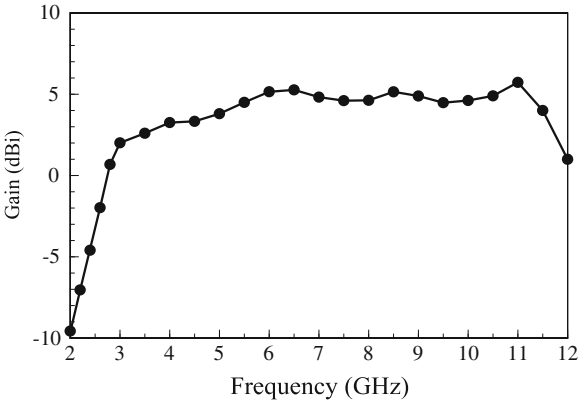

Fig. 10.6 Measured antenna gain versus frequency for proposed antenna

excited current distribution was 16 mm, which was nearly a quarter-wavelength corresponding to 5 GHz. Consequently, we can explain all the variation of VSWR in our experiment.

The radiation patterns and gain values of the proposed antenna were measured in the far-field anechoic chamber. Figure 10.5 describes the measured radiation pattern at 4 and 8 GHz. A figure-of-eight radiation pattern in the x–z plane and a nearly omni-directional radiation pattern in the y–z plane were acquired. The results in x–z plane indicated that radiation intensity in $\pm x$ directions much smaller than $\pm z$ directions. These characteristic suggested that the radiating performance of proposed QSCA was similar to a simple dipole antenna. Figure 10.6 presents the measured antenna gain versus frequency. The gain varied in a range of 2.1–5.7 dBi. It can be seen that the gain values within the operation bands were generally stable and sufficient for UWB applications.

10.3 Conclusions

A bow-tie quasi-self-complementary antenna for UWB applications was successfully designed and implemented. With a CPW-like matching technique consisting of a central strip and a triangular piece, the proposed QSCA operated from 3.04 to 11.47 GHz. Dipole-like antenna radiation performance was also obtained, which was suitable for the complex wave propagation environments. Furthermore, the antenna had a compact size of 10×35 mm^2, making it easy to be integrated with the radio-frequency terminals of wireless devices for satisfying miniaturizing tendency.

References

1. Mushiake, Y. (1992). Self-complementary antennas. *IEEE Antennas and Propagation Magazine, 34*, 23–29.
2. Mushiake, Y. (2003). A report on Japanese developments of antennas from Yagi-Uda antenna to self-complementary antennas. *IEEE Antennas and Propagation Magazine, 3*, 841–844.
3. Azadegan, R., & Sarabandi, K. (2007). Bandwidth enhancement of miniaturized slot antennas using folded, complementary, and self-complementary realizations. *IEEE Transactions on Antennas and Propagation, 55*, 2435–2444.
4. Guo, L., Chen, X., Parini, C. G. (2008). A printed quasi-self-complementary antenna for UWB applications, IEEE International Symposium on Antennas and Propagation and USNC/URSI National Radio Science Meeting, APSURSI.
5. Guo, L., Chen, X., & Parini, C. G. (2012). Miniature ultra-wideband antenna for wireless universal serial bus dongle applications. *IET Microwave and Antennas Propagation, 6*, 113–119.
6. Lin, C. C., Huang, C. Y., & Su, J. Y. (2011). Ultra-wideband quasi-self-complementary antenna with band-rejection capability. *IET Microwave, Antennas and Propagtion, 5*, 1613–1618.
7. Ansoft HFSS ver. 13, ANSYS (2009). Canonsburg, PA. Retrieved from http://www.ansoft.com/products/hf/hfss/
8. Mayhew-Ridgers, G., Odendaal, J. W., & Joubert, J. (2003). Single-layer capacitive feed for wideband probe-fed microstrip antenna elements. *IEEE Transactions on Antennas and Propagation, 51*, 1405–1407.

Chapter 11
A 0.33 mW Bulk Injection Downconverter RFIC for WSN Applications

Jian-Ming Wu, Ming-Yin Ko and Tzong-Lin Yang

Abstract A 2.4 GHz downconverter is designed using the TSMC 0.18 μm CMOS standard process for wireless sensor networks (WSN). An important goal of the design is to achieve the low supply voltage and low power consumption that is required in WSN receivers. The bulk injection technique is used to reduce the supply voltage and power consumption of the downconverter. A voltage of 0.6 V is supplied to the downconverter and the power consumption is then 0.33 mW. The simulated results of the 2.4 GHz downconverter include that a conversion gain is 8.6 dB, an input-referred 1 dB compression point (IP_{1dB}) is −18.4 dBm, an input-referred third-order intercept point (IIP_3) is −8.8 dBm, a noise figure (NF) is 16.2 dB, and a port-to-port isolation exceeds 30 dB.

Keywords Downconverter · Mixer · Bulk injection

11.1 Introduction

Wireless sensor networks (WSN) have been extensively used in localization [1], vehicle automation [2], biotelemetry [3], and health care [4, 5]. WSN adopting energy harvesting techniques demand that RF receivers have to consume low power. In RF receivers, downconverters are primarily responsible for converting frequencies. Proposed techniques to design downconverters with power consumption below 1 mW include the: (1) current reuse [6] and (2) bulk injection [7] techniques. The current reuse technique provides high conversion gain but at the cost of a poor linearity. The bulk injection technique is simple to implement but a high LO power is required to drive the transistors.

J.-M. Wu (✉) · M.-Y. Ko · T.-L. Yang
Department of Electronic Engineering, National Kaohsiung Normal University, Kaohsiung 824, Taiwan, Republic of China
e-mail: jianmingwu@nknucc.nknu.edu.tw

J. Juang et al. (eds.), *Proceedings of the 2nd International Conference on Intelligent Technologies and Engineering Systems (ICITES2013)*, Lecture Notes in Electrical Engineering 293,
DOI: 10.1007/978-3-319-04573-3_11,

The goal of this work is to design a 2.4 GHz downconverter using the TSMC 0.18 μm CMOS standard process for WSN applications. The bulk injection technique is used for reducing power consumption due to its simplicity. In this paper, the circuit design of the downconverter is presented in Sect. 11.2. Section 11.3 demonstrates the simulation results. The conclusion of this paper is shown in Sect. 11.4.

11.2 Circuit Design

Figure 11.1 schematically depicts the circuit of the bulk injection downconverter. The NMOS transistors M_1, M_2, M_3, and M_4 comprise the multiplication core. Each NMOS transistor has four ports, which are gate, drain, source, and bulk. The source is connected to ground, forming that the NMOS transistor is in a common-source configuration. The input differential RF signal is applied to the gate while the differential LO signal is injected to the bulk.

Figure 11.2 plots the simulated drain current versus the gate-source voltage of NMOS transistor that is driven by the 0-dBm differential LO signal. The simulation results are generated using an Agilent Advanced Design System (ADS). In Fig. 11.2, LO+ denotes the positive cycle of input LO signal while LO− represents the negative cycle of input LO signal. When the gate-source voltage of NMOS transistor is 0.5 V, as indicated in Fig. 11.2, the drain current of NMOS transistor in the positive cycle of input LO signal is 0.53 mA, but in the negative cycle of input LO signal its drain current is 0 mA. This clearly shows that the injected LO signal can switch on and off the NMOS transistor.

When the LO signal is applied to switch on and off the NMOS transistors from M_1 to M_4, the RF and LO signals are mixed to generate the output differential IF signal at the drain of NMOS transistor. To reduce further the supply voltage, the inductor (L_D) is used as an output load because no dc voltage drop exists across it. The output voltage swing of the differential IF signal drops on the inductive load.

11.3 Simulation Results

The bulk injection downconverter circuit is designed using the TSMC 0.18 μm CMOS foundry process. The bulk of NMOS transistor can be isolated by a deep N-well process. Figure 11.3 shows the chip layout of the downconverter RFIC. Notably, the inductor L_D is arranged off-chip to reduce the chip area. The chip area is 0.35 mm × 0.35 mm. The downconverter RFIC is now being fabricated. A supply voltage of 0.6 V is used with a power consumption of 0.33 mW. In a continuous-wave test the RF, LO, and IF frequencies that are used in this

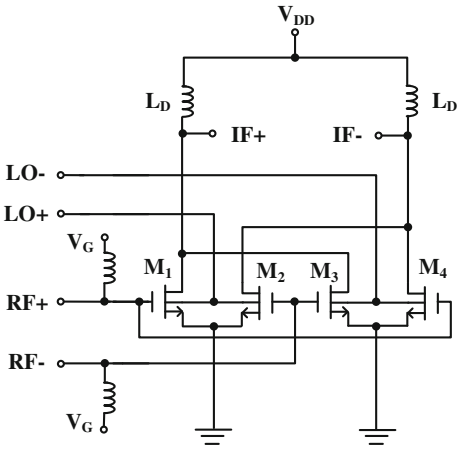

Fig. 11.1 Circuit schematic of bulk injection downconverter

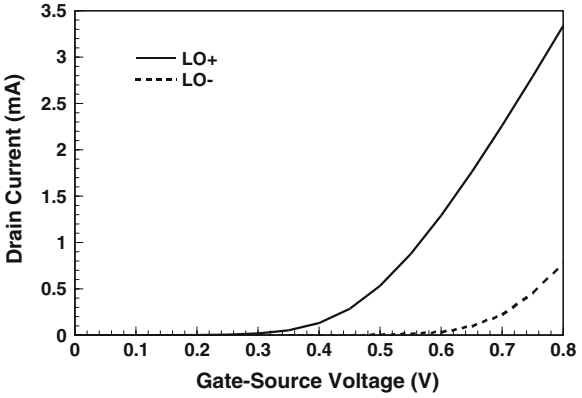

Fig. 11.2 Simulated drain current versus the gate-source voltage of NMOS transistor that is driven by the 0-dBm differential LO signal

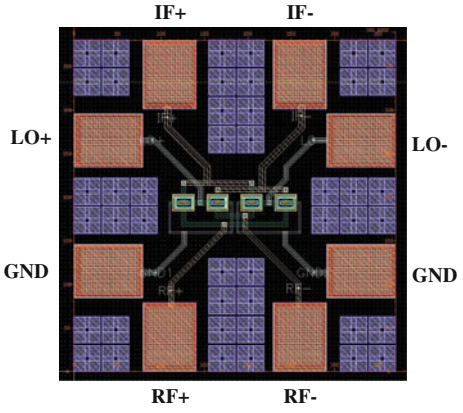

Fig. 11.3 Chip layout of bulk injection downconverter

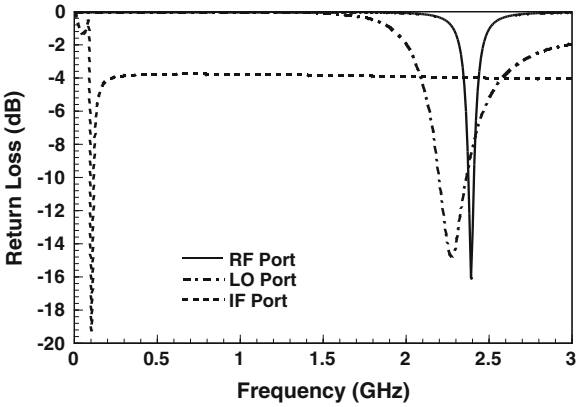

Fig. 11.4 Simulated return loss of RF, LO, and IF ports for bulk injection downconverter

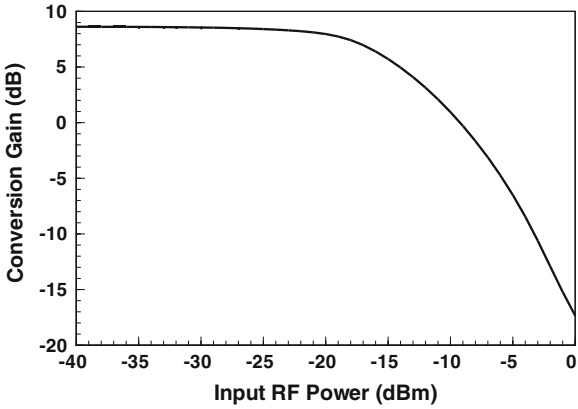

Fig. 11.5 Simulated gain compression of bulk injection downconverter

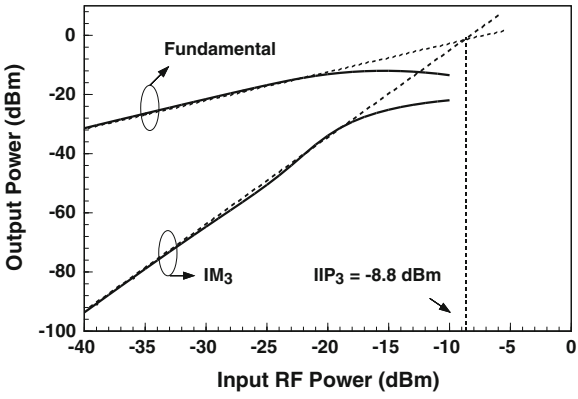

Fig. 11.6 Simulated output powers for the fundamental and IM_3 products in bulk injection downconverter

Table 11.1 Performance summary for this work and comparison with prior works

	[6]	[7]	This work[a]
RF frequency (GHz)	2.4	2.4	2.4
Supply voltage (V)	0.8	0.77	0.6
Power consumption (mW)	0.33	0.48	0.33
LO power (dBm)	−1	5	0
Conversion gain (dB)	18.7	5.7	8.6
IP_{1dB} (dBm)	−21	−16	−18.4
IIP_3 (dBm)	−14.9	−5.7	−8.8
NF (dB)	11.5	15	16.2

[a] Simulated results

downconverter are 2400, 2300, and 100 MHz, respectively. The applied LO power is 0 dBm. The frequency spacing in a two-tone test is set to 5 MHz.

Figure 11.4 plots the simulated return loss of RF, LO, and IF ports. Figure 11.4 reveals that the downconverter has good impedance match at all RF, LO, and IF ports. Figure 11.5 shows the simulation results of gain compression. It can be seen that the simulated conversion gain is 8.6 dB. Figure 11.5 also indicates that an input-referred 1 dB compression point (IP_{1dB}) is −18.4 dBm. The simulated output powers of fundamental and third-order intermodulation (IM_3) products are plotted in Fig. 11.6. Figure 11.6 demonstrates that the simulated input-referred third-order intercept point (IIP_3) is equal to −8.8 dBm. For this downconverter, the simulated noise figure (NF) is below 16.4 dB and the simulated port-to-port isolation exceeds 30 dB. Table 11.1 summarizes the performance merits of this work and compares it with previous proposed downconverter designs in [6, 7]. The comparison shows that the presented downconverter has the lowest supply voltage among the works listed in Table 11.1.

11.4 Conclusion

A low power downconverter with a bulk injection technique has been designed using the TSMC 0.18 μm standard CMOS process. The 2.4 GHz downconverter RFIC achieves a conversion gain of 8.6 dB and an IIP_3 of −8.8 dBm when the power only consumes 0.33 mW.

Acknowledgments This research was supported by the ROC (Taiwan) Ministry of Education. The authors wish to thank the R.O.C. (Taiwan) National Chip Implementation Center for providing the TSMC 0.18 μm CMOS foundry service.

References

1. Simek, M., Moravek, P., Komosny, D., & Dusik, M. (2012). Distributed recognition of reference nodes for wireless sensor network localization. *Radioengineering, 21*, 89–98.
2. Carmo, J. P., Mendes, P. M., Couto, C., & Correia, J. H. (2010). A 2.4-GHz CMOS short-range wireless-sensor-network interface for automotive applications. *IEEE Transactions on Industrial Electronics, 57*, 1764–1771.
3. Wong, A. C. W., Kathiresan, G., Chan, C. K. T., Eljamaly, O., Omeni, O., Mcdonagh, D., et al. (2008). A 1 V wireless transceiver for an ultra-low-power SoC for biotelemetry applications. *IEEE Journal of Solid-State Circuits, 43*, 1511–1521.
4. Daly, D. C., & Chandrakasan, A. P. (2007). An energy-efficient OOK transceiver for wireless sensor networks. *IEEE Journal of Solid-State Circuits, 42*, 1003–1011.
5. Seo, H.-M., Moon. Y. K., Park, Y.-K., Kim, D., Kim, D.-S., Lee, Y.-S., et al. (2007). A low power fully CMOS integrated RF transceiver IC for wireless sensor networks. *IEEE Transactions on Very Large Scale Integration (VLSI) Systems, 15*, 227–231.
6. Kraimia, H., Taris, T., Begueret, J., & Deval, Y. (2011). A 2.4 GHz ultra-low power current-reuse bleeding mixer with resistive feedback. In: *18th IEEE International Conference on Electronics, Circuits and Systems* (pp. 488–491). IEEE Press, New York.
7. Liang, K.-H., Chang, H.-Y., & Chan, Y.-J. (2007). A 0.5–7.5 GHz ultra low-voltage low-power mixer using bulk-injection method by 0.18-μm CMOS technology. *IEEE Microwave and Wireless Components Letters, 17*, 531–533.

Chapter 12
Expedited Stabilization of Furnace Slag Produced from Basic Oxygen Steelmaking

Da-Yun Huang, Shu-Lan Ke, Chien-Kuei Chang and Chao-Ming Hsu

Abstract Steelmaking plants in Taiwan using basic oxygen processes generate over a million tons of basic oxygen furnace slag (BOFS) annually. The slag contains free CaO and f-CaO, which are characterized by high pH values and high expansion rates, thus significantly compromising the potential of the slag for resource reuse. Various techniques have been adopted in attempts to stabilize the slag, but none have been effective in terms of completely depleting the f-CaO, leaving the slag unusable and raising serious waste disposal issues. This research explores the effects of the immersion method on the stabilization process for BOFS in a series of experiments. Results show that even long periods of immersion fail to produce complete f-CaO depletion, and indicate that the slag's porous and closed microstructure may be the cause of this problem. SEM and EDS analysis on slag cross-sections verify that the f-CaO is partially covered by metals, such as Fe and Mn, or other compounds, such that stabilizing processes are only able to partially degrade the f-CaO content.

Keywords Basic oxygen furnace slag (BOFS) · f-CaO · Chemical immersion · Porous

D.-Y. Huang · C.-M. Hsu (✉)
Department of Mechanical Engineering, National Kaohsiung University of Applied Science, Kaohsiung 80778, Taiwan, Republic of China
e-mail: jammy@cc.kuas.edu.tw

D.-Y. Huang
e-mail: dayun.huang@gmail.com

S.-L. Ke · C.-K. Chang
Department of Chemical and Materials Engineering,
National Kaohsiung University of Applied Science, Kaohsiung 80778,
Taiwan, Republic of China
e-mail: ga01455@yahoo.com.tw

C.-K. Chang
e-mail: isaac@cc.kuas.edu.tw

J. Juang et al. (eds.), *Proceedings of the 2nd International Conference on Intelligent Technologies and Engineering Systems (ICITES2013)*, Lecture Notes in Electrical Engineering 293,
DOI: 10.1007/978-3-319-04573-3_12,

12.1 Introduction

Basic oxygen steelmaking is a special process used by plants implementing consistent steel manufacturing procedures. The process involves pouring molten iron from a blast furnace into the basic oxygen furnace and blowing pure oxygen to trigger the smelting process. During the smelting process, substances, including quicklime and iron ore, are loaded into the furnace to absorb the gas or induce the formation of slag. These substances are introduced to reduce the content of C, Si, Mn, P, and S in the molten iron and thus achieve the proper chemical composition in the hot metal, since they react with pure oxygen to form slag. After the smelting process is completed, the residue is then poured off to cool, and the solidified residue is called basic oxygen furnace slag.

In Taiwan, BOFS has been applied to road pavements but according to [1] problems persist. First, the high iron content gives BOFS a higher level of hardness expediting wear-off or damaging grinding machines. Second, BOFS often contains unreacted free calcium oxide (free CaO or f-CaO) in granules which expand and disintegrate after absorbing moisture. These issues seriously impede the reusability of BOFS.

BOFS is a fusion of multiple minerals; CaO is one of the major components in BOFS and excessive content of this element causes massive crystallization (sedimentation). In particular, dusting occurs under a slow cooling process [2]. BOFS is mainly composed of C_2S (Di-calcium silicate) and C_3S (Tri-calcium Silicate) [3], and contains a ternary system of $CaO–Al_2O_3–SiO_2$ and the ratio of simple steel falls in between Portland cement clinker and BOFS [4].

Results from [5] indicate that f-CaO reacts with water and CO_2 in the air to form $Ca(OH)_2$ and $CaCO_3$, which, after weathering, disintegrate and expand at a rate ranging from 100 to 300 %. In addition, MgO disintegrates into $Mg(OH)_2$ with an expansion rate of 77 %. Based on the above, BOFS will only reach a stable state once the f-CaO and MgO are completely disintegrated. Results in [6] suggest that, when the pH value of BOFS ($CaO/SiO_2 + P_2O_5$) is higher than 1.8, the slag contains between 60 and 80 % of both C_3S and C_2S and, when the pH value increases, C_3S becomes more active, increasing the content of f-CaO along with the expansion rate. On the other hand, [7] suggests that the content of f-CaO in fresh BOFS is not relevant to the expansion rate, but that the pH value is directly correlated to the expansion rate.

In [8], the authors noted that f-CaO comes in two forms: one is residual free calcium oxide, which can be further broken down into free CaO granules and porous free CaO, while the other is free CaO deposits on the surface of the coarse granules of dicalcium ferrite and inside alite ($3CaO·SiO_2$) crystals. The authors of [9] suggest that BOFS is highly porous and water permeable, but [10] disagrees since the specific surface area of granules between 53 and 62 μm screened through BET is 1.45 m^2/g while that of granules smaller than 44 μm is 2.78 m^2/g.

12.2 Materials and Experiments

12.2.1 Acid Immersion

This research uses BOFS supplied by CHC Resources. The experiment proceeded through the following steps. One kilogram of BOFS was placed in a sample can, which was then filled with one liter of 0.1 % (v/v) HCl immersion solution. The mixture was then set aside for to observe changes in the pH value and samples were taken for analysis of f-CaO content. A control group was set up using RO water as the immersion solution.

12.2.2 Vacuuming

In Fig. 12.1, a vacuum device was constructed form a 10 L sealed S_3O_4 stainless steel tank. A manometer was installed along the pipeline linked to the pressure relief valve to monitor and maintain the vacuum state. BOFS was placed in the tank and the pump was used to create a vacuum of <1 Torr. The vacuum state was maintained for a period of time to ensure that the air inside of the pores of BOFS was completely drawn out. After vacuuming, the pump was turned off and then the pumping valve was close before the water inlet was opened. RO water was then drawn into the tank to immerse the BOFS and permeate the pores. After 1 h, the pressure relief valve was opened and the BOFS was retrieved along with the water for further treatment.

12.2.3 Fixed pH Acid Immersion

The experiment proceeded through the following steps. BOFS was placed in the sample can which then filled with one liter of 0.1 % (v/v) RO water. This was then adjusted to a fixed pH level with an acid. The pH value of the immersion solution was configured at 2, 3, 4, and 5, and these values were tested and adjusted daily. Samples were taken from the mixture for analysis of f-CaO content. Several solutions were tested, including H_2SO_4, HCl, and HNO_3.

12.2.4 Testing and Analysis

12.2.4.1 CaO Analysis (Reference: CNS 1384) and Metal Analysis (Reference: ASTM E1479)

Following CNS1384 and ASTME1479.

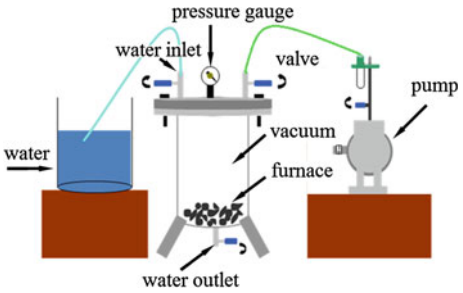

Fig. 12.1 Vacuum device

12.2.4.2 Scanning Electron Microscope Analysis (SEM)

Scanning Electron Microscope (SEM, Philips, XL30) for analysis.

12.3 Results and Conclusion

12.3.1 Effect of Acid Immersion

The sample was kept under continuous immersion for 10 days, and the pH value and f-CaO content were measured daily, with results shown in Fig. 12.2. The pH value in Fig. 12.2a was seen to rise quickly during the first 2 days, indicating that quick release of the alkaline substances from the BOFS. However, the process slowed dramatically after 2 days. Comparison with results statistics collected from the RO water experiment, the acid immersion solution is seen to be more effective but lack of uniformity among the slag samples leads to increased fluctuation in the content of f-CaO, as shown in Fig. 12.2b.

12.3.2 Effect of Vacuum Treatment

Figure 12.3 shows the f-CaO values of different BOFS samples treated with the vacuuming process and immersed in RO water for 10 days. Results show that vacuum treatment did not significantly improve the poor degradation rate of f-CaO, which argues against [5] porous BOFS theory.

12.3.3 Effect of Fixed pH Immersion Solution

Figures 12.4 and 12.5 show the results of immersion in RO water, HCl, H_2SO_4 and HNO_3 for a period of 3 months. Experimental results show that changes in the f-CaO content is not related to the duration of immersion and the fluctuation is due only to lack of uniformity among the slag samples.

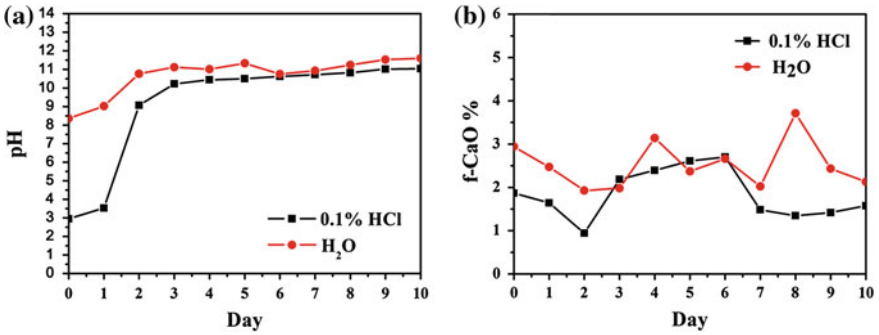

Fig. 12.2 Acid immersion treatment on BOFS **a** pH level **b** f-CaO content

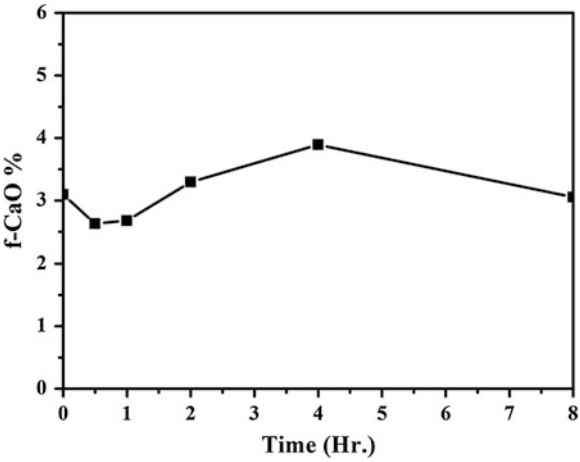

Fig. 12.3 Correlation between vacuuming treatment duration and f-CaO content

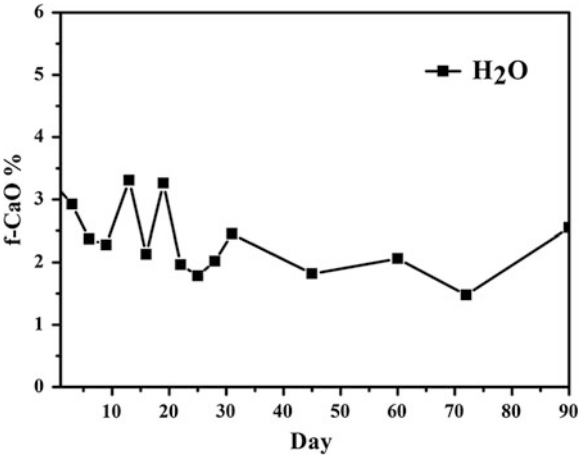

Fig. 12.4 Correlation between RO water immersion duration and changes in f-CaO content

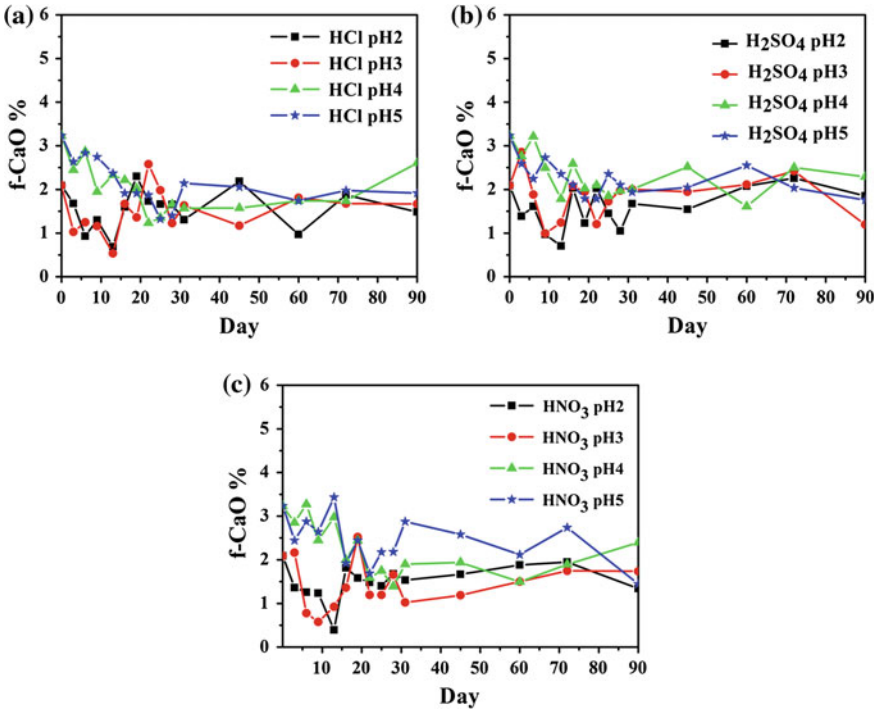

Fig. 12.5 Correlation between **a** HCl, **b** H_2SO_4 and **c** HNO_3 immersion duration and changes in f-CaO content

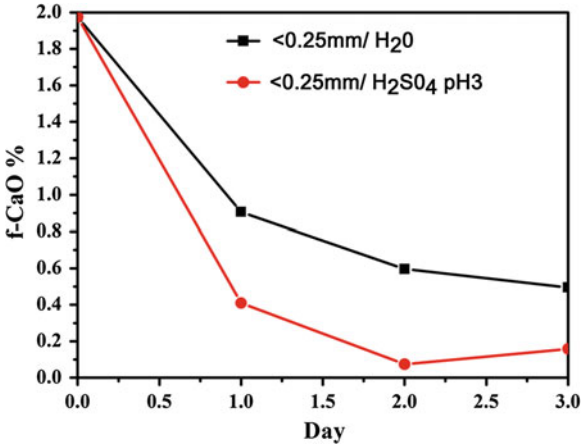

Fig. 12.6 Correlation between f-CaO content released from the fine slag granules and immersion duration

Table 12.1 ICP–OES analysis on BOFS

Al	0.1444
Ca	17.723
Cr	0.2050
Fe	26.720
Mg	3.0530
Mn	3.4958
P	0.9712
Si	4.7430
Ti	0.3239

12.3.4 Physical Properties of BOFS

Based on the above experiments, the following conclusions were drawn:

1. Long-periods of immersion in various acid solutions were unable to effectively degrade f-CaO, suggesting the influence of non-chemical impediments.
2. The slag samples used in the experiments were obtained from CHC Resources after 3-months of natural attenuation. Although the natural attenuation process had already caused f-CaO degradation, experimental results indicated residual remains of between 1 and 4 %. This fluctuation is considered significant and complete degradation is difficult to achieve.
3. Based on the results of the vacuum treatment, the slag structure is probably entirely or partially nonporous.

To explain this phenomenon that crushed and sieved the slag for granules smaller than 0.25 mm and then immersed in chemical solutions. Figure 12.6 shows that f-CaO content in the slag granules smaller than 0.25 mm immersed in RO water was reduced 1.0 after 1 day of immersion and to 0.6 % after 3 days of immersion. The f-CaO content in the granules immersed in H_2SO_4 at pH3 was reduced to 0.4 % on the first day. These results does not explicitly indicate that smaller granules trigger higher mass transfer efficiency because, if the slag is porous, the effect of immersion in relation to the changes in the f-CaO content should not be undetectable after a period of 90 days. Table 12.1 summarizes content analysis. Inside of BOFS deduced that closed areas covered by fine substances may exist, thus the immersion solutions were unable to dissolve the f-CaO content because it is inside the closed-off areas.

Via conducted cross-section analysis through SEM and EDS. Figure 12.7 shows that the Ca compounds inside the slag (which may be partially f-CaO) were covered by metals such as Fe and Mn, or by other compounds. The results of the above-mentioned immersion experiment with fine slag granules may thus be explained by damage to part of the closed-off areas, allowing for the quick release of the f-CaO content.

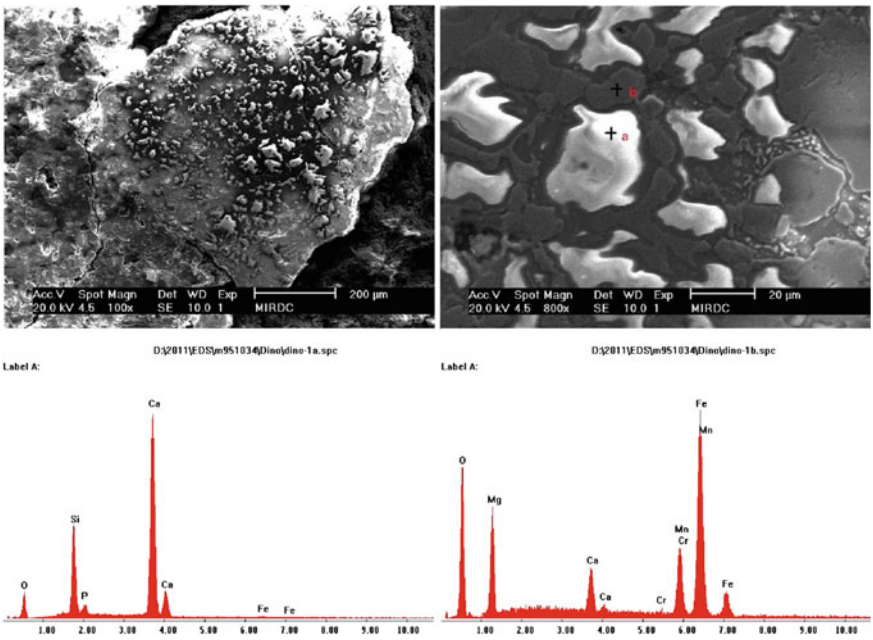

Fig. 12.7 SEM and EDS analysis on the cross-section of BOFS

12.4 Conclusion

BOFS can only be used to develop high value civil engineering aggregate materials if the f-CaO content is completely degraded; otherwise, it is only useful for road paving or landfill. None of the experiments designed to expedite the degradation process of f-CaO used in this research achieved total degradation, but certain useful knowledge has been derived. Different opinions have been suggested regarding the porosity of BOFS, but the results of this research indicate that the slag is porous with closed capsules. Immersing crushed and sieved slag granules for over 3 months mostly degraded the f-CaO contained in the porous areas and the remainder was easily released in liquid, but the f-CaO contained in the closed capsules was not removed by any means. SEM and EDS analysis indicate that the closed capsules were covered by metals, such as Fe and Mn, or other compounds. The difficulty in verifying whether the content of f-CaO has been completely released suggests that BOFS cannot feasibly be used into a resource for the development of structural aggregate.

References

1. Yang, G.-Y. (1992). Furnace slag resource. The past and future of furnace slag utilization in the China Steel Corp. *Technology and Training, 17*(1), 31–46 (Kaohsiung).
2. Huang, C.-L. (1986). Application of furnace clinker and fly ash in concrete engineering. Taipei: Taipei Construction.
3. CIMME. (1986). Introduction to ferrous metallurgy. *Ferrous Metallurgy, 1*.
4. Shi, T.-H. (1992). Utilization of metallurgical slag. Mining Technology (pp. 266–267). Sichuan, China.
5. Li, C.-H., Wang, C.-C., & Li, T.-H. (2002). *Expansion of basic oxygen furnace slag* (pp. 219–245). Collection of Public Engineering Conference Dissertations.
6. Koide, H. (1993). Research on using BOF slag for road construction. Nakayama Steel Works Technical Report, Osaka, Japan.
7. Wang, C.-C. (2005). Using BOF slag as a base material and its engineering attributes. Graduate Institute of Civil Engineering, National Cheng Kung University, Tainan, Taiwan.
8. Motzh, G. J. (2001). Products of steel slag—An opportunity to save natural resources. *Waste Management*, *21*(3), 285–293.
9. Li, C.-H. (1992). *Study on the solutions to repress expansion of BOF slag supplied by China Steel Corp*. Graduate Institute of Civil Engineering, National Cheng Kung University, Tainan, Taiwan.
10. Chiang, B.-C. (1993). Physical properties of active carbon and its absorbency to VOCs. *Industrial Pollution Prevention, 58*.

Chapter 13
Abstracting Zinc Flakes from Crude Zinc Oxide Through the Reclamation of Electric Arc Furnace (EAF) Dust

Sing-Jhen Wu, Jyun-Hong Huang, Ah-Der Lin and Chien-Kuei Chang

Abstract In recent years, factories in Taiwan have successively installed dust processing equipment in electric arc steel smelting furnaces (EAF) to reclaim crude zinc oxide which is then sold for profit. The price of crude zinc oxide, however, is directly correlated to their purity, as lower purity requires downstream factories to install additional purification technology [1, 2]. A case is presented in which the low quality of zinc oxide flakes produced make it difficult for a firm to justify its initial investment. To raise the value of its product, the firm requires an efficient manufacturing process to turn crude zinc oxide into high-purity zinc flakes. In this study, hydrometallurgy technology was used to transform zinc oxide into high-purity zinc flakes through a three-step process including leaching, purification and electrodialysis. Results show that zinc dissolution reaches its highest rate after 48 h of stirring in 7 N-NaOH as the leach agent with a solid–liquid ratio of 1:10 at room temperature. Using a strong alkaline as the leach agent can prevent the dissolution of iron oxide; however, the leach solution still contains a large amount of lead which must be removed to avoid degrading the purity of the electrodialyzed zinc powder. Using sheet zinc recycled from batteries as a displacement for purifying leach solution yielded a level of quality comparable to commercial zinc powder, but at a cost only 1/30 of that for the zinc powder

S.-J. Wu · J.-H. Huang · C.-K. Chang (✉)
Department of Chemical and Materials Engineering,
National Kaohsiung University of Applied Science, Kaohsiung 80778,
Taiwan, Republic of China
e-mail: isaac@cc.kuas.edu.tw

S.-J. Wu
e-mail: mbh5039@gmail.com

J.-H. Huang
e-mail: jhhuang79416@gmail.com

Ah-Der Lin
Department of Mechanical Engineering, Cheng-Shiu University, Kaohsiung 83374,
Taiwan, Republic of China
e-mail: ahder@csu.edu.tw

J. Juang et al. (eds.), *Proceedings of the 2nd International Conference on Intelligent Technologies and Engineering Systems (ICITES2013)*, Lecture Notes in Electrical Engineering 293,
DOI: 10.1007/978-3-319-04573-3_13,

process. This process also yielded high purity lead slag as a byproduct, which adds to its value. The purified leach solution is then electrolyzed into zinc flakes and the zinc powder manufactured from the above flakes achieves a purity as high as 99.1 % [3–5].

Keywords Electric arc furnace steel smelting · EAF dust · Crude zinc oxide · Hydrometallurgy · Zinc flakes

13.1 Introduction

The steelmaking process can be divided into two major types. Integrated steelmaking uses iron ore as the raw material, using a blast furnace followed by basic oxygen steelmaking (BOS) [6]. The quality of recycled steel scrap used in EAF is variable and much is characterized by a huge volume of highly diverse impurities, resulting in EAF dust contaminated by environmentally-threatening Dioxin [7]. However, the high zinc content from galvanizing steel surfaces makes EAF dust an important source of zinc [1, 2].

This study documents the experience of a steel plant using the Primus process developed by Paul Wurth in Luxembourg which can simultaneously reclaim steel and crude zinc oxide [2]. Increased impurity of the crude zinc oxide raises the difficulty of the purification process at downstream factories and thus directly affects its value. The company would thus benefit from developing an efficient manufacturing process to transform crude zinc oxide into valuable high-purity zinc flakes.

Zinc metal smelting technologies can be grouped into two categories: pyrometallurgy uses a carbon reduction process under high temperatures, and hydrometallurgy uses a solvent as a leaching agent followed by electrolysis [1, 8]. Hydrometallurgy can also be divided into two systems, acidic leach and alkaline leach. To prevent dissolving iron oxide in the product, and to simplify the purification procedure, this study uses alkaline hydrometallurgy through a three-step process including leaching, purification and electrolysis [1, 6, 7]. Nevertheless, the leach agent still contains a significant amount of lead ions which must be removed as much as possible to ensure the purity of the electrodeposited zinc power [2, 9]. The purification procedure is based on the displacement reactions of the reduction potential and the crude zinc powder is the general displacer [9]. Other metals with lower oxidizing powers are reduced into deposits and removed from the product, while zinc is oxidized into zinc ions and becomes part of the product in the electrolysis procedure.

Since the displacer is often added in excessive amounts to induce a complete reaction, the deposits from the purification procedure are mixed with a large amount of unreacted zinc powder, resulting not only in high wastage but also presenting disadvantages for the subsequent reclamation. For this reason, this study also tested the feasibility of using sheet zinc recycled from MZ batteries as the displacer, rather than crude zinc powder.

Fig. 13.1 Appearance of crude zinc dioxide

13.2 Experiments and Materials

13.2.1 Sample Pre-processing

Figure 13.1 shows crude zinc oxide collected from the factory. The crude zinc oxide is sieved with a 60mesh screen and then dried in an over at 103 °C. With reference to the standard NIEA S321.63B method published by the Environmental Analysis Laboratory (EPA), metal component analysis is conducted using an inductively coupled plasma atomic emission spectrometer (ICP-OES).

13.2.2 Leaching Experiment

The solid-liquid ratio was 1:10 throughout the experiment. First, 5 N-$NaOH_{(aq)}$ was used as the leach agent under room temperature and the solution was well stirred to ensure contact between the solids and liquids. The zinc content of the leach solution was analyzed based on standard leaching times (i.e., 4, 8, 12, 24, 48, and 72 h). Four different concentrations of $NaOH_{(aq)}$, 3, 5, 7 and 9 N, were prepared as the leach solutions and the zinc content leached from the above solutions was analyzed to determine the best concentration for the leaching agent. To derive the most effective heating temperature, the 5 N-$NaOH_{(aq)}$ leaching agent is tested at 60 °C to determine the effect on zinc content.

The leach volume is defined as the number of grams of zinc dissolved from every 100 grams of crude zinc oxide, following the following formula:

$$\begin{aligned} &\text{leach volume}(\text{g}) = \{[(\text{A} * \text{D}/1000000) * \text{V}]/\text{W}\} * 100 \\ &\text{A} = \text{AA analysis value}\,(\text{mg}/\text{L}) \\ &\text{D} = \text{dilution factor} \\ &\text{V} = \text{leach solution volume}\,(\text{ml}) \\ &\text{W} = \text{weight of crude zinc oxide}\,(\text{g}). \end{aligned} \tag{13.1}$$

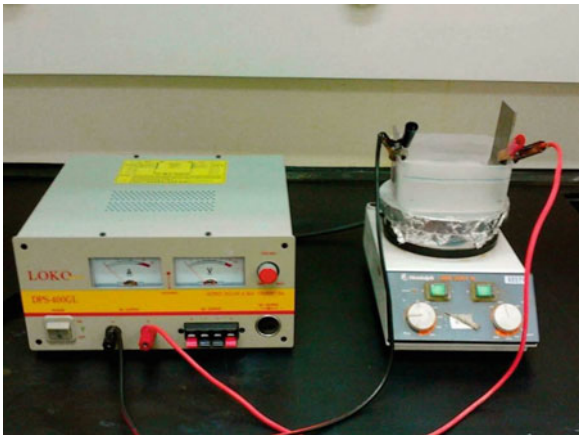

Fig. 13.2 Electrolysis device

13.2.3 Purification Experiment

Zinc shells recycled from batteries were initially cleaned in an ultrasonic cleaning machine. The cleaned zinc shell and zinc powder were then added into the leach agents for a 24-h displacement reaction. The liquid was drained and the residues were then repeatedly washed with RO processed water until the PH value dropped to neutral before they were filtered out by drying in nitrogen gas. The dried residues were then weighed and melted in a double boiler, followed by ICP-OES analysis of the amount of metal content.

13.2.4 Electrolysis Analysis

Using a stainless steel board as the anode and a magnesium board as the cathode, electrolysis was carried out for zinc reclamation using the device shown in Fig. 13.2. The magnesium board was grinded with sandpaper of various grades to compare the effects of different board roughness on the final product.

13.3 Results and Discussion

13.3.1 Composition of Crude Zinc Dioxide

Table 13.1 summarizes the composition of the crude zinc dioxide used in this study, with iron, zinc and lead being the major elements, and low ratios of other elements favorable conditions for the reclamation of metals such as zinc and lead.

Table 13.1 Composition of crude zinc dioxide (metals only)

Metals	Percentage in total composition
Fe	51.0697
Zn	45.5158
Pb	3.2781
Mn	0.0909
Si	0.0224
Cu	0.0105
Cd	0.0091
Cr	0.0035

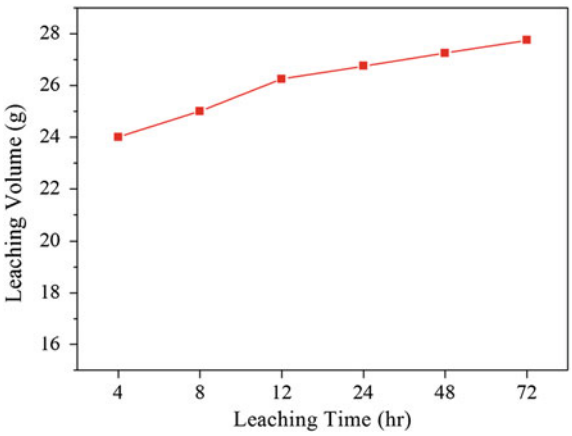

Fig. 13.3 Effect of leaching time on leaching volume

Table 13.1 shows the ICP-OES result of the percentage of metal compositions. Iron, zinc and lead respectively make up 41.0, 36.5 and 2.6 % of the crude zinc dioxide, while other metals make up 19.9 %.

13.3.2 Leaching Experiment

As shown in Table 13.3, longer leaching duration results in a larger volume of reclaimed zinc; however, the difference in the effect of leaching between 48 and 72 h is rather insignificant. In actual factory practice, longer reaction hours imply the need for larger reaction tanks. To avoid wasted investment, a time of 48 h is chosen for the follow-up experiments (Figs. 13.3 and 13.4).

Figure 13.3 shows that leaching agent concentration is positively correlated with the volume of zinc leached; however, there is no significant increase in the volume of the leached zinc when the concentration exceeds 7 N. Due to cost considerations, 7 N is determined to be the optimum NaOH leaching agent concentration. Under this criterion, approximately 36 g of zinc can be reclaimed from

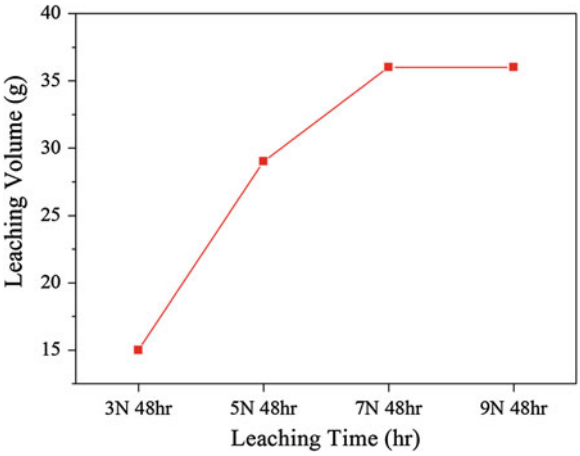

Fig. 13.4 Effect of leaching agent concentration on leaching volume

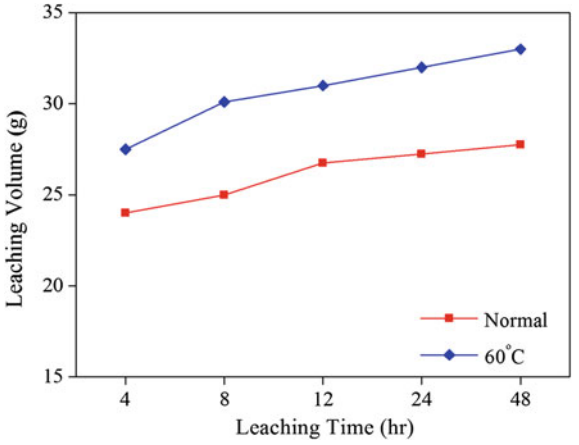

Fig. 13.5 Effect of leaching temperature on leaching volume

every 100 g of crude zinc dioxide, which is almost the entire zinc content in the crude zinc dioxide.

Figure 13.5 shows that higher temperatures enhance the leaching effect but, as seen in Fig. 13.4, only given increased leaching agent concentrations. However, the cost effectiveness of raising the temperature to shorten the leaching time remains to be confirmed before being applied to actual factory practice.

13.3.3 Leaching Solution Purification

As shown in Table 13.2, after the displacement reaction, metals with oxidation potential lower than zinc in the leaching agent are significantly reduced and the

Table 13.2 Effect of leach agent purification with displacement method

Metal name	Percentage before displacement	Zinc percentage after displacement (zinc powder)	Zinc percentage after displacement (sheet zinc)
Zn	88.7889	98.6151	98.4927
Pb	9.6149	0.0014	0.0085
Si	1.3112	1.3775	1.4720
Cu	0.2181	0.0001	0.0001
Cd	0.0317	0.0015	0.0153
Cr	0.0276	0.0018	0.0062
Fe	0.0075	0.0023	0.0050
Mn	0.0001	0.0004	0.0002

Table 13.3 Composition of displacement deposit

Name of metal	Percentage of zinc in the deposit (zinc powder)	Percentage of zinc in the deposit (sheet zinc)
Pb	49.6467	97.6332
Zn	4.2813	1.4461
Cu	0.6712	0.6057
Si	0.2072	0.1316
Cd	0.0710	0.0650
Cr	0.0657	0.0710
Fe	0.0367	0.0446
Mn	0.0201	0.0028

portion of zinc is relatively increased. Table 13.3 shows that high-purity lead slag (97.6 %) can be reclaimed by using sheet zinc recycled from batteries as the displacer. Due to the small particle size, the unreacted zinc powder is coated by the lead slag, making it difficult to separate. This not only decreases the purity of the lead slag, but also creates wastage. It is noteworthy that using sheet zinc as the displacer results in the same effect as zinc powder, but at 1/30th the cost. Therefore, using sheet zinc as the displacer not only reduces costs but also contributes to improved lead reclamation.

13.3.4 Electrolysis Experiment

In this experiment, the stainless steel anode board and the leaching agent concentration are fixed; only the roughness of the magnesium cathode board and the size of the electric current are variable to explore the electrolysis results in the products. Figure 13.6 compares the products reclaimed from the magnesium boards grinded by 250#, 500#, 2000# and 3000# sandpaper the results show that

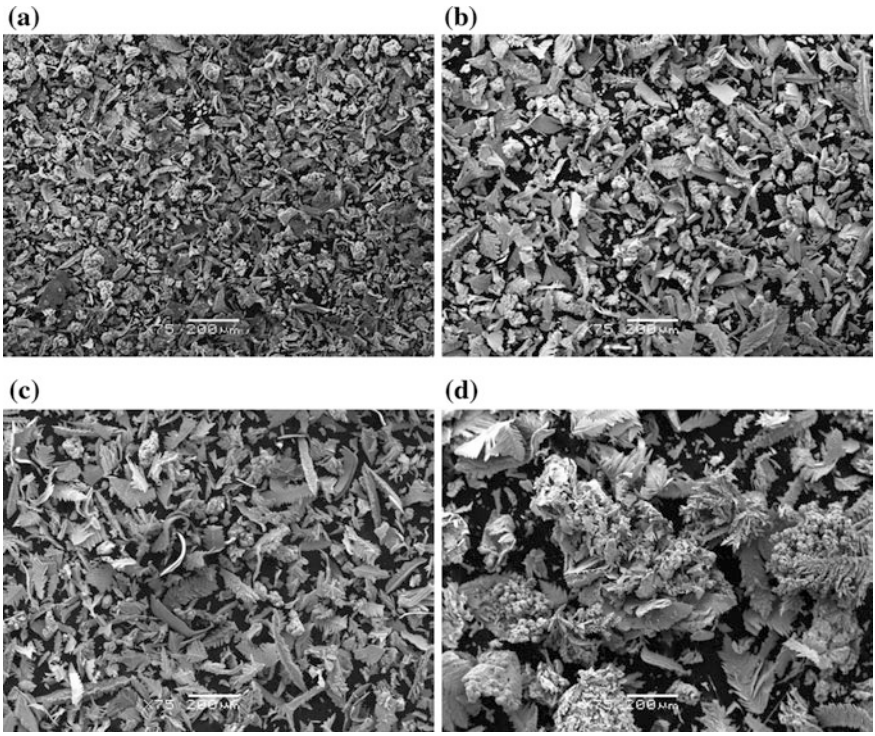

Fig. 13.6 SEM photograph of electrolyzed zinc powder appearance from magnesium board grinded with **a** 250#; **b** 500#; **c** 2000#; **d** 3000# sandpaper

the diameter of the zinc powder increases gradually with the fineness of the sandpaper. This phenomenon can be observed through SEM photos and reconfirmed through comparison under identical magnification.

13.4 Conclusion

High purity zinc flakes can be produced from low quality crude zinc dioxide through a three-step production process of leaching, purification and electrolysis. A solution of 7 N-NaOH is used as the leaching agent with a solid-liquid ratio of 1:10. The zinc dissolution rate approaches its maximum after forty-eight hours of stirring at room temperature. The leaching solution contains a large volume of lead which needs to be removed to avoid degrading the purity of the electrolyzed zinc powder. In the process of purifying the leaching agent, the effect of using sheet zinc recycled from batteries as a displacer is comparable to the effect of using zinc powder, but at 1/30th the cost, and with the added benefit of reclaiming high purity

lead in the form of slag as a byproduct. Using smoother magnesium board surfaces increases the diameter of the zinc flake particles.

References

1. Lo, H-R. (1998). *Caustic extraction of zinc from electric arc furnace steel dust*. Department of Chemical and Materials Engineering, National Kaohsiung University of Applied Sciences, Kaohsiung.
2. Chen, W-S, Zhou, W-S., Wu, J-Y., Shen, Y-H, Cai, M-H. (2010). *Steel smelting dust processing in Taiwan*. Industrial Pollution Prevention.
3. Carrillo-Abad, J., Garcia-Gabaldon, M., Ortega, E., Perez-Herranz, V. (2011). Electrochemical recovery of zinc from the spent pickling baths coming from the hot dip galvanizing industry. Potentiostatic operation. *Separation and Purification Technology, 81*(2), 200–207.
4. Wua,M., She, J-H., Nakano, Michio. (2001). An expert control system using neural networks for the electrolytic process in zinc hydrometallurgy. *Engineering Applications of Artificial Intelligence*, *14*(5), 547–702.
5. Zheng, H., Gu, Z., Zheng, Y. (2007). *Electrorefining zinc dross in ammoniacal ammonium chloride system*. ScienceDirect.
6. Chen, T-M. (1999). *Recycling zinc from electric arc furnace dust through alkaline dissolution*. School of Environmental Engineering, National Pingtung University of Science and Technology, Neipu.
7. Zhang, T-J., Wang C-F., Wang Y-R., Tu B-C., Wei Y-H., Qiu Y-Z. et al. (1995). *Characteristics and recycling of steel smelting dust*. Environmental Protection Agency, Executive Yuan, Development Program.
8. Zhao, Y., Stanforth, R. (2000). Technical note extraction of zinc from zinc ferrites by fusion with caustic soda. *Minerals Engineering*, *13*(13), 1417–1421.
9. You, Z-F., Chang, C-K., Tu, Y-R., Shen, M-L., Chen Q-Y. (2012). *Recycling batteries through acid dissolution, chemical displacement, and ferrite program*. Environmental Protection Agency, Executive Yuan, Development Program.

Chapter 14
Process Parameters Optimization of Micro Plasma Welding for Small-Scaled SUS 304 Pipe

Xiao-Qing Lin, Jhao-Jhong Su, Chao-Ming Hsu and Ah-Der Lin

Abstract This study discusses the parameter optimization of a SUS304 micro-tube using a micro-plasma welding process. The micro plasma welding machine used in this study is a self-designed, semi-automatic welding machine with self-designed fitting clasps. The Taguchi method was used to design an experiment for the optimization of the process parameters including welding current, speed of the automatic turntable, and the flow rate of the back-blown air. The standard of optimization is the tensile strength and the auxiliary standards include metallographic microscopic observation of the weld bead and tensile breaking forms.

Keywords Taguchi method · Micro-plasma welding process · SUS304 · Optimization

14.1 Introduction

Few studies have been conducted on tube welding for traditional manufacturing. This study focuses on using adjustments to welding device parameters to achieve full pipe permeation [1]. The orthogonal table proposed by Taguchi is applied as

X.-Q. Lin · J.-J. Su · C.-M. Hsu
Department of Mechanical Engineering, National Kaohsiung University of Applied Science, Kaohsiung 80778, Taiwan, Republic of China
e-mail: xiaoqing.linn@gmail.com

J.-J. Su
e-mail: jhaojhong.su@gmail.com

C.-M. Hsu
e-mail: jammy@cc.kuas.edu.tw

A.-D. Lin (✉)
Department of Mechanical Engineering, Cheng-Shiu University, Kaohsiung 83347, Taiwan, Republic of China
e-mail: ahder@csu.edu.tw

J. Juang et al. (eds.), *Proceedings of the 2nd International Conference on Intelligent Technologies and Engineering Systems (ICITES2013)*, Lecture Notes in Electrical Engineering 293,
DOI: 10.1007/978-3-319-04573-3_14,

Fig. 14.1 Micro plasma welding system equipments

the basis for pursuing optimized processing parameters. Three experiments, tensile test, fracture surface analysis and metallographic microscopic observation, were conducted, with ANOVA analysis indicating the influence of the control factors on the tensile strength of the test pieces [2].

14.2 Experiment Setting

Experimental equipment used in this study include a welding machine, a cooling water tank, an air compressor, three bottles of pure argon, a bottle of argon mixed with hydrogen, and a micro welding automatic turntable (with control panel), which was modified from a desktop lathe machine. Figure 14.1 shows the equipment used in the micro plasma welding system [3, 4].

14.3 Taguchi Experiment Method

14.3.1 Experimental Process

This study started with parameter setting, followed by the pre-treatment of the test pieces, setup and testing of the machines, and planning of the orthogonal table for the welding process based on the Taguchi method. The entire welding process consisted of 16 sets of experiments, with each set of experiments tested on four thin tube samples. Optimized process parameters were predicted based on the ANOVA analysis of the tensile test results, metallographic microscopic observation, and fracture surface analysis. Further experiments were carried out to verify the accuracy of the parameters. The experiment flowchart is shown in Fig. 14.2.

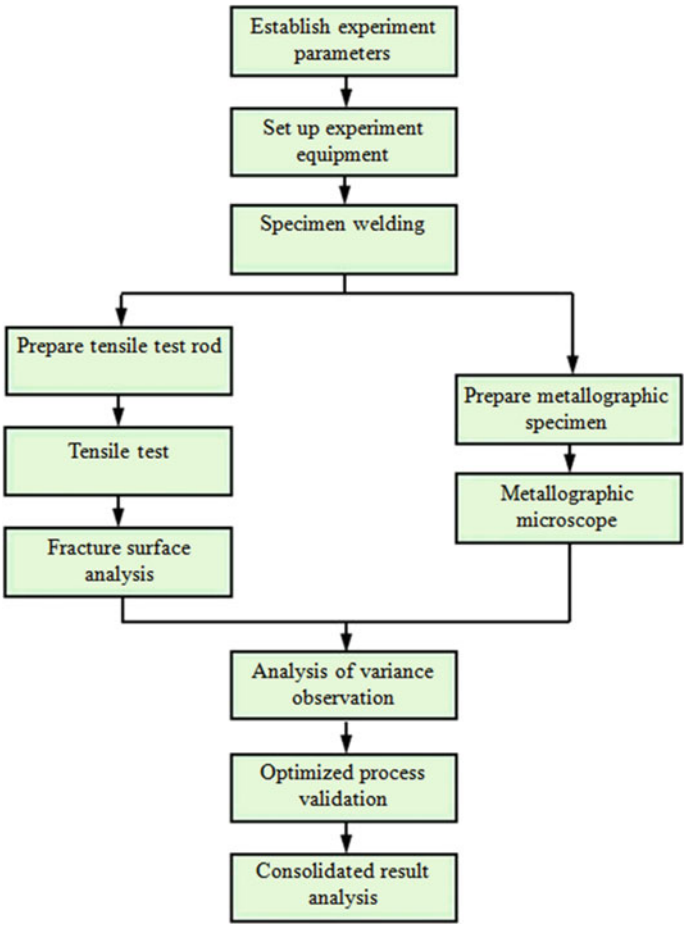

Fig. 14.2 Experimental flowchart

14.3.2 S/N Ratio

In the Taguchi method, the standard applied for robustness assessment is the ratio of signal and noise, S/N ratio. Equation (14.1) is applied in this study to evaluate the mechanical properties of the welded experimental pieces. LTB proposes that quality improves with a higher.

The S/N ratio is found as follows:

$$S/N = -10 \log \frac{\sum_{i=1}^{n} \frac{1}{y_i^2}}{n} \tag{14.1}$$

where n is the number of experimental measurements and y_i is the measured value.

For example, the S/N reaction value of factor A at the first level is the sum of the S/N ratios of all welding processes using the A1 parameter divided by the number of groups, which is represented by $\overline{\eta}_{A1}$. The average variation amount from the first level to the second level is represented by E_A^{1-2}. The formula is shown in Eqs. (14.2) and (14.3).

The S/N response value (a sample of the first level of factor A) is derived as follows:

$$\overline{\eta}_{A1} = \frac{\sum_{i=1}^{n} S/N}{n} \tag{14.2}$$

where n is the number of sets at the same level.

The average variation amount between levels (i.e., variations of factor A between the first and the second level) is derived as follows:

$$E_A^{1-2} = \overline{\eta}_{A2} - \overline{\eta}_{A1}. \tag{14.3}$$

14.3.3 Orthogonal Table

In this study, prior to parameter setting, initial testing was conducted on the range of parameters. The range of the control factors were selected based on the results of initial testing. Welding current, welding rotation speed and flow of the back-blown gas were used as the control factors, with four levels in each factor. Fixed parameters included the tungsten rod angle, ion gas flow, shielding gas flow, and isolation gas flow. SUS304 seamed stainless steel pipe was used as experimental specimens. Table 14.1 is the control factors planning table which summarizes the experimental parameters. Table 14.2 is the orthogonal table of the Taguchi method L_{16} (4^3). Table 14.3 is the fixed parameters and specifications of the test pieces.

14.4 Results and Discussion

In this study, the tensile strength is the major evaluation basis of the welding process parameters, thus tests were simultaneously conducted on the base materials and welding test pieces to provide a basis for comparison before and after welding.

The original base material was processed with work hardening through the pull process thus its tensile strength was far higher than that of ordinary SUS304 stainless steel. The fractured surface indicated that the presented structure of the original base material was characterized by ductility fractures. Table 14.4 presents the tensile strength test values while Fig. 14.3 presents the metallographic microstructure of the original base material, which was set as the control group.

Table 14.1 Experimental parameters: control factors planning table

	A Welding current (A)	B Welding rotation speed (RPM)	C Back-blown gas flow (kgf/cm^2)
Level 1	3	4	10
Level 2	4	6	13
Level 3	5	8	16
Level 4	6	10	19

Table 14.2 Orthogonal table of Taguchi method L_{16} (43)

Process	A Welding current (A)	B Welding rotation speed (RPM)	C Back-blown gas flow (kgf/cm^2)
1	1	1	1
2	1	2	2
3	1	3	3
4	1	4	4
5	2	1	2
6	2	2	1
7	2	3	4
8	2	4	3
9	3	1	3
10	3	2	4
11	3	3	1
12	3	4	2
13	4	1	4
14	4	2	3
15	4	3	2
16	4	4	1

Table 14.3 Fixed parameters and material specifications of test pieces

Fixed parameters	Specifications	Material specifications of test pieces	
Tungsten rod diameter	1.0 mm	Test pieces material	SUS304
Tungsten rod angle	35°	Test pieces form	Seam pipe
Fire nozzle diameter	1.2 mm	Test pieces outer diameter	4 mm
Electric ion gas flow	0.2 l/min	Test pieces thickness	0.5 mm
Protect gas flow	5 l/min	Test pieces length	40 mm
Isolated gas flow	15 kgf/cm^3		

Figure 14.4 shows the fracture surface of the original base material. Based on the above S/N ratio formula calculated the manufacturing process S/N ratio (Table 14.5) and the S/N ratio factor reaction of each set. Figure 14.5 shows the S/N ratio factor reaction (Table 14.6).

The S/N ratio factor reaction diagram based on the Taguchi method shows that the combination of optimized parameters in the welding process is A3B2C2. The

Table 14.4 Tensile strength value of the original base material

Original base material	
Test piece	Tensile strength (N/mm^2)
Original base material 1	1243.08
Original base material 2	1252.00
Original base material 3	1257.54
Original base material 4	1257.72

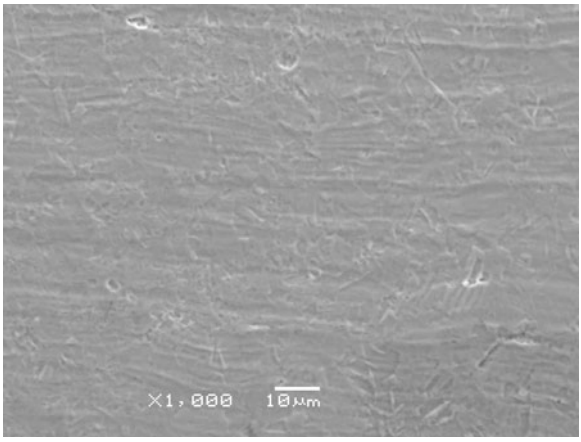

Fig. 14.3 Metallographic microstructure of the original base material, magnified −1000x

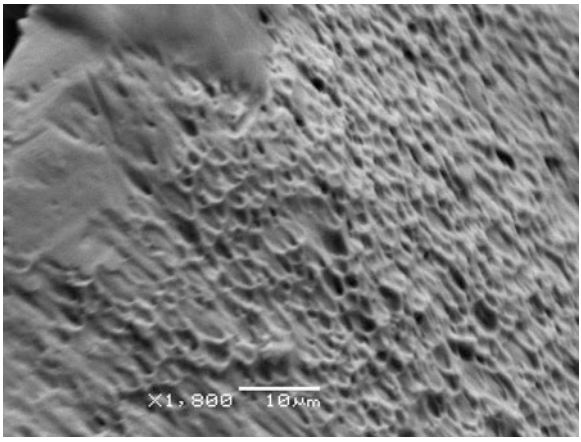

Fig. 14.4 Fractured surface of the original base material (ductility fracture), magnified −1800x

S/N ratio of the optimized welding process predicted by the Taguchi method is 61.22. However, empirical experiments verified the existence of a gap between the actual and predicted S/N ratio. The verification data of the optimized parameters is shown in Table 14.7.

Table 14.5 Tensile strength of each welding process and its S/N ratio

Welding process	A	B	C	Tensile strength (N/mm^2)			Average	S	S/N
				Group 1	Group 2	Group 3			
1	1	1	1	84.44		665.72	375.08	411.03	41.47
2	1	2	2	378.83	410.61	616.99	468.81	129.31	52.86
3	1	3	3	193.52	429.71	384.01	335.75	125.27	48.87
4	1	4	4	136.22	262.08	472.38	290.23	169.84	46.14
5	2	1	2	439.71	610.56	508.26	519.51	85.98	54.08
6	2	2	1	670.54	614.13	528.79	604.49	71.37	55.50
7	2	3	4	217.09	609.49		413.29	277.47	49.22
8	2	4	3	403.47	553.43	256.18	404.36	148.63	50.85
9	3	1	3	709.64	704.11	695.54	703.10	7.10	56.94
10	3	2	4	747.85	715.53	684.83	716.07	31.51	57.08
11	3	3	1	753.02	743.38	723.92	740.11	14.82	57.38
12	3	4	2	763.2	699.64	719.64	727.49	32.50	57.22
13	4	1	4	544.5	553.07	516.12	537.90	19.34	54.60
14	4	2	3	563.96	613.06	651.62	609.55	43.94	55.65
15	4	3	2	611.09	639.3	665.9	638.76	27.41	56.09
16	4	4	1	640.91	657.33	640.37	646.20	9.64	56.21

S/N average value = 53.14

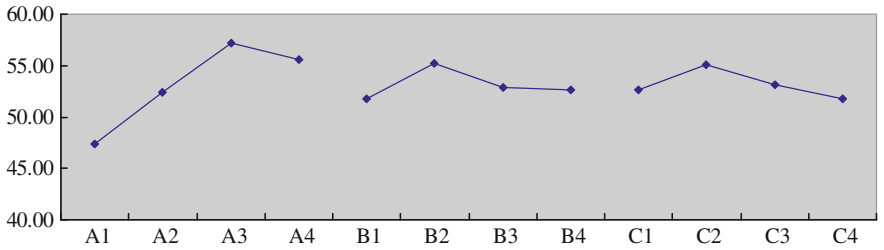

Fig. 14.5 S/N ration factor reaction

Table 14.6 S/N ratio factor reaction

	A	B	C
Level 1	47.34	51.77	52.64
Level 2	52.41	55.27	55.06
Level 3	57.16	52.89	53.08
Level 4	55.64	52.61	51.76
E^{1-2}	5.08	3.50	2.42
E^{2-3}	4.74	−2.38	−1.98
E^{3-4}	−1.52	−0.29	−1.32
Range	9.82	3.50	3.30
Rank	1	2	3

Table 14.7 Verification data of optimized parameter combination (A3B2C2)

Welding process	A	B	C	Tensile strength (N/mm^2)			Average	S	S/N
				Group 1	Group 2	Group 3			
	3	2	2	679.83	710.71	551.47	647.34	84.45	56.06

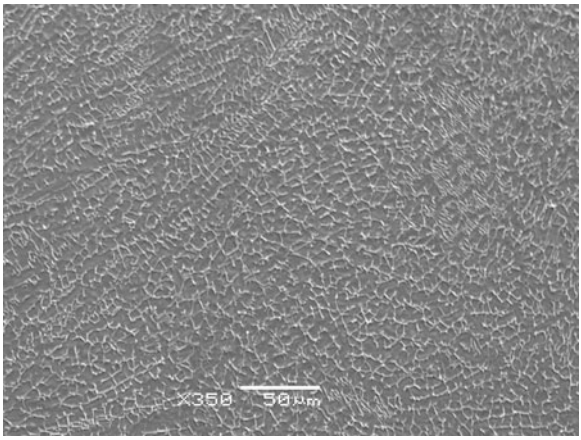

Fig. 14.6 Optimizing process of welding bead structure 350x

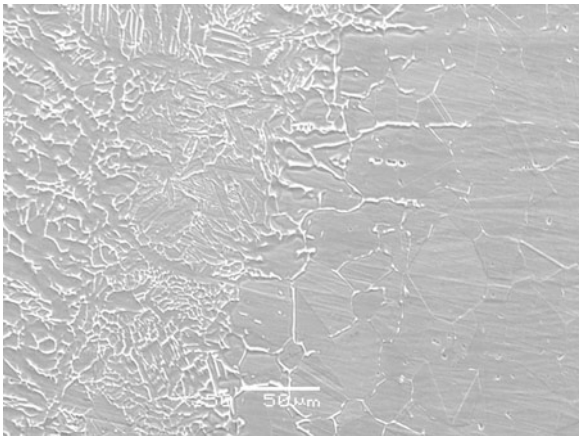

Fig. 14.7 Optimizing process of welding bead structure and heat affected area 350x

The statistical analysis results above indicate insufficient control over the experimental factors and fail to provide an overall explanation of this research. Photos of the metallographic microscopic observation provide supplementary results not expressed by the Taguchi analysis. The photos show insufficient permeation of the weld bead on part of the test pieces (with all parameters configures for welding processes 3 and 4) which is seen as the major cause of the unstable tensile strength.

14.5 Conclusion

1. The Taguchi method was used to predict the optimized parameter combination A3B2C2, which is considered representative to a certain level. The structure of the weld bead is shown in Figs. 14.6 and 14.7 (Fig. 14.6 shows the weld bead structure, while Fig. 14.7 shows the right side of the weld bead structure and the left-side of the structure of the heat affected area).
2. Based on Taguchi analysis and the principle of half, factor A (welding current) is found to be the most crucial factor in the S/N ratio factor reaction, followed by factor B (welding rotation times). Factor C is found to have very little impact.
3. The uneven thickness of permeation is caused the instability in the parameter combination of welding processes 1–8, the uneven thickness of permeation is caused the instability in the tensile strength, which can be modified by adjusting the rotation speed to achieve full permeation.

References

1. Zhou, Z.-B., Cai P.-C., & Guo Y.-C. (2003). *Welding Institution*. Taipei: Chuan Hwa Science & Technology Book Co.
2. Lee, H.-H. (2010). *Taguchi methods principles and practices of quality design*. Taipei: Gau Lih Book Co., Ltd.
3. Lai, G.-Z. (2010). *Development of plus type process of gas tungsten arc welding on 6061 aluminum alloy*. Thesis, Department of Mechanical Engineering, Cheng Shiu University.
4. Lin, S.-J., Ye, J.-W., Liu Z.-F., Li, & S.-L. (2003). *Materials engineering experiments and theory*. Taipei: Chuan Hwa Science & Technology Book Co.

Chapter 15
The Fatigue Life Analysis of the VCSEL with Sn/Pb and Sn/Ag/Cu Solder

Bo-Rong Qiu, Cheng-Han Lin, Ah-Der Lin and Chao-Ming Hsu

Abstract The Coffin-Manson equations of Sn/Ag/Cu and Sn/Pb solder joints are presented in this paper. The experimental results of CSP thermal cycle fatigue test and ball shear test are used to formulate Coffin-Manson equations. The maximum amplitude of equivalent plastic shear strain corresponding to these two experiments are employed. The MARC finite element package is used to calculate the plastic shear strain. Different published fatigue experiment results have been used to show the accuracy and the feasibility of these proposed equations. The 3-D finite element models of the VCSEL assembly are employed to simulate the thermal cycling fatigue. Results indicate that the fatigue life of solder predicted by using the proposed equations have good agreement with those measured from experimental tests.

Keywords Coffin-Manson · VCSEL · Equivalent plastic shear strain

B.-R. Qiu
Department of Mechanical Engineering, National Kaohsiung University of Applied Science, Kaohsiung 80778, Taiwan, Republic of China
e-mail: ab88321@yahoo.com.tw

C.-H. Lin · A.-D. Lin · C.-M. Hsu (✉)
Department of Mechanical Engineering, Cheng-Shiu University, Kaohsiung 83347, Taiwan, Republic of China
e-mail: jammy@cc.kuas.edu.tw

C.-H. Lin
e-mail: chenghan.linux@gmail.com

A.-D. Lin
e-mail: ahder@csu.edu.tw

J. Juang et al. (eds.), *Proceedings of the 2nd International Conference on Intelligent Technologies and Engineering Systems (ICITES2013)*, Lecture Notes in Electrical Engineering 293,
DOI: 10.1007/978-3-319-04573-3_15,

15.1 Introduction

According to a 2003 report from the Industrial Technology Research Institute (ITRI) [1], BGA and CSP are the dominant technologies in Taiwan's packaging industry, while I was in demand as a high-level substrate, and the market for FC was expected to begin expanding in the latter half of 2004. Therefore, the report said, solder balls would be continuously and widely applied in packaging industry production process. Sn/Ag/Cu alloy is a mild lead-free solder (with a molten point between 200 and 230 °C). It features good wettability, high strength, and high creep resistance, and is a highly replacement for Sn/Pb solder. Currently, a standard has not been set for the composition percentage of Sn/Ag/Cu in solder. Different national organizations have recommended various replacements, with the United States National Electronics Manufacturing Initiative (NEMI), recommending Sn/3.4–4.1Ag/0.45–0.9Cu, Japan's Electronics and Information Technology Industries Association (JEITA) recommending Sn/3.0Ag/0.5Cu, and the EU's IDEALS plan recommending Sn/1.0Ag/0.5Cu [2].

The calculation of fatigue life as a function of energy was first proposed in 1911 [3], and is generally expressed in terms of cyclic loading. Most solders have a fatigue life around or below 10^3 cycles, which is considered a low-cycle fatigue life range. Coffin-Manson's low cycle fatigue life model can be used to calculate the cycles of fatigue life of various types of materials or solder. Strain is local, and size is not a detrimental factor for isotropic materials. Therefore, this research adopts the Solomon model [4] as a reference and uses plastic sheer strain to predict the fatigue life of a solder ball.

The optical transceiver module uses two types of light sources, a laser diode (LD) and a laser emitting diode (LED). Depending on the light emission mode, LDs can be categorized as edge-emitting of surface-emitting. VCSEL, a type of surface-emitting laser, offers advantages of high transmission speed and low cost, making it suitable for mid-to-long distance telecommunications.

A surface-emitting laser diode module features three major components [5], see Fig. 15.1:

(1) VCSEL Structure: Gallium arsenide (GaAs) is the major component of this structure. Aluminum is added in the epitaxial process, but has a rather limited influence to the mechanical properties of the epitaxial layer. Therefore, the whole structure is GaAs when conducting the analyses.
(2) Silicon Bench.
(3) A micro solder ball is used to connect the VCSEL structure and the silicon bench, as shown in Fig. 15.1.

Flip chip (FC) technology is used with a micro solder ball, to connect the VCSEL structure and the silicon bench. Due to the significant differences in the thermal expansion coefficient between the upper and lower layers of the micro solder balls, the micro solder ball is easily damaged by relative displacement in its upper and lower layers when the whole package experiences thermal expansion.

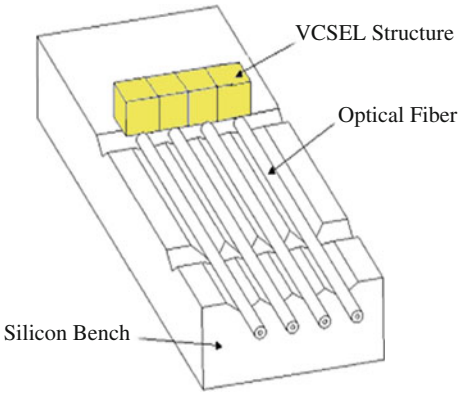

Fig. 15.1 Schematic diagram of surface-emitting laser diode module packaging

15.2 Relevant Theories and Analysis of Finite Elements

For the plasticity hardening rule, this research adopts the isotropic strain-hardening rule to simulate the plastic behavior while ignoring the Bauschinger effect. The von Mises yield criterion is applied as the criterion for yield determination, and the stress–strain curve of perfect elasticity or perfectly-elastic plastic materials is applied for all materials. A MARC subroutine is written only for the solder material to describe the stress–strain curve in relation to temperature fluctuations.

MARC is a software package for finite element analysis of thermal and mechanical coupling. First, use the heat transfer element to calculate the increment in each node, and then calculated the displacement caused by the rise in temperature. The horizontal and vertical convective heat transfer coefficient h is derived from the natural convection formula proposed by Ellison [6], and the average convective heat transfer coefficient h_m is derived from the method organized by Fan [7].

15.3 Prediction of Solder Ball Fatigue Life

Finite elements are used to simulate the equivalent plastic strain $\Delta\bar{\gamma}^p$ generated from the micro solder ball when the VCSEL components are heated, which is then used to predict the fatigue life of micro solder balls. The simulation components include the VCSEL structure, the micro solder ball, and the underlying silicon substrate. The VCSEL structure is symmetrical; thus, only half of the structure is constructed for the simulation. Figure 15.2 shows the finite elements mesh and material distribution of the VCSEL components. The upper part of the illustration shows the overall model of VCSEL elements, and the left half, framed by green dash lines, is the simulated portion. The lower part of the illustration presents a schematic diagram of the simulated portion from a different angle. The length,

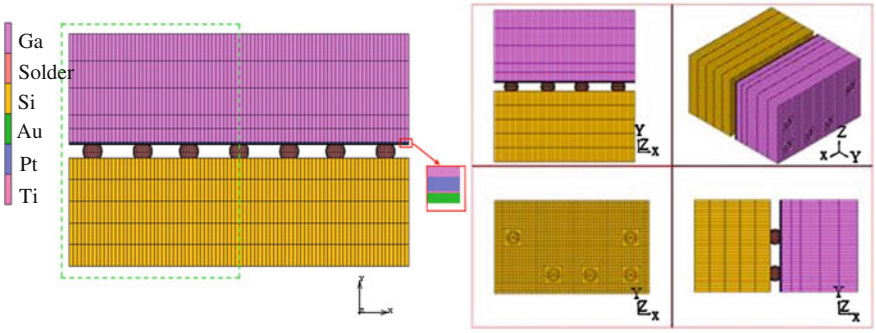

Fig. 15.2 Finite elements mesh and material distribution of VCSEL elements

Table 15.1 Material factor of VCSEL components

Property	GaAs	Si	Au	Pt	Ti
Young's modulus (GPa)	34.95	190	78	172	110
Poisson ratio	0.31	0.28	0.42	0.39	0.34
Yielding strength (MPa)	42.03	34.45	207	205	140
CTE (ppm/°C)	5.72	2.4	14.2	9.5	8.9
Conductivity (W/m °K)	54	148	315	71.1	17
Specific heat (J/kg °C)	322	712	128	132	522
Mass density (kg/m^3)	5320	2330	19320	21450	4510

width, and height of the VCSEL structure are 1000, 300, and 265.59 μm respectively. The diameter of the micro solder ball is 50 μm and its height is 30 μm. The length, width, and height of the silicon substrate board are 4200, 12000, and 24000 μm respectively. Only the part directly below the structure, which has an equivalent size is used for the analysis. For material factors, please refer to Table 15.1.

For the boundary conditions, set the symmetric displacement of all nodes on the symmetric plane to 0. The symmetric plane is heat isolated, so the exterior surface of the components is subjected thermal convection. The coefficient is obtained from the modifier formulas proposed by Ellison. The convergence criterion is derived based on the Residual Force principles, and the default value is 0.1. Computation is done based on an 8-node hexagonal 3-D element, which consists of a total of 15,468 elements and 19,070 nodes. The equivalent shear strain is used as the analysis parameter to derive the fatigue life formula for Sn/Pb and lead-free Sn/Ag/Cu solder balls, as listed below.

The prediction formula for the fatigue life of a Sn/Ag/Cu solder ball based on thrust test and thermal-cycle test of the solder ball is as follows:

$$N_f = 11.313527 \times (\Delta\bar{\gamma}^p)^{-2.044624} \tag{15.1}$$

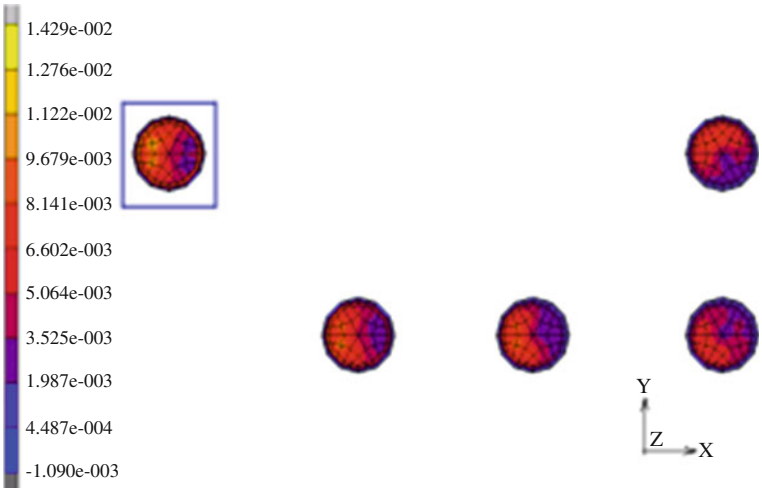

Fig. 15.3 Schematic diagram of equivalent plastic strain distribution of the micro solder ball

The prediction formula for the fatigue life of a Sn/Ag/Cu solder ball based on the thrust test and isothermal low cycle fatigue test of the solder ball is as follows:

$$N_f = 10.327870 \times (\Delta\bar{\gamma}^p)^{-1.957369} \tag{15.2}$$

The prediction formula for the fatigue life of Sn/Pb solder balls based on the thrust test and isothermal low cycle fatigue test of the solder ball is as follows:

$$N_f = 3.506668 \times (\Delta\bar{\gamma}^p)^{-1.6425} \tag{15.3}$$

15.4 Results and Discussion

In the finite element simulation, if the silicon substrate removed and observed the $\bar{\gamma}^p$ distribution of the equivalent plastic strain from bottom to top, along the direction indicated by the blue arrow in the upper part of Fig. 15.3, that can see a $\bar{\gamma}^p$ distribution of the underside of the micro solder balls, similar to the structure illustrated in Fig. 15.3. The ones framed with blue solid lines are the solder balls furthest from the symmetric plane. Regardless of whether the VCSEL components are under high or low temperature, $\bar{\gamma}^p$ of the solder balls furthest from the symmetric plane is still greater than that of the others. Figure 15.4a and b respectively present examples of $\bar{\gamma}^p$ distributions for Sn/Ag/Cu micro solder balls at high and low temperatures under the JESD22-A104A regulatory process.

Figure 15.5 shows the equivalent plastic shear strain–temperature–time relationship of a specific node drawn on the mesh, such as point D, through a thermal

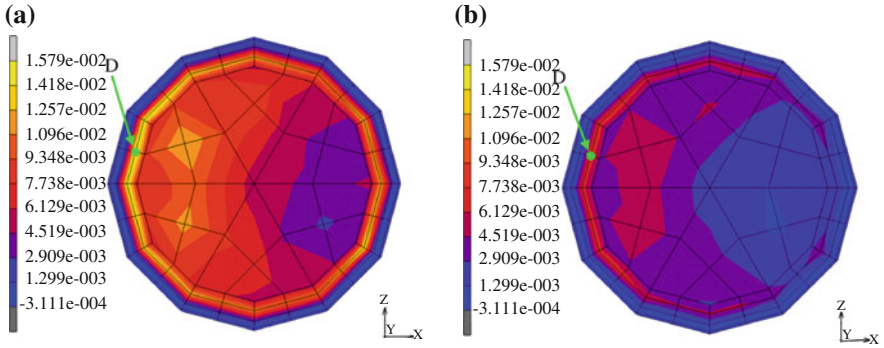

Fig. 15.4 **a** Schematic diagram of Sn/Ag/Cu micro solder ball distribution under 125 °C high temperature. **b** The schematic diagram of $\bar{\gamma}^p$ distribution under −40 °C low temperature

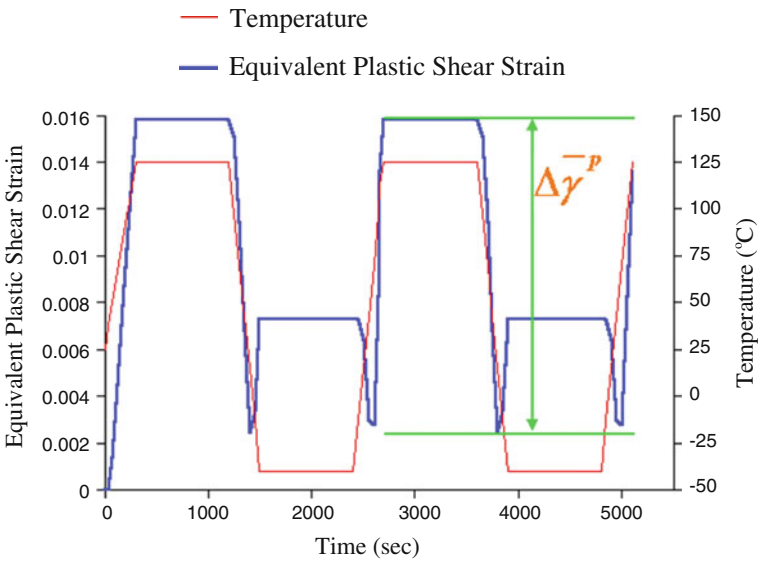

Fig. 15.5 Temperature–equivalent plastic shear strain diagram of D point

cycle. The area framed with fine red lines is the temperature–time curve under the JESD22-A104A standard. The first 300 s is the preheating phase followed by the first thermal cycle (300–2,700 s) and the second thermal cycle (2,700–5,100 s). The blue bold line is the equivalent plastic shear strain–time curve. The difference between the maximum and the minimum values of $\bar{\gamma}^p$ in a cycle (i.e., maximum minus minimum) is the equivalent plastic shear strain amplitude $\Delta\bar{\gamma}^p$ of the point. The $\Delta\bar{\gamma}^p$ value of each cycle falls in an approximate range. The $\Delta\bar{\gamma}^p$ marked in Fig. 15.5 falls in the second thermal cycle. Based on the calculation for point D,

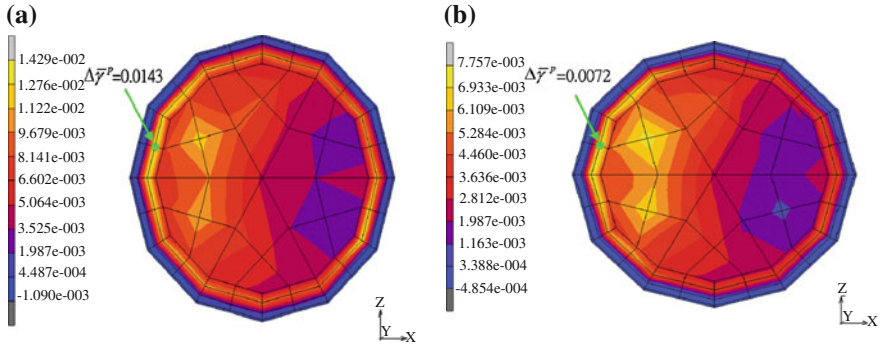

Fig. 15.6 Sn/Ag/Cu micro solder ball in thermal cycle specification. **a** JESD22-A104A, **b** TA-TSY-000983. The $\Delta\bar{\gamma}^p$ distribution schematic diagram after one thermal cycle

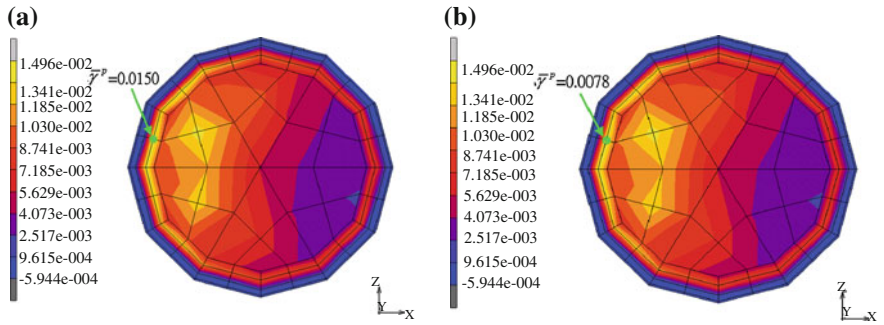

Fig. 15.7 Sn/Pb micro solder ball in thermal cycle specification. **a** JESD22-A104A, **b** TA-TSY-000983. The $\Delta\bar{\gamma}^p$ distribution schematic diagram after one thermal cycle

the MARC subroutine was written to compute the equivalent plastic shear strain amplitude $\Delta\bar{\gamma}^p$ of all the nodes in a thermal cycle, and the maximum value coincides with point D, on the underside of the solder ball furthest from the symmetric plane.

Using VCSEL components with different solders, Figs. 15.6 and 15.7 exhibit $\Delta\bar{\gamma}^p$ distribution of the underside of the micro solder balls furthest from the symmetric plane after a thermal cycle. The corresponding fatigue lives of the Sn/Ag/Cu and Sn/Pb solders are calculated to derive the maximum value, with results shown in Fig. 15.8. Under JESD22-A104A standards (−40 to 125 °C), the fatigue life of the Sn/Ag/Cu solder is nearly 26 times higher than that of Sn/Pb solder. Under TA-TSY-000983 standards (−40 to 85 °C), the fatigue life of the Sn/Ag/Cu solder is up to 270,000 cycles, which is far beyond the range of low-cycle fatigue life. However, the fatigue life of Sn/Pb falls within the normal range. Therefore, thermal cycle specifications with higher temperature requirements should be adopted for Sn/Ag/Cu low-cycle fatigue testing.

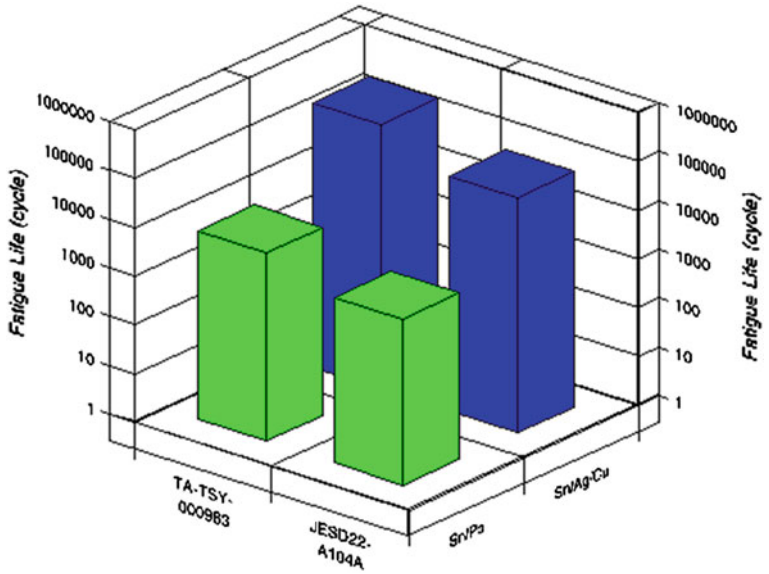

Fig. 15.8 Prediction results of micro solder ball fatigue life of VCSEL components

15.5 Conclusion

This research aims to establish the Coffin-Manson relation targeting on the fatigue life of Sn/Ag/Cu and Sn/Pb solder balls, as well as discuss the prediction of fatigue life using the Coffin-Manson correlation formula, targeting the VCSEL components under thermal cycle loads. The results of this research are summarized as follows:

(1) The Coffin-Manson correlation formula predicts that solder balls made of Sn/Ag/Cu will have a longer fatigue life those made of Sn/Pb for use in the VCSEL structure of optoelectronic packaging. Under identical thermal cycle specifications (−40 to 125 °C), the fatigue life of VCSEL components with Sn/Ag/Cu solder balls is 26 times longer than those with Sn/Pb solder balls.
(2) The molten temperature of lead-free Sn/Ag/Cu solder balls (217 °C) is higher than that of Sn/Pb solder balls (183 °C). In the thermal cycle process at identical high temperatures, a Sn/Ag/Cu solder ball has greater strength and thus longer fatigue life.
(3) The Coffin-Manson fatigue life prediction formula used here is based on the concept of equivalent plastic strain amplitude of the welded area and outperforms other published formulas for reliably predicting the fatigue life of Sn/Pb solder balls. No equivalent comparison could be made for the fatigue life of lead-free Sn/Ag/Cu solder balls given the lack of relevant research. However, consistency in the experimental statistics indicates good applicability and reliability.

References

1. Chen, L.-R. (2004). Electronic components market sentiment and industry trends. *Journal of Industrial Materials, 207*, 80–84.
2. Su, T.-L. (2002). *A study of Ball Grid Array Package interface reactions of Sn–3.5Ag/Ag thick film solder*. Thesis, Department of Materials Science and Engineering, National Taiwan University, Taipei, Taiwan.
3. Desai, C. S., & Whitenack, R. (2001). Review of models and the disturbed state concept for thermomechanical analysis in electronic packaging. *ASME Journal of Electronic Packaging, 123*, 19–33.
4. Frear, D., Morgan, H., Burchett, S., & Lau, J. (1994). *The mechanics of solder alloy interconnects* (pp. 199–313). New York: Van Nostrand Reinhold.
5. Hsu, C.-M. (2001). *Stress and alignment shift analyses in the vertical cavity surface emitting laser module*. Thesis, Department of Mechanical and Electro-Mechanical Engineering, National Sun Yat-Sen University, Kaohsiung City, Taiwan.
6. Ellison, G. N. (1989). *Thermal computations for electronic equipment* (pp. 31–48). Malabar, FL: R.E. Krieger Publishing Co.
7. Fan, S. H., Chan, Y. C., & Lai, J. K. L. (2001). Fatigue lifetimes of PBGA solder joints reflowed at different conveyor speeds. *ASME Journal of Electronic Packaging, 123*, 290–294.

Chapter 16
Research on Structure and Sorption Properties of Affiliative Polymer Piezoelectric Sensor Film Coating

Yu Gu, Qiang Li, Fang-fang Tian and Bao-jun Xu

Abstract Thin nanocomposite organic film coating with exactly thickness and high uniformity on the surface of the affiliative polymer piezoelectric sensor may be obtained using vacuum electron beam dispersion (EBD) coating technology. Structure and sorption properties of the thin film coating are studied. An experimental survey shows that EBD coating technology can produce a uniform thickness of the thin film coating when the cellulose treated as raw materials, and the physical and chemical analyses show that the coating has a high performance of absorption using the method of infrared spectroscopy. Meanwhile, the absorption and sensitivity performance of the thin film coating will change if other organic materials are added to the thin film coating. It is shown that cellulose based coatings have high sorption properties and may be used for gas sensing layers.

Keywords EBD · Thin film coating · Cellulose · Structure · Sorption properties

16.1 Introduction

Mass sensitive sensors with thin absorptive layers are very perspective for gas composition checking and analysis. Piezoelectric sensors are a kind of mass sensitive sensors taking quartz piezoelectric crystal as the basal material and thin film coating for improving absorbing properties. When a sensor absorbs characteristic materials, the quality, electrical conductivity, dielectric properties and the dielectric of the crystal will change, and these changes will be captured by computers to express some informations. Because of the features of simple structure, small volume, low quality, low consumption, long life, in particular,

Y. Gu (✉) · Q. Li · F. Tian · B. Xu
Department of Mechanics, School of Civil Engineering, Beijing JiaoTong University, Beijing 100044, China
e-mail: yugu@bjtu.edu.cn

J. Juang et al. (eds.), *Proceedings of the 2nd International Conference on Intelligent Technologies and Engineering Systems (ICITES2013)*, Lecture Notes in Electrical Engineering 293,
DOI: 10.1007/978-3-319-04573-3_16,

piezoelectric sensors have been widely used in food monitoring, cosmetic and pharmaceutical industries, achieving real-time detection and early warning of product quality and ingredients during the process of production [1–4], so researches on performance of piezoelectric sensors has great significance.

Piezoelectric sensors' sensitivity is determined by the absorption properties of thin film coating. The methods of thin film coating preparation mainly include chemical vapor deposition, physical vapor deposition, sol–gel, self-assembly, electro deposition method, glue coating, thermal spraying technology, etc. Due to imperfect technology to produce thin film coating, there are widespread problems such as the uncontrollability of the film thickness and uniformity, and poor interfacial adhesion.

The vacuum electron beam dispersion (EBD) coating technology is widely used to produce thin film coating. It employs the energy of laser, ion beam and electron beam to heat the nano structured non-metal polymer, which has absorption properties, and the energy makes the polymer disperse for coating. This dispersed polymer deposits on the surface of quartz piezoelectric crystal, and develops into stable and uniform coating. The main advantages of the EBD coating technology are that we can take wide raw materials in the coating and obtain a composite multi-layer coating. Most importantly, we can easily control the thickness of thin film, growth speed, and ensure the thin-film uniformity [5–7].

16.2 Model and Research

We know that the sensitivity of the affiliative polymer piezoelectric sensor is strongly depended on the properties of the thin film coating, such as the thickness, continuity and surface structure. The absorbability of the thin film coating to characteristic materials plays a vital role in applications in piezoelectric sensors. For our piezoelectric sensor, which was plated using nanometer non-metal thin polymer, the thickness, uniformity, and framework determine the sensitivity and the accuracy of the piezoelectric sensor directly. The more stable of the thin film coating, the higher sensitivity of the sensors. For EBD coating technology, we can employ many polymers such as cellulose, polyethylene, and polytef as raw materials for film coating. We can also add other function polymers which have different kinds of absorption functions into the raw materials for changing the absorption property of the thin film coating notably. In this paper, the structure and sorption properties of thin cellulose based coatings on mass sensitive sensors surface were studied, and the affiliative polymer piezoelectric sensor film coating model is shown in Fig. 16.1.

As shown in Fig. 16.1, the piezoelectric sensor is made of polymer film coating and quartz piezoelectric, and the diameter is 8 mm. The thin film coating was plated onto quartz resonators surface from active gas phase formed by electron beam dispersion (EBD) of raw materials in vacuum. Cellulose was used as raw materials for the coating.

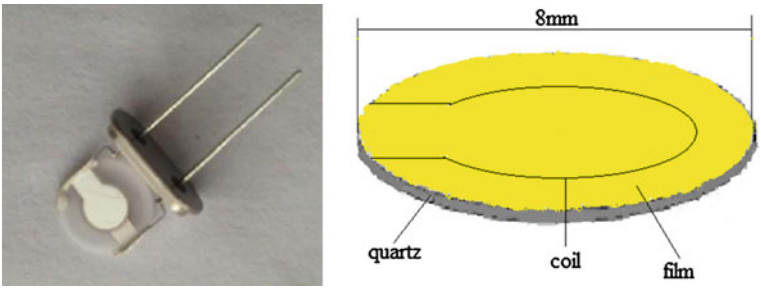

Fig. 16.1 Affiliative polymer piezoelectric sensor film coating model

Sorption properties of sensor layers to different analyses were studied using multi-channel device "electronic nose". Coatings were deposited onto mass sensitive sensors surface for investigation of sorption properties. Quartz resonators were used as sensors. Investigation of sorption processes was executed using 8 channels frequency measuring system. Sensor array was placed into chamber blown by dried air. Air flow was periodically terminated and chamber was filled by analyzed gas composition.

Nanocomposite cellulose film coatings were formed by several methods. As shown in Fig. 16.2, the first one was the filling of coating by doped material after deposition, the second method was composite obtaining during electron beam dispersion of different components mixture.

Chemical structure of coatings, formed out of PTFE, PE and PU, is neighbor to the initial material structure with characteristic nanoheterogeneous morphology. Structure of the cellulose coating, formed out of cellulose EBD products, differs significantly from the initial material structure. Surfaces of the coatings, deposited on the silicon monocrystal, have roughness of about 1–2 nm. Uniformly distributed on the surface radial spherulites are of 0.5–1 μm size. Cellulose coatings have a smooth surface with feebly marked structure (Fig. 16.2, left). No any structure formations were found in SEM image of coating obtained by dispersion of cellulose with reduced palladium nanoparticles (Fig. 16.2, right).

Figures 16.3 and 16.4 show the difference between the raw materials and the corresponding coating, based on the infrared spectroscopy in different wavelength ranges.

As shown in Fig. 16.3, the coating materials' structure is different from that of the raw materials under the condition of the infrared spectroscopy technology in the range 0.10–0.15 cm^{-1}. This means that the coating material is amorphous and there exists breaking of hydrogen bond.

As shown in Fig. 16.4, compared to the raw materials, there is little absorption in the range 400–700 cm^{-1} for the coating material. This is related to the fact that the coating material is amorphous while the raw materials are crystalline.

As shown in Fig. 16.5, the emerge of the 1110 cm^{-1} peak indicates that pyranose's periodical absorption and vibration intensity display a remarkable

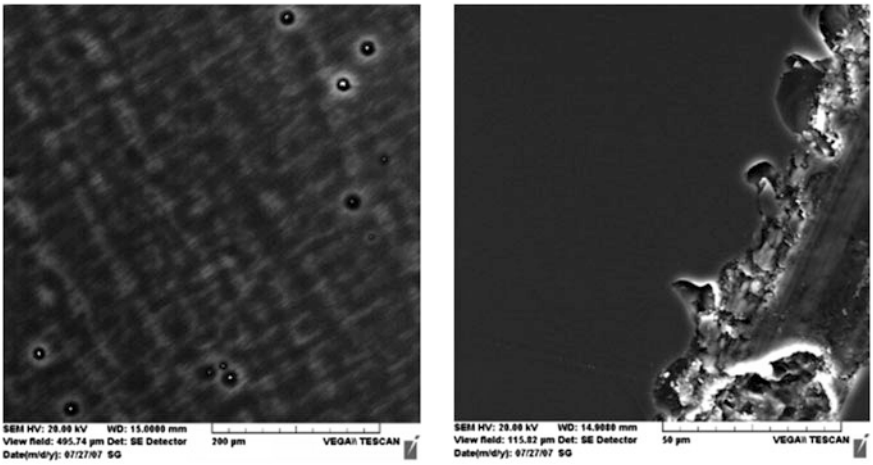

Fig. 16.2 SEM images of cellulose coatings

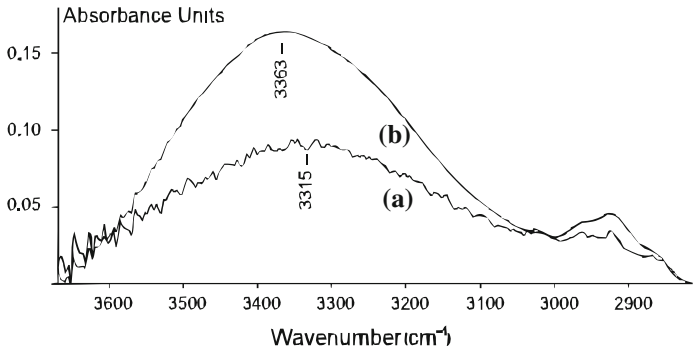

Fig. 16.3 Absorption properties of materials in the range 2800–3700 cm^{-1}: **a** raw materials, **b** coating materials

decrease, which demonstrates the fracture of the crystalline structure of the raw materials. The emerge of the 1050 cm^{-1} and 890 cm^{-1} peaks indicates the existence of glucosidic bond. The emerge of the 1000–1040 cm^{-1} indicates the periodical vibration change, which means that pyranose's structure exists fracture in the coating materials. The 1135 cm^{-1} peak is a new wave which has not been identified.

As shown in Fig. 16.6, the periodical absorption and vibration intensity of the 1680–1800 cm^{-1} indicate that the hydroxyl of the coating materials becomes more in comparison to the raw materials, which means that some structures of the coating materials are broken, then the hydroxyl increases, and the glucosidic bond remains unchanged.

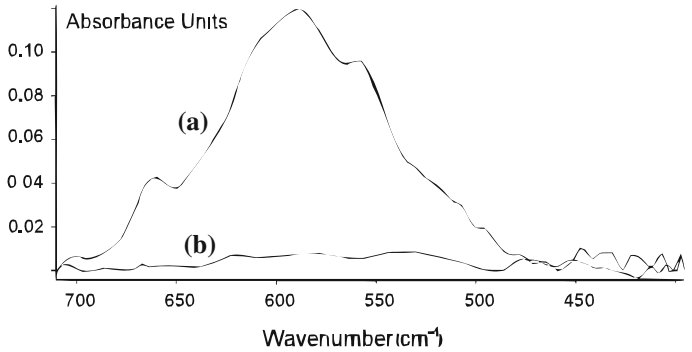

Fig. 16.4 Absorption properties of materials in the range 400–700 cm^{-1}: **a** raw materials, **b** coating materials

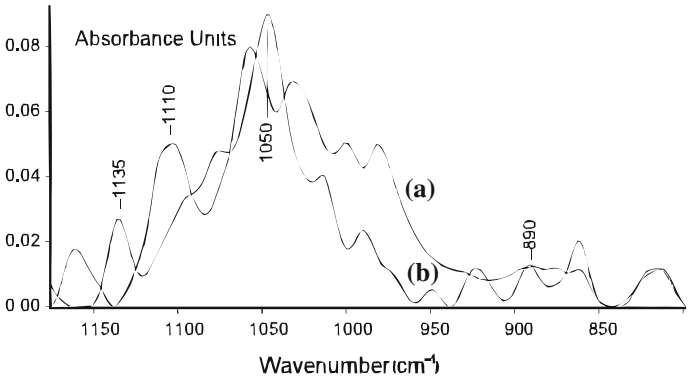

Fig. 16.5 Infrared spectra of materials: **a** original cellulose, **b** coating material

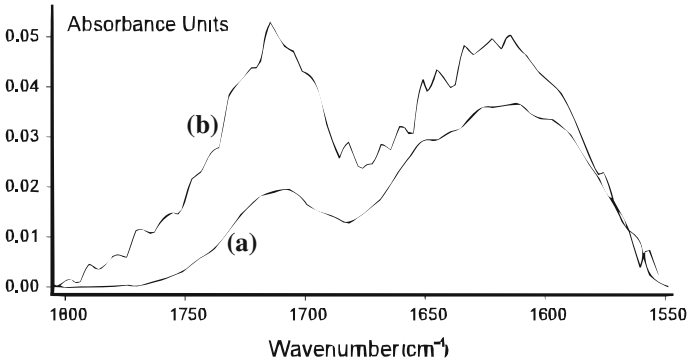

Fig. 16.6 Infrared spectra of materials: **a** original cellulose, **b** coating material

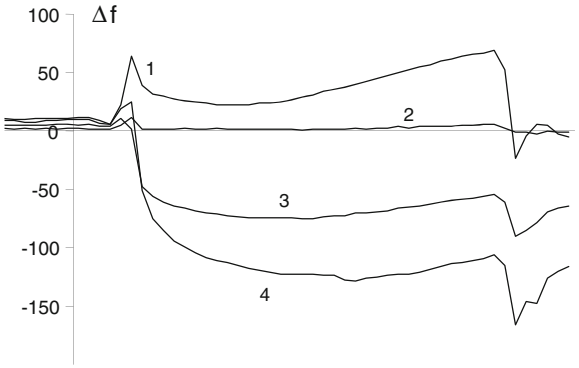

Fig. 16.7 Variation of resonance frequency of sensors on ammonia impact. *1* pure cellulose, *2* cellulose + brilliant green, *3* cellulose + pyridoxine hydrochloride, *4* cellulose + brilliant green + pyridoxine hydrochloride

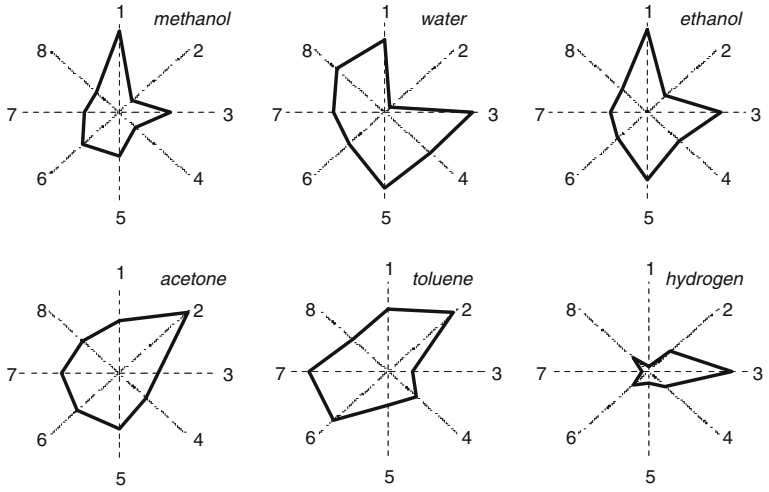

Fig. 16.8 Different structure cellulose coatings reactions on hydrogen impact and humidity variation. *1* pure cellulose, *2* cellulose coating treated by $PdCl_2$, *3–8* different coatings obtained by dispersion of cellulose filled

Based on the above analyses, we may conclude that cellulose film coating has a high absorption intensity. The piezoelectric sensor's property depends on the organic materials, which have different functions. Therefore, we may add different materials to monitor the performance of coating in the experiments. The above analyses show that cellulose film coating has high adsorption properties after the EBD coating technology. In the experiments, a sensor is made by the quartz piezoelectric crystal and cellulose which is filled by organic materials with different sensitivity to ammonia, such as the Brilliant Green(a material), pyridoxine

hydro chloride. In the experiments, natural frequency is measured, and the results are shown in Fig. 16.7.

As shown in Fig. 16.7, a cellulose coating is filled by different organic materials, and each sensor has obvious difference in frequency, indicating a high sensitivity to ammonia. Experimental results show that adding specific organic substance which has adsorption to materials into the basic material can achieve selective identification function of the coating.

Based on the above principle, sensors with different adsorption properties due to different thin film coatings are investigated by using an 8-channel frequency measurement system to measure the change of frequency after absorbing characteristic substances in the compound gases. Figure 16.8 shows the vibration spectra come from six substances, each spectrum contains eight frequencies provided by the coating sensors. We can distinguish the substances from the spectra.

16.3 Conclusions

In summary, thin nanocomposite film coating for affiliative polymer piezoelectric sensor may be obtained by EBD method. This method gives a possibility to form coatings with exactly thickness and high uniformity. Thin cellulose coatings have a wide range of absorption properties and are very perspective for sensing gas information. This concerned with amorphous structure of cellulose coatings and increased quantity of carbonyl groups. Cellulose base layers consisted of pyridoxine hydrochloride have a high selective sensitivity to ammonia. Introduction of palladium into cellulose coating leads to selective sorption of hydrogen. It is shown that cellulose based coatings have high sorption properties and may be used for gas sensing layers.

Acknowledgments The financial support from the National High Technology Research and Development Program of China (863 Program, No. 2013AA030901) is acknowledged.

References

1. Luo, J., Huang, Y. Y., Xiong, S. X., Liu, G. Q., & Zhao, R. (2007). Study on peptide-peptide interaction using high-performance affinity chromatography and quartz crystal microbalance biosensor. *Chinese Science Bulletin, 52*(10), 1311–1319.
2. Peris, M., & Escuder-Gilabert, L. (2009). A 21st century technique for food control: Electronic noses. *Analytica Chimica Acta, 638*, 1–15.
3. De Cesare, F., Pantalei, S., Zampetti, E., & Macagnano, A. (2008). Electronic nose and SPME techniques to monitor phenanthrene biodegradation in soil. *Sensors and Actuators B, 131*, 63–70.
4. Macagnano, A., Zampetti, E., & Pistillo, B. R., et al. (2008). Double layer sensors mimic olfactive perception: A case study. *Thin Solid Films, 516*, 7857–7865.

5. Rudnitskaya, A., & Legin, A. (2008). Sensor systems, electronic tongues and electronic noses, for the monitoring of biotechnological processes. *The Journal of Industrial Microbiology and Biotechnology, 35*, 443–451.
6. Panin, V. E., Belyuk, S. I., Durakov, V. G., Panin, S. V., Galchenko, N. K., & Samartsev, V. P. (2003). Structure and mesoscale plastic deformation and fracture patterns of materials coated by electron-beam deposition. *Fatigue and Fracture of Engineering Materials and Structures, 26*, 349–361.
7. Koshets, I. A., Kazantseva, Z. I., & Shirshov, Y. M. (2003). Polymer films as sensitive coatings for quartz crystal microbalance sensors array. *Semiconductor Physics Quantum Electronics & Optoelectronics, 6*(4), 505–507.

Chapter 17
Design of Bended Multimode Interference Demultiplexer with Multi-Sectional Coherent Coupled Bended Waveguides

Wei-Sung Weng, Yu-Tai Huang, Kun-Yi Lee, Yao-Chang Jeng, Wei-Yu Lee and Wei-Ching Chuang

Abstract A 1310/1550 nm demultiplexer constructed from a bended multimode interference (MMI) structure is proposed and the optical characteristics of the devices are analyzed and optimized as well. The multi-sectional coherent coupled bend waveguides are employed to optimize the output loss of the devices.

Keywords Demultiplexer · Multimode interference · Coherent coupled waveguides

17.1 Introduction

A 1310/1550-nm multiplexer plays important roles in WDM and PON networks [1, 2], which efficiently exploits the large capacity of optical fibers, and is becoming a promising broad-band optical access solution for next-generation network. There have been several approaches to implement 1310/1550-nm WDM such as the fused biconical taper fiber technology, the use of Mach-Zehnder-type interferometers, directional couplers, multimode interference (MMI) waveguide couplers, and arrayed waveguide gratings (AWGs). Amid these devices, multi-mode interference (MMI) couplers are attractive optical devices for controlling

W.-S. Weng · Y.-T. Huang · W.-C. Chuang
Department of Electro-Optical Engineering, National Formosa University, Yunlin County 632, Taiwan, Republic of China

K.-Y. Lee (✉) · W.-Y. Lee
Department of Electrical Engineering, China University of Science and Technology, Taipei City 115, Taiwan, Republic of China
e-mail: kelvin119@gmail.com

Y.-C. Jeng
Department of Automation Engineering, National Formosa University, Yunlin County, Taiwan, Republic of China

J. Juang et al. (eds.), *Proceedings of the 2nd International Conference on Intelligent Technologies and Engineering Systems (ICITES2013)*, Lecture Notes in Electrical Engineering 293,
DOI: 10.1007/978-3-319-04573-3_17,

and manipulating the power of lights in optical integrated circuits due to their advantageous characteristics such as compact size, relaxed fabrication tolerance, and wide bandwidth as well as polarization insensitivity [2]. The applications of such devices include splitters, combiners, mode converters, and wavelength multiplexers/demultiplexers in wavelength division multiplexing (WDM) systems. Furthermore, not only to the optical communications, they also can be applied to integrated optics sensors for chemical and biological sensing [3]. However, for the conventional 1310/1550-nm MMI couplers with low refractive index contrast, they suffered from the larger axial length caused by effective width of the devices. Some researchers increased the index contrast to minimize the device length [2]; nevertheless, the coupling loss between optical fibers and MMI devices increases due to Fresnel reflections. Besides, the fabrication complexity is raised substantially because of employing the high index materials.

In this paper, we propose a novel 1310/1550-nm MMI coupler, comprising of a bi-sectional bended MMI coupler and coherent coupled multi-sectional bended waveguides at the input and output terminals of the devices, so as to reduce the length of the devices with low index contrast. By using the beam propagating method (BPM), the optimum analysis is demonstrated as well.

17.2 Theory for Design and Analysis

17.2.1 MMI Design Theory

The operation and design theory of the multimode interference is based on the self-imaging principle, which is originated by the Bryngdahl [4]. The input fields are reproduced at the image plane $L_c = 3pL_\pi$, $p = 0, 1, 2, 3,\ldots$ Here, L_π is the beat length and defined as [5]

$$L_\pi = \frac{\pi}{\beta_0 - \beta_1} = \frac{4n_g W_e^2}{3\lambda_0}, \tag{17.1}$$

where β_0 and β_1 are the propagation constants of the fundamental and first order modes, respectively, λ_0 is the free space wavelength, n_g is the slab effective index (vertical analysis) at the guiding region, and W_e, which is slightly larger than W, is the effective width of the fundamental mode of the multimode guide. A direct or mirror image of the input field is formed if p is even or odd integer, respectively. An MMI coupler can perform dual-channel wavelength demultiplexing when it uses the difference between the beat lengths at these wavelengths to make the bar-couple for one wavelength and cross-couple for the other. The beat lengths can be adjusted so that the beat length ratio of the two wavelengths λ_1 and λ_2 is given by [5]

$$\frac{L_\pi(\lambda_1)}{L_\pi(\lambda_2)} = \frac{p+q}{q}, \tag{17.2}$$

where p is a positive integer and q is an odd one. If the length (L_{mmi}) of MMI region could be adjusted to satisfy [2]

$$L_{mmi} = p \cdot L_{\pi}(\lambda = 1310 \text{ nm}) = (p+1) \cdot L_{\pi}(\lambda = 1550 \text{ nm}), \tag{17.3}$$

there will be a direct image and mirror image for two wavelengths e.g., 1310- and 1550-nm, respectively.

17.2.2 Bended Waveguide Design and Analysis

The successive bended waveguides are employed as input and output waveguides of the devices. Such structures are analyzed based on coherent coupled effect, which is essential to a number of proposals for fabricating low-loss waveguide bends and the other applications [6, 7]. Coherently coupled effect is the basic mechanism of the coupled bending optical waveguide, and it represents the power oscillates between the guiding modes and radiation modes at the corner of bend. The structure of a tri-sectional bended waveguide is schematically illustrated in Fig. 17.1.

By employing beam propagation method (BPM), the output power of the bended waveguide for wavelengths of 1310- and 1550-nm with respect to the length of the central-sectional waveguide, is calculated and depicted in Fig. 17.2 when the bending angle, θ, is fixed at 5°. The power fluctuation shows that the power couples between guided and un-guided modes. It has been shown that the bending loss in a single mode waveguide will be minimized when [8]

$$L = \frac{(2m+1)}{2\Delta n}\lambda_0, \quad m = 0, 1, 2, \ldots \tag{17.4}$$

Here, λ_0 is the wavelength of the light in vacuum, and Δn is the difference between the effective index of the guided mode and the weighted average effective index of the unguided modes excited at the bends.

17.3 Design and Simulation Results

The topology of the proposed device is prototyped as in Fig. 17.3 and the related parameters are listed in Table 17.1. The MMI is abruptly bended by two sections with total bending angle, θ. The SiO_2 (the refractive index of 1.46) is employed as a substrate material for the device.

The total length, denoted by L_{mmi}, of the MMI demultiplexer is calculated from an un-bended MMI demultiplexer with device width of 6.46 μm by using Eq. (17.3); and simulated and optimized employing 2D BPM_CAD (R-soft Inc.) as well.

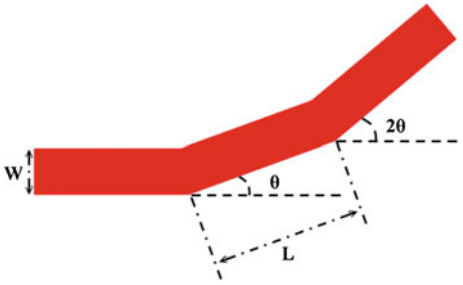

Fig. 17.1 The three-sectional structure of the coherent-coupled bended waveguide

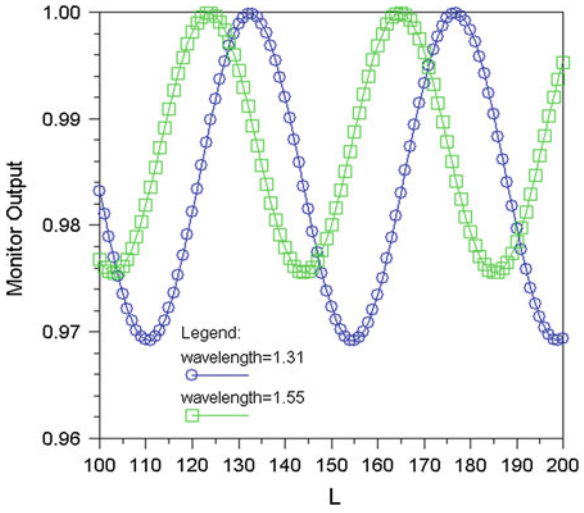

Fig. 17.2 The relative output power for coherent coupled waveguide with respect to the length of the centered waveguide. The unit of the length is μm and the relative output power is defined as the ratio of output to input powers

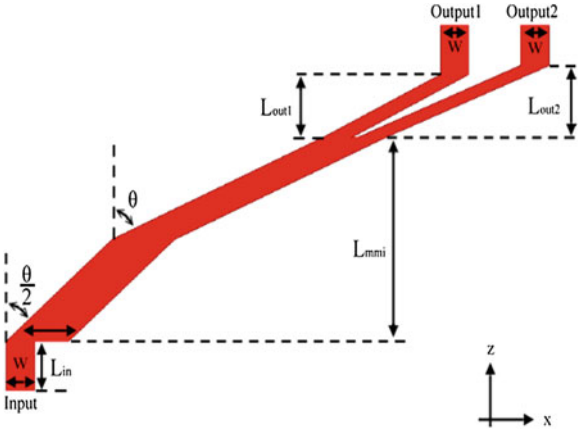

Fig. 17.3 Prototype of the bended MMI 1310/1550-nm demultiplexer

Table 17.1 Parameters for prototype of the bended MMI 1310/1550-nm demultiplexer

Parameters	L_{in} (μm)	W (μm)	L_{mmi} (μm)	W_{mmi} (μm)	Δn	L_{out1} (μm)	L_{out2} (μm)	W (μm)	θ (°)
	120	2.9	500	6.46	0.1	154	175	2.9	5

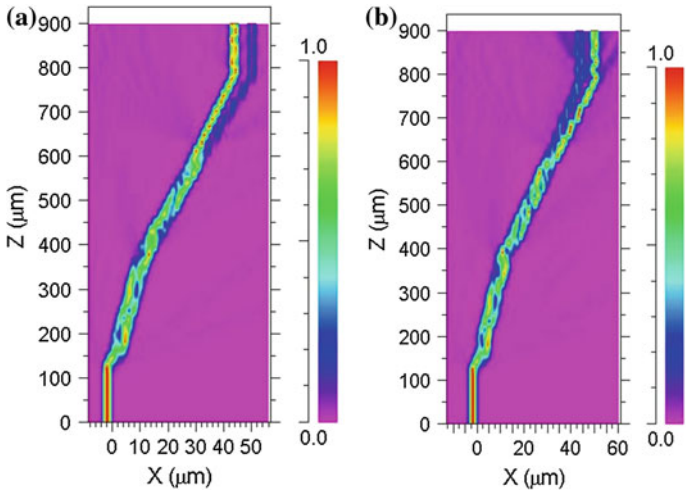

Fig. 17.4 2D-BPM simulations of the field distribution of the demultiplexer for different wavelengths, **a** wavelength of 1310 nm, and **b** wavelength of 1550 nm

The simulation results are depicted in Fig. 17.4a, b for 1310 and 1550 nm, respectively. The simulated output power of the device with respect to the total bending angles is plotted in Fig. 17.5. It is noted that the power loss increases dramatically as the bending angle increases.

The other transmission characteristics of the structure are simulated and listed in Table 17.2 as well.

In Table 17.2, it reveals the output loss is large in output 2 as well as in output 1. That is because of the large abrupt bended angle of the input waveguides and different optimal lengths of the output waveguides for wavelength of 1310 and 1550 nm. In order to reduce the output loss apparently, a coherent coupled bended waveguide was introduced to the input and output waveguides; and the output waveguide lengths are adjusted to be optimal as well. The modified structure is schematically depicted in Fig. 17.6.

In the input terminal, the waveguide is bended by $\frac{1}{3}\theta$ with respect to z direction at the first corner; and in the MMI section, the waveguide is bended by $\frac{2}{3}\theta$ and θ with respect to z direction at the initial and center position, respectively. The other design parameters are listed as in Table 17.3.

The simulated output power distributions are shown in Fig. 17.7a, b for wavelength of 1310- and 1550-nm, respectively.

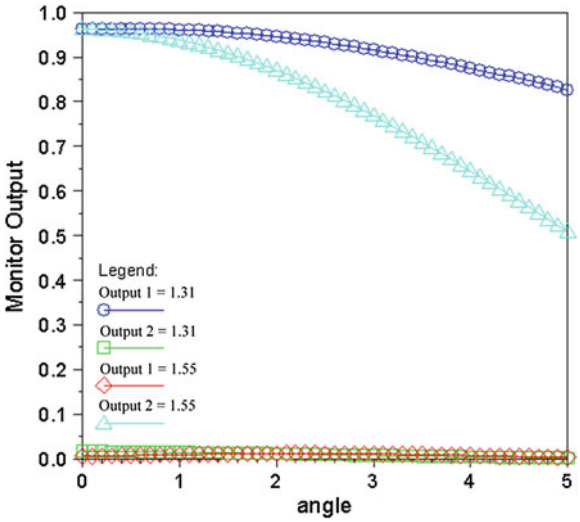

Fig. 17.5 The output power (normalized to the input power) from output 1 and 2 versus the bending angle θ

Table 17.2 Simulated transmission characteristics of the prototype demultiplexer

	Angle	Output 1	Output 2	Insertion loss (dB)	Extinction ratio (dB)
$\lambda = 1.31$ μm	5°	0.82651	0.0015989	0.8275	−27.13
$\lambda = 1.55$ μm	5°	0.0025834	0.50879	2.9346	−22.94

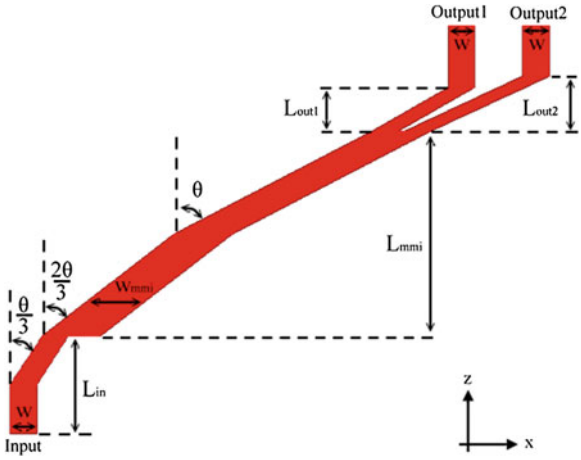

Fig. 17.6 A bended MMI 1310/1550 nm demultiplexer with bi-sectional coherent coupled waveguides as input and output waveguides

Table 17.3 The simulation parameters of the bended MMI with bi-sectional coherent coupled input/output waveguides

Parameter	L_{in} (μm)	W (μm)	L_{mmi} (μm)	W_{mmi} (μm)	Δn	L_{out1} (μm)	L_{out2} (μm)	W (μm)	θ (°)
	240	2.9	500	6.46	0.1	106	135	2.9	5

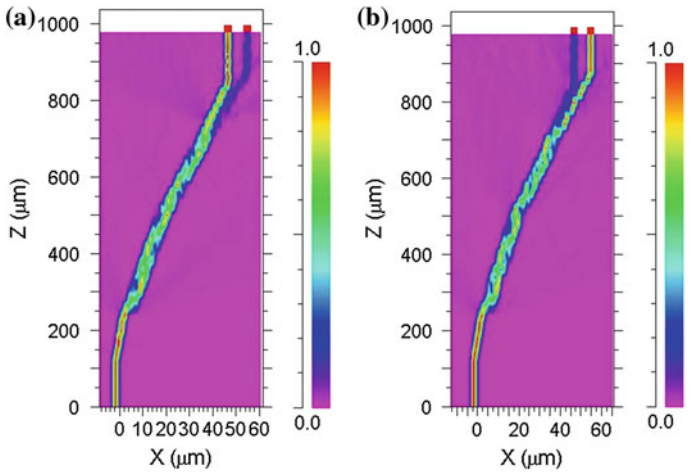

Fig. 17.7 2D-BPM simulations of the field distribution of the bended MMI demultiplexer with bi-sectional coherent coupled waveguides for different wavelengths, **a** wavelength of 1310 nm, and **b** wavelength of 1550 nm

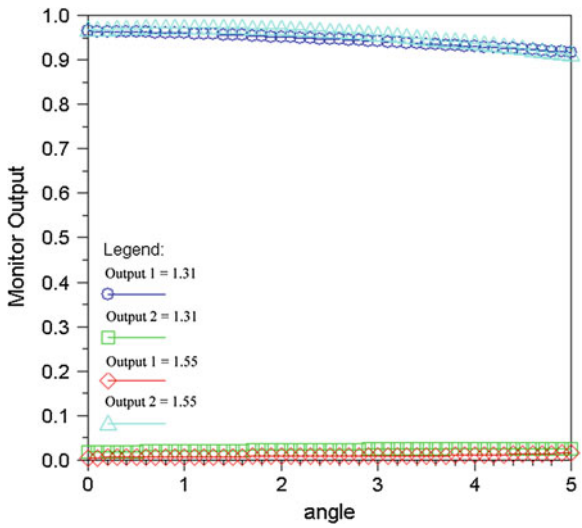

Fig. 17.8 The output power of output 1 and 2 versus the bending angle, the unit of angle is degree

Table 17.4 Simulated transmission characteristics of the bended MMI demultiplexer with bi-sectional coherent coupled waveguides

	Angle	Output 1	Output 2	Insertion loss (dB)	Extinction ratio (dB)
$\lambda = 1.31$ μm	5°	0.92186	0.0053269	0.3533	-22.38
$\lambda = 1.55$ μm	5°	0.0098389	0.91206	0.4067	-19.67

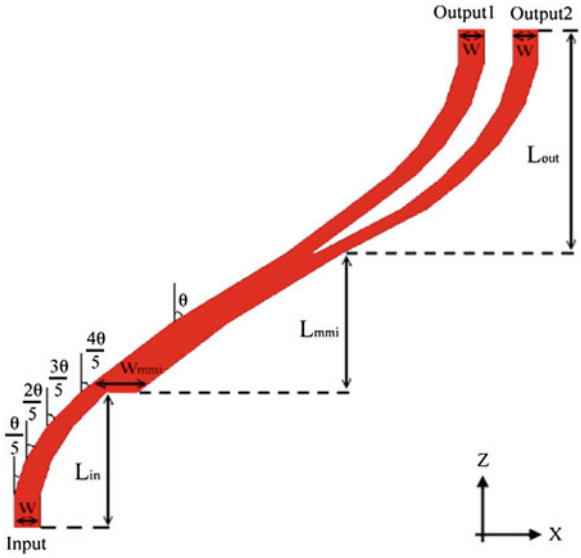

Fig. 17.9 The bended MMI demultiplexer with multi-sectional coherent coupled waveguides

The output power of the two output waveguides of the modified devices versus the bending angle θ for 1310- and 1550-nm are calculated as shown in Fig. 17.8 and the other transmission characteristics are listed in Table 17.4.

The transmission power of output-1 ($\lambda_0 = 1310$-nm) and output-2 ($\lambda_0 = 1550$-nm) reaches 92.2 and 91.2 %, respectively. It shows that the output power loss dramatically decreases.

To optimize the output power, the input and output waveguides are further segmented as multi-sectional coherent coupled waveguides. Figure 17.9 shows the schematic of the proposed optimum structure. The input waveguide is formed by a four-equal-segment coherent coupled bended waveguide with a sequence of bended angles, $\frac{\theta}{5}, \frac{2\theta}{5}, \frac{3\theta}{5}, \frac{4\theta}{5}$, and the output waveguides are bended in the reverse sequence of the input one with the equal segments.

The design parameters are listed in Table 17.5.

The output power distribution of the optimal device for the wavelength of 1310- and 1550-nm are simulated and shown in Fig. 17.10a, b, respectively.

The output powers of the two multi-sectional waveguides of the optimized demultiplexer versus the bending angle, θ, for wavelengths of 1310 and 1550-nm are depicted in Fig. 17.11 and the other transmission characteristics are listed in Table 17.6.

Table 17.5 The design parameters for the bended MMI with multi-sectional input/output waveguides

Parameter	L_{in} (μm)	W (μm)	L_{mmi} (μm)	W_{mmi} (μm)	Δn	L_{out} (μm)	W (μm)	θ (°)
	480	2.9	500	6.46	0.1	800.7	2.9	5

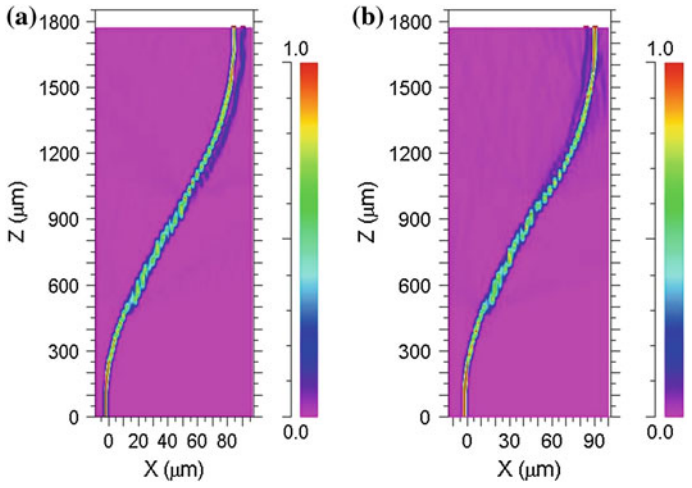

Fig. 17.10 2D simulated field distribution of a bended MMI demultiplexer with multi-sectional coherent coupled waveguides for **a** wavelength of 1310-nm and **b** wavelength of 1550-nm

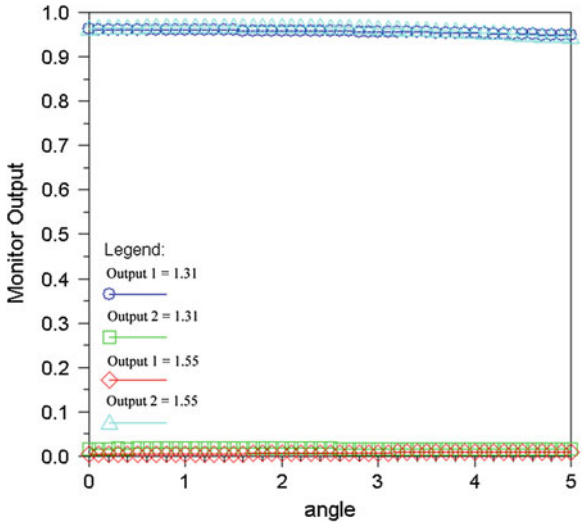

Fig. 17.11 The output power of output 1 and 2 for optimized device versus the bending angle. The unit of angle is degree

Table 17.6 Simulated transmission characteristics of the bended MMI demultiplexer with multi-sectional coherent coupled waveguides

	Angle	Output 1	Output 2	Insertion loss(dB)	Extinction ratio(dB)
$\lambda = 1.31$ μm	5°	0.94835	0.016421	0.2303	−17.62
$\lambda = 1.55$ μm	5°	0.01032	0.94396	0.2505	−19.61

The results show the output power of the optimized device reaches 94.8 and 95.4 %; and the loss reduce to 0.23- and 0.25-dB for wavelengths of 1310- and 1550-nm, respectively.

17.4 Conclusion

We successfully designed a novel 1310/1550 nm wavelength demultiplexer based on bended MMI structure with multi-sectional coherent coupled bended waveguides as input and output terminals. The results show that the output losses have been dramatically reduced due to the low bending loss for bended MMI and coherent coupled bended output waveguides.

References

1. Maier, G., Martinelli, M., Pattavina, A., & Salvadori, E. (2000). Design and cost performance of the multistage WDM-PON access networks. *IEEE Photonics Technology Letters, 18*, 125–143.
2. Shi, Y., Anand, S., & He, S. (2007). A polarization-insensitive 1310/1550-nm demultiplexer based on sandwiched multimode interference waveguides. *IEEE Photonics Technology Letters, 19*, 1789–1791.
3. Mayeh, M., Viegas, J., Srinivasan, P., Marques, P., Santos, J. L., Johnson, E. G., et al. (2009). Design and fabrication of slotted multimode interference devices for chemical and biological sensing. *Journal of Sensors, 2009*, 1–11.
4. Bryngdahl, O. (1973). Image formation using self-imaging techniques. *Journal of Optical Society of America, 63*, 416–419.
5. Paiam, M. R., & MacDonald, R. I. (1997). Polarisation-insensitive 980/1550 nm wavelength (de)multiplexer using MMl couplers. *Electronics Letters, 33*, 1219–1220.
6. Johnson, L. M., & Yap, D. (1984). Theoretical analysis of coherently coupled optical waveguide bends. *Applied Optics, 23*, 2988–2990.
7. Kawakami, S., & Baba, K. (1985). Field distribution near an abrupt bend in single-mode waveguides: A simple model. *Applied Optics, 24*, 3643–3647.
8. Johnson, L. M., & Leonberger, F. J. (1983). Low-loss $LiNbO_3$ waveguide bends with coherent coupling. *Optics Letters, 8*, 111–113.

Chapter 18
The Construction of a Zigbee-Based Factory Safety Monitoring System

Chih-Chiang Weng and Chin-Sung Hsiao

Abstract A factory safety monitoring system based on wireless sensor network, Zigbee, is proposed and constructed in the work. With the function of automatically monitoring of gas and smoke happening in factory and converting into image then to transmit to personal and phone call to security guiders for emergency treatment. The constructional system is able to authentically uplift the leveling of safety protection and significantly reduce the loss of human life and property. Consequently, one believes that this Zigbee-based system used for wireless messages transmission of abnormal cases coming in factory for safety monitoring can certainly provide a solution advangtable to achieve protection of lives and property.

Keywords Zigbee · Real-time · MYSQL database · Microprocessor

18.1 Introduction

The boost of the factory safe level has been a crucial issue and been emphasized recently for which it is related to the human life and belongings. Generally, some accidental events occurring in factory are unpredictable and usually resulting in catastrophic failure; so that the factory safety monitoring is imperative for protection of human life and property. Various secure monitoring parameters of factory such as carbon monoxide, oxygen, smoke and so on, have been

C.-C. Weng
Department of Computer Science and Information Engineering, Asia University, Taichung 41354, Taiwan, Republic of China

C.-S. Hsiao (✉)
Department of Photonics and Communications Engineering, Asia University, Taichung 41354, Taiwan, Republic of China
e-mail: cshsiao@asia.edu.tw

J. Juang et al. (eds.), *Proceedings of the 2nd International Conference on Intelligent Technologies and Engineering Systems (ICITES2013)*, Lecture Notes in Electrical Engineering 293,
DOI: 10.1007/978-3-319-04573-3_18,

traditionally watched by wired technology, which is expansive and ineffective. We here propose and build a factory security monitoring system based on Zigbee with the advantages of a reliable short-distance wireless communications capability to implement an automatic monitoring system [1, 2]. In this system, some hardware components such as gas, smoke sensors and magnetic reed switch are installed in rear-end of the present system for detection of the peculiar signals and for conversion of all pictures or images in factory to transmit to cell-phone and personal computer for emergency treatment.

18.2 Structure of the Designed System

The developed system with three divisions is shown in Fig. 18.1. The fore-end contains smoke, gas sensor and magnetic reed switch to detecting any abnormal parameters such as fire accident or dense smoke happening in factory. The middle part with a Zigbee is used for signals transmission and acceptance. The back-end includes a user interface with a webcam and a message platform for real-time images monitoring.

18.2.1 Smoke and Gas Sensor

TGS135, a semiconductor-type gas sensor, is installed in the front-end of the proposed system; the gas sensor has the characteristic of changing its conductivity as the leaks of gas are detected anytime. Figure 18.2 shows the basic testing circuit diagram of TGS135.

HS-129, a photonic-type sensor with smoke sensing function, is installed in the proposed system, which has the ability to interrupt an infrared signal as smoke appearing. The basic testing circuit diagram of smoke sensor HS-129 is given in Fig. 18.3.

18.2.2 Zigbee Wireless Telemetering

The present system for telemetering purpose consists of a PICDEM-Z CC2420 card; it is a RF card with the capability of 200 ft signal transmission on providing maximum supportable 65536 interconnection points and it is compatible with IEEE 802.15.4 working at 2.4 GHz frequency [3, 4]. Therefore, this constructed system is with the competence of providing versatile, easy operation and unstained interfaces.

The mission of the front-end sensors is to sense and collect all the eccentric signals occurring in abnormal event and to transfer those into images or pictures by 89c51 microprocessor and then transmit them to cell-phone and/or PDA via Zigbee.

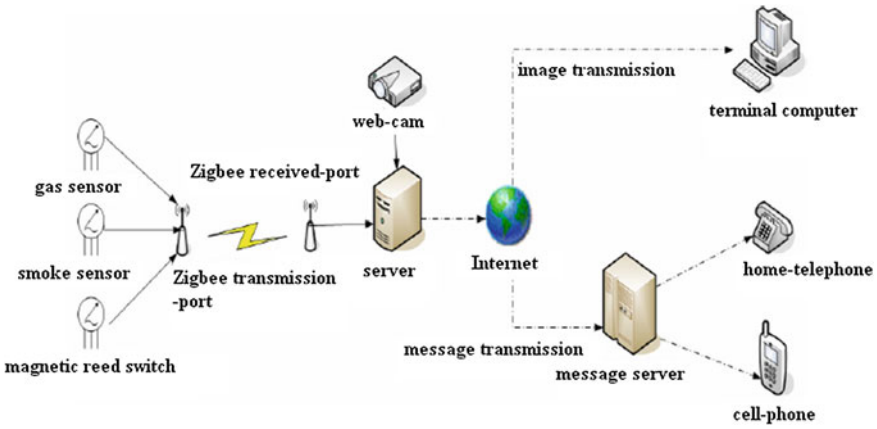

Fig. 18.1 The schematic diagram of the proposed system

Fig. 18.2 The basic testing circuit diagram of gas sensor TGS135

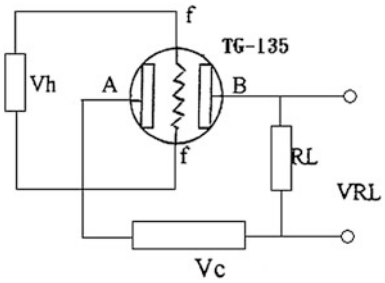

Fig. 18.3 The basic testing circuit diagram of smoke sensor HS-129

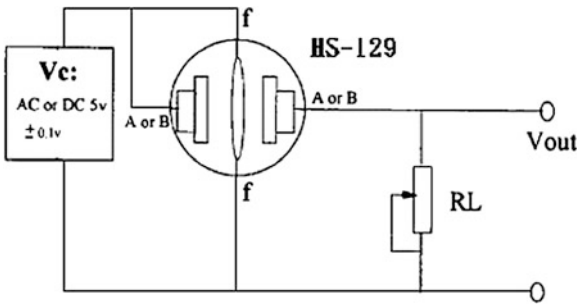

18.2.3 Development of Message Platform

The core work of the proposed system is to enable all messages to be transmitted immediately. The voice mode, a methodology by transmitting a word to the message server and converting a word into a voice mode to avoid the word message and a short ring in cell phone ignored by the people, is employed to notify the remote user via telephone.

18.2.4 Planning of Software Interface

There are five operational items included in the proposed system; the first item is the selection of communication ports, the exhibition of all the received signals is in the second item, the third item is the messages status display, the fourth item is the message platform and the final item is for image monitoring.

18.2.5 Real-Time Webcam Image

The aim of this real-time webcam image is to make the user with the capability of remotely viewing all factory images via Internet. In this case, the users need to enter the client program and input the IP address for observation of real-time dynamic images. In the meantime the remote users also can catch all static images by inputting the IP address before the server with function of broadcasting. The schematic drawing for images transmission is shown in Fig. 18.4.

In the webcam video system depicted above, a new picture is stored per second and the previous picture is covered simultaneously; the server transmit the updated image to the client end if a request were proffered.

18.2.6 Requirement of System Hardware

89c51, a microprocessor included in real-time controller for signal control, has been widely used in various fields latterly for safety monitoring application. 89c51 with ports such as p1.0, p1.1, p1.2 and p1.3 for some input-end signal connections of magnetic reed switch, smoke sensor and gas sensor is used in this developed system. The personal computer and RS-232 port are communicated serially with 89c51 microprocessor via a MAX232 voltage up-down chip. The hardware of the proposed system is also equipped with a server, MySQL database and PHP home page interface. The specifications for the factory monitoring system are listed in Table 18.1.

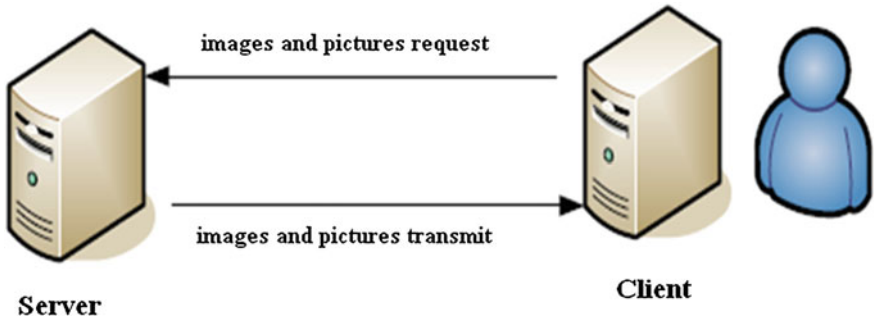

Fig. 18.4 The diagrammatic sketch for image transmission

Table 18.1 Specifications of the factory monitoring system

Item	Specification
Operating system	Windows XP Professional SP2
CPU	Inter(R) Pentium(R)M processor 1.86 GHz
Motherboard	ASUSTeK Computer Inc. M9 V
Memory	512 MB
Display card	ATI Mobility Radeon 7500
Harddisk	60 GB
Network card	Realtek RTL8139 Family Ethernet

18.3 Results

The completed work is with the competence of sensing irregular signals of the factory safety monitoring system. The operational procedure of message platform and the urgent message notification by point-to-point automatic transmission (video system) is provided in the constructional system. The operational description for the system is given as below.

18.3.1 Reception and Judgment of the Front-End Signal

The front-end of the proposed system with the function of the signals received from the installed sensors are transferred into voltage or current for identifying any abnormal events happening in the system. Figure 18.5 pictures clearly the hardware of front-end of the constructed system.

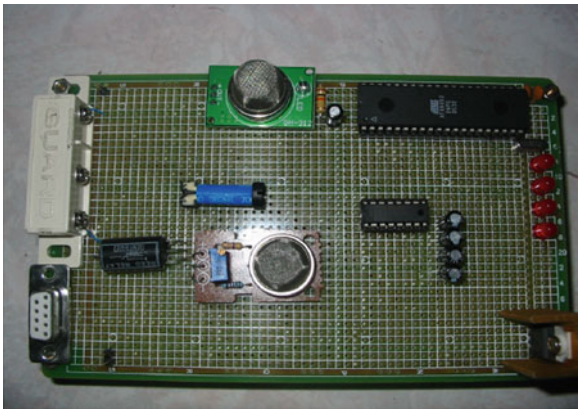

Fig. 18.5 The hardware of the front-end of the constructed system

Fig. 18.6 The received picture at the client end

18.3.2 Operational Procedure of Message Platform

This message platform will automatically and immediately notify the users for emergency treatment as any abnormal events happening in factory. The whole procedures in the message platform include four steps: opening the communication port, receiving messages, judging abnormal events and actuating the message platform. The message system will display all related data such as the IP address, password, message mode, telephone number and message content as the platform prepare to receive message.

18.3.3 Video System

This video system is to provide any abnormal messages to the user as soon as possible for emergency treatment in order to lessen the loss of human life and property. Figure 18.6 gives the received picture at the client-end.

18.4 Conclusion

In this work, a factory safety monitoring system with hardware circuit being installed and software being planned based on wireless sensor network technology, Zigbee, is proposed, described and built in detail. This present system is with the capability of detecting the occurring of gas and smoke and then tracing the location of abnormal events transpiring in factory. The constructed system not only can accurately monitor some eccentric parameters of sensors installed in factory, but also can automatically notify the user as uncommon cases existing for urgent treatment, so that the proposed system can ameliorate the level of factory safety and diminish the loss of property.

Acknowledgments This work is jointly supported by the grants 100-a-28 and 100-A-11 from Asia University and the grant 101-2221-E-468-014 from NSC, Taiwan, R.O.C.

References

1. Egan, D. (2005). The Emergence of ZigBee in building automation and industrial controls. *Journal of IEE Computing & Control Engineering, 16*, 14–19.
2. Song, G., Ding, F., Zhang, W., & Song, A. (2008). A wireless power outlet system for smart homes. *IEEE Transactions on Consumer Electronics, 54*, 1688–1691.
3. Lee, J.-S., Su, Y.-W., & Shen, C.-C. (2007). A comparative study of wireless protocols: Bluetooth, UWB, ZigBee, and Wi-Fi. In *IEEE International Symposium on Industrial Electronics Society, Taipei, Taiwan* (pp. 46–51).
4. Baker, N. (2005). ZigBee and Bluetooth strengths and weaknesses for industrial applications. *Computing and Control Engineering Journal, 16*, 20–25.

Chapter 19
Properties of the Highly Textured (200) NiO Thin Film Deposited by RF Magnetron Sputtering

F. H. Wang, P. J. Li, C. C. Diao, C. C. Huang, H. H. Huang and C. F. Yang

Abstract Nickel oxide (NiO) thin films are a well-known functional p-type material which can be used for many applications such as electrodes, sensors, and electrochromic devices. This work investigated the effect of different deposition power on the crystal structural, electrical, and optical properties of NiO thin films prepared by RF magnetron sputtering at room temperature in a pure argon atmosphere. The structural and optical properties of NiO thin films were examined by using X-ray diffraction and UV–Vis-NIR spectrum, respectively. The thickness and the composition of NiO thin films were analyzed by glow discharge spectrum, and the thickness increased with increasing deposition power. SEM observations showed that the surface particle sizes of NiO thin films increased with increasing deposition power. The crystal structure varied from amorphous phase to (200) orientation as the deposition power increased from 75 to 150 W. The electrical results showed that the 125 W-deposited NiO thin films had the lowest resistivity and the largest mobility and carrier concentration. The absorption edges in the UV region shifted toward lower optical length as deposition power (or thickness) increased. Findings from GDS analysis indicated that the obtained NiO thin films were Ni-rich non-stoichiometric films, which possessed excellent electronic properties.

F. H. Wang · C. C. Huang
Department of Electrical Engineering, National Chung Hsing University, Taichung, Taiwan, Republic of China

P. J. Li · C. F. Yang (✉)
Department of Chemical and Materials Engineering, National University of Kaohsiung, Kaohsiung, Taiwan, Republic of China
e-mail: cfyang@nuk.edu.tw

C. C. Diao
Department of Electronic Engineering, Kao Yuan University, Kaohsiung, Taiwan, Republic of China

H. H. Huang
Department of Electrical Engineering, Cheng-Shiu University, Kaohsiung, Taiwan, Republic of China

J. Juang et al. (eds.), *Proceedings of the 2nd International Conference on Intelligent Technologies and Engineering Systems (ICITES2013)*, Lecture Notes in Electrical Engineering 293,
DOI: 10.1007/978-3-319-04573-3_19,

Keywords Nickel oxide film · Transmittance · Structure · Textured

19.1 Introduction

Nickel oxide (NiO) is an attractive material due to its excellent chemical stability, as well as optical, electrical, and magnetic properties. It has also been used as antiferromagnetic material [1], material for electrochromic display devices [2], and functional layer material for chemical sensors [3]. Furthermore, it is considered to be a model semiconductor with p-type conductivity thin films due to its wide band-gap energy range from 3.6 to 4.0 eV [4]. NiO thin films can be fabricated by various deposition techniques, which include spray pyrolysis [5], plasma-enhanced chemical vapor deposition [6], and reactive sputtering [3]. Among these methods, the radio frequency (RF) magnetron sputtering has been most widely used. Many researches [6–8] have developed the influences of sputtering parameters on the properties of NiO thin films. The conduction properties of NiO thin films are primarily determined by holes generated from nickel vacancies, oxygen interstitial atoms, and the use of a dopant. As the substrate temperature is increased, the evaporation ratio of the solution is too swift, resulting in the formation of inferior NiO thin films. Many reference data and previous studies [6–8] show that superior electronic and optical properties of NiO thin films can be obtained by RF magnetron sputtering with sputtering pressure in the range of 10^{-3}–10^{-2} Torr and in a pure argon atmosphere with a heated substrate. In this study, optimal sputtering parameters, as being suggested in Refs. [6–8], are employed to RF magnetron sputtering NiO target in a pure Ar atmosphere. The effects of sputtering parameters on the electrical and optical properties of NiO thin films, such as the crystalline structure and transmittance were all investigated. The structural and optical properties of NiO thin films were characterized by scanning X-ray diffraction (XRD) patterns, electron microscopy (SEM), UV–visible spectroscopy, and Hall measurement, respectively. The value variations in the optical band gap (E_g) of NiO thin films were also evaluated from the plots of $(\alpha hv)^2 = c(hv\text{-}E_g)$.

19.2 Experimental Procedure

Nickel oxide (NiO) thin films were deposited on the Corning 1737 glass substrates with a thickness of 0.7 mm by a RF magnetron sputtering system, a NiO ceramic with 99.99 % purity was used a target and deposited in a pure argon atmosphere. The chamber was evacuated to a base pressure below 3×10^{-6} Torr before deposition. Deposition of NiO thin films was performed at a gas pressure of 5×10^{-3} Torr for 20 min, and the deposition power of cathode was changed from 75 to 150 W. The crystal structure of the deposited NiO thin films was identified

by X-ray diffraction (XRD) analysis. XRD patterns of NiO thin films were determined with PANalytical, 18 kW Rotating Anode X-ray Generator using monochromatic high-intensity CuKα radiation ($\lambda = 1.5406$ Å). The surface morphology of the deposited NiO thin films was analyzed by a Field emission scanning electron microscope (FESEM). The transmittance was measured at normal incidence in visible spectrum using JASCO V-570 spectrometer. The thickness and the composition of NiO films were analyzed by glow discharge spectrum (GDS). The chemical bonding states of oxygen and Ni in NiO thin films were investigated using an X-ray photoelectron spectroscopy (XPS).

19.3 Results and Discussion

The structure of NiO thin films deposited at various RF powers in pure Ar atmosphere was examined by XRD patterns (not shown here). As 75 W was used as deposition power, no apparent diffraction peak was observed, and NiO thin films showed the amorphous structure. As the deposition power was equal to and more than 100 W, the (200) diffraction peak were observed. The diffraction intensity of (200) peak increased rapidly with increasing deposition power, particularly as the deposition was higher than 100 W. The stronger diffraction peaks indicate that NiO thin films have a highly crystallized and (200)-textured structure.

The concentration profiles of NiO thin films were then analyzed with a GDS system, and the GDS depth profile of NiO thin films was shown in Fig. 19.1. As the deposition power were 75, 100, 125, and 150 W, the thicknesses of NiO thin films were about 36, 47, 56, and 72 nm, respectively. The GDS depth profiles confirm that the thicknesses of NiO thin films increased with deposition power. Figure 19.1 also shows that the deposited NiO thin films had a non-stoichiometric composition, which existed a Ni excess and oxygen vacancy. The results show that Ni-rich in NiO thin films creates vacancies in the normally occupied O sites to preserve overall electrical neutrality in the deposited thin films. Two Ni^{2+} ions must be converted to Ni^{3+} for every vacant Ni^{2+} site formation. Thus, Ni^{3+} ions could be considered to be positive centers capable of jumping from one Ni^{2+} site to another. When an electron hops from a Ni^{2+} to a Ni^{3+} site, it is as if a positive hole moves through the Ni^{2+} sites. Thus, NiO with Ni-rich film will reveal as a P-type semiconductor [8]. Applying band model to NiO with excess of oxygen, the Ni^{3+} sites act as impurity levels above the filled band and the excitation of an electron to these sites leave mobile holes in the band.

Figure 19.2 shows the SEM micrographs of NiO thin films as a function of deposition power. Figure 19.2 clearly shows that the morphology of NiO thin films had a granular structure, with individual grains appearing most clearly as bright spots on the dark field image. The volumes and sizes of the bright spots increased with increasing deposition power. When deposition power of NiO thin films is increased, the mobility of the molecules on the surface is improved, and that has resulted in an increase of the surface grain size and the thickness. Figure 19.2 also

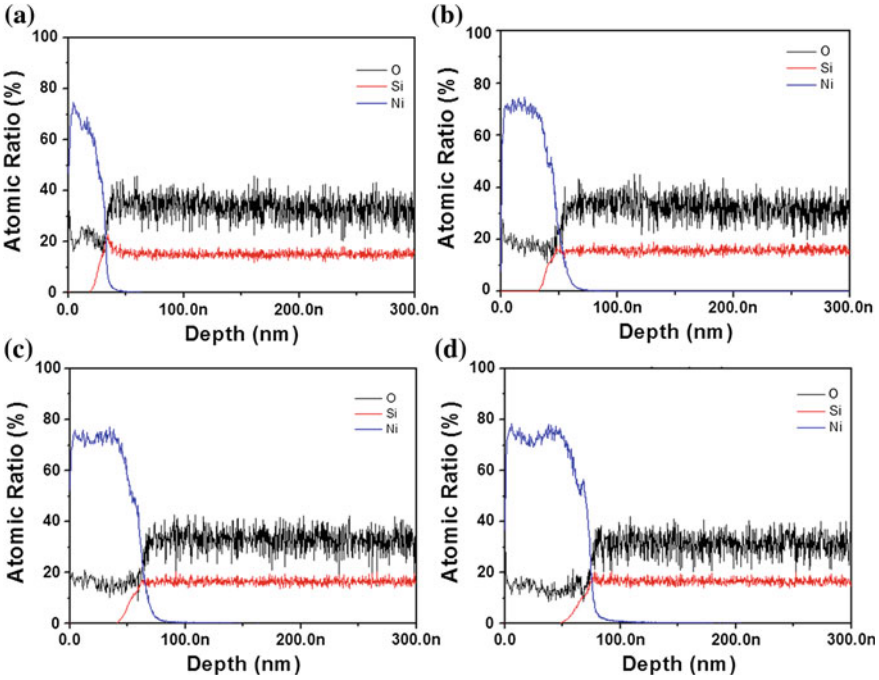

Fig. 19.1 GDS results of NiO thin films: **a** 75 W, **b** 100 W, **c** 125 W, and **d** 150 W

shows that the roughness of NiO thin films increased with increasing deposition power.

Figure 19.3 shows the UV absorbed spectra and the calculated energy gaps (Eg) of NiO thin film under various deposition powers. Figure 19.3a shows that the transmittance ratio decreased with increasing deposition power. The decrease of transmittance ratio with increasing deposition power results in increasing the proportion of nickel caused the light to be absorbed, the results in GDS analysis can prove this result. In the past, determination of the optical band gap (*Eg*) was often necessary to develop the electronic band structure of a thin-film material. However, using extrapolation methods, the *Eg* values of films can be determined from the absorption edge for direct interband transition, which can be calculated using the relation in Eq. (19.1)

$$(\alpha hv)^2 = c(hv - Eg) \tag{19.1}$$

where α is the optical absorption coefficient, c is the constant for direct transition, h is Planck's constant, and v is the frequency of the incident photon [9]. The linear dependence of $(\alpha hv)^2$ on hv indicates that NiO thin films are direct transition type semiconductors. The Eg value of 75 W-deposited NiO thin films was 3.38 eV; As the deposition power of NiO thin films increased from 100 to 150 W, the Eg values increased from 3.20 to 3.34 eV. As we know the Eg values of NiO thin film

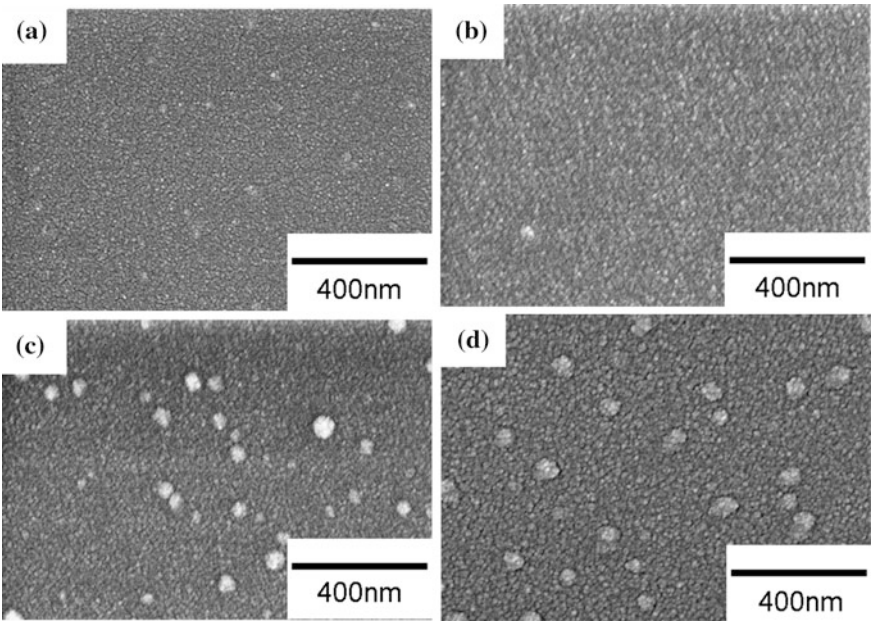

Fig. 19.2 SEM images of NiO films deposited at **a** 75 W, **b** 100 W, **c** 125 W, and **d** 150 W

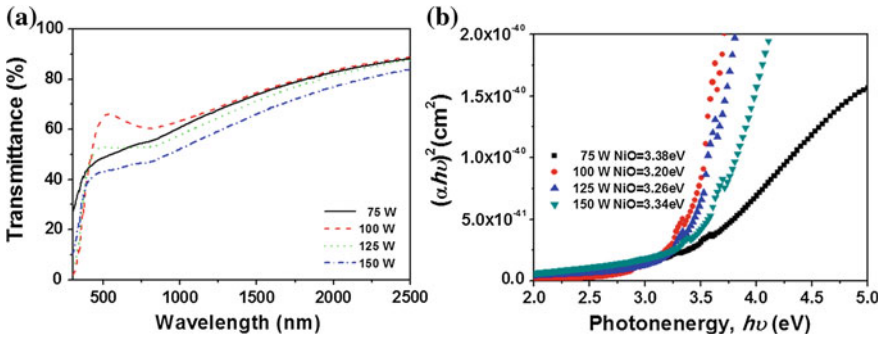

Fig. 19.3 **a** Transmittance and **b** energy gap of NiO thin films

is ranged from 3.6 to 4.0 eV [4] and, except the 75 W-deposited samples, the Eg value obviously increased with deposition power as shown in Fig. 19.3b.

Figure 19.4 shows the results of Hall-effect measurement of NiO thin films at various deposition powers, which indicates the value variations of resistivity, mobility, and carrier concentration were dependent deposition power. The lowest resistivity (2.49×10^{-2} Ω·cm), the largest mobility (3.63×10^{1} cm^2/V·s), and carrier concentration (6.91×10^{17} cm^{-3}) was obtained at the deposition power of 125 W. The electrical conductivity of undoped NiO thin films has a strong

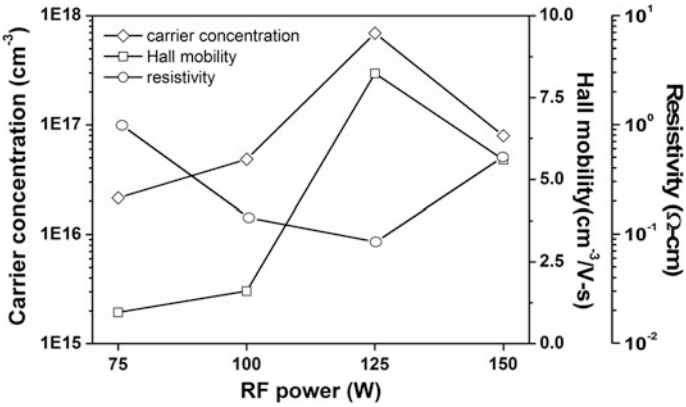

Fig. 19.4 Hall measurements of NiO thin films as a function of deposition power

dependence on the microstructural defects existing in NiO crystallites, such as nickel vacancies and interstitial [6–10]. The microstructure, composition, the deposition parameters are the main factors that will affect the electrical properties of NiO thin films. As we know, the variation in carrier concentration of deposited thin films depends on both crystalline microstructures and surface chemical reactions during the sputtering process. The drift velocity and mean free path of the charge carriers were used to determine the value of mobility. Reducing the scattering by the lattice imperfections increases the mobility of carrier with larger grain means less grain boundaries existing, and the scattering effect at the grain boundary is reduced [7]. Nakahata et al. [10] prepared polycrystalline silicon thin films on glass by PECVD and found that the value of Hall mobility depends strongly on the grain size, the texture, the crystallinity, or the fluctuation of grain orientation. For that, we suggest that the observed variation of carrier concentration and Hall mobility are associated with the NiO crystalline microstructure change and point defects.

The Ni $2p_{3/2}$ XPS spectra of NiO thin films are shown in Fig. 19.5. The NiO peaks at 853.6 eV and Ni_2O_3 peak at 855.6 eV, respectively, were revealed in the XPS spectrum, and no significant peak shift was observed in the Ni $2p_{3/2}$ spectrum as the deposition power increased. For Ni $2p_{3/2}$ electron binding energy, the intensity of Ni^{2+} bonding state decreased and Ni^{3+} bonding state increased as deposition power increased from 75 to 125 W and saturated at 125 W. The ratio (fitting area) of Ni^{3+}/Ni^{2+} increased from 1.83, 7.78, 8.85, and 12.1 as deposition power was 75, 100, 125, and 150 W, respectively. It coincides with the tendency observed in the Ni $2p_{3/2}$ peak where the Ni^{2+} (NiO) bonding state decreases over Ni^{3+} (Ni_2O_3) bonding state with increasing deposition power. The past literature had demonstrated that the formation of holes in a NiO thin film is due to an increase in the Ni^{3+} ions or to the formation of Ni^{2+} vacancies and the presence of interstitial oxygen atoms [11]. The results in Fig. 19.1 also demonstrate that the formation of holes in NiO thin films is due to the increase of the Ni^{3+} ions or the

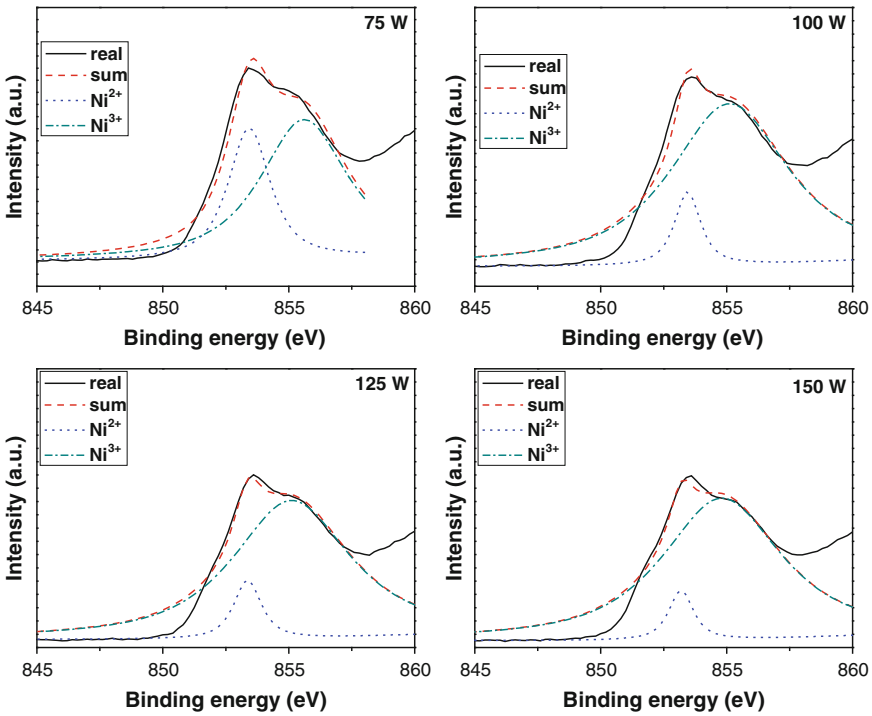

Fig. 19.5 Deconvolution of Ni $2p_{3/2}$ XPS spectra of NiO thin films

formation of the Ni^{2+} vacancies and the interstitial oxygen atoms. With increase of the hole concentration, the carrier concentration increases, then the resistivity of NiO thin films decrease, as the results shown in Fig. 19.4.

19.4 Conclusions

In this study, the thickness of NiO thin films increased with increasing deposition power. The highest deposition rate and lowest surface roughness were obtained at deposition power of 125 W. XRD spectra indicated that NiO thin films had highly crystalline and (200)-textured structure. For NiO thin films, the lowest resistivity (2.49×10^{-2} Ω·cm), high mobility (3.63×10^{1} $cm^2/V{\cdot}s$), and high carrier concentration (6.91×10^{17} cm^{-3}) were obtained at deposition power of 125 W. The transmittance of NiO thin films decreased with increasing deposition power, the increases of thickness and Ni^{+3} ions were the reasons. The optical energy band was evaluated from the plots of $(\alpha hv)^2 = c(hv - E_g)$, and Eg values were 3.38, 3.20, 3.26, and 3.34 eV, respectively, as the deposition powers were 75, 100, 125, and 150 W.

References

1. Fujii, E., Tomozawa, A., Torii, H., & Takayama, R. (1996). Preferred orientations of NiO films prepared by plasma-enhanced metalorganic chemical vapor deposition. *Japanese Journal of Applied Physics, 35*, L328–L330.
2. Yoshimura, K., Miki, T., & Tanemura, S. (1995). Nickel oxide electrochromic thin films prepared by reactive dc magnetron sputtering. *Japanese Journal of Applied Physics, 34*, 2440–2446.
3. Bogner, M., Fuchs, A., Scharnagl, K., Winter, R., Doll, T., & Eisele, I. (1998). Thin $(NiO)_{1-x}$ $(Al_2O_3)_x$, Al doped and Al coated NiO layers for gas detection with HSGFET. *Sensors and Actuators B: Chemical, 47*, 145–152.
4. Sato, H., Minami, T., Takata, S., & Yamada, T. (1993). Transparent conducting p-type NiO thin films prepared by magnetron sputtering. *Thin Solid Films, 236*, 27–31.
5. Puspharajah, P., Radhakrishna, S., & Arof, A. K. (1997). Transparent conducting lithium-doped nickel oxide thin films by spray pyrolysis technique. *Journal Materials Science, 32*, 3001–3006.
6. Yeh, W. C., & Matsumura, M. (1997). Chemical vapor deposition of Nickel Oxide films from Bis-p- Cyclopentadienyl-Nickel. *Japanese Journal of Applied Physics, 36*, 6884–6887.
7. Lu, Y. M., Hwang, W. S., Yang, J. S., & Chuang, H. C. (2002). Properties of nickel oxide thin films deposited by reactive magnetron sputtering. *Thin Solid Films, 420–421*, 54–61.
8. Hotovy, I., Huran, J., Spiess, L., Liday, J., Sitter, H., & Hascık, S. (2003). The influence of process parameters and annealing temperature on the physical properties of sputtered NiO thin films. *Vacuum, 69*, 237–242.
9. Moss, T. S. (1954). The interpretation of the properties of indium antimonide. *Proceedings of the Physical Society, London, Section B, 67*, 775–782.
10. Nakahata, K., Miida, A., Kamiya, T., Fortmann, C. M., & Shimizu, I. (1999). Carrier transport, structure and orientation in polycrystalline silicon on glass. *Thin Solid Films, 337*, 45–50.
11. Nandy, S., Saha, B., & Mitra, M. K. (2007). Effect of oxygen partial pressure on the electrical and optical properties of highly (200) oriented p-type $Ni_{1-x}O$ films by DC sputtering. *Journal Materials Science, 42*, 5766–5772.

Chapter 20
Using a Simple and Effective Method to Design Microstrip-Line Single-Band and Dual-Band Bandpass Filters with Frequency Adjustable Characteristic

Ming Cheung, Jui-Chan Chung, Kou-Tan Wu and Cheng-Fu Yang

Abstract In this study, a novel compact and effective method was developed to design the single-band and dual-band bandpass filters with frequency adjustable characteristics. The designed filters were comprised of two uniform microstrip lines but with one shorter pairs of open-loop ring resonators (OLLRs) or one longer pairs of OLLRs to be placed between two microstrip lines. The shorter OLLRs had shorter current path and then had higher resonant frequency, they were designed for a single-band filter. The longer OLLRs had longer current path and then had lower resonant frequency, they were designed for a dual-band filter during the 0–8 GHz. A pairs of shunt quarter wavelength open stubs were also added to eliminate the unwanted harmonic frequencies and transmit the desired passbands. Finally, we would design a 5.3 GHz single-band filter and a 3.4/6.6 GHz dual-band filter to prove that the proposed theorem was a compact method and it could be used to design the microwave filters with the number and the frequency of passband adjustable characteristics.

Keywords Microstrip-line · Single-band · Dual-band · Frequency adjustable

M. Cheung
Discipline of Media School and Humanities, The University of Adelaide, Adelaide, Australia

J.-C. Chung · K.-T. Wu
Department of Electrical Engineering, National University of Kaohsiung, Kaohsiung, Taiwan, Republic of China

C.-F. Yang (✉)
Department of Chemical and Materials Engineering, National University of Kaohsiung, Kaohsiung, Taiwan, Republic of China
e-mail: cfyang@nuk.edu.tw

J. Juang et al. (eds.), *Proceedings of the 2nd International Conference on Intelligent Technologies and Engineering Systems (ICITES2013)*, Lecture Notes in Electrical Engineering 293,
DOI: 10.1007/978-3-319-04573-3_20,

20.1 Introduction

In the past decade, simple peer-to-peer communication has rapidly changed to complicated networks, especially in wireless systems. Multi-band bandpass filters with wide bandwidth, high selectivity, and small insertion loss have recently become essential requirements for next-generation wireless communication systems. For that the multi-band filters [1, 2] and frequency and bandwidth adjustable filters [3] have been proposed and exploited extensively as a key circuit block in the wireless communication systems. In the past, there were many different methods used and combined to design the filters with single wideband, multiband, or multi-wideband. However, only few reports have developed the filters with single-band and multi-band bandpass filters with frequency adjustable characteristic. By properly selecting the relevant impedance or strip width ratio, the dual-band and quad-band filters using stepped-impedance resonators can be created [4, 5]. Those results suggest that the structure sizes are the most important factor to influence the characteristics of the designed filters. In the past literatures, Yang et al. positioned two different types of open-loop resonators (a winding line-shaped resonator and a stepped impedance resonator) with the same coupling lengths and coupling gap widths in parallel at the two sides of input/output microstrip lines [6]. They controlled the phase difference for the signals in the two resonators in negative, for that energy cancellation occurred, resulting in wide bandwidths and deep transmission zeros.

Chen and Hsu investigated that they used folded open-loop ring resonators (OLLRs) to design the low loss dual-band microstrip filters [7], as shown in Fig. 20.1. The OLRRs were placed between two microstrip lines and each had a perimeter about a half-wavelength, which could be applied to design the planar bandpass and bandstop filters [8]. Kung et al. also used two open-loop rectangular ring resonators as the elements of coupling connection in order to increase the bandwidths of the dual passbands at around 2.4 and 5.2 GHz [9]. They used the diverging U-shaped dual feed input/output transmission lines for strong coupling and using a shunt quarter wavelength open stub to eliminate the unwanted harmonic frequencies and to transmit the desired passbands. A groove structure was also used to regulate the coupling of the two modes and eliminate the ripple at the designed 5.2 GHz band. In this study, the designed filters were comprised of two uniform microstrip lines but with one shorter pairs of OLLRs or one longer pairs of OLLRs to be placed the correct position between two microstrip lines for single-band or dual-band bandpass filters. As we know, each of the fold half-wavelength ring resonators has the maximum electric field density near the open ends of the line, and the maximum magnetic field density around the center valley of the line at resonance [7]. A pairs of shunt quarter wavelength open stubs were also added to eliminate the unwanted harmonic frequencies and transmit the desired passbands. The proposed single-band and dual-band filters using respective coupling

mechanism had the advantages of low insertion loss, frequencies adjustable of either passband, and easy to design. Finally, two high performance filters with single-band at around 5.3 GHz and dual-band at around 3.4/6.6 GHz were optimally designed.

20.2 Design Procedure and Experimental Procedure

In this study, a novel microstrip single-band and dual-band passband filters were also proposed based on OLRRs shown in Fig. 20.1 [7]. Some Rogers Duroid printed boards have a high dielectric constant of 10.2 and low dielectric loss, but they are too expensive for popularly commercial applications. The Al_2O_3 ceramic substrates have a comparably higher dielectric constant of 9.4, a dielectric loss of less than 0.001, and a low price. For these reasons, the filter was designed on 1 mm thick Al_2O_3 ceramic substrates for pattern minimization. Because as a filter was designed on Al_2O_3 ceramic substrates, a printing method with low environmental impact could be used to fabricate the proposed dual-band bandpass filter (the method did not require $FeCl_3$ solution to etch the Cu plate from the surfaces of Duroid or FR4 substrates) [10]. An Ansoft full-wave electromagnetic field simulator (HFSS) was used to adjust and optimize the pattern parameters. After confirmed the used substrates, in order to obtain the maximum magnetic coupling between the OLRRs and micostrip lines the center valley of the OLRRs was positioned in the proper location, where magnetic field intensity had maximum value. This study used Al_2O_3 ceramic as the substrates, the variations in electric field and magnetic field intensity along the line could be determined using the HFSS by studying wave motions on a microstrip line.

Figure 20.2 shows the simulation results for the current distribution of 2.4, 5.2, and 5.7 GHz on a transmission line formed by using Al_2O_3 ceramic substrates. At the first, the approximate length of 2.4 GHz was calculated and used as the based length. From the uniform section of transmission line, the magnetic field intensity was about 0.5 of length under operation frequency of 2.4 GHz. With operation frequency of 5.2 GHz was applied to the same line, the magnetic field intensity occurred at a distance of 0.27 and 0.73 from the output end. Similarity, as 5.7 GHz was applied to the same line, the magnetic field intensity occurred at a distance of 0.09, 0.48, and 0.91 from the output end. However, as the OLLRs and microstrip lines were used to design the microwave filters, enough signal energy passed from microstrip line to OLLRs and then passed from OLLRs to microstrip line is very important. If coupling is too weak, the insertion loss in the passband of the designed bandpass filters will be large; If coupling is too strong, the ripple will appear in the passband of the designed filters. However, the two conditions will degrade the performance of the designed bandpass filters.

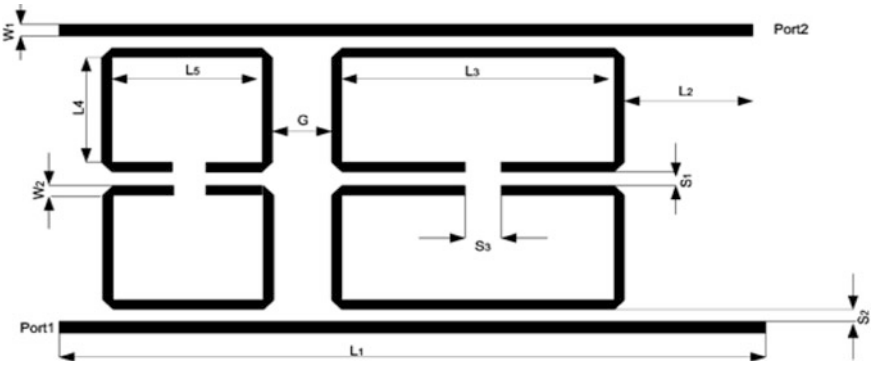

Fig. 20.1 Open-loop ring resonators used in Ref. [7] to design a dual-band filter

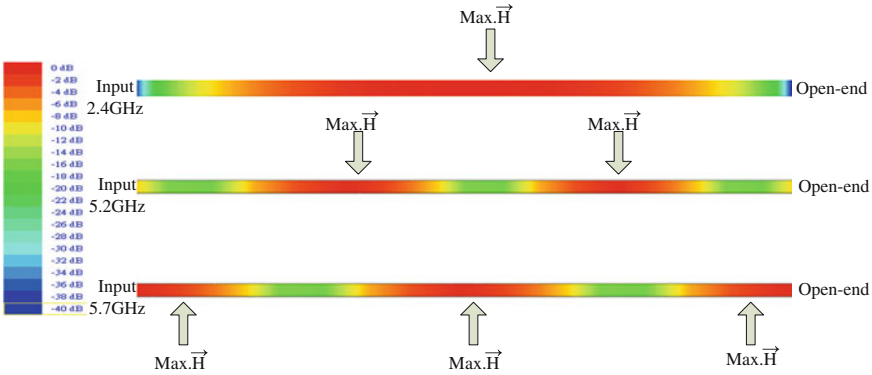

Fig. 20.2 Current distribution of microstrip line terminated at open end

20.3 Results and Discussion

After the most optimal parameters of the designed single-band and dual-band bandpass filters were found, we would leave one parameter to demonstrate the designed parameters had large effects on the characteristics of the designed filters. For the single-band filter shown in Fig. 20.3a, the optimally designed parameters were W1 = 1 mm, W2 = 0.4 mm, W3 = 0.3 mm, L1 = 0.1 mm, L2 = 18 mm, L3 = 3.8 mm, L4 = 2.8 mm, L5 = 12 mm, L6 = 1 mm, and L7 = 3 mm, respectively. As W4 was increased from 2 to 3 mm, as Fig. 20.4 shows, even the shape factor of the passband was improved but the bandwidth decreased and the S21 value of the out-of-band rejection also decreased.

For the dual-band filter shown in Fig. 20.3b, the optimally designed parameters were W1 = 1 mm, W2 = 0.4 mm, W3 = 0.6 mm, W4 = 2 mm, L1 = 0.1 mm, L2 = 2.6 mm, L3 = 3.8 mm, L4 = 6.2 mm, L5 = 2 mm, respectively. As W5

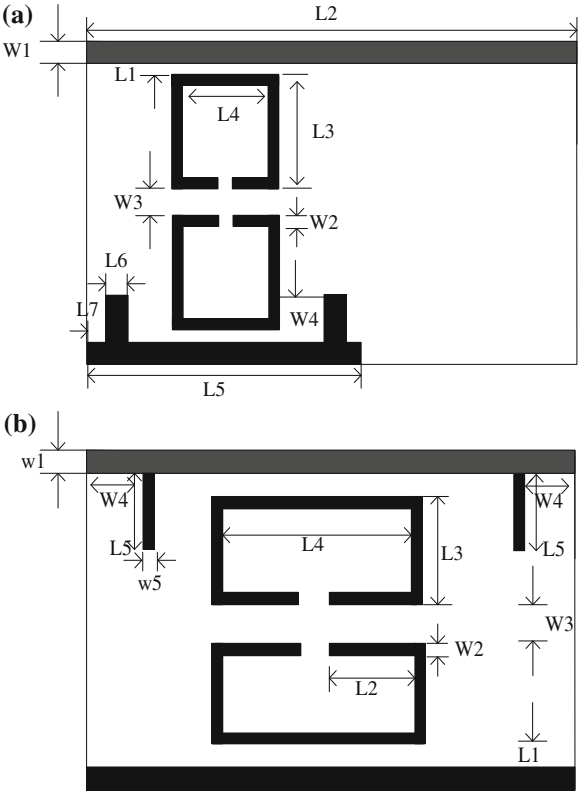

Fig. 20.3 The proposed **a** single-band and **b** dual-band bandpass filters designed on Al_2O_3 ceramic substrates

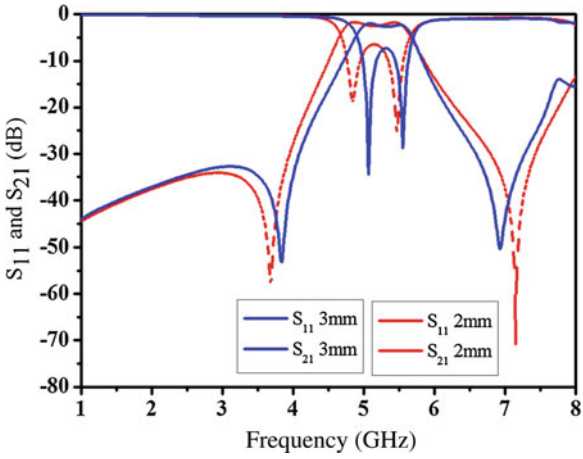

Fig. 20.4 Simulated frequency responses of single-band filter as a function of W4 length

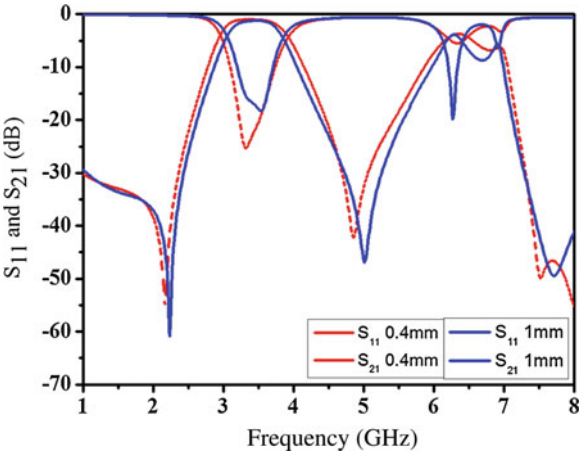

Fig. 20.5 Simulated frequency responses of dual-band filter as a function of W4 length

increased from 0.4 to 1 mm, as Fig. 20.5 shows, the characteristics of the designed filter had no apparent change. Because the length of the OLRRs in Fig. 20.3b was longer than that of Fig. 20.3a, the based resonant frequency was decreased from around 5.2 to 3.4 GHz. Then the first spurious resonant frequency was generated to from the second passband at around 6.6 GHz. The results show that the centre frequency of the designed filter can be accurately controlled to a desired frequency band once the right position and the right size of OLLRs are found. The results in Figs. 20.4 and 20.5 demonstrate that we can design the single-band and dual-band bandpass filters by using the different lengths of the OLRRs and by putting them in the optimal position of the microstrip lines. Figures 20.4 and 20.5 also demonstrate that the lengths of the OLRRs are the most important parameter to design a single-band filter or a dual-band filter in the coupling structure of OLRRs and microstrip lines.

20.4 Conclusions

From the results of this study, a simple and effective method based on standing wave and different sizes of open-loop ring resonators (OLLRs) for designing microstrip single-band and dual-band filters had successfully been investigated. By using the proposed method and finding the optimal structure parameters of OLLRs by HFSS, the centre frequencies of the designed filters could be tuned separately and it was possible to design the single-band and dual-band bandpass filters using the same designed structure depending on the different sizes of OLLRs. As the proposed examples, as the sizes of OLLRs decreased, the based-resonant frequency of the designed filters decreased from 5.2 to 3.4 GHz. A first spurious resonant frequency was generated to form the second passband at around 6.6 GHz, then a dual-band filter was formed. Those results proved that we had proposed a compact method to design a microwave filer with frequency adjustable characteristics.

References

1. Chen, W. N., Chia, W. K., Yang, C. F., & Shih, C. L. (2007). Design of dual-band bandpass filter using stepped impedance resonator and defected ground structure. *Microwave and Optical Technology Letters, 49*, 3099–3103.
2. Kung, C. Y., Chen, Y. C., Yang, C. F., & Chen, H. M. (2009). The miniature square-ring 2.4/5.2 GHz dual-band bandpass filter. *Microwave and Optical Technology Letters, 51*, 515–518.
3. Chen, W. N., Chia, W. K., Cheung, M., & Yang, C. F. (2010). Compact etched ground structure ultra-wideband bandpass filter with adjustable bandwidth. *Journal of Electromagnetic Waves and Applications, 24*, 1375–1385.
4. Chang, S. F., Jeng, Y. H., & Chen, J. L. (2004). Dual-band step-impedance bandpass filter for multimode wireless LANs. *Electronics Letters, 40*, 38–39.
5. Chang, S. F., Chen, J. L., & Chang, S. C. (2003). New dual-band bandpass filters with step-impedance resonators comb and hairpin structures. In *Proc*eedings of *Asia Pacific Microwave Conference* (pp. 793–796).
6. Yang, C. F., Chen, Y. C., Kung, C. Y., Lin, J. J., & Sun, T. P. (2011). Desigan and fabrication of a compact quad-band bandpass filter using two different single-stage open-loop resonators with parallel positioned structure. *Progress in Electromagnetics Research, PIER, 115*, 159–172.
7. Chen, C. Y., & Hsu, C. Y. (2006). A simple and effective method for microstrip dual-band filters design. *IEEE Microwave and Wireless Components Letters, 16*, 246–248.
8. Hong, J. S., & Lancaster, M. J. (1995). Canonical microstrip filter using square open-loop resonators. *Electronics Letters, 31*, 2020–2022.
9. Kung, C. Y., Chen, Y. C., Wu, S. M., Yang, C. F., & Sun, J. S. (2011). A novel compact 2.4/5.2 GHz dual wideband bandpass filter with deep transmission zero. *Journal of Electromagnetic Waves and Applications, 25*, 617–628.
10. Yang, C. F., Cheung, M., Huang, C. Y., & Sun, J. S. (2010). Print a compact single- and quad-band slot antenna on ceramic substrate. *Journal of Electromagnetic Waves and Applications, 24*, 1697–1707.

Chapter 21
Dynamic Economic Dispatch Incorporating Wind Power Generation with Carbon Trading

Tung-Sheng Zhan, Chih-Cheng Kao and Bo-Ru Niu

Abstract This paper proposed an issue aiming at the goal of pierces the relationship between the emission trading scheme and dynamic economic dispatch (DED) problem for the electricity utility. A model of the CO_2 emission trading market will be introduced into DED problem incorporating wind power plants and independent power providers (IPPs). The CO_2 emission trading is treated as the inner-cost, and the superfluous CO_2 quotas will be resale into the market, whereas the shortage quotas should be purchased from the market. The accelerated particle swarm optimization (APSO) algorithm, which avoid prematurity convergence of the original PSO and improve searching efficiency, is introduced to determine the DED strategy of the utility with incorporation of renewable power generation and contribution of IPPs.

Keywords Dynamic economic dispatch · CO_2 emission · Independent power providers · Particle swarm optimization

21.1 Introduction

The "Murakush Documents" was carried out by the seventh conference of the United Nations Framework Convention on Climate Change. These documents laid the firm foundation to the CO_2 emission trading, which permits the transferring and obtaining of the emission unit among the contracting parties. The purpose of "Cap-and-Trade Mechanism", one of those documents, is to put the number of CO_2 emission of each contracting party into the control. In the mechanism, "Cap" represents the maximum number of emission under the control, which guarantees

T.-S. Zhan (✉) · C.-C. Kao · B.-R. Niu
Department of Electrical Engineering, Kao-Yuan University, Kaohsiung 82151, Taiwan, Republic of China
e-mail: t21016@cc.kyu.edu.tw

J. Juang et al. (eds.), *Proceedings of the 2nd International Conference on Intelligent Technologies and Engineering Systems (ICITES2013)*, Lecture Notes in Electrical Engineering 293,
DOI: 10.1007/978-3-319-04573-3_21,

the fulfilling of the goals that the amount of emission will be reduced. "Trade" is a restrictive objective that this goal for emission reduction can be achieved at a minimum cost.

This paper proposed a research focused on optimal DED problem with a predicted daily-load curve under the carbon trading scheme and IPPs incorporation. The optimum power purchasing strategy of electricity industry was determined to minimize power generating cost; on the other hand, the trading of carbon emission right is considered to investigate influence between various electricity purchasing price and DED results for electrical utility. The DED problem is more complicated than the conventional economic dispatch model, due to the relevance and continuity in different time section is taken into the consideration of DED.

Additionally, the wind power generation is involved. Wind velocity is unstable and unpredictable, and by the use of the historic record of average wind velocity, the power generation of wind turbine could be found. The wind power generation is treated as a share or substitute generation of the utility for decreasing the CO_2 emission when it is operated.

21.2 Problem Formulation

The carbon trading cost certainly will become one burden of the cost to the electricity industry, the relevant research and analysis should be pre-made. According to the framework mentioned in the previous section, the DED problem can be described as follows:

Object Function

$$Min. \quad f = \sum_{t}^{\mathrm{T}} \left[\sum_{p}^{NP} FC_{t,p}(\bullet) + \sum_{i}^{NI} PC_{t,i}(\bullet) + [PQ_t(\bullet) - SQ_t(\bullet)] \right]. \qquad (21.1)$$

NP number of dispatchable units of the utility(including the sets which take coal, oil, LNG and wind power as fired fuel)
NI number of IPPs
T number of hours in the time horizon
$FC_{t,p}$ the power production cost of the pth unit in the tth time interval for utility
$PC_{t,i}$ the power purchasing cost of utility caused by purchasing power from the ith IPP in the tth time interval
PQ_t the emission quotas purchasing cost of utility in the tth time interval
SQ_t the emission quotas selling cost of utility in the tth time interval

Constraints of the Dynamic Economic Dispatch
The power balance constraint (in each interval) is shown as follows

$$\sum_{i}^{NP} P_{Gi} + \sum_{j}^{NI} BP_j \geq P_D + P_{res}. \tag{21.2}$$

P_D is the predicted daily peak load, P_{res} is the spinning reserve capacity, set as $0.2P_D$. BP_j is the amount of power purchasing from the jth IPP.

Besides, the generator constraint and ramp-up/ramp-down constraint of each interval are mentioned in Ref. [1].

Wind Power Generation Model [2]
Due to wind velocity is unstable and unpredictable, the author use the historic record of wind speed to calculate the power generation of wind turbine. When the average wind velocity $\overline{v}$ and the standard deviation σ are calculated according to the statistics of actual collected wind velocity, a round of calculation as follows:

$$\overline{v} = \frac{1}{n}\sum_{i=1}^{n} v_i, \sigma = \left[\frac{1}{n-1}\sum_{i=1}^{n}(v_i - \overline{v})^2\right]^{\frac{1}{2}}, k = \left(\frac{\sigma}{\overline{v}}\right)^{-1.086}, c = \frac{\overline{v}}{\Gamma\left(1+\frac{1}{k}\right)}.$$

$\Gamma(x)$ is the gamma function, and since the wind power density is $P = \frac{1}{2}\rho v^3$, so the formula of average wind power density is written like:

$$\overline{P} = \frac{1}{2}\rho c^3\left[\Gamma\left(1+\frac{1}{k}\right)\right]^3. \tag{21.3}$$

As a result, the output power of wine turbine is:

$$P_W = \frac{1}{2}\rho c^3\left[\Gamma(1+\frac{1}{k})\right]^3 C_p A. \tag{21.4}$$

P_w output of the wind turbine generator (W)
C_p coefficient of the wind power efficiency
ρ air density = 1.225 kg/m^3
v wind speed (m/s)
A sweeping area of the blade (m^2).

CO_2 Emission Model
The CO_2 emission model of each generating unit is closely related with the fuel used. In the paper, the author, will use the formula proposed by the Intergovernmental Panel on Climate Change (IPCC) to estimate the amount of carbon emission. Firstly, the thermal conductivity of each kind of unit should be estimated as follows:

$$H(P_{Gp}) = \alpha_{Gp} + \beta_{Gp}\cdot P_{Gp} + \gamma_{Gp}\cdot P_{Gp}^2 + \delta_{Gp}\cdot P_{Gp}^3. \tag{21.5}$$

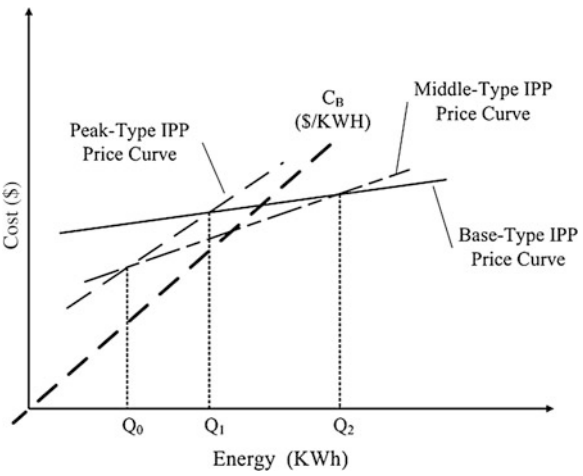

Fig. 21.1 Curve diagram of power trading behavior

Then the amount of carbon emission can be calculated by the use of the following formula:

$$E_p\left(P_{Gp}\right) = H(P_{Gp}) \cdot 4.1868 \cdot \frac{44}{12} \cdot CEP_p \cdot COR_p. \tag{21.6}$$

where E_p indicates the amount of CO_2 emission of the pth unit (Ton./h). α_{Gp}, β_{Gp}, γ_{Gp} and δ_{Gp} are emission coefficients of the pth unit. *CEP* is carbon emission parameter (for oil is 21.1 kgC/GJ, coal is 25.8 kgC/GJ, natural gas is 15.3 kgC/GJ) and *COR* is carbon oxidizing rate(for oil is 0.99, coal is 0.98, gas is 0.995).

Power Trading Model

Figure 21.1 illustrated the proposed model of power trading behavior in this paper. It shows the higher purchasing price (C_B) is, the bigger the slope is. Four conclusions can be observed from the diagram of the different kinds of the IPP

Conclusion 1 when purchasing power by the utility is below the Q_0, the peak-type IPP has the largest competitive edge and the auction price would be higher than the others

Conclusion 2 when purchasing power is between the Q_0 and the Q_2, the middle-type IPP has the largest competitive edge

Conclusion 3 when the purchasing power is beyond the Q_2, the base-type IPP is more competitive

Conclusion 4 the utility could purchase energy not from only one IPP, thus the utility can purchase power according to the cost sequence in different energy section, for instance, when the purchase energy is between Q_0 and Q_1, the purchase sequence is middle-type, peak-type, base-type. But, if purchasing cost is higher than the utility generation cost due to the power increase, the utility will choose to generate by its own units.

Scheme of Carbon Trading
The carbon trading scheme is shown as following programming procedures,

$$
\begin{aligned}
&\textit{if} \quad \sum_{n}^{N} PGCo2_n > Co2\_allow \ \textit{then} \\
&\quad \Delta Co2 = \sum_{n}^{N} PGCo2_n - Co2\_allow \\
&\quad \textit{if } Co2\_buy\_\cos t < P\_reduce\_\cos t \ \textit{then} \\
&\qquad \text{buy deficit of carbon credits.} \\
&\quad \textit{elseif } Co2\_buy\_\cos t > P\_reduce\_\cos t \ \textit{then} \\
&\qquad \text{reduce generation \& increase power purchase.} \\
&\quad \textit{end} \\
&\textit{elseif } Co2\_allow > \sum_{n}^{N} PGCo2_n \ \textit{then} \\
&\quad \text{sell surplus of carbon credits.} \\
&\textit{end}
\end{aligned}
$$

where $PGCo2_n$ is the power plant carbon emission quantity of the utility and IPPs, *Co2_allow* is carbon emission quota(metric-tons.) of the utility and IPPs. *Co2_buy_cost* is the cost due to carbon emission quota purchasing. *P_reduce_cost* means the avoid cost of the utility due to purchasing energy to instead of generate power by its own plants.

21.3 Optimal Algorithm

The accelerated particle swam optimization (APSO), which introduces the flying acceleration mechanism [3], was developed on the basis of PSO. The positional information of the last generation of the particle was introduced to describe speed variation exactly of particle. The APSO is introduced in order to avoid prematurity convergence of the original PSO and improve searching efficiency.

21.4 Case Study and Discussion

To verify the feasibility of the proposed DED model and APSO algorithm, a utility which with fourteen power-plants including three Coal-fired plants, three Oil-fired plants, five LNG plants and three wind-turbines were simulated in this paper. The wind-turbine is with capacity 25, 50 and 75 MW relatively. And, there are there

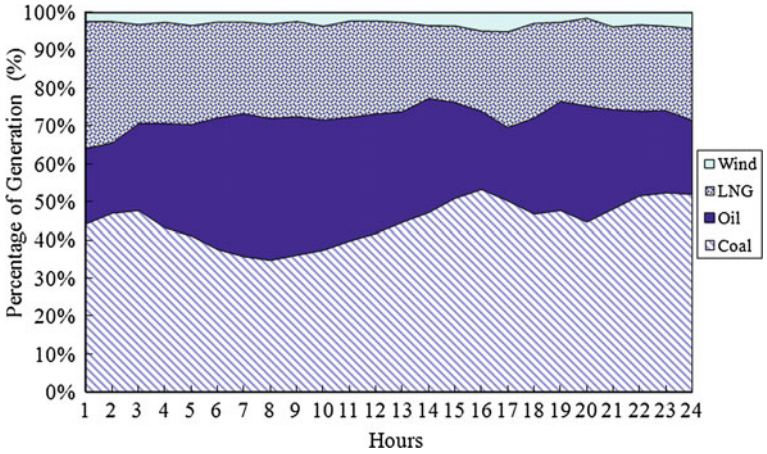

Fig. 21.2 Cumulated generation percentage of dispatch result of Case 1

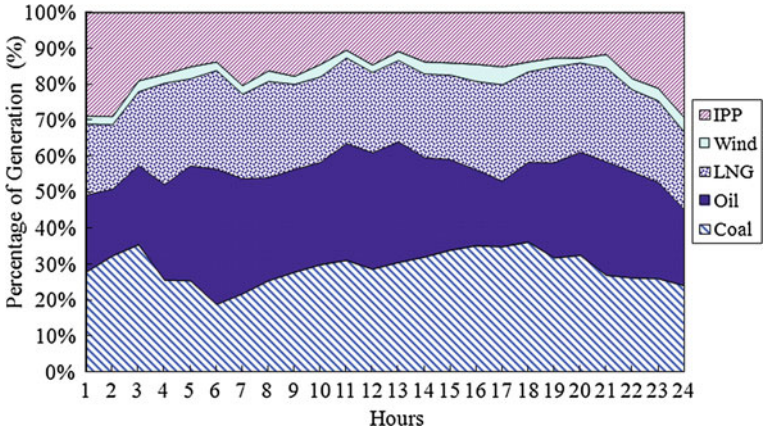

Fig. 21.3 Cumulated generation percentage of dispatch result of Case 2

Table 21.1 Cost analysis of the utility

Case	Total cost ($)	Percentage of generating cost of existing generator (%)	Percentage of power purchasing cost (%)	Percentage of the carbon trading cost (%)
1	1015247	100	–	–
2	1377801	60.2	32.0	7.8

type IPPs: base-type, middle-type and peak-type. The optimal DED strategy and optimal power purchasing price in each hour will be determined by APSO. The test divided into two scenarios, Case 1: the demand load is wholly supplied by the

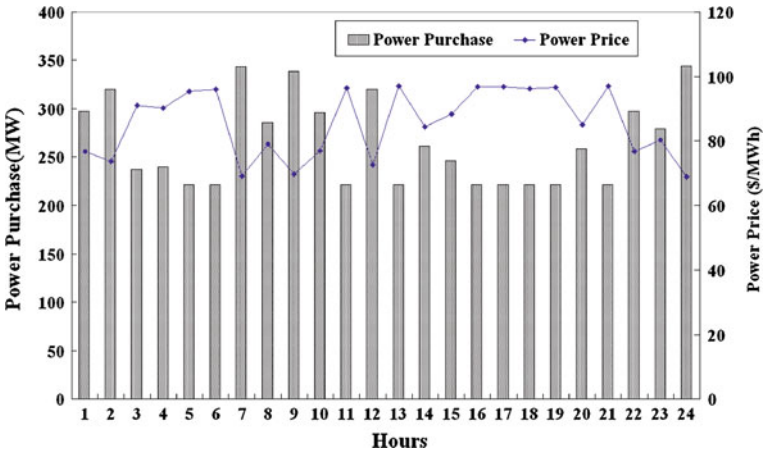

Fig. 21.4 Relationship between power purchase and price

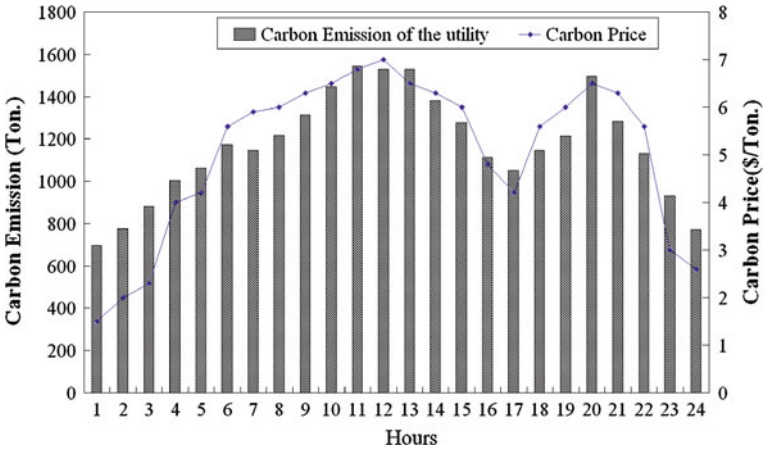

Fig. 21.5 Relationship between carbon emission and carbon price

utility owned power plants, and the carbon trading and constraint of total carbon emission were also not taken into the consideration; Case 2: the load is not only supplied by the utility, but also the electricity can be purchased from the IPPs, and the carbon trading mechanism was considered. Figures 21.2 and 21.3 shows daily cumulated generation percentage of dispatch result of Case 1 and Case 2, then the cost analysis shows that the utility generation cost increases under the carbon trading scheme (Table 21.1).

Moreover, the implementation of the carbon trading will result in higher electricity purchasing price and increase generation cost of utility under the most circumstances (Figs. 21.4 and 21.5).

In order to meet constraint of the carbon quota, it probably makes the utility purchase power instead of self-generating. However, the emission produced by the utility will transfer to the IPPs. In some time, the utility may purchase the emission quota from the carbon market and generate power by its owned units to ease cost sudden increase due to large amount of power purchasing.

References

1. Wollenberg, B. F. (1996). *Power generation operation and control* (2nd ed.). New York: Wiley.
2. Celik, A. C. (2003). A statistical analysis of wind power density based on the Weibull and Rayleigh models at the southern region of Turkey. *Renewable Energy*, *29*, 593–604.
3. Hu, J., & Zeng, J. (2007). A two-order particle swarm optimization model. *Journal of Computer Research and Development*, *44*(11), 1825–1831.

Chapter 22
Liquid-Crystal–Carbon-Nanotube Composite: A Chemophysical Point of View

Andy Ying-Guey Fuh, Wei Lee and Kevin Yu-Chia Huang

Abstract This paper aims to provide insight into the chemophysical nature of the composite of liquid crystal (LC) and carbon nanotube (CNT). A dilute colloid of CNT dispersed in a nematic was prepared for dielectric and birefringence measurements. Molecular dynamics calculations revealed that the polarizability anisotropy of CNT, which induces anisotropic dipolar moments when the composite is subjected to an electric field, plays an important role in enhancing the dielectric anisotropy of the nematic host. Based on the results, field-activated LC materials containing tiny amounts of CNT are expectable for potential applications in LC devices.

Keywords Liquid crystal · Carbon nanotube

A. Y.-G. Fuh · K. Y.-C. Huang (✉)
Institute of Electro-Optical Science and Engineering, National Cheng Kung University, Tainan 70101, Taiwan, Republic of China
e-mail: kevin.starter@hotmail.com

A. Y.-G. Fuh
Department of Physics and Advanced Optoelectronic Technology Center, National Cheng Kung University, Tainan 70101, Taiwan, Republic of China

W. Lee
College of Photonics, National Chiao Tung University, Tainan 71150, Taiwan, Republic of China

K. Y.-C. Huang
Department of Electrical Engineering, Cheng Shiu University, Kaohsiung, Taiwan, Republic of China

J. Juang et al. (eds.), *Proceedings of the 2nd International Conference on Intelligent Technologies and Engineering Systems (ICITES2013)*, Lecture Notes in Electrical Engineering 293,
DOI: 10.1007/978-3-319-04573-3_22,

22.1 Introduction

In the recent years, many researchers have been at the vanguard of studying binary mixtures of nematic liquid crystals (LCs) and carbon nanotubes (CNTs), primarily motivated by their common high geometric aspect ratios and anisotropically physical properties. Among them, Lee et al. observed a great nonlinear-index-change coefficient enhanced by CNTs as a dopant in nematic films [1, 2]. Lynch et al. discovered that CNTs can be orientationally ordered by LC when dispersed in a nematic matrix [3]. Dierking et al. confirmed the guest–host effect exhibited in a LC:CNT sandwiched glass cell, in which CNTs are oriented cooperatively with LC molecules in a sufficient electric field [4]. With potential for display applications, improved electro-optical performances of LCs on introduction of CNTs were also disclosed by various research groups. [See, for example [5–7]] Fundamental physics in reference to LC:CNT was studied by Park et al. who calculated the binding energy of a LC molecule on a CNT sidewall to be up to −2 eV [8]. Recently, efforts were made by Basu et al. to investigate the dielectric behavior of a dilute 5CB:CNT suspension, and the characteristic local *pseudonematic* domains stabilized by the strong anchoring force were experimentally demonstrated [9].

In this work, an *extradilute* LC:CNT was prepared for rigorous LC measurements. Our molecular dynamics (MD) calculations reveal that, in addition to an electromechanical mechanism for the LC:CNT mixture [10], there exists a chemophysical mechanism associated with the induced dipole of CNT that contributes to the enhancement of the dielectric anisotropy of the LC host when the mixture is subjected to an applied electric field.

22.2 Experimental and Molecular Dynamic Calculations

A preliminary mixture of 5CB (Merck; nematic range: 24–35 °C) and 0.02 wt% as-grown multiwalled CNT (MWCNT) (ITRI, Taiwan; purity >95 %) was first prepared by direct impregnations. The mixture was then under a high-power agitation of tip-sonication (Sonics and Materials VC505) to thoroughly debundle the CNT clusters and to obtain a temporary monodispersion. The supernatant was decanted after microcentrifugation (Heraeus Biofuge) at 13000 rpm for 30 min without disturbing the precipitates. The supernatant, though having the same appearance as that of pure 5CB with naked eyes, was sparsely populated by CNTs as verified by the observed discrepancy in optical transmittance between the pure and the prepared samples. Also, the CNTs percolated from 5CB into pellets *in vitro* about 2 weeks after the sample was prepared.

To obtain the dielectric properties, the 5CB:CNT mixture was sandwiched in an homogeneous cell (gap d: 4 μm, ITO-coated area A: 1 cm^2). The capacitance of each empty cell, C_{cell}, was measured to be typically 230 pF, and the relative permittivity of the empty cell, ε_{cell}, was determined by $C_{cell} = \varepsilon_0 \varepsilon_{cell} A/d$, where ε_0

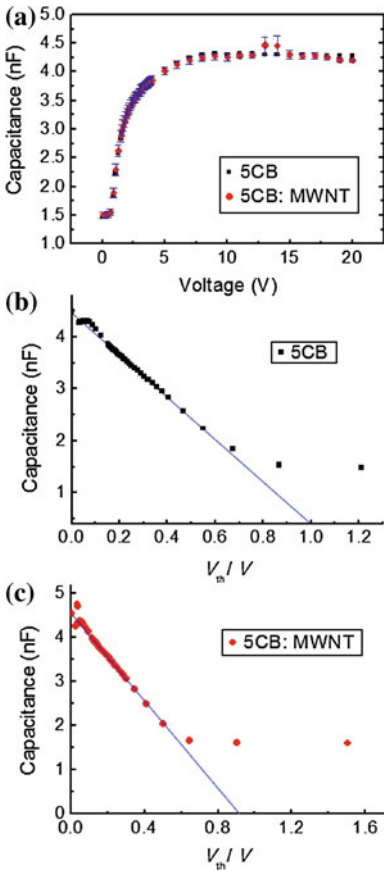

Fig. 22.1 (Color online) **a** Measured capacitance–voltage (*C–V*) responses at 1 kHz of the *extradilute* 5CB:MWCNT composite and the pure 5CB counterpart. Replots of (**a**) and the mostly linear *C* as a function of V_{th}/V for pure and MWCNT-doped 5CB obtained after a simple mathematic operation are shown in (**b**) and (**c**,) respectively

is the vacuum permittivity. The 5CB:CNT cell was subjected to the nematic measurement using the "single-cell" method that involves an extrapolation procedure [11, 12]. This allowed the dielectric constant parallel to the molecular long axis, $\varepsilon_{\|}$, to be dully measured since the so-called hard-boundary condition was eliminated by extrapolating the applied voltage to infinity. Figure 22.1 shows the results using LCAS 1 [13] at an ambient temperature of 27 °C. The dielectric constant perpendicular to the LC director, $\varepsilon_{\perp}$, was determined by the capacitance at voltage of 0.3 V (just below the threshold of the Fréedericksz transition). The nematic measurement yielded the dielectric anisotropies ($\Delta\varepsilon \equiv \varepsilon_{\|} - \varepsilon_{\perp}$) of $\Delta\varepsilon_{5CB} = 13.9$ and $\Delta\varepsilon_{5CB:CNT} = 14.31$.

With the previous studies [7, 9], it becomes evident that $\Delta\varepsilon_{LC}$ can be enhanced by the incorporation of CNT. It is reasonable to postulate that the enhanced $\Delta\varepsilon_{LC}$ is due to the increased effective dipole moment of the composite based on the mean field theory derived by Maier and Meier [14], which correlates the microscopic molecular parameters with the macroscopic dielectric anisotropy of LCs

$$\Delta\varepsilon \equiv \varepsilon_{||} - \varepsilon_{\perp} = \frac{NhFS}{\varepsilon_0}\left[\Delta\alpha + \frac{\mu^2 F}{2K_B T}(3\cos^2\beta - 1)\right], \tag{22.1}$$

where N is the number of molecules per unit volume, h and F are the correction factors for the internal and reactive fields, respectively, S is the orientational order parameter of the nematic LC, μ is the electric dipole moment, $\Delta\alpha \equiv \alpha_{||} - \alpha_{\perp}$. is the polarizability anisotropy, and β is the angle between the molecular long axis and dipole moment. To confirm this postulation, we performed birefringence measurement and MD calculations for the 5CB:CNT combination.

The birefringence measurement investigates the change in polarizability anisotropy of 5CB on introduction of CNT, while the MD calculations examine the local impact of a CNT on the dipole distribution of a 5CB molecule. The anisotropic refractive indices of 5CB and 5CB:CNT were measured using an Abbe refractometer (Atago DR-M4) at 589 nm and 25.8 °C, yielding birefringences $\Delta n_{5CB} = 0.1769$ and $\Delta n_{5CB:CNT} = 0.1798$. Invoking the Vuks model [15] which relates $\Delta\alpha_{LC}$ to the LC's birefringence at optical frequencies

$$\Delta n_{LC} = \frac{4\pi}{3}\frac{n_{LC}^2 + 2}{n_{||} + n_{\perp}} N\Delta\alpha_{LC}, \tag{22.2}$$

where $n_{\perp}$ and $n_{||}$ denote the refractive index of the ordinary and extraordinary rays, respectively, $\langle n_{LC}^2 \rangle = (2n_{\perp}^2 + n_{||}^2)/3$ is the average refractive index in the nematic phase, and N is the number density of LC molecules, the increase in optical anisotropy of the mixture compared with that of the pristine LC can be attributed to the increased $\Delta\alpha_{5CB}$ on addition of CNT, since the constituent CNTs possess high $\Delta\alpha_{CNT}$ owing to their immense "ocean" of delocalized π electrons along the CNT tubular axes. Thus, the high $\Delta\alpha_{CNT}$ is coupled to the LC matrix, contributing collectively to the enhanced birefringence of LC.

Computationally, a triple-walled CNT constructed from the innermost wall with $(N, M) = (5, 5)$ and with a 3.35 Å wall separation was assumed to represent a MWCNT, in which each successive outer wall was built by keeping M constant and increasing N until the distance between the walls exceeded the specified wall separation. Thus, the outermost wall of the representative MWCNT was of helical configuration. The *ab initio* calculation was started by the geometry optimization for the respective constituents and the generation of the equilibrium substrate-adsorbate configuration for the mixture. Thus, the preferential geometry of the 5CB–MWCNT pair was first identified using Adsorption Locator in the software Materials Studio [16]. Then, the structure optimization for 5CB–MWCNT (and for 5CB–SWCNT as a reference) (Fig. 22.2) and the subsequent MD calculations were performed using Forcite code in the same software, with Universal force field at $T = 25$ °C. A time step of 1 fs per integration cycle, for 10^7 cycles, yielded the simulation duration of 10 ns. The conformations of 5CB–MWCNT were recorded from frames that were output every 5000 steps. Accordingly, a total of 2×10^3 conformations were reproduced for posterior analyses.

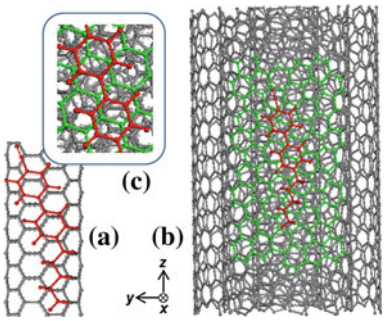

Fig. 22.2 (Color online) *Top views* of the fully relaxed geometries of 5CB combined with **a** a (5, 5) SWCNT and **b** a triple-walled MWCNT. *Red and green colors* represent 5CB molecule and part of the first-layer MWCNT, respectively, to express the stacking configuration for the two constituents, **c** is the zoom-in for the aromatic parts of 5CB positioned on the MWCNT

Intriguingly in Fig. 22.2b, the aromatic parts of 5CB do *not* proximately overlap the hexagonal rings on the CNT sidewall as indicated by Fig. 22.2a, inferring less π–π electron stacking interaction between 5CB and MWCNT. This finding is inconsistent with a previous study that shows perfect overlap between an LC molecule and a SWCNT [8]. Likely, this "off-ring" stacking configuration is the most significant chemophysical difference between LC:SWCNT and LC:MWCNT. On the other hand, the calculated *electrostatic* dipole moments for pure 5CB and its combination with MWCNT are listed in Table 22.1, which shows that the calculated resultant dipole moment for 5CB (4.04 D) agrees decently with a previously reported value (4.03 D) [17]. It is worth mentioning that the MD calculation for the dipole moment of a MWCNT gives a trivial solution attributable to the same electron negativity between C–C atoms, indicating that an "uncapped" MWCNT is a non-polar material. It can be seen from the table that the lateral ($\hat{x}$ and $\hat{y}$) dipole moments of the 5CB–MWCNT pair are increased at the expense of the decreased longitudinal ($\hat{z}$) dipole moment, leading to the increased β in comparison with the pristine LC. Also, the polar 5CB adsorbate seems to impart its permanent dipole moment μ_p to the nonpolar CNT substrate. Note that the phenomena of the increased β angle of 5CB, and the "off-ring" stacking were also observed in a variety of 5CB–CNT combinations regardless the tubular wall configurations in our MD study [18].

Since the differential polarizability of the mixture $\Delta\alpha_{5CB:CNT}$ is small in value according to Eq. (22.2), the dielectric anisotropy of 5CB:MWCNT depends mainly on the resultant/effective dipole moment and its angle with respect to the host molecular long axis at constant frequency and temperature; namely, the second term in Eq. (22.1). However, in addition to the possible decrease in the order parameter S, mixing the pure 5CB with the 5CB–MWCNT compound would diminish the polarity (i.e., reduce the magnitude of the resultant dipole) and increase β of the 5CB molecules, resulting in the decreased dielectric anisotropy of the mix, which contradicts the experimental results.

Table 22.1 Calculated average dipolar components (in Debye unit) for 5CB and the 5CB–MWCNT pair in directions referring to the coordinates in Fig. 22.2. μ_p is the resultant permanent dipole moment

Sample	$\langle \mu_x \rangle$	$\langle \mu_y \rangle$	$\langle \mu_z \rangle$	$\langle \mu_p \rangle$
5CB	0.07	0.49	4.01	4.04
5CB–MWCNT	0.19	0.83	2.85	2.97

Having knowledge of the abundant π-electron conjugation in CNT, one can anticipate that there must be a non-trivial component of the induced dipole moment when the mixture is subjected to an applied electric field. That is,

$$\boldsymbol{\mu}_{\mathrm{e,\,LC:CNT}}(\mathbf{E}) = \mathbf{M}_{\mathrm{LC}} + \mathbf{M}_{\mathrm{LC-CNT}} + \mathbf{P}_{\mathrm{CNT}}(\mathbf{E}), \tag{22.3}$$

where $\mathbf{M}_{\mathrm{LC}} = \sum_{i=1}^{m} \boldsymbol{\mu}_{i,\mathrm{LC}}$, $\boldsymbol{\mu}_{i,\mathrm{LC}}$ is the permanent dipole moment of the ith free LC molecule; $\mathbf{M}_{\mathrm{LC-CNT}} = \sum_{j=1}^{n} \boldsymbol{\mu}_{j,\mathrm{LC-CNT}}$ is the resultant dipole moment of the jth LC–CNT pair; $\mathbf{P}_{\mathrm{CNT}}$ is the induced dipole of the CNT defined by $\mathbf{P}_{\mathrm{CNT}} = \alpha_{\mathrm{CNT}}\mathbf{E}_{\mathrm{t}}$, where α_{CNT} is the frequency-dependent polarizability tensor of the CNT and $\mathbf{E}_{\mathrm{t}}$ is the total electric field felt by the mobile π electrons uncompressed due to delocalization. This induced dipole moment of the CNT was previously studied by Benedict et al. [19], who expressed that the polarizability for external fields in the tubular direction is considerably larger than that for fields along the lateral direction. Thus, $\mathbf{P}_{\mathrm{CNT}}$ indeed plays an important role in contributing the enhancement of the effective dipole moment and, in turn, the dielectric anisotropy of the mixture when both LC and CNT are cooperatively aligned by the electric field.

22.3 Conclusion

In conclusion, LC:CNT acquires enhanced dielectric anisotropy compared with the pure LC as a consequence of the inherent geometric and dielectric anisotropy of CNT. The chemophysical mechanism used to elucidate this notable phenomenon should include both of the *static* resultant and the *dynamic* induced dipole moments under an external electric field. Such unique electroactive characteristic of CNT-doped LCs can therefore be applied for ion trapping [6, 20] and for the development of new field-driven LC materials.

Acknowledgments This work is supported by the National Science Council of Taiwan (Grant No. NSC 98-2112-M-006-001-MY3). The authors acknowledge Professors T.-Y. Chen and C.-Y. Chen and Drs. W,-Y. Wu and M. Wand for experimental assistance and H.-Y. Lee and Dr. K.-T. Cheng for valuable discussion.

References

1. Lee, W., & Chiu, C.-S. (2001). *Optics Letters, 26*, 521.
2. Lee, W., & Yeh, S.-L. (2001). *Applied Physics Letters, 79*, 4488.
3. Lynch, M. D., & Patrick, D. L. (2002). *Nano Letters, 2*, 1197.
4. Dierking, I., Scalia, G., & Morales, P. (2005). *Journal of Applied Physics, 97*, 044309.
5. Lee, W., Wang, C.-Y., & Shih, Y.-C. (2004). *Applied Physics Letters, 85*, 513.
6. Baik, I. S., Jeon, S. Y., Lee, S. H., Park, K. A., Jeong, S. H., An, K. H., et al. (2005). *Applied Physics Letters, 87*, 263110.
7. Huang, C.-Y., Pan, H.-C., & Hsieh, C.-T. (2006). *Japanese Journal of Applied Physics, 45*, 6392.
8. Park, K. A., Lee, S. M., Lee, S. H., & Lee, Y. H. (2007). *Journal of Physical Chemistry C, 111*, 1620.
9. Basu, R., & Iannacchione, G. S. (2010). *Physical Review E, 81*, 051705.
10. Basu, R., & Iannacchione, G. (2008). *Applied Physics Letters, 93*, 183105.
11. Clark, M. G., Raynes, E. P., Smith, R. A., & Tough, R. J. A. (1980). *Journal of Physics D, 13*, 2151.
12. Welford, K. R., & Sambles, J. R. (1987). *Molecular Crystals and Liquid Crystals, 147*, 25.
13. LCAS 1 is a commercially available system configured in accordance with Refs. 13 and 14 for liquid crystal parameter measurements.
14. Maier, W., & Meier, G. (1961). *Zeitschrift Für Naturforschung, 16*, 262.
15. M. F. Vuks, Optika I Spektroskopiya, **60**, 644 (1966).
16. Materials Studio is a registered program from AccelrysTM Inc.
17. Dawid, A., & Gburski, Z. (2007). *The Journal of Non-Crystalline Solids, 353*, 4339.
18. So far includes: (10, 0) and (5, 4) SWCNTs and (15, 15) and (21, 0) (in terms of the outermost wall) MWCNTs.
19. Benedict, L. X., Louie, S. G., & Cohen, M. L. (1995). *Physical Review B, 52*, 8541.
20. Lee, C.-W., & Shih, W.-P. (2010). *Materials Letters, 64*, 466.

Chapter 23
Modified DC Load Flow Based Optimal DG Installations with Fast Feeder Reconfiguration

Rung-Fang Chang, Sung-Ling Chen, Ya-Chin Chang, Chan-Nan Lu and Yu-Wun Wang

Abstract With proper installation of distributed generation (DG), the performances of distribution grid, such as system loss, power quality and reliability, can be improved effectively. In this paper, the particle swarm optimization (PSO) based solution procedure, including the simplified load flow and the proposed modified DC load flow models, is used to solve for the optimal DG installation problem with the proposed fast feeder reconfiguration procedure. The computing efficiency is increased with the load flow fast estimated by the simplified load flow model and the tie switches to open to make a radial feeder structure selected based on the modified DC load flow model. Numerical results indicate that the proposed method can efficiently make a suitable feeder structure with a small system loss and a big DG penetration level.

Keywords Distributed generation capacity · Feeder reconfiguration · Modified DC load flow model · Particle swarm optimization

R.-F. Chang (✉) · Y.-W. Wang
Department of Electrical Engineering, Kao Yuan University, Kaohsiung 821, Taiwan Republic of China
e-mail: rfchang@cc.kyu.edu.tw

S.-L. Chen · Y.-C. Chang
Department of Electrical Engineering, Cheng Shiu University, Kaohsiung 833, Taiwan Republic of China

C.-N. Lu
Department of Electrical Engineering, National Sun Yat-Sen University, Kaohsiung 804, Taiwan Republic of China

J. Juang et al. (eds.), *Proceedings of the 2nd International Conference on Intelligent Technologies and Engineering Systems (ICITES2013)*, Lecture Notes in Electrical Engineering 293,
DOI: 10.1007/978-3-319-04573-3_23,

23.1 Introduction

The number of requests for non-controllable DG interconnections in the medium and low voltage network is increasing. Several system operational benefits, such as system losses reduction and reliability enhancement, could be realized by DG installation on existing networks. DG operation would cause various impacts on the network depending on the system structure and strength at the point of common coupling (PCC). In some cases, DG impact assessments are performed by using simple screening formula. These impact studies are often based on certain feeder configuration without considering time-varying effects of feeder load and DG power outputs. Such assessments could lead to optimistic or conservative results.

The allowable DG capacity is restricted by network operation constraints. In certain cases, if there is no network reinforcement planned for DG integrations the maximum capacity would be restricted. In order to reduce interconnection costs, feeder reconfiguration could be considered for accommodating higher DG capacity. Based on the customer demand data provided by advanced metering infrastructure (AMI) and the distribution feeder structure, the problem to maximize DG penetration by feeder reconfiguration can be formulated as a discrete nonlinear optimization problem.

Many applications and algorithms related to feeder reconfiguration have been proposed [1–3]. To restructure primary feeders for loss reduction, a simple formula which removes the need to conduct many load flow studies, was presented in [1]. Approximated power flow and loss reduction formula with varying degree of accuracy were developed to aid the search for optimal feeder configuration [2, 3]. The impacts of DG in the distribution feeder reconfiguration were shown in [4] and an ordinal optimization (OO) technique based method for distribution feeder reconfiguration was proposed in [5].

Previous studies have shown that through cooperation and competition among the population, particle swarm optimization (PSO) technique can often find good solutions for complicated problems [6–8]. In this paper, a PSO based solution method is proposed to solve the feeder reconfiguration problem to maximize the DG penetration while reduce system loss. The problem to reconfigure the feeders by optimally determining the status of the tie switch on each feeder section and the location and capacity for each DG installation, is formulated as a mixed discrete nonlinear optimization problem.

23.2 Problem Formulation

To investigate the effects when solving the feeder reconfiguration problem to determine the optimal DG installation, the objective function to minimize system loss is:

$$Min \quad P_{loss}(u)/P_{lose,base} \tag{23.1}$$

The security constraints include the supply limits of all transformers [7],

$$\sum_{k \in K_p} S_{pk}(u) \leq S_p^{\max} \quad \forall p \in N_T \tag{23.2}$$

the thermal ratings of all feeders,

$$S_{kj}(u) \leq S_{kj}^{\max} \quad \forall k - j \in N_l \tag{23.3}$$

and the voltage limits for all nodes,

$$V_i^{\min} \leq V_i(u) \leq V_i^{\max} \quad \forall i \in N_d \tag{23.4}$$

where $P_{lose,base}$ is system loss at base state, $P_{loss}(u) = \sum_{i=1}^{N_l} r_i \frac{P_i^2(u)+Q_i^2(u)}{V_i^2(u)}$ is system loss at state u, K_p is the set of the nodes receiving power from transformer p, N_T is the set of all substation transformers, N_d is the set of nodes, N_l is the set of branches, w_1, w_2 is weighting factors, u is the vector of the control variables including the capacity and location for each DG installation, and the status of the tie switch on each feeder section.

Basically, the problem can be solved directly by using a PSO-based solution algorithm with an AC power flow analysis to determine the fitness for each particle in each iteration.

23.3 Proposed Method

In the proposed PSO-based solution algorithm, the modified DC load flow model helps fast select the tie switches to open to make a radial network structure first, and then the simplified load flow model is used to fast inspect the feasibility and evaluate the fitness for each particle representing the location and capacity for each DG installation. Finally, to refine the solution obtained, an AC load flow analysis is executed upon the end of the proposed solution procedure.

23.3.1 Fast Tie Switches Selection Criterion

When using the proposed PSO solution procedure, for each iteration, to make a radial network structure and further improve the computing efficiency, the tie switches most necessary to open should be selected effectively.

In the proposed criterion, with all tie switches closed, the distribution network becomes a meshed grid and the modified DC load flow model is applied. As a result, in each circuit loop, the tie switch on the feeder section with minimum branch current is selected to open. In this way, the control variables for the PSO

procedure are reduced and only the location and the number of DG units (or capacity) for each DG installation left to be determined. Therefore, this criterion would greatly enhance the computing efficiency as compared to the basic PSO solution method. In the modified DC load flow model, the nodal balance equations expressed in complex form are:

$$S_i = V_i I_i^* = \sum_{k=1}^{N_d} |V_i V_k| [\cos(\delta_i - \delta_k) + j \sin(\delta_i - \delta_k)] Y_{ik}^* \tag{23.5}$$

where S_i and V_i are the complex power injection and phasor voltage at node i. Since $(\delta_i - \delta_k)$ is quite small, $\cos(\delta_i - \delta_k) \approx 1$ and $\sin(\delta_i - \delta_k) \approx \delta_i - \delta_k$, (23.5) can be rewritten as:

$$S_i \approx \sum_{k=1}^{N_d} \mathrm{V_i V_k} [1 + j(\delta_i - \delta_k)](Y_{ik}^*) \approx \sum_{k=1}^{N_d} \mathrm{V_i V_k} [Y_{ik}^* + j(\delta_i - \delta_k)(Y_{ik}^*)] \tag{23.6}$$

Because the node voltage magnitudes $\mathrm{V_i} \approx 1 \forall i$ and Y_{ik}^* are constant for all i and k, (23.6) can be changed to:

$$S_i' \approx \sum_{k=1}^{N_d} j(\delta_i - \delta_k)(Y_{ik}^*) \approx j \left(\left(\left(\sum_{k=1}^{N_d} Y_{ik}^* \right) - Y_{ii}^* \right) \delta_i - \sum_{\substack{k=1 \\ k \neq i}}^{N_d} Y_{ik}^* \delta_k \right) \tag{23.7}$$

where $S_i' = S_i - \sum_{k=1}^{N_d} Y_{ik}^*$, as expressed in matrix form below:

$$\mathbf{S'} \approx j[\mathbf{Y_Z}] \cdot \boldsymbol{\delta} \text{ or } \boldsymbol{\delta} \approx -j[\mathbf{Y_Z}]^{-1} \cdot \mathbf{S'} \tag{23.8}$$

Taking apparent power form at both sides of (23.8), it becomes:

$$\boldsymbol{\delta} \approx \left| -j[\mathbf{Y_Z}]^{-1} \cdot \mathbf{S'} \right| \tag{23.9}$$

where $Y_{Z_{ii}} = (\sum_{k=1}^{N_d} Y_{ik}^*) - Y_{ii}^*$ for $i \neq ref$, $Y_{Z_{ii}} = 0$ for $i = ref$, $Y_{Z_{ik}} = -Y_{ik}^*$ for i and $k \neq ref$, $Y_{Z_{ik}} = 0$ for i or $k = ref$.

Similar to the traditional DC load flow method, with the nodal phase angles obtained from (23.9) and as referred to (23.7), the apparent power flow on branch i–k is estimated by:

$$\mathrm{S_{ik}} \approx \sqrt{1 + (\delta_i - \delta_k)^2} \cdot \mathrm{Y_{ik}} \tag{23.10}$$

and with the node voltage magnitudes $\mathrm{V_i} \approx 1 \ \forall i$, the current magnitude flowing on branch i-k can be estimated as:

$$\mathrm{I_{ik}} \approx \mathrm{S_{ik}} / \mathrm{V_i} \tag{23.11}$$

23.4 Numerical Results and Discussions

The simple distribution system with 3 feeders is used for testing [1, 7]. The meshed grid with all 16 tie switches closed has three circuit loops respectively consisting of three sets of feeder sections, that are {S2, S5, S9, S8}, {S7, S11, S14} and {S3, S4, S16, S15, S13}. In order to maintain the three feeders in radial operation, a feeder section should be disconnected from each loop. The nominal voltage of the distribution system is 22.8 kV, the current rating of each feeder is 400 A, and the total real power demand of the system is 28.7 MW. Under the base state without DG installation, when the tie switches on feeder sections S5, S11 and S16 are opened, the system loss in the radial grid is 511.4 kW.

In the study, except substation buses 1, 2 and 3, the other nodes are considered to be the candidate locations for DG installation. A DG unit is rated at 630 kW with unity power factor assumed. The capacity for each DG installation is calculated by summing up the installed DG units. In the followings, the test results respectively for one and two DG installations are presented.

First, using minimum system loss as the objective function, Fig. 23.1 shows the convergence trends and system losses of the test case with one DG installation that are solved by using the basic PSO and proposed PSO methods respectively. As seen that at 15th iteration the proposed method approaches the minimum system loss at 137.5 kW, with system loss, 134.8 kW, estimated by the crude load flow analysis method, while using the basic PSO method, bigger iteration number is necessary for achieving a better solution.

Table 23.1 shows the statistical results of solving the feeder reconfiguration problem for respective 10 trials by the proposed and basic PSO methods, with iteration numbers set to 50 and 100, respectively. As seen that, using the proposed method to solve the problem for 10 trials, the mean (standard deviation) of the execution times are 0.244 (0.008) and 0.481 (0.019) s respectively. Solving the problem with basic PSO for 10 trials, the mean and standard deviation of the execution times are 0.898 (0.034) and 1.755 (0.04) s, respectively. Obviously, in this view, the proposed method outperforms the basic PSO method. It can also be justified with the technical results shown in Table 23.2.

Table 23.2 shows one and two DG installations respectively by using the proposed and basic PSO methods to solve the feeder reconfiguration problem for 10 trials with minimum system loss as objective. The solutions obtained from the proposed method are found to be the same with node 9 used as the location and 26 DG units or 16.38 MW as the capacity for DG installation. Also, in the solution, the tie switches at sections s2, s14 and s16 are selected to open to make the network in a radial structure, which can largely reduce the system loss from 511.43 to 137.5 kW. The average system loss and DG capacity directly obtained from the basic PSO method is 151.7 kW and 14.36 MW respectively, which are worse than the proposed method.

The best solution of the two DG installations includes 25 and 13 DG units as the capacities for the DG installations at nodes 9 and 16 respectively, system loss at

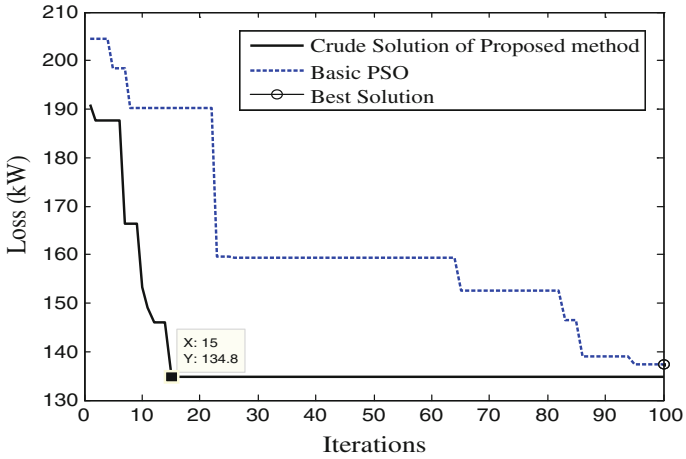

Fig. 23.1 Solution curves of minimum loss for the simple system

Table 23.1 Statistic computing times for 10 trials associated with various iteration numbers

Time	Iteration			
	Proposed PSO method		Basic PSO method	
	50	100	50	100
Mean (s)	0.244	0.481	0.898	1.755
Std. (s)	0.008	0.019	0.034	0.040

Table 23.2 Specific results from 10 trials solved using proposed and basic PSO solution methods for the study case of one and two DG installations

DG Num.	Best solution of 10 trials				Pro. (Avg.)		Basic (Avg.)	
	Node/Num.	Tie Sw.	Loss[a]	Cap.[a]	Loss[a]	Cap.[a]	Loss[a]	Cap.[a]
1	9/26	s2, s14, s16	137.5	16.38	137.5	16.38	151.7	14.36
2	9/25, 16/13	s2, s7, s3	90.2	23.94	92.8	20.8	106.3	20.0

[a] The units of system loss and DG capacity are kW and MW respectively

90.2 kW and the tie switches at sections s2, s7 and s3 selected to open for the feeders to operate in a radial structure. As can also be seen, the average system losses for the proposed and basic PSO methods are 92.8 and 106.3 kW respectively. Since the former is much closer to the best, 90.2 kW, than the latter, thus, in this concern, the proposed method is validated to outperform the basic PSO method.

23.5 Conclusion

In the paper, the optimal DG installation problem with feeder switching controls is formulated as a discrete nonlinear optimization problem. The problem is solved by using the proposed method with the fast feeder reconfiguration scheme, based on three objectives to investigate various possible effects caused by DG installation. Simulation results have demonstrated that, compared to the basic PSO method, the proposed method has better performance in terms of solution quality and computing efficiency. Test results also indicate that a proper DG installation strategy could have positive effects on feeder voltage quality, system loss reduction and allowable DG integrations in the existing distribution networks.

Acknowledgments The authors gratefully acknowledge the financial supports from National Science Council of Taiwan under Grants NSC 102-3113-P-110-007.

References

1. Civanlar, S., et al. (1988). Distribution feeder reconfiguration for loss reduction. *IEEE Transactions on Power Delivery, 3*(3), 1217–1223.
2. Baran, M. E., & Wu, F. F. (1989). Network reconfiguration in distribution systems for loss reduction and load balancing. *IEEE Transactions on Power Delivery, 4*(2), 1401–1407.
3. Darling, G. R., Chiang, H. D., & Wang, J. C. (1996). An efficient algorithm for real-time network reconfiguration in large scale unbalanced distribution systems. *IEEE Transactions on Power Systems, 11*(1), 511–517.
4. Olamaei, J., Niknam, T., & Gharehpetian, G. (2007). Impact of distributed generators on distribution feeder reconfiguration. In *Proceedings of IEEE Lausanne Power Tech*, *2007*.
5. Li, F. (2009). Application of ordinal optimization for distribution system reconfiguration. In *Proceedings of Power Systems Conference and Exposition, IEEE/PES*, *2009*.
6. Su, S. Y., Lu, C. N., Chang, R. F., & Gutiérrez-Alcaraz, G. (2011). Distributed generation interconnection planning: A wind power case study. *IEEE Transaction on Smart Grid, 2*(1), 181–1189.
7. Chang, R.F., et. al. (2010). Modified particle swarm optimization for solving distribution feeder reconfiguration problem with distributed generation. In *Proceedings of IEEE TENCON, November 21–24, 2010*.
8. Clerc, M. (1999). The Swarm and The Queen: Towards a deterministic and adaptive particle Swarm optimization. In *Proceedings of the 1999 Congress on Evolutionary Computation* (Vol. 3, pp. 1951–1957).

Chapter 24
Effects of Thickness on the Properties of Indium-Doped Zinc Oxide Films

Chia-Ching Wu, Chien-Chen Diao, Chih-Chin Yang, Yi-Chieh Chao, Chin-Guo Kuo and Cheng-Fu Yang

Abstract In this study, radio frequency magnetron sputtering was used to deposit indium-doped zinc oxide (IZO) films with varying deposition time on glass substrates. The structural, optical, and resistivity properties of IZO films were investigated with field emission scanning electron microscope, X-ray diffraction patterns, UV–visible spectroscopy, and Hall-effect analysis. XRD analysis on IZO films showed that only the (002) diffraction peak was observable, indicating that the IZO films showed a good c-axis orientation perpendicular to the glass substrates. As the deposition time of IZO films increased from 30 to 90 min, the thickness increased from 237 to 389 nm, the grain size increased from 12.3 to 87.6 nm, and the resistivity decreased from 9.08×10^{-3} to 2.85×10^{-3} Ω-cm. The transmittance was found to slightly decrease with the increasing thickness of IZO films.

Keywords Transparent conductive oxide · Indium-doped zinc oxide · RF magnetron sputtering · Thickness

C.-C. Wu · C.-C. Diao
Department of Electronic Engineering, Kao Yuan University, Kaohsiung, Taiwan, Republic of China

C.-C. Yang
Department of Microelectronics Engineering, National Kaohsiung Marine University, Kaohsiung, Taiwan, Republic of China

Y.-C. Chao · C.-G. Kuo
Department of Industrial Education, National Taiwan Normal University, Taipei, Taiwan, Republic of China

C.-F. Yang (✉)
Department of Chemical and Materials Engineering, National University of Kaohsiung, Kaohsiung, Taiwan, Republic of China
e-mail: cfyang@nuk.edu.tw

J. Juang et al. (eds.), *Proceedings of the 2nd International Conference on Intelligent Technologies and Engineering Systems (ICITES2013)*, Lecture Notes in Electrical Engineering 293,
DOI: 10.1007/978-3-319-04573-3_24,

24.1 Introduction

Transparent electronics is an advanced technology concerning the creation of visible electronic devices. To realize transparent electronic and optoelectronic devices, transparent conducting oxides (TCOs) have been widely utilized [1, 2]. Good TCOs should have wide optical band gap (>3.5 eV), low electrical resistivity ($<10^{-3}$ Ω-cm), high optical transmittance (>80 % in the visible region), and good etching property. Impurity doped indium oxides, tin oxides, and zinc oxides are known to satisfy these conditions well [3, 4]. Especially, impurity-doped indium oxide systems, such as tin-doped indium oxide (ITO), have been most widely used for numerous optoelectronic applications. However, in order to have high electrical conductivity and high transmittance, ITO films must be deposited and then annealed at high temperature (>300 °C). This high temperature makes the ITO films rough due to the crystallization, which leads to significant deterioration of the device reliability [5, 6].

Zinc oxide (ZnO) is an n-type semiconductor with a large binding energy and a wide bandgap. Doped ZnO films are promising alternatives to replace ITO films as TCOs due to the former's stable electrical and optical properties. The low resistivity of ZnO-based films arises from the presence of oxygen vacancies and zinc interstitials [7]. Al [8], Ga [9], and Ti [10] have been widely studied as dopants to enhance the n-type conductivity of ZnO-based films. Also, the ZnO-based films can be deposited using variety of techniques, such as sputtering [11], pulsed laser deposition (PLD) [12], metal organic chemical vapor deposition (MOCVD) [13], and spray pyrolysis (SP) [14]. Indium-doped zinc oxide (IZO) films can be deposited by RF magnetron sputtering technique which has been widely used due to its advantageous features including simple apparatus, high deposition rates, and low deposition temperature.

In this study, IZO films of a fixed composition (ZnO = 98 mol % and In_2O_2 = 2 mol %) were deposited by radio frequency magnetron sputtering from an oxide target mixed with ZnO and In_2O_3, near which composition the lowest resistivity was observed when processed at room temperature. The structural, optical, and electrical properties of IZO films were characterized by scanning electron microscopy (SEM), X-ray diffraction (XRD) pattern, UV–visible spectroscopy, and Hall measurement.

24.2 Experimental Procedures

Raw materials (ZnO and In_2O_2, 99.99 % in purity) were weighed according to the composition formula ZnO = 98 mol % and In_2O_2 = 2 mol % (IZO), and ball-milled with deionized water for 1 h. After being dried and ground, the powder was calcined at 800 °C for 2 h and ground again. The calcined powder was uniaxially pressed into a 2-inch plate in a steel die, and sintering was carried out at 1400 °C

in air for 2 h. 20 mm × 20 mm × 1 mm Corning 1737 glass were used as substrates, then the substrates were cleaned with acetone, isopropyl alcohol, deionized (D.I.) water, and dried under blown nitrogen gas, then IZO films were deposited on glass substrates. The working distance between the substrate and target was fixed at 10 cm. The base pressure was 5×10^{-6} torr and the working pressure was maintained at 5×10^{-3} torr. The deposition temperature of IZO films was kept at room temperature, the RF power was 100 W, and the deposition times varied from 30 to 90 min. The crystalline structures of IZO films were determined with an X-ray diffractometer using CuKα radiation (K = 1.5418 Å). The surface morphology and thickness of IZO films were measured by using the field emission scanning electron microscope (FE-SEM). The mobility, carrier concentration, and resistivity were obtained from Hall-effect measurements using the Van der Pauw method. Optical transmittance was measured by a UV spectrophotometer in the wavelength range of 200–1100 nm.

24.3 Results and Discussion

Figure 24.1 shows the surface SEM images of IZO films as a function of deposition time. The surface micrographs of the 30, 50, and 70 min-deposited IZO films had the similar morphologies. The surfaces of IZO films are smooth and compact, the average grain sizes of the 30, 50, and 70 min-deposited IZO films were about 12.3, 22.6, and 45.5 nm, respectively. However, as deposition time was increased to 90 min, the grain size of IZO films increased and the abnormal particles were also formed, and the roughness would critically increase. These results suggest that the deposition time of IZO films shorter than 90 min is better. The cross-section FE-SEM images of IZO films with different deposition times are shown in inset Fig. 24.1. The thickness of IZO films increased with deposition time is considerable. The thickness increased from 237 to 389 nm as the deposition times increased from 30 to 90 min. In addition, the crystallization IZO film reveals that preferential orientation growth with the columnar structure, as shown in Fig. 24.2a–d.

Figure 24.2 shows the mobility, carrier concentration, and resistivity of IZO films as a function of deposition time. As the deposition time increased from 30 to 90 min, the mobility increased from 19.26 to 43.69 cm^2/V-s. This result cause by the better crystal quality and larger particle sizes of IZO films. Therefore, a reduced grain boundary barrier is obtained, leading to an increase in carrier mobility. The carrier concentration of IZO films slightly decreased from 9.95×10^{18} to 1.21×10^{18} cm^{-3} as the deposition time increased from 30 to 90 min. The resistivity of TCO films is proportional to the reciprocal of the product of carrier concentration (N_e) and mobility (μ):

$$\rho = 1/N_e\mu \tag{24.1}$$

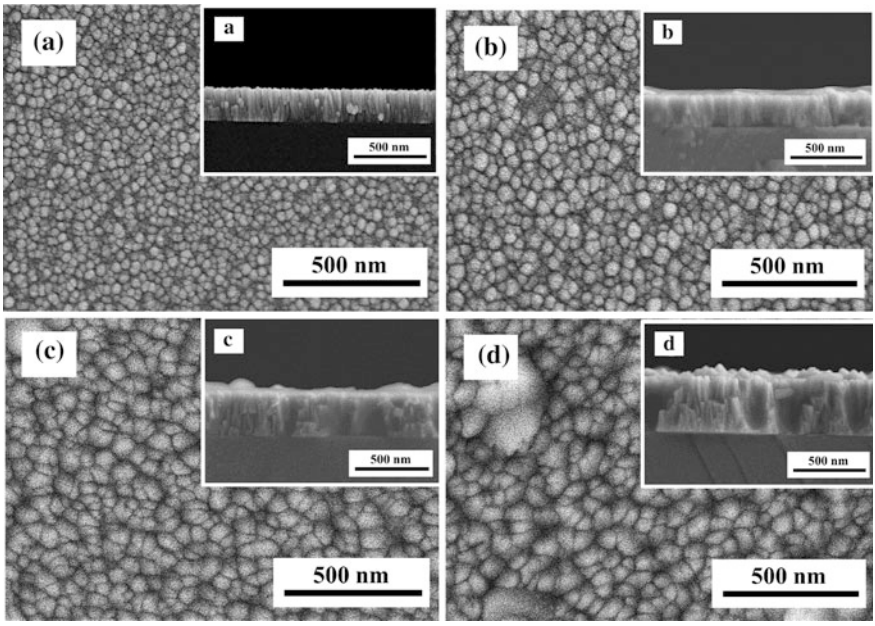

Fig. 24.1 Surface SEM images and cross-section SEM images (*inset*) of the IZO films as a function of deposition times. **a** 30 min, **b** 50 min, **c** 70 min, and **d** 90 min

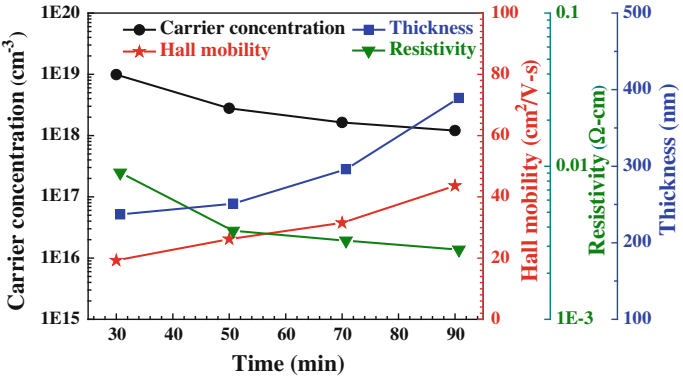

Fig. 24.2 Carrier concentration, resistivity, hall mobility, and thickness of the IZO films as a function of deposition times

which is a combined result of both the mobility and the carrier concentration. The resistivity of IZO films decreased from 9.08×10^{-3} to 2.85×10^{-3} Ω-cm when film thickness increased from 237 nm (deposition time was 30 min) to 389 nm (90 min), as shown Fig. 24.2.

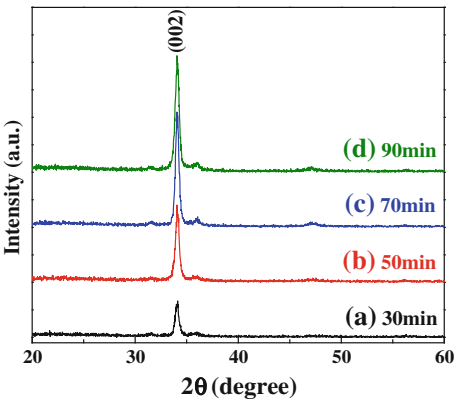

Fig. 24.3 XRD patterns of IZO films as a function of deposition times: **a** 30 min, **b** 50 min, **c** 70 min, and **d** 90 min

XRD patterns of IZO films with different deposition times are shown in Fig. 24.3. All patterns exhibited the (002) peaks of IZO crystallization preferential orientation along the c axis at diffraction angles (2θ) near 34.1°, with a hexagonal structure; no characteristic peak of In_2O_3 phase was found. As deposition time increased from 30 to 90 min, the full width at half maximum (FWHM) values decreased from 0.459 to 0.413. The decrease in FWHM value suggests the crystallization of IZO films increases with increasing deposition time. Those results reveal that the crystallization of IZO films is enhanced as longer deposition time is used, for that the resistivity of IZO films will closely depend on the deposition time. Compared the diffraction spectra show that the 2θ value of the (002) peak shifted from 34.29° to 34.05° as the deposition time of IZO films increased from 30 to 90 min, it means that the lattice constant c increased with increasing deposition time. This result is caused by that the ionic radius of In^{3+} (80 pm) is larger than that of Zn^{2+} (74 pm), and longer deposition time the more In^{3+} ionic will influence the characteristics of IZO films, then the 2θ value of the (002) peak is expected to shift downwards.

The optical transmittance spectra of IZO films in the wavelength range of 200–1100 nm are shown in Fig. 24.4. The average transmittance rate of IZO film is about 85 % in the 400–700 nm range as deposition time was 30 min, and the average transparency of IZO films slightly decreased as deposition time increased. In the ultraviolet range, all the IZO films showed a sharp absorption edge and exhibited a stronger redshift phenomenon with increasing deposition time. This redshift can be explained by the Burstein-Moss shift, a shift of the Fermi level into the conduction band, the energy of which enhances the optical bandgap [15, 16]:

$$\Delta E_g^{BM} = \frac{\hbar^2 k_F^2}{2}\left(\frac{1}{m_e} + \frac{1}{m_h}\right) = \frac{\hbar^2 k_F^2}{2m_{vc}^*} \tag{24.2}$$

where k_F stands for the Fermi wave vector and is given by $k_F = (3\pi^2 n_e)^{1/3}$, m_e is the effective mass of electrons in the conduction band, and m_h is the effective mass

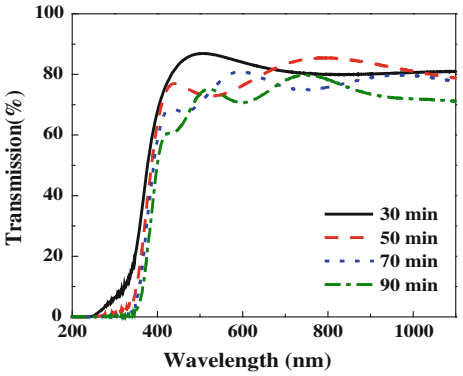

Fig. 24.4 Transmittance spectra of the IZO films as a function of deposition times

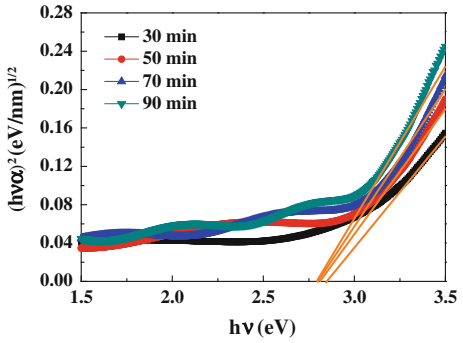

Fig. 24.5 The energy gap of the IZO films as a function of deposition times

of holes in the valence band, which can be simplified as the reduced effective mass m^*_{vc}. ΔE_g^{BM} can be rewritten by inducing k_F for the carrier concentration (n_e):

$$\Delta E_g^{BM} = \frac{\hbar^2 k_F^2}{2m^*_{vc}} (3\pi^2 n_e)^{2/3} \tag{24.3}$$

Equation (24.3) shows that the Burstein-Moss shift of the absorption edge to the longer wavelength region is due to the decrease in carrier concentration, as demonstrated in Fig. 24.2.

The corresponding optical bandgap (E_g) of IZO films were determined by applying the Tauc model and the Davis and Mott model [17] using Eq. (24.4):

$$(\alpha h\nu)^2 = c(h\nu - E_g) \tag{24.4}$$

where α is the optical absorption coefficient, c is the constant for direct transition, h is Planck's constant, and ν is the frequency of the incident photon. Figure 24.5 shows $(\alpha h\nu)^2$ vs. $h\nu$ plots of IZO films. Their E_g values decreased when the deposition time of IZO films increased from 30 to 90 min. The variations in E_g values roughly agree with the variations of the carrier concentrations shown in Fig. 24.2 and Eq. (24.3).

24.4 Conclusions

In this study, crystalline indium zinc oxide (IZO) films were deposited on glass substrates using RF magnetron sputtering technique. The (200) preferred orientation of IZO films increased as the deposition time increased, which would cause the better conductive properties in IZO films. The resistivity of IZO films linearly decreased from 9.08×10^{-3} to 2.85×10^{-3} Ω-cm with increasing in the thickness of IZO films, which could be explained by an increase of carrier mobility with decreasing grain boundary scattering. The average transmittance rate of IZO films was about 75 % in the wavelength range from 400 to 800 nm as the deposition time increased from 30 to 90 min.

Acknowledgments The authors acknowledge financial support from NSC 102-2221-E-244 -019 - and NSC 102-2622-E-244 -001 -CC3.

References

1. Orgiu, E., Manunza, I., Sanna, M., Cosseddu, P., & Bonfiglio, A. (2008). Transparent dielectric films for organic thin-film transistors: A perspective for low cost, low size technologies. *Thin Solid Films, 516*, 1533–1537.
2. Paine, D. C., Yaglioglu, B., Beiley, Z., & Lee, S. (2008). Amorphous IZO-based transparent thin film transistors. *Thin Solid Films, 516*, 5894–5898.
3. Haacke, G. (1977). Transparent conducting coatings. *Annual Review of Materials Science, 7*, 73–93.
4. Chena, K. J., Fang, T. H., Hung, F. Y., Ji, L. W., Chang, S. J., Young, S. J., et al. (2008). The crystallization and physical properties of Al-doped ZnO nanoparticles. *Applied Surface Science, 254*, 5791–5795.
5. Taga, N., Maekawa, M., Shigesato, Y., Yasui, I., Kamei, M., & Haynes, T. E. (1998). Deposition of heteroepitaxial In_2O_3 thin films by molecular beam epitaxy. *Japanese Journal of Applied Physics, 37*, 6524–6529.
6. Tuna, O., Selamet, Y., & Aygun, G. (2010). High quality ITO thin films grown by dc and RF sputtering without oxygen. *Journal of Physics. D. Applied Physics, 43*, 055402–055409.
7. Chen, X. L., Geng, X. H., Xue, J. M., & Li, L. N. (2007). Two-step growth of ZnO films with high conductivity and high roughness. *Journal of Crystal Growth, 299*, 77–81.
8. Chang, H. P., Wang, F. H., Wu, J. Y., Kung, C. Y., & Liu, H. W. (2010). Enhanced conductivity of aluminum doped ZnO films by hydrogen plasma treatment. *Thin Solid Films, 518*, 7445–7449.
9. Le, H. Q., Lim, S. K., Goh, G. K. L., Chua, S. J., & Ong, J. X. (2010). Optical and electrical properties of Ga-doped ZnO single crystalline films grown on $MgAl_2O_4$ (111) by low temperature hydrothermal synthesis semiconductor devices, materials, and processing. *Journal of the Electrochemical Society, 157*, H796–H800.
10. Huang, C. C., Wang, F. H., Wu, C. C., Huang, H. H., & Yang, C. F. (2013). Developing high-transmittance heterojunction diodes based on NiO/TZO bilayer thin films. *Nanoscale Research Letters, 8*(206), 1–8.
11. Minami, T., Yamamoto, T., & Toda, Y. (2000). Transparent conducting zinc-co-doped ITO films prepared by magnetron sputtering. *Thin Solid Films, 373*, 189–194.

12. Naghavi, N., Marcel, C., Dupont, L., Rougier, A., Leriche, J. B., & Guery, C. (2000). Structure and physical characterization of transparent conducting pulsed laser deposited In_2O_3–ZnO thin films. *Journal of Materials Chemistry, 10*, 2315–2319.
13. Wang, A. C., Dai, J. Y., Cheng, J. Z., Chudzik, M. P., & Marks, T. J. (1998). Charge transport, optical transparency, microstructure, and processing relationships in transparent conductive indium-zinc oxide films grown by low-pressure metal-organic chemical vapor deposition. *Applied Physics Letters, 73*, 327–329.
14. Pasquarelli, R., Hest, M., Miedaner, A., Curtis, C., Perkins, J., & Berry, J., et al. (2009). Solution deposition of amorphous IZO films by ultrasonic spray pyrolysis. In *Conference Record of the IEEE Photovoltaic Specialists Conference, USA,* Golden, CO: Colorado School of Mines.
15. Burstein, E. (1954). Anomalous optical absorption limit in InSb. *Physical Review, 93*, 632–633.
16. Hamberg, I., Granqvist, C. G., Berggren, K. F., Sernelius, B. E., & Engstrom, L. (1984). Band-gap widening in heavily Sn-doped In_2O_3. *Physical Review B, 30*, 3240–3249.
17. Wu, C. C., & Yang, C. F. (2013). Fabricate heterojunction diode by using the modified spray pyrolysis method to deposit nickel-lithium oxide on indium tin oxide substrate. *ACS Applied Materials & Interfaces, 5*, 4996–5001.

Chapter 25
Mechanism Design and Analysis for Solar Tracking System with 500W Power Output

Cheng-Yi Chen, Xiaoqing lin, Sung-Tsun Shih, Chao-Ming Hsu and Chien-Yuan Liu

Abstract This paper proposed a two-axis solar tracking system to enhance the efficiency of solar power conversion and to reduce the system cost with the consideration of easy manufacturing and assembling. Based on the solar information of the southern Taiwan, the two-axis motional mechanism with distinguished rotational limitation is designed to achieve the solar tracking objective. According to the reactive force and equivalent von Mises stress of the finite element analysis, the proposed mechanism can provide a safety and stable operation for the solar tracking system.

Keywords Solar tracking system · Photovoltaic power generation · Finite element analysis

X. lin · C.-M. Hsu
Department of Mechanical Engineering, National Kaohsiung University of Applied Science, Kaohsiung, Taiwan, Republic of China

C.-Y. Chen (✉)
Department of Electrical Engineering, Cheng Shiu University, Kaohsiung, Taiwan, Republic of China
e-mail: albert@csu.edu.tw

S.-T. Shih
Department of Electronic Engineering, Cheng Shiu University, Kaohsiung, Taiwan, Republic of China

C.-Y. Liu
Department of Computer Science and Information Engineering, Cheng Shiu University, Kaohsiung, Taiwan, Republic of China

J. Juang et al. (eds.), *Proceedings of the 2nd International Conference on Intelligent Technologies and Engineering Systems (ICITES2013)*, Lecture Notes in Electrical Engineering 293,
DOI: 10.1007/978-3-319-04573-3_25,

25.1 Introduction

Owing to the world crude oil reserves are running out in near future and the supplies of new oil fields tend to becoming difficulty, the petroleum price is prone to drastic fluctuation [1]. Since the problem of energy shortage worldwide, every country is aggressively searching for alternative green energies. Currently, the available power generation manners contain thermal power generation, hydraulic power generation, nuclear power generation, wind power generation, solar cell power generation, etc. Among them, the wind and solar cell power generations belong to the green energy paradigm, and are deemed as one of the most potential technologies in the energy development because of the design of their systems are simpler and convenient for application.

Solar tracking system is usually considered for efficient conversion of the solar energy. According the source of driving, the solar tracking system could be classified into active type and passive type. The active type applies the sensing devices to detect whether sunlight is perpendicular to the panel of the solar cells or not, then drives the angle of the solar tracking mechanism to proper position [2?10]. For instance, the research in [6] adopted a PLC control system to develop the single-axis solar tracking system for the panel of $1m^2$ area. The consumed power of the tracking system is rated as 3% of the collected energy of the solar cells system. However, the active solar tracking system is tend to being influenced by the environmental interference and is prone to appearing instable.

On the other hand, the passive solar tracking system simply applies the trajectory of the sunlight. Based on the latitude of the photovoltaic site, the trajectory time routes per days for a whole year could be calculated in advance. Via the design of the mechanism, several methods could be adopted for the passive solar tracking systems, e.g. the simple control strategy [9], constructed by the heat expansion or contraction material or shape memory alloy. The mechanism would move the tracker to keep itself in equilibrium status [2, 11]. The control algorithms of the systems are usually pertained to open-loop control. Therefore, the disadvantage of the passive tracking is the lack of higher accuracy while tracking.

At present, there are some patents related to the solar tracking systems, containing the two-axis steel mechanism [12], the two-axis spur gear set [13], the two-axis linkage mechanism [14], the two-axis worm gear and pulley mechanism [15], and the two-axis linkage and ball joining mechanism [14], etc. In order to improving the efficiency of photovoltaic energy conversion, this article presents a simple mechanical design with the integration of the active and passive tracking methods for the two-axis solar tracking system. The mechanism could be simply constructed. In addition, the safety and stability of the system were validated through the functional design and strength analysis.

25.2 Mechanism Design

The efficiency of photovoltaic energy conversion depends on the total electrical power generated by the solar panels and the power consumption of the solar tracking system. The accuracy of sunlight angle and the frequency of angle adjusting, therefore, are very important factors for the design of the solar tracking systems. The solar tracking systems could be categorized as fixed type, single-axis type, and two-axis type, etc. Intuitively, two-axis mechanism could absorb the most sunlight among the three types, if the electrical power consumed by the movement of mechanism during tracking could be ignored. Next, the sunlight absorption rate of the single-axis mechanism is the second one in comparing with that of the two-axis one. Finally, the fixed mechanism absorbs the least sunlight among them. Thus, we chose the two-axis mechanism to design the solar tracking system. The hybrid control of the system majorly utilized the passive type tracking assisted by the active one. It reduced the electrical power consumption by decreasing the frequency of tracking movement as less as possible in order to increasing the total electrical power generated by the photovoltaic system.

Table25.1 is the altitude angle and azimuth angle of the Sun at Tainan and Hengchun, which is released by the Taiwan Central Weather Bureau. Figure25.1 shows the Sun paths of four seasons in Taiwan. Based on the Table25.1 and Fig. 25.1, it is observed that the two-axis tracking system needs to adjust the altitude angle and azimuth angle of the sun. The range of the altitude angle is between 13 and 90 degrees, meanwhile, the range of the Azimuth angle is between 65 and 300 degrees. The period of tracking movement is denoted as half hour.

The outline size of the mechanism should be shrunk within the border of the solar panel. Therefore, the available space for the design is very limited. The selection of transmission mechanism certainly tends to simple structure and convenient assembler. A belt is a convenient power transmission part from one axis to another. The positive drive belt is the most accurate belt to transfer the amount of energy according to the belt speed. Thus, the positive drive belt was chosen as the element of power transmission. Geometric formula of the positive drive belt is expressed as Eq.(25.1).

$$c^2 = \frac{1}{4}[l - \pi(r_1 + r_2)]^2 - (r_2 - r_1)^2 \tag{25.1}$$

where l is the standard length, c is the distance between the centers of two gears, and $r_1?r_2$ is the radius of two gears, respectively.

Two 250W polycrystalline silicon solar panels were adopted in the experimental system. The outline dimension of the assembled solar panels is 1665æ 999æ40mm. Therefore, the designed mechanism of the two-axis tracking system for the photovoltaic panel is shown in Fig.25.2. Figure25.2a is the assembled mechanism of the two-axis tracking system. Figure25.2b, c are the exploded view diagrams of the mechanism. Meanwhile, four light dependent resistors (LDR or CDS) were placed at the middles of four edges of the solar panel. To provide higher strength with

Table25.1 The altitude angle and azimuth angle of the Sun

Tinan (North Latitude 23.00? Longitude 120.2)														
Season	Hour	6	7	8	9	10	11	noon	12	13	14	15	16	17	18
SS	AA	09.4	22.4	35.7	49.2	62.9	76.6	89.5	89.4	75.8	62.1	48.4	34.9	21.6	08.7
	ZA	068.3	072.9	076.8	080.1	083.0	085.0	0	218.7	264.9	277.1	280.0	283.4	287.3	292.0
SE	AA	00.9	14.2	27.8	41.0	53.2	63.0	67.0	67.0	62.5	52.5	40.2	27.0	13.4	00.1
AE	ZA	090.2	096.2	102.9	111.7	124.6	146.4	180.0	181.2	215.3	236. 4	249.0	257.5	264.2	269.8
WS	AA		04.1	15.8	26.5	35.3	41.4	43.5	43.5	41.1	34.9	25.9	15.1	03.5	
	ZA		117.6	124.7	134.0	146.3	162.1	180.0	180.5	198.9	214.5	226.6	235.7	242.7	
Hengchun (North Latitude 22.00? Longitude 120.73)															
Season	Hour	6	7	8	9	10	11	noon	12	13	14	15	16	17	18
SS	AA	09.5	22.5	35.9	49.5	63.2	77.0	88.5	88.3	75.2	61.5	47.8	34.2	21.6	07.9
	ZA	068.4	072.7	076.2	079.1	081.1	080.7	0	329.4	278.9	279.0	281.2	284.2	287.3	292.3
SE	AA	01.3	14.8	28.5	41.8	54.2	64.1	68.0	68.0	63.0	52.6	40.1	26.7	13.1	
AE	ZA	090.4	096.1	102.7	111.2	124.0	146.3	180.0	182.6	217.4	238.0	250.1	258.3	264.7	
WS	AA		05.0	16.7	27.5	36.4	42.5	44.5	44.5	41.9	35.4	26.2	15.3	03.5	
	ZA		117.8	124.8	134.0	146.4	162.4	180.0	181.2	199.8	215.4	227.3	236.2	243.0	

SS Summer Solstice, *SE* Spring Equinox, *AE* Autumn Equinox, *WS* Winter Solstice

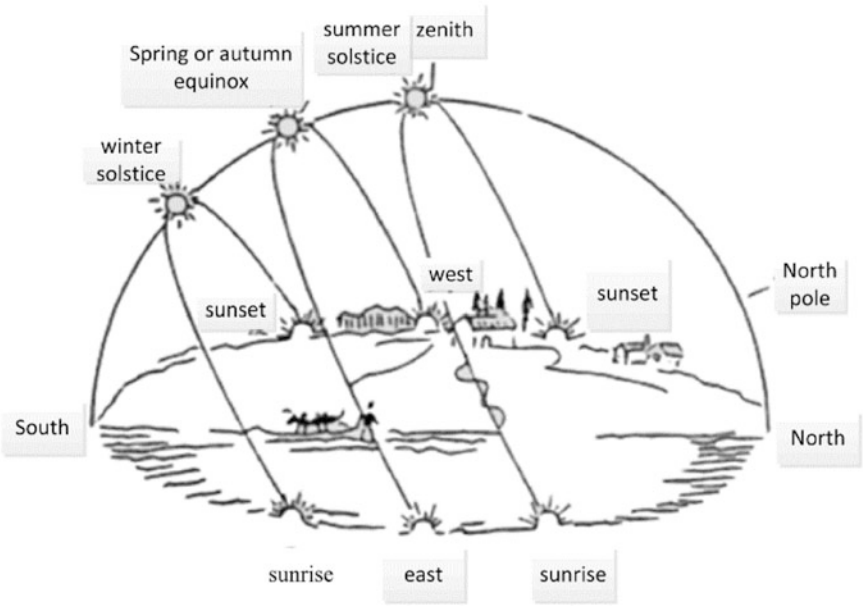

Fig.25.1 The Sun paths of four seasons in Taiwan

lower cost, the ?-shape 6061-T6 aluminum truss was selected as the structure to support the panel. The other structures utilized aluminum grooves and were joined by welding method. A steel-ball bearing with 38.1mm diameter was applied between the aluminum-alloyed rotational base and the stainless-steel body-fix frame. As for the transmission mechanism, a standard component was chosen as the positive driving belt. The teeth numbers of the big gear and small gear for the belt are 50 and 25. The width and the length of the belt are 25.4 and 345.4mm. The precision of the rotational mechanism has been restricted within one degree. Thus, the high-ratio reducer gear boxes were utilized to increase the rotation accuracy, and to raise the torque to meet the minimun requirement of 120Nm. To eliminate the power loss during electrical transformation, we adopted two DC motors to drive the mechanism as Fig.25.2c. The motor at the upper layer is in charge of the rotation of the XY plain. The motor at the lower layer rotates whole body along Z axis.

25.3 Computer Aided Analysis

In the article, a finite element analysis (FEA) software, named the ANSYS, was applied to analyze the mechanical strength of the solar tracking mechanism with the safety coefficient of 4.5. The finite element mesh of solar tracking mechanism is shown in Fig.25.3. Figure25.3a shows the mesh of photovoltaic panel and truss.

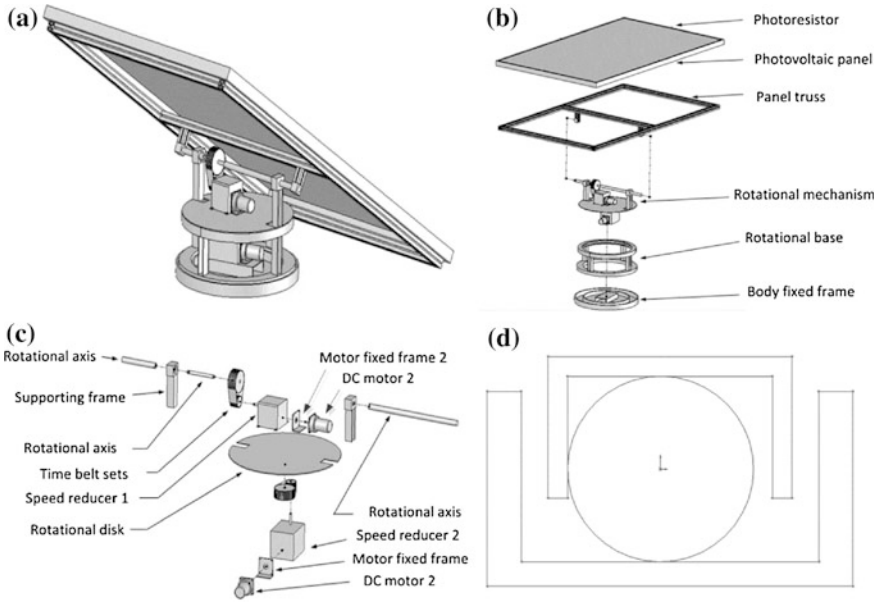

Fig.25.2 The solar tracking mechanism. **a** Assembled mechanism. **b** Exploded diagram. **c** Exploded diagram of the rotational mechanism. **d** Rotational trough

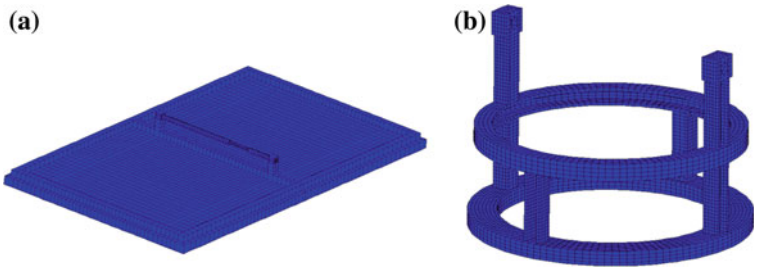

Fig.25.3 Finite element mesh of solar tracking mechanism. **a** Photovoltaic panel and truss mesh. **b** Base mechanism mesh

Figure25.3a shows the mesh of base mechanism. The base mechanism was decomposed to four portions for simplifying FEA. The reactive force of the first portion was applied as the active force to the second portion. Other portions were analyzed with same manner. Note that all cells of the mesh are regular hexahedron. The parameters of the aluminum structures were set by Young?s modulus=68.9Gpa, Possion?s rate=0.35; Density=2710kg/m^3. The gravity in z direction was set as ?9.8 m/s^2. The element type was set as 7. The results of FEA were selected to be the reactive force and the EVMS S_y. S_y is computed based on distortion energy theory, as shown in Eq.(25.2).

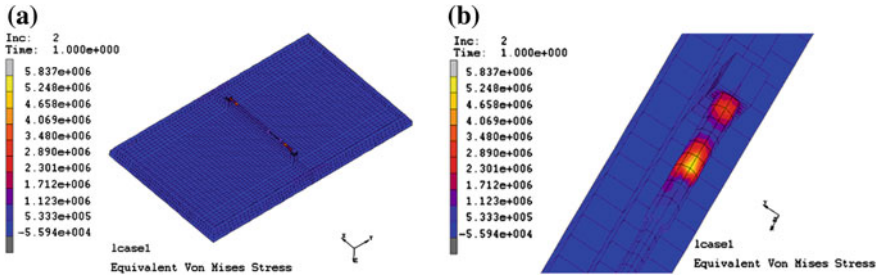

Fig.25.4 FEA result for photovoltaic panel and truss. **a** EVMS for Photovoltaic panel. **b** EVMS for local area of truss

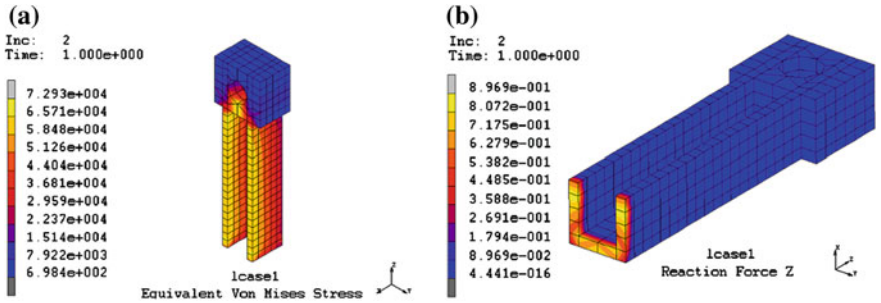

Fig.25.5 FEA result for first portion. **a** EVMS. **b** Reactive force in Z direction

$$s_y = \sqrt{\frac{(\sigma_1 - \sigma_2)^2 + (\sigma_2 - \sigma_3)^2 + (\sigma_3 - \sigma_1)^2}{2}} \tag{25.2}$$

where $?_1$, $?_2$ and $?_3$ are the main stress in x, y and z direction, respectively. Assume that $?_y$ is the yield strength of the aluminum material. When $S_y > ?_y$, the structure would break.

Figure25.4 shows the result of FEA for the photovoltaic panel and its supporting truss. The maximal EVMS of the result was 5.837MPa which is less than 270MPa, the yield strength of aluminum. Thus, the design of the panel and the truss are proper. The FEA result of first portion is shown in Fig.25.5. The reactive force of node at the bottom side was 17.39kg and its EVMS was 72.93Kpa. Figure25.6 shows the result of the second portion. The reactive forces at the four points were 20.80, 20.79, 3.84, and 3.83kg. The EVMS of the portion was 10.46kPa. Figure 25.7 depicts the result of the third portion. The reactive forces at the four points were 21.66, 21.65, 4.86, and 4.85kg. The EVMS of the portion was 145.2kPa. The FEA result of the fourth portion is shown in Fig.25.8. The EVMS of the portion was 507kPa. Since the yield strength of aluminum is 270MPa, the EVMS results of all portions were conformed to the constraint.

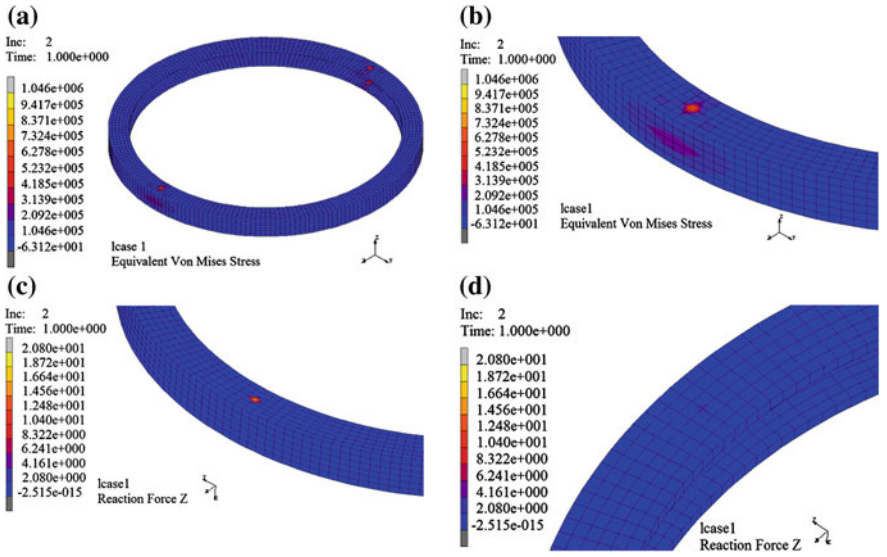

Fig.25.6 FEA result for the second portion. **a** EVMS. **b** Partial enlargement EVMS. **c** Maximum reactive force in Z direction. **d** Minimum reactive force in Z direction

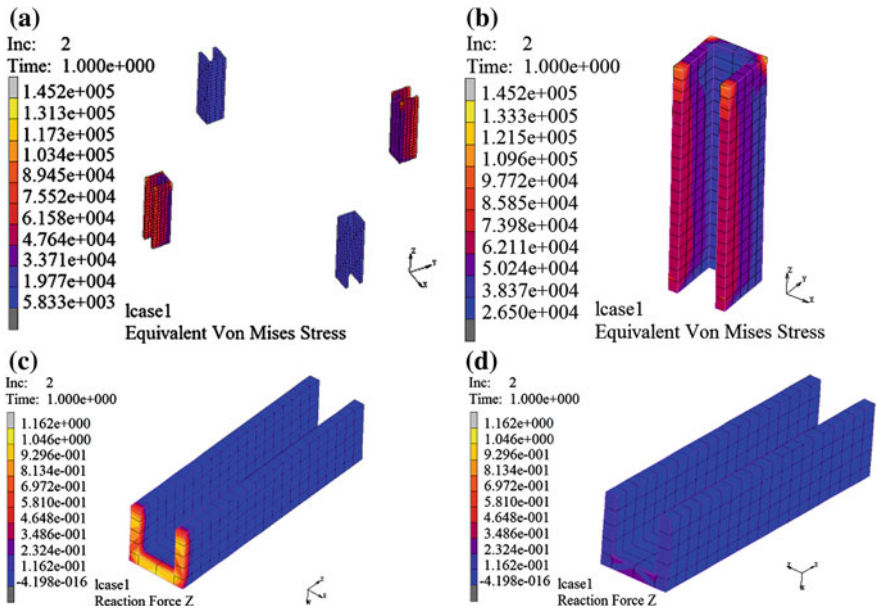

Fig.25.7 FEA result for the third portion. **a** EVMS. **b** Partial enlargement EVMS. **c** Maximum reacting force in Z direction. **d** Minimum reacting force in Z direction

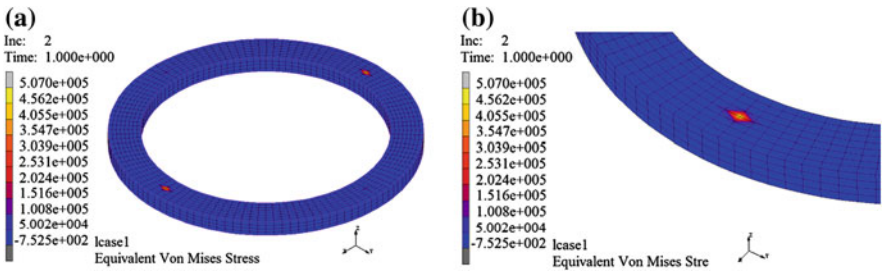

Fig.25.8 FEA result for the fourth portion. **a** EVMS. **b** Partial enlargement EVMS

25.4 Conclusions

Through functional design and strength calculation, this article proposed an easy-fabricated and simple-assembled solar tracking system. After finite element analysis, the maximal equivalent von Mises stress of each part of the mechanism was validated to be less than 270MPa, the yield strength of the aluminum structure. Therefore, the safety and stability of the tracking mechanism is conformed to the requirement. In future, the hybrid control strategy would be applied in the solar tracking system to enhance the efficiency of electrical power generation. Moreover, the supervising control system would be designed for the green power generation system to contribute to the green earth and the sustainable society.

Acknowledgments The authors would like to thank the National Science Council, the Republic of China, for financial support of this research under the grant NSC 101-2632-E-230-001-MY3.

References

1. http://www.bp.com/statisticalreview/.
2. Clifford, M. J., & Eastwood, D. (2004). Design of a novel passive solar tracker. *Solar Energy, 77*, 269?280.
3. Mwithiga, G., & Kigo, S. N. (2006). Performance of a solar dryer with limited sun tracking capability. *Journal of Food Engineering, 74*, 247?252.
4. Roth, P., Georgiev, A., & Boudinov, H. (2004). Design and construction of a system for sun tracking. *Renewable Energy, 29*, 393?402.
5. Georgiev, A., Roth, P., & Olivares, A. (2004). Sun following system adjustment at the UTFSM. *Energy Conversion and Management, 45*, 1795?1806.
6. Abdallah, S., & Nijmeh, S. (2004). Two axes sun tracking system with PLC control. *Energy Conversion and Management, 45*, 1931?1939.
7. Bakos, G. C. (2006). Design and construction of a two-axis sun tracking system for parabolic trough collector (PTC) efficiency improvement. *Renewable Energy, 31*, 2411?2421.
8. Huang, B. J., & Sun, F. S. (2007). Feasibility study of one-axis three positions tracking solar PV with low concentration ratio reflector. *Energy Conversion and Management, 48*, 1273?1280.

9. Rubio, F. R., Ortega, M. G., Gordillo, F., & Lopez-Mart?nez, M. (2007). Application of new control strategy for sun tracking. *Energy Conversion and Management, 48*, 2174?2184.
10. Abdallah, S., & Badran, O. O. (2008). Sun tracking system for productivity enhancement of solar still. *Desalination, 220*, 669?676.
11. R.O.C. Patent No. M346679, July, 2008.
12. R.O.C. Patent No. M296359, March, 2006.
13. U.S. Patent No. 2913583, 1954.
14. U.S. Patent No. 4649899, 1987.
15. R.O.C. Patent No. M334301, 2007.

Chapter 26
Sliding Mode Voltage Control of the DC to DC Buck Converters

Cheng-Yi Chen, Jung-Yi Shiau, Chien-Yuan Liu, Kuo-Jui Wu and Marvin H. Cheng

Abstract In comparison with the conventional power converters, the switching power converters, which possess the advantages of higher efficiency, smaller size, lighter weight, and wider ranges of voltage regulation, are widely applied in the application of portable electronic products and equipment in recent years. This article mainly focuses on the development and implementation of a buck converter with a sliding mode voltage controller, to achieve the stable desired voltage output. Firstly, based on Lyapunov stable analysis, the controller is proposed to enforce the system trajectory from the arbitrary point toward the sliding surface in finite time, and then slides along the surface to an equilibrium point exponentially. According to a fixed frequency pulse width modulation mechanism, the proposed controller is realized by controlling the duty cycle of the switching regulator to achieve the desired stable voltage output under the influences of loading variations. From the simulation results obtained by the PSpice simulation software, the encouraged system performance was validated by the testing of different loadings.

Keywords Switching power supply · Sliding mode · Bulk converter

C.-Y. Chen (✉) · J.-Y. Shiau · K.-J. Wu
Department of Electrical Engineering, Cheng Shiu University, Kaohsiung 83347, Taiwan, Republic of China
e-mail: albert@csu.edu.tw

C.-Y. Liu
Department of Computer Science and Information Engineering, Cheng Shiu University, Kaohsiung 83347, Taiwan, Republic of China

M. H. Cheng
Department of Mechanical and Aerospace Engineering, West Virginia University, Morgantown, WV 26506-6106, USA

J. Juang et al. (eds.), *Proceedings of the 2nd International Conference on Intelligent Technologies and Engineering Systems (ICITES2013)*, Lecture Notes in Electrical Engineering 293,
DOI: 10.1007/978-3-319-04573-3_26,

26.1 Introduction

In recent years, electronic products are nearly inseparable from humans' daily living. But the power adapters of familiar electronic products are typically different for various applications, e.g. mobile phones, digital cameras, or notebooks, etc. Generally the power adapters have to be redesigned and replaced for the stable operations of the electronics. Hence, to supply a stable direct current (DC) and low voltage power source is an essential requirement. The DC power sources are usually converted from battery power banks or wall power supplies, such as Taiwan Power Company. Therefore, the DC to DC conversion is a critical stage during the process of the transformation in a power supply.

Switching-mode power supplies (SMPS) are gradually deemed as the valuable parts in industry, in sequence of their higher efficiency, lighter weight, and broader ranges during the voltage raising or lowering conversions. A SMPS incorporates a switching regulator to convert electrical power efficiently. The voltage regulation is working in PWM mode which was achieved by varying the ratio of a duty cycle in a fixed frequency [1]. Guo [2] applied PID controllers during the voltage regulation, and added the design concepts of the dead bands and the averaging digital filters to the converter to improve the ripple effect. Gentry [3] proposed the disturbance accommodation control (DAC) for the SMPS. With the DAC, the disturbance to the external was greatly reduced, the settling time and the overshoot were obviously improved. Leung [4] presented the state trajectory prediction (STP) of hysteresis controllers to improve the computation complexity of the STP and to enhance the transcient respose effects of the voltage regulators. Veerachary [5] recommended utilizing the state-space averaging method, variable references and capacitances for hysteresis controlled 3-level step-down converters to improve the system's robustness. The experimential results showed that the dynamic responses of the system has better performance.

Itkis presented the book concerning the variable structure control system (VSCS) [6]. The switching control structure creates a sliding surface on a phase-angle plane and it switches from one smooth condition to another based on the position of the state trajectory. The method is insensitive to external disturbance and parameter fluctuations. It also has good robustness and dynamic responses. Hence, sliding mode control has been applied in the control system of the switching mode power suppliers [7]. A fixed frequency PWM control and a simple analog circuit are utilized to realize the sliding mode bulk converter [8]. In addition, the PSpice simulation software has been widely applied on the design of the DC converters to decrease the cost of hardware circuit design. Muhamad [9] also utilized the PSpice to simulate the power electronic converters and the sliding mode controllers. In that simulation, two power converters were simulated, i.e. a bulk converter and a single phase inverter, the results of simulation and that of the theoretic model were proven to be coincident.

Therefore, this article proposed a fixed frequency PWM scheme for the control of the raising or lowering the voltage of a bulk converter. In addition, a sliding mode controller adopting integral and differential functions was utilized for the bulk converter to reduce external disturbance and the influences from parameters' fluctuations, to eliminate stable deviation and to improve transient phenomena, and to enhance the robustness of the control system.

26.2 Mathematic Model of the Sliding Mode Control

A sliding mode control must provide a stable sliding surface. Then, the design of the sliding mode control maintains the state trajectory of the system toward the equilibrium point on the surface. This article utilized a fixed frequency PWM scheme to the control of the raising or lowering the voltage of a bulk converter. Figure 26.1 shows the architecture of the sliding mode bulk converter.

Three state variables were denoted as follows,

$$X_1 = V_{ref} - \beta V_o \tag{26.1}$$

$$X_2 = \dot{X}_1 = -\frac{\beta}{C} i_C = \frac{\beta}{C}\left(\frac{V_o}{R_L} - \int \frac{uV_i - V_o}{L} dt\right) \tag{26.2}$$

$$X_3 = \int X_1 dt \tag{26.3}$$

where X_1 denotes the voltage difference, X_2 denotes the derivative of the voltage difference, and X_3 denotes the integral of the voltage difference. C, L, R_L represents capacitance, inductance, and resistance of the load, respectively. i_C, i_L, i_O represents the current of capacitor, the current of inductor, and the current of the load, respectively. V_{ref}, V_i, βV_O represents the reference voltage, input voltage, and output voltage, respectively. u denotes the switching state in "1" or "0" of power transistor.

The system state Eqs. (26.1)–(26.3) could be presented as the form of the following matrix,

$$\dot{X} = AX + Bu + D \tag{26.4}$$

where

$$A = \begin{bmatrix} 0 & 1 & 0 \\ -\frac{1}{LC} & -\frac{1}{R_L C} & 0 \\ 1 & 0 & 0 \end{bmatrix} \quad B = \begin{bmatrix} 0 \\ -\frac{\beta V_i}{LC} \\ 0 \end{bmatrix} \quad D = \begin{bmatrix} 0 \\ \frac{V_{ref}}{LC} \\ 0 \end{bmatrix} \quad X = \begin{bmatrix} X_1 \\ X_2 \\ X_3 \end{bmatrix} \tag{26.5}$$

To define $u = \frac{1}{2}(1 + sgn(S))$ and the sliding surface $S = \alpha_1 X_1 + \alpha_2 X_2 + \alpha_3 X_3 = J^T X$; $J^T = [\alpha_1 \quad \alpha_2 \quad \alpha_3]$; α_1, α_2, and α_3 are sliding coefficients.

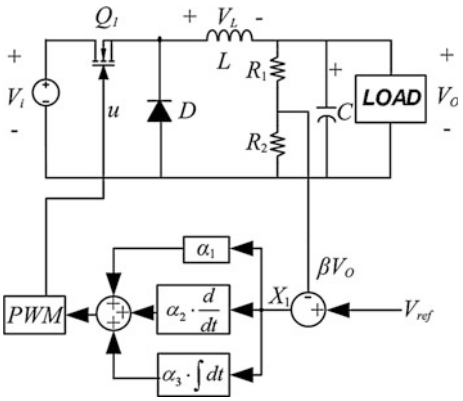

Fig. 26.1 The architecture of the sliding mode bulk converter

Frist of all, the mathematical expression of $\dot{S}$ is derived as below,

$$\dot{S} = J^T \dot{X}\, \dot{S} = J^T AX + \frac{1}{2} J^T B + \frac{1}{2} J^T B \mathrm{sgn}(S) + J^T D \tag{26.6}$$

To define a Lyapunov function $V = \frac{1}{2} S^2$ and its derivative is

$$\dot{V} = S\dot{S} = S\left(J^T AX + \frac{1}{2} J^T B + J^T D \right) + \frac{1}{2} |S| J^T B < 0 \tag{26.7}$$

It means that the above system is Lyapunov sensing stable. Furthermore, based on Filppov's method [6], Equivalent Control, u_{eq} can be derived as below, by considering $\dot{S} = 0$.

$$\begin{aligned} u_{eq} &= -\left(J^T B\right)^{-1} J^T (AX + D) \\ &= \frac{LC}{\beta V_i \alpha_2} \left[\alpha_1 X_2 - \frac{1}{LC} \alpha_2 X_1 - \frac{1}{R_L C} \alpha_2 X_2 + X_1 \alpha_3 + \frac{V_{ref}}{LC} \alpha_2 \right] \\ &= \frac{LC}{\beta V_i \alpha_2} \left[\left(-\frac{\alpha_2}{R_L C} + \alpha_1 \right) X_2 + \frac{\beta V_o}{LC} \alpha_2 + X_1 \alpha_3 \right] \\ &= \frac{LC}{\beta V_i} \left(\frac{\alpha_1}{\alpha_2} - \frac{1}{R_L C} \right) X_2 + \frac{V_o}{V_i} + \frac{\alpha_3 LC}{\alpha_2 \beta V_i} X_1 \end{aligned} \tag{26.8}$$

Since $1 > u_{eq} > 0$, thus the above equation could be rewritten as below,

$$\beta V_i > u_{eq}^* = LC \left(\frac{\alpha_1}{\alpha_2} - \frac{1}{R_L C} \right) X_2 + \beta V_o + \frac{\alpha_3}{\alpha_2} LC X_1 > 0 \tag{26.9}$$

where $u_{eq}^* = \beta V_i \cdot u_{eq}$. To substitute Eqs. (26.1)–(26.3) into Eq. (26.9), we obtain Eq. (26.10).

$$\beta V_i > u_{eq}^* = \beta L i_C \left(\frac{1}{R_L C} - \frac{\alpha_1}{\alpha_2} \right) + \beta V_o + \frac{\alpha_3}{\alpha_2} LC (V_{ref} - \beta V_o) > 0 \tag{26.10}$$

As for the duty cycle d could be expressed as below,

$$d = \frac{V_C}{V_{ramp}} \tag{26.11}$$

where V_C is the signal of voltage difference, V_{ramp} is the signal of saw wave. Since $1 > d > 0$, thus Eq. (26.11) could be rewritten as below,

$$V_{ramp} > V_C > 0 \tag{26.12}$$

To compare Eq. (26.10) and formula (26.11), we could obtain the Eqs. (26.13) and (26.14) as below,

$$V_C = u_{eq}^* = \beta L i_C \left(\frac{1}{R_L C} - \frac{\alpha_1}{\alpha_2}\right) + \beta V_o + \frac{\alpha_3}{\alpha_2} LC(V_{ref} - \beta V_o) \tag{26.13}$$

$$V_{ramp} = \beta V_i \tag{26.14}$$

26.3 System Experiment and Result

The design specification of the proposed DC-to-DC converter is as follows: input voltage $V_S = 24$ V, output voltage $V_O = 12$ V, switching frequency 200 kHz. Since the bulk converter wants to operate the system on the continuous current mode, the edge current mode is applied for obtaining the critical inductance, $L_{critical}$ is 7.5 μH. The value of inductance must be larger than the critical inductance for the system to operate under the continuous current mode. The loading capacitance could be obtained as 100 μF when the ripple of output voltage is set within 1 mV. Assume the response bandwidth is set to 20 KH, the slope coefficients could be designated as $\alpha_1/\alpha_2 = 251.32 \times 10^3$ and $\alpha_3/\alpha_2 = 15.79 \times 10^9$, Table 26.1 shows the specification of the bulk converter.

Equation (26.13) is rewritten as below when it is substituted by all constant parameters depicted above. We obtain Eq. (26.15).

$$V_C = -9.39 i_C + \beta V_O + 284.22(V_{ref} - \beta V_O) \tag{26.15}$$

With selected reference voltage and output voltage, β is obtained from the calculation of $\beta = V_{ref}/V_{od}$. Since the 2.5 V reference voltage is generated by the TL431 diode in the controller circuit, thus $\beta = 0.208$ is simply calculated. According the voltage division principle, the calculation formula $R_2 = R_1 \times \beta/(1 - \beta)$ is established. The current signal i_C is captured by the current sensor CS1100. It could be transferred into equivalent voltage. To satisfy Eq. (26.15), the gain of the current signal and the signal $(V_{ref} - V_O)$ must be as follows, respectively.

Table 26.1 The specification of the bulk converter

Parameter	Notation	Value	Parameter	Notation	Value
Input voltage	V_S	24 V	Output voltage	V_{od}	12 V
Switching frequency	f	200 kHz	Inductor	L	180 μH
Capacitance	C	100 μF	Load	R	6–24 Ω
Bandwidth	f_{BW}	20 kHz			

Table 26.2 The resistances for the controller

Parameter	Value	Parameter	Value	Parameter	Value
R1	950 Ω	*R2*	250 Ω	*R3*	10 KΩ
R4	1.1 KΩ	*R5*	1 MΩ	*R6*	3.5 KΩ
RS	10 KΩ				

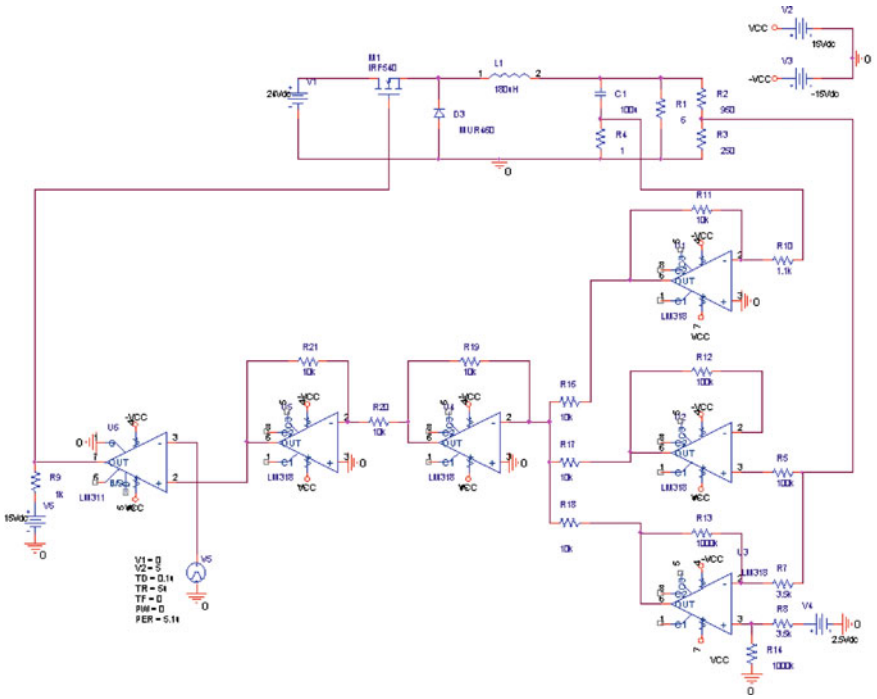

Fig. 26.2 Converter schematic for simulation

$$\beta L\left(\frac{1}{R_L C}-\frac{\alpha_1}{\alpha_2}\right) i_C = \frac{R_3}{R_4} = -9.39 \text{ and } \frac{\alpha_3}{\alpha_2} LC = \frac{R_5}{R_6} = 284.22$$

From the above descriptions, the values of all resistors are depicted in Table 26.2.

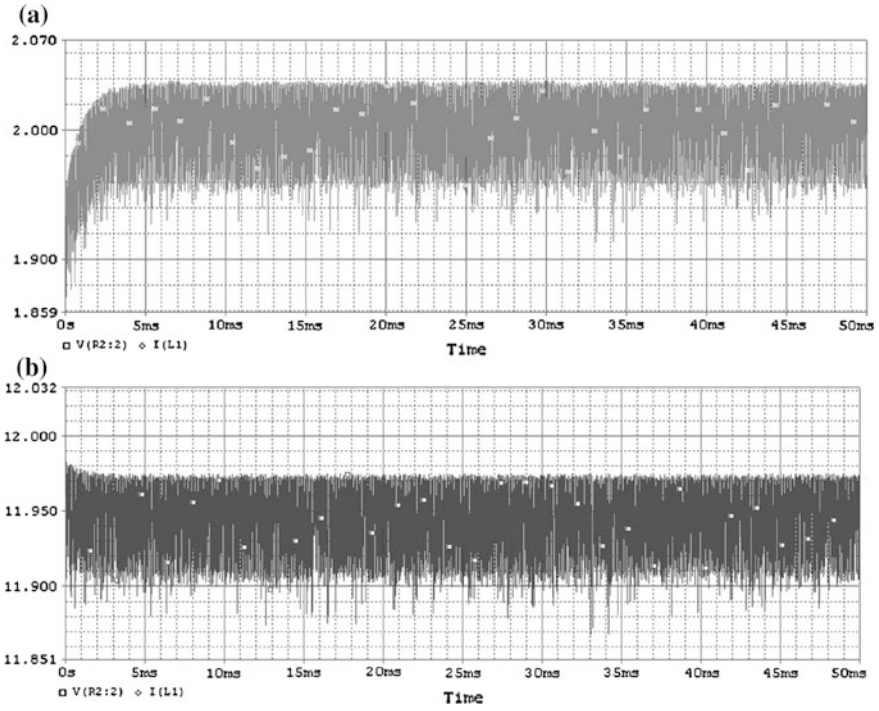

Fig. 26.3 Output waveform of full-load simulation under parameter fluctuation

Figure 26.2 is the schematic of the DC to DC converter designed by the simulation software PSpice, where the feedback voltage is expressed as Eq. (26.15). In the case of full load, the load resistance is 6 Ω. The current of inductor and the ripple of output voltage is described in Fig. 26.3a, b. From these figures, we know that the inductor current is about 2 A, the output voltage is 11.94 V, and the output response delay is approaching zero. The results conform to the design requirement. In the case of half load, the load resistance is 12 Ω. Figure 26.4a, b shows the current of inductor and the ripple of output voltage. Meanwhile, the inductor current is about 1 A and the output voltage is 11.94 V. The results also conform to the design requirement. In the case of very light load, the load resistance is 240 Ω. Figure 26.5a, b shows the output voltage for varying input voltage with 20 and 28 V, respectively. The fluctuations of output voltages is trivial, hence the goal of stable output voltage is achieved. From the output waveforms of all figures, therefore, we know that the ripples of output voltages are extremely stable. However, the output voltage levels are a little lower than that of the rated. In comparison to different loadings, we know that the level of output voltage is slightly increased when the loading resistance is increased.

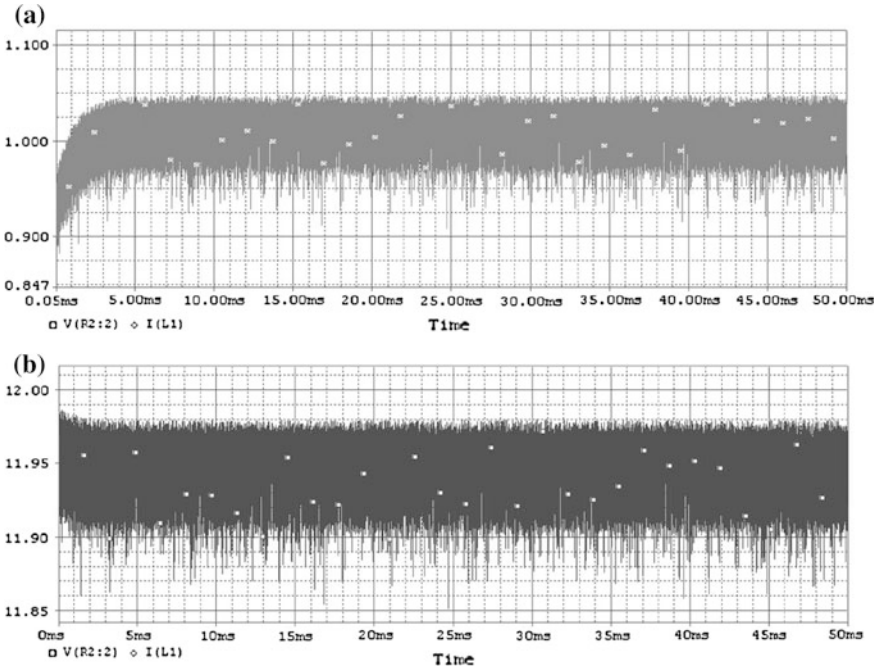

Fig. 26.4 Output waveform of half-load simulation under parameter fluctuation

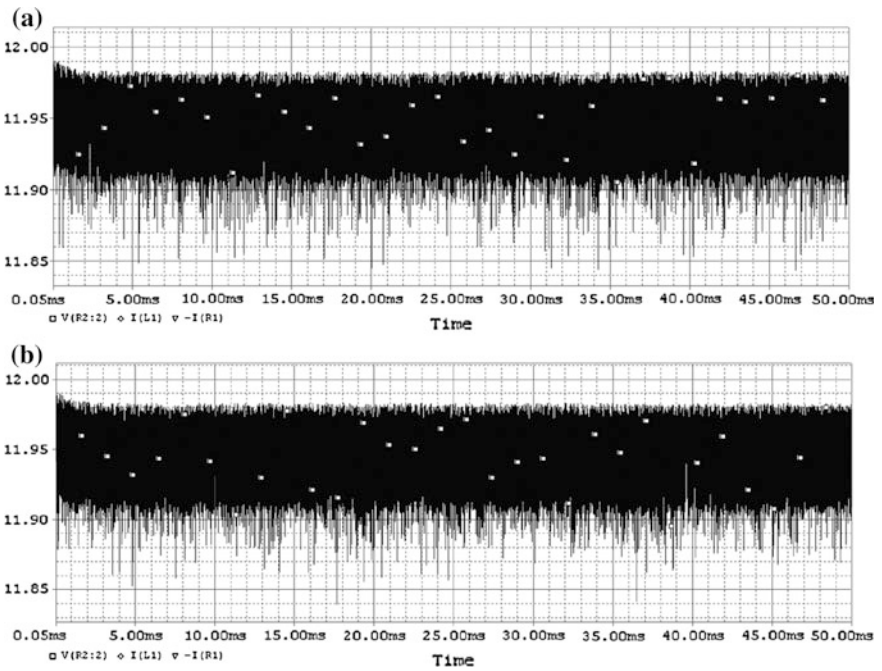

Fig. 26.5 Output waveform of no-load simulation under parameter fluctuation

26.4 Conclusions

This article presents a control scheme of the sliding mode control theorem. Based on the scheme, a sliding mode controller is designed for a bulk converter system. The controller not only assists the system in conforming to the prerequisite conditions, but also maintains the system stability under the sliding mode operation. Furthermore, the system is able to preserve its robustness under the influence of parameter fluctuations. Moreover, an integral and a differential term of the sliding mode function are designed into the bulk converter. In addition, the converter utilizes the feedback and slope signals as the trigger for the PWM control for the industrial transistors, therefore, to enhance the robustness over the loading variation, to eliminate the stable deviation, and to improve the transient phenomena.

Acknowledgments The authors would like to thank the National Science Council, the Republic of China, for financial support of this research under the grant NSC 101-2632-E-230-001-MY3.

References

1. Shepherd, W., & Zhang, L. I. (2004). *Power converter circuits*. NY: Marcel Dekker.
2. Guo, L., Hung, J. Y., & Nelms, R. M. (2002). PID controller modifications to improve steady-state performance of digital controllers for buck and boost converters. In *Seventeenth Annual IEEE Applied Power Electronics Conference and Exposition* (Vol. 1, pp. 381–388).
3. Gentry, B. N., Schmitt, N. M., & Martin, T. W. (2005). Improving performance of a switching converter using compensator with disturbance accommodation control. In *Proceedings of the IEEE International Symposium on industrial Electronics (ISIE 2005)*, Vol. 2, pp. 805–807.
4. Leung, K. K., & Chung, S. S. (2005). Dynamic hysteresis band control of the buck converter with fast transient response. *IEEE Transaction on Circuits and Systems, 52*(7), 398–412.
5. Veerachary, M., & Sharma, D. (2006). Adaptive hysteretic control of 3rd order buck converter. In *Power Electronics Drives and Energy Systems (PEDES 2006)* (pp. 1–4).
6. Utkin, V. I., Guldner, J., & Shi, J. (1999). *Sliding mode control in electromechanical systems*. London: Taylor and Francis.
7. Castilla, M., Vicuña, L. G., & López, M. (2000). On the design of sliding mode control schemes for quantum resonant converters. *IEEE Transactions on Power Electronics, 15*(6), 960–973.
8. Tan, S. C., Lai, Y. M., & Tse, C. M. (2005). A fixed-frequency pulsewidth modulation based quasi-sliding-mode controller for buck converters. *IEEE Transactions on Power Electronics, 20*(6), 1379–1392.
9. Muhamad, N. D., & Aziz, J. A. (2008). Simulation of power electronic converters with sliding mode control using PSpice. In *2nd IEEE International Power and Energy Conference (PEC 2008)* (pp. 231–236), Malaysia.

Chapter 27
Light Emitter Diode Display Design and Applications Using Time Triggered Control Network

Cheng-Yi Chen, Chen-Hung Hsiao, Tsung-Wei Liu, Chiu-Chan Kuo and Shun-Yu Chan

Abstract Light Emitter Diode (LED) character and graphic display are currently the better products for LED application, which include LED lighting, LED display board, traffic sign indication and so on. Those products can involve the full-color display system so that their outdoor applications are better than that of LCD display. However, the designs and applications of LED display board belong to the customized products such that the application field will be limited by its flexibility. Therefore, in order to provide a free assembly LED display module for increasing the extendable capability, this paper proposes an embedded LED display module and application architecture using real-time controller area network. The customized LED character and graphic display board system can be easily achieved by the firmware design of the main control board and slave display module, based on timer-trigged controller area network (TTCAN). Eventually, the proposed embedded display modules is verified by the practical testing of 109 × 36.5 cm (144 × 48 LED points) display board system with encouraged performance.

Keywords Light emitting diode · Embedded controller · Time-triggered controller area network

27.1 Introduction

In recent years, the Light Emitter Diode (LED) has gained its extensive applications ranging from indoor domestic lighting to outdoor public lighting. Featured with merits of rich colors, compactness, power saving, low heat dissipation, long life, fast response, and EMI-free, LED has found its wide-spreading applications in

C.-Y. Chen (✉) · C.-H. Hsiao · T.-W. Liu · C.-C. Kuo · S.-Y. Chan
Department of Electrical Engineering, Cheng Shiu University, Kaohsiung 83347, Taiwan, Republic of China
e-mail: albert@csu.edu.tw

J. Juang et al. (eds.), *Proceedings of the 2nd International Conference on Intelligent Technologies and Engineering Systems (ICITES2013)*, Lecture Notes in Electrical Engineering 293,
DOI: 10.1007/978-3-319-04573-3_27,

3C product display, lighting apparatus, traffic lights, and backlighting modules. After the mass production of high brightness blue-light LED was made possible in 1994, the three primitive colors, i.e. red, green, and blue, was successfully mixed to generate full range color spectrum and led to extensive area of application. Besides, with the fast development of LED, the high brightness LEDs are far more pervasive and applied not only in lighting equipment, indicator and vehicle headlight, but also in display including well-liked subtitle machine and advertisement wall. Furthermore, subtitle machine has evolved from mono color to duo color, and further to full color. It can perform font color changing and, even more, display animation and video image. Also, the display has progressed from small-size to large-size due to the combination of LEDs and the far-reaching application even cover stage lighting, artistic lighting, building landscaping, and so forth [1].

The latest applications of LED has come into sight in the areas of character and pattern display as well as dot matrix subtitle machine, which appears on public bus, mass railway transit and advertisement board, and generally comprised multiple 5×8 or 8×8 LED matrix. For curtailing the production cost of LED dot matrix drive circuit, the amount of output connectors of microcontroller is reduced by integrating multiple output driving integrated circuits such as SPI, I2C, serial communication, and so on. Whereas, microcontroller still uses part of its resource in LED matrix display scanning and, thus, leading to difficulty on programming and trouble on brightness control. For solving this problem, Holtek semiconductor Inc. has released a driving IC named HT1632C which can directly drive 32×8 or 24×16 LED dot matrix [2] and can, therefore, effectively reduce the amount of hardware circuit and device as well as decrease developing cost of drive circuit.

LED display is generally a customized design and allows no more modification and refurbishment. From application point of view, the module design of LED display panel is to assemble various modules according to customers' requirements. The control and communication can be merely accomplished through the usage of communication interfaces. The well-known communication interface includes RS-232, RS-422, RS-485, and CAN-Bus, etc. [3, 4]. RS-232/422/485 are categorized as open type communication format and the correctness of communication is evaluated and performed by microcontroller. However, Control Area Network (CAN) attributes to hardware design type and, therefore, can drastically decrease the burden of microcontroller. In addition, CAN is featured with collision-free and low interference and widely used in car, special vehicle, robot, liquid pressure system, distributed type I/O, even more, in ships and airplanes, elevators, medical instrument, tool machine, and building automation [5–7]. Unfortunately, as the amount of node in network increases, CAN experiences the problem of data sending failure for those with lower arbitration. To overcome this problem, CAN is modified to the communication hardware interface triggered by timing [8–11]. As all nodes in network possess synchronous mechanism, the transmission of message can be triggered based on cycling time or system matrix sequence and, accordingly, the arbitration problem can be conquered [12]. Thus, the transmission performance of CAN is promoted. In this paper, a modular LED panel using

TTCAN is proposed. It is a customization-based implementation that can be expanded and assembled freely according to different requirements of customers. Being employed in subtitle machine and graphic display, it will possess the function of brightness adjustment and the practical application, thus, leading to economic value of LED panel being enhanced. The end users can easily assemble the required LED panel without needing any decent electronic circuit background and training.

27.2 LED Display Board Hardware and Firmware Design

In this paper, the 8-bit microcontroller chip AT89C51CC01/CC02 of ATMEL [15] is used to integrate and realize LED panel. AT89C51CC01 plays the roles of communicator with PC and major controller of triggering function for TTCAN in CAN bus. The integration design of AT89C51CC02 and HT1632C (LED drive IC) is developed into a modularized LED panel that can build a customized module combination and connect CAN with power source to meet the customers' requirements. Figure 27.1 demonstrates hardware architecture for LED display system.

The modular design of LED display majorly consists of LED display panel, LED drive IC, microcontroller and CAN converter, as is shown in Fig. 27.2. Microcontroller chip 89C51CC02 of ATMEL is chosen since it encompasses control local network and serial transmission interface. Control area network interface offers the communication among various modules with host controller board. Microcontroller supervise LED driver of HT1632C via serial transmission interface to drive LED display board. It can be seen that merely two HT1632C drive ICs are connected in series to constitute a 48 $\times$ 16 LED module to display 3 Chinese characters or graphic symbols.

Figure 27.3 shows the hardware architecture design for the LED display host controller. With AT89C51CC01 being the core microcontroller, the integration design encompasses features of host controller communication for supervisory controlling, CAN bus communication for controlling LED display, external memory circuit for display data storage and real time clock with battery backup. The serial transmission interface USB/RS232 furnishes the plug and play function for connecting with computer. External memory circuit provides 32 k bytes memory space to store the display data of LED display board. Real Time Clock circuit with battery backup offer real-time display information. Through the integration of LED display host controller board and LED display board, the proposed LED display system can construct a subtitle machine equipped with both Chinese and English display capability and build a customized LED display panel system with graph display and real-time display function, as is illustrated in Fig. 27.1.

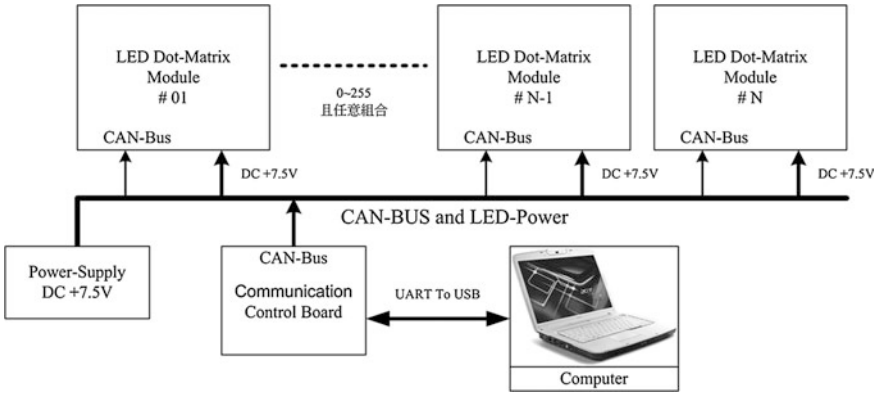

Fig. 27.1 Hardware architecture for LED display system

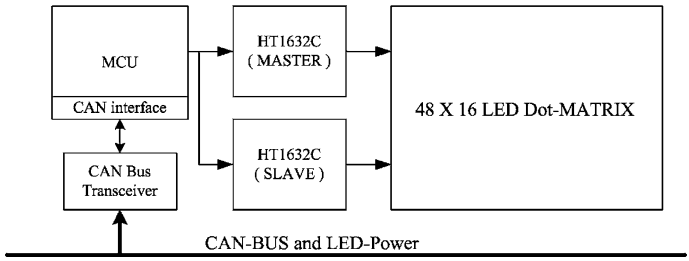

Fig. 27.2 Hardware architecture for LED display module

Fig. 27.3 Hardware architecture design for the LED display host controller

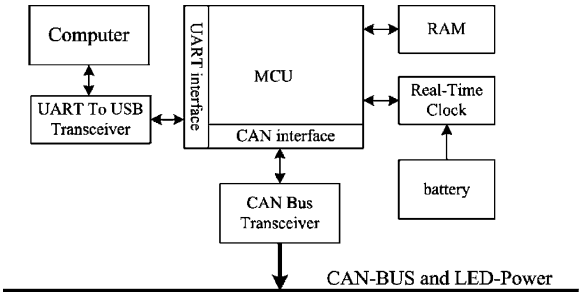

Figure 27.4 illustrates the software architecture for the LED display system. Through the human–machine interface, the display data are written or loaded into display system and converted to display code or graphic code. After that, the converted codes are linked to communication control board and stored in external extended memory. When display data are completely received and stored, the stored data in memory will permute according to setting and be sent, via CAN communication, to LED panel. In the meanwhile, the host controller will

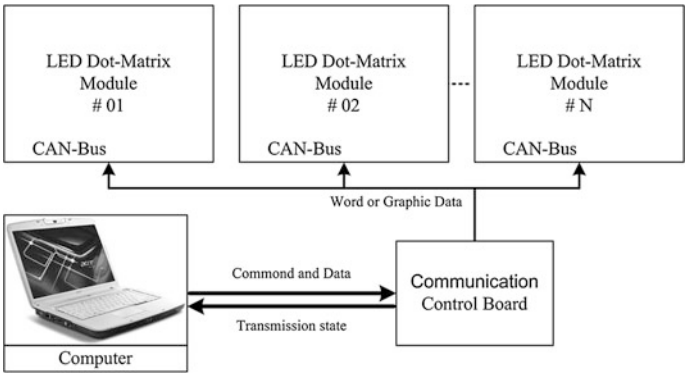

Fig. 27.4 Software architecture for the LED display system

continually send out synchronous updating display command in accordance with host computer. The display contents and store modes can, thus, exhibit on LED display system.

27.3 Experiment Results

The objective of experiment is to examine expanding method of LED panel and data transmission mode of control area network. Initially, virtual basic development tool is used to program the human–machine interface in host computer as shown in Fig. 27.5. The display data are transmitted via USB and converted through UART interface to reach communication control board. Next, by using CAN interface, display data are transmitted to corresponding individual module. The transmission scheme of CAN belongs to time triggering architecture. Based on presetting time sequence, data are sent to designated LED display module at fixed time interval. After being transmitted, the display data are renewed and displayed on LED panel successively. Figures 27.6 and 27.7 demonstrate the character data and graphic data, respectively, appearing on the LED display system. By observing the overall performance of the LED display system, the proposed fixed time triggering scheme used on CAN communication is an acceptable method in the LED display panel application. Compared with the earlier scanning circuit type of LED display system, the required amount of LED drive IC and electronic device is reduced and the displaying effect is superior. In the past, LED display panels were always customized ones. However, the presented LED display panel in this paper is a modularized one that can be assembled of customers' own accord. Therefore, it is far more valuable than the traditional one.

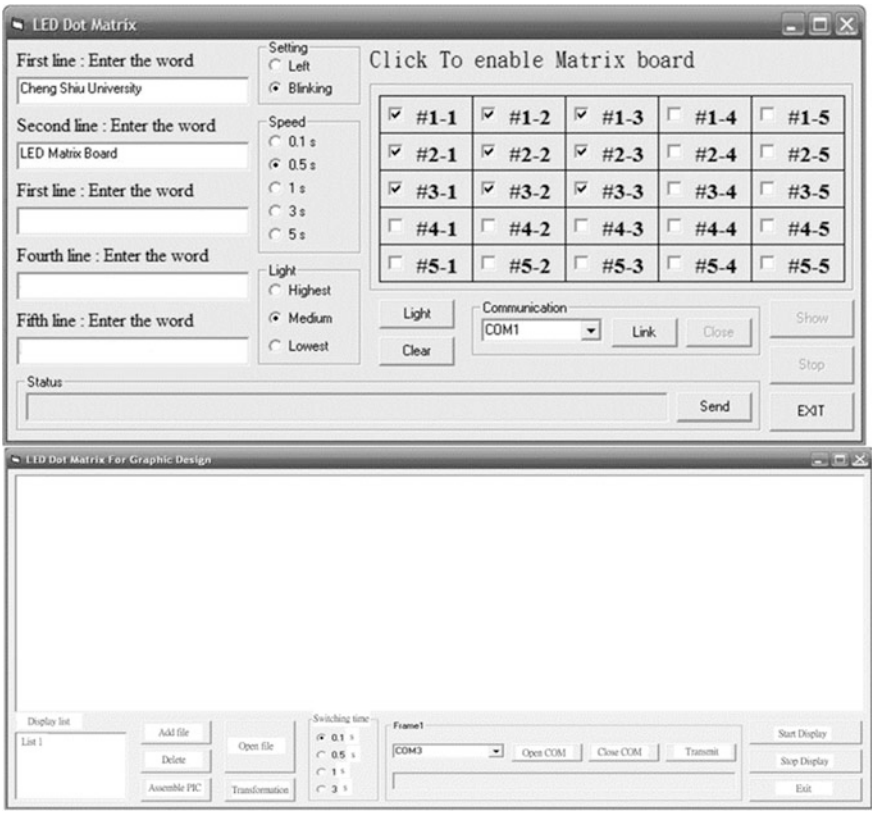

Fig. 27.5 Character and graphic human–machine interface using VB development tool

Fig. 27.6 LED display system for character data

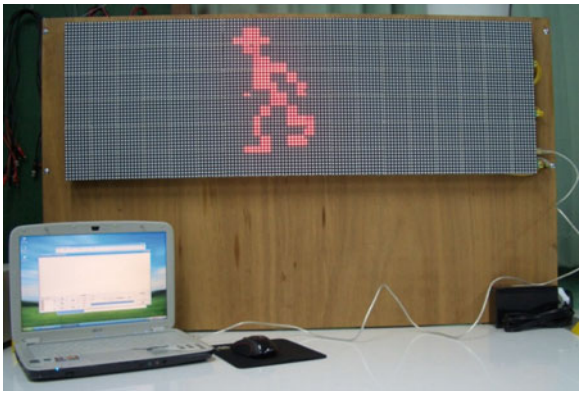

Fig. 27.7 LED display system for graphic data

27.4 Conclusions

In this paper, a time triggering method is proposed and used for data transmission and control of control area network communication. A LED display panel is built up accordingly. By utilizing LED drive IC with scanning function, the screen flickering and display delay problem of LED display module can be circumvented effectively. The simplified scanning circuit can further reduce the overall development cost and accomplish the modularized predominance. Through the laboratory experiments and measurements, the time triggering method is verified to be useful in control area network communication and validate the advantage of modularization. From the experimental results, it is clearly inspected that time triggering control of CAN unquestionably facilitate precise and updated renewal for data transmission. Moreover, the overall performance can be promoted accordingly. Furthermore, the experiment results convince that the time triggering method for CAN communication and expandable LED panel have disclosed the preponderance of system controllability. Future study will concentrate on controlling LED display system via wirelessly transmission by using smart phone. Hopefully, LED could encompass more and more economic benefit.

Acknowledgments The authors would like to thank the National Science Council, the Republic of China, for financial support of this research under the grant NSC 102-2622-E-230-002-CC3.

References

1. Wang, T.-L. (2005). *Development of high-light LED display system with embedded micro-controller", master thesis*. Chia-yi, Taiwan: National Chung Cheng University.
2. HOLTEK Co. Ltd (2008). HT1632C 32 8/2416 LED driver datasheet.
3. Chen, C.-Y., & Cheng, M. H.-M. (2010). Open architecture design of embedded controller for industrial communication gateway. *ICIC Express Letter Part B: Applications, 1*(1), 51–56.

4. Chen, C.-Y., & Yang, J.-Y. (2009). Design and application of gateway controller for heterogeneous industry protocol. *Journal of Cheng Shiu University, 22*, 135–155.
5. Park, W.-K., Han, I., & Park, K.-R. (2007). ZigBee based dynamic control scheme for multiple legacy IR controllable digital consumer devices, *IEEE Transactions on Consumer Electronics*, *53*(1): 172–177. (Rosemont, IL USA, 10–14 January).
6. Huang, H.-Y., Yen, J.-Y., Chen, S.-L., & Ou, F.-C. (2004). Development of an intelligent energy management network for building automation. *IEEE Transactions on Automation Science and Engineering, 1*(1), 14–25.
7. Alain, G. (2004). A hybrid controller for autonomous vehicles driving on automated highways. *Transportation Research Part C: Emerging Technologies, 12*(6), 421–452.
8. Qiao, X., Wang, K.-F., Sun, Y., Huang, W.-L., & Wang, F.-Y. (2007). A genetic algorithms based optimization for TTCAN, *IEEE International Conference on Vehicular Electronics and Safety* (pp. 1–7). Beijing, China, 13–15 December, 2007.
9. Saha, I., & Roy, S. (2007). A finite state analysis of time-triggered CAN (TTCAN) protocol using spin, *International Conference on Computing: Theory and Applications* (pp. 77–81), Kolkata, 5–7 March, 2007.
10. Galicki, M. (2009). Collision-free control of an omni-directional vehicle. *Robotics and Autonomous Systems, 57*(9), 889–900.
11. Talbot, S. C., & Shangping, R. (2009). Comparison of fieldbus systems CAN, TTCAN, flexray and LIN in passenger vehicles, *29th IEEE International Conference on Distributed Computing Systems Workshops* (pp. 26–31). Montreal, QC Canada, 22–26 June, 2009.
12. ATMEL Corporation. (2007). Enhanced 8-bit microcontroller with CAN controller and flash memory (AT89C51CC01/CC02) datasheet.

Chapter 28
Sensitivity and Response Time Analyses of a Wireless Thermal Convection Non-Floating Type Inclinometer with Hemispherical Chamber Filled by Carbon Dioxide

Jium-Ming Lin and Cheng-Hung Lin

Abstract The sensitivity and response time of a RFID-based thermal convection non-floating type inclinometer with hemispherical chamber filled by carbon dioxide are analysed in this paper, it is not mentioned in the previous literature. Several new ideas are presented. The first one is to fabricate it on a flexible substrate; it can save more energy than silicon. The second one is to integrate both an inclinometer and a RFID antenna on the same substrate, such that it becomes a wireless sensor. The third idea is to apply a hemispherical chamber instead of a rectangular one, so the gas flow field is more streamlined to increase the respond speed. The fourth idea is to use a non-floating structure instead of the floating one, thus it is very simple without making a cavity in the substrate. The fifth idea is to apply a stacking material for the temperature sensors, so the sensitivity is not only larger, but the curve is more close to a theoretical sinusoid one. Different combinations of stacking material (such as alumina nitride, copper and silicon) and their height (such as 1, 1.5 and 2 mm) are also studied. One can see the combinations of AlN/2 mm are always better.

Keywords Flexible Substrate · Inclinometer · RFID-Based · Thermal Convection

J.-M. Lin (✉)
Department of Communication Engineering, Chung-Hua University,
Hsin-Chu 30012, Taiwan
e-mail: jmlin@chu.edu.tw

C.-H. Lin
Program in Eng. Science College of Engineering, Chung-Hua University,
Hsin-Chu 30012, Taiwan Republic of China

J. Juang et al. (eds.), *Proceedings of the 2nd International Conference on Intelligent Technologies and Engineering Systems (ICITES2013)*, Lecture Notes in Electrical Engineering 293,
DOI: 10.1007/978-3-319-04573-3_28,

28.1 Introduction

This research proposes a novel wireless RFID-based thermal convection type inclinometer. Several new ideas are presented. The first one is to make the device on a flexible substrate, thus the leak energy is lower than that of the conventional silicon [1–11]. The second one is to integrate an inclinometer and a wireless RFID antenna on the same substrate as in Fig. 28.1, such that it is very convenient for usage. The third idea is to apply a hemispherical chamber instead of the rectangular one, so the gas distribution is more streamlined to increase the respond speed. The fourth idea is to use a non-floating structure instead of the floating one with a cavity or a groove in the substrate, thus it is very simple. The fifth idea is to apply a stacking material for the temperature sensors, so that the sensitivity is not only larger, but the curve is more close to a theoretical sinusoid one except at larger tilt angles. The fabrication steps of a non-floating type thermal convection inclinometer is given in this paper.

The results using floating and non-floating structures are studied first; note that the sensitivity curves by applying the non-floating one are better. Besides, different combinations of stacking material (such as alumina nitride, copper and silicon) and their height (such as 1, 1.5 and 2 mm) are also studied. One can see the combinations of AlN/2 mm are always better. The paper organization is as follows: the first section is the introduction. The second one is fabrication steps. The third one is simulation and discussion. The last part is the summary.

28.2 Fabrication Steps

Step 1: Deposit SiO_2 on both sides of substrate for thermal, electrical and humidity isolation. Cover Photo Resist (PR) to protect the layers of SiO_2. Deposit layers of aluminium nitride and p-type amorphous silicon successively. The aluminium nitride is used as a stacking material of the themisters. Use mask #1 and Photolithography And Etching Processes (PAEP) to retain two stripes of PR for forming the thermisters, use KOH solution or RIE process to remove the layers of poly-silicon and AlN without PR protection. Remove the PR; the result is as shown in Fig. 28.2a

Step 2: Deposit a layer of Cr and Ni as heater, RFID antenna, and the conductors connected to the power supply. Use mask #2 and PAEP to retain the PR on the heater, RFID antenna, and the conductors connected to the power supply. Finally, use sulfuric acid solution or RIE process to remove the layers of Cr and Ni without PR protection. Remove the PR; the result is as shown in Fig. 28.2b

Step 3: Use mask #3 and PAEP to retain PR on heater, and flash gold on Ni by electroless-plating to increase the conductivity of RFID antenna, and the

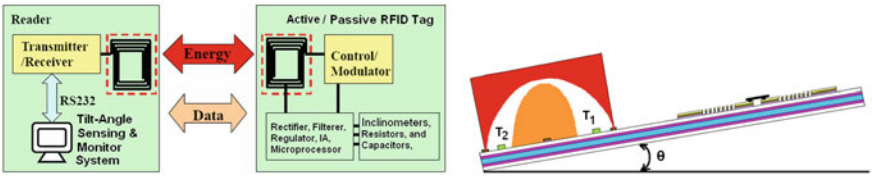

Fig. 28.1 Block diagram and operation principle of RFID-based inclinometer

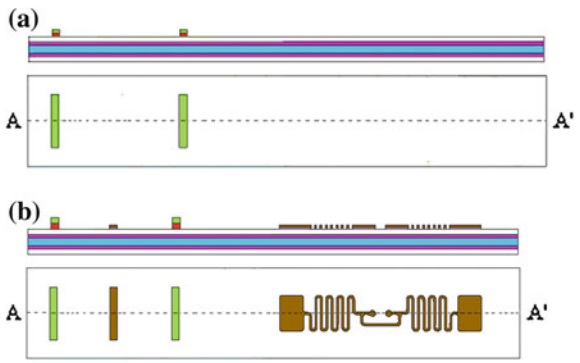

Fig. 28.2 Device top and side views. **a** Step 1. **b** Step 2

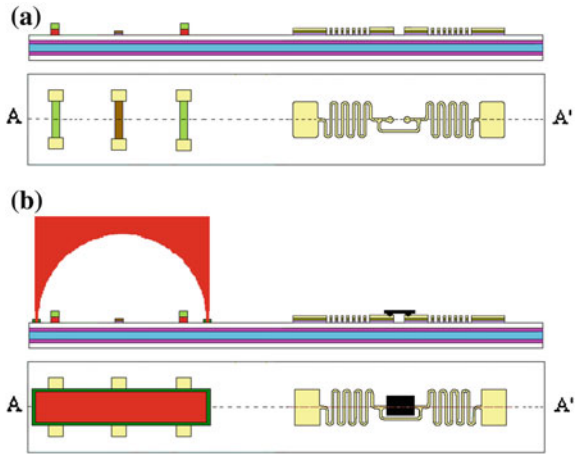

Fig. 28.3 Device top and side views. **a** Step 3. **b** Step 4

conductors connected to the power supply. Remove PR, the result is as shown in Fig. 28.3a

Step 4: Screen print plastic or polymer material around the inclinometer as dam bar, then put a cap with hemispherical chamber on the dam bar and curing, before sealing it one can fill it with carbon dioxide gas. Finally, the chip with metal bump is flip chip bonded to the RFID feed terminal, then the result is in Fig. 28.3b.

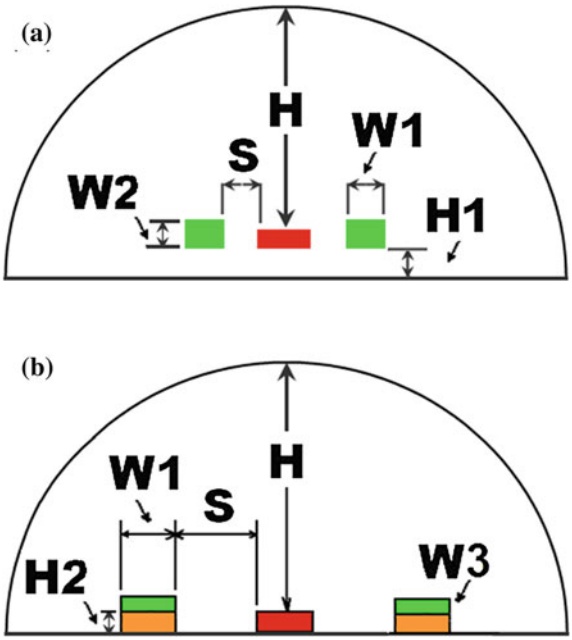

Fig. 28.4 Inclinometer geometry definition. **a** Floating type. **b** Non-floating type

28.3 Simulation and Discussions

The ESI-CFD$^+$ software is applied in this paper for simulation. Let the lengths of thermisters and heater are 9 mm and 1 mm, respectively. Figure 28.4a and b show the geometry definition of the inclinometers with floating and non-floating structures, in which W1 = 0.5 mm, W2 = 1 mm, S = 1.25 mm and H = 8.7 mm. Besides, the temperature of the package boundaries and the heater are set as 300 and 400 K, respectively. The chamber is filled with carbon dioxide gas.

Figure 28.5a, b and c show the temperature differences at the center points of thermisters versus the tilt angles (sensitivity) for the floating height (H1) as 1, 1.5 and 2 mm, respectively. Note that the floating structure is not suitable, so the non-floating structure is tested the next. Moreover, to increase the sensitivity the thermisters are stacked on one material as shown in Fig. 28.4b, in which W1 = 0.5 mm, W3 = 0.5 mm, S = 1.25 mm and H = 9 mm. The stacking material can be anyone of alumina nitride, copper and silicon. The thermal conductivity and the specific heat of these materials are listed in Table 28.1. Three values of stacking height H2, e.g. 1, 1.5, and 2 mm, are tested for comparison. The sensitivity curves with various stacking materials are as shown in Fig. 28.6a, b and c for the stacking height as 1, 1.5 and 2 mm, respectively. Note the sensitivity curve by using AlN/2 mm is better as shown in Fig. 28.6c; it is very close to a theoretical sinusoid one except at larger tilt angles.

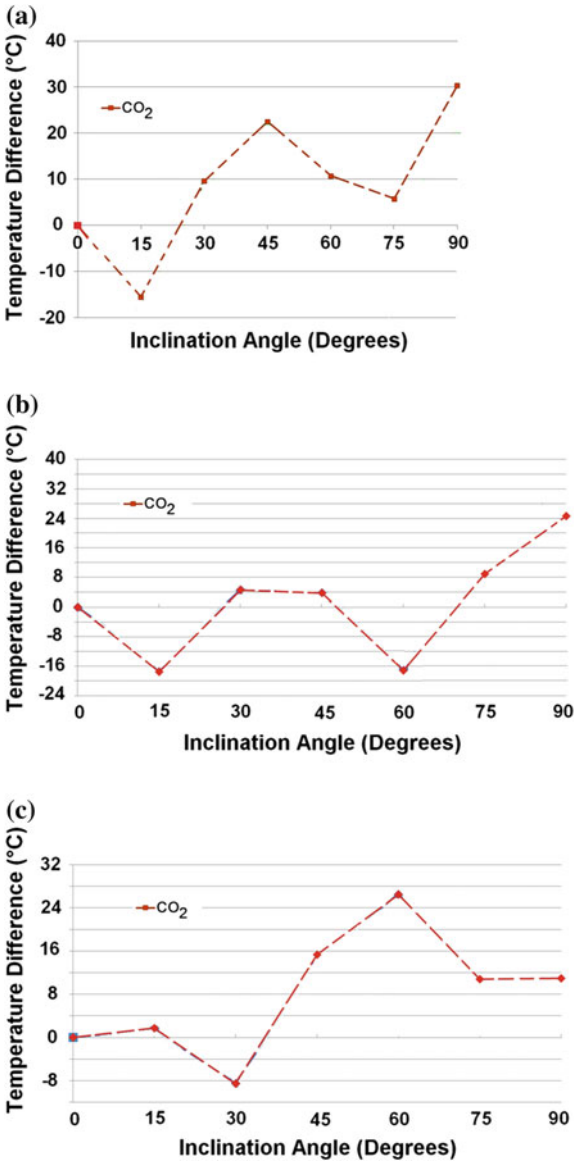

Fig. 28.5 Floating type sensitivity curves for three values of H1. **a** 1 mm. **b** 1.5 mm. **c** 2 mm

Table 28.1 Thermal conductivity and specific heat of materials

Stacking materials	Thermal conductivity	Specific heat
Aluminum nitride	160	740
Copper	385	385
Silicon	124	702

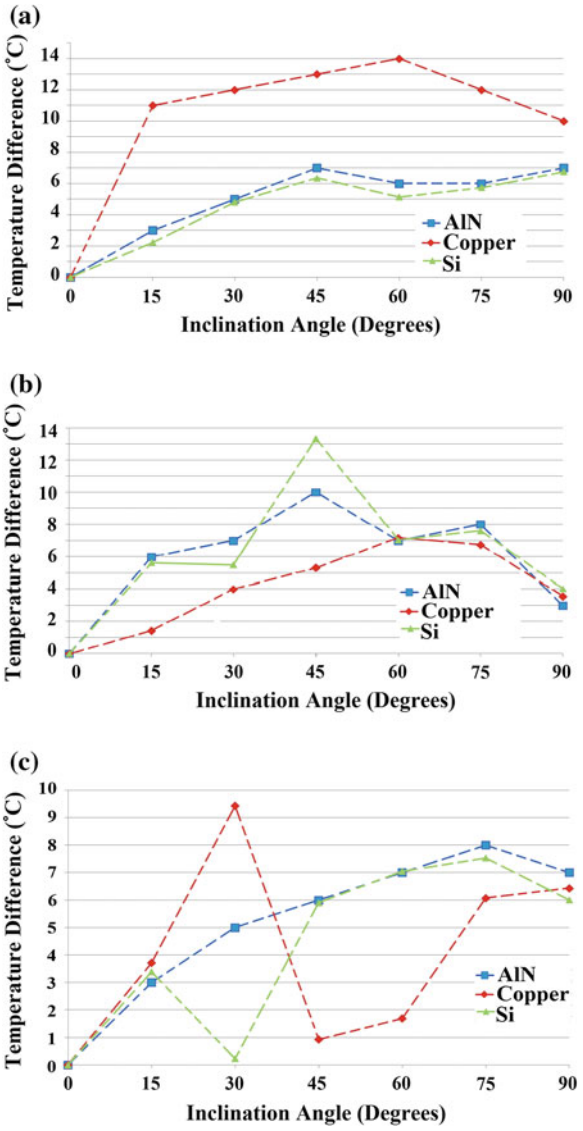

Fig. 28.6 Sensitivity curves by using different stacking materials and stacking heights **a** 1 mm. **b** 1.5 mm. **c** 2 mm

Besides, the step-input response curves of the velocities and total entropy for the angular displacement angle θ be 30° (H2 = 2 mm) are as shown in Figs. 28.7 and 28.8, respectively. The step-input response times of various angular displacements for three kinds of stacking height are listed in Table 28.2. The average value of angular displacements for each stacking height is also listed in Table 28.2 for comparison. Note that the response time for stacking height as 2 mm is always

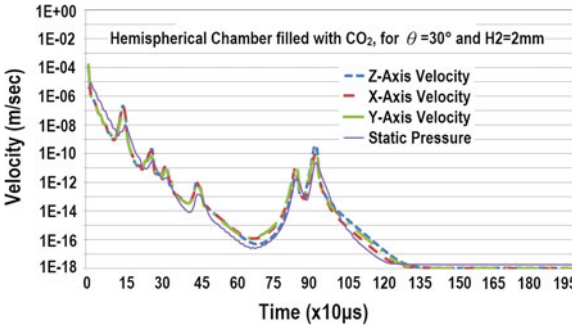

Fig. 28.7 Step-input response curve of velocities for 30° angular displacement (H2 = 2 mm)

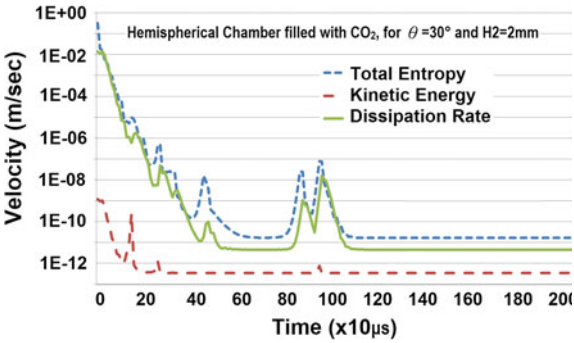

Fig. 28.8 Step-input response curve of total energy for 30° angular displacement (H2 = 2 mm)

Table 28.2 Step-input response times of various angular displacements for three kinds of stacking height (H2)

H2 (mm)	15° (μs)	30° (μs)	45° (μs)	60° (μs)	75° (μs)	90° (μs)	Average (μs)
1.25	1010	1160	990	1020	950	1080	1035
1.5	1660	1445	600	1140	1360	1120	1220
2	930	1240	1070	1670	1290	1120	1221

the quicker. Thus one can get the conclusion that both the sensitivity curve and the response speed are better for the non-floating structure with stacking combination as AlN/2 mm.

28.4 Conclusion

This research proposes a novel wireless RFID-based thermal convection type inclinometer design. Five new ideas are presented. The results by using floating and non-floating structures are studied the first; note that the sensitivity curves for

the floating structures are not good, so the non-floating structure is applied in this paper. To increase the sensitivity, the thermisters are stacked on some materials such as alumina nitride, copper and silicon. Three kinds of stacking height are also studied such as 1, 1.5 and 2 mm. Note that the combinations of AlN/2 mm are always better. This study is not proposed in the previous literature.

Acknowledgments This research was supported by National Science Council Taiwan, R.O.C. with contracts NSC-101-2622-E-216-001-CC3, 101-2221-E-216-006-MY2, and 101-2221-E-216-019-.

References

1. Billata, S., Glosch, H., Kunze, M., Hedrich, F., Frech, J., & Auber, J., et al. (2002). Micromachined inclinometer with high sensitivity and very good stability. *Sensors and Actuators, A: Physical, 97–98*, 125–130.
2. Billat, S., Glosch, H., Kunze, M., Hedrich, F., Frech, J., & Auber, J., et al. (2001). Convection-based micromachined inclinometer using SOI technology. *MEMS, 01*, 159–161.
3. Baxter, R. R., Ohno, S., Hawley, S. D., & Wilson, D. M. (2003). On a micromachined fluidic inclinometer, transducers. *Solid-State Sensors. Actuators and Microsystems, 2*, 1279–1282.
4. Leung, A. M., Jones, J., Czyzewska, E., Chen, J., & Woods, B. (1998). Micromachined accelerometer based on convection heat transfer. *MEMS, 98*, 627–630.
5. Milanovic, V., Bowen, E., Tea, N., Suehle, J., Payne, B., & Zaghloul, M., et al. (1998). Convection based accelerometer and tilt sensor implemented in standard CMOS. *MEMS, 98*, 290–487.
6. Honschoten, J. V., Baar, J. V., Bree, H. E. D., Lammerink, T., Krijnen, G., & Elwenspoek, M. (2000). Application of a microflown as a low-cost level sensor. *Journal of Micromechanics and Microengineering, 10*, 250–253.
7. Zhao, Y., & Cai, Y. Y. (2011). U. S. Patent 7,862,229 B2.
8. Alain, B., Alain, R., Bernard, V., & Alain, G. (2010). EP1550874 B1.
9. Ma, A. H., & Leung, A. M. (2008). Three-axis thermal accelerometer based on buckled cantilever microstructure. *IEEE Sensors* (pp. 1492–1495).
10. Courteaud, J., Combette, P., Crespy, N., Cathebras, G., & Giani, A. (2008). Thermal simulation and experimental results of a micromachined thermal inclinometer. *Sensors and Actuators, A: Physical, 141*, 307–313.
11. Akella, M. R., Halberta, J. T., & Kotamraju, G. R. (2003). Rigid body attitude control with inclinometer and low-cost Gyro measurements. *Systems and Control Letters, 49*, 151–159.

Chapter 29
Development of Portable Rehabilitation Device Using Flexible Spherical Actuator and Embedded Controller

Yasuko Matsui, Tetsuya Akagi, Shujiro Dohta, Mohd Aliff and Changjiang Liu

Abstract The purpose of our study is to develop a potable rehabilitation device which can be safe enough to apply to the human body. A novel flexible pneumatic actuator that can be used even if it is deformed by external force has been developed in our previous study. In this paper, a portable rehabilitation device using the flexible spherical actuator that consists of two ring-shaped flexible pneumatic cylinders is proposed and tested. The low-cost control system using small-sized quasi-servo valves and an embedded controller is also developed. The spherical actuator is also improved so as to apply to the portable device. In addition, the attitude measuring system for attitude control of the device using a tiny embedded controller and accelerometers is constructed and tested. As a result, we can confirm that the tested measuring system can measure the attitude angle of the device at the handling position. The light-weight portable device with a mass of 310 g was realized.

Keywords Portable rehabilitation device · Flexible pneumatic cylinder · Flexible spherical actuator · Embedded controller · Low cost

29.1 Introduction

Recently, it has been desired to develop a system to aid in nursing care [1, 2] and to support the activities of daily life for the elderly and the disabled [3]. The actuators required for such a system need to be flexible so as not to injure the human body [4]. The purpose of our study is to develop a portable rehabilitation device that can be safe enough to use it while handling it with hands. In our

Y. Matsui · T. Akagi · S. Dohta (✉) · M. Aliff · C. Liu
Department of Intelligent Mechanical Engineering, Okayama University of Science, Okayama 700-0005, Japan
e-mail: dohta@are.ous.ac.jp

J. Juang et al. (eds.), *Proceedings of the 2nd International Conference on Intelligent Technologies and Engineering Systems (ICITES2013)*, Lecture Notes in Electrical Engineering 293,
DOI: 10.1007/978-3-319-04573-3_29,

previous study, a novel flexible pneumatic cylinder that can be used even if the cylinder is deformed by external forces has been proposed and tested [5]. Several kinds of flexible actuators using the flexible pneumatic cylinders were proposed and tested. It is also better to apply this cylinder to a rehabilitation device. Therefore, we developed a compact flexible actuator with multi degrees of freedom so as to use it on a table or in human hands as a rehabilitation device for human wrist and arm [6]. In this paper, a portable rehabilitation device using flexible spherical actuator that consists of two flexible pneumatic cylinders is proposed and tested. The spherical actuator can realize larger bending motion along the spherical surface. In order to apply the spherical actuator to the portable rehabilitation device, the attitude measuring system at the handling points is required. Therefore, a compact and inexpensive measuring system using an embedded controller (a tiny micro-computer) and two accelerometers is proposed and tested. An attitude control system of the portable device using a superior embedded controller and quasi-servo valves which is composed of inexpensive on/off control valves is also proposed and tested.

29.2 Flexible Pneumatic Cylinder and Spherical Actuator

29.2.1 Flexible Pneumatic Cylinder

Figure 29.1 shows the construction of a novel rod-less type flexible pneumatic cylinder that we had developed [5]. The cylinder consists of a flexible tube as a cylinder and gasket, one steel ball as a cylinder head and a slide stage that can slide along the outside of the tube. The steel ball is pinched by two pairs of brass rollers from both sides of the ball. The operating principle of the cylinder is as follows. When the supply pressure is applied to one side of the cylinder, the inner steel ball is pushed. At the same time, the steel ball pushes the brass rollers and then the slide stage moves while it deforms the tube. Table 29.1 shows the properties of the cylinder as a pneumatic cylinder. The specifications of the cylinder such as a minimum radius of curvature of the cylinder, a maximum working pressure and an allowable working temperature depend on the properties of the soft polyurethane tube (SMC Co. Ltd., TUS 1208).

29.2.2 Flexible Spherical Actuator

Figure 29.2 shows the construction of a spherical actuator. The actuator consists of two ring-shaped flexible pneumatic cylinders. They are intersected at right angle and are fixed on the base. Each slide stage is set on the different acrylic plate of the base in order to decrease the gap at cross position of tubes. This gap is 12 mm.

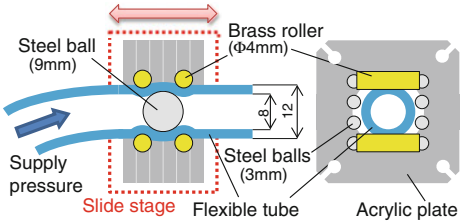

Fig. 29.1 Construction of flexible cylinder

Table 29.1 Properties of flexible cylinder

Min. driving pressure	120 kPa
Generated force	16 N (supply:500 kPa)
Max. moving speed	> 1 m/s
Weight (stroke of 1 m)	< 0.1 kg
Min. radius of curvature	about 30 mm
Max. working pressure	600 kPa
Working temperature	from −20 to +60 deg. C
Movement	push–pull actions

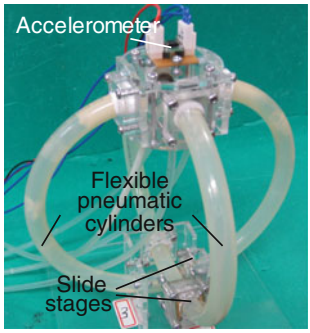

Fig. 29.2 Flexible spherical actuator

Each cylinder is also hold by an additional slider set on the opposite acrylic plate of the base that has a distance of 43 mm from the sliding stage. The diameter of each ring-shaped cylinder is 160 mm. The size of the tested actuator is 160 mm in width and 170 mm in height. The total mass of the actuator is 300 g.

Figure 29.3 shows the relation between supplied pressure and the generated torque of the tested actuator. The torque is calculated from the measured generated force and radius of the tested actuator. The torque of x and y direction were calculated based on the distance of 85 and 80 mm from the center of each ring-shaped cylinder to a fixed position of the force sensor, respectively. From Fig. 29.3, it can be seen that the maximum generated torque in the x-direction is 0.45 Nm and the y-direction is 0.47 Nm. The tested actuator has a dead zone of the generated torque for supplied pressure. This corresponds to a minimum driving pressure of the flexible pneumatic cylinder caused by a friction of the cylinder. Furthermore, the characteristic is not linear. This is caused by a larger friction between the tube and slide stage by adding the additional slider on the base.

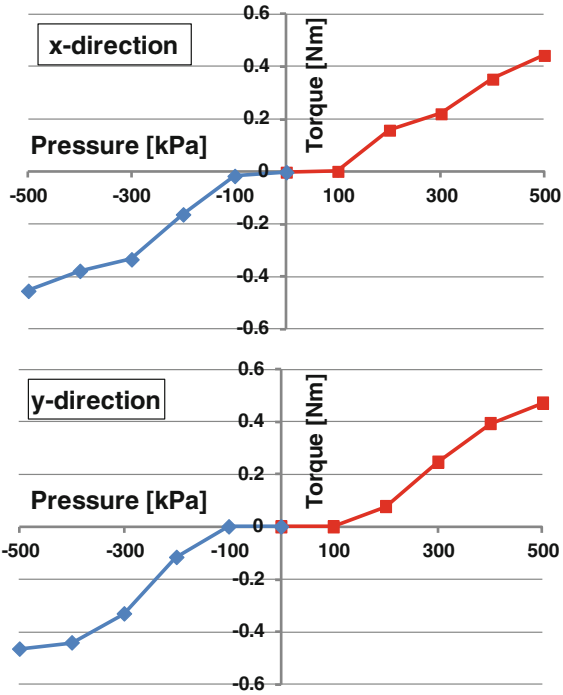

Fig. 29.3 Generated torque of tested actuator

29.3 Portable Rehabilitation Device

29.3.1 Construction and Attitude Control System

Figure 29.4 shows the view of a portable rehabilitation device using the spherical actuator. The device is developed as a rehabilitation device for shoulders and arms. We image that patients will have both handling stages of the device by their both hands in the rehabilitation. In order to apply the spherical actuator to the rehabilitation device, it is necessary to increase the moving area and the generated torque of the actuator. Therefore, the diameter of the ring-shaped flexible pneumatic cylinder is changed from 160 mm to 260 mm. Compared with the previous spherical actuator, two slide stages of each flexible cylinder are not connected with one side base, that is, each slide stage of the flexible cylinder is fixed on each handling stage. The size of the actuator is 260 mm in width and 270 mm in height. The total mass of the actuator is 310 g. In addition, to measure the attitude angle of the each handling stage, two accelerometers are used as angular sensors.

Figure 29.5 shows the schematic diagram of the attitude control system of tested portable rehabilitation device. The control system consists of the tested spherical actuator with two accelerometers, four quasi-servo valves [7] to operate two flexible pneumatic cylinders and a microcomputer (Renesas Co. Ltd., SH7125).

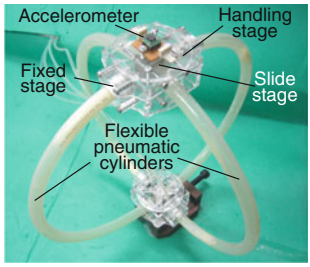

Fig. 29.4 Portable rehabilitation device

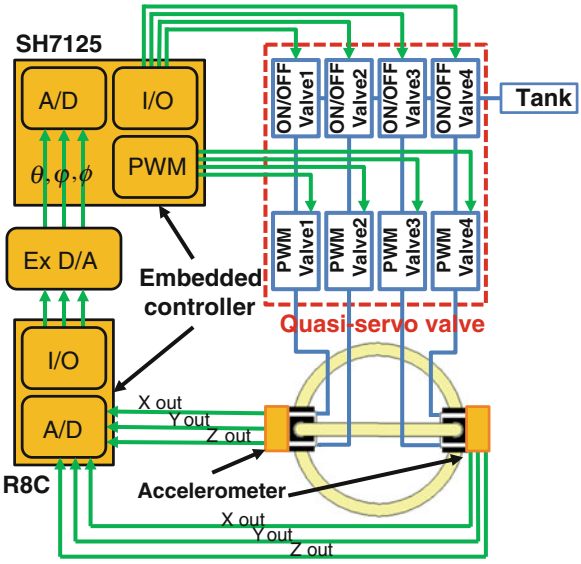

Fig. 29.5 Attitude control system of the device

The accelerometers were used as angular sensors of the both handling stages. The attitude control of the device is done as follows. The desired angles between both stages are given by the sequential data or input device operated by physical therapist. For measuring the angle between both stages, the microcomputer gets the output voltages from two accelerometers. By the control scheme, the quasi-servo valves are driven and the flexible pneumatic cylinders are driven. The sampling period of the control is 2.3 ms. The PWM period of the quasi-servo valve is 10 ms.

Figure 29.6 shows the transient view of movement of the device. In the experiment, the sequential on/off operation of the quasi-servo valve every 0.8 s was applied. The supply pressure of 450 kPa is applied. From Fig. 29.6, it can be seen that the device can move smoothly. We found that the device can work while the human hold it by both hands.

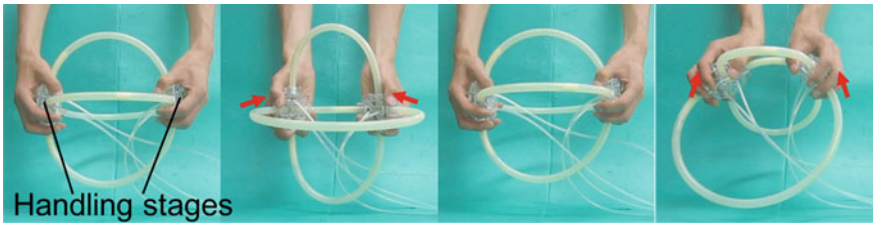

Fig. 29.6 Transient view of the movement of the rehabilitation device

29.3.2 Attitude Measuring System

In order to control the attitude of the device, it is necessary to measure the angular change of both stages that are holding points of the device. Figure 29.7 shows the construction of the tested attitude measuring system. The system consists of two accelerometers, a tiny embedded controller (Renesas Co. Ltd., R8C/M12A) and D/A convertor with SPI communication (Linear Technology Co. Ltd., LTC1660). Three output ports from each accelerometer are connected with A/D converter in the embedded controller. The angular change θ, ψ and φ defined as shown in Fig. 29.8 are given by the following equations, respectively [8].

$$\theta = \tan^{-1}\left(\frac{A_{xout}}{\sqrt{A_{yout}^2 + A_{zout}^2}}\right) \tag{29.1}$$

$$\psi = \tan^{-1}\left(\frac{A_{yout}}{\sqrt{A_{xout}^2 + A_{zout}^2}}\right) \tag{29.2}$$

$$\varphi = \tan^{-1}\left(\frac{\sqrt{A_{xout}^2 + A_{yout}^2}}{A_{zout}}\right) \tag{29.3}$$

where, A_{xout}, A_{yout} and A_{zout} are incremental A/D values for x, y and z axis in the accelerometer. These calculation algorism were embedded in the tiny controller. The controller can send the six calculated angles to the personal computer through the serial communication. In addition, the tiny embedded controller can send these data to the superior embedded controller for attitude controller of the device as voltage changes through D/A converter. The sampling period using serial communication method with 9600 bps of tiny embedded controller is about 52 ms. By using the low-cost embedded controller and MEMS based accelerometer, the estimated cost of tested measuring system is very low, that is less than 30 US dollars.

Figure 29.9 shows the transient responses of the incremental angles for θ and φ between both stages of the device by using the tested attitude measuring system. In

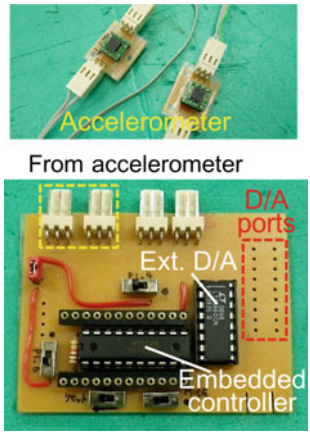

Fig. 29.7 Attitude measuring system

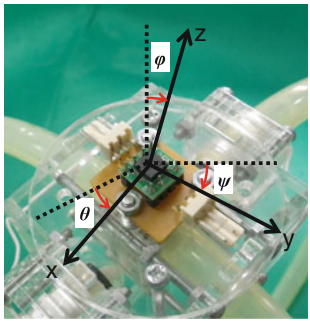

Fig. 29.8 Attitude angle (θ, ψ and φ)

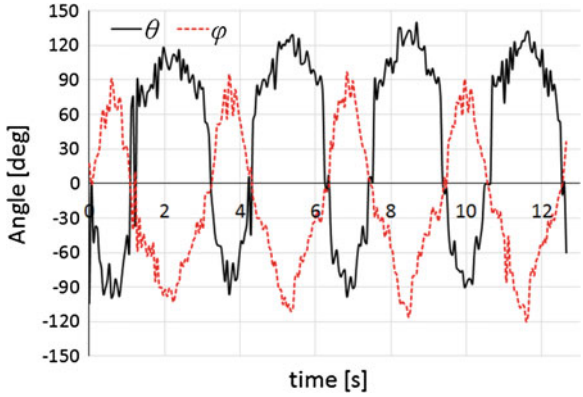

Fig. 29.9 Transient response of stage angle θ and φ

the experiment, the device was driven by the attitude control system as shown in Fig. 29.5 so that the angles for x and y directions of the device are changed every 0.8 s. In Fig. 29.9, the solid line shows the incremental angle of θ, and the broken line shows the incremental angle of φ. From Fig. 29.9, we can confirm that the

attitude of both stages in the device can be measured. By using the measuring system, it will be possible to control the motion of the device according to the desired incremental angle changes.

29.4 Conclusions

This study that aims to develop the portable rehabilitation device can be summarized as follows.

(1) The portable rehabilitation device that is redesigned flexible spherical actuator using two flexible pneumatic cylinders was proposed and tested. The driving test using the device was executed. As a result, we could confirm the validity of the portable device because of its light-weight and flexibility.
(2) The low-cost attitude measuring system that consists of two accelerometers and a tiny embedded controller was proposed and tested. By using the tested system, the attitude of the device could be also measured.

As our future work, we are going to execute the tracking control of the device for desired sequential angular change by using the tested attitude measuring and control systems.

This study was supported by the Education Ministry of Japan through a Financial Assistance Program for QOL Innovative Research (2012-) and a Grant-in-Aid for Scientific Research (C) (Subject No. 24560315).

References

1. Ishii, M., Yamamoto, K., & Hyodo, K. (2005). Stand-alone wearable power assist suit-development and availability-. *Journal of Robotics and Mechatronics, 17*, 575–583.
2. Noritsugu, T., Takaiwa, M., & Sasaki, D. (2009). Development of power assist wear using pneumatic rubber artificial muscles. *Journal of Robotics and Mechatronics, 21*, 607–613.
3. Kobayashi, H., Shiban, T., & Ishida, Y. (2004). Realization of all 7 motions for the upper limb by a muscle suit. *Journal of Robotics and Mechatronics*, *16*, 504–512.
4. Nagata, Y. (Ed) (2004). Soft actuators -forefront of development-. NTS ltd., pp. 291–335.
5. Akagi, T., & Dohta, S. (2007). Development of a rodless type flexible pneumatic cylinder and its application. *Transactions of JSME, Series C, 73*, 2108–2114.
6. Krebs, H. I., Volpe, B. T., Williams, D., Celestino, J., Charles, S. K., Lynch, D., et al. (2007). Robot-aided neurorehabilitation a robot for wrist rehabilitation. *IEEE Transactions on Neural Systems and Rehabilitation Engineering, 15*, 327–335.
7. Moriwake, Y., Akagi, T., Dohta, S., & Zhao, F. (2012). Development of low-cost pressure control type quasi-servo valve using embedded controller. *Journal of Procidia Engineering, 41*, 493–500.
8. Christopher, J. F. (2010). Using an accelerometer for inclination sensing. analog devices application note AN-1027, pp. 1–8.

Chapter 30
Large-Stroke Control of a Telescopic Two-Stage Linear Motor

Jyh-Chyang Renn, Chin-Yi Cheng and Nien-Ting Ho

Abstract In this paper, a novel two-stage large-stroke proportional linear motor for fluid power valve technology is developed. It is found that the linear effective stroke is around 10 mm and the maximal output force reaches 15 N for the maximal excitation current of 1.0 A. In the design of the larger 2nd-stage linear motor, the hollow stator with embedded coil and permanent magnet covers and incorporates the smaller 1st-stage linear motor. It is also observed that both the stator and the armature of the 1st-stage linear motor are independently movable and form translational two-dimensional motion. Experiments further prove that such a two-stage large-stroke proportional linear motor can produce diverse modes of motion output even though the motions of the two armatures in the two-stage large-stroke proportional linear motor are translational rather than rotational. It is worth mentioning that the output force/stroke characteristic of the larger 2nd-stage linear motor is actually more nonlinear. However, such a non-linearity is not of great importance since the final precision linear force output control and the precision plunger position control are both accomplished by the armature of smaller 1st-stage linear motor. Finally, in this paper only open loop control scheme is required for the precision large-stroke plunger position control. In addition, the electro-magnetic software FLUX 2D is used as a tool to accomplish the design task and analysis of the two-stage linear motor.

Keywords Linear motor · Hydraulics and pneumatics · Proportional technique · Fluid power · Flux2D

J.-C. Renn (✉) · C.-Y. Cheng · N.-T. Ho
Department of Mechanical Engineering, National Yunlin University of Science and Technology, Douliou 640, Taiwan, Republic of China
e-mail: rennjc@yuntech.edu.tw

J. Juang et al. (eds.), *Proceedings of the 2nd International Conference on Intelligent Technologies and Engineering Systems (ICITES2013)*, Lecture Notes in Electrical Engineering 293,
DOI: 10.1007/978-3-319-04573-3_30,

30.1 Introduction

Nowadays, electro-mechanical transducers are widely used in the design of electro-hydraulic and electro-pneumatic valves [1, 2, 4–8]. Among these different electro-mechanical transducers, the switching solenoid is perhaps the most commonly used one and has been widely applied to the design of conventional fluid power on–off solenoid valves. On the other hand, the proportional solenoid has been successfully applied to the design of fluid power proportional valves. The linear force/stroke relation of the proportional solenoid is the key requirement for the design of a fluid power proportional valve [1, 3]. The spool, which is subjected to a constant force within the linear working stroke, reaches a definite position in the valve body according to Hook's law. This definite position of the spool signifies a definite opening area of the valve orifice. Therefore, the volumetric flowrate may be varied continuously by electrically adjusting the opening area of the proportional valve orifice. In this paper, a two-stage large-stroke linear motor for fluid power proportional valve is proposed and realized as shown in Fig. 30.1. It is observed that the whole two-stage motor consists of two linear motors, the smaller 1st-stage and the larger 2nd-stage motor. Clearly, its function and structure is actually very similar to a telescope. The detailed schematic layout of the 1st-stage linear motor is shown in Fig. 30.2. Two significant features of the 1st-stage linear motor are the available linear force/stroke characteristic as well as the movable pair of permanent magnets that are directly embedded into the output plunger of armature as shown in Fig. 30.2[9]. The coil is wound around the bakelite to generate the control magnetic flux. However, the permanent magnet on each side of the plunger produces its own magnetic flux as well. Consequently, the proposed 1st-satge linear motors is able to provide bi-directional force output. It is also worth mentioning that two cylindrical permanent magnets are embedded into both ends of the movable plunger respectively. Such a novel design enables the linear force/stroke characteristic as long as the geometry and dimension are properly determined. On the other hand, Fig. 30.3 shows the schematic layout of the larger 2nd-stage linear motor. Due to the more massive motor body design, the proposed 2nd-stage linear motor is able to produce larger stroke output. However, the output force/stroke characteristic of the larger 2nd-stage linear motor is more nonlinear because two sets of permanent ferrite magnets are embedded into the stator rather than rotor (armature) and hence are not movable. Strictly speaking, such a nonlinearity is not of great importance since the final precision linear force output control and the precision plunger position control are both accomplished by the armature of the smaller 1st-stage linear motor. In this paper, the commercial FLUX 2D software is utilized as a tool to obtain the most suitable dimensions for the linear motors. In the following, the design procedure using FLUX 2D is briefly outlined.

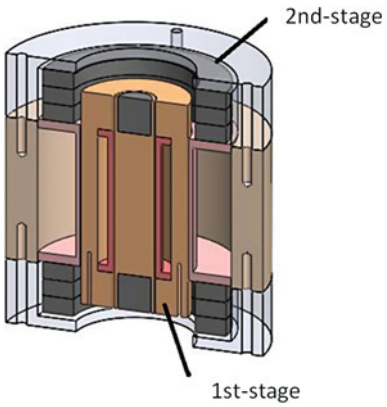

Fig. 30.1 Schematic layout of the proposed two-stage, large-stroke linear motor

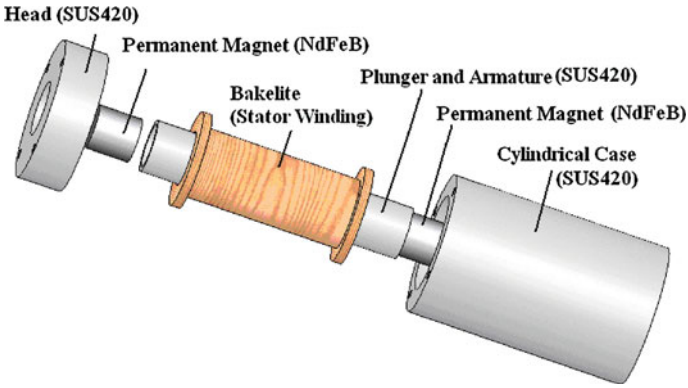

Fig. 30.2 Schematic layout of the smaller 1st-stage linear motor

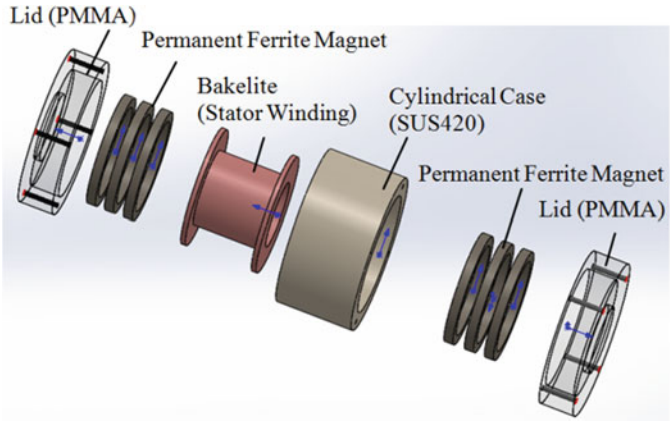

Fig. 30.3 Schematic layout of the larger 2nd-stage linear motor

30.2 Designing the TWO-STAGE Linear Motor Using FLUX 2D

In this paper, the commercial FEM software package FLUX 2D is chosen as a tool to design the electro-mechanical linear motor. Generally speaking, conventional design approach based on equivalent circuit method and trial-and-error are time-consuming [2]. However, the introduction of FLUX 2D helps to test new ideas quickly and design a successful prototype rapidly. First of all, according to the design dimension of the 1st-stage liner motor shown in Fig. 30.2, the construction of the study domain for the 1st-stage linear motor by creating the necessary points is shown in Fig. 30.4. Similarly, Fig. 30.5 shows the construction of the study domain for the 2nd-stage linear motor. Since the geometry of the linear motor is axis-symmetric, a two-dimensional cylindrical coordinate model of the magnetic field is established for the quantitative analysis of the armature's output force. Then, as an example, the FLUX 2D's automatic mesh points generator accomplishes the meshing in finite elements for the 2nd-stage linear motor as shown in Fig. 30.6. Before the simulations, the value of the excitation current as well as the magnetization (B–H) curves for different magnetic materials must be given in advance. The former is the known input signal and the latter can be found in the data sheets of corresponding magnetic materials. In addition, the boundary condition assuming all the field lines are perpendicular to the boundary is applied throughout the simulations. For the 1st-stage linear motor, the remnant flux density of the NdFeB permanent magnet is set to be 1.45 Tesla. The diameter of the coil-wire is 0.4 mm and the number of coil turns is 1000 which results in a total winding resistance of 19.9 Ω. For the 2nd-stage linear motor, however, the remnant flux density for the permanent ferrite magnet is found to be 0.95 Tesla. The diameter of the coil-wire is 0.4 mm and the number of coil turns is set to be 1150 which results in a total winding resistance of 22 Ω.

After simulations, the magnetic flux density near the winding of the 1st-stage linear motor for the input current of 0.25 A can be derived as shown in Fig. 30.7. Similarly, the magnetic flux density for the 2nd-satge linear motor using the same input current is shown in Fig. 30.8. From their numerical tables, the average flux density can be determined. Consequently, the static force/stroke relation for a given excitation current can be numerically derived. Similar simulations may be repeated for different input currents and at different strokes of the armature (plunger). Figure 30.9 shows the numerical static force/stroke characteristic curve for the 1st-stage linear motor using eight different excitation currents. It is observed that the static force/stroke relation is quite linear within the stroke range of ±1 mm. Similarly, Fig. 30.10 shows the numerical static force/stroke characteristic curve for the 2nd-stage linear motor using eight different excitation currents. It is noticeable that the static force/stroke relation is more nonlinear as compared to Fig. 30.9. However, the effective range of working stroke is around ±10 mm which is 10 times larger than that of the 1st-stage linear motor. In addition, the maximal output forces corresponding to different values of input current for the smaller 1st-stage linear motor are depicted in Table 30.1. Similarly, Table 30.2 shows the similar data

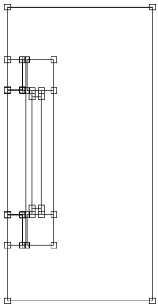

Fig. 30.4 Construction of the study domain for the 1st-stage linear motor by creating the necessary points

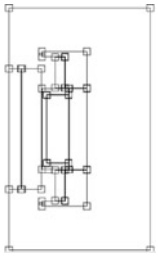

Fig. 30.5 Construction of the study domain for the 2nd-stage linear motor by creating the necessary points

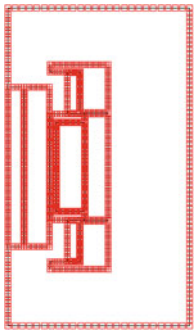

Fig. 30.6 The meshing in finite elements for the 2nd-stage linear motor

numerically derived for the larger 2nd-stage linear motor. It is worth mentioning that the 1st-stage and 2nd-stage linear motors possess approximately the same maximal output force even though their effective ranges of working stroke are quite different. This provides an advantage that the switching of force control between two linear motors can be seamlessly accomplished (Fig. 30.11).

30.3 Experimental Test Devices

In this study, two experimental test devices are developed for evaluating the performances of the proposed two-stage linear motor. The first one is the static test rig as shown in Fig. 30.12. An open-loop controlled micro-stepping motor is

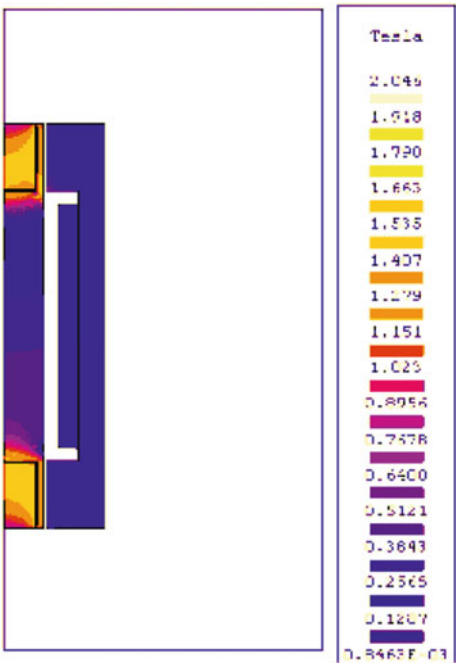

Fig. 30.7 Magnetic flux density in units of Tesla for the 1st-stage linear motor (Input current: 0.25 A)

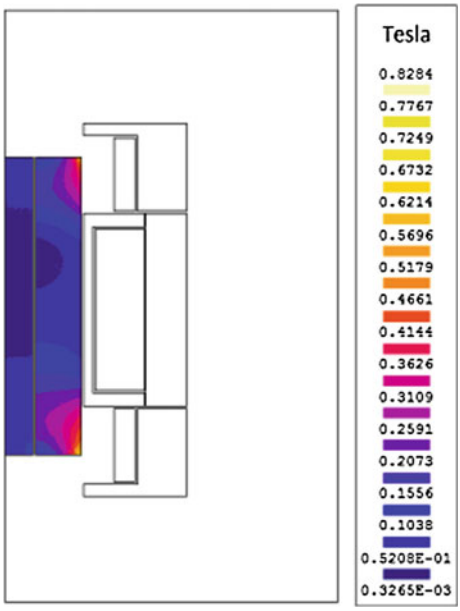

Fig. 30.8 Magnetic flux density of in units of Tesla for the 2nd-stage linear motor (Input current: 0.25 A)

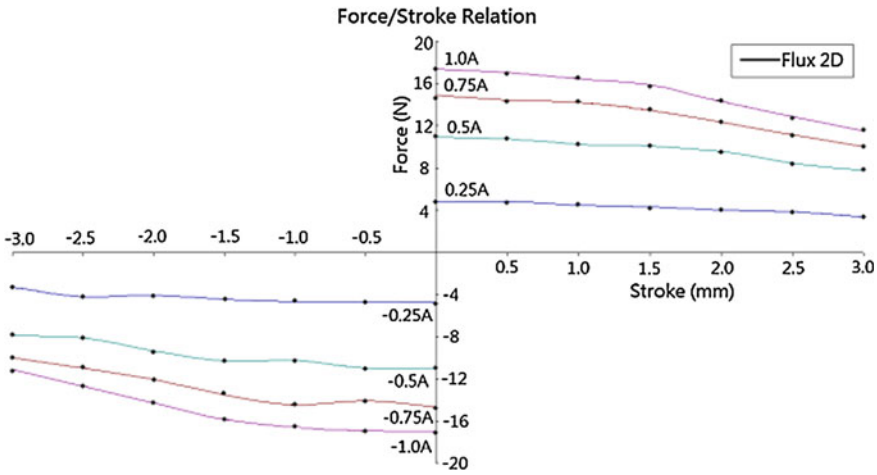

Fig. 30.9 Numerical static force/stroke relation using 8 different excitation currents for the 1st-stage linear motor

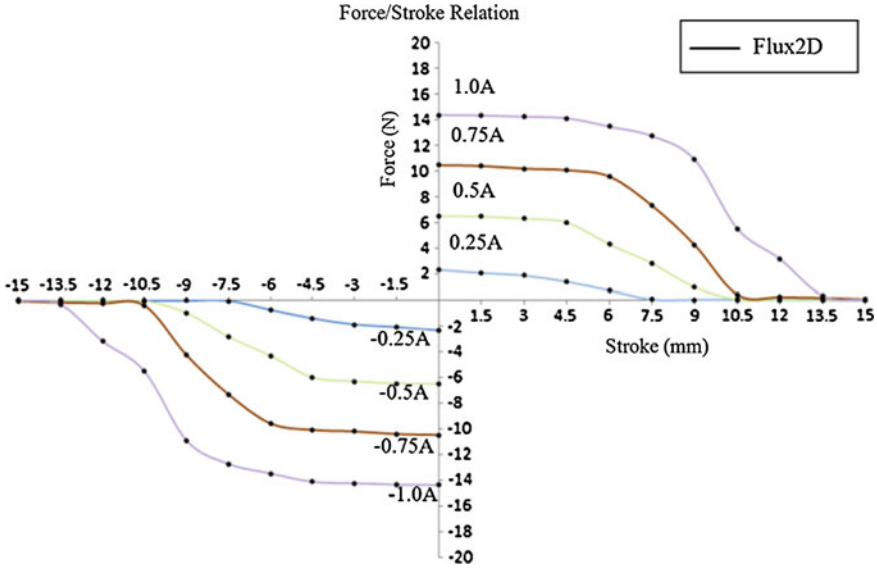

Fig. 30.10 Numerical static force/stroke relation using 8 different excitation currents for the 2nd-stage linear motor

utilized to control the position of armature (plunger) of the tested linear motor. The rotational angle and speed of the micro-stepping motor are derived directly from the number of pulses and the frequency of the generated pulse signal sent to the driver, respectively. Besides, the test device provides a position sensor (LVDT) as

Table 30.1 Simulation results of input current versus maximal output forces for the 1st-stage linear motor

Input current (A)	Max. force (N)	Input current (A)	Max. force (N)
0.25	4.24	−0.25	−4.3
0.5	9.17	−0.5	−9.12
0.75	13.99	−0.75	−13.93
1	17.24	−1	−17.19

Table 30.2 Simulation results of input current versus maximal output forces for the 2nd-stage linear motor

Input current (A)	Max. force (N)	Input current (A)	Max. force (N)
0.25	2.36	−0.25	−2.34
0.5	6.61	−0.5	−6.51
0.75	10.52	−0.75	−10.47
1	14.45	−1	−14.38

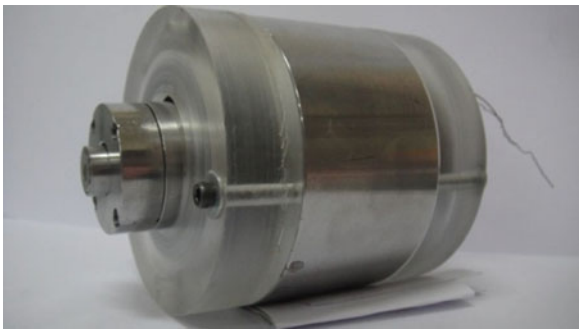

Fig. 30.11 Photograph of the realized prototype of two-stage linear motor

well as a load cell for the measurement of the stroke and the output force of the armature (plunger). Finally, the control of the unit as well as the acquisition and processing of measured data are all integrated in a PC-based LabView software controller. The second one is the open-loop dynamic test device as depicted in Fig. 30.13.

30.4 Experimental Results and Discussion

The experimental static force/stroke family curves of the smaller 1st-stage linear motor can be evaluated by using the static test device shown in Fig. 30.12 and the corresponding results are depicted in Fig. 30.14. Similarly, the experimental static force/stroke relation for the larger 2nd-stage linear motor can also be derived as shown in Fig. 30.15. In addition, the comparisons of simulation and experimental

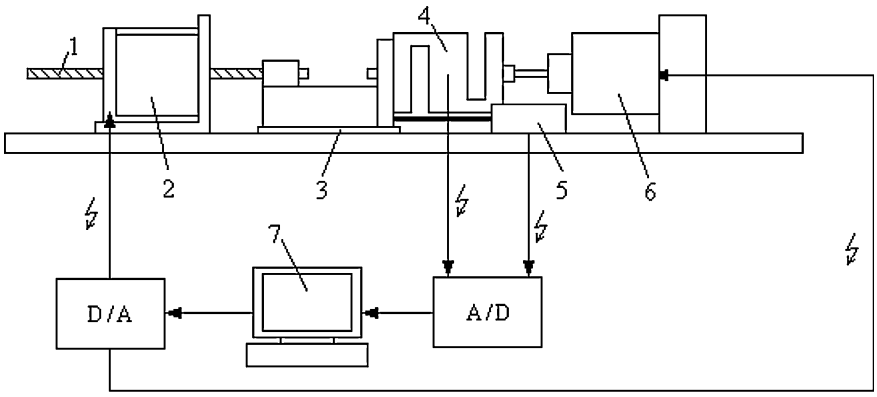

1. Ball Screw
2. Micro-stepping motor
3. Linear ball-bearing
4. Load-cell
5. LVDT
6. Tested linear motor
7. PC

Fig. 30.12 The static force/stroke test device

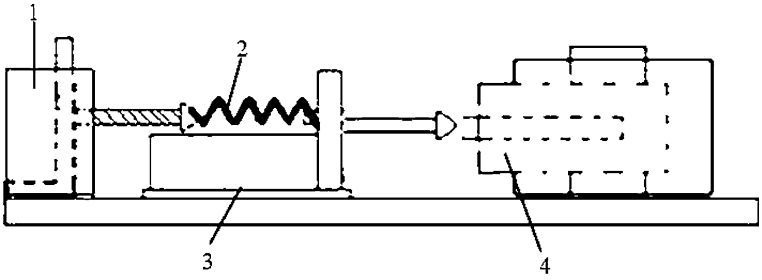

1. Laser displacement meter
2. Spring
3. Linear ball-bearing
4. Tested linear motor

Fig. 30.13 The open-loop dynamic test device

results are depicted in Figs. 30.14 and 30.15 as well. For the 1st-stage linear motor, it is observed that the maximal output force and the linear working stroke are around 16 N and 1.0 mm for the maximal input current of 1.0 A. Similarly, for the 2nd-stage linear motor, the maximal output force and the effective working stroke are around 15 N and 10 mm for the maximal input current of 1.0 A. This proves the initial design criterion that the 1st-stage and 2nd-stage linear motors should possess approximately the same maximal output force even though their effective ranges of working stroke are quite different. Furthermore, it is also noticeable that the simulation results agree quite well with the experimental ones. For the 1st-stage linear motor, the maximal error is around 5 % and for the

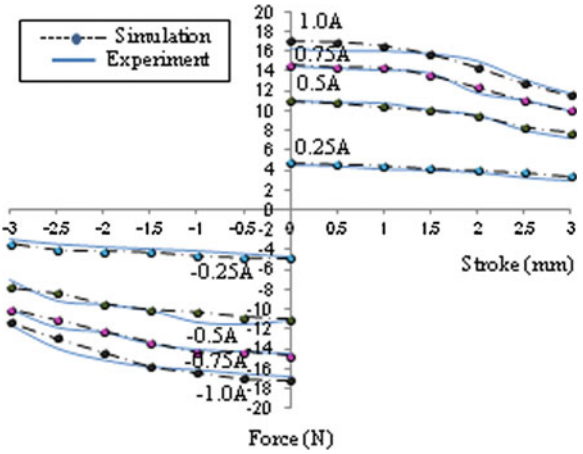

Fig. 30.14 Comparison of simulation and experimental force/stroke results of the 1st-stage linear motor

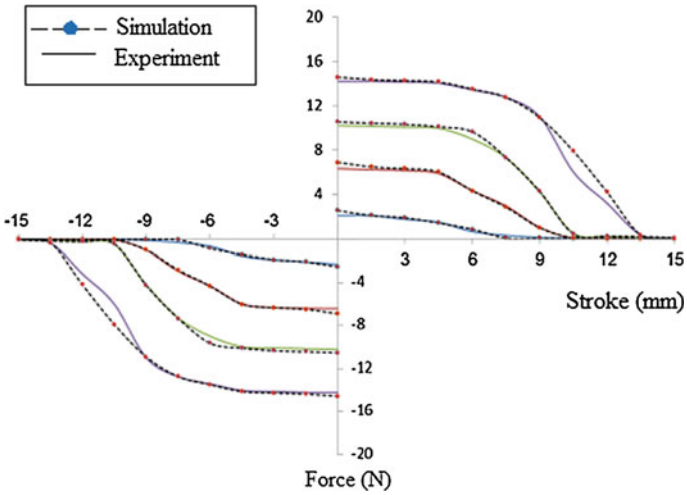

Fig. 30.15 Comparison of simulation and experimental force/stroke results of the 2nd-stage linear motor

2nd-stage linear motor, the maximal error is around 3 %. This proves the effectiveness of utilizing the software FLUX2D as the initial design tool.

For the 2nd-stage linear motor, the input excitation current for a rough (accuracy: 1 mm) but large-stroke position control can be determined directly from Fig. 30.16. The intersection of the spring-constant straight line and the nonlinear force curve gives the value of input excitation current. As an example, if the desired stroke is 7.5 mm, then the intersection gives the value of 0.75 A as the

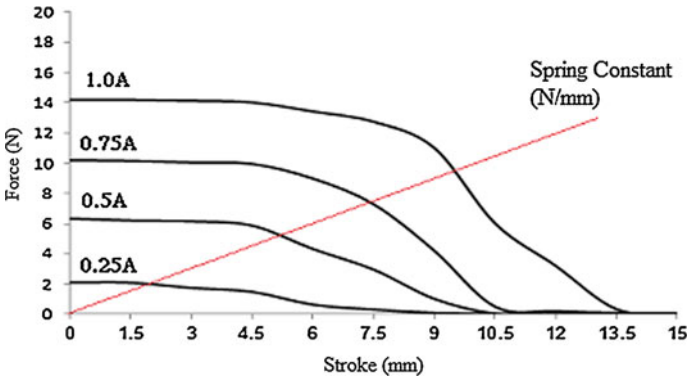

Fig. 30.16 Determination of the input excitation current for the 2nd-stage linear motor

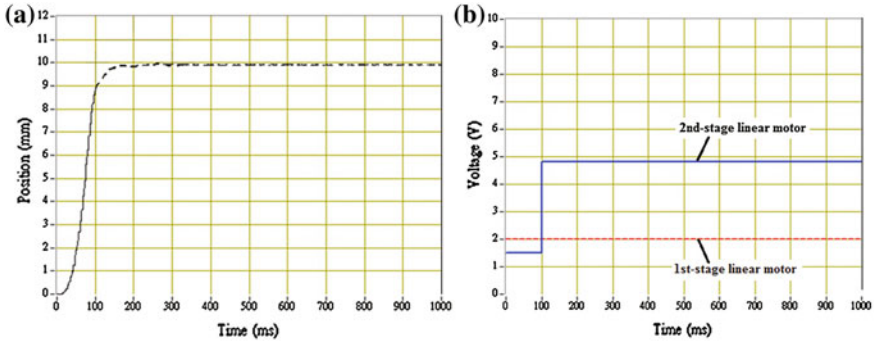

Fig. 30.17 Telescopic two-step armature position control using proposed two-stage linear motor (Total displacement: 10 mm), **a**: Position signal, **b**: Input voltage signal

input current to the 2nd-stage linear motor. On the other hand, the 1st-stage linear motor is responsible for the more precise (accuracy : 100 μm) armature (plunger) position control. However, the available linear range of working stroke is limited within ±1 mm. Thus, if the desired target position is 10 mm, it is suggested that the initial 9 mm position control can be done by the 2nd-stage linear motor. The remaining 1 mm position control can be switched and accomplished by the 1st-stage linear motor. Using the test device depicted in Fig. 30.13, the corresponding experimental results are shown in Fig. 30.17. In Fig. 30.17a, the solid line represents the initial 9 mm position control by the 2nd-stage linear motor while the dashed line above 9 mm describes the armature position control by the 1st-stage linear motor. The input voltages to the 2nd-stage and 1st-stage linear motor are also depicted in Fig. 30.17b. Clearly, after reaching 9 mm, the input voltage to the 2nd-stage linear motor drops very quickly to nearly 5 V meaning that the input excitation current to the 2nd-stage linear motor becomes nearly zero. Thus the proposed two-stage linear motor fulfills and complies with the energy-efficient requirement.

30.5 Conclusions

In this paper, a novel two-stage linear motor is successfully developed and realized. After experimental tests, four conclusions may be drawn from this research.

(1) For the 1st-stage linear motor, the maximal output force and the linear working stroke are 16 N and 1.0 mm for an input current of 1.0 A. For the 2nd-stage linear motor, the maximal output force and the effective working stroke are around 15 N and 10.0 mm for an input current of 1.0 A.
(2) The simulation results agree very well with the experimental ones. For the 1st-stage linear motor, the maximal error is approximately 5 % and for the 2nd-stage linear motor, the maximal error is around 3 %. This proves the effectiveness of utilizing the software FLUX2D as the initial design tool.
(3) The proposed novel precision telescopic large-stroke armature position control by open loop scheme is proved experimentally to be effective.
(4) The proposed two-stage linear motor fulfill the energy-efficient requirement because the input excitation current to the 2nd-stage linear motor drops to zero immediately after the 1st-stage linear motor takes over the position control of the remaining stroke.

Acknowledgments The financial supports of the National Science Council under grant number NSC 100-2221-E-224-022-MY2 is greatly appreciated.

References

1. Backe, W. (1993). *Steuerung- und Schaltungstechnik II, Umdruck zur Vorlesung* (4th ed.). Germany: RWTH Aachen.
2. Renn, J.-C., & Xu, Z.-L. (2003). State-space modeling and FEM design of moving-coil transducer for fluid-technical proportional valves. *Journal of the CSME*, *24*(2), 119–125.
3. Renn, J.-C., & Tsai, C. (2002). Linearization of the force/stroke characteristic of switching solenoid using Fuzzy-logic-controller. *Proceedings of Fifth JFPS International Symposium on Fluid Power* (Vol. 1, pp. 193–198). Nara, Japan.
4. Gamble, J., & Tappe, P. (2008). A Novel bi-directional proportional hydraulic valve actuator, NCFP 108-11.3, (pp. 301–305).
5. Li, Q., Ding F., & Wang, C. (2005). Novel bidirectional linear actuator for electrohydraulic valves, *IEEE Transactions on Magnetics*, *41*(6), 2199–2202.
6. Yamahata, C., Lacharme, F., Burri, Y., & Gijs, M. A. M. (2005). A ball valve micro pump in glass fabricated by powder blasting. *Sensors and Actuators, 110*(1), 1–7.
7. Renn, J.-C., & Chen, H.-M. (2005). Design of a novel semi-active suspension for motorcycles with Fuzzy-sliding mode controller. *Journal of the CSME, 26*(3), 287–291.
8. Renn, J.-C., Chen, C.-Y., & Lu, C.-H. (2008). Gap control for a proportional floating vacuum pad, JMES. *Proceedings of the Institution of Mechanical Engineers: Part C, 222*(11), 2069–2072.
9. Renn, J.-C. & Liao, B.-J. (2010). A novel linear motor with movable integrated permanent magnets. *Proceedings of the 7th International Fluid Power Conference,* (Vol. 2, pp. 343–354). Aachen, Germany.

Chapter 31
A Method for Extracting the Characteristic of Capacitors Using Transmission Matrix

Yu-Yung Wu, Sung-Mao Wu, Ching-Fu Yang, Lung-Shu Hung, Yung Mau Cheng and Chia-Lin Chen

Abstract In this paper, we propose a method for analyzing the dielectric loss and resonance effect of capacitor through transforming S-parameter which is from EM-simulation or measurement to transmission matrix (ABCD matrix). The equivalent model of capacitor is also built by this method. In order to validate the method, we measure the different size of capacitor sample. Due to measurement result and the proposed method, not only the characteristic of capacitor is analyzed but also the stability of process is observed.

Keywords Transmission matrix · S-parameter · Capacitor

31.1 Introduction

Recently, as the developing of electronic products to high operating frequency and versatility, products are lessened gradually. Because size of them are minified, passive devices have to be integrated. For this reason, integrated passive device (IPD) is advanced. Therefore, designing a passive device which is high accuracy and small size is significant.

Usually, in order to extract the accurate value of capacitor or inductor, formula of impedance is used to calculate value of them. However, the conventional

Y.-Y. Wu (✉) · S.-M. Wu · L.-S. Hung
Department of Electrical Engineering, National University of Kaohsiung, Kaohsiung, Taiwan Republic of China
e-mail: pc9160906@hotmail.com

C.-F. Yang
Department of Chemical and Materials Engineering, National University of Kaohsiung, Kaohsiung, Taiwan Republic of China

Y. M. Cheng · C.-L. Chen
Metal Industries Research Development Center, Kaohsiung, Taiwan Republic of China

J. Juang et al. (eds.), *Proceedings of the 2nd International Conference on Intelligent Technologies and Engineering Systems (ICITES2013)*, Lecture Notes in Electrical Engineering 293,
DOI: 10.1007/978-3-319-04573-3_31,

formula, Z-parameter, is suited for one-port measurement. For two-port measurement, transmission matrix (ABCD matrix) is more appropriate than the convention for extracting value. Another reason for using transmission matrix is that it can ignore many effects like end-effect.

In this paper, the capacitor is a sample to verify the method proposed in this paper. The stack-up of capacitors is silicon substrate and Aluminum plates. Besides, the size of capacitors is changed for analyzing and comparing. Though measuring different the size of capacitors, resonate of them is estimated preliminarily. Furthermore, by transforming transmission matrix from measurement S-parameter, each characteristic of capacitors can be compared and analyzed obviously [1, 2].

31.2 Theorem

From the S-parameter of EM-simulation or measurement, the characteristic of capacitor can be analyzed. However, the dielectric loss and resonate effect of it are not obviously observed by S-parameter. So, a method is proposed in this paper to easily solve these problems.

The structure of capacitor fabricated in this paper is showed in Fig. 31.1a. The equivalent model can be determined from this structure and showed in Fig. 31.1b. Moreover, a reciprocal two-port network which is composed of a series impedance Z is depended on this equivalent model. The transmission matrix can be let A = D = 1, B = Z, C = 0 [3]. With a reciprocal network, the transmission matrix can be built through Eq. (31.1). Because the S-parameter is known by EM-simulation or measurement, Eqs. (31.2) and (31.3) are also built through conversion between S-parameter and transmission matrix.

$$\begin{bmatrix} A & B \\ C & D \end{bmatrix} = \begin{bmatrix} 1 & Z \\ 0 & 1 \end{bmatrix} \tag{31.1}$$

$$S_{11} = \frac{A + {}^{B}/_{Z_0} - CZ_0 - D}{A + {}^{B}/_{Z_0} - CZ_0 + D} = \frac{{}^{Z}/_{Z_0}}{2 + {}^{Z}/_{Z_0}} \tag{31.2}$$

$$S_{21} = \frac{2}{A + {}^{B}/_{Z_0} + CZ_0 + D} = \frac{2}{2 + {}^{Z}/_{Z_0}} \tag{31.3}$$

Because the S-parameter consists of magnitude and phase, S_{11} and S_{21} can be regarded as real and imaginary part. Impedance Z also has real part R and imaginary part X. Furthermore, Eqs. (31.4) and (31.5) are derived by dividing Eqs. (31.2) and (31.3). According to derived R and X, the dielectric loss and resonance effect can be observed easily and extracted an equivalent model.

$$\mathrm{R} = 2Z_o \frac{Re[S_{11}] \times Re[S_{21}] + Im[S_{11}] \times Im[S_{21}]}{Re[S_{21}]^2 + Im[S_{21}]^2} \tag{31.4}$$

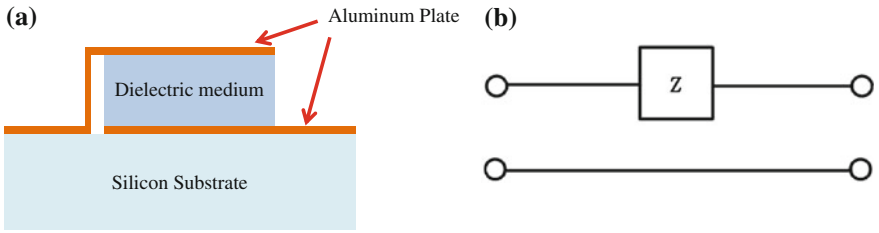

Fig. 31.1 **a** The structure of capacitor in this paper. **b** The equivalent model of capacitor

$$X = 2Z_o \frac{-Re[S_{11}] \times Im[S_{21}] + Im[S_{11}] \times Re[S_{21}]}{Re[S_{21}]^2 + Im[S_{21}]^2} \tag{31.5}$$

The RLC model is simulated by Agilent ADS to verify the proposed equations. The model and its frequency response show in Fig. 31.2. The value of capacitor is 1 pF, inductor is 4 nH and resistor is 50 ohm. Furthermore, the S-parameter of simulation is substituted into the Eqs. (31.3) and (31.4) and then the result shows in Fig. 31.3. From Fig. 31.3, the real part is value of resistor and the imaginary part is impedance of inductor and capacitor. The resonance frequency is also observed when the impedance is zero in the RLC series. Moreover, the resonance frequency is matched the S-parameter. Therefore, Eqs. (31.3) and (31.4) is useful to analyze the loss and resonance frequency in the two-port network.

31.3 Measurement Result

The proposed capacitors are fabricated in different lengths showed in Fig. 31.4. The capacitors are with different length: 2000, 1000, 500, and 250 um for measuring. The S-parameter of them is measured by Agilent 5071C vector network analyzer. The S-parameters of real and imaginary part of measurement results show in the Figs. 31.5 and 31.6.

Furthermore, through the measurement result, the real and imaginary part of capacitors are calculated by using the Eqs. (31.4)–(31.5) and the calculating result are showed in Figs. 31.7 and 31.8. From Fig. 31.7, the loss of capacitors can be observed obviously by the value of real part. The wider the length of capacitors is changed to, the larger the loss of them is become. Moreover, as the length of them is change to, long, not only the loss of them is large but also resonate is moved to low frequency. Furthermore, the value of capacitors can be calculated by the Eq. (31.6). The value of capacitor is calculated by imaginary part which is Eq. (31.5). The characteristic of capacitor or inductor isn't evident in the capacitors fabricated in this paper at the S-parameter, so the characteristic of them can be easily determined by observing imaginary part.

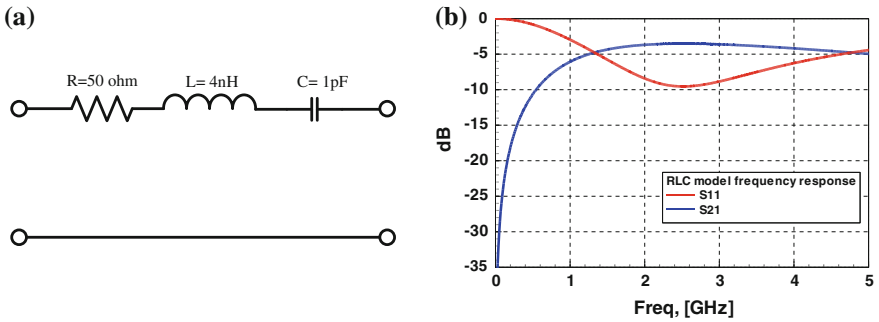

Fig. 31.2 **a** The RLC model and value. **b** The frequency response of RLC model

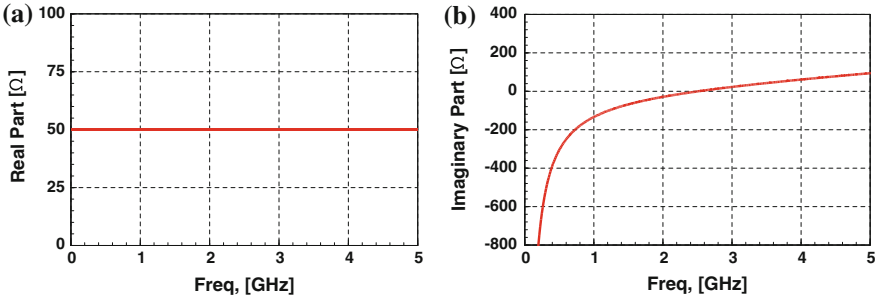

Fig. 31.3 **a** Real part of RLC model. **b** Imaginary part of RLC model

Fig. 31.4 The capacitors which are fabricated in this paper are with different length for measuring

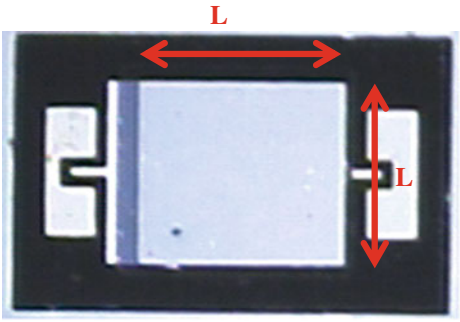

$$C = \frac{1}{\omega \times imag(Z)} \tag{31.6}$$

The Eq. (31.7) is the traditional formula of capacitor and propoed method is verified by it. Table 31.1 and Fig. 31.8 show the value of capacitors which is calculated by Eq. (31.6) and by Eq. (31.7). From Table 31.1, the error is between

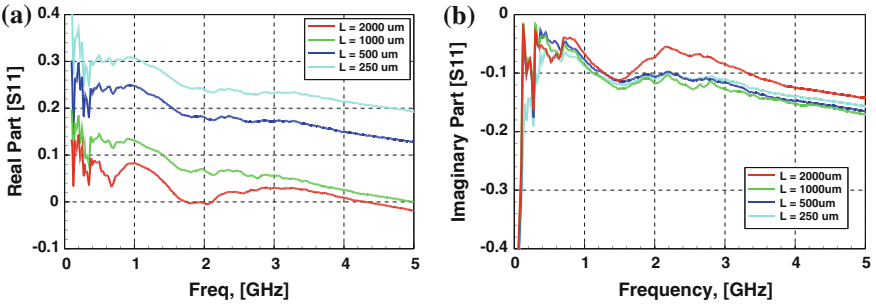

Fig. 31.5 The measurement of capacitors **a** Real part of S11, **b** Imaginary part of S11

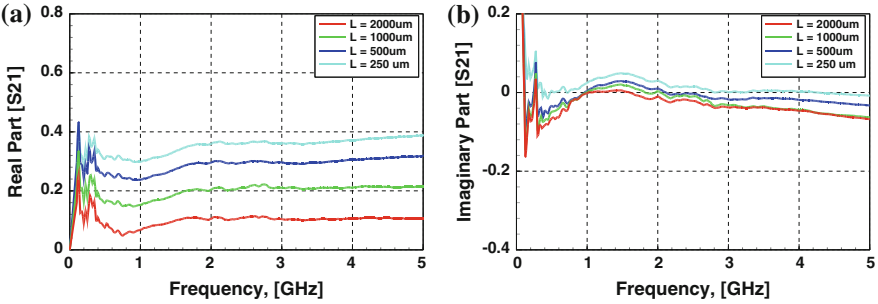

Fig. 31.6 The measurement result of capacitors **a** Real part of S21, **b** Imaginary part of S21

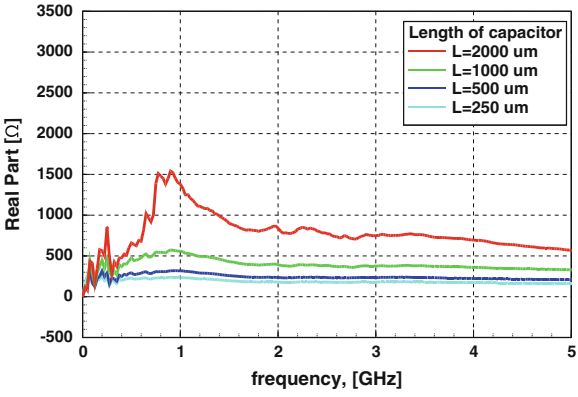

Fig. 31.7 The real part of measurement result with different length of capacitors are calculated by Eqs. (31.4)–(31.5)

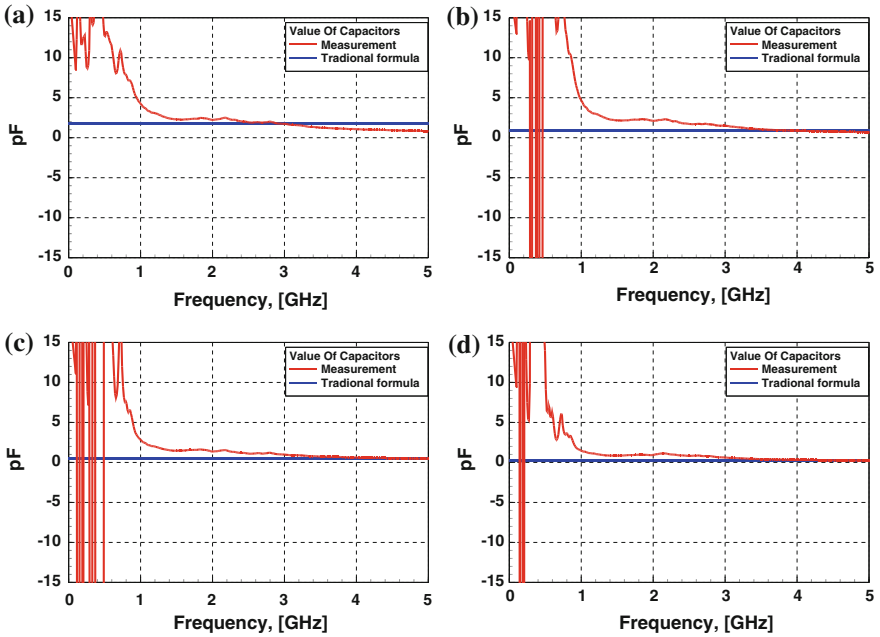

Fig. 31.8 Comparing value calculation of capacitors between measurement and tranditional formula **a** L = 2000 um, **b** L = 1000 um, **c** L = 500 um, **d** L = 250 um

Table 31.1 The value of capacitors is calculated by Eqs. (31.4)–(31.5) and by Eq. (31.6) with different frequency

By Eq. (31.6)				
Frequency (GHz)	L = 2000 um (pF)	L = 1000 um (pF)	L = 500 um (pF)	L = 250 um (pF)
2	2.223	2.104	1.364	0.953
3	1.742	1.494	0.991	0.682
4	1.070	0.881	0.613	0.326
5	0.823	0.673	0.453	0.239
By Eq. (31.7)				
	1.760	0.880	0.440	0.220

measurement result and traditional formula. When the value of capacitors is calculated by Eq. (31.6), inductance effect isn't ignored. Therefore, the value of them is composed of inductance effect which is result in inexact value.

$$C = \varepsilon_0 \varepsilon_r \frac{A}{d} \tag{31.7}$$

31.4 Conclusion

A method extracted the analyzing the dielectric loss and resonance effect of a two-port device is proposed. In this paper, the capacitor is a sample to be observed characteristic. However, without directly observing S-parameter, transforming from it to transmission matrix is the way to determine the characteristic of capacitors. Therefore, by the proposed equations in this paper, not only the characteristic of capacitors can be captured but also stability of process is verified.

Acknowledgments The authors acknowledge financial supports of NSC 102-2622-E-390 -002 -CC3 and Metal Industries Research Development Center.

References

1. Chen, K. Y., Brown, W. D., Schaper, L. W., Ang, S. S., & Naseem, H. A. (2000). A study of the high frequency performance of thin film capacitors for electronic packaging. *IEEE Transactions on Advanced Packaging, 23*(2), 293–302.
2. Shutzberg, B. A., Huang, C., Ramesh, S., Giannelis, E. P. (2000). Integral thin film capacitors: Materials, performance and modeling. *Proceedings of the 50th Electronic Components and Technology Conference, 2000* (pp. 1564–1567).
3. Pozar, D. M. (2005). *Microwave engineering 3rd ed*. Norwood: Wiley, pp. 183–187.

Chapter 32
Stability Control for Two-Wheeled Mobile Robot Using Robust Pole-Placement Method

Yoko Amano

Abstract In order to guarantee a robotic stability, a robust pole-placement method is proposed in this paper, the proposed method combines a linear quadratic regulator (LQR) into the pole-placement design. Firstly, a mathematical model of Two-Wheeled Mobile Robot (TWMR) is analytically derived from the real TWMR. Secondly, the LQR for the TWMR's model is designed, and optimal poles can be obtained from the designed LQR. Thirdly, according to the following conditions in selecting best poles: (1) a convergence speed, (2) vibration times, (3) saturation evasion of control inputs to TWMR's actuators, (4) the ratio of an imaginary part and a real part are carried out near one of selected poles. Ultimately, the robotic stability of the proposed method with the best poles is confirmed by experiment results.

Keywords Robotic stability · Inverted two-wheeled mobile robot · Robust control · Pole-placement method · Linear quadratic regulator

32.1 Introduction

A two-wheeled mobile robot (TWMR) shown in Fig. 32.1 always exhibits many problems existing in industrial applications, for example, various nonlinear behaviors under different operation conditions, external disturbances and physical constraints on some variables. Thus, the task of on-line real time control for the high nonlinear unstable inverted TWMR has been a challenge for the modern control field. It is difficult to produce a suitable control system that realizes on-line

Y. Amano (✉)
Graduate School of Electrical and Electronics Engineering, Department of Electronics and Electrical Engineering, Nihon University, Tokyo 963-8642, Japan
e-mail: amano@ee.ce.nihon-u.ac.jp

J. Juang et al. (eds.), *Proceedings of the 2nd International Conference on Intelligent Technologies and Engineering Systems (ICITES2013)*, Lecture Notes in Electrical Engineering 293,
DOI: 10.1007/978-3-319-04573-3_32,

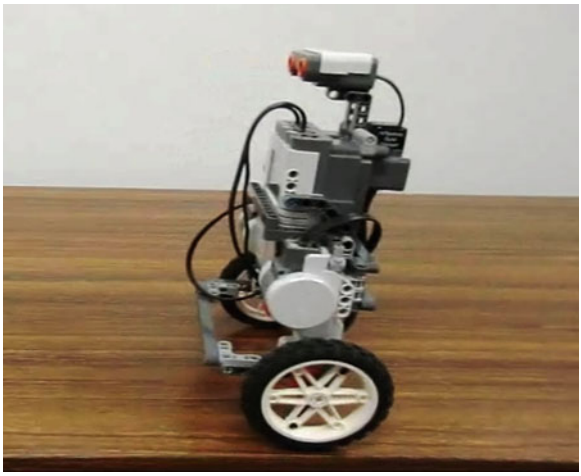

Fig. 32.1 Inverted two-wheeled mobile robot

real time control and accurate balancing control at all time for the inverted TWMR.

On the other hand, many research results of the TWMR have been applied to various real problems for designing walking gaits of humanoid robots, robotic wheelchairs, personal transport systems, and so on. Recently, control problems of the TWMR have been intensively studied due to the challenging demands of fast and precise operation.

Besides protecting the safety of humans and robotic operators, the robotic stability is very important research topic at the longest. There have been many studies on the robotic stability problem, for example, Integrated modeling and analysis [1], sliding-model control [2], fuzzy switched swing-up control [2], and adaptive control are explored on the TWMR. But, these control systems are very complex and slow response times for on-line real time control to the TWMR.

In order to guarantee a robotic stability, a robust pole-placement method is proposed in this paper, the proposed method combines a linear quadratic regulator (LQR) into the pole-placement design. Firstly, a mathematical model of the TWMR is analytically derived from the real TWMR. Secondly, a LQR for the TWMR's model is designed, and optimal poles can be obtained from the designed LQR. Thirdly, according to the following conditions in selecting best poles: (1) a convergence speed, (2) vibration times, (3) saturation evasion of control inputs to the TWMR's actuators, (4) the ratio of an imaginary part and a real part are carried out near one of selected poles. Ultimately, the robotic stability of the proposed method with the best poles by the LQR is confirmed by experiment results.

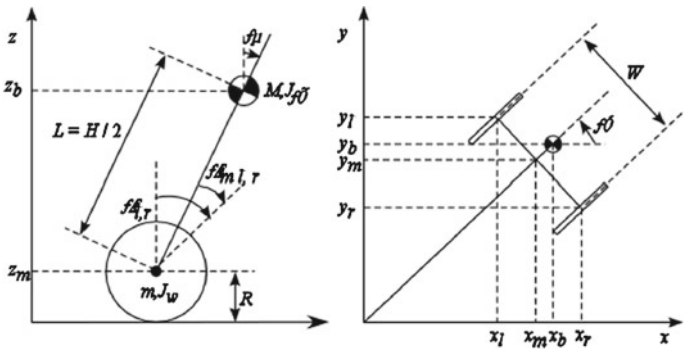

Fig. 32.2 Side and plane view of TWMR. Ψ: body pith angle, $\theta_{l,r}$: left and right wheel angles, $\theta_{m_{l,r}}$: DC motor angles

32.2 TWMR's Model

Figure 32.2 shows a side and a plane view of the TWMR, a coordinate system of Fig. 32.2 has used the TWMR model, and physical parameters by measurements are shown in [3].

Motion equations from the TWMR are driven by the Lagrangian method based on the coordinate system, the generalized forces, F_Ψ, F_ϕ can be expressed and make use of motor voltages v_l and v_r of the left and right DC motors in the TWMR.

$$F_\theta = \left[(2m + M)R^2 + 2J_m + 2n^2 J_m\right]\ddot{\theta} + (MLR - 2n^2 J_m)\ddot{\psi} \tag{32.1}$$

$$F_\psi = (MLR - 2n^2 J_m)\ddot{\theta} + (ML^2 + J_\psi + 2n^2 J_m)\ddot{\psi} - MgL\psi \tag{32.2}$$

$$F_\phi = \left[\frac{1}{2}mW^2 + \frac{W^2}{2R^2}(J_w + n^2 J_m)\right]\ddot{\phi} \tag{32.3}$$

here, θ, ψ and ϕ are the wheel mean rotation angle, the body grade angle and the body plane angle of the TWMR, respectively; consider the limit $\psi \to 0$, and neglect the second order term like ψ^2.

32.2.1 State Space Model

Now, from (32.1) to (32.3), the following state space model of the TWMR can be obtained.

$$\dot{x}_1(t) = A_1 x_1(t) + B_1 u(t) \tag{32.4}$$

$$y_1(t) = C_1 x_1(t) \tag{32.5}$$

where, the state variable $x_1(t) = [\theta, \psi, \dot{\theta}, \dot{\psi}]^T$, the input $u(t) = [v_r, v_l]^T$, and the output $y_1(t) = [\theta, \psi, \dot{\theta}, \dot{\psi}]^T$, the parameter matrices of the state space model (32.4), (32.5) can be described as the following.

$$A_1 = \begin{bmatrix} 0 & 0 & 1 & 0 \\ 0 & 0 & 0 & 1 \\ 0 & A_1(3,2) & A_1(3,3) & A_1(3,4) \\ 0 & A_1(4,2) & A_1(4,3) & A_1(4,4) \end{bmatrix}, \quad B_1 = \begin{bmatrix} 0 & 0 \\ 0 & 0 \\ B_1(3,1) & B_1(3,2) \\ B_1(4,1) & B_1(4,2) \end{bmatrix},$$

$$C_1 = \mathrm{diag}[\,1 \quad 1 \quad 1 \quad 1\,], \quad E = \begin{bmatrix} E(1,1) & E(1,2) \\ E(2,1) & E(2,2) \end{bmatrix},$$

$$A_1(3,2) = -\frac{gMLE(1,2)}{\det(E)}, \quad A_1(3,3) = -\frac{2[(\beta + f_\omega)E(2,2) + \beta E(1,2)]}{\det(E)},$$

$$A_1(3,4) = \frac{2[(\beta + f_\omega)E(1,2) + \beta E(1,1)]}{\det(E)}, \quad A_1(4,2) = \frac{gMLE(1,1)}{\det(E)},$$

$$A_1(4,3) = \frac{2\beta[E(2,2) + E(1,2)]}{\det(E)}, \quad A_1(4,4) = -\frac{2\beta[E(1,1) + E(1,2)]}{\det(E)},$$

$$B_1(3,1) = \frac{\alpha[E(2,2) + E(1,2)]}{\det(E)}, \quad B_1(4,1) = -\frac{\alpha[E(1,1) + E(1,2)]}{\det(E)},$$

$$\det(E) = E(1,1)E(2,2) - E(1,2)E(2,1),$$

$$E(1,1) = (2m + M)R^2 + 2J_\omega + 2n^2 J_m, \quad E(1,2) = MLR - 2n^2 J_m,$$

$$E(2,1) = MLR - 2n^2 J_m, \quad E(2,2) = ML^2 + J_\psi + 2n^2 J_m,$$

$$B_1(3,1) = B_1(3,2), \quad B_1(4,1) = B_1(4,2), \quad \alpha = \frac{nK_t}{R_m}, \quad \beta = \frac{nK_t K_b}{R_m} + f_m.$$

32.2.2 LQR Design for TWMR

In this section, the LQR design for the TWMR is considered as an expansive state space equation, the θ as a reference state $\theta_{ref} = C_\theta x_{1ref}$, and define an error $e(t) = C_\theta x_{1ref} - \theta(t)$,$\dot{z}(t) = e(t)$, then the expansive state space equation can be expressed by

$$\dot{\bar{x}}(t) = \bar{A}\bar{x}(t) + \bar{B}\bar{u}(t) \tag{32.6}$$

$$\dot{\bar{x}}(t) = \begin{bmatrix} \dot{x}(t) \\ \dot{z}(t) \end{bmatrix}, \quad \bar{A} = \begin{bmatrix} A_1 & 0 \\ 0 & C_\theta \end{bmatrix}, \quad \bar{B} = \begin{bmatrix} B_1 & 0 \\ 0 & -C_\theta \end{bmatrix}, \quad \bar{u}(t) = \begin{bmatrix} u(t) \\ x_1(t) \end{bmatrix}.$$

According to an optimal feedback gain matrix K such that the feedback control law as given below

$$\overline{u^*}(t) = -K\bar{x}(t), \quad \overline{u^*}(t) = [-k_f \quad -k_i]\begin{bmatrix}\dot{x}(t)\\ \dot{z}(t)\end{bmatrix}, \quad K = R^{-1}\bar{B}^T P \tag{32.7}$$

here, the matrix P of (32.7) is the unique positive-definite solution of the following associated matrix Riccati Equation

$$\bar{A}^T P + P\bar{A} + Q - P\bar{B}R^{-1}\bar{B}^T P = 0 \tag{32.8}$$

As stated above, a servo control for the TWMR is shown in Fig. 32.3, where $C_\theta = \text{diag}[1, \ 0, \ 0, \ 0]$, and the weight matrices Q, R of (32.8) by experimental trial and error can be expressed as

$$Q = \text{diag}[1, \ 6 \times 10^5, \ 1, \ 1, \ 4 \times 10^2], \quad R = \text{diag}[1 \times 10^3, \ 1 \times 10^3]$$

Then, the LQR problem is solved, and obtained the gain K is the following

$$K = [k_\theta, \ k_\psi, \ k_{\dot{\theta}}, \ k_{\dot{\psi}}, \ k_i]. \tag{32.9}$$

32.3 Proposed Method

A design of the proposed method called a robust combined pole-placement method is presented in this section; assuming that all state variables are measurable and available for the closed-loop system shown in Fig. 32.3. If the system is completely state controllable, then poles of the closed-loop system may be placed at any desired locations by means of state feedback through an appropriate state feedback gain matrix.

The design begins with determination of desired closed-loop poles based on the requirements of the transient and frequency response, such as speed, damping ratio, and bandwidth, as well as steady-state requirements.

32.3.1 Pole-Placement for TWMR

From the expansive state space Eq. (32.6) and the optimal control input (32.7), the closed-loop system can be expressed as

$$\dot{\bar{x}}(t) = \bar{A}\,\bar{x}(t) - \bar{B}K\,\bar{x}(t) = (\,\bar{A} - \bar{B}K)\bar{x}(t) \tag{32.10}$$

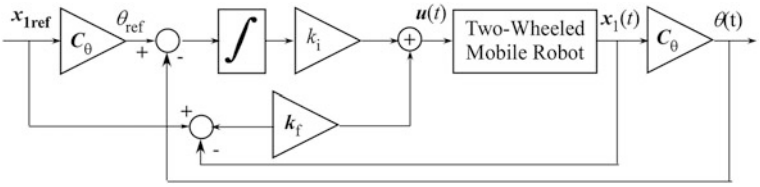

Fig. 32.3 Servo control system block diagram for TWMR

The desired characteristic equation is

$$\begin{aligned} |sI - \bar{A} + \bar{B}K| &= (s - p_1)(s - p_2)\cdots(s - p_n) \\ &= s^n + a_{n-1}s^{n-1} + \cdots + a_0 = 0 \end{aligned} \tag{32.11}$$

where, p_i (i = 1,2,…,n) are poles of the closed-loop system (32.11). The first step in the pole-placement design approach is to choose the locations of the desired closed-loop poles. The most frequently used approach is to choose such poles on the basis of experience in root-locus analysis, placing a dominant pair of closed-loop poles and choosing other poles so that is farther to the left of the dominant closed-loop poles.

It have to note that if the dominant closed-loop poles are farther from the $j\omega$-axis, so that the system's response becomes very fast, the signals in the system become very large shown in Fig. 32.4, the system will become nonlinear and should be avoided.

Another approach is based on LQR and determines the desired closed-loop poles such that the system balance between the acceptable response and the amount of control energy require.

In the complex coordinate of Fig. 32.4, an angle $\delta = tan^{-1}(\sqrt{1-\zeta^2}/\zeta)$, here ζ is a damping ratio. For a servo control system of robotics, the TWMR and so on, ζ = 0.6–0.8 and δ = 37°–53° have been generally accepted.

32.3.2 Choosing Location of Desired Closed-Loop Poles

From K of (32.9), the pole p_0 can be derived from the designed LQR, and shows the following

$$P_0 = [-284.41,\ -10.92,\ -1.3 \pm j0.73,\ -1.47] \tag{32.12}$$

Because it is with a guidance of the pole placement that the result is better than the pole p_0 about responsiveness and stability is provided, the damping ratio ζ at 0.87 is maintained and a value of the natural frequency ω_n is given. When changing real part of conjugate complex number of the pole p_0 by 0.2 at the same time, keeping the damping rate ζ at 0.87, and obtaining poles p_i (i = 6,…,8), their

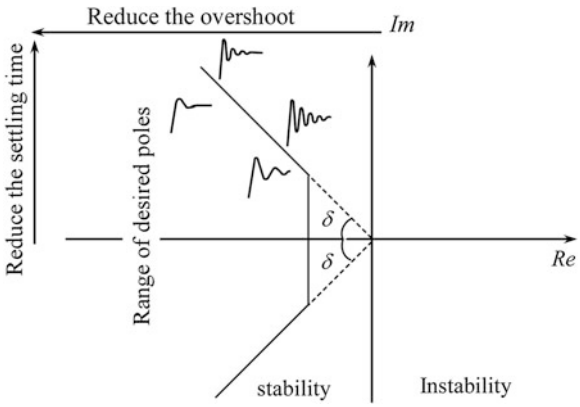

Fig. 32.4 Range of desired poles

feedback gains, the ζ and ω_n are shown in Tables 32.1, 32.2 and 32.3, respectively. Figure 32.5 shows unit step responses of the closed-loop with P_i.

On the same method, the ζ is kept, and change the real number of the conjugate number $-1.3 \pm j0.73$ with 0.2 steps in negative direction. The good pole can be obtained as the pole $P_6 = [-284.4, \ -10.9, \ -1.5 \pm \text{j}0.84, \ -1.47]$ with gain margin 5.0 [dB], resonant peak -10.1 [dB], setting time 4.79 (sec.), overshoot -0.41, and $\zeta = 0.87$, $\omega_n = 1.72$ (rad/sec.).

32.4 Experimental Results

A real TWMR is established practice to illustrate the effectiveness of the proposed method. Using the same parameters, real stable position experiment is implemented to verify the feasibility of the proposed method with the pole p_6 and the LQR method with p_0, respectively.

Figure 32.5 presents responses of the wheel mean rotation angle for a unit step with $P_i$which tests the stability of the TWMR, a small shaking of the body angle with the pole P_6 than the pole P_0. Figure 32.6 shows body angles at an appointed position in a state of rest, and a small position error using the proposed method with the pole P_6 than the LQR with pole p_0. Figure 32.7 indicates moving distances of the TWMR at the appointed position, and a large distance error using the LQR is produced, but, the proposed method generates very small moving distance from the appointed position than the LQR method.

Table 32.1 Closed-loop poles

	p_1	p_2	p_3, p_4	p_5
P_0	−284.41	−10.9	$-1.3 \pm j0.73$	−1.47
P_6	−284.41	−10.9	$-1.5 \pm j0.84$	−1.47
P_7	−284.41	−10.9	$-1.7 \pm j0.96$	−1.47
P_8	−284.41	−10.9	$-1.9 \pm j1.07$	−1.47

Table 32.2 Feedback gains

	k_θ	k_ψ	$k_{\dot{\theta}}$	$k_{\dot{\psi}}$	k_i
P_0	−0.867	−31.931	−1.154	−2.784	−0.447
P_6	−1.061	−33.120	−1.228	−2.797	−0.524
P_7	−1.274	−34.349	−1.304	−3.099	−0.764
P_8	−1.501	−35.608	−1.381	−3.262	−0.953

Table 32.3 Damping ratio and Natural frequency

	Damping ratio ζ	Natural frequency ω_n (rad/s)
P_0	0.87	1.49
P_6	0.87	1.72
P_7	0.87	1.95
P_8	0.87	2.18
P_9	0.87	2.40
P_{10}	0.87	2.64

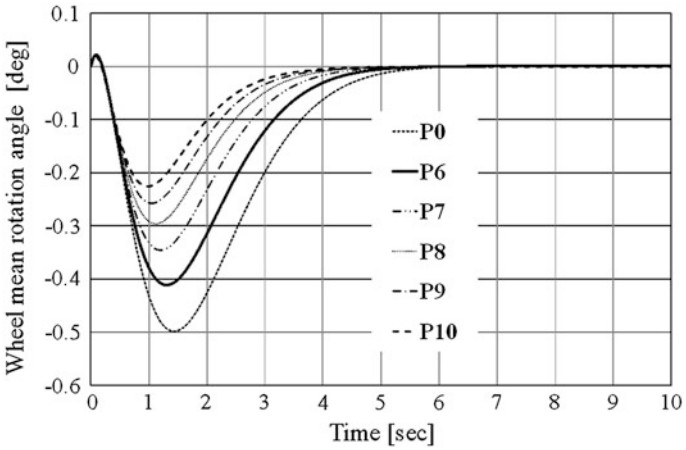

Fig. 32.5 Unit step responses with P_i

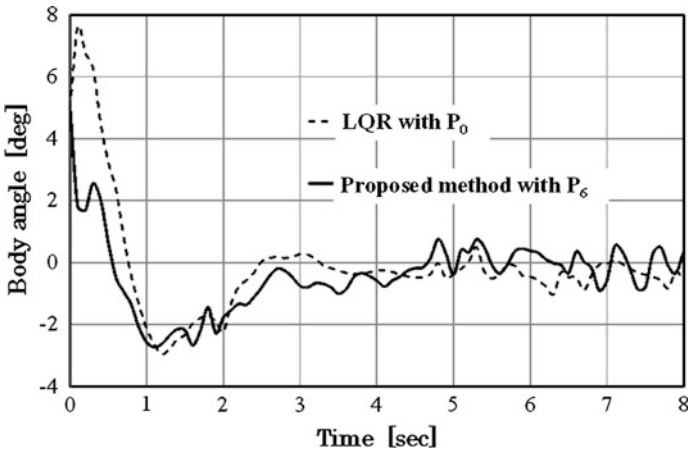

Fig. 32.6 Experimental results of body angles

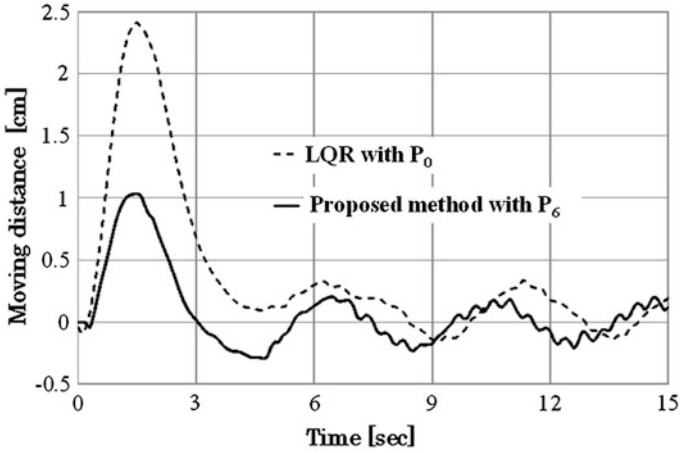

Fig. 32.7 Experimental results of shifting distance, experimental results of body angle

32.5 Conclusion

In this paper, the robust pole-placement method has been newly proposed to control the TWMR achieving the desired control behaviors. The experiment of stable position control was executed using the proposed method and the LQR method; experimental results have verified that the proposed method is effective for the real TWMR's stability than the LQR method. The proposed method will be used to new applications.

References

1. Rahman, M., Ahmad, S., & Akmeliawati, R. (2013). *Integrated modeling and analysis of an extendable double-link two-wheeled mobile robot*. *Advanced Intelligent Mechatronics (AIM), 2013 IEEE/ASME International Conference on Date of Conference*, doi:10.1109/AIM.2013.6584358
2. Huang, J., Guan, Z.-H., Matsuno, T., Fukuda, T., & Sekiyama, K. (2011). Sliding-model velocity control of mobile-wheeled inverted-pendulum system. *IEEE Transactions on Robotics, 26*(4), 750–758.
3. Huang, C.-H., Wang, W.-J., & Chiu, C.-H. (2011). Design and implementation of fuzzy control on a two-wheel inverted pendulum. *IEEE Transactions on Industrial Electronics, 58*(7), 2988–3001.

Chapter 33
Transconductance Enhancement Dependence on the Channel Length of CESL-Strained nMOSFETs

Wen-Teng Chang and Pin-Hung Kuo

Abstract Stress is distributed unequally along channels by both uniaxial and biaxial stressors. This study investigated channel-length-related performance enhancement by using contact etching stop layer (CESL) as the stressor. Devices with low tensile (L.T.) and high tensile (H.T.) stresses use CESLs with different thicknesses on nMOSFETs. Results indicate that transconductance enhances the shortest channel in H.T. devices compared with L.T. devices. The threshold voltage difference between L.T. and H.T. nMOSFETs verifies the high stress in H.T. nMOSFETs. However, this threshold voltage difference cannot verify the considerable decrease in the threshold voltage of the shortest channel of H.T. devices compared with L.T. devices.

Keywords Contact etch stop layer (CESL) · Transconductance · Threshold voltage · Channel length

33.1 Introduction

Strain engineering is widely used in enhancing carrier mobility [1–8]. Various strained approaches have been developed by fabrication, lattice mismatch, or packaging. However, strains vary along channel lengths [9]. Studies have reported that the strains induced by uniaxial or biaxial stressors are unequally distributed along channels [1–3]. Electrical properties related to strain structures have also been reported to be channel-length dependent [4–8]. Several researchers have found that the piezoresistance coefficients of silicon channels under external stress are larger on long channels than on short channels [7], i.e., the piezoresistance

W.-T. Chang (✉) · P.-H. Kuo
Department of Electrical Engineering, National University of Kaohsiung, Kaohsiung, Taiwan
e-mail: wtchang@nuk.edu.tw

J. Juang et al. (eds.), *Proceedings of the 2nd International Conference on Intelligent Technologies and Engineering Systems (ICITES2013)*, Lecture Notes in Electrical Engineering 293,
DOI: 10.1007/978-3-319-04573-3_33,

coefficients exhibit more obvious changes on long channels than on short channels. On the contrary, devices with shorter channels have higher mobility variations than devices with longer channels [10]. However, the above measurements used external stress rather than the intrinsic stress generated by the embedded structure. Contact etching stop layer (CESL), which exhibits effective mass transformation, is one of the most commonly used technologies on uniaxial stress to improve mobility performance and significantly change carrier mobility. A previous report demonstrated that uniaxial tension by CESL enhances nMOSFET [11, 12], which uses a layer of capped film that can be adjusted to tensile stress or compressive stress by plasma-enhanced chemical vapor deposition. The current study is the first to use CESL configurations rather than external stresses on various channel dimensions to evaluate the uniaxial strain that leads to different levels of performance enhancement.

33.2 Experiments

The silicon-on-insulator (SOI) wafers in this study were developed via smart-cut technology by using a 200 nm-thick buried oxide. The thickness of SOI (t_{SOI}) nMOSFETs was 90 nm. Thereafter, a 1.6 nm nitride gate oxide was developed. Arsenic and boron ion implantations were used for source and drain junctions. The 36.8 nm-thick poly-Si gate was subjected to spike annealing, and a 24 nm-thick Ni was deposited because of its low thermal budget. The capping CESL layers with low tensile (L.T.) and high tensile (H.T.) stresses by silicon nitride had thicknesses of 70 and 38 nm, respectively. The Nickel fully silicided metal gate approach was used because the work function of this approach can be adjusted by implantation doping. The contact pads of the gate, source, drain, and body were connected by manipulating probes. The devices were characterized by HP4156 semiconductor parameters. The widths of the nMOSFET channels were 9.99, 3.598, 0.898, 0.448, and 0.222 μm and their lengths were 0.135, 0.45, and 10 μm.

33.3 Results and Discussion

33.3.1 Characteristics of nMOSFETs with Low and High Tensile CESL

Figure 33.1a shows the drain current of nMOSFETs with L.T. and H.T. CESL at $V_G = 0.05$ and 2 V. The enhancement of tensile CESL enhances and degrades the <110> n-channel and p-channel in the longitudinal configuration, respectively [6]. Furthermore, the H.T. CESL improves the drive current at $V_G = 2$ V. The drain current is further enhanced at high V_G when the strained channel improves the

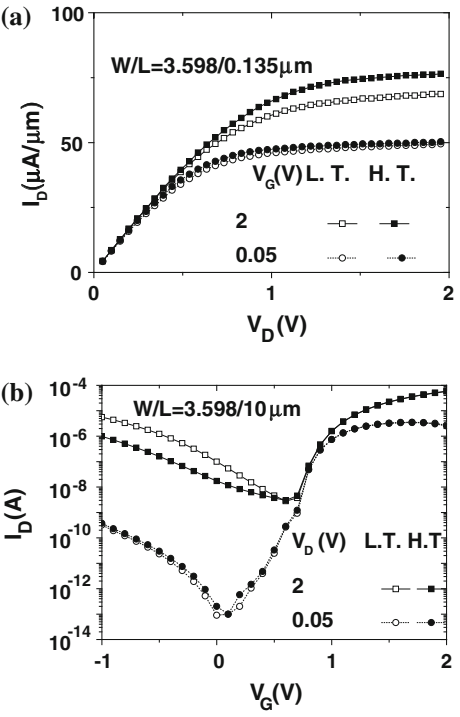

Fig. 33.1 **a** $I_D - V_D$ curves measured at $V_G = 2$ and 0.05 V and **b** $I_D - V_G$ curves measured at $V_G = 2$ and 0.05 V for CESL with L.T. and H.T. stresses on channels

carrier mobility and the gate voltage and mobility products produce the drain current. Figure 33.1b shows the $I_D - V_G$ plot at $V_D = 0.05$ and 2 V. The gate-induced drain leakage is substantially high at $V_D = 2$ V but indifferent at $V_D = 0.05$ V for nMOSFETs with L.T. and H.T. CESLs.

33.3.2 Performance Enhancement on Channel Length Dependence of CESL Strained nMOSFETs

Figure 33.2 shows the transconductance (G_m) enhancement of L.T. and H.T. CESLs with channel lengths of 0.135, 0.45, and 10 μm. The different channel lengths show that G_m is enhanced more with H.T. CESL than with L.T. CESL. The enhancement rate (*Enh.*) can be defined as the difference in G_m between H.T. and L.T. ($\Delta G_m = G_{m,\ H.T.} - G_{m,\ L.T.}$) over $G_{m,\ L.T.}$:

$$Enh. = \frac{G_{m,H.T.} - G_{m,L.T.}}{G_{m,L.T.}} \tag{33.1}$$

Enhancement rate differs with different channel lengths. Table 33.1 lists the enhancement rate and threshold voltage difference for all L.T. and H.T. CESL

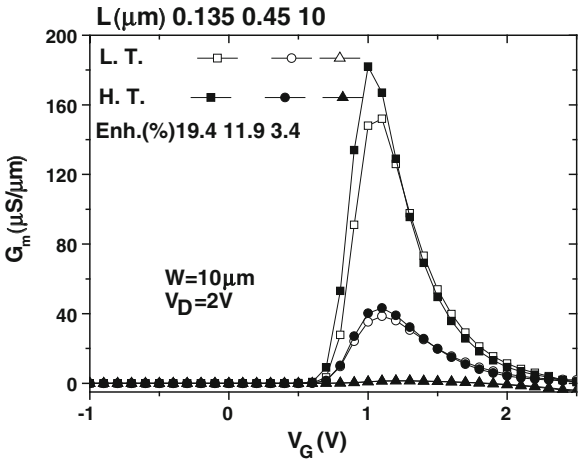

Fig. 33.2 Transconductance enhancement for L.T. and H.T. CESLs with 0.135, 0.45, and 10 μm channel lengths

Table 33.1 Transconductance enhancement rate ($\Delta Gm/Gm$) and threshold voltage difference for all measured L.T. and H.T. CESL nMOSFETs

$V_D = 2$		L.T.	H.T.	ΔVth (mV)	L.T.	H.T.	$\Delta G_m/G_m$ (%)
W	L	Vth(mV)			G_m (μS/μm)		
9.99	0.135	869	843	−26	152.2	181.8	19
	0.45	867	866	−1	38.7	43.3	12
	10	970	949	−21	1.4	1.5	3
3.598	0.135	855	855	0	138.7	201.0	45
	0.45	913	913	0	39.8	42.3	6
	10	879	876	−3	1.7	1.7	−2
0.898	0.135	859	825	−34	127.0	159.7	26
	0.45	910	906	−5	35.8	39.9	12
	10	877	877	0	1.9	1.8	−2
0.448	0.135	861	858	−3	94.0	130.0	38
	0.45	895	899	4	42.8	38.1	−11
	10	870	870	0	2.4	2.4	−2
0.222	0.135	866	840	−27	102.2	113.6	11
	0.45	861	840	−21	45.5	45.4	0
	10	860	860	0	3.2	3.2	−1

nMOSFETs with widths ranging from 9.99 μm to 0.222 μm and lengths of 0.135, 0.45, and 10 μm. The threshold voltage difference between L.T. and H.T. CESLs were compared because stress is related to this difference [4].

Figure 33.3a summarizes the transconductance enhancement rate of H.T. nMOSFETs compared with L.T. nMOSFETs with different dimensions. The trend indicates that the enhancement is related to the channel length. The shortest channel length ($L = 0.135$ μm) has the highest enhancement rate compared with short channel lengths with different channel widths. Figure 33.3b shows the threshold voltage between H.T. and L.T. nMOSFETs. The negative difference

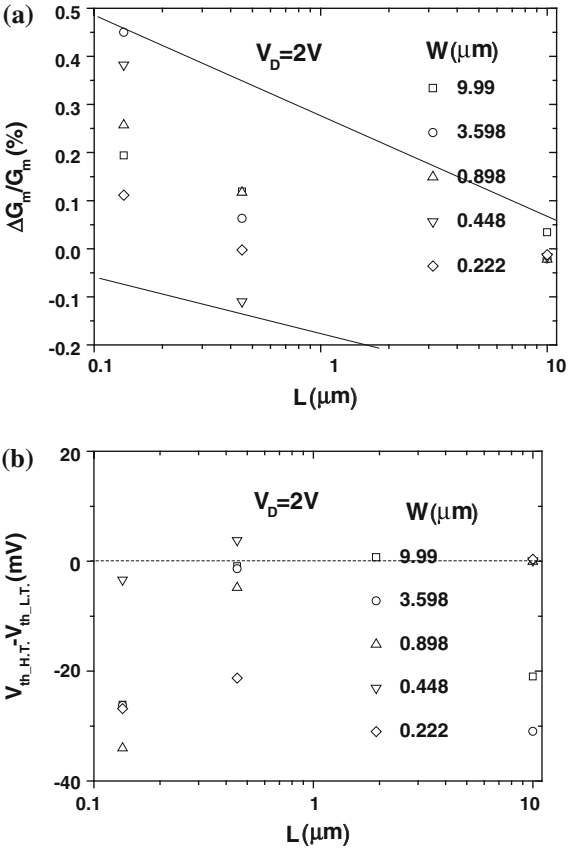

Fig. 33.3 **a** Enhanced transconductance with decreased channel lengths and different channel widths; **b** threshold voltage difference between H.T. and L.T. nMOSFETs with channel lengths of 0.135, 0.45, and 10 μm

indicates that the H.T. channel suffers higher stress (strain) than the L.T. channel. However, the threshold difference plot cannot provide sufficient evidence that the shortest channel suffers the largest stress (strain).

33.4 Conclusion

This study is the first to investigate embedded CESL configurations rather than external mechanical stress on channels to evaluate the channel-length-related uniaxial CESL stress on nMOSFETs. The CESL configurations included 70 and 38 nm H.T. and L.T. CESL films, respectively. The results indicate that transconductance enhancement by CESL configuration is more significant in devices with small channel lengths than in devices with long channel lengths. However, threshold voltage shifting provides only a slight difference on various channel lengths under the same CESL thickness. This result shows that the threshold voltage shifting is insensitive. The fringe stress of the CESL film on devices with

small channel lengths is more significant than on devices with long channel lengths because the capping thickness is prominent in short channels (i.e., 135 nm channels). According to previous literature, induced structural stress is unevenly distributed along channels, thus resulting in different levels of performance enhancement/degradation on short or long channels because of embedded or external stresses.

Acknowledgments The authors thank the National Science Council for its financial support under contract number 101-2221-E-390-001-MY2, and the staff at United Microelectronics Corporation for their informative discussions.

References

1. Irie, H., Kita, K., Kyuno, K., & Toriumi, A. (2004). In-plane mobility anisotropy and universality under uni-axial strains in NAND p-MOS inversion layers on (100), (110) and (111) Si. In IEDM Technical Digest, pp. 225–228.
2. Liu, J. P., Li, K., Pandey, S. M., Benistant, F. L., See, A., Zhou, M. S., et al. (2008). Strain relaxation in transistor channels with embedded epitaxial silicon germanium source/drain. *Applied Physics Letters, 93*, 221912.
3. Chang, W. T., Wang, C. C., Lin, J. A., & Yeh, W. K. (2010). External Stresses on Tensile and Compressive Contact Etching Stop Layer SOI MOSFETs. *IEEE Transactions on Electronics Devices, 57*, 1889–1894.
4. Lim, J. S., Thompson, S. E., & Fossum, J. G. (2004). Comparison of threshold-voltage shifts for uniaxial and biaxial tensile-stressed n-MOSFETs. *IEEE Electron Device Letters, 25*, 731–733.
5. Sugii, N., Hisamoto, D., Washio, K., Yokoyama, K. N., & Kimura, S. (2002). Performance enhancement of strained-Si MOSFETs fabricated on a chemical-mechanical-polished SiGe substrate. *IEEE Transactions on Electronics Devices, 49*, 2237–2243.
6. Rochettea, F., Casséa, M., Mouisb, M., Reimbolda, G., Blachiera, D., Lerouxa, C., et al. (2007). Experimental evidence and extraction of the electron mass variation in [110] uniaxially strained MOSFETs. *Solid-State Electronics, 51*, 1458–1465.
7. Zhao, W., He, J., Belford, R. E., Wernersson, L. E. E., & Seabaugh, A. (2004). Partially depleted SOI MOSFETs under uniaxial tensile strain. *IEEE Transactions on Electronics Devices, 51*, 317–323.
8. Yang, P., Lau, W. S., Lai, S. W., Lo, V. L., Siah, S. Y., & Chan, L. (2010). Effects of switching from ‹110› to ‹100› channel orientation and tensile stress on n-channel and p-channel metal-oxide-semiconductor transistors. *Solid-State Electronics, 54*, 461–474.
9. Hoshi, Y., Sawano, K., Yamada, A., Nagakura, S., Usami, N., Arimoto, K., et al. (2011). Line width dependence of anisotropic strain state in sige films induced by selective ion implantation. *Applied Physics Express, 4*, 095701.
10. Haugerud, B. M., Bosworth, L. A., & Belford, R. E. (2003). Mechanically induced strain enhancement of metal–oxide–semiconductor field effect transistors. *Journal of Applied Physics, 94*, 4102.
11. Komoda, T., Oishi, A., Sanuki, T., Kasai, K., Yoshimura, H., Ohno, K., et al. (2004). Mobility improvement for 45 nm node by combination of optimized stress and channel orientation design. In IEDM Technical Digest, pp. 217–220.
12. Rim, K., Hoyt, J. L., & Gibbons, J. F. (2000). Fabrication and analysis of deep submicron strained-Si n-MOSFET's. *IEEE Transactions on Electronics Devices, 47*, 1406–1415.

Chapter 34
Stability Analysis and Verification of End Milling Process

Te Ching Hsiao and Shyh Chour Huang

Abstract Chatter is a self-excited vibration during the cutting process. This condition will increase the wear and the breakage of the cutting tools; the surface roughness of the workpiece become worse, the damage of the machine tool and reduce the material removal rate (MRR). It leads to the relative increasing cost of the working time, materials, energy, etc. In order to avoid the chatter during the milling process, it is necessary to build a chatter stability lobes to forecast the chatter stability. This article focus on the most effective regenerative chatter . Using Floquet Nyquist method (FLN) and convolution milling mode to forecast the chatter stability of the milling process and then knowing the influence of milling parameter on the milling system's stability. The research shows that there is a consistency of the method in this article, Altintas Zero Order Analytical (ZOA) and Insperger Semi-discretization Method (SDM). If the radial depth of cut and diameter ratio become smaller, it will increase the stability of the milling system.

Keywords Chatter · Milling · Stability

34.1 Introduction

On some certain condition during the milling process, the cutting tools will cause violent vibration between the workpiece. This vibration can influence the surface roughness of the workpiece and furthermore it makes milling force and vibration

T. C. Hsiao (✉) · S. C. Huang
Department of Mechanical Engineering, National Kaohsiung University of Applied Sciences, Kaohsiung 80778, Taiwan, Republic of China
e-mail: hugo@cc.kuas.edu.tw

S. C. Huang
e-mail: shuang@cc.kuas.edu.tw

J. Juang et al. (eds.), *Proceedings of the 2nd International Conference on Intelligent Technologies and Engineering Systems (ICITES2013)*, Lecture Notes in Electrical Engineering 293,
DOI: 10.1007/978-3-319-04573-3_34,

quantity result in unstable oscillation and then the milling system becomes unstable. The self-excited vibration which caused by itself during the milling process calls chatter. Chatter can be divided into Regenerative Chatter, Mode Coupling Chatter and Friction Chatter, etc. Regenerative Chatter is considered the most direct and important mechanism in the cutting system. Regenerative Chatter's conception is the change of cutting thickness effect. Due to the vibration caused by the cutting tool during the cutting process, it will leave some ripple cutting grain. The previous cutting grain has phase difference with the present cutting grain. If the phase difference is not the equal of zero, the cutting thickness will change. This change will cause the undulation of cutting force and relative vibration between the cutting tool and workpiece. It will also leave chatter marks again. This kind of repetition causes chatter.

In 1958, Tobias and Fishwick [1] used linear theory to analyze the stability of cutting chatter, and brought up the idea of Stability Lobes Diagram (SLD). Merritt addressed an explanatory chart which is about the theory of the maximum of stability in 1965 [2]. This chart is called Merritt Chart and it is in connection with the cutting system. The cutting system links up with the cutting process dynamics and structure dynamics. In 1990, Smith and Tlusty [3, 4] gave the further evidence of the analysis of Stability Lobes Diagram become more important when it talks about high speed milling.

In 1993, Minis and Yanushevsky et al. [5] used Floquet's theorem to cooperate with Fourier series and Nyquist Stability Criterion. After transforming the system into limitless multi-stage frequency domain equation, directly delete the high order term, and it will show simplified system characteristic equation. Substitute the function into spindle speed and cutting depth, and it will turn out the eigenvalue of the system which is for judging the stability situation of the system. And then, it shows the stability chart of the milling system. Budak and Altintas [6–9] considered the dynamic connection between the cutters and the work pieces and improved the method which is addressed by Minis et al. They aimed at cylindrical end milling cutter and brought up Zero Order Analytical, ZOA. This method is based on average force, and use the DC component of Fourier series to show the dynamics milling factor.

In 2001, Bayky et al. [10] aimed at the single degree of freedom milling situation and brought up temporal finite element analysis (TFEA) to judge the stability of cutting process at first. In 2002, Insperger [11, 12] brought up Semi-Discretization (SD), to solve the stability problem of milling system. Later, use the calculated system situation to divert the eigenvalue of Function for judging the chattering frequency. In 2003, Wang et al. [13] combined with the convolution force mode and Minis' Fourier analytics (FLN) to lead the analysis formula of milling system stability characteristic equation. This method applies to multi-freedom, multi-chatter, and it can include the influence of the weight of dynamic milling force. Also, the effect of helix angle is clearly included in the mode. This article uses the method of [13] to discuss down and up milling processed form and the influence of helix angle to chatter stability chart.

34.2 Dynamic Milling Force Model

Wang [14] and other people find out milling force can get from tooth sequence function,chip width density function and elementary cutting function by convolution operation. The mode is as below.

$$\begin{Bmatrix} f_x \\ f_y \end{Bmatrix} = k_t[ts(\phi) * cwd(\phi) * p(\theta)] \begin{pmatrix} t_{xd} \\ t_{yd} \end{pmatrix} \tag{34.1}$$

where

$$cwd(\phi) = \begin{cases} \frac{R}{\tan\alpha} & 0 \le \phi \le \beta_a \\ 0 & otherwise \end{cases} \tag{34.2}$$

$$p(\theta) = \begin{bmatrix} 1 & k_r \\ -k_r & 1 \end{bmatrix} \begin{pmatrix} \sin\theta\cos\theta & -\cos^2\theta \\ \sin^2\theta & -\sin\theta\cos\theta \end{pmatrix} w(\theta) \tag{34.3}$$

Symbol '*' in Eq. (34.1) denotes the convolution operation. $cwd(\phi)$ is the chip width density function. Using Fourier transform can get:

$$\begin{Bmatrix} F_x \\ F_y \end{Bmatrix} = k_t TS(\omega) CWD(W) P(\omega) \begin{pmatrix} t_{xd} \\ t_{yd} \end{pmatrix} \tag{34.4}$$

where

$$TS(\omega) = N \sum_{k=-\infty}^{\infty} \delta(\omega - NK)$$

$$CWD(\omega) = \frac{2R}{\tan\alpha} \frac{\sin\frac{\omega\beta_a}{2}}{\omega} e^{-j\omega\frac{\beta_a}{2}} \tag{34.5}$$

We can indicate the milling force as the Fourier series through Fourier integration

$$\begin{aligned} \begin{Bmatrix} f_x \\ f_y \end{Bmatrix} &= \frac{1}{2\pi} \int_{-\infty}^{\infty} \begin{Bmatrix} F_x \\ F_y \end{Bmatrix} e^{j\omega\phi} d\omega \\ &= \sum_{k=-\infty}^{\infty} \begin{Bmatrix} A_{xx}[NK] & A_{xy}[NK] \\ A_{yx}[NK] & A_{yy}[NK] \end{Bmatrix} e^{jNK\phi} \end{aligned} \tag{34.6}$$

where

$$\begin{bmatrix} A_{xx}[NK] & A_{xy}[NK] \\ A_{yx}[NK] & A_{yy}[NK] \end{bmatrix} = \frac{Nk_t}{2\pi} CWD[NK] \begin{bmatrix} 1 & k_r \\ -k_r & 1 \end{bmatrix} \begin{bmatrix} P_1[NK] & P_3[NK] \\ P_2[NK] & P_4[NK] \end{bmatrix} \tag{34.7}$$

A is the process stiffness of a two-dimensional milling system. A_{xx} and A_{yy} represent the process stiffness of one-dimension milling system in X and Y direction.

34.3 Stability Analysis

According to Minis et al. [4] derivation, the characteristic equation of the milling system stable limitations can be showed like the following:

$$\det[\delta_{um} I + W_{u-m}(\lambda + jm\omega)] = 0 \tag{34.8}$$

In the equation, δ_{um} is Kronecker delta function, I is unit matrix, W_{u-m} is the $u - m$ Fourier series of the transforming function which is defined by Rozenvasser [15] for the linear periodicity system.λ is based on Floquet's theorem to solve the characteristic equation of the milling dynamics equation. If the system is stable, the characteristic equation λ must be on the left half plane of the complex number plane. Based on the definition of [15], $W_{u-m}(\lambda + jm\omega)$ can be showed like the following:

$$W_{u-m}(\lambda + jm\omega) = A_d[N(u-m)]G_m(\lambda + jm\omega) \tag{34.9}$$

where

$$G_m(\lambda + jm\omega) = (1 - e^{-\lambda T})G(\lambda + jm\omega) \tag{34.10}$$

Generally, milling force has infinite terms Fourier series, so $A_d[N(u-m)]$ also has infinite terms, because milling force has very little milling force AC component in the high frequency of harmonics. Therefore, the milling system stability characteristic equation simplified like the followings.

$$\det\begin{bmatrix} 1 + A_d[0]G_m[0] & A_d[-1]G_m[1] & A_d[1]G_m[-1] \\ A_d[1]G_m[0] & 1 + A_d[0]G_m[1] & A_d[2]G_m[-1] \\ A_d[-1]G_m[0] & A_d[-2]G_m[1] & 1 + A_d[0]G_m[-1] \end{bmatrix} = 0 \tag{34.11}$$

If using the average force to predict the stable limit value, the Eq. (34.11) can be simplified like the following.

$$\det[1 + A_d[0]G_m[0]] = 0 \tag{34.12}$$

No matter which equation is, the Eq. (34.9) or (34.11), They can be written down as the follow:

$$1 + \psi(c^*, \lambda, \omega) = 0 \tag{34.13}$$

In the equation, $\psi(c^*, \lambda, \omega)$ is Nyquist contour function, c* is the parameter for predicting. According to Nyquist criterion, it can be given the rotational speed, and then give the cutting parameter for predicting. Therefore, the Nyquist contour function will be evaluated in a series of different frequency. When the dot $(-1, 0)$ on the real axis is out of Nyquist contour curve, the system is in a stable situation. On the contrary, when the dot $(-1, 0)$ is in the Nyquist contour curve, the system is in an unstable situation. And the stable limit value of the cutting parameter is when the dot $(-1, 0)$ is exactly on the Nyquist contour curve, and the corresponding frequency is the beginning chattering frequency at this time.

Table 34.1 System parameters

Modal parameters for single DOF	$k = 2.18 \times 10^6$ N/m
	$\omega_n = 146.5$ Hz
	$\xi = 0.0032$
Cutting force coefficients	$k_t = 6.0 \times 10^8$ N/m^2
	$k_r = 0.364$
Tool parameters	$\alpha = 0$
	D = 20 mm

34.4 Simulation and Certification

The imitation case used the example of end milling which is presented in [16] to compare with the article for proving. The system Parameters and the cutting conditions is in the Table 34.1.

There is a high consistency between chatter stability lobes and the forecast from the scholar, as Fig. 34.1 shows. We can get the critical cutting depth in different rotational speed, the chatter's limit cutting depth. The area above the curve is unstable cutting area. The area below the curve is stable cutting area. Figure 34.2 is the Nyquist contour plot of milling process. We can know when the milling system is in the limit stability. Nyquist curve passed through the critical point (−1, j0) as Fig. 34.2b; When Nyquist curve surround the critical point (−1, j0), the system becomes unstable as Fig. 34.2a. On the contrary, when the curve do not surround the critical point (−1, j0), the system will keep stable as Fig. 34.2c.

34.5 Conclusion

1. Using Semi-discretization Method will emerge Hopf bifurcation and flip bifurcation's additional Lobe chart. When up milling $dr/D \leq 0.5$, flip will appear at the right side of Hopf and down milling flip will appear at the left side of Hopf.
2. For the structure which is parallel to feed direction, Lobe chart will have a tendency of going up by the decreasing of radial cutting depth and the enlarging of critical axial depth of cut; Comparing to the uninterrupted cutting of big radial cutting depth, small radial cutting depth has raised.
3. The additional Lobe chart appears in the prediction of Semi-discretization method in small radial cutting depth's stability will increase stable cutting rotational speed area in small radial cutting depth.
4. For imitating chatter stability lobes, using ZOA to imitate is the fastest and easiest. Because of not think of the influence of high harmonic of periodic function, it will effect the precision of low radial cutting depth. SDM thinks of high harmonic during the measuring process so the precision is more accurate.

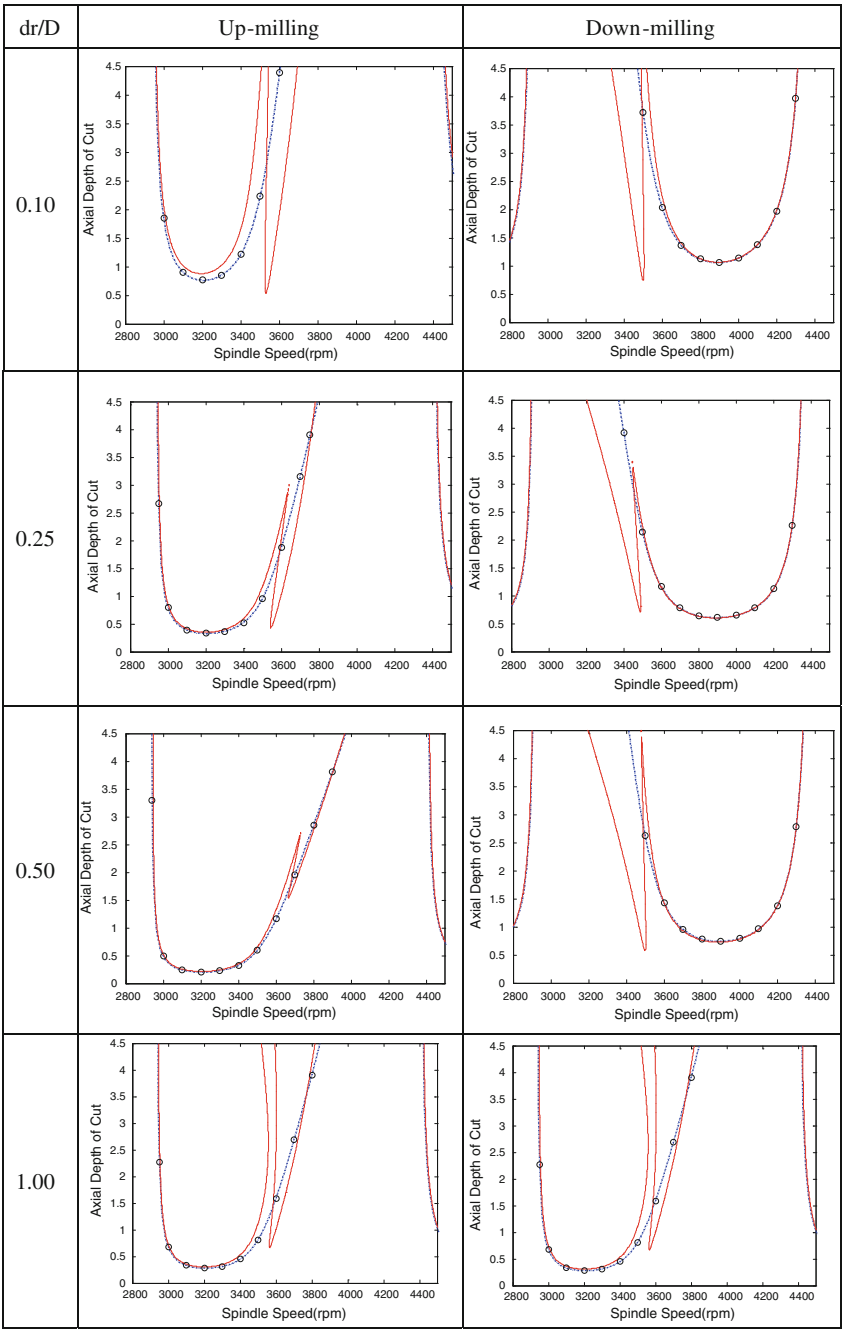

Fig. 34.1 The comparison of stability lobes for up-milling and down-milling

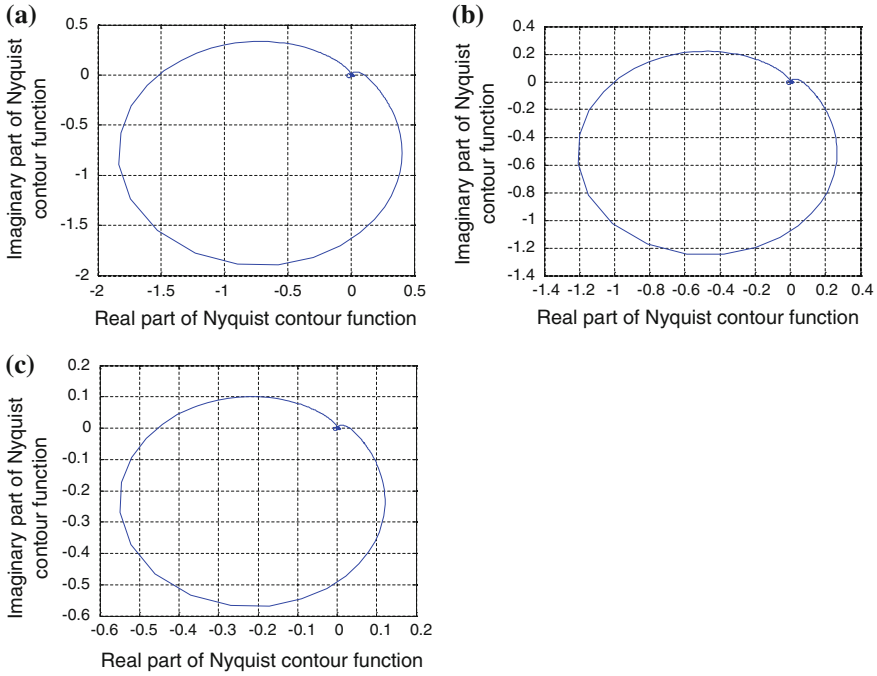

Fig. 34.2 Nyquist contour plot for **a** unstable system. **b** critical stable system. **c** stable system. Cutting parameters: **a** $\omega = 3200$ rpm, da $= 0.50$ mm; **b** $\omega = 3200$ rpm, da $= 0.33$ mm; **c** $\omega = 3200$ rpm, da $= 0.15$ mm

But the cost of time will redouble. The methods mentioned in this article can be used in multi-degree of freedom and it can contain the influence of dynamic force and helix angle. The prediction has a high precision.

References

1. Tobias, S.A., & Fishwick, W. (1958). Theory of regenerative machine tool chatter. *Engineering*, *205*, 199–203.
2. Merritt, H. E. (1965). Theory of self-excited machine tool chatter. *Journal of Engineering for Industry, 87*, 447–454.
3. Smith, S., & Tlusty, J. (1990). Update on high speed milling dynamics. *ASME Journal of Engineering for Industry, 112*, 142–149.
4. Smith, S., & Tlusty, J. (1992). Stabilizing chatter by automatic spindle speed regulation. *Annals of the CIRP, 41*(1), 433–436.
5. Minis, I., Yanushersky, R. (1993). A new theoretical approach for the prediction of machine tool chatter in milling. *Journal of Engineering for Industry*, *ll5*, l–8.
6. Altintas, Y., & Budak, E. (1995). Analytical prediction of stability lobes in milling. *Annals of the CIRP, 44*, 357–362.

7. Budak, E., & Altintas, Y. (1998a). Analytical prediction of stability lobes in milling-part i: General formulation. *ASME Journal of Engineering for Industry, 120*, 22–30.
8. Budak, E., & Altintas, Y. (1998b). Analytical prediction of chatter stability in milling-part ii: application of the general formulation to common milling systems. *ASME Journal of Dynamic Systems, Measurement, and Control, 120*, 31–36.
9. Budak, E. (2006). Analytical models for high performance milling part II: Process dynamics and stability. *International Journal of Machine Tools & Manufacture, 46*, 1489–1499.
10. Bayly, P. V., Halley, J. E., Mann, B. P. et al. (2001). Stability of interrupted cutting by temporal finite element analysis. *Proceedings of the ASME Design Engineering Technical Conference*, (vol. 6C, pp. 2361–2370).
11. Insperger, T., & Stepan, G. (2002). Semi-discretization method for delayed systems. *International Journal for Numerical Methods in Engineering, 55*, 503–518.
12. Insperger, T., & Stepan, G. (2004). Stability analysis of turning with periodic spindle speed modulation via semi-discretization. *Journal of Vibration and Control, 10*(12), 1835–1855.
13. Wang, J. J., Zheng, C. M. & Huang, C.Y. (2003). The effect of harmonic force components on regenerative stability in end milling. *ASME/IMECE*, November 15–21, Washington, D.C.
14. Wang, J. J., & Liang, S. Y. (1996). Convolution analysis of milling force pulsation. *ASME Journal of Engineering for Industry, 116*, 17–25.
15. Rozenvasser, E. N. (1972). Computation and transformation of transfer functions of linear periodic system. *Automatic and Remote Control, 33*, 220–227.
16. Bayly, P.V., Schmitz, T.L., Mann, B.P., Peters, D.A., Stepan, G., & Insperger, T. (2002). Effects of radial immersion and cutting direction on chatter instability in endmilling. *Proceedings of IMEC, ASME International Mechanical Engineering Congress & Exposition*, November 17–22, New Orleans, Louisiana.

Chapter 35
Real Option Analysis for Renewable Energy Investment Under Uncertainty

Jen-Nan Sheen

Abstract This paper is aimed to using the fuzzy real option analysis to evaluate project's economic effectiveness for highly uncertain wind power investment. The performance of the proposed model has been verified by applying the model to a simple numerical example. It is found that an appropriate options strategy allows the real option value model to reduce investment implementation costs, enhance investment performance, and facilitate an estimation of substantial benefits created by specific policies.

Keywords Decision-making · Fuzzy mathematics · Real option analysis · Mellin transform

35.1 Introduction

Prior to adopting an investment project, potential participants must explore the soundness of the project by performing a feasibility study which investigates all aspects of the project, including its anticipated future financial and economic performance. The discounted cash flow method (DCF method) is the traditional adopted methods for evaluating the value of an investment plan [1, 2]. However, its analytical framework and assumptions are based on irreversible and non-deferrable investment. DCF is thus applicable only for evaluating short-term investment projects with low uncertainties. Moreover, the DCF method cannot accurately reflect managerial flexibility in investment decisions efficiently, possibly understanding the opportunity and actual value of an investment. Importantly, DCF is limited in its inherent role in many project types, e.g., renewable energy (RE) technology [3–6].

J.-N. Sheen (✉)
Department of Electrical Engineering, Cheng Shiu University, Kaohsiung 83347, Taiwan, Republic of China
e-mail: sheenjn@csu.edu.tw

J. Juang et al. (eds.), *Proceedings of the 2nd International Conference on Intelligent Technologies and Engineering Systems (ICITES2013)*, Lecture Notes in Electrical Engineering 293,
DOI: 10.1007/978-3-319-04573-3_35,

Financial options are known from the financial world where they represent the right to buy or sell a financial value (mostly a stock) for a predetermined price (exercise price), without having the obligation to do so. Real options analysis (ROA) in option thinking is based on the same principals as financial options. ROA has its roots in the model developed for financial options by Fischer Black and Myron Scholes and later modified by Robert Merton. In real options, the options involve real assets as opposed to financial ones. To have a real option means to have the possibility for a certain period to either choose for or against something, without binding oneself up front [7].

In the case of deficient data, most decision-makers tend to rely on an expert's knowledge of financial information when carrying out their financial modeling activities. Since the nature of this knowledge often tends to be vague rather than random, Dr. Zadeh introduced fuzzy set theory, which aimed to rationalize the uncertainty caused by vagueness or imprecision. However, practical applications of fuzzy set theory in the profitability arena require two laborious tasks, namely fuzzy mathematical operations and the comparison or ranking of the resultant complex fuzzy numbers [8, 9].

The task of comparing or ranking the resultant complex fuzzy numbers can invoke a problem because fuzzy numbers do not always yield a totally ordered set in the same way that crisp numbers do [10]. The Mellin Transform [11, 12] has been proposed as a means to calculate the mean and variance values of the approximated fuzzy resulted indexes.

In order to reduce emissions, to guarantee security of energy supply, and to ensure adequacy of energy resources (so-call 3E-problems), many governments set policy targets for the exploitation of renewable energy (RE). In the valuation, we account for the special characteristics of RE sources such as wind power, and solar power. In contrast to conventional power generation, the intermittency of these power sources, notably wind power, renders generation largely incontrollable and only partly predictable. Moreover, the value of a RE project depends on a number of uncertain factors. Very importantly, the profitability of most renewable electricity investments strongly depends on public incentives, and this is our motivation for considering support scheme uncertainty.

This paper is structured as follows: Sect. 35.2 introduces the basic concepts of probabilistic real option analysis. Section 35.3 introduces fuzzy mathematic using extended principle and ranking fuzzy numbers based on the mean and variance of a fuzzy number derived by the Mellin Transform. Meanwhile, Sect. 35.4 develops fuzzy real option analysis and its application in a highly uncertain project investment. Finally, Sect. 35.5 presents the conclusions of the present study.

35.2 Probabilistic Real Option Analysis

A firm that decides to make an irreversible investment exercises an option. The lost option value is an opportunity cost that must be incorporated in the assessment of the investment cost, i.e., an essential feature in explaining the lack of consistency

between neoclassical investment theory and investment behavior. The real option rule is that one should invest today only if the net present value is high enough to compensate for giving up the value of the option to wait. Because the option to invest loses its value when the investment irreversibly made, this loss is an opportunity cost of investing. The option pricing theory of Black and Scholes (B&S) [13], Eq. (35.1) was subsequently applied to value non-financial or real investment planning and acquire real assets with learning and flexibility.

$$C_0 = S_0 N(d_1) - X e^{-rT} N(d_2). \tag{35.1}$$

$$\text{Where} \qquad d_1 = \frac{\ln(S_0/X) + (r + \sigma^2/2)T}{\sigma\sqrt{T}},\ d_2 = d_1 - \sigma\sqrt{T}. \tag{35.2}$$

And, where C_0 is the option price, S_0 is the current stock price, X is the exercise price, r is the annualized continuously compounded rate of a safe asset with the same maturity as the expiration of the option, T is the time to maturity of the option (in years) and σ is denotes the standard deviation of the annualized continuously compounded rate of return of the stock, N(d) is the probability that a random draw from a standard normal distribution will be less than d, means $N(d_1)$ denotes the proportion of shares required to replicate the call option and $N(d_2)$ is the probability that the call option will be exercised on expiry.

In 1973 Merton extended the Black-Scholes option pricing formula to dividends-paying stocks as Eq. (35.3) [14].

$$C_0 = S_0 e^{-\delta T} N(d_1) - X e^{-rT} N(d_2). \tag{35.3}$$

$$\text{Where} \qquad d_1 = \frac{\ln(S_0/X) + (r - \delta + \sigma^2/2)T}{\sigma\sqrt{T}},\ d_2 = d_1 - \sigma\sqrt{T}. \tag{35.4}$$

where δ denotes the dividends pay out during the life time of the option. Following [6], we will compute the value of a real option by Eq. (35.5).

$$ROV = S_0 e^{-\delta T} N(d_1) - X e^{-rT} N(d_2). \tag{35.5}$$

$$\text{Where} \qquad d_1 = \frac{\ln(S_0/X) + (r - \delta + \sigma^2/2)T}{\sigma\sqrt{T}},\ d_2 = d_1 - \sigma\sqrt{T}. \tag{35.6}$$

The ROV denotes the current real option value, S_0 is the present value of expected cash flows from the investment opportunity on which the option is purchased, X is the present value of all the fixed costs expected over the lifetime of the investment opportunity, *r* is the annualized continuously compounded rate of a safe asset with the same maturity as the expiration of the option. δ denotes the value that drains away over the duration of the option. Also, σ denotes the uncertainty of expected cash flows related to the asset, more precisely, the standard deviation of the growth rate of the value of future cash flows associated with it. Time to expiry T, denotes the period for which the investment opportunity is valid.

This will depend on technology (a product's life cycle), competitive advantage (intensity of competition), and contracts (patents, leases, licenses). $N(d_1)$ denotes the proportion of shares required to replicate the call option and $N(d_2)$ is the probability that the call option will be exercised on expiry.

35.3 Mathematic and Ranking of Fuzzy Numbers

A fuzzy set $\tilde{A}$, is designated as $\forall x \in X,\ \mu_A(x) \in [0, 1]$, where $\mu_A(x)$ is the grade of membership, ranging from 0 to 1, of a vague predicate, $\tilde{A}$, over the universe of objects, X. The membership function may be viewed as representing an opinion poll of human thought or as an expert's opinion. A fuzzy number is a normal and a convex fuzzy set, and its membership function can be denoted as: $\mu_A(x) = (a_1,\ f_{A_1}(\alpha)/a_2,\ a_3/f_{A_2}(\alpha),\ a_4)$, for $0 \le \alpha \le 1$. The Trapezoidal Fuzzy Number (*TrFN*) is a particular form of fuzzy number in which $f_{A_1}(\alpha)$ and $f_{A_2}(\alpha)$ are both straight-line segments, and in the case of $a_2 = a_3$, this *TrFN* becomes a Triangular Fuzzy Number (*TFN*). The *TFN* of the vague predicate $\tilde{A}$ can be expressed simply as $\tilde{A} = (a_1,\ a_2,\ a_3)$, where the vertexes a_1, a_2, a_3, denote *the smallest possible value*, *the most promising value*, and *the largest possible value* describing a fuzzy event, respectively. Of these values, the *most promising value* can be considered as the conventional (classic) crisp number. The membership function of the vague predicate $\tilde{A}$ is described by the following linear relationships:

$$\mu_A(x) = \begin{cases} \mu_{A_1}(x) = \frac{x - a_1}{a_2 - a_1}, & a_1 \le x \le a_2 \\ \mu_{A_2}(x) = \frac{a_3 - x}{a_3 - a_2}, & a_2 \le x \le a_3 \end{cases} \tag{35.7}$$

The α-cut of the fuzzy set $\tilde{A}$ is given by:

$$A_\alpha = [f_{A_1}(\alpha), f_{A_2}(\alpha)] = [a_1 + (a_2 - a_1)\alpha,\ a_3 - (a_3 - a_2)\alpha]. \tag{35.8}$$

Possibility (or confidence level) analysis is performed by using the membership function of the fuzzy number given in Eq. (35.7). At a specific membership grade or at a specific possibility α, the range of x can be calculated from the α-cut given in Eq. (35.8).

Fuzzy mathematics is based on the extended principles presented in [15–17], in which the traditional addition, subtraction, multiplication, division, power, logarithmic and exponent mathematical operations are applied to fuzzy numbers. Unfortunately, financial and engineering applications involving fuzzy sets typically require the more complex nonlinear mathematical operations such as product, division, power and logarithmic manipulations. In some cases, fuzzy operations of this type may require an insurmountable computational effort. Consequently, it has been proposed that approximated triangular fuzzy numbers be used to examine the resultant fuzzy profitability indexes [1, 18].

Many authors have investigated the use of alternative fuzzy set ranking methods, and these methods have been reviewed and compared by Chen and Hwang [10]. The Mellin Transform [11, 12] has been proposed as a mean to calculate the mean and variance values of the approximated fuzzy resulted indexes. A rigorous ranking of the fuzzy numbers can then be obtained by simply comparing the means and variances of the fuzzy numbers [9]. In an earlier study [1, 2], the current author suggested using the Mellin transform to perform the fuzzy ranking of normalized fuzzy numbers. The Mellin transforms of the *TFN* $\tilde{A} = (a_1, a_2, a_3)$ were summarized in Eq. (35.1) in [1], gives the mean and variance of the Triangular Fuzzy Number $\tilde{A} = (a_1, a_2, a_3)$ as:

$$\mu_A = M_x(2) = \frac{a_1 + a_2 + a_3}{3}. \tag{35.9}$$

$$\sigma_A^2 = \frac{1}{18}(a_1^2 + a_2^2 + a_3^2 - a_1a_2 - a_2a_3 - a_3a_1). \tag{35.10}$$

After calculates means and variances of fuzzy numbers, fuzzy numbers which share the same mean value are ranked as *Rule 1*, while the remaining fuzzy numbers are ranked using Rule 2. *Rule 1*: a fuzzy number with a lower variance is ranked above fuzzy numbers whose variances are higher. *Rule 2:* a fuzzy number with a superior mean is ranked above fuzzy numbers having inferior means.

35.4 Fuzzy Real Option Analysis

The cash flow models applied in economic decision-making problems relating to project evaluation frequently involve an element of uncertainty the expected cash flows cannot be characterized by a single number. In this paper, the triangle fuzzy numbers, *TFNs*, are presented to estimate the expected cash flows. The present value, $\tilde{S}_0$, of expected cash flows from the investment opportunity on which the option is purchased, $\tilde{X}$ is the present value of all the fixed costs expected over the lifetime of the investment opportunity, i.e. $\tilde{S}_0 = (s_1, s_2, s_3)$, $\tilde{X} = (x_1, x_2, x_3)$denoted fuzzy expected cash inflows from the investment opportunity on which the option is purchased and fuzzy present value of all the fixed costs expected over the lifetime of the investment opportunity, respectively. The fuzzy real option value presented as Eq. (35.11),

$$\mathrm{FROV} = \tilde{S}_0 e^{-\delta T} N(d_1) - \tilde{X} e^{-rT} N(d_2). \tag{35.11}$$

Where $$d_1 = \frac{\ln(E(\tilde{S}_0)/E(\tilde{X})) + (r - \delta + \sigma^2/2)T}{\sigma\sqrt{T}},\ d_2 = d_1 - \sigma\sqrt{T}. \tag{35.12}$$

And where, $E(\tilde{S}_0)$ and $E(\tilde{X})$ denoted the fuzzy mean values of expected cash inflows and expected cost, respectively. σ is the variance of the present of expected cash inflow value.

The triangle fuzzy real option value of Eq. (35.11) then can be represented as Eq. (35.13),

$$\begin{aligned} \text{FROV} &= (s_1, s_2, s_3)e^{-\delta T}N(d_1) - (x_1, x_2, x_3)e^{-rT}N(d_2) \\ &= \begin{pmatrix} (s_1 e^{-\delta T}N(d_1) - x_3 e^{-rT}N(d_2)), (s_2 e^{-\delta T}N(d_1) - x_2 e^{-rT}N(d_2)), \\ (s_3 e^{-\delta T}N(d_1) - x_1 e^{-rT}N(d_2)) \end{pmatrix} \end{aligned} \tag{35.13}$$

The value of a fuzzy real option will also be a fuzzy number, and it can be easily be shown that if the $\tilde{S}_0 = (s_1, s_2, s_3)$ and $\tilde{X} = (x_1, x_2, x_3)$ are of symmetric triangle form then ROV = E(FROV) [3].

Numerical Example: Suppose a company want to find fuzzy real option value of a new project under the following assumptions: $\tilde{S}_0 = (\$300, \$400, \$500)$ million dollar (M$), $\tilde{X} = (\$450, \$500, \$550)$ M$, and $\boldsymbol{r} = 5$ %/year, $\boldsymbol{T} = 5$ years, $\boldsymbol{\delta} = 0.03$/year.

The variance of the present of expected cash inflow value is calculated as:

$$\sigma(\tilde{S}_0) = \sqrt{\frac{1}{18}(s_1^2 + s_2^2 + s_3^2 - s_1 s_2 - s_2 s_3 - s_3 s_1)} = 173.21\,\text{M\$}, \quad \text{i.e.}\ \sigma(\tilde{S}_0) = 43.30\%,$$

$$E(\tilde{S}_0) = \frac{(300 + 400 + 500)}{3} = 400\,\text{M\$}, \text{ and } E(\tilde{X}) = \frac{(450 + 500 + 550)}{3} = \$500\ \text{M\$},$$

$d_1 = 0.357$, $d_2 = -0.611$, then $N(d_1) = 0.6498$, $N(d_2) = 0.2712$.

The fuzzy value of the real option then can be calculated by Eq. (35.13), FROV = ($51.619,$118.108,$184.191) M$, the expected value of FROV then calculated by Eq. (35.11) as $117.973 M$.

A possibility analysis can be performed by setting a specific confidence level in the fuzzy real option models in order to obtain a possible economic value range. If two specific confidence levels of 0.6, and 0.4 are selected, the possible FROV range can be calculated to be [91.512, 144.541]M$ and [78.215, 157.758]M$, respectively. It should be noted that a fuzzier (larger interval) economic index is obtained as the lower confidence level is adopted.

35.5 Conclusions

This study has derived fuzzy real option analysis model which enable the company to perform a financial evaluation of project investment under highly uncertainty. The real option rule is that an investor should invest today only if the net present value of the planning project is high enough to compensate for giving up the value

of option to wait. The performance of the proposed model has been verified by applying the model to a simple numerical example. It is found that an appropriate options strategy allows the *FROV* model to reduce investment implementation costs, enhance investment performance, and facilitate an estimation of substantial benefits created by specific policies.

References

1. Sheen, J. N. (2005). Fuzzy financial profitability analyses of demand side management alternatives from participant perspective. *Information Sciences, 169*, 329–364.
2. Sheen, J. N. (2005). Fuzzy financial decision-making: Load management programs case study. *IEEE Transactions on Power Systems, 20*, 1808–1817.
3. Carlsson, C., Fuller, R., & Adams, L. B. (2003). A fuzzy approach to real option valuation. *Fuzzy Sets and Systems, 139*, 297–312.
4. Lee, S. C. (2011). Using real option analysis for highly uncertain technology investment: The case of wind energy technology. *Renewable and Sustainable Energy Reviews, 15*, 4443–4450.
5. Ho, S. H., & Liao, S. H. (2011). A fuzzy real option approach for investment project valuation. *Expert Systems with Application, 38*, 15296–15302.
6. Leslie, K. J., & Michaels, M. P. (1997). The real power of real options. *The McKinsey Quarterly, 3*, 5–22.
7. Lamarre, E., Pergler, M., & Vainberg, G. (2009, April). Reducing risk in your manufacturing footprint, *The McKinsey Quarterly*. http://www.mckinsey.com/insights/corporate_finance/reducing_risk_in_your_manufacturing_footprint
8. Kaufmann, A., & Gupta, M. M. (1988). *Fuzzy mathematical models in engineering and management science*. New York: Elsevier Science Publishers B.V.
9. Chiu, C. Y., & Park, C. S. (1994). Fuzzy cash flow analysis using present worth criterion. *The Engineering Economist, 39*, 113–137.
10. Chen, S. J., & Hwang, C. L. (1992). *Fuzzy multiple attribute decision making methods and applications*. Lecture Notes in economics and mathematical systems. New York: Springer
11. Giffin, W. C. (1975). *Transform techniques for probability modeling*. New York: Academic Press.
12. Debnath, L. (1995). *Integral transform and their application*. New York: CRC Press.
13. Black, F., & Scholes, M. (1973). The pricing of options and corporate liabilities. *Journal of Political Economics, 81*, 637–659.
14. Merton, R. (1973). Theory of rational option pricing. *The Bell Journal of Economics and Management Science, 4*, 41–183.
15. Park, C. S. (1987). The Mellin transform in probabilistic cash flow modeling. *The Engineering Economist, 32*, 115–134.
16. Dubois, D., & Prade, H. (1980). *Fuzzy sets and systems: Theory and applications*. New York: Academic Press.
17. Bortolan, G., & Degani, R. (1985). A review of some methods for ranking fuzzy subsets. *Fuzzy Sets and Systems, 15*, 1–19.
18. Buckley, J. J. (1987). The fuzzy mathematics of finance. *Fuzzy Sets and Systems, 21*, 257–273.

Chapter 36
The Optimal Placement of Wind Turbine in a Distribution System

Ming-Tang Tsai, Sung-Ling Chen, Szu-Wzi Wu and Cheng-Pin Lin

Abstract This paper presents an approach for determining optimal placement of wind turbine in the distribution systems. In order to minimize the system losses the optimization approach is solved by the Particle Swarm Optimization (PSO). To enhance the performance of the optimization approach, a load flow model with Equivalent Current Injection (ECI) is used to analyze the power flow of distribution systems for getting better convergent characteristics. Example of Taipower distribution feeder is presented to illustrate the efficiency and feasible of the proposed algorithm. Simulation results show that with proper placement of wind turbine can be used to reduce system loss, and maintain the voltage profile.

Keywords Optimal placement · Dsitribution feeder · Particle swarm optimization · Wind turbine

36.1 Introduction

In the past few years, utilities has faced many challenges in a competitive market due to increased investment cost and required the high level of reliability. They have the obligation for customers to supple the service reliability with their limited resource. Integration of Wind Turbines (WTs) into an existing distribution systems will bring several advantages, which largely depended on the allocation of WTs. Several advantages cover wide varieties of benefit, such as, line loss reduction, peak shaving, reduction emission, and increased system voltage profile [1–5]. It can also relieve distribution congestion as well as gird reinforcement. However, the optimal locations of the winds are gaining interest in the electricity industries.

M.-T. Tsai · S.-L. Chen (✉) · S.-W. Wu · C.-P. Lin
Department of Electrical Engineering, ICITES, Cheng-Shiu University,
Kaohsiung, Taiwan, Republic of China
e-mail: sungling@csu.edu.tw

J. Juang et al. (eds.), *Proceedings of the 2nd International Conference on Intelligent Technologies and Engineering Systems (ICITES2013)*, Lecture Notes in Electrical Engineering 293,
DOI: 10.1007/978-3-319-04573-3_36,

Due to advances in small wind energy technologies, utilities began to integrate the WTs in the distribution system for reducing the system loss and improving service reliability. The objective function of minimizing system losses is very common for the optimal allocation of WTs. WTs are mostly installed in demand system and directly connected to distribution networks. The inappropriating locations of WTs may lead to greater system loss. However, integration of WTs into the distribution systems takes a major challenge to system operators and planners due to the high uncertainty and variability in the characteristics of WTs. The proper placement of WTs will become a important issue in the future.

This paper presents an approach for determining optimal placement of wind turbine in the distribution systems. The Particles Swarm Optimization with Constriction Factor (PSO-CF) [6] was applied to optimally incorporate WTs into a distribution system. The proposed algorithm combines PSO-CF with power flow algorithm to find the best combination of locations. To enhance the performance of the new approach, a load flow model with Equivalent Current Injection (ECI) [7] is used to analyze the power flow of distribution systems. A Taipower distribution system [8] had been used to validate the proposed method. Simulation results can help decision makers perform the proper installation site selection of wind turbine to reduce system loss and maintain the voltage profile.

36.2 The Problem Formulation

The objective of this paper is to find the optimal WTs locations that minimize the system loss of the radial distribution network while satisfying operational constraints. The objective can be formulated as

$$\text{Min } P_{loss} = \frac{1}{2}\sum_{i=1}^{NB}\sum_{j=1}^{NB}\text{Re}\left[Y_{ij}\right]\left[|V_i|^2 + |V_j|^2 - 2|V_i||V_j|\cos\theta_{ij}\right] \tag{36.1}$$

where,

Y_{ij}	the admittance of branch $i-j$
Re	the real part of complex quantity
NB	the total number of branches in the system
V_i	The bus voltage
$\theta_{ij} = \theta_i - \theta_j$	the angle of voltage.

The constraints considered are described as follows

1. Power balance constraints

$$P_i = |V_i|\sum_{j=1}^{NB}|V_j||Y_{ij}|\cos(\theta_i - \theta_j - \delta_{ij}) \tag{36.2}$$

$$Q_i = |V_i| \sum_{j=1}^{NB} |V_j| |Y_{ij}| \sin(\theta_i - \theta_j - \delta_{ij}) \tag{36.3}$$

2. Voltage limit constraints

$$|V_i^{\min}| \leq |V_i| \leq |V_i^{\max}| \tag{36.4}$$

3. Line flow limit constraints

$$S_{ij} \leq S_{ij}^{\max} \tag{36.5}$$

4. WTs real power output constraints

$$P_{wind,i}^{\min} \leq P_{wind,i} \leq P_{wind,i}^{\max} \tag{36.6}$$

δ_{ij}	the angle of branch i–j element of the admittance
S_{ij}	The line flow in the branch i–j
$S_{ij}^{\max}$	the upper bound of line flow in the branch i–j
$P_{wind,i}$	the real power output of i-th WTs
$P_{wind,i}^{\min}$, $P_{wind,i}^{\max}$	the lower and upper bounds of the real power output of i-th WTs.

36.3 The Proposed Methodology

In this paper, Particles Swarm Optimization with Constriction Factor (PSO-CF) [6] was selected to trace the *pbest* value and *gbest* value. The proposed algorithm combines PSO-CF with load flow to find the best combination of locations. This load flow analysis can be used for ECI-based Newton–Raphson (NR) algorithm. NR algorithm is a gradient minimization problem in solving the non-linear equations, where the Jacobian matrix provides the optimal direction to find the root. Due to use the constant Jacobian matrix approximations in ECI-NR algorithm, the computation could be compensated for improving overall performance. The proposed methodology can be summarized in the following steps.

(1) Randomly initialize 30 particle (WTs) with feasible position in the system buses.
(2) Randomly assign suitable velocities (V_{wind}) and pitch angles (θ) of WTs to each particle. The power output of WTs can be calculated. If the power output is less 100 KW, the velocities and pitch angles of WTs are re-generated.

(3) Perform the load flow model with Equivalent Current Injection (ECI) and calculated the loss of distribution systems.
(4) Determine the best particle (*pbest* and *gbest*) performance dependent upon the system loss of entire particles.
(5) Update velocity vectors of each particle due to the position of individuals gradually close to *pbest* and *gbest*.
(6) Modified the current position vectors of each particle.
(7) The terminating condition is maximal number of iterations. If the preset target is not yet attained, then go back to Step (1) and repeat operation. In this paper, 500 generations is set to stop condition.

36.4 Case Study

The proposed algorithm was applied to solve the Taipower distribution system as shown in Fig. 36.1. The associated data is adapted from [8]. The maximal output of WTs is 200 KW. The numerical computations were performed using the Matlab language on a PIV-2.6 GHZ computer with 512 MB RAM.

The PSO parameter used in this paper is 30 particles. 500 generations is set as the stopping criteria. The power output of WTs ranges from 100 KW to 200 KW dependent upon the pitch angle and wind speed. The number of WTs are located in the buses to find the optimal system loss. Table 36.1 shows the generation outputs, wind speed, and optimal locations of WTs. It is clear from the obtained results that the locations of WTs are placed on ADa0 bus, BIa0 bus, and BK0 bus and the generation output is 143.5 KW for each WT, respectively.

Table 36.2 shows the summary of simulation results. The original system loss before WTs installed is 96.5 KW. From the results, the number of WTs installed is set 3, which the system loss ranges from 78.45 to 80 KW. It is clear from the obtained results that the number of WTs has significantly improved the system loss. The loss reduction ranges from 15.2 to 18.7 % due to the WTs are added in the distribution system. Figure 36.2 shows the convergent characteristics of the proposed method. The convergent generation was about the 70-th generation.

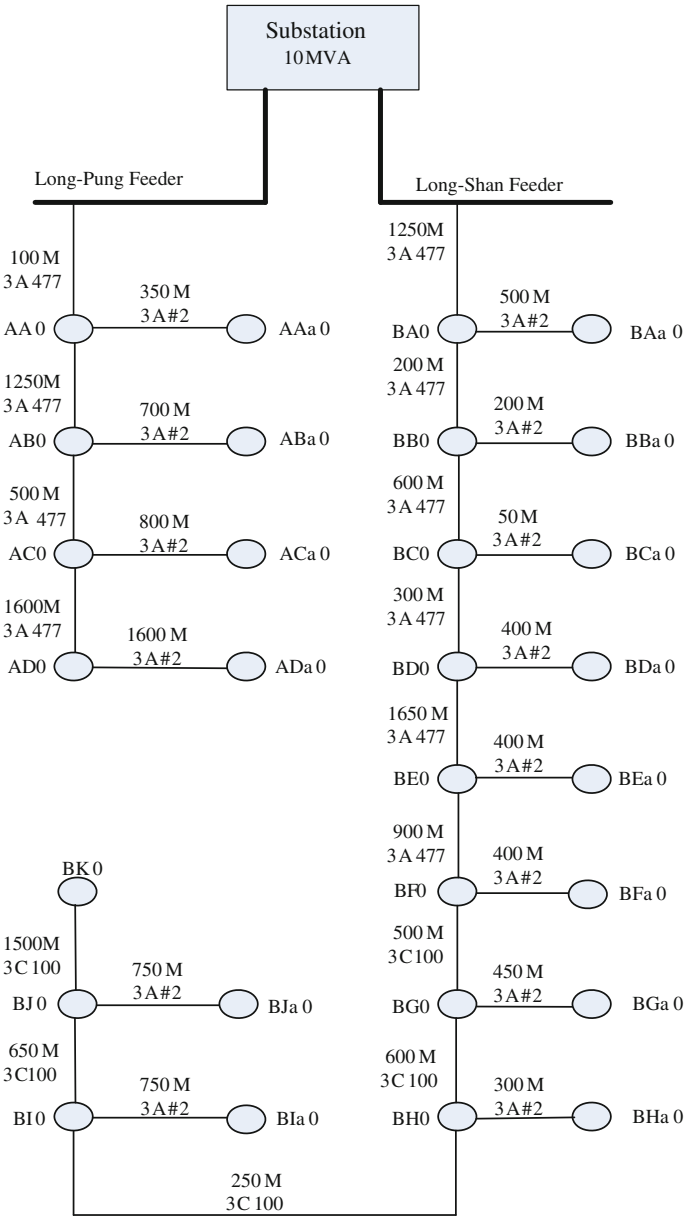

Fig. 36.1 The Taipower distribution system

Table 36.1 The summary for optimal placement of WTs

Wind speed (rpm)	88	88	88
Angle	0	0	0
Generation output (KW)	143.5	143.5	143.5
Optimal location (bus)	ADa0	BIa0	BK0

Table 36.2 The summary of simulation results

The system loss without WTs installed (KW)	96.5
The number of WTs installed	3
The best system loss after WTs installed (KW)	78.45
The average system loss after WTs installed (KW)	80
The worst system loss after WTs installed (KW)	81.47
The best percentage of loss reduction (%)	18.7
The average percentage of loss reduction (%)	17.1
The worst percentage of loss reduction (%)	15.2

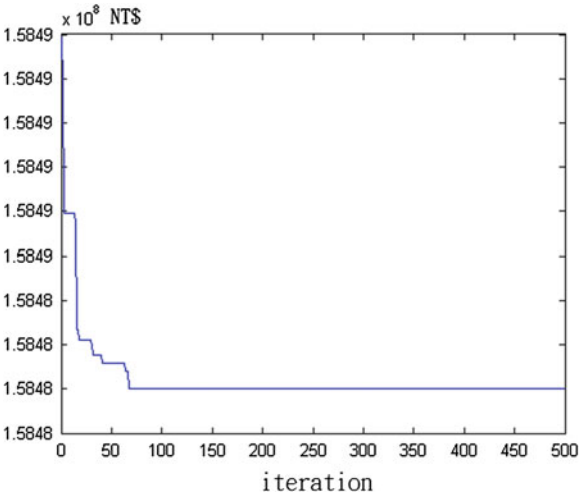

Fig. 36.2 The convergent characteristics of the proposed method

36.5 Conclusion

This paper presented a PSO for the location of wind turbine in the distribution systems in order to minimize the system loss. Technical constraints such as feeder capacity limits, bus voltage profile, and load balance are considered. To enhance the performance of the new approach, a load flow model with Equivalent Current Injection (ECI) is used to analyze the power flow of distribution systems. The effectiveness of the proposed algorithm is demonstrated and tested on Taipower

distribution system. Results show that incorporating the WTs in the distribution system can reduce the system loss. In addition, the results show that the different location of WTs could also produce multi-solutions to achieve the real global or nearly global solution.

Acknowledgments Financial support for this work by the National Science Council of R.O.C. under contract number NSC101-2221-E-230-021 is gratefully appreciated.

References

1. Borges, C. L. T., & Falcao, D. M. (2006). Optimal distributed generation allocation for reliability, losses, and voltage improvement. *International Journal of Electrical Power and Energy Systems, 28*, 413–420.
2. Tuba, G., & Hocaoglu, M. H. (2009). An analytical method for the sizing and siting of distributed generators in radial systems. *Electric Power Systems Research, 79*(6), 912–918.
3. Kumar, A., & Gao, W. (2010). Optimal distributed generation location using mixed integer non-linear programming in hybrid electricity markets. *IET Generation, Transmission and Distribution, 4*(2), 281–298.
4. Singh, R. S., & Goswami, S. K. (2010). Optimum allocation of distributed generations based on pricing for profit, losses reduction, and voltage improvement including voltage rise issue. *International Journal of Electrical Power and Energy Systems, 32*, 637–644.
5. Khalesi, N., Rezaei, N., & Haghifam, M. R. (2011). DG allocation with application of dynamic programming for loss reduction and reliability improvement. *International Journal of Electrical Power and Energy Systems, 33*, 288–295.
6. Shi, Y., & Eberhart, R. C. (1998). A modified particle swarm optimizer. In *Proceedings of the IEEE International Conference on Evolutionary Computation Anchorage* pp. 69–73.
7. Lin, W. M., & Teng, J. H. (1996). Phase-decoupled load flow method for radial and weakly-meshed distribution networks. *IEE Proceedings-Generation, Transmission and Distribution, 143*(1), 39–42.
8. Kuo, Z. Y. (1994). *A study on the impacts of grid connection wind power generations*. The thesis of master degree in National Sun-Yat University.

Chapter 37
A Novel Successive Approximation Register ADC Based on Vernier Caliper Design

Chih-Feng Huang, Chien-Yuan Liu and Yi-Chin Chen

Abstract This study presents a new method for the design of a N-bit successive approximation register (SAR) analog-to-digital converter (ADC) which employs the main-scale Vernier-scale characteristics of a Vernier caliper. The proposed design is similar to a half-SAR design where the main half-SAR ADCs the N/2 most significant bits (MSBs) from comparisons of the input signal with all of the quantization thresholds, while the Vernier (scale) half-SAR ADCs the N/2 least significant bits (LSBs). Relative to previous designs, this architecture reduces the number of comparators while maintaining high resolution and speed. A 12-bit prototype is tested by code density analysis, showing Integral Nonlinearity (INL) within ±1.0 LSB and Differential Nonlinearity (DNL) within ±0.5 LSB. Resolution is strongly dependent on precision current sources and resistor ladders. Such requirements, however, are easily met with very-large-scale integrated (VLSI) technologies, making the Vernier SAR ADC is a good candidate for high-performance low-cost low-power SAR ADC designs.

Keywords Vernier caliper · SAR ADC · Code density analysis

37.1 Introduction

In order to digitize modern sensor signals, data acquisition systems must have relatively high-precision and fast analog-to-digital converter (ADC) [1]. The common higher resolution ADCs such as dual slope and sigma-delta modulation

C.-F. Huang (✉) · C.-Y. Liu
Department of Computer Science and Information Engineering, ICITES, Cheng Shiu University, Kaohsiung 83347, Taiwan, Republic of China
e-mail: hcf0937@csu.edu.tw

Y.-C. Chen
Department of Computer Science, National Kinmen Agriculture and Industrial Vocational Senior High School, Kinmen 89142, Taiwan, Republic of China

J. Juang et al. (eds.), *Proceedings of the 2nd International Conference on Intelligent Technologies and Engineering Systems (ICITES2013)*, Lecture Notes in Electrical Engineering 293,
DOI: 10.1007/978-3-319-04573-3_37,

types are all low speed [2]. The parallel A/D architecture, commonly called flash A/D, is known for its high-speed conversion rate. While flash ADCs is the traditional choice for these specifications, a comparative potential energy savings of the successive approximation register (SAR) ADCs, which requires only a linear number of comparisons versus exponential for flash ADCs [3].

Conventional N-bit full-SAR ADC architecture needs N-bit digital-to-analog converter (DAC). The drawbacks of full-SAR architecture are a large number of R-2R resistor ladder network for N-bit DAC. In this article, a novel N-bit SAR ADC is constructed from a main half-SAR ADC and a Vernier half-SAR ADC.

The main half-SAR ADC is used essentially as a "pointer" to the segment of two successive main reference voltages where the input signal lies, thus determining the N/2 MSBs for the coarse conversion, while the Vernier half-SAR ADC determines the N/2 LSBs for the fine conversion. The new N-bit SAR ADC only needs three N/2-bit DACs for requiring fewer R-2R resistor ladder networks. Compared with traditional designs, the proposed SAR ADC is easy to design, lower power consumption, cooler operation, reduced physical size, lower cost, higher linearity and is easier to manufacture.

37.2 Method

The N-bit SAR ADC consists of a sample and hold circuit, a N-bit DAC, a voltage comparator circuit (Comparator) and a SAR controller. A N-bit of SAR ADC principle of operation is as follows. The analog input voltage through a sample and hold circuit provides a stable voltage to the comparator. The output voltage of the N-bit DAC is compared with the analog input voltage. The SAR controller will use binary search algorithm to control DAC output. A N-bit SAR ADC which converts an analog voltage value to the digital signal requires N cycles.

In Fig. 37.1, the new N-bit SAR ADC is based on the emulation of the Vernier caliper and uses the main N/2-bit SAR ADC and the Vernier N/2-bit SAR ADC to evaluate the voltages of the input analog signals. The divisions of the main full scale voltages (VFS) on the main half-SAR ADC and the Vernier full scale voltages (VFS*(1−1/M)) on the Vernier half-SAR ADC are all equal to M = N/2. The resolution of the main half-SAR ADC is VFS/M and the resolution of the Vernier half-SAR ADC is VFS/M^2. A given measured voltage Va may be represented as

$$V_a = \frac{mV_R}{M} + r = \frac{mV_R}{M} + \frac{vV_R}{M^2} + \frac{eV_R}{M^2}. \tag{37.1}$$

Where $0 \le m < (M - 1)$ $0 \le r < 1$, $0 < v < (M - 1)$, $0 \le e < 1$.

In Eq. (37.1), m and v are integer, r and e are real numbers. The value m is read from the main-scale reference voltage and the value r is the residual part of the

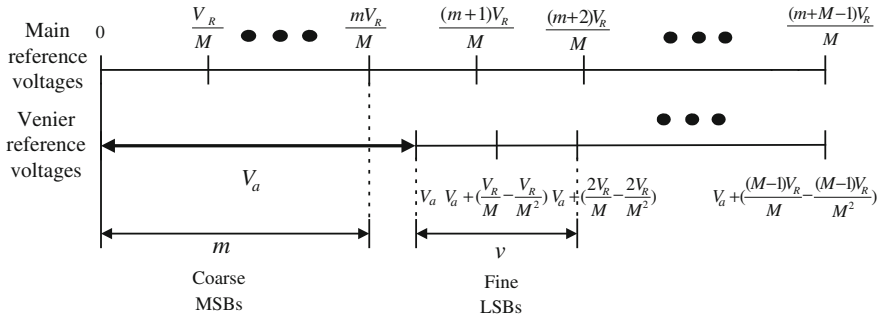

Fig. 37.1 Main and Vernier voltage references based on Vernier caliper emulation

input voltage Va that is less than the difference between two successive main reference voltages. After Va is determined on the main reference voltages, the movable Vernier reference voltages are compared with the main reference voltages to obtain the value read from the Vernier reference voltages. At the beginning of measurement, the value Va is r greater than m*VFS/M. The value of the vth Vernier reference voltage will be r-v*VFS/M^2 greater than the main reference voltage. If r-v*VFS/M^2 is less than zero, the value of the vth Vernier reference voltage will be smaller than the main reference voltage. The Vernier half-SAR ADC obtains the value v from the Vernier scale by electronically comparing the reference voltages on the two scales and locating the pair with the smallest voltage difference between them; v is the value of the Vernier-scale side of this pair. The resolution of the Vernier half-SAR ADC is VFS/M^2, and the value e is the residual part of the input signal Va that is less than the resolution of the Vernier SAR ADC, so the term e*VFS/M^2 can be eliminated. Equation (37.1) is then

$$V_a = \frac{mV_R}{M} + \frac{vV_R}{M^2}. \tag{37.2}$$

37.3 System Implementation

A block diagram of the new N-bit SAR ADC is shown in Fig. 37.2. This system consists of two sample and hold circuit, a main half-SAR ADC, a Vernier half-SAR ADC, and two digital data latches. Analysis of the operation of the system can be conveniently divided into five parts. The operation of each module is described as follows. If the input analog signal is not stable during the conversion process, then serious distortion will be present in the digital output. Therefore, a sample and hold circuit samples the input signal and holds the input signal on a capacitor for a short period of time in order for all of the distributed comparators to sample the same input signal level.

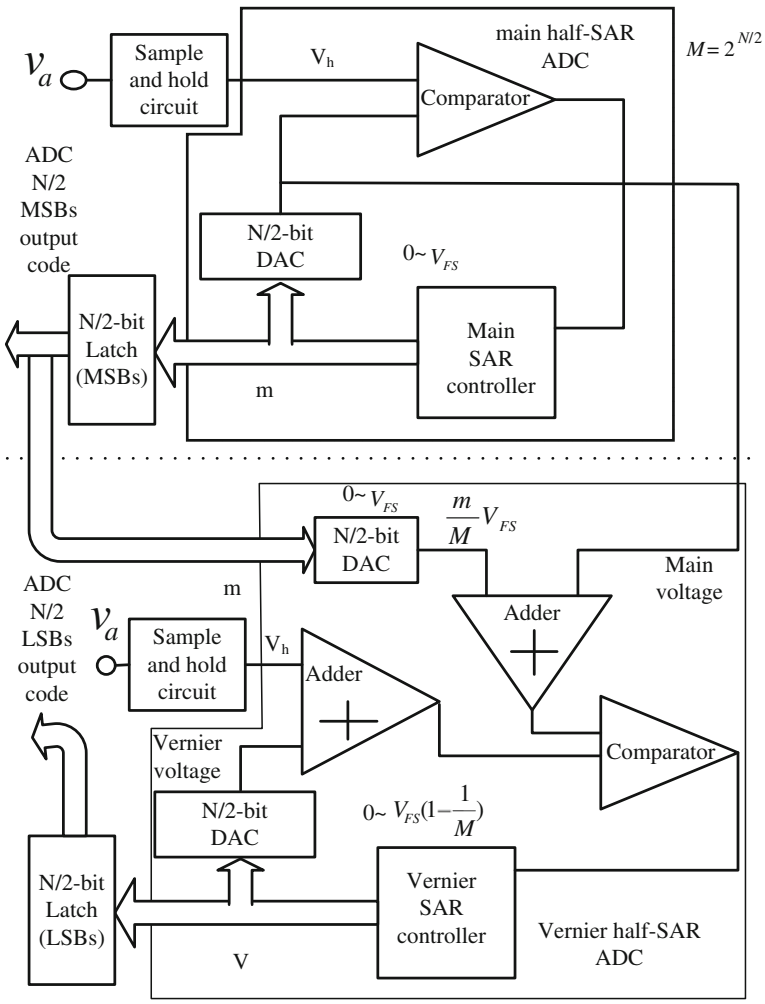

Fig. 37.2 Block diagram of the proposed Vernier N-bit SAR ADC

In Fig. 37.2, the input signal is held at a constant voltage Vh during the comparisons. To design an N/2-bit main half-SAR ADC, one needs an N/2-bit DAC, a main SAR controller and a comparator. The main SAR controller will use binary search algorithm to control N/2-bit DAC output. The main reference voltage using the full scale voltage (VFS) divided by M is equal to VFS/M. The comparator performs comparisons of the input-held signal Vh with the N/2-bit DAC output. If Vh is greater than mVFS/M and less than (m + 1)VFS/M, the SAR ADC outputs code represented as m.

A Vernier half-SAR ADC designed to emulate a Vernier caliper. To design an N/2-bit Vernier half-SAR ADC, one needs two N/2-bit DACs, two adder, a

Vernier SAR controller and a comparator. The N/2-bit Vernier half-SAR ADC performs comparison between the main reference voltages and the Vernier reference voltages. The both ends of the comparator are the main scale and Vernier scale voltage. The main scale voltage is (m + v)*FS/M which controlled by the main scale SAR controller. The Vernier scale voltage is Va + (vFS/M)*(1 − 1/M) which controlled by the main scale SAR controller. The output value v of the N/2-bit Vernier half-SAR ADC is the main scale voltage greater than the Vernier voltage. When the SAR ADC performs the conversion, the previous digital data must be latched until the next conversion to avoid instability in the conversion cycle. Two edge-triggered registers are used to latch the main scale (m) and the Vernier scale (v) of the converted value for the digital signal processing system.

37.4 Testing the System

Code density analysis is widely used for the dynamic characterization of ADCs. Code density analysis requires repeated sampling of an input sinusoid with random phases, forming a histogram which reports the number of occurrences of each code [4]. A 12-bit prototype of the proposed SAR ADC constructed in our lab from discreet commercial components was tested to check accuracy and nonlinearity. Tests were performed using the code density testing system shown in block diagram in Fig. 37.3, consisting of the prototype ADC, a HP33120A function generator, two banks of 256 KB Static Random Access Memory (SRAM), a clock generator, a 20-bit counter and a microcontroller. The sine wave signals were generated by a HP33120A function generator and used to test the SAR ADC. The ADC sampling rate was set by the clock generator. The clock generator also set the rate of the 20-bit counter generating memory addresses in two banks of 256 KB SRAM used to save the 12-bit digital data. Therefore, the digital data converted by the new SAR ADC is saved sequentially in the SRAM. The microcontroller controls system operation and transfers the digital data to a PC system via RS-232 interface. The PC contains code density testing software written by our group on MATLAB. This software can display, process and analyze data from the code density analysis system.

A prototype 12-bit, SAR ADC was tested at full speed using the code density testing system with a 100 kHz input sinusoid. 64 K samples were captured for analysis. Figure 37.4 shows the integral nonlinearity (INL) is less than ±1.0 LSB at the 12-bit level. Figure 37.5 shows the differential nonlinearity (DNL) is less than ± 0.5 LSB at the 12-bit level.

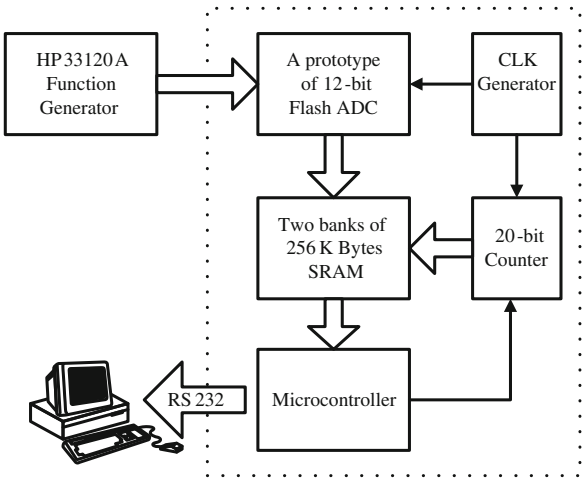

Fig. 37.3 Block diagram of the code density testing system

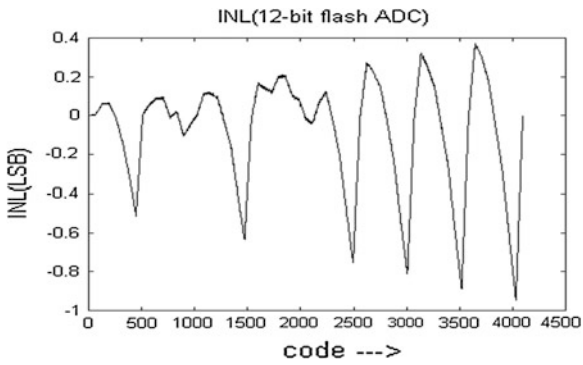

Fig. 37.4 INL at the 12-bit level

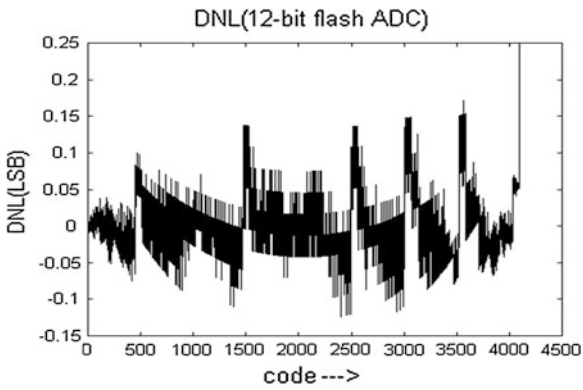

Fig. 37.5 DNL at the 12-bit level

37.5 Conclusions

The proposed SAR ADC emulates Vernier caliper operation theory. Compared with traditional designs, the proposed Vernier SAR ADC offers comparable linearity. The proposed design is easy to design, lower power consumption, cooler operation, reduced physical size, lower cost and is easier to manufacture. Improved performance could presumably be achieved by use of higher precision and speed components. The proposed Vernier SAR ADC is approximately as fast as traditional SAR ADC.

Acknowledgments This work was supported in part by the National Science Council under the Grant NSC 101-2514-S-821-001. The authors also greatly appreciate to the support of the National Science Council, R.O.C., under the Grant no. NSC-101-2632-E-230-001-NY3.

References

1. Huang, C. F., Huang, S. S., & Fu, I.-Y. (2004). Flash A/D converter based on Vernier caliper design. *Review of Scientific Instruments, 75*, 2328–2333.
2. Kim, M. G., Ahn, G.-C., Hanumolu, P. K., Lee, S.-H., Kim, S.-H., You, S.-B., et al. (2008). A 0.9 V 92 dB double-sampled switched-RC delta-sigma audio ADC. *IEEE Journal of Solid-State Circuits, 43*, 1195–1206.
3. Ginsburg, B. P., & Chandrakasan, A. P. (2007). Dual time-interleaved successive approximation register ADCs for an ultra-wideband receiver. *IEEE Journal of Solid-State Circuits, 42*, 247–257.
4. Chiorboli, G., Franco, G., & Morandi, C. (1996). Analysis of distortion in A/D converters by time-domain and code-density techniques. *IEEE Transactions on Instrumentation and Measurement, 45*, 45–49.

Chapter 38
Decubitus Prevention System Based on Mechanical Switches and Temperature Sensors

Chih-Feng Huang, Chien-Yuan Liu, S. P. Cao and Yi-Chin Chen

Abstract Bedsores (also known as Decubitus) are the adverse effects and emerge when skin under long-time pressured (including bones, and joints). The skin will cause poor blood loop so that cells cannot obtained nutrient, eventually cause injury to skin tissue. Unfortunately we will currently find that we are vulnerable to it. Bedsores have always been a threat to handicapped, illness or elderly persons who stays in bed or wheelchair for hours. Although normal human body is not threatened by bedsore, but there is no guarantee that any one of us can stay healthy forever. The price of existing medical instruments designed for bedsores are costly. Therefore we use mechanical switches and temperature sensors which are much cheaper to measure local pressure and temperature of body parts. The blood circulation of certain parts of the body can be monitored to solve bad blood circulation problem caused by local overpressure.

Keywords Decubitus · Bedsore · Temperature sensor · Mechanical switch

38.1 Introduction

Kosiak [1] found that bedsores will produce when the pressure imposed on the skin for 1–5 days. Its severity depends on the stress intensity and pressure duration [2]. The most important method to prevent bedsores produce is reducing or eliminating these factors. The time and pressure factors can quickly use by turning the patient

C.-F. Huang (✉) · C.-Y. Liu · S. P. Cao
Department of Computer Science and Information Engineering, ICITES, Cheng Shiu University, Kaohsiung 83347, Taiwan, Republic of China
e-mail: hcf0937@csu.edu.tw

Y.-C. Chen
Department of Computer Science, National Kinmen Agriculture and Industrial Vocational Senior High School, Kinmen 89142, Taiwan, Republic of China

J. Juang et al. (eds.), *Proceedings of the 2nd International Conference on Intelligent Technologies and Engineering Systems (ICITES2013)*, Lecture Notes in Electrical Engineering 293,
DOI: 10.1007/978-3-319-04573-3_38,

Table 38.1 Parts of body that bed sores most likely to occur [1]

Body in sitting	Body in lying
Heel	Shoulder Blade
Tail Bone	Tail Bone
Elbow	Ischium
Shoulder Blade	Foot
Back of the head	Heel
	Buttock

frequently, turning to alternate sides every three hours, and use of special decompression mattress are effective ways to improve [3]. Bedsores are most likely to occur in the bones prominent parts shown as Table 38.1.

Bedsores wounds would have serious consequences. It could take several weeks to heal the wound for small delays. Even the patients were suffering from sepsis, amputation or death. Not only for the patients have a serious impact, are more likely to cause irreversible sequela resulting in the loss and waste of medical resources.

About 6–10 % hospitalized patients suffering from pressure sore according to Haalboom and Bakker 1992 assessment. The bedsore prevention and treatment were spent about 700 million ANG (about 309,541,797.72 Euros). Braden and Bergstrom [4] pointed out that almost 40 % ICU (Intensive Care Unit) patients suffering from bedsores. Prevalence survey of Affiliated Hospital of Netherlands Amsterdam shows 43 % of ICU patients suffering from bed sores problem (Gunning-Scheper et al. [5]) and 50 % of patients suffering from bedsore problem in ICU as the lack of manpower (Barratt 1990). This thesis will show how to use mechanical switches and temperature sensors to achieve local pressure measurement as the main target while meet the efficiency of care, and patient health status [6, 7].

38.2 Method

This thesis is presented that health care workers enhance the alertness of bedsore for patients to reduce the possibility of follow-up care of medical human resources, so as to indirectly reduce the waste of medical resources. The design concepts are simplicity to achieve savings in medical costs. We design the 16 × 16 array of the mechanical switches and 4 × 4 array of the temperature sensors to implement the system. The system can measure 256 pressure points and 16 temperature points. The patients can sit or lying on mechanical switches and temperature for monitor the pressured parts of the body. The system also can measure the pressured time for reminding the caregiver to move or turn the body.

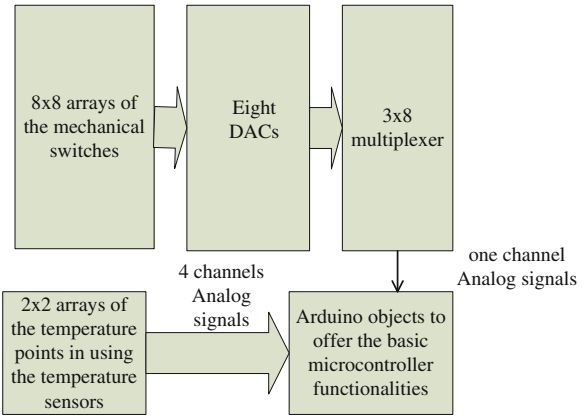

Fig. 38.1 Block diagram of the small basic module

38.3 System Implementation

The system is divided into mechanical switches, processors and temperature sensors. We use the small basic modules to implement the full system. The small basic modules include the 8 × 8 array of the mechanical switches and 2 × 2 array of the temperature sensors for the easy design and expansion. The small basic module uses the 8-bit digital to analog converter (DAC) to sense the pressing operation of eight mechanical switches as shown in Fig. 38.1. The small module uses Arduino objects to offer the basic microcontroller functionalities, analog to digital converters (ADCs) and digital controls. The pressing operation of eight mechanical switches will converter to analog signal. Eight DACs will be designed for 8 × 8 array of the mechanical switches. The 3 × 8 multiplexer is used to select the analog signal of eight DACs. Then the small module can use one channel of ADCs in Arduino for sensing the pressing operation of the 8 × 8 array of the mechanical switches. The other four channels of ADCs in Arduino are used to measure the 2 × 2 array of the temperature points in using the temperature sensors.

The Decubitus prevention system uses four basic modules to design the 16 × 16 array of the mechanical switches and 4 × 4 array of the temperature sensors as shown in Fig. 38.2. Four small modules and computer transmit the pressure and temperature data using RS-232 serial ports. The computer is the master and four small modules are slaves. The pressure and temperature sensing data are processed in computer using the LabVIEW (short for Laboratory Virtual Instrument Engineering Workbench) software. The pressing points of the 16 × 16 array of the mechanical switches are shown as two dimensions picture with 256 points. The 4 × 4 array of the temperature points are shown as a graph that displays 16 channel data in a time sequence.

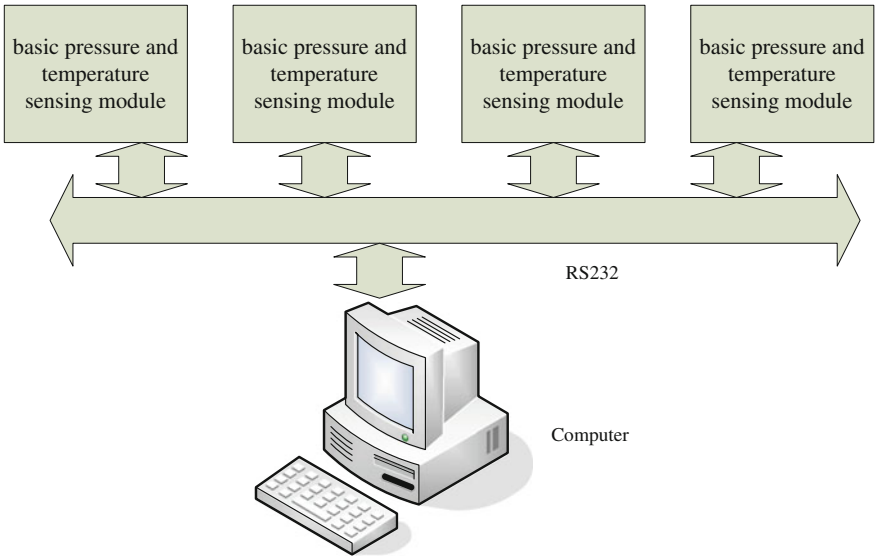

Fig. 38.2 Block diagram of the Decubitus prevention system

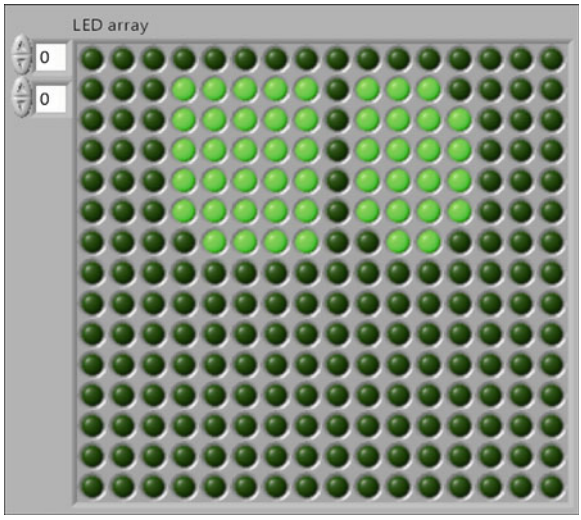

Fig. 38.3 The pressing points of the 16 × 16 array of the mechanical switches are displayed as LED array

38.4 Testing the System

In this experiment, the patients are sitting on the Decubitus prevention system. We use LabVIEW to show the pressing points of the 16 × 16 array of the mechanical switches. The LED is bright (ON) to present that this point is pressed. The LED is

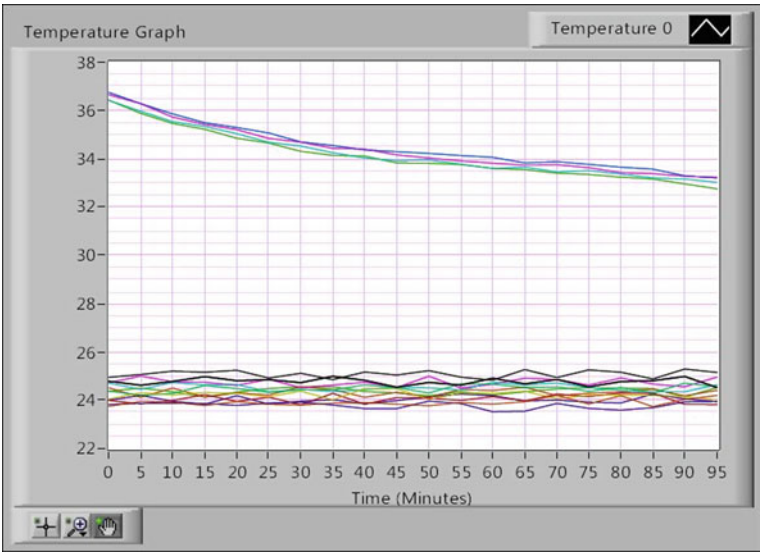

Fig. 38.4 A 16 channels temperature data are got and displayed in a time sequence

dark to present that this point is not pressed. The 16 × 16 LED array are shown as in Fig. 38.3. LED bright points are sat by the patient.

The 4 × 4 array of the temperature points are shown as in Fig. 38.4 that displays 16 channel temperature data in a time sequence. The top four channel signals are the four temperature measurement points that are sat by the patient ant the temperatures are decreased from about 36–33° after 100 min. The skin will cause poor blood loop so that the temperatures of skin are decreased. The other channel signals are not sat by the patient so the temperatures are displayed as the room temperatures.

38.5 Conclusions

In this paper, the Decubitus prevention system uses mechanical switches and temperature sensors which are much cheaper to measure local pressure and temperature of body parts. The system also can measure the pressured time for reminding the caregiver to move or turn the body. The blood circulation of certain parts of the body can be monitored to solve bad blood circulation problem caused by local overpressure.

Acknowledgments This work was supported in part by the National Science Council under the Grant NSC 101-2514-S-821-001. The authors also greatly appreciate to the support of the National Science Council, R.O.C., under the Grant no. NSC-101-2632-E-230-001-NY3.

References

1. Kosiak, M. (1959). Etiology and pathology of ischemic ulcer. *Archives Physical Medicine & Rehabilitation*, *40*, 62–68.
2. Taking Care of Pressure Sores. Retrieved from http://web.it.nctu.edu.tw/~hcsci/hospital/sci/sore.htm#cause
3. Weststrate, J. T. M., & Bruining, H. A. (1996). Pressure sores in an intensive care, unit and related variables: a descriptive study. *Intensive and Critical Care Nursing, 12*(5), 280–284.
4. Braden, B., & Bergstrom, N. (1987). A conceptual schema for the study of the etiology of pressure stores. *Rehabilitation Nursing*, *12*(1), 8–16.
5. Gunning-Scheper, et al. (1993). A model to estimate the health benefits of prevention. In *Tools for Health Future Research* (pp. 7–12). Geneva: World Health Organization.
6. Trinkoff, A. M., Johantgen, M., Storr, C. L., Gurses, A. P., Liang, Y., & Han, K. (2011). Nurses' work schedule characteristics, nurse staffing, and patient mortality. *Nursing Research, 60*(1), 1–8.
7. Yang, M.-C., Li, Y.-F., & Wei, S.-L. (2007). An analysis of the working hours and related factors associated with attending physicians and residents in teaching hospitals. *Journal of Medical Education, 11*(3), 40–51.

Chapter 39
A Niche-Related Particle Swarm Meta-Heuristic Algorithm for Multimodal Optimization

Chien-Jong Shih, Tso-Liang Teng and Shiau-Kai Chen

Abstract A niche-related particle swarm meta-heuristic algorithm for dealing with multimodal optimization problem is proposed in this paper. The inspiration and numerical algorithm are presented and the Rastrigin function with numerous local optima is adopted as the illustrative example. Proposed multimodal particle swarm optimization (MPSO) is sensitive to predetermined multimodal numbers, particle numbers, niche radius, and convergent iterations. The results show that the proposed MPSO is accurate and stable. The presented MPSO is ready for applied engineering optimization and further application.

Keywords Particle swarm optimization algorithm · Multimodal function · Niche · Bio-logical based optimization

39.1 Introduction

The simulated flock is an elaboration of a particle system, the simulated birds being the particles. Each simulated bird is implemented as an independent actor that navigates according to its local perception of the dynamic environment, the laws of simulated physics that rule its motion, and a set of behaviors programmed into it by the "animator" [1]. Particle swarm optimization (PSO) was originally attributed to Kennedy, Eberhart and modified by Shi [2]. It was first intended for simulating social behaviour as a stylized representation of the movement of

C.-J. Shih (✉) · S.-K. Chen
Department of Mechanical and Electro-Mechanical Engineering, Tamkang University, 25137 Danshui, New Taipei, Taiwan, Republic of China
e-mail: cjs@mail.ksu.edu.tw

T.-L. Teng
Department of Mechanical Engineering, Hsiuping University of Science and Technology, Dali, Taichung 41280, Taiwan, Republic of China

J. Juang et al. (eds.), *Proceedings of the 2nd International Conference on Intelligent Technologies and Engineering Systems (ICITES2013)*, Lecture Notes in Electrical Engineering 293,
DOI: 10.1007/978-3-319-04573-3_39,

organisms in a bird flock. An inertia weight w is brought into the original equation as shown in Eqs. (39.1) and (39.2) [2]. This w plays the role of balancing the global search and local search. It can be a positive constant or even a linear or nonlinear function of time.

$$x_{i,j}^{(k+1)} = x_{i,j}^{(k)} + v_{i,j}^{(k+1)} \tag{39.1}$$

$$v_{i,j}^{(k+1)} = w \times v_{i,j}^{(k)} + c_1 \times rand() \times (P_{i,j} - x_{i,j}^{(k)}) + c_2 \times Rand() \times (P_{g,i} - x_{i,j}^{(k)}) \tag{39.2}$$

Bergh et al. in PSO study [3] empirically found that the inertia weight w of 0.729, and acceleration coefficients c_1 and c_2 of 1.4945 are good choices, leading to convergent trajectories. Representations of *rand*() and *Rand*() are random number between 1 and 0. This PSO algorithm provides a critical platform for dealing with general optimization problem containing single objective function.

A multimodal optimization problem has more than one optimum, or exist only one global optimum and several useful local optima in feasible domain. There are a large number of such problems existing in the real world. In order to offer a variety of options and more information to decision makers, multimodal function optimization (MFO) tries to locate all these global optima and useful local optima. The use of PSO to solve multimodal optimization problems is just in starting stage. Parsopoulos et al. [4] applied compression and stretching techniques to solve multimodal problems. Brits et al. [5] proposed NichePSO by using sub-swarm. Ozca [6] improved the performance of NichePSO by using fanaticism mechanism and climbing mechanism. Most of existing multimodal PSO algorithms are based on species conservation and fitness sharing.

From long time investigation of animals learning models, the niche-related learning approach provides the basis for resulting in traditional general-process learning paradigms [7]. A niche-related approach can generate predictions for classic anomalies; provide a more secure and productive path for integration of the behavioral study of learning with neurophysiology, evolution, genetics, and development. This behavior science inspired us applying bird's niche-related learning approach to develop MPSO of dealing with multimodal optimization problems. The results obtained in this paper were compared with that obtained in NichePSO [5].

39.2 Multimodal PSO (MPSO) Algorithm

A general multimodal function optimization (MFO) is written as follows: Find $\boldsymbol{X} = [X_1, X_2, \ldots, X_{N_m}]^T$ where $X_i = [x_1, x_2, \ldots, x_n]_i^T, i = 1, 2, \ldots, N_m$. Each X_i represents the ith set of design variables corresponding to the ith extreme value. By

minimizing $f(X)$ subjected to $x_i^L \le x_i \le x_i^U$. One can see that the minimization of multimodal points corresponding to extreme values are written as: $f_1(X_1)$, $f_2(X_2)$, …,$f_{N_e}(X_{N_e})$. If only one global exists, then $f_1(X_1)$ indicates $f_{\min}(X^*)$. A niche-related MPSO proposed herein is stated as follows:

1. Define and select parameters: w (0.729), $c_1 = c_2(1.4945)$, $k_{\max}$(maximum evolutionary number), δ(convergent tolerance), M(preset multimodal numbers), N (particle numbers for search), R (niche radius), K_C(convergent iterations for the extreme), and $v_{\max}$(allowable velocity limit).
2. Evolutionary number $k = 1$. Within x_i^L and x_i^U, M multimodal points are averagely generated. Each pre-assumed extreme point is $X_m = (gbest)_m$, $m = 1, 2, \ldots, M$.
3. Uniformly random generate N-1 search points within the circle of center X_m with radius R. Include the point X_m, there are $(M \times N)$ search points in total. Each variable is represented as $(x_{i,j}^{(k)}, i = 1, 2, \ldots, n), j = 1, 2, \ldots, N$.
4. Compute function value of $(M \times N)$ search points. Each initial point is marked as $(pbest)_j$, $j = 1, 2, \ldots, N$. Make comparison for all search points and renew each $(gbest)_m$ and $(pbest)_j$.
5. Apply Eqs. (39.2) and (39.1) for updating locations of all search points.
6. If any updated x_i satisfies $x_i < x_i^L$; let $x_{i,j}^{(k+1)} = x_i^L$. If any updated x_i satisfies $x_i > x_i^U$; let $x_{i,j}^{(k+1)} = x_i^U$. If $x_{i,j}^{(k+1)} > v_{\max}$, let $x_{i,j}^{(k+1)} = v_{\max} \times rand()$. If $x_{i,j}^{(k+1)} < v_{\max}$, let $x_{i,j}^{(k+1)} = -v_{\max} \times rand()$.
7. Compute $f(X_i)$, $i = 1, 2, \ldots, M$. Renew each $(gbest)_m$ and $(pbest)_j$.
8. Based on Eq. (39.3), examine $(gbest)_m$ of mth niche continues K_C iterations convergence, it is concluded convergence and recorded number M_1.

$$\frac{(gbest)_m^{(k+1)} - (gbest)_m^{(k)}}{(gbest)_m^{(k+1)}} \le \delta \tag{39.3}$$

9. Continuously examine 100 times evolutionary number without finding new convergence point, go to step 13.
10. Calculate the distance d_g between any two niche center points of $(gbest)_m$ by:

$$d_g = \sqrt{\sum_{i=1}^{n} [(gbest_i)_{m+1} - (gbest_i)_m]^2} \tag{39.4}$$

If any distance of two $(gbest)_m$ points is less than R, reserve the one with smaller function value of $f(gbest)_m$. Thus M_2 points are reserved in the storing space. There are M_3 points were deleted from the space.

11. If $k \geq k_{\max}$, go to step 13.
12. Within x_i^L and x_i^U uniformly re-distribute $(M_1 + M_3)$ multimodal points. Include M_2 reserved points, totally M points is still maintained. Each pre-assumed extreme point is $X_m = (gbest)_m$, $m = 1, 2, \ldots, M$. Let $k = k + 1$ and go to step 3.
13. Terminate computation and output results.

Some explanations in above algorithm are introduced as follows. The maximum evolutionary number $k_{\max}$ depends on the problem; in general, 2000 was used. The convergent iterations K_C is depending on problem; and δ is 0.0001 predetermined. Niche radius R is related to the numbers of predetermined multimodal points. In general, R may be considered around $0.01(x_i^U - x_i^L)$. The allowable velocity limit in here used is defined as $v_{\max} = R$. Because $v_{\max}$ means searching step size, it shall not beyond local region.

39.3 Illustrative Example and Comparison

Brits et al. [5] proposed NichePSO algorithm used the GCPSO technique as a sub-swarm optimization method. The NichePSO's ability to scale to massively multimodal domain was investigated by adopting the Rastrigin function written in Eq. (39.5) required minimization.

$$f(\boldsymbol{X}) = \sum_{i=1}^{n} [x_i^2 - 10\cos(2\pi x_i) + 10] \tag{39.5}$$

Each variable x_i is restricted within -1.5 and 1.5. Figure 39.1 represents the configuration plot of two-dimensional Rastrigin function. Figure 39.2 shows all optimum points with one global located at center. The number of minima increases exponentially as dimension increases.

Apply the algorithm of MPSO proposed in previous session, parameters used are: $N = 5$, $R = 0.025$, $K_C = 100$ where $M = 10$ for $n = 1, 2$; $M = 100$ for $n = 3, 4$; and $M = 150$ for $n = 5$. There are five sub-problems, each one solved by MPSO with 30 times. Table 39.1 indicates the results of MPSO and NichePSO. The number "1" within the parenthesis indicates the number of global point. All global and local multimodal solutions can be averagely obtained except $n = 5$. However, 99.2 % can be found that still is superior to NichePSO with 92.0 % successful. It is noted that MPSO begin with a small quantity of particle numbers that will adaptively increased when it needed. In NichePSO, the swarm number must be assigned about four times of total searching points.

Figure 39.3 shows the convergence of global point for $n = 2$ for 30 times searches. Every converged after 100 iterations but until 300 iterations all optimum were found. Figure 39.4 represents global convergent history of all niches search.

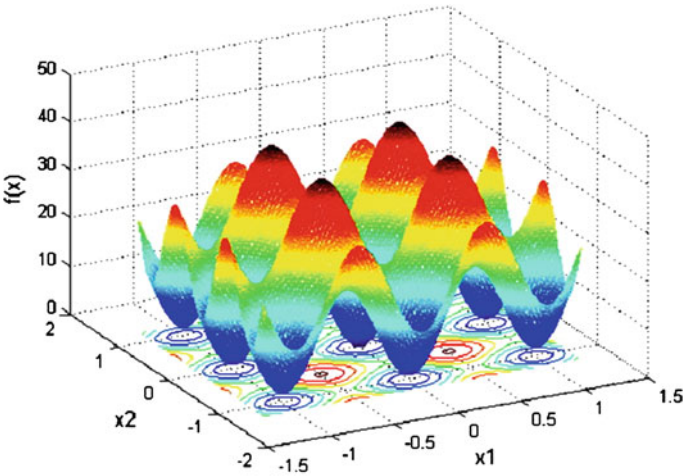

Fig. 39.1 Two-dimensional Rastrigin function

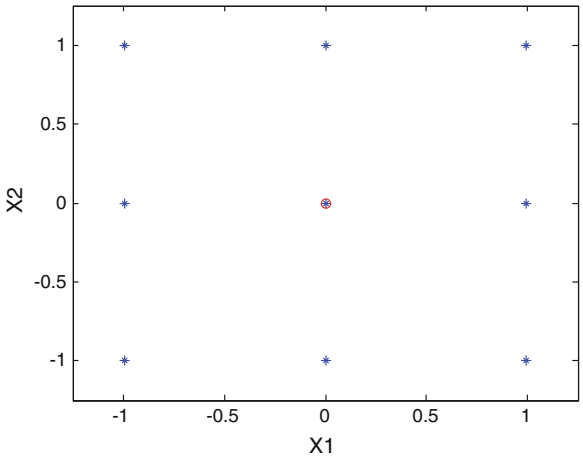

Fig. 39.2 MPSO result for Rastrigin function

Table 39.1 Results and comparison of Rastrigin function

Standard		MPSO			NichePSO [5]	
n	Opt.	Avg. opt.	%	Iterations	Avg. opt.	%
1	3(1)	3(1)	100	169	3(1)	100
2	9(1)	9(1)	100	249	9(1)	100
3	27(1)	27(1)	100	267	26(1)	97.4
4	81(1)	81(1)	100	317	79(1)	97.1
5	243(1)	240(2)	99.2	786	224(1)	92.0

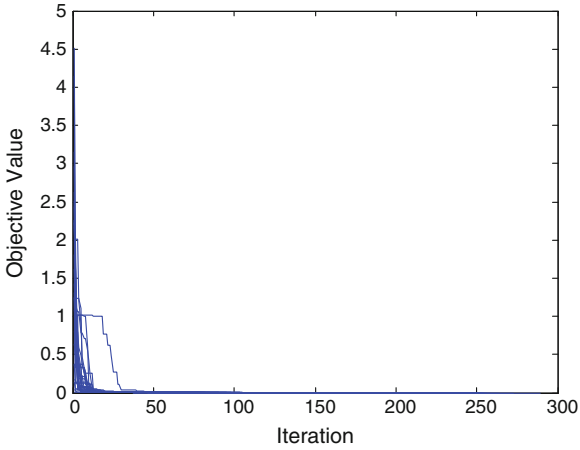

Fig. 39.3 Iteration history of global point

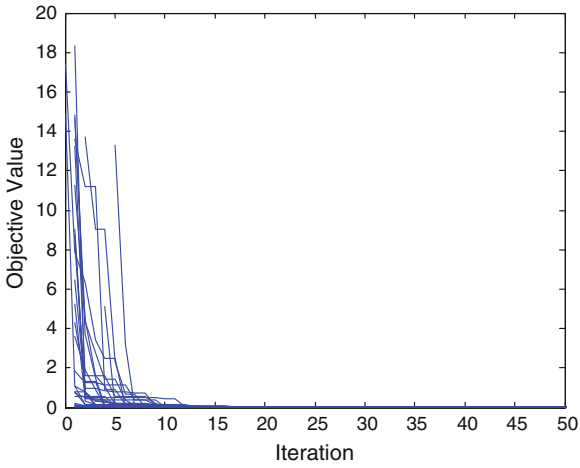

Fig. 39.4 Global search history of all niches

One line of search of 30 times search shown in Fig. 39.4 can be separately plotted in Fig. 39.5. For example, since 8th iteration, certain m's niche starts search with $f(X) = 14.033$ and converge to $f(X) = 0.000111$ at 45th iterations with $K_C = 100$. Figure 39.6 shows the plot of all 9 optimum with iterations for 30 times search. All multimodal are obtained at 249th iteration confirmed in Table 39.1.

Similar plots for $n = 5$ are shown in Figs. 39.7 and 39.8. Since $n = 5$ means more variables and more multimodal exist that makes the solutions search more difficult. It is reasonable use larger $M = 150$. This problem contains single global optimum, ten secondary-optimums and 232 local optimums. The global optimum can be obtained around 100 iterations. During 30 times search computation, in average 240.23 local optimums can be obtained. From Fig. 39.7 one can read that

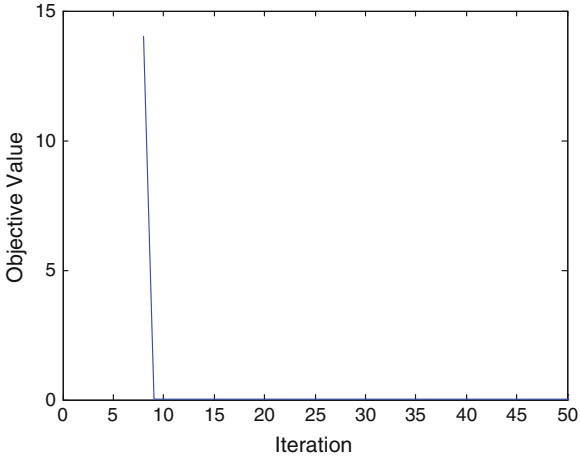

Fig. 39.5 Global search history of 8th niche

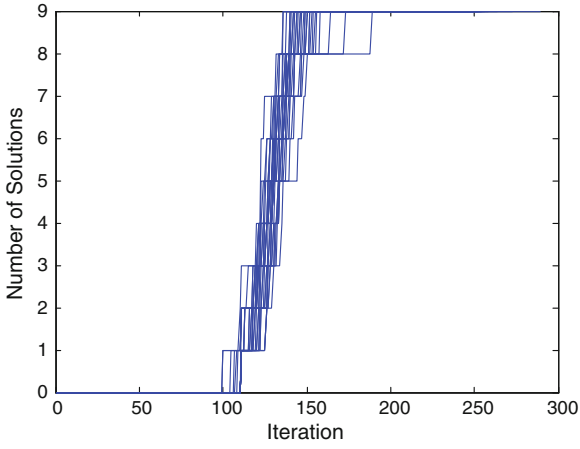

Fig. 39.6 All optimum and iterations

before 300 iterations the solution velocity is fast, after 800 iterations all optimum are converged. The solution search history of ten secondary-optimums for one representative search is shown in Fig. 39.8. From these observations, one can conclude that the proposed MPSO algorithm is stable and accurate.

39.4 Conclusion

A niche-related particle swarm meta-heuristic algorithm for multimodal optimization problems is presented. The complete algorithm is given for numerical programming with convenience and application. The anatomy of the Rastrigin

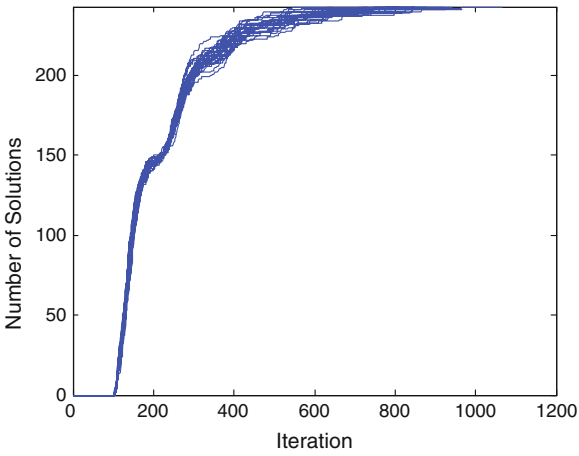

Fig. 39.7 All optimum and iterations ($n = 5$)

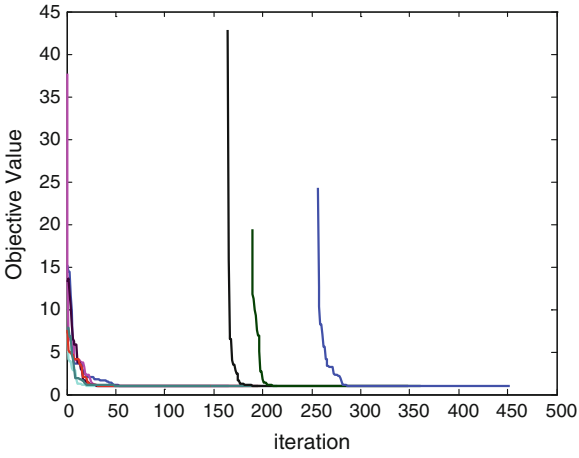

Fig. 39.8 Ten secondary-optimums iterations

function is provided as suitable illustrations of MPSO characteristics. The numerical result verifies the proposed MPSO algorithm is accurate and reliable, as compare to published multimodal PSO algorithm. The further research will extend to constraints handling technique combined presented algorithm for engineering design optimization.

Acknowledgments The support received from the National Science Council, Taiwan under Grant No. NSC 102-2221-E-032-010, is gratefully acknowledged.

References

1. Reynolds, C. W. (1987). Flocks, herds and schools: A distributed behavioral model. *Computer Graphics, 21*(4), 25–34.
2. Shi, Y., & Eberhart, R. C. ((1998)). A modified particle swarm optimizer. In *Proceedings of IEEE International Conference on Evolutionary Computation* (pp. 69–73).
3. van den Bergh, F., & Engelbrecht, A. P. (2006). A study of particle swarm optimization particle trajectories. *Information Sciences, 176*(8), 937–971.
4. Parsopoulos, K E., & Vrahatis, M. N. (2004). On the computation of all global minimizers through particle swarm optimization. *IEEE Transactions on Evolutionary Computation,* 8(3), 211–224.
5. Brits, R., Engelbrecht, A. P., & van den Bergh, F. (2007). Locating multiple optima using particle swarm optimization. *Applied Mathematics and Computation, 189*, 1859–1883.
6. Ozca, E., & Yilmaz, M. (2007). Particle swarms for multimodal optimization. In *ICANNGA 2007, Part I, LNCS 4431* (pp. 366–375).
7. Timberlake, W. (2001). Integrating niche-related and general process approaches in the study of learning. *Behavior Processes, 54*, 79–94.

Chapter 40
Investigation of Ceria Truncated Nano-Tetrahedron Island, Triangular Plate Stack Structure, and Columns Made by Using Electron Beam Deposition

Ming-Hsiu Wu, Jow-Lay Huang, Jui-Chao Kuo and Ding-Fwu Lii

Abstract Ceria truncated nano-tetrahedron islands, triangular plate stacks, and columns were deposited using EB-PVD and the application of glancing angle deposition (GLAD). The film surface morphology and nano-structures were characterized using FE-SEM, and TEM, respectively. The {111} facets were the dominant plane on the film surface, and the islands grew in a particular direction toward these plates.

Keywords Ceria · Glancing angle deposition · Truncated tetrahedron islands

40.1 Introduction

Ceria nano-structures have been widely studied for several years. Ceria can be applied in the solid electrolyte of solid oxide fuel cells [1], ultraviolet absorbers [2], oxygen sensors [3], and low-temperature catalysts [4]. Various types of nano-structures have been fabricated, such as nano-particles, nano-rods [5], and nano-tubes. Several methods are used for synthesizing specific facet-folded nano-structures to obtain superior catalysis, such as {110} or {100} facet-folded crystals, morphologies are usually finalized as {111} facet-folding [6].

Ceria film was grown using an electron beam deposition (EB-PVD) system with the influence of glancing angle deposition (GLAD) on crystal growth [7]. For understanding the influence of the high temperature application, the annealed

M.-H. Wu · J.-L. Huang · J.-C. Kuo
Department of Materials Science and Engineering, National Cheng Kung University, No. 1, Dashiue Road, Dung Chiu, Tainan 701, Taiwan, Republic of China

D.-F. Lii (✉)
Department of Electrical Engineering, Cheng Shiu University, Kaohsiung 833, Taiwan, Republic of China
e-mail: dflii888@csu.edu.tw

J. Juang et al. (eds.), *Proceedings of the 2nd International Conference on Intelligent Technologies and Engineering Systems (ICITES2013)*, Lecture Notes in Electrical Engineering 293,
DOI: 10.1007/978-3-319-04573-3_40,

samples were also examined. The obtained columnar structure exhibited a large surface area and specific crystal facets with excellent potential for the application of catalysts and SOFCs in the future [2, 3].

40.2 Experimental Procedure

EB-PVD was used to grow ceria film. The evaporation source was ceria pellets. Effectively milled ceria powder was compressed into pellets and sintered at 1,500 °C for 24 h. During film deposition, the voltage and current of the electron gun for evaporation were 8 kV and 40 mA, respectively, and the temperature of the system was maintained at 250 °C. Ceria (220) epitaxial films on (220) YSZ single crystal were used as substrates.

The ceria nano-columns were grown with the application of GLAD. The substrate holder was glanced at an angle of 10° relative to the perpendicular. The rotation speed was 5 rpm. The detailed setup of the system was presented in a previous paper [8].

Glancing incident angle diffraction (Rigaku 18 kW Rotating Anode X-ray Generator) was used to identify the crystal structure. The microstructure of the film surface and cross-section was examined using field-emission (FE-SEM) (Hitachi S4000). JEOL JSM-7001FE-SEM equipped with electron backscatter diffraction (EBSD) was used to resolve the crystal and texture information of the ceria film using TexSEM Laboratories OIM Analysis software. The nano-scale observation and the analysis of as-deposited and annealed crystals were conducted using transmission electron microscopy (TEM) (FEI E.O Tecnai F20 G2 MAT S-TWIN Field-Emission Gun Transmission Electron Microscopy).

40.3 Results and Discussion

40.3.1 Non-glancing Deposition of Ceria Film

The morphology of the ceria film became a triangular nano-plate stack, on which a number of islands were grown, as shown in the SEM image in Fig. 40.1a. This type of triangular plate structure has been investigated by Kopia et al. In their works, the tetrahedron-like structure became stable with {111} facets [9].

In contrast to the formation of nano-octahedron synthesized using hydrothermal or other chemical methods, the islands on triangular plates in this study were six-facet [10]. The islands can be observed as tips from the cross-section (Fig. 40.1b), and the film thickness was 500 nm. The two structures had a particular orientation to each other. The horns at the bottom of all islands pointed at

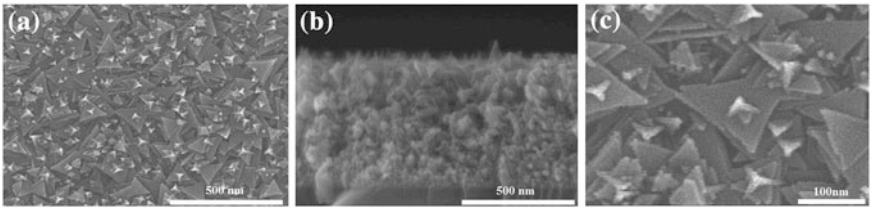

Fig. 40.1 **a** The surface morphology of the ceria film, **b** cross-section of the ceria film, and **c** higher magnification image for the island

the straight edge of the flat triangular plates. Relatively small plates were also observed at the side of the islands (Fig. 40.1c).

Details of the triangle and the island structure were obtained by using TEM. In the bright field image (Fig. 40.2a-1), and the boundary between the two facets is observed. As shown in the cropped area with HR mode (Fig. 40.2a-2), the {111} lattice planes with 3.2 Å spacing are parallel to the bottom of the island.

Electron diffraction shows that the triangular plate (Fig. 40.2b-1) was in the [-111] beam direction (Fig. 40.2b-2). The {220} lattice planes with 2.0 Å spacing were perpendicular to the straight edge of the triangle (Fig. 40.2b-2).

40.3.2 Deposition with Application of GLAD Method

With the application of GLAD, the ceria film became nano-column perpendicular to the substrate, as shown in the SEM image in Fig. 40.3a. As shown in the bright field image of a single column (Fig. 40.3b), the column was composed of multiple sections with the same crystal orientation, and a number of spikes were observed on the side of the column. According to the {111} lattice spacing fringes in the HR image (Fig. 40.3c) from the top of the rod, the growth direction of the rod was [111], which was the same as that of ceria film grown using the conventional method. Two {111} electron diffraction spots were imaged through nano-beam mode (Fig. 40.3d), and the angle between the two diffraction spots was equal to that of the two {111} lattice spacing fringes in Fig. 40.3c. The nano-rod was folded with {110} facets.

The {111} HR lattice fringes and nano-beam diffraction of the side spikes had the same orientation with the main structure of the rod, as shown in Fig. 40.3e, f. The growth from the side of the ceria island did not receive sufficient ceria molecules to grow into a {111} facet flat plane as the film grown using the non-glancing deposition method because of periodic shadowing [11].

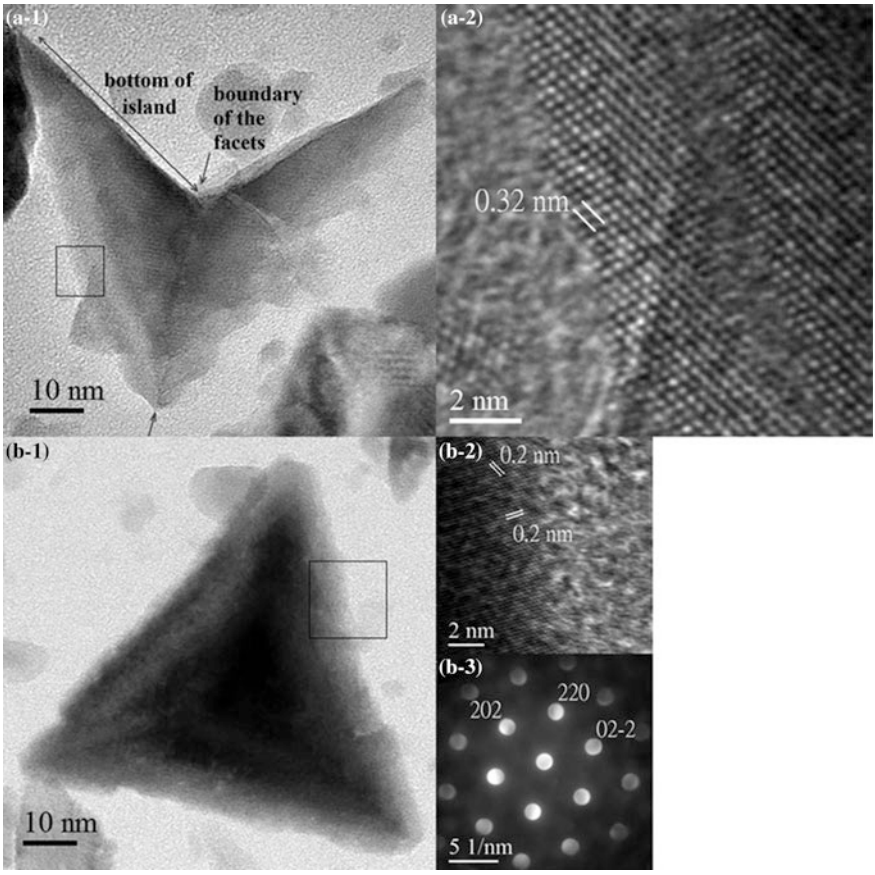

Fig. 40.2 **a-1** BF image of the ceria islands and **a-2** HR image of the circled area of (**a-1**); **b-1** BF image of the triangular plate; **b-2** HR image of the circled area of (**b-1**); and nanobeam diffraction of the triangular plate (**b-3**)

40.3.3 Annealing Effect on the Ceria Columns

As shown in Fig. 40.4, the XRD of the as-deposited columns and columns after annealing at 900 °C were compared. The (220) diffraction was contributed by the ceria epitaxial layer. The as-deposited and annealed ceria columns had a [111] preferred orientation; however, the diffraction intensity ratio of (111) to (220) decreased from 0.53 to 0.45 after annealing.

As shown in the bright field image in Fig. 40.5a, the surface of the annealed ceria columns became smooth, and the spike of the side growth shrank because of the effect of Ostwald Ripening. The catalysis is reduced due to the decrease in the surface area at high temperature. The whole column experienced distortion, which

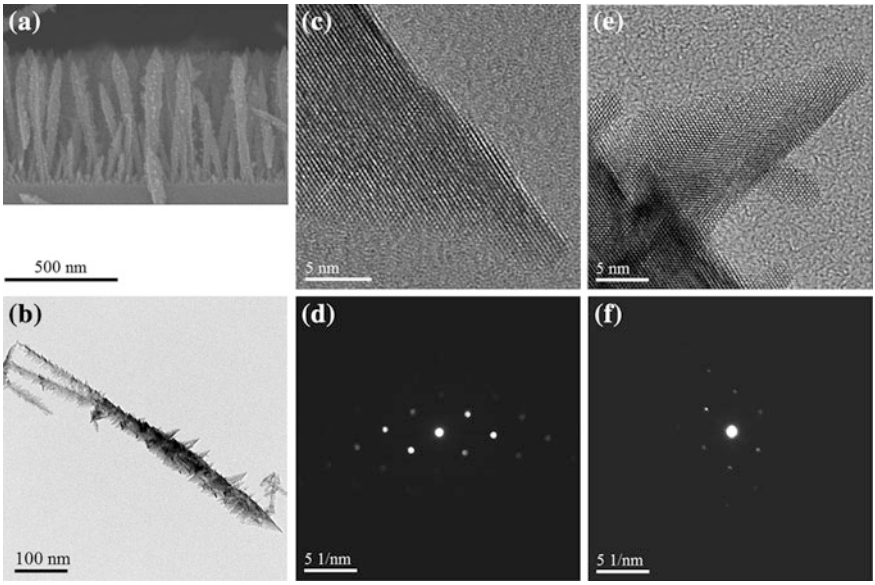

Fig. 40.3 **a** SEM image of the cross-section; **b** TEM bright field image of a single nanorod; **c**, **d** the HR image and nanobeam diffraction of the top of the nanorod; **e**, **f** the HR image and nanobeam diffraction of the side spike of the nanorod

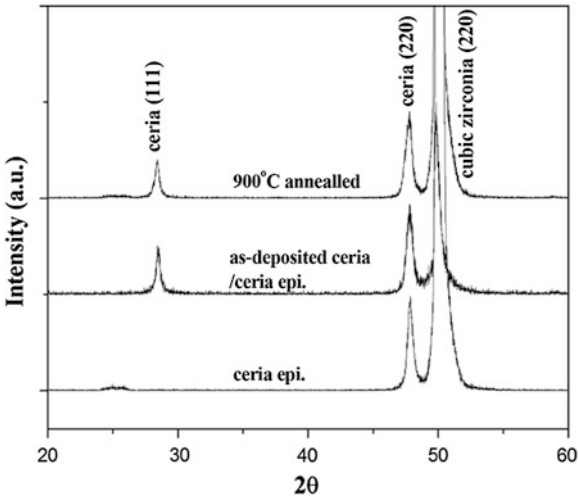

Fig. 40. 4 X-ray diffraction of the substrate, as-deposited, and annealed

was verified by selected area diffraction (Fig. 40.5b), in which the diffraction spots became a small arc rather than spots. It resulted in the decrease of the (111) diffraction, shown in Fig. 40.5.

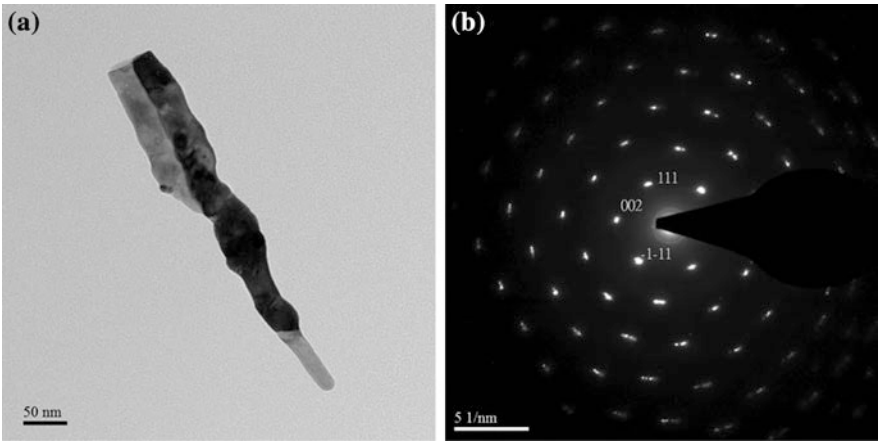

Fig. 40.5 **a** Bright field image of annealed ceria column, **b** selected area diffraction of this column

40.4 Conclusion

In summary, ceria six-facet islands and triangular nano-plate stacks were grown using a PVD system. The TEM analyses indicate that the ceria film had a preferred orientation, the surface of the triangular nanoplate stack had {111} facets, and the thin walls of the tetrahedron-like island were {110} facets. The evolution of these two structures was attributed to the driving force that reduced the surface of thin walls on the islands. During deposition using the GLAD method, the nano-rod was able to maintain a larger surface area with {110} facets because the substrate rotation imitated the growth of {111} facets. After annealing at 900 °C, the ceria columns became smooth with the same crystal orientation.

Acknowledgments The authors are grateful for the support from the National Science Council of Taiwan program under grant no. NSC 96–2221-E-006–123-MY3.

References

1. Tuller, H. L., & Nowick, A. S. (1975). *Journal of the Electrochemical Society, 122*(2), 255–259.
2. Li, R. X., Yabe, S., Yamashita, M., Momose, S., Yoshida, S., Yin, S., et al. (2002). *Solid State Ionics, 151*(1–4), 235–241.
3. Jasinski, P., Suzuki, T., & Anderson, H. U. (2003). *Sensors and Actuators B-Chemical, 95*(1–3), 73–77.
4. Trovarelli, A. (1996). *Catalysis Reviews-Science and Engineering, 38*, 439.
5. Du, N., Zhang, H., Chen, B., Ma, X. Y., & Yang, D. (2007). *Journal of Physical Chemistry C, 111*, 12677–12680.

6. Kuchibhatla, S. V. N. T., Karakoti, A. S., Sayle, D. C., Heinrich, H., & Seal, S. (2009). *Crystal Growth and Design, 9*(3), 1614–1620.
7. Robbie, K., & Brett, M. J. (1997). *Journal of Vacuum Science and Technology A, 15*, 1460.
8. Wu, M. S., Hunag, J. L., Fung, K. Z., & Lii, D. F. (2010). *Surface and Coatings Technology, 205*, 30–34.
9. Kopia, A., Kowalski, K., Chmielowska, M., & Leroux, Ch. (2008). *Surface Science, 602*, 1313–1321.
10. Yan, L., Yu, R., Chen, J., & Xing, X. (2008). *Crystal Growth and Design, 8*(5), 1474–1477.
11. Tucker, R. T., Beaudry, A. L., LaForge, J. M., Taschuk, M. T., & Brett, M. J. (2012). *Applied Physics Letters, 101*, 193.

Chapter 41
Intelligent Control for Wind Power Generator Using Neural Networks

Yoko Amano

Abstract This paper proposes a new intelligent control that can adaptively perform a wind power generator with various nonlinear uncertainties including nonlinear modeling errors and nonlinear parameter variations. The proposed intelligent control uses neural networks for various nonlinear uncertainties, and a new PD (Proportional Differential) learning rule for the neural networks is derived. In order to illustrate the validity and the practicality of the proposed intelligent control, it is applied to a simulation model of the wind power generator that includes most general nonlinear uncertainties.

Keywords Intelligent control · Neural networks · Wind power generator · Optimal control · Power electronics

41.1 Introduction

Wind power provides a golden opportunity for clean and cheap energy; so many countries have set an ambitious goal for wind power development. In order to that, various efficient control methods are proposed [1–4]. However, there are many elements which are not made of measurement and has difficulty in predicting in the power generator, it becomes the left difficult problem.

In this paper, for improvement of the efficiency of wind power generator, a new intelligent control which performs compensation of nonlinear uncertainties is proposed. First, the nonlinear uncertainties of the wind power generator are analyzed, and a control model including the nonlinear uncertainties is designed. Next,

Y. Amano (✉)
Graduate School of Electrical and Electronics Engineering,
Department of Electrical and Electronics Engineering, College of Engineering,
Nihon University, Tokyo 963-8642, Japan
e-mail: amano@ee.ce.nihon-u.ac.jp

J. Juang et al. (eds.), *Proceedings of the 2nd International Conference on Intelligent Technologies and Engineering Systems (ICITES2013)*, Lecture Notes in Electrical Engineering 293,
DOI: 10.1007/978-3-319-04573-3_41,

the intelligent control of the wind power generator using neural networks is constructed. Finally, simulated experiments are carried out, and most experimental results of the optimal regulator and the intelligent control are compared, the validity and the partiality of this proposal are confirmed.

41.2 Configuration of Maximum Electrical Wind Power Generator

In order to carry out the maximum electrical power, the configuration of the wind power generator is shown in Fig. 41.1 by [1]. Its attention is directed to the optimum rotational speed of the windmill and the single phase AC generator; it can obtain the maximum electrical power from the single phase AC generator according to the natural wind speed.

It becomes the experimental equipment that added the conversion with the optimum rotational speed N_r^* for the natural wind speed versus the rotational speed shown in Fig. 41.1, a wind speed meter, a laser speed meter that measures the rotational speed N_r of the single phase AC generator, a controller, a Pulse-Width Modulation (PWM) controller and the Field-Effect Transistor (FET) device as the generated power brake.

41.2.1 Equivalent Circuit of Wind Power Generator

An equivalent circuit of the wind power generator obtained from Fig. 41.1 is shown in Fig. 41.2, where, R_a, L and R_L are an armature resistance, an armature inductance, and a load resistance with the regulator and the direct current load and so on, $e(t)$ is a generated electric power from the single AC generator, and $V_i(t) = g_m r_{ds} V_{gs}(t) = V_{ds}(t)$ is a drain-source voltage, here g_m and r_{ds} are a transfer conductance and a resistance of the FET's drain-source, respectively. From Fig. 41.2, an equation of the equivalent circuit is the following

$$e(t) = Ri(t) + L\frac{di(t)}{dt} + V_i(t)\,, \quad e(t) = k_b\omega(t)\,, \tag{41.1}$$

$$J\dot{\omega}(t) + D\omega(t) = \tau\,, \quad \tau(t) = k_t i(t)\,, \quad R = R_a + R_L + r_{ds} \tag{41.2}$$

where, R, k_b, k_t, J, D and $\omega(t)$ are a synthetic resistance, a back electromotive force constant, a torque constant, an inertia moment of the single phase AC generator and the windmill, a viscous friction and an angular velocity, respectively. From formulas (41.1), (41.2), a state equation of the wind power generator is represented as

$$\begin{bmatrix} \dot{\omega}(t) \\ \dot{i}(t) \end{bmatrix} = \begin{bmatrix} -\frac{D}{J} & \frac{k_t}{J} \\ \frac{k_b}{L} & -\frac{R}{L} \end{bmatrix} \begin{bmatrix} \omega(t) \\ i(t) \end{bmatrix} + \begin{bmatrix} 0 \\ -\frac{1}{L} \end{bmatrix} V_i(t) \tag{41.3}$$

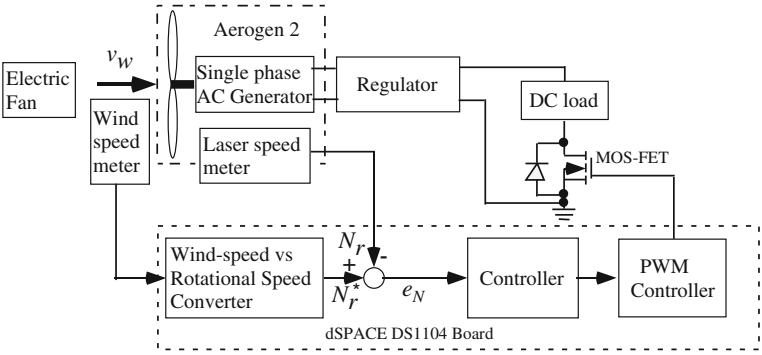

Fig. 41.1 Block diagram of wind power generator

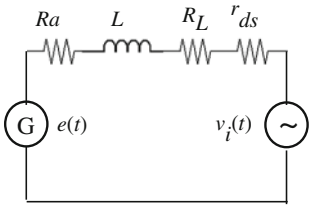

Fig. 41.2 The equivalent circuit of the wind power generator

41.2.2 Model with Uncertainties of Wind Power Generator

When the wind power generator is permanently operated, the heat of the wind power generator is produced, so that, the synthetic resistance changes with the heat, and the armature inductance is changed by the copper wire's heat expansion of the coil. Considering those various nonlinear uncertainties as stated above, formula (41.3) is rewritten as

$$\begin{bmatrix} \dot{\omega}(t) \\ \dot{i}(t) \end{bmatrix} = \begin{bmatrix} -\frac{D}{J} + \Delta_{D/J} & \frac{k_t}{J} + \Delta_{k_t/J} \\ \frac{k_b}{L} + \Delta_{k_b/L} & -\frac{R}{L} + \Delta_{R/L} \end{bmatrix} \begin{bmatrix} \omega(t) \\ i(t) \end{bmatrix} + \begin{bmatrix} 0 \\ -\frac{1}{L} \end{bmatrix} V_i(t), \quad y(t) = [1 \quad 0] \begin{bmatrix} \omega(t) \\ i(t) \end{bmatrix} \tag{41.4}$$

here, each item Δ represents the nonlinear uncertainties of the wind power generator. If formula (41.4) is simplified and can be expressed as

$$\dot{x}(t) = Ax(t) + Bu(t), \quad y(t) = Cx(t), \quad A = A_n + \Delta_A$$
$$x(t) = \begin{bmatrix} 0 \\ -\frac{1}{L} \end{bmatrix}, \quad A_n = \begin{bmatrix} -\frac{D}{J} & \frac{k_t}{J} \\ \frac{k_b}{L} & -\frac{R}{L} \end{bmatrix}, \quad B = \begin{bmatrix} 0 \\ \frac{-1}{L} \end{bmatrix}, \quad \Delta_A = \begin{bmatrix} \Delta_{D/J} & \Delta_{k_t/J} \\ \Delta_{k_b/L} & \Delta_{R/L} \end{bmatrix},$$
$$C = [1 \quad 0], \quad u(t) = V_i(t) \tag{41.5}$$

where, $x(t)$, $u(t)$ and $y(t)$, are the state, the input and the output variables, respectively; A, B, C are the parameter matrices; and Δ_A is the nonlinear uncertainties.

The goal of the control is to find the optimal input that minimizes a quadratic performance index described as

$$J = \int_0^\infty [x^T(t)Qx(t) + u^T(t)Ru(t)]dt, \tag{41.6}$$

where, $Q(\in \Re^{2\times 2}) \geq 0$ and $R(\in \Re^{1\times 1}) > 0$ are the weight matrices specified by the designer. The nonlinear regulator problem for the system (41.5) is very difficult and is generally solved using linearization techniques that synthesize an observer and a linear optimal regulator. However, there are many control problems where (41.5) cannot be linearization appropriately, so that the nonlinear compensation is particularly required.

In the next section, we propose the intelligent control using the neural networks with excellent capabilities of nonlinear mapping, learning ability and parallel computation.

41.3 Intelligent Control for Wind Power Generator

41.3.1 Quadratic Optimal Regulator

The optimal control input $u^*(t)$ that minimizes the performance index J of (41.6) is given as $u^*(t) = -R^{-1}B^TPx(t)$, where $P \in \Re^{2\times 2}$ is a unique solution of the Riccati equation $PA + A^TP - PBR^{-1}B^TP + Q = 0$. here the solution P is assumed as $P = P_n + \Delta_P$, where $P_n \in \Re^{2\times 2}$ and $\Delta_P \in \Re^{2\times 2}$ express respectively, the solution for the known linear part A and the compensatory solution for the unknown nonlinear uncertainty part Δ_A of the system (41.5).

Figure 41.3 shows a block diagram of the intelligent control proposed in this paper, an identification system shown in Fig. 41.3 is described as

$$\hat{\dot{x}}(t) = A_n x(t) + Bu(t) + x_{NN}(t) \tag{41.7}$$

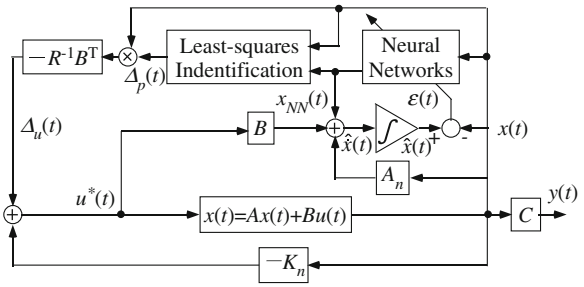

Fig. 41.3 Block diagram of the intelligent control

where, $\hat{x}(t) \in \Re^{2\times 1}$ and $x_{NN}(t) \in \Re^{2\times 1}$ are a predicted state variable of the identification system and an output of the neural networks, respectively. The optimal control input $u^*(t)$ is given as

$$\begin{aligned} u^*(t) &= u_n(t) + \Delta_u(t), u_n(t) = -K_n x(t), \\ K_n &= R^{-1}B^T P_n, \Delta_u(t) = -R^{-1}B^T \Delta_P x(t) \end{aligned} \tag{41.8}$$

where, $K_n \in \Re^{1\times 2}$ is a feedback gain of the linear optimal regulator. The identified state error $\varepsilon(t) \in \Re^{2\times 1}$ between the predicted state $\hat{x}(t)$ and the state $x(t)$ is defined as

$$\varepsilon(t) = \hat{x}(t) - x(t) = \int_0^t \zeta(\tau)d\tau, \quad \zeta(\tau) = [x_{NN}(\tau) - \Delta_x(\tau)] \tag{41.9}$$

where, $\zeta(\tau) \in \Re^{2\times 1}$ represents an error between the neural networks output $x_{NN}(t)$ and state uncertainties $\Delta_x(t)$. However, even if the identified error $\varepsilon(t)$ becomes zero, the integrand term $\zeta(\tau)$ of (41.9) may not be zero. So, we define an energy function $E(t)$ for training the neural networks as

$$\begin{aligned} E(t) &= \frac{1}{2}\bar{\varepsilon}^T(t)\bar{\varepsilon}(t) + \frac{1}{2}\varepsilon^T(t)\varepsilon(t) = E^{(1)}(t) + E^{(2)}(t), \\ E^{(1)}(t) &= \frac{1}{2}\zeta^T(t)\zeta(t), \quad E^{(2)}(t) = \frac{1}{2}\varepsilon^T(t)\varepsilon(t). \end{aligned} \tag{41.10}$$

When $E(t)$ will become zero, the output $x_{NN}(t)$ of the neural networks agrees with the state uncertainties $\Delta_x(t)$, that is $x_{NN}(t) = \Delta_x(t)$. According to training the neural networks, we can expect that the control input shown in Fig. 41.3 will be gradually approaching the optimal control input $u^*(t)$.

41.3.2 Multi-layer Neural Networks

The multi-layer neural networks used in the proposed intelligent control is shown in Fig. 41.4, here the unit numbers of the input layer, the hidden layer and the

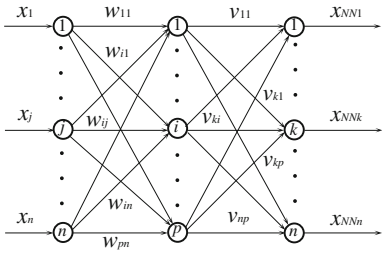

Fig. 41.4 Three-layer neural networks

output layer are described as n, p and n, respectively; w_{ij} represents a weight that connects the unit j of the input layer to the unit i of the hidden layer; v_{ki} represents a weight that connects the unit i of the hidden layer to the unit k of the output layer. These weight matrices are represented as $W(t) \in \Re^{p\times n}$ and $V(t) \in \Re^{n\times p}$, respectively. Also, the input and output vectors of the neural networks are represented as $x(t)$ and $x_{NN}(t)$, respectively. Let the unit j 's output of the input layer ($j = 1,\ldots,n$) be $I_j = x_j(t)$ the unit i 's output of the hidden layer ($i = 1,\ldots,p$) is

$$H_i = \sigma(s_i), \quad s_i = \sum_{i=1}^{n} w_{ij} I_j, \quad \sigma(\mu) \equiv (1/\gamma)\tanh(\gamma\mu) \tag{41.11}$$

where, $\sigma()$ is the sigmoid function, and γ is the positive parameter related to the shape of the sigmoid function. In the training process, the energy function of (41.10) is minimized by changing the weights w_{ij} and v_{ki}. According to the back-propagation algorithm, the weight updating rules can be described as

$$\begin{aligned} v_{kj}(t+\Delta t) =& v_{kj}(t) - \eta\left[\frac{\partial E^{(1)}(t)}{\partial v_{kj}(t)} + \frac{\partial E^{(2)}(t)}{\partial v_{kj}(t)}\right], \\ w_{ij}(t+\Delta t) =& w_{ij}(t) - \eta\left[\frac{\partial E^{(1)}(t)}{\partial w_{ij}(t)} + \frac{\partial E^{(2)}(t)}{\partial w_{ij}(t)}\right] \end{aligned} \tag{41.12}$$

As the result to the above mention, the updating rules of (41.12) are the following

$$\begin{aligned} v_{ki}(t+\Delta t) &\approx v_{ki}(t) - \eta[\bar{\varepsilon}_k(t) + \varepsilon_k(t)\Delta t_s]\frac{\partial x_{NN_k}(t)}{\partial v_{ki}(t)}, \\ w_{ij}(t+\Delta t) &\approx w_{ij}(t) - \eta\sum_{q=1}^{n}[\bar{\varepsilon}_q(t) + \varepsilon_q(t)\Delta t_s]\frac{\partial x_{NN_q}(t)}{\partial w_{ij}(t)}. \end{aligned} \tag{41.13}$$

Since (41.13) mean that the error signal for training the neural networks is the weighted sum of $.\varepsilon(t)$. and $\bar{\varepsilon}(t)$, this learning rule is corresponding to the PD control rule of the feedback control. Therefore, it is called as a PD updating rule in this paper. It should be noted that, if the energy functions of (41.10) are modified as

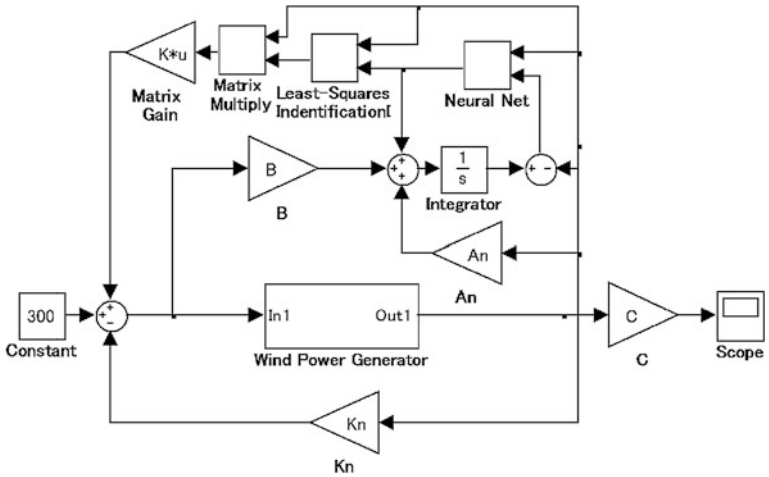

Fig. 41.5 The simulation model with MATLAB/Simulink

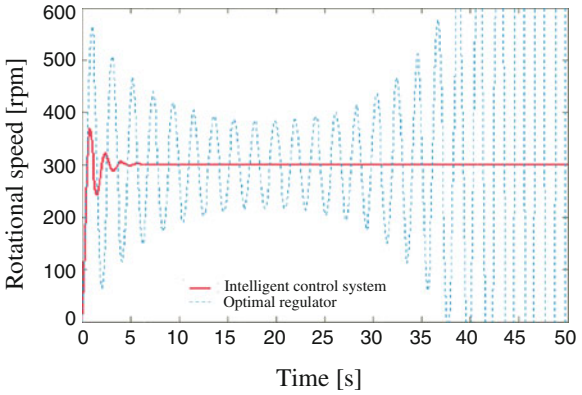

Fig. 41.6 The simulation result for case3: $\Delta_A = A_n \times M \cdot e^{nt}$

$$E^{(1)}(t) = \frac{1}{2}\bar{\varepsilon}^T(t)B_I\bar{\varepsilon}(t), \qquad E^{(2)}(t) = \frac{1}{2}\varepsilon^T(t)K_I\varepsilon(t). \tag{41.14}$$

The energy function $E(t)$ can be adjusted by learning gains $B_1 \in \Re^{n\times n}$, $K_1 \in \Re^{n\times n}$ defined as the positive definite matrices. In the intelligent control, the unit number in the input layer and the output layer $n = 2$, the unit number in the hidden layer $p = 5$ are respectively set.

41.4 Simulated Experiments

The simulated experiments are performed in order to confirm the usefulness and the validity of the intelligent control proposed in this paper. These experiments assume that the optimal rotational speed of the wind power generator is 300 (rpm), and compares experiment results between the optimal regulator and the proposed intelligent control. In the three-layer NN's used in the proposed system, the sampling time $\Delta t_s = 0.\ 1$ (s) and the learning rate $\eta = 0.025$ are set. In consideration of the heat characteristic of the coil's copper etc., the nonlinear uncertainties are made exponential function as $\Delta_A = A_n \times M \cdot e^{nt}$ here,M defines a constant and t is the time second. Figure 41.5 gives a MATLAB/Simulink model.

The experimental result is shown in Fig. 41.6; the solid line is as a result of the proposed intelligent control and the dotted line is as a result of the optimal regulator. The result of the optimal regulator is always vibrating; now, the result of the intelligent control system is converged on the target rotational speed, and is very stable. From the above-mentioned experimental results, it has confirmed that the intelligent control system for the nonlinear uncertainties using the neural networks is very effective than the optimal regulator.

41.5 Conclusion

In this paper, the intelligent control using the neural networks for the wind power generator was proposed, and the simulated experiments with the nonlinear uncertainties that often occur in the wind power generator were carried out. These experimental results of the optimal regulator and the intelligent control confirm the usefulness and the validity of the proposed intelligent control.

References

1. Amano, Yoko. (2013). Variable-speed wind generator system with maximum output power control. *LNEE, 234*, 437–443.
2. Belfedhal, S. (2013). Flywheel energy storage system with induction machine associated to a variable-speed wind generator. doi: 10.1109/EVER, p. 6521598.
3. Amano, Y., & Hiroyuki, K. (2008). Maximum electrical power control system of variable-speed small wind generators. Wiley Periodicals, Inc., A Wiley Company. *Electrical Engineering in Japan*, *165*(1), 9–17.
4. Adachi, G., Amano, Y. (2005). Identification system of wind power system using neural network. In *Proceedings of the 2005 Japan Industry Society Conference, II*.

Chapter 42
A Transmission Expansion Plan Considering Uncertainties and Risk Assessment Under a Deregulated Market

Rong-Ceng Leou, Chuo-Yean Chang and Shun-Yu Chan

Abstract In a deregulated power market, the transmission is required to supply a nondiscriminatory service. The location of power producers and power purchasers does not matter in terms of participation in national electricity market. Therefore, criteria for transmission planning in a deregulated market are different from those in a monopoly power market. These criteria must be amended to meet the requirement of the deregulated power market. The entrance/closure of the generation units is subject to delay or even cancellation, and it will increase uncertainties for the planning. This paper will propose a transmission expansion plan to meet these requirements. The contingency analysis and nodal price analysis are used to find all the candidate lines to add to the transmission system. Considering the investment cost, operation cost, and risk cost, a method combining the Monte Carlo Simulation and the Greedy Algorithm is proposed to find the optimal transmission expansion plan.

Keywords Transmission planning · Deregulation of power markets · Greedy algorithm · Monte carlo simulation

42.1 Introduction

The deregulation of the power industry leads to separation of the transmission planning from the generation expansions. This will increase the uncertainties and challenges of the transmission planning. Uncertainties can be classified in two categories: random and nonrandom uncertainties. Random uncertainties are deviation of those parameters which are repeatable and have a known probability

R.-C. Leou (✉) · C.-Y. Chang · S.-Y. Chan
Department of Electrical Engineering, Cheng Shiu University,
Niao-Song, Kaohsiung, Taiwan, Republic of China
e-mail: leou@csu.edu.tw

J. Juang et al. (eds.), *Proceedings of the 2nd International Conference on Intelligent Technologies and Engineering Systems (ICITES2013)*, Lecture Notes in Electrical Engineering 293,
DOI: 10.1007/978-3-319-04573-3_42,

distribution. Hence, their statistics can be derived from the past observation. Nonrandom uncertainties are evolution of parameters which are not repeatable and hence their statistics cannot be derived from the past observations. Many papers that are presented to deal with these uncertainties are discussed below.

Following the full competition of the generation and supply in England and Wales [1], there is no centrally coordinated planning of new generation or closure of existing generation. New generation enters into a contract with the transmission company for connection. Although this generation has entered into a transmission contract with the transmission company, this project is subject to cancellation or delay in commissioning to a later year. This paper shows that planning future transmission capacity is an exercise in risk management and identifies a portfolio of measures that facilitates trading and competition in the energy pool and at the same time optimizes the value of the transmission service.

In [2], transmission network expansion plans determined considering deterministic or uncertain conditions are evaluated under demand and cost scenarios different from the original design scenarios. Test results show that transmission plans considering uncertainty performed better than plans under deterministic conditions both in terms of minimization of the total expected cost and the range of operational costs. In [3], in order to provide a fair environment for all market participants, this paper proposed a reasonable expansion plan taking the operation cost, load curtailment cost, and investment cost into account.

In [4–6], a new market-based transmission planning in deregulated environments is presented in these papers. These papers introduce a new probabilistic tool to compute the probability density functions of nodal prices to handle the random uncertainties and present a new approach for transmission expansion planning. The scenario technique is used to model nonrandom uncertainties. The final plan is selected using risk assessment or fuzzy risk assessment.

In [7], some important issues related to transmission planning under a competitive market environment are extensively discussed. One of the challenges is more uncertain factors and risks faced by the transmission planning under competitive environment. In [8], a new transmission planning model is developed to consider a variety of market-driven power-flow patterns while a decision analysis scheme is incorporated to minimize the risk of the selected plan.

From surveys of these papers, it can be seen that uncertainties play an important role on the transmission planning under competitive environment. This brings a new challenge to the transmission planning problem. A new transmission planning strategy is therefore proposed in this paper. In order to provide a security and nondiscrimination of service, the security analysis and nodal price analysis are used to form the candidates of the transmission planning model. Considering the investment cost, operation cost, and risk cost, a method combining the Monte Carlo Simulation [9] and the Greedy Algorithm [10] is proposed to deal with the random uncertainties and find the optimal transmission expansion plan. In addition, scenario analysis is used to model the load growth rate and the change of the generation expansion plan. The IEEE 24-bus reliability test system [11] is adopted to verify the proposed model.

42.2 The Proposed Model

In order to provide a security and nondiscrimination of service, the security analysis and nodal price analysis are used to form the candidates of the transmission planning model. According to the scenarios of the load growth rate and the change of the generation expansion plans, the optimal transmission expansion plan is solved by the method combining the Monte Carlo Simulation and the Greedy Algorithm for each scenario. Finally, the risk assessment is used to select the final plan. Fig. 42.1 demonstrates the flow diagram of the proposed model. Detailed descriptions are given below.

1. Security analysis

The security analysis contains the line outage analysis and the generator outage analysis. The line outage analysis is to measure how much a particular line outage might affect the power system. The performance index (PI) of this analysis is shown in (42.1).

$$\mathrm{PI} = \sum_{\text{all branches } \ell} \left(\frac{\mathrm{P}_{\mathrm{flow},\ell}}{\mathrm{P}_{\ell}^{\max}} \right)^2, \tag{42.1}$$

where $\mathrm{P}_{\mathrm{flow},\ell}$ is the line flow of the line ℓ, and $\mathrm{P}_{\ell}^{\max}$ is the maximum line flow rating of the line ℓ.

A larger PI value indicates that outage of the line will lead to much more severe overload of the transmission lines. Therefore, the first five lines are considered as the candidates of the line outage analysis. The generator outage analysis is to let one generator outage one time and selects the overloaded lines.

2. Nodal price analysis

In a deregulated power market, the transmission is required to supply a nondiscriminatory service. The location of power producers and power purchasers does not matter in terms of participation in national electricity market. In order to have a competitive electric market, nodal prices must be made equal and congestion must be alleviated. Nodal prices are computed by the following optimization. The objective function is to minimize the operation cost. The first constraint is dc power flow. The second and third constraints are line flow limit and generator output limit respectively. Nodal prices are the Lagrange multiplier of dc power flow constraints.

$$\begin{aligned} \text{Min} \quad & \sum_{\mathrm{i} \in \mathrm{NG}} \mathrm{C_i P_{Gi}} \\ \text{S.T.} \quad & \mathbf{B}' \vec{\theta} = \mathbf{P_G} - \mathbf{P_D} \\ & -\mathrm{P}_{\ell}^{\max} < \frac{\theta_{\mathrm{i}} - \theta_{\mathrm{j}}}{\mathrm{x}_{\ell}} < \mathrm{P}_{\ell}^{\max} \quad \text{for all line } \ell \\ & \mathrm{P}_{\mathrm{Gi}}^{\min} < \mathrm{P_{Gi}} < \mathrm{P}_{\mathrm{Gi}}^{\max} \quad \mathrm{i} \in \mathrm{NG}, \end{aligned} \tag{42.2}$$

where $\mathrm{C_i}$ is the operational cost of generator i, NG is the generator bus set.

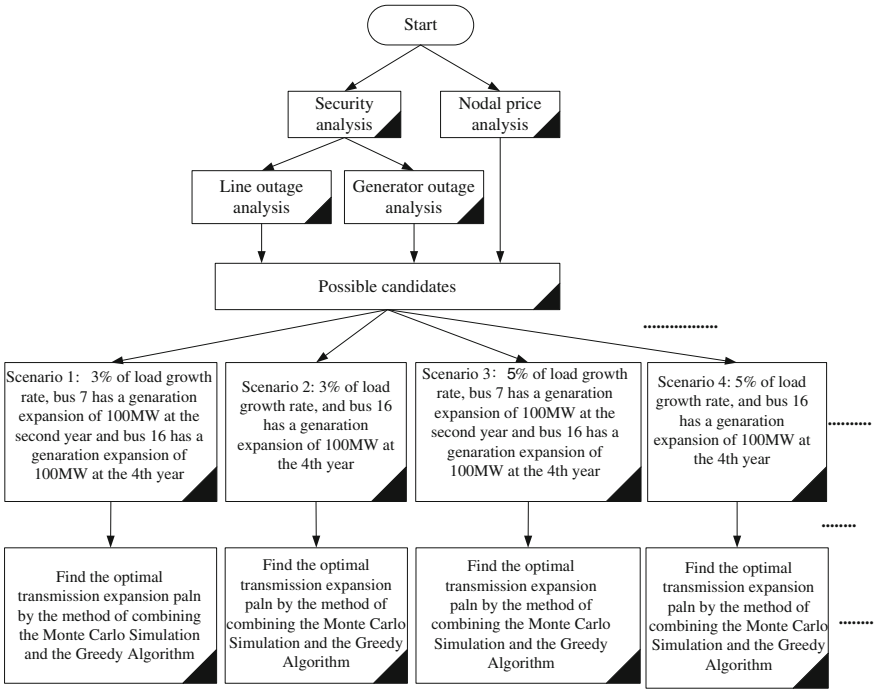

Fig. 42.1 The flow diagram of the proposed model

The new candidate line is created between the maximum nodal price bus and the minimum nodal price bus. The process lasts until the nodal price difference is small than the tolerance. For this system, the new candidate lines created by the nodal price analysis are line 16–17, and line 8–9.

3. Cost analysis

The costs of the transmission expansion plan contain the investment, operation, and risk costs. The objective function is to minimize these three costs as shown in (42.3).

$$\text{Min TC} = \text{IC} + \text{OC} + \text{RC}. \tag{42.3}$$

where TC is the total cost, IC is the investment cost, OC is the operation cost, and RC is the risk cost.

The annual investment cost of the transmission line is shown in (42.4). The operation cost and the risk cost are calculated by the Monte Carlo simulation according to the load data, parameters and outage rates of the transmission lines, and generators described in Sect. 42.2. Equation (42.5) is the operation cost and the risk cost for each hour. The first part of the objective function is the operation cost, and the second part is the risk cost. Accumulating the cost of each hour, the cost of one year can be obtained.

$$\mathrm{Inv} = \mathrm{V} * \frac{\mathrm{i}(1+\mathrm{i})^{\mathrm{n}}}{(1+\mathrm{i})^{\mathrm{n}} - 1}, \tag{42.4}$$

where Inv is the annual investment cost, V is the actual investment cost, i is the discount rate, and n is the economic life of the investment.

$$\begin{aligned} \text{Min} \quad & \sum_{\mathrm{i}\in\mathrm{NG}} \mathrm{C_i P_{Gi}} + \sum_{\mathrm{i}\in\mathrm{ND}} \mathrm{d_c Cur_i} \\ \text{S.T.} \quad & \mathbf{B}'\vec{\theta} = \mathbf{P_G} + \mathbf{Cur} - \mathbf{P_D} \\ & -\mathrm{P}_\ell^{\max} < \frac{\theta_\mathrm{i} - \theta_\mathrm{j}}{\mathrm{x}_\ell} < \mathrm{P}_\ell^{\max} \quad \text{for all line } \ell \\ & 0 \le \mathrm{Cur_i} \le \mathrm{P_{Di}} \quad \mathrm{i} \in \mathrm{ND} \\ & \mathrm{P}_{\mathrm{Gi}}^{\min} < \mathrm{P_{Gi}} < \mathrm{P}_{\mathrm{Gi}}^{\max} \quad \mathrm{i} \in \mathrm{NG}, \end{aligned} \tag{42.5}$$

where ND is the load bus set, $\mathrm{Cur_i}$ is the curtailment of electricity at bus i, and $\mathrm{d_c}$ is the curtailment cost.

The investment cost, operation cost, and risk cost of one year can be obtained by (42.4) and (42.5). During the planning horizons, the present value of the total cost is calculated by (42.6).

$$\mathrm{PV} = \sum_{\mathrm{j}=1}^{\mathrm{m}} \frac{\mathrm{TC_j}}{(1+\mathrm{i})^{\mathrm{j}-1}}, \tag{42.6}$$

where PV is the present value, $\mathrm{TC_j}$ is the total cost of the jth year, and m is the planning horizon.

4. The method combining the Monte Carlo Simulation and the Greedy Algorithm

According to the security analysis and nodal price analysis, the 11 possible candidate lines are listed in Table 42.1. This paper proposed a method of combining the Monte Carlo Simulation and the Greedy Algorithm to find the optimal expansion plan. The planning horizon is 5 years, and one line from the 11 possible candidate lines is added to the network one time to perform the Monte Carlo Simulation. If the minimum total cost of these 11 network topologies is smaller than the original network topology, update the original topology by adding this line as the initial network topology for the next iteration of the Greedy Algorithm. This iteration process continues until no line added to the network can reduce the total cost. The description of this process is shown below.

a. According to the outage rates of the lines and generators, create the network topology randomly

The reliability data and parameter data of lines and generators are used to create the network topology randomly. A random number between 0 and 1 is created to determine whether a line or a generator is broken-down.

b. Check convergence of the Monte Carlo Simulation

Table 42.1 All possible candidate lines of the test system

Candidate lines created by the line outage analysis	3–24
	15–24
	11–13
	15–21
	10–12
Candidate lines created by the generator outage analysis	18–21
	20–23
	7–8
	14–16
Candidate lines created by the nodal price analysis	16–17
	8–9

The variance of the total cost is used to check the convergence of the Monte Carlo Simulation. The simulation stops when the variance is smaller than the tolerance.

c. Check convergence of the Greedy Algorithm

The Greedy Algorithm converges when no any candidate line added to the network topology can reduce the present value of the total cost calculated by (42.6). When one of the 11 candidate line added to the network, the Monte Carlo Simulation is used to consider the uncertainties and calculate the present value of the total cost.

42.3 Test Results

This paper adopts the IEEE 24 bus reliability test system as the test system. The transmission network consists of 24 bus locations connected by 38 lines and transformers, as shown in [11]. The generating capacity data and load data are twice of the data in [11]. The transmission line data and their investment costs of [8] are applied in this paper. The outage data of these transmission lines are described in [11]. The reliability data and marginal costs of these generating units are shown in Table 42.2 and 42.3 respectively.

In this system, the economic life of the transmission line is 45 years, the planning horizon is 5 years, and the discount rate is 10 %. The load curtailment cost US$1964/MW-h is calculated according to [12] which is based on a gross domestic product divided by total electric energy consumption. Four scenarios are considered in the proposed model shown in Fig. 42.1. According to the planner's judgement, more scenarios can be included in this model. The first part of the test results will show the optimal expansion plan for each scenario, and then the risk analysis is discussed in the second part.

Table 42.2 The reliability data of the generating units

Capacity (MW)	Outage rate
24	0.02
40	0.1
100	0.01
152	0.02
200	0.04
310	0.04
394	0.05
700	0.08
800	0.12

Table 42.3 The marginal costs of the generating units

Bus	Marginal cost (US$/MW-h)
1	30
2	30
7	46
13	23
15	57
16	65
18	35
21	35
22	5
23	25

42.3.1 The Optimal Expansion Plan for Each Scenario

According to the proposed model shown in Fig. 42.1, the first scenario is that the load growth rate is 3 %, bus 7 will have a generation expansion of 100 MW at the second year, and bus 16 will have a generation expansion of 100 MW at the fourth year. The iterative process of this scenario is shown in Table 42.4. The optimal expansion plan is adding two lines between bus 7 and 8, and one line between 11 and 13. The total cost of no transmission expansion is $3.29485*10^7$ US$, and this cost can be downed to $3.22179*10^7$ US$ after performing the expansion plan solved by the proposed model.

The scenario 2 is the same as scenario 1 but the generation expansion at bus 7 is cancelled. The iterative process of this scenario is shown in Table 42.5. Due to the cancellation of the generation expansion at bus 7, the optimal expansion plan of the scenario 2 contains only one line between bus 7 and 8, and the total cost is also higher than that of the scenario 1.

The scenario 3 has a load growth of 5 %, and the generation expansion plan is the same as that of the scenario 1. In this case, the optimal expansion plan is shown in Table 42.6. The same lines as those of the scenario 1 are added to the network,

Table 42.4 The iterative process of the optimal expansion plan of scenario 1

Iteration	Network state	Total cost (US$)
0	Initial network state	$3.29485*10^7$
1	Add line 7–8	$3.23076*10^7$
2	Add line 7–8	$3.22454*10^7$
3	Add line 11–13	$3.22179*10^7$

Table 42.5 The iterative process of the optimal expansion plan of scenario 2

Iteration	Network state	Total cost (US$)
0	Initial network state	$3.29485*10^7$
1	Add line 7–8	$3.23932*10^7$
2	Add line 11–13	$3.23133*10^7$

Table 42.6 The iterative process of the optimal expansion plan of scenario 3

Iteration	Network state	Total cost (US$)
0	Initial network state	$3.71735*10^7$
1	Add line 7–8	$3.56565 *10^7$
2	Add line 7–8	$3.52285*10^7$
3	Add line 11–13	$3.51406*10^7$

Table 42.7 The iterative process of the optimal expansion plan of scenario 4

Iteration	Network state	Total cost (US$)
0	Initial network state	$3.71735*10^7$
1	Add line 7–8	$3.58358*10^7$
2	Add line 11–13	$3.57536*10^7$
3	Add line 16–17	$3.57219*10^7$
4	Add line 14–16	$3.57017*10^7$

but the total cost is higher than that of the scenario 1 due to the larger load growth rate.

The scenario 4 also has a load growth rate of 5 %, but the generation expansion at bus 7 of the second year is cancelled. The optimal expansion plan is shown in Table 42.7. Comparing with the scenario 2, two additional lines, line 16-17 and line 14-16, are included in this optimal expansion plan due to the higher load growth rate.

42.4 Conclusions

A new model to perform transmission expansion is proposed in this paper. This model considers the uncertainties of generation expansions. The possible candidate lines are obtained by the security analysis and the nodal price analysis. The Monte Carlo Simulation and the Greedy Algorithm is proposed to find the optimum transmission expansion plan. For further research, the risk analysis technique can be used to find the maximum expected value option.

References

1. Hiorns, A. (1998). Probabilistic transmission planning in England and Wales. In *IEE Colloquium on Tools and Techniques for Dealing with Uncertainty*, (1998).
2. Cedeno, E. B., & Arora, S. (2011). Performance comparison of transmission network expansion planning under deterministic and uncertain conditions. *Electrical Power and Energy Systems, 33*, 1288–1295.
3. Leou, R. C. (2011). A multiyear transmission planning under a deregulated market. *Electrical Power and Energy Systems, 33*, 708–714.
4. Buygi, M. O., Balzer, G., Shanechi, H. M., & Shahidehpour, M. (2004). Market-based transmission expansion planning. *IEEE Transactions on Power Systems, 19*, 2060–2067.
5. Buygi, M.O., Shanechi, H.M., Balzer, G., Shahidehpour, M., & Pariz, N. (2006). Network planning in unbounded power systems. *IEEE* Transactions *on Power Systems*, *21*, 1379–1387.
6. Buygi, M.O., Balzer, G., Shanechi, H.M., & Shahidehpour, M. (2004). Market based transmission expansion planning: fuzzy risk assessment. In *Proceedings of the 2004 IEEE International Conference on Electric Utility Deregulation, Restructuring and Power Technologies*, vol. 2, pp. 427–432.
7. David, A. K., & Wen, F. (2001). Transmission planning and investment under competitive electricity market environment. *IEEE PES Summer Meeting, 3*, 1725–1730.
8. Fang, R., & Hill, D. J. (2003). A new strategy for transmission expansion in competitive electricity markets. *IEEE Transactions on Power Systems, 18*, 374–380.
9. Billinton, R., & Li, W. (1994). *Reliability assessment of electrical power systems using Monte Carlo methods*. New York: Plenum Press.
10. Nemhauser, G., & Wolsey, L. (1999). *Integer and combinatorial optimization*. New York: Wiley.
11. The Reliability Test System Task Force of the Application of Probability Methods Subcommitte. (1976). IEEE reliability test system. *IEEE* Transactions *on Power Systems*, *PAS-98*, 2047–2054.
12. Li, W., & Choudhury, P. (2007). Probabilistic transmission planning. *IEEE Power and Energy Magazine*, pp. 46–53.

Chapter 43
Model Based Axial Displacement Measurement of Rubber Artificial Muscle Using Inner Diameter Sensor

Tetsuya Akagi, Shujiro Dohta, Yuji Kenmotsu, Shota Jinno and Ken-ichi Taniguchi

Abstract The purpose of this study is to develop a soft actuator which can be used as nursing care task in a bathing. In our previous study, a rubber artificial muscle with the inner diameter sensor was proposed and tested. The inner diameter sensor consists of two electric circuit boards with two photo reflectors. The sensor is inserted into the tube of the artificial muscle. It could be also obtained an empirical relation between the inner diameter and the axial directional displacement of the muscle with a strong correlation. By using the sensor and the empirical equation, the feedback position control of the muscle in the water could be also realized. In this paper, the model based axial displacement measurement of the muscle is described in order to estimate the condition of the muscle such as the inner diameter exactly. As a result, the design parameters of the muscle were obtained.

Keywords Inner diameter sensor · Rubber artificial muscle · Embedded controller · Low cost

43.1 Introduction

Recently, the ageing of Japanese society has caused to make worse "Quality of Life". It also caused the increase in the finical burden for healthcare. Especially, the lack of welfare care worker for the elderly and the disabled will be serious problem. In such a situation, it has been strongly desired to develop a system to aid in nursing care [1, 2] and to support the activities of daily life for the elderly and the disabled. The actuators required for such a system need to be flexible so as not to injure the human body [3]. The actuator also needs the larger generated force to support the nursing care task and water resistance to wash it. The purpose of this

T. Akagi (✉) · S. Dohta · Y. Kenmotsu · S. Jinno · K. Taniguchi
Department of Intelligent Mechanical Engineering, Okayama University of Science, Okayama 700-0005, Japan
e-mail: akagi@are.ous.ac.jp

J. Juang et al. (eds.), *Proceedings of the 2nd International Conference on Intelligent Technologies and Engineering Systems (ICITES2013)*, Lecture Notes in Electrical Engineering 293,
DOI: 10.1007/978-3-319-04573-3_43,

study is to develop a high-power flexible actuator with a sensor for positioning which can be used in supporting a bathing and in the rehabilitation device in warm water for heat therapy. In our previous study, the rubber artificial muscle with inner diameter sensor was proposed and tested [4]. The position control of the muscle in the water was also executed. The proposed measuring method is superior than other studies about measuring the displacement of the muscle from the outer side of the muscle [5, 6]. However, the proposed method required the empirical formula to calculate the axial displacement of the muscle from the senor outputs. Therefore, the inner diameter of the muscle to estimate the volume of the muscle could not be calculated. Therefore, in this paper, the geometric model for axial displacement measurement of the rubber artificial muscle using the inner diameter sensor is proposed and tested.

43.2 Rubber Artificial Muscle with Inner Diameter Sensor

43.2.1 Construction and Measuring Principle

Figure 43.1 shows the construction of the inner diameter sensor developed in our previous study. The sensor consists of two photo reflectors (GENIXTEK Co. Ltd., TPR-105F), an electronic circuit board and an acrylic board to adjust their height. The output terminal from two photo reflectors is set at the base of the sensor and is connected with the bulkhead with the outer diameter of 12 mm and the thickness of 2 mm. Figure 43.2 shows the inner construction of the rubber artificial muscle (FESTO Co. Ltd., MXAM-10-AA: a natural length of 250 mm) with the inner diameter sensor. The sensor has a bulkhead to hold it at a constant position and keep a seal at the same time. The measuring principle of the inner diameter is as follows. When the muscle is pressurized, the distance between the photo reflector and the inner wall of the muscle becomes longer until the maximum distance of 5.5 mm. The output voltage from the photo reflector becomes lower as increasing the distance. The embedded controller (Renesas Co. Ltd. H8/3664) can detect the voltage change through the inner A/D converter. By using the empirical formula based on the relation between the output voltage of the sensor and the axial displacement of the muscle that was investigated, the displacement of the sensor can be estimated. The mass of the inner diameter sensor is only 10 g. The total mass including the sensor and the muscle is very small, that is 70 g.

43.2.2 Measurement Based on Empirical Formula

Figure 43.3 shows the relation between output value from the sum of incremental A/D values from two photo reflectors in the sensor and the axial displacement of

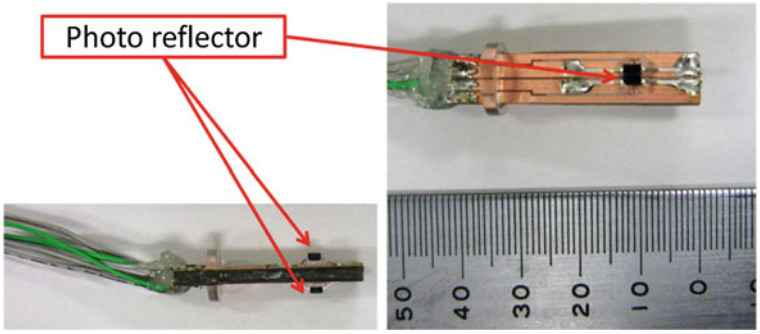

Fig. 43.1 Inner diameter sensor

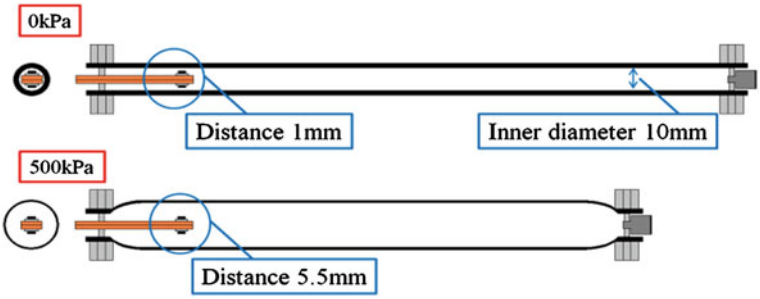

Fig. 43.2 The muscle with inner diameter sensor

the rubber artificial muscle. In the experiment, when the supplied pressure to the muscle was given from 0 to 500 kPa and from 500 to 0 kPa every 50 kPa, both the sensor output (A/D value) and the displacement of the muscle were measured. The measurement was repeated five times. The initial value of the sensor is defined as zero when no pressure is applied to the muscle. From Fig. 43.3, it can be seen that the relation between the displacement and the output from the sensor has no hysteresis. It means that the sensor is useful as a feedback senor of positioning the muscle that has larger hysteresis in relation between the input pressure and the displacement. The nonlinear relationship depends on the characteristics of the rubber artificial muscle and the photo-reflector. As a result, the following approximate equation between the displacement y [mm] and the sensor value x [A/D value] can be obtained.

$$y = 2.003 \times 10^{-13}x^6 - 1.477 \times 10^{-10}x^5 + 3.878 \times 10^{-8}x^4 - 3.235 \times 10^{-6}x^3 - 1.091 \times 10^{-4}x^2 + 6.086 \times 10^{-2}x \tag{43.1}$$

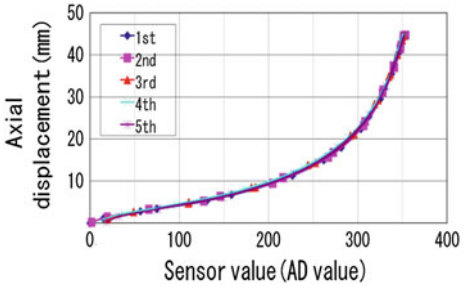

Fig. 43.3 Static characteristics of the sensor

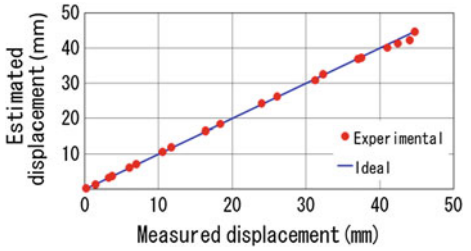

Fig. 43.4 Comparison with measured value

Figure 43.4 shows the relation between the actual displacement of the rubber artificial muscle measured with the potentiometer (Sakae Tsushin Kogyo Co. Ltd., 18FLPA50) and the calculated displacement using the sensor and the empirical formula of Eq. (43.1). In Fig. 43.4, symbols and the solid line show the calculated displacement and the ideal case that both the measured and actual displacement are same, respectively, As a result, we can confirm that the estimated displacement agrees well with the actual displacement. We found that the standard deviation of the error is 0.4 mm and the maximum estimated error is less than 2.0 mm.

43.3 Model Based Measurement Using Improved Sensor

43.3.1 Model of the Muscle and Improved Inner Diameter Sensor

By using the empirical formula to obtain the axial displacement of the muscle, the simple and low-cost measuring system using the tiny embedded controller could be realized. However, the unknown parameter such as the inner diameter of the muscle to estimate the condition of the muscle also existed. In the next step, the method to measure both displacement and inner diameter of the muscle is proposed. Figure 43.5 show the geometric model of the rubber artificial muscle proposed by Chou [7]. The model shows the string with the length of b is n-times

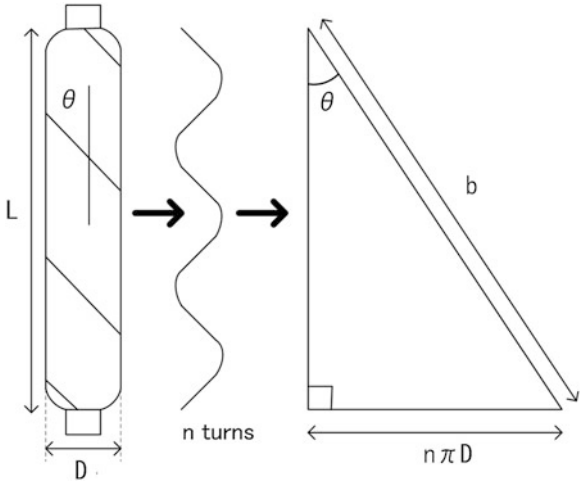

Fig. 43.5 Model of rubber artificial muscle

turned on the elastic tube with inclined angle of θ. From the geometric relation, the following equation can be obtained.

$$L = \sqrt{b^2 - (n\pi D)^2} \tag{43.2}$$

where, D and L show the effective inner diameter and length of the muscle, respectively. From Eq. (43.2), by measuring the effective inner diameter of the muscle exactly, the length of the muscle is calculated theoretically. In addition, it can also identify the design parameters of n and b that are useful to estimate the physical property of the muscle.

Figure 43.6 shows the construction of the improved inner diameter sensor. Compared with the previous sensor, the improved sensor has four photo-reflectors (GENIXTEK Co. Ltd., TPR-105F) to compensate the inclined angle of the sensor. The sensor also has three through holes between two electric circuit boards so as to realize compact electric lines and circuit. The size of the sensor is $9 \times 60 \times 8$ mm. The estimated cost of the sensor is low, that is less than 3 US dollars. By using a tiny embedded controller (Renesas Electronic Co. Ltd., R8CM12A), the total cost of the measuring system is about 4 US dollars. In addition, the compensation of inclined angle of the sensor while measuring the inner diameter was also executed by the tiny embedded controller [4].

43.3.2 Experimental Results

In order to estimate the output from the inner diameter sensor when the muscle is pressurized, it is necessary to measure the true value of the inner diameter. However, it is difficult to measure the inner diameter while the supply pressure is

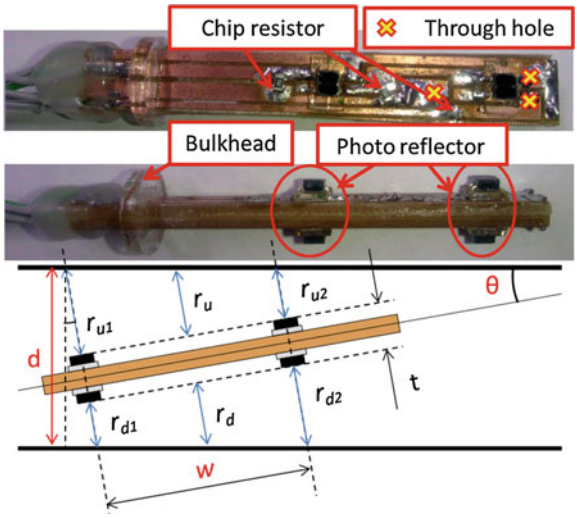

Fig. 43.6 Improved inner diameter sensor

applied because of seal and narrow space of the muscle. Therefore, the inner diameter was measured indirectly by measuring the outer diameter of the muscle when the brass rod with a certain outer diameter was inserted into the muscle as shown in Fig. 43.7. Figure 43.8 shows the relation between the square values of the effective inner diameter D^2 and length L^2 of the muscle. The inner diameter was measure by the method as shown in Fig. 43.7. The effective inner diameter means the diameter of the reinforced string in the muscle. From Fig. 43.8, we can confirm that the relation between both squared values D^2 and L^2 has a linear relationship based on the theoretical equation (43.2). From these results, we also identified the length of the string b of 270.2 mm and the number of turns n of 2.97 for the muscle with natural length of 247.5 mm.

Figure 43.9 shows the relation between the calculated effective inner diameter using the sensor and the actual inner diameter. The circles show the calculated results. The solid line shows the ideal case that the calculated diameter and the actual diameter are same. The calculated diameter can be obtained by using 4th order approximate equation based on the relation between the A/D values from the senor output and the measured effective inner diameter. In the experiment, the value of the diameter is calculated by the embedded controller and sent to PC through serial communication from the controller. The embedded controller also compensates the inclined angle of the inner diameter sensor by using outputs from four photo-reflectors. From Fig. 43.9, it can be seen that the inner diameter of the muscle can be calculated within standard deviation of error of 0.10 mm.

Figure 43.10 shows the relation between the measured and calculated length of the muscle using the calculated effective inner diameter, the model of the muscle given by Eq. (43.2) and identified parameters such as n and b. The calculation was done by the embedded controller (Renesas Co. Ltd. H8/3664). In Fig. 43.10, the circles show the calculated length, the solid line shows the ideal case that the

Fig. 43.7 Measurement of inner diameter

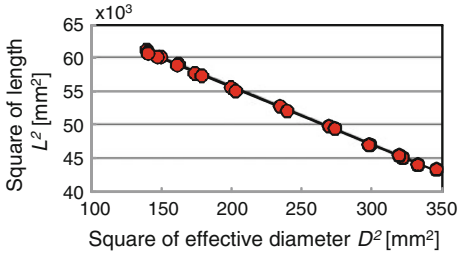

Fig. 43.8 Relation between D^2 and L^2

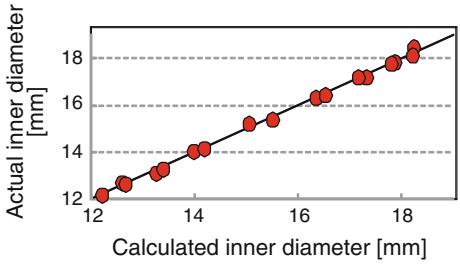

Fig. 43.9 Calculated effective inner diameter

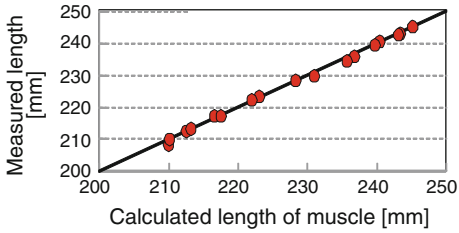

Fig. 43.10 Calculated length of the muscle

calculated and measured lengths of the muscle are same. From Fig. 43.10, we can confirm that the length of the muscle can be obtained based on the analytical model. The standard deviation of error is about 0.6 mm. This value is not superior to the previous method using the empirical formula from the sensor output. However, the proposed method can be also obtained the inner diameter that is useful to estimate the volume of the muscle. By using the measured inner diameter and identified parameters b and n, the length of the muscle can be also calculated even if the natural length of the muscle is changed. In addition, the error depends on the measurement accuracy of inner diameter. By using the superior photo-reflector, the whole measurement accuracy will be improved.

43.4 Conclusions

This study that aims to develop a high-power flexible actuator with a sensor for positioning which can be used in the water can be summarized as follows.

(1) The inner diameter of the muscle was measured by inserting brass cylinders with various diameters. The relation between the inner diameter and length of the muscle was investigated. As a result, we could confirm that the geometric model is useful to calculate the length of the muscle from the inner diameter. The design parameters of the rubber artificial muscle were also identified.
(2) By using the improved inner diameter sensor, the inner diameter could be measured with standard deviation of the error of 0.10 mm. The length of the muscle could be also obtained with standard deviation of the error of 0.6 mm by using the model and identified parameters.

As our future work, we are going to apply the tested rubber artificial muscle with the inner diameter sensor to rehabilitation device in the warm water.

Acknowledgments This study was supported by the Education Ministry of Japan through a Financial Assistance Program for QOL Innovative Research (2012-) and a Grant-in-Aid for Scientific Research (C) (Subject No. 24560315).

References

1. Noritsugu, T., Takaiwa, M., & Sasaki, D. (2009). Development of power assist wear using pneumatic rubber artificial muscles. *Journal of Robotics and Mechatronics, 21*, 607–613.
2. Kobayashi, H., Shiban, T., & Ishida, Y. (2004). Realization of all 7 motions for the upper limb by a muscle suit. *Journal of Robotics and Mechatronics, 16*, 504–512.
3. Nagata, Y. (Ed.). (2004). *Soft actuators—Forefront of development* (pp. 291–335). Tokyo: NTS Ltd.

4. Akagi, T., Dohta, T., Kenmotsu, Y., Zhao, F., & Yoneda, M. (2012). Development of smart inner diameter sensor for position control of Mckibben artificial muscle. *Journal of Procedia Engineering, 41*, 105–112.
5. Kuriyama, S., Ding, M., Kurita, Y., Ueda, J., & Ogasawara, T. (2009). Flexible Sensor for McKibben Pneumatic Artificial Muscle Actuator. *International Journal of Automation Technology, 3*, 731–740.
6. Wakimoto, S., Suzumori, K., & Kanda, T. (2005). Development of intelligent McKibben actuator with built-in soft conductive rubber sensor. In *International Conference on Solid-State Sensors, Actuators and Microsystems*, (Vol. 1, pp. 745–748).
7. Chou, C., & Hannaford, B. (1996). Measurement and modeling of McKibben pneumatic artificial muscles. *IEEE Transactions on Robotics and Automation, 12*, 90–102.

Chapter 44
Estimation of Pressure Control Performance in Low-Cost Quasi-Servo Valve Using Embedded Controller

So Shimooka, Shujiro Dohta, Tetsuya Akagi, Yoshinori Moriwake and Feifei Zhao

Abstract In our previous study, a small-sized and light-weight pressure control type quasi-servo valve was developed to reduce the burden of the user in a power-assisted system. The valve consists of inexpensive on/off control valves and embedded controller. In this study, the pressure control performances using four kinds of control scheme were investigated and compared by experiment and simulation. The frequencies up to 5 Hz were applied to the tested pressure control system. As an index of control performance, we used the mean absolute error. As a result, the sliding mode controller gave smaller error on the whole and PD controller gave the good performance in the higher frequency. It was confirmed that the introducing the dead zone to a control input and the lowering the supply pressure were effective to suppress the impulsive pressure change.

Keywords Quasi-servo valve · Small-sized control valve · Embedded controller

44.1 Introduction

Today, the care and welfare pneumatic equipment to support a nursing care and a self-reliance of the elderly and the disabled are actively researched and developed by many researchers [1, 2]. These wearable devices require many servo valves for multi degrees of freedom and precise control performance of the wearable actuator. The total weight load of the wearable devices increases according to the

S. Shimooka · S. Dohta (✉) · T. Akagi · Y. Moriwake
Department of Intelligent Mechanical Engineering, Okayama University of Science, Okayama 700-0005, Japan
e-mail: dohta@are.ous.ac.jp

F. Zhao
Tsuyama National College of Technology, Tsuyama, Okayama 708-8025, Japan

J. Juang et al. (eds.), *Proceedings of the 2nd International Conference on Intelligent Technologies and Engineering Systems (ICITES2013)*, Lecture Notes in Electrical Engineering 293,
DOI: 10.1007/978-3-319-04573-3_44,

degree of freedom. Therefore, we aim to develop a small-sized, light-weight and low-cost quasi-servo valve using on/off control valves to reduce the burden of the user instead of expensive and bulky electro-pneumatic servo valves. In our previous studies [3, 4], an inexpensive pressure control type quasi-servo valve using a low-cost embedded controller and a pressure transducer was proposed and tested. An analytical model of the pressure control type quasi-servo valve was also proposed. In this paper, the control performance of frequency response is estimated using the analytical model. In addition, the control performance of the valve is investigated experimentally by the tested pressure control system.

44.2 Quasi-Servo Valve

44.2.1 Construction

Figure 44.1 shows the schematic diagram of the quasi-servo valve. The valve consists of two on/off type control valves (Koganei Co. Ltd., G010HE-1) whose both output ports are connected each other. One valve is used as a switching valve to supply or exhaust, and the other is used as a PWM (Pulse Width Modulation) control valve that can adjust output flow rate like a variable fluid resistance [3]. The size of the on/off valve is 33 × 20 × 10 mm, and the mass is only 15 g. The maximum output flow rate is 38 l/min at the supply pressure of 500 kPa.

44.2.2 Analytical Model of Quasi-Servo Valve

In our previous study, the analytical model of the quasi-servo valve as shown in Fig. 44.2 was proposed, and the validity of the model and identified parameters was confirmed [3]. Here, the relation between pressure and flow rate which is important in control is described. The mass flow rates Q_s and Q_a shown in Fig. 44.2 are given as follows.

$$Q_s = A_s P_s \sqrt{\frac{2}{RT}} f(z), \quad z = \frac{P_o}{P_s} \tag{44.1}$$

$$Q_a = A_a P_o \sqrt{\frac{2}{RT}} f(z), \quad z = \frac{P_a}{P_o}. \tag{44.2}$$

where, A_s, A_a, P_s, P_o, P_a, R and T mean the sectional area of the supply orifice, the sectional area of the exhaust orifice, the supply pressure, pressure in the connected chamber, atmospheric pressure, a gas constant and an absolute temperature, respectively. The function *f(z)* that expresses the state of flow is given as follows.

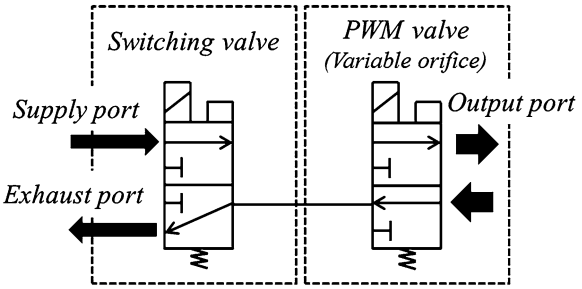

Fig. 44.1 Schematic diagram of quasi-servo valve

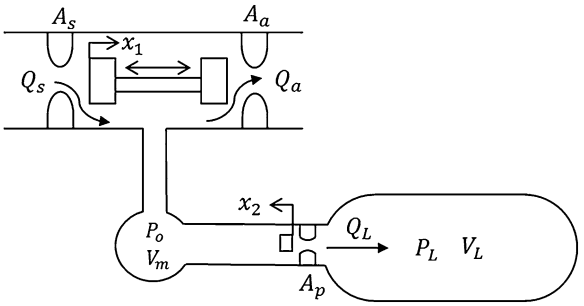

Fig. 44.2 Analytical model of the valve

$$f(z) = \sqrt{\frac{\kappa}{\kappa - 1}\left(z^{\frac{2}{\kappa}} - z^{\frac{(\kappa+1)}{\kappa}}\right)} \ (0.528 < z \leqq 1) \tag{44.3a}$$

$$f(z) = \sqrt{\frac{\kappa}{\kappa + 1}\left(\frac{2}{\kappa + 1}\right)^{\frac{2}{(\kappa-1)}}} \ (0 \leqq z \leqq 0.528) \tag{44.3b}$$

where κ means a specific heat ratio (=1.4).

If the pressure change in the connected chamber volume V_m is assumed as an adiabatic change, the relation between P_o and the output flow rate Q_o is given by

$$\frac{dP_o}{dt} = \frac{\kappa RT}{V_M} Q_o \tag{44.4}$$

$$Q_o = Q_s = Q_a - Q_L. \tag{44.5}$$

where Q_L is the flow rate through the orifice in the PWM valve and is expressed by

$$Q_L = A_p P_o \sqrt{\frac{2}{RT}} f(z), \quad z = \frac{P_L}{P_o} \ (Po \geqq P_L) \tag{44.6a}$$

$$Q_L = -A_p P_L \sqrt{\frac{2}{RT}} f(z), \quad z = \frac{P_o}{P_L} \ (Po < P_L). \tag{44.6b}$$

where A_p is the sectional area of the orifice in the PWM valve. The relation between pressure P_L in the volume and Q_L is given by

$$\frac{dP_L}{dt} = \frac{\kappa RT}{V_L} Q_L. \tag{44.7}$$

44.3 Pressure Control

The pressure control system consists of the quasi-servo valve, a pressure transducer (Matsushita Electronics Co. Ltd., ADP5160) and an inexpensive embedded controller (Renesas Co. Ltd. R8C12M). The pressure control is carried out as follows. First, the embedded controller gets the sensor output voltage and the reference voltage through an inner 10 b A/D converter. Then, the error between sensor output voltage and the reference voltage is calculated by a controller, and the control input is calculated based on a control scheme. Finally, the control input is applied to the quasi-servo valve. P, PD, PID control and sliding mode control (SMC for short) are used.

44.3.1 PID Control

The PID controller is expressed by following equations.

Switching valve:

$$\begin{array}{ll} u > 0 & \text{Switching valve : on} \quad \text{(Supply)} \\ u \leq 0 & \text{Switching valve : off} \quad \text{(Exhaust)} \end{array} \tag{44.8}$$

PWM valve:

$$u = K_p e_{c(i)} + K_i \sum_{j=0}^{i} e_{c(j)} + K_d (e_{c(i)} - e_{c(i-1)}) \tag{44.9}$$

$$u_s = u \frac{f(z)_{\max}}{f(z)} + 47.5, \quad z = \frac{P_L}{P_S} \quad \text{(Supply)} \tag{44.10}$$

$$u_s = u \frac{P_s}{P_L} \frac{f(z)_{\max}}{f(z)} + 47.5, \quad z = \frac{P_a}{P_L} \quad \text{(Exhaust)} \tag{44.11}$$

where u, K_p, K_i, K_d and e_c mean the input duty ratio for supply and exhaust, the proportional gain, the integral gain, the derivative gain and the error from the reference pressure, respectively. $f(z)_{\max}$ means the maximum value of $f(z)$ when the flow is sonic flow which is $f(z)_{\max} = 0.484$. $f(z)_{\max}/f(z)$ in Eq. (44.10) and (P_S/P_L)

$f(z)_{\max}/f(z)$ in Eq. (44.11) are for the compensation of the flow rate [3]. Because the valve has a dead zone for output flow rate, the input duty ratio of the PWM valve is always added by 47.5 %. In addition, when u is positive, the switching valve turns on, that is the supply state. In the opposite case, the valve turns off as shown in Eq. (44.8).

44.3.2 Sliding Mode Control

The sliding mode controller is expressed by following equations.

Switching valve:

$$s = e_{c(i)} + \alpha(e_{c(i)} - e_{c(i-1)}) \tag{44.12}$$

$$\begin{array}{ll} s > 0 & \text{Switching valve : on} \quad \text{(Supply)} \\ s \leq 0 & \text{Switching valve : off} \quad \text{(Exhaust)} \end{array} \tag{44.13}$$

PWM valve:

$$u_s = \left|K_p e_{c(i)}\right| \frac{f(z)_{\max}}{f(z)} + 47.5, \quad z = \frac{P_L}{P_S} \quad \text{(Supply)} \tag{44.14}$$

$$u_e = \left|K_p e_{c(i)}\right| \frac{P_s}{P_L} \frac{f(z)_{\max}}{f(z)} + 47.5, \quad z = \frac{P_a}{P_L} \quad \text{(Exhaust)} \tag{44.15}$$

where s and α mean the switching function and switching constant, respectively.

44.4 Control Performance

Figure 44.3 shows an example of frequency response of the output pressure. The broken line, dotted line and solid line show the reference, calculated and experimental pressure. In the simulation, the model of the embedded controller includes a 10 bit A/D converter and PWM port with PWM period of 5 ms. The sampling period of calculation is 0.01 ms and the sampling period of control is 3.2 ms. From Fig. 44.3, it can be seen that the calculated result agrees with the experimental. In both results, we can observe the impulsive pressure changes. It is considered that this impulsive change is caused by the use of on/off control valve.

Figure 44.4 shows the experimental results between the frequency and the mean absolute error (MAE for short) for four kinds of control scheme; P, PD, PID control and SMC. The applied frequency is from 0.1 to 5 Hz. The control parameters in P, PD and PID control were decided by trial and error and are shown in Table 44.1. The switching constant α in SMC is 0.1. It can be found that MAE for P, PD, PID control and SMC are almost constant in low frequency of 0.1–1 Hz;

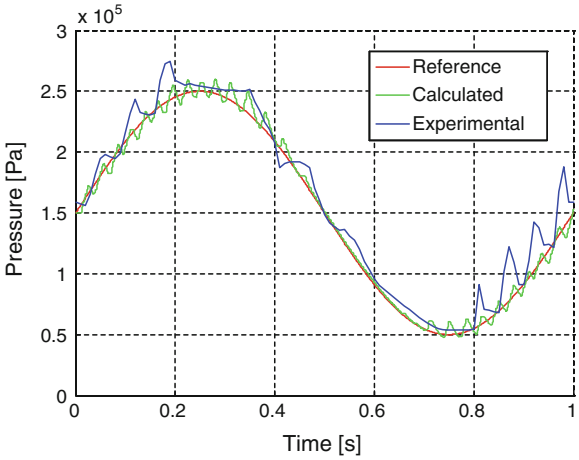

Fig. 44.3 Example of frequency response at 1 Hz

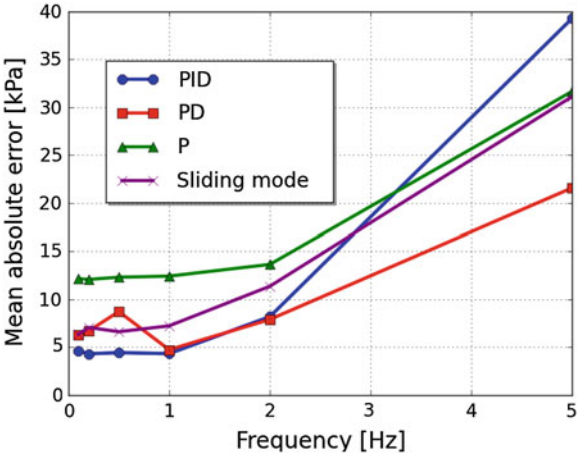

Fig. 44.4 Comparison of control performance

Table 44.1 Control parameters used in pressure control

Control scheme	K_p (%/kPa)	K_i (%/kPa)	K_d (%/kPa)
P	0.60	–	–
PD	0.79	–	1.99
PID	0.56	0.034	0.98

12, 7, 4.4 and 7 kPa. Thus, PID controller gives the good performance in low frequency. In the higher frequency of 2–5 Hz, PD controller gives the good performance. In the range from 0.1 to 5 Hz, the sliding mode controller shows smaller MAE on the whole.

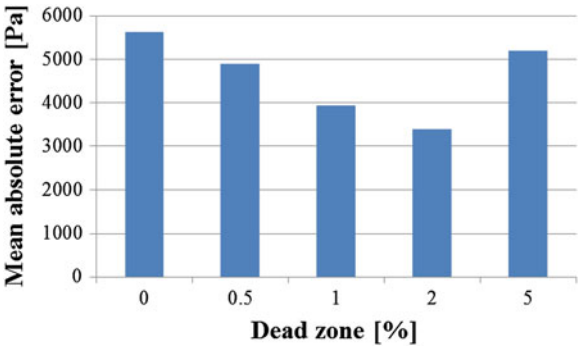

Fig. 44.5 Effect of dead zone

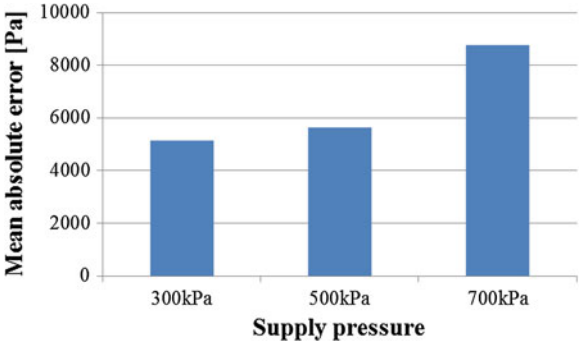

Fig. 44.6 Effect of supply pressure

In order to suppress the impulsive pressure change as shown in Fig. 44.3, a dead zone was introduced to a control input and the supply pressure was decreased. Figure 44.5 shows the relation between the dead zone and MAE for 1 Hz. From Fig. 44.5, it is found that the dead zone of 2 % shows the lowest MAE of 3.4 kPa. Figure 44.6 shows the effect of the supply pressure on MAE for 1 Hz. It can be seen that supply pressure of 300 kPa shows the lowest MAE of 5.1 kPa. Thus, it can be confirmed that the introducing the dead zone to a control input and the lowering the supply pressure are effective to suppress the impulsive pressure change.

44.5 Conclusions

This study can be summarized as follows. The pressure control was simulated by means of the analytical model of the pressure control system using the quasi-servo valve. The simulated results agree well with the experimental results. The control performances of frequency response using several control schemes were

investigated and compared by experiment and simulation. The frequencies of 0.1–5 Hz were applied to the pressure control system. The control schemes are P control, PD control, PID control and sliding mode control. As an index of control performance, the mean absolute error was selected and compared. As a result, PID controller gave the good performance in low frequency of 0.1–1 Hz. In the higher frequency of 2–5 Hz, PD controller gave the good performance. In the range from 0.1 to 5 Hz, the sliding mode controller gave smaller MAE on the whole. It was confirmed that the introducing the dead zone to control input and the lowering the supply pressure were effective to suppress the impulsive pressure change.

Acknowledgments This study was supported by the Ministry of Education, Culture, Sports, Science and Technology of Japan through a Financial Assistance Program for QOL Innovative Research (2012–).

References

1. Noritsugu, T., Takaiwa, M., & Sasaki, D. (2009). Development of power assist wear using pneumatic rubber artificial muscles. *Journal of Robotics and Mechatronics, 21*, 607–613.
2. Kobayashi, H., Shiban, T., & Ishida, Y. (2004). Realization of all 7 motions for the upper limb by a muscle suit. *Journal of Robotics and Mechatronics, 16*, 504–512.
3. Moriwake, Y., Akagi, T., Dohta, S., & Zhao, F. (2012). Development of low-cost pressure control type quasi-servo valve using embedded controller. *Journal of Procedia Engineering, 41*, 493–500.
4. Moriwake, Y., Akagi, T., Dohta, S., & Zhao, F. (2013). Improvement of pressure control type quasi-servo valve and on/off valves using embedded controller. In: IEEE/ASME International Conference on Advanced Intelligent Mechatronics (pp. 882–887).

Chapter 45
Computationally Improved Optimal Supervisory Control Policy for FMSs Using Petri Nets

Yen-Liang Pan, Cheng-Chung Yang, Mu-Der Jeng and Wei-Hsiang Liao

Abstract One novel control policy named selective siphon control policy [1] is proposed to solve deadlock problems in flexible manufacturing systems (FMSs). The novel policy not only solves the deadlock problem successfully but obtains maximally permissive controllers. In existing literature, the policy is the first one to achieve the goal of obtaining maximally permissive controllers for all Systems of Simple Sequential Processes with Resources (S^3PR) models. However, the proposed policy cannot check the exact number of maximally permissive states of a deadlock net in advance. After all iterating steps, the final maximally permissive can then be known. Additionally, all legal markings still to be checked again and again until all critical markings vanished. In this work, one computationally improved supervisory control methodology is proposed to solve the two problems. Experimental results show that the proposed methodology is practical and better than existing literatures.

Keywords Petri nets · Flexible manufacturing system · Supervisory control

45.1 Introduction

Deadlock prevention in FMSs includes structural analysis and reachability graphs. Deadlock prevention avoidance schemes have been developed for controlling FMS by using the former. In particular, deadlock prevention problems [2–4] are solved

Y.-L. Pan (✉) · W.-H. Liao
Department of Avionic Engineering, Air Force Academy, Kaohsiung 82047, Taiwan, Republic of China
e-mail: peterpan960326@gmail.com

C.-C. Yang
Department of Aeronautical and Mechanical Engineering, Air Force Academy, Kaohsiung 82047, Taiwan, Republic of China

M.-D. Jeng
Department of Electrical Engineering, National Taiwan Ocean University, keelung 20224, Taiwan, Republic of China

J. Juang et al. (eds.), *Proceedings of the 2nd International Conference on Intelligent Technologies and Engineering Systems (ICITES2013)*, Lecture Notes in Electrical Engineering 293,
DOI: 10.1007/978-3-319-04573-3_45,

using the concept of siphons. Unfortunately, those siphon control algorithms cannot obtain optimal controlled systems.

For improving above disadvantage of conventional siphon control, Piroddi et al. [1] proposed a novel control policy named selective siphon control for solving deadlock problem. According to our awareness, the above policy is the first deadlock prevention policy to achieve the goal which can obtain maximally permissive controllers for all S^3PR models in existing literature. However, the selective siphon control policy cannot explicitly calculate what the number of maximally permissive markings is in the first stages. Under their policy, all legal markings are needed to check again and again until all critical markings are vanished. This is time consuming since all legal markings are needed to check in each iterative step.

In this paper, one computationally improved methodology is proposed to solve above two problems. First of all, reachability graph is needed. Second, identify all markings and all markings of a reachability graph can be divided into three groups: legal markings (M_L), quasi-dead markings (M_Q), and dead markings (M_D). Therefore, the number of maximally permissive markings can then be obtained. Furthermore, the selective siphon control is only used for these critical markings so that all critical markings vanished. Most importantly, the computational efficiency is enhanced.

This work aims to develop a computationally optimal supervisory control policy. Section 45.2 presents the basic definitions and selective siphon control method. Section 45.3 describes the proposed policy. Section 45.4 presents the experimental results. Section 45.5 gives the comparisons and conclusions.

45.2 Preliminaries

45.2.1 Petri Nets (PN)

Due to limitation of paper space, the detailed theory of Petri net refers to [5].

45.2.2 Critical Markings and Selective Siphons Control Method [1]

Piroddi et al. [1] proposed the selective siphon control approach. The key of the policy is that once the selected siphons are controlled, all the paths from legal markings to critical markings are accordingly forbidden. In the following, uncontrolled siphons, critical markings, and selected siphons are defined.

Definition 45.1 [1] Uncontrolled siphons and critical markings:
Let $\Pi = \{S_1, \ldots, S_n\}$ the set of minimal siphons of *PN*.

(i) The set $\Pi_u = \{S_j \in \Pi | E_{Sj} \neq \emptyset\}$, where $E_{Sj} = \{M \in R(N, M_0) | \lambda_{Sj}^T M = 0\}$, is the set of uncontrolled siphons.
(ii) The set $\Pi_M = \{S_j \in \Pi_u | \lambda_{Sj}^{\mathrm{T}} M = 0\}$ denotes the set of empty siphons in the marking M.
(iii) For any $\Pi^* \subseteq \Pi_u$, $E_{\Pi^*} = \cup_{Sj \in \Pi^*} E_{Sj}$ is the set of markings where at least one siphon in Π^* is empty.
(iv) The set $E_{\Pi u}$ denotes the *set of critical markings*.
(v) A *covering set of uncontrolled siphons* (CSUS) is a subset of siphons $\Pi_c \subseteq \Pi_u$, such that $E_{\Pi c} = E_{\Pi u}$.

In sum, a siphon that is marked at any reachable marking is termed a controlled siphon, whereas an uncontrolled siphon gets empty of tokens in at least one reachable marking [1].

45.2.3 Synthesis Problem [6, 7]

It is assumed that a deadlock-prone PN model contains at least a dead marking in its reachability graph at which no transition is enabled. Based the reason, one can formally define the dead marking M_D as follows.

Definition 45.2 The set of *dead markings* $M_D = \{M \in R(N, M_0) |$ at M, no transition is enabled$\}$.

Definition 45.3 A zone consisting of M_D is called a *dead zone*, denoted by Z_D.

Once a marking enters a dead zone, the system is dead. Besides, all markings of a reachability graph can be divided into three groups: legal markings (M_L), quasi-dead markings (M_Q), and dead markings (M_D).

Definition 45.4 The set of *quasi-dead markings* $= \{M \in R(N, M_0) |$ M must eventually evolve to a dead one regardless of transition firing sequences$\}$.

Definition 45.5 A zone consisting of M_Q is called a *quasi-dead zone*, denoted by Z_Q.

Definition 45.6 A zone consisting of all quasi-dead and dead markings, i.e., $Z_I = Z_D \cup Z_Q$, is called an *illegal zone*.

Markings except quasi-dead and dead markings are legal ones.

Definition 45.7 A zone consisting of M_L is called a *legal zone*, i.e., $Z_L = R(N, M_0) - Z_I$.

No doubt, a system has the maximally permissive behavior if the system behavior equals Z_L. In other words, one must remove all the markings in illegal zone from $R(N, M_0)$ if one wants to obtain the maximally permissive behavior.

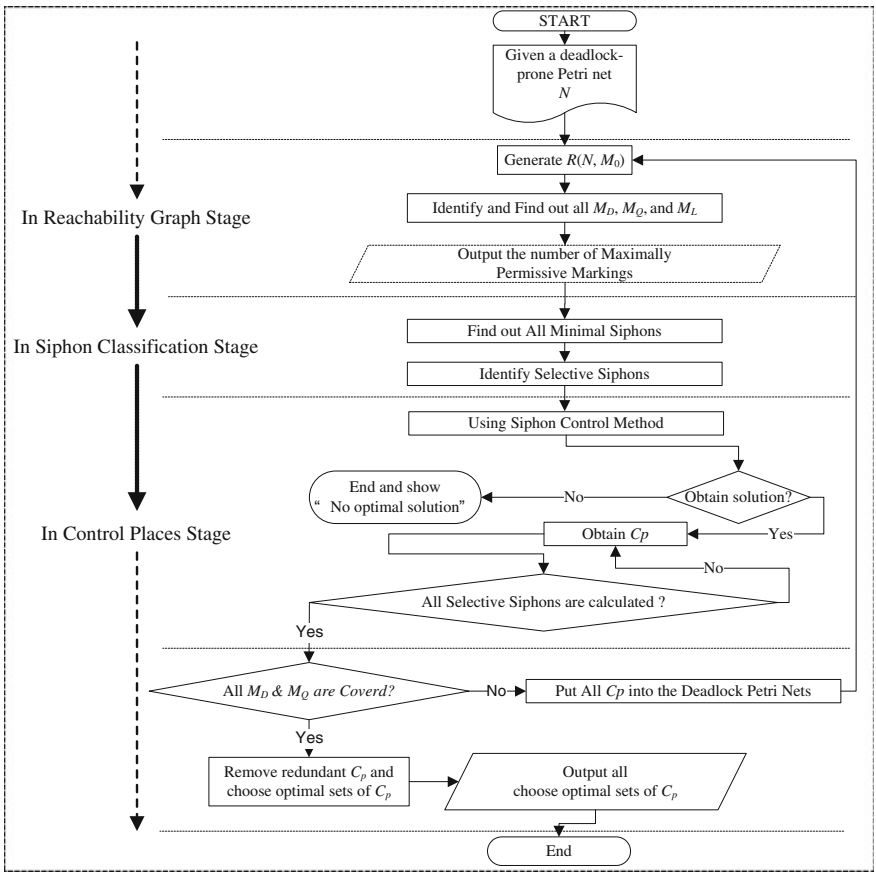

Fig. 45.1 Flow chart of the proposed deadlock prevention

45.3 The Proposed Methodology

In this paper, one computationally improved methodology is proposed to enhance the computational efficiency of conventional selective siphon control technology. The methodology is main consist of four stages. They are reachability graph running stage, siphon classification stage, siphon controlling stage, and maximally permissive live markings obtaining. The follow chart is shown in Fig. 45.1.

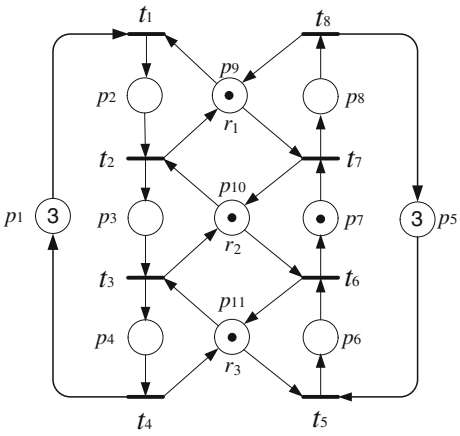

Fig. 45.2 One classical FMS PN model [8]

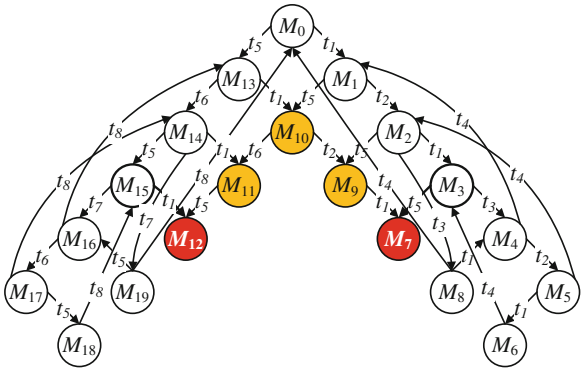

Fig. 45.3 The reachability graph of a classical example

45.4 Experimental Results

In this section, one classical FMS example shown in Fig. 45.2 is used to evaluate our deadlock prevention policy. It is taken from [8]. This PN is a system of S^3PR, denoted by (N_1, M_0). To do our deadlock prevention policy, $R(N_1, M_0)$ of the PN system can be constructed as shown in Fig. 45.3.

Additionally, five illegal markings are identified. Their detailed information is shown in Table 45.1. Hence, the number of legal markings (i.e. $20 - (2 + 3) = 15$) can then be determined. In other words, the number of maximally permissive markings is 15. In the following, three sets of minimal siphons $S_1 = \{p_3, p_8, p_9, p_{10}\}$, $S_2 = \{p_4, p_7, p_{10}, p_{11}\}$, and $S_3 = \{p_4, p_8, p_9, p_{10}, p_{11}\}$ are obtained in this example. Additionally, according to the definition in [1], S_1 and S_2 are the two sets of selective siphons. The detailed information of selective siphons in first stage is shown in Table 45.2. In siphon control stage, two control places

Table 45.1 The detailed information of dead and quasi-dead markings

Marking no.	Information of marking [p_1, p_2, p_3, p_4, p_5, p_6, p_7, p_8, p_9, p_{10}, p_{11}]	Classification
M_7	[1, 1, 1, 0, 2, 1, 0, 0, 0, 0, 0]	M_D
M_{12}	[2, 1, 0, 0, 1, 1, 1, 0, 0, 0, 0]	M_D
M_9	[2, 0, 1, 0, 2, 1, 0, 0, 1, 0, 0]	M_Q
M_{10}	[2, 1, 0, 0, 2, 1, 0, 0, 0, 1, 0]	M_Q
M_{11}	[2, 1, 0, 0, 2, 0, 1, 0, 0, 0, 1]	M_Q

Table 45.2 The detailed information of selective siphons in first stage for example 1

	S_1	S_2	S_3
$\boldsymbol{M_7}$		x	x
$\boldsymbol{M_{12}}$	x		x
$\boldsymbol{M_9}$		x	
$\boldsymbol{M_{10}}$			
$\boldsymbol{M_{11}}$	x		

Table 45.3 The first stage additional control places in example 1

Control places	$M_0(C_{pi})$	$\bullet(C_{pi})$	$(C_{pi})\bullet$
P_{C1}	1	t_2, t_7	t_1, t_6
P_{C2}	1	t_3, t_6	t_2, t_5

Table 45.4 The detailed information of selective siphons in second stage for example 1

	S_4	S_5	S_6	S_7
$\boldsymbol{M_{10}}$	x	x	x	X

shown in Table 45.3 are then obtained by siphon control method [3]. Please note that the quasi-dead marking M_{10} is not covered by all siphons. Therefore, for seeking selective siphon in second is necessary. Furthermore, in this work we just focus on the critical marking (quasi-dead marking) M_{10} while the conventional selective siphon method has to check all markings.

In second stage, four sets of minimal siphons $S_4 = \{p_3, p_7, p_{12}, p_{13}\}$, $S_5 = \{p_3, p_8, p_9, p_{12}, p_{13}\}$, $S_6 = \{p_4, p_7, p_{11}, p_{12}, p_{13}\}$, and $S_7 = \{p_4, p_8, p_9, p_{11}, p_{12}, p_{13}\}$ are obtained after the two control places are added into the example.

Besides, the elements of critical marking M_{10} become [2, 1, 0, 0, 2, 1, 0, 0, 0, 1, 0, 0, 0] since above two control places are added. All empty siphons are selective siphons since all places of these selective siphons are empty in M_{10}. Their relation is shown in Table 45.4. Therefore, we just pick one simply siphon to calculate. The final control Cp_3 can then be obtained shown in Table 45.5. No doubt, the example is deadlock free when control place P_{C3} is added.

Table 45.5 The second stage additional control place in example 1

Control Places No	$M_0(C_{pi})$	$\bullet(C_{pi})$	$(C_{pi})\bullet$
P_{C3}	1	t_2, t_6	t_1, t_5

Table 45.6 The comparison results in example 1

Important parameter comparison	[1]	This work
Optimal (Maximally permissive) control?	Yes	Yes
Can make sure the exact number of optimal states in first stage?	No	Yes
How many reachable markings are needed to check in first stage?	20	5
How many reachable markings are needed to check in second stage?	16	1

45.5 Comparison and Conclusions

Based on Table 45.6, our deadlock prevention can make sure the exact number of maximally permissive live (legal) markings in the reachability running stage. Besides, there are just five markings in first stage and only one marking is needed to check by selective siphons, respectively. To summarize, our work presents a computationally improved optimal control algorithm than the existing literature [1].

References

1. Piroddi, L., Cordone, R., & Fumagalli, I. (2008). Selective siphon control for deadlock Prevention in Petri Nets. *IEEE Transaction on Systems, Man, and Cybernatics, Part A: Systems and Humans, 38*, 1337–1348.
2. Ezpeleta, J., Colom, J. M., & Martinez, J. (1995). A Petri net based deadlock prevention policy for flexible manufacturing systems. *IEEE Transactions on Robotics and Automation, 1*, 173–184.
3. Huang, Y. S., Jeng, M. D., Xie, X. L., & Chung, S. L. (2001). A deadlock prevention policy based on Petri nets and siphons. *International Journal of Production Research, 39*, 283–305.
4. Li, Z. W., & Zhou, M. C. (2004). Elementary siphons of Petri nets and their application to deadlock prevention in flexible manufacturing systems. *IEEE Transaction on Systems, Man, and Cybernatics, Part A: Systems and Humans, 34*, 38–51.
5. Murata, G. T. (1989). Petri nets: Properties, analysis and applications. *Proceedings of the IEEE, 77*, 541–580.
6. Huang, Y. S., Pan, Y. L., & Zhou, M. C. (2012). Computationally improved optimal deadlock control policy for flexible manufacturing systems. *IEEE Transaction on Systems, Man, and Cybernatics, Part A: Systems and Humans, 42*, 404–415.
7. Pan, Y. L. (2012). *A computationally improved optimal solution for deadlocked problem of flexible manufacturing systems using theory of regions*. Petri Nets—Manufacturing and Computer Science (Chap. 3, pp. 51–74). InTech. (ISBN 978-953-51-0700-2).
8. Abdallah, I. B., & ElMaraghy, H. A. (1998). Deadlock prevention and avoidance in FMS: A petri net based approach. *International Journal of Advanced Manufacturing Technology, 14*, 704–715.

Chapter 46
An Improved Random Decrement Algorithm with Time-Varying Threshold Level for Ambient Modal Identification

Chang-Sheng Lin, Tse-Chuan Tseng and Din-Goa Huang

Abstract Modal Identification from response data only is studied for structural systems under nonstationary ambient vibration. The topic of this paper is the estimation of modal parameters from nonstationary ambient vibration data by applying the random decrement algorithm with time-varying threshold level. In the conventional Random Decrement Algorithm, the threshold level for evaluating randomdec signatures is defined as the standard deviation value of response data of the reference channel. However, the distortion of randomdec signatures may be induced by the error involved in the noise obtained from the original response data in practice. To improve the accuracy of identification, a modification of the sampling procedure in random decrement algorithm is proposed for modal-parameter identification from the nonstationary ambient response data. The time-varying threshold level is presented for the acquisition of more sample time history to perform averaging analysis, and defined as the temporal root-mean-square function of structural response, which can appropriately describe a wide variety of nonstationary behaviors in reality. Numerical simulations confirm the validity and robustness of the proposed modal-identification method from nonstationary ambient response data under noisy conditions.

Keywords Modal identification · Nonstationary ambient vibration · Random decrement algorithm · Time-varying threshold level · Temporal root-mean-square function

C.-S. Lin (✉) · T.-C. Tseng · D.-G. Huang
Precision Mechanical Engineering Group, Instrumentation Development Division, National Synchrotron Radiation Research Center, Hsinchu 30076, Taiwan, Republic of China
e-mail: lin.changsheng@nsrrc.org.tw

J. Juang et al. (eds.), *Proceedings of the 2nd International Conference on Intelligent Technologies and Engineering Systems (ICITES2013)*, Lecture Notes in Electrical Engineering 293,
DOI: 10.1007/978-3-319-04573-3_46,

46.1 Introduction

The basic idea behind the RDD algorithm is to pick out time segments and average them each time the response satisfies a given initial condition. The RDD algorithm helps extract free-decay response data that can be further used for operational modal analysis. In the previous studies of modal identification through the RDD algorithm, the threshold level of RDD algorithm were defined as the standard derivation value of response data of the reference channel [1]. However, the distortion of randomdec signatures may be induced by the error involved in the noise obtained from the original response data in practice. In the present paper, we propose a technique to improve the effectiveness of modal identification through the RDD algorithm with time-varying threshold level. The time-varying threshold level for the acquisition of sample time history and defined as the temporal root-mean-square function of structural response, which can properly describe the approximate time variation as nonstationary trends. Numerical simulations confirm the validity and robustness of the proposed modal-identification method from nonstationary ambient response data under noisy conditions.

46.2 Improved Nonstationary Random Decrement Algorithm with Time-Varying Threshold Level

According to the theory of conventional random decrement algorithm, to obtain the random decrement signature, the response is pre-divided into N averaged time segments, each with the same time length τ. Note that all of these segments should have the same initial condition, which is usually referred to as the so-called triggering value. Through the ensemble averaging of N pre-selected sample segments of the response measurement, the following time function can be obtained:

$$\delta(\tau) = \frac{1}{N}\sum_{i=1}^{N} q_r(t_i + \tau) \tag{46.1}$$

where $q_r(t)$ denotes the rth component of the modal displacement response $q(t)$, $\delta(\tau)$ denotes the random decrement signature obtained from the ensemble average of the N segments, and t_i denotes the time instant when the random signal crosses the threshold condition. Equation (46.1) implies that constant time segments $[t_i, t_i + \tau]$ were extracted from $q_r(t)$. The following equation can be obtained as follows:

$$\begin{aligned}\delta(\tau) &= \frac{1}{N}\sum_{i=1}^{N} -e^{-\xi_r\omega_r\tau}\left[q_{t_i r}\cos\omega_{dr}\tau + \frac{\dot{q}_{t_i r} + \xi_r\omega_r q_{t_i r}}{\omega_{dr}}\sin\omega_{dr}\tau\right] \\ &\quad + \frac{1}{N}\sum_{i=1}^{N} -e^{-\xi_r\omega_r\tau}\left[q_{t_i rp}\cos\omega_{dr}\tau + \frac{\dot{q}_{t_i rp}\sin\omega_{dr}\tau}{\omega_{dr}}\right] + \frac{1}{N}\sum_{i=1}^{N} q_{rp}(t_i+\tau) \qquad (46.2) \\ &= e^{-\xi_r\omega_r\tau}\left[A_r\cos\omega_{dr}\tau + \frac{B_r + \xi_r\omega_r A_r}{\omega_{dr}}\sin\omega_{dr}\tau\right] + \Theta(\tau)\end{aligned}$$

where the $e^{-\xi_r\omega_r\tau}\left[A_r\cos\omega_{dr}\tau + \frac{B_r+\xi_r\omega_r A_r}{\omega_{dr}}\sin\omega_{dr}\tau\right]$ term in Eq. (46.2) implies that $\delta(\tau)$ contains the behavior of free-decay vibration, while

$$\begin{aligned}\Theta(\tau) &= -e^{-\xi_r\omega_r t}\left[\frac{1}{N}\sum_{i=1}^{N} q_{rp}(t_i)\ \cos\omega_{dr}\tau + \frac{\xi\omega_n\sum_{i=1}^{N} q_{rp}(t_i) - \sum_{i=1}^{N}\dot{q}_{rp}(t_i)}{\omega_{dr}}\sin\omega_{dr}\tau\right] \\ &\quad + \frac{1}{N}\sum_{i=1}^{N} q_{rp}(t_i+\tau)\end{aligned}$$

corresponds to the behavior due to force vibration. If the input excitation is assumed to be a nonstationary random process with zero-mean, the behavior due to force vibration will be vanished by performing the random-decrement averaging [2]. It has been shown that an improvement to the random decrement algorithm is presented for modal identification from zero-mean nonstationary ambient vibration data. We can perform the random-decrement averaging over the nonstationary-responses samples to obtain good improved RDD signatures, as quasi free-vibration data for further modal identification. By treating the sample improved RDD signatures of measured response as output from free vibration decay, a time-domain modal identification method, such as the Ibrahim Time-Domain method [3], can then be employed to extract (complex) modal parameters of a structure.

It has been shown in a previous paper [4] that the temporal root-mean-square functions of the response histories describe the same time variation as given by the envelope function. This suggests that if the original nonstationary data could be represented by the product model with a slowly varying envelope function, the temporal root-mean-square functions of the data also have the same nonstationary trend as that of the original data. The temporal root-mean-square function can thus be determined by using interval average and then applying curve-fitting technique. The temporal root-mean-square function of each DOF is proportional to the same envelope function of time, and can properly describe the approximate time variation as nonstationary trends. Based on the concept mentioned above, in this paper, we introduce the temporal root-mean-square function of structural response as the time-varying threshold level to acquire more sample time history for performing random-decrement average in the procedure of RDD algorithm, and therefore could avoid the distortion of randomdec signatures may be induced by the error involved in the noise obtained from the original response data in practice.

The randomdec signatures of response data can then be obtained, which are in turn treated as the free-decay responses corresponding to each DOF, without reducing the nonstationary problem to a stationary one by extracting the amplitude-modulating function from the original nonstationary data via curve-fitting technique. The modal parameters of the system can then be obtained via a time-domain modal-identification method.

46.3 Numerical Simulation

To demonstrate the effectiveness of the proposed method, we consider a linear 6-dof chain model with viscous damping. A schematic representation of this model is shown in Fig. 46.1. The mass matrix $\boldsymbol{M}$, stiffness matrix $\boldsymbol{K}$, and the damping matrix $\boldsymbol{C}$ of the system are given as follows:

$$\boldsymbol{M} = \begin{bmatrix} 2 & 0 & 0 & 0 & 0 & 0 \\ 0 & 2 & 0 & 0 & 0 & 0 \\ 0 & 0 & 2 & 0 & 0 & 0 \\ 0 & 0 & 0 & 2 & 0 & 0 \\ 0 & 0 & 0 & 0 & 3 & 0 \\ 0 & 0 & 0 & 0 & 0 & 4 \end{bmatrix} \text{Kg}, \quad \boldsymbol{K} = 600 \cdot \begin{bmatrix} 1 & -1 & 0 & 0 & 0 & 0 \\ -1 & 2 & -1 & 0 & 0 & 0 \\ 0 & -1 & 2 & -1 & 0 & 0 \\ 0 & 0 & -1 & 2 & -1 & 0 \\ 0 & 0 & 0 & -1 & 3 & -2 \\ 0 & 0 & 0 & 0 & -2 & 5 \end{bmatrix},$$

$$\boldsymbol{C} = 0.05\boldsymbol{M} + 0.001\boldsymbol{K} + 0.2 \begin{bmatrix} 1 & \dots & 1 \\ \vdots & \ddots & \vdots \\ 1 & \dots & 1 \end{bmatrix}_{6\times 6} \text{N} \cdot \text{s/m}$$

Note that the damping matrix $\boldsymbol{C}$ is not a linear combination of $\boldsymbol{M}$ and $\boldsymbol{K}$, so that the system has non-proportional damping (and so complex modes). Consider that the ambient vibration input can be modeled as nonstationary white noise as represented by the product model. The stationary white noise is generated using the spectrum approximation method [5] as a zero-mean band-pass noise, whose standard deviation is $0.02\,\text{N}^2 \cdot \text{s/rad}$ with a frequency range from 0 to 50 Hz. The sampling interval is chosen as $\Delta t = 0.01\,\text{s}$, and the sampling period is $T = N_t \cdot \Delta t = 1310.72\,\text{s}$, where N_t was chosen as 2^{17} to assure that more than 500 good samples of shifted signals can be obtained for performing the random-decrement averaging. The stationary white noise simulated is then multiplied by an amplitude-modulating function $\Gamma(t) = 4 \cdot (e^{-0.002t} - e^{-0.004t})$to obtain the nonstationary white noise, which serves as the excitation input acting on the sixth mass point of the system. The displacement responses of the system were obtained through Newmark's method [6]. To examine the robustness of the proposed identification approach under noisy conditions, 10 % noise is added to the simulated displacement response data. By examining the Fourier spectra associated with each of the response channel, we chose the third channel's response $X_3(t)$,

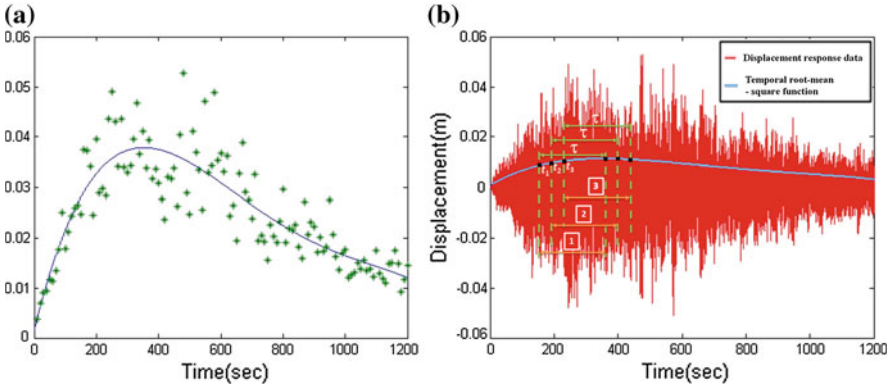

Fig. 46.1 Schematic plot of the time-varying threshold level in the procedure of RDD algorithm **a** temporal root-mean-square function obtained from curve-fitting technique, and introduced as **b** time-varying threshold in RDD algorithm

which contains richer overall frequency information, as the reference channel to evaluate the randomdec signatures of the system. According to the theory presented in the previous sections, by introducing the time-varying threshold level in the procedure of RDD algorithm, as shown in Fig. 46.1, the randomdec signatures of a system can be obtained through the improved RDD algorithm without reducing the nonstationary problem to a stationary problem by extracting the amplitude-modulating function from the original nonstationary data. The improved randomdec signatures thus obtained, are treated as free-vibration data. The Ibrahim time-domain method could then be applied to identify modal parameters of the system.

The results of modal identification through the improved RDD algorithm with time-varying threshold level and the conventional RDD algorithm in conjunction with a curve-fitting technique are summarized in Tables 46.1. Note that the "exact" modal damping ratios listed in Table 46.1 are actually the equivalent modal damping ratios obtained by utilizing ITD from the free vibration response data of the nonproportionally damped structure. The identified mode shapes obtained from the improved RDD algorithm with time-varying threshold level are compared with exact values in Fig. 46.2, where good agreement is observed.

The errors of identified modal parameters of the system through the conventional RDD algorithm coupled with a curve-fitting technique are also summarized in Table 46.1, which show that the errors in natural frequencies are less than 1 % and the maximum error in damping ratios is about 33 %, and are somewhat larger than those through the improved RDD algorithm with time-varying threshold level, especially for the identified damping ratios. The modal-identification results of the numerical simulations indicate that the robustness of the improved RDD algorithm with time-varying threshold level is better than that of the conventional RDD algorithm coupled with curve-fitting technique, and this proposed method

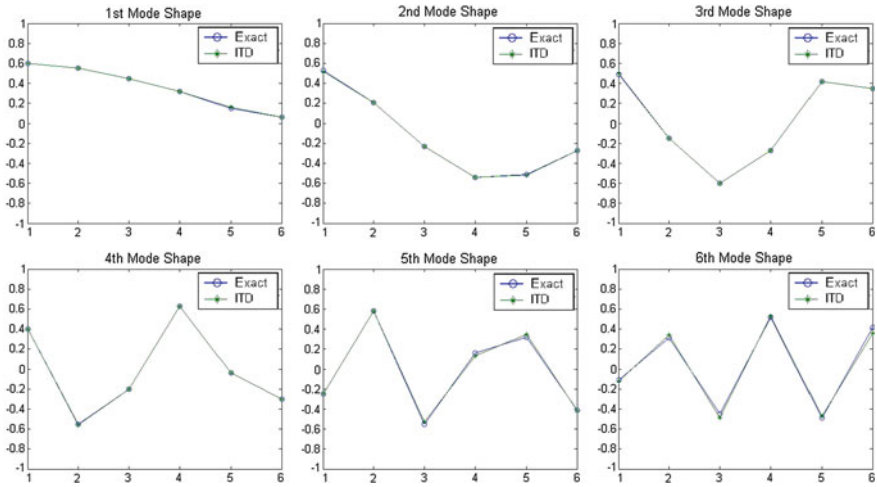

Fig. 46.2 Comparison between the identified mode shapes (the improved RDD algorithm with time-varying threshold level) and the exact mode shapes of the 6-DOF chain system subjected to nonstationary white-noise input

Table 46.1 Results of natural frequency and damping ratio identification

Mode	Time-varying threshold level			Curve-fitting technique		
	Exact	ITD	Error (%)	Exact	ITD	Error (%)
Natural frequency (rad/sec)						
1	5.03	5.02	0.11	5.03	5.04	0.14
2	13.45	13.43	0.13	13.45	13.43	0.12
3	19.80	19.73	0.36	19.80	19.73	0.34
4	26.69	26.48	0.80	26.69	26.44	0.95
5	31.66	31.41	0.78	31.66	31.47	0.60
6	33.73	33.47	0.78	33.73	33.54	0.57
Damping ratio (%)						
1	5.24	6.10	16.41	5.24	6.95	32.63
2	1.07	1.12	4.67	1.07	1.18	10.28
3	1.13	1.17	3.54	1.13	1.18	4.42
4	1.43	1.38	3.50	1.43	1.69	18.18
5	1.66	1.92	15.66	1.66	1.86	12.05
6	1.74	1.94	11.49	1.74	2.26	29.89

Obtained from the simulated ambient response data contaminated with 10 % noise, of the 6-dof chain system subjected to nonstationary white-noise input

may be relatively applicable to identify modal parameters of a system from the ambient response data under noisy conditions. It should be mentioned that, the errors of identified damping ratios are somewhat larger than those of identified natural frequencies, due to the fact that the system response generally has lower sensitivity to damping ratios than to the natural frequencies.

46.4 Conclusions

For the purpose of identifying dynamic characteristics of structures, the modal-analysis method of using measured responses to ambient nonstationary excitation is studied. To improve the accuracy of identification, a modification of the sampling procedure in random decrement algorithm is proposed for modal identification from the nonstationary ambient response data without the restriction of stationary response in conventional RDD algorithm. The time-varying threshold level is presented for the acquisition of more sample time history and defined as the temporal root-mean-square function of structural response, which can appropriately describe a wide variety of nonstationary behaviors in reality. Through numerical simulations, the effectiveness and robustness of the proposed identification method is demonstrated. By taking advantage of the computation of improved randomdec signatures through the time-varying threshold level introduced in the procedure of RDD algorithm to perform modal identification, we avoid a distortion in the modal parameters of identification induced by the error involved in the approximate quasi-stationary response obtained through curve-fitting technique.

References

1. Cole, H. A., Jr. (1971). "Method and apparatus for measuring the damping characteristics of a structure." United States Patent No. 3, 620, 069,
2. Lin, C. S., & Chiang D. Y. (2013). Modal identification from nonstationary ambient response data using extended random decrement algorithm. *Computers & Structures*, *119*, 104–114.
3. Ibrahim, S. R., & Mikulcik, E. C. (1977). A method for the direct identification of vibration parameters from free response. *Shock and Vibration Bulletin, 47*(4), 183–198.
4. Chiang, D. Y., & Lin, C. S. (2008). Identification of modal parameters from nonstationary ambient vibration data using correlation technique. *AIAA Journal, 46*(11), 2752–2759.
5. Shinozuka, M., & Jan, C.-M. (1972). Digital simulation of random processes and its applications. *Journal of Sound and Vibration, 25*(1), 111–128.
6. Newmark, N. M. (1959). A method of computation for structural dynamics. *Journal of Engineering Mechanics, ASCE, 85*(EM3), 67–94.

Chapter 47
Applying Virtual Reality to Remote Control of Mobile Robot

Gin-Shan Chen and Jih-Ping Chen

Abstract Aiming at remotely operating robots in Virtual Reality, an experiment site with solid experimental equipment is first placed; then, the experimental equipment and scene modeling are input to Virtual Reality for establishing an environment similar to the reality; and finally, the remote mobile robot is controlled to operate assembly through wireless communication by the object operation in Virtual Reality. The robot consists of a movable robot platform and robotic arm with seven degrees of freedom; the Virtual Reality is constructed by Quest3D software; and, the wireless connection is equipped the wireless AP (Access Point), which is set the same domain as the router in the control site for the connection control. With experimental tests to verify the robot in Virtual Reality and the wireless remote control, the robot could be operated and controlled to successfully complete assembly in reality.

Keywords Virtual reality · Quest3D · Mobile robot · Assembly · Remote control

47.1 Introduction

Virtual Reality (VR) has been widely applied to various industries with the development of science and technology, such as entertainment, education, military affairs, medical science, space science, industrial design, architecture, and manufacturing. Playing a critical role in such domains, VR integrates the machinery equipment and becomes the development of human machine interface (HMI). VR is often applied to aided instruction, training, or simulation of manufacturing process and restoring the real scenes. In addition to excluding the restrictions of

G.-S. Chen (✉) · J.-P. Chen
Graduate School of Mechatronic Technology, Yung-Ta Institute of Technology and Commerce, Pingtung 909, Taiwan, Republic of China
e-mail: gschen@mail.ytit.edu.tw

J. Juang et al. (eds.), *Proceedings of the 2nd International Conference on Intelligent Technologies and Engineering Systems (ICITES2013)*, Lecture Notes in Electrical Engineering 293,
DOI: 10.1007/978-3-319-04573-3_47,

location and space, it could avoid people and machine damage and reduce educational costs.

The popularity of mechanical automation has resulted in many manufacturers largely replacing manpower with robots. Mobile robots are expected to enhance the ability of the users in executing complex work in a remote environment [1, 2]; however, wrong operation or errors would still occur when robots are set and operated by manpower that on-site danger and machinery breakdown could be caused. For this reason, trainings with VR replacing the real operartion training could reduce the maintenance costs resulted from on-site accident and machinery breakdown.

Furthermore, the development costs for a real prototype is considerably high, and the assembly process could not be repeatedly applied that assembly presents equal importance to the design and manufacturing process [3, 4]. For machinery assembly, the aid of reinforced reality could reduce errors and establish a virtual team collaboratively completing the machinery assembly.

This study expects to applied the interactive VR to having the users rapidly and clearly understand the operation, implementing the simulation of robot operation in the actual environment, and operate and control the mobile robot in the reality through wireless remote monitoring and control so as to successfully complete the assembly by a robot.

47.2 System Structure

The experimental framework for controlling mobile robotic arm proceeding assembly with the integration of VR and remote control is explained as follows.

The hardware framework contains robotic arm, mobile robot, wireless broadband router, and Laptop. The model for the robotic arm with seven degrees of freedom is Cyton Alpha 7D 1G. The model for the mobile robot platform is MOBILE ROBOTS Pioneer 3–DX. The model for the wireless broadband router is D-Link DI-624. COMPAC Laptop is used for the control, which is equipped with ADM Turionx2 Dual-Core Mobile RM-70 2.00 GHz processing unit, Windows Vista operating system, 2G memory (RAM), and ATI Mobility Radeon HD3450 graphics card.

An ODE (Open Dynamics Engine) is included in Quest3D, functions to present the physical properties of an object, such as physical collision, friction, and gravity effect, so as to vivify the objects in VR. The solid graphic module of robotic arm and mobile robot are constructed with Inventor 10 software and transferred into DirectX.X file with PolyTrans software for being edited in Quest3D. The remote control software in this study is designed by ARIA especially for mobile robot. Action Viewer is developed by Energid for controlling robotic arm. A Laptop is used for connecting with Wireless Network.

47.3 Virtual Reality

The Robot Association started studying the applications of VR in 1990 and regarded the great potential of VR for HMI [5, 6]. The applications of VR have expanded the remote monitoring field for human beings. With the effects of computer speed and network transmission rate, the early research could merely transmitted noncontinuous frames and limited information. To overcome the delay, robots and the 3D interface for the work environment were utilized for remote operation, providing an operator with real scenes for replacing the delayed images [7]. Regarding the applications of robotic arms, 2D plane displays could not satisfy the high-degree of freedom movements of robotic arms. 3D graphs therefore is utilized for displaying various information to better correspond to an operator's demands.

The control of virtual object is also described as follows. To have identical motions of virtual objects and real objects, the rotation and movement of a real object should be understood. Figure 47.1 shows the rotation of robotic arms in various angles, including Roll, Pitch, and Yaw. In consideration of the control power being the key in machinery design, virtual simulation should present the same concept [8]. For this reason, the movement and overall moving procedure of a real object should be actually realized in advance so as to establish the control of virtual objects in Quest3D.

With the example of wheel control of a mobile robot, the wheel control is equipped as in Fig. 47.2, in which A + B stands for being operated when one of or both Channels A and B functions; (A − B) * C represents being operated after reading the parameter in Channel C when merely one of Channels A and B is accepted. Such two judgments could control the rotation direction of wheels; besides, the parameters for forward, backward, left turn, right turn, and distance movement are set, which are respectively operated by ⌜↑⌟, ⌜↓⌟, ⌜←⌟, and ⌜→⌟ on the keyboard. The adjustment of damping parameter could change the speed of module motion.

47.4 Virtual Reality Integrated Mobile Robot Control

The virtual scenes are first input to the module in Quest3D, Channel is used for setting the control parameters of objects, and mobile robot and communication framework are further installed. The robot test is then proceeded in VR, as the following procedure.

47.4.1 Control Procedure

An indoor solid experiment is first setup, which includes mobile robot, robotic arm, work platform, and communication framework. A similar scene is also

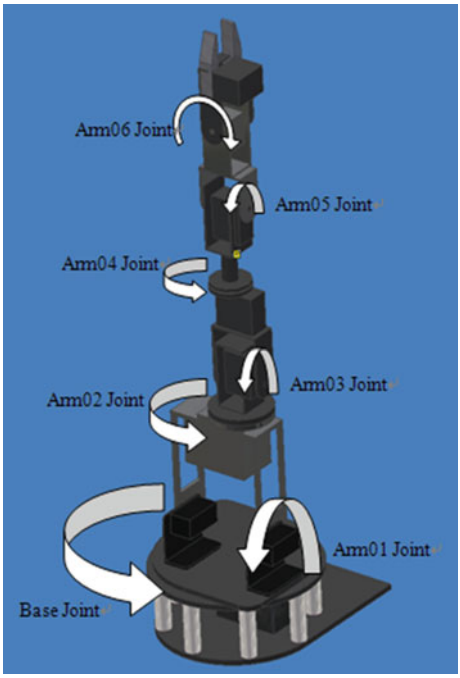

Fig. 47.1 Definitions of robotic arm

established in VR to verify the synchronous operation of the robot. In the experimental scene, a mobile robot equipped with robotic arm and two platforms are established; No. 1 platform is equipped with peg and No. 2 platform is equipped three holes with different shapes. The robot is controlled to walk a straight line from No. 1 platform, takings the peg and turning 90 degree to No. 2 platform, peg insertions in the hole with the same shape, and return to the start point, Fig. 47.3.

47.4.2 Connection of Robot

The connection is proceeded with DOS; then, the robot motion, which is originally controlled by Mobile Eyes and Action Viewer, is called out the connection function in DOS by Channel in Quest3D. The synchronous connection control could be operated through VR scenes.

The wireless communication control utilizes the wireless transmission specifications and standards of IEEE 802.11 b/g bandwidth.

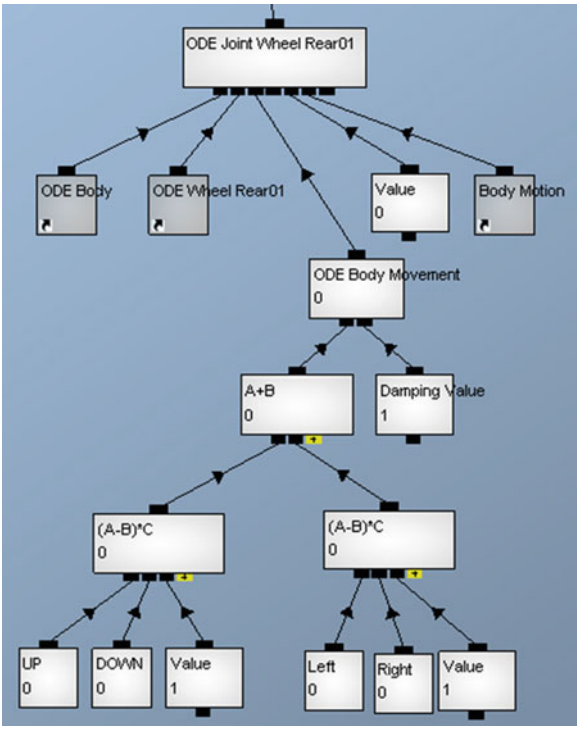

Fig. 47.2 ODE joint wheels rear channel

47.4.3 Operation and Control of Robotic Arms

The mobile robot motion mentioned in Sect. 47.3 is controlled by ⌜↑⌟, ⌜↓⌟, ⌜←⌟, and ⌜→⌟ on the keyboard. The control of robotic arm is similar to it of wheels, but with more joints, buttons, and Channels. Robotic arm, on the other hand, are divided and controlled by ⌜R⌟ for moving backward and ⌜T⌟ for moving forward for Arm01 Joint, ⌜Q⌟ for moving backward and ⌜E⌟ for moving forward for Arm03 Joint, ⌜A⌟ for moving backward and ⌜D⌟ for moving forward for Arm05 Joint, ⌜S⌟ for moving backward and ⌜w⌟ for moving forward for Arm06 Joint, and ⌜z⌟ for the gripper and ⌜x⌟ for the release for the gripper of an arm.

The mobile robot and arm, gripper could simultaneously move without any effects. However, simultaneously moving forward and backward at the same part would not appear any motions.

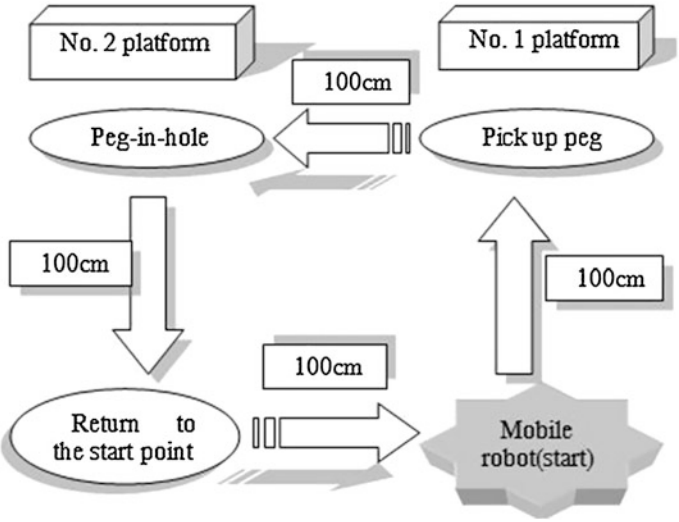

Fig. 47.3 Control procedure

Table 47.1 Mobile robot speed parameter relative speed in virtual and reality

Speed parameter	Virtual mobile robot speed (dis/sec)	Reality mobile robot speed (cm/sec)
30	0.531	5.31
50	0.574	5.74
100	0.680	6.80
150	0.787	7.87
200	0.893	8.93
250.2	1.000	10.0

47.4.4 Experimental Results and Discussions

With the experimental test, the robot rate appears 10 cm/sec in reality, while the virtual robot rate without being adjusted the speed parameter reveals 0.531dis/sec (displacement/sec), about 5.31 cm/sec, and the virtual robot rate with the speed parameter 200 appears 0.893 dis/sec, about 8.93 cm/sec. The detailed data are shown in Table 47.1. Apparently, 1 unit speed parameter could affect 0.00213 the displacement. When the virtual robot rate equals to it of the robot in reality, the virtual robot rate should achieve 1 dis/sec. According to the above data, the required speed parameter 250.5 is further revised 250.5 for testing. The result corresponds to the rate of 1 dis/sec.

The revision of speed parameter for robotic arm is similar to it for a mobile robot, which is finally revised to 104.2, the same as the turning speed of real robotic arms. The follow-up adjustment of speed parameter reduces the operation

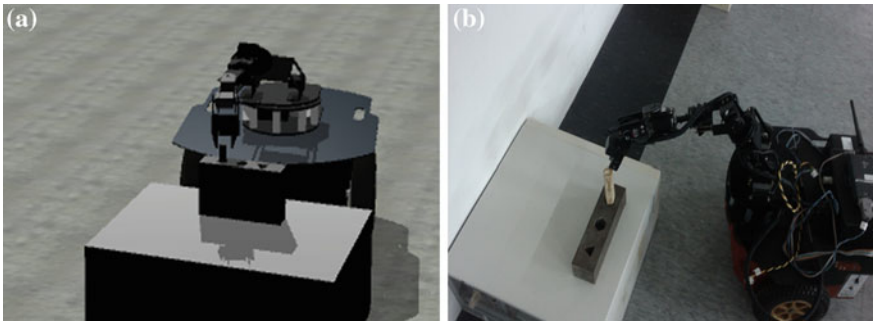

Fig. 47.4 **a** Insertion assembly successfully in the VR. **b** Insertion assembly successfully in the reality at same time

errors between VR and the real robot down to the least so that the movement and assembly of the robot in VR and the solid robot are almost synchronous. Furthermore, the wireless remote control assists in successfully controlling the robot in reality to complete the assembly, as shown in Fig. 47.4.

47.5 Conclusions

Quest3D is utilized for real-time connection control of solid robot to automatically complete the assembly in VR. The past research mostly reduced the errors by improving the transmission speed after the camera transmitting the on-site images. In this study, VR, replacing a camera, revises the speed parameter of the robot for synchronism between virtual and real frames. Moreover, ODE engine in Quest3D is applied to presenting the real physical properties of an object, such as the moving speed and collision of a mobile robot and arm.

In the real operation, it requires several attempts and corrections to grab the peg and successfully complete the assembly. VR allows freely changing the angles of view to make the grab and assembly be more easy. A new function to show the information of coordinate, moving distance, and rotation angle of the robot or other objects in VR frames could have the users more clearly understand the situation in the field. Or, including a virtual guidance could assist the users more easily operation the process, which are considered as a different research field.

References

1. Hsu, F. C. (2000). VR-based teleoperation system for industrial robots. Master's thesis, Department of Mechanical Engineering, Chung-Yuan Christian University.
2. Huang, Y. H. (2007). Applying virtual guidance for robot teleoperation. Master's thesis, Department of Electrical and Control, National Chiao Tung University.

3. Chuang, S. W. (1997). Virtual assembly modeling. Master's thesis, Department of Mechanical Engineering, National Central University.
4. Ke, T. J. (1998). Personal computer assembly by virtual reality technique. Master's thesis, Department of Computer Science, National Chiao Tung University.
5. Orady, E. A., & Osman, T. A. (1997). Virtual reality software for robotics and manufacturing cell simulation. In *21st International Conference on Computers and Industrial Engineering*, (Vol. 33, pp. 87–90).
6. Freund, E., & RoBmann, J. (2001). Multimedia and virtual reality techniques for the control of ERA, the first free flying robot in space. In *Proceedings of the 2001 IEEE International Conference on Robotics and Automation* (pp. 21–26).
7. Xie, X., Sun, L., Du, Z., & Zong, Z. (2006). Predictor display in robotic teleoperation over internet. In *Proceedings of the 6th World Congress on Intelligent Control and Automation* (pp. 21–23).
8. Jönsson, A., Wall, J., & Broman, G. (2005). A virtual machine concept for real-time simulation of machine tool dynamics. *International Journal of Machine Tools and Manufacture, 45*, 795–801.

Chapter 48
Influence of Carbon Nanotubes on the Electrochemical Properties of Lithium-Ion Battery Anode Materials

Yu-Shiang Wu and Kai-Ling Hu

Abstract Due to the quick leap on battery technology in recent years, the application of lithium-ion battery is expanding very fast. However, related researches mostly focus on surface modification of graphite anode materials. By contrast, subjects about conductive additives are relatively rare. This research investigated the adding carbon nanotubes (CNTs) on natural graphite anode materials. Due to the poor dispersing effect of CNTs, PVA was utilized as the dispersant in the process. After coating the natural graphite with PVA, modification was carried on by adding CNTs in different ratio in order to increase the electrochemical properties as well as raise rate and cycle performance of the battery. The results show that the coating natural graphite with 3 wt% PVC and then adding 2 wt% CNTs as conductive additive could achieve 361.0 mAh/g in discharge capacity. Moreover, rate and cycle performance were greatly improved at the same time.

Keywords Lithium ion battery · Natural graphite · Carbon nanotubes · Rate performance · Cycle performance

48.1 Introduction

In recent years, the increasing effects of global warming as well as the oil crisis have led to worldwide concerns on environmental protection and alternative energy. The application of lithium-ion battery has been extended from electric vehicles to renewable energy electricity storage systems, even to various electronic products, electric tools and electric vehicles. The lithium-ion battery has the

Y.-S. Wu (✉) · K.-L. Hu
Department of Mechanical Engineering and Graduate School of Optomechatronics, China University of Science and Technology, Taipei 11502, Taiwan, Republic of China
e-mail: yswu@cc.cust.edu.tw

J. Juang et al. (eds.), *Proceedings of the 2nd International Conference on Intelligent Technologies and Engineering Systems (ICITES2013)*, Lecture Notes in Electrical Engineering 293,
DOI: 10.1007/978-3-319-04573-3_48,

advantages of high operating voltage, high energy density, long cycle life, high rate and environmental protection [1]. In the lithium-ion battery field, the anode material is undergoing innovation and is developed extensively. Related studies focus on the active material doping and surface modification of the anode, but seldom on the conductive additive to the anode material [2, 3].

As the specific surface area increasing of carbon nanotubes (CNTs) within the graphite anode materials, the graphite expansion with lithium ion intercalation and de-intercalation is decreased effectively to improve the cycle life and rate performance [4–7]. This study investigated the CNTs addition in natural graphite anode material.

As the CNTs have a poor dispersion effect, polymer resin PVA was used as a dispersant coated the natural graphite, and then different ratios of CNTs were added in the experiment. This study aimed to improve the electrochemical properties of the lithium-ion battery and enhance the charge and discharge cycles and rate performance of the battery.

48.2 Experimental Method

48.2.1 Sample Preparation and Material Analysis

The CNTs were added as a conductive additive in the anode slurry. However, due to the agglomeration of CNTs, the polymer resin polyvinyl alcohol (PVA) was used as a dispersant covered the natural graphite surface layer (as shown in Table 48.1 and 48.2). The CNTs were added in anode slurry at 0–3 wt%. The anode plate containing CNTs was obtained after drying, oven drying, rolling and cutting procedures. The plate was then analyzed, and the electrochemical properties were tested.

The surface morphology of CNTs dispersed in the anode plate with different ratios of CNTs was observed through SEM (JEOL JSM-6500F) and FESEM (LEO-1530). The electrochemical properties were tested by charge and discharge tester (Arbin BT2000).

48.2.2 Battery Assembly

The coin cell lithium-ion battery was used for testing electrochemical properties. The active material was graphite (92 wt%), and the dispersant was polymer resin PVA (3, 10 wt%). CNTs (0, 1, 2 and 3 wt%) and Super-P (3 wt%) were used as conductive additive. The PVDF was used as a binder (5 wt%) dissolved in NMP solvent. The mixture was stirred by magnetic stirrer for 3 h to form an uniform slurry before vacuum defoaming. The slurry was poured into the rewinding coating

Table 48.1 Experimental materials and function

Raw materials	Function
Natural graphite	Active material
Super-P	Conductive additive
CNTs	Conductive additive
PVA	Dispersant

Table 48.2 Addition ratio of PVA and CNTs

Samples	Amount of PVA addition (wt%)	Amount of CNTs addition (wt%)	Amount of Super-P addition (wt%)
A-1	3	0	3
A-2	3	1	3
A-3	3	2	3
A-4	3	3	3
A-5	10	0	3
A-6	10	1	3
A-7	10	2	3
A-8	10	3	3

machine, covering the copper foil before vacuum drying. The battery test consisted of cathode lithium metal and anode graphite composites, separated by porous polypropylene separator film. The electrolyte was 1 M $LiPF_6$/EC:EMC:DMC (1:1:1 wt%). The coin cell battery was assembled in a glove box with full nitrogen, put aside for one day, and then the cycle life and rate performance were tested by charge–discharge tester.

48.3 Results and Discussion

48.3.1 SEM Analysis

Figure 48.1 is the schematic diagram of CNTs distribution within graphite. The morphology and microstructure of the anode material plate were observed through the SEM. Figure 48.2 is the SEM images of anode plate without polymer resin PVA dispersant (0 wt%) and CNTs addition 1–3 wt% The dispersion of Super-P particles could be observed in detail. Since the agglomeration of CNTs was severe, the CNTs dispersion effect was poor before the addition of the dispersant.

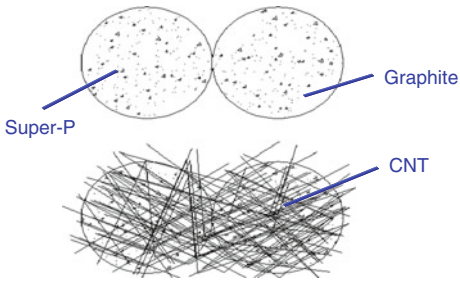

Fig. 48.1 Schematic diagram of CNTs distribution within graphites

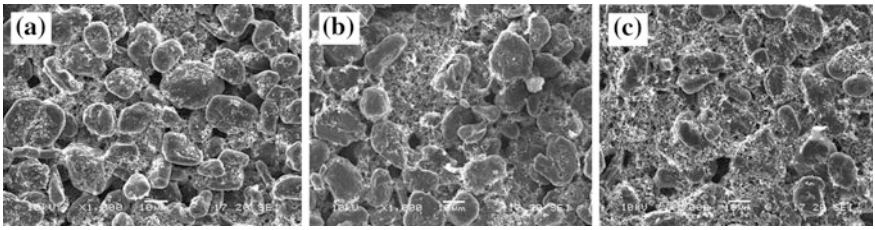

Fig. 48.2 SEM images in different CNTs addition with PVA 0 wt% **a** CNTs 1 wt%; **b** CNTs 2 wt%; **c** CNTs 3 wt%

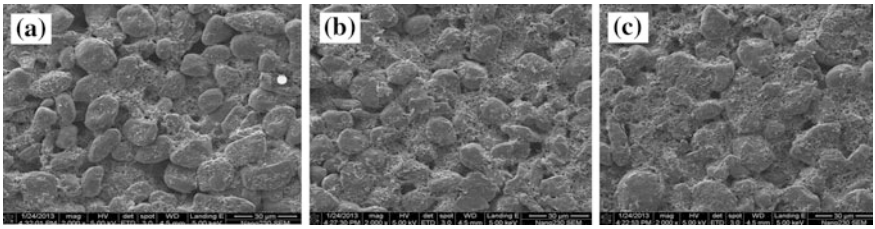

Fig. 48.3 FESEM images in different CNTs addition with PVA 3 wt% **a** CNTs 1 wt%; **b** CNTs 2 wt%; **c** CNTs 3 wt%

48.3.2 FESEM Analysis

Figure 48.3 is the FESEM images of the anode plate with PVA 3 wt% and CNTs addition 1–3 wt%. The CNTs completely dispersed in the plate were observed clearly through the FESEM. The polymer resin PVA covers the graphite, effectively improving the agglomeration of CNTs. The extension of the polymer chain inhibited the agglomeration of solid particles, thereby enhancing the dispersion effect of the CNTs. Moreover, the CNTs were not dispersed one by one, but distributed uniformly in different directions. Furthermore, the net-like bridge structure increased the specific surface area of natural graphite powder that can increase the contact areas between the graphites.

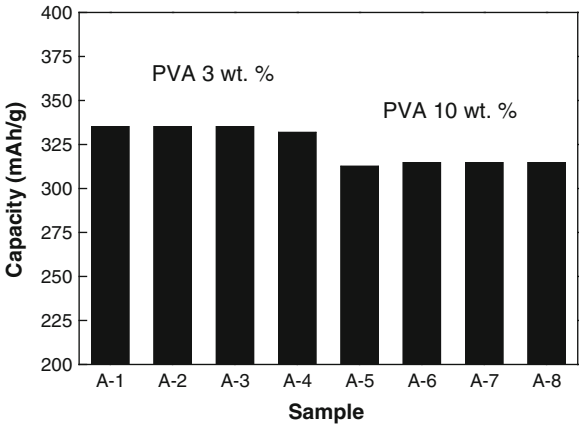

Fig. 48.4 The first discharge capacity with different PVA amount

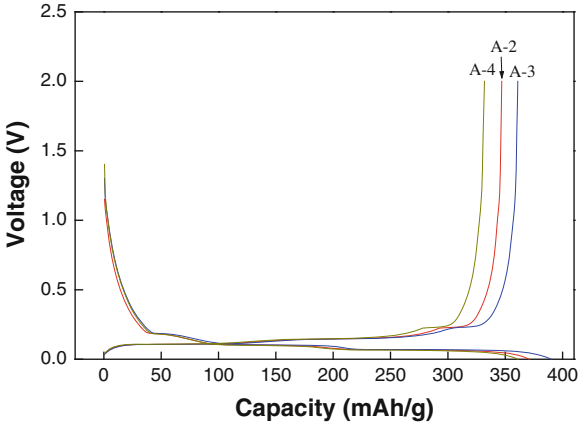

Fig. 48.5 The first charge–discharge capacity with 1–3 wt% CNT (A-2–A-4)

48.3.3 Capacity Test

For the lithium-ion battery performance, the first charge–discharge capacity, the first irreversibility, the first irreversible capacity and the first coulombic efficiency were observed in the capacity relations. The first discharge capacity of A-1–A-8 was 336.9, 347.0, 361.0, 331.9, 312.6, 321.6, 335.7 and 325.5 mAh/g, respectively. The polymer resin PVA was used as the dispersant coating material. When the coating ratio was 10 wt%, the first discharge capacity was 312.6 mAh/g. However, when the coating ratio was 3 wt%, the first discharge capacity was about 336.9 mAh/g. It is obvious that at a high PVA coating ratio, the capacity was low (as shown in Fig. 48.4). Therefore, the PVA was used as dispersant, and the optimal coating ratio was 3 wt%. Figure 48.5 compares the first charge–discharge capacity of polymer resin PVA 3 wt% and CNTs 1–3 wt%. The result shows that the discharge capacity of 361.0 mAh/g was better when CNTs was 2 wt%. The

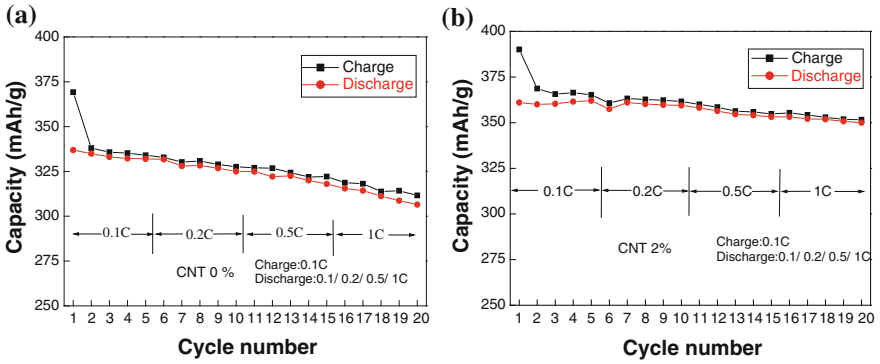

Fig. 48.6 Cycle life and rate test of PVA 3 wt% **a** CNT 0 wt%; **b** CNT 2 wt%

addition of CNTs (A-2–A-4, A-6–A-8) could effectively reduce the irreversibility of the battery. The first irreversibility of the battery without CNTs was 8.7 % and 8.6 %, respectively. After the addition of 1–3 wt% of CNTs, the first irreversibility was 6.4 % (A-2), 7.5 % (A-3), 8.1 % (A-4), 7.9 % (A-6), 5.1 % (A-7) and 7.1 % (A-8), respectively. Therefore, the addition of CNTs could effectively reduce the first irreversibility of the battery. When the CNTs were dispersed in the graphite anode, the bridge structure built in the anode graphite powders enlarged the specific surface area of the graphite, and improved the electrochemical activity of lithium ions intercalation and de-intercalation of the graphites, thereby reducing the first irreversibility of the battery.

48.3.4 Cycle Life and Rate Performance Test

For the electrochemical properties, the cycle life and rate performance were showed in Fig. 48.6. It was charged at 0.1C, and then discharged at 0.1, 0.2, 0.5 and 1C, cycled five times, respectively. The charge and discharge cycles and rate of the plate with PVA 3 wt% and CNT 0–3 wt% were tested in order to compare the performance of cycle and rate. Figure 48.6a showed that the decay of the battery was obvious before the addition of CNT. Figure 48.6b shows that the decay of the battery was improved after the addition of CNT 2 wt%, and the battery performance of cycle and rate were the best. The discharge capacity was still keeping 350.0 mAh/g after the fifth 1C discharge. In the discharge capacity of cycle life shown in Fig. 48.7, the PVA 3 wt% was used as the dispersant to cover the natural graphite, and then when the CNTs 2 wt% was added as the conductive agent, the capacity and cycle life were the best electrochemical property. The addition of CNTs could effectively enhance the rate and cycle of battery, and in the case of discharge at a high rate, the discharge capacity was more stable than the capacity without CNTs.

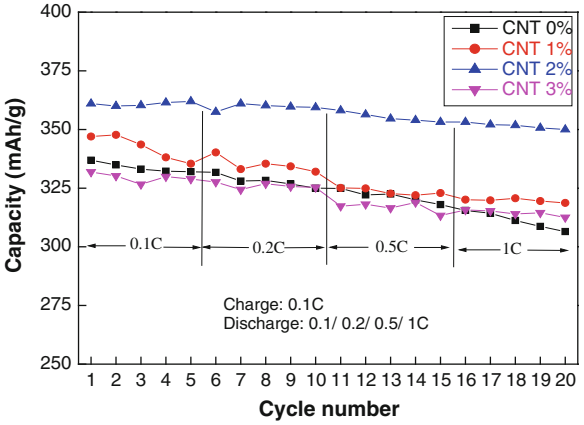

Fig. 48.7 Comparison of discharge capacity in different CNTs addition and rate

48.4 Conclusion

The CNTs have poor dispensability and are likely to agglomerate before it is mixed with a dispersant. When the natural graphite surface is coated with polymer resin PVA as the dispersant, the CNTs dispersion effect is clearly improved. In this study, the PVA was used as coating material. The results indicated that when the PVA coating ratio was 10 wt%, the first discharge capacity was 312.6 mAh/g; but when the PVA coating ratio was 3 wt%, the first discharge capacity was 336.9 mAh/g. Therefore, the PVA was used as dispersant, and the optimal coating ratio was 3 wt%. When the anode was coated with PVA 3 wt% and mixed with different ratios of CNTs as conductive agent, the CNTs 2 wt% had the best performance. There was no apparent capacity decay at different charge and discharge rates tests.

References

1. Zhao, T. F., Ren, J., He, X., Li, J., Jiang, C., & Wen, C. (2008). Modification of natural graphite for lithium ion batteries. *Solid State Sciences, 10*, 612–617.
2. Guilmard, M., Rougier, A., Grune, M., & Delmas, C. (2003). Effects of aluminum on the structural and electrochemical properties of $LiNiO_2$. *Journal of Power Sources, 155*, 305–314.
3. Dominko, R., Bele, M., Gaberscek, M., Remskar, M., Hanzel, D., Pejovnik, S., et al. (2003). Impact of the carbon coating thickness on the electrochemical performance of $LiFePO_4$/C composites. *Journal of the Electrochemical Society, 152*, 607–610.
4. Li, X. L., Du, K., Huang, J. M., Kang, F. Y., & Shen, W. C. (2010). Effect of carbon nanotubes on the anode performance of natural graphite for lithium ion batteries. *Journal of Physics and Chemistry of Solids, 71*, 457–459.
5. Wang, W., Epur, R., & Kumta, P. N. (2011). Vertically aligned silicon/carbon nanotube (VASCNT) arrays: hierarchical anodes for lithium-ion battery. *Electrochemistry Communications, 13*, 429–432.

6. Zhang, Y., Chen, T., Wang, J., Min, G., Pan, L., Song, Z., et al. (2012). The study of multi-walled carbon nanotubes with different diameter as anodes for lithium-ion batteries. *Applied Surface Science, 258*, 4729–4732.
7. Shao, Q. G., Chen, W. M., Wang, Z. H., Qie, L., Yuan, L. X., Zhang, W. X., et al. (2011). SnO_2-based composite coaxial nanocables with multi-walled carbon nanotube and polypyrrole as anode materials for lithium-ion batteries. *Electrochemistry Communications, 13*, 1431–1434.

Chapter 49
A Cloud-Based Chinese Web 5-Gram Query System

Chee Sin Lim and Liang-Chih Yu

Abstract This paper presents a cloud-based Chinese language query system which provides n-gram and skip n-gram frequencies retrieved from the Chinese Web 5-gram corpus. Language learners can learn frequently co-occurring context words or other contextual information from the retrieval results. The system was implemented using a MySQL relational database and PHP script language. Experimental results show the retrieval time for some sample queries which reveals that the system achieves high retrieval efficiency.

Keywords Natural language processing · Information retrieval · Computer-assisted language learning · n-gram

49.1 Introduction

Computer-assisted language learning (CALL) systems have been demonstrated their effectiveness in synonym learning/vocabulary learning [1?7] and sentence correction [8]. This paper presents a cloud-based Chinese language query system which provides n-gram and skip n-gram frequencies retrieved from the Chinese Web 5-gram corpus released by Linguistic Data Consortium (LDC). In this online language learning system, we use n-gram models [9] to develop the system that allows users to query words so that they can learn frequently co-occurring context words or other contextual information from retrieval results.

C. S. Lim · L.-C. Yu (✉)
Department of Information Management, Yuan Ze University, Chungli 32003, Taiwan
e-mail: lcyu@saturn.yzu.edu.tw

J. Juang et al. (eds.), *Proceedings of the 2nd International Conference on Intelligent Technologies and Engineering Systems (ICITES2013)*, Lecture Notes in Electrical Engineering 293,
DOI: 10.1007/978-3-319-04573-3_49,

Table49.1 Time spent to create dictionary tables

n-gram	Time spent to create Unigram table (in seconds)
n=2	15,950
n=3	41,077
n=4	41,012
n=5	50,627
Total time	148,666

Table49.2 Time spent to import data

n-gram	Time spent to import data (in seconds)
n=2	353,651
n=3	552,056
n=4	1,655,199
n=5	439,006
Total time	2,999,912

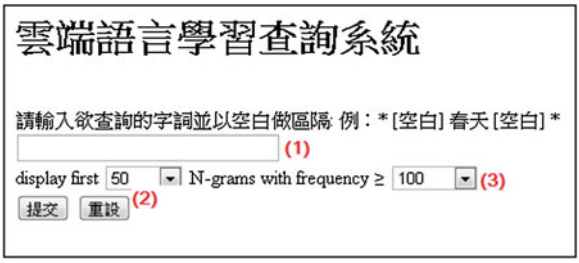

Fig.49.1 Screenshot of the user interface

49.2 System Description

49.2.1 MySQL Database

? **Data conversion**: The encoding of the original data was Big-5. We use the converter software?ConvertZ to convert the encoding of data from Big-5 to UTF-8. The purpose is to avoid the garbled data.

? **Data checking**: Use the program to ensure that was not unrecognized word in the data. If have, we have to modify the error data by refer the original data manually.

? **Dictionary table**: Import the data into the database?s Unigram table to create the dictionary. Every word was given by a unique ID and the frequency of the words was counted. This stage also run by a program and there was a text file created to record the time that had spent after a file of data was imported successfully (Table 49.1).

? **Importing data tables**: After create the dictionary table, the data from file of 2 to 5gms were imported into the database by the program. Each file of data will

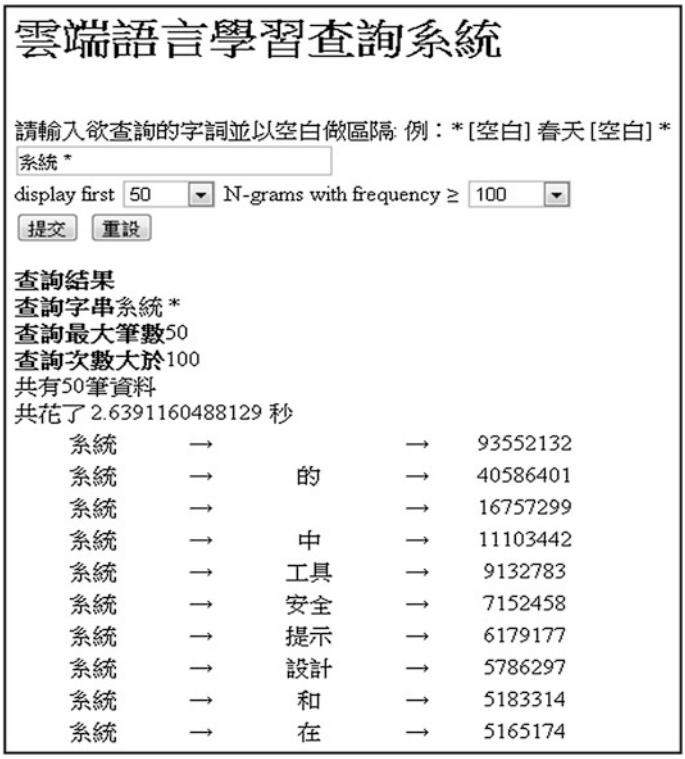

Fig.49.2 Screenshot of a query example for the first run

create a new table to import its own data. Example: the data in the file 2gms will be imported to the table which name ?two?. While importing the data, every data?s words will be turn into their ID which refers to the Unigram table (Table 49.2).

49.2.2 User Interface

In the part of web page, we use the PHP as the language to design. We built the connection between the MySQL database and web page. Users can inquiry through the web page and the results of inquiry will also display on the web page.

Users can input the words which they want to inquiry in the textbox (1) (see Fig. 49.1). Users can set the condition through the two drop-down lists and the webpage will only show the data of results which correspond to the condition. One of the drop-down lists is to set how many data of results users want to show in the

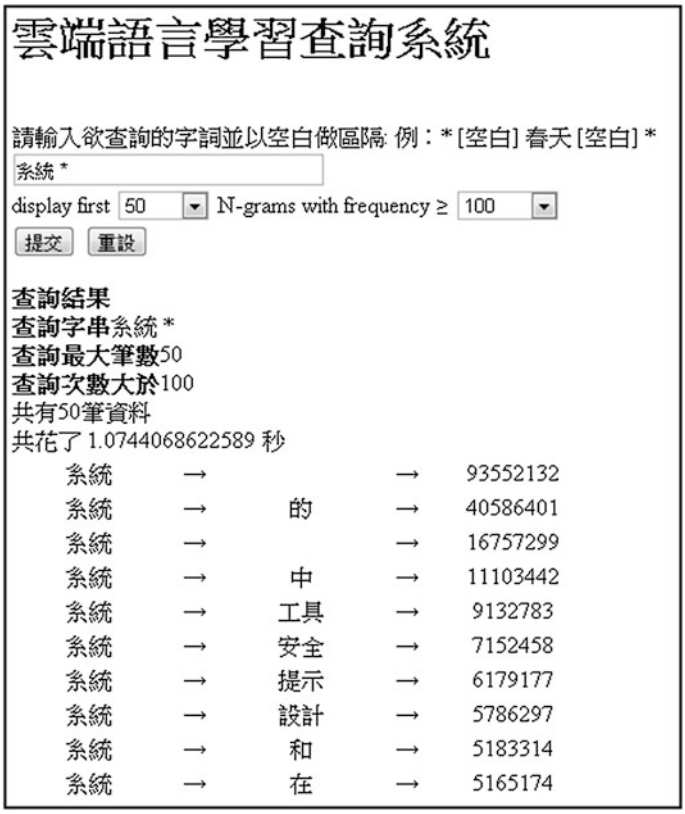

Fig.49.3 Screenshot of a query example for the second run (cache)

webpage (2) (eg. only show the first 50 results). Besides that, users also can decide to show the data which have the frequency greater than the amount they have set in the webpage through another drop-down list (3).

49.3 Experimental Results

The system was installed on a personal computer. The specification is described as follows.

? CPU: Intel(R) Core(TM)2 Duo CPU E8400 3.00GHz
? Memory: 8GB; Harddisk: 1TB
? OS: Windows 7 Professional

In this project to develop a system, we used the MySQL+Apache+PHP and Notepad++. MySQL is the most widely used relational database management

Table49.3 Retrieval efficiency for the first and second runs

Query		Time spent to retrieve the first 100 results (in seconds)	
		1st run	2nd run
n=2	?? *	8.17	1.07
n=2	* ??	25.30	1.05
n=5	* * ?? * *	20.74	1.12
n=5	* * * * ??	24.90	1.09

Table49.4 Retrieval efficiency in [4]

Query		Time spent to retrieve the first 100 results (in seconds)	
		1st run	2nd run
n=2	banana *	0.4	0.1
n=2	* banana	11.9	0.5
n=5	* * cake * *	33.6	1.6
n=5	* * * * cake	47.3	1.7

system. Apache is a web server software program. PHP is a server-side scripting language designed for web development and we used Notepad++ to edit the PHP language?s web page. Figure49.2 and 49.3 show a query example for the first run query and second run query (cache). We inquiry the word ???*? and set to show the first 50 result which the data frequency is greater than 100. As shown in Fig.49.2, the system spent 2.639s to complete the inquiry for the first run, and 1.074s for the second run (Fig.49.3).

Table49.3 shows the retrieval efficiency for the first and second runs with input queries of different n-grams. All the inquiries are setting to return first 50 results which with the frequency greater than 100. Table49.4 shows the retrieval efficiency of the English language presented in [4]. The comparative results show that our system is more efficient for n=5 in both first and second runs.

49.4 Conclusion

This work has presented a Chinese language query system which provides n-gram and skip n-gram frequencies retrieved from the Chinese Web 5-gram corpus. Experimental results also show the efficient retrieval time for some sample queries. Future work will incorporate more useful contextual information such as pointwise mutual information (PMI) to improve the usability of the system for language learners.

Acknowledgments This work was partially supported by National Science Council, Taiwan, under Grant No. NSC102-2221-E-155-029-MY3, and Bureau of Energy, Ministry of Economic Affairs, Taiwan, under Grant No. 102-E0616. The authors would like to thank the anonymous reviewers for their constructive comments.

References

1. Cheng, C. C. (2004). Word-focused extensive reading with guidance. *Proceedings of the 13th International Symposium on English Teaching* (pp. 24?32).
2. Inkpen, D. (2007). A statistical model of near-synonym choice. *ACM Transactions on Speech and Language Processing, 4*(1), 1?17.
3. Ouyang, S., Gao, H. H., & Koh, S. N. (2009). Developing a computer-facilitated tool for acquiring near-synonyms in Chinese and english. *Proceedings of IWCS-09* (pp. 316?319).
4. Lam, Y. C. (2010). Managing the google web 1T 5-gram with relational database. *Journal of Education, Informatics and Cybernetics, 2*(2), 1?6.
5. Yu, L. C., Wu, C. H., Chang, R. Y., Liu, C. H., & Hovy, E. H. (2010). Annotation and verification of sense pools in ontoNotes. *Information Processing and Management, 46*(4), 436?447.
6. Yu, L. C. & Hsu, K. H. (2012). Developing and evaluating a computer-assisted near-synonym learning system. *Proceedings of the 24th International Conference on Computational Linguistics* (pp. 509?516).
7. Yu, L. C., & Chien, W. N. (2013). Independent component analysis for near-synonym choice. *Decision Support Systems, 55*(1), 146?155.
8. Wu, C. H., Liu, C. H., Matthew, H., & Yu, L. C. (2010). Sentence correction incorporating relative position and parse template language models. *IEEE Transactions on Audio, Speech and Language Processing, 18*(6), 1170?1181.
9. Manning, C., & Schtze, H. (1999). *Foundations of statistical natural language processing*. Cambridge: MIT Press.

Chapter 50
A Pulse-Type Angular Position Mechanism for Quadrature Signals

Ping-Sung Liao and Chien-Hua Lee

Abstract Quadrature signals are often found in angular position sensors such as linear scales and 2-axis Hall sensors. The phase of quadrature signals always carries the moving direction and position of a working platform. To increase the phase resolution, this paper presents a novel phase chopping method to convert the phase information into pulse sequences. With the help of an 8-bit analog-to-digital conversion upon each $\pi/4$ phase interval, the full 2π phase cycle can be digitized into 1,600 quasi-equipollent pulse resemblances and the phase error is bound within near one splitting phase division.

Keywords Quadrature signals · Mechanical division · Amplitude-to-phase conversion · Phase division · Mapping phase range

50.1 Introduction

Optical encoder and optical meter are the typical sources of quadrature signals. In manufacturing automation, optical encoder is usually mounted to the shaft of an electrical machine and its internal mechanical divisions cast in either simple division or Gray-coded division for detecting the angular position [1]. Optical meter, also named as linear scale, has the similar optical property like an optical encoder. It can accurately measure the position of working platform that moves in linear motion quickly within 3, 5 m and even 7 m [2, 3].

In general, the accuracy of a manufacturing machine relies on the resolution of mechanical divisions embedded in optical encoder and optical meter. However, the phenomenon of light variation for ray penetrating the mechanical divisions is often

P.-S. Liao (✉) · C.-H. Lee
Department of Electrical Engineering, Cheng Shiu University, Kaohsiung 83347, Taiwan
e-mail: bsliao@csu.edu.tw

J. Juang et al. (eds.), *Proceedings of the 2nd International Conference on Intelligent Technologies and Engineering Systems (ICITES2013)*, Lecture Notes in Electrical Engineering 293,
DOI: 10.1007/978-3-319-04573-3_50,

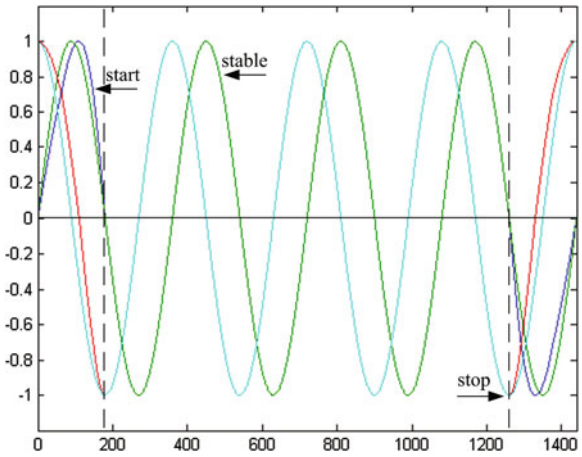

Fig. 50.1 Periodic quadrature signals {sin(θ) in light *blue* and cos(θ) in *green*} and aperiodic quadrature signals {$\sin_{\Delta}(\theta)$ in *red* and $\cos_{\Delta}(\theta)$ in *blue*}

ignored. Actually, the light variation through these mechanical divisions appears sinusoidal, hence the outputs of optical encode and optical meter are a kind of quadrature signals preserving the clue of phase position [3, 4].

The output of 2-axis Hall sensor used for sensing the rotation of a rotating target is another example of quadrature signals [5, 6]. It can sense the magnetic vector of the field from the magnet and generates a pair of quadrature signals. Therefore, it usually is applied in the joystick, electronic compass and steering wheel. In this paper more useful tiny angular position information will be derived from these quadrature signals arising from the aforementioned devices for precision phase measure.

50.2 Phase Chopping Upon Quadrature Signals

Quadrature signals are composed of one sine signal and another cosine signal simultaneously. Because the mechanical transition at least involves start stage, stable stage and stop stage due to inertial law, the phase information of quadrature signals sensing from angular devices usually appears aperiodic cycle at start timing and stop timing. Figure 50.1 shows one ideal phase periodic waveform and the other actual aperiodic phase waveform of quadrature signals. It clearly uncovers that the angular position is indeterminate with the running frequency, but pertains to their amplitudes. For finding the angular position speedily, a look-up memory map of quadrature signals was ever investigated in [6].

Liau proposed differentiation and synchronization method to promote the resolution of the optical encoder four times than before [7]. To further increase the measuring accuracy of phase angle in an optical meter, Lee and Chiu proposed a resolution-scale division method to improve the accuracy of phase resolution up to

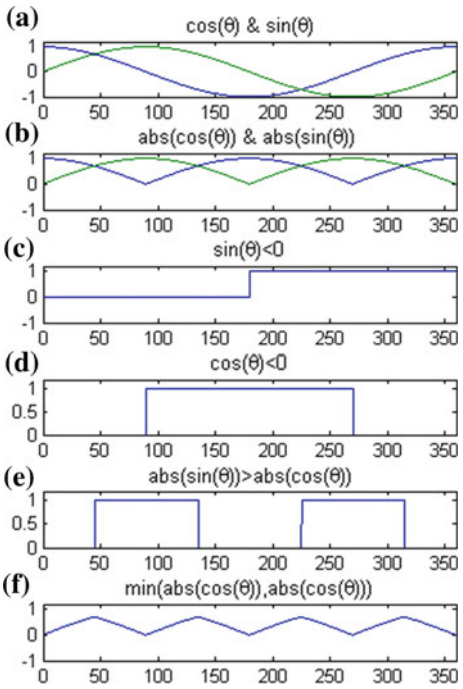

Fig. 50.2 **a** Quadrature signals, **b** their absolutes, **c**, **d** and e other binary waveforms in derived from the amplitude comparison, **f** the last deterministic waveform for discreteness

32 times [2]. The kernel of the latter resolution-scale division method involves (50.1) to choose the minimal splitting phase angle at phase π for a cosine signal, and (50.2) to use a conversion table between the phase angle and the amplitude of input signal to generate a sequence of pulses of quasi-equipollent interval [1]. Apparently, the more phase divisions are generated, the more accurate phase position can be improved.

In this paper authors develop an alternative discrete method to chop the phase of quadrature signals into pulse-type sequence. The minimal splitting phase angle in [2, 7] is altered to be a phase of $\pi/4$ (45°) for quadrature signals. Observing at Fig. 50.2c and d, we can conclude that the full phase cycle of 360° can be spliced into 4 phase intervals of 90°. Oppositely, the proposed combination among Fig. 50.2c, d and e can yield twice phase intervals, that is, 8 phase intervals of 45°. Consequently, the chopping action will be conducted on this new phase intervals instead of the phase intervals of 90° in [2, 7].

50.2.1 Amplitude-to-Phase Conversion

As for an n-bit A/D converter, the amplitude from peak to peak for a cosine signal could be divided into 2^n levels. Because the relationship between the amplitude and the phase of a cosine signal is nonlinear, the mapping phase range

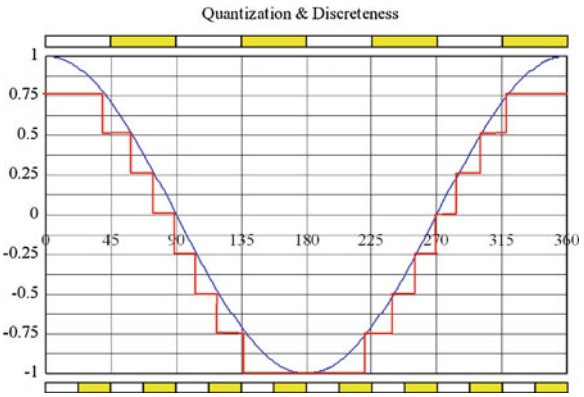

Fig. 50.3 There are eight quantization levels in amplitude axis. For the phase division in phase axis, the top one is 45° at *top* and the *bottom* one is 22.5°

corresponding to the quantization level at phase 0 and π would be the greatest as shown in Fig. 50.3. Therefore, in [2], the greatest mapping phase range for A/D conversion is chosen as

$$\theta_{\max} = \cos^{-1}(1 - \frac{1}{2^n}) \tag{50.1}$$

The phase division (splitting phase unit) θ_s in phase axis must be greater than the greatest mapping phase range. Otherwise, it is possibly conflicting to assign one phase division to a reasonable mapping phase range if more than two mapping phase ranges are happened. For the instance of 3-bit A/D converter in Fig. 50.3, the upper phase division with 45° is legal one, but the lower phase division with 22.5° is illegal one due to the failure of identifying the first mapping phase range (amplitude: 0.75–1.0). Thus, the minimal phase division $\theta_{s,\min}$ greater than the greatest mapping phase range $\theta_{\max}$ is strongly recommended.

According to Eq. (50.1), the maximal multiplier $D_{\max}$ to chop a phase interval of 180° must satisfy the inequality below in [2],

$$D_{\max} \leq \frac{\pi}{\theta_{\max}} \tag{50.2}$$

Regarding to an 8-bit A/D converter, the minimal phase division $\theta_{s,\min}$ equals 5.07° and the maximal multiplier $D_{\max}$ is 35.5. Thus, the maximal multiplier of chopping pulse was chosen to be 32 [2] for the phase interval π.

50.2.2 Abundant Phase Chopping Interval

Good selection of phase chopping interval is the key factor to improve the accuracy of phase measuring. In Fig. 50.2f each phase interval is obviously either the replica or the mirror of sine signals from 0 to 45°. This adaptation of new abundant phase chopping interval brings two advantages: (1) the number of phase

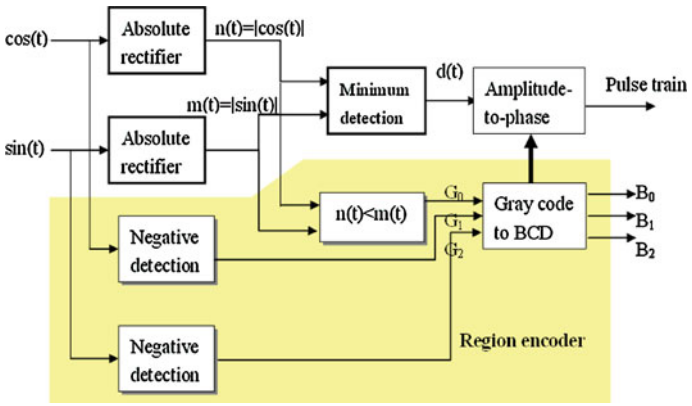

Fig. 50.4 Phase chopping diagram

chopping interval doubles that of the aforementioned methods in [2, 7], (2) the amplitude for quantization is more accurate over $[-1, 1]$ instead of $[0, \sqrt{2}/2]$.

Consequently, for an 8-bit A/D converter, the amplitude of a sine signal can be quantized into 256 discrete levels for the amplitude ranging between 0 and 45°, and the greatest phase mapping range $\theta_{\max}$ approximates 0.2234° for a phase interval of $\pi/4$ (45°). The new inequality of maximal multiplier will be

$$D_{\max} \leq \frac{\pi/4}{\theta_{\max}} \tag{50.3}$$

Finally, the span of this phase division is chosen to be 0.225°, that is, 45°/200, and the number of chopping phase interval $\pi/4$ into quasi-equipollent phase divisions is 200, and maximal total multiplier $D_{\max,FS}$ along full 2π phase interval is 1600.

50.3 Phase Chopping Diagram and Simulation

The integrated phase chopping diagram is given in Fig. 50.4 in which the amplitude-to-phase conversion and the index finding of each 45° phase interval by regional encoder are realized. The number ($B_2B_1B_0$) of region encoder reflects the logical function over three comparisons. In Fig. 50.2f, odd phase intervals get the same chopping pulse sequences and the chopping pulse sequences of even phase intervals are reverse-in-order and complement to that of odd phase intervals. Interleaving these chopping pulse sequences of both odd phase intervals and even phase intervals will comprise the complete chopping pulse sequences in association with the full phase interval from 0 to 360° for quadrature signals. Fig. 50.5 is the simulated result of the proposed phase chopping diagram over the first phase interval of quadrature signals.

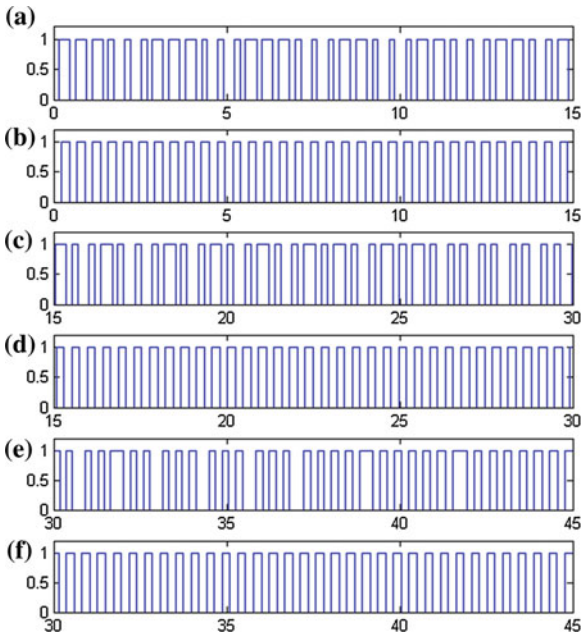

Fig. 50.5 **a**, **c** and **e** are the actual phase divisions with respect to 0°-15°, 15°-30°, and 30°-45°. **b**, **d** and **f** are the ideal phase divisions 0°-15°, 15°-30°, and 30°-45° derived from the proposed phase chopping method

It is worth noting that the multipliers $D_{\max,FS}$ of the proposed chopping phase method in practice may be one of 1600, 1000, 800, 500, 400, 200, 100, 64, 32, 16, 8 and so on. Once the total multiplier is assigned, the great mapping phase range is still nears 0.2234° for a phase interval of $\pi/4$ (45°), and the span of its corresponding phase division is determined by $360^\circ/D_{\max,\mathrm{FS}}$. The smaller the chosen total multiplier $D_{\max,FS}$ is, the greater the error will be.

50.4 Conclusions

The success of the proposed phase chopping mechanism is summarized below. First, region encoder is designed to reduce the span of phase interval for chopping. Hence, the proposed amplitude-to-phase quantization is more accurate over a phase range from 0 to 45° than that from 0 to 180°. Second, the greatest mapping phase range proposed here is smaller than that proposed in [2]. Third, each mapping phase range has a unique numbering index of phase division because the inequality $\theta_{s,\,\min} \geq \theta_{\max}$ always holds, and the maximal error bound between the actual phase division and the ideal phase division is restricted within θ_s. Once this proposed method is applied to the manufacturing machines, the band width of electronic phase chopping circuit will be trivial because mechanical position detection of a working platform is always determined at the low-speed stop stage.

References

1. Lucas-Nulle. (1987). *Measurement of Geometric Quantities*. IMT-3, SO 5157-2P.
2. Lee, H. Y., & Chiu, H. H. (1998). Resolution-scale division method of linear scale and its implementation (in Chinese). *Journal of Technology, 13*(1), 95–102.
3. Lee, H.Y. (1998). *Sensors and transducer application* (in Chinese) (pp.53–64). Kao-Le. ISBN 957584560-9.
4. Gurley Precision Instruments: Rotary Incremental Encoder. (2012) http://www.gpi-encoders.com/
5. Popovic, R. S., Drljaca, P., Schott, C., & Racz, R. (2001). A new CMOS hall angular position sensor. *Technisches Messen, 68*(6), 286–291.
6. SENTRON, Angular Position Sensing with 2-Axis Hall IC 2SA-10 (2004). Retrieved February 12, 2004, from AN-101
7. Liau, W. H. (1993). The analysis and realization for four multiplier circuit with optical encoder (in Chinese). *Journal of Technology, 8*(3), 327–331.

Chapter 51
Optical Security System by Using Image Dyadic Displacement and Manipulations in Fractional Fourier Domain

Hsuan-T Chang, Chien-Yi Lu, Mn-Ta Lee and Mu-Liang Wang

Abstract Most of the conventional optical security verification systems based on the domain of the fractional Fourier transform use a principal phase and fractional factors as keys. These systems will not be secure if the illegal users have the right phase key and know the fractional factors. Therefore, how to enhance the secure level of these systems is an important issue. A new architecture using the image dyadic displacement and manipulations to provide more parameters as supplementary keys is proposed. By using the image dyadic displacement to encrypt and decrypt the target image, as well as using the image manipulations, such as the image scaling factor and image interpolation methods to generate a dynamic lock, the security capability of the optical verification system is enhanced furthermore.

Keywords Fractional fourier transform · Dyadic displacement · Projection-onto-constraint sets

51.1 Introduction

Because information can be parallel processed and hidden in phase or spatial frequency by optical systems, many optical information security systems had been proposed in the past decades [1]. Different kinds of techniques were used in those

H.-T. Chang · C.-Y. Lu
Department of Electrical Engineering, National Yunlin University of Science and Technology, Yunlin 64002, Taiwan, Republic of China

M.-T. Lee (✉)
Department of Electronic Engineering, Kao Yuan University, Kaohsiung 82151, Taiwan, Republic of China
e-mail: mtlee@cc.kyu.edu.tw

M.-L. Wang
Department of Computer Science and Information Engineering, Shu-Te University, Kaohsiung 82445, Taiwan, Republic of China

J. Juang et al. (eds.), *Proceedings of the 2nd International Conference on Intelligent Technologies and Engineering Systems (ICITES2013)*, Lecture Notes in Electrical Engineering 293,
DOI: 10.1007/978-3-319-04573-3_51,

security systems, such as random phase encoding [2], joint transform correlator [3], as well as computer-generated hologram [4].

Since Refregier and Javidi [2] proposed the double random phase encryption algorithm in analog optical information processing to encrypt an image into stationary white noise, several methodologies [5–7] based on this technique had been proposed. Recently, some optical information security systems based on the domain of the fractional Fourier transform (FRT) were proposed in the literatures [8–10]. The main advantages of the FRT are its extra parameters which are provided by the fractional orders in both x-axis and y-axis, so that the security levels of the optical information security systems can be enhanced moreover. As an example, Unnikrishnan et al. [8] used the flexibility of a quadratic phase system to encrypt a primary image into stationary white noise by using two statistically independent random phase codes. There are three planes in their encryption system, i.e. input, encryption, and output planes. The distributions in these planes are related by a FRT with three parameters, input and output scale factors and order of FRT. Thus, the random phase codes as well as the parameters of the FRT constitute the keys to decrypt the stationary white noise.

In the paper, a novel optical security verification system based on using the image dyadic displacement and manipulations in the domain of the FRT is proposed to provide more parameters as supplementary keys. The image dyadic displacement is used to encrypt the target image. On the other hand, the image manipulations, such as the image scaling factor and image interpolation methods, acted on the image of organization logo, is adapted to generate different locks instead of using a fixed lock in the encryption plane. These locks are stored in a lock database and each lock can stand for an organization or a community. Therefore, users who want to access the security verification system must use parameters of the image manipulations as supplementary keys to select the exact lock form the lock database, besides the random phase codes as well as the fractional orders of the FRT. Hence, the security level of the optical verification system can be improved moreover. Furthermore, we use dyadic displacement to encrypt the target image. So, even if the illegal users have the ability to choose the right lock, it still cannot decrypt the target image properly.

51.2 Background Knowledge

In this section, the FRT and the image dyadic displacement are briefly introduced and used in the later sections.

Conceptually, the FRT is a generalization of the conventional Fourier transform and can be used to describe wave propagation in graded index media. For simplicity, we consider one-dimensional FRT. If $f(x)$ is a one-dimensional function, then the αth-order continuous FRT of the function $f(x)$ can be defined for $0 < |\alpha| < 2$ as follows [11]:

$$\{\Im^{\alpha} f\}(u) = \int_{-\infty}^{\infty} K_{\alpha}(u,\ x) f(x) dx$$
$$K_{\alpha}(u,\ x) = K_{\phi} \exp[i\pi(u^2 \cot\phi - 2ux\ \csc\phi\ + x^2 \cot\phi)], \tag{50.1}$$

where $\phi = \alpha\pi/2$ and $K_{\phi} = \exp(-\mathrm{i}(\pi\mathrm{sgn}(\phi)/4 - \phi/2))/|\sin(\phi)|^{0.5}$. The kernal $K_{\alpha}(u, x)$ is defined as $\delta(u-x)$ and $\delta(u + x)$ for the special cases $\alpha = 0$ and $\alpha = \pm 2$, respectively. When $\alpha = 1$, the FRT reduces to the conventional Fourier transform.

Image dyadic displacement (IDD) is considered an address permutation of image pixels and can be used to the image encryption [12, 13]. It is implemented by performing the exclusive OR (XOR) operations for the key and the addresses of the image pixels. By proper key selection, the image pixels can be scrambled and difficult to decrypt the encrypted image.

51.3 The Proposed Optical Security Verification System

The architecture of the proposed optical security verification system is shown in Fig. 51.1. In this proposed security verification system, there are two chief procedures, i.e. the encryption and decryption procedures. For the encryption procedure, there are two main processes, i.e. generating a lock and encrypting the target image into a white noise as a principal key. For the decryption procedure, there are also two main processes, i.e. deciding lock used in the encryption plane and decrypting the white noise in the input plane into a recovered image.

The diagram of the encryption procedure is shown in Fig. 51.2. There are two main parts, i.e. generating a lock using a logo image and encrypting a target image into a white noise. Both of the two processes are executed by computer. While generating a lock, the image of organization logo is first manipulated by different parameters such as the image compression format, scaling factor, and interpolation method. Then, the manipulated image is transformed by Fourier transform (FT) into complex values. After that, the phase part of the complex values is stored into a database and as a lock.

While encrypting the target image into a white noise, the algorithm named projection-onto-constraint sets (POCS) [14, 15] is used to disturb the target image into a white noise according to the lock generated through the prior process. The POCS algorithm is a function which transforms forth and back between two domains and is projected onto a constraint set which is included in one of the two domains. The forward step simulates digitally the propagation of light from the left side to the right side of the optical setup, while the backward step simulates in the reversed direction. When all the constraints in every domain are satisfied simultaneously, the process is terminated and an input phase is gotten. The goal of using the POCS algorithm in the proposed verification system is to retrieve an input phase which an approximate image of the scrambled target image will be shown at output plane as a coherent plane wave is incident to the input plane.

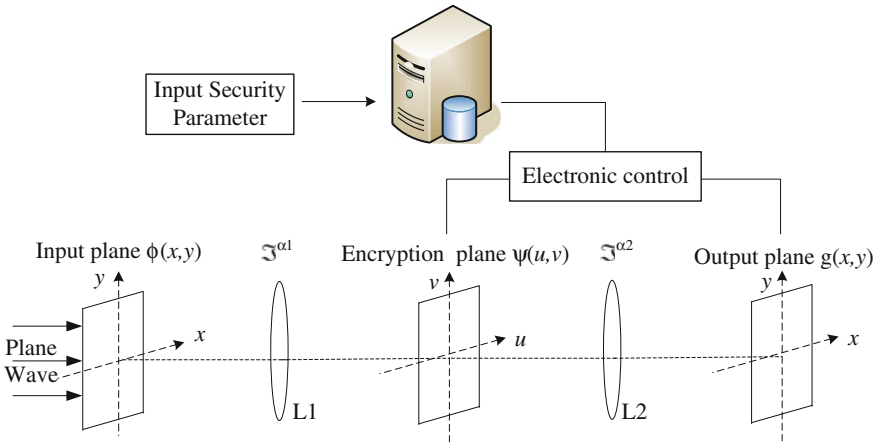

Fig. 51.1 The architecture of the proposed optical security verification system

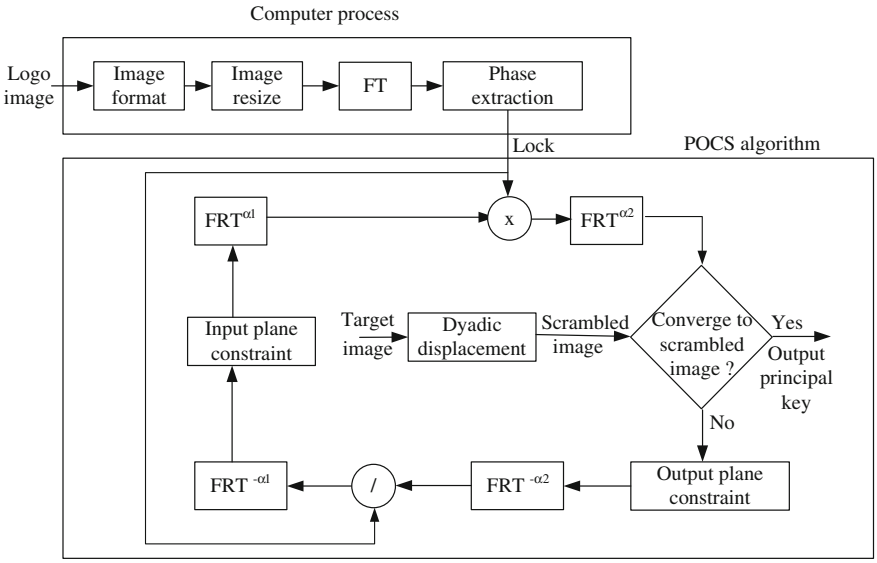

Fig. 51.2 The diagram of the encryption procedure

For decrypting the white noise, i.e. the retrieved input phase, into a retrieved image, the users input the correct security parameters, such as the fractional factors, the image of organization logo, image compression format, image scaling factor, and image interpolation method, etc., to select a lock from the lock database, and put the retrieved input phase in the input plane. When a coherent plane wave is incident to the input plane, a retrieved image will be shown at the output

Fig. 51.3 **a** The organization logo **b** the target image **c** the recovered image

plane. Through using the dyadic displacement with two choice keys j and k on the vertical and horizontal addresses of the retrieved image, an approximate image of the target image is recovered to present the verification result.

51.4 Simulation Results

We execute some simulations to demonstrate the performance of our scheme. In these simulations, the logo of size 64×64 with 256 gray levels, shown in Fig. 51.3a, is used as the image of organization logo, and the Lena image of size 128×128 with 256 gray levels, shown in Fig. 51.3b, is used as the target image. The sizes of both phase masks are as the same as the size of the Lena image in Fig 51.3b. The peak signal-to-noise ratio (PSNR) value of the recovered image is evaluated to estimate the similarity between the target and recovered image. If the PSNR value of the recovered image is larger than a predefined threshold value, then the verification result of the security system is true, otherwise it is false. Two situations which the optical security verification system could be encountered are simulated, i.e. under correct and incorrect input parameters.

First of all, the exactitude of the security verification system while it is under correct input parameters is verified. At the beginning, the logo image in Fig. 51.3a is enlarged eight times by bilinear interpolation method, and then reduced to the same size of the Lena image in Fig. 51.3b by nearest interpolation method. The fractional orders α_1 and α_2 of the FRT are 0.7 and 0.9, and the two keys j and k of the IDD are 30 and 60. Figure 51.3c shows the recovered image with all the correct scaling factors, interpolation methods, fractional orders, and keys of the IDD. From Fig. 51.3c, we can observe that the recovered image is very similar to the target image in Fig. 51.3b with PSNR $= 20.14$. So, it can pass the check of the optical verification system correctly.

After that, we consider the situation that the system is only with incorrect keys j or k of the IDD. Figure 51.4a shows the corresponding recovered image with incorrect key $j = 20$ and its PSNR is 13.8. Figure 51.4b shows the corresponding recovered image with incorrect key $k = 70$ and its PSNR is 10.7.

Finally, we consider the situation that the system is only with one incorrect fractional factor. We observe the effect of error fractional order α_1 from value

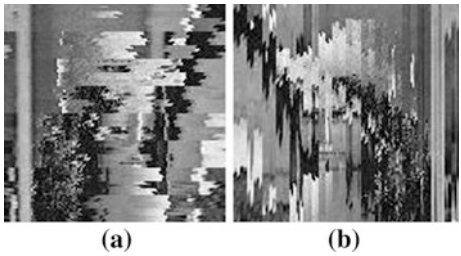

Fig. 51.4 The recovered image due to selecting an incorrect key of IDD. **a** $j = 20$, **b** $k = 70$

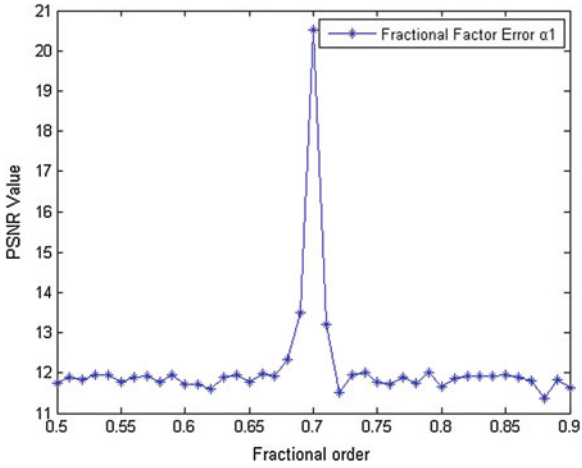

Fig. 51.5 The PSNR value versus different fractional order α_1

0.5 to 0.9. The corresponding PSNR values of the recovered images are shown in Fig. 51.5. From Fig. 51.5, we can find it has high PSNR value at fractional factor 0.7 because the exact fractional order α_1 is 0.7.

51.5 Conclusion

With the image dyadic displacement and manipulations, an optical security verification system based on the fractional Fourier domain is proposed to enhance the security level. In addition to using fractional factors as keys in conventional FRT domain, the image manipulation methods, are used as supplement keys to choose the exact lock from the lock database. Moreover, the parameters of the image dyadic displacement are also used as sub-keys to encrypt and decrypt the target image. Therefore, users who want to access the security system must provide all supplementary keys exactly. Otherwise they cannot pass the check of the optical security verification system. So, the security capability is promoted further.

References

1. Horner, J. L., & Javidi, B. (1996). Special issue on optical security. *Optical Engineering, 35*(9), 2451–2541.
2. Refregier, P., & Javidi, B. (1995). Optical image encryption based on input plane and fourier plane random encoding. *Optics Letters, 20*(7), 767–769.
3. Chang, H. T., & Chen, C. T. (2004). Enhanced optical image verification based on joint transform correlator adopting fourier hologram. *Optical Review, 11*(3), 165–169.
4. Liu, M., Yang, G., Xie, H., Xia, M., Hu, J., & Zha, H. (2007). Computer-generated hologram watermarking resilient to rotation and scaling. *Optical Engineering, 46*(6), 060501.
5. Wang, R. K., Watson, I. A., & Chatwin, C. (1996). Random phase encoding for optical security. *Optical Engineering, 35*(9), 2464–2469.
6. Li, Y., Kreske, K., & Rosen, J. (2000). Security and encryption optical systems based on a correlator with significant output images. *Applied Optics, 39*(29), 5295–5301.
7. Chang, H. T., Lu, W. C., & Kuo, C. J. (2002). Multiple-phase retrieval for optical security systems using random phase encoding. *Applied Optics, 41*(23), 4825–4834.
8. Unnikrishnan, G., Joseph, J., & Singh, K. (2000). Optical encryption by double-random phase encoding in the fractional fourier domain. *Optics Letters, 25*(12), 887–889.
9. Liu, S., Yu, L., & Zhu, B. (2001). Optical image encryption by cascaded fractional fourier transforms with random phase filtering. *Optics Communications, 187*, 57–63.
10. Zhang, Y., Zheng, C. H., & Tanno, N. (2002). Optical encryption based on iterative fractional fourier transform. *Optics Communications, 202*, 277–285.
11. Candan, Ç., Kutay, M. A., & Ozaktas, H. M. (2000). The discrete fractional fourier transform. *IEEE Transactions on Signal Processing, 48*(5), 1329–1337.
12. Castaneda, R., Garcia-Sucerquia, J., Henao, R., & Trabocchi, O. (2001). Information encryption through dyadic permutations. *Optics and Lasers in Engineering, 36*, 537–544.
13. Chang, Y. C., Chang, H. T., & Kuo, C. J. (2004). Hybrid image cryptosystem based on dyadic phase displacement in the frequency domain. *Optics Communications, 236*, 245–257.
14. Rosen, J. (1993). Learning in correlators based on projection onto constrain sets. *Optics Letters, 18*(14), 1183–1185.
15. Abookasis, D., Arazi, O., Rosen, J., & Javidi, B. (2001). Security optical system based on the joint transform correlator with significant output images. *Optical Engineering, 40*(8), 1584–1589.

Chapter 52
Intelligent Decision Model of House Evaluation

Chia-Yu Hsu, Julaimin Goh and Pei-Chann Chang

Abstract House purchasing is an important decision. Customers usually search house information such as total house price, purchasing ability, location and house size through the websites of agency. However the information regarding the house attributes and surrounding environments is incomplete in most real estate agency, customers are difficult to consider the overall factors effectively and only can search candidates by sorting-based approach. This study aims to develop an intelligent decision model for house evaluation, in which information of customer preference, house attributes and house facilities, total price are integrated into house value and purchasing cost simultaneously. A case study was conducted to evaluate the validity of this study. The result demonstrated that the proposed approach can capture ideal candidate house for customer than Simple Multi-Attribute Ranking Technique (SMART).

Keywords Decision support system · House purchasing · Decision analysis · Simple multi-attribute ranking technique

52.1 Introduction

House purchasing is one of the important decisions due to the large expenses in life. Secondhand houses are usually considered first for house purchasing based on different customer demand and purchasing ability. With advanced development in information technology and intelligent applications in recent years, market of real estate has been driven to adopt innovative e-transformations [1]. However, most

C.-Y. Hsu (✉) · J. Goh · P.-C. Chang
Department of Information Management, Yuan Ze University, Chungli 32003, Taiwan, Republic of China
e-mail: cyhsu@saturn.yzu.edu.tw

J. Juang et al. (eds.), *Proceedings of the 2nd International Conference on Intelligent Technologies and Engineering Systems (ICITES2013)*, Lecture Notes in Electrical Engineering 293,
DOI: 10.1007/978-3-319-04573-3_52,

websites of house agencies only provide ranking-based results by area, price, or house size for customers without considering the overall customer preferences.

To maintain the competitive advantage and capture the market sharing, house agencies need to match requirement of customers effectively. House attributes and surrounding environment of house are considered for the evaluation before make purchasing. Most house agency website only provides complete basic information but rough information for surrounding environments of real estate. Therefore, house information location is derived by using the web-scrapper in the internet and the spatial information of surrounding area needs to be identified. However, most information available on the web is only readable to humans through presentation oriented H.T.M.L pages [2, 3].

In order to collect more house information before purchasing house, customers will typically search the candidates through the house agency website. However, most house agency only provides basic house information and less information about house facilities. To collect information detailed of house facilities, customers must collect through other websites that wasting a lot of time and difficult to find an ideal house in a short time. Therefore, integration information of house and facilities is important for customer to shorten times in searching ideal house based on customer preference.

This study aims to develop an intelligent decision model of house evaluation considering both house value, and purchasing ability simultaneously. In particular, total house price is applied to evaluate user purchasing ability and Simple Multi-Attribute Ranking Technique (SMART) is used for house evaluation based on customer preference as the house value. The case study demonstrated that the proposed approach can provide information of basic house and house facilities completely, shorten time for customer in searching ideal house, and provide users to comparing each house in different house agency.

52.2 Approach

The proposed intelligent decision model for the house evaluation and purchasing is shown in Fig. 52.1. First, the preferences, housing attribute and facilities are selected. In considered housing attributes, we use price per ping rather than total price to measure the cost of purchasing house because buyers bargain house price by discount in price per ping. Total price represents the purchasing ability which calculates in purchasing cost. Preference weight of each different attribute is calculated. The score of house evaluation is calculated according to each house attribute by different mathematic equations. The overall evaluation of candidate houses is performed by maximizing house value and minimizing purchasing cost.

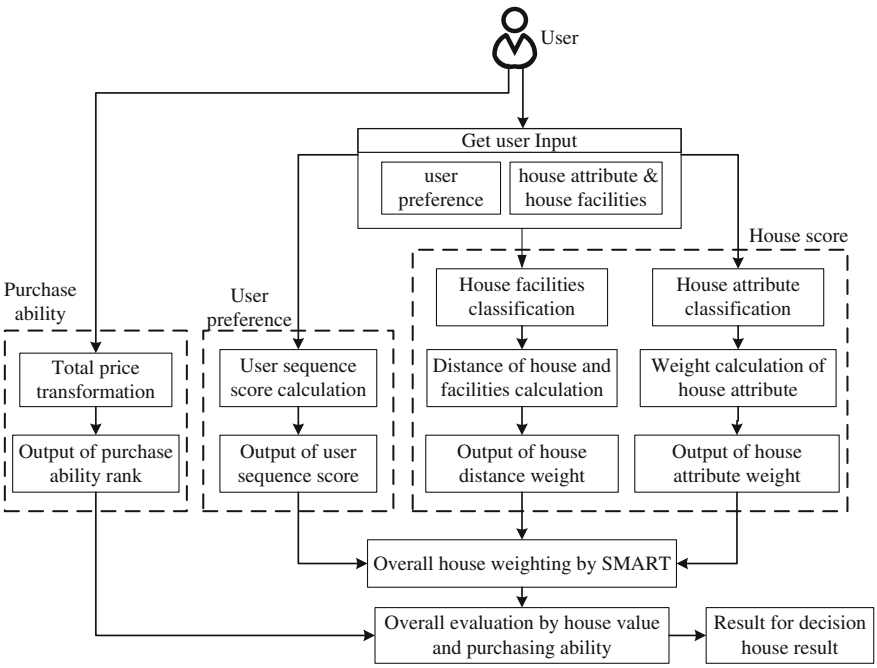

Fig. 52.1 Proposed approach for house evaluation

52.2.1 House Value

The house value is consisted of customer preference and house score. First, score for each house attribute and surrounding facilities are calculated by different mathematic equation. Score of price per ping is calculated by curve line method as seen in Eqs. (52.1, 52.2). Each minimum and maximum input value will add 20 % due to some customer may accept higher or cheaper 20 % of house price per ping input according to house agency expert experience.

$$A_{ij} = 1 - \exp\left[-\frac{p_{\max} - x_{ij}}{p}\right] \Big/ 1 - \exp\left[-\frac{p_{\max} - p_{\min}}{p}\right] \tag{52.1}$$

$$p = p_{\min} - (p_{\min} \times 0.7) \tag{52.2}$$

where A_{ij} is the score of each house j in different attribute i. $p_{\max}$ is the maximal house price per ping input, and $p_{\min}$ is minimal house price per ping input. P is a parameter of house price per ping and x_{ij} is house j of different attribute i.

Similarly, score of house size using the curve line algebra is as shown in Eqs. (52.3, 52.4). Also in each minimum and maximum input value will add 20 %. The difference in this attribute calculation is decades until 0.4 as shown in Eq. (52.4). For calculation house size attribute is decreased until 0.4 because not to

make a difference with each house score too far, and user input value added 20 % because want to search a result that a bigger house size and with the cheaper price.

$$A_{ij} = \begin{cases} A_{ij} \leq 0.4 \, A_{ij} = 0.4 \\ A_{ij} > 0.4 \, A_{ij} = 1 - \exp\left[-\frac{x_{ij} - h_{\min}}{h}\right] \Big/ 1 - \exp\left[-\frac{h_{\max} - h_{\min}}{h}\right] \end{cases} \tag{52.3}$$

$$h = h_{\max} - (h_{\min} \times 0.9) \tag{52.4}$$

where h is parameter of house size, $h_{\min}$ is minimal house size input, and $h_{\max}$ is maximal house size input.

Next, the score of number of room is determined based on what user input and compare to how many rooms that house have as shown in Eq. (52.5). In this research room attribute, score of more rooms is larger than few rooms because most of the user may accept that house room is match with desire amount or more than that.

$$x = \begin{cases} x_{ij} - 1 & A_{ij} = 0.6 \\ x_{ij} & A_{ij} = 1 \\ x_{ij} + 1 & A_{ij} = 0.8 \\ x_{ij} + 2 & A_{ij} = 0.2 \end{cases} \tag{52.5}$$

The score of house accessory is depended on whether the house included the parking lot or security. For example if user preferences want parking lot and security, then if there is one house match with the both conditions than the weight will be 1 and if just match in one condition the weight will be 0.5.

Customer usually considers not only house attribute but also traffic conditions, surrounding facilities and environmental. Harvesine formula [4] is used to evaluate the score of house facilities including education, social living, transportation and negative facilities according to the distance between the house and facilities. The evaluation of each facility is depended on how many sub- type that user consider, and each sub-type score count in average method as the evaluation score for each different type of facilities. The calculation on each facility score is determined by the nearest distance between each facility and house as showed in Table 52.1.

52.2.2 Aggregation Model

The house value (W_j) is calculated as follows:

$$W_j = \sum_{i=1}^{n} r_{ij} A_{ij} \tag{52.6}$$

where the weight of house j in attribute i (r_{ij}) is determined by Eq. (52.7) based on the preference order of attribute i (R_i).

Table 52.1 Score of house facilities

Facility type	Facility sub-type	Distance (in Km)	Interval score
Education	Kindergarten, elementary school, junior school, high school, university	0–2	1
		2–5	1–0
		more than 5	0
Social living	Clinic, bank, post office	0–2	1
		2–5	1–0
		more than 5	0
	Super market, department store	0–1	1
		1–5	1–0
		more than 5	0
Transportation	Train station, bus station, high speed rail (HSR)	0–1	1
		1–5	1–0
		more than 5	0
	Science park	0–3	1
		3–5	1–0
		more than 5	0
Negative facility	Gas station, funeral, tomb, recycle	0–1	−1
		1–3	−1 to 0
		more than 3	0

$$r_{ij} = \frac{n + 1 - R_i}{n(n+1)/2} \tag{52.7}$$

Furthermore, this study considers house value and purchasing cost, in which the rank of house value (M_j) depends on house value as shown in Eq. (52.8).

$$M_j = \begin{cases} w_j \geq 0.9 & M_j = 10 \\ 0.9 > w_j \geq 0.8 & M_j = 9 \\ 0.8 > w_j \geq 0.7 & M_j = 8 \end{cases} \tag{52.8}$$

In addition, rank of purchase ability is used in different total price multiplying the minimal input price per ping, minimal house size and maximal house size as follows:

$$B_j = \begin{cases} x_{ij} \leq b_{\min} + (b_{\min} \times 20\,\%) & B_j = 10 \\ b_{\min} + (b_{\min} \times 20\,\%) > x_{ij} > b_{\max} & B_j = 9 \\ x_{ij} \geq b_{\max} & B_j = 8 \end{cases} \tag{52.9}$$

$$b_{\min} = p_{\min} \times h_{\min},\ b_{\max} = p_{\min} \times h_{\max} \tag{52.10}$$

Table 52.2 Result of house evaluation by proposed approach

House ID	Score				Total house value	Total price	House value rank	Purchasing ability rank
	Price per ping	House size	Room	Transportation distance (km)				
273	1.00 (6.55)	1.00 (55)	0.60 (1)	1.00 (0.89)	0.96	360	10	10
991	1.00 (5.96)	1.00 (50)	0.60 (1)	1.00 (0.93)	0.96	298	10	10
166	1.00 (7.00)	1.00 (50)	0.20 (4)	0.70 (1.43)	0.80	350	9	10
2372	0.89 (13.86)	0.96 (32.5)	0.60 (1)	1.00 (0.91)	0.92	450	10	9
2596	0.93 (12.61)	0.57 (26)	0.60 (1)	1.00 (0.91)	0.85	328	9	10
255	0.99 (9.06)	1.00 (55)	1.00 (2)	0.69 (1.46)	0.87	498	9	9
624	1.00 (6.63)	1.00 (60)	1.00 (2)	0.60 (1.66)	0.84	398	9	9
1194	0.96 (11.96)	1.00 (50)	1.00 (2)	1.00 (0.89)	0.99	598	10	8
1519	1.00 (7.76)	1.00 (39.7)	0.8 (3)	0.36 (2.79)	0.72	308	8	10
1558	0.98 (10.95)	0.96 (32.7)	0.8 (3)	0.36 (2.79)	0.71	358	8	10

Table 52.3 Result of house evaluation by SMART

House ID	Price per ping	House size	Room	Transportation distance (km)	House value	Total price
1194	1.00 (11.96)	1.00 (50)	1.00 (2)	1.00 (0.89)	1.00	598
1760	0.98 (15.24)	0.99 (38)	1.00 (2)	1.00 (0.91)	0.99	580
361	1.00 (13.17)	1.00 (60)	0.80 (3)	1.00 (0.94)	0.98	790
486	1.00 (13.09)	1.00 (55)	0.80 (3)	1.00 (0.19)	0.98	720
1618	0.98 (15.49)	1.00 (58)	0.80 (3)	0.99 (1.01)	0.97	898
1835	0.99 (14.75)	1.00 (54.1)	0.80 (3)	0.94 (1.06)	0.96	798
2132	0.92 (16.78)	1.00 (59.5)	0.80 (3)	1.00 (0.93)	0.96	998
2313	0.92 (16.96)	1.00 (58.9)	0.80 (3)	1.00 (0.76)	0.96	998
2372	1.00 (13.86)	0.97 (32.5)	0.60 (1)	1.00 (0.91)	0.95	450
681	0.92 (16.29)	0.99 (35)	0.60 (1)	1.00 (0.60)	0.93	570

52.3 Case Study

To validate the proposed approach, a case study was conducted from a real estate agency in Hsinchu, Taiwan. Total 2,807 houses collected from house agency around eight months were used as candidates. There are total 1,853 facilities collected in this study until 2012. Assuming a customer wants to purchase a house in the Hsinchu City, and price per ping in between 10 to 15 thousand per area with affordable price around 300 until 500 thousand, house size is between 30 ping (1 ping = 36 sq ft.) and 50 ping, and Hsinchu High Speed Rail (HSR) nearby. The preference order for the housing factors are transportation, price per ping, house area size, number of room.

Tables 52.2 and 52.3 show the first 10 house candidates by proposed approach and using SMART only. Although house #624 is bigger than house #273, but user preference wants house with near HSR and total price of house #273 is cheaper than #624. With same distance of house facility in #2732 and #2596, which shows that proposed method recommended house #2372 first because house size of house

#2372 is bigger than house #2596. To compare both methods based on customer preference, there are six candidates by SMART exceeding user purchasing ability. Indeed, total house price multiplying by price per ping and house size is also critical to purchase house. Comparing the analysis results, the candidate houses by proposed approach have cheaper price per ping with the nearest distance to HSR than using SMART.

52.4 Conclusion

This study proposes an intelligent decision model with considering the preference and condition of house attribute and house facilities rather than using ranking individual house attribute. Geographic information system is to incorporate the information of surrounding facilities for evaluating the living quality of the surrounding area. House value evaluation and purchasing cost of the total house price are considered simultaneously for house evaluation rather than sorting by price only. We also have developed a decision support system to implement into a real estate company.

Further research can consider other important facilities including subway, work place and future business area. Additionally, adding some area that have government plan on building project as consider evaluation for example in Taichung city will build a metro rapid transit system in the future, many customer will buy house in location nearby.

Acknowledgments This research is appreciatively supported by National Science Council, Taiwan (NSC99-2622-E-007-015-CC3; NSC 100-2410-H-155-048) and Ministry of Economic Affairs, Taiwan (102-E0616).

References

1. Zavadskas, E. K., Kaklauskas, A., & Banaitis, A. (2010). Real estate's knowledge and device—Based decision support system. *International Journal of Strategic Property Management, 14*(3), 271–282.
2. Xiao, Q. P., Fu, M. C., Wang, G. J., & Zhang, J. J. (2009). *House site selection decision support system based on ArcGIS. International conference on management and service science* (pp. 1–4).
3. Shi, G., & Barker, K. (2011). Thematic data extraction from web for GIS and applications. *International conference on spatial data mining and geographical knowledge services* (pp. 27–278).
4. Sinnott, R. W. (1984). Virtues of the haversine. *Sky and Telescope, 68*(2), 158.

Chapter 53
A Trident Shape CPW Antenna for UWB Applications

Wen-Shan Chen and Chun-Lin Ciou

Abstract This article presents a coplanar waveguide (CPW) antenna with a trident shape for ultra-wideband (UWB) applications. First, a basic shape of trident CPW antenna is proposed to excite three resonant modes. The three resonances create a wide operating band but cannot cover the entire UWB band. To increase the impedance matching, the parameters of the proposed antenna are modified, which include adding two strips on the two outer arms and truncating two slots on the bottom of the middle arm. The ground plane of the proposed design is also modified to obtain better impedance matching. Finally, the 10 dB return loss that covers the UWB applications is accomplished. Besides, the dimensions of the proposed design occupy a small area of 32 mm × 17 mm × 0.8 mm with planar structure, which is convenient to apply in wireless devices. This article will provide the experimental measurements of return loss, radiation patterns.

Keywords CPW antenna · UWB · Trident shape · 2-D structure

53.1 Introduction

In recent years, many wireless products for ultra-wideband (UWB) applications are investigated for the advantages of high-speed transmission, low power consumption, and simple hardware configuration. Antenna, the most important component for wireless system, is developed in various configurations and substrate materials in the previous publications. Coplanar waveguide (CPW) feeding having the benefits of 2-D planar structure, small dimensions, and wide impedance bandwidth becomes an optimal design mechanism in designing wideband

W.-S. Chen (✉) · C.-L. Ciou
Department of Electronic Engineering,
Southern Taiwan University of Science and Technology,
Tainan City 71005, Taiwan, Republic of China
e-mail: chenws@mail.stust.edu.tw

J. Juang et al. (eds.), *Proceedings of the 2nd International Conference on Intelligent Technologies and Engineering Systems (ICITES2013)*, Lecture Notes in Electrical Engineering 293,
DOI: 10.1007/978-3-319-04573-3_53,

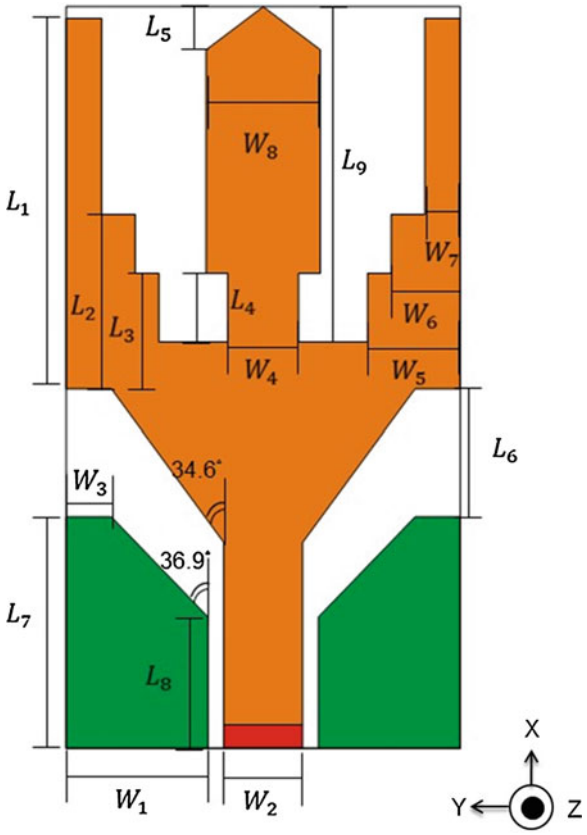

Fig. 53.1 Geometry of the proposed antenna

microwave communication elements. In [1–6], the CPW antennas use circular shape or bevel edge on both antenna portion and ground plane, which reduce the impedance variations to obtain wider impedance bandwidth and meet the UWB application bands. The reference antennas use the popular monopole type or slot type antenna as their main structures. In the proposed design, a trident CPW antenna which excites three fundamental modes and two higher modes to achieve wider impedance bandwidth (2.4–10.6 GHz), is proposed for UWB applications. The proposed design not only performs a wide operating bandwidth but also has a compact dimension of 32 mm × 17 mm × 0.8 mm.

53.2 Antenna Design and Results

The proposed trident shape antenna shown in Fig. 53.1 is fabricated on an FR4 substrate with thickness of 0.8 mm, area of 32 mm × 17 mm, permittivity constant of 4.4, and loss tangent of 0.0245 S/m. The main structure of the trident

Table 53.1 Detailed dimensions of the proposed antenna

Antenna parameters						unit: mm	
L_1	L_2	L_3	L_4	L_5	L_6	L_7	L_8
16	7.5	5	3	1.9	5.5	10	5.6
W_1	W_2	W_3	W_4	W_5	W_6	W_7	W_8
6.1	3.4	2	3	4	3	1.5	5

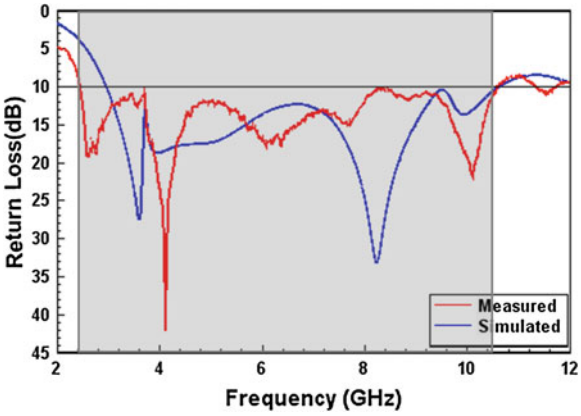

Fig. 53.2 Simulated and measured return losses of the proposed antenna

antenna consists of two outer arms on both sides and a middle arm. To increase the impedance matching, the two outer arms is added two strips (L_2 and L_3) to smooth the guiding current and the middle arm is truncated two slots (L_4) to match the impedance. In addition, the angle of the bevel edge in antenna geometry is 34.6° while that of antenna ground is 36.9°. The antenna ground is fabricated on both ends of the substrate and a 50-ohm CPW-fed line with width of 3.4 mm (W_2) is printed through the ground plane. Detailed dimensions of the proposed antenna are listed in Table 53.1.

To confirm the antenna's application bands, the measured and simulated return losses of the proposed antenna are shown in Fig. 53.2. The simulated results of this paper are obtained through high frequency simulation software (HFSS). From the results, the agreements of the measured and simulated return losses can be seen although small variations of resonances and impedance matching are existing, which are occurred by the fabrication errors. The measured result based on 10 dB return loss (2.4–10.6 GHz) covers the UWB application.

The surface current distributions of the proposed antenna at the five resonant frequencies (3.6, 3.9, 5, 8.2 and 9.9 GHz) are plotted in Fig. 53.3. From Fig. 53.3a, b, c, the surface current distributions at 3.6, 3.9, and 5 GHz are concentrated on the middle arm, the two outer arms, and the 34.6° bevel edge, respectively. The results indicate that the three resonances are obtained from their fundamental modes. The higher operating bands at 8.2 and 9.9 GHz are achieved from higher modes of the two outer arms and the middle arm as shown in

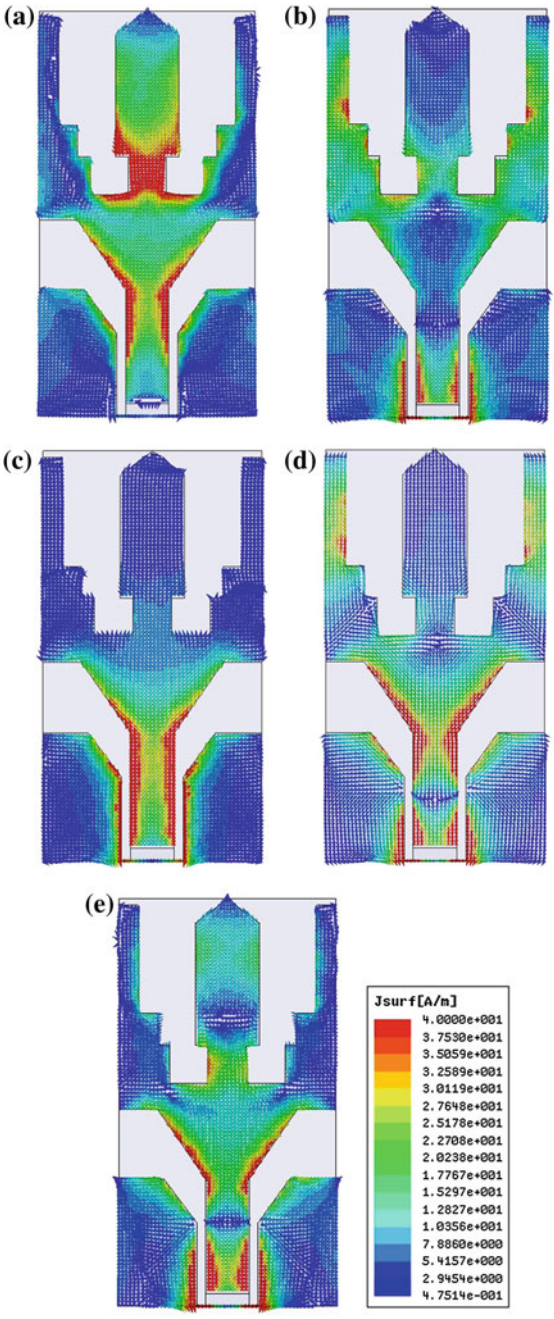

Fig. 53.3 Simulated current distributions at different frequencies **a** 3.6 GHz, **b** 3.9 GHz, **c** 5 GHz, **d** 8.2 GHz, **e** 9.9 GHz

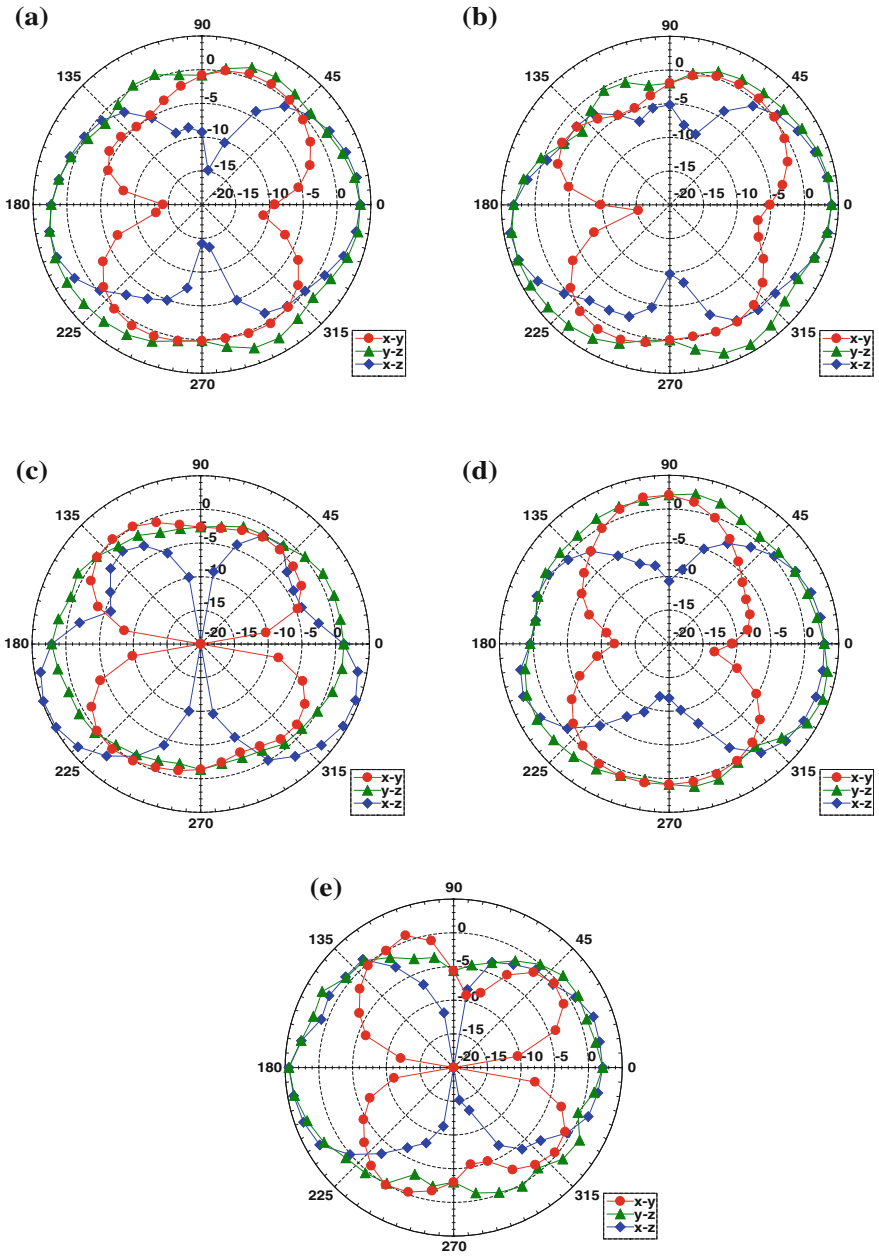

Fig. 53.4 Simulated radiation patterns at **a** 3.6 GHz, **b** 3.9375 GHz, **c** 5.05 GHz, **d** 8.23125 GHz, **e** 9.94375 GHz

Fig. 53.3d, e. In Fig. 53.4, the simulated radiation patterns at 3.6, 3.9, 5, 8.2 and 9.9 GHz are presented. From the results, the patterns in the Y–Z plane perform an omni-directional characteristic and that in the X–Y and X–Z plane have the shape of number 8. Because the 8.2 and 9.9 GHz bands are higher modes, the patterns are slightly twisted. Besides, the patterns are similar to the conventional dipole antennas that have a benefit of stable reception.

53.3 Conclusion

The trident CPW antenna for UWB applications is proposed and verified. Three fundamental modes and two higher modes obtained by the middle arm, the two outer arms, and the 34.6° bevel edge produce a wide operating band. The measured bandwidth based on 10 dB return loss is from 2.4 to 10.6 GHz that covers the UWB application bands (3.1–10.6 GHz). The proposed design not only operates broad operating band but also occupies a compact dimensions of 32 mm × 17 mm × 0.8 mm. The compact and 2-D planar structure has advantages of easy fabrication and applying in the wireless devices. Beside, the radiation patterns perform an omni-directional characteristic in the Y–Z plane and the shape of number 8 in the X–Y and X–Z plane.

Acknowledgments This work was supported by the National Science Council of Taiwan under grant numbers of NSC 101-2221-E-218-032-, NSC 102-2221-E-218-005- and NSC 101-2632-E-218-001-MY3.

References

1. Xu, J., Shen, D. Y., Zhang, X. P., & Wu, K. (2012). A compact disc ultrawideband (UWB) antenna with quintuple band rejections. *IEEE Antennas and Wireless Propagation Letters, 11*, 1517–1520.
2. Jiang, Y. T., Zhang, H., Xu H. Y., Zhang, R., & Zeng X. F. (2012). A novel ultra-wideband antenna with band notch characteristic. In *2012 International Conference on Microwave and Millimeter Wave Technology (ICMMT)* (Vol. 3, pp. 1–4). Shenzhen, China.
3. Bod, M., Hassani, H. R., & Taheri, M. M. S. (2011). Compact printed UWB antenna with a tunable extra band. In *Antennas and Propagation Conference (LAPC), 2011 Loughborough* (pp. 1–3). Loughborough, UK.
4. William, J., & Nakkeeran, R. (2009). CPW-fed UWB slot antenna with band notched design. In *Microwave Conference on APMC 2009, Asia Pacific* (pp. 1833–1836). Suntec City, Singapore.
5. Bialkowski, M. E., & Abbosh, A. M. (2008). Design of UWB planar antenna with improved cut-off at the out-of-band frequencies. *IEEE Antennas and Wireless Propagation Letters, 7*, 408–410.
6. Jalil, M. E., Rahim, M. K. A., Abdullah, M. A., & Ayop, O. (2012). Compact CPW-fed ultra-wideband (UWB) antenna using denim textile material. In *2012 International Symposium on Antennas and Propagation (ISAP 2012)* (pp. 30–33). Yokohama, Japan.

Chapter 54
Core Competence of Information Security Service Specialists in System Integration Service Provider

Chun-Yi Chen, Chen Lin, Tsung-Hui Lu, Hsin-Fu Chen and Jung Nien Chou

Abstract In Taiwan, about 80 % information security services companies are system integration services provider. In the era of recession, system integration service companies are not only promising, there are also a large job market in Taiwan. This research use Modified Delphi and AHP to study core competence and core competence relationship between four information security service specialists working in system integration service provider. The results provide statistics to be reference by industries and academic.

Keywords System integration service provider · Information security service specialists · Core competence · Modified delphi · Analytic hierarchy process

C.-Y. Chen (✉) · C. Lin · H.-F. Chen · J. N. Chou
Department of Information Management, Huafan University, Taipei County 22301, Taiwan, Republic of China
e-mail: konamiei88@gmail.com

C. Lin
e-mail: linchen@cc.hfu.edu.tw

H.-F. Chen
e-mail: skywingsc@gmail.com

J. N. Chou
e-mail: dtlhp.chou@gmail.com

T.-H. Lu
Department of Mechatronic Engineering, Huafan University, Taipei County 22301, Taiwan, Republic of China
e-mail: jeffth.lu@gmail.com

J. Juang et al. (eds.), *Proceedings of the 2nd International Conference on Intelligent Technologies and Engineering Systems (ICITES2013)*, Lecture Notes in Electrical Engineering 293,
DOI: 10.1007/978-3-319-04573-3_54,

54.1 Introduction

This study try to find out the core competence of information security service specialists aspiring to enter the system integration services provider industries, and the core competence relationship between the four different specialists to make personal career planning reference in this industries.

54.2 Literature Reviews

54.2.1 System Integration Service Provider

Taiwan's information security industry chain, including upstream of the information security manufacturer, in the middle of distributors, agents, as well as downstream services provided directly to end-users: systems integrated service providers, information security consulting company, carriers, etc. [1]. System integration service providers (SI) to the needs of enterprise customers based on providing solutions to selected problems for the customer information systems, including the integration of Internet, telecommunications, hardware and also software or custom software packages, technical consulting and training, etc. [2].

54.2.2 Information Security Service Specialists

System integration projects directly related information security service specialists can be divided into the following four categories:

1. Product Tech Manager (PTM): PTM need to understand product line relevant market information, price competition, also need the overall information systems experience to make the right plan to suit customer security system environment.
2. Project Manager (PM): Main tasks of the PM perform project management, coordinate internal resources and external customer and suppliers, in order to effectively control the progress of the project.
3. Account Manager (AM): AM needs to promote business, maintain a good customers relationship, enhance customer service, handle customer complaints.
4. Engineer: Engineer responsible for equipment installation and setting, solve client problems, device repair, upgrades, maintenance and troubleshooting.

54.2.3 Core Competence

For PTM core competence of view, Lehmann and Winner [3] research this role by product management. Kim Clark [4] Investigate PTM by project plan.

For PM core competence of view, Cleland and King [5] proposed a PM in addition to professional basic knowledge, practical work experience and also prepare special personality traits. American Project Management Association [6] developed a project management body of knowledge. Harrison [7] believes PM is a variety of role combination.

For AM core competence of view, Spencer and Spencer [8] believe AM should have power and influence infection and other 11 major items core competence. Robinson [9] thinks a good AM to have a keen mind, right work ethic and other characteristics.

For Engineer core competence of view, Spencer and Spencer [8] discussed the importance of tech staff capabilities included teamwork, expertise…12 items.

54.3 Research Methodology: Synthesis of Overall Priority Matrix

This research conducted related literature to find out the Modified Delphi assessment criteria and then apply analytic hierarchy process (AHP) for analyzing core competence of Specialists working in SI. This study considers the Panel of Experts' familiarity and representative indicators, to select 20 experts currently working in SI, and hold positions seniority from 7 to 23 years.

Core competence factors and assessment criteria divided into three levels: the first layer goal is: Core Competence of Specialists, the second layer core competence factors are: "expertise", "management", "personality", the third layer is the core competence criteria according to the Specialists. Research framework refers to Fig. 54.1.

54.4 Data Analysis and Findings

Table 54.1 below shows the AHP questionnaire analyzing and criteria sorting of Specialists.

Critical core competence interactions between Information Security Service Specialists can be used as personal career plan working in the system integration provider, refer to Table 54.2.

Specialist core competence comparing in three factors and proportion in expertise factor refer to Fig. 54.2,

Analyze the proportion in factors of management and personality, refer to Fig. 54.3.

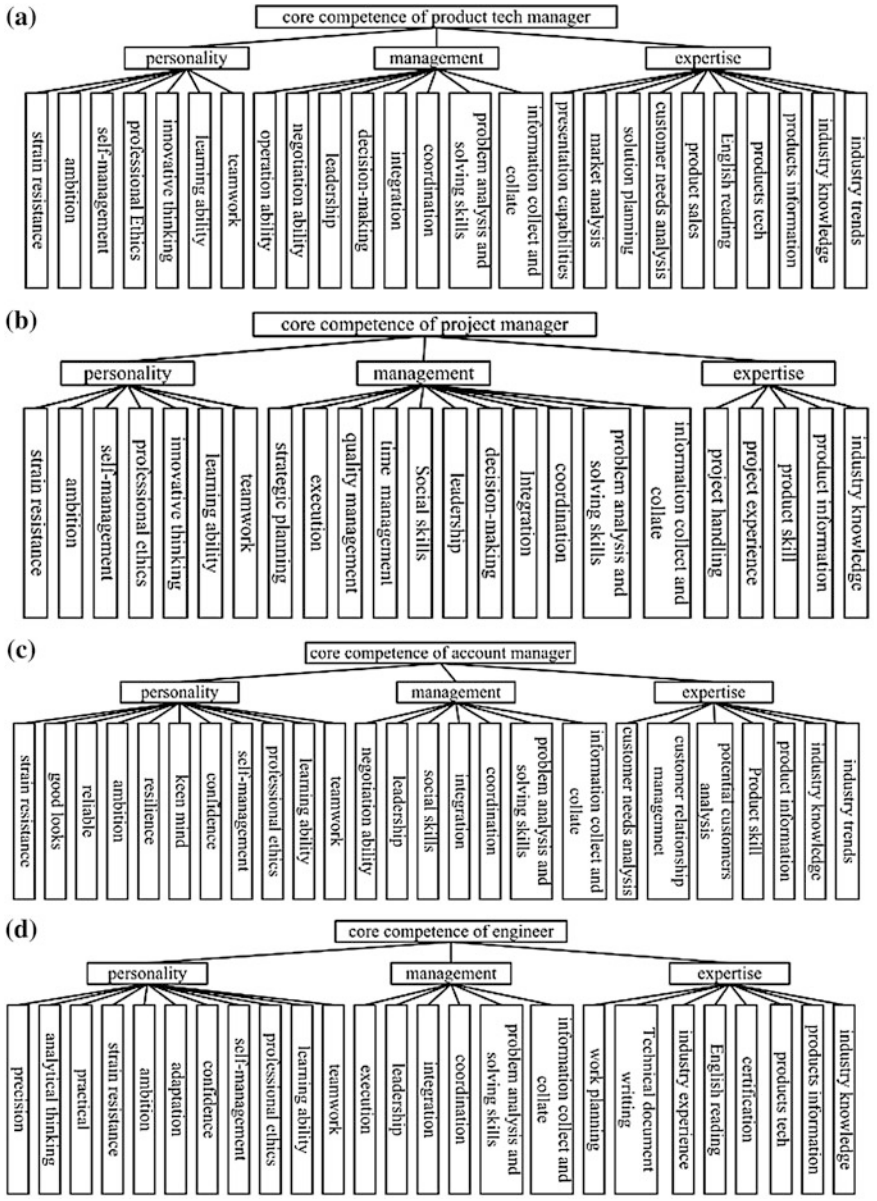

Fig. 54.1 Specialists core competence research framework. **a** Product tech manager (PTM). **b** Project manager (PM). **c** Account manager (AM). **d** Engineer

Table 54.1 Specialists core competence importance sorting table

	Factor	Relative weights	Absolute	Ranking by factor	Total ranking
Core competence of product tech manager (*PTM*)					
Goal	Expertise	0.49		1	
	Management	0.28		2	
	Personality	0.23		3	

	Criteria	Relative weights	Absolute	Ranking by factor	Total ranking
Expertise	Solution planning	0.34	0.17	1	1
	Customer needs analysis	0.23	0.11	2	2
	Product information	0.14	0.07	3	7
	Industry knowledge	0.11	0.05	4	8
	Market analysis	0.1	0.05	5	9
	Industry trends	0.08	0.04	6	11
Management	Problem analysis and solving skills	0.36	0.1	1	3
	Information collect and collate	0.3	0.09	2	4
	Integration	0.16	0.05	3	10
	Coordination	0.1	0.03	4	13
	Negotiation ability	0.06	0.02	5	15
Personality	Learning ability	0.34	0.08	1	5
	Teamwork	0.34	0.08	2	6
	Self-management	0.14	0.03	3	12
	Innovative thinking	0.11	0.02	4	14
	Professional ethic	0.08	0.02	5	16

	Factor	Relative weights	Absolute	Ranking by factor	Total ranking
Core competence of project manager (*PM*)					
Goal	Expertise	0.32		3	
	Management	0.35		1	
	Personality	0.34		2	

	Criteria	Relative weights	Absolute	Ranking by factor	Total ranking
Expertise	Project execution	0.3	0.09	1	2
	Project handling	0.29	0.09	2	3
	Project experience	0.2	0.06	3	8
	Product information	0.11	0.04	4	13
	Industry knowledge	0.11	0.04	5	15
Management	Coordination	0.31	0.11	1	1
	Problem analysis and Solving skills	0.24	0.08	2	4
	Integration	0.19	0.07	3	7
	Leadership	0.14	0.05	4	11
	Decision-making	0.13	0.05	5	12

(continued)

Table 54.1 (continued)

	Criteria	Relative weights	Absolute	Ranking by factor	Total ranking
Personality	Teamwork	0.24	0.08	1	5
	Learning ability	0.23	0.08	2	6
	Interpersonal relationship handling	0.18	0.06	3	9
	Strain resistance	0.16	0,05	4	10
	Ambition	0.1	0.04	5	14
	Self-management	0.09	0.03	6	16

	Factor	Relative weights	Absolute	Ranking by factor	Total ranking
Core competence of account manager (AM)					
Goal	Expertise	0.33		2	
	Management	0.33		3	
	Personality	0.36		1	

	Criteria	Relative weights	Absolute	Ranking by factor	Total ranking
Expertise	Customer needs analysis	0.26	0.09	1	1
	Customer relationship management	0.26	0.09	2	2
	Potential customers analysis	0.24	0.08	3	4
	Product information	0.14	0.05	4	10
	Industry knowledge	0.1	0.03	5	16
Management	Negotiation ability	0.26	0.09	1	3
	Coordination	0.23	0.08	2	5
	Social skills	0.22	0.07	3	6
	Integration	0.11	0.04	4	15
	Problem analysis and solving skills	0.1	0.03	5	17
	Information collect and collate	0.09	0.03	6	19
Personality	Teamwork	0.17	0.06	1	7
	Strain resistance	0.15	0.06	2	8
	Ambition	0.13	0.05	3	9
	Confidence	0.12	0.04	4	11
	Keen mind	0.12	0.04	5	12
	Reliable	0.12	0.04	6	13
	Resilience	0.1	0.04	7	14
	Learning ability	0.09	0.03	8	18

	Factor	Relative weights	Absolute	Ranking by factor	Total ranking
Core competence of engineer					
Goal	Expertise	0.42		1	
	Management	0.32		2	
	Personality	0.26		3	

	Criteria	Relative weights	Absolute	Ranking by factor	Total ranking
Expertise	Product tech	0.39	0.16	1	1
	Technical document writing	0.2	0.08	2	3
	Work planning	0.18	0.08	3	4
	Work execution	0.17	0.07	4	7
	Product information	0.07	0.03	5	15

(continued)

Table 54.1 (continued)

	Criteria	Relative weights	Absolute	Ranking by factor	Total ranking
Management	Problem analysis and solving skills	0.36	0.11	1	2
	Analytical thinking	0.22	0.07	2	5
	Integration	0.22	0.07	3	8
	Coordination	0.21	0.07	4	9
Personality	Learning ability	0.27	0.07	1	6
	Teamwork	0.17	0.04	2	10
	Self-management	0.15	0.04	3	11
	Strain resistance	0.15	0.04	4	12
	Practical	0.14	0.04	5	13
	Precision	0.12	0.03	6	14

Table 54.2 Critical core competence interactions between speclists

Item	Criteria	Factor	PTM (%)	PM (%)	AM (%)	Engineer (%)
1	Problem analysis and solving skills	Management	10.2	8.2		11.4
2	Learning ability	Personality	7.7	7.6		7.0
3	Teamwork	Personality	7.6	8.1	5.9	
4	Coordination	Management		10.6	7.6	
5	Customer needs analysis	Expertise	11.3		8.7	

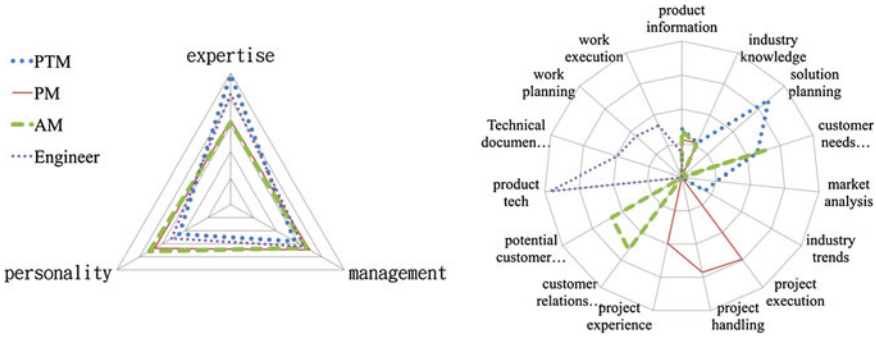

Fig. 54.2 Specialists' core competence comparing in three factors (*left fig.*) and proportion in expertise factor (*right fig.*)

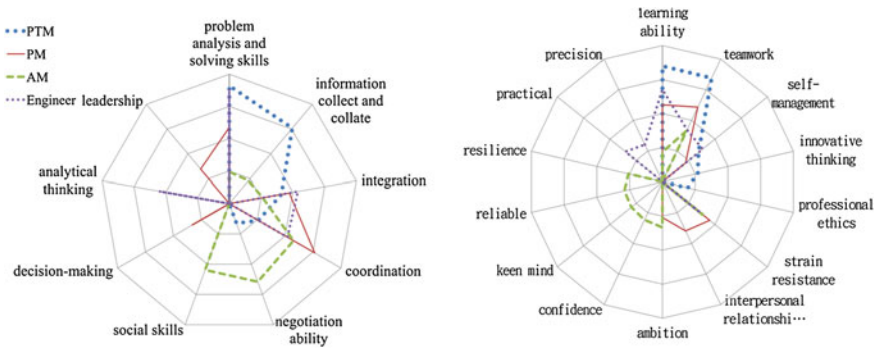

Fig. 54.3 Specialists core competence comparing in managemnet (*left fig.*) and personality factors (*right fig.*)

54.5 Conclusion

Core competence of Information Security Service Specialist is as follows:

1. Product Tech Manager: criteria of solution planning, customer needs analysis, problem analysis and solving skills, information collect and collate, learning ability, teamwork, the total weighted ratio is up to 62.0 % as PTM the most critical indicators of core competence.
2. Project Manager: criteria of coordination, project execution, project handling, problem analysis and solving skills, teamwork, learning ability, integration, the total weighted ratio is up to 59.6 % as PM the most critical indicators of core competence.
3. Account Manager: criteria of customer needs analysis, customer relationship management, negotiation ability, potential customer analysis, coordination, social skills, teamwork, strain resistance, the total weighted ratio is up to 59.9 % as AM the most critical indicators of core competence.
4. Engineer: criteria of products tech, problem analysis and solving skills, Technical document writing, work planning, analytical thinking, learning ability, the total weighted ratio is up to 57.5 % as Engineer the most critical indicators of core competence.

References

1. Institute for Information Industry-MIC. (2009). *Information security trends and opportunities in Taiwan*. R.O.C: Ministry of Economic Affairs.
2. Institute for Information Industry- MIC. (2001). *2000–2003 project integration of market development status and trend analysis*. R.O.C: Ministry of Economic Affairs.
3. Lehmann, D. R., & Winner, R. S. (1994). *Product management*. Burr Ridge: Irwin.

4. Clark, k. B., & Wheel Wright, S. C. (1992). Creating project plans to focus product development. *Harvard Business Review*, *72*(2), 70–82.
5. Cleland, D. I., & King, W. R. (1983). *System analysis and project management* (2nd ed.). New York: McGraw-Hill.
6. Project Management Institute. (1984). Project management body of knowledge (PMBOK). New York: Project Management Institute.
7. Harrison, F. L. (1993). *Advanced project management*. England: Gower.
8. Spencer, L. M., & Spencer, S. M. (1993). *Competence at work: Models for superior performance*. New York: John Wiley and Sons.
9. Robinson, D. (1981). The salesman ambassador of progress. *Journal of Business Research, 8*, 275–284.

Chapter 55
Development of a Low-Cost Flight Simulation Training Device for Research and Education

Lung-Nan Wu and Yun-Ping Sun

Abstract A low-cost and high-fidelity flight simulation training device (FSTD) has been developed for the purpose of research and education. With inexpensive and easy obtained materials, the FSTD duplicates a realistic cockpit and relevant hardware of the airplane Beech 1900C. The computational platform is a PC-based cluster system. The commercial-off-the-shelf (COTS) software of Microsoft Flight Simulator 2004 is the computational kernel of the simulation system. Two middleware, named as FSUIPC and WideFS, are used for data interchange between cluster computers. An instructor workstation is included in this system to manage the mission of the flight simulation. USB 2.0 interface is also adopted for connecting the cockpit hardware and the hardware control computer (HCC).

Keywords Flight simulation training device (FSTD) · Systems integration · Human-in-the-loop (HITL) · Commercial-of-the-shelf (COTS)

55.1 Introduction

The flight simulation training device (FSTD) is a highly integrated engineering system. It involves many knowledge domains and integrates numerous technologies to comprise a sophisticated human-in-the-loop (HITL) simulation system. It has given a substantial contribution to aviation and will play an important role continuously in the future. The FSTD is also a valuable topic for the study in

L.-N. Wu (✉)
Department of Avionics Engineering, R.O.C. Air Force Academy, Kaohsiung 82047, Taiwan Republic of China
e-mail: rolandwu@cc.cafa.edu.tw

Y.-P. Sun
Department of Mechanical Engineering, Cheng Shiu University, Kaohsiung 83347, Taiwan Republic of China

J. Juang et al. (eds.), *Proceedings of the 2nd International Conference on Intelligent Technologies and Engineering Systems (ICITES2013)*, Lecture Notes in Electrical Engineering 293,
DOI: 10.1007/978-3-319-04573-3_55,

academia. However, a high-fidelity flight simulator in the business market is very expansive and unaffordable for general universities. It has confined study aspect to a limit area for academics in former days. However, owing to the benefit by the emerging of the Commercial-off-the-shelf (COTS) hardware and software in this decade, building a high-fidelity and affordable FSTD on campus becomes feasible.

Since 2007, the Chinese research team of School of Mechatronics Engineering in Harbin Institute of Technology has published their works [1, 2] to present they achievements using COTS products to develop a low-cost and high-fidelity Boeing 737-300 flight simulator. In 2009, Professor Swenson had reported their efforts for developing a Boeing 737-NG flight simulator, base on Field Programmable Gate Array (FPGA) technique as a multidisciplinary education platform [3]. The Brazilian research group in Federal University of Minas Gerais [4] had also published a work to propose the development of a PC-based flight simulator for the pilot assistance research in 2010. The common features of the above researches are using COTS software and hardware to come down cost and reduce the complexity of the development. In this work, an experimental FSTD of Beech 1900C (BE-1900C), based on the advantage of COTS products, has been built. The PC-based hardware and COTS software of Microsoft Flight Simulator 2004 (FS2004) and relevant add-on software were used to construct the main framework. Visual C++ was used for developing interface software to link PC to the cockpit hardware. Moreover, Keil C was used for programming the firmware to drive the microprocessor on the cockpit hardware.

Microsoft Flight Simulator (MSFS) is a series of flight simulator programs for the Microsoft Windows operating system. It has been developed for over 25 years. It was originally marketed as video games and afterward evolved into a visual simulation platform of COTS software for military and commercial applications. The older version of MSFS, FS2004 released in 2003, was adopted in this work to construct the simulation platform according to the study in Ref. [5]. Reference [5] concluded that FS2004 has better real-time characteristics and temporal stability than the newest version of MSFS, Flight Simulator X, especially while it runs in a common PC with cozy computing power and storage resources.

55.2 Overview of System Architecture

This section describes the physical structure and computational architecture of the FSTD, as shown in Fig. 55.1. The constructed system is categorized into two major parts of hardware and software. The hardware is a simulated cockpit with a functional flight deck and a visual & audio system which are driven by a PC cluster. The software is composed of FS2004 simulation platform, aircraft and scenery add-on modules, FSUIPC and WideFS middleware, USB interface software, and microprocessor firmware. USB interface software and microprocessor firmware have been programmed in this work. The following is the details.

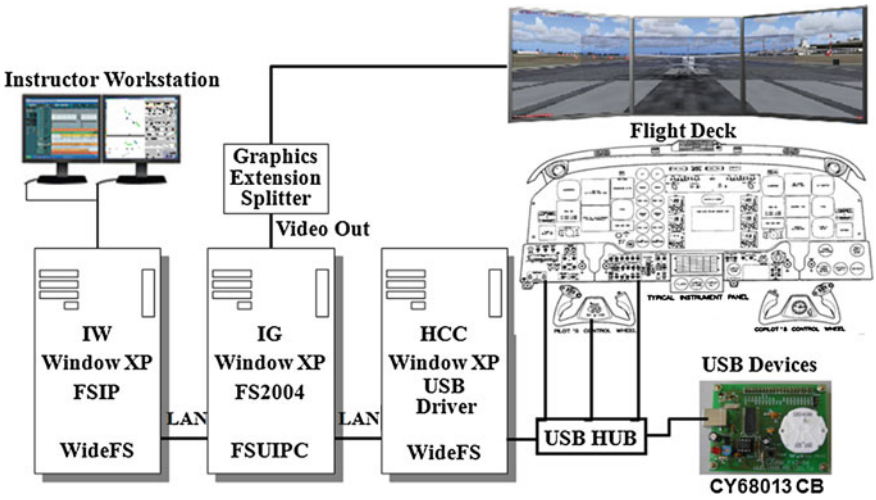

Fig. 55.1 Physical structure and computational architecture of the FSTD

There are many types of equipments installed on the flight deck of BE-1900C. They include a main instrument panel, four instrument subpanel, fuel control panel, circuit breaker panel, overhead light control and electrical instrument panel, and power control pedestal and central console. The above modules are important equipments of human–machine interfaces. They feature a great effect in fidelity for FSTD. This work employed inexpensive and easy obtained materials to duplicate a 1:1 scale highly resembled cockpit and relevant hardware according to the size, function, and operation method of aircraft BE-1900C. All equipments inside the simulated cockpit are functionally accurate.

The simulated fidelity of a flight simulator is closely related to the real-time computation capability of operating computers. Frame time is a small period of time that the simulator completes numerical calculation, updates data, and refreshes cuing system. In general, the frame time of a real-time flight simulator should be less than 33.3 ms in order to cheat human sense and let human feel that the simulation is smooth. The frame rate for modern FSTD is up to 60 Hz. In order to improve the efficiency of computation, a PC-based cluster system was adopted. Three PC, illustrated in Fig. 55.1, were used and linked via Local Area Network (LAN) to comprise a distributed simulation system. The first PC is image generator (IG) for running the FS2004 and outputting dynamic data and the scenery image. The second PC is a hardware control computer (HCC), responsible for a human–machine interface I/O control. The third PC is instructor workstation (IW), charged with a mission management.

Surrounding multi-projection visual system has been widely adopted in high-end FSTD. A simplified and cheap multi-channel LCD visual system was substituted in this work. Three 20-inch LCD monitors were installed in front of the cockpit to display three different angle-of-view, which are front, left, and right

scenery, simultaneously. In order to deliver the wide angle of simulated image to three LCDs, a graphic splitter, Matrox TripleHead2Go, was employed for splitting the wide angle of the image and then outputting to three VGA ports. Audio signals were directly generated from FS2004 and output to speakers inside the cockpit.

The kernel of FS2004 has a build-in 6-DOF flight dynamic module. It incorporates with an aircraft module, weather module, and scenery module to calculate the dynamic behavior of the simulated airplane and generate the scenery image. FS2004 includes a few lower fidelity aircraft modules and lower resolution scenery modules. Therefore, many high quality add-on modules for aircraft, scenery, and utility are produced by 3rd party of MSFS and sold on SimMarket [6]. PMDG's BE-1900C aircraft module and Samsoft's "The Sky of Taipei" scenery module are add-on software for FS2004 and were adopted in this work to enhance the quality of visual cue.

Two COTS middleware of FS2004, FSUIPC (Flight Simulator Universal Interprocess Communication) and WideFS [7], are employed for the data interchange between cluster computers. FSUIPC and WideFS form a client–server application. FSUIPC is an add-on module of FS2004. It enables an external process to communicate with FS2004. WideFS is composed by WideClient and WideServer. WideServer is packed into FSUIPC module. FSUIPC module including WideServer was installed in IG. WideClient was independently installed in HCC and IW. WideClient in HCC gets control data that generated from the flight yoke, power lever, rudder paddle and various control devices. Then, WideServer in IG gets the data from the WideClient via LAN and handed it on to FSUIPC. Afterward FSUIPC outputs data to FS2004 by the method of memory mapping. In the counter way, FSUIPC gets data from FS2004 by the same method, and hands it on to WideServer. Then, WideClient in HCC gets the data from WideServer via LAN and outputs it to various indicators to drive them. USB 2.0 was used for connecting the HCC and cockpit hardware. Therefore, the USB interface software must be developed for all USB devices. It was developed in Visual C++. It runs in HCC to communicate WideClient with USB data bus. Furthermore, the cockpit hardware with a USB micro-processor is driven by a firmware which accesses data from endpoints of USB data bus and controls the relevant electronic parts. It was developed in Keil C.

An instructor management software, FSIP (FS Instructor Panel) [8], was installed in IW. FSIP is an application software for FS2004. It is used to act as a workstation for the flight instructor in combination with any kind of procedure training. It can be used for the flight tracking, flight logging and for any manipulation on lots of parameters, such as weather, aircraft systems, positioning data, etc. It also provides a detailed overview to the actual flight situation. FSIP also communicates with FS2004 by way of WideFS and FSUIPC.

55.3 Hardware Construction

According to the function and geometric shape of a real BE-1900C airplane, a duplicated flight deck has been built in this work. Figure 55.2 shows some of completed modules.

The most important and complex hardware are various indicators. There are total 49 miscellaneous indicators required. In order to cost down the budget of this work, all those indicators, except a flight hour indicator that has been gotten from a retired airplane, were planned to be built. Cyress EZ-USB CY68013 microprocessor is a high-speed USB peripheral controller. It was adopted for accessing data from USB data bus and controlling electronic parts such as step motor, servo motor, LED, LCD, rotary encoder, switch, etc. Figure 55.3 shows some built indicators of an amount up to 33. Another 16 indicators are still under construction or test. Figure 55.4 shows the flight deck module.

In Fig. 55.4, COTS hardware of flight yoke, throttle quadrant, and rudder pedal are adopted temporally. They are lower fidelity in geometric shape and operation method. A highly alike customized power console, dual flight yoke and rudder pedal system for pilot and co-pilot control are under development.

55.4 Systems Integration

The FSTD of this work integrated many hardware and software to make up a versatile training system. A mission of the simulated flight starts from input a set of parameters to FSIP, as shown in Fig. 55.4, to set simulated conditions. Those initialized status data are sent to FS2004 in IG to activate the mission. While the mission starts, control signals are input to HCC and then sent to FS2004. FS2004 incorporates control data with the aircraft module and environment module to calculate dynamic behavior of the aircraft and produce new status data. Some of those data are returned to HCC to drive various indicators. Meanwhile, FS2004 also refreshes the visual and audio system, which let pilots see and hear the moment situation and make a response to the FSTD. These processes are iterated continuously to form a human-in-the-loop, virtual reality system.

The data of the flight situation also inputs to IW and displays on a status window of FSIP synchronously, as shown in Fig. 55.5. It provides the flight instructors with a detailed overview to manage flight lessons. Instructors can track flights and add some abnormalities or change the flight conditions or even pause or stop the mission. Instructors can also log the flight lesson and analyze it later to improve the flight training efficiency. This work integrates a mission management system with a physically cueing system of flight to comprise an FSTD.

Fig. 55.2 Two control panel module of the FSTD

Fig. 55.3 Various indicators on instrument panel

Fig. 55.4 The flight deck of BE-1900C FSTD

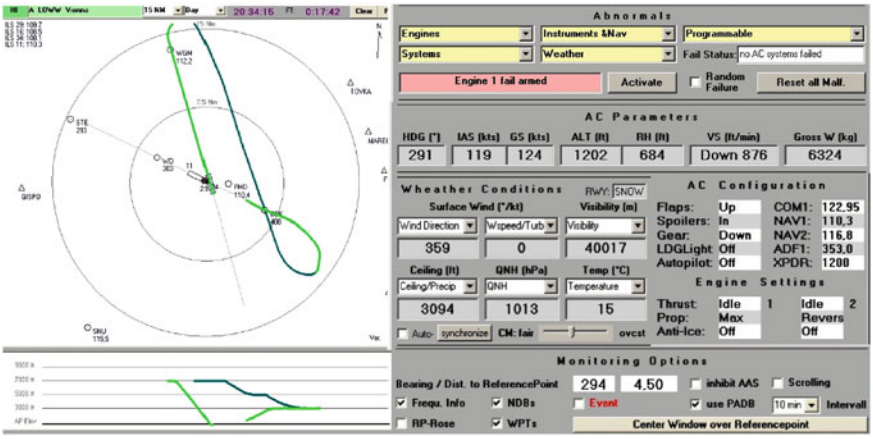

Fig. 55.5 Flight instructor operation window of FSIP

55.5 Conclusion

A low-cost PC-based FSTD has been developed. A duplicated cockpit of BE-1900C with a highly resembled flight deck was constructed. FS2004 and relevant add-on software were successfully setting up the simulation platform on a PC. FSUIPC and WideFS middleware were successfully linking three PC becoming a PC cluster. The simulated data were interchanged between cluster computers via LAN. USB 2.0 interface connects the cockpit hardware and HCC. USB interface software and firmware were developed by Visual C++ and Keil C, respectively. An instructor workstation was included in this FSTD for the mission management. In order to build a completed multidisciplinary education platform for the application of relevant research and education, more works are needed and are under construction.

References

1. Zhang, L., Jiang, H., & Li, H. (2007). PC based high quality and low cost flight simulator. In *Proceedings of the IEEE International Conference on Automation and Logistics* (pp. 1017–1022). Jinan, China.
2. Zheng, S., Huang, Q., Jin, J., & Han, J. (2009). Flight simulator architecture development and implementation. In *International Conference on Measuring Technology and Mechatronics Automation* (pp. 230–233). IEEE C.S.
3. Swenson, R., & Cuellar, R. (2009). A flight simulation training device based on FPGAs: A multidisciplinary educational platform. In *AIAA Modeling and Simulation Technologies Conference, AIAA* (2009–5826), Chicago, Illinois.
4. Oliverira, P. H. I. A., Pereira, G. A. S., Torres, L. A. B., Rebelo, D. R., Junqueira, G. H. C., Silva Filho, A. R., & Santana, G. A. (2010). Development of a PC-based flight simulator for

pilot assistance research. In *AIAA Modeling and Simulation Technologies Conference, AIAA* (pp. 2010–8103), Toronto, Ontario, Canada.
5. Louali, R., Belloula, A., Djouadi, M. S., & Bouaziz, S. (2011). Real-time characterization of Microsoft Flight Simulator 2004 for integration into Hardware in the Loop Architecture. In *19th Mediterranean Conference on Control and Automation IEEE* (pp. 1241–1246). ThBT3.4, Corfu, Greece.
6. SimMarket Web Store, http://secure.simmarket.com
7. Peter Dowson's Support Forum, http://www.schiratti.com
8. FS Instructor Panel 200X, http://www.fsip200x.com

Chapter 56
One-Day-Ahead Hourly Load Forecasting of Smart Building Using a Hybrid Approach

Chao-Ming Huang, Hong-Tzer Yang, Yann-Chang Huang and Kun-Yuan Huang

Abstract This paper proposes a hybrid approach to solve the one-day-ahead hourly load forecasting of smart building. The electricity consumption of a smart building is inherently nonlinear and dynamic and heavily dependent on the habitual nature of power demand, activities of daily living and on holidays or weekends, so it is often difficult to construct an adequate forecasting model for this type of load. To address this problem, this paper proposes a hybrid approach combining self-organizing map (SOM), learning vector quantization (LVQ), and fuzzy inference method to offer more adequate forecasting model for smart building. The proposed model comprises classification stage, forecasting stage, and correction stage. The forecasting results show that the proposed approach provides a robust and appropriate forecasting model.

Keywords Load forecasting · Smart building · Fuzzy inference method

56.1 Introduction

In recent years, the smart grid has raised more attentions in Taiwan. The smart grid integrates advanced metering infrastructure (AMI), communication facilities, and effective energy management strategies to achieve the goals of energy-saving and

C.-M. Huang (✉)
Department of Electrical Engineering, Kun Shan University, Tainan 710, Taiwan, Republic of China
e-mail: h7440@ms21.hinet.net

H.-T. Yang
Department of Electrical Engineering, National Cheng Kung University, Tainan 701, Taiwan, Republic of China

Y.-C. Huang · K.-Y. Huang
Department of Electrical Engineering, Cheng Shiu University, Kaohsiung 833, Taiwan, Republic of China

J. Juang et al. (eds.), *Proceedings of the 2nd International Conference on Intelligent Technologies and Engineering Systems (ICITES2013)*, Lecture Notes in Electrical Engineering 293,
DOI: 10.1007/978-3-319-04573-3_56,

carbon reduction under limited transmission and distribution capacities. Smart building is the basic construction of smart grid. To reduce the cost of power consumption and achieve energy-saving effect, the customers of smart building usually need to install some basic equipments, such as smart metering, power generation units of renewable energy (i.e. photovoltaic power generation and wind power generation), electric vehicles (EV) charging station and energy management system. Since the electricity consumption of a smart building is inherently nonlinear and dynamic and heavily dependent on the habitual nature of power demand, activities of daily living and on holidays or weekends, it is often difficult to construct an adequate forecasting model for this type of load.

Some novel approaches have been developed to cope with load forecasting on demand side. These techniques comprise nonparametric regression techniques [1], evolutionary-based linear and nonlinear models [2], a hybrid method based on PSO and ant colony algorithm [3], fuzzy regression-time series algorithm [4] and neural network based similar days approach [5]. The methods mentioned above can serve as useful tools to produce accurate load forecasting.

This paper develops an alternative approach to tackle the one-day-ahead load forecasting of smart building. The proposed approach combines SOM, LVQ, and fuzzy inference method to offer a robust and appropriate forecasting model. Because it is eminently capable of dealing with diverse load profiles and the load changed with season, the proposed approach is suitable for smart building forecasting environment.

56.2 The Proposed Approach

As shown in Fig. 56.1, the schematic diagram of the proposed method comprises classification, forecasting and correction, which are introduced in order as follows.

56.2.1 Classification

The SOM is an unsupervised, competitive learning, clustering network, in which only one neuron in a group is "on" at a time. The learning rule can be expressed as

$$w_i(k+1) = \begin{cases} w_i(k) + \mu(k)[x(k) - w_i(k)] & \text{if } i \in N_q(k) \\ w_i(k) & \text{if } i \notin N_q(k) \end{cases} \tag{56.1}$$

where x is an input vector, w_i is the ith synaptic weight vector, N_q is a neighborhood set (q is a winning neuron evaluated by Euclidean norm), and $\mu(k) \in [0, 1]$ is the learning rate parameter.

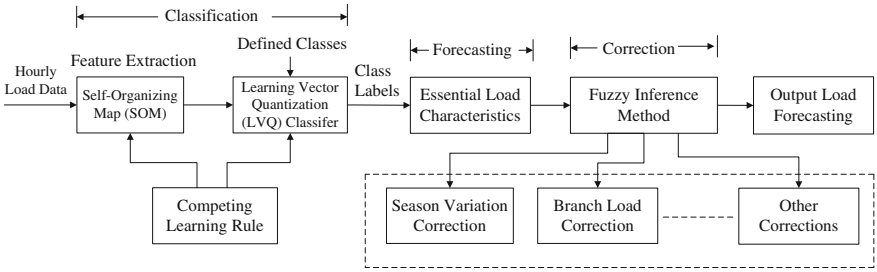

Fig. 56.1 Schematic diagram of the proposed method

Equation (56.1) shows that the synaptic weight vector is updated associated with the winning neuron and the neurons within a defined neighborhood of the winning neuron. When the learning process is converged, each input vector is mapped onto a discrete array of output neurons, in which the feature of input vector is identified.

The LVQ is a supervised learning network that can classify input vectors based on vector quantization, as follows.

$$w_q(k+1) = \begin{cases} w_q(k) + \mu(k)[x(k) - w_q(k)] & \text{if } C_q = C_i \\ w_q(k) - \mu(k)[x(k) - w_q(k)] & \text{if } C_q \neq C_i \end{cases} \tag{56.2}$$

where C_q is the class that is associated with the weight vector w_q and C_i is the class label of the ith input vector.

As shown in (56.2), the weight vector w_q is moved in the direction of the input $x(k)$ if the class labels of the input vector and of the weight vector agree. However, if the class is not correct, the weight vector is moved in the opposite direction away from the input vector.

56.2.2 Forecasting

In this stage, the one-day-ahead hourly forecast of essential load characteristic is produced based on the mean load of the similar day and the variation of mean load, as follows.

$$y'(k) = \overline{y} + (y(k) - \overline{y_c}) \tag{56.3}$$

$$\overline{y} = \frac{1}{24}\sum_{k=1}^{24} y(k) \tag{56.4}$$

where $y'(k)$ is the forecasting load at the kth hour, $\overline{y}$ is the mean load at the same day of last week, $\overline{y_c}$ is the mean load of the similar days of last week, and $y(k)$ is the load of the kth hour at the same day of last week.

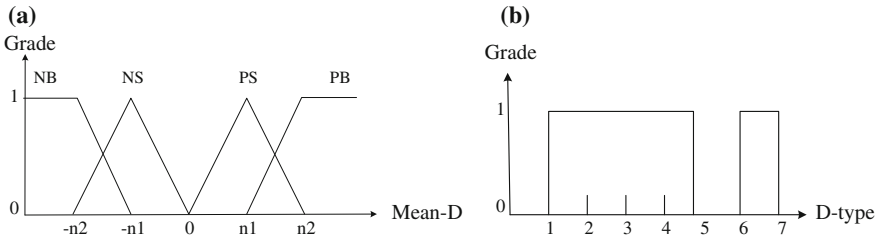

Fig. 56.2 Membership function of fuzzy input variables. *NB* Negative Big, *NS* Negative Small, *PS* Positive Small, *PB* Positive Big, **a** Deviation of mean load of the similar day. **b** Day type

56.2.3 Correction

The correction stage includes season variation correction, branch load correction, and other corrections needed. This stage is developed using the object-oriented method and implemented by the fuzzy inference method. The operators can insert (or draw out) an effective correction program to (from) the system anytime.

56.2.3.1 Season Variation Correction

The season variation correction updates the forecasted value according to the mean load and load deviation of the similar day. For mean load correction, the input variables are the deviation of mean load of the similar day and day type while the output variable is the corrected value. Figures 56.2 and 56.3 show the input and output variables of mean load correction, respectively. As shown in Figs. 56.2 and 56.3, there are eight fuzzy rules in the inference system, as follows.

R1: If Mean-D is NB and D-type is Weekday, Then output is NB
R2: If Mean-D is NB and D-type is Weekend/Holiday, Then output is NS
: : :
R8: If Mean-D is PB and D-type is Weekend/Holiday, Then output is PS

where Mean-D is the deviation of mean load of the similar day and D-type is the day type.

For load deviation correction, the input variables are the variation of load deviation and day type, while output variable is the corrected value. The form of the membership function of fuzzy input and fuzzy output variables is the same as mean load correction. Therefore, eight fuzzy rules are also included in the inference system.

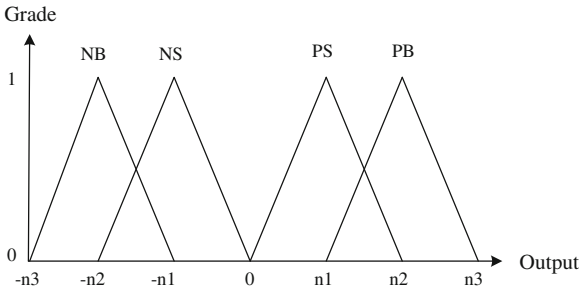

Fig. 56.3 Membership function of fuzzy output variable

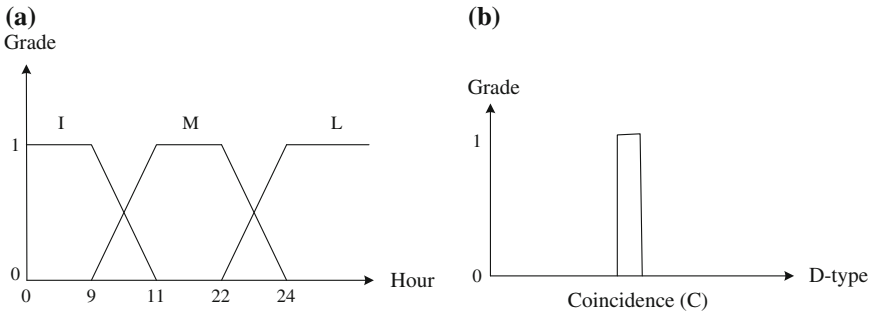

Fig. 56.4 Membership function of fuzzy input variables. *I* Initial, *M* Middle, *L* Last, **a** Time, **b** Day type

56.2.3.2 Branch Load Correction

The branch load correction is developed for some special time and day type. If branch load consumption on weekend day before dawn is higher than weekday, then the forecasted value must be corrected during these times. Figures 56.4 and 56.5 show the input and output variables of branch load correction, respectively. As shown in these figures, there are three fuzzy rules in the inference system, as follows.

R1: If Hour is I and D-type is C, Then D-load is B
R2: If Hour is M and D-type is C, Then D-load is M
R3: If Hour is L and D-type is C, Then D-load is S

where D-load represents the increasing of load variation.

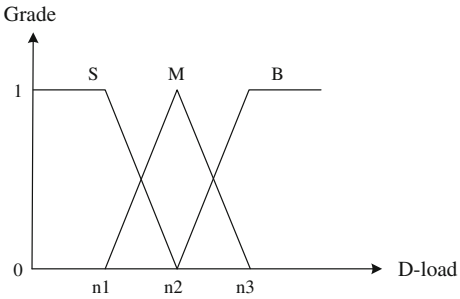

Fig. 56.5 Membership function of fuzzy output variable. *S* Small, *M* Middle, *B* Big

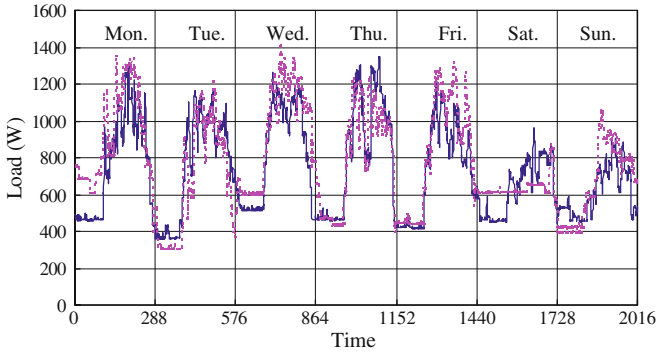

Fig. 56.6 Forecasting results of essential load characteristic from Nov. 19 to 25th in year 2011. (*solid line* actual load; *dot line* forecasted load before correction)

56.3 Numerical Results

The proposed approach was implemented and tested using practical load data which were collected in the year 2011. Due to the limited of space, only the forecasting results in November were presented in this paper. The load data was sampled every 5 min, so 288 load data were collected each day.

Figure 56.6 show the one-day-ahead hourly forecasting results of essential load characteristic by using (56.3) and (56.4). This figure reveals that the forecasting errors are large that needs to be corrected. Figure 56.7 shows the forecasting results by using the correction method described in Sect. 56.2.3. The proposed correction stage increases the forecasting accuracy of load demand. Table 56.1 shows the comparison between the load forecast of essential load characteristic and the load forecast using correction. The mean absolute percentage errors (MAPE) can be expressed as follows.

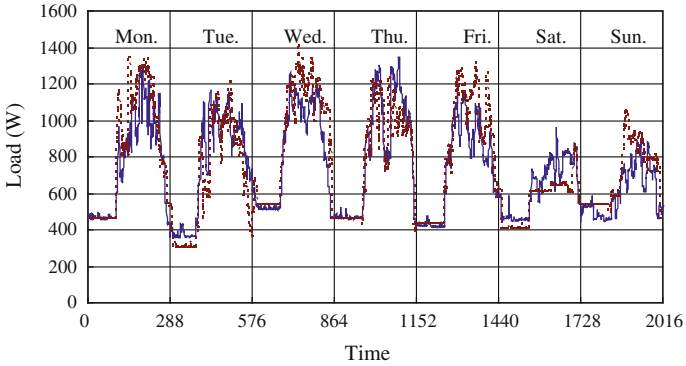

Fig. 56.7 Forecasting results using correction stage from Nov. 19 to 25th in year 2011. (*solid line* actual load; *dot line* forecasted load after correction)

Table 56.1 The comparison between the load forecast of essential load characteristic and the forecast using correction

	Mon. (%)	Tue. (%)	Wed. (%)	Tue. (%)	Fri. (%)	Sat. (%)	Sun. (%)	Average
Forecast[1]	26.21	17.97	18.78	9.71	11.30	19.59	17.95	17.36
Correction[2]	10.74	13.76	12.75	7.63	10.81	12.32	15.16	11.88

[1] Load forecast of essential load characteristic; [2] Load forecast using correction

$$MAPE = \frac{1}{N}\sum_{i=1}^{N}\frac{\left|P_{forecast} - P_{actual}\right|}{P_{actual}} \times 100\% \tag{56.6}$$

The results of Table 56.1 indicate that the proposed method improves the forecasting accuracy after correction.

56.4 Conclusions

A hybrid approach combining SOM, LVQ, and fuzzy inference method has been proposed and implemented in this paper. The proposed approach uses fuzzy inference technique to correct the forecasted load and provides a better forecasting model for smart building. Testing results show that the proposed approach produces acceptable forecasting results and offers a more robust process for the load predictors. Although only one type of load data was implemented in this paper, an extension of the proposed method to deal with diverse load level is feasible, through appropriate design of the fuzzy input variables and heuristic rules.

Acknowledgments The authors gratefully acknowledge the financial supports from the National Science Council, Taiwan, R.O.C. under Grant No. 102-3113-P-006-015.

References

1. Vilar, J. M., Cao, R., & Aneiros, F. (2012). Forecasting next-day electricity demand and price using nonparametric functional methods. *International Journal of Electrical Power & Energy Systems, 39*(1), 48–55.
2. Piltan, M., Shiri, H., & Ghaderi, S. F. (2012). Energy demand forecasting in Iranian metal industry using linear and nonlinear models based on evolutionary algorithms. *Energy Conversion and Management, 58*(1), 1–9.
3. Kiran, M. S., et al. (2012). A novel hybrid approach based on particle swarm optimization and ant colony algorithm to forecast energy demand of Turkey. *Energy Conversion and Management, 53*(1), 75–83.
4. Azadeh, A., Saberi, M., & Gitiforouz, M. (2011). An integrated simulation based fuzzy regression-time series algorithm for electricity consumption estimation with non-stationary data. *Journal of the Chinese Institute of Engineers, 34*(8), 1047–1066.
5. Mandal, P., Senjyu, T., Urasaki, N., & Funabashi, T. (2006). A neural network based several-hour-ahead electric load forecasting using similar days approach. *Electrical Power & Energy Systems, 28*, 367–375.

Chapter 57
Robust Exponential Stability of Uncertain Discrete-Time Systems with Interval Time-Varying Delay

Chang-Hua Lien, Jenq-Der Chen, Ker-Wei Yu, Chin-Tan Lee, Ruey-Shin Chen and Chyi-Da Yang

Abstract In this paper, the problem of robust exponential stability for uncertain discrete-time systems with interval time-varying delay is investigated. By choosing appropriate Lyapunov functional and using discrete Jensen inequality, an LMI-based delay-dependent condition is proposed to guarantee the robust exponential stability for such system with parametric perturbations. Without ignoring any negative terms in the difference of Lyapunov functionals and using any free-weighting matrices, the presented result is less conservative and less computational burdens than those in the existing paper. Finally, some numerical examples are illustrated to show the obtained result.

Keywords Robust exponential stability · Discrete-time system · Interval time-varying delay

C.-H. Lien · K.-W. Yu
Department of Marine Engineering, National Kaohsiung Marine University, Kaohsiung, Taiwan, Republic of China

J.-D. Chen (✉) · C.-T. Lee
Department of Electronic Engineering, National Quemoy University, Kinmen, Taiwan, Republic of China
e-mail: tdchen@nqu.edu.tw

R.-S. Chen
Department of Computer Engineering, National Quemoy University, Kinmen, Taiwan, Republic of China

C.-D. Yang
Department of Microelectronics Engineering, National Kaohsiung Marine University, Kaohsiung, Taiwan, Republic of China

J. Juang et al. (eds.), *Proceedings of the 2nd International Conference on Intelligent Technologies and Engineering Systems (ICITES2013)*, Lecture Notes in Electrical Engineering 293,
DOI: 10.1007/978-3-319-04573-3_57,

57.1 Introduction

Time-delay phenomena are usually encountered in many practical systems, such as AIDS epidemic, aircraft stabilization, chemical engineering systems, hydraulic systems, inferred grinding model, manual control, neural network, nuclear reactor, population dynamic model, rolling mill, ship stabilization, and systems with lossless transmission lines. It is also well known that the existence of delay in a system may cause instability or bad performance in closed control systems. Hence stability analysis and stabilization for continuous and discrete systems with time delay have received some attention by many researchers in recent years [1–13]. The stability for discrete-time systems with interval time-varying delay has been an attractive research topic [6–13].

In recent years, the system models always contain some uncertain elements. These uncertainties may be due to additive unknown noise, environmental influence, poor plant knowledge. At the same time, many robust stable technologies are developed to analyze the uncertain discrete-time systems with time-varying delay [7, 11].

In the past, there were many approaches been proposed to guarantee the stability and the stabilision for discrete time-delay systems. Delay-dependent conditions is applied to slove ouput feedback stabilisation problem in [7, 11]. Lyapunov theory and LMI approach are provided to guarantee the asymptotic stability for discrete-time systems with interval time-varying delay [8–10, 12]. In this paper, the Lyapunov theory and the discrete Jensen inequality are proposed to guarantee the exponential stability problem for uncertain switched systems with interval time-varying delay. Delay-dependent sufficient conditions are proposed to guarantee the exponential stability. Our proposed approach is a new method and easy to apply to the uncertain switched systems with interval time-varying delay. Some numerical examples are provided to demonstrate the effectiveness of the obtained results. From the simulation results, our proposed approach will provide less conservative and useful results.

The notations are used throughout this paper. For a matrix A, we denote the transpose by A^T, spectral norm by $\|A\|$, symmetric positive (negative) definite by $A > 0$ ($A < 0$),maximal eigenvalue by $\lambda_{\max}(A)$, minimal eigenvalue by $\lambda_{\min}(A)$, $n \times m$ dimension by $A_{(n\times m)}$. $A \leq B$ means that matrix $B - A$ is symmetric positive semi-definite. 0 and I denote the zero matrix and identity matrix with compatible dimensions. $diag\{\cdots\}$ stands for a block-diagonal matrix. For a vector x, we denote the Euclidean norm by $\|x\|$. Define $\|x_k\|_s = \max_{\theta=-r_M,-r_M+1,\cdots,0} \|x(k+\theta)\|$.

57.2 Problem Formulation and Main Result

Consider the following uncertain discrete-time system with interval time-varying delay

$$\begin{aligned} x(k+1) &= (A + \Delta A(k))x(k) + (A_d + \Delta A_d(k))x(k - r(k)), \\ x(\theta) &= \phi(\theta), \quad \theta = -r_M, \ -r_M + 1, \ \cdots, \ 0, \end{aligned} \tag{57.1}$$

where $x(k) \in \Re^n$ is the state vector, x_k is the state at time k defined by $x_k(\theta) := x(k + \theta)$, $\forall \theta \in \{-r_M, -r_M + 1, \cdots, 0\}$, A and $A_d \in \Re^{n \times n}$ are some given constant matrices, and $\phi(k) \in \Re^n$ is a vector-valued initial state function. The time-varying delay $r(k)$ is a function from $\{0, 1, 2, 3, \cdots\}$ to $\{0, 1, 2, 3, \cdots\}$, and satisfies the following condition:

$$0 < r_m \le r(k) \le r_M, \tag{57.2}$$

where r_m and r_M are two given positive integers. The $\Delta A(k)$ and $\Delta A_d(k)$are some perturbed matrices and satisfy the following conditions

$$[\,\Delta A(k) \quad \Delta A_d(k)\,] = MF(k)[N_1 \quad N_2\,], \tag{57.3}$$

where M, N_1 and N_2 are some given constant matrices of system with appropriate dimensions, and $F(k)$ is unknown matrices representing the parameter perturbations which satisfy

$$F^T(k)F(k) \le I. \tag{57.4}$$

In order to derive our main results, the Lemmas are introduced as follows:

Lemma 57.1 *Let* U, V, W and M *be real matrices of appropriate dimensions with* M *satisfying* $M = M^T$, *then* $M + UVW + W^TV^TU^T < 0$ *for all* $V^TV \le I$, *if and only if there exists a scalar* $\varepsilon > 0$ *such that*

$$M + \varepsilon^{-1} \cdot UU^T + \varepsilon \cdot W^TW = M + \varepsilon^{-1} \cdot UU^T + \varepsilon^{-1} \cdot (\varepsilon W)^T(\varepsilon W) < 0.$$

Lemma 57.2 Zhu and Yang [12]. *For any constant matrix* $M \in \Re^{n \times n}$, $M = M^T > 0$, *integers* $\gamma_2 \ge \gamma_1$, *vector function* $\omega : \{\gamma_1, \gamma_1 + 1, \cdots, \gamma_2\} \to \Re^n$ *such that the sums in the following are well defined, then*

$$-(\gamma_2 - \gamma_1 + 1)\sum_{\theta=\gamma_1}^{\gamma_2} \omega^T(\theta)M\omega(\theta) \le -\left[\sum_{\theta=\gamma_1}^{\gamma_2} \omega(\theta)\right]^T R_1 \left[\sum_{\theta=\gamma_1}^{\gamma_2} \omega(\theta)\right].$$

The aim of this paper is to derive a new novel delay-dependent stability criterion which is less conservative than the existing results.

Theorem 57.1 *System* (57.1) *with* (57.3)–(57.4) *is exponentially stable with convergence rate* $0 < \alpha \le 1$ *for any time-varying delay* $r(k)$ *satisfying* (57.2), *if there exist some* $n \times n$ *matrices* $P > 0$, $S > 0$, $T > 0$, $Q > 0$, $R_i > 0$, $i = 1, 2, 3, 4$, *and a positive number* ε, *such that the following LMI conditions are satisfied*:

$$\Xi_i = \begin{bmatrix} \Xi_{11}^i & \Xi_{12} & \Xi_{13} \\ * & \Xi_{22} & \Xi_{23} \\ * & * & \Xi_{33} \end{bmatrix} < 0, \ i = 1, \ 2, \tag{57.5}$$

where

$$\Xi_{11}^{1} = diag\{ -P + S + (r_{Mm}+1) + T \quad -\alpha^{2r_m}\cdot S \quad -\alpha^{2r_M}\cdot Q \quad -\alpha^{2r_M}\cdot T \} - \alpha^{2r_m}\cdot W_1^T R_1 W_1 - \alpha^{2r_M}\cdot \left(W_2^T R_2 W_2 + W_3^T R_3 W_3 + 2\cdot W_4^T R_4 W_4 + W_5^T R_4 W_5\right),$$

$$\Xi_{11}^{2} = diag\{ -P + S + (r_{Mm}+1) + T \quad -\alpha^{2r_m}\cdot S \quad -\alpha^{2r_M}\cdot Q \quad -\alpha^{2r_M}\cdot T \} - \alpha^{2r_m}\cdot W_1^T R_1 W_1 - \alpha^{2r_M}\cdot \left(W_2^T R_2 W_2 + W_3^T R_3 W_3 + W_4^T R_4 W_4 + 2\cdot W_5^T R_4 W_5\right),$$

$$\Xi_{12} = \begin{bmatrix} A^T P & r_m\cdot (A-I)^T R_1 & \hat{r}_{Mm}\cdot (A-I)^T R_2 & r_M\cdot (A-I)^T R_3 & r_{Mm}\cdot (A-I)^T R_4 \\ 0 & 0 & 0 & 0 & 0 \\ A_d^T P & r_m\cdot A_d^T R_1 & \hat{r}_{Mm}\cdot A_d^T R_2 & r_M\cdot A_d^T R_3 & r_{Mm}\cdot A_d^T R_4 \\ 0 & 0 & 0 & 0 & 0 \end{bmatrix},$$

$$\Xi_{22} = -diag\{ \alpha^2\cdot P \quad R_1 \quad R_2 \quad R_3 \quad R_4 \},\ \Xi_{13} = \begin{bmatrix} 0 & \varepsilon\cdot N_1^T \\ 0 & 0 \\ 0 & \varepsilon\cdot N_2^T \\ 0 & 0 \end{bmatrix},$$

$$\Xi_{23} = \begin{bmatrix} PM & 0 \\ r_m\cdot R_1 M & 0 \\ \hat{r}_{Mm}\cdot R_2 M & 0 \\ r_M\cdot R_3 M & 0 \\ r_{Mm}\cdot R_4 M & 0 \end{bmatrix},$$

$$\Xi_{33} = -diag\{ \varepsilon\cdot I \quad \varepsilon\cdot I \},\ r_{Mm} = r_M - r_m,\ \hat{r}_{Mm} = \sqrt{\frac{r_M}{2}(r_{Mm}+1)\cdot (r_M + r_m)},$$

$$W_1 = [I \quad -I \quad 0 \quad 0]_{(n\times 4n)},\ W_2 = [I \quad 0 \quad -I \quad 0]_{(n\times 4n)},\ W_3 = [I \quad 0 \quad 0 \quad -I]_{(n\times 4n)},$$
$$W_4 = [0 \quad 0 \quad I \quad -I]_{(n\times 4n)},\ W_5 = [0 \quad I \quad -I \quad 0]_{(n\times 4n)}.$$

Proof The Lyapunov–Krasovskii functional candidate is given by

$$
\begin{aligned}
V(x_k) = {} & \alpha^{-2k} \cdot x^T(k) P x(k) + \sum_{\theta=k-r_m}^{k-1} \alpha^{-2\theta} \cdot x^T(\theta) S x(\theta) + \sum_{\theta=k-r_M}^{k-1} \alpha^{-2\theta} \cdot x^T(\theta) T x(\theta) \\
& + \sum_{\theta=k-r(k)}^{k-1} \alpha^{-2\theta} \cdot x^T(\theta) Q x(\theta) + \sum_{l=-r_M+1}^{-r_m} \sum_{\theta=k+l}^{k-1} \alpha^{-2\theta} \cdot x^T(\theta) Q x(\theta) \\
& + r_m \cdot \sum_{l=-r_m+1}^{0} \sum_{\theta=k-1+l}^{k-1} \alpha^{-2\theta} \eta^T(\theta) R_1 \eta(\theta) \\
& + r_M \cdot \left[\sum_{l=-r(k)+1}^{0} \sum_{\theta=k-1+l}^{k-1} \alpha^{-2\theta} \cdot \eta^T(\theta) R_2 \eta(\theta) + \sum_{l=-r_M+1}^{-r_m} \sum_{\theta=k+l}^{k-1} \alpha^{-2\theta} \cdot (\theta - k - l + 1) \cdot \eta^T(\theta) R_2 \eta(\theta) \right] \\
& + r_M \cdot \sum_{l=-r_M+1}^{0} \sum_{\theta=k-1+l}^{k-1} \alpha^{-2\theta} \cdot \eta^T(\theta) R_3 \eta(\theta) + r_{Mm} \cdot \sum_{l=-r_M}^{-r_m-1} \sum_{\theta=k+l}^{k-1} \alpha^{-2\theta} \cdot \eta^T(\theta) R_4 \eta(\theta),
\end{aligned}
\tag{57.6}
$$

where $\eta(\theta) = x(\theta + 1) - x(\theta)$. The difference of Lyapunov functional along the solutions of system (57.1) is given by

$$
\begin{aligned}
\Delta V(x_k) \le {} & \alpha^{-2k} \cdot \{ \alpha^{-2} \cdot x^T(k+1) P x(k+1) + x^T(k)[-P + S + (r_{Mm} + 1) \cdot Q + T] x(k) \\
& - \alpha^{2r_m} \cdot x^T(k - r_m) S x(k - r_m) - \alpha^{2r_M} \cdot x^T(k - r_M) T x(k - r_M) - \alpha^{2r_M} \cdot x^T(k - r(k)) Q x(k - r(k)) \\
& + \eta^T(k) \left[r_m^2 \cdot R_1 + \hat{r}_{Mm}^2 \cdot R_2 + r_M^2 \cdot R_3 + r_{Mm}^2 \cdot R_4 \right] \eta(k) - \alpha^{2r_m} \cdot W_1^T R_1 W_1 \\
& - \alpha^{2r_M} \cdot \left(W_2^T R_2 W_2 + W_3^T R_3 W_3 + W_4^T R_4 W_4 + W_5^T R_4 W_5 + \lambda(k) \cdot W_4^T R_4 W_4 + (1 - \lambda(k))_5^T R_4 W_5 \right) \} \\
= {} & \alpha^{-2k} \cdot \beta^T(k) \cdot (\lambda(k) \cdot \bar{\Xi}_1 + (1 - \lambda(k)) \cdot \bar{\Xi}_2) \beta(k),
\end{aligned}
\tag{57.7}
$$

where $\beta^T(k) = \begin{bmatrix} x^T(k) & x^T(k - r_m) & x^T(k - r(k)) & x^T(k - r_M) \end{bmatrix}$, $\lambda(k) = \frac{r(k) - r_m}{r_{Mm}}$,

$$
\bar{\Xi}_i = \Xi_{11}^i + \begin{bmatrix} \bar{A}^T P \\ 0 \\ \bar{A}_d^T P \\ 0 \end{bmatrix} (\alpha^2 \cdot P)^{-1} \begin{bmatrix} \bar{A}^T P \\ 0 \\ \bar{A}_d^T P \\ 0 \end{bmatrix}^T + \begin{bmatrix} (\bar{A} - I)^T \\ 0 \\ \bar{A}_d^T \\ 0 \end{bmatrix} \left(r_m^2 \cdot R_1 + \hat{r}_{Mm}^2 \cdot R_2 + r_M^2 \cdot R_3 + r_{Mm}^2 \cdot R_4 \right) \begin{bmatrix} (\bar{A} - I)^T \\ 0 \\ \bar{A}_d^T \\ 0 \end{bmatrix}^T,
\tag{57.8}
$$

with Ξ_{11}^i, W_j, $i = 1, 2, j = 1, 2, 3, 4, 5$, are defined in (57.5). Since $0 \le \lambda(k) \le 1$, the $\lambda(k) \cdot \bar{\Xi}_1 + (1 - \lambda(k)) \cdot \bar{\Xi}_2$ is a convex combination of $\bar{\Xi}_1$ and $\bar{\Xi}_2$. Hence, $\lambda(k) \cdot \bar{\Xi}_1 + (1 - \lambda(k)) \cdot \bar{\Xi}_2 < 0$ will imply $\bar{\Xi}_1 < 0$ and $\bar{\Xi}_2 < 0$. Define

$$
\hat{\Xi}_i = \begin{bmatrix} \Xi_{11}^i & \Xi_{12} \\ * & \Xi_{22} \end{bmatrix} + \Lambda F(k) \Gamma^T + \Gamma F^T(k) \Lambda^T, \ i = 1, 2,
\tag{57.9}
$$

where $\Lambda^T = \begin{bmatrix} 0 & 0 & 0 & 0 & M^T P & r_m \cdot M^T R_1 & \hat{r}_{Mm} \cdot M^T R_2 & r_M \cdot M^T R_3 & r_{Mm} \cdot M^T R_4 \end{bmatrix}$, $\Gamma^T = [N_1 \quad 0 \quad N_2 \quad 0 \quad 0 \quad 0 \quad 0 \quad 0 \quad 0]$, and Ξ_{11}^i, Ξ_{12}, Ξ_{22} are defined in (57.5). By Lemma 57.1 and Schur complement in [13], the condition $\Xi_i < 0$ in (57.5) will imply the condition $\hat{\Xi}_i < 0$ in (57.9). The condition $\hat{\Xi}_i < 0$ in (57.9) implies the condition $\bar{\Xi}_i < 0$ in (57.8). The condition $\bar{\Xi}_i < 0$ in (57.9) is also equivalent to $\lambda(k) \cdot \bar{\Xi}_1 + (1 - \lambda(k)) \cdot \bar{\Xi}_2 < 0$ in (57.7). From the above condition with (57.5), we have

Table 57.1 Comparing the maximum r_M for $\alpha = 1$ and different values of r_m

Results	$r_m = 4$	$r_m = 6$	$r_m = 7$	$r_m = 10$	$r_m = 15$	$r_m = 20$
[7]	8	9	10	12	16	20
[8]	13	14	14	15	18	22
[9]	13	14	15	17	20	24
[10]	15	16	16	18	21	25
Corollary 57.1	15	16	17	20	24	28

Table 57.2 Comparing the maximum $\bar{\alpha}$ for $\alpha = 1$, different values of r_m and r_M

Results	$2 \le r(k) \le 7$	$3 \le r(k) \le 9$	$10 \le r(k) \le 15$	$20 \le r(k) \le 25$
[8]	0.0830	infeasible	infeasible	infeasible
[9]	0.1901	0.1457	0.0655	infeasible
[10]	0.1920	0.1548	0.1023	0.0886
Theorem 57.1	0.2351	0.1897	0.1391	0.1100

$$\Delta V(x_k) = V(x_{k+1}) - V(x_k) \le 0,\ k = 0,\ 1,\ 2,\ 3,\ \cdots,\ V(x_{k+1}) \le V(x_k),\ k = 0,\ 1,\ 2,\ 3,\ \cdots.$$

This implies

$$V(x_k) \le V(x_0),\ k = 0,\ 1,\ 2,\ 3,\ \cdots,\ \alpha^{-2k} \cdot \lambda_{\min}(P) \cdot \|x(k)\|^2 \le V(x_k) \le V(x_0) \le \delta \cdot \|x_0\|_s^2,$$

where

$\delta = \lambda_{\max}(P) + r_m \cdot \lambda_{\max}(S) + r_M \cdot \lambda_{\max}(T) + \left(r_M^2 - r_M r_m + r_m\right) \cdot \lambda_{\max}(Q) + r_m^2 \cdot \lambda_{\max}(R_1) + \left(r_M^2 + \frac{1}{2}(r_M + r_m + 1) \cdot (r_M - r_m) \cdot (r_M - 1)\right) \cdot \lambda_{\max}(R_2) + r_M^2 \cdot \lambda_{\max}(R_3) + (r_M - r_m) \cdot r_M \cdot \lambda_{\max}(R_4)$.

By some simple derivations, we have $\|x(k)\| \le \sqrt{\delta / \lambda_{\min}(P)} \cdot \alpha^k \cdot \|x_0\|_s$. We conclude that system (57.1) is exponentially stable with $0 < \alpha \le 1$. This completes this proof.

Remark 57.1 By setting $\alpha = 1$ in Theorem 57.1, global asymptotic stability of system (57.1) can be achieved.

57.3 Illustrative Examples

Example 57.1 Consider the system (57.1) without perturbation and the following parameters [7]:

$$A = \begin{bmatrix} 0.8 & 0 \\ 0.05 & 0.9 \end{bmatrix},\ A_d = \begin{bmatrix} -0.1 & 0 \\ -0.2 & -0.1 \end{bmatrix}. \tag{57.10}$$

In order to show the obtained results, the allowable delay upper bounds that guarantee the asymptotic stability for system (57.1) with (57.10) is provided in Table 57.1 with $\alpha = 1$. From Table 57.1, we can see that the presented stability results in this paper are less conservative than ones in [7–10].

Example 57.2 Consider the system (57.1) with the following parameters: (Example 57.2 of [8])

$$A = \begin{bmatrix} 0.8 + \alpha(k) & 0 \\ 0 & 0.9 \end{bmatrix}, A_d = \begin{bmatrix} -0.1 & 0 \\ -0.1 & -0.1 \end{bmatrix}, M = \begin{bmatrix} \bar{\alpha} \\ 0 \end{bmatrix}, \\ N_1 = [1 \quad 0], N_2 = [0 \quad 0], F(k) = \frac{\alpha(k)}{\bar{\alpha}}. \tag{57.11}$$

In order to show the obtained results, the allowable bounds that guarantee the asymptotic stability for system (57.1) with (57.11) are provided in Table 57.2. From Table 57.2, we can see that Theorem 57.1 in this paper presents some less conservative results.

57.4 Conclusions

In this paper, the robust exponential stability problem for uncertain discrete-time systems with interval time-varying delay has been considered. Without applying free-weighting matrices, the computational complexity of the derived stability criteria has been reduced. The obtained results have been shown to be less conservative than some existing published results by some numerical examples.

Acknowledgments This report was supported by the National Science Council of Taiwan, R.O.C. under grant no. NSC 100-2221-E-507-001 and NSC 101-2221-E-022-009.

References

1. Hale, J. K. (1977). *Theory of functional differential equations*. New York: Springer.
2. Gu, K., Kharitonov, V. L., & Chen, J. (2003). *Stability of time-delay systems*. Boston: Birkhauser.
3. Yu, K. W., & Lien, C. H. (2008). Stability criteria for uncertain neutral systems with interval time-varying delays. *Chaos, Solitons & Fractals, 38*, 650–657.
4. He, Y., Wang, Q. G., & Lin, C. (2006). An improved H_∞ filter design for systems with time-varying interval delay. *IEEE Transactions on Circuits and Systems II: Express Briefs, 53*, 1235–1239.
5. Peng, C., & Tian, Y. C. (2008). Improved delay-dependent robust stability criteria for uncertain systems with interval time-varying delay. *IET Control Theory and Applications, 2*, 752–761.
6. Elaydi, S. (2005). *An introduction to difference equations*. New York: Springer.
7. Gao, H., Lam, J., Wang, C., & Wang, Y. (2004). Delay-dependent output feedback stabilisation of discrete-time systems with time varying state delay. *IEE Proceedings: Control Theory and Applications, 151*, 691–698.

8. Gao, H., & Chen, T. (2007). New results on stability of discrete-time systems with time-varying state delay. *IEEE Transactions on Automatic Control, 52*, 328–334.
9. Zhang, B., Xu, S., & Zou, Y. (2008). Improved stability criterion and its applications in delayed controller design for discrete-time systems. *Automatica, 44*, 2963–2967.
10. Huang, H., & Feng, G. (2010). Improved approach to delay-dependent stability analysis of discrete-time systems with time-varying delay. *IET Control Theory and Applications, 4*, 2152–2159.
11. Liu, X. G., Martin, R. R., Wu, M., & Tang, M. L. (2006). Delay-dependent robust stabilisation of discrete-time systems with time-varying delay. *IEE Proceedings: Control Theory and Applications, 153*, 689–702.
12. Zhu, X. L., & Yang, G. H. (2008). Jensen inequality approach to stability analysis of discretetime systems with time-varying delay. In *Proceedings* of the *American Control Conference* (pp. 1644–1649).
13. Boyd, S., El Ghaoui, L., Feron, E., & Balakrishnan, V. (1994). *Linear matrix inequalities in system and control theory*. Philadelphia: SIAM.

Chapter 58
Particle Swarm Optimization Based on Elitism for Fractal Image Compression

Ming-Sheng Wu

Abstract In this paper, a particle swarm optimization (PSO) algorithm based on elitism is proposed to speedup the fractal encoder. Using the elitism, the particles in the swarm are divided into two groups. Two evolutionary strategies are separately applied to the two groups to search better match. Such a method can speedup the encoder and also preserve the image quality. Simulations show that the encoding time of our method is 42 times faster than that of the full search method, while the retrieved image quality is still acceptable. Moreover, a comparison of the proposed PSO to the baseline PSO is done to demonstrate when the elitism is embedded into the PSO, the performance of PSO has significant improvement.

Keywords Fractal image compression · Particle swarm optimization · Elitism

58.1 Introduction

Fractal image compression (FIC) is the one of the famous encode algorithms. The original idea was proposed by Barnsley and Demko in 1985 [1] and the practical FIC algorithm was implemented by Jacquin in 1992 [2]. It is very time-consuming. The reason is that each range block must search for the best matched block from the large domain pool. Considerable time will be wasted on a large number of the redundant similar computations to slow down the encoding speed of the FIC. Therefore, the main research of the FIC is focus on how to reduce the encoding time.

In the past, many encoding algorithms were presented to speedup the fractal encoder. These techniques include classification techniques [3, 4], quad-tree

M.-S. Wu (✉)
Department of Electrical Engineering, Cheng Shiu University, Kaohsiung 83347, Taiwan, Republic of China
e-mail: sheng@csu.edu.tw

J. Juang et al. (eds.), *Proceedings of the 2nd International Conference on Intelligent Technologies and Engineering Systems (ICITES2013)*, Lecture Notes in Electrical Engineering 293,
DOI: 10.1007/978-3-319-04573-3_58,

technique [5, 6], no search technique [6, 7], and spatial correlation [8, 9] etc. Recently, the researchers focus their eyes on the evolutionary algorithms to solve the problem of the encoding of the FIC [9–12], in which PSO is the one of the most interested methods. PSO is a population-based algorithm for searching global optimum. The original idea is to simulate a simplified social behavior, like bird flocking or fish schooling, and has some common features of evolutionary computation such as fitness evaluation. It provides a mechanism the particles in the swarm can communication and exchange information each other, which is similar to the behavior of insects and human society. Since imitate the sharing of information of society, PSO particles can search optimal solution more effectively.

In this paper, we propose a particle swarm optimization (PSO) algorithm based on elitism to overcome the problem of encoding time is too long. All the particles in the swarm are divided into two groups, superiority group and inferiority group, according to the degree of similarity. A particle in the superiority group is belonging to elitism and has good similarity match with the range block. Hence the probability that the neighborhood around the particle also has good similarity match with the range block is high. Such a particle will carry out the PSO evolutionary to find better similarity match. On the contrary, a particle in the inferiority group is not belonging to elitism and has not good similarity match with the range block. The probability that the neighborhood around the particle has good similarity match with the range block is low. The particle will be compelled to escape from the origin position in order to find good match solution in the other areas. Such a search strategy can speedup the encoder and also preserve the image quality.

In the next section, the theoretical basis of fractal image compression is outlined. The proposed PSO algorithm is introduced in Sect. 58.3. The experimental results of comparing the proposed PSO algorithm with the full search and the baseline PSO algorithms are provided in Sect. 58.4. Finally, a conclusion is stated in Sect. 58.5.

58.2 Fractal Image Compression

The fractal image compression is based on the local self-similarity property in a nature image. The fundamental idea is coming from the Partitioned Iterated Function System (PIFS). Suppose the original gray level image f is of size 256×256. Let the range pool R be defined as the set of all non-overlapping blocks of size 8×8 of the image f, which makes up $(256/8)^2 = 1024$ blocks. For obeying the Contractive Mapping Fixed-Point Theorem, the domain block must exceed 2 times than the range block in length. Thus, let the domain pool D be defined as the set of all possible blocks of size 16×16 of the image f, which makes up $(256 - 16 + 1)^2 = 58081$ blocks. For each range block v from the R, the fractal affine transformation is constructed by searching all of the domain blocks in

the D to find the most similar one and the parameters representing the fractal affine transformation will form the fractal compression code of v.

To execute the similarity measure between range block and domain block, the size of the domain block must be first sub-sampled to 8×8 such that its size is the same as v. Let u denote a sub-sampled domain block. The similarity of two image blocks u and v of size $n \times n$ is measured by mean square error (MSE) defined as

$$MSE(u,v) = \frac{1}{n \times n} \sum_{j=0}^{n-1} \sum_{i=0}^{n-1} (u(i,j) - v(i,j))^2 \tag{58.1}$$

The fractal affine transformation allows the eight transformations of the domain block u in the Dihedral. The eight transformations $T_k : k = 0, 1, \cdots, 7$ can be expressed by the diagrams in Fig. 58.1. Thus for a given block from the range pool, there are $58081 \times 8 = 464, 648$ MSE computations must be done in order to obtain the most similar block from the domain pool. Thus, in total, one needs $1024 \times 464, 648 = 475, 799, 552$ MSE computations to encode the whole image using this full search compression method.

The fractal affine transformation also allows the contrast scaling p and the brightness offset q on the transformed blocks. Thus the similarity is to minimize the quantity $d = \|p \cdot u_k + q - v\|$. Here, p and q can be computed directly by

$$p = \frac{[N < u_k, v > - < u_k, \vec{1} > < v, \vec{1} >]}{[N < u_k, u_k > - < u_k, \vec{1} >^2]} \text{ and } q = \frac{1}{N}[< v, \vec{1} > - p < u_k, \vec{1} >]$$

, respectively, where N is the number of pixels of the range block and $\vec{1} = [1 \quad 1 \quad \cdots \quad 1]^T$.

Finally, as u runs over all the 58081 blocks in the domain pool, a set of parameters t_x, t_y, p, q, and k are obtained and constitute the fractal compression code of v, in which t_x and t_y represent the position of the domain block. For 256×256 image, both t_x and t_y require 8 and 8 bits, respectively. For contrast p, brightness q, and the Dihedral transformation k, 5, 7 and 3 bits are required, respectively. Hence one needs 31 bits in total to encode a range block. Finally, as v runs over all 1024 blocks in the range pool, the encoding process is completed.

58.3 A Particle Swarm Optimization Algorithm Based on Elitism for Fractal Image Compression

The original idea of the PSO is to mimic a simplified social behavior to evolve. Its main feature is that the particles and the swarm have memory. In other word, by communication and exchange of information each other, the particles in the swarm evolve toward the best individual experience (PBEST) and the best social experience (GBEST).

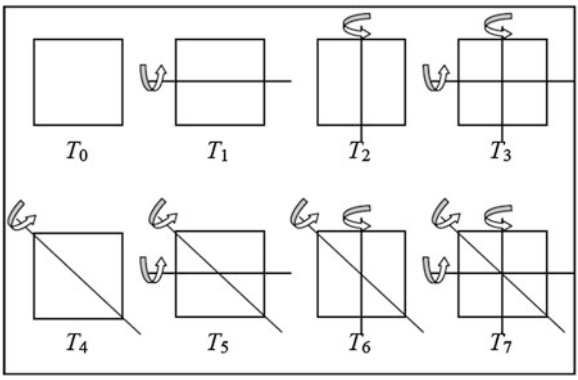

Fig. 58.1 The diagram of eight transformations in the Dihedral group

Let $x_{j,d}(t)$ and $v_{j,d}(t)$ denote the dth dimensional value of the vector of position and velocity of jth particle in the swarm, respectively, at time t. The PSO model can be expressed as

$$v_{j,\,d}(t) = v_{j,\,d}(t-1) + c_1 \cdot r_1 \cdot (x^*_{j,d} - x_{j,d}(t-1)) + c_2 \cdot r_2 \cdot (x^{\#}_d - x_{j,d}(t-1)), \tag{58.2}$$

$$x_{j,d}(t) = x_{j,d}(t-1) + v_{j,d}(t), \tag{58.3}$$

where $x^*_{j,d}(t)$ denotes the dth dimension value of the best position $x^*_j(t)$ (PBEST) of jth particle up to time t-1 and $x^{\#}_d$ denotes the dth dimension value of the best position $x^{\#}$ (GBEST) of the whole swarm up to time t-1, c_1 and c_2 represent the individuality and sociality coefficients, respectively, and r_1 and r_2 are random numbers.

First, the swarm size is determined. The position and velocity of each particle are initialized randomly. The fitness of all the particles is calculated. The fitness is the reciprocal of the MSE and represents the degree of the similarity with the range block. According to the fitness, all the particles are divided into two groups: superiority group D_S and inferiority group D_I. The particles in the D_S has good similarity match with the range block. It represents the probability is high that finding the better similarity match at the neighborhood around the particle. Such a particle will moves according to (58.2) and (58.3) to find better similarity match. On the contrary, a particle in the D_I has not good similarity match with the range block. It means that the probability of finding good similarity match at the neighborhood around the particle is low. The particle will escapes from the area to explore the whole image in order to find good match solution in the other areas. Meanwhile, the best positions $x^*_j(t)$ and $x^{\#}$ of each particle and the swarm are updated. Finally, as the stopping criterion is satisfied, the best position of the swarm is the final solution. The main steps of the proposed PSO algorithm are given as follows:

Step 1: Set the swarm size, the individuality coefficient c_1, and the sociality coefficient c_2. Initialize the position and the velocity of each particle randomly.

Step 2: For each j, evaluate the fitness value of the particle and update the individual best position $x_j^*(t)$ if the fitness of the new position is better than that of the previous individual best position.

Step 3: Find the best one of all the particles at the current position. Update the swarm best position $x^{\#}$ if the fitness of the new best position is better than that of the previous swarm best position.

Step 4: If the stopping criterion is satisfied, then stop. Record the affine parameters of the swarm best position $x^{\#}$ as fractal code. Otherwise, go to next step.

Step 5: Divide the particles into two groups D_S and D_I according to the fitness.

Step 6: For the particles in D_S, update the velocity and the position according (58.2) and (58.3).

Step 7: For the particles in D_I, assign the new position randomly and keep the velocity unchanged. Back to Step 2.

58.4 Experimental Results

The comparison of proposed PSO, baseline PSO, and full search methods for fractal image compression is done to verify the performance of the proposed one. The tested image is Lena, Pepper, F-16, and Baboon, each of which is of size 256 × 256. The size of range block is 8 × 8. For the two PSO algorithms, the swarm size is 100. Both the individuality coefficient c_1 and the sociality coefficient c_2 are set to be 1. In addition, the two groups D_S and D_I in the proposed PSO algorithm divide the swarm equally. The simulation programs implemented by using Borland C++ Builder v. 6.0 are run on a Pentium Core2 Duo 2.0 GHz, 2G RAM, windows XP PC. The quality distortion of the retrieved image $g(i, j)$ to the original image $f(i, j)$ is measured in Peak Signal to Noise Ratio (PSNR) defined by

$$PSNR = 10 \times \log_{10}\left(\frac{255^2}{\mathrm{MSE}(f, g)}\right) \tag{58.4}$$

where MSE(f, g) is given in Eq. (58.1).

Figure 58.2 shows the comparison of performances of proposed PSO algorithm and baseline PSO algorithm for Lena, in which x-coordinate is the number of the iteration and y-coordinate is PSNR. At 16th iteration, the PSNR of the proposed PSO and baseline PSO algorithms are 27.85 and 27.72 dB, respectively. The difference at retrieved image quality for the two methods is 0.13 dB. As shown in Fig. 58.2, in all the iteration process, the proposed PSO algorithm indeed has better retrieved quality than the baseline PSO algorithm.

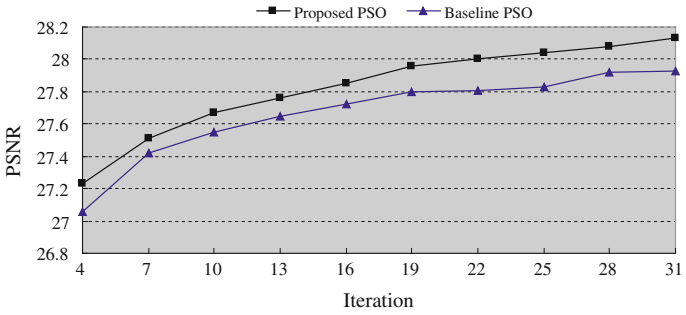

Fig. 58.2 PSNR versus number of iterations for Lena

Table 58.1 The comparison of proposed PSO, baseline PSO, and full search algorithms

	Algorithm	Time (s)	No. of MSE computations	PSNR (dB)
Lena	Full search	2514.58	475,799,552	28.91
	Baseline PSO	59.83	13,107,200	27.72
	Proposed PSO	59.88	13,107,200	27.85
Pepper	Full search	2515.62	475,799,552	29.84
	Baseline PSO	59.75	13,107,200	28.36
	Proposed PSO	59.76	13,107,200	28.67
F-16	Full search	2516.85	475,799,552	25.21
	Baseline PSO	59.77	13,107,200	23.44
	Proposed PSO	60.08	13,107,200	24.26
Baboon	Full search	2515.34	475,799,552	20.15
	Baseline PSO	59.83	13,107,200	19.73
	Proposed PSO	59.94	13,107,200	19.84

Table 58.1 lists the performance differences of the proposed PSO algorithm to the baseline PSO and the full search methods for Lena, Pepper, F-16, and Baboon. The number of the iteration is 16. All the PSO parameters of the two PSO algorithms are the same. The number of the MSE computation of the proposed PSO algorithm is equal to that of the baseline PSO algorithm, since their PSO parameters are the same. As we have seen, the retrieved quality of the proposed PSO algorithm is indeed superior to that of baseline PSO algorithm. The improvements in PSNR are 0.13, 0.31, 0.82, and 0.11, respectively, for the four images. Moreover, in comparison to the full search method, the encoding time is 42 times faster while the retrieved image quality can still be preserved.

The retrieved images obtained by using full search, baseline PSO, and proposed PSO algorithms are shown in Fig. 58.3. The parameters are the same as Table 58.1. Figure 58.3a is the original Lena image. Figure 58.3b, c are the retrieved images using the full search and baseline PSO algorithms, respectively. Figure 58.3d is the retrieved image using proposed PSO algorithm. As demonstrated, the proposed method does preserve the image visual effects.

Fig. 58.3 **a** Original image, Lena of size 256 × 256. **b** Full search algorithm. **c** Baseline PSO algorithm. **d** Proposed PSO algorithm

58.5 Conclusion

In this paper, a strategy embedding elitism into the PSO has been considered. By using the elitism, two groups, superiority group D_S and inferiority group D_I, are formed. A particle in the D_S is belonging to the elitism and move according to Eqs. (58.2) and (58.3) to find better similarity match. On the contrary, a particle in the D_I is not belonging to the elitism. Hence it escapes from the origin position to explore the whole image to find good match solution in the other areas. Experimental results show that the speed of the proposed PSO algorithm is about 42 times faster than that of the full search method with the acceptable decay of the retrieved image. Moreover, under the same number of the MSE computations, the decay of the retrieved quality of the proposed PSO algorithm is less about 0.11–0.82 dB than that of the baseline PSO algorithm.

References

1. Barnsley, M. F., & Demko, S. G. (1985). Iterated function systems and the global construction of fractals. *Proceedings of the Royal Society of London, A399*, 243–275.
2. Jacquin, A. E. (1992). Image coding based on a fractal theory of iterated contractive image transformations. *IEEE Transactions on Image Processing, 1*, 18–30.
3. Kova'cs, T. (2008). A fast classification based method for fractal image encoding. *Image and Vision Computing, 26*, 1129–1136.
4. Duh, D. J., Jeng, J. H., & Chen, S. Y. (2008). Speed quality control for fractal image compression. *The Imaging Science Journal, 56*, 79–90.
5. Wang, X. Y., Li, F. P., & Chen, Z. F. (2009). An improved fractal image coding method. *Fractals, 17*(4), 451–457.
6. Wang, X. Y., & Wang, S. G. (2008). An improved no-search fractal image coding method based on a modified gray-level transform. *Computers & Graphics, 32*, 445–450.
7. Furao, S., & Hasegawa, O. (2004). A fast no search image coding method. *Signal Processing Image Communication, 19*, 393–404.
8. Truong, T. K., Kung, C. M., Jeng, J. H., & Hsieh, M. L. (2004). Fast fractal image compression using spatial correlation. *Chaos, Solitons & Fractals, 22*(5), 1071–1076.
9. Wu, M. S., Teng, W. C., Jeng, J. H., & Hsieh, J. G. (2006). Spatial correlation genetic algorithm for fractal image compression. *Chaos, Solitons & Fractals, 28*, 497–510.

10. Wang, X. Y., Li, F. P., & Wang, S. G. (2009). Fractal image compression based on spatial correlation and hybrid genetic algorithm. *Journal of Visual Communication and Image Representation, 20*(8), 505–510.
11. Muruganandham, A., & Wahida Banu, R. S. D. (2010). Adaptive fractal image compression using PSO. *Procedia Computer Science, 2*, 338–344.
12. Wu, M. S., & Lin, Y. L. (2010). Genetic algorithm with a hybrid select mechanism for fractal image compression. *Digital Signal Processing, 20*(4), 1150–1161.

Chapter 59
A Short Note on Derandomization of Perfect Target Set Selection

Yan-Liang Chen and Ching-Lueh Chang

Abstract Consider the following process on a simple undirected connected graph $G(V, E)$. At the beginning, only a set S of vertices are active. Subsequently, a vertex is activated if at least an $\alpha \in (0, 1)$ fraction of its neighbors are active. The process stops only when no more vertices can be activated. Following earlier papers, we call S an α perfect target set, abbreviated α-PTS, if all vertices are activated at the end. Chang [1] proposes a randomized polynomial-time algorithm for finding an α-PTS of expected size $(2\sqrt{2}+3)\lceil\alpha|V|\rceil$, where the expectation is taken over the random coin tosses of the algorithm. We note briefly that the method of conditional expectation can be used to derandomize Chang's algorithm. So the derandomized algorithm finds an α-PTS of size no more than $(2\sqrt{2}+3)\lceil\alpha|V|\rceil$ given any simple undirected connected graph.

Keywords Target set selection · Repetitive polling game · Fault propagation · Global cascade

59.1 Introduction

Consider the following process on a simple undirected connected graph $G(V, E)$: Initially, only a set S of vertices are active. Subsequently, a vertex is activated if at least an $\alpha \in (0, 1)$ fraction of its neighbors are active. The process stops when no more vertices remain to be activated. The set of active vertices at the end is

Y.-L. Chen
Zen Voce, No 53, Jinggong Road, Hsinchu county 304, Taiwan, Republic of China

C.-L. Chang (✉)
Department of Computer Science and Engineering, Yuan-Ze University,
Taoyuan 320, Taiwan
e-mail: clchang@saturn.yzu.edu.tw

J. Juang et al. (eds.), *Proceedings of the 2nd International Conference on Intelligent Technologies and Engineering Systems (ICITES2013)*, Lecture Notes in Electrical Engineering 293,
DOI: 10.1007/978-3-319-04573-3_59,

denoted by $\sigma(S)$. Following the literature, we call S an α perfect target set, or α-PTS for short, if $\sigma(S) = V$. The perfect target set selection problem aims to find the minimum size of α perfect target sets.

The aforementioned process with α close to 1/2 models fault propagation in fault-tolerant computing systems because majority voting is a common way to amend errors [2]. In this regard, Flocchini et al. [3–5] and Adams et al. [6] study the perfect target set selection problem and its variants for chordal rings, tori, complete trees, rings, butterflies, cube-connected cycles, shuffle-exchanges and hypercubes. For general graphs, the perfect target set selection problem has been studied by Chang and Lyuu [1, 7], Ackermann et al. [8] and Khoshkhah et al. [9]. Algorithmic and complexity-theoretic aspects are also well investigated [10–13]. In statistical physics, the process of this paper is known as a global cascade or bootstrap percolation [14, 15]. There are also reversible variants, where active vertices may be deactivated later [4, 5, 16–20].

Using a method of Ackermann et al. [8], Chang [1] gives a randomized polynomial-time algorithm outputting an α-PTS of expected size at most $(2\sqrt{2}+3)\lceil\alpha|V|\rceil$, where the expectation is taken over the random coin tosses of the algorithm. This paper briefly notes that the method of conditional expectation can be used to derandomize Chang's algorithm. So the derandomized algorithm outputs an α-PTS of expected size at most $(2\sqrt{2}+3)\lceil\alpha|V|\rceil$. For information on the method of conditional expectation, please see [21].

59.2 Derandomizing Chang's Algorithm

Some standard notations will be useful in the sequel: The set of neighbors of a vertex v is denoted N(v), and $d(v) = |N(v)|$. Below is Chang's [1] randomized algorithm.

Input : Simple undirected graph $G(V, E)$, $\varphi : V \to Z^+$ and $\lambda \in (0, 1)$

1: $L \leftarrow \{v \in V \mid \varphi(v) > 1\}$;

2: $R \leftarrow V \setminus L$;

3: $A \leftarrow \emptyset$;

4: $B \leftarrow \emptyset$;

5: **while** there exists $v \in L \setminus A$ with $|N(v) \cap (R \setminus \sigma(A))| \geq \lambda d(v)$ **do**

6: $A \leftarrow A \cup \{v\}$;

7: **end while**

8: Pick a bijection $\boldsymbol{\pi}: \mathrm{V} \rightarrow \{1, 2, \ldots, |\mathrm{V}|\}$ uniformly at random;

9: **for** each $\mathrm{v} \in \mathrm{L} \setminus \mathrm{A}$ **do**

10: **if** $|\mathrm{N}(\mathrm{v}) \cap (\{\mathrm{u} \in \mathrm{L} \mid \boldsymbol{\pi}(\mathrm{u}) < \boldsymbol{\pi}(\mathrm{v})\} \cup \sigma(\mathrm{A}))| < \varphi(\mathrm{v})$ **then**

11: $\mathrm{B} \leftarrow \mathrm{B} \cup \{\mathrm{v}\}$;

12: **end if**

13:**end for**

14: Output $\mathrm{A} \cup \mathrm{B}$;

Suppose that each vertex v can be activated when at least $\varphi(\mathrm{v})$ of its neighbors are active, and the process continues until no more vertices can be activated. Then the output of Chang's algorithm, when considered to be the set of initially active vertices, will cause all vertices to be active at the end [1].

Fact 1 [1]. Let $\mathrm{G}(V, E)$ be a simple connected undirected graph and $\varphi(\mathrm{v}) = \lceil \alpha \mathrm{d}(\mathrm{v}) \rceil$ for all $\mathrm{v} \in \mathrm{V}$, where $\alpha \in (0, 1)$. Then the output of Chang's algorithm is an α-PTS of expected size no more than $\left(2\sqrt{2} + 3\right)\alpha|\mathrm{V}|$, where the expectation is taken over the random coin tosses of the algorithm.

We now note that Chang's algorithm can be derandomized using the method of conditional expectation.

Theorem 2 Given any simple undirected connected graph, an α-PTS of size no more than $\left(2\sqrt{2} + 3\right)\lceil \alpha|\mathrm{V}| \rceil$ can be computed in deterministic polynomial time, where $\alpha \in (0, 1)$.

Proof Denote $\mathrm{V} = \left\{\mathrm{v}_1, \mathrm{v}_2 \ldots, \mathrm{v}_{|\mathrm{V}|}\right\}$. Clearly, for distinct $x_1, x_2, \ldots, x_i \in \{1, 2, \ldots, |\mathrm{V}|\}$,

$$\begin{aligned}
&\mathbf{E}[|\mathbf{B}||\boldsymbol{\pi}(\mathbf{v}_1) = \mathbf{x}_1, \ldots, \boldsymbol{\pi}(\mathbf{v}_\mathbf{i}) = \mathbf{x}_\mathbf{i}] \\
&= \frac{1}{|\mathbf{V}| - \boldsymbol{i}} \sum_{\boldsymbol{y} \in \{1,2,\ldots,|\mathbf{V}|\} \setminus \{\boldsymbol{x}_1, \boldsymbol{x}_2 \ldots \boldsymbol{x}_i\}} \mathbf{E}[|\mathbf{B}||\boldsymbol{\pi}(\mathbf{v}_1) = \mathbf{x}_1, \ldots, \boldsymbol{\pi}(\mathbf{v}_\mathbf{i}) = \mathbf{x}_\mathbf{i}, \boldsymbol{\pi}(\mathbf{v}_{\mathbf{i}+1}) = \mathbf{y}].
\end{aligned} \tag{59.1}$$

For each $y \in \{1, 2, ..., |\mathrm{V}|\} \setminus \{x_1, x_2 \ldots x_i\}$,

$$\begin{aligned}
&\mathbf{E}[|\mathbf{B}||\boldsymbol{\pi}(\mathbf{v}_1) = \mathbf{x}_1, \ldots, \boldsymbol{\pi}(\mathbf{v}_\mathbf{i}) = \mathbf{x}_\mathbf{i}, \boldsymbol{\pi}(\mathbf{v}_{\mathbf{i}+1}) = \mathbf{y}] \\
&= \sum_{\boldsymbol{v} \in \mathbf{V}} \mathbf{Pr}[\mathbf{v} \in \mathbf{B} | \boldsymbol{\pi}(\mathbf{v}_1) = \mathbf{x}_1, \ldots, \boldsymbol{\pi}(\mathbf{v}_\mathbf{i}) = \mathbf{x}_\mathbf{i}, \boldsymbol{\pi}(\mathbf{v}_{\mathbf{i}+1}) = \mathbf{y}] \\
&= \sum_{\boldsymbol{v} \in \mathbf{L} \setminus \mathbf{A}} \mathbf{Pr}\left[\left|N(\mathbf{v}) \bigcap \left(\{\mathbf{u} \in \mathbf{L} | \boldsymbol{\pi}(\mathbf{u}) < \boldsymbol{\pi}(\mathbf{v})\} \bigcup \sigma(\mathbf{A})\right)\right| < \varphi(\mathbf{v}) | \boldsymbol{\pi}(\mathbf{v}_1) = \mathbf{x}_1, \ldots, \boldsymbol{\pi}(\mathbf{v}_\mathbf{i}) = \mathbf{x}_\mathbf{i}, \boldsymbol{\pi}(\mathbf{v}_{\mathbf{i}+1}) = \mathbf{y}\right].
\end{aligned} \tag{59.2}$$

Above, Eq. (59.2) can be seen from lines 9–13 of Chang's algorithm.

Observe that each summand in the right-hand side of Eq. (59.2) can be computed deterministically in polynomial time. Hence we may pick in deterministic polynomial time an $x_{i+1} \in \{1, 2, \ldots, |V|\} \backslash \{x_1, x_2 \ldots x_i\}$ with

$$\begin{aligned}
&E[|B||\pi(v_1) = x_1, \ldots, \pi(v_i) = x_i, \pi(v_{i+1}) = x_{i+1}] \\
&= \min_{y \in \{1,2,\ldots,|V|\} \backslash \{x_1, x_2 \ldots x_i\}} E[|B||\pi(v_1) = x_1, \ldots, \pi(v_i) = x_i, \pi(v_{i+1}) = y] \\
&\leq E[|B||\pi(v_1) = x_1, \ldots, \pi(v_i) = x_i],
\end{aligned}$$

where the last inequality follows from Eq. (59.1). Repeat the above to obtain distinct $x_1, x_2 \ldots, x_{|V|}$ in polynomial time such that for each $i \in \{1, 2, \ldots, |V| - 1\}$,

$$\begin{aligned}
&E[|B||\pi(v_1) = x_1, \ldots, \pi(v_i) = x_i, \pi(v_{i+1}) = x_{i+1}] \\
&\leq E[|B||\pi(v_1) = x_1, \ldots, \pi(v_i) = x_i],
\end{aligned}$$

implying

$$E\left[|B||\pi(v_1) = x_1, \ldots, \pi\left(v_{|V|}\right) = x_{|V|}\right] \leq E[|B|].$$

This is equivalent to

$$E\left[|A \cup B|\middle|\pi(v_1) = x_1, \ldots, \pi\left(v_{|V|}\right) = x_{|V|}\right] \leq E[|A \cup B|]$$

because $A \cap B = \emptyset$ in Chang's algorithm. Therefore, by **Fact 1**,

$$E\left[|A \cup B|\middle|\pi(v_1) = x_1, \ldots, \pi\left(v_{|V|}\right) = x_{|V|}\right] \leq \left(2\sqrt{2} + 3\right)\alpha|V|.$$

Finally, note that the set $A \cup B$ is deterministic conditional on $\pi(v_1) = x_1, \ldots, \pi\left(v_{|V|}\right) = x_{|V|}$. QED

59.3 Conclusions

Chang [1] gives a randomized polynomial-time algorithm for finding an α-PTS of expected size $(2\sqrt{2} + 3)\lceil\alpha|V|\rceil$ in any connected graph. We note briefly that the method of conditional expectation can be used to derandomize his algorithm. So the derandomized algorithm finds an α-PTS of expected size no more than $(2\sqrt{2} + 3)\lceil\alpha|V|\rceil$ given a simple undirected connected graph.

Acknowledgments Ching-Lueh Chang is supported in part by the Ministry of Economic Affairs under grant 102-E0616 and the National Science Council under grant 101-2221-E-155-015-MY2.

References

1. Chang, C. -L. (2011). Triggering cascades on undirected connected graphs. *Information Processing Letters*, *11*(19), 973–978.
2. Peleg, D. (2002). Local majorities, coalitions and monopolies in graphs: A review. *Theoretical Computer Science, 282*(2), 231–257.
3. Flocchini, P., Geurts, F., & Santoro, N. (2001). Optimal irreversible dynamos in chordal rings. *Discrete Applied Mathematics, 113*(1), 23–42.
4. Flocchini, P., Královic, R., Ruzicka, P., Roncato, A., & Santoro, N. (2003). On time versus size for monotone dynamic monopolies in regular topologies. *Journal of Discrete Algorithms, 1*(2), 129–150.
5. Flocchini, P., Lodi, E., Luccio, F., Pagli, L., & Santoro, N. (2004). Dynamic monopolies in tori. *Discrete Applied Mathematics, 137*(2), 197–212.
6. Adams, S. S., Troxell, D. S., & Zinnen, S. L. (2011). Dynamic monopolies and feedback vertex sets in hexagonal grids. *Computers and Mathematics with Applications, 62*(11), 4049–4057.
7. Chang, C. -L., & Lyuu, Y. -D. (2010). Bounding the number of tolerable faults in majority-based systems. In *Proceedings of the 7th International Conference on Algorithms and Complexity* (pp. 109–119). Rome, Italy.
8. Ackerman, E., Ben-Zwi, O., & Wolfovitz, G. (2010). Combinatorial model and bounds for target set selection. *Theoretical Computer Science, 411*(44–46), 4017–4022.
9. Khoshkhah, K., Soltani, H., & Zaker, M. (2012). On dynamic monopolies of graphs: The average and strict majority thresholds. *Discrete Optimization, 9*(2), 77–83.
10. Chen, N. (2008). On the approximability of influence in social networks. In *Proceedings of the 19th Annual ACM-SIAM Symposium on Discrete Mathematics* (pp. 1029–1037).
11. Dreyer, P. A., & Roberts, F. S. (2009). Irreversible k-threshold processes: Graph-theoretical threshold models of the spread of disease and of opinion. *Discrete Applied Mathematics, 157*(7), 1615–1627.
12. Kempe, D. Kleinberg, J, & Tardos, E. (2003). Maximizing the spread of influence through a social network. In *Proceedings of the 9th ACM SIGKDD International Conference on Knowledge Discovery and Data Mining* (pp. 137–146).
13. Kralovic, R. (2001). On majority voting games in trees. In *Proceedings of the 28th Conference on Current Trends in Theory and Practice of Informatics* (pp. 282–291.
14. Gleeson, J. P., & Cahalane, D. J. (2002). Seed size strongly affects cascades on random networks. *Physical Review E, 75*(5), 056103.
15. Watts, D. J. (2002). A simple model of global cascades on random networks. *Proceedings of the National Academy of Sciences 99*(9), 5766–5771.
16. Berger, E. (2001). Dynamic monopolies of constant size. *Journal of Combinatorial Theory Series B, 83*(2), 191–200.
17. Goles, E., & Olivos, J. (1980). Periodic behaviour of generalized threshold functions. *Discrete Mathematics, 302*, 187–189.
18. Kleinberg, J. (2000). The small-world phenomenon: An algorithm perspective. In *Proceedings of the 32nd Annual ACM Symposium on Theory of Computing* (pp. 163–170.
19. Morris, S. (2000). Contagion. *Review of Economic Studies, 67*(1), 57–78.
20. Peleg, D. (1998). Size bounds for dynamic monopolies. *Discrete Applied Mathematics, 86*(2–3), 263–273.
21. Motwani, R., & Raghavan, P. (1995). *Randomized algorithms*. Cambridge: Cambridge University Press.

Chapter 60
Electric Power Usage Data Acquisition Module Composed of Two Sensors and a Microcontroller

Chien-Yuan Liu, Chih-Feng Huang and Yann-Chang Huang

Abstract This article presents an electric power usage data acquisition module which was designed and developed by a microcontroller, a current sensor, a voltage sensor, and an acquisition firmware. The electric power usage data is obtained from the multiplication of the acquired current value and the acquired voltage value. At present stage, power factor is deemed as 100 % for simplifying the computation for general household electric appliances. Next stage, PF would be detected by the phase angle deviation of the current waveform and the voltage waveform. The layout of the printed circuit board of the module was drawn by the open-source Fritzing. The PCB was successfully fabricated and validated by a light AC load during experimental measurement.

Keywords Current sensor · Voltage divider · Electric power · Data acquisition

60.1 Introduction

Recently, the need of energy saving is globally emphasized as the increase of the price of fossil energy [1]. Therefore, electric power data acquisition systems are more important for conserving electric power consumption under such trend of energy saving [2].

There are several ways to acquire the data of electric power usage for various applications. For instance, a certified power meter is installed to measure and

C.-Y. Liu (✉) · C.-F. Huang
Department of Computer Science and Information Engineering, Cheng Shiu University, Kaohsiung 83347, Taiwan Republic of China
e-mail: cyliu@csu.edu.tw

Y.-C. Huang
Department of Electrical Engineering, Cheng Shiu University, Kaohsiung 83347, Taiwan Republic of China

J. Juang et al. (eds.), *Proceedings of the 2nd International Conference on Intelligent Technologies and Engineering Systems (ICITES2013)*, Lecture Notes in Electrical Engineering 293,
DOI: 10.1007/978-3-319-04573-3_60,

accumulate the power usage for commercial billing. For research and laboratory, precise instruments are popular for further analysis [3, 4], e.g. LabVIEW and MATLAB. Modular data acquisition systems [5] are often designed for prototyping projects.

This research developed the electric power data acquisition module implemented by a microcontroller and sensors in low cost. The electric power usage data is calculated by the sensed voltage data multiplied by the sensed current data. The result of the measurement is precise enough for the practical application of smart home [6]. At present, however, the precision of it is still insufficient for the commercial metering purpose [7].

60.2 The Design and Development of the Acquisition Module

The electric power usage data acquisition module is composed of sensors, a microcontroller, and man–machine interface (MMI). The sensors are consisted of one current transformer (CT) and one potential transformer (PT). Traditional CT and PT [8] are made of coil transformers to isolate the high power and the low power sides, meanwhile, to reduce the detecting voltage level and current level to match the input level of a microcontroller. Next, the transformed low level analog signals are input to the ADC of the microcontroller for converting the sensed values to digital data. The sensed data are calculated by the microprocessor and are stored in the flash memory for accumulation. The calculated results are display by the LCD unit of MMI. Few buttons are utilized to operate the control firmware of the module for displaying various contents (see Fig. 60.1).

In this design, a current sensor IC of ACS758 [9] is adopted as the CT. The current sensor IC is based on the Hall Effect to detect the loading current with 100 μΩ internal resistance to the load path, thus providing very low power loss. ACS758-*x*050 B features with up to 50 A sampling current, 4 μs response time, 120 kHz bandwidth, liner voltage output in response to sampling current, 40 mV/A sensitivity, 1.2 % total error, and the quiescent output voltage V_Q at $V_{CC}/2$. Rated V_{CC} is 5 V, hence, output voltage for zero sampling current is 2.5 V. Typical circuit of ACS758 is connected as Fig. 60.2. The sensed current I_{LOAD} is calculated by formula (60.1). To simplify the current sensing and conversion, only V_{outmax} is sensed for calculation. Therefore, the effective value of load current is obtained by the multiplication of $1/\sqrt{2}$ and V_{outmax}.

$$I_{LOAD} = \frac{1}{\sqrt{2}} \times \left(V_{out} - \frac{V_{CC}}{2} \right) \times \frac{1}{Sensitivity} \tag{60.1}$$

Figure 60.3 illustrates the voltage sensor circuit. The AC power source is rectified by a diode bridge. The bridge provides a full-wave rectification for the output. A voltage divider is utilized as the potential transformer. The sensed

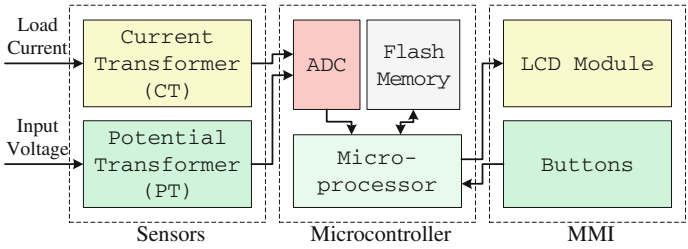

Fig. 60.1 The block diagram of electric power acquisition module

Fig. 60.2 The schematic diagram of the ACS758 current sensor

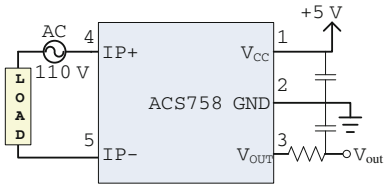

voltage V_{AC} is calculated by formula (60.2). To simplify the voltage sensing and conversion, only V_{outmax} is sensed for calculation. Therefore, effective value of V_{AC} is obtained by the multiplication of $1/\sqrt{2}$ and V_{DCmax}.

$$V_{AC} = \frac{1}{\sqrt{2}} \times V_{out} \times \frac{R_1 + R_2}{R_1} \tag{60.2}$$

Finally, the electric power usage value could be computed by the effective V_{AC} multiplied by the effective I_{LOAD}. At present revision, PF is assumed to be 100 % for most of household electric appliances. In future extension, actual PF of various household electric appliances would be detected by the phase angle deviation between the sensed voltage waveform and the sensed current waveform. The more precise PF, voltage, and current date would produce more accurate electric power usage data. In this case, however, higher sampling rate and more computation capability is required. Comprehensive experiments will be necessary to fully utilize the computation power of the microcontroller in order to extend the sampling rate. The parameters about the current sensor and the voltage sensor are listed in Table 60.1.

60.3 The Implementation and Measurement of Acquisition Module

The selection of microprocessor vendors is pretty versatile from TI, Renesas, Microchip, NXP, Atmel, and ARM, etc. For implementation, the Atmel ATmega328P [10] was chosen to be the microcontroller for the acquisition module.

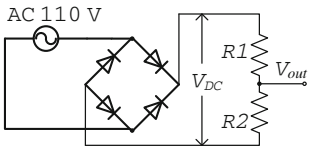

Fig. 60.3 The schematic diagram of the voltage sensor

Table 60.1 The parameters of the current sensor and the voltage sensor

Parameter	Value
V_{CC}	5 V
V_Q	$V_{CC}/2 + V_{Q\_Offset}$
Sensitivity	40 mV/A
R_1	2 KΩ
R_2	150 KΩ
V_{Q_Offset}	Experimental value
Sampling rate	1 kHz
Max. sampling rate	10 kHz (in future)

The RISC ATmega328P features with 20MIPS, 1 KB EEPROM, 2 KB SRAM, 32 KB Flash memory, 6-ch 10-bit ADC, 23 programmable IO, and power-save mode, etc. HD44780U-based LCD module [11] with 2-line by 16-character is utilized as the display unit. Two buttons are allocated to adjust the displayed content to up or down direction.

The layout of the acquisition module is routed by the open-source PCB tool, named Fritzing [12]. The output formats could be in BOM list, in PDF for printer, or in Gerber for mass production. In this work, the top and bottom layouts in PDF format are printed for PCB. Then, the photo-resist PCB is exposed, developed, etched, drilled, and soldered with all components. The top tracks and the bottom tracks of the module routes are illustrated in Figs. 60.4 and 60.5.

The acquisition firmware was developed by the open-source Arduino IDE [13]. It is an integrated development environment, including text-sensitive editor, C++ compiler, and USB-burn up loader. The current sample and voltage sample are acquired by the IO statement as below,

Line no.	Acquisition statement
1	`ct_vout = analogRead(ACS758_Vout_Pin)`
2	`pt_vout = analogRead(VoltageDivider_Vout_Pin)`

The ct_vout is converted to the effective line current by the formula (60.1) and the pt_vout is converted to the effective line voltage by the formula (60.2). Various sampling rates were applied for sensing experiment. The integrated acquisition module is depicted in Fig. 60.6. During validation stage, a light load was plugged to the module to verify the functionality and correctness of the module.

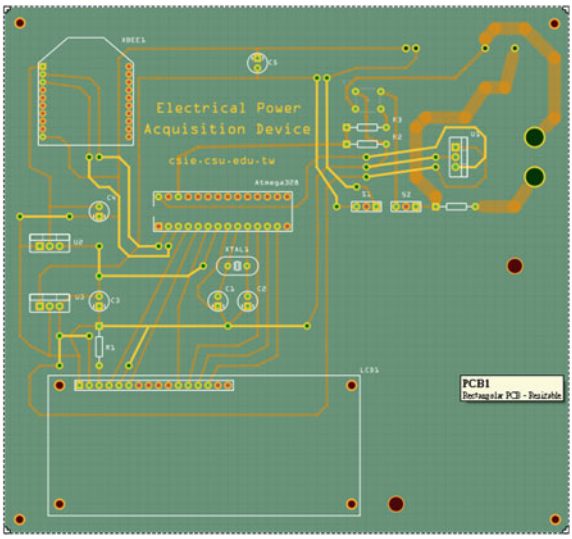

Fig. 60.4 The top tracks of the DAQ module

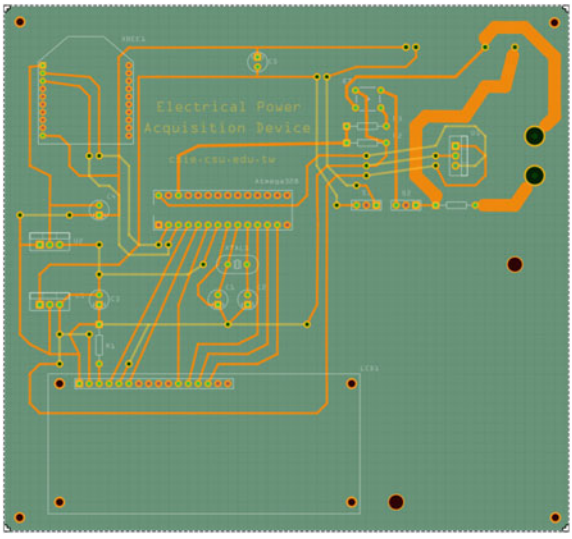

Fig. 60.5 The bottom tracks of the DAQ module

The acquired current and voltage data are shown in Fig. 60.7. The waveforms in Fig. 60.7 are not smooth enough. The reason of this is because the sampling interval is set to 1 ms. If the sampling rate could be increased to 10 KHZ or even more, a high-quality sampling curve would be obtained. In that case, the PF is possible to be observed from the deviation of the phase angles between the sampled waveform of the current and that of the voltage.

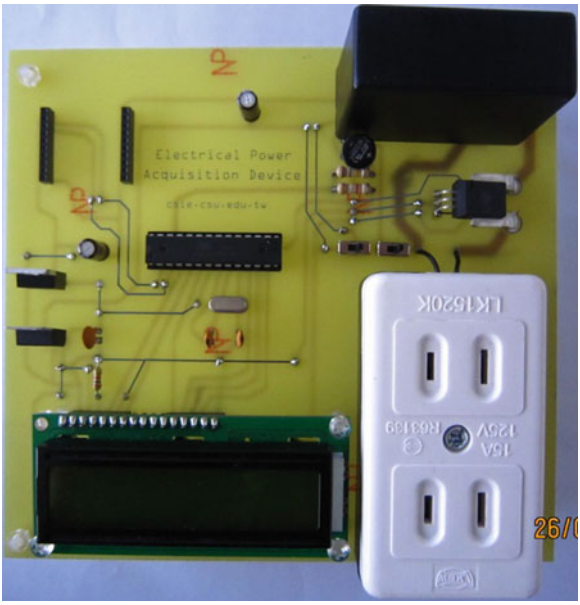

Fig. 60.6 The completed acquisition module

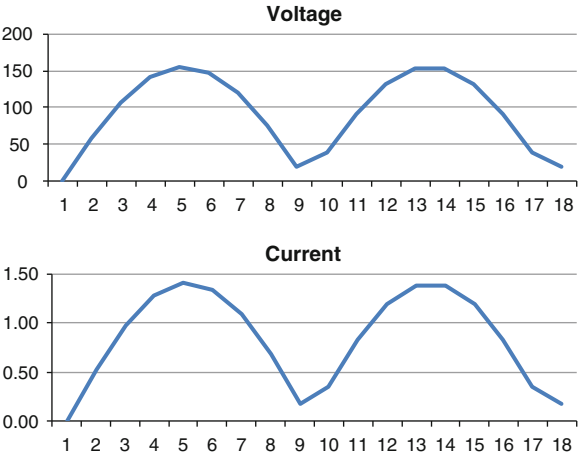

Fig. 60.7 The sampled voltage and current data

60.4 Conclusions

The electric power usage value is critical for commercial billing and the requirement under the power-save trend. In this research, the electric power usage data acquisition system is designed and developed by a current sensor, a voltage sensor and a microcontroller. From the multiplication of the acquired current and voltage values, the electric power usage value could be calculated. The system

module is majorly implemented by a common microcontroller and two sensing schematics. With the uploaded firmware, the effective loading current and line voltage were acquired by the sensors and ADC of the microcontroller. In future, the module is expected to extend as follows,

- Increase the sampling rate to acquire more records such that the PF could be observed from the acquired waveforms of the loading current and the line voltage.
- Extend wireless communication capability such that the module could transmit the sampled (*V, I*) data and the calculated power data to an energy-management system or could accept the control command from the manager in order to turn ON/OFF the power plug on this module.
- Refine the hardware module such that a smaller module could be developed and could be installed within a common electric socket on wall. Therefore, it becomes an intelligent socket for the automation of smart home.

Acknowledgments The authors greatly appreciate to the support of the National Science Council, R.O.C., under the Grant no. NSC 101-2632-E-230-001-NY3 and NSC 101-2514-S-821-001.

References

1. Sterner, T., & Coria, J. (2011). *Policy instruments for environmental and natural resource management*. Washington DC: Resources for the Future Press.
2. Utkarsh Seetha, U., & Sharma, P. (2013). Meter data acquisition system in power utilities. *International Journal of Innovative Research in Science, Engineering and Technology, 2*(4), 970–974.
3. Kaston, D. G. (2000). Integrating Computerized data acquisition and analysis into an under graduate electric machines laboratory. In *Proceedings of 30th ASEE/IEEE Frontiers in Education Conference*, Oct.18-21, Kansas City, MO.
4. Dimitrijević, M., & Litovski, V. (2006). Power factor and distortion measuring for small loads using USB acquisition module. In *Proceedings of Conference REV2006*, June 29-30, Maribor, Slovenia.
5. Beer, B., & Tong, L. (2008). *Modular data acquisition system for alternative energy solutions*. Wayne: Senior Project of Indiana-Purdue University Fort Wayne.
6. Jahn, M., et al. (2010). The energy aware smart home. In *The IEEE 5th International Conference on Future Information Technology*, May 21-23 May, Busan, Korea.
7. Pihala, H. (1998). *Non-intrusive appliance load monitoring system based on a modern kWh-meter*. Finland: Valtion Teknillinen Tutkimuskeskus.
8. http://www.mccdaq.com/. Electrical Measurements. Measure Computing (2013).
9. http://www.allegromicro.com/. ACS758-Datasheet (2013).
10. http://www.atmel.com/. Atmel-AVR-328P-Datasheet.pdf. (2013).
11. http://en.wikipedia.org/wiki/Hitachi_HD44780_LCD_controller (2013).
12. http://fritzing.org/download/0.8.3b/windows/fritzing.2013.07.27.pc.zip (2013).
13. http://arduino.googlecode.com/files/arduino-1.0.5-windows.exe (2013).

Chapter 61
USB Dongle Antenna for WLAN Applications

Wen-Shan Chen, Chin-Kai Yang, Ching-Yu Huang and Ssu-Han Ting

Abstract A monopole antenna and a truncated slot in ground plane with broadband operation are proposed for USB dongle applications. The monopole and ground plane excite a broad operating band that starts at 2.05 GHz and ends at 2.8 GHz for WLAN application at 2.4 GHz. By adding the truncated slot, the impedance matching of the 2.4 GHz band is improved to meet the WLAN requirement. An important feature of the design is that the resonances are easily controlled by changing the lengths of the monopole and the slot. Using the design mechanisms, the antenna not only can reach small size for portable devices but also can meet the wide application band for Bluetooth, Wi-Fi, and WLAN.

61.1 Introduction

Recently, the rapid developments of the wireless systems result in the wireless devices using in various applications, such as mobile phone, GPS, RFID, and WLAN. To attract consumers' interests, portable and multi-purposes are the important features. Among the wireless devices, USB dongle is the most convenient device for its smallest dimensions and plug and play. In practice, IEEE 802.11 standards of 2.4 GHz (2.4–2.484 GHz) band can be used for WLAN, Bluetooth, and Wi-Fi systems. To use in wireless dongle, the antennas must keep their dimensions in small and compact. In the prior of arts, many small and compact printed antennas were proposed for WLAN USB dongle. The antennas in

W.-S. Chen (✉) · C.-K. Yang · C.-Y. Huang
Department of Electronic Engineering, Southern Taiwan University of Science Technology, Tainan 71005, Taiwan, Republic of China
e-mail: chenws@mail.stust.edu.tw

S.-H. Ting
Department of Electronic Engineering, National Cheng Kung University, Tainan 70146, Taiwan, Republic of China

J. Juang et al. (eds.), *Proceedings of the 2nd International Conference on Intelligent Technologies and Engineering Systems (ICITES2013)*, Lecture Notes in Electrical Engineering 293,
DOI: 10.1007/978-3-319-04573-3_61,

[1–3] are designed with 20 mm in width and that in [4] is 15 mm. The antenna widths in these references are too wide to apply in today's dongle. In this design, a monopole antenna on top of FR-4 substrate excites a resonant band at 2.4 GHz for IEEE 802.11 b/g applications. A truncated slot in the ground plane is applied to increase the impedance matching of the 2.4 GHz band. In [5, 6], loop-type ground antennas, which establish the spread loop-type current distributions on the ground plane, acts as the major radiator. Thus, the truncated slot performs as the loop-type ground antenna and operates another resonance at 3.4 GHz. The truncated slot also modifies monopole's impedance to increase its matching. Beside the mechanism of truncated slot, the proposed antenna can easily control its resonance by changing antenna's parameters.

61.2 Antenna Design and application Bands

The geometry of the proposed antenna shown in Fig. 61.1 is fabricated on an FR4 substrate with thickness of 1.6 mm, relative permittivity of 4.4, and loss tangent of 0.024. The overall dimensions 55 × 13 mm (L1 × W1) consist of an antenna portion 10 × 13 mm and a system ground plane 45 × 13 mm. The detailed dimensions are listed in Table 61.1 and the size is suitable to apply in wireless USB dongle devices. A 50-ohm coaxial line is used for RF signal input. At top of the substrate, a monopole geometry and the ground plane are used to excite a resonant band at 2.4 GHz but has poor impedance matching. To increase its impedance matching, the ground plane is truncated a slot to excite another resonant band at 3.4 GHz and increase the impedance matching of the monopole. By optimizing the antenna parameters, both the simulated and measured return losses meet the WLAN application band (2.4 to 2.484 GHz) as shown in Fig. 61.2. The measured and simulated return losses also show good agreements to ensure the reliability of the design. The simulated results are obtained through HFSS simulation software.

61.2.1 Printing Area

See Figs. 61.1, 61.2 and Table 61.1.

61.3 Results and Discussions

The effects of the antenna's parameters including length of the monopole, length of the truncated slot, and size of the ground plane are discussed in this paragraph. In Fig. 61.3, the simulated return losses show that the low band at 2.4 GHz is

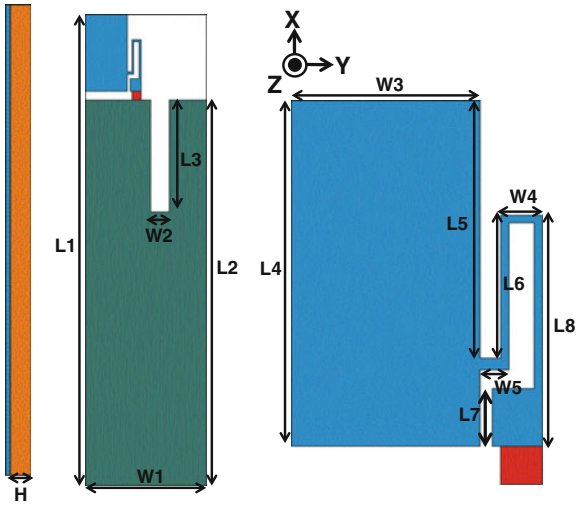

Fig. 61.1 The geometry of the proposed antenna

Table 61.1 Detailed dimensions of the proposed antenna

Parameter	Unit (mm)	Parameter	Unit (mm)
L1	55	L8	6
L2	45	W1	13
L3	13	W2	2
L4	9	W3	4.5
L5	6.7	W4	1
L6	3.7	W5	0.7
L7	1.5	H	1.6

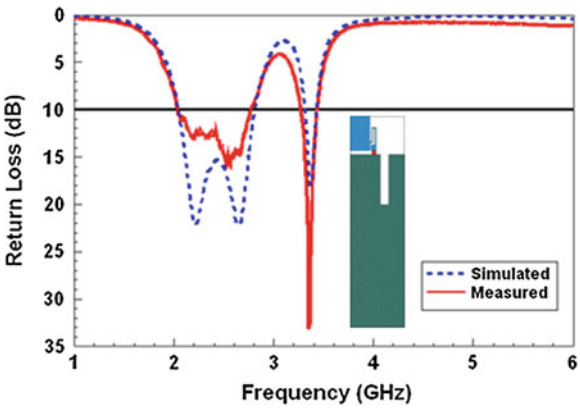

Fig. 61.2 Simulated and measured return loss of the proposed antenna

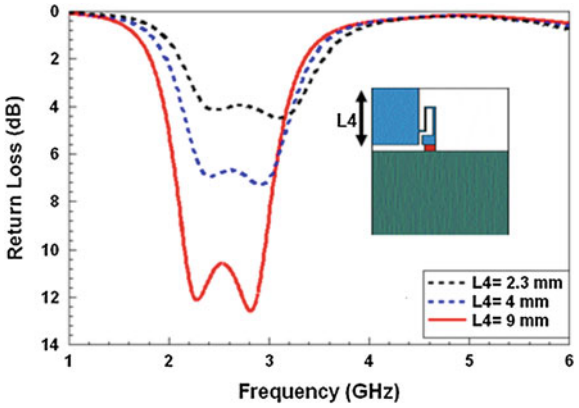

Fig. 61.3 Simulated return losses of the proposed antenna with various of monopole size

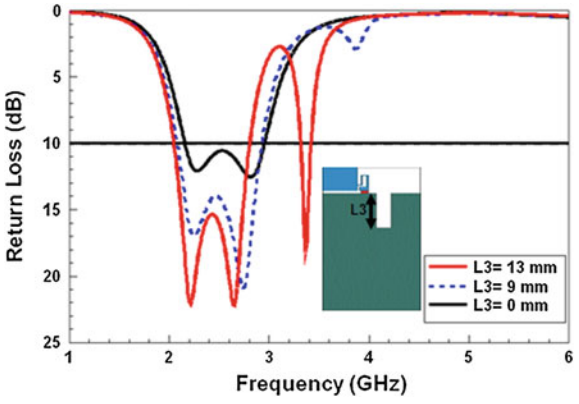

Fig. 61.4 Simulated return losses of the proposed antenna with different lengths of the truncated slot

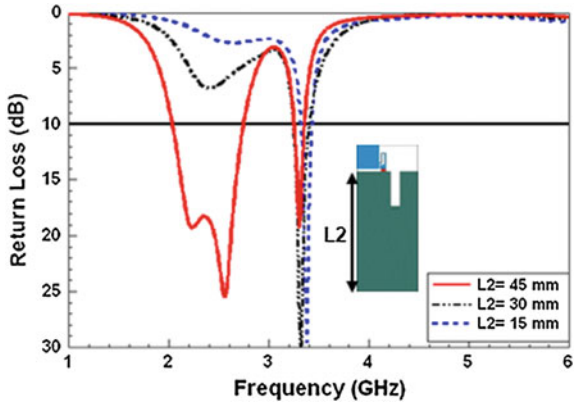

Fig. 61.5 Simulated return losses of the proposed antenna with different ground plane

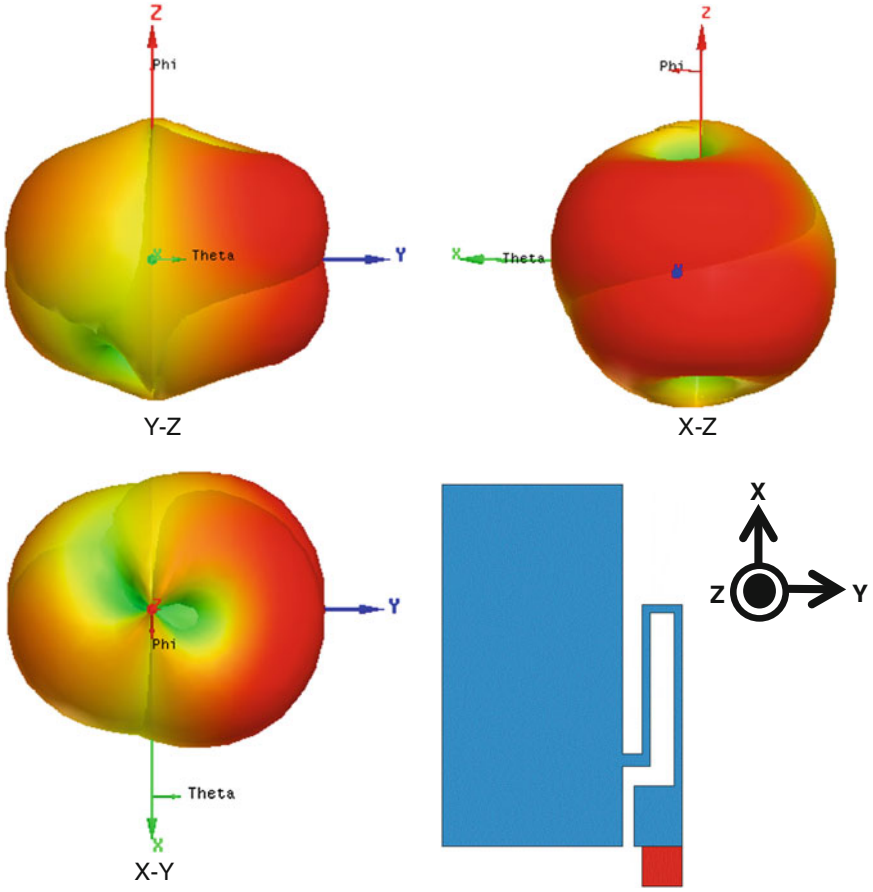

Fig. 61.6 Simulated 3-D radiation patterns in Y–Z, X–Z, and X–Y plane at 2.4 GHz

shifted lower and impedance matching is improved when L4 is increased. The results indicate that 2.4 GHz band is excited by the monopole. The simulated return losses of different lengths of the truncated slot is shown in Fig. 61.4. When the length of the truncated slot is increased, the higher mode within operating band is shifted lower and the impedance matching of low band at 2.4 GHz is improved. In Fig. 61.5, the simulated return losses are presented for different sizes of the ground plane. When the ground is decreased, the resonances have small influence but the impedance matching at 2.4 GHz is obviously changed. Figure 61.6 shows the simulated 3-D radiation patterns at 2.4 GHz. The pattern in X–Z plane shows a near omni-directional characteristic.

61.4 Conclusion

A compact and small wireless USB Dongle antenna for WLAN application was proposed and verified. The resonant frequency band is easily adjusted by changing antenna's current path and the measured and simulated 10 dB impedance bandwidth cover the WLAN 2.4 GHz application bands. The simulated radiation patterns perform an omni-directional feature. The proposed antenna with an overall antenna dimensions of 55 × 13 mm is suitable to be applied to small USB devices.

Acknowledgments This work was supported by the National Science Council of Taiwan under grant numbers of NSC 101-2221-E-218-032-, NSC 102-2221-E-218-005- and NSC 101-2632-E-218-001-MY3.

References

1. Qi, L., Pereira, J. R., & Salgado, H. M. (2009). Fractal Monopole Antenna for WLAN USB Dongle. In *2009 Loughborough Antennas & Propagation Conference*, pp. 245–247.
2. Lee, S. H., & Sung, Y. (2011). Multiband antenna for wireless USB dongle applications. *IEEE Antennas Wireless Propagation Letters, 10*, 25–28.
3. Lin, C. C., Kuo, S. W., & Chuang, H. R. (2005). A 2.4-GHz printed meander-line antenna for USB WLAN with notebook-PC housing. *IEEE Microwave and Wireless Components Letters, 15*, 546–548.
4. Kim, D., Kim, U., & Choi, J. (2010). Design of a wideband internal monopole antenna for wireless USB dongle application. In *Proceedings of Asia-Pacific Microwave Conference*, pp. 231–234.
5. Zhang, R., Liu, Y., Kim, H. H., & Kim, H. (2013). Bandwidth enhancement of ground antenna using resonant feeding circuit. *Electronics Letters, 49*(7), 441–442.
6. Cho, O., Choi, H., & Kim, H. (2011). Loop-type ground antenna using capacitor. *Electronics Letters, 47*(1), 11–12.

Chapter 62
Integration of Mean–Variance Model and Stochastic Indicator for Portfolio Optimization

Jun-Lin Lin, Chien-Hao Wu and Laksamee Khomnotai

Abstract The mean–variance model proposed by Harry Markowitz is widely used for portfolio optimization. It helps the investors to allocate their capital to a number of assets, however, it does not guide the investors when to buy or sell these assets. In contrast, technical indexes are widely used to help the investors to decide when to buy/sell an asset. In this paper, we integrate the mean–variance model with a commonly used technical index, called stochastic indicator or KD index, to derive three investment strategies. Preliminary performance study is conducted to compare these investment strategies against the mean–variance model during the uptrend, downtrend and correction periods.

Keywords Mean–variance model · KD index · Portfolio optimization

62.1 Introduction

Modern portfolio theory attempts to maximize portfolio expected return for a given level of portfolio risk, or to minimize portfolio risk for a given level of expected return. It was pioneered by Harry Markowitz, who proposed a mathematical formulation of the portfolio optimization problem, and derived a mean–variance model to yield optimized portfolios [1]. These mean–variance optimized portfolios help the investors to allocate their wealth on a number of assets to achieve the goal of diversification.

J.-L. Lin · C.-H. Wu · L. Khomnotai (✉)
Department of Information Management, Yuan Ze University, Taoyuan 32003, Taiwan, Republic of China
e-mail: k.laksamee@hotmail.com

L. Khomnotai
Faculty of Management Science, Nakhon Ratchasima Rajabhat University, Nakhon Ratchasima 30000, Thailand

J. Juang et al. (eds.), *Proceedings of the 2nd International Conference on Intelligent Technologies and Engineering Systems (ICITES2013)*, Lecture Notes in Electrical Engineering 293,
DOI: 10.1007/978-3-319-04573-3_62,

A mean–variance optimized portfolio, however, does not provide enough agility to the investors on the timing of buying and selling an asset. In the single-period model, the investors simply buy and sell these assets as suggested by the portfolio at the beginning and the end of a period, respectively [2]. In the multiple-period model, an optimized portfolio is generated for each period, and thus the investors need to adjust his/her holdings at the beginning of each period to match the portfolio of the period through a process called rebalancing [2]. Therefore, it is assumed that there is no buying and selling within each period except at the beginning or the end of a period. In practice, an investor may want to buy/sell an asset anytime with response to the dynamic market conditions. Consequently, using the mean–variance optimized portfolios alone may not be agile enough to meet the investors' need.

Technical analysis is a popular technique to decide the timing of buying and selling an asset. In this paper, we integrate the stochastic indicator (also called KD index) from technical analysis with a mean–variance optimized portfolio to derive three new investment strategies. On one hand, the mean–variance optimized portfolio is responsible of asset allocation. On the other hand, the KD index helps to determine the timing of buying and selling an asset. Overall, the resulting investment strategies provide more agility to the investors than the mean–variance optimized portfolio.

The rest of this paper is organized as follows. Section 62.2 reviews the mean–variance model and the KD index. Section 62.3 describes the proposed investment strategies. Section 62.4 presents the preliminary experimental results. Section 62.5 concludes this paper.

62.2 Preliminaries

62.2.1 Mean–Variance Model

Markowitz's mean–variance model uses the expected return of each asset and the covariance between the returns of any two assets as input. Given the expected returns of n risky assets $\mathbf{r} = (r_1, r_2, \ldots, r_n)$ and their variance–covariance matrix $\boldsymbol{\sigma} = (\sigma_{ij})_{n\times n}$, the expected return and the risk of a portfolio $\mathbf{w} = (w_1, w_2, \ldots, w_n)$ are measured as $\mathbf{r}\mathbf{w}^T$ and $\mathbf{w}\boldsymbol{\sigma}\,\mathbf{w}^T$, respectively. Then, the mean–variance model is formulated as the following optimization problem.

$$\begin{aligned}
&\text{Maximize } \mathbf{r}\mathbf{w}^T \\
&\text{s.t. } \mathbf{w}\boldsymbol{\sigma}\,\mathbf{w}^T \le \mathrm{E}, \\
&\sum_{i=1}^{n} w_i = 1, \text{ and} \\
&0 \le w_i \le 1, \text{ for } i = 1 \text{ to } n.
\end{aligned}$$

Here, E is the given level of risk provided by the investor. Alternatively, this problem can be formulated as maximizing the risk (i.e., $\mathbf{w}\boldsymbol{\sigma}\ \mathbf{w}^T$) for a given level of return. The second constraint enforces that all wealth is invested, and the third constraint prohibits short selling.

62.2.2 KD Index

The stochastic indicator (or the KD index) is a commonly used indicator among future traders. The idea behind the indicator is that asset's price tends to close near the upper/lower end of an uptrend/downtrend period. Thus, the stochastic indicator first calculates the raw stochastic value (RSV) as follows:

$$RSV_n = \frac{(P_n - L_n)}{(H_n - L_n)} \times 100$$

where P_n, L_n, and H_n represent the current closing price, the lowest closing price and the highest closing price during n periods, respectively. Then, the KD index is defined as follows:

$$K_n = RSV_n \times \left(\frac{1}{3}\right) + K_{n-1} \times \left(\frac{2}{3}\right)$$
$$D_n = K_n \times \left(\frac{1}{3}\right) + D_{n-1} \times \left(\frac{2}{3}\right)$$

where $K_1 = D_1 = 50$. In this study, whenever $K_{n\ -\ 1} \leq D_{n\ -\ 1}$ and $K_n > D_n$, a buying signal is generated; whenever $K_{n\ -\ 1} \geq D_{n\ -\ 1}$ and $K_n < D_n$, a selling signal is generated.

62.3 Proposed Investment Strategies

This section proposes three investment strategies. The first strategy (called the *conservative strategy*) simply uses mean–variance model to derive the optimized portfolio, but uses KD index to decide when to buy an asset, as shown below.

1. Solve the mean–variance model to yield the optimized portfolio $\mathbf{w} = (w_1, w_2, \ldots, w_n)$;
2. For each asset i;
3. If KD index shows a buying signal, then buy asset i with wealth w_i;
4. Else invest wealth w_i to risk-free asset.

The second strategy (called the *moderate strategy*) relies on both the mean–variance optimized portfolio and the KD index's buying signal to choose assets for investment, but allocate equaled weight to each chosen asset, as follows:

1. Solve the mean–variance model to yield the optimized portfolio $\mathbf{w} = (w_1, w_2, \ldots, w_n)$;
2. $\mathrm{B} = \phi$;
3. For each asset i satisfying $w_i > 0$;
4. If KD index shows a buying signal, then add i to B;
5. For each asset $i \in \mathrm{B}$;
6. Buy asset i with wealth $1/|\mathrm{B}|$.

The third strategy (called the *aggressive strategy*) simply relies on the KD index's buying signal to choose assets for investment, but allocate equaled weight to each chosen asset, as follows:

1. $\mathrm{B} = \phi$;
2. For each asset i;
3. If KD index shows a buying signal, then add i to B;
4. For each asset $i \in \mathrm{B}$;
5. Buy asset i with wealth $1/|\mathrm{B}|$.

62.4 Experimental Results

The experiment is conducted using a moving window approach. In each window, the last month is used as test data, and the rest as training data. The training data is used both to calculate KD index to generate buying signal, and to construct the mean–variance model to yield the optimized portfolio. The resulting portfolio and the buying signal are then applied to the test data to gather the performance (i.e., return) of each investment strategies.

The experiment uses five assets as recommended in [3]. They are exchange traded funds (ETF): VTI, VEU, BND, VNQ, and DBC. The data spans from May of 2007 to March of 2013. The period from June 2008 to February 2009 is selected for the downtrend period; from February 2009 to December 2009 is for the uptrend period; from January 2010 to March 2013 is for the correction period.

Tables 62.1, 62.2 and 62.3 show the average monthly return during the downtrend, uptrend and correction periods, respectively. During downtrend and correction periods, all three strategies perform better than the mean–variance model. The conservative strategy performs the best and the worst for the downtrend period and the uptrend period, respectively. The aggressive strategy performs the best for the uptrend period, and the moderate strategy performs the best for the correction period.

Table 62.1 Average monthly return during the downtrend period

Strategy	Average monthly return	Standard deviation of monthly return
Conservative	0.0000	0.00018
Moderate	−0.0016	0.00470
Aggressive	−0.0016	0.00470
Mean–variance model	−0.0227	0.07702

Table 62.2 Average monthly return during the uptrend period

Strategy	Average monthly return	Standard deviation of monthly return
Conservative	0.0007	0.00112
Moderate	0.0120	0.03266
Aggressive	0.0284	0.03618
Mean–variance model	0.0022	0.00889

Table 62.3 Average monthly return during the correction period

Strategy	Average monthly return	Standard deviation of monthly return
Conservative	0.0014	0.00362
Moderate	0.0057	0.01306
Aggressive	0.0034	0.01986
Mean–variance model	0.0000	0.01454

62.5 Conclusions

In the literature, mean–variance optimized portfolios have been shown to put excessive weights on assets with large expected returns [4–7]. Instead of simply buying assets according the mean–variance optimized portfolios, this paper proposes the use of KD index to withhold some wealth to risk-free assets (as in the conservative strategy), or to yield an equaled weighted portfolio of selected assets (as in the moderate and aggressive strategies). Compared to the mean–variance model, the three proposed strategies show promising performance in term of monthly return. The mean–variance model only outperforms the conservative strategy during the uptrend period.

Further study with more datasets is needed to strengthen the results of this study. Also, we leave as future study for investigating the possibility of integrating more sophisticate techniques from technical analysis to improve the performance of the proposed strategies.

Acknowledgments This research is supported by the National Science Council under Grants 99-2221-E-155-048-MY3 and 102-2221-E-155-034-MY3.

References

1. Markowitz, H. (1952). Portfolio selection. *The Journal of Finance, 7*, 77–91.
2. Chapados, N. (2011). *Portfolio choice problems: An introductory survey of single and multiperiod models*. New York: Springer.
3. Faber, M. T., & Richardson, E. W. (2009). *The Ivy Portfolio: How to invest like the top endowments and avoid bear markets*. Hoboken, NJ: Wiley.
4. Huang, X. X. (2010). *Portfolio analysis from probabilistic to credibilistic and uncertain approaches*. Berlin: Springer.
5. Best, M. J., & Grauer, R. R. (1991). Sensitivity analysis for mean-variance portfolio problems. *Management Science, 37*(8), 980–989.
6. Green, R. C., & Burton, H. (1992). When will mean-variance efficient portfolios be well diversified? *The Journal of Finance, 47*(5), 1785–1809.
7. Lin, J.-L. (2013). On the diversity constraints for portfolio optimization. *Entropy, 15*(11), 4607–4621.

Chapter 63
Applying Image Processing Technology to Monitor the Disabilities' Security

Yu-Xian Huang and Yi-Nung Chung

Abstract In order to enhance the disabilities' security all alone at home, a way of home care services for detecting the disabilities whether they tumble or not is proposed in this paper. This experiment is mainly applied for detecting the disabilities and avoiding the accidents in daily life all alone. In this paper, the system combines the image tracking technology with the image subtraction of the original background image and the current image which are from camera to identify the moving objects. Then, it make the detecting identification for human body in daily life and mark it as region of interest (ROI) to differentiate from other objects which regard as background or obstacles. Furthermore, it can judge whether the human body lie down or not. Also, it can judge the area where the human bodies lie down is proper or not. The system will give the alarm once it judges the abnormal phenomenon that the human body lies down. According to the consequence of the experiment, this system obtains a satisfactory outcome and accuracy from the algorithm.

Keywords Image tracking · Home care · Region of interest

63.1 Introduction

Lots families make big changes of life style due to the economic and technology, thus, it is an important issue of taking care of the elderly. The average life of human has been increasing by the improvement of technology, on the other hand, more and more people choose to leave hometown and go to other places in order to seek for jobs and opportunities due to the economic downturn, that is, a new

Y.-X. Huang · Y.-N. Chung (✉)
Department of Electrical Engineering, National Changhua University of Education, Changhua 50007, Taiwan, Republic of China
e-mail: ynchung@cc.ncue.edu.tw

J. Juang et al. (eds.), *Proceedings of the 2nd International Conference on Intelligent Technologies and Engineering Systems (ICITES2013)*, Lecture Notes in Electrical Engineering 293,
DOI: 10.1007/978-3-319-04573-3_63,

problem comes out—the elder disabilities may face some difficulties all alone at home because of the degenerative joint disease and slowly reaction, such as the tumble.

However, most families cannot afford the expense of home care services. Moreover, unwilling to accept well care of the professional care institute is the big problem for the elderly above all. Therefore, some unexpected accidents happen while the elderly are alone at home. Without assistance and proper reaction at prime time, some tragedies happen.

For these reasons and circumstances, we conduct experiments for the tumble detection [1] of the elderly in limited range of walking indoors where the home environment we establish in advance just as the following picture one. The following are the description of the action. Under morphological image processing conditions, filtering targets (the figure image of the elderly) we need through the image subtraction and mark the position of the target we seek from ROI [2, 3]. Moreover, it can judge whether tumble or not by comparing the position of the target marked from ROI with figure height ratio. Once the judgment is the state of tumbling, it means the accidents happen, and it needs people to assist or seek for the doctor.

63.2 Image Detection and Tracking

63.2.1 The Image Processing

The continuous original images from camera must go through the steps of image processing to get the available image data then via the system to make the judgments. The image processing takes a lot of time of the CPU's. Thus, using the image pre-processing to delete unnecessary part of image message is an efficient way to save time and get the result.

63.2.2 Image Pre-processing

The way to make RGB color image into the image gray level belongs to the conversion of color space which makes the images from RGB color space into YUV color space or YIQ color space. And Y is the intensity of black to white which is called luminance. If it just retains the luminance Y that it means to make the color image into the image gray level [4].

The system can use image subtraction to remove the background and retain the target on the same background of the images. In this paper, it uses the matrix subtraction of two images and the absolute value which can reflect the difference from two original images. According to the application of image tracking,

Fig. 63.1 The original images

Fig. 63.2 Result of image subtraction

assuming to capture the images is fast enough, in other words, the background of these two continuous images almost unchanged. The original image is shown in Fig. 63.1.

Therefore, the location of the moving objects can be got from the image by using image subtraction [5]. It is worth mentioning that the result of the image subtraction is the union of two images of moving objects not the single object. Moreover, the image from image subtraction will be affected by external force during the shot of two images to cause the noise such as wind, the object vibration of photographic equipment, and etc. The picture is shown in Fig. 63.2. That's why we need to delete the noise.

In some specific range, there is the noise usually caused from the external force. And they can be deleted by the image processing. In the image processing method, the expansion is the algorithm of the binary image which makes the object to enlarge or thicken. Conversely, the erosion is the algorithm of the binary image which makes the object to shrink or thinned. A binary image is controlled by the structure elements of the expansion and the erosion [6] which can effectively remove most of the noise in the picture. But, there are still some of the noise needs to be filtered through a filter. The picture is shown in Fig. 63.3.

Median filtering is a way of nonlinear processing which can effectively reduce the noise of salt and pepper. Simultaneously, it can also maintain the image of

Fig. 63.3 Morphological processing

Fig. 63.4 Image after median filter

cunny operator. The picture is shown in Fig. 63.4. The principle of median filtering is using an n * n mask in every pixel which sorts the pixels of the proximal area, then selects the specified pixel values to replace the pixel values of the proximal area. And it selects the 50th % to be the pixel of the proximal area. In spatial filtering, the usage of low-pass filtering will be limited while there are great difference between the pixel values of the image noise and the pixel values of the proximal area. The mask's sizes of median filtering have 3 * 3, 5 * 5, and 7 * 7, etc. [2]; it can remove the impact of the shadow on the ground.

63.2.3 Moving Figure Detection and Tracking

After removing most of the noise, there will be a lot of types of targets in an image space. In order to avoid affecting the tracking results from non-detection targets, the system need to use ROI to detect the objects and detect the target from the image. Before doing ROI, it will get the edge of image from the canny edge detector, and then remove the irrelevant edge by background subtraction and image pre-processing. Finally, to find out whether there is the appearance of the human body by detecting [7, 8]. The picture is shown in Fig. 63.5, which means the detection of the target.

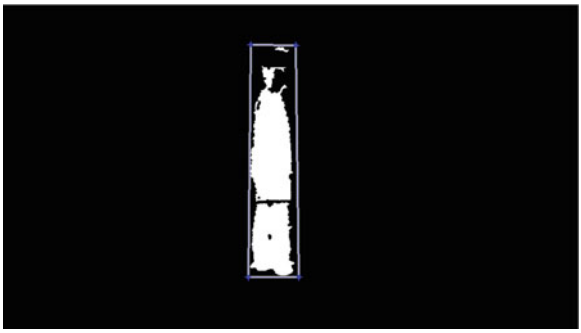

Fig. 63.5 Result of region of interest

ROI is mainly used to locate the searching range of the tracked target. So, the calculation of central point only needs to sum the internal total score of ROI and calculate by sum the pixels from the regional range. The system can locate the regional pixels of the tracked target quickly in the smaller searching range. It will recognize if the human body lies down and predictive calculation.

63.3 The Analysis of the Experimental Result

To reduce the possibility of biased in sampling procedures, the best way of samples is selected independently and randomly which can get the value of the observations. The $\overline{X}$ is the sample mean and the Xi is the pixels in ROI and n is the number of samples. The sample mean is shown in Eq. (63.1). The sample, S^2 means the sample variance. The sample variance is shown in Eq. (63.2). S means sample standard deviation which is the positive square root of sample variance. The sample standard deviation is shown in Eq. (63.3). Dealing with the predictive interval of the future observation values in unknown variance case. The $t_{a/2}$ is to make the right side area for the degree of freedom v = n + 1 of t value [63.5]. The criterion is shown in Eq. (63.4).

$$\overline{X} = \sum_{i=1}^{n} \frac{Xi}{n} \tag{63.1}$$

$$S^2 = \sum_{i=1}^{n} \frac{(Xi - \bar{X})^2}{n-1} \tag{63.2}$$

$$S = \sqrt{\sum_{i=1}^{n} \frac{(Xi - \bar{X})^2}{n-1}} \tag{63.3}$$

Fig. 63.6 The region of interest human lying (ratio 0.1983)

$$\bar{X} - t_{a/2}s\sqrt{1+\frac{1}{n}} < x_0 < \bar{X} + t_{a/2}s\sqrt{1+\frac{1}{n}} \tag{63.4}$$

For example, the experiment is conducted on the walkway where the human bodies stand or lie down. In order to monitor the security of the elderly at home, the system uses the difference locations and angles from the images to recognize if the elderly lie down. We use the location ratio from ROI to recognize if the elderly lie down. It can get the ratio by comparing the height with width from human body. In order to avoid the inaccuracy of the target image from the distance of the figure and the different camera, using the ratio way to recognize is much better. Moreover, the height ratio of human body is different. According to the calculation, the processing image ratio of human standing is about 3.284–3.926. The value is under 0 due to the ratio of the lying human body. And the processing image ratio of human lying is about 0.192–0.315. The picture is shown in Fig. 63.6.

The result is shown in Table 63.1. Although it can recognize from the value if the human body lies down, avoiding the inaccuracy from the system and gives the wrong alarm such as sitting human body or bending human body is necessary. So, the system set the range of the ratio value from images to make the recognition which recognize if the human body stands or lies.

The experiment data is mainly used to analyze the ratio of the target image which is used to determine standing or lying. The picture is shown in Table 63.1. According to the experiment results, it achieves about 91 % average recognition rate.

63.4 Results and Discussion

The research is discussed that the original digital images from camera as well as the technology of the human body detection and the moving target tracking. The experiment analysis is using Matlab 2009a software. Three results are achieved. (1) The original images by the pre-processing of filtering can reduce the impact on the color of the clothes. And it can remove the noise which made from the camera. (2) According to the tracking system, the following procedures such as the analysis

Table 63.1 Experimental data

Number	Type	Image ratio	Fall down?
1	Face to camera	3.288	No
2	Side 45°	3.452	No
3	Side (people face to the right)	3.324	No
4	Side (people face to the left)	3.606	No
5	Side 45°	0.220	Yes
6	Side (people face to the down)	0.231	Yes
7	Side (people face to the up)	0.195	Yes
8	Side (people face to the left)	0.263	Yes
9	Side (people face to the right)	0.307	Yes
10	Side 45°	0.417	Yes
11	Sit	0.417	Other

of image background → image processing of binarization → the continuous image subtraction → morphology processing → Median filtering → object moving are used, it can reach the goal of the human body tracking fast and accurately. (3) The algorithm can accurately recognize if the human body lies down.

Acknowledgments The work was supported by the National Science Council under Grant NSC 101-2221-E-018-031-

References

1. Lou, H., & Jinxiang, C. (2010). Example-based human motion denoising. *IEEE Trans on Visualization and Computer Graphics, 16*(5), 870–879.
2. Hidayatullah, P., & Konik, H. (2011). CAMSHIFT improvement on multi-hue object and multi-object tracking. In *Visual Information Processing (EUVIP), 3rd European Workshop on 2011* (pp 143–148).
3. Lin, H. H., Chiang, W. C., Shu, S. G., Shih, L. M., & Yu, S. S. (2011). The effect of ROI normalization for hand radiographic image segmentation. *International Journal of Innovative Computing, Information and Control, 7*(10), 5669–5688.
4. Chen, K.-Y., Chien, C.-C., Chang, C.-L., & Chang, Y.-P. (2006). A stereo vision system for image tracking using fuzzy logic control. *Journal of Advanced Engineering, 1*(1), 21–29.
5. Yang, H., Kot, A. C., & Jiang, X. (2011). Binarization of low-quality barcode images captured by mobile phones using local window of adaptive location and size. *IEEE Transaction on Image processing, 21*(1), 418–425.
6. Zhang, X., Yang, J., & Tang, Z. (2011). Edge detection using image segmentation and Sobel operators. *ICIC Express Letters, Part B, 2*(4), 809–814.
7. Huang, C.-R., (Julia) Chung, P.-C., Lin, K.-W., & Tseng, S.-C. (2010). Wheelchair detection using cascaded decision tree. *IEEE Transactions on Information Technology in Biomedicine*, *14*(2), 292–300.
8. Hu, Z., & Ding, Y. (2011). Lips detection based on skin model and adaboost algorithm in the human-wheelchair interaction. In *International Conference on Information Technology, Computer Engineering and Management Sciences (ICM)* (Vol. 2, pp. 169–172), Sept 2011.

Chapter 64
System Design and Implementation of the Electrical Power Usage Reminders for Smart Homes

Chien-Yuan Liu, Chih-Feng Huang and Ming-Chang Hsiao

Abstract This article presents a system concerning the electrical power usage reminders for smart homes. The system was designed by famous open source software and was implemented by common electronic components for lowering the cost of the system. ZigBee network is adopted for wireless communication between the devices of the system. The electrical power usage information is captured and derived by a current sensor and a voltage sensor. The information is sent from an acquisition device to multiple reminding devices via ZigBee, is displayed on a LCD, and is mapped onto a vertical LED bar of the reminding indicator. The implementation result shows that the low-cost system would actively assist homeowners to save their power usage.

Keywords Electrical power conservation · LED reminder · ZigBee

64.1 Introduction

In recent years, the shortages of natural resources have been greatly rising up the price of mineral substance and crude oil worldwide [1]. It also increases the expenses of petroleum and electrical consumptions of common families. Moreover, the financial meltdowns of the European Union debts and the home-loan storms in the United States of America have severely depressed the economic growth in the E.U. and the U.S.A. All countries over the world, especially the

C.-Y. Liu (✉) · C.-F. Huang
Department of Computer Science and Information Engineering, Cheng Shiu University, Kaohsiung 83347, Taiwan, Republic of China
e-mail: cyliu@csu.edu.tw

M.-C. Hsiao
Department of Computer Science and Information Engineering, WuFeng University, Chiayi 62153, Taiwan, Republic of China

J. Juang et al. (eds.), *Proceedings of the 2nd International Conference on Intelligent Technologies and Engineering Systems (ICITES2013)*, Lecture Notes in Electrical Engineering 293,
DOI: 10.1007/978-3-319-04573-3_64,

developing nations, are tremendously influenced by the above factors [2]. Thus, the revenue of export and the rate of economic growth are obviously run down [3].

In Taiwan, the annual income of average family is declined rather than going up. In addition, the financial pressure is approaching the suffocating level of common family under the stress of swelled prices of gasoline and electricity. Therefore, the makeshift strategy of the families is to save the expenditure as much as possible to compensate the earnings decline. Preserving the electrical power usage by turn-off the switches at hand is a prevailing slogan, however, is an uneasy rule to follow up. This is because the saving amount is implicit until the receiving of electrical bill bimonthly. Instead of inconveniently checking the figure of the power meter in the yard or at the electrical main distribution panel (MDP) near the main gate, assume that there are several indoor low-cost and convenient-lookup reminders to prompt the users with a simple LED indicator, we believe that there would be more chances for the users to discover their electrical power consumption, hence, hopefully to save their electrical power usage [4].

Consequently, this research conceived to design and to develop the reminder by prevalent microcontrollers and sensors. Furthermore, to untether the installation positional constraint of a traditional electrical power meter, a wireless link would be adopted to communicate between the power sensing modules and the indoor indicators. Multiple reminders could be flexibly placed at the most accessible locations, e.g. on the tea table in living room, on the mid-island cabinet in kitchen, or on the bed aside table, to increase the reminding chance and to decrease the electrical power wastage as much as possible.

64.2 System Design and Implementation

64.2.1 System Hardware

The electrical power usage reminding system is composed of two subsystems. The first subsystem is the electrical power acquisition device which is equipped with one current sensor, one voltage sensor, one LCD, and one ZigBee chip for wireless communication. As formula 64.1, it calculates the electrical real power P usage by the multiplication of the effective values of the sensed load current i_{rms}, the supplied voltage v_{rms}, and cos [5]. The cos is also named as the power factor. Since the indicator is applied for reminding purpose but not for commercial billing, the power factor could be deemed as one for calculating simplification. In order to sense the load current and voltage, the acquisition device is usually installed beside the electrical MDP.

$$P = v_{rms} \times i_{rms} \times \cos\theta \tag{64.1}$$

The block diagram of the electrical power acquisition device is shown in Fig. 64.1. In this diagram, the voltage sensor is consisted of a bridge rectifier and a

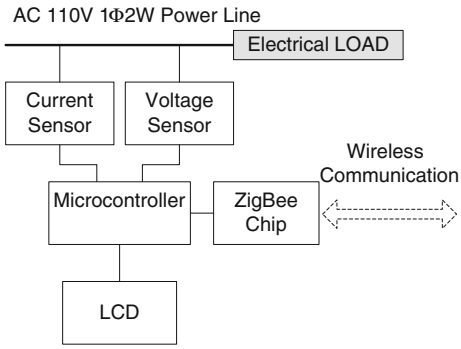

Fig. 64.1 The block diagram of the electrical power acquisition device

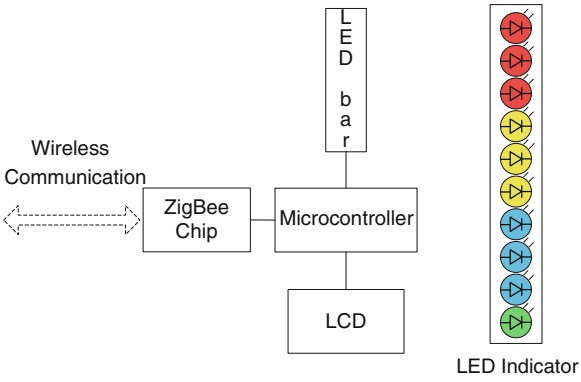

Fig. 64.2 The block diagram of the electrical power usage reminding device

voltage divider and the part no. of the current sensor is ACS758 [6]. It also accumulates the present power usage values into kilowatt per hour (KWH) value for the reference of homeowners. The real time electrical power, load current, voltage, and the KWH of the acquisition device will be sent to the second subsystem as described below.

The second subsystem is the electrical power usage reminding device, which is equipped with one LED indicator, one LCD unit, and one ZigBee chip for wireless communication as shown in Fig. 64.2. On the reminder, the type of microcontrollers of the acquisition device and the reminding device is Atmel ATMEGA 328P. The XBee pro serial 2 chip (Part No. XBP24-CIT-04) is selected as the ZigBee chip. The LCD is a usual text based display unit with two rows and 16 characters per row. The enlarged LED indicator diagram is illustrated on the right side of Fig. 64.2. The power load of a typical home is divided into ten equal levels. Each level is corresponding to a LED. The current of light load to heavy load is mapped from the bottom green LED up to the top red LED.

Through the wireless communication between the ZigBee chip of the reminder and the ZigBee chip of the acquisition device, the reminder could receive the real

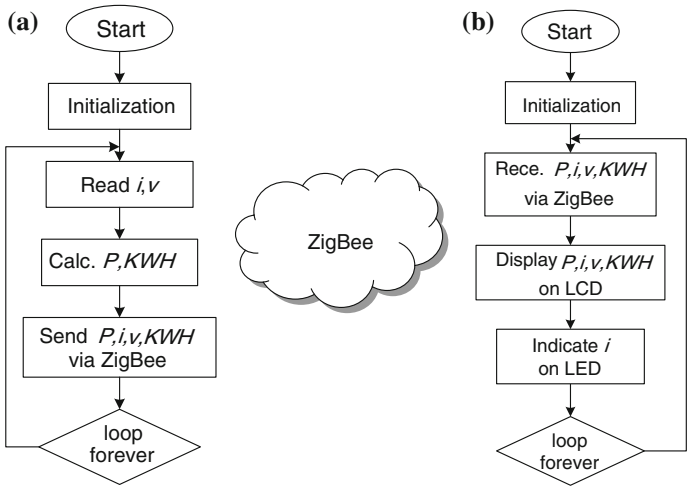

Fig. 64.3 **a** The firmware flowchart of the acquisition device. **b** The firmware flowchart of the reminding device

time electrical power, load current, voltage, and the KWH from the acquisition device. Then, the reminder could show the values on the LCD and would transform the present load current onto the LED indicator for easy reminding.

64.2.2 System Software

The flowcharts of the firmware of the acquisition device and the firmware of the reminding device are depicted in Fig. 64.3a, b respectively. The real time values of current and voltage are read per second by the microcontroller of the acquisition device. Thus, the electrical power for the second is calculated by the multiplication of the current value and the voltage value. Meanwhile, The KWH is accumulated from the calculated power for the second. Then, the present values of the power, current, voltage, and the accumulated KWH are sent to the reminding device through the ZigBee network. The ZigBee link is treated as a serial interface to the microcontroller. The baud rate of it could be set from 9600 to 115200 bps. In this implementation, 9600 bps is enough for sending four values per second.

After receiving the values of present power, current, voltage, and KWH, via the ZigBee network, the reminder would show them on the LCD display and would map the current onto the LED indicator in the manner mentioned in Sect. 64.2.1. Since these values are sent by broadcasting frames, multiple reminders at different rooms would receive the frames according the topological sequence. Table 64.1 shows the algorithm utilized by the firmware in the acquisition device. Note that the maximal values of load current and voltage for each second should be

Table 64.1 The algorithm of the electrical power usage in the acquisition device

Line	Pseudo Statement
1	kwh=0, accp=0 // initial KWH and hourly accumulated pwr
2	loop forever {
3	loop for 60 minutes { // calc. power for the hour
4	loop for 60 seconds { // calc. power for the minute
5	read i_m,v_m per second // stably read max.i & max.v
6	calculate i_{rms}, v_{rms} // i_{rms}= i_m × 0.7071 (so do the v_{rms})
7	calculate p = i_{rms} × v_{rms} // calc. power for the second
8	accp = accp + p // accumulate the power
9	} // end of minute
10	} // end of hour
11	kwh = kwh + (accp/K) // K constant = 1/(3600×1000)
12	accp=0 // reset accp // K would normalize accp to KWH
13	}

extracted from the reading values and should be changed to effective values for real power calculation.

The Arduino IDE (integrated development environment) is chosen for developing the firmware of the system. The Arduino is an open source project [7] and is really prevalent in recent years. It contains an IDE, the c-code compiler, the bootstrap loader for microcontroller, the USB-interface firmware burner, common libraries for various sensors, actuators, and communication interfaces, etc. With the assist of the Arduino IDE, the development task for the electrical power usage reminder is quite productive.

64.3 Results and Discussions

The result of implemented system composes of one electrical power usage acquisition device as shown in Fig. 64.4a and one electrical power usage reminding device as shown in Fig. 64.4b. The hardware schematics are designed according the block diagram in Sect. 64.2.1. The layout of schematic is drawn by the Fritzing, which is an open source electronic design automation (EDA) software for schematic PCB design. The output file format of the Fritzing layout includes PDF and Gerber for PCB production. The bill of material (BOM) could be generated by the Fritzing too. With the hardcopy schematic layout, the target PCB was fabricated in accordance with the standard PCB manufacturing process.

In this implementation, there are only one acquisition device and one reminder. For practical smart home applications [8], however, additional acquisition devices could be installed for each heavy load electrical appliances in order to monitoring

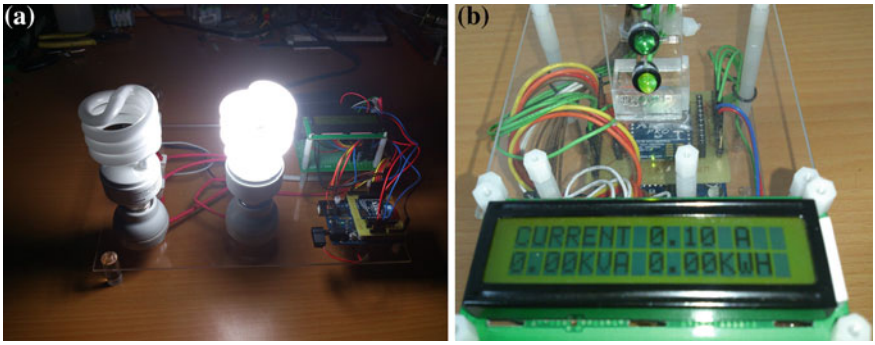

Fig. 64.4 **a** The implemented electrical power usage acquisition device. **b** The implemented electrical power usage reminding device

their usage situations. Furthermore, additional reminders could also be deployed to helping homeowners to further manage their electrical power usage [9–11].

The frequency of the ZigBee transmissions is set to one time per second. This period is examined by common homeowners for comfortable inspection. For saving power consideration, it could be prolonged to extend the battery operation lifetime of the reminding devices. As shown in Fig. 64.4, when the load is changed by turned on different number of lamps, the LED indicator exhibits varying height of lighted LED.

64.4 Conclusions

The power conservation and the automation of electrical home appliances are important applications for smart homes. In this research, an electrical power usage reminding system is proposed and designed. The system is implemented by popular microcontroller, current sensor, voltage sensor, ZigBee wireless network, LCD module, and LED indicating bar, etc. The low cost devices of the system are pretty practical for promoting the saving power actions of homeowners. In future, the control capability could be enhanced to the system to assist direct saving power actions executed by the homeowners.

Acknowledgments The authors greatly appreciate to the support of the National Science Council, R.O.C., under the Grant no. NSC 101-2632-E-230-001-NY3 and NSC 101-2514-S-821-001.

References

1. Sterner, T., & Coria, J. (2011). *Policy instruments for environmental and natural resource management*. Washington DC: Resources for the Future Press.
2. Grick, R., & Spiegel, M. M. (2009) *Asia and the global final crisis*. Paper presented at Asia Economic Policy Conference, Federal Reserve Bank of San Francisco, California.
3. Bai, L. (2012). *Effects of global financial crisis on Chinese export: A gravity model study*. Denmark: Jonkoping University Press.
4. Pihala, H. (1998). *Non-intrusive appliance load monitoring system based on a modern kWh-meter*. Finland: Valtion Teknillinen Tutkimuskeskus.
5. Robbins, A. H., Miller, W. C. (2012) *Circuit analysis: Theory and practice* (5th Edition). Delmar: Cengage Learning.
6. http://www.digikey.com/
7. http://www.arduino.cc/
8. Han, D. M., & Lim, J. H. (2010). Design and implementation of smart home energy management systems based on zigbee. *The IEEE Transactions on Consumer Electronics, 56*(3), 1417–1425.
9. Jahn, M., et al (2010) The energy aware smart home. In *Proceedings of the IEEE 5th International Conference on Future Information Technology, 21-23 May*, Busan, Korea.
10. Vázquez, F. I., & Kastner, W. (2012). Thermal comfort support application for smart home control. *Ambient Intelligence-Software and Applications Advances in Intelligent and Soft Computing, 153*, 109–118.
11. Tariq, M., et al. (2012) Smart grid standards for home and building automation. In *Proceedings of the IEEE International Conference on Power System Technology (POWERCON), Oct 30–Nov 2*, Auckland, New Zealand.

Chapter 65
The Carpets with Indication Function

Hsieh-Ping Chen

Abstract A very common thing can turn into something very special with a few changes. Carpets are quite common. But this invention is quite different. It can guide people through complicated buildings. Have you ever been to a mall such gigantic that you it would take a whole week just to visit all the floors? It is very easy to get lost. This carpet can solve the problem. When someone steps on the first LED bar on the carpet, it would send a signal to the second one, lighting it up, then to the third one, and so on. This can also guide people through dark rooms without turning on the lights. The device is very thin so the bump is less likely to trip people. The lines can be guided to a central control box. The main switches would be in there. All you have to do is sort the lines and plug it in. Installation is pretty easy.

Keywords LED · Carpet

65.1 Introduction

Most of nursing homes for old people have rooms that have many beds for many old people. When people want to go the bathroom, they would not turn on the lights to not wake the others. It is pretty inconvenient.

A survey points out, a subway station in Stockholm, Sweden with colorful stairs can encourage people to take the stairs instead of the escalators or elevators. Experiments confirm that 66 percent of people wouldn't take the escalator just because there are piano colored stairs.

H.-P. Chen (✉)
Department of Electrical Engineering, Cheng Shiu University,
Kaohsiung 83347, Taiwan, Republic of China
e-mail: k0304@gcloud.csu.edu.tw

J. Juang et al. (eds.), *Proceedings of the 2nd International Conference on Intelligent Technologies and Engineering Systems (ICITES2013)*, Lecture Notes in Electrical Engineering 293,
DOI: 10.1007/978-3-319-04573-3_65,

The same thing applies to this invention. When people see the special LED [1–3] carpet, they would want to try it out. Wouldn't everybody? People would think walking or climbing the stairs is pretty interesting, not tiring.

During the night, you don't have to turn on the night to get someplace else. One of the reasons this carpet is made is because of this. In nursing homes, the LED bars are instantly activated when somebody steps on the floor. It can also guide anybody from the toilet back to the bed.

This device can be also used for other purposes. It can guide people to their rooms in a hotel, or lead people through certain public facilities. The sensors can be easily moved. There are also different modes, automatic and manual. People can manually activated, or automatically. The two main functions of this invention is to guide people and provide light [4–6].

65.2 Design Concept

Other from providing light, this invention can guide people. The first prototypes don't have the carpet on, just like the pictures below. During the night, people don't have to turn on the lights to get somewhere. When you step on to the carpet, the sensors will sense it and activate the first LED bar, then the second, and so on. People can follow the light to certain places, such as the toilet. It can guide people back the same way, as shown in Fig. 65.1.

People don't have to turn on the lights with this carpet. The LED light on the carpet turns on instantly when people step on it, guiding people to the destination. This is solar powered, as shown in Fig. 65.2. The light bars are very thin, and are installed on the carpet. The wires are pretty simple, and are put under the carpet all going to a control box. The sensors are thin and light, and can be placed on the entrances and exits under the carpet. When somebody steps on it, the sensors will activate the lights. The solar panels and the control box can be placed anywhere.

To guide pedestrians, the sensors are put on the end of walkways, as shown in Fig. 65.3. This device can stretch as long as the environment needs.

If pedestrians finished using the telephone booth in the hotel and wants to go to the bathroom, all they have to do is step on the icon with WC on it. The lights will light up in order, guiding them to the bathroom; if they want to go to the lobby, they can just step on the light, and same with the rooms, as shown in Fig. 65.4.

65.3 Product Benefits and Usage

The carpets, lights, and light bars are together. The sensors are put in the entrance or the exit, in the carpet. The light bars are on the carpet, and the wires can be sorted. There is a thin control box under the carpet, which provides electricity, so the way to power it up is to plug it. Installation is very easy.

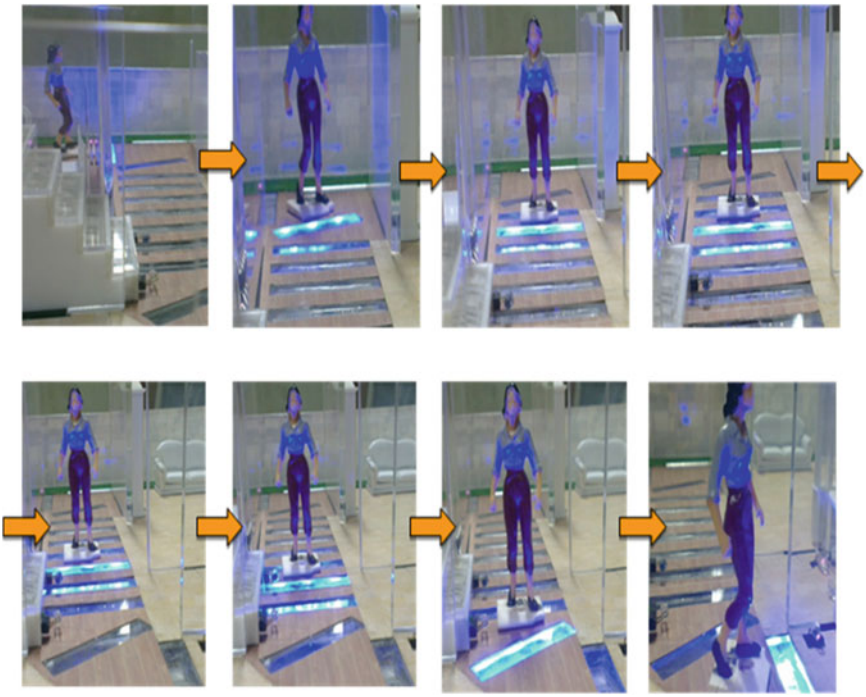

Fig. 65.1 LED light bar process

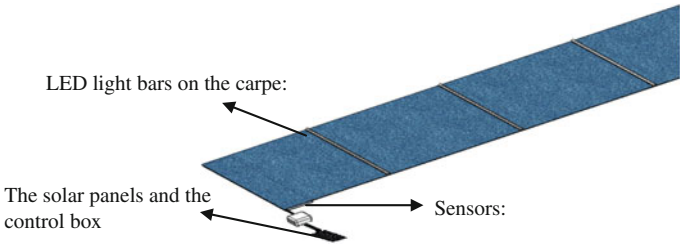

Fig. 65.2 Functions on the carpet

This carpet can be used in many places like

1. Nursing Homes: Most nursing homes have a big room with plenty of space for many old people. Some of them may want to go to the bathroom during the night. They do not wish to wake the others up, so they walk in the dark. It is very inconvenient for them. This guiding carpet can solve this problem.
2. Hotels: Using the carpet on the floor as a guide, you can go anywhere you like. It can help the customers find what they want to find without asking the hotel staff.

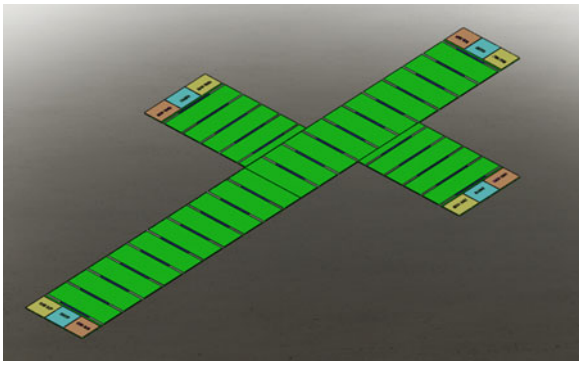

Fig. 65.3 Carpet design

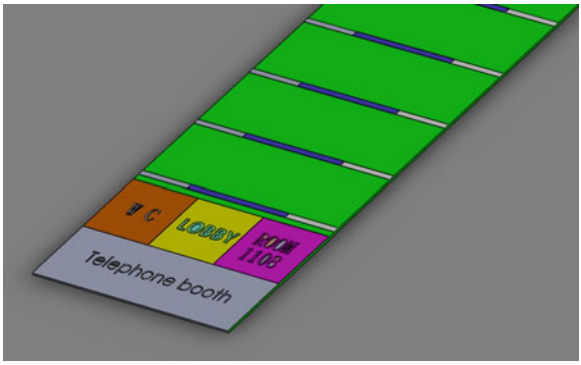

Fig. 65.4 Carpet entrance design

3. Welcoming: It can be used as a "red carpet." After using it, all you have to do is roll it up.
4. Public facilities and guiding: This can also be used on public facilities. It can guide people to certain places.
5. Hospitals: The personnel can use it to send the patients to the right rooms during emergencies.
6. Outdoor stages: The wire goes under the carpet, so people won't trip. During the day, it can charge using solar energy.

65.4 Conclusions

It is unnecessary to switch the power by hand. The LED light bar embedded in the carpet is automatic. It is very convenient for anybody walking on the carpet. The carpet can also guide people through dark rooms without turning on the lights.

References

1. Tseng, C.-K., Lee, M.-C. M., Hung, H.-W., Huang, J.-R., Lee, K.-Y., Shieh, J.-M., et al. (2012). Silicon-nanocrystal resonant-cavity light emitting devices for color tailoring. *Journal of Applied Physics, 111*, 074512.
2. Chen, C.-C., Y.-H., Lin, Shih, M. H., Lin, G.-R., & Kao H.-C., (2011). Light enhancement of silicon-nanocrystal-embedded SiOx film on silicon-on-insulator substrate. *Japanese Journal of Applied Physics, 50*(4), 04DJ09–04DJ09.
3. Tsai, M.-A., Yu, P.-c., Chao, C. L., Chiu, C. H., Kuo, H. C., Lin, S. H., et al. (2009). Efficiency enhancement and beam shaping of GaN–InGaN vertical-injection light-emitting diodes via high-aspect-ratio nanorod arrays. *IEEE Photonics Technology Letters, 21*(4), 257–259.
4. Lee, J.-H., Huang, J. J., Liao, C.-C., Hu, P.-J., & Chang, Y. (2005). Operation lifetimes of organic light-emitting devices with different layer structures. *Chemical Physics Letters, 402*, 335–339.
5. Lin, H.-Y., Ho, Y.-H., Lee, J.-H., Chen, K.-Y., Fang, J.-H., Hsu, S.-C., et al. (2008). Patterned microlens array for efficiency improvement of small-pixelated organic light-emitting devices. *Optics Express, 16*, 11044–11051.
6. Lin, H.-Y., Lee, J.-H., Wei, M.-K., Dai, C.-L., Wu, C.-F., Ho, Y.-H., et al. (2007). Improvement of outcoupling efficiency of an organic light-emitting device by attaching microstructured film. *Optics Communications, 275*, 464–469.

Chapter 66
A Study of Breaker Characteristics for Progressive Gravity Waves on Gentle Sloping Bottoms

Wen-Jer Tseng

Abstract This paper studies the periodic gravity surface waves propagating on non-steep sloping bottom in two-dimension. A new mathematical derivation is developed to describe the periodic gravity surface waves propagating on sloping bottoms. In the Eulerian system, the velocity potential is obtained as a function of the wave steepness ε and the bottom slope α to the second order. Then, the wave profile and the breaker characteristics are found by transforming the flow field into a Lagrangian system. According to the solution coupled with the wave breaker criteria, the wave deformation and the continuous wave breaking processes for the progressive water waves propagating on a sloping bottom can be derived. Furthermore, by comparing the theoretical values of wave asymmetry with the experimental study of other scholars, it is found that theoretical results of the present solution has similar tendency with the experimental data of other scholars.

Keywords Eulerian system · Velocity potential · Lagrangian system · Breaker

66.1 Introduction

In the process of wave propagation from deep to shallow, wave deformation in shoaling water appears when the depth is shorter than half a wave length. As a result of the phenomenon that the steepening of wave crests in shallow water, the wave profile gradually becomes asymmetric, unstable, and meanwhile, wave will slow down, wave length will shorten, wave height and its steepness will increase and wave will finally breaks, which do much damage to the coast structure, like breakwater.

W.-J. Tseng (✉)
Department of Civil Engineering and Geomatics, Cheng Shiu University, Kaohsiung 83347, Taiwan, Republic of China
e-mail: jwj@csu.edu.tw

J. Juang et al. (eds.), *Proceedings of the 2nd International Conference on Intelligent Technologies and Engineering Systems (ICITES2013)*, Lecture Notes in Electrical Engineering 293,
DOI: 10.1007/978-3-319-04573-3_66,

Most investigators have discussed and inducted formulas from experimental studies. For example, Tang [1] has proposed empirical formulas for the breaking wave height as a function of deep wave height, wave steepness, and bottom slope in accordance with experiments or reliable field data. Gotoh et al. [2] studied the characteristics of breaking wave by means of numerical simulation and Tsai et al. [3] took experimental data to examine some empirical formulas of breaking wave.

A theoretical analysis of a surface-wave propagating on a gently sloping bottom has been given in Biesel [4] based on a small amplitude assumption, but the wave breaking and the nonlinear effects are not treated in his research. Furthermore, how the formula was derived is not explained in detail. Extensions of Biesel's theory is available in Chen and Tang [5] and Hsu et al. [6], but the explicit analytic solution for breaking waves on a gently sloping bottom is still not yet perfect. In this paper, the analytical solution for velocity potential function is derived to the second order of perturbation in the Eulerian system, then the wave profile and breaking wave are found by using a transformation in the Lagrangian system.

66.2 Formulation of the Problem

For describing the surface-wave propagation on a small, uniformly slope bottom, the Cartesian rectangular coordinate axis OX and OY are used in two dimensions as shown in Fig. 66.1. The axis OX is located at mean water level, with positive in direction of wave propagation and OY is directed vertically upwards.

In order to obtain the equations of irrotational motion of an incompressible fluid, it is sufficient to find a velocity potential function $\phi\,(x, y, t)$, from which the particle velocity components are deduced by $u = \partial\phi/\partial x$ and $v = \partial\phi/\partial y$.

This function $\phi\,(x, y, t)$ is harmonic with respect to x and y, such that:

$$\nabla^2\phi = \frac{\partial^2\phi}{\partial x^2} + \frac{\partial^2\phi}{\partial y^2} = 0. \tag{66.1}$$

The wave motion has to satisfy a number of boundary conditions at the bottom and on the free water surface:

1. On an immovable and impermeable sloping plane with an inclination $\alpha\,(0 \le \alpha < 1)$ to the horizon, represented by $f(x, y) = y + h = y - \alpha x = 0,\ x \le 0$, the no-flux bottom boundary condition gives

$$\nabla\phi \cdot \nabla f/|\nabla f| = \left(\phi_y - \alpha\phi_x\right)\Big/\sqrt{1+\alpha^2} = 0 \quad \text{at} \quad y = -h. \tag{66.2}$$

2. The kinematic and dynamic free surface boundary conditions are respectively

$$\phi_y = d\eta/dt\ ;\ \phi_t + g\eta + \frac{1}{2}\nabla(\nabla\phi)^2 = 0\ ;\text{at} \quad y = \eta. \tag{66.3}$$

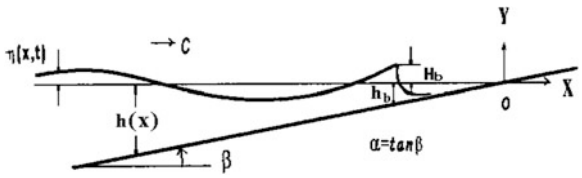

Fig. 66.1 Sketch definition for surface-wave propagation on a gentle slope bottom. Among $\eta(x,t)$: water surface elevation; $h(x)$: water depth; H_b, h_b: breaking height, breaking depth; c: wave celerity; wave steepness $\varepsilon = H_o/L_o$

Eliminating the free surface displacement η, can obtain an equation for $\phi(x, y, t)$ alone in the following form:

$$\phi_{tt} + g\phi_y + \left[(\nabla\phi)^2\right]_t + \nabla\phi \cdot \nabla(\nabla\phi)^2 \Big/ 2 = 0 \quad \text{at} \quad y = \eta. \tag{66.4}$$

This combined condition will replace the kinetic free surface boundary condition in the following.

3. A time-averaged mass flux conservation condition is required: The water mass bounded by the shoreline of the sloping bottom rushes up and down the beach face and the total mass does not change. Therefore, at any cross section where x = constant, the time-averaged mass flux should vanish. This condition gives

$$y\text{-direction}: \frac{1}{T}\int_0^T \int_{-h}^{\eta} \phi_y \, dydt = \overline{\int_{-h}^{\eta} \phi_y \, dy} = \overline{(\phi)_{y=\eta}} - \overline{(\phi)_{y=-h}} = 0, \tag{66.5}$$

$$\begin{aligned} x\text{-direction}: & \frac{1}{T}\int_0^T \int_{-h}^{\eta} \phi_x \, dydt - \frac{U(\alpha)}{T}\int_0^T \int_{-h_0}^{\eta^c} \phi_x^c \, dydt \\ & = \overline{\int_{-h}^{\eta} u \, dy} - U(\alpha)\overline{\int_{-h_0}^{\eta^c} u^c \, dy} = 0; \; U(\alpha) = \begin{cases} 0, & \alpha \neq 0 \\ 1, & \alpha = 0 \end{cases}. \end{aligned} \tag{66.6}$$

Both the superscript c and the subscript 0 express the physical quantity at infinite depth. Because of the nonlinear effect, waves over constant depth induce a net flux of water. Thus, a deep-water streaming term is introduced in Eq. (66.6) which is adjusted by a unit function $U(\alpha)$ to ensure that it can be reduced to the deep-water condition when the bottom slope is equal to zero. Only in the condition of a small bottom slope (α), the solutions for Eqs. (66.1)–(66.6) can be derived and checked in Sect. 66.3.

66.3 Theoretical Analysis

First, use Eqs. (66.1)–(66.6), on a small bottom slope and assume that the relevant physical quantities can be expanded as a double power series of the nonlinear ordering parameter ε and the bottom slope α. Thus, the velocity potential ϕ, the free-surface displacement η, the wave number k and the angular frequency σ can be obtained as

$$\begin{aligned}\phi &= \sum_{m=1}^{\infty}\sum_{n=0}^{\infty}\varepsilon^m\alpha^n\left(\phi'_{m,n}+\phi_{m,n}\right)\\ &= \sum_{m=1}^{\infty}\sum_{n=0}^{\infty}\varepsilon^m\alpha^n\left\{\phi'_{m,n}(t,\sigma_0,a_0)+\sum_{i=0}^{m}A_{m,n,i}(\lambda h,\lambda y,\lambda;\sigma_0,a_0)\right.\\ &\qquad\left.\times F_{m,n,i}(S)E_{pm}(\lambda h,\lambda;\alpha)+\int_{x_0}^{x}M_{m,n,0}(\lambda h,\lambda;\sigma_0,a_0)dx'\right\},\end{aligned} \tag{66.7}$$

$$\eta=\sum_{m=1}^{\infty}\sum_{n=0}^{\infty}\varepsilon^m\alpha^n\eta_{m,n}(\lambda h,\ S;\ \lambda_0,\ a_0)=\sum_{m=1}^{\infty}\sum_{n=0}^{\infty}\sum_{i=0}^{m}\varepsilon^m\alpha^n\eta_{m,n,\,i}(\lambda h,\ S;\ \lambda_0,\ a_0), \tag{66.8}$$

$$k=\sum_{r=0}^{\infty}\sum_{l=0}^{\infty}\varepsilon^r\alpha^l k_{r,l}\left(k_{0,0},\ k_{0,0}h;\ \lambda_0\ a_0\right), \tag{66.9}$$

$$\sigma=\sum_{\beta=0}^{\infty}\varepsilon^\beta\sigma_\beta(\lambda_0,\ a_0)=constant. \tag{66.10}$$

where S is the phase function $\left(S=\int_{x_0}^{x}k\,dx'-\sigma t\right)$; $\lambda=k_{0,0}.k_0=\lambda_0=2\pi/L_0$; $E_{pm}(\lambda h,\lambda,\alpha)=\exp\left[m\sum_{j=2}^{\infty}\alpha^j\int_{x_0}^{x}e_j(\lambda h,\lambda)\,dx'\right]=E_{pm}$. x_0 notes the x value at infinite depth, ε a small nonlinear ordering parameter characterizing the wave steepness, e_j the wave amplitude influence factor, $M_{m,n,0}$ the return flow and $k_{0,0}$ has been replaced by λ for simplicity. Note that the bottom slope α is assumed to be small, thus the q-th differentiations of $k_{r,l}$, e_j, $A_{m,n,i}$ and $M_{m,\,n,\,0}$ with respect to x are of order α^q:

$$\left(\frac{d^qk_{r,l}}{dx^q},\frac{d^qe_j}{dx^q},\frac{\partial^qA_{m,n,i}}{\partial x^q},\frac{d^qM_{m,n,0}}{dx^q}\right)=O(\alpha^q). \tag{66.11}$$

Upon substituting Eqs. (66.7)–(66.11) into the governing equations and the boundary conditions Eqs. (66.1)–(66.6), using the Taylor series expansion of functions at $y=0$ instead of $y=\eta$, and collecting terms of the same ε and α orders yield the necessary equations to each order of approximation. Then different

orders of $\varepsilon(m)$, $\alpha(n)$ and harmonic (i) may be separated, yielding a set of partial differential equations for each index (m,n,i). The boundary-value problems can be solved sequentially for each order of m, n, and i. The solution will be given in the following statements, where the notations below will be used for convenience:

$$\cosh = \mathrm{ch},\ \sinh = \mathrm{sh},\ \tanh = \mathrm{th};\ I = \coth \lambda h. \tag{66.12}$$

The solutions are solved and presented as follow:

For $O(\varepsilon^1\alpha^1)$, the solution for velocity potential function ϕ and the corresponding free-surface displacement η can be obtained from the boundary-value problem obtained from the terms of the corresponding orders. The results are

$$\phi = \left[\left(A_{1,0,1}\right)\sin S + \left(\alpha A_{1,1,1}\right)\cos S\right], \tag{66.13}$$

$$\eta = \left[\left(\alpha a_{1,1,1}\right)\sin S + (a)\cos S\right], \tag{66.14}$$

$$\sigma = \sigma_0 = k\ c\ ;\ \sigma^2 = gk\ \cdot\ \tanh kh = gk\ \cdot\ \mathrm{th}kh\ ;\ k = k_0, \tag{66.15}$$

where

$$A_{1,0,1} = \frac{ag}{\sigma_0}\frac{ch\lambda(h+y)}{ch\lambda h}; a_{1,1,1} = a\left(\frac{\lambda^2 h^2}{Dsh2\lambda h} - \lambda h + \frac{I^2}{D^2}\lambda h\right),$$

$$A_{1,1,1} = \frac{ag}{\sigma_0}\left\{\left[-\frac{\lambda^2(h+y)^2}{Dsh2\lambda h} + \lambda(h+y)\right]\frac{ch\lambda(h+y)}{ch\lambda h} - \frac{\lambda(h+y)}{D^2 th\lambda h}\frac{sh\lambda(h+y)}{ch\lambda h}\right\},$$

$$a = a_0\Big/\sqrt{Dth\lambda h}; D = 1 + 2\lambda h/sh2\lambda h. \tag{66.16}$$

Among $\sigma = \sigma_0 = 2\pi/T$: angular frequency; a_0: wave amplitude of deep water.

66.4 Study of Breaking Wave

66.4.1 Wave Deformation

For a constant depth, it is very advantageous to utilize the Lagrangian coordinate system to express the results of third order theory; a wave motion that is very similar to reality that is thereby obtain, and the existence of limiting value of wave camber is immediately evident. Contrarily, the theories expressed in Eulerian coordinate system with no limiting camber. It is reasonable to expect that the Lagrange coordinate system will also be advantageous for wave in water with a gentle sloping bottom.

Thus, transfer the equations to the Lagrangian system. Then the fluid particle in the initial average position (*x*,*y*) and the displacement components X and Y are derived and presented as follow:

$$u = \partial\phi/\partial x + \left(\int^t u dt\right)\frac{\partial u}{\partial x} + \left(\int^t v dt\right)\frac{\partial u}{\partial y} = \sigma_0 a\left\{\left[(\alpha C_1)\frac{\cosh\lambda(h+y)}{\sinh} + (\alpha S_1)\right.\right.$$
$$\left.\left.\times\frac{\sinh\lambda(h+y)}{\sinh\lambda h}\right]\sin S + \left[\frac{\cosh\lambda(h+y)}{\sinh\lambda h}\right]\cos S\right\} = u_1\sin S + u_2\cos S, \tag{66.17}$$

$$v = \partial\phi/\partial y + \left(\int^t u dt\right)\frac{\partial v}{\partial x} + \left(\int^t v dt\right)\frac{\partial v}{\partial y} = \sigma_0 a\left\{\left[\frac{sh\lambda(h+y)}{sh\lambda h}\right]\sin S\right.$$
$$\left.+\left[-(\alpha C_1)\frac{sh\lambda(h+y)}{sh\lambda h} - (\alpha S_1)\frac{ch\lambda(h+y)}{sh\lambda h}\right]\cos S\right\} = v_1\sin S + v_2\cos S, \tag{66.18}$$

where

$$u_1 = \sigma_0 a\left[(\alpha C_1)\frac{ch\lambda(h+y)}{sh\lambda h} + (\alpha S_1)\frac{sh\lambda(h+y)}{sh\lambda h}\right];\ u_2 = \sigma_0 a\left[\frac{ch\lambda(h+y)}{sh\lambda h}\right],$$

$$v_1 = \sigma_0 a\left[\frac{sh\lambda(h+y)}{sh}\right];\ v_2 = \sigma_0 a\left[-(_1)\frac{sh\lambda(h+y)}{sh} - (\alpha S_1)\frac{ch\lambda(h+y)}{sh\lambda h}\right].$$

The displacement components *X* and *Y* can be written as

$$X = \int^t u dt$$
$$= a\left\{\left[(-1)\frac{\mathrm{ch}\lambda(h+y)}{\mathrm{sh}\lambda h}\right]\sin S + \left[(\alpha C_1)\frac{\mathrm{ch}\lambda(h+y)}{\mathrm{sh}\lambda h} + (\alpha S_1)\frac{\mathrm{sh}\lambda(h+y)}{\mathrm{sh}\lambda h}\right]\cos S\right\}, \tag{66.19}$$

$$Y = \int^t v dt$$
$$= a\left\{\left(\alpha C_1\frac{\mathrm{sh}\lambda(h+y)}{\mathrm{sh}\lambda h} + \alpha S_1\frac{\mathrm{ch}\lambda(h+y)}{\mathrm{sh}\lambda h}\right)\sin S + \left[\frac{\mathrm{sh}\lambda(h+y)}{\mathrm{sh}\lambda h}\right]\cos S\right\}, \tag{66.20}$$

where $C_1 = \frac{\lambda^2(h+y)^2}{D\mathrm{sh}\,2\lambda h} - \lambda(h+y) + \frac{1}{D^2\mathrm{th}\lambda h}$; $S_1 = \frac{2(D+\mathrm{ch}^2\lambda h)}{D^2\mathrm{sh}2\lambda h}\lambda(h+y) - 1$.

By applying Eqs. (66.17–66.20) and $y = 0$, can get

$$(u)_0 = (u_1)_0\sin S + (u_2)_0\cos S, \tag{66.21}$$

$$(v)_0 = (v_1)_0\sin S + (v_2)_0\cos S. \tag{66.22}$$

Among $(u_1)_0 = \sigma_0 a\,[(\alpha C_{10})\coth\lambda h + (\alpha S_{10})]$; $(u_2)_0 = \sigma_0 a\,[\coth\lambda h]$; $(v_1)_0 = \sigma_0 a$; $(v_2)_0 = \sigma_0 a\,[(-\alpha C_{10}) - (\alpha S_{10})\coth\lambda h]$,

$$\xi = x + (X)_{y=0} = x + a\{[(-1)\coth\lambda h]\sin S + [(\alpha S_{10}) + (\alpha C_{10})\coth\lambda h]\cos S\}, \tag{66.23}$$

$$\varsigma = (Y)_{y=0} = a\{[(\alpha C_{10}) + (\alpha S_{10})\coth\lambda h]\sin S + \cos S\}, \tag{66.24}$$

where $C_{10} = \frac{\lambda^2 h^2}{D\mathrm{sh}2\lambda h} - \lambda h + \frac{1}{D^2\mathrm{th}\lambda h}$; $S_{10} = \frac{2(D+\mathrm{ch}^2\lambda h)}{D^2\mathrm{sh}2\lambda h}\lambda h - 1$, $(\xi,\ \varsigma)$ is the coordinate of the fluid particle on the free-surface.

66.4.2 Kinematic Stability Parameter and Wave Breaking

Why does the breaking wave happen? In briefly, because the water depth changes, the breaking wave happens on the process of wave moving from deep to shallow and the results of shoaling, refraction and friction, etc. That will make wave velocity reduced, which result in the phenomenon—the fluid particle velocity of wave crest is faster than celerity, and then the breaking wave happens.

By $\partial(u)_0/\partial t = 0$, can obtain

$$\tan S = (u_1)_0/(u_2)_0 = \tan\theta_b \ \ or \ \ S = \tan^{-1}[(u_1)_0/(u_2)_0] = \theta_b, \tag{66.25}$$

and

$$(u_b)_0 = \sqrt{(u_1)_0^2 + (u_2)_0^2} \tag{66.26}$$

$(ub)_0$: the fluid particle horizontal velocity of breaking wave on the surface.

By Eq. (66.16), can rewrite "a" and "D" as:

$$a_b = \frac{a_0}{(D_b\tanh k_b h_b)^{1/2}};\ D_b = \left(1 + \frac{2k_b h_b}{\sinh 2k_b h_b}\right). \tag{66.27}$$

Through Eq. (66.15), when the surface-waves propagation on the gentle slope bottom to breaking point, and then

$$\sigma^2 = gk_b\tanh k_b h_b\ ;\ \sigma = k_b c_b\ ;\ L_b = \frac{2\pi}{k_b}\ ;\ k_b = (k_0)_b, \tag{66.28}$$

where $\sigma = 2\pi/T$: angular frequency; k_b: the wave number of breaking wave; c_b: the celerity of breaking wave; h_b: the breaking depth; L_b: the breaking length.

In order to describe the breaking wave mechanism, the kinematic stability parameter (KSP) is applied and the breaking criteria is simply

$$KSP = (u_b)_0/c_b = 1. \tag{66.29}$$

Equation (66.29) is used as the qualification for how the breaking wave happens.

Using the viewpoint of the Eq. (66.29), this paper solves the characteristics of breaking waves on the gentle sloping bottom. Methods are stated as the following:

Substituting Eqs. (66.26)–(66.29) into Eq. (66.30), can obtain

$$k_b a_b \left\{ [\alpha C_{10b} \coth k_b h_b + \alpha S_{10b}]^2 + [(\coth k_b h_b)]^2 \right\}^{1/2} = 1, \tag{66.30}$$

where C_{10b}, S_{10b} and k_b are exact C_{10}, S_{10} and k with the substitution $a = a_b$, $D = D_b$, $k = k_b$ and $h = h_b$, where the subscript 0 represents the free surface.

By Eqs. (66.25), (66.28) and (66.30), can solve h_b, k_b and θ_b. By means of Eq. (66.24), can obtain the maximum surface elevation $\varsigma_{\max}$, which appears when a wave breaks

$$\varsigma_{\max} = a_b \{ (\alpha C_{10b} + \alpha S_{10b} \coth k_{0b} h_b) \sin \theta_b + \cos \theta_b \}. \tag{66.31}$$

By Eq. (66.24) and the variance of phase, can solve the minimum elevation of breaker depth $\varsigma_{\min}$ and the breaking height H_b is derived as

$$H_b = (\varsigma_{\max} - \varsigma_{\min}). \tag{66.32}$$

Among H_b: breaking height; θ_b: phase angle of the breaking wave.

66.4.3 Results and Discussion

Whether breaking wave happens or not is influenced by the factors, such as wave steepness, wave height, and bottom etc. The breaking phenomenon is so complicated that most of the previous studies gave breaker characteristics only based on experimental studies, empirical, or semi-empirical formulas calibrated from laboratory data. However, the present study is the only research that gives theoretical characteristics for breaking waves. In Fig. 66.2, the relative breaker height H_b/H_0 is given for different incident wave steepness H_0/L_0 with α = 1/50, 1/80, 1/110 and 1/600. And then based on the results of Tang (1966) [1], the semi-empirical formula is plotted in Fig. 66.3 to compare with the present theory.

Where H_0, L_0, T: the incident wave height, length and period of deep water.

The above associated figures show that the analytical solution in this paper has similar tendency with the results of other scholars. So the results of this paper can express the characteristics about the breaking phenomenon on practical gentle slope bottom.

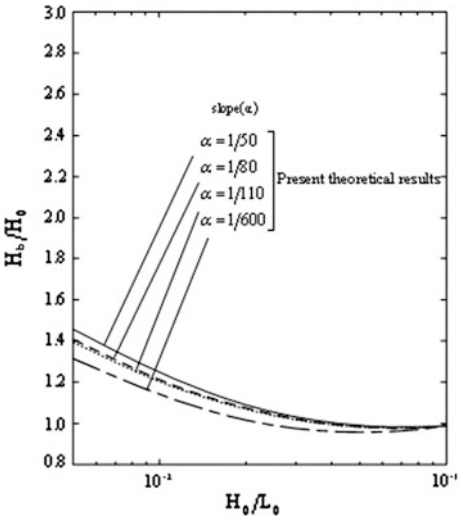

Fig. 66.2 Relationship between H_b/H_0 and H_0/L_0

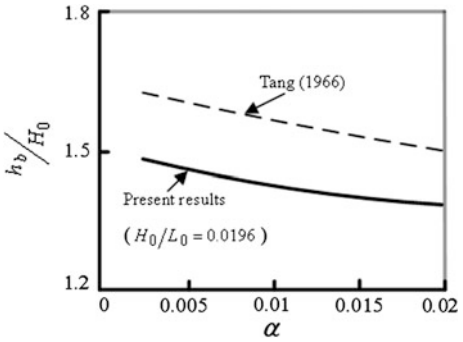

Fig. 66.3 Relationship between h_b/H_0 and α for $H_0/L_0 = 0.0196$

66.5 Conclusion

This paper provides an analytic solution for breaking waves on a gentle slope, which the writers believe was not treated appropriately in previous studies. The velocity potential was developed in explicit form as a function of the bottom slope α and the wave steepness ε in an Eulerian system. Then, after transferring to a Lagrangian system, these explicit expressions enable a proper description for wave shoaling and wave breaking. However, the bottom friction, the reflect waves and wave set-down are neglected in this theoretical study. For clearly describing the fact about the wave breaking, an extended study on the basis of this study is needed. The bottom friction, the reflect waves and wave set-down should be taken into consideration, and furthermore, higher order expansion is required. Nevertheless, what I obtained in this paper can be applied for future study.

References

1. Tang, L.W. (1966). Coastal engineering researches on the western coast of Taiwan. In *Proceedings 10th Conference on coastal Engineering, Tokyo, Japan*.
2. Gotoh, H., & Sakai, T. (1999). Lagrangian simulation of breaking waves using particle method. *Coastal Engineering Journal, 41*(3–4), 303–326.
3. Tsai, C. P., Chen, H. B., Hwung, H. H., & Huang, M. J. (2005). Examination of empirical formulas for wave shoaling and breaking on steep slopes. *Ocean Engineering, 32*(4), 469–483.
4. Biesel, F. (1952). Study of propagation in water of gradually varying depth. In *Gravity waves* (pp. 43–253). U.S.: U.S. National Bureau of Standards (NBS circular 521).
5. Chen, Y. Y., & Tang, L. W. (1992). Surface-wave propagation on gentle sloping bottom. In *Proceedings of the 14th Ocean Engineering Conference in Taiwan* (pp. 1–22).
6. Hsu, H. C., Chen, Y. Y., Hwung, H. H. (2001). Surface wave propagation on a gentle sloping bottom. In *Proceedings of the 23rd Ocean Engineering Conference in Taiwan* (pp. 33–40).

Chapter 67
Investigation of Breaking Criteria on a Mild Sloping Bottom in Lagrangian System

Wen-Jer Tseng

Abstract During moving from deep to shallow, wave in shoaling water will deform when the depth is shorter than half a wave length, then even break. There is a new asymptotic solution describes water wave propagation on the surface of a mild sloping bottom which derived in the Lagrangian system. By the perturbation method to develop a new mathematical derivation, and Lagrangian velocity potential is derived as the functions of the bottom slope α to first order. And then can find the wave profile and the breaker characteristics. In Lagrangian form, the analytical solution satisfies the zero pressure at the free surface. Combined the solution and the kinematic stability parameter (*KSP*), can derive the wave deformation, the continuous wave breaking processes and the criteria of breaking wave. The Lagrangian solution not only can describe the features of the wave which shoaling from deep water to shallow water, but also the processes of successive deformation of a wave profile and the wave breaking which leaded by water particle trajectories. The theoretical results and experimental data have well uniformity.

Keywords Mild sloping · Lagrangian system · Perturbation · Velocity potential

67.1 Introduction

In the process of wave propagation from deep to shallow, the motion of a fluid particle within a propagating surface wave may be described by either the trajectory of a particle that is carried along with the flow or observing the fluid velocity at a fixed position. These alternative descriptions are called Lagrangian

W.-J. Tseng (✉)
Department of Civil Engineering and Geomatics, Cheng Shiu University, 83347 Kaohsiung, Taiwan, Republic of China
e-mail: jwj@csu.edu.tw

J. Juang et al. (eds.), *Proceedings of the 2nd International Conference on Intelligent Technologies and Engineering Systems (ICITES2013)*, Lecture Notes in Electrical Engineering 293,
DOI: 10.1007/978-3-319-04573-3_67,

and Eulerian approach, respectively. In the Lagrangian approach, however, the surface elevation is specified through the position of a surface particle, unlike an Eulerian surface, which is given as an implicit function. It is also well known that the Eulerian description for a free surface can always be expressed in Taylor series at a fixed water level, which implicitly assumes that the surface profile is a differentiable single-valued function. Hence, many researchers [1–3] paid attention solving the wave transformation on sloping bottoms in the Eulerian system. However, since the sloping bottom was approximated by a large number of steps, the effect of the bottom could not be fully exhibited and the wave breaking profile still can not be evidently described by the Eulerian coordinate.

The first water wave theory in Lagrangian coordinates was obtained by Gerstner [4] who assumed the flow possesses finite vorticity. To date, only a limited few analytic solutions are derived for wave transformation on a slope beach in Lagrangian coordinates [5–7]. Some investigators have discussed and inducted formulas from experimental studies. For example, [8–10] took experimental data to examine some empirical formulas of breaking wave.

This paper is to develop a rational and explicit analytical solution for surface waves propagating over a sloping bottom in Lagrangian description. And then the wave profile and the breaker characteristics are found by Lagrangian system.

67.2 Mathematical Formulation of the Problem

Considering a two-dimensional monochromatic wave propagating on a gentle slope, the Cartesian rectangular coordinate axis OX and OY are used in two dimensions as shown in Fig. 67.1. The negative x-axis (OX) is outward to the sea from the mean water level, while the positive y-axis (OY) taken vertically upward.

where $\eta(x, t)$ is the water surface elevation, $h(x)$ is water depth, α is bottom slope, is breaking wave height, and h_b is breaking depth.

The fluid motion in the Lagrangian representation is described by tracing an individual fluid particle. For two-dimensional flow, a fluid particle is distinguished by the horizontal and vertical parameters (x_0, y_0) known as Lagrangian labels. Then fluid motion is described by a set of trajectories $x(x_0, y_0, t)$ and $y(x_0, y_0, t)$, where x and y are in Cartesian coordinates. The dependent variables x and y indicate the position of any particle at time t and are function of the independent variables x_0, y_0 and t. The governing equations and boundary conditions can be derived to the n-th order of bottom slope α for two-dimensional incompressible, inviscid and irrotational free-surface flow are summarized as below:

The governing equations and boundary conditions as follow:

(1). Continuity equation under conservation of mass

$$\frac{\partial(x, y)}{\partial(x_0, y_0)} = x_{x_0} y_{y_0} - x_{y_0} y_{x_0} = 1, \tag{67.1}$$

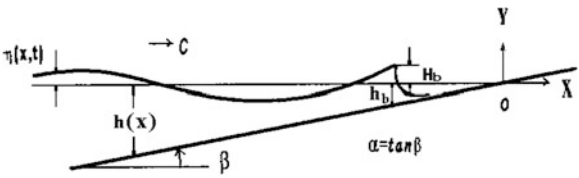

Fig. 67.1 Definition sketch for surface-wave propagation on a gentle slope bottom

or

$$x_{x_0t}y_{y_0} - x_{y_0t}y_{x_0} + x_{x_0}y_{y_0t} - x_{y_0}y_{x_0t} = \frac{\partial(x_t, y)}{\partial(x_0, y_0)} + \frac{\partial(x, y_t)}{\partial(x_0, y_0)} = 0. \tag{67.2}$$

(2). Energy equation under conservation of energy

$$\frac{P}{\rho} = -\frac{\partial\phi}{\partial t} - gy + \frac{1}{2}\left(x_t^2 + y_t^2\right). \tag{67.3}$$

(3). Irrotational condition

$$x_{x_0t}x_{y_0} - x_{y_0t}x_{x_0} + y_{x_0t}y_{y_0} - y_{y_0t}y_{x_0} = \frac{\partial(x_t, x)}{\partial(x_0, y_0)} + \frac{\partial(y_t, y)}{\partial(x_0, y_0)} = 0, \tag{67.4}$$

$$\frac{\partial\phi}{\partial x_0} = x_t x_{x_0} + y_t y_{x_0}, \frac{\partial\phi}{\partial y_0} = x_t x_{y_0} + y_t y_{y_0}. \tag{67.5}$$

The wave motion has to satisfy a number of boundary conditions at the bottom and on the free water surface as follow:

(1). On an immovable and impermeable sloping plane with an inclination to the horizon, the no-flux bottom boundary condition gives

$$y_t - \alpha x_t = 0, \quad y = y_0 = -h. \tag{67.6}$$

(2). The dynamic free surface boundary conditions are respectively

$$P = 0, y_0 = 0. \tag{67.7}$$

In Eqs. (67.1–67.7), subscripts x_0, y_0, and t denote k partial differentiation with respect to the specified variable, $P(x_0, y_0, t)$ is water pressure, $\phi(x_0, y_0, t)$ a velocity potential function in Lagrangian system. The fundamental physical relationships defining the equations above have been derived previously.

67.3 Asymptotic Solutions Analysis

To solve Eqs. (67.1–67.7), it is assumed that relevant physical quantities can be expanded in terms of the bottom slope α. Thus, the particle displacements x and y, the potential function ϕ, pressure P, wave number k and Lagrangian wave frequency σ can be obtained as below:

$$\begin{aligned} x &= x_0 + \sum_{n=0}^{\infty} \alpha^n X_n(x_0, y_0, t) \\ &= x_0 + [A(x_0)\cosh k_0(y_0 + h) + \sum_{n=1}^{\infty} \alpha^n A_n(x_0, y_0)]\, e^{i(\int k dx_0 - \sigma t)} \;\; ; \;\; i = \sqrt{-1}, \end{aligned} \tag{67.8}$$

$$\begin{aligned} y &= y_0 + \sum_{n=0}^{\infty} \alpha^n Y_n(x_0, y_0, t) \\ &= y_0 + [B(x_0)\sinh k_0(y_0 + h) + \sum_{n=1}^{\infty} \alpha^n B_n(x_0, y_0)]\, e^{i(\int k dx_0 - \sigma t)}, \end{aligned} \tag{67.9}$$

$$\phi = \sum_{n=0}^{\infty} \alpha^n \Phi_n(x_0, y_0, t) = \left[f(x_0, y_0) + \sum_{n=1}^{\infty} \alpha^n f_n(x_0, y_0) \right] e^{i(\int k dx_0 - \sigma t)}, \tag{67.10}$$

$$P = P_0(x_0, y_0, t) + \sum_{n=1}^{\infty} \alpha^n P_n(x_0, y_0, t), \tag{67.11}$$

$$k = k_0(x_0) + \sum_{n=1}^{\infty} \alpha^n k_n(x_0) \tag{67.12}$$

where $X_n(x_0, y_0, t)$ and $Y_n(x_0, y_0, t)$ are the particle displacements and the Lagrangian variable (x_0, y_0) of the n-th order. $\sigma(=2\pi/T)$ is the angular frequency of the particle motion or the Lagrangian angular frequency for a particle reappearing at the same elevation and T is the period of particle motion. For a relatively gentle bottom slope α, it may be assumed that the j-th differentiation of A_m, A, B_m, B, f_n, f, P_n, P_0, k_n and k_0 with respect to x_0 are in the order of $\alpha^j (j \in N)$.

Substituting Eqs. (67.8–67.12) into Eqs. (67.1–67.7), can get the necessary equations of approximation. Then, can obtain the $a_0\alpha$ order solution as below:

$$\theta = \int k dx_0 - \sigma t, \tag{67.13}$$

$$\mathrm{Re}[x(x_0, y_0, t)] = x_0 - B\cosh k_0(y_0 + h) \cdot \sin\theta + \alpha A_1 \cos\theta, \tag{67.14}$$

$$\mathrm{Re}[y(x_0, y_0, t)] = y_0 + B\sinh k_0(y_0 + h) \cdot \cos\theta + i\alpha B_1 \sin\theta, \tag{67.15}$$

$$\mathrm{Re}[\phi] = \frac{\sigma}{k_0} B \cosh k_0(y_0 + h) \cdot \sin\theta + \alpha f_1 \cos\theta, \tag{67.16}$$

$$\mathrm{Re}\left[P/\rho\right] = -g y_0 - gB(\ \sinh k_0 y_0 / \cosh k_0 h\ ) \cos\theta + \alpha \mathrm{Re}\left[P_1/\rho\right]. \tag{67.17}$$

The detail had been referred in [5].

67.4 Wave Deformation and Breaker Wave

67.4.1 Wave Deformation

The surface profile of a gravity wave is not prescribed in the Eulerian description, which is derived from the solution restricted to single valued functions of the spatial position. Besides, the dynamic boundary condition at the free surface can only be satisfied in an approximate manner. This assumption limits the applicability of Eulerian description to a near-breaking condition. When a wave getting shallow, the particle motion has to be transformed from the Eulerian to Lagrangian descriptions to imitate the asymmetric waveform [1, 2]. However, the free surface is directly represented by an explicit parametric function of the particles in the Lagrangian description, and it has more flexibility to describe the actual wave shape and kinematics above the mean water level. Furthermore, the Lagrangian solution can satisfy the dynamic boundary and find out the zero pressure condition at the free surface motion. Hence, when the height of a wave reaches its limit, the crest is also developed as a summit which can be calculated as the spatial surface profile by the Lagrangian coordinates system. So the water particle $x(x_0, y_0, t)$ and $y(x_0, y_0, t)$, which are new displacement components, to the first order approximation can be obtained from Eqs. (67.14) and (67.15). And then the free-surface displacements are evaluated by substituting $y_0 = 0$ into the previous equations and the results are

$$\begin{aligned}\xi(x_0, 0, t) = x_0 - (B\cosh k_o h)\sin\theta + \alpha B\big\{&[k_0^2 h^2/(D \times \sinh 2k_0 h) - k_0 h + 1/(D^2 \tanh k_0 h)] \\ &\times \cosh k_0 h + [k_0 h/(D^2 \tanh k_0 h) + 2k_0 h/(D \sinh 2k_0 h) - 1]\sinh k_0 h\big\}\cos\theta,\end{aligned} \tag{67.18}$$

$$\begin{aligned}\zeta(x_0, 0, t) = B\sinh k_o h \cos\theta + \alpha B\{\ &[k_0^2 h^2/(D \sinh 2k_0 h) - k_0 h + 1/(D^2 \tanh k_0 h)] \\ &\times \sinh k_0 h + [k_0 h/(D^2 \tanh k_0 h) + 2k_0 h/(D \sinh 2k_0 h) - 1]\cosh k_0 h\}\sin\theta\end{aligned} \tag{67.19}$$

(ξ, ζ) is the position of fluid particle on the free-surface.

67.4.2 Breaker Wave

Because of the change of water depth, the wave shoals and is refracted in the propagation process from deep water to shallow water. The celerity is reduced; hence, the particle velocity of the wave crest is faster than the celerity and the wave breaks. In order to describe the breaking wave mechanism, the kinematic stability parameter (*KSP*) is applied and the breaking criteria is simply

$$KSP = u_m / u_m c.c = 1 \tag{67.20}$$

where c is celerity and u_m is the horizontal maximum velocity of the particle at the wave crest.

The Lagrangian velocities u and v evaluated at (x_0, y_0) can be simplified to

$$u = \frac{\partial x(x_0, y_0, t)}{\partial t} = (u_1)\cos\theta + (u_2)\sin\theta, \tag{67.21}$$

$$v = \frac{\partial y(x_0, y_0, t)}{\partial t} = (v_1)\sin\theta + (v_2)\cos\theta \tag{67.22}$$

And then the Lagrangian velocities evaluated at $y_0 = 0$ can be simplified to

$$(u)_0 = (u_1)_0 \cos\theta + (u_2)_0 \sin\theta, \tag{67.23}$$

$$(v)_0 = (v_1)_0 \sin\theta + (v_2)_0 \cos\theta. \tag{67.24}$$

where $(u_1)_0$, $(u_2)_0$, $(v_2)_0$ and $(v_2)_0$ are exact u_1, (u_2), (v_1) and (v_2) given with the substitution $y_0 = 0$, where the subscript 0 represents the free surface.Then, the Eq. (67.23) can be rewritten in the more specific form

$$(u)_0 = \sqrt{(u_1)_0^2 + (u_2)_0^2}\cos(\theta - \theta_m)\ ;\ \theta_m = \tan^{-1}\frac{(u_2)_0}{(u_1)_0}. \tag{67.25}$$

By means of Eq. (67.25), to command $\theta = \theta_m = \theta_b$ and $h = h_b$ that can get the resulting Lagrangian maximum horizontal velocity of the breaking point at the wave crest on the free surface ($y_0 = 0$), is denoted as $(u_b)_0$:

$$(u_b)_0 = \sqrt{(u_1)_0^2 + (u_2)_0^2} = u_m\ ; \quad \theta_b = \tan^{-1}\frac{(u_2)_0}{(u_1)_0}. \tag{67.26}$$

where the subscripts b express the physical quantity breaking point and h_b are breaking depth. Hence, D, B, σ, L, c *and* k can be rewritten as D_b, B_b, σ_b, L_b, c_b *and* k_b.

$$\sigma^2 = g k_{0b} \tanh k_{0b} h_b; \quad \sigma = k_b c_b; \quad L_b = 2\pi / k_b. \tag{67.27}$$

Thus, the breaking criterion can be rewritten in the more specific form

$$KSP = (u_b)_0 / c_b \tag{67.28}$$

This criterion, after substituting the previous Lagrangian velocity, becomes

$$(k_b)\left\{(B_b\cosh k_{0b}h_b)^2+\alpha^2B_b^2\left[\left(\frac{k_{0b}^2h_b^2}{D_b\sinh 2k_{0b}h_b}-k_{0b}h_b+\frac{1}{D_b^2\tanh k_{0b}h_b}\right)\right.\right.$$
$$\left.\left.\times\cosh k_{0b}h_b+\left(\frac{k_{0b}h_b}{D_b^2\tanh k_{0b}h_b}+\frac{2k_{0b}h_b}{D_b\sinh 2k_{0b}h_b}-1\right)\sinh k_{0b}h_b\right]^2\right\}^{1/2}=1\ . \tag{67.29}$$

By means of Eq. (67.26), Eq. (67.27) and Eq. (67.29), can solve h_b, k_b and θ_b. And then the maximum surface elevation $\zeta_{\max}$, which appears when a wave breaks

$$\zeta_{\max}=B_b\sinh k_{0b}h_b\cos\theta_b+\alpha B_b\{[k_{0b}^2h_b^2/(D_b\sinh 2k_{0b}h_b)-k_{0b}h_b+1/(D_b^20bh_b)]$$
$$\times\sinh k_{0b}h_b+[k_{0b}h_b/(D_b^2\tanh k_{0b}h_b)+2k_{0b}h_b/(D_b\sinh 2k_{0b}h_b)-1]\cosh k_{0b}h_b\}\sin\theta_b. \tag{67.30}$$

In the same way, the minimum elevation $\zeta_{\min}$ can be obtained also and the breaker height H_b is derived as

$$H_b=(\zeta_{\max}-\zeta_{\min}). \tag{67.31}$$

67.5 Results Analysis and Discussion

The breaker characteristics depend on the bottom slope, wave steepness and wave height etc. The breaking phenomenon is so complicated that most of the previous studies gave breaker characteristics only use experimental studies, empirical, or semi-empirical formulas measured from laboratory data. However, the present study is the only research that gives theoretical characteristics for breaking waves. In Fig. 67.2, the relative breaker depth h_b/H_0 of the theoretical analysis is given for different incident wave steepness H_0/L_0 with $\alpha = 1/20$, 1/80, 1/110 and 1/600. And then based on the results of [9], the experimental result is plotted in Fig. 67.3 to compare with the present theory.

Where H_0, a_0 , L_0 , T: the incident wave height, amplitude, length and period of deep water; H_b, h_b: breaking height, breaking depth; α: the bottom slope. The above associated figures show that the analytical solution in this paper has similar tendency with the results of other scholar. So the results of this paper can express the characteristics about the breaking phenomenon on practical gentle slope bottom.

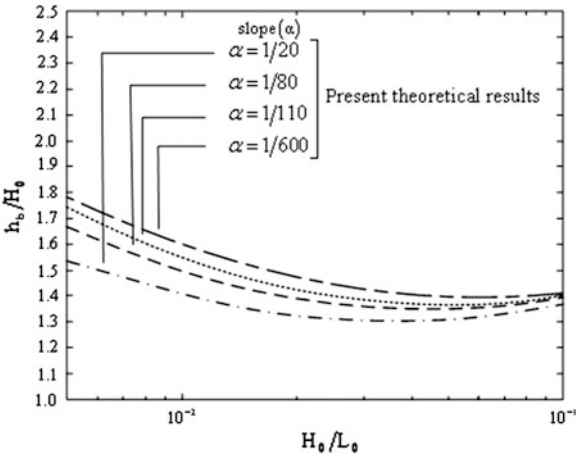

Fig. 67.2 Relationship between the relative breaker depth h_b/H_0 and the incident wave steepness H_0/L_0 for $\alpha = 1/20, 1/80, 1/110, 1/600$

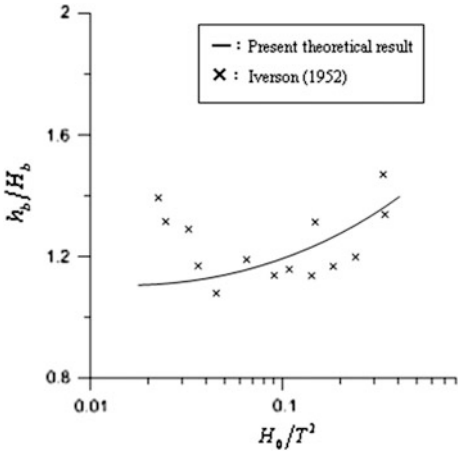

Fig. 67.3 Relationship between h_b/H_b and H_0/T^2 ($\alpha = 1/150$)

67.6 Conclusion

This paper provides an analytic solution for breaking waves on a gentle slope, which the writer believe was not treated appropriately in previous studies. The velocity potential was developed in explicit form as a function of the bottom slope α in a Lagrangian system. However, the bottom friction, the reflect waves and wave set-down are neglected in this theoretical study. For clearly describing the fact about the wave breaking, an extended study on the basis of this study is needed. The bottom friction, the reflect waves and wave set-down should be taken into consideration, and furthermore, higher order expansion is required. Nevertheless, what I obtained in this paper can be applied for future study.

References

1. Biesel, F. (1952). *Study of propagation in water of gradually varying depth*. U.S. National Bureau of Standards, Gravity Waves NBS Circular 521 243–253.
2. Chen, Y. Y., Hsu, H. C., Chen, G. Y., & Hwung, H. H. (2006). Theoretical Analysis for Surface Waves Propagation on Sloping Bottoms, Part 2. *Wave Motion, 43*, 339–356.
3. Hsu, H. C., Chen, Y. Y., & Hwung, H. H. (2001). Surface wave propagation on a gentle sloping bottom. *Proceeding of the 23rd Ocean Engineering Conf. in Taiwan Republic of China*, (pp. 33–40).
4. Gerstner, F. J. (1802). Theorie de wellen. In *Abh. d. K. bohm. Ges. Wiss*. Reprinted in *Ann der Physik* 32, pp. 412–440.
5. Chen, Y. Y., & Huang, C. Y. (2000). Surface-wave propagation on a gentle bottom with Lagrangian Form. In *Proceeding of the 22th Ocean Engineering Conference*, *Taiwan Republic of China* (pp. 79–88).
6. Chen, Y. Y., Yang, B. D., Hsu, H. C., Li, M. S., & Yang, K. S. (2010). Lagrangian nonlinear progressive water waves on sloping bottoms. In *Proceedings of the Twentieth International Offshore and Polar Engineering Conference Beijing*, June 20–26, 2010 Vol. 3, (pp. 806–814).
7. Li, M. S., Chen, Y. Y., Hsu, H. C., & Torres-Freyermuth, A. (2013). Experimental and Lagrangian modeling of nonlinear water waves propagation on a sloping bottom. *Ocean Engineering, 64*, 36–48.
8. Tang, L. W. (1966). Coastal engineering researches on the western coast of Taiwan Republic of China*: Proceeding 10th conference on coastal engineering*.
9. Iverson, H. W. (1952). Waves and breakers in shoaling water. In *Proceeding 3rd Conference, on Coastal Engineering,* (pp. 1–12) ASCE.
10. Tsai, C. P., Chen, H. B., Hwung, H. H., & Huang, M. J. (2005). Examination of empirical formulas for wave shoaling and breaking on steep slopes. *Ocean Engineering, 32*(4), 469–483.

Chapter 68
A Three-Phase Grid-Connected PV Generation System with a Constant Voltage Based Maximum Power Point Tracking

Shun Lee

Abstract This paper utilizes the characteristic that the maximum power point (MPP) voltage of a solar panel can be regarded as an approximate constant value, and applies the linear relationship between the MPP voltage and the open-circuit voltage for photovoltaic (PV) modules to assist the maximum power point tracking (MPPT) in a three-phase grid-connected PV generation system. A simple technique to identify the range of approximate MPP voltages and then to determine a constant MPP voltage is suggested to do a constant voltage based control on the PV panels for the MPPT in the paper. Some experimental tests are also conducted and discussed.

Keywords Three-phase · Grid-connected · PV · MPPT · Constant voltage based

68.1 Introduction

The main types for applying solar energy to generate electricity are the photoelectric conversion type and the type with thermal-electric conversion. The first is chosen to study in this paper. Tracking the maximum power point (MPP) for solar cells (modules or panels) is required for enhancing the overall efficiency of solar power generation systems. In the past, the perturbation and observation method [1] was a popular approach to do the maximum power point tracking (MPPT) for a solar panel. This method needed to consider how much control effort taken to perturb the controlled systems, and required the observing time to wait for the system responses falling into a next steady-state point after a control action induced. In addition, this tracking approach possessed larger deviations around the

S. Lee (✉)
Department of Electrical Engineering, Cheng Shiu University, Kaohsiung 83347, Taiwan, Republic of China
e-mail: shunlee@csu.edu.tw

J. Juang et al. (eds.), *Proceedings of the 2nd International Conference on Intelligent Technologies and Engineering Systems (ICITES2013)*, Lecture Notes in Electrical Engineering 293,
DOI: 10.1007/978-3-319-04573-3_68,

MPP. Therefore, driving a solar panel encountering a disturbance entered the MPP state with a small deviation around the MPP in a short time became a hard work, and it was a weakness for this MPPT approach. Consequentially, the incremental conductance (INC) methods [2] for MPPT operations were proposed. Although the INC approach can get a nearer MPP for solar modules, the observing time was still a weak spot for this approach. Masoum et al. [3] used the linear relationship between the MPP voltage and the open-loop voltage to track the MPP for a solar module. These authors completed the sampling operation on the open-circuit voltage of a solar panel through a transient interruption between the solar panels and loads, but it therefore caused a non-continuous operation for PV generation systems and complicated the control system. Authors in [4] also presented a tracking approach for a solar array. The terminal voltage of a diode injected a constant current and mounted on the back of a solar array was taken as a reference of the open-circuit voltage of a solar array. Since diode characteristics and its surrounding environment were different from the ones of solar arrays, the measured values on the diode were not a precise reaction for the open-circuit voltage of a solar array.

The utilization of solar powers, generally, can be divided into stand-alone systems [5] and grid-connected systems [6]. Stand-alone systems typically require the use of batteries, diesel generators and other auxiliary power to reduce instability and intermittent characteristics, and therefore are cost less economical. Consequentially, the grid-connected generation systems currently are more widely utilized, and will be investigated in this study.

Following the more installation of the single-phase grid-connected PV generation systems, it is foreseeable that the unbalance situation on the three-phase utility power systems will be gradually serious in the future. The installation of three-phase grid-connected PV generation systems with a MPPT function therefore become quite importances for maintaining a good power quality in utility power systems. In this paper, a three-phase grid-connected PV generation systems with a constant voltage based maximum power point tracking will be constructed and tested. The results from experimental tests will be also observed and discussed to provide more knowledges about the application of grid-connected PV generation systems and to benefit utility power systems.

68.2 P–V Characteristics of a Photovoltaic Module

The P–V curve of a photovoltaic module (called a solar panel) is depicted in Fig. 68.1.

The voltage generating a maximum power point (MPP) is denoted V_{max}. In general, the decision, how to control the appearance of the MPP of a solar panel, can be made by detecting the operating voltage of a photovoltaic module. When the solar panel operates at the right side of the MPP in Fig. 68.1, it implies that the panel has the ability to bear more loading; otherwise the solar module needs to

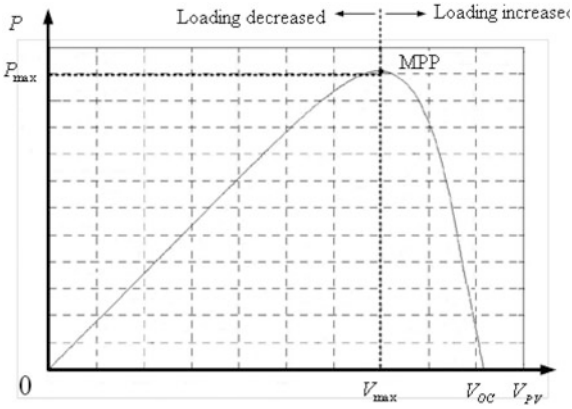

Fig. 68.1 The P–V curve of a photovoltaic module

decrease its loading. If the panel works at the voltage V_{max}, it means that the photovoltaic module reaches to the MPP and generates maximum output powers.

Under different sunlight conditions by day, the variation among the MPP voltages of a solar panel is generally a little, so the MPP voltage can be regarded as a constant value. In addition, the solar module also exist the linear relationship between the MPP voltage V_{max} and the open-circuit voltage V_{oc} [3]. Hence, these properties will be adopted in this paper to control the maximum power outputs generated from solar panels in a three-phase grid-connected photovoltaic (PV) generation system.

68.3 System Configurations and Controls

A three-phase grid-connected PV generation system with a control frame is shown in Fig. 68.2. In order to simplify the control of a three-phase grid-connected PV generation system, a coordinate transformation method is adopted in the paper.

As to the control of three-phase inverters in Fig. 68.2, the line to line voltages v_{ab}, v_{bc}, v_{ca} are firstly detected, and through a sensing gain k_v and a block with functions transferring three-phase coordinate quantities (line to line voltages) to two-phase coordinate quantities, the two-phase coordinate quantities v_d, v_q are obtained. The d, q axis voltages v_d, v_q are sent to a sine/cosine function generator to get unit sine and unit cosine signals. The d, q-axis reference currents i_d^*, i_q^* of the line currents i_a, i_b, i_c injected into the utility power system are therefore generated after unit sine and unit cosine signals multiplying, respectively, a current command $I_{COM}^{`}$. The currents i_a, i_b, i_c are sensed, and through a sensing gain k_s and a block with functions transferring three-phase coordinate quantities to two-phase coordinate quantities, the two-phase coordinate quantities i_d, i_q of the i_a, i_b, i_c are therefore achieved. The i_d, i_q currents compare with the reference currents i_d^*, i_q^* in a current controller with a proportional gain k_P, and then this controller determines

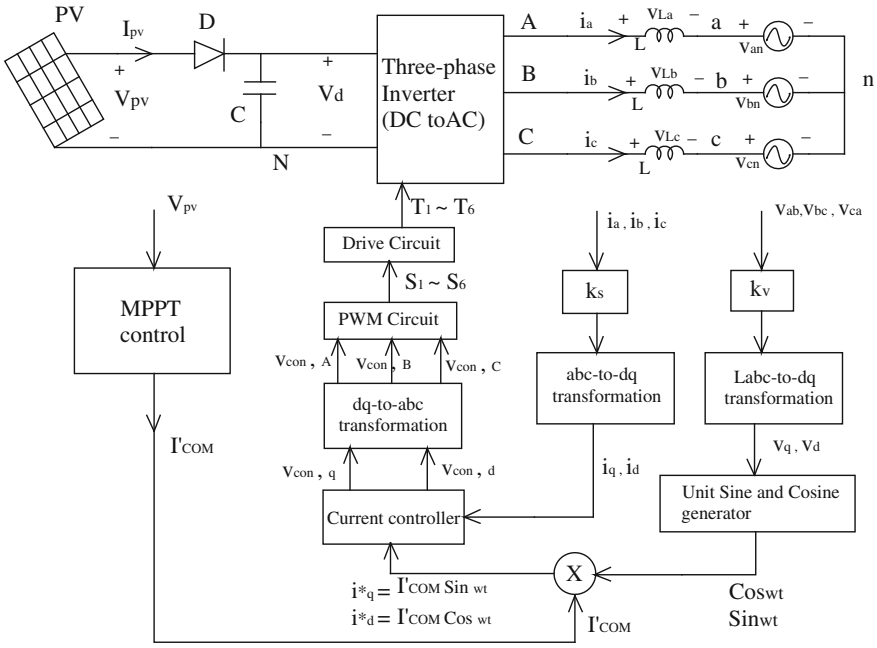

Fig. 68.2 A three-phase grid-connected PV generation system with a control frame

the d, q axis components $v_{con,d}$, $v_{con,q}$ of a PWM control signal v_{con}. The d, q coordinate quantities $v_{con,d}$, $v_{con,q}$ are transferred to three-phase coordinate quantities $v_{con,A}$, $v_{con,B}$, $v_{con,C}$ through a function block with transferring two-phase coordinate quantities to three-phase coordinate quantities. The control signals $v_{con,A}$, $v_{con,B}$, $v_{con,C}$ are sent to a PWM circuit to generate the triggering signals for power electronic switches in the three-phase inverter. The triggering signals are amplified by a drive circuit to control the switching of the three-phase inverter. Since the phase angles of reference currents i_d^*, i_q^* refer to the d, q axis components v_d, v_q of the utility power source voltages, it can urge the injected currents i_a, i_b, i_c synchronizing to the phase voltages v_{an}, v_{bn}, v_{cn} and obtains an unity power factor. For stimulating the PV panel to generate maximum power outputs, the operating voltage V_{pv} from solar panels PV are detected and sent to a MPPT block with functions to track the maximum power point of PV panels. The MPPT block then determines an amplitude command $I_{COM}^{'}$ of the reference currents i_d^*, i_q^*.

The control principle of this MPPT block is shown in Fig. 68.3. If the constant MPP voltage $V_{pv,max}$ can be properly set in advance, the solar panel will work nearly at the MPP through a constant voltage based control on the PV panel. The MPP voltage $V_{pv,max}$ comparing with the measured one V_{pv} in real time gets an error voltage V_e. The error voltage V_e is sent to a voltage controller with a proportional gain K_1. The output from this controller is added to the I_{COM} (an amplitude of the i_d or the i_q), and it will generate a current command $I_{COM}^{'}$. Based

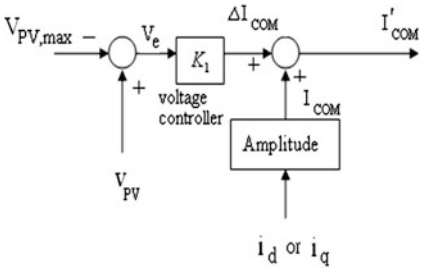

Fig. 68.3 Control principle for the MPPT block

on the linear relationship between the MPP voltage and the open-circuit voltage and on an approximate constant value for MPP voltage on the PV module, a good set value $V_{pv,max}$ can be easily determined through providing the known and necessary electrical specifications of the installed PV modules and measuring, in advance, the open-circuit voltages on the solar panels under a sunny day. The function blocks in the control system mostly will be implemented by using a Matlab/Simulink real-time control software package to avoid the usage of a complicated hardware.

68.4 Experimental Tests and Discussions

The solar panel PV in Fig. 68.2 consists of six pieces of 10 watts photovoltaic modules connected in series, and are installed toward the south tilted 23.5°. The known electrical specifications given by the manufacturer for each piece of photovoltaic modules are open-circuit voltages $V_{oc} = 21.6$ V, short-circuit currents $I_{sc} = 0.63$A, maximum power voltages $V_{max} = 17.2$ V, maximum power currents $I_{max} = 0.58$A. A three-phase power converter module in the JUBILEE PE-8A equipment placed at the Green-Energy Laboratory, Department of Electrical Engineering, Cheng Shiu University is taken as a three-phase inverter through some proper modifications. The three-phase voltage source is given via three 220 V/24 V transformers connected in Δ-Δconnection from utility power systems with 220 V line to line voltages.

Choosing one piece of photovoltaic modules, and measuring its open-circuit voltage V_{oc} from 8:00 am to 17:00 pm in a sunny day, the measured values are probably between 18.5 V and 19.5 V. On the other hand, since the real solar modules have the linear characteristic between the MPP voltage V_{max} and the open-circuit voltage V_{oc} (i.e. $V_{max}/V_{oc} = K_r$, a constant) in different sunlight, a linear constant $K_r = 0.8$ can be calculated and obtained from the known electrical specifications and then an MPP voltage range, $V_{max} = 14.8$– 15.6 V, can be estimated for each piece of solar modules used. Therefore, an MPP voltage range 88.8 V–93.6 V for the solar panel PV in Fig. 68.2 can also be evaluated, approximately. Based on the expectation that the approximate maximum power

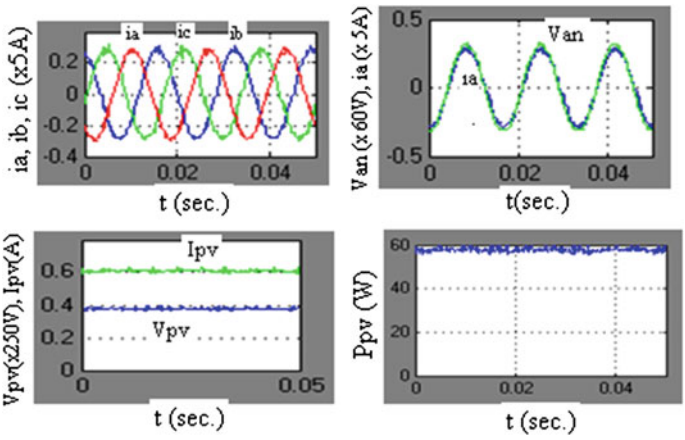

Fig. 68.4 Waveforms of the experimental results

Fig. 68.5 P-V curves of the solar panel PV under different sunlight conditions

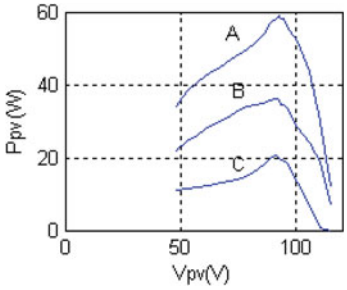

A: sunny; B: sunny but with cloud; C:cloudy

outputs from the solar panel PV under different sunlight conditions are still attainable, the middle value of the previously evaluated MPP voltages for the PV panel, i.e. a 91.2 V, is chosen as the setting value of the $V_{pv,max}$ to control the MPPT operation in this paper. Experimental tests are then conducted under a sunny weather condition. The waveforms of the injected currents i_a, i_b, i_c, the phase voltage v_{an} and line current i_a, the PV panel's voltage V_{PV}, current I_{PV} and output power P_{PV} are all shown in Fig. 68.4. The P–V curve (curve A) of the solar panel PV working at 48–115.2 V is depicted in Fig. 68.5. Figure 68.4 shows the injected currents i_a, i_b, i_c with some high-frequency harmonics are always balance and approximately sine wave. Output powers from the PV panel are about 58 watts in Fig. 68.4. The curve A in Fig. 68.5 also reveals the output powers P_{pv} are about 57–59 W when the PV panel operates at 88.8–93.6 V. The PV panel has an only 2.0 W (3.4 %) differences in these operating voltages, so the range 88.8–93.6 V can be called as an approximate MPP voltage range for the solar panel PV. Since the PV panel operates at 91.2 V involved in the approximate MPP voltage range,

the solar panel PV certainly obtains the generation effects with approximate maximum power outputs.

To confirm the MPP voltage setting $V_{PV,max} = 91.2$ V still keeps effectiveness for different sunlight conditions, two different P–V curves (curves B and C) corresponding to a sunny but with cloudy weather and a cloudy weather, respectively, for the solar panel PV working at 48–115.2 V are also depicted in Fig. 68.5. The curve B shows that the maximum power of the P_{pv} is 36 W, and has an only 1.0 W (2.8 %) differences on the P_{pv} for the PV panel operating at the approximate MPP voltage range (88.8–93.6 V). The curve C shows that the maximum power of the P_{pv} is 20.5 W, and has an only 1.0 W (4.9 %) differences on the P_{pv} for the PV panel working at the approximate MPP voltage range. The determined setting $V_{PV,max} = 91.2$ V is therefore justified in a good and proper value for the solar panel PV to generate approximate maximum power outputs under different sunlight conditions.

The waveforms of the line current i_a (injected into utility power systems) and the phase voltage v_{an} are also shown in Fig. 68.4. This figure shows that current i_a almost synchronizes to voltage v_{an}, and then the outcome with unity power factor ($\cos\theta = 1.0$) for the injected powers into utility power system is produced. The results with $\cos\theta = 1.0$ implies that the three-phase inverter has the ability to stimulate that the injected powers into utility power systems are mostly real powers. Consequently, the utility power systems can get rid of the improper injection of reactive powers, and then the disposal costs for the power quality owing to the improper injection of reactive powers do not happen.

Considering the system operation with unity power factor and ignoring harmonic components for the injected currents and voltage sources of the utility power sources in the test system, the Fig. 68.4 exhibits that the maximum values for v_{an} and i_a are 20.2 V and 1.4A, respectively, and then a $0.5*20.2*1.4*3 = 42.4$ W injected power into the utility power system is estimated. The 58 W generated power (average values) by the solar panel PV is also observed in the same figure. It can be concluded that the overall conversion efficiency of the three-phase grid-connected PV generation system is about 73.1 %.

68.5 Conclusions

A three-phase grid-connected PV generation system with a constant voltage based maximum power point tracking has been constructed in this study. The experimental tests show that the approximate maximum power point tracking for solar panels can be realized via a constant voltage based control on the solar panel PV through a decoupling control (a coordinate transformation method) on the three-phase inverter. The currents injected into utility power systems retain a three-phase balance state and are without most of harmonic contents in addition to near sine wave. The power injected into utility power sources are mostly real power components, and then the utility power system gets rid of the disposal costs for the

power quality. The conversion efficiency of the three-phase grid-connected PV generation system is about 73.1 % and needs to be further advanced. Additionally, the suggested MPPT approach in the paper is simple, effective and easy to be implemented.

References

1. Femia, N., Petrone, G., Spagnuolo, G., & Vitelli, M. (2005). Optimization of perturb and observe maximum power point tracking method. *IEEE Transactions on Power Electronics, 20*, 963–973.
2. Liu, F., Duan, S., Liu, F., Liu, B., & Kang, Y. (2008). A Variable Step Size INC MPPT Method for PV Systems. *IEEE Transactions on Industrial Electronics, 55*, 2622–2628.
3. Masoum, M. A. S., Dehbonei, H., & Fuchs, E. F. (2002). Theoretical and experimental analysis of photovoltaic systems with voltage and current-based maximum power-point tracking. *IEEE Transactions on Energy Conversion, 17*, 514–522.
4. Kobayashi, K., Matsuo, H., & Sekine, Y. (2006). An excellent operating point tracker of the solar-cell power supply system. *IEEE Transactions on Industrial Electronics, 53*, 495–499.
5. Koutroulis, E., Kalaitzakis, E. K., & Voulgaris, N. C. (2001). Development of a microcontroller-based photovoltaic maximum power point tracking control system. *IEEE Transactions on Power Electronics, 16*, 46–54.
6. Kadri, R., Gaubert, J. P., & Champenois, G. (2011). An improved maximum power point tracking for photovoltaic grid-connected inverter based on voltage-oriented control. *IEEE Transactions on Industrial Electronics, 58*, 66–75.

Chapter 69
Remotely Operated Vehicle System Implementation in Open-Water

Ling-Ji Mu, Carlos Sardinha, Chin-Yin Chen, Ya-Chao Yang, Chao-Ming Yu and Yi-Ming Chiu

Abstract Oceans cover most of the earth's surface, and average depth more than 3800 m. It is rich in biological resources and mineral resources. With the depletion of land resources, marine resources development and utilization is increasingly apparent. However, accompanied by the development of marine resources such as oil, natural gas from offshore extension to the deep ocean, Remotely Operated Vehicle (ROV) for its safety, high efficiency, large range of operating depths, work long hours, is increasingly becoming the development of marine resources important tool. Accordingly, in this study, the exploring ocean results in open-water for science/work-class ROV which configuration by Taiwan Ocean Research Institute (TORI) and built by Forum is discussed.

Keywords Remotely operated vehicle · Underwater robot · System integrated

69.1 Introduction

Marine environments cover approximately 70 % of surface for the earth still has many unknown parts. Therefore various studies and development about the ocean such as submarine environment, ocean life, and marine resources research and so on are carried out. Consequently, data exploration and visualization systems are

L.-J. Mu · C.-Y. Chen (✉) · Y.-C. Yang · C.-M. Yu
National Applied Research Laboratories, Taiwan Ocean Research Institute, Kaohsiung, Taiwan, Republic of China
e-mail: cychen@tori.narl.org.tw

Y.-M. Chiu
Ship and Ocean Industries R&D Center, New Taipei City, Taiwan, Republic of China

C. Sardinha
Bluelaguna Incrporation, Jupiter, Florida

J. Juang et al. (eds.), *Proceedings of the 2nd International Conference on Intelligent Technologies and Engineering Systems (ICITES2013)*, Lecture Notes in Electrical Engineering 293,
DOI: 10.1007/978-3-319-04573-3_69,

particularly important to oceanography. In last half-century, Remotely Operated Vehicles (ROVs) have satisfied to all of these needs as above. ROV are controlled by operator (pilots) outside the vehicle. Generally the pilots work from a surface ship to which the ROV is tethered by an umbilical. This umbilical cable provides electrical power and control commands to the ROV and transmits sensor and feedback data to the pilots. ROVs are often operated from a control console where monitors display the images of the seafloor or water column in real time. The advantage of the control console is that it allows a number of scientists or engineers to discuss the data in real time and make decisions about the operations or missions. Because the ROV uses an umbilical cable to provide power to the vehicle, the vehicle potentially can remain subsea for days without coming back up to the surface. The umbilical cord, however, represents a constraint on operations because the range of the vehicle with respect to the ship cannot exceed a few 100 or 1000 m (based on length of the cable). The ship must therefore anticipate the movements of the vehicle, which requires a ship prepared with a dynamic positioning system. Moreover, the presence of a tether limits maneuverability and can introduce entanglement problems in rugged terrain such as hydrothermal fields with high chimney structures [2].

Currently, there are many science/work-class ROVs being deployed for research purposes, such as ROPOS, Jason, ISIS, Victor and KAIKO were developed for exploring ocean resources and carrying out scientific studies [1]. In past years, Taiwan has been building up facilities and supply for marine industry. In addition to ocean resource, shipbuilding, and offshore engineering, the government has also provided sustained support for the development of underwater technology more than decade. Underwater technology has attracted increasing attention because it is the basis for sustainable development and preservation of our ocean environment. In this study, a result for 3000 m science/work-class ROV which designed by Taiwan Ocean Research Institute (TORI) and built by Perry is discussed.

69.2 Components for ROV

As Fig. 69.1 shown, the ROV system can be broken into vehicle, control console and Launch and Recovery System (LARS). The characteristics of those components are discussed as below.

69.2.1 Vehicle Specifications

The overview and specifications of the vehicle for TORI's ROV are shown in Fig. 69.2 and Table 69.1, respectively. This ROV designed using modular design

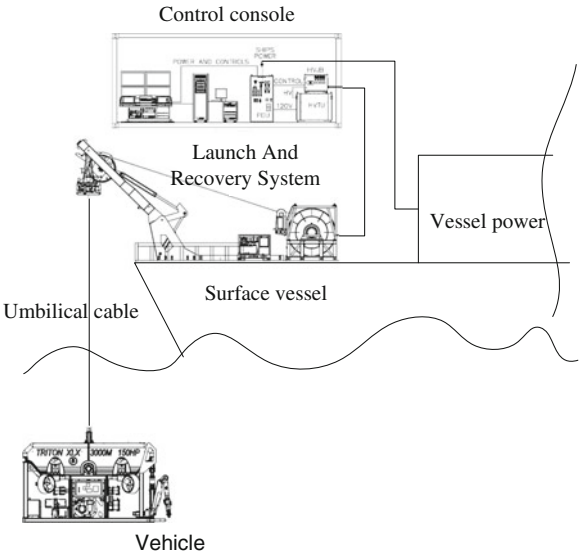

Fig. 69.1 Components of TORI's ROV

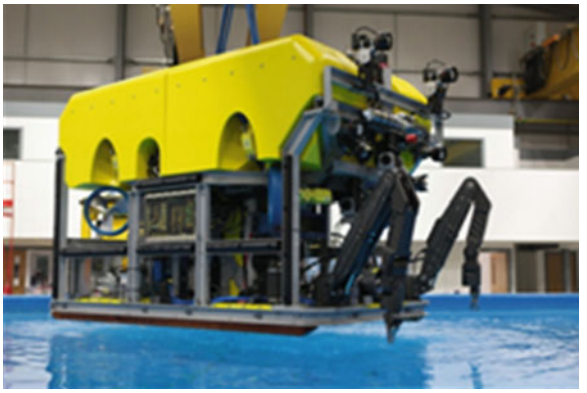

Fig. 69.2 Vehicle overview

method, which consists of mechanical modular, propulsion modular, vision modular, light modular, sampling modular and sensor modular [1, 2].

69.2.2 Control Console

As Fig. 69.3 shown, ROV control systems are built within two containers. The control room is divided into five separate modular sections: modular 1 as video panel, modular 2 as control system, modular 3 as information transfer, modular 4 as power modular, and modular 5 as scientist interface, respectively.

Table 69.1 Vehicle specification

Items	Specification
Mechanical characteristic	Size: L 3 m, W 1.8 m, H 2.2 m
	Air weight: 5.2 Ton (w/o tools sled)
	Max payload: 350 kg
Propulsion	Max hydraulic power: 150 Hp
	Thruster:
	Sub-Atlantic SA-300-20 (vertical) max force 900 kg
	Sub-Atlantic SA-380-30 (horizontal) max force 1100 kg
Light	No.: 6
	Power: 4–400 W, 2-LED
Vision system	Video camera:
	Science observation—Insite Pacific Inc.-Zeus Plus 1080p
	Operation—Insite Pacific Inc.-Mini Zeus 1080i
	Environment sensor—Insite Pacific Inc.-Pegasus Plus
	Camera:
	Insite Pacific Inc.-Scorpio Plus @Flash
Sampling system	Manipulator—2-*Kraft-Predator* with master–slave 7 function force feedback
	Max load: 230 kg (normal), 93 kg (full extension)
Sensors	Sonar: Kongsberg Mesotech Multi Frequency 1171
	USBL Beacon: Ixsea Posidonia Beacon POSI-Beacon-S
	INS with DVL: Ixsea PHINS 6000 + RDI DVL
	Altimeter: Kongsberg Mesotech 1007
	Depth sensor: Paroscientific Inc. Digiquartz Model 8CB4000-I part number 1700-003-0

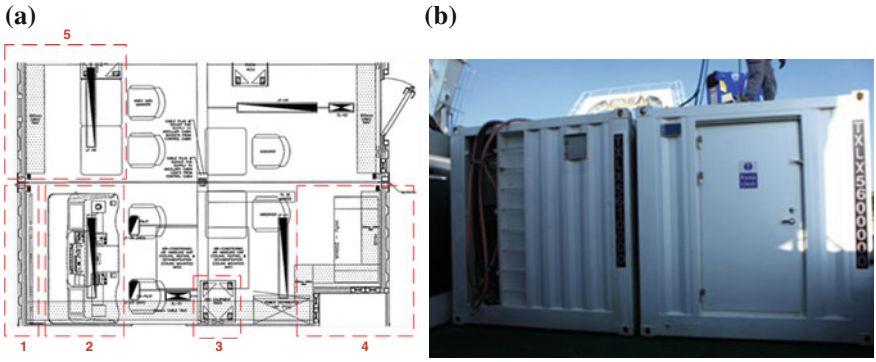

Fig. 69.3 Control console for ROV. **a** Modular for control system. **b** Control containers

Generally, ROV control systems is broken down into two sections, a Surface Control and Subsea control system, that provides the basic commination between the Surface Control system and the Subsea computer. Below is the Perry integrated control architecture is shown in Fig. 69.4.

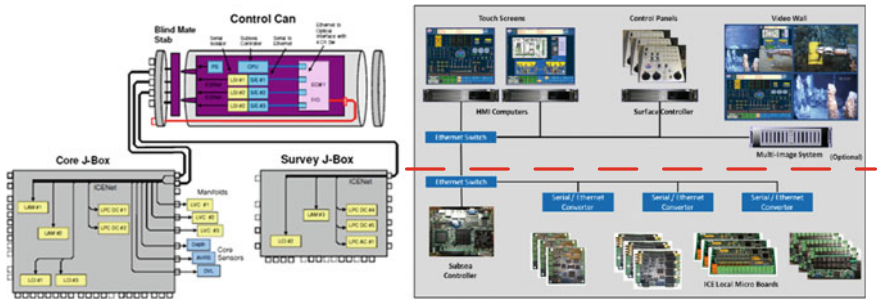

Fig. 69.4 Integrated control architecture [3]

A. *Vehicle control*

For the vehicle control, the control diagram is illustrated in Fig. 69.4. In this configuration, 10-inch diameter, 57-inch long anodized aluminum canister with removable end caps. The control tray connector end slides into the canister. All of electronic sensors and control signals are connected with core junction-box and survey junction-box, those supports 110 VAC, 48, 24, 12 and 5 VDC power for over 50 connectors. In the control canister, the Explicitly Parallel Instruction Computing (EPIC) 1.0 is used as main subsea controller, which great enhance 1.8 GHz Pentium M Processor. Moreover, there is also provision PID based such as auto heading mode, auto heading park mode, auto depth mode, auto altitude mode and auto position for pilot to enhance control performance.

B. *System telemetry*

For system telemetry, the architecture GUI shown in Fig. 69.5 is runs by ICE and under the Microsoft Windows XP operating system. In this structure, the HMI computers (Human Machine Interface) are industrial rack mount and labeled HMI #1, HMI #2 and surface controller. Furthermore, Fig. 69.5 shows GUI (Graphic User Interface) screens are organized using a paneling concept, where functional panels are placed on each page to build the screen. Finally, the all of the surface control environment is built in the 20 ft container and shown in Fig. 69.6. In this container, right hand side site, left hand side site and in front of container are for pilot, co-pilot and videos information TVs.

69.3 System Implementation in Open-water

The TORI's ROV system was operated up to maximum 1400 m depth and has performed over 10 successful dives off the southwest waters in Taiwan by some deep-sea projects [4]. The ROV is docked and launched from the mother vessel (Ocean Researcher V) using the deep-sea winch (see the Fig. 69.7). A 3500 m of electro-optic umbilical cable is housed in a hydraulic deck storage winch and its

Perry Slingsby Systems, (2012). ICE Computer Control System and Graphical User Interface. Perry Slingsby Systems.

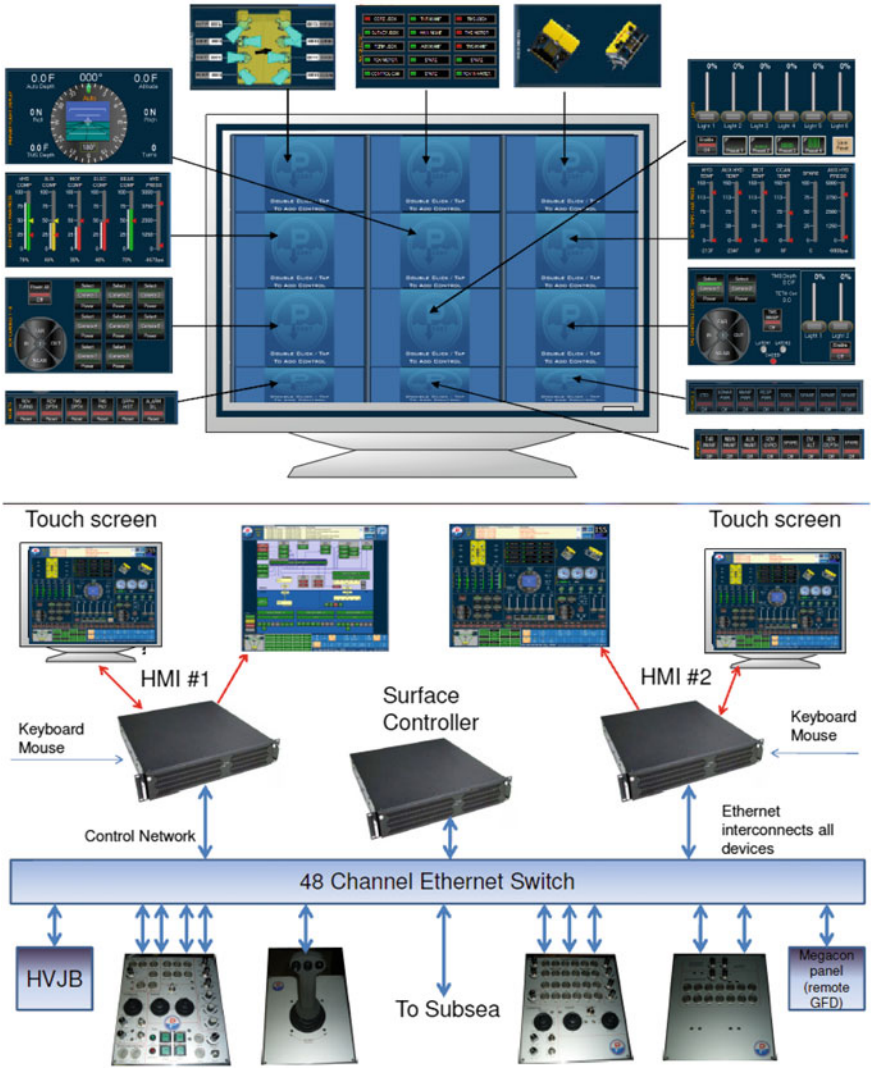

Fig. 69.5 System telemetry architecture and GUI screens [3]

operation is with the winch. The winch handles the ROV system and transfer the load to the umbilical cable it below the water surface. The ROV is propelled by thrusters and can be operated in any desired direction from the pilot command from the ship and move with mother vessel together (see the Fig. 69.7). Manipulators are used to carry out subsea intervention tasks. After the completion of the subsea task, the ROV shall be recovered back to the ship.

Fig. 69.6 Control container

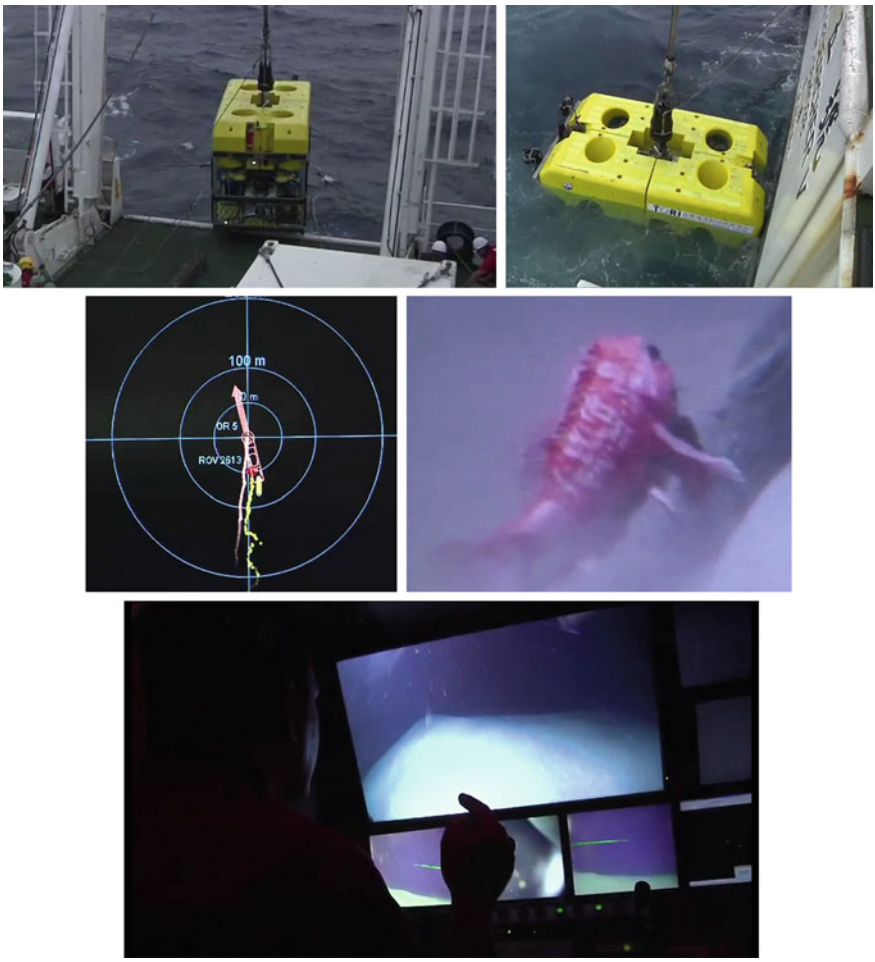

Fig. 69.7 Results in open-water

69.4 Conclusion

In this study, the TORI's ROV is presented. For this system, it is not only for science observation but also work for offshore engineering. However, in this study, it just focuses on the environment observation; the seafloor sampling will be prepared in the near future.

References

1. Mu, L. J., Chen, E., Huang, S. W., Chen, K. L., Chao, J, C., & Shih, C. S. et al. (2012). System integrated design and implementation for under water explorer in TORI. In *The 43rd International Symposium on Robotics*.
2. Steele, J., Thorpe, S., & Turekian, K. (2009). *Measurement techniques platforms and sensors*. Waltham: Academic Press.
3. Triton XLX Training Course: ICE Computer Control System and Graphical User Interface. Perry Slingsby Systems.
4. Mu, L. J., Chen, C. Y., Liu, C. S., Yu, C. M., Yang, Y. C., & Jang, J. P. et al. (2013). Integrated multiple underwater vehicles for underwater topography measurement and observation in southwest Taiwan. In *The 35th Ocean Engineering Conference in Taiwan* (Accepted).

Chapter 70
A Nonlinear-Multivariate Regression Prediction of Compressive Strength of Waste Glass Concrete

Chien-Chih Wang, Her-Yung Wang, Chao-Wei Tang and Jyun-Jie Huang

Abstract In this study, a predictive model on compressive strength of waste LCD glass concrete was developed by analyzing a series of laboratory test results. The compressive strength prediction model with parameters of the water-binder ratio w/b, curing age t, and waste glass content G was progressed by nonlinear-multivariate regression analysis. The calculated results are appropriate with the laboratory measured data. In addition, the coefficient of determination R^2 value is 0.93–0.96, were obtained by regression analysis using the model predicted compressive analysis value and test result are also excellent.

Keywords Compressive strength · Concrete · Waste glass · Prediction

70.1 Introduction

Liquid crystal glass is of a rising industry of high-tech industry in Taiwan at present. Thus, Taiwan was the worldwide key manufacturer of panel displays with the highest market share of TFT-LCD (Thin film transistor-Liquid crystal display) in the world, namely 43 % in 2007 [1]. The main chemical constituents of waste LCD glass are SiO_2, Na_2O and a small amount of indium-tin-oxide conducting film. Therefore, direct landfill, incineration or composting treatment is not appropriate to treat waste LCD glass [2]. Because of the glass contains a large amount of silicon and calcium, and it is of Portland material in nature. Its physical

C.-C. Wang (✉) · C.-W. Tang · J.-J. Huang
Department of Civil Engineering and Geomatics, Cheng Shiu University, Kaohsiung 83347, Taiwan, Republic of China
e-mail: ccw@csu.edu.tw

H.-Y. Wang
Department of Civil Engineering, National Kaohsiung University of Applied Sciences, Kaohsiung 80778, Taiwan, Republic of China

J. Juang et al. (eds.), *Proceedings of the 2nd International Conference on Intelligent Technologies and Engineering Systems (ICITES2013)*, Lecture Notes in Electrical Engineering 293,
DOI: 10.1007/978-3-319-04573-3_70,

properties, such as unit weight, compressive strength, elasticity modulus, thermal expansion coefficient and heat transfer coefficient, are very close to concrete, thus, adding the crushed waste glass in concrete as fine aggregate can reduce the air content and unit weight of concrete [3]. The waste glass recycling can reduce the material cost and the impact on the environment, as well as the emission of CO_2. It has become a necessary trend of sustainable environmental protection.

The characteristics of concrete made with waste glass have discussed by many studies, most of them focus on the compressive strength, surface resistance, shrinkage, workability, ultrasonic pulse velocity and durability [3–8], while seldom discuss the prediction model and regression analysis of compressive strength of the concrete. Therefore, based on the results of our previous studies on the mixture ratio of concrete made with waste LCD glass [7, 9], the water-to-binder ratios were 0.28, 0.32, and 0.36, and four kinds of glass sand were added at volume replacement ratios of 0, 10, 20, and 30 %. Fly ash, water-quenched slag and superplasticizer were added and blended by means of a simple SCC mixing design method. This study aimed to determine the relationships between multiple influencing factors of compressive strength and waste glass content, water-binder ratio and age. Moreover, a predictive analysis model was established for evaluating the compressive strength reasonably.

70.2 Characteristics of Glass Concrete

Kou and Poon [10] used recycled glass sand in particle diameter less than 5 mm with specific gravity of 2.45 and fineness modulus of 4.25 to study self-consolidating concrete (SCC). The findings indicated that the unit weight and air content decreased as the addition level of waste glass increased, but the decreasing amplitude was small, and the variance in slump flow was influenced by the waste glass content slightly. In addition, the expansion increased slowly as the addition level of waste glass increased. The trend of slump flow and ASR test result [10] was slightly different from the results of Topcu and Canbaz [3].

Topcu and Canbaz [3] used waste glass to replace coarse aggregate. The slump, air content and unit weight of the concrete decreased as the proportion of additional waste glass increased, but the slump flow related to the workability increased. In addition, the mechanical properties of concrete, such as compressive strength, flexural strength, splitting tensile strength and dynamic modulus of elasticity, decreased by degrees as the waste glass content increased. The concrete expansion slowed down as the addition of waste glass content increased. Terro [11] found the same trend in the waste glass concrete with replacement of recycled crushed glass in different particle diameters for aggregate.

As for mechanical properties, the compressive strength, splitting tensile strength and static elasticity modulus decreased by degrees as the waste glass content increased. The test result show that the compressive strength of waste LCD glass concrete decreased as the replacement of waste glass for aggregate increased

[8, 12–14]. In addition, the compressive strength of all the concrete with waste glass is similar to behavioural characteristic of general concrete, the compressive strength increases by degrees with the curing time. However, after a certain age, the increase in compressive strength becomes smooth. Similarly, the compressive strength decreases as the water-binder ratio increases.

70.3 Development of Compressive Strength Prediction Model

Murat et al. [15] found that the compressive strength of fly ash concrete increased by degrees with age, but the trend became smooth over time. The relationship was rapid raised in initial state, but converted to an approximately horizontal curve after a certain age. The results of other studies on the compressive strength of concrete revealed the same trend [12, 15, 16]. In terms of the influence of additives in concrete on the compressive strength, including the influence of replacement of fly ash, furnace slag and waste glass for partial cement or sandy soil content, under the same conditions, the compressive strength of the concrete with any additive increased with the age, and the trend of increase in compressive strength became smooth over time. The compressive strength of waste glass concrete increased as the addition level of waste glass decreases [3, 8, 10–14]. Therefore, for the model, the behavior of compressive strength of waste glass concrete decreases as the waste glass content increases in the same mixture ratio was assumed in this study. Duncan and Chang [17] conducted a triaxial test on soil, and found that the nonlinear stress–strain relation of soil could be evaluated reasonably by using the hyperbolic model. The trend of compressive strength and age of concrete is very similar to hyperbolic model. As long as variables are changed appropriately, it can be applied to predictive analysis of trend of compressive strength of concrete. Thus, this study constructed the prediction model for compressive strength of multivariate self-compacting waste LCD glass concrete considering water-binder ratio w/b, age t and replacement percentage of waste glass G based on hyperbolic model.

Figure 70.1 illustrates the test result of normalized ratio of compressive strength at different curing ages and on Day 28 when the water-binder ratio w/b is 0.28 and the waste glass replacement ratio G is 0–30 %. For the same waste glass content G, the compressive strength f'_c increases by degrees with the age t, but the increase becomes smooth as the age goes on. Therefore, the relation between compressive strength and age is simulated by hyperbolic model, as shown in Eq. (70.1).

$$\frac{f'_c}{f'_{c,28}} = f(t) = \frac{t}{a + bt} \tag{70.1}$$

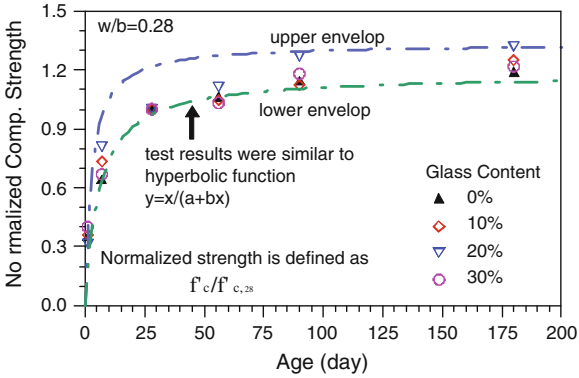

Fig. 70.1 Normalized compressive strength versus curing time with different glass content (w/b = 0.28)

where parameters a and b are the coefficients of hyperbolic function, t is the age, and parameters a and b are the functions of waste glass content G according to the test result in Fig. 70.1, expressed as Eq. (70.2) and Eq. (70.3). The test results of other water-binder ratios have the same trend, so the test results can be further integrated. The parameters m and n are the functions of water-binder ratio w/b.

$$a = f(G) = (m + \alpha \times G) \tag{70.2}$$

$$b = f(G) = (n + \beta \times G) \tag{70.3}$$

where α and β are parameters related to waste glass content G, m and n are coefficients related to water-binder ratio w/b. Eq. (70.2) and Eq. (70.3) are combined, Eq. (70.1) can be expressed as Eq. (70.4). And the normalized compressive strength can be derived as Eq. (70.5).

$$\frac{f'_c}{f'_{c,28}} = \frac{t}{(m + \alpha \times G) + (n + \beta \times G)t} \tag{70.4}$$

$$\frac{f'_c}{f'_{c,28}} = \frac{t}{[(m_1 + m_2(w/b)) + \alpha \times G] + [(n_1 + n_2(w/b)) + \beta \times G] \times t} \tag{70.5}$$

70.4 Comparison Between Predictive Analysis and Test Result of Compressive Strength

Figure 70.2 show the test results of compressive strength of self-compacting waste LCD glass concrete with replacement of waste LCD glass for fine aggregate (sandy soil) by weight percentage G of 0, 10, 20 and 30 %, respectively, for water-binder ratio (w/b) is 0.28. It is shown that the compressive strength of the specimen decreases slightly as the waste glass content increases at the same age. However,

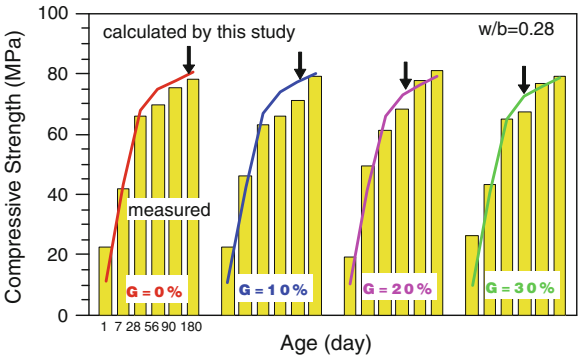

Fig. 70.2 Comparison results of experimental value and predicted model (w/b = 0.28)

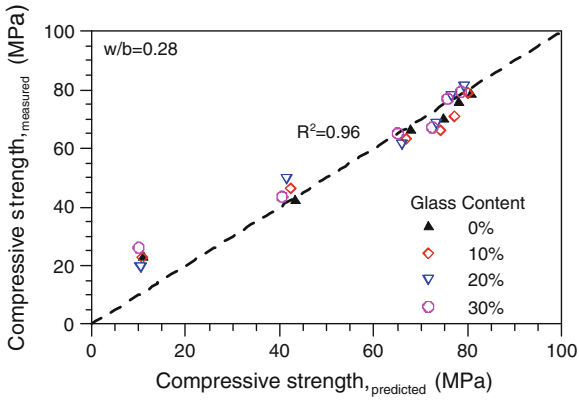

Fig. 70.3 Relationship between predicted and measured compressive strength (w/b = 0.28)

the change is not obvious, and the strength is approximately distributed in a range. And compressive strength decreases as the water-binder ratio increases at the same mixed condition. When the prediction model for compressive strength of concrete planned in Sect. 70.3 is used for model regression analysis of test results, the model parameters are $\alpha = 1.48$, $\beta = 0$, $m_1 = 4.30$, $m_2 = 2.58$, $n_1 = 1.07$ and $n_2 = -1.09$. Thus, the value of compressive strength on Day 28 must be obtained from test results or calculated, when the predicted model was used.

The multivariate concrete compressive strength prediction model considering water-binder ratio w/b, age t and waste glass content G, was developed. In addition, it can evaluate the compressive strength in different w/b, t and G conditions reasonably. As seen, the strength analysis value of prediction model is overrated and underrated sometimes, but the overall analysis result is reasonable, as shown in Fig. 70.2.

Figure 70.3 illustrated the coefficient of determination R^2 obtained by regression analysis using the model predicted compressive strength analysis value and test result is also excellent, when w/b is 0.28, $R^2 = 0.96$. When w/b is 0.32, $R^2 = 0.93$, when w/b is 0.36, $R^2 = 0.95$. It is noteworthy that Mousavi et al. [16] studied high performance concrete and found that in the comparison between the analytic result of prediction model and the experimental value, if the coefficient of determination

R^2 value is greater than 0.8, there is excellent relevance between them. Therefore, the prediction model for compressive strength of self-consolidating waste LCD glass concrete built in this study can evaluate compressive strength of concrete in different states in the range of mixture ratio of this study reasonably.

70.5 Conclusion

A compressive strength prediction model considering multiple variables of water-binder ratio, waste glass content and age simultaneously was constructed by combining compressive strength characteristic of waste glass concrete based on hyperbolic model. According to the comparison analysis of predicted value and test result, the coefficient of determination R^2 was as high as 0.93–0.96, so the built compressive strength prediction model was reasonable. In addition, the compressive strength of specimen f'_c increased by degrees with the age, but decreased as the water-binder ratio increased. Under the same mixture ratio, the compressive strength of specimen f'_c decreased as the waste glass content increased, which is consistent with previous studies.

References

1. Tseng, C. C. (2009). Competitiveness analysis of display panel industry in Taiwan and Korea (II). *Quality Magazine, 45*(2), 48–52.
2. Lin, K. L. (2007). The effect of heating temperature of thin film transistor-liquid crystal display (TFT-LCD) electric-optical waste glass substitute partial clay as eco-brick. *Journal of Cleaner Production, 15*, 1755–1759.
3. Topcu, I. B., & Canbaz, M. (2004). Properties of concrete containing waste glass. *Cement and Concrete Research, 34*, 267–274.
4. Bashar, T., & Ghassan, N. (2009). Utilizing waste recycled glass as sand/cement replacement in concrete. *Journal of Materials in Civil Engineering ASCE, 21*(12), 709–721.
5. Chen, S. H., Chang, C. S., Wang, H. Y., & Huang, W. L. (2011). Mixture design of high performance recycled liquid crystal glasses concrete (HPGC). *Construction and Building Materials, 25*, 3886–3892.
6. Kin, K. L. (2007). Use of thin film transistor liquid crystal display (TFT-LCD) waste glass in the production of ceramic tiles. *Journal of Hazardous Materials, 148*, 91–97.
7. Wang, H. Y., & Huang, W. L. (2010). A study on the properties of flesh self-consolidating glass concrete (SCGC). *Construction and Building Materials, 24*, 619–624.
8. Wang, H. Y. (2011). The effect of the proportion of thin film transistor–liquid crystal display (TFT–LCD) optical waste glass as a partial substitute for cement in cement mortar. *Construction and Building Materials, 25*, 791–797.
9. Wang, H. Y., & Huang, W. L. (2010). Durability of self-consolidating concrete using waste LCD glass. *Construction and Building Materials, 24*, 1008–1013.
10. Kou, S. C., & Poon, C. S. (2009). Properties of self-compacting concrete prepared with recycled glass aggregate. *Cement and Concrete Composites, 31*, 107–113.
11. Terro, M. J. (2006). Properties of concrete made with recycled crushed glass at elevated temperatures. *Building and Environment, 41*, 633–639.

12. Lin, K. L., Shiu, H. S., Shie, J. L., Cheng, T. W., & Hwang, C. L. (2012). Effect of composition on characteristics of thin film transistor liquid crystal display (TFT-LCD) waste glass-metakaolin-based geopolymers. *Construction and Building Materials, 36*, 501–507.
13. Park, S. B., Lee, B. C., & Kim, J. H. (2004). Studies on mechanical properties of concrete containing waste glass aggregate. *Cement and Concrete Research, 34*, 2181–2189.
14. Wang, H. Y. (2009). A study of the engineering properties of waste LCD glass applied to controlled low strength materials concrete. *Construction and Building Materials, 23*, 2127–2131.
15. Murat, P., Erdogan, O., Ahmet, O., & Yuce, M. I. (2007). Appraisal of long-term effects of fly ash and silica fume on compressive strength of concrete by neural networks. *Construction and Building Materials, 21*, 384–394.
16. Mousavi, S. M., Aminian, P., Gandomi, A. H., Amir Hossein Alavi, A. H., & Bolandi, A. H. (2012). A new predictive model for compressive strength of HPC using gene expression programming. *Advances in Engineering Software, 45*, 105–114.
17. Duncan, J. M., & Chang, C. Y. (1970). Nonlinear analysis of stress and strain in soil. *Journal of the soil mechanics and foundations division, ASCE, 96*(SM5), 1629–1653.

Chapter 71
Optimal Power Flow Control Using a Group Search Optimizer

Chao-Ming Huang, Chi-Jen Huang, Yann-Chang Huang and Kun-Yuan Huang

Abstract This paper proposes a group search optimizer (GSO) for optimal power flow (OPF) control based on a flexible AC transmission system (FACTS). FACTS has been successfully applied to steady-state control of power system, which determines the optimal location of FACTS devices and their associated values in the transmission lines. To solve the optimal solution of FACTS devices, a GSO inspired by animal searching behavior is used in this paper. GSO is a population-based optimization algorithm which has been successfully applied to deal with optimization problem. The proposed method is verified using the IEEE 30-bus 41-transmission system. The results demonstrate that the proposed method improves the total transfer capability and provides better steady-state control of power systems than existing methods.

Keywords Power flow · Flexible AC transmission system · Group search optimizer · Optimization algorithm

71.1 Introduction

The FACTS devices have been widely used to improve the total transfer capability of the power system, which requires determining the optimal location of FACTS devices and their associated values. Some novel approaches have been developed to cope with the OPF control using FACTS devices. These techniques contain

C.-M. Huang (✉) · C.-J. Huang
Department of Electrical Engineering, Kun Shan University, Tainan 710, Taiwan, Republic of China
e-mail: h7440@ms21.hinet.net

Y.-C. Huang · K.-Y. Huang
Department of Electrical Engineering, Cheng Shiu University, Kaohsiung 833, Taiwan, Republic of China

J. Juang et al. (eds.), *Proceedings of the 2nd International Conference on Intelligent Technologies and Engineering Systems (ICITES2013)*, Lecture Notes in Electrical Engineering 293,
DOI: 10.1007/978-3-319-04573-3_71,

Newton method [1], interior point algorithm [2], particle swarm optimization (PSO) algorithm [3] and evolution computing (EC) method [4]. The techniques mentioned above can serve as useful tools to produce optimal solution for OPF control problem.

This paper develops an alternative approach using GSO [5] to determine the optimal solution for FACTS devices. The GSO inspired by animal searching behavior is a population-based optimization algorithm. In animal behavioral ecology, the group living is a widespread phenomenon and has been studied for a long time. The most adopted strategies are producing and joining. Joining is a ubiquitous trait found in most social animals. It usually searches around the producers to get resources and so is called the scroungers. The rangers use the random search method to make the group search process more complete. Based on producer–scrounger (PS) model, GSO has the ability to offer global or near global solution for the OPF control problem.

The rest of the paper is organized as follows. In Sect. 71.2, the FACTS devices and proposed approach using GSO to produce OPF solution is briefly reviewed. In Sect. 71.3, the numerical results of different methods for the IEEE 30-bus system are illustrated. Finally, conclusions are given in Sect. 71.4.

71.2 The Proposed Approach

71.2.1 FACTS Devices

As shown in Fig. 71.1, FACTS can be categorized into four types: thyristor-controlled series capacitor (TCSC), thyristor-controlled phase shifting transformer (TCPST), thyristor-controlled voltage regulator (TCVR) and static var compensator (SVC). Figure 71.1a shows the circuit symbol of TCSC, which is composed of a capacitor, an inductor, and a short-circuit line. In this paper, the capacitor is used to improve the power flow of the transmission system. As shown in Fig. 71.1b, TCPST is used to control the angle of bus voltage. The TCVR, as shown in Fig. 71.1c, is mainly used to tune the bus voltage amplitude. Figure 71.1d shows the circuit symbol of SVC, which usually connects in parallel to the transmission line to inject (absorb) reactive power to (from) the bus.

71.2.2 Objective Functions

(1) Active power transmission loss (P_{loss})
The active power transmission loss, P_{loss}, can be expressed as follows:

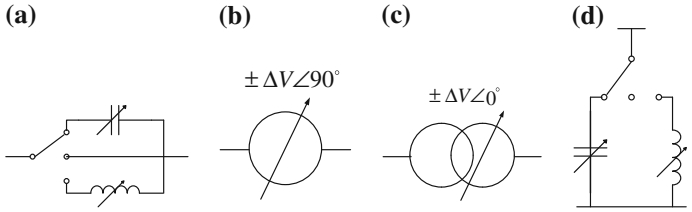

Fig. 71.1 The circuit symbol of FACTS devices **a** TCSC **b** TCPST **c** TCVR **d** SVC

$$P_{loss} = \sum_{i=1}^{N_m} \sum_{j=1}^{N_m} \left[g_{ij} \left(|V_i|^2 + |V_j|^2 - 2|V_i||V_j| \cos(\delta_i - \delta_j) \right) \right] j \neq i, \tag{71.1}$$

where N_m is the number of buses, g_{ij} is the conductance between bus i and j, $|V_i|$ is the voltage magnitude of bus i, and δ_i is the phase angle of bus i.

(2) The performance index of the active power flow (PI_{line})

The PI_{line} is used to evaluate the degree of congestion in the transmission line, as follows:

$$PI_{line} = \sum_{i=1}^{L} \frac{P_i}{P_i^{rated}}, \tag{71.2}$$

where P_i is the active power flow in the ith line, P_i^{rated} is the rated value of the active power flow in the ith line and L is the number of transmission lines.

(3) The performance index of the voltage difference between buses (PI_{bus})

The PI_{bus} is used to determine the voltage stability of the power system, as follows:

$$PI_{bus} = \sum_{\substack{i=1 \\ j=1}}^{N_m} \left(|V_i| - |V_j| \right) \quad j \neq i, \tag{71.3}$$

where $|V_i|$ is per unitized. Note that the value of PI_{bus} is evaluated only when the transmission lines between buses are connected.

The three objective functions can be converted to a single optimization problem, as follows:

$$\min F = \lambda_1 \bar{P}_{loss} + \lambda_2 PI_{line} + \lambda_3 PI_{bus}, \tag{71.4}$$

where $\bar{P}_{loss} = P_{loss} / P_{loss}^b$, P_{loss}^b is the active power transmission loss obtained by the basic load flow solution; λ_i is the weight of the ith objective function and $\Sigma \lambda_i = 1$.

The objective functions of the model (71.4) must satisfy a number of constraints, including a power balance constraint, a reactive generation constraint, a bus voltage constraint and capacitor and transformer tap-setting constraints [6].

71.2.3 Group Search Optimizer

The GSO inspired by animal searching behavior is a population-based optimization algorithm which employs producer–scrounger (PS) model as a framework. In a n-dimensional search space, the ith member at the kth generation has a position $X_i^t \in \Re^n$ and a head angle $\varphi_i^t = (\varphi_{i1}^t, \ldots, \varphi_{i(n-1)}^t) \in \Re^{n-1}$. The search direction of the ith member can be calculated as follows.

$$d_{ij}^t = \begin{cases} \prod_{q=1}^{n-1} \cos(\varphi_{iq}^t), j = 1 \\ \sin(\varphi_{i(j-1)}^t) \prod_{q=j}^{n-1} \cos(\varphi_{iq}^t), j = 2, \ldots, n-1 \\ \sin(\varphi_{i(n-1)}^t), \; j = n \end{cases} \tag{71.5}$$

In the GSO, a group consists of three types of members: producers, scroungers and rangers, which are introduced in order as follows.

(1) Producers

In each generation, the member with the best fitness value will be chosen as the producer. The producers mainly search through the 'vision', which includes a maximum pursuit angle ($\theta_{\max} \in \Re^1$) and a maximum pursuit distance ($l_{\max} \in \Re^1$), as shown in Fig. 71.2.

The producer will scan at zero degree and then scan by randomly sampling three points in the scanning field, as follows.

$$\mathrm{X}_z^t = \mathrm{X}_p^t + r_1 l_{\max} \mathrm{D}_p^t(\varphi^t) \tag{71.6}$$

$$\mathrm{X}_x^t = \mathrm{X}_p^t + r_1 l_{\max} \mathrm{D}_p^t(\varphi^t + r_2 \theta_{\max}/2) \tag{71.7}$$

$$\mathrm{X}_y^t = \mathrm{X}_p^t + r_1 l_{\max} \mathrm{D}_p^t(\varphi^t - r_2 \theta_{\max}/2) \tag{71.8}$$

where $X_p^t$is the location of the producers at the tth generation, $r_1 \in \Re^1$ is a normally distributed random number and $r_2 \in \Re^{n-1}$is an uniformly distributed random number.

For each generation, the producer will find the location with the best fitness value. If the location has a better fitness value than its current position, then it will move to this position. Otherwise, it will stay in its current position and randomly turn its head to a new angle, as follows.

$$\phi^{t+1} = \phi^t + r_2 \delta_{\max} \tag{71.9}$$

where $\delta_{\max} \in \Re^1$ is the maximum turning angle. If the producer cannot find a better position through many generations, it will turn its head back to zero degree, i.e. $\varphi^{t+d} = \varphi^t$, $d \in \Re^1$ is a constant.

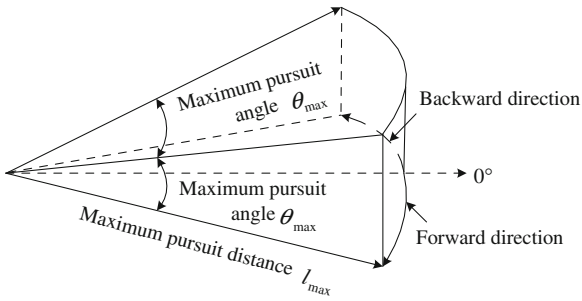

Fig. 71.2 The 3-dimensional scanning field of producer [5]

(2) Scroungers

For each generation, a number of group members (about 80 %) are selected as scroungers. The scroungers use the 'area coping' strategy to keep opportunities to connect with the resources found by the producer, as follows.

$$X_i^{t+1} = X_i^t + r_3\left(X_p^t - X_i^t\right) \tag{71.10}$$

where $r_3 \in \Re^{n-1}$ is an uniformly distributed random number in the range (0, 1). Equation (71.10) reveals that the *i*th scrounger will turn its head to a new randomly generated angle.

(3) Rangers

In the GSO, the rangers employ 'random walk' strategy to randomly distributed resources, which is thought to be the most efficient searching method.

At the *i*th iteration, the rangers generate a head angle using (71.9), choose a random distance and then move to a new position, as follows.

$$l_i = b \times r_1 l_{\max} \tag{71.11}$$

$$X_i^{t+1} = X_i^t + l_i D_i^t\left(\phi^{t+1}\right) \tag{71.12}$$

where $b \in \Re^1$ is a constant. To maximize the changes of finding the best resources, the rangers also employs the bounded search method to restrict their search to a profitable patch. When a member is outside the search space, it will be turned back into the search space by randomly generating a proper position.

71.2.4 The Scheme of GSO to OPF Control

Step 1: Set the associated parameters: maximum pursuit angle, maximum pursuit distance, the size of group and the maximum number of iterations

Step 2: Randomly generate an initial group $X_i = [X_{i1}, X_{i2}, \ldots, X_{im}]$, $i = 1,\ldots, J$, m is the dimension of the member and J is the size of the group. Each member in the group is composed of the optimal location of FACTS devices and their associated values in the transmission lines
Step 3: For each member in the group, perform power flow analysis and evaluate the objective value using (71.4)
Step 4: Select the best objective value in the group as the producer
Step 5: Perform producer operation from (71.6) to (71.9)
Step 6: Perform scrounger and ranger operations as described in (71.10) and (71.12), respectively
Step 7: For the current group, perform step 3 and step 4 again to obtain a new producer
Step 8: Repeat steps 5–7 until the maximum number of iterations is reached
Step 9: Output the optimal solution for the FACTS. The solution with the lowest objective value in the group is regarded as the optimal solution for the FACTS.

71.3 Numerical Results

The proposed method was verified using the IEEE 30-bus system [6]. For comparison purpose, the PSO [3] and EC [4] methods were also tested using the same database.

In the IEEE system, bus 1 is a slack bus, buses 2, 5, 8, 11 and 13 are generation buses and the others are load buses. The control variables are the location of the FACTS devices and their associated values in the transmission lines. The size of group and the number of maximum iterations for each method are set at 20 and 50, respectively. The weights of P_{loss}, PI_{line} and PI_{bus} are set at 0.4, 0.3 and 0.3, respectively. Note that the generation buses do not connect with TCVR or SVC and that each transmission line or bus has only one FACTS device. To ensure a similar investment cost, the same type and amount of FACTS devices are used in the optimization process.

Table 71.1 shows a comparison of the different methods with eight FACTS devices. There are 24 control variables in each member. The basic load flow solution that uses the Newton method [1] is regarded as the benchmark. The reduction of active power loss by using the EC, PSO and proposed method are 57.64, 53.92 and 72.51 %, respectively. The proposed method also achieves better performances than EC and PSO methods, in terms of PI_{line} and PI_{bus}. Table 71.2 shows the best location and the associated value of each FACTS device. The average convergence time for EC, PSO and proposed methods through 30 random runs are 13.25, 11.41 and 10.35 s, respectively.

Table 71.1 Results of different methods with eight FACTS devices

Method	ΣP_G (MW)	ΣQ_G (MVar)	P_{loss} (MW)	Q_{loss} (MVar)	Reduction of P_{loss} (%)	PI_{line}	PI_{bus}	Objection value
	288.683	102.766	5.2830	−23.434	None	0.6564	0.5782	0.7704
EC	285.638	68.471	2.2377	−25.249	57.64	0.5903	0.5481	0.5109
PSO	285.834	73.181	2.4345	−24.717	53.92	0.5916	0.5442	0.5251
GSO	284.853	75.350	1.4525	−21.225	72.51	0.5812	0.5242	0.4416

Note $P_D = 283.4$(MW), $Q_D = 126.2$(MVar)

Table 71.2 Location and their associated values with eight FACTS devices

FACTS	EC		PSO		GSO	
	Location	Value	Location	Value	Location	Value
TCSC	Line 12-14	0.10pu	Line 6-11	0.10pu	Line 4-12	0.15pu
	Line 23-24	0.20pu	Line 4-12	0.10pu	Line 25-27	0.10pu
TCPST	Line 14-15	+5°	Line 12-15	+5°	Line 3-4	+5°
	Line 15-23	+5°	Line 10-17	+5°	Line 2-4	+5°
TCVR	Line 18-19	1.02pu	Line 15-23	1.02pu	Line 18-19	1.01pu
	Line 21-22	0.99pu	Line 21-22	0.98pu	Line 10-22	1.01pu
SVC	Bus 14	5 MVar	Bus 15	3 MVar	Bus 14	5 MVar
	Bus 15	4 MVar	Bus 26	3 MVar	Bus 23	5 MVar

71.4 Conclusions

A novel approach using GSO to determine the optimal solution of FACTS devices in the transmission lines is proposed in this paper. The paper first introduces the FACTS devices and the objective functions. Then the proposed GSO and the scheme of GSO to OPF control are briefly reviewed. Because there is an almost global search scheme, the proposed approach is more likely to converge toward a global solution than the EC and PSO methods. Testing on IEEE 30-bus system demonstrates that the proposed approach results in a greater reduction in active power transmission losses and allows more secure operation. Although only one scenario with eight FACTS devices was studied, other scenarios that use more or less FACTS devices are feasible using the proposed approach.

Acknowledgments Financial supports from the National Science Council, Taiwan, R.O.C. under the Grant No. NSC 101-2221-E-168-045 are acknowledged.

References

1. Abdel-Moamen, M. A., & Padhy, N. P. (2003). Power flow control and transmission loss minimization model with TCSC for practical power networks. *Proceedings of IEEE Power Engineering Society General Meeting*, *2*, 880–884.
2. Xiao, Y., Song, Y. H., Liu, C. C., & Sun, Y. Z. (2003). Available transfer capability enhancement using FACTS devices. *IEEE Transaction on Power Systems, 18*(1), 305–312.
3. Saravanan, M., Slochanal, S. M. R., Venkatesh, P., & Prince Stephen Abraham, J. (2007). Application of particle swarm optimization technique for optimal location of FACTS devices considering cost of installation and system loadability. *Electrical Power System Research*, *77*(3–4), 276–283.
4. Hao, J., Shi, L. B., & Chen, C. (2004). Optimising location of unified power flow controllers by means of improved evolutionary programming. *IEE Proceedings—Generation, Transmission and Distribution*, *151*(6), 705–712.
5. He, S., Wu, Q. H., & Saunders, J. R. (2009). Group search optimizer: An optimization algorithm inspired by animal searching behavior. *IEEE Transaction on Evolution Computation, 13*(5), 973–990.
6. Zhao, B., Guo, C. X., & Cao, Y. J. (2005). A multiagent-based particle swarm optimization approach for optimal reactive power dispatch. *IEEE Transaction on Power Systems, 20*(2), 1070–1078.

Chapter 72
Bridge's Scour Monitoring System

Yuan Ping Luh and Ying Chang Liu

Abstract The scour of pier in riverbed is one of the major causes for bridge failure. The riverbed around the pier footing can be eroded in scouring event. Erosion of soil around the bridge foundation could lead to problems from instability of substructure to complete bridge failures. An effective scour risk countermeasure is to deploy bridge scour monitoring system. It is difficult to measurement and monitor the depth variation of scouring at piers, especially during flood event. In this paper, a bridge's scour monitoring system is proposed. It is integrated with RFID, Wireless Charging and Geographic Information System (GIS) technology. The prototype system was installed in field and successful work in 2010. It demonstrates the adoptability and potential of this system.

Keywords Scour · Bridge failure · RFID

72.1 Introduction

Scour is defined as the erosion or removal of streambed or bank material from bridge's foundations due to flowing water [1]. Although it may be greatly affected by the presence of structures encroaching on the channel, scour is a natural phenomenon caused by the flowing of water over an erodent boundary. Scour at bridge piers has long been recognized as an issue of considerable importance as it pertains to pier hydraulic design, according to a large number of scour studies conducted over the past 10 years. The current study, which was based on field evaluations of pier scour failures in rivers with cohesionless beds, focused on a general view of the scouring process [2]. Flood flow in natural rivers scours the river bed and

Y. P. Luh · Y. C. Liu (✉)
Graduate Institute of Mechanical and Electrical Engineering, National Taipei University of Technology, Taipei 10608, Taiwan, Republic of China
e-mail: flag.liu@gmail.com

J. Juang et al. (eds.), *Proceedings of the 2nd International Conference on Intelligent Technologies and Engineering Systems (ICITES2013)*, Lecture Notes in Electrical Engineering 293,
DOI: 10.1007/978-3-319-04573-3_72,

Table 72.1 Comparison of existing instrument for measuring bridge scour

Instrument	Advantages	Disadvantages or limitations	Cost
RFID	Monitor depth; extensive area monitor integrated GIS		Medium
Bridge mounted sonar	Monitor depth	Mild slope river/estuary; gravel or sandstone interference	Medium
Acoustic Doppler	Monitor velocity and depth	Not applicable to high sediment concentration condition	High
Ground penetrating radar	Monitor depth	More time consuming; specialized training required	High
Fiber Bragg grating	Monitor depth	Avoid stone or rock hitting	High
Numbered bricks	Applicable to high turbulent or rapid flows	Excavation of riverbed required suitable for ephemeral rivers	Low

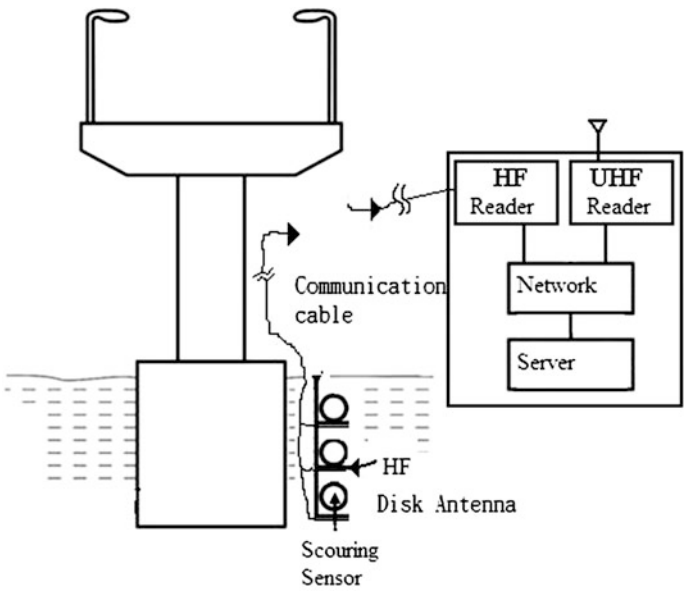

Fig. 72.1 Bridge's scour monitoring system architecture

creates large holes around bridge piers that gradually extend beneath them, eventually destroying them.

More than 1000 bridges have collapsed over the past 30 years in the U.S.A., with 60 % of the failures due to scour [3]. Many bridges will experience floods which can cause damage each year. To minimize future bridge flood damage and ensure public safety requires developing and implementing real-time monitored

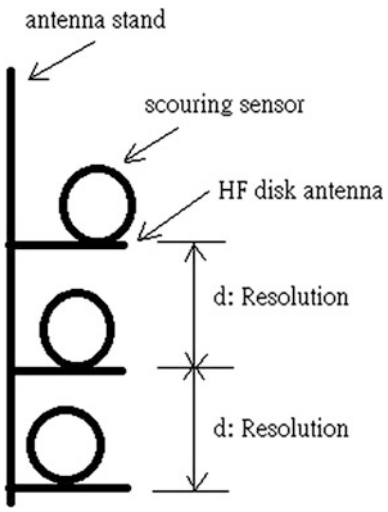

Fig. 72.2 Antenna stand

system for scour. But it is difficult to measure or monitor the depth variations of scouring at piers, especially during flood event. Erosion of soil around the bridge foundation could lead to problems from instability of substructure to complete bridge failures. An effective scour risk countermeasure is to deploy bridge scour monitoring system.

There are many techniques, and practices available for countering scour [4–8]. They have compared the advantages, disadvantages or limitations, and relative costs of existing instruments for measuring bridge scour in Table 72.1.

72.2 System Architecture

The system architecture is shown as Fig. 72.1. This system consists of Sensors, HF disk antenna, RFID HF readers, UHF Antenna, RFID UHF readers and application server. The HF disk antenna provides wireless charging and communication function to several sensors. And the UHF antenna is used to receive sensors' signal. The application server links RFID HF reader and RFID UHF readers via Ethernet. It is adopted Geographic Information System (GIS) to monitor sensors' working status and location.

72.2.1 Antenna Stand

As Fig. 72.2 to shown, the antenna stand consists of several HF disk antennas. Each HF disk antenna interval is relative to scouring depth sensing (d: measuring

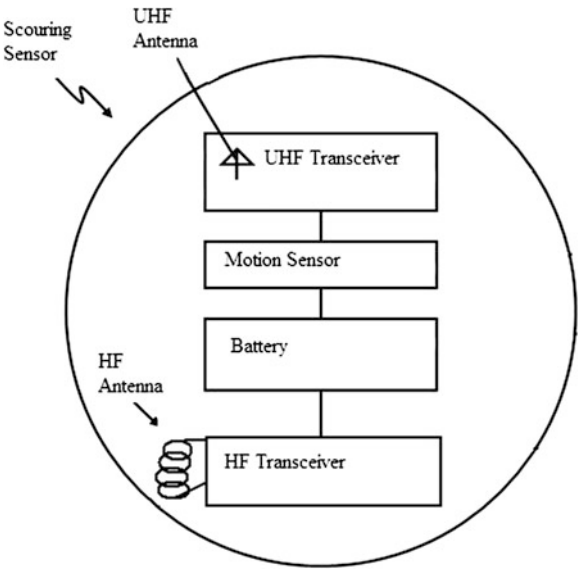

Fig. 72.3 Scouring sensor composition

resolution). Normally, the antenna stand is buried in riverbed. For example, the scouring sensor A was buried under riverbed at 3 m. If the scouring sensor A was scoured to water surface, it means the scouring depth more than 3 m in flood. It can make HF disk antenna intervals to adjust monitoring resolution of scouring depth.

72.2.2 Scouring Sensors

As Fig. 72.3 to shown, the scouring sensor consists of UHF antenna, UHF transceiver, motion sensor, battery, HF antenna and HF transceiver. The HF transceiver communicates with scour monitoring system and gets energy via HF antenna. Normally, the scouring sensor was put on HF disk antenna. The system can communicate with scouring sensors via external HF disk antennas and internal HF antenna. The Sensor looks like a ball and can float in the water. Its battery keeps one side, another side located UHF transceiver's antenna. This setup lets scouring sensor like a tumbler ball in the water. When the bridge foundation scouring by a flood, the sensor will be flushed and surfaced. And there is a motion detector inside of the scouring sensor, the UHF transceiver will be waked up to work. The scouring sensor can like a tumbler ball that float and transmission data on the water surface. See Fig. 72.4.

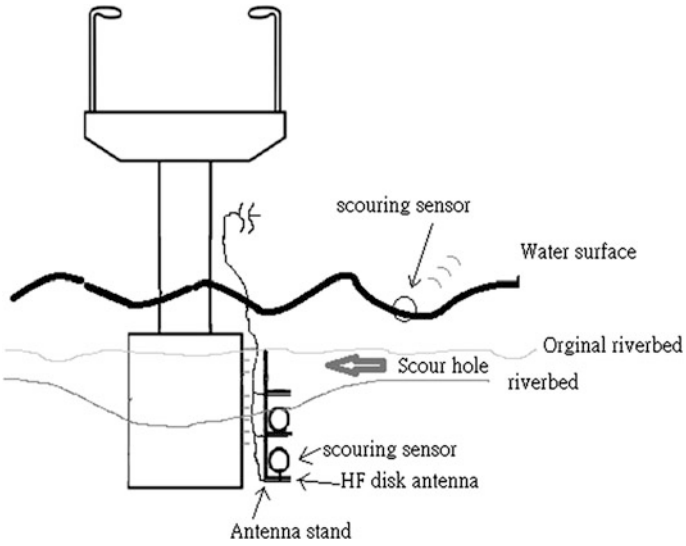

Fig. 72.4 Scouring sensor working scenario

72.2.3 Scour Monitor Server

The scour monitor server links RFID HF readers and RFID UHF readers. Each scouring sensor has HF tag's ID and UHF tag's ID. And the IDs data are registered in server database. This server combines with Geographic Information System (GIS) and IDs database. The UHF ID of scouring sensor is an index. When scouring sensor was waked up in the water, the RFID UHF readers will receive its ID. And system server got the ID data to mapping registered information (GPS address, bridge name, pier Number and buried depth). Finally, the system will display the map, information and alarm (buried depth >= scour depth threshold).

The server has at least one RFID HF reader because each bridge has more than one pier. And in this practice, the system has installed seven RFID UHF readers at river side. The interval distance of the RFID UHF readers is 150 m. If scouring sensors had scoured out, they could have received RF signal from scouring sensors. This configuration is necessary. Because the scouring sensor was scoured out in that time, it may be or not to float on water. It may drift a period in the water. If the system designer has not to extend receiving area or distance, it will lose the sensor signal.

Fig. 72.5 Scouring sensor worked during TALIM typhoon flood in 2012

72.3 Practice Result

The system was installed at Yufeng bridge in the upstream of Dahan river. The monitoring depth resolution is 1 m. And the top scouring sensor was installed 1 m under riverbed. The scour monitoring result is shown in Fig. 72.5 during TALIM typhoon flood in 2012, Taiwan. The scour monitoring system has received data from scouring sensor #A, #B and #A1. It means the Yufeng bridge's pier #2 and #3 was scouring at that time. And scouring depth of the pier #2 had 2 m at least under riverbed.

It is shown in Fig. 72.6 that the server received RF signal status from scouring sensors during TALIM typhoon raided TAIWAN. The server links seven RFID UHF readers of river side via WIFI and Ethernet network. The RF signal strength of scouring sensor should be reach to −12 dB for system design. In fact, the signal strength was smaller. Because the water of rain in the air and mud–water in the river could destroy and attenuate the RF signal.

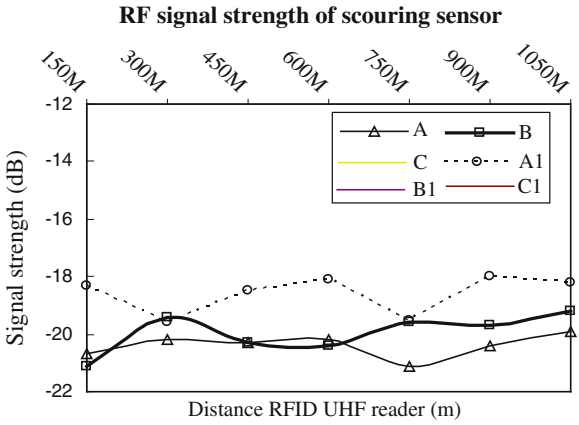

Fig. 72.6 RF signal status from scouring sensors

72.4 Conclusion

The scour of pier in riverbed is one of the major causes for bridge failure. The riverbed around the pier footing can be eroded in scouring event. Erosion of soil around the bridge foundation could lead to problems from instability of substructure to complete bridge failures. But it is difficult to measure or monitor the depth variations of scouring at piers, especially during flood event. In this paper, it is shown that the scour monitoring system has demonstrated the capability to measure scouring depth and alarm. The field result indicates that scour monitoring system using scouring sensor and antenna stand has the potential for real world application.

References

1. John, K., & Merv, E. (1998). *Bridge scour evaluation: Screening, analysis, and countermeasures*. Technical report, San Dimas, CA: Technology and Development Center.
2. Behzad, G. (2008). A field study of scour at bridge piers in flood plain rivers. *Turkish Journal of Engineering and Environmental Sciences*, *32*, 189–199.
3. Deng, L., & Cai, C. (2010). Bridge scour: Prediction, modeling, monitoring, and countermeasures—review. *Practice Periodical on Structural Design and Construction*, *15*(2), 125–134.
4. Sheppard, D. M., & William, M, Jr. (2006). Live-bed local pier scour experiments. *Journal of Hydraulic Engineering Division of the American Society of Civil Engineers, 132*(7), 635–642.
5. Millard, S. G., Bungey, J. H., Thomas, C., Soutsos, M. N., Shaw, M. R., & Patterson, A. (1998). Assessing bridge pier scour by radar. *NDT International*, *31*(4), 251–258.
6. Deng, L., & Cai, C. (2010) Bridge scour: Prediction, modeling, monitoring, and countermeasures—review. *Practice Periodical on Structural Design and Construction*, *15*(2), 125–134.
7. Yu, X., & Yu, X. (2007). Algorithm for time domain reflectometry bridge scour measurement system. In *Proceedings 7th International Symposium on Field Measurements in Geomechanics, FMGM, Boston* (pp. 1–10).
8. Deng, L., & Cai, C. S. (2007). Application of fiber optic sensor in civil engineering. *Structural Engineering* and *Mechanics*, *25*(5), 577–596.

Chapter 73
Intelligent Approaches for Vibration Fault Diagnosis of Steam Turbine-Generator Sets

Yann-Chang Huang, Chien-Yuan Liu and Chao-Ming Huang

Abstract To enhance diagnosis accuracy of vibration faults for steam turbine-generator sets (STGS), this paper presents evolutionary programming-based radial basis function (EP-RBF) networks. The proposed EP automatically determine the optimal parameters for the RBF network, which includes the number of neurons in the hidden layer, the centers of hidden neurons, the spread parameters, and the weights in the output layer of the RBF network. The test results demonstrate that the proposed EP-RBF network has a higher diagnostic accuracy than the RBF network and multilayer perceptron (MLP) network trained by error back-propagation algorithm. Moreover, this paper reveals that the proposed EP-RBF network can apply to effectively diagnose vibration fault of STGS.

Keywords Intelligent approaches · Fault diagnosis · Steam turbine-generator sets

73.1 Introduction

Artificial intelligence (AI)-based methods have been used to diagnose vibration faults of STGS, which include expert systems, fuzzy logic systems, and artificial neural networks (ANNs). The expert systems [1, 2] combined an inference engine

Y.-C. Huang (✉)
Department of Electrical Engineering, Cheng Shiu University, Kaohsiung, Taiwan, Republic of China
e-mail: huangyc@csu.edu.tw

C.-Y. Liu
Department of Computer Science and Information Engineering, Cheng Shiu University, Kaohsiung, Taiwan, Republic of China

C.-M. Huang
Department of Electrical Engineering, Kun Shan University, Tainan, Taiwan, Republic of China

J. Juang et al. (eds.), *Proceedings of the 2nd International Conference on Intelligent Technologies and Engineering Systems (ICITES2013)*, Lecture Notes in Electrical Engineering 293,
DOI: 10.1007/978-3-319-04573-3_73,

with a range of knowledge to develop guidelines for fault diagnosis of STGS; however, design an efficient inference engine to draw conclusions from a large body of rule-based knowledge is difficult, and the inference processes are time-consuming.

Fuzzy logic systems [3, 4] were expressed in imprecise linguistic terms; they have been developed to solve vibration fault problems with uncertain and inaccurate information. However, like an expert system, a fuzzy system depends heavily on the operators' experience to determine the fuzzy inference rules and their associated membership functions. Therefore, practical vibration fault data collected from a machine may not be applied to solve the diagnosis problems.

The ANNs [5, 6] captured complex input–output relations with well interpolated and extrapolated capabilities; they provided real-time response in practical applications. Although ANNs have been successfully applied to diagnose vibration faults of STGS, some problems remain unsolved, including the local and slow convergence during training, and determining network structure and parameters.

Support vector machines (SVMs) adopted the best hyperplane to extract the feature from linear or nonlinear data [7, 8]; however, determining a best hyperplane in SVM is often difficult and depends strongly on the operators' experience or trial-and-error experiments. Moreover, to enhance the effectiveness of PSO [9] in designing the optimal SVM model, an enhanced PSO algorithm was presented to increase the diagnosis accuracy of fault in STGS [8]. In comparison with MLP network trained by error back-propagation algorithm, the RBF network [10] had a more compact topology and requires less training time. However, the performance for such a simple mechanism to deal with complex vibration fault diagnosis problems in a STGS must be further evaluated.

73.2 The Intelligent Approaches

Vibration signals are often used to evaluate the operating status of the STGS. Mechanical vibration of the STGS is caused by misalignment of the rotor, rotor unbalance, loose bearings, rubbing, oil whirl, and steam whirl. In this paper, signals associated with mechanical vibration were used as basic data to train the EP-RBF network. Then, the trained network was adopted to diagnose faults in a STGS. Figure 73.1 presents the structure of the intelligent approaches that describes as follows.

73.2.1 The RBF Network

An RBF network is similar to multilayer perceptron (MLP) network with three layers (input, hidden layer, and output) [11]. The major difference between the RBF network and the MLP network is that an RBF network does not use raw input

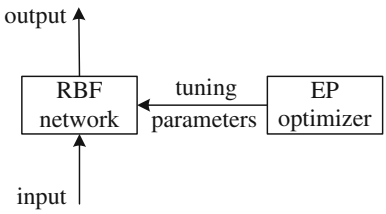

Fig. 73.1 The structure of the proposed intelligent approaches

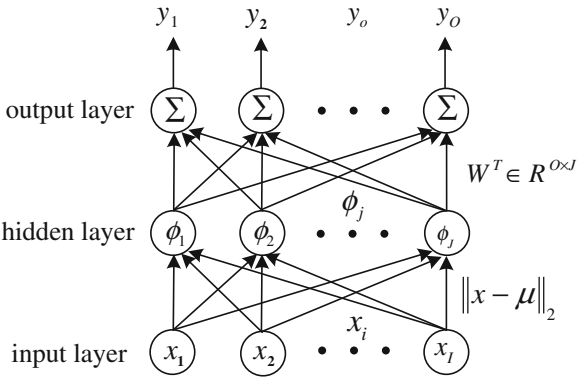

Fig. 73.2 The structure of the RBF network

data, but rather passes a distance measure from the inputs to the hidden layer. This distance is measured from some center value in the range of the variables to a given input value about a Gaussian function. The number of input nodes depends on the dimensionality of the input vector; that of hidden nodes equals the number of basis functions used in the network; that of output nodes equals the number of distinct classes.

Figure 73.2 shows the structure of the RBF network. The input and output layers of the RBF network are presented with training pairs, each consisting of a vector from an input space and a desired network output. The error between the actual and desired output is minimized according to the supervised learning algorithm and optimization criterions. As shown in Fig. 73.2, the oth output node of the RBF network can be described as

$$y_o = \sum_{j=1}^{J} \varphi_j\left(\|x-\mu_j\|_2\right) \times w_{oj}, = 1, 2, \ldots, O \tag{73.1}$$

where $x \in R^{I\times 1}$ is an input vector, $\mu_j \in R^{J\times 1}$ are the RBF network centers in the input vector space, $\|\bullet\|_2$ denotes the Euclidean norm, $\varphi_j(x) = \exp(-x^2/\sigma^2)$ is the Gaussian function of the jth center with spread parameter σ, and $w_{oj} \in R^{O\times J}$ are the weights between hidden and output layers.

Four sets of parameters govern the mapping properties of the RBF network: the number of hidden nodes, the centers of hidden neurons, the spread parameters, and the weights in the output layer. A sufficient number of centers are randomly chosen

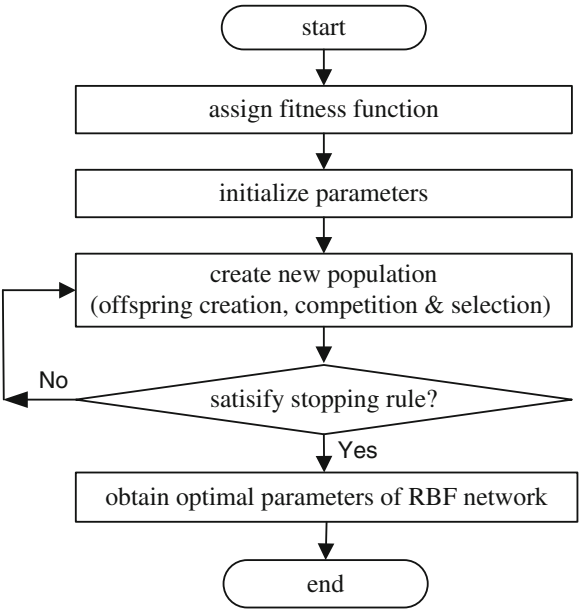

Fig. 73.3 Flowchart of the evolutionary programming algorithm

as a subset of the input space according to the probability density function of the training data. Then the gradient approach is used to tune the weights in the output layer. The disadvantage of this method is that it is prone to fall into the local minimum. Therefore, the EP algorithm was adopted to tune the parameters.

73.2.2 The EP Algorithm

The proposed evolutionary programming [12] determine the optimal parameters for the RBF network, which includes the number of neurons in the hidden layer, the centers of hidden neurons, the spread parameters, and the weights in the output layer of the RBF network. Figure 73.3 presents flowchart of the evolutionary programming algorithm. The proposed evolutionary programming with global search ability can simultaneously determine the optimal parameters for the RBF network, while avoiding the limitation of the gradient-descent technique.

73.3 Results and Discussion

This paper presented the fault vibration signals to identify the faults in a STGS using the EP-RBF network. A total of 90 samples, as shown in Table 73.1, collected from [8] was used to train and test the diagnosis accuracies of the proposed approach. Each sample contains eight input features and one fault class. The eight

Table 73.1 The 90 test dada for vibration fault of STGS

No.	Frequency bands (B)								Fault type
	b_1	b_2	b_3	b_4	b_5	b_6	b_7	b_8	
1	0.01	0.02	0.01	0.03	0.42	0.55	0.08	0	Misalignment
…	…	…	…	…	…	…	…	…	
15	0.02	0	0.02	0.01	0.39	0.58	0.12	0.04	
16	0.01	0.04	0.02	0.05	0.7	0.17	0.22	0.1	Unbalance
…	…	…	…	…	…	…	…	…	
30	0.05	0.03	0.03	0.06	0.85	0.25	0.27	0.13	
31	0.93	0.01	0.02	0	0.05	0.07	0	0.15	Looseness
…	…	…	…	…	…	…	…	…	
45	0.87	0.05	0.04	0.01	0.08	0.02	0.03	0.2	
46	0.08	0	0.05	0.18	0.29	0.12	0.13	0.19	Rubbing
…	…	…	…	…	…	…	…	…	
60	0.17	0.2	0.09	0.15	0.32	0.18	0.23	0.17	
61	0.06	0.91	0.12	0.08	0.18	0.01	0.03	0.14	Oil whirl
…	…	…	…	…	…	…	…	…	
75	0.02	0.69	0.1	0.09	0.15	0.01	0.02	0.12	
76	0.08	0.06	0.1	0.47	0.08	0.35	0.23	0.08	Steam whirl
…	…	…	…	…	…	…	…	…	
90	0.12	0.06	0.09	0.42	0.19	0.39	0.28	0.1	

input features represent the vibration amplitudes of different frequency bands: $<0.4f$, 0.4–0.49f, 0.5f, 0.51–0.99f, f, 2f, 3–5f, and $>5f$, which expressed by an input vector $B = [b_1, b_2, \ldots, b_8]$. The six typical mechanical vibration faults are misalignment, unbalance, looseness, rubbing, oil whirl, and steam whirl. To verify the diagnosis accuracy of the EP-RBF network, the performance was compared with that of the RBF and the MLP network methods, using the same database.

In the test cases, all of the parameters for the MLP and the RBF networks were determined by experience or by trial-and-error experiments. For the MLP network, 10 neurons were selected in the hidden layer; learning rate was set to 0.01 for training by a steepest-descent gradient algorithm. The spread parameter of the RBF network was set to 0.5; 10 neurons were chosen in the hidden layer. For the RBF and the EP-RBF networks, the maximum number of iterations was set to 5,000; the goal was set to 10^{-5}.

The diagnostic accuracies of the MLP, the RBF, and the proposed EP-RBF networks with different training and testing samples are compared in Table 73.2. The results indicate that these methods obtained 100 % accuracy for historical training data. For all models, the test accuracies were improved with increasing training samples, and the ratio of training to testing samples with 2:1 obtained the best diagnosis accuracy. The proposed EP-RBF achieved 93.33 % accuracy and outperformed the RBF and the MLP networks. Moreover, the best spread parameter of the EP-RBF network was 0.45, and the best number of neuron in hidden layer was 15. The average time ratio required to construct the diagnostic models for the MLP, the RBF, and the EP-RBF networks was 1:0.06:1.51. The

Table 73.2 Diagnosis accuracy of different models

Network	Ratio of training to testing samples	Training accuracy (%)	Testing accuracy (%)
MLP	1 : 2	100	83.33
	1 : 1	100	84.44
	2 : 1	100	86.67
RBF	1 : 2	100	81.67
	1 : 1	100	82.22
	2 : 1	100	83.33
EP-RBF	1 : 2	100	86.67
	1 : 1	100	88.89
	2 : 1	100	93.33

time required to construct the diagnostic model using the EP-RBF network was slightly longer than that required for the other networks.

73.4 Conclusions

This paper has proposed the EP-RBF network to diagnose vibration faults of STGS. The proposed EP automatically determines the optimal parameters for the RBF network, which includes the number of neurons in the hidden layer, the centers of hidden neurons, the spread parameters, and the weights in the output layer of the RBF network. The following conclusions can be derived from this paper:

(1) The RBF network trained much faster than the MLP; however, the RBF network generally cannot quite achieve the accuracy of the MLP network.
(2) The MLP and the RBF networks trained by the gradient-based algorithm seem prone to becoming stuck in a local minimum. The proposed EP-RBF network obtains a higher diagnostic accuracy than the MLP and the RBF networks.
(3) The test results demonstrate that EP increases the diagnostic accuracy of the EP-RBF and improves the existing disadvantages of the RBF network.

Acknowledgments Financial supports from the National Science Council, Taiwan, R.O.C. under the Grant No. NSC 102-2221-E-230-006 are acknowledged.

References

1. Kirk, R. G., & Guo, Z. (2003). Expert system source identification of excessive vibration. *International Journal of Rotating Machinery, 9*, 63–79.
2. Yang, B. S., Lim, D. S., & Tan, A. C. C. (2005). VIBEX: An expert system for vibration fault diagnosis of rotating machinery using decision tree and decision table. *Expert Systems with Applications, 28*, 735–742.

3. Zhang, X., Miao, X., & Zhu, J. (2000). A study on fuzzy neural network diagnosis modeling. *Journal of Aerospace Power, 15*, 196–200.
4. Zhang, S., Asakura, T., Xu, X., & Xu, B. (2003). Fault diagnosis system for rotary machines based on fuzzy neural networks. In *Proceedings of the 2003 IEEE/ASME International Conference on Advance Intelligent Mechatronics* (pp. 199–204).
5. Wang, C. C., Kang, Y., Shen, P. C., Chang, Y. P., & Chung, Y. L. (2010). Applications of fault diagnosis in rotating machinery by using time series analysis with neural network. *Expert Systems with Applications, 37*, 1696–1702.
6. De Moura, E. P., Souto, C. R., Silva, A. A., & Irmao, M. A. S. (2011). Evaluation of principal component analysis and neural network performance for bearing fault diagnosis from vibration signal processed by RS and DF analyses. *Mechanical Systems and Signal Processing, 25*, 1765–1772.
7. Baccarini, L. M. R., Silva, V. V. R., De Menezes, B. R., & Caminhas, W. M. (2011). SVM practical industrial application for mechanical faults diagnostic. *Expert Systems with Applications, 38*, 6980–6984.
8. Sun, H. C., Huang, C. M., & Huang, Y. C. (2013). Fault diagnosis of steam-generator sets using an EPSO-based support vector classifier. *IEEE Transaction on Energy Conversion, 28*, 164–171.
9. Hsu, C. W., & Lin, C. J. (2002). A comparison of methods for multi-class support vector machines. *IEEE Transaction on Neural Network, 13*, 415–425.
10. Kennedy, J., & Eberhart, R. (1995). Particle swarm optimization. *IEEE International Conference on Neural Networks, 4*, 1942–1948.
11. Meng, K., Dong, Z. Y., Wang, D. H., & Wong, K. P. (2010). A self-adaptive RBF neural network classier for transformer fault analysis. *IEEE Transaction on Power Systems, 25*, 1350–1360.
12. Fogel, D. B. (1994). An introduction to simulated evolutionary optimization. *IEEE Transaction on Neural Networks, 5*, 3–14.

Chapter 74
Uniform Design and Kriging Surrogate Modeling in Improvement of Warpage and Ejection Time of an Injection Molded Plastic Spur Gear

Cheng-Kang Lee and Pang-Chieh Lin

Abstract This paper aims to present the application of uniform design of experiments, mold flow analysis, Kriging surrogate modeling, and optimization algorithms to the improvement of warpage and ejection time of an injection molded plastic spur gear. Firstly, uniform design method is applied to build a set of experiments. Secondly, for each experiment, simulation software Moldflow is employed to analyze the warpage distribution and ejection time of the plastic spur gear. Thirdly, Kriging surrogate modeling method is applied to construct the maximum warpage and ejection time surrogate models. Fourthly, a genetic algorithm and a sequential quadratic programming algorithm are used to solve the optimal solutions of parameters minimizing the maximum warpage surrogate model. Finally, a verification experiment is executed in Moldflow to ensure that the optimal solutions determined via surrogate model can act as near-optimal solutions to the real problem.

Keywords Ejection time · Kriging · Plastics injection molding · Spur gear · Uniform design · Warpage

74.1 Introduction

Injection molding is the most commonly used manufacturing process for fabricating plastic parts by injecting molten plastics into a mold. A wide variety of products can be manufactured by injection molding. Influenced by shrinkage effect, the shape of part finally obtained is usually different from the shape of cavity in the mold. It is necessary to optimize process parameters to reduce their

C.-K. Lee (✉) · P.-C. Lin
Department of Industrial Engineering and Management, Cheng Shiu University, Kaohsiung 833, Taiwan
e-mail: leeck588@csu.edu.tw

J. Juang et al. (eds.), *Proceedings of the 2nd International Conference on Intelligent Technologies and Engineering Systems (ICITES2013)*, Lecture Notes in Electrical Engineering 293,
DOI: 10.1007/978-3-319-04573-3_74,

difference. Much work has been done on the improvement of warpage problems [1–4]. However, little is known about using uniform design, Kriging surrogate modeling, and optimization algorithms to deal with warpage problems. Besides, the production cost of an injection molded part is proportional to the cycle time, which can be broken down into the injection time, cooling time, and resetting time. As long as the cycle time is reduced, cost can be reduced and efficiency can be advanced. This paper employs the uniform design method, injection molding simulation software Moldflow, Kriging surrogate modeling technique, genetic and sequential quadratic programming algorithms to improve the warpage and ejection time of an injection molded plastic spur gear.

74.2 Injection Molding Simulation of a Plastic Spur Gear

The injection molded part is an involute spur gear with a module of 5 mm, a pressure angle of 20°, a tooth face width of 10 mm, and 14 teeth. The injection molding simulation software Moldflow is employed to analyze the warpage and ejection time of the injection molded part. Since to create a solid model of spur gear in Moldflow is difficult, it is suggested to apply professional CAD software such as AutoCAD or SolidWorks. This paper uses SolidWorks to create the solid model of spur gear. In Moldflow, the model created in SolidWorks is imported using the IGES file exchange format. According the result of gate location analysis, four gates are designed in the central hole of gear. Figure 74.1 shows the designed runner system and the cooling water channels. The runner system is composed of a sprue and four gates. The diameters of sprue on the top and bottom ends are 2.8 and 6 mm, respectively. The diameter of gate in the sprue side is also 6 mm. The diameter of gate in the part side is 2.4 mm. The diameters of all cooling water channels are 5 mm. The distance from the central line of cooling water channel to the side surface of gear is 7 mm. The gear is meshed by 3D volume elements since it is not a thin-shell part. The number of elements is 84165. The maximum value of aspect ratio is 25. Since 25 is smaller than 30, the mesh of part is a qualified mesh.

The polymer to be injected is PA 66. The trade name of the polymer is Zytel 101 F NC010 DAM, which is manufactured by DuPont. The range of melt temperature suggested by DuPont is from 260 to 360 °C. The part is molded at the following conditions. The melt temperature is 290 °C. The fill time is 1 s. The V/P switchover is 99 % volume filled. The packing pressure curve is composed of a horizontal line and an oblique line. The horizontal line is provided with a height of 85 % of maximum pressure and a lasting time of 2 s. The oblique line is provided with a lasing time of 2 s. In other words, the total time of packing pressure phase is 4 s. Before packing pressure is released, all gates are frozen totally. The temperature of cooling water is 25 °C. Under such molding conditions, warpage distribution of the molded gear is analyzed by Moldflow and is shown in Fig. 74.2. The maximum warpage is 0.7403 mm. The ejection time, which is defined by the time to reach ejection temperature, is 102.3 s.

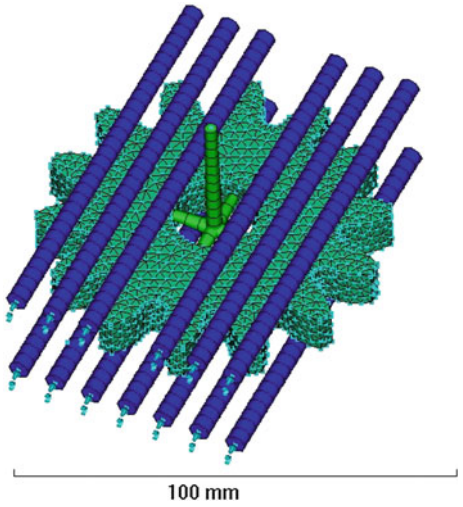

Fig. 74.1 The model created in Moldflow

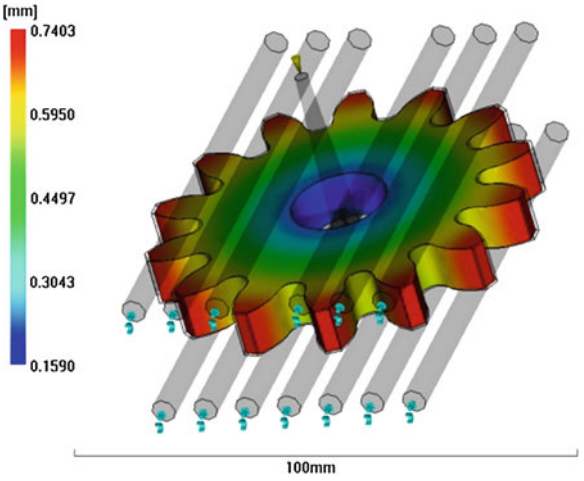

Fig. 74.2 Warpage distribution

74.3 Improvement of Warpage and Ejection Time

74.3.1 Uniform Design of Experiments

Uniform design, proposed by Fang [5] and Wang and Fang [6], is a kind of space filling design method and is able to construct a set of experimental points uniformly scattered in the continuous design space of design parameters. Unlike the orthogonal design, the uniform design only considers the uniform distribution rather than symmetrical comparability of the experiment points. The uniform design is very suitable for the problem with multiple factors which have multiple levels.

Table 74.1 Definitions, units, and ranges of process parameters

Parameter	Definition	Unit	Range
A	Diameter of sprue in the lower end	mm	4–8
B	Melt temperature	°C	260–300
C	Diameter of sprue in the upper end	mm	2–3.6
D	Temperature of cooling water	°C	20–40
E	Diameter of gate in the end near cavity	mm	1.6–3.2
F	Fill time	s	0.8–1
G	Height of the horizontal packing pressure curve	%	80–90

Table 74.2 Uniform table $U_{12}^{*}(12^{7})$ and allocation of parameters

Exp.	A	B	C	D	E	F	G
1	1	6	8	2	9	10	12
2	2	12	3	4	5	7	11
3	3	5	11	6	1	4	10
4	4	11	6	8	10	1	9
5	5	4	1	10	6	11	8
6	6	10	9	12	2	8	7
7	7	3	4	1	11	5	6
8	8	9	12	3	7	2	5
9	9	2	7	5	3	12	4
10	10	8	2	7	12	9	3
11	11	1	10	9	8	6	2
12	12	7	5	11	4	3	1

The process parameters considered herein are shown in Table 74.1. As there are seven parameters, the uniform design table applied here is $U_{12}^{*}(12^{7})$, which is shown in Table 74.2. All parameters are divided into 12 levels in their own ranges. The experiments planned by using $U_{12}^{*}(12^{7})$ are shown in Table 74.3. Each experiment represents a deterministic processing scenario. The injection molding simulation software Moldflow is also employed to analyze the warpage and ejection time for each experiment. The results of experiments are shown in Table 74.4. It can be found that experiment 11 has the smallest maximum warpage and the smallest ejection time.

74.3.2 Surrogate Modeling and Optimization of Process Parameters

With the data given in Tables 74.3 and 74.4, the surrogate models of the maximum warpage and ejection time can be created based on the Kriging surrogate modeling method. Kriging, named after the South African mining engineer D. C. Krige, is a

Table 74.3 The experiments planned by using uniform table $U_{12}^{*}(12^{7})$

Exp.	A	B	C	D	E	F	G
1	4	278.182	3.018	21.818	2.764	0.96364	90
2	4.364	300	2.291	25.455	2.182	0.90909	89.09
3	4.727	274.545	3.455	29.091	1.6	0.85455	88.18
4	5.091	296.364	2.727	32.727	2.909	0.8	87.27
5	5.455	270.909	2	36.364	2.327	0.98182	86.36
6	5.818	292.727	3.164	40	1.745	0.92727	85.45
7	6.182	267.273	2.436	20	3.055	0.87273	84.55
8	6.545	289.091	3.600	23.636	2.473	0.81818	83.64
9	6.909	263.636	2.873	27.273	1.891	1	82.73
10	7.273	285.455	2.145	30.909	3.200	0.94545	81.82
11	7.636	260	3.309	34.545	2.618	0.89091	80.91
12	8	281.818	2.582	38.182	2.036	0.83636	80

Table 74.4 Results of experiments analyzed by Moldflow

Exp.	Maximum warpage (mm)	Ejection time (s)
1	0.7133	92.75
2	0.7678	107.9
3	0.6863	95.81
4	0.7572	110.6
5	0.7043	98.06
6	0.7385	112.1
7	0.6954	88.88
8	0.7133	101
9	0.6844	89.29
10	0.7535	103.9
11	0.6660	88.17
12	0.7318	104.9

geo-statistical interpolation technique that considers both the distance and the degree of variation between known data points when estimating values in unknown area. Sacks et al. [7] proposed a framework for the construction of Kriging surrogate models for deterministic outputs of expensive computer experiments. This paper uses a free-of-charge Matlab toolbox, DACE software [8], to create the Kriging surrogate models of maximum warpage and ejection time. The Kriging model applied herein is ordinary Kriging and the correlation function applied herein is Gaussian function. Figure 74.3 shows the Kriging surrogate model of the maximum warpage. It can be found that the impact of parameter B is larger than the impact of parameter A.

Now that the maximum warpage surrogate model is obtained, the next step is to regard the minimization of the surrogate model as the objective function and apply optimization algorithms to find the optimal solutions of process parameters. In order not to fall in local optima, this paper applies an optimization strategy with two phases. The first is to apply a genetic algorithm to execute a global search.

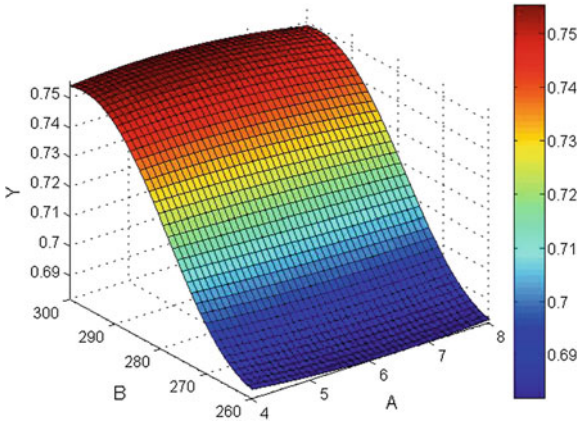

Fig. 74.3 Response surface plot of maximum warpage

Table 74.5 Optimal solutions of parameters

Parameter	Unit	Optimal	Original
A	mm	5.386	6
B	°C	260	290
C	mm	3.6	2.8
D	°C	20	25
E	mm	3.2	2.4
F	s	0.8	1
G	%	86.46	85

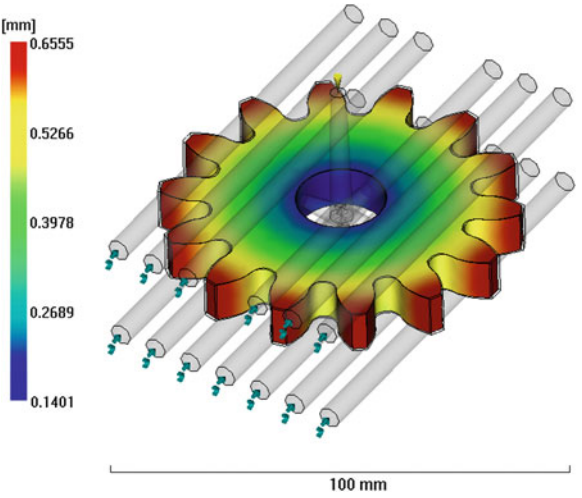

Fig. 74.4 Warpage distribution at the optimal solutions

The second is to apply a sequential quadratic programming algorithm to exploit the solutions found in the first phase. Table 74.5 shows the optimal solutions of process parameters. The minimized value of maximum warpage predicted by the

Table 74.6 Maximum warpage and ejection time in various states

State	Maximum warpage (mm)	Ejection Time (s)
Original design	0.7403	102.3
After executing uniform design	0.666	88.17
After executing surrogate modeling and optimization	0.6555	85.63

surrogate model is 0.6482 mm. At the optimal solutions, an injection molding simulation is executed in Moldflow again and the simulation value of maximum warpage is 0.6555 mm as shown in Fig. 74.4. The difference between the predicted value and the simulation value is just 1.1 %. Therefore, the optimal solutions are acceptable. Table 74.6 shows the improvement of maximum warpage and ejection time. The maximum warpgage deformation is reduced from 0.7403 to 0.6555 mm. The ejection time is also reduced from 102.3 to 85.63 s.

74.4 Conclusions

This paper has presented a systematic process which integrates the uniform design method, simulation of plastics injection molding, Kriging surrogate modeling, and optimization algorithms to improve the warpage problem of an injection molded part, a plastic spur gear. The injection molded spur gear has a larger warpage and a longer ejection time if process parameters are not optimized. After executing the experiments planed by the uniform design, the maximum warpage has an improvement rate of 10.03 % and the ejection time has an improvement rate of 13.8 %. After executing surrogate modeling and optimization, the warpage improvement rate will go up to 11.45 % and the ejection time improvement rate will go up to 16.29 %. The presented process is a general process, which can be applied to other manufacturing problems.

References

1. Hwang, M. C., & Tai, C. C. (2001). The effective factors in the warpage problem of an injection-molded part with a thin shell feature. *Journal of Materials Processing Technology, 110*, 1–9.
2. Liao, S. J., Chang, D. Y., Chen, H. J., Tsou, L. S., Ho, J. R., Yau, H. T., et al. (2004). Optimal process conditions of shrinkage and warpage of thin-wall parts. *Polymer Engineering and Science, 44*, 917–928.
3. Liao, S. J., Hsieh, W. H., Wang, J. T., & Su, Y. C. (2004). Shrinkage and warpage prediction of injection-molded thin-wall parts using artificial neural networks. *Polymer Engineering and Science, 44*, 2029–2040.

4. Erzurumlu, T., & Ozcelik, B. (2005). Minimization of warpage and sink index in injection-molded thermoplastic parts using taguchi optimization method. *Materials and Design, 27*, 853–861.
5. Fang, K. T. (1980). The uniform design: Application of number theoretic methods in experimental design. *Acta Mathematicae Applicatae Sinica, 3*, 363–372.
6. Wang, Y., & Fang, K. T. (1981). A Note on Uniform Distribution and Experimental Design. *Kexue Tongbao, 26*(6), 485–489.
7. Sacks, J., Welch, W. J., Mitchell, T. J., & Wynn, H. P. (1989). Design and analysis of computer experiments. *Statistical Science, 4*, 409–435.
8. Lophaven, S.N., Nielsen, H.B., & Søndergaard, J. DACE a matlab Kriging toolbox, http://www.imm.dtu.dk/∼hbn/dace/.

Chapter 75
10 Bit 1.5b/Stage Pipeline ADC Design for Video Application

Chin-Fa Hsieh, Chun-Sheng Chen and Jimmy Lin

Abstract This paper proposes a design of a 10-bit fully differential pipeline analog-to-digital converter (ADC). The main component of this ADC is the sample and hold (S/H) circuit and eight stages of 1.5 bit sub-ADC and a 1.5 bit flash ADC. This ADC is designed by using TSMC 0.18 μm single-poly, six-metal CMOS process. It operates by 3.3 V power supply and at 10 MHz sampling frequency. The simulation results show that signal-to-noise ratio (SNR), differential nonlinearity (DNL), integral nonlinearity (INL) are 58.29 dB, −0.604–0.286 LSB, and −0.399–1.413 LSBs, respectively.

Keywords Pipeline ADC · Flash ADC · Sample and hold · DNL · INL

75.1 Introduction

Analog to digital converters (ADC) which can convert a measured analog signal to a digital representation play a very important role in an electronic systems. The performance of ADC is usually evaluated based on its speed and resolution. With high speed and resolution, an ADC enhances a system performance, which can be applied in many fields. For example, a direct-conversion ADC (flash ADC) provides the highest conversion rate by using $2^n - 1$ comparators to convert an analog signal into a digital signal in parallel, in which the comparator generates a code for each voltage range. Though it achieves very high-speed conversion, it results in large die area, high input capacitance, and high power dissipation. This type of ADC is often used for video, wideband communications or other fast signals processing devices [1, 2]. A Successive-Approximation-Register ADC

C.-F. Hsieh (✉) · C.-S. Chen · J. Lin
Department of Electronic Engineering, China University of Science and Technology, Taipei 11581, Taiwan, Republic of China
e-mail: c0935@cc.cust.edu.tw

J. Juang et al. (eds.), *Proceedings of the 2nd International Conference on Intelligent Technologies and Engineering Systems (ICITES2013)*, Lecture Notes in Electrical Engineering 293,
DOI: 10.1007/978-3-319-04573-3_75,

(SAR ADC) uses a comparator to successively narrow a range that contains the input voltage step by step. It requires n compare cycles for a n-bit output. Therefore, a SAR ADC effectively saves power consumption and area, but its convert rate is very slow due to the successive comparison operation [3]. The Delta-Sigma (ΔΣ) ADCs are widely used in the digital audio application. Its features of oversampling and noise-shaping can reduce the noise and move the in-band quantization error out of the band. The digital filter used filters the noise at high frequency of signals, significantly improving the resolution. Its conversion speed is between those of the flash ADC and SAR ADC. ΔΣ ADC is mainly used in the application of high resolution and high cost effective, such as audio, measurement instruments, and so on [4–6].

In this paper, a 10 bit 1.5b/stage pipeline ADC for video application has been presented first and then it is designed using 0.18 μm CMOS technology. It is organized as follows. Section 75.2 describes the principal of pipeline ADC and the common parameters, including the dynamic performance and static performance. Section 75.3 designs and simulates all the function of this paper which uses a differential operational amplifier circuit with the telescope architecture. It comprises high gain and high swing circuit. The proposed pipeline ADC is designed and its simulation results are presented in Sect. 75.4. Finally, Sect. 75.5 gives a conclusion.

75.2 Principal of Pipeline ADC

Figure 75.1 shows a pipeline ADC system diagram. This ADC is composed of a sample-and-hold (S/H) circuit and eight stage a sub-ADC, a digital-to-analog converter (DAC) and a gain amplifier. The function is described below. After a first S/H circuit, the input signal is sampled and kept in a certain voltage range. Then, the sampled signal is quantized by the sub-ADC to produce a digital output. The digital value is then converted into the rough reconstruction analog signals. After that, the difference between these two analog signals, the original input analog signal and the rough reconstruction analog signals, is calculated. The result is amplified by the gain stage and then sent to the next stage for another converting [7]. The pipeline ADC is composed by cascading several of these stages to achieve required resolution.

75.3 Circuit Design

As mentioned in Sect. 75.2, the block diagram of a pipeline ADC can be designed as Fig. 75.2 shown. The architecture is composed of the differential CMOS comparator circuit, the clock generator, the S/H circuit, 8-stage sub-ADCs and one-stage flash ADC. The main component function of the architecture is described as follows.

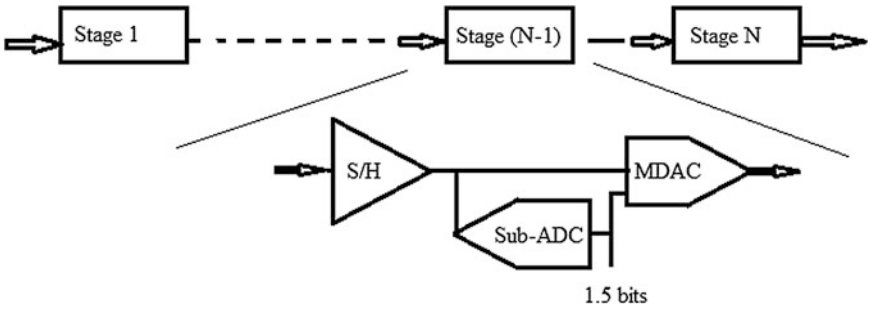

Fig. 75.1 Diagram of the pipeline ADC

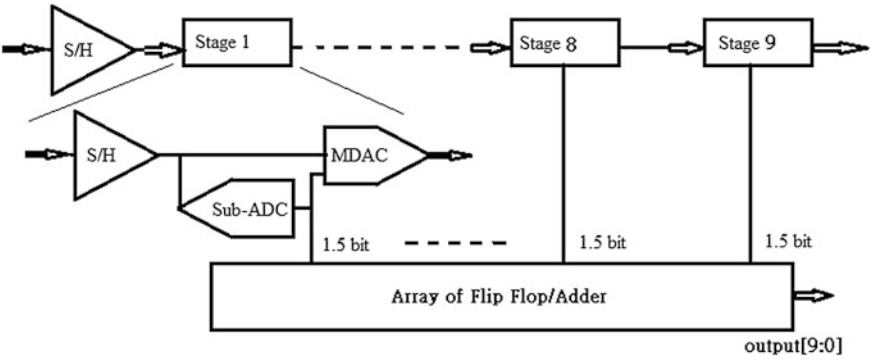

Fig. 75.2 Block diagram of the pipeline ADC

The performance of the pipeline ADC is influenced by the accuracy of the comparator. The digital error correction in the proposed architecture is 1.5 bits in each stage. The maximum allowable error range is $-1/4 \times$ VREF to $+ 1/4 \times$ VREF (VREF = VREFP − VREFN), therefore a less accurate fully-differential dynamic comparator is chosen [8]. The comparator shown in Fig. 75.3 is mainly composed of the two CMOS latch-controlled current sources coupled to the differential pair. The dynamic current source connects between the supply voltage and the differential input pair, so it has no static power consumption and has better noise immunity to the common-mode noise.

In order to generate non-overlapping clocks, an appropriate size inverter chain is used to adjust time delay. The block diagram is shown in Fig. 75.4. S/H circuit is the first stage circuit which samples the input signal by the control signals, PHA1 and PHA2, and then the signal is sent to the next stage. The fully differential S/H with switched-capacitor common mode feedback (CMFB) circuit is shown in Fig. 75.5.

Sub-ADC converts the sampled voltage into digital code, amplifies two times and aand greater thandds +VREF, 0VREF, or −VREF according to three intervals, less than −1/4VREF, between −1/4–1/4VREF, +1/4VREF, respectively. The

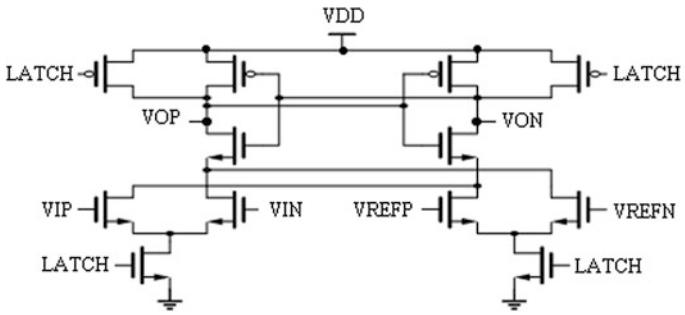

Fig. 75.3 Differential CMOS comparator

Fig. 75.4 Clock generator

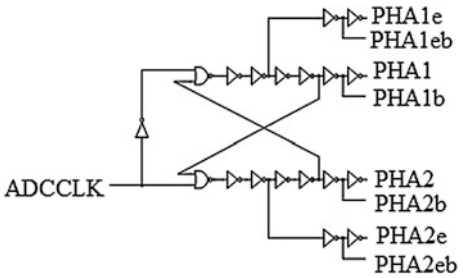

Fig. 75.5 S/H circuit

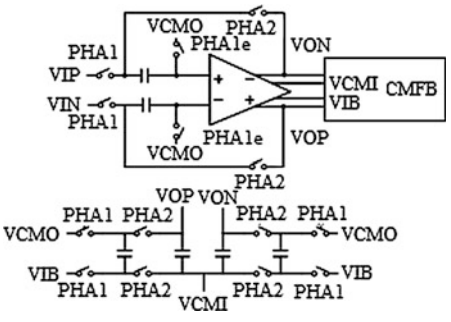

Fig. 75.6 Sub-ADC

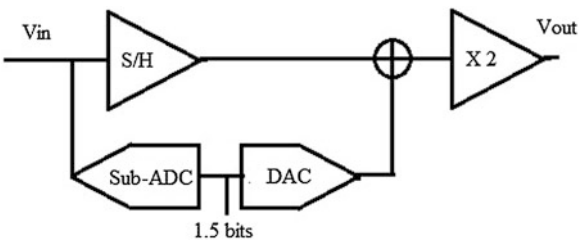

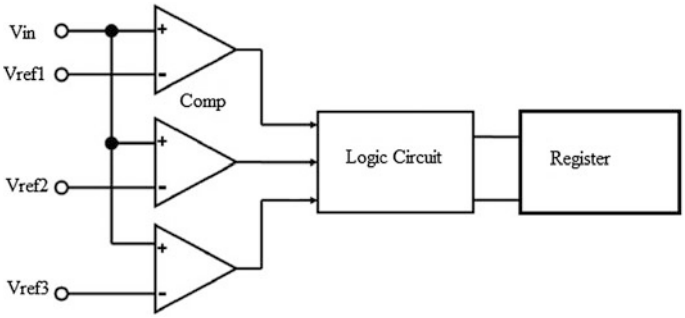

Fig. 75.7 Flash-ADC

block diagram is shown in Fig. 75.6. The last stage of this architecture is the 1.5-bit flash ADC as shown in Fig. 75.7.

75.4 Simulation Result

The design of such a 10-bit pipeline ADC circuit is shown in Fig. 75.8. The first stage S/H circuit samples the differential input analog signal and transmits it to the next sub-ADCs. There are a total of eight sub-ADCs plus the final one of the flash ADC. Each of them outputs two-digit bits. By summing the highest bit, an output of 10-digital bits is obtained. The simulation results are shown in Figs. 75.9 and 75.10. They show that the total harmonic distortion (THD) is −68.02 dB, the signal-to-noise pulse harmonics ratio (SNDR) of 58.29 dB, the output valid bit ENOB is 9.37, the spurious free dynamic range (SFDR) is 68.02 dB, the differential nonlinearity DNL = − 0.604–0.286 LSB and the integral nonlinearity INL = − 0.399–1.413 LSB. The result compared with Wen [9] and Balasubramaniam and Hofmann [10] is shown in Table 75.1.

75.5 Conclusion

This paper presents a 10-bit fully differential pipeline ADC designed in TSMC 0.18 μm single-poly six-metal CMOS process. The design includes the S/H circuit, eight stage 1.5-bit sub-ADCs, one stage 1.5-bit Flash ADC, and a nonoverlapping clock generator. In this architecture, the fully differential dynamic comparator is used to gain a better noise immunity for a common mode. The model verification was successfully implemented in MATLAB Simulink. All the functions of the proposed ADC are successfully tested and proven through HSPICE simulations.

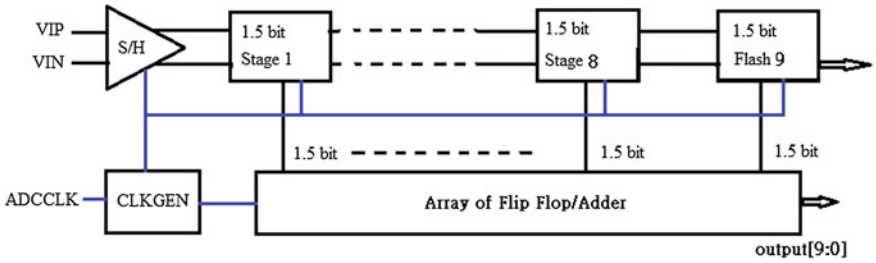

Fig. 75.8 Proposed pipeline ADC

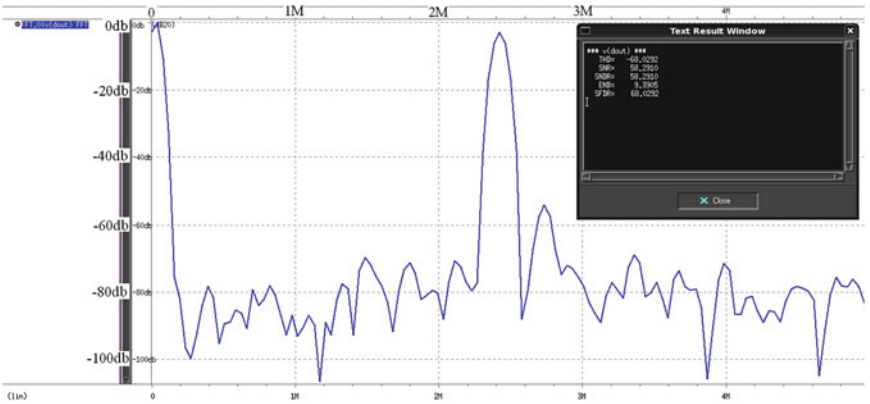

Fig. 75.9 Simulation result

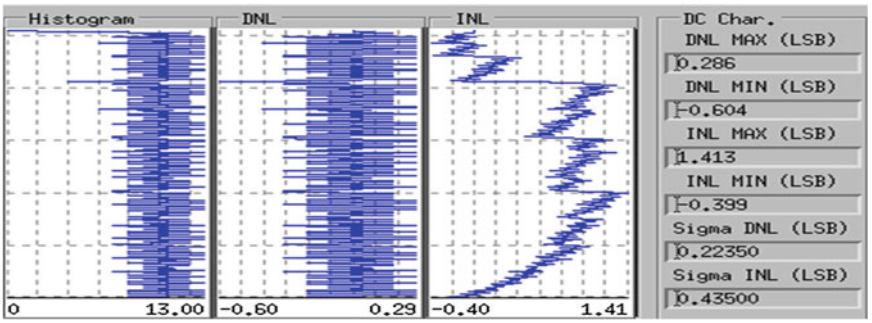

Fig. 75.10 DC result of ADC

By the simulation results, the total harmonic distortion (THD), the signal-to-noise plus harmonics ratio (SNDR), the effective number of bits (ENOB), and the spurious free dynamic range (SFDR) is shown to be −68.02, 58.29, 9.37, and

Table 75.1 Results for comparison

	Wen [9]	Balasubramaniam and Hofmann [10]	Proposed
Process	0.35 μm	90 nm	0.18 μm
Supply voltage (V)	3.3	1	3.3
Sampling speed (MHz)	12.5	10	10
INL (LSB)	±0.8	±1.4	1.413–– 0.399
DNL (LSB)	±0.4	±0.6	0.286–– 0.604
ENOB (LSB)	7.3	8.9	9.37

68.02 dB, respectively. Pipelined ADCs have very useful applications. The proposed work is very suitable for data conversion employed in the video applications.

References

1. Sall, E., Vesterbacka, M., & Andersson, K. O. (2004). A study of digital decoders in flash analog to digital converters. *IEEE International Symposium on Circuits System, Vancouver, Canada*.
2. Kale, A. V., Palsodkar, P., & Dakhole, P. K. (2012). Comparative analysis of 6 bit thermometer-to-binary decoders for flash analog-to-digital converter. *2012 International Conference on Communication Systems and Network Technologies (CSNT)* (pp. 543–546).
3. Cho, S. H., Lee, C. K., Lee, S. G., & Ryu, S. T. (2010). A two-channel asynchronous SAR ADC with metastable-then-set algorithm. *IEEE Transactions on Very Large Scale Integration (VLSI) Systems, 20*(4), 765–769.
4. Signore, B. P., Kerth, D. A., Sooch, N., & Swanson, E. (1990). A monolithic 20-b delta-sigma A/D converter. *IEEE Journal of Solid-State Circuits, 25*, 1311–1317.
5. Mahajan, D., Kakkar, V., & Singh, A. K. (2011). Analysis of delta sigma modulator. *2011 International Conference on Computational Intelligence and Communication Networks (CICN)* (pp. 182–186).
6. Fujimoto, Y., Re, P. L., & Miyamoto, M. (2005). A delta-sigma modulator for a 1-bit digital switching amplifier. *IEEE Journal of Solid-State Circuits, 40*(9), 1865–1871.
7. Jamal, S. M., Fu, D., Chang, N. C. -J., Hurst P. J. & Lewis, S. H. (2002). A 10-b 120-Msample/s time-interleaved analog-to-digital converter with digital background calibration. *IEEE Journal of Solid State Circuits, 37*(12), 1618–1627.
8. Lee, C. C., & Flynn, M. P. (2010). A 12b 50MS/s 3.5mW SAR assisted 2-stage pipeline ADC. *2010 IEEE Symposium on VLSI Circuits* (pp. 239–240).
9. Wen, Y. C. (2007). Novel step-ramp signal for testing ADCS and DACS. *IEEE 14th International Conference on Mixed Design of Integrated Circuits and Systems* (pp. 517–522).
10. Balasubramaniam, H., & Hofmann, K. (2011). A 10 bit, 1.5b/stage pipeline ADC using a fully differential current conveyor with foreground calibration. *IEEE 10th International Symposium on Signals, Circuits and Systems (ISSCS)* (pp. 1–4).

Chapter 76
The Effect of Annealing on the Microstructure and Scratch Behavior of Copper Deposited Film

Chun-Chieh Huang, Yi-Feng Lin and Ching-An Jeng

Abstract In this study, copper film with thickness 5 μm was deposited by electron beam evaporation on slightly oxidized silicon substrates. Ti and Al metals were used as adhesion or barrier layers. The effect of annealing on the microstructure, resistivity and scratch behavior of Cu film was investigated using a scratch indenter of radius of 2.5 μm. Results revealed that the resistivity decreases, but scratch resistance increases after annealing. Compared to as-deposited film, the annealed one exhibited not only higher friction coefficient, but also lower loading of the first fracture, due to grain growth.

Keywords Cu film · Resistivity · Scratch · Annealing

76.1 Introduction

Thin layer of copper films on Si substrate is an important structure in electronic industry. The thin film multilayer substrates have been used in multichip module and electronic packaging applications [1]. In general, Cu does not bond well to the dielectric, it leads to adhesion and agglomeration problems, when a high current density is passed through the Cu line [2]. Hence, it is necessary to use a thin metal layer to serve as an adhesion promoter as well as diffusion barrier between Cu and the dielectric layer. In addition, in order to maintain stability of the microstructure of the multilayer at high temperatures, inter-diffusion as well as interface phase transformation should be minimized.

C.-C. Huang · Y.-F. Lin
Department of Electrical Engineering, Cheng Shiu University, Kaohsiung 83347, Taiwan, Republic of China

C.-A. Jeng (✉)
Department of Mechanical and Automation Engineering, I-Sou University, Kaohsiung, Taiwan, Republic of China
e-mail: cajeng@isu.edu.tw

J. Juang et al. (eds.), *Proceedings of the 2nd International Conference on Intelligent Technologies and Engineering Systems (ICITES2013)*, Lecture Notes in Electrical Engineering 293,
DOI: 10.1007/978-3-319-04573-3_76,

The scratch test is a simple and widely used method for investigating adhesion in thin films [3]. Scratch testing has been used recently to probe the tribological properties of multilayered materials [4]. During scratch testing both normal and tangential forces are applied under dynamic loading. Usually, an indenter tip is moved across the sample surface with increasing normal load.

In this study, we have investigated the microstructure, resistivity and scratch behavior of Cu films after heat treatment. The evolution of the friction coefficient, contact stiffness and the ratio of elastic to plastic deformation were also discussed.

76.2 Experimental Details

Copper films were deposited in an electron beam evaporation system with a pure Cu source material. No external substrate heating was used. However, it is estimated that the substrates may have been oxidized to a thickness of 100 nm in the vicinity of 25 °C. An in situ quartz crystal oscillator was used to monitor the film thickness. Ti and Al metals were used as adhesion or barrier layers with a thickness of 0.3 μm. These Cu films (5 μm) were annealed in an atmosphere of high purity grade argon gas at two different temperatures −200 and 300 °C, for 60 min. The sheet resistance was measured by a four-point probe.

Scratch testing was carried out by using a Universal Nanomechanical (UNAT, ASMEC GmbH, Germany) with a Rockwell C indenter of radius of 2.5 μm. The load can be increased at a specified loading rate 13.45 mN/s. Load can be measured at any place as we know the loading rate and the length of the track. A progressive load from 0 to 700 mN was applied with a scratch length of 45 μm and the scratch speed of 0.86 μm/s. In all scratch tests, the friction coefficient was defined by the ratio of "tangential force divided by the applied normal load" which corresponds to the apparent friction coefficient. Pre-scans at minimum load were performed to obtain the surface profile and post-scans were utilized to obtain the residual depth and, thus, estimate the ratio of elastic to plastic deformation. The microstructure and surface morphology of the films were observed using field emission scanning electron microscopy (FESEM) (Hitachi S-4300) with the operating voltage of 15 kV. XRD and Energy dispersive X-ray spectroscopy (EDX) (INCA Energy) were utilized to investigate the contents of each element in the films with the accelerating voltage of 15 kV and collection time of 100 s.

76.3 Results and Discussion

76.3.1 Resistivity Variation

Figure 76.1 shows the resistivity of the Cu–Ti and Cu–Al films before and after heat treatment. The resistivity of the films for both cases decreased with increasing

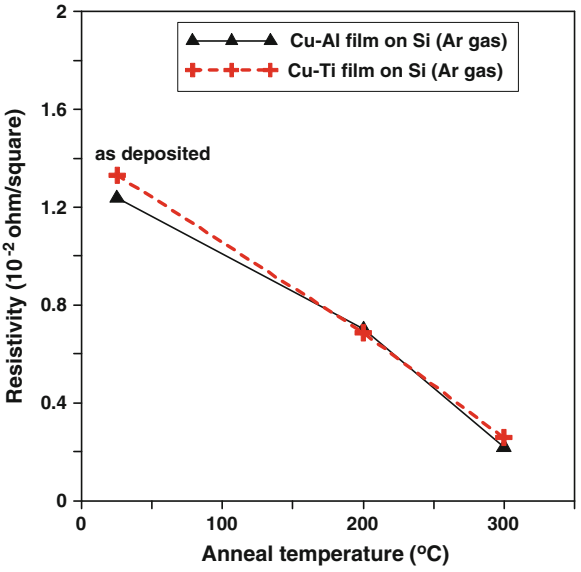

Fig. 76.1 The resistivity as a function of anneal temperature for two different adhesion layers

heat treatment temperature. As-deposited films showed the resistivity ranging from 0.012 to 0.013 Ω/square, while the resistivity of the films ranged from 0.002 to 0.007 Ω/square after annealing. The resistivity of the films decreased by almost half one order of magnitude after annealing at 200 °C (Ar). This change in the resistivity with respect to the treated temperature was very closely related to changes in the microstructure.

The typical microstructure of annealed samples (300 °C) (Ar) is shown in Fig. 76.2a, b. These results implied that the improved electrical property was due to grain growth. The grain growth is confirmed by XRD analysis. In Fig. 76.3a, the XRD spectra from the Ar gas annealed Cu–Ti films show that the $Cu_{(111)}$ peak intensity increases and become sharper with anneal temperatures. The intermixing of Ti into the Cu is found in the as-deposited film. The original $CuTi_3$ peak vanished and a new CuO phase was observed after annealing. This is an indication of grain growth and oxidization. In Fig. 76.3b, the XRD spectra from the Ar gas annealed Cu–Al films show that the $Cu_{(111)}$ peak intensity does not increases, but $Cu_{(200)}$ become sharper with anneal temperatures.

76.3.2 Scratch Behavior

The observed evolution of the friction coefficient with increased normal load is shown in Fig. 76.4a, b. The coefficient of friction (COF) of annealed samples is larger than as deposited one, indicating that grain growth by annealing treatment can enhance scratch resistance. An average value ranging from 0.35 to 0.379 can

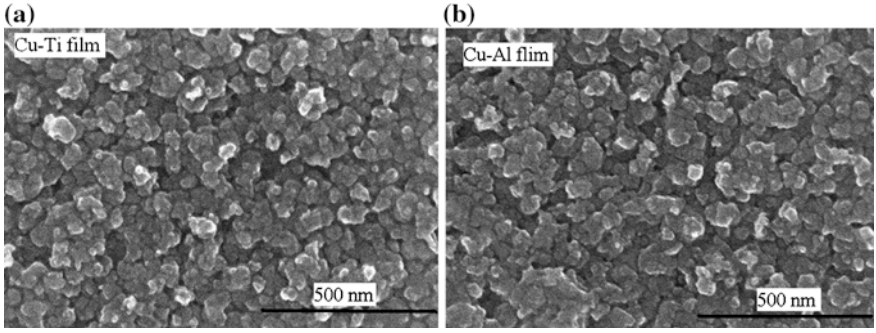

Fig. 76.2 Typical SEMs of Cu–Ti film (**a**) and Cu–Al film (**b**), annealed at (300 °C) (Ar)

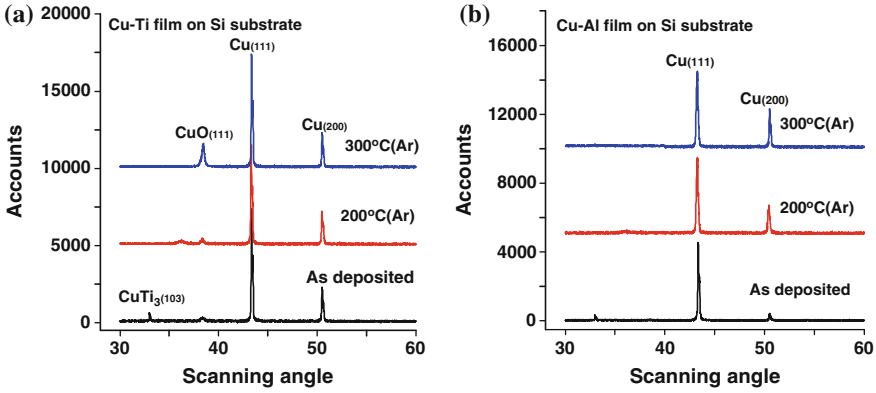

Fig. 76.3 X-ray diffraction spectra for the Cu–Ti film (**a**) and Cu–Al film (**b**) samples

be achieved with 200 °C (Ar)-annealed samples for both Al and Ti-containing films. The friction coefficients of the 300 °C (Ar)-annealed samples are higher than those of the 200 °C (Ar)-annealed films. For Cu–Ti films, the magnitudes of features in the first fracture were different for the as-deposited and annealed films at loads close to 425 and 70 mN, respectively. During temperature increases, the first fracture event takes place at a slightly higher load. After annealing, the Cu film may be controlling the degree of grain growth during the scratch experiment. A similar behavior is observed in the Cu–Al films annealed samples.

Tables 76.1 and 76.2 show typical data obtained from a scratch test. Both tables show the maximum depth under load (h_{max}) and maximum depth under load (h_e) for both all Al and Ti-containing annealed samples. For Cu–Ti films, the as-deposited, the 200 °C (Ar)-annealed samples and annealing (300 °C) (Ar) samples, the ratios of the residual depth ($h_{max} - h_e$) to the maximum depth (h_{max}) were estimated to be 0.63, 0.24 and 0.19, respectively. It indicates that the as-deposited films capable of sustaining larger amounts of plastic deformation than those of annealing samples. The maximum plastic deformation depth is also illustrated in

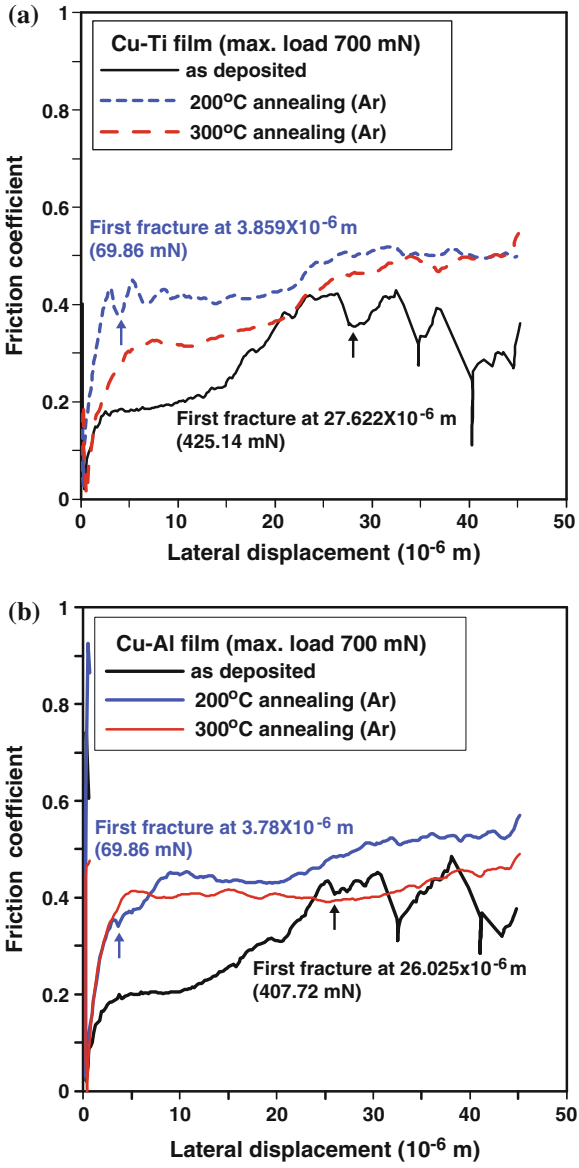

Fig. 76.4 Friction response for Cu-Ti film (**a**) and Cu-Al film (**b**) in a progressive load test

tables. The maximum plastic deformation occurred almost same as the maximum depth under load for 200 °C (Ar)-annealed samples. However, the annealed samples (300 °C) (N_2) revealed a slightly different depth. For Cu–Al films, the as-deposited, the 200 °C (Ar)-annealed samples and annealing (300 °C) (Ar) samples, the ratios of the residual depth ($h_{max} - h_e$) to the maximum depth (h_{max}) were estimated to be 0.32, 0.18 and 0.19, respectively.

Table 76.1 Scratch testing of Cu–Ti film on Si substrate with different annealing temperatures

Name	As deposited	200 °C (Ar)	300 °C (Ar)
Max. loading depth			
(under load) h_{max} (μm)	5.213	6.344	6.158
(after unload) h_e (μm)	1.949	4.808	4.983
Plastic deformation (max.) depth h_p (μm)	1.879	4.703	4.041
Lateral displacement of the first fracture (μm)	27.622	3.859	3.879
Normal force of the first fracture (mN)	425.137	69.86	82.493
COF (average)	0.316	0.379	0.41

Table 76.2 Scratch testing of Cu–Al film on Si substrate with different annealing temperatures

Name	As deposited	200 °C (Ar)	300 °C (Ar)
Max. loading depth			
(under load) h_{max} (μm)	5.506	6.414	5.741
(after unload) h_e (μm)	3.726	5.252	4.607
Plastic deformation (max.) depth h_p (μm)	3.325	5.113	4.124
Lateral displacement of the first fracture (μm)	26.025	3.781	3.815
Normal force of the first fracture (mN)	407.718	69.86	82.763
COF (average)	0.323	0.35	0.388

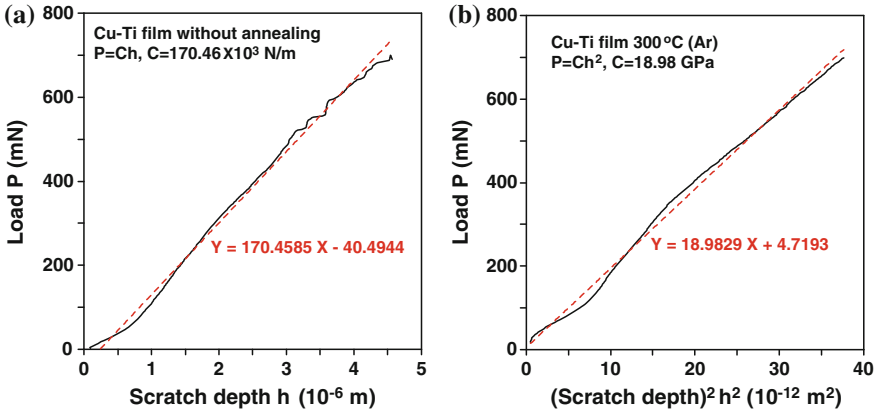

Fig. 76.5 Typical compliance curve of as-deposited Cu–Ti film (**a**) and P-h^2 relation of Cu–Ti film annealed at (300 °C) (Ar) (**b**)

The typical load-depth compliance curve of as deposited Cu–Ti film is indicated in Fig. 76.5a. The contact stiffness (dP/dh) was estimated to be at a fixed value of 170 × 10^3 N/m. Joslin and Oliver [5] proposed that the contact stiffness could be related to the resistance of plastic penetration. Fig. 76.5b shows that the loading curve of the annealing Cu–Ti film can be described using a linear

relationship between the load P and the square of the depth ($P = Ch^2$) [6]. The constants of proportionality C for the Cu–Al films annealed at 200 °C (Ar) and 300 °C (Ar) were found to be 17.5 GPa and 21.81 GPa, respectively.

76.4 Conclusion

Copper films were deposited in an electron beam evaporation system with a Ti (Al) barrier layer and annealed in Ar gas. Scratch testing was carried out by using a progressive loading device with a Rockwell C indenter of radius of 2.5 μm. It was found that the different temperature annealing affected both the resistivity and scratch resistance. The annealed films exhibited not only higher COF, but also more influence from loading of the first fracture, due to grain growth.

References

1. Kumar, N., & Nelson, B. H. (1990). Multi-chip module interconnect and packaging technology for the 90's. *Proceedings* of *Asm International's 3rd Electronic Materials and Processing Congress* (pp. 99–109).
2. Kim, H., Koseki, F., Ohta, T., Kojima, Y., Sato, H., & Shimogakia, Y. (2005). Cu wettability and diffusion barrier property of Ru thin film for Cu metallization. *Journal of the Electrochemical Society, 152*, 594–600.
3. Bull, S. J., & Berasetegui, E. G. (2006). An overview of the potential of quantitative coating adhesion measurement by scratch testing. *Tribology International, 39*, 99–114.
4. Shen, W., Sun, J., Liu, Z., Mao, W., Nordstrom, J. D., Ziemer, P. D., et al. (2004). Methods for study of mechanical and tribological properties of hard and soft coating with a nanoindenter. *Journal of Coatings Technology and Research, 1*(2), 117–125.
5. Joslin, D. L., & Oliver, W. C. (1990). A new method for analyzing data from continuous depth-sensing microindentation tests. *Journal of Materials Research, 5*, 123–126.
6. Hainsworh, S. V., Chandler, H. W., & Page, T. F. (1996). Analysis of nanoindentation load-displacement loading curves. *Journal of Materials Research, 11*, 1987–1995.

Chapter 77
Piezoelectric Properties of Cement-Based Piezoelectric Composites Containing Fly Ash

Huang Hsing Pan, Chang-Keng Chiang, Rui-Hao Yang and Neng-Huei Lee

Abstract Piezoelectric properties of 0–3 type cement-based piezoelectric composites with fly ash are investigated, where the piezoelectric inclusion is PZT, and the binder consists of cement and fly ash. Cement was replaced by fly ash from 10 % to 50 vol.% in the binder. Experimental results indicate that all fly ash/cement piezoelectric composites can be successfully polarized. Prior to polarization, relative dielectric constant ε_r increases with fly ash, but diminishes with curing time. Piezoelectric properties are stable at the 50th day after the polarization. Curing time is not sensitive to piezoelectric properties, but polarizing voltage is. A 20 vol.% replacement of cement by fly ash in cement-based piezoelectric composite with 50 vol.% PZT reaches a maximum value of 54 pC/N and 28 $\times$ 10^{-3} V-m/N for d_{33} and g_{33}, respectively.

Keywords Cement · Piezoelectricity · Fly ash · Curing · Polarization

77.1 Introduction

Sensors and actuators installed in civil engineering structure are usually made by piezoelectric ceramics and polymers. Among piezoelectric materials, lead zirconate titanate (PZT) is a ceramic with higher piezoelectric strain factor (d_{33}) that have been used in, such as, ceramic micro-electro-mechanical systems (C-MEMS), ultrasonic generators, ferroelectric thin films and small actuators.

H. H. Pan (✉) · C.-K. Chiang · R.-H. Yang
Department of Civil Engineering, Kaohsiung University of Applied Sciences, Kaohsiung 80778, Taiwan, Republic of China in Affiliation
e-mail: pam@cc.kuas.edu.tw

N.-H. Lee
Department of Business Administration, Quemoy University, Kinmen 89250, Taiwan, Republic of China in Affiliation

J. Juang et al. (eds.), *Proceedings of the 2nd International Conference on Intelligent Technologies and Engineering Systems (ICITES2013)*, Lecture Notes in Electrical Engineering 293,
DOI: 10.1007/978-3-319-04573-3_77,

To overcome the matching problem in concrete structures that conventional sensors and actuators do not contact simultaneously with concrete, 0–3 type cement-based piezoelectric composites have been developed since last decade [1–7]. Common 0–3 type cement-based piezoelectric composites (PZT/cement composites) consist of cement binder as the matrix and randomly oriented PZT particles as the inclusion. To create piezoelectricity, we need to apply poling voltage to PZT/cement composites. No piezoelectric properties are found without the polarization.

Many factors affect the dielectric and piezoelectric properties of 0–3 type cement piezoelectric composites. Currently, PZT/cement composites containing PZT from 20 to 90 vol.% can be manufactured by pressure forming. The effect of volume fraction and particle size of piezoelectric ceramics was discussed [8–10]. The other factors such as poling time [11], poling temperature [12], poling field [13], the thickness and the forming of specimens [4, 14–16] were also investigated. To produce higher piezoelectric strain factor (d_{33}), adding carbon black into 0–3 type cement-based composites was reported [17], and adding 80 vol.% nano-PZT powder can obtain $d_{33} = 53.7$ pC/N [7].

Dielectric and piezoelectric properties of PZT/cement composites containing pozzolanic materials were rarely reported until a PZT-silica fume cement composite was conducted, where 5–10 wt.% silica fume were added [10]. Recently, d_{33} value up to 70 pC/N for 60 vol.% PZT and 20 wt.% silica-based replacement in cement was manufactured at 38 aging days [18]. No piezoelectric properties of PZT/cement composites containing fly as were investigated previously.

In this study, we focus on PZT/cement composites containing fly ash, and examine the influence of age effect including curing time and aging time after the polarization. Cement-based piezoelectric composites containing 50 vol.% PZT and partial cements were replaced by fly ash with 10–50 vol.% in the binder.

77.2 Materials and Experiments

PZT ceramics (piezoelectric inclusion) are randomly oriented in cement-based binders (matrix) to form a 0–3 type PZT/cement composite. The diameter of PZT particle is 75–150 μm, with a specific gravity of 7.9, $d_{33} = 470$ pC/N, piezoelectric voltage factor (g_{33}) of 24×10^{-3} V-m/N, and relative dielectric factor (ε_r) of 2100. Cement is type I Portland cement with the fineness of 349 m^2/kg and specific gravity of 3.16. Fly ash belongs to Class F produced by Hsinta thermal power plant (Taiwan) with a fineness of 326 m^2/kg and specific gravity of 2.11.

Six kinds of PZT/cement composites are made. The composite denoted by PP is a cement-based piezoelectric composite with 50 % PZT and 50 % cement by volume, and no PZT found in PP is named as PC (100 % cement). PP material containing fly ash is referred as FA groups. There are five replacements of cement by fly ash in PP material from 10 to 50 %, for example, FA10 represents 10 vol.% of cement replaced by fly ash in the binder, and FA50 is a 50 % replacement of fly ash.

PZT powders, cement and fly ash were pre-mixed without adding water. The mixture was placed in a cylindrical steel mold of 15 mm in diameter, and then applied by a compressive stress of 80 MPa for 5 min to form a disk-like shape. Before the polarization, specimens were cured in 90 °C and relative humidity of 100 % for 7, 28 and 56 days (curing time), respectively. After curing, specimens were polished to 2 mm in thickness, coated by silver paint as an electrode, and then, baked at 150 °C for 30 min in oven. During the polarization, the specimen was subjected to three poling voltages, 0.5, 1.0 and 1.5 kV/mm, respectively, in a 150 °C silicone oil bath for 30 min (polarizing time).

After the polarization, specimens were placed in the air for 24 h and measured piezoelectric and dielectric properties based on aging time. Piezoelectric strain factor d_{33} was directly measured by d_{33} Piezometer, and other piezoelectric properties were captured by Impedance Phase Analyzer. Each experimental value shown as follows is an average of three specimens, and was measured at 24 °C and 50 % humidity condition.

77.3 Results and Discussion

77.3.1 Properties Before Polarization

Cement-based composites do not have piezoelectric properties unless the addition of piezoelectric inclusions and a successful polarization [1, 4, 11, 16]. Prior to the polarization, electric properties including capacitance (C), dielectric loss (D) and relative dielectric factor ε_r were measured and calculated.

Table 77.1 displays the capacitance of PC, PP and FA-group materials. Capacitance gradually decreases as curing time increases. FA-group materials with increasing fly ash always have a higher capacitance, compared with PP material. While the content of fly ash greater than 30 vol.% in the binder, the capacitance of PZT/cement composites raises tremendously.

Materials with high dielectric loss are difficult to be polarized, and easy to induce current breakdown in the specimen during the polarization. Table 77.2 indicates that cement-based materials at longer curing time own the lower dielectric loss. PC materials (pure cement) cannot be polarized due to a higher D, and lead to no piezoelectric properties. Compared with PC material, dielectric loss of PP and FA-group materials is lower.

Before the polarization, relative dielectric factor ε_r of cement-based composites is shown in Table 77.3. The development of ε_r is similar to the capacitance in Table 77.1, so that increasing curing time will reduce ε_r. Cement containing PZT (PP material) has the lowest ε_r, and continues to develop with increasing fly ash. Obviously, relative dielectric factors of FA40 and FA50 material are dramatically high, compared with the others materials.

Table 77.1 Capacitance before the polarization (unit: pF)

Curing time	PC	PP	FA10	FA20	FA30	FA40	FA50
7 days	108	75	84	95	165	644	742
28 days	80	70	78	87	158	466	552
56 days	56	68	74	71	121	285	398

Table 77.2 Dielectric loss before the polarization

Curing time	PC	PP	FA10	FA20	FA30	FA40	FA50
7 days	0.94	0.21	0.31	0.39	0.49	0.68	0.73
28 days	0.85	0.20	0.27	0.37	0.43	0.62	0.71
56 days	0.76	0.19	0.25	0.34	0.39	0.51	0.69

Table 77.3 Relative dielectric factor before the polarization

Curing time	PC	PP	FA10	FA20	FA30	FA40	FA50
7 days	138	96	107	121	165	824	949
28 days	102	90	100	111	158	596	706
56 days	72	86	95	91	121	365	508

77.3.2 Piezoelectric Properties

Polarizing voltages applied to PZT/cement composites to create piezoelectric properties as the curing time reached. After the polarization, specimens were measured daily until 60 days. To discuss aging effect (the time after polarization), results of piezoelectric properties are shown in Figs. 77.1, 77.2, 77.3, 74.4, 75.5, 77.6 for the material undergone 1.5 kV/mm at 7 and 56 curing days.

Figures 77.1 and 77.2 show relative dielectric factor of PP and FA-group materials at 7 and 56 curing days respectively. Relative dielectric factors increase with aging time, and the growth of ε_r displays less fluctuant after the polarization of 50 days, where ε_r values are between 150 and 200. From Figs. 77.1 and 77.2, choosing the day after the polarization of 24 h to determine ε_r is not adequate because of rapid variations of the property at early age. After the polarization of 50 days, increasing fly ash to PP material will diminish ε_r no matter what curing day is, and this trend is different from that prior to polarization in Table 77.1.

Piezoelectric strain factor d_{33} and piezoelectric voltage factor g_{33} are important piezoelectric properties for sensors and actuators. Aging effect for d_{33} and g_{33} are shown in Figs. 77.3, 77.4, 77.5, 77.6, where d_{33} and g_{33} are on the increase with aging time. Figure 77.3 shows d_{33} at 7 curing days, and d_{33} values of PP (with 50 % PZT) are 18, 40, 43 and 44 pC/N at aging time of 0, 21, 28 and 60 days respectively. It seems that adding fly ash to PP material does not increase d_{33} except for FA10 and FA20 material after 40 days. d_{33} values of FA20 material are

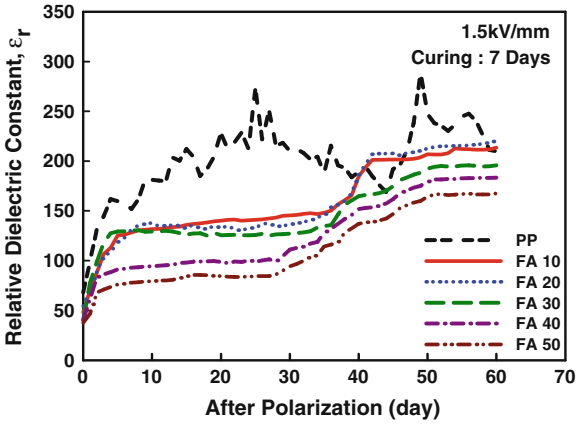

Fig. 77.1 Aging effect of ε_r at 7 curing days

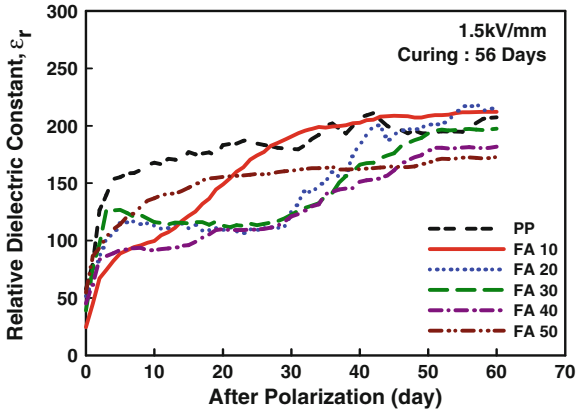

Fig. 77.2 Aging effect of ε_r at 56 curing days

23, 42, 45 and 54 pC/N for aging time of 0, 21, 28 and 60 days respectively. In Fig. 77.4, the trend of d_{33} at 56 curing days is similar to Fig. 77.3.

Figure 77.5 shows experimental results for g_{33} at 7 curing days, and indicates that g_{33} reduces tremendously at early aging time. g_{33} values for FA10 and FA20 at the 28th day of aging time are 30.6 and 37.4 mV-m/N respectively, those even greater than that for PZT ceramic ($g_{33} = 24$ mV-m/N). The replacement (fly ash) less 30 vol.% is a better choice to increase g_{33}. In Fig. 77.6, the trend of g_{33} with the aging day is also similar to Fig. 77.5.

Experimental results display that all FA-group materials can be successfully polarized. Now, we select the experimental data at the 60th day after the polarization to show the effect of curing time and fly ash contents. In Fig. 77.7, curing time shows less effective to enhance ε_r, and increasing poling voltage will reduce ε_r. A 20 % replacement by fly ash is the most effective to improve the dielectric constant.

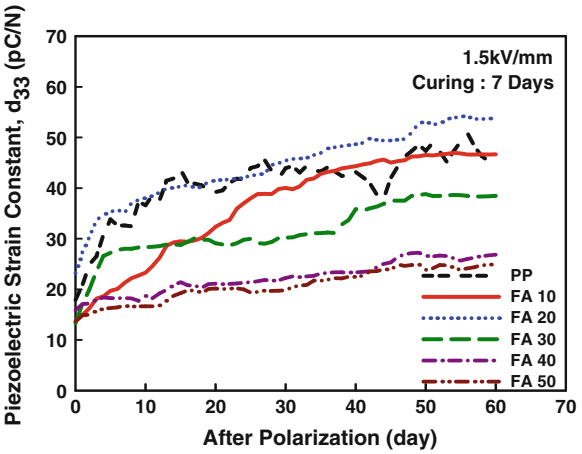

Fig. 77.3 Aging effect of d_{33} at 7 curing days

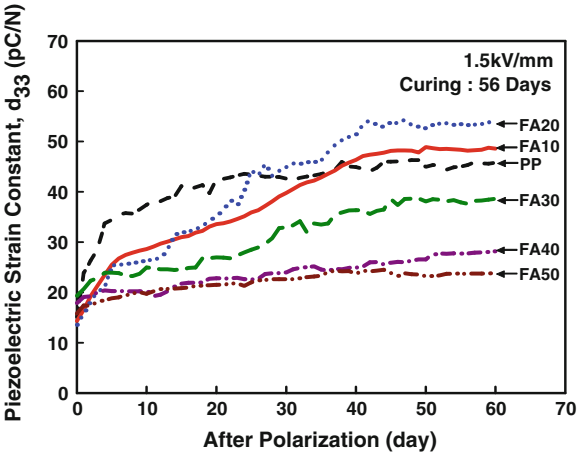

Fig. 77.4 Aging effect of d_{33} at 56 curing days

The results for d_{33} and g_{33} at 60 days are shown in Figs. 77.8 and 77.9 respectively. d_{33} and g_{33} have a less fluctuation for different curing times at the constant poling voltage, but increase with poling voltages. Both figures indicate that a 20 % replacement by fly ash is the best choice to promote piezoelectric properties. d_{33} values for PZT/cement piezoelectric composites with fly ash from 0 to 50 % at 56 curing days and 1.5 kV/mm are 46, 49, 54, 39, 28 and 24 pC/N respectively, and g_{33} are 24.9, 25.9, 28.0, 22.1, 17.5 and 15.6 mV-m/N in turn. Hence, d_{33} and g_{33} of FA20 material reaches a maximum value, where $d_{33} = 54$ pC/N and $g_{33} = 28.0$ mV-m/N.

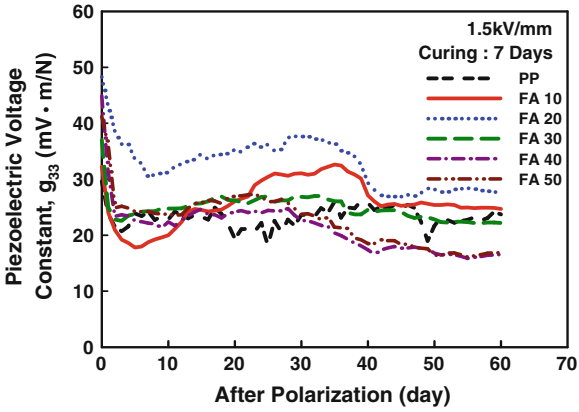

Fig. 77.5 Aging effect of g_{33} at 7 curing days

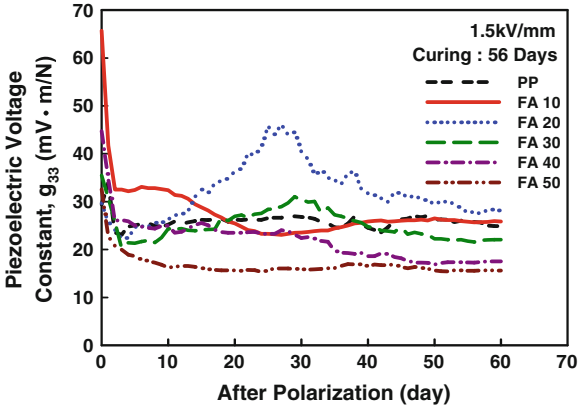

Fig. 77.6 Aging effect of g_{33} at 56 curing days

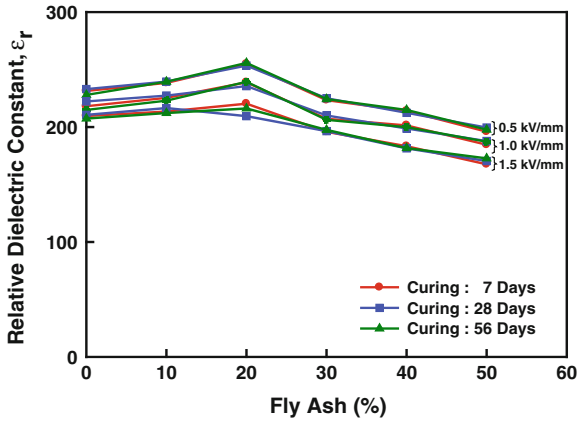

Fig. 77.7 Volume fraction of fly ash and ε_r

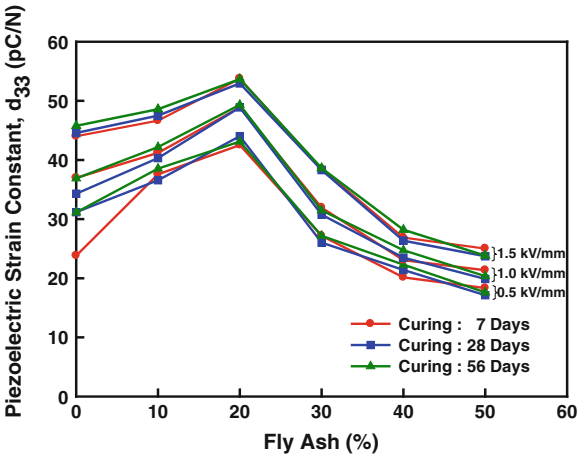

Fig. 77.8 Volume fraction of fly ash and d_{33}

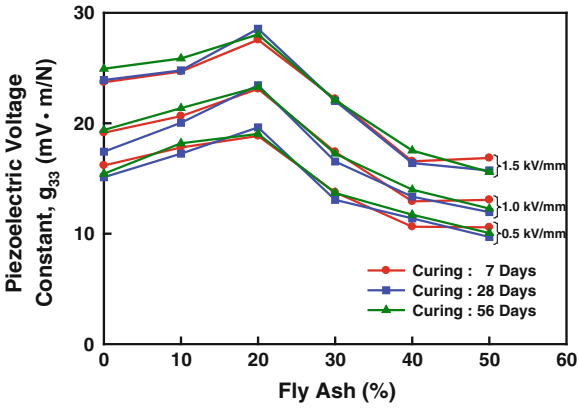

Fig. 77.9 Volume fraction of fly ash and g_{33}

77.4 Conclusions

Cement-based piezoelectric composites without adding water were pressed by a 80 MPa compression and cured for 7, 28 and 56 days respectively, after that, specimen were polarized by three poling voltages. Experimental data were measured daily till 60 days after the polarization. Experimental results are concludes as follows.

(1) Prior to polarization, capacitance, dielectric loss, and relative dielectric factor of FA-group materials increase as increasing fly ash, but decrease with curing time. However, adding fly ash to PP material will diminish ε_r after the polarization.
(2) All FA-group materials containing fly ash up to 50 vol.% replacement can be successfully polarized.

(3) Relative dielectric factor, d_{33} and g_{33} of PP and FA-group materials gradually increase with aging time, but have less effective to the effect of curing time. Meanwhile, increasing poling voltage will reduce ε_r, but increase d_{33} and g_{33}.
(4) To promote d_{33}, the content of fly ash had better not exceed 20 vol.% replacement of cement.
(5) Some g_{33} values of FA/cement composites, for example FA10 and FA20, are even greater than that of PZT ceramic.
(6) A 20 vol.% replacement of cement by fly ash is the best choice to improve the dielectric constant, piezoelectric strain factor and piezoelectric voltage factor of PZT/cement composites.
(7) Due to rapid increase of piezoelectric properties (ε_r, d_{33} and g_{33}) at early aging time, a suitable timing to represent piezoelectric properties of PZT/cement is to choose a relatively stable value after 50 days of the polarization.

Acknowledgments This study was financially supported by the Taiwan National Science Council under NSC 101-2625-M-011-001.

References

1. Li, Z., Zhang, D., & Wu, K. (2002). Cement-based 0–3 piezoelectric composites. *Journal of the American Ceramic Society, 85*, 305–313.
2. Wen, S., & Chung, D. D. L. (2002). Cement-based materials for stress sensing by dielectric measurement. *Cement and Concrete Research, 32*, 1429–1433.
3. Sun, M., Li, Z., & Song, X. (2004). Piezoelectric effect of hardened cement paste. *Cement Concrete Composites, 26*, 717–720.
4. Dong, B., & Li, Z. (2005). Cement-based piezoelectric ceramic smart composites. *Composites Science and Technology, 65*, 1363–1371.
5. Chaipanich, A. (2007). Effect of PZT particle size on dielectric and piezoelectric properties. *Current Applied Physics, 7*, 574–577.
6. Jaitanong, N., Chaipanich, A., & Tunkasiri, T. (2008). Properties 0–3 PZT-portland cement composites. *Ceramics International, 34*, 793–795.
7. Li, Z., Gong, H., & Zhang, Y. (2009). Fabrication and piezoelectric of 0–3 cement based composite with nano-PZT powder. *Current Applied Physics, 9*, 588–591.
8. Li, Z., Dong, B., & Zhang, D. (2005). Influence of polarization on properties of 0–3 cement-based PZT composites. *Cement Concrete Composites, 27*, 27–32.
9. Huang, S., Chang, J., Liu, F., Lu, L., Ye, Z., & Cheng, X. (2004). Poling process and piezoelectric properties of lead zirconate titanate/sulphoaluminate cement composites. *Journal Materials Science, 39*, 6975–6979.
10. Chaipanich, A. (2007). Dielectric and piezoelectric properties of PZT-silica fume cement composites. *Current Applied Physics, 7*, 532–536.
11. Chaipanich, A., & Jaitanong, N. (2008). Effect of poling time on piezoelectric properties of 0–3 PZT-portland cement composites. *Ferroelectric Letters, 35*, 73–78.
12. Dong, B., Xing, F., & Li, Z. (2007). The study of poling behavior and modeling of cement-based piezoelectric ceramic composites. *Materials Science and Engineering A, 456*, 317–322.
13. Huang, S., Chang, J., Lu, L., Liu, F., Ye, Z., & Cheng, X. (2006). Preparation and polarization of 0–3 cement based piezoelectric composites. *Materials Research Bulletin, 41*, 291–297.

14. Cheng, X., Huang, S., Chang, J., Xu, R., Liu, F., & Lu, L. (2005). Piezoelectric and dielectric properties of piezoelectric ceramic-sulphoaluminate cement composites. *The Journal of the European Ceramic Society, 25*, 3223–3228.
15. Huang, S., Ye, Z., Hu, Y., Chang, J., Lu, L., & Cheng, X. (2007). Effect of forming pressures on electric properties of piezoelectric ceramic/sulphoaluminate cement composites. *Composites Science and Technology, 67*, 135–139.
16. Pan, H. H., & Chen, Y. N. (2011). Manufacturing and polarization process of 0–3 cement-based PZT composites. *Journal of the Chinese Institute of Civil and Hydraulic Engineering, 23*, 1–10.
17. Gong, H., Li, Z., Zhang, Y., & Fan, R. (2009). Piezoelectric and dielectric behavior of 0–3 cement-based composites mixed with carbon black. *The Journal of the European Ceramic Society, 29*, 2013–2019.
18. Wang, F., Wang, H., Song, Y., & Sun, H. (2012). High piezoelectricity 0–3 cement-based piezoelectric composites. *Materials Letters, 76*, 208–210.

Chapter 78
Mining Company Competitor/ Collaborator Network from Online News for Competitive Intelligence

Chin-Sheng Yang and Hong-Cheng Ye

Abstract To gain sustainable competitiveness in an unstable and turbulent business environment, companies need to adapt to their environments and develop competitive intelligence that helps managers make crucial business decisions. Automatic discovery of competitors and collaborators represents a critical and essential task of competitive intelligence. This study proposes an approach that incorporates the state-of-the-art text mining and natural language processing techniques to effectively discover competitors and collaborators of a focal company from online news. Empirical evaluation results are promising.

Keywords Competitive intelligence · Competitor mining · Collaborator mining · Text mining · Natural language processing

78.1 Introduction

In the global economy era, business environment becomes more turbulent and the uncertainty faced by companies increases significantly. To gain sustainable competitiveness in such competitive and uncertain marketplaces, companies need to monitor their environments to produce competitive intelligence that helps managers make crucial business decisions efficiently and effectively [2, 3].

Automatic discovery of competitor/collaborator network (CCN) of a focal company represents a critical and essential task of competitive intelligence and is important and valuable for the stakeholders. From companies' perspective, CCN discovery helps them understand the important players in their target marketplace(s) and formulate competition strategies accordingly. On the other hand, for

C.-S. Yang (✉) · H.-C. Ye
Department of Information Management, Yuan Ze University, Chung-Li 32003, Taiwan, Republic of China
e-mail: Csyang@saturn.yzu.edu.tw

J. Juang et al. (eds.), *Proceedings of the 2nd International Conference on Intelligent Technologies and Engineering Systems (ICITES2013)*, Lecture Notes in Electrical Engineering 293,
DOI: 10.1007/978-3-319-04573-3_78,

individual shareholders or venture capitals, a comprehensive and up-to-date list of competitors and collaborators is essential to determine the value of a focal company.

There are several commercial databases (e.g., Hoover's, Mergent, Yahoo Finance) which provide the competitor lists of publicly traded companies. Some prior studies also developed several methods for the automatic discovery of competitors. However, they all encounter some critical limitations. First, it is time- and human-consuming for commercial databases to maintain comprehensive and up-to-date CCNs. Second, they all neglect the essential task of collaborator mining in competitive intelligence. Last but not least, the strengths of competing or collaborating relationships between a focal company and its competitors and collaborators may not be identical and should be determined properly. In response, this study concentrates on proposing an approach, which incorporates state-of-the-art text mining and natural language processing techniques to address the above-mentioned limitations and automatically discover competitors and collaborators of a focal company from online news. The proposed approach is empirically evaluated and the results are promising.

78.2 Literature Review

Some prior studies have concentrated on the issue of competitive intelligence for companies. Most of them adopted either Web pages or news documents as the information sources for competitive intelligence discovery. Bao et al. [1] proposed the CoMiner system to mine competitors from the Web automatically. Given a focal company *f*, CoMiner generated comparative queries for *f* based on some linguistic patterns and then applied these queries for candidate competitor extraction. CoMiner also had the ability to rank the competitors and find the competitive domain and evidence of a pair of competitors. CoMiner is a powerful technique for competitor mining. However, the coverage of the CoMiner may not be sufficient since only 7 linguistic patterns are adopted for competitor extraction.

Some studies adopted an alternative approach by exploiting news documents and network analysis for the discovery of competitor networks [5]. Specifically, candidate company names were identified by stock tickers and then treated as nodes in a competitor network. Subsequently, the link between a pair of nodes is estimated by the degree-based attributes, centrality-based attributes and structural equivalence-based attributes. Supervised learning algorithms are applied to induce a classifier to differentiate competitors from non-competitors. The major limitation of this approach is that the quantity and quality of training data affect the system effectiveness greatly.

Last, Pang and Sheng [6] combined Web pages and news documents for competitor mining. The similarities of in-link and out-link structures between a pair of companies were estimated based on the network constructed from news documents. In additional, the similarity of Website contents, co-occurred news

counts, and search engine counts were also incorporated as additional independent variables. Predictive models were then built using supervised learning algorithms. Similar to the previous approach, the quantity and quality of training data is crucial.

In summary, among the three approaches reviewed, they all have difficulty in differentiating competitors and collaborators. Moreover, they do not deal with the issue of relationship strength determination. These limitations motivate this study.

78.3 Competitor/Collaborator Network (CCN) Discovery

To support effective competitor/collaborator network (CCN) discovery, we propose an approach which combines several text mining and natural language processing techniques and is capable of mining competitors and collaborators of a focal company an then determining the strength of relationship between each pair of companies. Overall process of the proposed CCN technique is illustrated in Fig. 78.1.

Relevant Document Retrieval: Given a focal company f (e.g., Intel) and a search engine, the relevant document retrieval phase searches for documents, which potentially hold relevant competitive information for the focal company f, from the WWW. Currently, only news documents N_f whose titles contain the company f are retrieved. Subsequently, a preprocessing procedure is conducted to remove irrelevant information (e.g., html tags, reporter, date, etc.) from the retrieved HTML news documents and retain only the textual contents for subsequent analysis.

Named Entity Recognition: Because the purpose of the CCN technique is to identify competitors and collaborators of a focal company, it is intuitive that only the named entities, more specifically named organizations, could be candidates. Consequently, a named entity recognition tool (i.e., the Stanford named entity recognizer [4]) is adopted to annotate named entities in the retrieved news documents N_f. Take a news sentence—"Intel falls deeper, fails to break ARM mobile supremacy"—as an example, it will be annotated as "*Intel/ORGANIZATION falls/O deeper/O,/O fails/O to/O break/O ARM/ORGANIZATION mobile/O supremacy/O*." All terms, annotated with "/ORGANIZATION" tag, represent organization names. Accordingly, "Intel" and "ARM" are extracted as candidates of competitors or collaborators. After the named entity recognition step, a set of organization names ON_f for the focal company f is extracted from the set of relevant news documents N_f.

Named Entity Disambiguation: There may be some noises in the set of extracted organizations names ON_f. Abbreviation represents a common type of noises. For example, "Advanced Micro Devices" is commonly abbreviated as "AMD." These two terms are semantically identical but syntactically different. Another common noise is annotation mistakes. For example, "Advanced Micro Devices" may be mis-annotated as "*Advanced/ORGANIZATION*

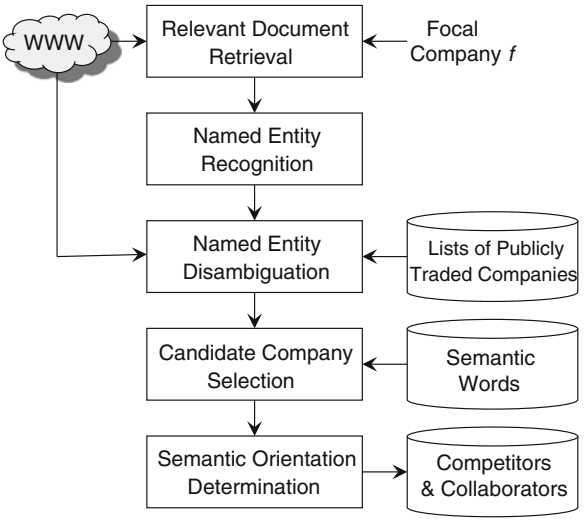

Fig. 78.1 Overall process of CCN

Micro/ORGANIZATION Devices/O." An incomplete company name, i.e., "Advanced Micro" may be extracted. This phase aims at eliminating the above-mentioned annotation noises. A two-step mechanism is designed.

A stock exchange market office generally maintains the listed companies and their abbreviations. Thus, the first step incorporates the lists of publicly traded companies as checking lists to overcome the problem of company name abbreviation. The lists of the three major stock exchange market offices (i.e., New York Stock Exchange, NASDAQ Stock Market, and American Stock Exchange) are adopted.

WWW is employed to design the second step. For each organization *on* (e.g., "Advanced Micro") in ON_f, it is submitted to a search engine (i.e., Google). The search results are used for disambiguation. We extracted the longest frequent noun phrase as the correct form of *on*. We first applied a part-of-speech tagger [7, 8] to syntactically tag each word. Subsequently, we implement a noun-phrase parser [9] to extract noun phrases. Finally, we select the longest frequent noun phrase (e.g., "Advanced Micro Devices") to represent the original organization name *on*.

Candidate Company Selection: Not all organization names ON_f are exact competitors or collaborators. Considering the following three news sentences for Intel: (1) **Intel** chips to ***challenge*** **AMD**, **ARM** in microservers. (2) **Dell** and **Intel** today ***jointly*** launched their first experience store in Pakistan. (3) Both **IBM** and **Intel** are scheduled to report quarterly earnings next Tuesday. AMD and ARM are competitors of Intel due to the occurrence of the word "challenge." Similarly, Dell and Intel are collaborators since "jointly" expresses the meaning of "in collaboration or cooperation." Last, IBM and Intel are neither competitors nor collaborators because there is no semantic word co-occurs. Therefore, we adopt a list of competing-related words and a list of collaborating-related words for candidate company selection. Specifically, the 228 power conflict words and the 118 power

cooperation words in General Inquirer (www.wjh.harvard.edu/~inquirer/) are employed and refined as the semantic words. For each organization name *on* in ON_f, we calculate its sentence-level co-occurrence frequency cf_{on} with the focal company *f* and the set of semantic words. If cf_{on} is higher than a threshold, *on* is regarded as candidate competitor or collaborator. A set of competitors and collaborators (CC_f) of *f* is obtained.

Semantic Orientation Determination: The purpose of the last phase is to determine the semantic relationship (i.e., competing or collaborating) and its strength between the focal company *f* and a company *c* in CC_f. Dichotomous classification is the simplest and intuitive approach for this problem. However, it is not an appropriate approach since a company could be a competitor and, at the same time, a collaborator of *f*. For example, Samsung is the manufacturer (i.e., collaborator) of Apple's A5 chip. On the other hand, Samsung's Galaxy-series mobile phones are major competing product of Apple's iPhone. Moreover, the strength of competing or collaborating varies and needs to be determined. For example, the competing strength between Ford Motor and General Motors is higher than that between Ford Motor and Mazda Motor since Mazda Motor has a partnership with the Ford Motor. Thus, we adopt an alternative approach for semantic orientation determination. Specifically, we divide the co-occurrence frequency cf_{on} of a company *on* into co-occurrence frequency of competing-related semantic words (i.e., $comp\text{-}cf_{on}$) and co-occurrence frequency of collaborating-related semantic words ($coll\text{-}cf_{on}$). By calculating the ratio between $comp\text{-}cf_{on}$ and $coll\text{-}cf_{on}$, we can determine the semantic orientation and the corresponding strength of *on* toward *f*. Figure 78.2 shows a sample output of the CCN using "Intel" as the focal company *f*.

78.4 Empirical Evaluation

Eight companies (i.e., Intel, Microsoft, Google, Yahoo, Ford Motor, General Motors, Amazon, and Wal-Mart) in the Fortune 500 are selected as our focal companies. News released by the Forbes and the Reuters from January 2010 to March 2011 are collected. 352, 622, 1018, 251, 480, 383, 280, and 393 news documents are collected for the eight focal companies respectively. To obtain the gold-standard lists of competitors and collaborators for the focal companies, we collect the competitors from three popular commercial databases, i.e., Hoover's, Mergent, and Yahoo Finance. However, not all companies are exactly competitors. For example, Mazda is listed as a competitor of Ford Motor in Hoover's but exactly a strategic partner of Ford Motor. Thus, three participants are asked to re-examine the semantic relationships in the lists. Table 78.1 shows the summary the gold-standard datasets of the eight focal companies. There are 28, 24, and 10 competitors for Intel in Hoover's, Mergent, and Yahoo Finance, respectively. The union of the three commercial databases (U) consists of 48 companies. Moreover, after the re-examination by this study, only 16 companies are exactly competitors

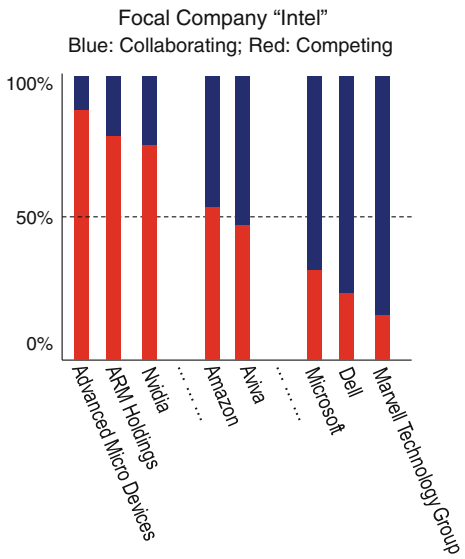

Fig. 78.2 Sample output of CCN

Table 78.1 Summary of the eight focal companies

	Inte.	Micr.	Goog.	Yaho.	Ford.	GM.	Amaz.	WalM.
Hoover's (H)	28	21	22	21	29	21	46	51
Mergent (M)	24	24	24	24	35	35	24	24
Yahoo (Y)	10	6	8	8	10	10	3	3
U = H∪M∪Y	48	38	48	48	58	38	67	67
Competitor	16	13	25	14	24	29	46	64
Collaborator	28	22	13	12	22	7	17	1
Neutral	4	3	10	22	12	2	4	2

of Intel. 28 companies are collaborators and 4 companies are neutral to Intel. The accuracy rate of U in Intel is 16/48 = 0.33. The macro- and micro-average accuracy rates of U are 0.54 and 0.56.

Evaluation Results: The outputs (denoted as O) of the CCN technique are also evaluated on the basis of the re-examined gold-standard dataset. As shown in Table 78.2, the accuracy rates (*Acc*) of the CCN technique are 0.55, 0.69, 0.64, 0.47, 0.68, 0.59, 0.67, and 0.48 for Inte., Micr., Goog., Yaho., Ford., GM., Amaz., and WalM., respectively. The macro- and micro-average accuracy rates are 0.60 and 0.60 accordingly. Furthermore, we analyze the performance of the CCN technique and the commercial databases (CD) on identifying competitors and collaborators. Since CD only identify competitors but ignore collaborators of a focal company, its *F* measure of the collaborator category (i.e., F_{coll}) are always 0 and worse than CCN. When the *F* measure of the competitor category (i.e., F_{comp}) are considered, CCN outperforms CD in Inte., Micr., Goog., Yaho., and Ford. but

Table 78.2 Comparative evaluation results

		Inte.	Micr.	Goog.	Yaho.	Ford.	GM.	Amaz.	WalM.	Macro	Micro
CCN	*Acc*	**0.55**	**0.69**	**0.64**	**0.47**	**0.68**	0.59	0.67	0.48	**0.60**	**0.60**
	F_{comp}	**0.63**	**0.61**	**0.74**	**0.5**	**0.72**	0.60	0.78	0.62	0.65	0.67
	F_{coll}	**0.69**	**0.74**	**0.50**	**0.63**	**0.71**	**0.70**	**0.72**	**0.55**	**0.66**	**0.67**
CD	*Acc*	0.33	0.34	0.52	0.29	0.41	**0.76**	**0.69**	**0.96**	0.54	0.56
	F_{comp}	0.50	0.51	0.68	0.45	0.59	**0.87**	**0.81**	**0.98**	**0.67**	**0.72**
	F_{coll}	0	0	0	0	0	0	0	0	0	0

is worse than CD in GM., Amaz., WalM., macro-average, and micro-average. Overall, CCN is slightly worse than CD in predicting competitors but significantly better than CD in predicting collaborators.

78.5 Conclusion and Future Research Directions

This study addresses the problem of automatic competitor/collaborator network discovery by proposing an approach which incorporates text mining and natural language processing techniques. According to our empirical evaluation results, the proposed CCN technique outperforms the commercial databases due to its ability on distinguishing collaborators from competitors and determining the strength of the relationships. Some ongoing and future research directions of this study are discussed. First, a large-scaled empirical evaluation with more focal companies from diverse industries and nations is essential to demonstrate the generalization ability of the CCN technique. Second, some designs of the CCN technique could be further refined. For example, relevant document retrieval phase could adopt an approach similar to Bao et al. [1] study to improve the quality of news documents for subsequent analysis. Moreover, the list of semantic words needs further refinement. Third, categorizing the collaborative relationship into more elaborate categories (e.g., suppliers, customers, and strategic partners) should be an essential and interesting future research direction.

Acknowledgments This work was supported by the National Science Council, R.O.C. under the grant NSC 100-2410-H-155-013-MY3 and the Ministry of Economic Affairs, R.O.C. under the grant 102-E0616.

References

1. Bao, S., Li, R., Yu, Y., & Cao, Y. (2008). Competitor mining with the web. *IEEE Transactions on Knowledge and Data Engineering, 20*, 1297–1310.
2. Chen, H., Chau, M., & Zeng, D. (2002). CI spider: A tool for competitive intelligence on the web. *Decision Support Systems, 34*, 1–17.

3. Choo, C. W. (1999). The art of scanning the environment. *Bulletin of the American Society for Information Science, 25*, 13–19.
4. Finkel, J. R., Grenager, T., & Manning, C. (2005). Incorporating non-local information into information extraction systems by Gibbs sampling. In *43th Annual Meeting of the Association for Computational Linguistics.*
5. Ma, Z., Pant, G., & Sheng, O. R. L. (2011). Mining competitor relationships from online news: A network-based approach. *Electronic Commerce Research and Applications, 10*, 418–427.
6. Pant, G., & Sheng, O. R. L. (2009). Avoiding the blind spots: Competitor identification using web text and linkage structure. In *International Conference on Information Systems*.
7. Toutanova, K., & Manning, C. D. (2000). Enriching the knowledge sources used in a maximum entropy part-of-speech tagger. In *Joint SIGDAT Conference on Empirical Methods in Natural Language Processing and Very Large Corpora.*
8. Toutanova, K., Klein, D., Manning, C., & Singer, Y. (2003). Feature-rich part-of-speech tagging with a cyclic dependency network. In *HLT-NAACL.*
9. Voutilainen, A. (1993). NPtool: A detector of English noun phrase. In *Workshop on Very Large Corpora.*

Chapter 79
An Extension of Gene Expression Programming with Hybrid Selection

Julie Yu-Chih Liu, Jeng-Her Alex Chen, Chiang-Tien Chiu and Juo-Chiang Hsieh

Abstract Premature convergence and suboptimal solutions are inevitable problems for evolutionary algorithms, such as Gene Expression Programming (GEP). This study proposes an extension of GEP which includes a hybrid selection method and a diversity maintenance mechanism to release local optimum of the GEP algorithm. The hybrid selection involves the Clonal selection and the Roulette wheel method. The experimental results show that the proposed algorithm outperforms Ferreira's GEP algorithm.

Keywords Evolutionary algorithm · Gene expression programming · Hybrid selection · Local optimum

79.1 Introduction

Gene Expression Programming (GEP) is an extension of Genetic Programming proposed by Ferreira [1]. The GEP allows individual expressions to be encoded easily with fixed length. GEP can be used to solve multiple problems such as symbolic regression, classification, combinational optimization and logic synthesis [2], modeling generation [3], and water resource management [4].

J. Y.-C. Liu · J.-H. A. Chen · C.-T. Chiu (✉) · J.-C. Hsieh
Department of Information Management, Yuan Ze University, Tau Yuan 32003, Taiwan, Republic of China
e-mail: s1019201@mail.yzu.edu.tw

J. Y.-C. Liu
e-mail: imyuchih@saturn.yzu.edu.tw

J.-H. A. Chen
e-mail: alex@saturn.yzu.edu.tw

J.-C. Hsieh
e-mail: s956210@mail.yzu.edu.tw

J. Juang et al. (eds.), *Proceedings of the 2nd International Conference on Intelligent Technologies and Engineering Systems (ICITES2013)*, Lecture Notes in Electrical Engineering 293,
DOI: 10.1007/978-3-319-04573-3_79,

It is well known that the performance of the evolutionary computation is influenced by the way of control parameter settings. Researchers have proposed adaptive methods to control the parameters such as adaptive probability of genetic operator control [5], adaptive population size [6], and adaptive gene selection method [7]. The search space of problem may contain many local extremes such as peaks or valleys, and the premature population will lead into local optimum. The literature of genetic programming consistently cites that the maintain diversity as a crucial factor to avoid local optimum [8, 9]. However, the approaches inevitably introduce heavy computation overhead.

This work proposes an algorithm to increase the diversity of population for evolution efficiency. The algorithm adds hybrid selection technique as an extension to gene expression programming, thus we call HS-GEP (Hybrid Selection-Gene Expression Programming) for short. It not only avoids local optimum but also prevents the heavy computational overhead. To examine the effectiveness of the proposed algorithm, this research compared our algorithm with Ferreira's GEP algorithm proposed in [2] by experimental testing on their fitness value and prediction power in both studies.

79.2 Gene Expression Programming

Gene Expression Programming (GEP) was proposed by Ferreira [1] as an alternative to overcome the common drawbacks of Genetic Algorithm (GA) and of Genetic programming for real-world problems. In GEP, likes in GA, a chromosome consists of a linear, symbolic string of fixed length composed of one or more genes. Despite their fixed length, GEP chromosomes code for expression trees (ETs) with different sizes and shapes. In order to evolve new populations, GEP follows the same Darwinian principle of the survival of the fittest and of the user populations of candidate solutions to a given problem. The evolving populations undergo selective pressure and their individuals are submitted to genetic operators.

GEP uses the well-known roulette wheel method for selecting individuals. The genetic operators of GEP include the replication operator, the mutation operator, crossover operator, insertion sequence (IS) operator, and root insertion sequence (RIS) operator. The RIS operator is similar to the IS operator, except that the insertion sequence must have a function as the first element and the target point must be also the first element of a gene (root).

To deal with numerical constants, Ferreira used random replacement approach for the transformation of expression tree in GEP [2]. This technique generated random numerical constants during the inception of the initial population and kept them in an array for each gene. It also used an extra symbol and an extra domain *Dc* composed of the symbols chosen to represent the random numerical constants. The extra symbols would be replaced with the numerical constant according to the position of constant array.

The GEP adopted the Clonal selection. The Clonal selection principle [10] was used to explain the basic features of an adaptive immune response to an antigenic stimulus. When antigens invalid into human body, nature immune system produces many antibodies to against antigens. The antibodies with higher recognition of antigen are selected to proliferate. These antibodies mutate to a new one in order to seek a better recognition of the antigen. The rest antibodies will be eliminated, and then the nature immune system will produce the new ones.

79.3 Methodology

The proposed algorithm HS-GEP adopts diversity maintenance and hybrid selection to increase the diversity of population and the number of elitism genes, respectively. The flowchart of the algorithm is illustrated in Fig. 79.1. Each process and the examination of condition are detailed below.

Initial population. The chromosome used in the method is the same as the structure given in [2]. The quality of initial population can influence the performance of gene expression programming. To obtain a good initial population, HS-GEP employs the Ramped-half and half method with the elitism selection method to generate the initial population. After numerous individuals are generated, the individuals with higher fitness value calculated by fitness function are chosen by the elitism selection method to form in the initial population.

Fitness function. The proposed algorithm uses the mean square error (MSE) to evaluate the fitness value of individual. The mean square error M_i of an individual is expressed by Eq. (79.1).

$$M_i = \frac{1}{n}\sum_{j=1}^{n}\left(P_{(i,j)} - T_j\right)^2 \tag{79.1}$$

where $P_{(i,j)}$ is the value predicted by the individual program i for fitness case j (out of n fitness cases) and T_j is the target value for fitness case j. For a perfect fit, $P_{(i,j)} = T_j$ is hold for all fitness cases, thus $M_i = 0$. The mean squared error ranges from 0 (the ideal value) to infinity. To measure the fitness of the evolved models, the fitness f_i of an individual i is evaluated by Eq. (79.2):

$$f_i = 1000 * \frac{1}{1 + M_i} \tag{79.2}$$

Which obviously ranges from 0 to 1000, and 1000 is the ideal value.

Termination. The evolution stops when either (1) the fitness value reaches the maximum $f_{\max} = 1000$, or (2) the number of generation reaches a user-define generation.

Low diversity. The diversity of population represents the extent of which the individuals are diverse in populations. Diversity is often regarded as the key factor

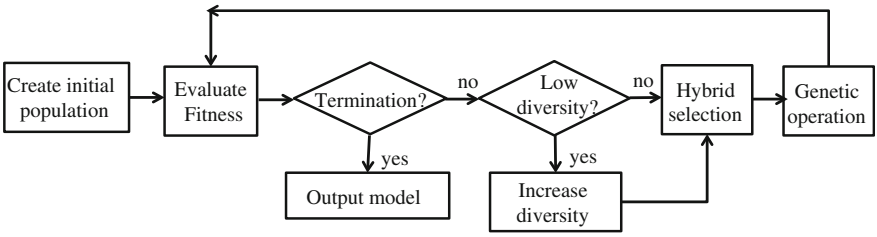

Fig. 79.1 The flowchart of HS-GEP

for the performance of an evolutionary algorithm. The diversity of a population is measured by the *entropy E* in Eq. (79.3) for every 20 generations.

$$E = -\sum_{k} p_k * \log p_k \tag{79.3}$$

where p_k is the proportion of the population P occupied by the population partition k. A partition is assumed to be each possible different fitness value. The procedure of increasing diversity will be executed if the entropy of the population is less than half of maximum entropy. Or, the hybrid selection algorithm is executed.

Increasing diversity. The proposed algorithm adopts the idea from a removal and addition of individuals in [6] to increase the diversity of population. It eliminates the worst 90 % individuals, and generating new individuals randomly into population. Different from [6], the size of population is fixed rather than variable in our algorithm to prevent the complicate computation overhead for deciding population size.

Hybrid selection algorithm. The hybrid selection algorithm adopted in the HS-GEP includes two selection methods, the Clonal special method and the Roulette wheel method. First, the Clonal special method selects the best α % individuals according to their fitness values. Then, the best α % individuals would clone β times and these cloned individuals would execute mutation operation. After mutation operation, the best offspring of each parent is selected for the next generation. The best offspring is the one whose fitness value is greater than the fitness value of its parent and sibling. If there are no qualified offspring, no one would be selected. After Clonal special method, the number of the offspring selected for the next generation is set at the number that individuals are cloned. Finally, the Roulette wheel method would be executed to produce offspring so that the population size of each generation will be fixed.

79.4 Experiments and Results

To test the performance of the HS-GEP and compare it with GEP-RNC (random numerical constants), dataset of sunspot series adopted from [2] was used. Two experiments were conducted for the comparison. One used100 data points

(1770–1869) for model training without testing. Another used 90 data points (1770–1859) for model training and the next 10 points for model testing. Here, the experiment of this study follows the experiments in [2] with the same parameter settings. The parameter settings of two experiments are listed as follows: number of runs = 100, gene head = 7, number of genes = 3, population size = 100, selection method: roulette wheel, number of generation = 5000, fitness function: MSE, function set = 4(+, −, *, /), linking function: +, *Dc* length = 10, *Dc* range = [−1, 1], mutation rate = 0.044, crossover rate = 0.3, reproduction rate = 0.3, inversion rate = 0.1, RIS rate = 0.1, IS rate = 0.1, gene transposition rate = 0.1, RNC-mutation rate = 0.01, *Dc*-mutation rate = 0.044, *Dc*-transposition rate = 0.1 and *Dc*-inversion rate = 0.1. Besides, Clonal special (α, β) was set to (0.1, 5) for the proposed algorithm.

The effect of the proposed approaches for the extension of GEP was examined with experiment by comparing the performance of the follows.

Method A: GEP-RNC.
Method B: GEP-RNC with the elitism selection method.
Method C: GEP-RNC with lightweight diversity maintenance method.
Method D: GEP-RNC with hybrid selection method.
Method E: Combination of approaches B and C.
Method F: Combination of approaches B, C and D.

Table 79.1 shows the comparison results, where F_{avg}, F_{max}, F_{min} and F_{std} respectively represent the average, maximum, minimum and standard deviation value of the fitness value of the best individuals with 20 runs. The results indicate that the GEP-RNC (method A) performed worse than any other methods except the GEP-RNC with elitism selection method B. The worse results of method B compared to A show that the elitism selection would lead to premature convergence, which in turn results into suboptimal solutions. The comparison of results of method D and method A (or B) verify that hybrid selection method would provide better solution than other selection mechanism considered. The comparison of the result on F_{avg} (4.3054) of method C and (3.9859) of A as well as the comparison of (5.1141) of method F and (4.9061) of method E prove that the proposed lightweight diversity maintenance method can improve the performance of GEP. In addition, the experiment (F) demonstrates that the three joint methods are superior (or favorable). Therefore, we adopted approach F as the proposed method for HS-GEP.

The influence of α and β, used for the Clonal selection, on HS-GEP were also examined. The results shows that The values F_{avg}, F_{max}, F_{min} and F_{std} vary with the value of α and β. For example, the best value of F_{avg} values is 5.8 at $\alpha = 0.4$, the worst is 4.9 at $\alpha = 0.9$. This confirms that variables α and β influence the performance of HS-GEP.

The comparison of GEP-RNC and HS-GEP using 100 data points and 90 data points are shown in Table 79.2, where *R* denotes the Pearson's correlation coefficient. The value of *R* reflects the extent of a linear relationship between the

Table 79.1 The comparison of using different selection methods

	F_{avg}	F_{max}	F_{min}	F_{std}
A (GEP-RNC)	3.9859	5.7863	3.1237	0.8401
B	3.8440	5.7918	2.9959	0.7152
C	4.3054	5.5598	3.2878	0.6594
D	4.8340	8.3379	3.2273	1.2987
E	4.9061	6.5698	3.2878	0.7767
F (HS-GEP)	5.1141	8.2706	3.8083	1.1117

Table 79.2 Comparison using 100 and 90 data points with 100 runs

	Using 100 data points		R of best model (90 data points)	
	Average f	Average R	Training	Testing
GEP-RNC	6.708	0.8803	0.9497	0.8785
HS-GEP	7.210	0.9439	0.9543	0.9484

predicted values and the target values. Both of the average of fitness and the average of R are used to measure the performance. The higher values of two measurements indicate the better performance. Accordingly, HS-GEP outperforms than original GEP-RNC.

79.5 Conclusion

The contribution of this work is three-fold. First, we design a hybrid selection method which chooses elitism genes for mutation operation and it works better than traditional single-selection methods. Second, we propose a lightweight diversity maintenance method which increases the diversity of population to prevent or reduce premature convergence without much overhead. Both of the methods work well with the evolution algorithms. Third, we propose HS-GEP which unites lightweight diversity maintenance and the hybrid selection with GEP. The HS-GEP reduces the suboptimal solutions of evolution.

This work demonstrates, through experimental comparison, that the lightweight diversity maintenance improves the performance of evolution algorithm. Besides, and our hybrid selection can release the premature convergence and reach better solution than the Clonal selection and the Elitism selection. By testing with dataset of sunspot series, the experimental results also prove that HS-GEP outperforms the original GEP-RNC on both of fitness value and prediction power.

Acknowledgments This work was supported by National Science Council of Taiwan under grant No. NSC 97-2410-H-155-029 and NSC 102-2410-H-155 -036 -MY2

References

1. Ferreira, C. (2001). Gene expression programming: A new adaptive algorithm for solving problems. *Complex Systems, 13*, 87–129.
2. Ferreira, C. (2006). *Gene expression programming: Mathematical modeling by an artificial intelligence (Studies in computational intelligence)*. Secaucus, NJ: Springer-Verlag New York Inc.
3. Colbourn, E., Roskilly, S., Rowe, R., & York, P. (2011). Modelling formulations using gene expression programming—A comparative analysis with artificial neural networks. *European Journal of Pharmaceutical Sciences, 44*, 366–374.
4. Guven, A., & Aytek, A. (2009). New approach for stage–discharge relationship: Gene-expression programming. *Journal of Hydrologic Engineering, 14*, 812–820.
5. Yin, Z., Brabazon, A., & O'Sullivan, C. (2007). Adaptive genetic programming for option pricing. In *Proceedings of the 2007 GECCO Conference Companion on Genetic and Evolutionary Computation* (pp. 2588–2594). ACM.
6. Rochat, D., Tomassini, M., & Vanneschi, L. (2005). *Dynamic Size Populations in Distributed Genetic Programming. Genetic Programming* (pp. 50–61). Berlin: Springer.
7. Fry, R., Smith, S. L., & Tyrrell, A. M. (2005). A self-adaptive mate selection model for genetic programming. In *Evolutionary Computation*, *The 2005 IEEE Congress on* (pp. 2707–2714). IEEE.
8. Ekárt, A., & Németh, S. Z. (2002). *Maintaining the Diversity of Genetic Programs. Genetic Programming* (pp. 162–171). Heidelberg: Springer.
9. Burke, E. K., Gustafson, S., & Kendall, G. (2004). Diversity in genetic programming: An analysis of measures and correlation with fitness. *Evolutionary Computation, IEEE Transactions on, 8*, 47–62.
10. De Castro, L. N., & Von Zuben, F. J. (2002). Learning and optimization using the clonal selection principle. *Evolutionary Computation, IEEE Transactions on, 6*, 239–251.

Chapter 80
Application to Biomimetic Robotic Wrist Based on Stewart Platform

Guo-Wei Weng and Yin-Fang Wei

Abstract An application to robotic wrist based on simplified Stewart platform by NI single-board RIO control system was investigated in this study. The positions of moving platform are changed by extension or shortening of three linear actuators. In order to obtain good control, the proportional-integral (PI) controller was employed in single axis control. Through experiments, the response time of robotic wrist to achieve the target position could be less than 0.3 s.

Keywords Biomimetic · Robotic · Stewart platform · NI single-board RIO

80.1 Introduction

In order to fulfill the motions like eversion, flexion, inversion and abduction, spherical joint with parallel mechanism became a good choice adopted in robotic arm [1, 2]. A parallel architecture was chosen over a serial chain due to the potential for higher stiffness, reduced inertia and higher accuracy. The most common parallel mechanism is 6-DOF (Degree of Freedom) known as the Stewart Platform [3, 4]. Reduced-DOF (i.e., less than six) architectures have the advantage of needing fewer actuators, thereby reducing the cost. The actuator can be pneumatic, hydraulic and motor. In this study, the DC motors were selected as the drives for their small sizes, high efficiency, and absolute position detecting.

NI single-board RIO (Reconfigurable I/O) developed by the National Instruments is a small industrial control system. By using LabVIEW graphical programming tools the single-board RIO FPGA embedded systems can rapidly

G.-W. Weng · Y.-F. Wei (✉)
Department of Electronic Engineering, Kao Yuan University, Kaohsiung 82151, Taiwan, Republic of China
e-mail: t10014@cc.kyu.edu.tw

J. Juang et al. (eds.), *Proceedings of the 2nd International Conference on Intelligent Technologies and Engineering Systems (ICITES2013)*, Lecture Notes in Electrical Engineering 293,
DOI: 10.1007/978-3-319-04573-3_80,

Fig. 80.1 Stimulated scheme of the robotic hand

Fig. 80.2 Stimulated scheme of a linear actuator

developed. Therefore, single-board RIO was employed as controller to implement the biomimetic robotic wrist.

The mechanical characteristics of the 3-axis pneumatic motion platform have been discussed [5]. Several research, the Fuzzy, and PID were employed in single axis trace control [6, 7]. In this study, PI was adopted.

80.2 Architecture

The specification of the whole robotic wrist includes central processor unit, PC, power system, NI single-board RIO, DC motors, encoder modules and. The power supplying is a 22.2 V/4000 mAh rechargeable battery for its durableness.

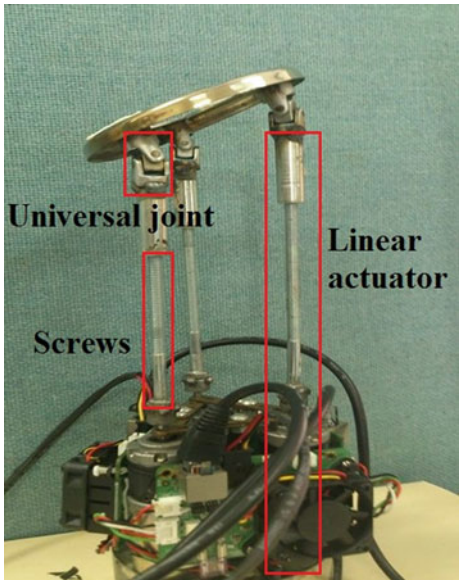

Fig. 80.3 Photo of 3-axis mobile platform

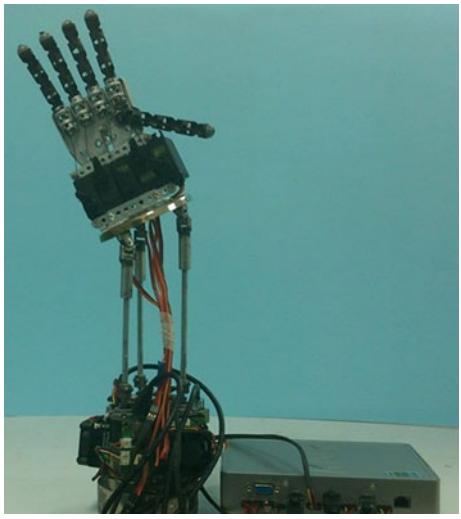

Fig. 80.4 Photo of biomimetic robotic hand

The figure of robotic hand was designed by computer-aid software, Solid-Works, as shown in Fig. 80.1. Linear actuator was fulfilled by a metal rod with screws linked a universal joint together, activated by motor, Fig. 80.2. Three linear actuators were driven shafts, connected to a plate, and became a 3-axis mobile platform. The photo of real object was in Fig. 80.3. The biomimetic robotic hand was pictured as Fig. 80.4.

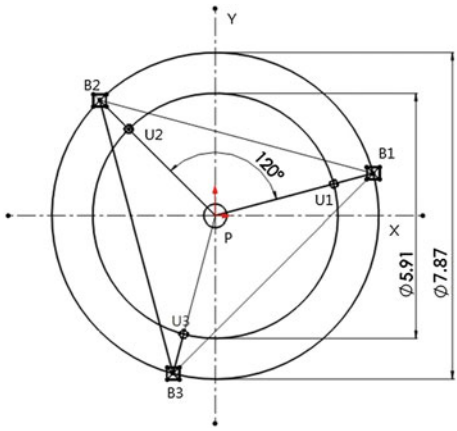

Fig. 80.5 The diagram of moving platform

80.3 Experiments Methods and Results

In this study, a robotic wrist with 3-DOF 3-axis simplified Stewart platform was implemented. The positions of the motion platform could be changed by lengthening or shortening of the actuator axis. The math model adopted to obtain the elongations of the three actuator axis is proposed by Cheng [8]. The inverse kinematics of the 3-axis mechanism was derived to get the center of the mobile plate and the elongation of the driven shaft. The diagram of moving platform was shown in Fig. 80.5. All connection points of the top and bottom could be obtained, and the locations are as follows:

$$^{U}U_i = r \cdot [\, C\theta_i \quad S\theta_i \quad 0 \quad 1\,]^T;\ \mathrm{i} = 1\text{–}3 \tag{80.1}$$

$$^{U}B_i = R \cdot [\, C\theta_i \quad S\theta_i \quad 0 \quad 1\,]^T \tag{80.2}$$

where r is the radius of circum-radius of the mobile plate, and R is the radius of circum-radius of the fixed plate. S and C indicate sinusoid and cosine function respectively. The coordinate points of the mobile platform could be transformed into the coordinate system of the fixed platform. The length of the connecting rods, Di can be expressed as:

$$D_i = \sqrt{^{B}U_{ix}^2 - 2^{B}B_{ix}{}^{B}U_{ix} + {}^{B}B_{ix}^2 + {}^{B}U_{iy}^2 - 2^{B}U_{iy}{}^{B}B_{iy} + {}^{B}B_{iy}^2 + {}^{B}U_{iz}^2} \tag{80.3}$$

In industrial control systems, PID (Proportional-Integral-Derivate) controller is widely used as feedback design. To minimize the error, the controller attempts to adjust the inputs. In this experiments, PI controller was adopted, as in Fig. 80.6, the proportional gain $k_p = 0.005$.

Figure 80.7 shown the length of the connecting rod with time, the scheme indicated the response of manipulator fully actuated. The maximum of elongation

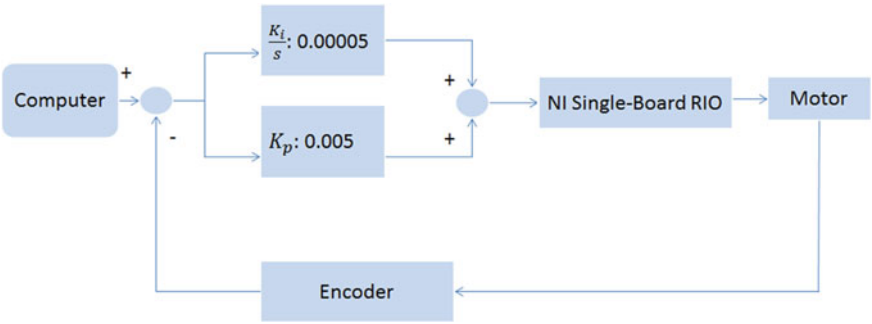

Fig. 80.6 The scheme of PI controller

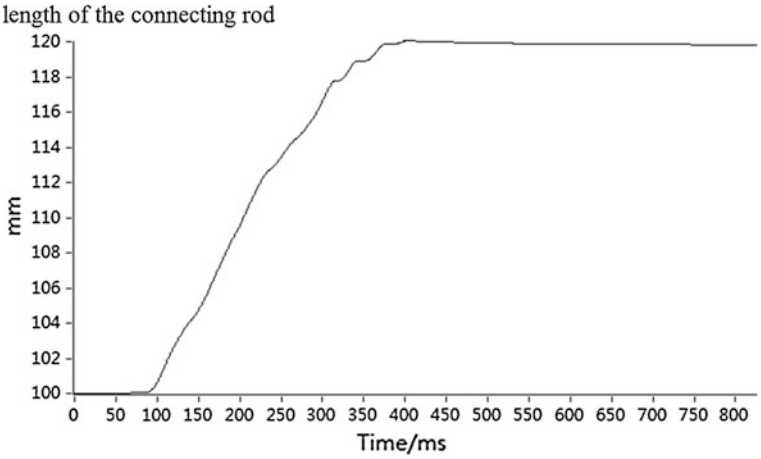

Fig. 80.7 The length of the connecting rod with time

was restricted to 20 mm. The rising time was approximately about 0.3 s. The inclination angle of motion platform was approached 22 degrees.

80.4 Conclusion

In this study, motors were used as drives of actuators, and NI single-board RIO was used to construct embedded control system. The biomimetic robotic wrist was implemented to fulfill the need of dexterousness with PI control.

The response time of robotic wrist to achieve the target position can be less than 0.3 s. The inclination angle of motion platform was approached 22 degrees.

This results in a single manipulative device which can operate in most situations where a human being could perform manipulative functions. Further it can also function in environments that would be dangerous or difficult for a human. Adaptations of the design could also function at different scales, under dangerous conditions.

References

1. Chia, P.-C., Dong, C.-W., & Kuo, C.-H. (2011). Implementations and controls of a 3-DOF parallel link joint module. *Communications in Computer and Information Science, 212*, 66–77.
2. Huapeng, W. (2008). *Parallel manipulators toward new applications*. Austria: I-Tech Education and Publishing.
3. Stewart, D. (1965). A platform with 6 degrees of freedom. *Proceedings of the Institute of Mechanical Engineering, 180*(1), 371–386.
4. António, M. (2009). Lopes: Dynamic modeling of a Stewart platform using the generalized momentum approach. *Communications in Nonlinear Science and Numerical Simulation, 14*, 3389–3401.
5. Chen, Y.-S., Chen, B.-Y., & Cheng, Y.-M. (2011). An investigation of a 3-PRS pneumatic parallel motion mechanism. In *Proceedings of 2011 MIIS Mechatronic and Industry Interact Cross Strait Conference*, *A09*, (pp. 116–121).
6. Hamdan, M., Gao, Z. (2000). A novel PID controller for pneumatic proportional valves with hysteresis. In *Record of the 2000 IEEE Industry Applications Conference*, (Vol. 2, pp. 1198–1201).
7. Parnichkun, M., & Ngaecharoenkul, C. (2000). Hybrid of fuzzy and PID in kinematics control of a pneumatics system. In *Proceedings of the 26th Annual Conference of the IEEE Industrial Electronics Society*, (Vol. 2, pp. 1485–1490).
8. Cheng, Y.-M. & Chen, Y.-S. (2013). An angle trajectory tracking for a 3-DOF pneumatic motion platform by the NI compact RIO embedded system, *Journal of Mechanics Engineering and Automation*, *3*, 14–21.

Chapter 81
VCT Protection IC for Li-Ion Battery

Tzung-Je Lee and Wei-Ren Lin

Abstract This paper proposes a VCT (Voltage, Current, and Temperature) protection IC for the Li-Ion battery cell 18650. By using the VCT protection IC, the BMS (Battery Management System) can be miniaturized into a SOC (System-on-a-Chip) to reduce the system size in the future. The proposed design is implemented using TSMC 0.25 um BCD HV G2 process. The over voltage and under voltage limits are simulated to be 4.1986 and 2.5037 V, respectively. The over temperature and under temperature limits are simulated to be 0.26383 and 44.849 °C, respectively. Besides, the charging current is detected linearly and the gain is 0.6610 (V/A) for the maximum charging current of 2.9997 A.

Keywords Li-Ion · Battery · Protection · Battery management system · BMS

81.1 Introduction

With the development of the material technologies, Li-Ion batteries have become a preferred choice for portable electrical products and smart home energy applications, because of their higher density than nickel–cadmium or nickel-metal hydride batteries.

However, it is quit dangerous if Li-Ion batteries are not dealt properly. In most cases, the only effect is simply that the life of the battery cell is reduced, or the cells are damaged, with no safety issues. However, abusing a Li-Ion battery cell in particular ways can be extremely dangerous and can result in physical damage and overheating. Li-Ion batteries will be quickly damaged and may burst into flames if they are not charged and discharged in the SOA (Safe Operating Area).

T.-J. Lee (✉) · W.-R. Lin
Department of Computer Science and Information Engineering, Cheng Shiu University
ICITES, Kaohsiung 83347, Taiwan, Republic of China
e-mail: tjlee@csu.edu.tw

J. Juang et al. (eds.), *Proceedings of the 2nd International Conference on Intelligent Technologies and Engineering Systems (ICITES2013)*, Lecture Notes in Electrical Engineering 293,
DOI: 10.1007/978-3-319-04573-3_81,

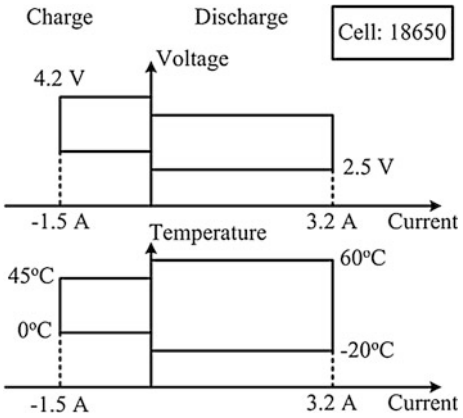

Fig. 81.1 Safe operating area (SOA) of the Li-Ion battery cell 18650

Figure 81.1 reveals the SOA of a Li-Ion battery cell 18650 provided by the manufacturer [1]. Referring to Fig. 81.1, the maximum voltage of the Li-Ion battery cell 18650 is limited to 4.2 V with the charging current of 1.5 A in the CC/CV (Constant Current/Constant Voltage) charging mode. At the same time, the charging temperature must be in the range from 0 to 45 °C. Otherwise, it will cause the battery cell overheating, damage and even bursting into flame. In the discharging mode, the voltage of the Li-Ion battery cell 18650 cannot be lower than 2.5 V with 3.2 A discharging current. Besides, the temperature should be limited from −20 to 60 °C. Otherwise, it will cause over-discharged for the cell and reduce its capacity and cycle life.

There are many battery management systems (BMSs) implemented using commercial battery protection ICs [2, 3]. These systems are huge and complicated. In order to implement a BMS in a SOC in the future, this paper proposes a VCT (Voltage, Current, Temperature) protector IC, which can be integrated in a SOC to reduce the size of the system, and make sure the Li-Ion battery cell operating in the SOA.

81.2 VCT Protection IC for Li-Ion Battery

Typically, an analog battery management system includes a Charger, and a VCT Protector. The Charger is composed of an AC/DC converter and a DC/DC converter to provide CC/CV charging procedure. The VCT Protector is to detect the voltage, current, and temperature of the battery cell and generate the control signals to the Charger to charge the battery cell in the SOA. Thus, the VCT Protector includes the Over Voltage Protector, the Over Current Protector, and the Over Temperature Protector.

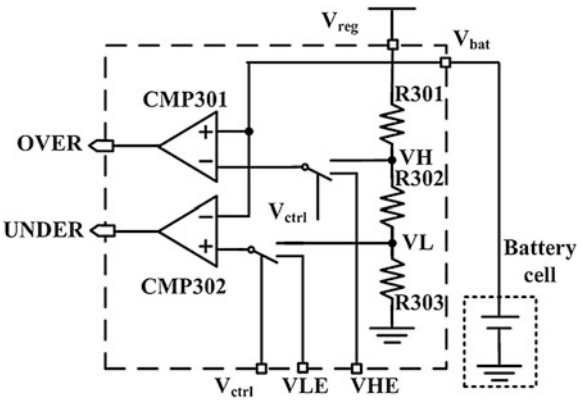

Fig. 81.2 Schematic of the Over Voltage Protector (OVP)

81.2.1 Over Voltage Protector

Figure 81.2 reveals the schematic of the Over Voltage Protector (OVP). The circuits in the dashed line refers to the circuits in the IC, which are composed of two Voltage Comparators (CMP301 and CMP302), and the resistor string with three resistors in series.

The serial resistor string is biased by the voltage, V_{reg}, provided by the system regulator. With the voltage division of the resistor string, two reference voltages, VH (=4.2 V) and VL (=2.5 V) are obtained and are biased to the negative input terminal of CMP301 and the positive input terminal of CMP302, respectively. On the other hand, the positive input terminal of CMP301 and the negative input terminal of CMP302 are biased to the battery cell's positive node, V_{bat}. With the comparison of the Voltage Comparators, two digital signals, OVER and UNDER are generated by CMP301 and CMP302, respectively. OVER refers to the over voltage of the battery cell. UNDER refers to the under voltage of the battery cell. Besides, the control signal, V_{ctrl}, is given for the two switches to determine whether the reference voltages are selected from the external or internal bias circuits. This mechanism is to make sure the functional work of the circuit.

81.2.2 Over Current Protector

Figure 81.3 shows the schematic of the Over Current Protector, which is composed of a Wide-Range Operational Amplifier (OPA), a MOS transistor, and three resistors, R401, R402, and R_{senI}. The inductor and the capacitor refer to the simplified schematic of a DC/DC converter, which plays the role of the Charger. V_{sup} refers to the input voltage of the Charger. The OCP senses the charging current of the battery cell and generates a proportional output voltage for the Charger to adjust the charging current. By connecting a small resistor, R_{senI}, in

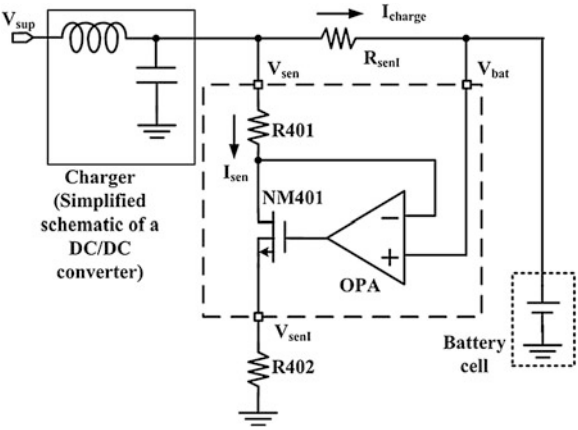

Fig. 81.3 Schematic of the Over Current Protector (OCP)

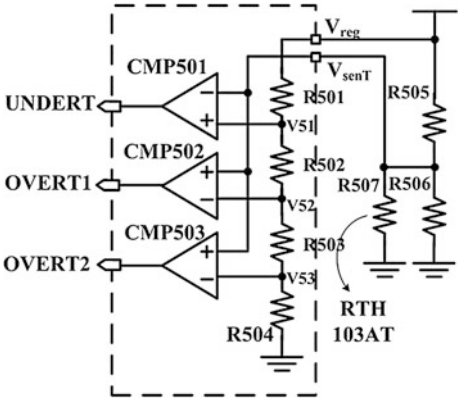

Fig. 81.4 Schematic of the Over Temperature Protector (OTP)

series to the charging path, the value of the charging current, I_{charge}, can be derive from the voltage drops across R_{senI} and the cell voltage, V_{bat}. After computation and simplification, the output voltage, V_{senI}, can be derived to be

$$V_{senI} = \frac{R_{senI} \cdot R_{402}}{R_{401}} \cdot I_{charge}, \tag{81.1}$$

Notably, R402 is an external resistor which can fine tune the gain of the OCP.

81.2.3 Over Temperature Protector

Figure 81.4 shows the schematic of the Over Temperature Protector, which is composed of three Voltage Comparators, CMP501–CMP503, and four internal resistors, R501–R504, and three external resistors, R505–R507. R507 is an thermal

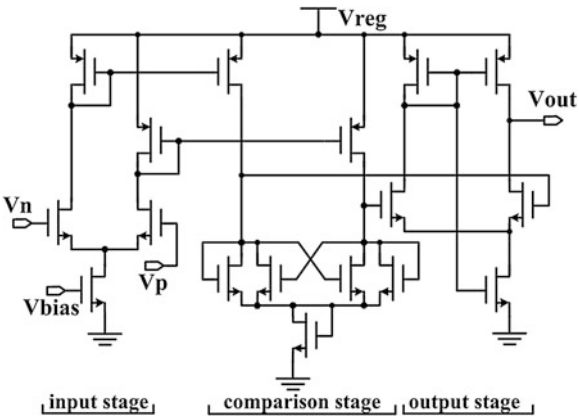

Fig. 81.5 Schematic of the voltage comparator

resistor with product model number RTH 103AT [4]. By parallel connected to the serial resistors, R506 and R507, a voltage, V_{senT}, whose value is reduced with the rise of the temperature, is obtained. V_{senT} is biased to the negative input terminal of CMP501 and the positive input terminals of CMP502 and CMP503. R501–R504 are the resistor string to generate three reference voltages, V51–V53. With the reference voltages, V51–V53, biased to the other input terminals of CMP501–CMP503, three digital output signals, UNDERT, OVERT1, and OVERT2 are generated to represent the operating temperature of the battery cell.

81.2.4 Voltage Comparator

Figure 81.5 shows the schematic of the Voltage Comparators utilized in the proposed VCT Protection IC. CMP is divided to three stages. The first stage is the input stage, which is a differential amplifier with active loads to receive the differential input signals. The second stage is the comparison stage, which is to determine the comparison result. It uses the cross-coupled structure to increase the comparison speed. Besides, the cross-coupled structure provides the hysteresis comparison to reject the noise. The output stage is a self-biased single output differential amplifier, which is to provide the required driving ability.

81.2.5 Wide-Range Operational Amplifier

Figure 81.6 reveals the schematic of the Wide-Range Operational Amplifier [5]. The OPA is composed of four stages, the bias stage, the input stage, the gain stage, and the output stage. The bias stage is to provide the operation current for the OPA by using diode-connected MOS strings. The input stage is composed of p-type and

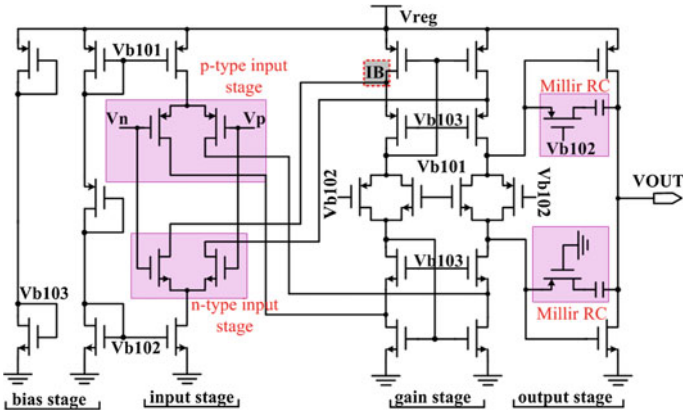

Fig. 81.6 Schematic of the wide-range operational amplifier

Fig. 81.7 Layout of the proposed VCT protection circuit

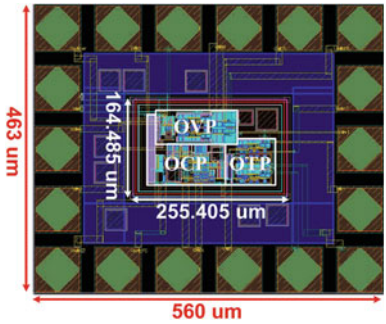

n-type MOS transistors. The p-type MOS transistors operate for the low input voltage and the n-type MOS transistors operate for the high input voltage. Thus, it is easy to carry out wide input range. The gain stage is composed of the cascade MOS transistors to increase the voltage gain. The two MOS resistors and the two capacitors are utilized for the Miller frequency compensation RCs. The output stage is to provide the required driving ability.

81.3 Implementation and Simulation

The proposed VCT Protection IC is implemented using TSMC 0.25 um BCD HV G2 process. The layout is shown in Fig. 81.7. The core area is 164.485 × 255.405 um^2. The chip area is 463 × 560 um^2. The simulation is based on HSPICE.

Figures 81.8, 81.9 and 81.10 reveals the worst case of the post-layout simulation results for the OVP, OCP, and OTP, respectively. Referring to Fig. 81.8, the digital signal, OVER, is activated when the cell voltage, V_{bat}, is at 4.1984 V to

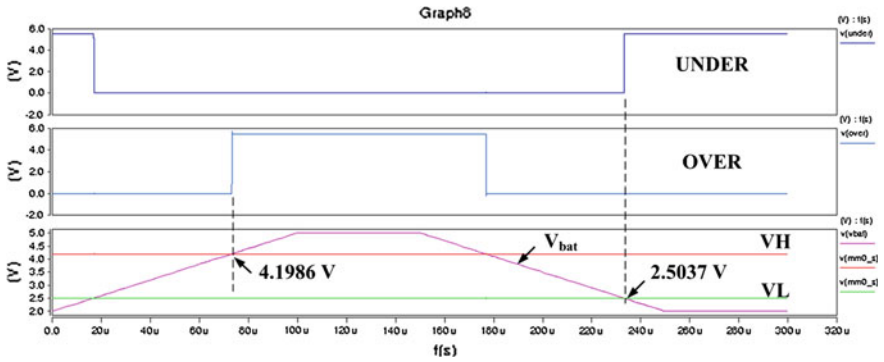

Fig. 81.8 Post-layout simulation results of the OVP at the worst-case of FF, VDD + 10 %, 45 °C

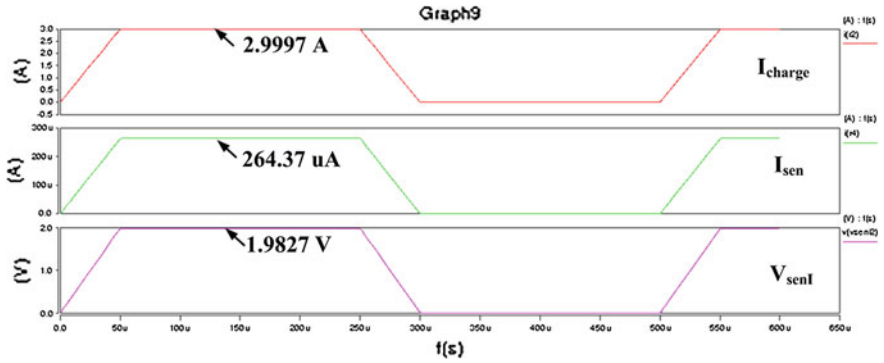

Fig. 81.9 Post-layout simulation results of the OCP at the corner of SS, VDD−10 %, 0 °C

avoid the over voltage occurred in the charging mode. Moreover, the digital signal, UNDER, is activated when V_{bat} is at 2.5037 to avoid the under voltage occurred in the discharging mode.

Referring to Fig. 81.9, the sense current, I_{sen}, is miniaturized to be 264.37 uA with I_{charge} of 2.9997 A. The current gain (=I_{sen}/I_{charge}) is $11{,}346^{-1}$. At the same time, the output voltage is 1.9827 V. Thus, the voltage gain is 0.6610 (V/A). Notably, the relation of V_{senI}, I_{sen}, and I_{charge} is linear. Thus, it is easy to be detected.

Referring to Fig. 81.10, the temperature voltage, V_{senT}, is reduced according to the rise of temperature. With the comparison of V_{senT} to V51, V52, and V53, the digital output voltage UNDERT, OVER1, and OVER2, are generated to refer to 0.26383, 29.552, and 44.849 °C, respectively. Thus, the under temperature and over temperature can be detected by UNDERT and OVER1 in the charging mode as shown in Fig. 81.1. Table 81.1 reveals the specifications and the simulated results of the pre-layout and post-layout simulation for the proposed VCT

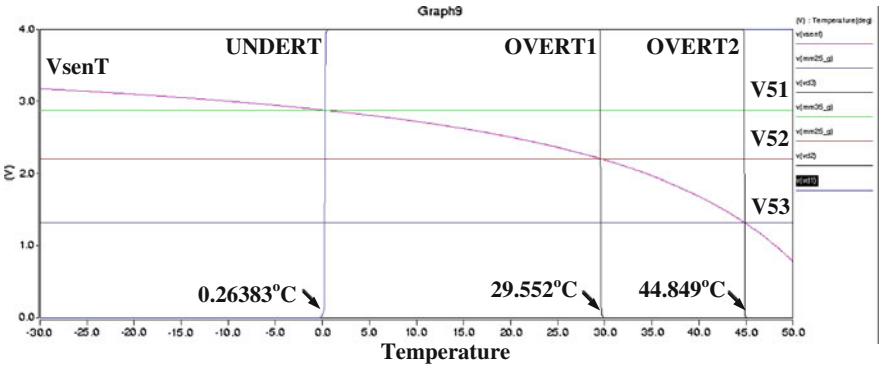

Fig. 81.10 Post-layout simulation results of the OTP at the corner of FF, VDD + 10 %

Table 81.1 Table of specifications and the simulated results of the pre-layout and post-layout simulation of the proposed VCT protection IC

	Specifications	Pre-sim	Post-sim
Power supply (for charging)	5.0 V	5.0 V	5.0 V
Battery voltage	3.6 V	3.6 V	3.6 V
Over voltage limit	<4.2 V	4.1984	4.1986
Under voltage limit	>2.5 V	2.5038	2.5037
Over temperature limit	<45 °C	44.849	44.849
Under temperature limit	>0 °C	0.3189	0.2638
Current gain (I_{sen}/I_{charge})	$<10{,}000^{-1}$	$11{,}048^{-1}$	$11{,}346^{-1}$
Voltage/current gain (V/A)	>0.5	0.6788	0.6610
Core Area (um^2)	N/A	255.405 ×164.485	255.405 × 164.485
Area (um^2)	N/A	560 × 463	560 × 463
Power dissipation	N/A	13.25 mW	12.56 mW

protection IC. Based on Table 81.1, the battery cell 18650 can be protected by the proposed VCT protection IC.

81.4 Conclusion

The VCT protection IC is proposed in this paper to reduce the BMS size. The over and under voltage limits are simulated to be 4.1986 and 2.5037 V, respectively. The over and under temperature limits are simulated to be 0.26383 and 44.849 °C, respectively. The charging current is detected linearly for the maximum charging current of 2.997 A. By using the proposed VCT protection IC, the Li-Ion battery cell 18650 can be properly protected.

Acknowledgments This research was partially supported by National Science Council under grant NSC 101-2632-E-230-001-MY3, as well as Cheng Shiu University under grant CS-2-102-023 (B1) and CS-B2-101-292. Besides, the authors would like to express their deepest gratefulness to CIC (Chip Implementation Center) of NARL (National Applied Research Laboratories), Taiwan, for their thoughtful chip fabrication service.

References

1. Lithium Ion Battery. (2010). Panasonic datasheet 18–50.
2. Synchronous Switch Mode, Li-Ion and Li-Polymer Charge-management IC with integrated power FETs. (2010). Texas Instruments Datasheet bq24105.
3. Kim,C.-H., Kim, M.-Y. Kim, Y.-D., & Moon, G.-W. (2011). A modularized charge equalizer using battery monitoring IC for series connected Li-Ion battery strings in an electric vehicle. *IEEE 8th International Conference on Power Electronics and ECCE Asia (ICPE & ECCE)*, 28(8), 304–309. (August 2013).
4. NTC Thermistors. (2012). Murata manufacturing datasheet R44E-15.
5. Baker, R. J., Li, H. W., & Boyce, D. E. (2010). *CMOS circuit design, layout, and simulation* (3rd ed.). New York: Wiley-Interscience.

Chapter 82
Energy Management Technologies for Smart Home Applications

Huo-Ching Sun, Yann-Chang Huang, Chao-Ming Huang and Chien-Chin Tung

Abstract This paper reviews previous and recent trends in energy management systems (EMS) and energy information communication technologies (EICT) for smart home applications. Relevant EMS and EICT publications on smart homes are reviewed. This paper first analyzes different energy management approaches for smart home applications, including fuzzy logic, neural networks, heuristic methods, and evolution-based approaches. Then, various EICT approaches are surveyed to evaluate the feasibility of smart home applications by discussing historical developments and introducing advanced EICT methods. Importantly, this paper contributes to efforts to further advanced energy management technologies for smart home applications.

Keywords Energy management systems · Energy information communication technologies · Smart home applications

82.1 Introduction

Smart grid integrates advanced information and communications technologies, automation, sensing and metering technologies, and energy management techniques to incorporate intelligence and bidirectional flows of information and electricity throughout a power grid. The smart grid is a modern power grid infrastructure for better efficiency, reliability, with possible integration of

H.-C. Sun · Y.-C. Huang (✉) · C.-C. Tung
Department of Electrical Engineering, Cheng Shiu University, Kaohsiung, Taiwan, Republic of China
e-mail: huangyc@csu.edu.tw

C.-M. Huang
Department of Electrical Engineering, Kun Shan University, Tainan, Taiwan, Republic of China

J. Juang et al. (eds.), *Proceedings of the 2nd International Conference on Intelligent Technologies and Engineering Systems (ICITES2013)*, Lecture Notes in Electrical Engineering 293,
DOI: 10.1007/978-3-319-04573-3_82,

renewable and alternative energy sources. Smart grid technologies can schedule loads at the consumer level to conserve energy, reduce electricity costs, and facilitate grid operations.

Figure 82.1 shows the smart grid conceptual model [1]. The smart grid enables the provision of real-time pricing information and other services to consumers, using smart meters, home automation networks, and advanced metering infrastructure (AMI). However, expecting a consumer to create an optimal schedule from many possibilities is unrealistic. Recently, millions of smart meters, sensors, and automatic control devices have been deployed in residential and commercial buildings via two-way communication networks. Furthermore, the on/off, cycling, or mode switching of appliances can be controlled and monitored wirelessly with a home energy management system by developing smart appliances and deploying home area networks (HANs).

Therefore, a smart home energy management system (SHEMS) must be developed, which requires little consumer attention to set up and allows consumers to compare costs/benefits with different load schedules. The SHEMS motivates consumers to actively participate in managing their energy consumption for their own benefit as well as for the efficient, reliable, and economical operations of a power grid.

82.2 Energy Management Systems

Several hardware and software platforms have been developed to realize a smart home from the perspective of energy conservation and management [2]. These systems allow end users to monitor and control key equipment remotely within their homes and also implement rule-based decision-making about their operations. Some systems also incorporate location-management frameworks that can either learn and predict occupant location and routes or learn and recognize occupant activities [3].

An information fusion-based smart home control system [4] was presented to integrate information from multiple sources to control home appliances. This system combined information acquisition and fusion, wireless/wired communication modes, central intelligent control algorithms, and user-friendly interfaces of the central control unit. The fuzzy logic and fuzzy neural network approaches were applied and both output acceptable lead alarm-time estimations, using information from physical sensors and open sources.

A proactive, autonomous, context-aware, unobtrusive lighting system [5] for a lab-based smart home environment was implemented using pattern recognition, continuous control, and online adaptation approaches. A data mining-based approach was presented to accurately estimate the prediction interval of the electricity price series [6]. A novel energy service simulation platform was presented to improve services delivery using maximizing net benefit derived from energy services [7]. The simulation platform maximized the value of required

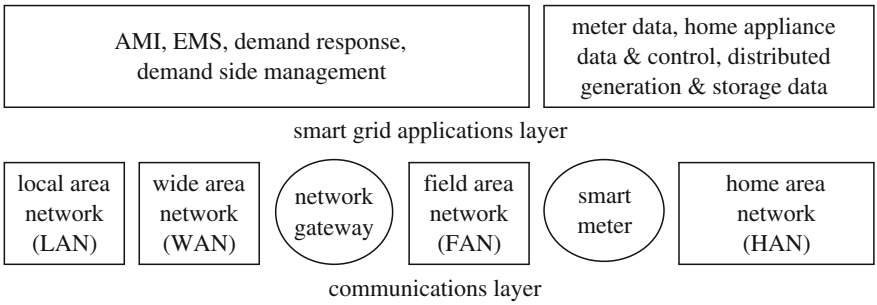

Fig. 82.1 The smart grid conceptual model

services while minimizing the cost of energy consumption by proposing a strategy, or a schedule for how available distributed energy resources (DERs) should be operated. To solve this optimization problem and generate effective strategies, particle swarm optimization (PSO) was applied because this algorithm can be implemented easily and has global search ability within reasonable computing times.

Designing smart home device descriptions and standard practices for demand response and load management applications was presented in [8]. The paper proposed smart home interfaces and device definitions to allow interoperability among ZigBee devices produced by various manufacturers of electrical equipment, meters, and smart energy enabling products. The control application domains include sensing device control, pricing and demand response and load control applications.

A decision-support system was applied to optimize energy provisions by allowing end users to first assign values to desired energy services, and then schedule their available DERs to maximize net benefits [9]. The PSO method was used to solve the optimization problem, and the basic formulation of cooperative PSO was enhanced by stochastic repulsion among particles, which adds additional randomness to particle trajectories during initial iterations and prevents premature convergence.

Linear programming-based energy consumption scheduling framework [10] was presented to achieve a desirable trade-off between minimizing electricity payment and minimizing wait time for operation of each appliance. Test results suggested that the proposed scheduling design and the price predictor filter combined significantly reduced user payments and the resulting peak-to-average ratio in load demand under various load scenarios. Moreover, the proposed optimal scheduling schemes are beneficial for both end customers and utilities.

To minimize payment or maximize user comfort preferences, two-step linear and sequential optimization-based algorithm [11] was applied to solve the appliance commitment problem, using price and consumption forecasts. The thermal dynamics of heating and coasting of the water heater load was modeled by

physical models; random hot water consumption was modeled using statistical methods. Moreover, user comfort settings were regarded as a set of linear constraints. Test results confirm that the solution may achieves an optimal balance between energy cost and user comfort level.

A hybrid forecasting framework [12] was presented to deal with dynamics for predicting electricity price and demand. The proposed framework integrated a multi-input multi-output forecasting engine for joint price and demand prediction with data association mining algorithms. A hybrid approach combing PSO and fuzzy inference for smart home one-step-ahead load forecasting was presented [13]. The PSO algorithm firstly determined the locations of fuzzy membership functions. Then, the fuzzy inference approach was adopted to develop the one-step-ahead load forecasting. Test results confirmed that the proposed approach possessed better forecasting accuracy than existing methods.

82.3 Energy Information Communication Technologies

A smart grid provides consumers with greater control over their individual energy costs, using technology that allows for monitoring of electricity consumption. Smart grid technologies can schedule loads at the consumer level to conserve energy, reduce electricity costs, and facilitate grid operations. The smart meter delivers real-time electricity prices to homes, allowing customers to leverage data via an in-home energy management controller (EMC). The EMC uses prices and user-defined preferences to control power use across a household. Demand response controls electricity consumption using varying the price of electricity over a 24-h day period to reduce peak demand.

Using a suite of hardware devices and software programs, SHEMS facilitates the demand response imperatives of the smart grid while empowering consumers with information and increasing the control functions automatically or manually. The SHEMS can be characterized as an electronic information display, allowing consumers to visualize their energy use, thus facilitating response to dynamic price signals. To supply real-time feedback on energy consumption, in-home displays (IHDs) enable residents to lower energy consumption by providing information on the cost of the energy consumed. In addition to displaying basic information (e.g., real-time power use and planed hourly electricity cost and consumption data), IHDs also allow customers to determine how behavioral changes alter energy expenditures and consumption. While many IHDs are commercially available, most are portable, wireless, or plug-in. IHD illustrates the power drawn from an electric meter using a clip-on device transformer to measure the electric current. The measured values are communicated to IHD via PLC or wireless radio frequencies.

AMI is an interactive system that includes smart meters, a wired or wireless communications network, computer hardware, and meter data management

software. AMI enables meters to measure and record customer electricity use and then transmits this data over the communications network to a central collection point, either a utility or a third-party aggregator. Progress in AMI has led to the development of demand-side management (DSM) programs. DSM is the implementation of policies and integrates various appliances with a smart controller, capable of bi-directional communication with the utility to control, regulate, and lower energy consumption.

HANs connect home appliances and devices into an integrated communicative system that links TVs, lights, appliances, computers, SHEMS, and security systems, among other home systems. All devices are connected to a central access point (i.e. a hub, node, or router) by wired or wireless networks. Complex HANs are constructed around a smart meter and a network of smart appliances and thermostats. HANs integrate multiple appliances and devices into a single cohesive wired or wireless communications command and control network that enables complete home automation and energy management. All HANs comprise the following elements: hub, gateway, operating system, network management software, information display, and smart appliances.

Two-way communications networks among utilities, grid operators, and consumers will lay the foundation for deploying SHEMS. The networks must be reliable and secure when transmitting enormous volumes of data. Their fault-tolerant design resists security breaches and repairs itself during extreme power demand conditions. Networks that incorporate advanced digital switches and ubiquitous sensing and response devices allow for the interconnection of many smart appliances. Several communications platforms are tested for this demanding and flexible networking system. The most common communications platforms are power line communications (PLC), broadband over power lines (BPL), ZigBee, Wi-Fi, Z-wave, and Worldwide interoperability for microwave access (WiMAX).

While various PLC and BPL-based communications are technically feasible, no current technologies and protocols are technically mature and cost competitive to represent a viable solution. Although BPL installations are currently limited in number, significant growth is expected as utilities attempt to improve communications for a smart grid. ZigBee and Wi-Fi network are integrated via a common home gateway that provides network interoperability and remote access to the system. ZigBee is designed for use in applications that require low data rate, low-cost, low power consumption, and two way wireless communications; Wi-Fi is designed to provide relatively high data rate communications. Z-Wave uses a low-power RF radio embedded or retrofitted into home electronics devices and systems; the Z-Wave wireless protocol is optimized for reliable, low-latency communication of small data packets. WiMAX is a 4G communication technology that attempts to satisfy the requirements of smart grid-minded utilities; WiMAX is a standards-based technology that allows for delivery of last mile wireless broadband access as an alternative to cable and digital subscriber line.

82.4 Conclusions

This paper aims to review different energy management approaches for smart home applications, including fuzzy logic, neural networks, heuristic methods, and evolution-based approaches. The fuzzy logic was used to combine heterogeneous sources of information and execute an inference mechanism using IF–THEN rules. However, the heuristic nature of membership functions and fuzzy rules defined by expert experience, limit fuzzy logic system performances in real-world applications. Artificial intelligence can be used to implement relatively more powerful, complex control, decision, and management systems. A hybrid intelligent system is a good solution when the environment model is so complex that a mathematical model would be markedly nonlinear or impossible to develop. Therefore, hybrid intelligent systems for generating control rules derived by learning from examples should be studied further.

The underlying EICT that enables SHEMS benefits consumers, and the utility is the availability of an AMI and HAN communication system. For efficacy and easy deployment, the HAN communication network must be based on a network technology that utilizes open data architecture, is cheap, consumes a minimum amount of energy, and does not require extensive new infrastructure. We conclude that PLC, ZigBee, and Wi-Fi optimally satisfy the requirements for smart home applications.

Acknowledgments Financial supports from the National Science Council, Taiwan, R.O.C. under the Grant No. NSC 102-3113-P-006-015 and NSC 101-2632-E-230-001-MY3 are acknowledged.

References

1. Leeds, D. J. (2009). *The smart grid in 2010: market segments, applications and industry players*. Greentech Media Inc.
2. Lien, C. H., Bai, Y. W., & Lin, M. B. (2007). Remote-controllable power outlet system for home power management. *IEEE Transactions on Consumer Electronics, 53*, 1634–1641.
3. Roy, A., Das, S., & Basu, K. (2007). A predictive framework for location-aware resource management in smart homes. *IEEE Transaction on Mobile Computer, 6*, 1270–1283.
4. Zhang, L., Leung, H., & Chan, K. (2008). Information fusion based smart home control system and its application. *IEEE Transactions on Consumer Electronics, 54*, 1157–1165.
5. Vainio, A. M., Valtonen, M., & Vanhala, J. (2008). Proactive fuzzy control and adaptation methods for smart homes. *IEEE Intelligent Systems, 23*, 42–49.
6. Zhao, J. H., Dong, Z. Y., Xu, Z., & Wong, K. P. (2008). A statistical approach for interval forecasting of the electricity price. *IEEE Transactions on Power Systems, 23*, 267–276.
7. Pedrasa, M. A. Spooner, E. D., & MacGill, I. F. (2009). Improved energy services provision through the intelligent control of distributed energy resources. In 2009 IEEE Bucharest Power Tech Conference, pp. 1–8.
8. Han, D., & Lim, J. (2010). Smart home energy management system using IEEE 802.15.4 and ZigBee. *IEEE Transactios on Consumer Electronics, 56*, 1403–1410.

9. Pedrasa, M. A. A., Spooner, T. D., & MacGill, I. F. (2010). Coordinated scheduling of residential distributed energy resources to optimize smart home energy services. *IEEE Transactions on Smart Grid, 1*, 134–143.
10. Mohsenian-Rad, A. H., & Leon-Garcia, A. (2010). Optimal residential load control with price prediction in real-time electricity pricing environments. *IEEE Transactions on Smart Grid, 1*, 120–133.
11. Du, P., & Lu, N. (2011). Appliance commitment for household load scheduling. *IEEE Transactions on Smart Grid, 2*, 411–419.
12. Motamedi, A., Zareipour, H., & Rosehart, W. D. (2012). Electricity price and demand forecasting in smart grids. *IEEE Transactions on Smart Grid, 3*, 664–674.
13. Huang, C. M., Yang, S. P., Yang, H. T., & Huang, Y. C. (2012). Combined particle swarm optimization and heuristic fuzzy inference systems for a smart home one-step-ahead load forecasting. *Journal of the Chinese Institute of Engineers, 35*, 1–10.

Chapter 83
Applying Kaizen Methods to Improve Voltage Regulator Subassembly Area

Jun-Ing Ker, Yichuan Wang and Hung-Yu Lee

Abstract Enhancing productivity and quality to gain competitive advantage has always been a primary goal for a manufacturer. Nowadays, companies frequently conduct Kaizen events to continue improve the process to achieve this goal. This paper presents a real world case to demonstrate how Kaizen methods were applied to improve a voltage regulator subassembly area in a leading electrical device manufacturer. Benefits gained form this project include eliminations of non-value added activities, reduction of overtime payments, better inventory control and more efficient process flows.

Keywords Kaizen · Lean manufacturing · Continuous process improvement · Two-bin Kanban system · Voltage regulator subassembly

83.1 Introduction

Improving productivity and quality to gain dynamic capabilities, thereby enhancing substantial competitive advantage has always been a primary goal for manufacturing industry. Lean manufacturing aims to apply effective lean tools to help companies reduce wastes and has generated promising results [1–3]. Although employing lean practice to improve production process is not new, many

J.-I. Ker (✉)
Industral Engineering Program, Louisiana Tech University, Ruston, LA, USA
e-mail: ker@latech.edu

Y. Wang
Department of Aviation and Supply Chain Management, Auburn Unviersity, Auburn, AL, USA

H.-Y. Lee
Department of Industrial and Systems Engingeering, Auburn University, Auburn, AL, USA

J. Juang et al. (eds.), *Proceedings of the 2nd International Conference on Intelligent Technologies and Engineering Systems (ICITES2013)*, Lecture Notes in Electrical Engineering 293,
DOI: 10.1007/978-3-319-04573-3_83,

companies have yet to realize the core value of process improvement [4]. Apparently, the key challenge lies in utilizing appropriate approaches to facilitate the continuous process improvement and advance the operational capabilities.

Kaizen means "improvement" in Japanese. The Kaizen method is an approach of continuous improvement, and it has been widely applied to various industries [5], particularly in manufacturing [6, 7] and healthcare [8]. The fundamental mechanism of Kaizen is to boost any possible improvement under the cycle of plan, do, check, and act (PDCA) [9, 10]. Practically, Kato and Smalley [10] emphasized the need of following specific steps when conducting Kaizen events in order to achieve process improvement effectively. They found most studies failed to take such step-by-step approach. This study illustrates how a voltage regulator manufacturer followed this stepwise approach in conducting Kaizen events to improve its voltage regulator subassembly area and the economical benefits gained from these Kaizen events.

83.2 Related Work

In recent years, lean manufacturing concepts have gained great attention in the field of production and operations management as organizations compete on the ability to sustain process improvement rather than increase production volume [11]. The concepts of lean manufacturing focus on improvement of workplaces and production areas through various lean tools. Rahani and al-Ashraf [12] demonstrated how the value stream mapping (VSM) method was applied in assembly processes to reduce production lead time and lower work-in-process (WIP) inventory. Ker and Wang [13] applied the principles of lean manufacturing to identify root causes for productivity variation in the conduit installation process. They then implemented several lean tools to standardize the process.

Kaizen methods often utilize a specific set of technical problem-solving tools, with the potential of impacting both production and employee performance. It has been proven to be an effective approach to help companies achieve the goals of lean manufacturing [14]. Glover et al. [7] identified the factors such as goal clarity, goal difficulty, and management support that influence the employee attitude and commitment to Kaizen events within work area.

83.3 Method

The six steps of Kaizen for process improvement were followed in this study to improve the voltage regulator subassembly area in this plant. The main goal and the steps of implementation of lean tools are summarized in Table 83.1.

Table 83.1 The steps of the Kaizen

Steps	Main goal	Lean practice
Discover improvement potential	To complete exercises in helping individuals learn to identify the waste and inefficiency problems	Seven types of waste
Analyze the current methods	To conduct job analysis methods for identifying inefficiency problems	Time study
Generate original ideas	To help individuals and teams learn to generate original ideas	Brainstorming
Develop an implementation plan	To create effective plans for communication and tracking purposes	Plan development
Implement the plan	To implement plans	5S and Spaghetti chart
Evaluate the new method	To evaluate the results of the action items performed in order to verify the actual level of improvement	Evaluations

83.4 Results

The steps and results of implementing Kaizen methods to combat many issues of the regulator subassembly area are presented below.

83.4.1 Step 1: Discover Improvement Potential

The way to get employees in the mode for discovery of improvement potential is simply to analyze the wastes in the process [10]. The seven forms of waste including transportation, inventory, motion, waiting, overproduction, processing, and defects were first analyzed by the team. In order to eliminate these wastes, the team observed the operations of the operator. Flow process analysis sheets were used to identify non-value added activities during the part assembly and transportation processes. The team also interviewed operators to identify additional wastes that could be eliminated in the process. This study revealed that three major wastes were (1) excessive inventory, (2) long waiting for WIP parts, and (3) extensive walking.

83.4.2 Step 2: Analyze the Current Methods

Time study technique was used to quantify the time spent in each activity. The results showed that the assembly processes of reactors, zenoxes and potential transformers were composed of 85 min of value added activity (VA) and 42 min of non-value added activity (NVA). The team also found that the operator walked 2,637 ft to complete a production cycle in the subassembly area.

83.4.3 Step 3: Generate Original Ideas

Because 2,637 ft of transportation accounts for about 10 min of NVA (calculated at 4.5 ft/s), the team decided that the most prominent task was to redesign the layout in order to eliminate the transportation waste. In addition, the team discovered that part shortages and overproduction of WIP were mainly caused by the ineffective material requirements planning system (MRP) currently used. Thus, the team concluded that a more effective way of counting inventory—a two bin Kanban supermarket system—had to be implemented in the subassembly area to allow the MRP system to react to the true need of the area so that part shortages and overproduction would not occur. The team also recommended that 5S be implemented in the newly design area. (Note that 5S is a workplace organization method that uses a list of five Japanese words: *seiri, seiton, seiso, seiketsu,* and *shitsuke* translated into English as *sort, set in order, shine, standardize, and sustain.*)

83.4.4 Step 4: Develop an Implementation Plan

In this step, tasks needed to be completed were itemized and time line for completing each task was established. The plan included the following major tasks: design the two-bin Kanban supermarket system, relocate the current operations to a temporary area, reconstruct the new subassembly area, move the operations back to the newly designed area, and implement 5S. A time frame of 6 weeks was given to complete these tasks.

83.4.5 Step 5: Implement the Plan

The team started the layout redesign task by first removing the giant green wall that separated the production area and the inventory area to bring inventory racks closer to assembly workstations. Figure 83.1 illustrates the differences of the subassembly area after the new inventory system and 5S were implemented. As a result, storages and overproduction were eliminated due to accurate inventory information maintained in the MRP system. Note that the two-bin Kanban supermarket system is gravity-fed so that workers do not have access to newer pars until older parts have been used. This results in the inventory being used on a first in, first out (FIFO) basis.

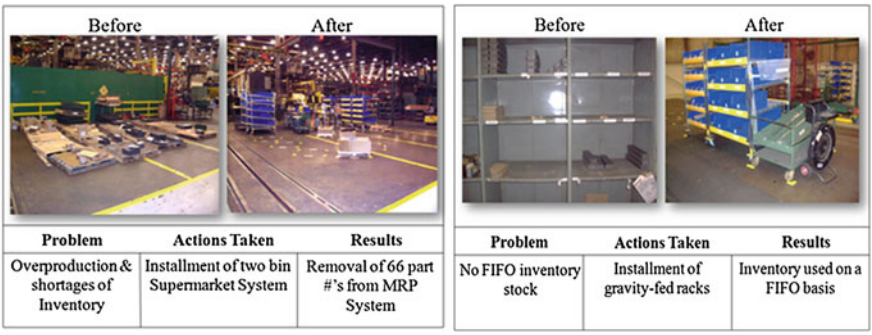

Fig. 83.1 The work area before and after implementation of Kanban inventory system

Spaghetti charts were used to measure the process flows while 5S was used to organize the work area for efficiency and effectiveness. The before and after spaghetti charts are shown in Fig. 83.2. It can be seen that the new layout effectively eliminates 877 ft of transportation waste, resulting in saving 3.22 min per work cycle.

83.4.6 Step 6: Evaluate the New Method

The results of the implementation of 5S and the redesign of the subassembly area are shown in Table 83.2. Note that shortages and overproduction were totally eliminated. Travel distance was reduced to 1760 ft, a 33.3 % reduction. Non-value added time was reduced by 38 % or 16 min.

The economic justification of improvement to the subassembly area is based on overtime payment reduction of the operators. In the past, the inaccurate inventory data on the MRP system frequently caused part shortages so workers would have to wait for parts to arrive from different fabricators in the facility and stay past standard hours to complete their jobs. By contrast, the implementation of the new system has helped reduce these occurrences significantly, resulting in $5000 reduction in overtime cost per quarter. The building of new two-bin Kanban inventory racks and reorganization of the new area cost approximately $6200. This gives a payback period of 1.24 quarters or 3.72 months. (Payback period = 6200/5000 = 1.24 quarters).

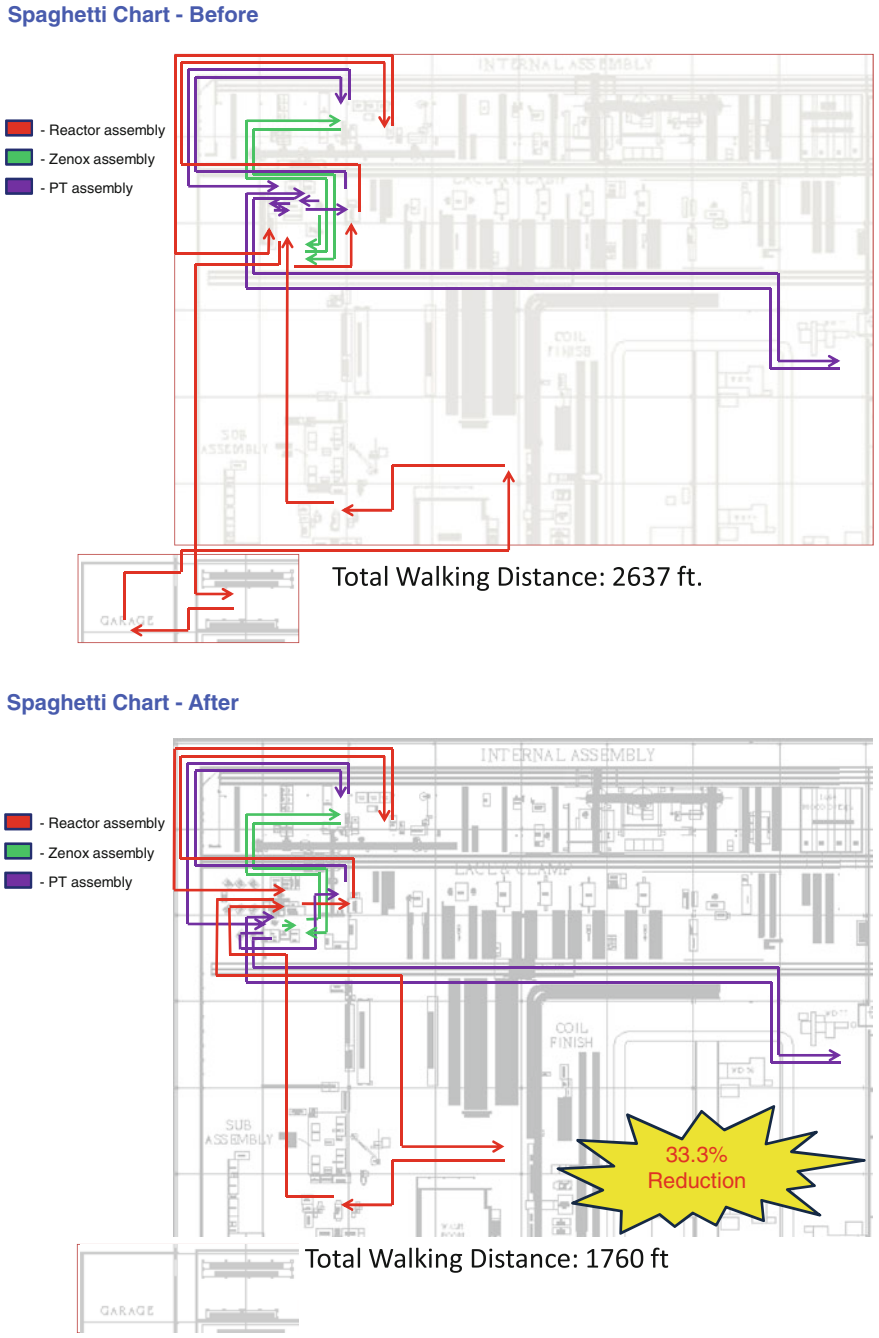

Fig. 83.2 The process flow before and after redesigned layout

Table 83.2 Results of voltage regulator subassembly Kaizen

Problem	Before Kaizen	After Kaizen	Amount changed	Outcome (%)
Shortages/overproduction	10	0	−10	100
Number of parts on MRP	66	0	−66	100
Travel distance	2,637 ft	1,760 ft	−877 ft	33.3
Reduction in NVA time	42 min	26 min	−16 mm	38
Rack capacity rating	N	Y	–	–

83.5 Conclusion

This paper presents the use of Kaizen methods to improve the process flow of a voltage regulator subassembly area by eliminating the non-value added processes in a leading electrical device manufacturer. Lean tools used in this project included process flow analysis, time study, plant layout, two-bin Kanban system, and 5S. The economic justification showed remarkable improvement in the subassembly area with a short payback period.

Acknowledgments The lead author would like to acknowledge the support of the James Emmett Smith Endowed Professorship that made this study possible. The James Emmett Smith Endowed Professorship is made available through the State of Louisiana Board of Regents Support Funds.

References

1. Anand, G., Ward, P. T., Tatikonda, M. V., & Schilling, D. A. (2009). Dynamic capabilities through continuous improvement infrastructure. *Journal of Operations Management, 27*, 444–461.
2. Browning, T. R., & Heath, R. D. (2009). Reconceptualizing the effects of lean on production costs with evidence from the F-22 program. *Journal of Operations Management, 27*, 23–44.
3. Herron, C., & Braiden, P. M. (2006). A methodology for developing sustainable quantifiable productivity improvement in manufacturing companies. *International Journal of Production Economics, 104*, 143–153.
4. Pullin, J. (2005). Room for improvement. *Professional Engineering, 18*, 38–138.
5. Farris, J. A., Van Aken, E. M., Doolen, T. L., & Worley, J. (2008). Learning from less successful Kaizen event: A case study. *Engineering Management Journal, 20*, 10–20.
6. Chan, F. T. S., Lau, H. C. W., Ip, R. W. L., Chan, H. K., & Kong, S. (2005). Implementation of total productive maintenance: A case study. *International Journal of Production Economics, 95*, 71–94.
7. Glover, W. J., Farris, J. A., Van Aken, E. M., & Doolen, T. L. (2011). Critical success factors for the sustainability of Kaizen Event human resource outcomes: An empirical study. *International Journal of Production Economics, 132*, 197–213.
8. Gene, S., Annah, P., Macon, H. L., & Randolph, G. D. (2012). Applying lean principles and Kaizen rapid improvement events in public health practice. *Journal of Public Health Management and Practice, 18*, 52–54.
9. Lyu, J. (1996). Applying Kaizen and automation to process reengineering. *The Journal of Manufacturing Systems, 15*, 125–132.

10. Kato, I., & Smalley, A. (2011). *Toyota Kaizen methods: Six steps to improvement*. New York: Taylor & Francis Group.
11. Teece, D. J. (2007). Explicating dynamic capabilities: The nature and micro-foundations of (sustainable) enterprise performance. *Strategic Management Journal, 28*, 1319–1350.
12. Rahani, A. R., & al-Ashraf, M. (2012). Production flow analysis through value stream mapping: A lean manufacturing process case study. *Procedia Engineering, 41*, 1727–1734.
13. Ker, J. I., & Wang, Y. (2013). Applying the principles of lean manufacturing to optimize Conduit installation process. In J. Juang & Y. C. Huang (Eds.), *Intelligent technologies and engineering systems* (Vol. 234, pp. 923–929)., LNEE Heidelberg: Springer.
14. Ortiz, C. (2010). Kaizen vs. Lean: Distinct but related. *Metal Finishing, 108*, 50–51.

Chapter 84
Advance in Neural Networks for Power Transformer Condition Assessment

Kun-Yuan Huang, Yann-Chang Huang, Hsing-Feng Chen and Hsieh-Ping Chen

Abstract Artificial neural networks (ANN) have emerged as rapidly evolving and highly practical approaches for condition assessment of power transformers. This study reviewed different ANN approaches for assessing power transformer conditions by discussing historical developments and presenting state-of-the-art ANN methods. Relevant publications from international journals covering a broad range of ANN methods were reviewed. This paper concludes that no single ANN approach enables detection of all faults of power transformers; therefore, overall and reliable assessment of power transformer conditions is necessary. Moreover, the most effective condition assessment technique is to combine artificial intelligent approaches to form hybrid intelligence-based systems and to aggregate them into an overall evaluation. This paper is helpful in the academics, research and engineering community, which is working on condition assessment of transformer fault diagnosis using artificial intelligence.

Keywords Neural networks · Power transformers · Condition assessment

84.1 Introduction

Power transformer is an important apparatus in power systems and its failure may interrupt power supplies and diminish profits. Minimizing the risk of power outages entails detecting incipient faults inside power transformers immediately. Moreover, the conditions must be assessed routinely, as well as the apparatus reliability maintained. Therefore, accurately evaluating power transformer conditions is essential.

K.-Y. Huang · Y.-C. Huang (✉) · H.-F. Chen · H.-P. Chen
Department of Electrical Engineering, ICITES, Cheng Shiu University, Kaohsiung, Taiwan, Republic of China
e-mail: huangyc@csu.edu.tw

J. Juang et al. (eds.), *Proceedings of the 2nd International Conference on Intelligent Technologies and Engineering Systems (ICITES2013)*, Lecture Notes in Electrical Engineering 293,
DOI: 10.1007/978-3-319-04573-3_84,

Time-based and condition-based monitoring strategies have been developed for transformer fault identification and diagnosis. Time-based monitoring uses various off-line tests to schedule tests for incipient faults in transformers; however, this labor-intensive strategy is costly and sometimes ineffective in detecting faults that develop between regular intervals of examination. Condition-based monitoring applies advanced fault diagnosis techniques to identify on-line and off-line incipient faults and to provide real-time transformer conditions; thus, it can also optimize maintenance schedules.

Various condition assessment techniques of power transformer have been developed to reduce operating costs, enhance the reliability of operation, and improve power supply and service to customers. Advances in artificial neural networks (ANN) techniques have rapidly improved transformer condition monitoring and assessment tools in recent years. Many practical transformer operation problems have been solved by ANN-based condition monitoring and assessment systems. This study reviews various ANN techniques for evaluating power transformer conditions. A review of the accumulating literature on the practicability, reliability, and automation of intelligent condition assessment systems was performed to determine the state of the art in this important area.

84.2 Transformer Condition Assessment

Dissolved gas analysis (DGA) [1–8] is among the most common techniques used for on-line condition assessment of power transformers. The DGA requires routine oil sampling and modern technologies for on-line gas monitoring. The key step in using gas analysis for fault detecting is correctly diagnosing the fault that generated the gases. Abnormal electrical or thermal stresses cause insulation oil to break down and to release small quantities of gases.

These dissolved gases include hydrogen (H_2), methane (CH_4), ethylene (C_2H_4), ethane (C_2H_6), acetylene (C_2H_2), carbon monoxide (CO), and carbon dioxide (CO_2). Each fault type produces gases that are generally combustible. An increase in total combustible gases (TCG) that correlates with an increase in gas generating rates may indicate the existence of any one or a combination of thermal, electrical or corona faults. The composition of these gases depends on the fault type. Faults in oil-filled transformers can be identified according to the gases generated and the gases that are typical or predominant at various temperatures.

The DGA can provide the early diagnosis needed to increase the chance of finding an appropriate cure. Interpretation schemes are generally based on defined principles such as gas concentrations, key gases, key gas ratios, and graphical representations. Common schemes mentioned in IEEE Standard C57.104-2008 include Key Gas Analysis [1, 2], Dornenberg Ratio [3] and Rogers Ratio [4] Methods, Nomograph [5], IEC Ratio [5], Duval Triangle [6, 7], and CIGRE Method [8]. The DGA can distinguish faults such as partial discharge, overheating, and arcing in many different power transformers.

Various DGA methods have been used by organizations and utilities to assess transformer conditions. These DGA interpretation schemes are based on empirical assumptions and practical knowledge gathered by experts worldwide. Nevertheless, if these interpretation schemes are not applied cautiously, they may incorrectly identify faults because they only indicate possible faults. In some cases, DGA interpretation schemes may differ about identified faults, which is clearly unacceptable for a reliable fault diagnosis system.

Because the conventional DGA diagnosis results may be imprecise and even incomplete, a suitable information integration method is needed to process DGA data to overcome such uncertainties. Therefore, the integration of available transformer DGA-based diagnostic approaches to generate an overall condition assessment is very important for asset management in modern power system operation.

84.3 Artificial Intelligence Applications

An ANN acquires knowledge through training, which is a major advantage when the training set is often composed of actual observations of the physical world rather than being formed of the human opinions used for fuzzy (or expert) systems. However, the training set must adequately represent the domain of interest. Otherwise, the network must make decisions that are not based on experience. Diagnosis accuracy evaluations of the ANN-based transformer fault diagnosis systems have confirmed their effectiveness and reliability.

Many works on applications of ANN in condition assessment of transformers have been published; the proposed systems have been promising because the ANN can learn hidden relations among fault types and dissolved gas concentrations. Besides their learning capabilities, another advantage of ANN is their capability to acquire new information by incremental training from newly obtained samples. Doing so is usually impossible in systems based on fuzzy rules unless the implementations also rely on a back-propagation procedure to evolve parameters. After training, the diagnostic accuracies of the ANN were tested with a new set of DGA results and compared with those obtained by inspection and analysis.

A two-step ANN method [9] was used to detect transformer faults. The first ANN classified the fault as overheating, corona, or arcing; the second ANN determined if the cellulose was involved. The results of the two-step ANN approach were promising even with limited sample data; however, additional training data should be needed for the ANN to learn more complex relationships. Moreover, the accuracy of fault diagnosis can be improved choosing the proper value of learning rate, momentum factor and activation functions.

The ANN diagnostic method has proven very effective for diagnosing the insulating properties of an oil-insulated power apparatus [10]. A comparative study of ANNs in detecting incipient transformer faults was presented in [11], and the

diagnosis accuracies obtained were about 87–100 %. An ANN trained with Levenberg–Marquardt learning algorithm demonstrated that the algorithm is apparently the fastest method for training a moderate-sized feedforward ANN [12].

Self-organizing polynomial modeling technique [13] was proposed to heuristically formulate the model using a hierarchical architecture with several layers of functional nodes using simple low-order polynomials. The networks can learn numerical, complicated, and uncertain relationships between dissolved gas content in transformers and fault conditions. A fuzzy-based vector quantization network was used to classify historical DGA data [14]. For each category of gas attributes, a learning vector quantization network was trained to classify potential faults caused by insulation deterioration. Remarkable classification accuracy has been achieved with substantially reduced training.

Evolutionary algorithms were used to automatically tune the network parameters (connection weights and bias terms) of the ANN to achieve the best model [15, 16]. The evolutionary algorithms based systems can identify complex relationships among the gases dissolved in transformer oil and corresponding fault types by combining the global search capabilities of evolutionary algorithms with the highly nonlinear mapping capabilities of the ANN.

Conventional ANN has difficulty determining the number of neurons in hidden layers, and training is time consuming. To overcome the drawbacks of traditional ANN, extension-based methods based on the matter-element model and extended relation functions have been used for diagnosing power transformer faults [17, 18]. A cerebellar model articulation controller neural network (CMACNN) method was presented for diagnosing power transformer faults [19]. The CMACNN fault diagnosis scheme functions like the human cerebellum and enables a powerful and efficient fault diagnosis. The results also confirm that multiple incipient faults can be detected simultaneously. An effective and flexible probabilistic neural network (PNN) overcomes the slow repeated iterative process and poor adaptation capability for structural data of the conventional ANN [20]; diagnostic results confirmed the effectiveness of the PNN approach.

Self-organizing map (SOM)-based approach to analyzing DGA data has demonstrated convincing performance in DGA for fault diagnosis [21]. The evolution of incipient faults can now be visualized by plotting DGA trajectories, and the incipient fault can thereby be monitored visually so that proper corrective actions can be taken at the right time. Studies have reported the use of wavelet networks (WN) and DGA samples for incipient fault detection in power transformers [22, 23]. A comparative study of evolving WN for incipient fault diagnosis in transformers indicated that the diagnostic accuracy and efficiency of five WN approaches are superior to those of conventional ANN and are suitable for fault diagnosis of power transformers [24].

The novel hybrid self-adaptive training approach-based radial basis function (RBF) neural network [25] showed several performance advantages over other ANN: better approximation capability, simpler network structure, and faster learning speed. The proposed method generated RBF neural network models based

Table 84.1 The advantages and disadvantages of artificial intelligence approaches

Method	Advantages	Disadvantages
ES	• Inference by specialized knowledge and experience	• Cannot obtain knowledge from new data samples by self-learning
	• Makes a decision similar to that made by human experts	• Relies heavily on knowledge engineers and domain experts
FLS	• Manages decisions that involve imprecise knowledge	• Requires identification of proper membership functions
	• Softens fault decision boundaries for solving uncertainty problems	• Cannot learn directly from data samples
ANN	• Accurately and efficiently captures input–output relations by training	• Accuracy depends on correct and complete training samples
	• Excellent interpolation and extrapolation capacity	• Difficulty in determining network structures and parameters

on fuzzy c-means and quantum-inspired particle swarm optimization (PSO), which can automatically configure network structures and automatically obtain model parameters.

84.4 Issuess for ANN Applications

Like expert system (ES), the ANN cannot directly handle fuzzy information. This limitation comes from the basic configuration of the network: knowledge is distributed over the entire pattern of weights, and the weights are involved in each decision. Moreover, operations of ANN are also obscured by nonlinearities. The ANN knowledge is discreetly distributed throughout the network according to the sample learning rather than stored in a knowledge base as in ES. When the difference between the training samples and the fault samples is very large, the reasoning used by ANN to reach a conclusion is not clear.

An ANN shares many similarities with a fuzzy logic system (FLS). They both use stored knowledge to make decisions about new inputs. Both can generalize; both produce correct responses despite minor variations in the inputs. Table 84.1 summarizes the advantages and disadvantages of artificial intelligence approaches for power transformer condition assessment. The performance of ES depends on the quantity and quality of the obtained knowledge. The FLS explicitly displays expert knowledge that is not extracted from the DGA data. The ANN performs in transformer fault diagnoses but the knowledge it captured remains hidden in the model. This paper suggests that hybrid intelligence-based systems, which combine an ES, FLS, ANN, and computational intelligence for diagnosing transformer faults, are the state-of-the-art condition assessment tools for power transformers.

84.5 Conclusions

This paper has reviewed literature on transformer fault diagnosis and the great progress made in recent decades. This review provides important information about research directions and trends in the field of transformer condition monitoring using ANN. Although condition assessment of ANN can offer early warning of insulation conditions, no single method can detect the full range of faults and reliably estimate remnant life. Each method has its own strengths and weaknesses. Moreover, a more useful method is to combine and integrate all the diagnosis results obtained from major DGA approaches to present an overall evaluation. Therefore, instead of using one diagnostic method, hybrid intelligent methods that combine the strengths of each method require further study to improve detection of incipient faults in power transformers.

References

1. IEEE Guide for the Interpretation of Gases Generated in Oil-Immersed Transformers. (2008). IEEE Standard C57.104.
2. Guide for the Sampling of Gases and of Oil-Filled Electrical Equipment and for the Analysis of Free and Dissolved Gases. (2005). IEC Standard 60567.
3. Dornenburg, E., & Strittmatter, W. (1974). Monitoring oil-cooled transformers by gas analysis. *Brown Boveri Review, 61*, 238–247.
4. Rogers, R. R. (1978). IEEE and IEC codes to interpret incipient faults in transformers using gas in oil analysis. *IEEE Transactions on Electrical Insulation, 13*, 349–354.
5. Mineral Oil-Impregnated Electrical Equipment in Service–Guide to the Interpretation of Dissolved and Free Gases Analysis. (2007). IEC Standard 60599.
6. Duval, M. (2002). A review of fault detectable by gas-in-oil analysis in transformers. *IEEE Electrical Insulation Magazine, 18*, 8–17.
7. Duval, M., & Dukarm, J. (2005). Improving the reliability of transformer gas-in-oil diagnosis. *IEEE Electrical Insulation Magazine, 21*, 21–27.
8. Mollmann, A., & Pahlavanpour, B. (1999). New guideline for interpretation of dissolved gas analysis in oil filled transformers. *Electra, 186*, 31–51.
9. Zhang, Y., Ding, X., Liu, Y., & Griffin, P. J. (1996). An artificial neural network approach to transformer fault diagnosis. *IEEE Transactions on Power Delivery, 11*, 1836–1841.
10. Vanegas, O., Mizuno, Y., Naito, K., & Kamiya, T. (1997). Diagnosis of oil-insulated power apparatus by using neural network simulation. *IEEE Transactions on Dielectrics and Electrical Insulation, 4*, 290–299.
11. Guardado, J. L., Naredo, J. L., Moreno, P., & Fuerte, C. R. (2001). A comparative study of neural network efficiency in power transformers diagnosis using dissolved gas analysis. *IEEE Transactions on Power Delivery, 16*, 643–647.
12. Gunes, I., Gozutok, A., Ucan, O. N., & Kiremitci, B. (2009). Power transformer fault type estimation using artificial neural network based on dissolved gas in oil analysis. *International Journal of Engineering Intelligent System, 17*, 193–198.
13. Yang, H. T., & Huang, Y. C. (1998). Intelligent decision support for diagnosis of incipient transformer faults using self-organizing polynomial networks. *IEEE Transactions on Power Systems, 13*, 946–952.

14. Yang, H. T., Liao, C. C., & Chou, J. H. (2001). Fuzzy learning vector quantization networks for power transformer condition assessment. *IEEE Transactions on Dielectrics and Electrical Insulation, 8*, 143–149.
15. Huang, Y. C. (2003). Evolving neural nets for fault diagnosis of power transformers. *IEEE Transactions on Power Delivery, 18*, 843–848.
16. Huang, Y. C. (2003). Condition assessment of power transformers using genetic-based neural networks. *IEE Proceedings-Science, Measurement and Technology*, *150*, 19–24.
17. Wang, M. H. (2003). A novel extension method for transformer fault diagnosis. *IEEE Transactions on Power Delivery, 18*, 164–169.
18. Wang, M. H. (2003). Extension neural network for power transformer incipient fault diagnosis. *IEE Proceedings-Generation, Transmission and Distribution*, *150*, 679–685.
19. Hung, C. P., & Wang, M. H. (2004). Diagnosis of incipient faults in power transformers using CMAC neural network approach. *Electric Power Systems Research, 71*, 235–244.
20. Lin, W. M., Lin, C. H., Tasy, M. X. (2005). Transformer-fault diagnosis by integrating field data and standard codes with training enhancible adaptive probabilistic network. *IEE Proceedings-Generation, Transmission and Distribution*, *152*, 335–341.
21. Thang, K. F., Aggarwal, R. K., McGrail, A. J., & Esp, D. G. (2003). Analysis of power transformer dissolved gas data using the self-organizing map. *IEEE Transactions on Power Delivery, 18*, 1241–1248.
22. Huang, Y. C., & Huang, C. M. (2002). Evolving wavelet networks for power transformer condition monitoring. *IEEE Transactions on Power Delivery, 17*, 412–416.
23. Huang, Y. C. (2003). A new data mining approach to dissolved gas analysis of oil-insulated power apparatus. *IEEE Transactions on Power Delivery, 18*, 1257–1261.
24. Chen, W., Pan, C., Yun, Y., & Liu, Y. (2009). Wavelet networks in power transformers diagnosis using dissolved gas analysis. *IEEE Transactions on Power Delivery, 24*, 187–194.
25. Meng, K., Dong, Z. Y., Wang, D. H., & Wong, K. P. (2010). A self-adaptive RBF neural network classifier for transformer fault analysis. *IEEE Transactions on Power Systems, 25*, 1350–1360.

Chapter 85
Simple Stabilization Design for Perturbed Time-Delay Systems

Chien-Hua Lee, Tsung-Lieh Hsien, Ping-Chang Chen and Hsin-Ying Huang

Abstract This paper addresses the stabilization design problem for the continuous perturbed systems subjected to a time delay. By using the Riccati equation approach associated with the upper bound of the solution of the Riccati equation, a new stabilizability criterion is proposed. This criterion is easy to be tested. According to the above criterion, a simple stabilization controller is developed. This controller is very simple and hence is easy to be implemented.

Keywords Stabilization · Time-delay · Perturbation · The Riccati equation · Upper solution bound

85.1 Introduction

It is known that time delay exist naturally in physical systems, engineering systems, and so on. Time delay can be considered as a of instability source of systems. On the other hand, perturbation is also a source of instability and must be integrated into system model. The control problem of systems with time delay(s) and/or perturbations then is complicate and hence has become an attractive research topic over past several decades. A number of research approaches have been proposed to solve control problems of systems with time delay(s) and/or perturbation(s) during the past decades [1–10]. In [2, 3, 5–10], stabilizability conditions have been developed and various feedback controllers have also been derived. It is

C.-H. Lee (✉) · P.-C. Chen · H.-Y. Huang
Department of Electrical Engineering, Cheng Shiu University, Kaohsiung 83347, Taiwan, Republic of China
e-mail: chienhua@csu.edu.tw

T.-L. Hsien
Department of Electrical Engineering, Kun Shan University, Tainan 71003, Taiwan, Republic of China

J. Juang et al. (eds.), *Proceedings of the 2nd International Conference on Intelligent Technologies and Engineering Systems (ICITES2013)*, Lecture Notes in Electrical Engineering 293,
DOI: 10.1007/978-3-319-04573-3_85,

seen that the proposed results often come to solving LMI. Since there are usually many free matrices in LMI, this might be a miscellaneous work. Therefore, to develop a simple stabilizability condition and a state feedback controller for perturbed time-delay systems is the objective of this paper. We first derive a simple upper matrix bound of the solution of the Riccati equation by choosing properly the positive definite matrix Q. Then, by using the Riccati equation approach associated with the proposed upper bound, a concise stabilizability criterion is presented. This criterion does not involve any Riccati equation and hence is easy to be tested. Furthermore, according to the obtained criterion, a simple stabilization controller is developed. This controller is very simple and hence is easy to be implemented. An algorithm is also proposed to construct the controller.

The following symbol conventions are used in this paper. Symbol $\mathbb{R}$ denotes the real number field. $A >\!\!=\!\!< B$ means matrix $A - B$ is positive (semi)definite; $\lambda_1(A)$ denote the maximal eigenvalue of a symmetric matrix A. $\|A\|$ is the norm of matrix A. Furthermore, the identity matrix with appropriate dimensions is represented by I.

85.2 Main Results

Consider the time-delay systems with nonlinear perturbations

$$\dot{x}(t) = Ax(t) + A_d x(t-d) + Bu(t) + f(x(t),t) + f_d(x(t-d),t) \tag{85.1}$$

where, $x \in \mathbb{R}^n$, $u \in \mathbb{R}^m$, $d > 0$, respectively, denote the state, the input to be designed, and the delay duration, A, A_d, and B represent constant matrices with appropriate dimensions and A is a stable matrix, and $f(x(t), t)$ and $f_d(x(t - d), t)$ are nonlinear perturbations with the following properties:

$$\|f(x(t),t)\| \le \delta\|x(t)\| \quad \text{and} \quad \|f_d(x(t-d),t)\| \le \delta_d\|x(t-d)\| \tag{85.2}$$

where δ and δ_d are positive constants. It is assumed that the pair (A, B) is completely controllable. The objective of this paper is to derive simple stabilizability conditions and design a memoryless state feedback controller in the form of

$$u(t) = -Fx(t) \tag{85.3}$$

where F is the gain matrix such that the resulting closed-loop system is stable.

Before developing the main results, we first give the following useful result.

Lemma 1 *If there exists a positive constant η such that*

$$A^T + A - 2\eta BB^T + 2\left(\delta + \delta_d + \frac{\|A_d\|}{2}\right)I + \frac{A_d^T A_d}{\|A_d\|} < 0 \tag{85.4}$$

then the positive solution P of the Riccati equation

$$A^T P + PA - PBB^T P = -Q \tag{85.5}$$

has the upper bound

$$P < qI \tag{85.6}$$

where the $n \times n$ real positive definite matrix Q is given as

$$Q = q\left[(2\delta + \|A_d\| + 2\delta_d)I + \frac{A_d^T A_d}{\|A_d\|}\right] \tag{85.7}$$

and q is a arbitrary positive constant.

Proof Let a positive semi-definite matrix R be defined by

$$R \equiv (P - \eta I)BB^T(P - \eta I). \tag{85.8}$$

Then, we can rewrite the Riccati equation (85.5) as

$$\begin{aligned}&\left(A - \eta BB^T\right)^T(qI - P) + (qI - P)\left(A - \eta BB^T\right)\\ &\quad = -R + Q + \eta^2 BB^T + q\left(A^T + A - 2\eta BB^T\right).\end{aligned} \tag{85.9}$$

In (85.9), we have

$$\begin{aligned}&Q + \eta^2 BB^T + q\left(A^T + A - 2\eta BB^T\right)\\ &\quad = q\left[A^T + A - 2\eta BB^T + 2\left(\delta + \delta_d + \frac{\|A_d\|}{2}\right)I + \frac{A_d^T A_d}{\|A_d\|} + \frac{\eta^2}{q}BB^T\right].\end{aligned} \tag{85.10}$$

It is obvious that if the condition (85.4) is satisfied, then there must exist a constant $q \gg \eta^2\|B\|^2$ such that the right-hand side of (85.10) is a negative definite matrix. Furthermore, the condition (85.4) also implies that $A^T + A - 2\eta BB^T < 0$, one hence can conclude that the matrix $A - \eta BB^T$ is stable. Therefore, Eq. (85.9) is a Lyapunov equation and then its solution is positive definite. That is, the solution of the Riccati equation (85.5) has the upper bound (85.6). Thus, this completes the proof.

Then, by utilizing lemma 1 and some linear algebraic techniques, a stabilization controller for the system (85.1) is designed as follows.

Theorem 1 *If the stabilizability condition (85.4) holds, the perturbed time-delay system (85.1) can be stabilized by a memoryless state feedback controller in the form of (85.3) with*

$$F = 0.5B^T P \tag{85.11}$$

where the positive definite matrix P satisfies the Riccati equation (85.5) and the positive definite matrix Q is given by (85.7).

Proof Using the controller (85.3) with (85.11), the system (85.1) becomes

$$\dot{x}(t) = (A - 0.5BB^T P)x(t) + A_d x(t-d) + f(x(t),t) + f_d(x(t-d),t). \quad (85.12)$$

For this system, we construct a Lyapunov function as

$$V(x(t),t) = x^T(t)Px(t) + q\int_{t-d}^{t} x^T(\tau)\left(\frac{A_d^T A_d}{\|A_d\|} + \delta_d I\right)x(\tau)d\tau \quad (85.13)$$

where the positive definite matrix P satisfies (85.5). For convenience, we use symbols V, x, and x_d to replace $V(x(t), t)$, $x(t)$, and $x(t - d)$, respectively, in the following and later descriptions. Furthermore, $f(x(t), t)$ and $f_d(x(t - d), t)$ are also replaced by f and f_d, respectively. Now, taking the derivative along the trajectories of (85.1) gives

$$\begin{aligned}\dot{V} = {} & x^T\left[A^T P + PA - PBB^T P + q\left(\frac{A_d^T A_d}{\|A_d\|} + \delta_d I\right)\right]x - qx_d^T\left(\frac{A_d^T A_d}{\|A_d\|} + \delta_d I\right)x_d \\ & + x_d^T A_d^T Px + x^T PA_d x_d + f^T Px + x^T Pf + f_d^T Px + x^T Pf_d.\end{aligned} \quad (85.14)$$

Since

$$\begin{aligned}x_d^T A_d^T Px + x^T PA_d x_d &\le \frac{1}{\|A_d\|}x_d^T A_d^T PA_d x_d + \|A_d\|x^T Px \\ &< q\left[\frac{1}{\|A_d\|}x_d^T A_d^T A_d x_d + \|A_d\|Ix^T x\right],\end{aligned} \quad (85.15)$$

$$f^T Px + x^T Pf \le \delta x^T Px + \frac{1}{\delta}f^T Pf < q\left[\delta x^T x + \frac{1}{\delta}f^T f\right] \le q2\delta x^T x, \quad (85.16)$$

and

$$\begin{aligned}f_d^T Px + x^T Pf_d &\le \frac{1}{\delta_d}f_d^T Pf_d + \delta_d x^T Px \\ &< q\left[\frac{1}{\delta_d}f_d^T f_d + \delta_d x^T x\right] \le q\delta_d\left[x_d^T x_d + x^T x\right],\end{aligned} \quad (85.17)$$

then

$$\begin{aligned}\dot{V} &< x^T\left[-Q + q\left(2\delta I + \|A_d\|I + \frac{A_d^T A_d}{\|A_d\|} + 2\delta_d I\right)\right]x \\ &= qx^T\left[-(2\delta + \|A_d\| + 2\delta_d)I - \frac{A_d^T A_d}{\|A_d\|} + 2\delta I + \|A_d\|I + \frac{A_d^T A_d}{\|A_d\|} + 2\delta_d I\right]x = 0\end{aligned} \quad (85.18)$$

where the upper bound (85.6) is used. Therefore, it is seen that if the condition (85.4) is satisfied, then the resulting closed-loop system (85.12) is asymptotically stable. Thus, the proof is completed.

Remark 1 An interesting consequence of this theorem is that the stabilizability condition (85.4) is independent of the Riccati equation (85.5). Furthermore, it is also independent of the free variable q.

Remark 2 Another benefit of the upper bound (85.6) is that we can use the bound qI to replace P in the memoryless feedback controller (85.3) to simplify the controller design. The result is given as follows.

Theorem 2 *If the stabilizability condition* (85.4) *is met, then the perturbed time-delay system* (85.1) *can be stabilized by making use of the feedback controller*

$$u(t) = -0.5B^T qIx(t) = -\eta B^T x(t) \tag{85.19}$$

where the positive constant η *defined by* $\eta \equiv 0.5q$ *is chosen by the designer.*

Proof From (85.19), the closed-loop system now becomes

$$\dot{x}(t) = (A - \eta BB^T)x(t) + A_d x(t-d) + f(x(t),t) + f_d(x(t-d),t). \tag{85.20}$$

Here, we choose the Lyapunov function as

$$V = x^T x + \int_{t-d}^{t} x^T(\tau)\left(\frac{A_d^T A_d}{\|A_d\|} + \delta_d I\right)x(\tau)d\tau. \tag{85.21}$$

This can lead to

$$\begin{aligned}\dot{V} &= x^T\left[A^T + A - 2\eta BB^T + \frac{A_d^T A_d}{\|A_d\|} + \delta_d I\right]x - x_d^T\left(\frac{A_d^T A_d}{\|A_d\|} + \delta_d I\right)x_d \\ &\quad + x_d^T A_d^T x + x^T A_d x_d + f^T x + x^T f + f_d^T x + x^T f_d \\ &\le x^T\left[A^T + A - 2\eta BB^T + 2\left(\delta + \delta_d + \frac{\|A_d\|}{2}\right)I + \frac{A_d^T A_d}{\|A_d\|}\right]x < 0.\end{aligned} \tag{85.22}$$

Therefore, it is seen that if the condition (85.4) holds, then the perturbed time-delay system (85.1) can be indeed stabilized by the controller (85.19). Thus, the proof is completed.

Note that the stabilization controller (85.19) is very simple. We also give the following algorithm for designing the positive constant η.

Algorithm 1

Step 1. Set $k = 0$. Give an initial value of $\eta_k = 0$.

Step 2. Substitute η_k into the stabilizability condition (85.4) and check it. If it is satisfied, then stop the algorithm and the controller is obtained. Otherwise, go to Step 3.

Step 3. Set

$$\eta_{k+1} = \eta_k + \varepsilon$$

where ε is an adequate positive constant. If $\eta_{k+1} > w$, then stop this algorithm and the stabilization controller can not be found where w is a default large value. Otherwise, go to Step 2.

85.3 Conclusions

The stabilization design problem of the continuous perturbed systems subjected to a time delay has been solved. A new stabilizability criterion is proposed to guarantee the existence of stabilization controller. This criterion does not involve any Riccati equation and hence is easy to be tested. Furthermore, a simple stabilization controller that is independent of the Riccati equation has also been developed. By the proposed algorithm, it is seen that this controller is easy to be implemented.

Acknowledgments The authors would like to thank the National Science Council, the Republic of China, for financial support of this research under the grant NSC 101-2221-E-230-010.

References

1. Erik, V., & Patrick, F. (1995). Stability of stochastic systems with uncertain time delays. *System & Control Letters, 24*, 41–47.
2. Feng, Z., Wang, Q. G., & Lee, T. H. (2005). Adaptive robust control of uncertain time delay systems. *Automatica, 41*, 1375–1383.
3. Fridman, E., & Shaked, U. (2003). Parameter dependent stability and stabilization of uncertain time-delay systems. *IEEE Transactions Automation Control, 48*, 861–866.
4. Hsien, T. L., & Lee, C. H. (1995). Exponential stability of discrete time uncertain systems with time-varying delay. *Journal of Franklin Institute, 332*(4), 479–489.
5. Lee, C. H. (1998). Simple stabilizability criteria and memoryless state feedback control design for time-delay systems with time-varying perturbations. *IEEE Transactions Circuit System-I, 45*, 1121–1125.
6. Liu, T., Gao, F., & Wang, Y. (2010). IMC-based iterative learning control for batch processes with uncertain time delay. *Journal Process Control, 20*, 173–180.
7. Liu, B., Teo, K. L., & Liu, X. Z. (2008). Robust exponential stabilization for large-scale uncertain impulsive systems with coupling time-delays. *Nonlinear Analysis, 68*, 1169–1183.
8. Mohammad, B., & Edward, D. (2006). Control of time delay processes with uncertain delays: Time delay stability margins. *Journal Process Control, 16*, 403–408.
9. Park, J. H., & Kwon, O. M. (2005). LMI optimization approach to stabilization of time-delay chaotic systems. *Chaos, Solitons Fractals, 23*, 445–450.
10. Xia, Y., Zhu, Z., Li, C., Yang, H., & Zhu, Q. (2010). Robust adaptive sliding mode control for uncertain discrete-time systems with time delay. *Journal of the Franklin Institute, 347*, 339–357.

Chapter 86
Robust Stabilization for Time-Delay Systems with Parametric Perturbations

Chien-Hua Lee and Ping-Sung Liao

Abstract The stabilization design problem for continuous time-delay systems subjected to time-varying parametric perturbations is discussed in this paper. By using the Riccati equation approach associated with an upper bound of the solution of the Riccati equation, we propose a new stabilizability condition. This condition does not involve any Riccati equation and hence is easy to be tested. It is also shown that the obtained criterion is sharper than a previous one. Furthermore, according to the aforementioned condition, two robust stabilization controllers are developed. A numerical algorithm is proposed to construct the controller.

Keywords Stabilization · Time-delay · Parametric perturbation · The Riccati equation · Upper solution bound

86.1 Introduction

Perturbation which is a result of nonlinearities, variation of parameters, approximate system model for simplicity, etc., is a source of instability and must be integrated into system model. Furthermore, the characteristic equation of linear systems would be changed and the eigenvalue number would be increased to infinite when systems possess time delay(s). Such situations might lead to unsatisfactory performances or unstable systems. Therefore, time delay is also considered as a instability source of systems. When systems possess time delay(s) and/or perturbations, the control problem is complicate and has become an attractive research topic over past several decades. In general, the study of time-delay systems can be classified into two topics: (i) stability analysis [2, 4, 5] and (ii) robust

C.-H. Lee (✉) · P.-S. Liao
Department of Electrical Engineering, Cheng Shiu University, Kaohsiung 83347, Taiwan, Republic of China
e-mail: chienhua@csu.edu.tw

J. Juang et al. (eds.), *Proceedings of the 2nd International Conference on Intelligent Technologies and Engineering Systems (ICITES2013)*, Lecture Notes in Electrical Engineering 293,
DOI: 10.1007/978-3-319-04573-3_86,

stabilization design [2–4, 6–9]. For robust stabilization design of the mentioned systems, stabilizability conditions have been proposed and the corresponding feedback controllers have also been derived in the literature. It is seen that the LMI approach is usually adopted to solve the stabilization problem of the aforementioned systems. However, there are usually many free matrices in LMI. The computer burdens might be very hard for solving this approach. Therefore, to avoid the difficulty of the previous approaches, a simple stabilizability condition and the corresponding state feedback controllers for time-delay systems with parametric perturbations will be developed in this paper. A simple stabilization condition will be developed by using the Riccati equation approach associated with a simple upper bound of the solution of the Riccati equation. This criterion does not involve any Riccati equation and hence is easy to be tested. It is also shown that this criterion is sharper than an existing one. Furthermore, two corresponding stabilization controllers then will be presented. These controllers are very simple and hence are easy to be implemented. We also propose an algorithm to check the stabilization condition and to construct the controllers. Finally, we demonstrate the applicability of the present schemes via a numerical example.

The following symbol conventions are used in this paper. Symbol $\mathbb{R}$ denotes the real number field. $A > (\geq) B$ means matrix $A - B$ is positive (semi) definite; $\lambda_1(A)$ denote the maximal eigenvalue of a symmetric matrix A. $\|A\|$ is the norm of matrix A. Furthermore, the identity matrix with appropriate dimensions is represented by I.

86.2 Main Results

Consider the time-delay systems with nonlinear perturbations

$$\dot{x}(t) = (A + \Delta A(k,t))x(t) + (A_d + \Delta A_d(r,t))x(t-d) + Bu(t). \tag{86.1}$$

where, $x \in \mathbb{R}^n$ denotes the state, $u \in \mathbb{R}^m$ is the input to be designed, $d > 0$ represents the delay duration, A, A_d, and B represent constant matrices with appropriate dimensions and A is a stable matrix, and $\Delta A(k,t)$ and $\Delta A_d(r,t)$ are time-varying perturbations with $(k,\ r) : \mathbb{R} \to \Phi$ are Legesque measurable and $\Phi \in \mathbb{R}^p$ is a compact set of $\mathbb{R}^p$. Furthermore, it is also assumed that

$$\max_{k\in\Phi}\|\Delta A(k,t)\| \leq \alpha \quad \text{and} \quad \max_{r\in\Phi}\|\Delta A_d(r,t)\| \leq \beta \tag{86.2}$$

where α and β are positive constants. It is assumed that the pair (A, B) is completely controllable. The objective of this paper is to derive a simple stabilizability condition and design corresponding state feedback controllers in the form of

$$u(t) = -Fx(t) \tag{86.3}$$

where F is the gain matrix such that the resulting closed-loop system is stable.

Theorem 1 If there exists a positive constant η such that

$$A^T + A - 2\eta BB^T + 2\left(\alpha + \beta + \frac{\|A_d\|}{2}\right)I + \frac{A_d^T A_d}{\|A_d\|} < 0, \tag{86.4}$$

the time-delay system (86.1) with time-varying parametric perturbations can be stabilized by the memoryless state feedback controller in the form of (86.3) with the gain matrix F as

$$F = 0.5B^T P \tag{86.5}$$

where the positive definite matrix P satisfies the following Riccati equation

$$A^T P + PA - PBB^T P = -Q. \tag{86.6}$$

where Q is a given $n \times n$ real positive definite matrix.

Proof Define a positive semi-definite matrix N as

$$N \equiv (P - \eta I)BB^T(P - \eta I). \tag{86.7}$$

Then, the Riccati equation (86.6) can be rewritten as

$$\begin{aligned}&\left(A - \eta BB^T\right)^T(qI - P) + (qI - P)\left(A - \eta BB^T\right)\\ &\quad = -N + Q + \eta^2 BB^T + q\left(A^T + A - 2\eta BB^T\right).\end{aligned} \tag{86.8}$$

Furthermore, define

$$Q \equiv q\left[(2\alpha + \|A_d\| + 2\beta)I + \frac{A_d^T A_d}{\|A_d\|}\right]. \tag{86.9}$$

Substituting (86.9) into (86.8) leads to

$$\begin{aligned}&Q + \eta^2 BB^T + q\left(A^T + A - 2\eta BB^T\right)\\ &= q\left[A^T + A - 2\eta BB^T + 2\left(\alpha + \beta + \frac{\|A_d\|}{2}\right)I + \frac{A_d^T A_d}{\|A_d\|} + \frac{\eta^2}{q}BB^T\right].\end{aligned} \tag{86.10}$$

Obviously if condition (86.4) is satisfied, then there must exist a positive constant $q \gg \eta^2\|B\|^2$ such that the right-hand side of (86.10) is a negative definite matrix. This means the right-hand side of (86.8) is also a negative definite matrix. Furthermore, condition (86.4) also implies that $A^T + A - 2\eta BB^T < 0$, one hence can conclude that $A - \eta BB^T$ is a stable matrix. Therefore, it is seen that equation (86.8) is a Lyapunov equation and then its solution $qI - P$ is positive definite. That is, the solution P of the Riccati equation (86.6) has the upper bound

$$P < qI. \tag{86.11}$$

Then, using the controller (86.3) with gain matrix (86.5), the system (86.1) becomes

$$\dot{x}(t) = \big(A - 0.5BB^T P + \Delta A(k,t)\big)x(t) + (A_d + \Delta A_d(r,t))x(t-d). \tag{86.12}$$

For this system, we construct a Lyapunov function as

$$V(x(t),t) = x^T(t)Px(t) + q\int_{t-d}^{t} x^T(\tau)\left(\frac{A_d^T A_d}{\|A_d\|} + \beta I\right)x(\tau)d\tau \tag{86.13}$$

where the positive definite matrix P satisfies (86.6). For convenience, we use symbols V, x, x_d, ΔA, and ΔA_d to replace $V(x(t),t)$, $x(t)$, $x(t-d)$, $\Delta A(k,t)$, and $\Delta A_d(r,t)$, respectively, in the following and later descriptions. Taking the derivative along the trajectories of (86.1) yields

$$\begin{aligned}\dot{V} = {} & x^T\left[A^T P + PA + \Delta A^T P + P\Delta A - PBB^T P + q\left(\frac{A_d^T A_d}{\|A_d\|} + \beta I\right)\right]x \\ & - qx_d^T\left(\frac{A_d^T A_d}{\|A_d\|} + \beta I\right)x_d + x_d^T A_d^T Px + x^T PA_d x_d + x_d^T \Delta A_d^T Px + x^T P\Delta A_d x_d.\end{aligned} \tag{86.14}$$

Using the upper bound (86.11) associated with linear algebraic tehniques, we have

$$\begin{aligned}x_d^T A_d^T Px + x^T PA_d x_d &\le \frac{1}{\|A_d\|}x_d^T A_d^T PA_d x_d + \|A_d\|x^T Px \\ &< q\left[\frac{1}{\|A_d\|}x_d^T A_d^T A_d x_d + \|A_d\|Ix^T x\right],\end{aligned} \tag{86.15}$$

$$\begin{aligned}x^T\Delta A^T Px + x^T P\Delta Ax &\le \alpha x^T Px + \frac{1}{\alpha}x^T\Delta A^T P\Delta Ax \\ &< q\left[\alpha x^T x + \frac{1}{\alpha}x^T\Delta A^T\Delta Ax\right] \le q2\alpha x^T x,\end{aligned} \tag{86.16}$$

and

$$\begin{aligned}x_d^T\Delta A_d^T Px + x^T P\Delta A_d x_d &\le \frac{1}{\beta}x_d^T\Delta A_d^T P\Delta A_d x_d + \beta x^T Px \\ &< q\left[\frac{1}{\beta}x_d^T\Delta A_d^T\Delta A_d x_d + \beta x^T x\right] \le q\beta\left[x_d^T x_d + x^T x\right],\end{aligned} \tag{86.17}$$

then

$$\begin{aligned}\dot{V} &< x^T\left[-Q + q\left(2\alpha I + \|A_d\| I + \frac{A_d^T A_d}{\|A_d\|} + 2\beta I\right)\right]x \\ &= qx^T\left[-(2\alpha + \|A_d\| + 2\beta)I - \frac{A_d^T A_d}{\|A_d\|} + 2\alpha I + \|A_d\| I + \frac{A_d^T A_d}{\|A_d\|} + 2\beta I\right]x = 0.\end{aligned} \tag{86.18}$$

Therefore, it is seen that if condition (86.4) is satisfied, then the resulting closed-loop system (86.12) is asymptotically stable. Thus, the proof is completed.

Remark 1 An interesting consequence of this theorem is that the stabilizability condition (86.4) is independent of the solution of the Riccati equation (86.6). Furthermore, it is also independent of the free variable q. Therefore, it is easy to check this condition.

Remark 2 If the stabilizability condition (86.4) holds, another simple state feedback controller can be developed as follows.

Theorem 2 If there exists a positive constant η such that the stabilizability condition (86.4) is met, then the perturbed time-delay system (86.1) can be stabilized by making use of the feedback controller (86.3) with

$$F = \eta B^T. \tag{86.19}$$

Proof From (86.19), the closed-loop system now becomes

$$\dot{x}(t) = \left(A - \eta BB^T + \Delta A\right)x(t) + (A_d + \Delta A_d)x(t-d). \tag{86.20}$$

Here, we choose the Lyapunov function as

$$V = x^T x + \int_{t-d}^{t} x^T(\tau)\left(\frac{A_d^T A_d}{\|A_d\|} + \beta I\right)x(\tau)d\tau. \tag{86.21}$$

This can lead to

$$\begin{aligned}\dot{V} &= x^T\left[A^T + A + ^T + \Delta A - 2\eta BB^T + \frac{A_d^T A_d}{\|A_d\|} + \beta I\right]x - x_d^T\left(\frac{A_d^T A_d}{\|A_d\|} + \beta I\right)x_d \\ &\quad + x_d^T A_d^T x + x^T A_d x_d + x_d^T \Delta A_d^T P x + x^T P \Delta A_d x_d \\ &\le x^T\left[A^T + A - 2\eta BB^T + 2\left(\alpha + \beta + \frac{\|A_d\|}{2}\right)I + \frac{A_d^T A_d}{\|A_d\|}\right]x < 0.\end{aligned} \tag{86.22}$$

Therefore, if condition (86.4) holds, then system (86.1) can be indeed stabilized by the controller (86.3) with the gain matrix (86.19). Thus, the proof is completed.

It is seen that the stabilization controller (86.3) with (86.19) is very simple. We also give the following algorithm for designing constant η and gain matrices (86.5) and (86.19).

Algorithm 1

Step 1. Set $k = 0$. Give an initial value of $\eta_k = 0$.
Step 2. Substitute η_k into the stabilizability condition (86.4) and check it. If it is satisfied, then stop the algorithm and gain matrices (86.5) and (86.19) are obtained where the positive matrix P in (86.5) satisfies (86.6). Otherwise, go to Step 3.
Step 3. Set

$$\eta_{k+1} = \eta_k + \varepsilon$$

where ε is an adequate positive constant. If $\eta_{k+1} > w$, then stop this algorithm and the stabilization controllers can not be found where w is a default large value. Otherwise, go to Step 2.

Remark 3 In existing researches for the control problems of systems by using Riccati equation approach, the selection of the positive matrix Q is an open problem. Most of them consider Q as a free matrix or choose it as cI for simplification. For example, by choosing $Q = cI$ and using maximal eigenvalue bound of the solution matrix P, Xia et al. [9] proposed a stabilizability criterion for system (86.1) as

$$\lambda_1(A^T + A - 2\eta BB^T) + 2(\alpha + \beta + \|A_d\|) < 0. \tag{86.23}$$

In light of the relation $A_d^T A_d \le \lambda_1(A_d^T A_d) I = \|A_d\|^2 I$ and the inequality $\lambda_1(A + B) \le \lambda_1(A) + \lambda_1(B)$ for $A^T = A \quad and \quad B^T = B$ [1], we have

$$\begin{aligned}
&A^T + A - 2\eta BB^T + 2\left(\alpha + \beta + \frac{\|A_d\|}{2}\right) I + \frac{A_d^T A_d}{\|A_d\|} \\
&\le \lambda_1 \left[A^T + A - 2\eta BB^T + 2\left(\alpha + \beta + \frac{\|A_d\|}{2}\right) I + \frac{A_d^T A_d}{\|A_d\|} \right] I \\
&\le \lambda_1 \left(A^T + A - 2\eta BB^T\right) I + 2\left(\alpha + \beta + \frac{\|A_d\|}{2}\right) I + \lambda_1 \left(\frac{A_d^T A_d}{\|A_d\|}\right) I \\
&\le \lambda_1 \left(A^T + A - 2\eta BB^T\right) I + 2(\alpha + \beta + \|A_d\|) I
\end{aligned} \tag{86.24}$$

Therefore, it is obvious that condition (86.4) is sharper than (86.23). This shows that by choosing properly the matrix Q associated with the upper matrix bound of the solution matrix P, we can obtain better stabilizability conditions.

To show the merits of the obtained results, we give the following numerical example.

Example 1 This example is given in [9]. Consider the perturbed time-delay system (86.1) with

$$A = \begin{bmatrix} 1 & 0 & 1 \\ -1 & -3 & 0 \\ 0 & 0 & 0 \end{bmatrix},\ A_d = \begin{bmatrix} 0.4 & 0 & 0 \\ -0.2 & 1 & 0 \\ 0 & 0 & 0.3 \end{bmatrix},\ B = \begin{bmatrix} 2 & 3 \\ 1 & 1 \\ 1 & 0 \end{bmatrix},\ d = 0.5,$$

$$\Delta A = \begin{bmatrix} 0.5\sin t & 0 & 0 \\ 0 & 0 & 0.3\sin 2t \\ 0 & -0.2\sin t & 0.1\cos 2t \end{bmatrix},\ \Delta A_d = \begin{bmatrix} 0.15\cos 3t & 0 & 0 \\ 0.1\sin 2t & 0 & 0 \\ 0 & 0.2\cos 2t & 0 \end{bmatrix}.$$

In [9], it was found that the gain matrix F must satisfy $F \geq 3.65B^T$ such that the closed-loop system is stable. Using Algorithm 1 and choosing $\varepsilon = 0.1$, we find the algorithm stop at $\eta = 3.3$. This means the gain matrix F can be chosen as $F \geq 3.3B^T$. Obviously the obtained result is better than that of [9]. Therefore, from (86.19), the memoryless feedback controller now can be designed as

$$u(t) = -3.3B^T x(t) = -\begin{bmatrix} 6.6 & 3.3 & 0 \\ 9.9 & 3.3 & 3.3 \end{bmatrix} x(t).$$

86.3 Conclusions

The stabilization design problem of the continuous time-delay systems subjected to parametric perturbations has been solved. A new stabilizability criterion is proposed to guarantee the existence of stabilization controller. This criterion does not involve the solution of any Riccati equation and hence is easy to be tested. Furthermore, two simple stabilization controllers have also been developed. One of them is also independent of the solution of the Riccati equation. By the proposed algorithm, it is seen that these controllers are easy to be implemented. Finally, a numerical example has been presented to show the applicability of the proposed schemes.

Acknowledgments The authors would like to thank the National Science Council, the Republic of China, for financial support of this research under the grant NSC 101-2221-E-230-010.

References

1. Amir-Moez, R. (1956). Extreme properties of eigenvalues of a Hermitian transformation and singular values of the sum and product of linear transformations. *Duke Mathematics Journal, 23*, 463–467.
2. Chen, W. H., Guan, Z. H., & Pei, Y. (2004). Delay-dependent stability and H_∞ control of uncertain discrete-time Markovian jump systems with mode-dependent time delays. *System Control Letters, 52*, 361–376.

3. Eun, T. J., Do, C. O., Kim, J. H., & Park, H. B. (1996). Robust controller design for uncertain systems with time delays: LMI approach. *Automatica, 32*, 1229–1231.
4. Fridman, E., & Shaked, U. (2003). Parameter dependent stability and stabilization of uncertain time-delay systems. *IEEE Transaction Automatic Control, 48*, 861–866.
5. Hsien, T. L., & Lee, C. H. (1995). Exponential stability of discrete time uncertain systems with time-varying delay. *Journal of Franklin Institute, 332*, 479–489.
6. Lee, C. H. (1998). Simple stabilizability criteria and memoryless state feedback control design for time-delay systems with time-varying perturbations. *IEEE Transaction Circuits and Systems I, 45*, 1121–1125.
7. Liu, T., Gao, F., & Wang, Y. (2010). IMC-based iterative learning control for batch processes with uncertain time delay. *Journal of Process Control, 20*, 173–180.
8. Su, N. J., Su, H. Y., & Chu, J. (1998). Delay-dependent robust H_∞ control for uncertain time-delay systems. *IEEE Transaction Automatic Control, 43*, 1727–1733.
9. Xia, Y., Zhu, Z., Li, C., Yang, H., & Zhu, Q. (2010). Robust adaptive sliding mode control for uncertain discrete-time systems with time delay. *Journal of Franklin Institute, 347*, 339–357.

Chapter 87
Extended Kalman Filter for Speed Sensorless Induction Motor Control with Torque Compensation

Tien-Chi Chen, Gang-Ming Fan, Chun-Jung Chen, Ming-Fang Wu, You-Je Lin and Ming-Bin Wang

Abstract A field-oriented control induction motor, without speed sensors, using the extended Kalman filter is proposed. With this method, the state is composed of stator current, rotor flux, motor speed, load torque and rotor time constant. The extended Kalman filter was used to estimate the motor speed, rotor flux, rotor time constant and load torque simultaneously by measuring the stator currents and voltages. The motor speed estimation was estimated using the extended Kalman filter and feedback to produce the speed control without speed sensors. The rotor time constant estimation was used to regulate the field-oriented mechanism to achieve the field orientation. The load torque estimation provided a torque feed-forward loop to realize a robust speed control against the load torque disturbance. Some experimental results demonstrate the proposed scheme's effectiveness.

Keywords Field-oriented control · Speed sensorless · Induction motor · Extended Kalman filter · Load torque estimation

87.1 Introduction

In recent years, variable induction motor drives have been widely applied in numerous industries. The increasing availability of low cost microcomputers has created great interest in the applications of field oriented control to induction motors. The field-oriented control method is the favored method in the industry today. However, its performance strongly depends upon the motor parameters,

T.-C. Chen (✉) · G.-M. Fan
Department of Computer and Communication, Kun Shan University, Tainan, Taiwan
e-mail: tchichen@mail.ksu.edu.tw

C.-J. Chen · M.-F. Wu · Y.-J. Lin · M.-B. Wang
Department of Electrical Engineering, Kun Shan University, Tainan, Taiwan

J. Juang et al. (eds.), *Proceedings of the 2nd International Conference on Intelligent Technologies and Engineering Systems (ICITES2013)*, Lecture Notes in Electrical Engineering 293,
DOI: 10.1007/978-3-319-04573-3_87,

particularly the rotor time constant. Therefore, rotor time constant identification is required for field-oriented control of induction motors.

In many industrial applications, a speed sensor at the machine shaft is often expensive or not feasible. Therefore, control must be instituted without the use of a speed sensor, without deteriorating the dynamic performance of the drive. The development of a sensorless shaft induction motor drive has become an important research topic.

In recent years, a wide variety of estimation techniques have been used for the parameter and speed estimation of an induction motor. This approach includes the model reference adaptive system method [1, 2], speed observer method [3, 4] and the extended Kalman filter [5–7]. The extended Kalman filter algorithm is an optimal recursive estimation algorithm for nonlinear systems. It processes all available measurements regardless of their precision, to provide a quick and accurate estimate of the variable of interest, and also achieves a rapid convergence.

This paper proposes using the extended Kalman filter (EKF) for a field-oriented induction motor control without the requirement for speed sensors. The proposed method can accurately estimate the motor speed, rotor flux, rotor time constant and load torque simultaneously by measuring the stator currents and voltages. The rotor flux and rotor time constant identification can be used to regulate the field-oriented mechanism in order to maintain the field orientation advantage. The load torque estimation can provide a torque feedforward loop to produce a robust speed control. Therefore, the proposed method is suitable for sensor-less speed control and is robust against load torque disturbance and rotor time constant variations. The proposed control scheme was implemented using a 32-bit TMS320C32 microprocessor. Some experimental results demonstrate that the proposed control scheme can rapidly and accurately estimate the motor speed, the load disturbance, the rotor time constant and has a robust speed response.

87.2 Dynamic Model of the Induction Motor

A block diagram of the proposed extended Kalman filter (EKF) for a field-oriented control induction motor without speed sensors is shown in Fig. 87.1. The diagram consists of the induction motor drive, the extended Kalman filter, the field-oriented mechanism, torque feed-forward loop and a conventional PI controller. The EKF was used to estimate the motor speed, rotor flux, rotor time constant and load torque. Using the speed estimation, an induction motor speed control with speed sensors was developed. The rotor flux and rotor time constant estimation were used to regulate the field-oriented mechanism to set the electrical angular frequency in order to maintain field orientation advantage. The load torque estimation, with torque feedforward loop, resulted in an equivalent control, such that the speed response of the induction motor is robust against a load disturbance.

The electrical dynamics of an induction motor in a stationary reference frame, d^s and q^s axis, can be expressed as

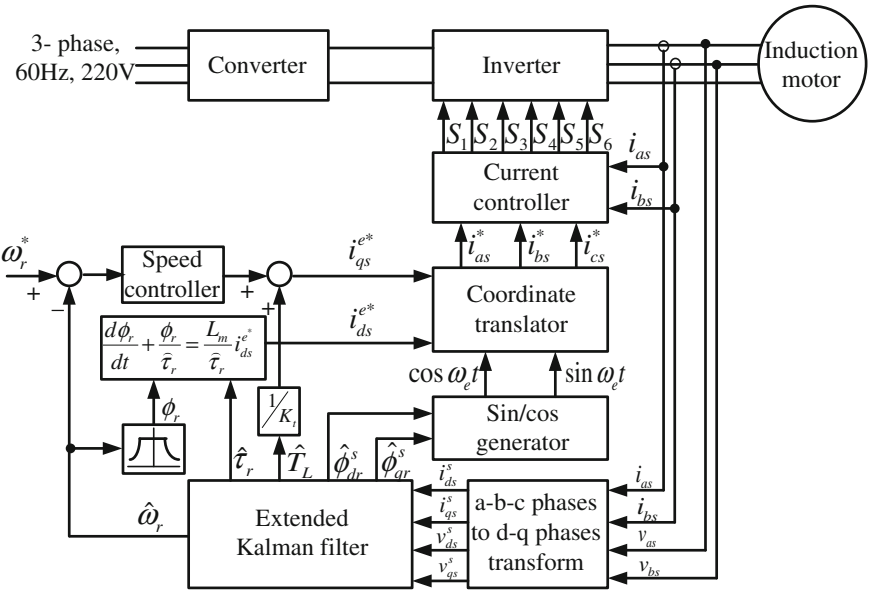

Fig. 87.1 Block diagram of the proposed the extended Kalman filter for an induction motor drive

$$\frac{d}{dt}\begin{bmatrix} i^s_{ds} \\ i^s_{qs} \\ \phi^s_{dr} \\ \phi^s_{qr} \end{bmatrix} = \begin{bmatrix} -\left(\frac{R_s}{\sigma L_s}+\frac{1-\sigma}{\sigma\tau_r}\right) & 0 & \frac{L_m}{\sigma L_s L_r \tau_r} & \frac{L_m \omega_r}{\sigma L_s L_r} \\ 0 & -\left(\frac{R_s}{\sigma L_s}+\frac{1-\sigma}{\sigma\tau_r}\right) & -\frac{L_m \omega_r}{\sigma L_s L_r} & \frac{L_m}{\sigma L_s L_r \tau_r} \\ \frac{L_m}{\tau_r} & 0 & -\frac{1}{\tau_r} & -\omega_r \\ 0 & \frac{L_m}{\tau_r} & \omega_r & -\frac{1}{\tau_r} \end{bmatrix} \begin{bmatrix} i^s_{ds} \\ i^s_{qs} \\ \phi^s_{dr} \\ \phi^s_{qr} \end{bmatrix} + \begin{bmatrix} \frac{1}{\sigma L_s} & 0 \\ 0 & \frac{1}{\sigma L_s} \\ 0 & 0 \\ 0 & 0 \end{bmatrix} \begin{bmatrix} v^s_{ds} \\ v^s_{qs} \end{bmatrix} \tag{87.1}$$

The generating torque of the induction motor can be rewritten as:

$$\frac{d\omega_r}{dt} = \frac{3PL_m}{4JL_r}\left(i^s_{qs}\phi^s_{dr} - i^s_{ds}\phi^s_{qr}\right) - \frac{B}{J}\omega_r - \frac{1}{J}T_L \tag{87.2}$$

where v^s_{ds}, v^s_{qs}: d^s and q^s axis stator voltages, i^s_{ds}, i^s_{qs}: d^s and q^s axis stator currents, ϕ^s_{dr}, ϕ^s_{qr}: d^s and q^s axis rotor fluxes, R_s, R_r: stator and rotor resistances, L_s, L_r, L_m: stator, rotor and mutual inductances, $\sigma = 1 - L_m^2/(L_s L_r)$: leakage coefficient, $\tau_r = L_r/R_r$: rotor time constant, ω_r: rotor angular velocity, P: pole number of the induction motor.

To simplify the observer's design, since the observation period in an actual system is short enough compared with the variation of T_L and τ_r. The following assumption can be made:

$$\frac{d}{dt}T_L = 0 \tag{87.3}$$

$$\frac{d}{dt}\left(\frac{1}{\tau_r}\right) = 0 \tag{87.4}$$

where τ_r is the rotor time constant.

According to Eqs. (87.1, 87.2, 87.3, 87.4), the dynamic behavior of an induction motor and the discrete-time measurement model can be written as

$$\dot{\mathbf{x}}(t) = \mathbf{f}(\mathbf{x}(t), \mathbf{u}(t), t) + \mathbf{w}(t) \tag{87.5}$$

$$\mathbf{y}(t_i) = \mathbf{h}[\mathbf{x}(t_i), t_i] + \mathbf{v}(t_i) \tag{87.6}$$

where

$$\mathbf{f}(\mathbf{x}, \mathbf{u}, t) = \begin{bmatrix} -\left(\frac{R_s}{\sigma L_s} + \frac{1-\sigma}{\sigma}x_7\right)x_1 + \frac{L_m}{{}_sL_r}x_3x_7 + \frac{L_m}{\sigma L_s L_r}x_4x_5 + \frac{1}{\sigma L_s}v_{ds} \\ -\left(\frac{R_s}{\sigma L_s} + \frac{1-\sigma}{\sigma}x_7\right)x_2 - \frac{L_m}{\sigma L_s L_r}x_3x_5 + \frac{L_m}{\sigma L_s L_r}x_4x_7 + \frac{1}{\sigma L_s}v_{qs} \\ L_m x_1 x_7 - x_3x_7 - x_4x_5 \\ L_m x_2 x_7 + x_3x_5 - x_4x_7 \\ \frac{3PL_m}{4JL_r}(x_2x_3 - x_1x_4) - \frac{B}{J}x_5 - \frac{1}{J}x_6 \\ 0 \\ 0 \end{bmatrix} \tag{87.7}$$

$$\mathbf{x}(t) = [\, i_{ds}^s \quad i_{qs}^s \quad \phi_{dr}^s \quad \phi_{qr}^s \quad \omega_r \quad T_L \quad \tau_r^{-1} \,]^{\mathrm{T}} \tag{87.8}$$

$$\mathbf{h}(\mathbf{x}, t) = \begin{bmatrix} i_{ds}^s \\ i_{qs}^s \end{bmatrix} = \begin{bmatrix} x_1 \\ x_2 \end{bmatrix} \tag{87.9}$$

The process noise $\mathbf{W}(t)$ and measurement noise $\mathbf{V}(t)$ are assumed to be white, zero-mean Guassian random vectors.

87.3 The Extended Kalman Filter Algorithm

The model of the induction motor is nonlinear. Therefore, the extended Kalman filter can be used to estimate the state variables of the induction motor. The algorithm of the extended Kalman filter for the nonlinear model (87.5) and (87.6) is summarized as follows.

(1) Prediction of state:

$$\widehat{\mathbf{x}}(k+1|k) = \widehat{\mathbf{x}}(k|k) + \int_{t_{k-1}}^{t_k} \mathbf{f}\Big(\widehat{\mathbf{x}}(t|t_k), \mathbf{u}(t), t\Big)dt \tag{87.10}$$

(2) Estimation of error covariance matrix:

$$\mathbf{P}_m(k+1|k) = \mathbf{\Phi}(k+1|k)\mathbf{P}_m(k|k)\mathbf{\Phi}^T(k+1|k) + \mathbf{Q}_d \tag{87.11}$$

where

$$\mathbf{\Phi}(k+1|k) = \exp(\mathbf{F}(k)t_s) \approx \mathbf{I_n} + t_s\mathbf{F}(k) \tag{87.12}$$

$$\mathbf{F}[k] = \frac{\partial \mathbf{f}[\mathbf{x}(t), \mathbf{u}(t), t]}{\partial \mathbf{x}(t)}\Big|\mathbf{x} = \widehat{\mathbf{x}}(k|k)$$

$$= \begin{bmatrix} -\left(a + b\widehat{x}_7\right) & 0 & c\widehat{x}_7 & c\widehat{x}_5 & c\widehat{x}_4 & 0 & \left(c\widehat{x}_3 - b\widehat{x}_1\right) \\ 0 & -\left(a + b\widehat{x}_7\right) & -c\widehat{x}_5 & c\widehat{x}_7 & -c\widehat{x}_3 & 0 & \left(c\widehat{x}_4 - b\widehat{x}_2\right) \\ L_m\widehat{x}_7 & 0 & -\widehat{x}_7 & -\widehat{x}_5 & -\widehat{x}_4 & 0 & L_m\widehat{x}_1 - \widehat{x}_3 \\ 0 & L_m\widehat{x}_7 & \widehat{x}_5 & -\widehat{x}_7 & \widehat{x}_3 & 0 & L_m\widehat{x}_2 - \widehat{x}_4 \\ -d\widehat{x}_4 & d\widehat{x}_3 & d\widehat{x}_2 & -d\widehat{x}_1 & \frac{-B}{J} & \frac{-1}{J} & 0 \\ 0 & 0 & 0 & 0 & 0 & 0 & 0 \\ 0 & 0 & 0 & 0 & 0 & 0 & 0 \end{bmatrix} \tag{87.13}$$

$$\mathbf{Q_d} = \int_{t_k}^{t_{k+1}} \mathbf{\Phi}(t_{k+1}|\tau)\mathbf{Q}(\tau)\mathbf{\Phi}^T(t_{k+1}|\tau)d\tau \tag{87.14}$$

where $a = \frac{R_s}{\sigma L_s}$, $b = \frac{1-\sigma}{\sigma}$, $c = \frac{L_m}{\sigma L_s L_r}$, $d = \frac{3PL_m}{4JL_r}$.

(3) Computation of Kalman filter gain:

$$\mathbf{K_m}(k+1) = \mathbf{P_m}(k+1|k)\mathbf{H}^T(k+1)[\mathbf{H}(k+1)\mathbf{P_m}(k+1|k)\mathbf{H}^T(k+1) + \mathbf{R}(k+1)]^{-1} \tag{87.15}$$

where

$$\mathbf{H} = \frac{\partial \mathbf{h}(\mathbf{x}, t)}{\partial \mathbf{x}}\Big|_{\mathbf{x}=\underline{\widehat{\mathbf{x}}}} = \begin{bmatrix} 1000000 \\ 0100000 \end{bmatrix} \tag{87.16}$$

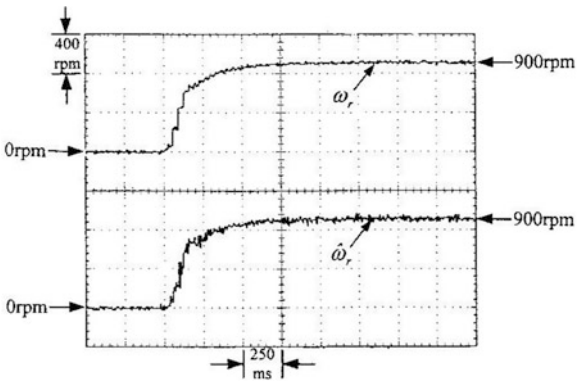

Fig. 87.2 The tracking responses of actual speed ω_r and estimated speed $\hat{\omega}_r$

(4) The update of the error covariance matrix is:

$$\mathbf{P_m}(k+1|k+1) = [\mathbf{I_n} - \mathbf{K_m}(k+1)\mathbf{H}(k+1)]\mathbf{P_m}(k+1|k) \tag{87.17}$$

(5) State estimation:

$$\hat{\mathbf{x}}(k+1\Big|k+1) = \hat{\mathbf{x}}(k+1|k) + \mathbf{K_m}(k+1)\mathbf{e}(k+1) \tag{87.18}$$

where

$$\mathbf{e}(k+1) = \mathbf{y}(k+1) - \mathbf{h}[\hat{\mathbf{x}}(k+1|k), k+1 \tag{87.19}$$

87.4 Experimental Results

In this section, some experimental results are provided to verify the effectiveness of the proposed scheme. Experiments have been realized using the following actual parameters of the induction motor: $R_s = 1.1\Omega$, $R_r = 1.3\Omega$, $L_s = 103.9$ mH, $L_r = 103.9$ mH, $L_m = 103$ mH, $J = 0.0027$ N · m · s^2/rad and $B = 0.000069$ N · m · s/rad.

As Fig. 87.1 indicates, the induction motor used here is a three-phase squirrel-cage. The rotor of the induction motor was coupled with a magnetic braking system used to vary the load torque. The converter and PWM inverter were implemented using a power diode and IGBT, respectively. The PI controller, extended Kalman filter, field-oriented mechanism, load torque compensation and axes transformation were implemented as a control program using a 32-bit TMS320C32 microprocessor.

The effectiveness of the proposed scheme was tested by experiments. First, the rotor time constant of the induction motor is fixed at its nominal value, $\tau_r = 0.0799$ s. The speed command is 900 rpm and a load torque of 2 N-m was applied. Figure 87.2 shows the tracking responses of actual speed ω_r and

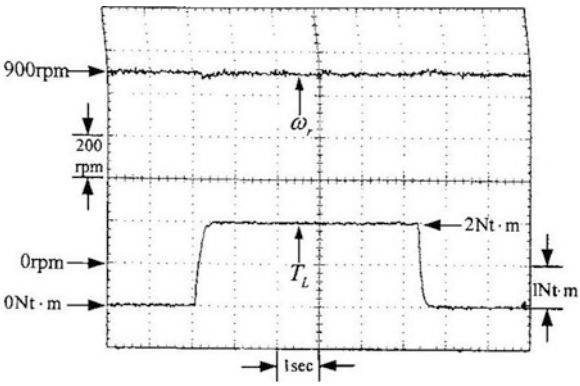

Fig. 87.3 The applied load torque T_L and the regulating response of actual speed ω_r when the speed control was performed using the proposed scheme

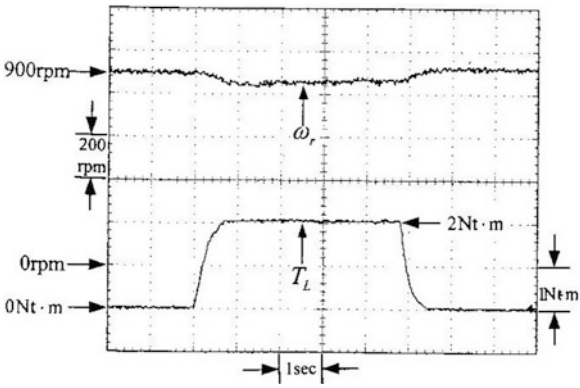

Fig. 87.4 The applied load torque T_L and the regulating response of actual speed ω_r if the extended Kalman filter does not introduce

estimated speed $\hat{\omega}_r$ when the speed control was performed using the estimated speed. It can be found that the extended Kalman filter estimates the motor speed very well. Second, the rotor time constant of the induction motor was fixed at its nominal value, $\tau_r = 0.0799$ s. The speed command is 900 rpm and a load torque of 2 N-m was applied. Figure 87.3 shows the applied load torque T_L and the regulating response of actual speed ω_r when the speed control was performed using the proposed scheme. If the extended Kalman filter does not introduce the load torque as a state variable, Fig. 87.4 shows the applied load torque T_L and the regulating response of actual speed ω_r. According to these figures, it is indicated that the extended Kalman filter estimates the load torque and computes a load torque compensation very well, such that the effects of a load torque disturbance on the speed response can be eliminated or reduced. However, the speed response has a long recovery time if the extended Kalman filter does not introduce the load torque as a state variable. Therefore, an improvement in the speed ripple using the proposed control scheme can be observed.

87.5 Conclusions

The extended Kalman filter for a field-oriented control induction motor without speed sensors was proposed. Using the rotor flux and rotor time constant estimation, the field-oriented mechanism can be regulated in order to maintain the field orientation. Furthermore, the load torque estimation can provide a torque feed-forward loop to produce a robust speed control. The proposed control scheme was implemented using a high-performance TMS320C32 microprocessor. According to Figs. 87.2, 87.3, 87.4, the experimental results demonstrate that the proposed method can accurately estimate the motor speed from low speed to high speed very well. The extended Kalman filter can estimate the rotor time constant, the load torque and produce a load torque compensation to obtain a robust speed response.

Acknowledgments This work is supported by Ministry of Economy Affairs for the Local Scientific Specialist Project under contract 101-EC-17-A-04-S1-220.

References

1. Uddin, M. N., Hao, W., Rebeiro, R. S., & Hafeez, M. (2011). Experimental performance of a model referenced aptive flux observer based NFC for IM drive. *2011 IEEE Industry Applications Society Annual Meeting* (pp. 1–8).
2. Ohara, M., & Noguchi, T. (2011). Sensorless control of surface permanent-magnet motor based on model reference adaptive system. *2011 IEEE 9th International Conference on Power Electronics and Drive Systems* (pp. 608–614).
3. Cirrincione, M., Accetta, A., Pucci, M., & Vitale, G. (2013). MRAS speed observer for high-performance linear induction motor drives based on linear neural networks. *IEEE Transactions on Power Electronics, 28*(1), 123–134.
4. Guzinski, J., Diguet, M., Krzeminski, Z., Lewicki, A., & Abu-Rub, H. (2009). Application of speed and load torque observers in high-speed train drive for diagnostic purposes. *IEEE Transactions on Industrial Electronics, 56*(1), 248–256.
5. Khanesar, M. A., Kayacan, E., Teshnehlab, M., & Kaynak, O. (2012). Extended Kalman filter based learning algorithm for type-2 fuzzy logic systems and its experimental evaluation. *IEEE Transactions on Industrial Electronics, 59*(11), 4443–4455.
6. He, H., Xiong, R., Zhang, X., Sun, F., & Fan, J. X. (2011). State-of-charge estimation of the lithium-ion battery using an adaptive extended Kalman filter based on an improved Thevenin model. *IEEE Transactions on Vehicular Technology, 60*(4), 1461–1469.
7. Kim, J. H., Lee, S. S., Kim, R. Y., & Hyun, D. S. (2012). A sensorless control using extended Kalman Filter for an IPM synchronous motor based on anextended rotor flux. *38th Annual Conference on IEEE Industrial Electronics Society* (pp. 1631–1636).

Chapter 88
Analysis and Implementation of SEPIC Power-Factor-Correction Rectifiers

Tsung-Lieh Hsien, Chien-Hua Lee and Cheng-Hung Hung

Abstract The objective of this paper is to analyze and implement the SEPIC Power-Factor-Correction (PFC) Rectifiers. The system transfer function is derived by the average current-mode control (ACC) and average power factor method for the active PFC technology. To achieve good output voltage regulation and higher power factor, the inner loop current controller and the outer loop voltage controller are designed to reduce the effects load fluctuation and provide a good disturbance rejection. Thus, less current harmonics is produced, while it also complies with the international current standards on power factor and fully improves the utilization rate of the power supplies.

Keywords SEPIC · PFC · Average current control · Average power factor

88.1 Introduction

The requirement of power quality and efficiency for electrical equipment becomes more and more demanding nowadays. Thus, EU organization regulates all electrical equipment sold in Europe to be confined with IEC 61000-3-2 current harmonic regulation [1].

SEPIC Power-Factor-Correction (PFC) Rectifiers is a good option for global power regulation. The circuit design of SEPIC PFC is based on SEPIC converter analysis. The current controller is based on combination of average current-mode

T.-L. Hsien (✉) · C.-H. Hung
Department of Electrical Engineering, Kun Shan University, Tainan 71003, Taiwan, Republic of China
e-mail: tlhsien@mail.ksu.edu.tw

C.-H. Lee
Department of Electrical Engineering, Cheng Shiu University, Kaohsiung 83347, Taiwan, Republic of China

J. Juang et al. (eds.), *Proceedings of the 2nd International Conference on Intelligent Technologies and Engineering Systems (ICITES2013)*, Lecture Notes in Electrical Engineering 293,
DOI: 10.1007/978-3-319-04573-3_88,

control (ACC) technique [2] and AC small signal analysis [3] to derive inner loop control block diagram. The voltage control is based on average power method [4] to analysis transfer function which comes from outer loop control signal to output voltage. By proper design of inner loop current controller and outer loop voltage controller, better output stability and higher power factor are achieved even under amplitude perturbation and load fluctuation.

88.2 Analysis of High Power Factor SEPIC Rectifier

88.2.1 Modeling of Inner Loop Current Control

The purpose of inner loop current control is to make average input current follow the input voltage to achieve high power factor, electric circuit structure as Fig. 88.1. Input voltage (v_g) is adjusted by K_v ($0 < K_v < 1$) as commend voltage (v_{ig}). Current resistance R_s feedback is utilized to input current, and commend voltage is compared to have current error signal e_i, through current controller $C_I(s)$ and PWM electric circuit, PWM driver signal is generated with its conducting duty ratio d to control ON/OFF of switch (S). This will make waveform of average input current follow the waveform of input voltage.

AC small signal of SEPIC converter is analyzed to design current controller $C_I(s)$. By using state-space averaging, the transfer function of electric circuit is derived, and this result will be applied to the voltage controller design. Electric circuit of state variables as inductance 'L_1, L_2'and capacitor 'C_1, C_o' are shown as Fig. 88.1. Two state equation results according to power factor switch (S) and conducting situation of diode (D) shown as bellow:

When S : ON, D : OFF When S : OFF, D : ON

$$L_1 \frac{di_{L_1}(t)}{dt} = v_g(t) \tag{88.1}$$

$$L_2 \frac{di_{L_2}(t)}{dt} = v_{c_1}(t) \tag{88.2}$$

$$C_1 \frac{dv_{c_1}(t)}{dt} = -i_{L_2}(t) \tag{88.3}$$

$$C_o \frac{dv_{c_o}(t)}{dt} = -\frac{1}{R_L} v_{c_o}(t) \tag{88.4}$$

$$L_1 \frac{di_{L_1}(t)}{dt} = v_g(t) - v_{c_1}(t) - v_{c_o}(t) \tag{88.5}$$

$$L_2 \frac{di_{L_2}(t)}{dt} = -v_{c_o}(t) \tag{88.6}$$

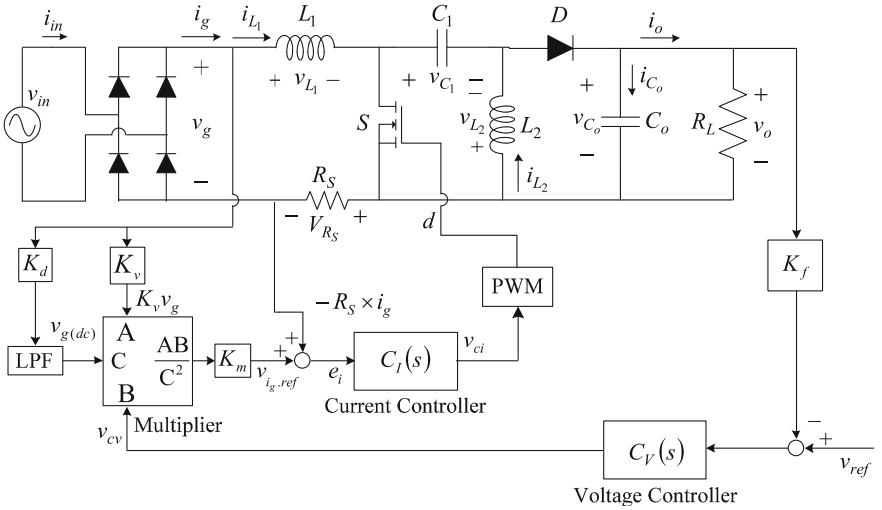

Fig. 88.1 High power factor SEPIC rectifier complete system framework

Table 88.1 Parameter of transfer function

n_1	$\frac{V_{c_1}+V_{c_o}}{L_1}$	d_1	$\frac{1}{C_o R_L}$
n_2	$\frac{V_{c_1}+V_{c_o}}{L_1 C_o R_L}+\frac{(1-D)(I_{L_1}+I_{L_2})}{L_1}\left(\frac{1}{C_1}+\frac{1}{C_o}\right)$	d_2	$\frac{(1-D)^2}{C_1 L_1}+\frac{(1-D)^2}{C_o L_1}+\frac{D^2}{C_1 L_2}+\frac{(1-D)^2}{C_o L_2}$
n_3	$\frac{(V_{c_1}+V_{c_o})D}{L_1 L_2 C_1}+\frac{(I_{L_1}+I_{L_2})(1-D)}{L_1 C_1 C_o R_L}$	d_3	$\frac{1}{C_1 C_o R_L}\left(\frac{D^2}{L_2}+\frac{(1-D)^2}{L_1}\right)$
n_4	$\frac{(V_{c_1}+V_{c_o})D}{L_1 L_2 C_1 C_o R_L}+\frac{(I_{L_1}+I_{L_2})(1-D)}{L_1 L_2 C_1 C_o}$	d_4	$\frac{(1-D)^2}{C_1 C_o L_1 L_2}$

$$C_1 \frac{dv_{c_1}(t)}{dt} = i_{L_1}(t) \tag{88.7}$$

$$C_o \frac{dv_{c_o}(t)}{dt} = i_{L_1}(t) + i_{L_2}(t) - \frac{1}{R_L} v_{c_o}(t) \tag{88.8}$$

The average of state equation is taken within a switch period (T_S) to introduce small signal disturbance to linearize DC operating point $Q(I_{L_1}, I_{L_2}, V_g, V_{c_1}, V_{c_o}, d)$. Also direct current item and AC product term are ignored, as state space form Eq. (88.9).

Small signal disturbance $\tilde{v}_g(t)$ is commended as zero to get transfer function of conduction duty ratio from output signal $\tilde{i}_{L_1}(t)$ to control signal via Laplace Transform as Eq. (88.10) and Table 88.1.

$$\begin{bmatrix} \frac{d\tilde{i}_{L_1}(t)}{dt} \\ \frac{d\tilde{i}_{L_2}(t)}{dt} \\ \frac{d\tilde{v}_{c_1}(t)}{dt} \\ \frac{d\tilde{v}_{c_o}(t)}{dt} \end{bmatrix} = \begin{bmatrix} 0 & 0 & -\frac{(1-D)}{L_1} & -\frac{(1-D)}{L_1} \\ 0 & 0 & \frac{D}{L_2} & -\frac{(1-D)}{L_2} \\ \frac{1-D}{C_1} & -\frac{D}{C_1} & 0 & 0 \\ \frac{1-D}{C_o} & \frac{1-D}{C_o} & 0 & -\frac{1}{C_o R_L} \end{bmatrix} \begin{bmatrix} \tilde{i}_{L_1}(t) \\ \tilde{i}_{L_2}(t) \\ \tilde{v}_{c_1}(t) \\ \tilde{v}_{c_o}(t) \end{bmatrix} + \begin{bmatrix} \frac{1}{L_1} \\ 0 \\ 0 \\ 0 \end{bmatrix} \tilde{v}_g(t)$$

$$+ \begin{bmatrix} \frac{V_{c_1}+V_{co}}{L_1} \\ \frac{V_{c_1}+V_{co}}{L_2} \\ -\frac{(I_{L_1}+I_{L_2})}{C_1} \\ -\frac{(I_{L_1}+I_{L_2})}{C_o} \end{bmatrix} \tilde{d}(t) \tag{88.9}$$

$$\left.\frac{i_{L_1}(s)}{d(s)}\right|_{\tilde{v}_g(s)=0} = \frac{n_1 s^3 + n_2 s^2 + n_3 s + n_4}{s^4 + d_1 s^3 + d_2 s^2 + d_3 s + d_4} \tag{88.10}$$

88.2.2 Modeling of Outer Loop Voltage Control

With assumed high power factor, the transfer function will be analyzed when the control signal (v_{cv}) from high power factor SEPIC rectifier is sent to output voltage (v_o). The result will be applied to the voltage controller design.

Multipliers are commonly used in voltage stabilization control. The complete control method uses output voltage and voltage divider feedback ($K_f\, v_o$) to compare with reference voltage (v_{ref}) to get voltage error signal (e_v). Through voltage controller ($C_V(s)$), control signal is generated. Meanwhile, input voltage ($K_v v_g$), voltage feed-forward ($v_{g(dc)}$) and control signal are used to generate commend voltage ($v_{ig.ref}$) which is multiplied by K_m to control the current and stabilize output voltage. v_{cv} controls current according to variation of output power factor, complete electric circuit shown as Fig. 88.1.

The control signal and input voltage average value are quite stable compared with the moving average of half-line voltage period T_{2L}, thus, it's regarded as constant. The average input power as Eq. (88.11) and the average output power as Eq. (88.12).

$$\langle P_{in}(t)\rangle_{T_{2L}} = \langle v_g(t) i_g(t)\rangle_{T_{2L}} = \frac{8K_v K_m v_{cv} v^2_{g(rms)}(t)}{\pi^2 R_S v^2_{g(dc)}} = \frac{K_v K_m v_{cv}}{R_S} \tag{88.11}$$

$$\langle P_o(t)\rangle_{T_{2L}} = \langle v_o(t) i_o(t)\rangle_{T_{2L}} = v_o \langle i_o(t)\rangle_{T_{2L}} \tag{88.12}$$

With assumed 100 % power transfer efficiency, that is, average input power equals average output power, according to $v_{g(dc)} = 2v_m/\pi$, Eqs. (88.11 and 88.12), the average output current $< i_o(t) >_{T2L}$ and the input current $< i_g(t) >_{T2L}$ is derived.

At DC working point $Q(I_g, I_o, V_{cv}, V_o, V_m)$, small signal disturbance to $< i_g(t) >_{T2L}$, $< i_o(t) >_{T2L}$, v_{cv}, v_o and v_m are introduced. Meanwhile, direct current item and AC product term are ignored. Hence,

$$\begin{aligned}\tilde{i}_{o\langle T_{2L}\rangle}(t) &= \left.\frac{\partial f_2}{\partial v_{cv}}\right|_Q \tilde{v}_{cv}(t) + \left.\frac{\partial f_2}{\partial v_o}\right|_Q \tilde{v}_o(t) = \frac{K_v K_m}{R_s V_o}\tilde{v}_{cv}(t) - \frac{K_v K_m V_{cv}}{R_s V_o^2}\tilde{v}_o(t) \\ &=: g_c \tilde{v}_{cv}(t) - \frac{1}{r_o}\tilde{v}_o(t)\end{aligned} \tag{88.13}$$

$$\begin{aligned}\tilde{i}_{g\langle T_{2L}\rangle}(t) &= \left.\frac{\partial f_1}{\partial v_{cv}}\right|_Q \tilde{v}_{cv}(t) + \left.\frac{\partial f_1}{\partial v_m}\right|_Q \tilde{v}_m(t) = \frac{4K_v K_m}{\pi R_s V_m}\tilde{v}_{cv}(t) - \frac{K_v K_m V_{cv}}{R_s V_m^2}\tilde{v}_m(t) \\ &=: g_i \tilde{v}_{cv}(t) - \frac{1}{r_i}\tilde{v}_m(t)\end{aligned} \tag{88.14}$$

$$\text{Where} \quad g_i = \frac{4K_v K_m}{\pi R_s V_m},\ r_i = \frac{R_s V_m^2}{K_v K_m V_{cv}},\ g_c = \frac{K_v K_m}{R_s V_o},\ r_o = \frac{R_s V_o^2}{K_v K_m V_{cv}} \tag{88.15}$$

According to Eqs. (88.13) and (88.14), small signal equivalent circuit is shown as Fig. 88.2. and, $R_L = 1/r_o$ according to average power Eq. (88.15). Transfer function from the voltage controller control signal $\tilde{v}_{cv}$ to the output voltage $\tilde{v}_o$ is derived through Laplace transform:

$$\frac{\tilde{v}_o(s)}{\tilde{v}_{cv}(s)} = g_c\left(r_o // R_L // \frac{1}{sC_o}\right) = g_c\left(\frac{R_L}{2} // \frac{1}{sC_o}\right) = \frac{\frac{K_v K_m}{R_s V_o C_o}}{s + \frac{2}{R_L C_o}} =: G(s) \tag{88.16}$$

88.3 Analysis and Design of High Power Factor SEPIC Rectifier Control System

To achieve power factor correction control, the design needs to be conformed to Table 88.2 circuit specification. Components which fit the SEPIC power factor specification are used to substitute in modeling analysis result to have actual transfer function of circuit. Controller for inner loop and outer loop are designed according to system frequency response chart.

Current loop needs to have sufficient bandwidth to allow followed half-line input voltage frequency 120 Hz waveform. So the system bandwidth setting should be 10 times larger than 120 Hz, i.e., above 2 kHz. However, in order to make input current precisely follow the waveform of input voltage, the system bandwidth should be 50 times larger than that of half-line voltage frequency, i.e.,

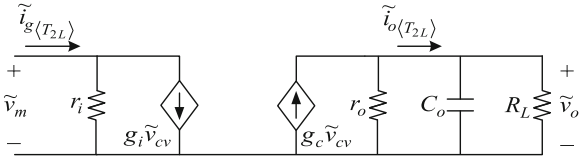

Fig. 88.2 Small signal equivalent circuit for high power factor SEPIC rectifier

Table 88.2 SEPIC circuit specification

Input voltage	v_{in}	90–260v_{ac}	Electric inductor	$L_1 = L_2$	2 mH
Output voltage	V_o	170 V	Blocking capacitor	C_1	1 μF
Output power	P_o	400 W	Output capacitor	C_o	940 μF

above 6 kHz. An integral plus phase lead controller as Eq. (88.17) is designed to fulfill system requirement.

$$C_I(s) = \frac{\mathrm{s}^2 + 125576730\mathrm{s} + 342817020000}{\mathrm{s}^2 + 9095000s} \tag{88.17}$$

Multipliers, inner loop current control, and transfer function of high power factor SEPIC rectifier all are derived from voltage loop modeling. In actual circuit, the resistance R_S is 0.125 Ω, multiplier output ratio, K_m as 3900, the input voltage ratio K_v as 0.000628, loading resistance R_L as 72.25 Ω when 400 W, the rest specification at Table 88.2. The actual transfer function of voltage loop is derived.

For DC output stabilization, the bandwidth of outer loop voltage control system should be way lower than half-line voltage frequency 120 Hz [5] to slow down the reaction of output voltage and avoid influence of load fluctuation. Meanwhile, the range should be within 50–200 ms, i.e., system bandwidth within 5–20 Hz to cover transient response settling time. An integral plus phase lead controller as Eq. (88.18) is designed to meet the system requirement.

$$C_V(s) = \frac{3500s + 87500}{s^2 + 350s} \tag{88.18}$$

88.4 Implementation Results

This section shows the performance of system high power factor and voltage stability, and its voltage and loading variation. When system fully loaded, the lowest and highest input voltage is measured as 90 V_{ac} and 260 V_{ac} when the high power factor performance as Figs. 88.3 and 88.4. The PF is 0.971 at 90 V_{ac} and

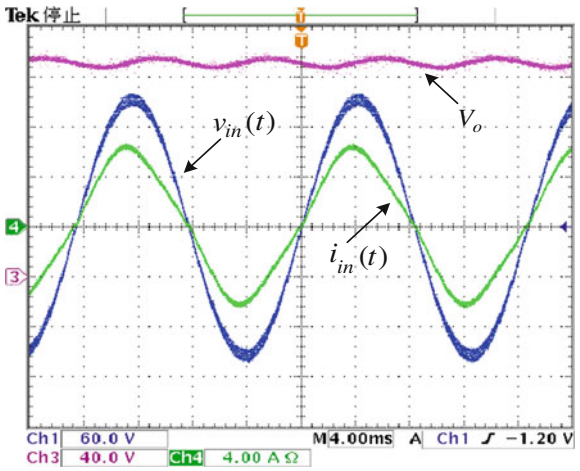

Fig. 88.3 Power factor characteristic when $v_{in} = 90$ V_{ac}

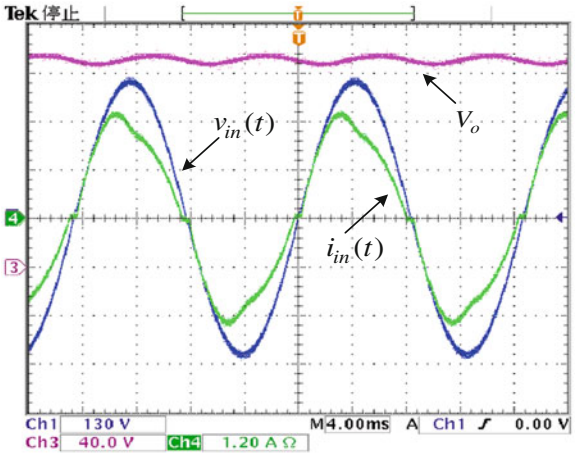

Fig. 88.4 Power factor characteristic when $v_{in} = 260$ V_{ac}

0.956 at 260 V_{ac}. Output power (P_o) change between 200 and 400 W is taken to measure system voltage stability, the response as Fig. 88.5. All perform their voltage stability within 200 ms. The transfer efficiency rate is between 86 and 89.8 %, curve chart as Fig. 88.6. The current spectrum compared with IEC 61000-3-2 for current harmonics as Fig. 88.7 and fits this regulation.

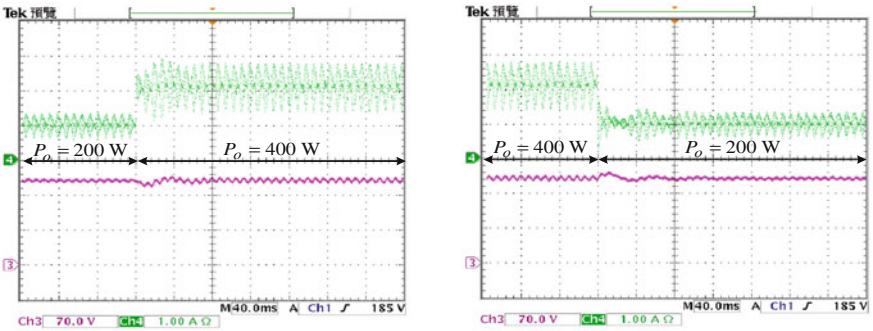

Fig. 88.5 Output voltage response when output power change between 200 and 400 W

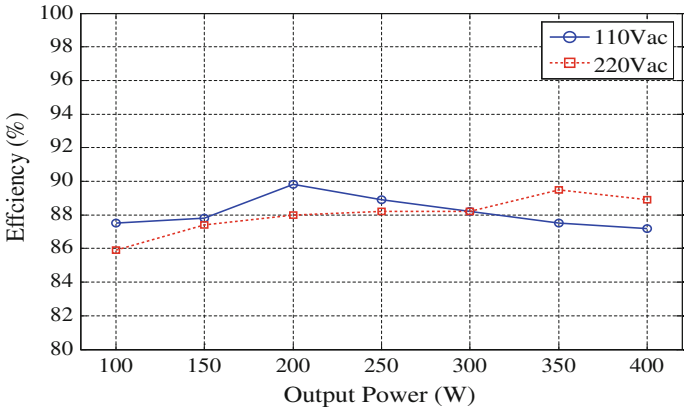

Fig. 88.6 System transfer efficiency curve

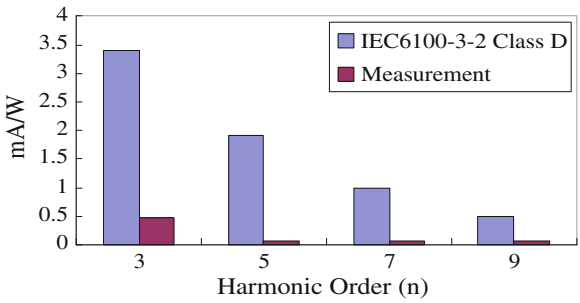

Fig. 88.7 Compared with Safety standard when $P_o = 400$ W

88.5 Conclusion

This paper adopts SEPIC convertor as structure of power factor corrector, utilizes active power factor correction as average current control method to achieve high power factor performance. Small signal math model is introduced by state space and average power method as design base for inner loop current controller and outer loop voltage controller, the result contributes to the developing of SEPIC PFC Rectifiers. According to implementation, in all power input domain, the system can achieve high power factor efficiency. The transfer efficiency can reach 90 % at most. When measuring loading variation, the system also retains voltage stability which fits IEC 61000-3-2 for current harmonics.

Acknowledgment This research is supported by National Science Council. Project number NSC 101-2221-E-168-022 and 100-EC-17-A-05-S1-192.

References

1. Electromagnetic Compatibility (EMC). (2001) *Limits for Harmonic Current Emissions (61000-3-2)*. Switzerland, IEC.
2. Ma, W., Wang, M., Liu, S., Li, S., and Yu, P. (2011). Stabilizing the Average-Current-Mode-Controlled Boost PFC Converter via Washout-Filter-Aided Method *IEEE Transactions on Circuits and Systems—II: Express Briefs, 58* (9).
3. Kanaan, H.Y. and AI-Haddad, K. (2008). Small-signal Averaged Model and Carrier-Based Linear Control of a SEPIC-Type Power Factor Correction Circuit. *Proc. IEEE 30th Int. Telecommunications Energy Conf.* (pp. 1–6).
4. Chen, S.J., Yang, S.P., and Wong, R.H. (2012). FPGA-based digital control for boost converters with power factor correction. *Proceedings for the IEEE ICIEA* (pp. 1089–1093).
5. Jovanovic, Z. M. (1992) Design trade-offs in continuous current-mode controlled boost power factor correction circuits. In: *Proceedings of the* HFPC*, San Diego* (pp. 209–220).

Chapter 89
Repetitive Control of Linear Servo System Based on Fuzzy Neural

Chun-Jung Chen, Tsung-Lieh Hsien, Chih-Hsuan Lee and Po-Young Kuo

Abstract This paper presents an innovative application to improve the repetitive control system on linear servomotor based on fuzzy-neural theorem. The proposed method provides the advantages self-tuning ability by neural algorithm and fuzzifier, defuzzifier of the fuzzy theorem. The fuzzy neural controller is employed to improve the traditional fixed repetitive controller for the second low-pass filter value. Experiments results can be proved the system have better motion response, reduce steady-state error and peak acceleration.

Keywords Fuzzy neural · Repetitive control

89.1 Introduction

Rotary motors are widely used in contemporary industrial application. Through transfer mechanism, the rotary motion is transferred into linear motion action for the fixed periodic repetitive control. Now, without any transmission mechanism, the linear motors achieve higher precision, faster production and less maintenance with its contact-drive system, unlike traditional transfer mechanism, there is no backlash and deflection happens.

In this paper, from the kinematic viewpoint, applicable motion characteristic curve is designed for the command of the linear servomotor [1, 2]. Combined with self-control characteristic from fuzzy neural control, a repetitive control scheme

C.-J. Chen · T.-L. Hsien (✉) · P.-Y. Kuo
Department of Electrical Engineering, ICITES, Kun Shan University, Tainan 71003, Taiwan, Republic of China
e-mail: tlhsien@mail.ksu.edu.tw

C.-H. Lee
Department of Electrical Engineering, Cheng Shiu University, Kaohsiung 83347, Taiwan, Republic of China

J. Juang et al. (eds.), *Proceedings of the 2nd International Conference on Intelligent Technologies and Engineering Systems (ICITES2013)*, Lecture Notes in Electrical Engineering 293,
DOI: 10.1007/978-3-319-04573-3_89,

[3–5] is proposed according to different motion characteristic curve to improve the bandwidth of second-order low-pass filter and optimize the linear servo position, speed and acceleration response. The result verifies the controller's good output response, elimination of steady-state error and lowest peak value of acceleration response.

89.2 Repetitive Control

The repetitive control based on the internal model principle [3] is employed to design a servo controller for reducing the steady-state error due to the periodic commands. The block diagram of repetitive control is shown as Fig. 89.1, where $G(s)$ is a linear servo system transfer function shown as Eq. (89.1), $K_q(s)$ is the second-order low-pass filter shown as Eq. (89.2), T_d is the time delay, and $K_b(s)$ is a phase compensator used to improve the closed-loop stability shown as Eq. (89.3).

$$G(s) = \frac{98676.9 \cdot (s^2 + 25.2s + 152.1)}{(s^5 + 129s^4 + 8336s^3 + 171845s^2 + 1004113.7s)} \tag{89.1}$$

$$K_q(s) = 1/(\frac{s^2}{\omega_q^2} + \frac{2\xi_q s}{\omega_q} + 1) \tag{89.2}$$

$$K_b(s) = e^{-\tau_b s} \tag{89.3}$$

According to Nyquist criteria, the original system characteristic equation,$1 + G(s) = 0$, must be stable under any time delay periodic. Join repetitive controller, the stability of system is determined by the regeneration spectrum $R(\omega)$ which is operated in any frequency less than 1 shown as Eq. (89.4).

$$R(\omega) = \left| K_q(j\omega) \cdot (1 - k_b(j\omega) \cdot \frac{G(j\omega)}{1 + G(j\omega)}) \right| < 1 \tag{89.4}$$

Periodic delay of the repetitive controller designed must be satisfied $T_d \geq 5/|\alpha|$ for the stable system [3], where α is the closest to the imaginary axis zero of the s-plane for the original system. The sensitivity function $S_o(s) = 1/(1 + G(s))$ is defined a system capability for outside disturbance exclusion function. The second-order low-pass filter and the frequency response of the sensitivity function schematic diagram are shown as Fig. 89.2, where ω_q is the second-order low-pass filter corner frequency, ω_s is the corresponding frequency of the sensitivity function such that $|S_o(j\omega_s)| = 1$, and M_s is the maximum value for the sensitivity function. Since sup $|S_o(j\omega)| \leq M_s$, and $|S_o(j\omega_s)| \geq 1$, $\forall \omega > \omega_s$ for the condition of $|R(\omega)| < 1$, we obtain the design criteria for the operating frequency of the filter $K_q(s)$ that must satisfy the Eq. (89.5) [3].

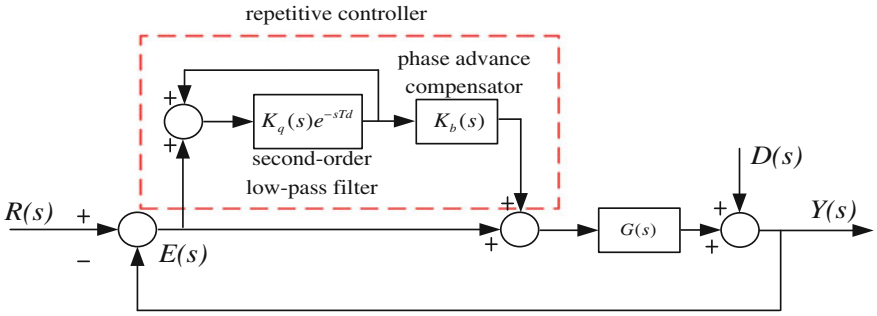

Fig. 89.1 Repetitive control block diagram

Fig. 89.2 Frequency responses of $S_o(s)$ and $K_q(s)$

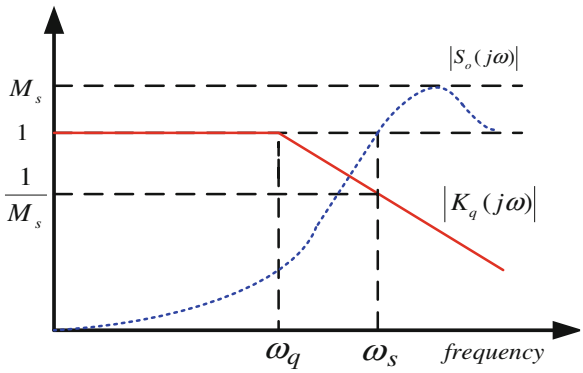

$$\left|K_q(j\omega_s)\right| < \frac{1}{M_s},\ \omega_q > \frac{\omega_s}{\sqrt{M_s}} \tag{89.5}$$

Selecting the appropriate operating frequency of filter $K_q(s)$ and phase angle of phase compensator $K_b(s)$ can be increased repetitive control system robustness. Therefore, the second-order filter damping ratio $\zeta_q = 0.7$ and operating frequency are chosen $\zeta_q = 0.7$ and $\omega_q < 20.4$, respectively. Phase compensator $K_b(s)$ can compensate for the phase lag of the original closed-loop system which is chosen as $|K_b(j\omega)| = |e^{-\tau bj\omega}| = 1$ with $\tau_b = 0.015$. Substituting the correlation coefficients into Eq. (89.4), the regeneration frequency spectrum is less than 1 which satisfies the criteria of repetitive control system shown as Fig. 89.3.

89.3 The Fuzzy Neural Repetitive Control

In this paper, the fuzzy neural theorem was employed in repetitive control system. The structure of the fuzzy neural networks is shown in Fig. 89.4. There are four layers in the network. They are input layer, membership layer, rule layer, and

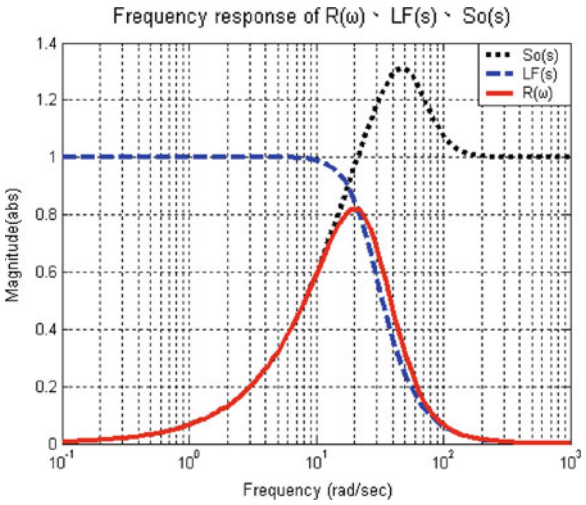

Fig. 89.3 Regeneration spectrum $R(\omega)$, the frequency response of $K_q(s)$ and $S_o(s)$

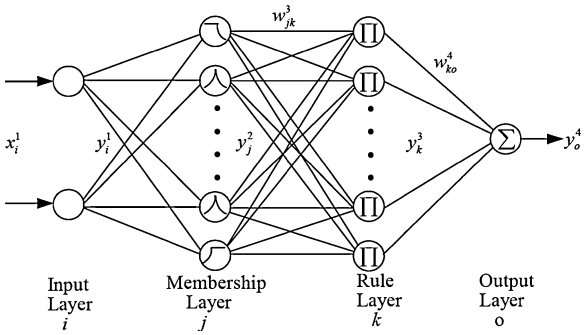

Fig. 89.4 The structure of fuzzy neural networks

output layer, individually. The algorithm of the fuzzy neural can be explained as following:

First layer: Input layer

$$x_1^1 = e = d_m - d \tag{89.6}$$

$$x_2^1 = \Delta e \tag{89.7}$$

where $x_1^1 = e$, $x_2^1 = \Delta e$ is represented the inputs of the input layer, d_m is represented input of the system, and d is output of the system.

Second layer: Membership Layer, the input x and output y can be expressed as

$$x_j^2 = -\sum_{i=1}^{2} \frac{(x_i^2 - m_{ij})^2}{\sigma_{ij}^2}, \quad i = 1, 2 \tag{89.8}$$

$$y_j^2 = \exp\left(-\sum_{i=1}^{2}\frac{\left(x_i^2 - m_{ij}\right)^2}{\sigma_{ij}^2}\right), \quad j = 1, \ldots n_2 \tag{89.9}$$

where m_{ij} and σ_{ij} are represented ith input of linguistic variable x_i^2 vs. jth neuron of the Gauss's function mean value and standard deviation. n_2 is the neurons number in membership layer.

Third layer: Rule layer,

$$x_k^3 = \prod_{j=11}^{n_2} w_{jk}^3 y_j^2, \text{ assume } w_{jk}^3 = 1 \tag{89.10}$$

$$y_k^3 = x_k^3 = \prod_{j=1}^{n_2} \exp\left(-\sum_{i=1}^{2}\frac{x_i^1 - m_{ij}}{\sigma_{ij}^2}\right), \quad k = 1, \ldots, n_3 \tag{89.11}$$

where x_k^3 is represented the input of the kth neurons of the rule layer, w_{jk}^3 is the weights between jth node at membership layer and kth node at rule layer, n_3 is the connection numbers, y_k^3 is the output of the kth neuron.

Forth layer: Output layer

$$x_o^4 = \sum_{k=1}^{n_3} w_{ko}^4 y_k^3, o = 1 \tag{89.12}$$

$$y_o^4 = x_o^4 = \sum_{k=1}^{n_3} w_{ko}^4 y_k^3 \tag{89.13}$$

where w_{ko}^4 is represented the weight between kth neuron of output layer and oth neuron of the output layer. Here $o = 1$, x_o^4 and y_o^4 are input, output of the fuzzy neural networks, individually.

The repetitive controller has effectively eliminated the steady state error due to the periodic commands, but if the values ω_q of the filter $K_q(s)$ are fixed in repetitive controller, the effect and the performance will be limited in different periodic input signals. Hence, the fuzzy neural theorem to be used in repetitive controller was proposed in this paper. Assume the system output error e and error change rate Δe, fuzzy neural is used to correct the operating frequency ω_q values of the filter $K_q(s)$ in repetitive controller. If the repetitive controller increases the operating frequency ω_q of the filter $K_q(s)$, it can enhance the precision of the position setting characteristics. But it may possible decrease the system's robust. Therefore, the fuzzy neural repetitive controller was proposed to be design according to the practical servomotor acceptable frequency ω_q values for filter $K_q(s)$. It contains better tolerance in variable periodic motion inputs and can correct relative operating value ω_q, it also ensure the system stable and to decrease the error.

Figure 89.5 shows the block diagram of the fuzzy neural repetitive controller system, the input and output signals of fuzzy neural are d_m and d, individually.

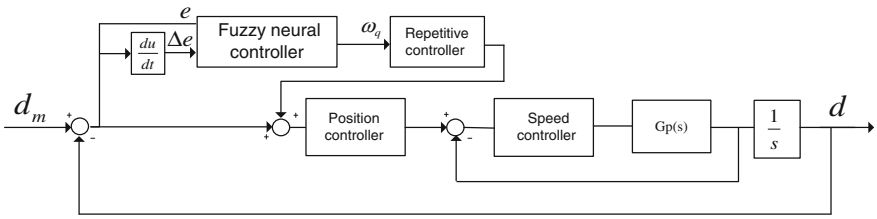

Fig. 89.5 The block diagram of the fuzzy neural repetitive controller system

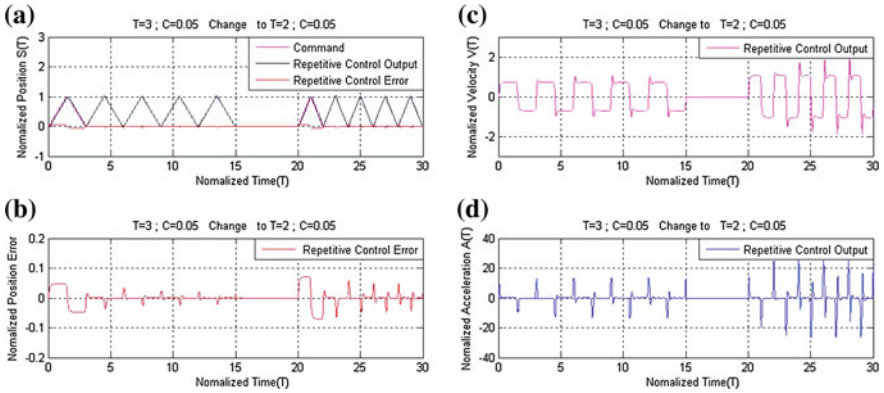

Fig. 89.6 $T = 3$ s to $T = 2$ s, repetitive controller response chart **a** position, **b** position error, **c** speed, **d** acceleration

Initially, the error e and error changing rate Δe to be created by random function. The rulers of the inference engine of the fuzzy system are defined by experts and can be automatically adjusted by neural algorithm. w_{ko}^4 is the weight between rule layer and output layer, m_{ij} is average value of the membership function layer. σ_{ij} is the standard error in membership function layer. The learning rates are chosen with tried and error method.

89.4 Experimental Results

In this section, periodic input is changed from $T = 3$ s to $T = 2$ s, (velocity changing parameter $c = 0.05$) [2], to measure the position, speed and acceleration response. From Fig. 89.6, with repetitive controller, the curve keeps converging after one period. This result verifies the repetitive controller can reduce periodical error, the bigger value of motion variation parameter, the longer time for acceleration or deceleration, and the more leveling of the acceleration response peak value. Also, the more steady-state error is reduced in the system.

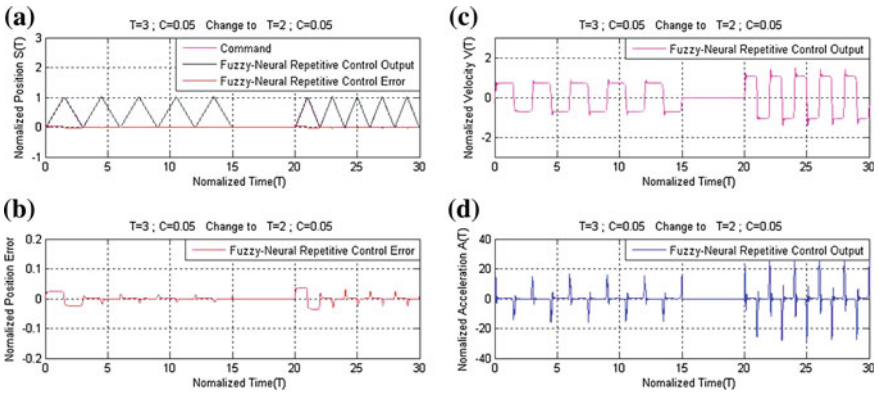

Fig. 89.7 $T = 3$ s to $T = 2$ s, fuzzy-neural network repetitive controller response chart. **a** position, **b** position error, **c** speed, **d** acceleration

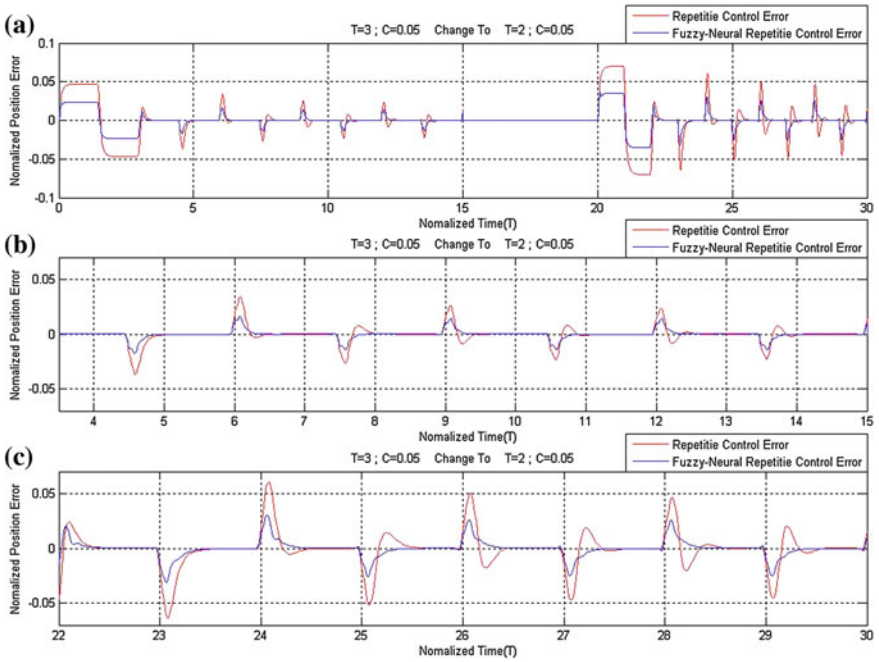

Fig. 89.8 $T = 3$ s to $T = 2$ s, comparison of repetitive controller and fuzzy-neural network repetitive controller. **a** position error, **b** position error from 4th second to 15th second, **c** position error from 22 to 30th second

From above, with the compensation of repetitive controller, the system has improved on steady-state error. But, still, there is always more to do. This paper utilizes fuzzy-neural network, via online dynamic learning to self-adjust operative frequency value, ω_q, in the second-order low-pass filter of repetitive controller. The weakness of fixed ω_q is improved to enhance the purpose of this repetitive controller. This enables the linear motor to swiftly reduce steady-state error according to variable periodical movement input commend shown as Fig. 89.7. Compare to a fixed ω_q of repetitive controller, the fuzzy-neural network repetitive controller has optimal transient response and steady state error shown as Fig. 89.8.

89.5 Conclusion

The paper analyzes the repetitive controller and fuzzy-neural repetitive controller design for the linear servomotor driver system. However, by using structure of fuzzy-neural repetitive controller and its online dynamic learning, the operative frequency value ω_q of second-order low-pass filter in repetitive controller is adjusted automatically. The weakness of fixed ω_q is improved to enhance the purpose of this repetitive controller and the precision control in position. After experimenting, the purposed controller performs good tracking ability, swiftly improves the zero steady-state error and reduces the peak value of acceleration.

Acknowledgments This research is supported by Ministry of Economy Affairs and National Science Council. Project number 101-EC-17-A-04-S1-220 and NSC 102-2221-E-168-025.

References

1. Liu, J. Y., Hsu, M. H., & Chen, F. C. (2001). On the design of rotating speed functions to improve the acceleration peak value of ball-screw transmission mechanism. *Mechanism and Machine Theory, 36*, 1035–1049.
2. Yan, H. S., Tsai, M. C., & Hus, M. H. (1996). A variable-speed method for improving motion characteristics of cam-follower systems. *ASME Transactions, Journal of Mechanical Design, 118*(1), 250–258.
3. Yau, W.-S & Tsai, M.-C. (1999). Repetitive control design for linear servo systems. *Proceedings of the American Control Conference* (pp. 3728–3732).
4. Tsai, M. C., & Yao, W. S. (2002). Design of a plug-in type repetitive controller for periodic inputs. *IEEE Transactions on Control Systems Technology, 10*(4), 547–555.
5. Chen, T.-C., Yua, C.-H., Chen, C.-J., & Tsai, M.-C. (2008). Neuro-fuzzy speed control of traveling-wave type ultrasonic motor drive using frequency and phase modulation. *Journal of ISA Transactions, 47*, 325–338.

Chapter 90
Controller Design for a Boost PFC Converter with Hybrid Particle Swarm Optimization

Shin-Ju Chen, Chao-Ming Huang, Sung-Pei Yang and Hung-Chi Chen

Abstract The controller design with on-line scheme for an active boost power-factor-correction (PFC) converter is proposed to comply with the international harmonic current standards. The average current-mode control (ACC) is used for the PFC boost converter. The ACC-controlled boost converter includes a fast inner current loop and a slow outer voltage loop. The current loop regulates the input current such that input average current follows the input voltage waveform to achieve high power factor. The outer voltage loop maintains the output voltage at a reference level against load variation and line voltage fluctuation. To optimize the control systems, a hybrid particle swarm optimization (HPSO) algorithm is used to determine the optimal controllers for both of the inner and outer loops. A 450 W converter prototype is built to validate the effectiveness of the approach. The experimental results show the proposed controllers can provide better performance in load regulation and line regulation than the conventional controller design.

Keywords Boost converter · Power factor correction · Average current-mode control · Hybrid particle swarm optimization

90.1 Introduction

Recently, relative regulations have come up to classify electronic equipments, such as IEC61000-3-2 to limit the input line current harmonics for the different electronic equipments. In order to comply with the standard, adding PFC AC-DC pre-regulator [1] is necessary for the switching power supply. The continuous-conduction-mode (CCM) boost topology is a popular choice for a PFC converter

S.-J. Chen (✉) · C.-M. Huang · S.-P. Yang · H.-C. Chen
Department of Electrical Engineering, Kun Shan University, Tainan 71003, Taiwan Republic of China
e-mail: sjchen@mail.ksu.edu.tw

J. Juang et al. (eds.), *Proceedings of the 2nd International Conference on Intelligent Technologies and Engineering Systems (ICITES2013)*, Lecture Notes in Electrical Engineering 293,
DOI: 10.1007/978-3-319-04573-3_90,

with high power rating because the inductor current ripple is small, and the converter has low current stress as well as a small filter for electromagnetic interference (EMI).

In order to achieve low input line current harmonics and well output voltage regulation, the average current-mode control (ACC) scheme is generally used in practice. The ACC-controlled boost PFC converter includes an inner current loop and an outer voltage loop. The current loop regulates the input current such that input average current follows the input voltage waveform to achieve high power factor. The voltage loop maintains the output voltage at a reference level against load variation and line voltage fluctuation. The conventional controller design requires an accurate mathematical model of the plant. However, the inherent nonlinear time-varying characteristics of PFC power converter impose difficulties to perform satisfactorily under parameter variation and load disturbance.

Many researches have been devoted to the PFC converter [2–4]. Theses techniques have served as effective tools to achieve high power factor and well output voltage regulation for the PFC converter. In this paper, an alternative method using hybrid particle swarm optimization (HPSO) [5] to on-line optimize the performance for a boost PFC converter based on the digital signal processor dsPIC30F4011. The control scheme is shown in Fig. 90.1. Finally, the experimental results based on a 450 W prototype are given to validate the effectiveness.

90.2 System Configuration

The scheme of an ACC-controlled PFC boost converter with HPSO optimal control is shown in Fig. 90.1. The system includes an inner current loop and an outer voltage loop. In the inner loop, the current controller is to shapes the average input current to be a sinusoidal waveform in phase with the AC line voltage. In the outer loop, the output voltage is sensed and compared with the voltage reference v_{ref}. The voltage controller output v_{cv} is the scaling factor for the magnitude of the current referencev_{iref} to balance the average input power and output power. The interface circuits include voltage scaling circuit, current sensing circuit and driver circuit. The block diagram of the PFC control system with HPSO-based optimal controllers is shown in Fig. 90.2.

Assume that the boost converter operates at CCM and the switching frequency is much higher than the line frequency. Therefore, the input voltage can be assumed as a constant within one switching period. When the switch S is on and the diode is off, the state equations can be described by

$$L\frac{di_L(t)}{dt} = v_g(t) \tag{90.1}$$

$$C_o\frac{dv_{C_o}(t)}{dt} = -\frac{v_{C_o}(t)}{R_L} \tag{90.2}$$

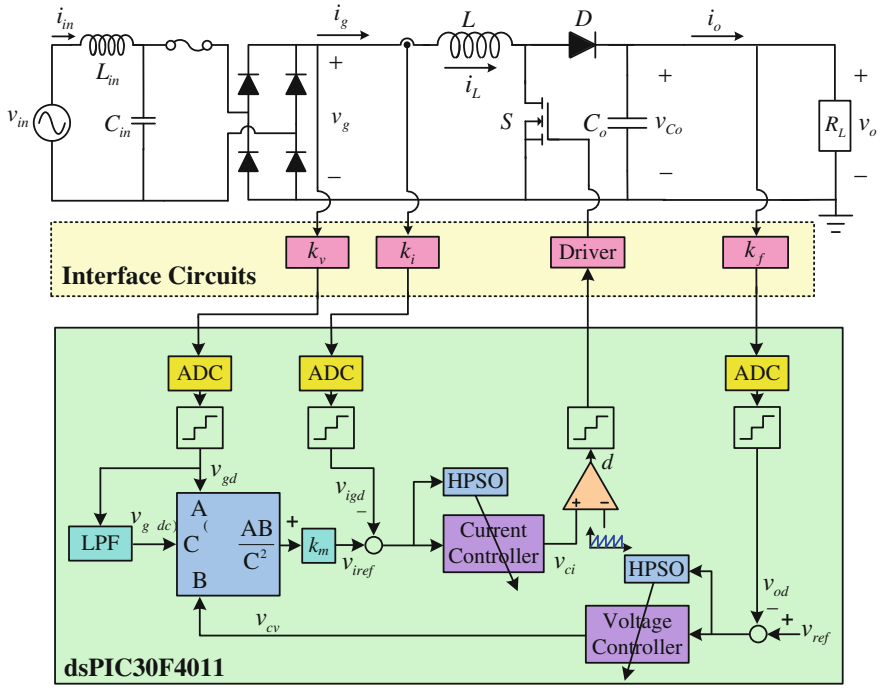

Fig. 90.1 HPSO-based optimal control of a boost PFC converter with dsPIC30F4011

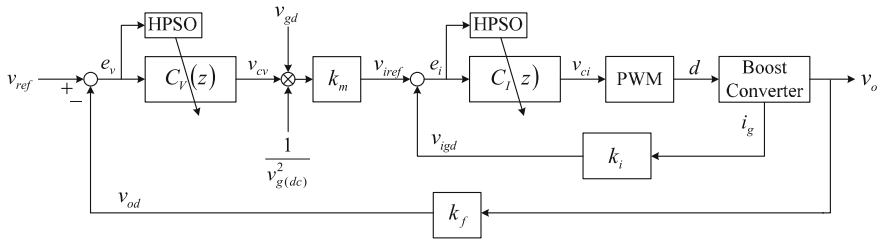

Fig. 90.2 The block diagram of the PFC control system

When the switch S is off and the diode is on, the state equations are given by

$$L\frac{di_L(t)}{dt} = v_g(t) - v_{C_o}(t) \tag{90.3}$$

$$C_o\frac{dv_{C_o}(t)}{dt} = i_L(t) - \frac{v_{C_o}(t)}{R_L} \tag{90.4}$$

The output equation is $v_o(t) = v_{Co}(t)$.

In general, the bandwidth of the inner current control system should be high enough to pass all significant harmonics of the rectified sine wave. Hence, the wide-bandwidth current controller varies the duty ratio d and forces the average input current to follow the waveform of the input voltage.

The outer voltage control loop is designed to maintain the output voltage equal to the reference voltage. In general, the bandwidth of the outer voltage control system is low, so that it can prevent the voltage controller output v_{cv} from introducing distortion and power factor degradation into the ac line current waveform. Let the input voltage $v_{in}(t) = V_m \sin(\omega t)$, then the variable v_{cv} can be viewed as a constant over one-half of the ac line period $T_{2L} = \pi/\omega$.

90.3 The HPSO Algorithm

In this paper, the hybrid particle swarm optimization (HPSO) algorithm is used to on-line determine the optimal controllers of the boost PFC converter. The particle swarm optimization (PSO) simulates the behavior of a swarm as a simplified social system. In a PSO system, each particle adjusts its position and velocity as follows:

$$R_i^d(t+1) = R_i^d(t) + v_i^d(t+1) \tag{90.5}$$

$$v_i^d(t+1) = wv_i^d(t) + \alpha_1 \times rand_1 \times [Pbest_i^d - R_i^d(t)] + \alpha_2 \times rand_2 \times [Gbest^d - R_i^d(t)] \tag{90.6}$$

where $R_i^d(t)$ is the current position of the ith particle, $v_i^d(t)$ represents the current velocity of the ith particle, d is the dimension of swarm, $Pbest_i^d$ means the best previous position of the ith particle, $Gbest^d$ represents the best previous position among all the particles in the swarm, w is the weighting function, α is an acceleration factor, and $rand$ represents the uniform random number between 0 and 1.

The basic PSO usually converges on a sub-optimal solution. To improve this drawback, a HPSO algorithm combined a mutation mechanism and basic PSO is used to help escape the local optimal points, as follows.

$$R_k^d(t+1) = R_k^d(t) + \psi_k(t+1) \tag{90.7}$$

where $R_k^d(t+1)$ is the position of the kth particle after mutation, $R_k^d(t)$ is the position of the kth particle selected randomly from the swarm, $\psi_k(t+1)$ is a mutation factor whose value is set between 0 and $0.2 \times (x_{max} - x_{min})$, x_{max} and x_{min} represent the upper and lower bounds of position, respectively.

90.4 Experimental Results

To demonstrate the validity of the proposed method, a 16 bit microprocessor dsPIC30F4011 is used to implement the control strategy for the PFC boost converter. The chip has 12 ADC modules with 10-bit resolution and is capable of a 500 ksps sampling rate. The 450 W prototype converter is built with the following parameters: $v_{in} = 90$–130 Vac, $v_o = 400$ V, inductor $L = 1$mH, output capacitor $C = 848$ μF, switching frequency f_{sw} =100 kHz, sensing gains $k_v = 1/39$, $k_i = 0.5$ and $k_f = 1/104$.

For comparison purpose, the conventional PI and Type II controllers are firstly designed for the inner current loop and the outer voltage loop respectively based on a linearized model around the operating point [6]. Then the proposed HPSO-based optimal controllers are implemented for the dual-loop PFC converter system.

Figure 90.3a shows the optimization processes of the current control with five different random seeds. After about 14 iterations, the best fitness value of the average input current sampled with 3000 data per second converges toward the value of 0.3468A, 0.3460A, 0.3454A, 0.3452A, and 0.3450A, respectively. The fitness value (FV) is calculated as follows.

$$\mathrm{FV} = \frac{1}{m}\sum_{i=1}^{m}(y_i - \hat{y}_i)^2 \tag{90.8}$$

where $\hat{y}_i$ is the ith measured output, y_i is the corresponding command, and m is the number of sampling data.

Equation (90.9) shows the controller obtained by the inner-loop current control. The results indicate that the proposed HPSO algorithm has good convergence performance for each stochastic optimization process.

$$v_{ci}(k) = 0.6977e_i(k) - 0.5589e_i(k-1) + v_{ci}(k-1) \tag{90.9}$$

For the outer-loop voltage control, the optimization processes with five different random seeds are shown in Fig. 90.3b. The convergence tendency of the best fitness value for position trajectory was obtained. After 10 iterations, the optimal controller is attained as follows.

$$v_{cv}(k) = 1.709e_v(k) - 1.56e_v(k-1) + 1.656v_{cv}(k-1) - 0.656v_{cv}(k-2) \tag{90.10}$$

In the steady state operation, the waveforms of the input current i_{in} and input voltage v_{in} at full load are depicted in Fig. 90.4. The measured comparisons of power factor at different load levels are listed in Table 90.1. It is clear that the proposed method gives higher power factor than the conventional methods. Moreover, the input line current satisfies current harmonic standard IEC61000-3-2 Class D.

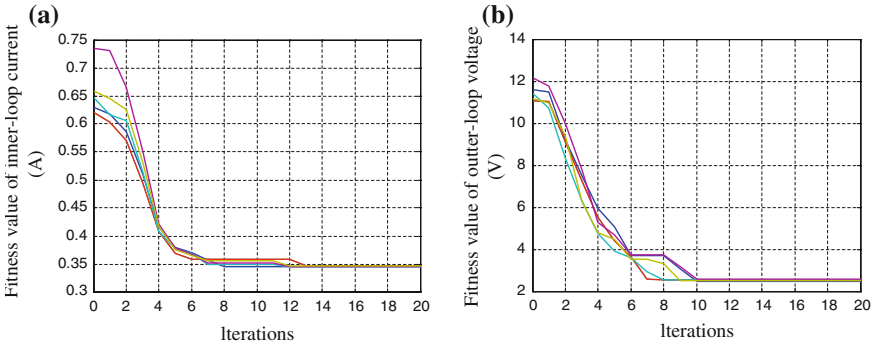

Fig. 90.3 Optimization processes: **a** inner-loop current control, **b** outer-loop voltage control

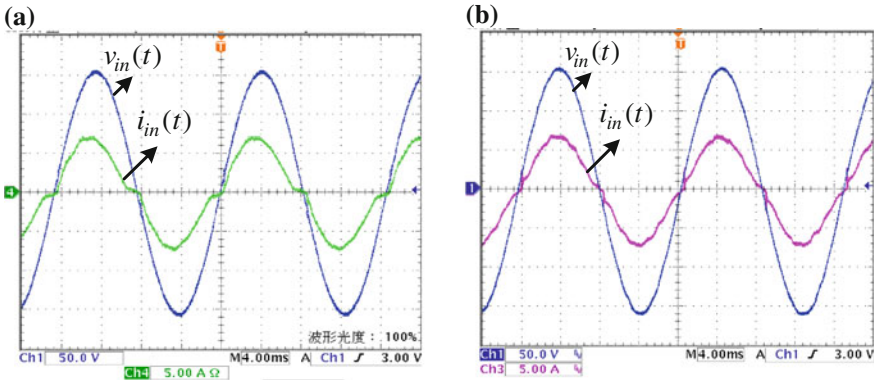

Fig. 90.4 Waveforms of i_{in} and v_{in}: **a** conventional control, **b** HPSO-based optimal control

Table 90.1 Comparison of power factor (PF) at different load levels

$P_o\,(W)$	150 W	200 W	250 W	300 W	350 W	400 W	450 W
PF with the conventional control	0.924	0.930	0.933	0.950	0.957	0.961	0.968
PF with the HPSO-based optimal control	0.981	0.980	0.983	0.983	0.980	0.981	0.981

To verify the improvement achieved by the proposed scheme, the comparative experimental response of the output voltage to a load variation from 450 to 250 W is depicted in Fig. 90.5. It is seen that the setting time and the peak of the output voltage deviation from the steady-state value are improved. It shows that the proposed scheme has better output voltage regulation than the conventional control scheme.

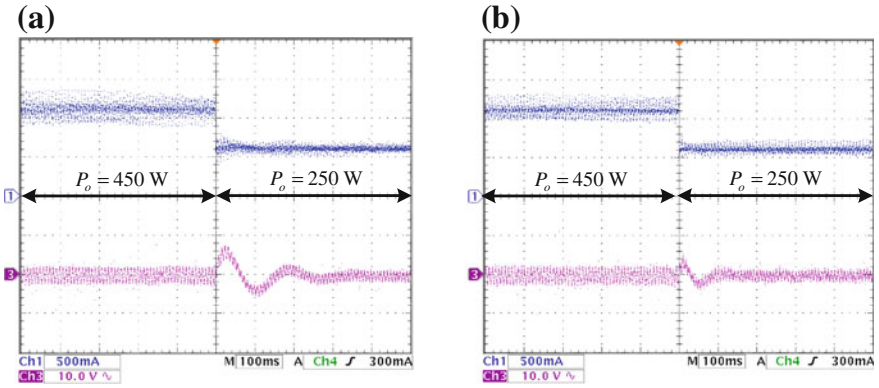

Fig. 90.5 The output voltage response: **a** conventional control, **b** HPSO-based optimal control

90.5 Conclusions

The dsPIC30F4011-based digital control for a PFC boost converter with ACC scheme is implemented to comply with the harmonic current standards. The inner current loop and outer voltage loop are designed by the on-line HPSO-based optimal controllers. A 450 W prototype is built to validate the effectiveness. The experimental results show that the superior performance of the proposed scheme in the power factor and output voltage regulation compared with the conventional control scheme.

References

1. Mohan, N., Undel, T. M., & Robbins, W. P. (2003). *Power electronics: Converters, applications, and design*. New York: Wiley.
2. Zhang, W. F., Feng, G., Liu, Y. F., & Wu, B. (2004). A digital power factor correction (PFC) control strategy optimized for DSP. *IEEE Transactions on Power Electronics, 19*, 1474–1485.
3. Zhang, W., Liu, Y. F., & Wu, B. (2006). A new duty cycle control strategy for power factor correction and FPGA implementation. *IEEE Transactions on Power Electronics, 21*, 1745–1753.
4. Hariprasath, S., & Balamurugan, R. (2013). A fuzzy logic controller based power factor correction for LED lighting applications, in *Proceedings of ICICES*, pp. 1118–1122.
5. Esmin, A. A., Lambert-Torres, G., & Zambroni de Souza, A. C. (2005). A hybrid particle swarm optimization applied to loss power minimization. *IEEE Transactions on Power Systems, 20*, 859–866.
6. Chen, S. J., Yang, S. P., & Cheng, Y. S. (2012). Analysis and design of digitally controlled boost PFC converters. *Journal of Kun-Shan University, 9*, 58–70.

Chapter 91
A Man–Machine Interface on the Cloud for Automatic Defect Detection

Chia-Yu Lee, Chin E. Lin, Chun-Jung Chen, Tien-Chi Chen, Min-Fang Wu and Tsung-Heng Ma

Abstract This paper presents a Man–Machine Interface (MMI) for Automatic Optical Inspection (AOI) using the Cloud computing system. The proposed system differs from the traditional MMI by implementing a Programmable Logic Controller (PLC) for manipulation. This system takes the advantage of the Qt Creator with C++ JavaScript to quickly develop drag and drop function. The system performance can be displayed on a smart phone including Android and iOS system. The preliminary operation of the proposed is tested with function capability for remote defect detection.

Keywords Man–Machine interface · Cloud system · Defect detection · Programmable logic controller

91.1 Introduction

In modern technology, display panels are one of the most valuable parts in livelihood devices, such as computers, cell phones and many consumer products. The Indium Tin Oxide (ITO) technology has become a new trend into mass production [1]. The performance of ITO display presents much better quality than any traditional technologies. The production quality and yield rate are two key factors to

C.-Y. Lee (✉) · C. E. Lin
Department of Aeronautics and Astronautics, National Cheng Kung University, Tainan, Taiwan, Republic of China
e-mail: chiayulee0519@gmail.com

C.-J. Chen · M.-F. Wu · T.-H. Ma
Department of Electric Engineering, Kun Shan University, Tainan, Taiwan, Republic of China

T.-C. Chen
Department of Computer and Communication, Kun Shan University, Tainan, Taiwan, Republic of China

J. Juang et al. (eds.), *Proceedings of the 2nd International Conference on Intelligent Technologies and Engineering Systems (ICITES2013)*, Lecture Notes in Electrical Engineering 293,
DOI: 10.1007/978-3-319-04573-3_91,

success. The automation defect detection is an important system to examine to semi-product and final product for quality assurance for production being running stably. An Automatic Detection System is used to inspect the blemishes of the ITO glass. The defects of the inspected glass include finger touches, pinholes, scratches, and particles.

In some large factories, there are usually multiple production lines running in parallel using different kinds of machines. Traditionally, each machine should require a specific production engineer to take care of the production control. It is basically wasteful in manpower if the system is well designed and running under perfect condition [2].

To deal with mass data from inspection and detection, a man–machine interface (MMI) is proposed onto the cloud via Internet to deliver scene from detection and collect production assessments for quality [3]. In high technology productions, automation with high performance MMI system design can be reliable to reduce manpower and enhance productivity [4].

In the detection data handling, real time operation via Internet into isolated computers is usually limited to wider interconnection for many participants in production control. While virtual database can be installed on a cloud system, the production control MMI can be designed into the cloud for more flexibility and efficiency in operation [5].

The advantages of the Cloud MMI are that convenient for engineers to manage many machines in the factory through multi-functional monitors directly interconnection to many machines simultaneously. The production control engineers can monitor MMI anytime anywhere by personal consumer devices, such as smart phone and tablet.

91.2 Cloud Computing

The Cloud Computing System is a new computing concept to interconnect many computers simultaneously to process data through Internet. The Cloud Computing shares the resources to all users during data access efficiently using resources that can be installed in the cloud. Therefore, the implementing system can be reduced into a feasible small scale that hardware cost can be saved.

Figure 91.1 shows a typical cloud computing system where users' device can be adequate on availability for any handy consumer electronics.

When a cloud system is adopted to handle system data, the acquired data can be transmitted to all qualified users anytime and anywhere for need. At present, handy consumer devices are convenient to modern life by connecting onto Internet, the cloud computing becomes most acceptable means as MMI displays. An engineer requires his authorization to hook on the cloud system to directly tune the parameters of duty machines on its control computer. In the development, the interconnection can make remote system operational and controllable by parameter adjustment via keypad to send commands.

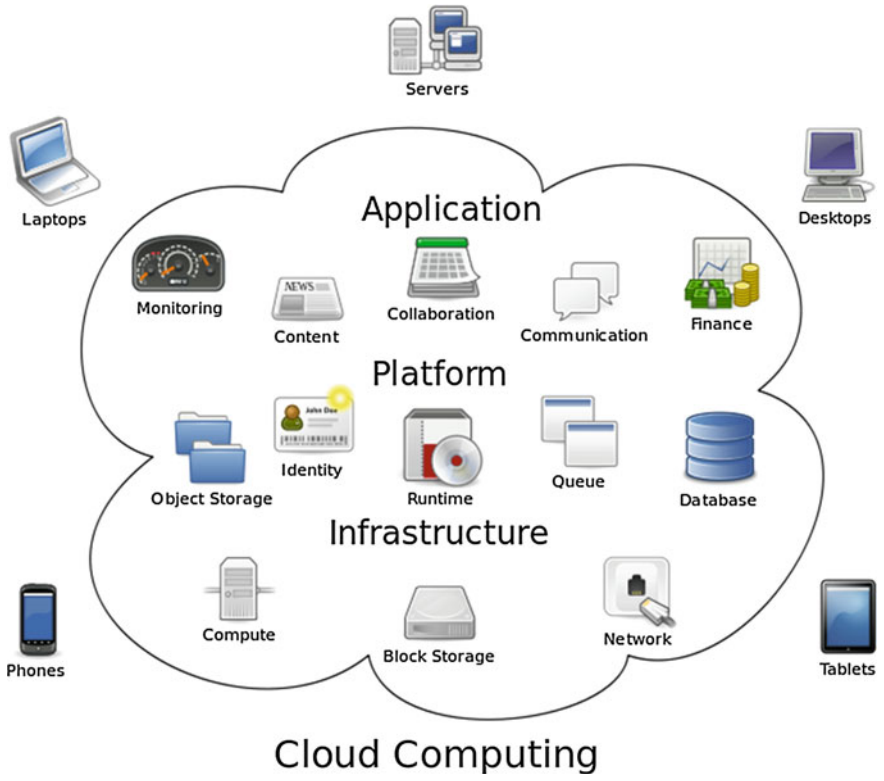

Fig. 91.1 The cloud computing system

91.3 Man–Machine Interface

Figure 91.2 shows the proposed man–machine interface (MMI) system, including three main parts as personal devices, system hardware and control software. For the devices, computer, smart phone, tablet for personal availability can be adopted. For the system hardware, the programmable logic controller and machine tool are adopted. For the control software, the MMI engine and communication interface are implemented.

A Man–Machine Interface (MMI) is designed with many fundamental functions as: password setting, system clock, normal monitor, malfunction alert, fault alarm, control data display, control chart display, control parameter adjustment, and machine setting. There are design pages to present the operation functions as: the image page, control page, defect history page, qualified page, and explore data page.

The most important function can be focused on the production engineer to adjust control parameters to the running machines if the operation condition is varying into unstable or inclining to fault situation.

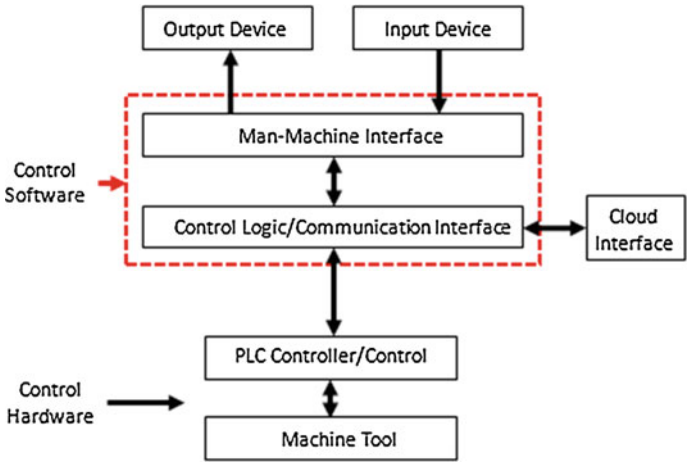

Fig. 91.2 The proposed man–machine interface

91.4 Development Tools

The PLC is a PC-based and common programming language system for real time operation. There are three ways to develop the MMI. The common programming language Qt Creator is employed to develop the proposed MMI for access into the cloud system.

The Qt Creator has the following advantages. It uses C++ JavaScript and QML code editor for prompt developing with an integrated UI designer. The system supports vision control to design user interfaces quickly with drag and drop functionality. The software can be customized in widgets or chosen from library with standard widgets to support desktop computers or any embedded and mobile devices.

91.5 Preliminary Results

First, a main window for MMI is created as shown in Fig. 91.3a. When the machine is started, the main window page will show directory of image page button, control page button, parameter page button, defect history table button, etc. for its operation.

In the image page, the production defect picture is taken by CCD and shown with the number of defects as shown in Fig. 91.4. In addition, this image page can be enlarged into better vision effect for the defect picture in more details.

In the control page, there are two control modes of the light control and motor control. The production engineer can manipulate the light control mode to adjust the light intensity and set the velocity, acceleration and target of the production line by the motor control mode. Different control parameters can be entered from the personal device in remote operation (Fig. 91.5).

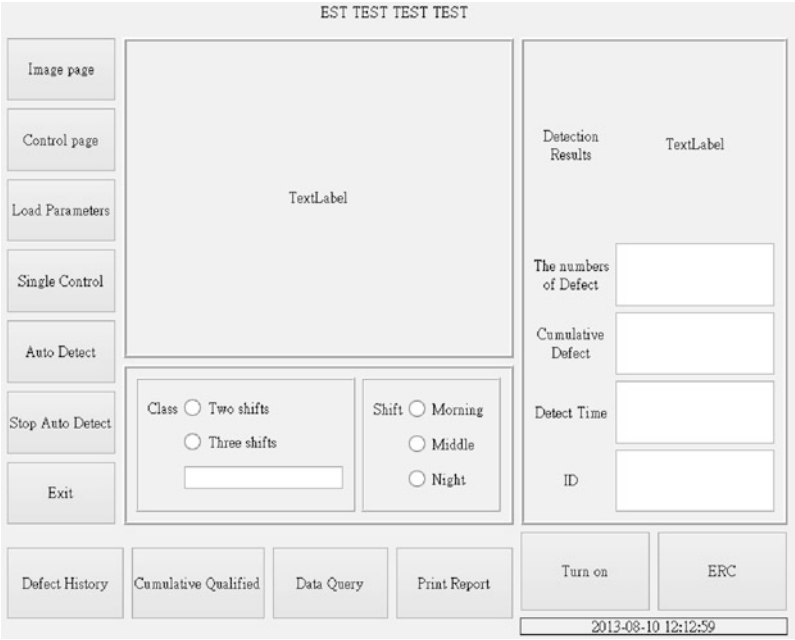

Fig. 91.3 Main window page

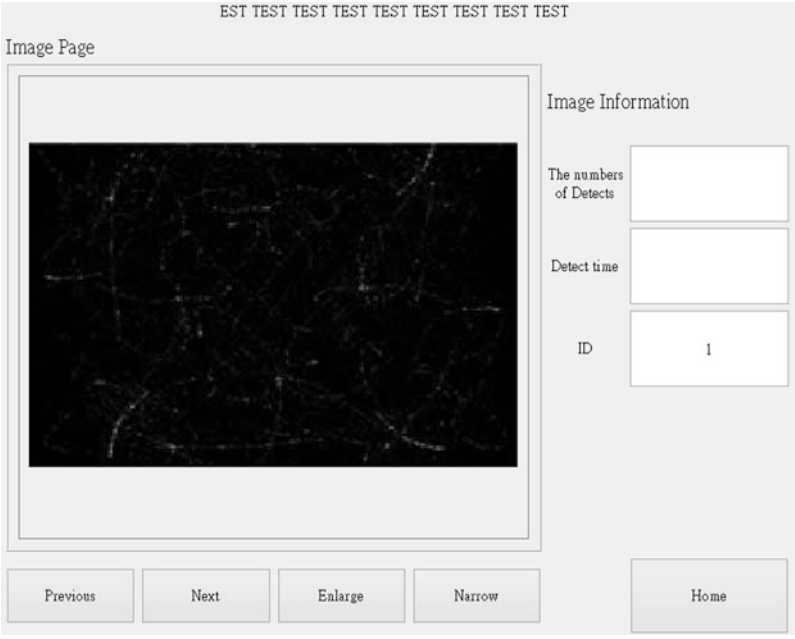

Fig. 91.4 image to show defects in production

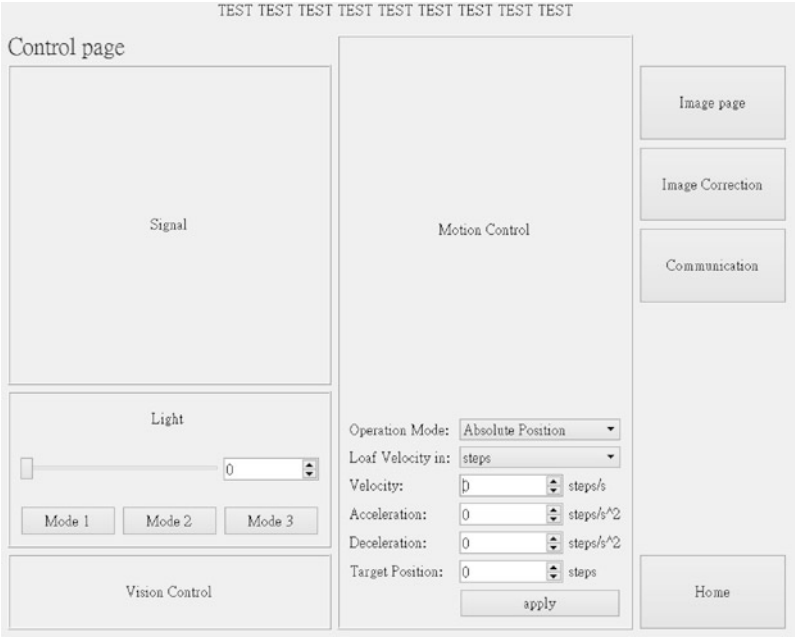

Fig. 91.5 Control page

Fig. 91.6 The defect history table

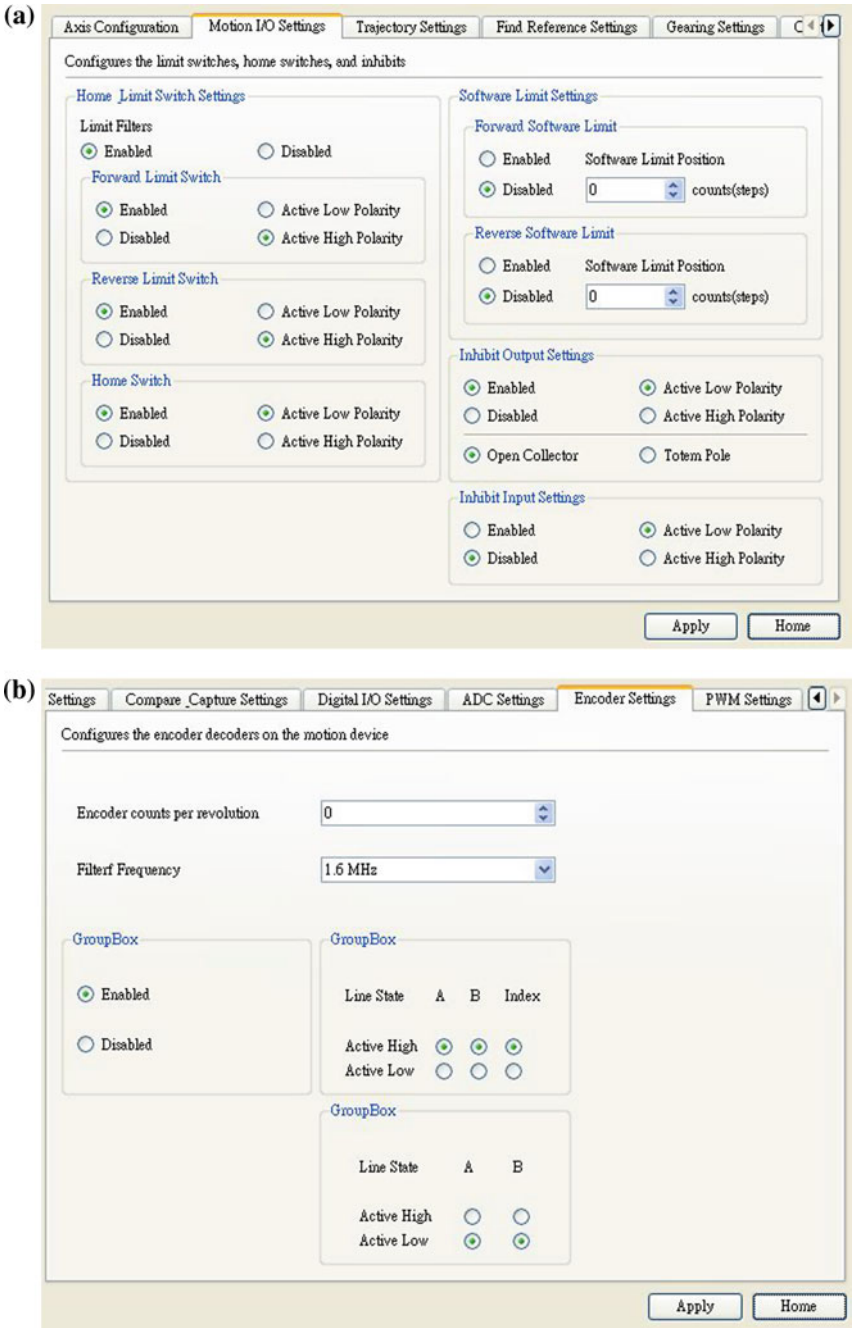

Fig. 91.7 **a** AOI parameters setting for batch page, **b** AOI parameters setting for batch page

The defect history table as shown in Fig. 91.6 is the most important part for AOI system because the production engineer needs to know the trend of defects in details. If the trend of defect is getting worsened, the production engineer can quickly consult with other experts to find a suitable solution.

The following parameters as shown in Fig. 91.7a, b should be set first when the production engineer starts the AOI system.

- Axis configuration
- Motion I/O settings
- Trajectory settings
- Find reference settings
- Gearing settings
- Digital I/O settings
- ADC settings
- Encoder settings
- PWM settings.

91.6 Conclusion

Smart phone and tablet are popular today therefore we have various ways to use the Cloud MMI system. The advantages of the Cloud MMI are that convenient for engineers to manage many machines in the factory through multi-functional monitors directly interconnection to many machines simultaneously. The production control engineers can monitor MMI anytime anywhere by personal consumer devices, such as smart phone and tablet. Therefore, the engineers can work efficiently and have lower loading.

There have many challenges for us to complete the Cloud MMI system. For example, we need to deliver comment from user to machine by internet and the safety is a big problem that we should check the safety if someone attacks our system from internet.

Acknowledgments This work is supported by Ministry of Economy Affairs for the Local Scientific Specialist Project under contract 101-EC-17-A-04-S1-220.

References

1. Nano Markets. (2008). The future of ITO: Transparent conductor and ITO replacement markets.
2. Bai, Y. W., Lin, H. E., & Jau, W. C. (2008). *Design and implementation of an integrated man-machine interface by touch panel for an embedded electronic measurement system* (pp. 14–16). Istanbul, Turkey: IEEE VECIMS.
3. de Chaves, S. A., Uriarte, R. B., & Westphall, C. B. (2011). Toward an architecture for monitoring private clouds. IEEE Communications Magazine, *49*, 130–137.

4. Kim, J. S., Lee, S. K., Ahn, H. Y., Seo, D. J., Park, S. Y., & Choi, C. L. (2013). Feasibility of employing a smartphone as the payload in a photogrammetric UAV system. *ISPRS Journal of Photogrammetry and Remote Sensing, 79*, 1–18.
5. Mednieks, Z., Dornin, L., Meike, G. B., & Nakamura, M. (2011). Programming Android. Cambridge: O'Reilly Media, e-Book ISBN: 978-1-4493-8970-3.

Chapter 92
Design and Implementation of EtherCAT Slave Based on ARM Cortex-M0

Yu-Wei Huang and Chih-Hung Wu

Abstract In this paper, EtherCAT slave module design and implementation based on Cortex-M0 is carried out. This paper designs a slave module with EtherCAT slave controller (ESC) and Cortex-M0 microcontroller. The slave module has eight 16-bits input ports and eight 16-bits output ports. The experimental results show that performance of the slave module can meet the real-time requirements in industrial automation. Combining with other modules, it could satisfy the varieties of control functions needed. It is easy to be made and operated.

Keywords EtherCAT slave · Cortex-M0 · Microcontroller

92.1 Introduction

With the requirement of industrial automation, Ethernet technology applied to industrial control systems become an important area for its cost and fast speed communication. The industrial fieldbus requires quick response time less than 1 ms. In order to meet the requirements, varieties of solutions based on Ethernet are proposed [1–4]. Real time Ethernet is based on conventional Ethernet technology. It could meet the requirements of fast speed communication in industrial control.

Fast development of Ethernet technology let more and more deployment and application of real-time Ethernet technology used in industry, and EtherCAT

Y.-W. Huang
Graduate Institute of Vehicle Engineering, National Changhua University of Education, Changhua 50007, Taiwan, Republic of China

C.-H. Wu (✉)
Department of Game and Product Design, Chienkuo Technology University, Changhua 50094, Taiwan, Republic of China
e-mail: zhwu@cc.ctu.edu.tw

J. Juang et al. (eds.), *Proceedings of the 2nd International Conference on Intelligent Technologies and Engineering Systems (ICITES2013)*, Lecture Notes in Electrical Engineering 293,
DOI: 10.1007/978-3-319-04573-3_92,

(Ethernet for Control Automation Technology) having less cycle time and high bandwidth is better to be considered applying. EtherCAT is a high-performance industrial network system based on the Ethernet system, so it is suitable used on machine control and automation in industry and can reduce development time.

In this paper, a solution of EtherCAT slave controller based on Cortex-M0 has been proposed. The slave module combines EtherCAT slave controller (ESC), microcontroller and input/output ports. The EtherCAT Controller Slave chip is Beckhoff ET1100. The microcontroller is NUC140VE3AN with ARM Cortex-M0. It has eight 16-bits input ports and eight 16-bits output ports. The experimental results show that performance of the slave module can meet the real-time requirements in industrial control fields.

92.2 EtherCAT Technology

Each EtherCAT slave node can transmit Ethernet frames in a short cycle time. The physical layer of EtherCAT uses the standard Ethernet technology, so the conventional Ethernet cables, connectors and tools are available. Because EtherCAT master adopts a standard network controller, it is very cost-effective without special hardware required.

EtherCAT uses standard IEEE 802.3 Ethernet frames and it has a reserved EtherType of 0x88A4. The EtherCAT Slave Controller processes the frame in hardware. An EtherCAT frame is subdivided into the EtherCAT header followed by one or more EtherCAT datagrams as shown in Fig. 92.1 [5]. The EtherCAT frame has at least one EtherCAT datagram. If the minimum Ethernet frame size requirement is not fulfilled, padding bytes have to be added. Otherwise the length of EtherCAT frame is equal to the sum of all EtherCAT datagrams plus EtherCAT frame header.

Figure 92.2 shows the structure of an EtherCAT frame. EtherCAT frame consists of header and at least one EtherCAT datagram. The Length of the EtherCAT datagrams is specified with 11 bits. The protocol type has 4 bits. Only EtherCAT command (Type = 0x1) is currently processed by ESCs.

Figure 92.3 shows the structure of an EtherCAT datagram. Each datagram has header, data and working counter. The working counter counts the number of devices that were successfully addressed by this EtherCAT datagram.

Instead of store and forward, EtherCAT passes the Ethernet frame through each salve node on the fly shown in Fig. 92.4. When frame passing through each node, the data is read and written in units of several nanoseconds to each corresponding area. The Ethernet frame is transmitted from the EtherCAT master throughout all slave nodes, and then sent back to the EtherCAT master by the last slave node. With this mechanism, EtherCAT achieves real time requirement of high-speed data transmission.

EtherCAT slave controllers utilize a device called a Fieldbus Memory Management Unit (FMMU) that can read, write and forward EtherCAT Ethernet

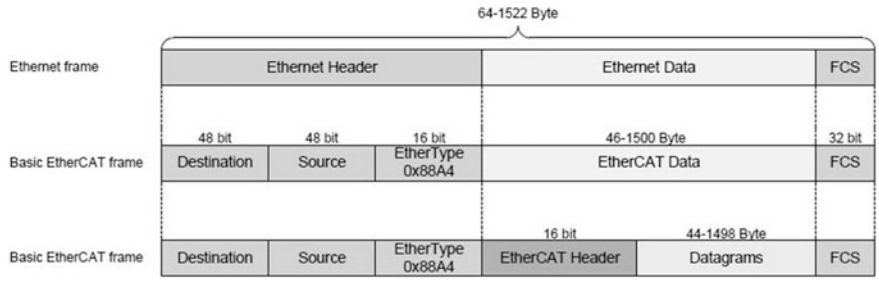

Fig. 92.1 Ethernet Frame with EtherCAT Data Format

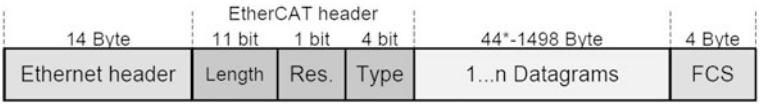

Fig. 92.2 The structure of EtherCAT Frame

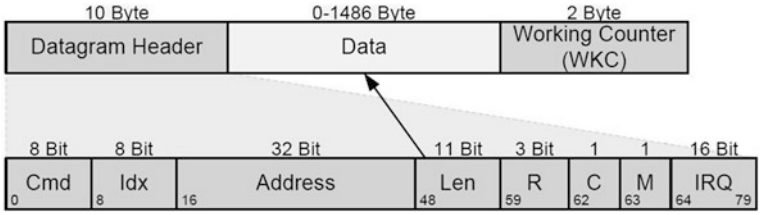

Fig. 92.3 The structure of an EtherCAT datagram

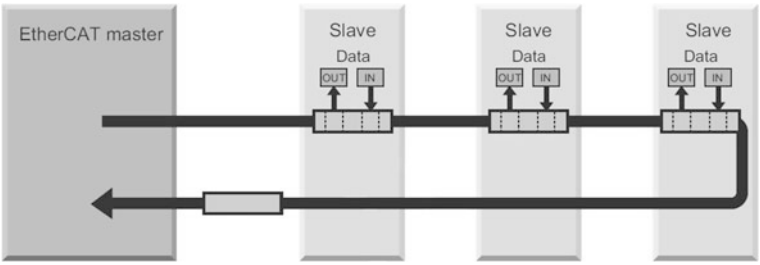

Fig. 92.4 EtherCAT frame pass through network

packets on-the-fly. FMMU convert logical addresses into physical addresses by the means of internal address mapping. Thus, FMMUs allow using logical addressing for data segments that span several slave devices: one datagram addresses data within several arbitrarily distributed ESCs. Each FMMU channel maps one

continuous logical address space to one continuous physical address space of the slave.

The registers in each slave that can be mapped by the FMMUs are known as Process Data Objects (PDOs). EtherCAT exchanges PDO data bi-directionally between the master and multiple slaves. In this paper, the first EtherCAT slave configured FMMU to map logical address 0x01000000 to physical register 0x1100 for output ports. Then, FMMU of second EtherCAT maps logical address 0x01000010 to physical register 0x1180 and so on.

92.3 Design of EtherCAT Slave

The slave module combines EtherCAT Piggyback controller boards FB1111-014X, NuTiny-SDK-NUC140 development board, input/output ports and other circuits.

The EtherCAT Piggyback controller boards FB1111-014X combine an ET1100 EtherCAT Slave Controller, two EtherCAT ports and a PDI-Connector on a printed circuit board. The ET1100 takes care of the EtherCAT communication as an interface between the EtherCAT nodes. The ET1100 is used as a part of a microcontroller design with 2 EtherCAT communication ports. The Process Data Interface (PDI) is used to communicate with external hardware.

NuTiny-SDK-NUC140 is the specific development board for NuMicro NUC140 series [6]. Users can use NuTiny-SDK-NUC140 to develop and verify the application program easily. NuTiny-SDK-NUC140 includes two portions. NuTiny-EVBNUC140 is the evaluation board and Nu-Link-Me is its Debug Adaptor. Thus, users do not need other additional ICE or debug equipment. NuTiny-EVB-NUC140 uses the NUC140VE3AN microcontroller to design, develop and verify applications for a real time system.

The asynchronous microcontroller NUC140 interface uses demultiplexed address and data busses to reduce pins. The width of bidirectional data bus is 16 bits. The NUC140 equips an external bus interface (EBI) for external device used. The EBI supports device whose address bus and data bus are multiplexed. For the external device with separated address and data bus, the connection to device needs additional logic to latch the address. The address latch enable (ALE) signal can differentiate the address and data cycle. The signals of connection between NUC140 and FB1111 are shown in Fig. 92.5.

The input/output connection panel has eight 16-bits input port and eight 16-bits output ports. The NUC140 microcontroller gets Ethercat output from registers of ESC and transfer to corresponding output ports. Then, NUC140 microcontroller gets data from input ports and transfers data to register of ESC respectively. A 4-to-16 line demultiplexer accepts four binary line inputs and provides 16 mutually exclusive active LOW outputs. The demultiplexer sets only one of the 8 inputs and 8 outputs as active (Fig. 92.6).

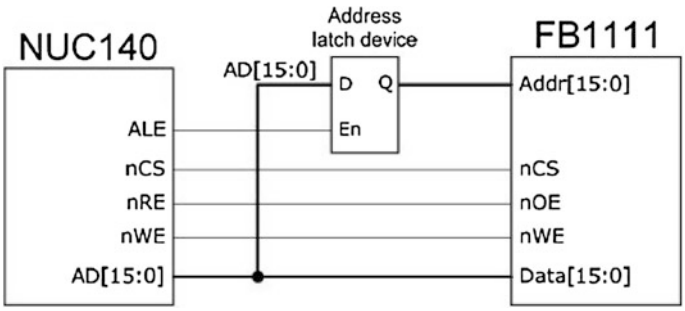

Fig. 92.5 The connection of EtherCAT slave module

Fig. 92.6 The appearance of EtherCAT slave module

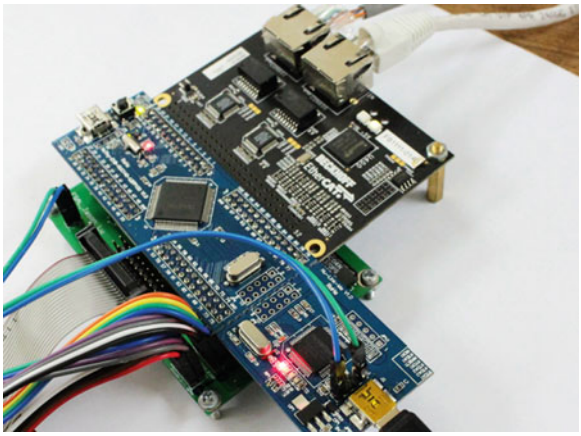

92.4 Experiment and Result

The test system contains a master and three slave nodes. The master includes a PC, standard Ethernet interfaces and TwinCAT software. The master connects EtherCAT slave module with unshielded twisted pair. The connection of the devices is shown in Fig. 92.4.

The I/O information of each EtherCAT slave is read from and entered in the TwinCAT System Manager. The TwinCAT software scan slave devices, the screen of inputs and outputs appeared as shown in Fig. 92.7. The operation state of EtherCAT slave BOX 1 is in OP. There are no communication problems in EtherCAT slave hardware circuit. Next, began the debugging of ESM(EtherCAT State machine) configuration file and the driver programs.

The slave program consists of three parts: microcontroller initialization function, ESC initialization function and main loop function as shown in Fig. 92.8. The microcontroller initialization function includes pin function, PLL and CPU clock,

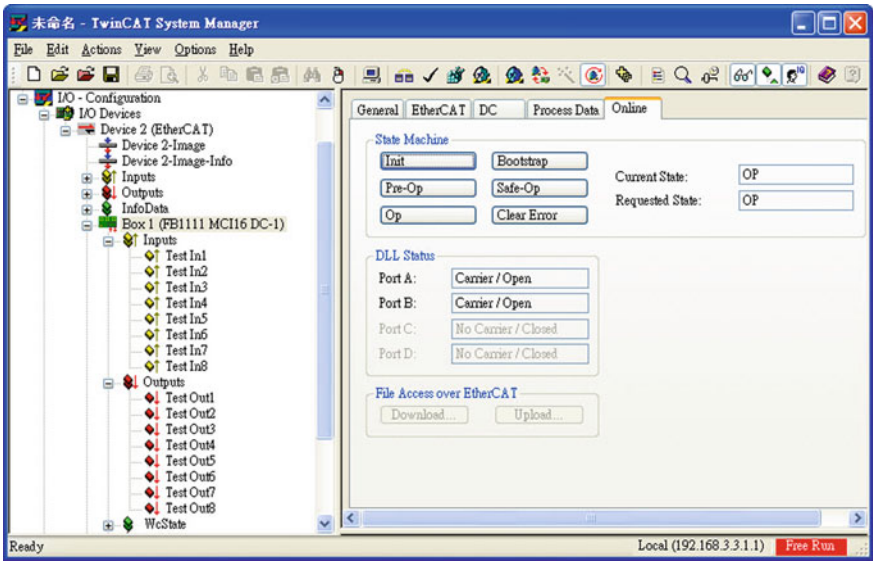

Fig. 92.7 TwinCAT System Manager

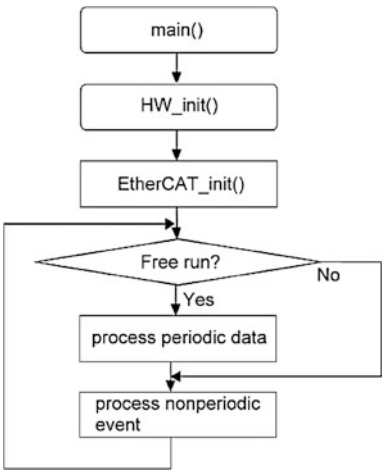

Fig. 92.8 The flow chart of EtherCAT slave program

timer, EBI settings, etc. The ESC initialization function initializes EtherCAT slave interfaces.

The main loop function consists of periodic process data and non-periodic events. The ESM is responsible for the coordination of master and slave applications at start up and during operation. State changes are typically initiated by requests of the master. Master is acknowledged by the slave non-periodic event

application after the associated operations have been executed. I/O data processing of EtherCAT are completed by the periodic process data function. In Operation state (OP), master transfer EtherCAT frames through all slave nodes. The frames are processed by the ESC on the fly. Data is read and written as the bits when passing the ESC.

92.5 Conclusions and Suggestions

This paper presents a slave module that based on EherCAT technology and Cortex-M0 microcontroller. The EherCAT frame passed through each slave node in units of several nanoseconds, so the slave module can meet the real-time requirements in industrial automation. With the excellent performance of the real-time EtherCAT technology, it would be accepted by more and more developers in industry control fields. For the future study, how to port the EherCAT master to various embedded platforms connected with the proposed EtherCAT slave is a challenge.

Acknowledgments This study was funded by grants from Foxnum Technology Co., Ltd. (project no. 302205501), so that the study can be completed smoothly.

References

1. Zhu, Z. H., & Wang, Y. E. (2010). The real-time technology research of industrial Ethernet in control field. In: *2010 International Conference on Mechanic Automation and Control Engineering (MACE)* (pp. 5274–5277). Wuhan, China.
2. Orfanus, D., Indergaard, R., Prytz, G., & Wien, T. (2013). EtherCAT-based platform for distributed control in high-performance industrial applications, in *2013 IEEE 18th Conference on Emerging Technologies and Factory Automation (ETFA)* (pp. 1–8). Cagliari, Italy.
3. Yiming, A., & Eisaka, T.: Development of an Ethernet protocol for industrial real-time communications, in *2004 IEEE International Symposium on Communications and Information Technology* (Vol. 2, pp. 1122–1125). Japan.
4. Decotignie, J. D.: Ethernet-based real-time and industrial communications. Proceedings of the IEEE, *93*(6), 1102–1117 (2005).
5. Hardware Datasheet ET1100. (2010). EtherCAT Slave Controller, BECKHOFF, Germany.
6. NuMicro NUC100 Series NUC130NUC140 Technical Reference Manual. (2011). NuMicro, Taipei.

Chapter 93
Decentralized Adaptive Control of Euler–Lagrange Mechanical System

Cheng-Fa Cheng and Tse-Han Chen

Abstract The problem of decentralized control Euler–Lagrange like mechanical systems with high-order interconnections is investigated in this paper. A new decentralized adaptation scheme is proposed to estimate the unknown structure bounds. Then, a decentralized adaptive controller is constructed to guarantee the uniformly ultimate boundedness of the system and the exponential convergence of the tracking error. Finally, a numerical example is given to demonstrate the validity of the results.

Keywords: Euler–Lagrange equations · Decentralized control · Adaptive · Uniformly ultimate

93.1 Introduction

With the rapid development of modern technology, the demands of planning, design and implementation of complex are generated. Due to the increasing fields of integration, such systems typically have complex structures and are usually higher interconnected dimensions. Thus when an interconnected system is concerned, the centralized pattern often fails to hold due to either lack of the overall information or lack of the centralized computing capability. Many approaches have been used by researchers to the stability and stabilization of interconnected systems [1–3].

When the knowledge of the system model is limited, adaptive control techniques should be applied to high-performance control system design. During the last two decades, different adaptive control techniques have been investigated

C.-F. Cheng (✉) · T.-H. Chen
Department of Communications, Navigation and Control Engineering, National Taiwan Ocean University, Keelung 20224, Taiwan, Republic of China
e-mail: cfcheng@ntou.edu.tw

J. Juang et al. (eds.), *Proceedings of the 2nd International Conference on Intelligent Technologies and Engineering Systems (ICITES2013)*, Lecture Notes in Electrical Engineering 293,
DOI: 10.1007/978-3-319-04573-3_93,

intensively from different perspectives by many researchers ([4, 5] and the references therein). However, these developed techniques must solve the special problems like constrained information structure, high-time consuming computation, and large storage requirement for large scale systems. Thus how to design decentralized adaptive controllers for large-scale nonlinear systems like power systems and robot manipulators such that the performance targets can be achieved is an important topic [6–8]. In this paper, the problem of decentralized control Euler–Lagrange like mechanical systems with high-order interconnections is explored. Based on the system structure, a new decentralized adaptation scheme is proposed to estimate the unknown structure bounds.

93.2 Systems Description and Problem Formulation

Consider the mechanical system described by Euler–Lagrange equations [9]

$$M_i(q_i)\ddot{q}_i(t) + C_i(q_i, \dot{q}_i)\dot{q}_i(t) + g_i(q_i) = \tau_i(t) \tag{93.1}$$

where $q_i(t) \in R^{n_i}$ are the generalized coordinates of the subsystem i, for $i = 1, 2, \ldots, N$, $M_i(q_i)$ denotes the $n_i \times n_i$, inertial matrix, $C_i(q_i, \dot{q}_i)\dot{q}_i(t)$ are Coriolois and centrifugal terms, $g_i(q_i)$ the potential energy term, and $\tau_i(t)$ the generalized forces applied to the subsystem. Furthermore, assume

$$\tau_i(t) = u_i(t) - Z_i(q, \dot{q}) - D_i(q_i, \dot{q}_i) \tag{93.2}$$

where $u_i(t)$ is the n_i-dimensional vector of control inputs, $Z_i(q, \dot{q})$ is the interconnections, $q^T(t) = \begin{bmatrix} q_1^T & q_2^T & \cdots & q_N^T \end{bmatrix} \in R^n$, $n = \sum_{i=1}^{N} n_i$, and $D_i(q_i, \dot{q}_i)$ is the disturbances. The disturbances $D_i(q_i, \dot{q}_i)$ depend only on the local states and the interconnections $Z_i(q, \dot{q})$ may depend on the states of all subsystems. The dynamical equations of the mechanical systems are now given by

$$M_i(q_i)\ddot{q}_i(t) + C_i(q_i, \dot{q}_i)\dot{q}_i(t) + g_i(q_i) + Z_i(q, \dot{q}) + D_i(q_i, \dot{q}_i) = u_i(t) \tag{93.3}$$

for $i = 1, 2, \ldots, N$. We make the following assumptions throughout this work.

Assumption 1. $\underline{m}_i I \le M_i(q_i) = M_i^T(q_i) \le \bar{m}_i I,\ q_i \in R^{n_i}$ with $0 < \underline{m}_i \le \bar{m}_i$.

Assumption 2. $\varsigma_i^T[\dot{M}_i(q_i) - 2C_i(q_i, \dot{q}_i)]\varsigma_i = 0,\ \forall \varsigma_i \in R^{n_i}$.

Assumption 3. Local dynamics of each subsystem are parameterized linearly

$$M_i(q_i)\ddot{q}_i(t) + C_i(q_i, \dot{q}_i)\dot{q}_i(t) + g_i(q_i) = Y_i(q_i, \dot{q}_i, \ddot{q}_i)\theta_i(t) \tag{93.4}$$

Assumption 4. $\|Z_i(q, \dot{q})\| \le \sum_{j=1}^{N} c_{ij} Q_j(t)$ with $c_{ij} \ge 0,\ p \ge 1$, and

$$Q_j(t) = 1 + \left\|q_j(t)\right\| + \left\|\dot{q}_j(t)\right\| + \cdots + \left\|\dot{q}_j(t)\right\|^p + \left\|q_j(t)\right\|^p$$

Assumption 5. $\|D_i(q_i, \dot{q}_i)\| \le d_i Q_i(t)$ with $d_i \ge 0$.

Let $q_i^d(t) \in R^{n_i}$ be a given smooth desired trajectory and define the tracking error as $\tilde{q}_i(t) := q_i(t) - q_i^d(t)$, $\dot{q}_i^r := q_i^d(t) - \Lambda_i \tilde{q}_i(t)$ be the reference velocity, and $s_i(t) := \dot{\tilde{q}}_i(t) + \Lambda_i \tilde{q}_i = \dot{q}_i(t) - \dot{q}_i^r(t)$ be the sliding variable with positive definite matrix $\Lambda_i \in R^{n_i \times n_i}$. The proposed decentralized adaptive control is

$$u_i(t) = Y_i(q_i, \dot{q}_i^r, \ddot{q}_i^r)\theta_i^o - K_i s_i(t) + w_i(t) \tag{93.5}$$

where K_i is a positive definite matrix and $w_i(t) \in R^{n_i}$ is designed to compensate for the parameter uncertainty, disturbances and interconnections. Thus the closed-loop system in terms of $s_i(t)$ will be

$$M_i(q_i)\dot{s}_i(t) + C_i(q_i, \dot{q}_i)s_i(t) + K_i s_i(t) = Y_i(q_i, \dot{q}_i, \dot{q}_i^r, \ddot{q}_i^r)\tilde{\theta}_i(t) - Z_i(q, \dot{q}) - D_i(q_i, \dot{q}_i) + w_i(t) \tag{93.6}$$

where $\tilde{\theta}_i(t) := \theta_i^o - \theta_i(t)$ denotes the parameter uncertainty and $(\cdot)_i^o$ is the nominal value of $(\cdot)_i$. According to Lemma 1 of [9], for sufficiently large $\lambda_m(\Lambda_i)$, we have $\left\|Y_i(q_i, \dot{q}_i, \dot{q}_i^r, \ddot{q}_i^r)\tilde{\theta}_i(t) - Z_i(q, \dot{q}) - D_i(q_i, \dot{q}_i)\right\| \le \sum_{j=1}^{N} \delta_{ij} S_j$, where $\delta_{ij} \ge 0$ and $S_i = 1 + \|s_i(t)\| + \cdots + \|s_i(t)\|^p$. In the following, an algorithm should be developed to estimate the parameter δ_{ij} since it is unknown in general. Before proceeding, some notations should be introduced: $\varepsilon_{ij} := \delta_{ij}^2$ for $i, j = 1, 2, \ldots, N$, $\varepsilon_i = \begin{bmatrix} \varepsilon_{i1} & \varepsilon_{i2} & \cdots & \varepsilon_{iN} \end{bmatrix}^T$. $s^T(t) = \begin{bmatrix} s_1^T(t) & s_2^T(t) & \cdots & s_N^T(t) \end{bmatrix}$, and $\phi = \begin{bmatrix} 1 & 1 & \cdots & 1 \end{bmatrix}^T$. Furthermore, let $\hat{\varepsilon}_i(t)$ be the estimates of the unknown bound ε_i and $\tilde{\varepsilon}_i(t) = \hat{\varepsilon}_i(t) - \varepsilon_i$, for $i = 1, 2, \cdots, N$.

93.3 Synthesis of Decentralized Adaptive Controller

Theorem 1. Consider the decentralized adaptive control (93.5) with the compensation

$$w_i(t) = -\frac{s_i(t)(\varphi^T \hat{\varepsilon}_i(t))^2}{\|s_i(t)\|\varphi^T \hat{\varepsilon}_i(t) + \beta_i e^{-\mu_i t}} - \frac{N s_i(t) S_i^4}{\|s_i(t)\| S_i^2 + \alpha_i^{-\bar{\mu}_i t}} \tag{93.7}$$

and the adaptive law

$$\dot{\hat{\varepsilon}}_i(t) = \Gamma_i \phi \|s_i(t)\| \tag{93.8}$$

where Γ_i is any positive definite matrices, and α_i, β_i, μ_i and $\bar{\mu}_i$ are all positive scalars. The resultant closed-loop system (93.6) is globally stable in the sense that the tracking error $\tilde{q}(t)$ converges asymptotically.

Proof: Consider the positive definite Lyapunov function candidate $V(t) = \sum_{i=1}^{N} V_i(t) = \sum_{i=1}^{N} \frac{1}{2}\{s_i^T(t)M_i s_i(t) + \tilde{\varepsilon}_i^T(t)\Gamma_i^{-1}\tilde{\varepsilon}_i(t)\}$. Taking the derivative of $V(t)$ along (93.6) and using Assumption 2 yield

$$\dot{V}(t) = -\sum_{i=1}^{N} s_i^T(t)K_i s_i(t) + \sum_{i=1}^{N} s_i^T(t)[Y_i\tilde{\theta}_i(t) - Z_i - D_i + w_i(t)] + \tilde{\varepsilon}_i^T(t)\Gamma_i^{-1}\dot{\tilde{\varepsilon}}(t) \tag{93.9}$$

Using the Chebyshev inequality and (93.8), we get

$$\sum_{i=1}^{N} s_i^T(t)[Y_i\tilde{\theta}_i(t) - Z_i - D_i + w_i(t)] \le \sum_{i=1}^{N}\{N\alpha_i e^{-\bar{\mu}_i t} + \beta_i e^{-\mu_i t}\} - \sum_{i=1}^{N}\|s_i\|\varphi^T\tilde{\varepsilon}_i \tag{93.10}$$

It follows from (93.5) and (93.10) that (93.9) can be rewritten as

$$\dot{V}(t) \le -\upsilon_1 \sum_{i=1}^{N} s_i^T(t)M_i s_i(t) + \sum_{i=1}^{N}(N\alpha_i + \beta_i)e^{-\upsilon_2 t} \tag{93.11}$$

where $\upsilon_1 = \min_{i=1,\cdots,N}\{\lambda_m(K_i)/\bar{m}_i\}$ and $\upsilon_2 = \min_{i=1,\cdots,N}\{\mu_i, \bar{\mu}_i\}$. It can be easily seen that $\lim_{t\to\infty}\sum_{i=1}^{N} s_i^T(t)K_i s_i(t) = 0$, i.e., $\lim_{t\to\infty} s_i(t) = 0$. Since $\dot{\tilde{q}}_i(t) = -\Lambda_i\tilde{q}_i(t) + s_i(t)$, $\tilde{q}_i(t)$ has the same property with $s_i(t)$, i.e., $\lim_{t\to\infty}\tilde{q}(t) = 0$. The proof is completed.

Furthermore, when the additive noise is present, the system parameter in (93.5) may diverge [10]. To avoid the parameter divergence, the parameter adaptation law can be modified as (93.7) with σ-modification term

$$\dot{\hat{\varepsilon}}_i(t) = -\Gamma_i\Sigma_i\hat{\varepsilon}_i(t) + \Gamma_i\phi\|s_i(t)\| \tag{93.12}$$

where Σ_i and Γ_i are any positive definite matrices.

Theorem 2. Consider the decentralized adaptive control (93.5) with (93.12) and the compensation signal

$$w_i(t) = -\frac{s_i(t)(\phi^T\hat{\varepsilon}_i(t))^2}{\|s_i(t)\|\phi^T\hat{\varepsilon}_i(t) + \beta_i} - \frac{Ns_i(t)S_i^4}{\|s_i(t)\|S_i^2 + \alpha_i} \tag{93.13}$$

with positive scalars α_i and β_i. The resultant closed-loop system (93.5) is globally stable in the sense that the tracking error $\tilde{q}(t)$ converges exponentially toward the final attractor $B(0, r)$, where r is a finite number determined by Γ_i, Σ_i, α_i, β_i and the actual bound of the parameter ε_i.

Proof: Similar to the proof of Theorem 1, we have

$$\sum_{i=1}^{N} s_i^T(t)[Y_i\tilde{\theta}_i(t) - Z_i - D_i + w_i(t)] \le \sum_{i=1}^{N}\{N\alpha_i + \beta_i\} - \sum_{i=1}^{N}\|s_i\|\phi^T\tilde{\varepsilon}_i \quad (93.14)$$

and $\tilde{\varepsilon}_i^T(t)\Gamma_i^{-1}\dot{\tilde{\varepsilon}}(t) \le -\kappa_i\lambda_m(\Sigma_i)\|\tilde{\varepsilon}_i(t)\|^2 + \frac{\lambda_M(\Sigma_i)}{2(1-\kappa_i)\lambda_m(\Sigma_i)}\|\varepsilon_i\|^2 + \|s_i(t)\|\phi^T\varepsilon_i$, where $0<\kappa_i<1$. It follows that $\dot{V}(t) \le -\bar{\upsilon}_1\|\aleph\|^2 + \bar{\upsilon}_2$, where $\aleph^T(t) = \begin{bmatrix} s^T(t) & \tilde{\varepsilon}^T(t)\end{bmatrix}$, $0<\bar{\upsilon}_1 = \min\limits_{i=1,\cdots,N}\{\lambda_m(K_i), \kappa_i\lambda_m(\Sigma_i)\}$, $\bar{\upsilon}_2 = \sum\limits_{i=1}^{N}\{N\alpha_i + \beta_i + \frac{\lambda_M(\Sigma_i)}{2(1-\kappa_i)\lambda_m(\Sigma_i)}\|\varepsilon_i\|^2 + \|s_i(t)\|\varphi^T\varepsilon_i\}$, and $\tilde{\varepsilon}^T(t) = \begin{bmatrix}\tilde{\varepsilon}_1^T(t) & \tilde{\varepsilon}_2^T(t) & \cdots & \tilde{\varepsilon}_N^T(t)\end{bmatrix}$. Furthermore, the inequality $\upsilon_3\|\aleph(t)\|^2 \le V(t) \le \upsilon_4\|\aleph(t)\|^2$ always holds with $0<\upsilon_3 = \min\limits_{i=1,\cdots,N}\{\underline{m}_i/2, \lambda_m(\Gamma_i^{-1})/2\}$ and $0<\upsilon_4 = \max\limits_{i=1,\cdots,N}\{\bar{m}_i/2, \lambda_M(\Gamma_i^{-1})/2\}$. It follows from [11] that for all finial attractor ball $\tilde{B}(0,r) := \{\aleph(t) \in R^n : \|\aleph(t)\| \le r\}$ with $r > r^* := \sqrt{\bar{\upsilon}_2/(\bar{\upsilon}_1\upsilon_3)}$ and any initial condition $\aleph_0$, there exists a finite constant $T[\aleph_0, \tilde{B}(0,r)] := 2/\bar{\upsilon}_1 \ln\{1/(r-r^*)\sqrt{\upsilon_4/\upsilon_3\|\aleph_0\|^2 - \bar{\upsilon}_2/(\bar{\upsilon}_1\upsilon_3)}\}$ for all $\aleph_0 \in R^n\backslash\tilde{B}(0,r)$ and $T[\aleph_0, \tilde{B}(0,r)] = 0$ for $\aleph_0 \in \tilde{B}(0,r)$, such that $\aleph(t) \in \tilde{B}(0,r)$, $\forall t \ge t_0 + T[\aleph_0, \tilde{B}(0,r)]$. Also $d[\aleph(t), \tilde{B}(0,r)] := \min\{\|\aleph(t) - \aleph^*\| : \aleph^* \in \tilde{B}(0,r)\} \le \sqrt{\upsilon_4/\upsilon_3\|\aleph_0\|^2 - \bar{\upsilon}_2/(\bar{\upsilon}_1\upsilon_3)}e^{-\bar{\upsilon}_1/2(t-t_0)}$ for all $\aleph_0 \in R^n\backslash\tilde{B}(0,r)$. This implies that $\begin{bmatrix} s^T(t) & \tilde{\varepsilon}^T(t)\end{bmatrix}$ converges exponentially with the degree $\bar{\upsilon}_1/2$ toward the finial attractor $\tilde{B}(0,r)$. It follows that $\tilde{q}_i(t)$ has the same property with $s_i(t)$ and thus $\tilde{q}^T(t) = \begin{bmatrix}\tilde{q}_1^T(t) & \tilde{q}_2^T(t) & \cdots & \tilde{q}_N^T(t)\end{bmatrix}$ is ultimately bounded toward the final attractor $B(0,r) := \{\tilde{q}(t) \in R^n : \|\tilde{q}(t)\| \le r\}$. The proof is completed.

93.4 Illustrative Example

Consider the coupled inverted pendulums which are subject to two distinct controls

$$m_i l_i^2\ddot{\theta}_i - m_i g l_i \sin\theta_i = u_i - b_i\dot{\theta}_i + Fa_i\cos(\theta_i - \varphi) \quad (93.15)$$

for $i = 1, 2$,where $a_i \in [0, l_i]$ is the position of the spring, b_i is the damping coefficient, $l_k = [(l + a_2\sin\theta_2 - a_1\sin\theta_1)^2 + (a_1\cos\theta_1 - a_2\cos\theta_2)^2]^{1/2}$, $m_i(t)$ is the payload with $m_i(t) = \bar{m}_i + \Delta m_i(t)$, $F = k[1 + A^2(l_k - l)^2](l_k - l)$, with $|A(l_k - l)|<1$, and $\varphi = \tan^{-1}[\frac{a_1\cos\theta_1 - a_2\cos\theta_2}{l - a_1\sin\theta_1 + a_2\sin\theta_2}]$. It can be shown that the disturbances D_i and interconnections Z_i satisfy Assumptions 4 and 5 with $p = 3$.

For demonstration purpose, taking $g = 9.8\,(\mathrm{m/s^2})$, $l = 1(\mathrm{m})$, $l_1 = 0.5(\mathrm{m})$, $l_2 = 0.4(\mathrm{m})$, $b_1 = b_2 = 0.008(\mathrm{Newton\cdot m\cdot s/rad})$, $k = 1(\mathrm{Newton\cdot m^{-1}})$, $A = 0.2$, $\bar{m}_1 = 1(\mathrm{kg})$, $\bar{m}_2 = 0.5(kg)$, $|\Delta m_1(t)| \le 0.1(\mathrm{kg})$, $|\Delta m_2(t)| \le 0.05(\mathrm{kg})$, $K_1 = 40$,

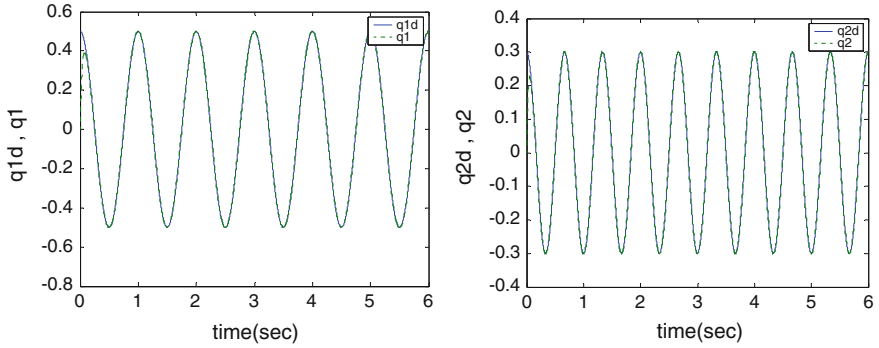

Fig. 93.1 The desired trajectories and the actual pendulum positions of (*left*) subsystem 1; (*right*) subsystem 2

$K_2 = 50$, $\Gamma_1 = \Gamma_2 = I$, $\Sigma_1 = \Sigma_2 = diag\{1, 2\}$, $\Lambda_1 = 30$, $\Lambda_2 = 40$, and $\alpha_1 = \alpha_2 = \beta_1 = \beta_2 = 0.01$, the local stabilizing control law are

$$u_1(t) = 0.25\ddot{q}_1^d(t) - 7.5(\dot{q}_1(t) - \dot{q}_1^d(t)) - 4.9\sin(q_1(t)) - 40s_1(t) + w_1(t) \tag{93.16a}$$

$$u_2(t) = 0.08\ddot{q}_2^d(t) - 3.2(\dot{q}_2(t) - \dot{q}_2^d(t)) - 1.96\sin(q_2(t)) - 50s_2(t) + w_2(t) \tag{93.16b}$$

with
$w_i(t) = -s_i(t)(\phi^T\hat{\varepsilon}_i(t))^2/(\|s_i(t)\|\phi^T\hat{\varepsilon}_i(t) + 0.01) - 2s_i(t)S_i^4(t)/(\|s_i(t)\|S_i^2(t) + 0.01)$,
$\dot{\hat{\varepsilon}}_i(t) = -5\hat{\varepsilon}_i(t) + \phi\|s_i(t)\|$, $S_i(t) = 1 + \|s_i(t)\| + \|s_i(t)\|^2 + \|s_i(t)\|^3$, $s_1(t) = \dot{q}_1(t) - \dot{q}_1^d(t) - 30(q_1(t) - q_1^d(t))$, and $s_2(t) = \dot{q}_2(t) - \dot{q}_2^d(t) - 40(q_2(t) - q_2^d(t))$.

Now with the initial conditions $q_i(0) = 0$, $\dot{q}_i(0) = 0.5$, $\hat{\varepsilon}_i(0) = [0 \quad 0]^T$, $i = 1, 2$, the uncertainties $\Delta m_1(t) = 0.1\sin t$, $\Delta m_2(t) = 0.05\sin 2t$, the desired trajectories $q_1^d(t) = 0.5\cos(2\pi t)$, $q_2^d(t) = 0.3\cos(3\pi t)$ and the positions of the springs $a_1(t) = \begin{cases} 0.2(\text{m});\ 0 \le t < 1\ (\text{s}) \\ 0.4(\text{m});\ 1 \le t < 4\ (\text{s}) \\ 0.1(\text{m});\ 4 \le t \le 6\ (\text{s}) \end{cases}$ and $a_2(t) = \begin{cases} 0.3(\text{m});\ 0 \le t < 2\ (\text{s}) \\ 0.1(\text{m});\ 2 \le t < 5\ (\text{s}) \\ 0.25(\text{m});\ 5 \le t \le 6\ (\text{s}) \end{cases}$, the desired trajectories and the actual pendulum positions are shown in Fig. 93.1.

93.5 Conclusion

The problem of decentralized control Euler–Lagrange like mechanical systems with high-order interconnections has been explored. A new decentralized adaptation scheme is constructed and the unknown structure bounds are estimated such

that the decentralized adaptive controllers can be synthesized. Global stability for the closed-loop system is guaranteed. The globally ultimate boundedness for tracking errors and parameter estimation errors are achieved and converges toward the final attractor exponentially.

References

1. Ugrinovskii, V. A., & Pota, H. R. (2005). Decentralized control of power systems via robust control of uncertain markov jump parameter systems. *International Journal of Control, 78*, 662–677.
2. Li, L., Ugrinovskii, V. A., & Orsi, R. (2007). Decentralized robust control of uncertain markov jump parameter systems via output feedback. *Automatica, 43*, 1932–1944.
3. Baric, M., & Borrelli, F. (2012). Decentralized robust control invariance for a network of storage devices. *IEEE Transactions on Automatic Control, 57*, 1018–1024.
4. Ioannou, P. A., & Fidan, B. (2006). *Adaptive control tutorial*. Philadelphia, PA: SIAM Book Series on Advances in Design and Control.
5. Narendra, K. S., & Han, Z. (2011). The changing face of adaptive control: the use of multiple models. *Annual Reviews in Control, 35*, 1–12.
6. Yan, R., Dong, Z. Y., Saha, T., & Majumder, R. (2010). A power system nonlinear adaptive decentralized controller design. *Automatica., 46*, 330–336.
7. Tan, K. K., Huang, S., & Lee, T. H. (2009). Decentralized adaptive controller design of large-scale uncertain robotic systems. *Automatica., 45*, 161–166.
8. Yang, Z. J., Fukushima, Y., & Qin, P. (2012). Decentralized adaptive robust control of robot manipulators using disturbance observers. *IEEE Transactions on Control Systems Technology, 20*, 1357–1365.
9. Tang, Y., Tomizuka, M., Guerrero, G., & Montemayor, G. (2000). Decentralized robust control of mechanical systems. *IEEE Transactions on Automatic Control*, *45*, 771–776.
10. Ioannou, P. (1986). Decentralized adaptive control for interconnected systems. *IEEE Transactions on Automatic Control, 31*, 291–298.
11. Gong, Z., Wen, C., & Mital, D. P. (1996). Decentralized robust controller design for a class of interconnected uncertain systems with unknown bound of uncertainty. *IEEE Transactions on Automatic Control, 41*, 850–854.

Chapter 94
Robust Feedback Stabilizability of Periodic Networked Control Systems

Cheng-Fa Cheng and Xuan-Ru Lin

Abstract In this paper, the problem of reducing the packet rate of a periodic networked control system using the model-based approach will be investigated. Firstly, the robust stabilization of the uncertain model-based networked control systems (MB-NCS) with transmission attenuation and randomly update time intervals will be conferred. Furthermore, the architecture of the *T*-periodic MB-NCS will be introduced and then the stability analysis will be explored. Finally, a numerical example with simulation results will be illustrated to demonstrate the effectiveness and flexibility of the proposed method.

Keywords Networked control systems · *T*-periodic · Robust · Transmission attenuation · Packet rate

94.1 Introduction

The feature of the networked control systems is the use of control system components (sensors, controllers, actuators etc.) of networks to exchange the information (reference input, plant output, control input, etc.) [1]. These channels can be shared using other feedback control loops. Point-to-point cables are usually used to build these connection schemes for feedback control in the traditional systems. Advantages over point-to-point cables, serial communication networks not only own the high system testability and resource utilization but also meet the low weight, space, power, and wiring requirements [1, 2]. These advantages have made the sensors/actuators via a network connection to the controller architecture more popular in traffic control, satellite clusters, mobile robots, and many other

C.-F. Cheng (✉) · X.-R. Lin
Department of Communications, Navigation and Control Engineering, National Taiwan Ocean University, Keelung 20224, Taiwan, Republic of China
e-mail: cfcheng@ntou.edu.tw

J. Juang et al. (eds.), *Proceedings of the 2nd International Conference on Intelligent Technologies and Engineering Systems (ICITES2013)*, Lecture Notes in Electrical Engineering 293,
DOI: 10.1007/978-3-319-04573-3_94,

applications. Most recently, the research of modeling, analysis and control for networked control systems with limited communications capabilities has given rise to the high level of interest in the control and computer communities [1–7].

Periodic system research in the fields of applied mathematics and control already has a long history [8]. Interested in periodic systems mainly due to natural and man-made systems often have periodic properties. Periodic system, one of the simplest time-varying systems, can be used to analyze the oscillation of communications systems, planets and satellites in orbit, windmills and helicopter rotors, sampled data systems and AC power systems [9, 10]. Besides, the appearance of multirate sampled data systems and the study of behavior description of circulation physical dynamics make this type of system is taken seriously. Most theoretical concepts and many standard numerical methods of general systems have been extended to periodic systems.

In this paper, the problem of reducing the packet rate of a periodic NCS using a novel approach called MB-NCS will be investigated. At each transmission times, the T-periodic plant model is updated with the measured plant state, and this control architecture has as its main objective the reduction of the data packets transmitted over the network. In addition, the effect of the transmission attenuation for the MB-NCS will be included.

94.2 Systems Description and Problem Formulation

Consider the system dynamics given by [3]

$$\text{Plant} : \dot{x}(t) = A(t)x(t) + B(t)u(t) \tag{94.1a}$$

$$\text{Model} : \dot{\hat{x}}(t) = \hat{A}(t)\hat{x}(t) + \hat{B}(t)u(t) \tag{94.1b}$$

$$\text{Controller} : u(t) = K(t)\hat{x}(t) \tag{94.1c}$$

where $A(t) \in R^{n\times n}$ and $B(t) \in R^{n\times p}$ denote the nominal system matrix and input connection matrix of the plant, respectively; and $\hat{A}(t) \in R^{n\times n}$ and $\hat{B}(t) \in R^{n\times p}$ denote the nominal system matrix and input connection matrix of the model, respectively. The state error is defined as $e(t) = x(t) - \hat{x}(t)$, and represents the difference between the plant state and the model state. The modeling error matrices $\tilde{A}(t) = A(t) - \hat{A}(t)$ and $\tilde{B}(t) = B(t) - \hat{B}(t)$ represent the difference between the plant and the model. The update times are denoted as τ_k, and $\tau_0 < \tau_1 < \tau_2 < \cdots$, $\lim_{k\to\infty} \tau_k = \infty$. The update intervals are $h_k = \tau_k - \tau_{k-1}$ for all $k \in \mathbb{N}$, where $\mathbb{N}$ denotes the set of natural numbers. Furthermore, due to the long distance transmission, the signal $x(t)$ will be attenuated with the attenuation ratio ϖ_k before entering the model (94.1b) for $0 < \varpi_k \leq 1$. Since the model state is updated every τ_k seconds, then

$$\hat{x}(\tau_k) = \zeta_k \hat{x}(\tau_k^-) + \varpi_k x(\tau_k^-) \tag{94.2}$$

with $\zeta_k \in \mathbb{R}$ for all $k \in \mathbb{N}$. This resetting of the state error every update time is a key factor in our control system.

The dynamics of the overall system for $t \in [\tau_k, \tau_{k+1})$ can be described by

$$\begin{bmatrix} \dot{x}(t) \\ \dot{e}(t) \end{bmatrix} = \begin{bmatrix} A(t) + B(t)K(t) & -B(t)K(t) \\ \tilde{A}(t) + \tilde{B}(t)K(t) & \hat{A}(t) - \tilde{B}(t)K(t) \end{bmatrix} \begin{bmatrix} x(t) \\ e(t) \end{bmatrix} \tag{94.3a}$$

and

$$\begin{bmatrix} x(\tau_k) \\ e(\tau_k) \end{bmatrix} = \begin{bmatrix} x(\tau_k^-) \\ (1 - \varpi_k - \zeta_k)x(\tau_k^-) + \zeta_k e(\tau_k^-) \end{bmatrix} \tag{94.3b}$$

Denoting $z(t) = \begin{bmatrix} x(t) \\ e(t) \end{bmatrix}$, $\Lambda(t) = \begin{bmatrix} A(t) + B(t)K(t) & -B(t)K(t) \\ \tilde{A}(t) + \tilde{B}(t)K(t) & \hat{A}(t) - \tilde{B}(t)K(t) \end{bmatrix}$, $M_k = \begin{bmatrix} 0 & 0 \\ (1 - \varpi_k - \zeta_k)I & (\zeta_k - 1)I \end{bmatrix}$, and $\Delta z = z(\tau_k) - z(\tau_k^-)$, for $t = \tau_k$, system (94.2) can be rewritten as

$$\begin{cases} \dot{z}(t) = \Lambda(t)z(t), & t \neq \tau_k \\ \Delta z(t) = M_k z(t^-), & t = \tau_k \end{cases} \tag{94.4}$$

for $k \in \mathbb{N}$. Furthermore, we assume that $\Lambda(t) \in \mathbb{R}^{2n \times 2n}$ is a continuous matrix bounded for $t \geq t_0 := \tau_0$ and $z(t) = z(t, z_0) = z(t, t_0, z_0)$ is any a solution of (94.3a, 94.3b) with initial condition $z(t_0) = \begin{bmatrix} x(t_0) \\ 0 \end{bmatrix} = z_0$. In this paper, our objective is to construct the model and controller schemes (94.1b) and (94.1c) such that $\lim_{t \to \infty} z(t) = 0$.

94.3 Robust Feedback Control

In this paper, the frequency at which the network updates the state in the controller is not necessary constant and no assumptions should be made on the plant dynamics.

Theorem 94.1 *Assume that $\Re(t_0, t)$ is the number of control impulses in the interval $[t_0, t)$ and γ is the largest eigenvalue of $\frac{1}{2}\left[\Lambda(t) + \Lambda^T(t)\right]$ for all $t \geq t_0$. The MB-NCS (94.1a, 94.1b, 94.1c) is asymptotically stable if*

$$\gamma + p \ln \bar{\alpha} < 0 \tag{94.5}$$

where

$$\bar{\alpha} = \max_{k\in\mathbb{N}} \left\{ \sqrt{\frac{\left(1+\zeta_k^2\right) + \alpha_k^2 + \sqrt{\left((1+\zeta_k)^2+\alpha_k^2\right)\left((1-\zeta_k)^2+\alpha_k^2\right)}}{2}} \right\} \tag{94.6}$$

with $\alpha_k = 1 - \varpi_k - \zeta_k$ *for all* $k \in \mathbb{N}$ *and the limit*

$$p = \lim_{t\to\infty} \frac{\Re(t_0, t)}{t} \tag{94.7}$$

exists and is uniform with respect to $t > t_0$.

Proof Let the initial condition be $z_0 = z(t_0, z_0) \in \mathbb{R}^{3n}$ then every solution of system (94.4) satisfies

$$\|z(t_0, z_0)\| \le \bar{\alpha}^{\Re(t_0,t)} e^{\gamma(t-t_0)} \|z_0\| \tag{94.8}$$

where $\bar{\alpha}$ is the square root of the largest eigenvalue of the matrix $(I + M_k)^T (I + M_k)$. It follows from (94.5) to (94.7) that we can find a constant $\mathrm{H} > 1$ and $\mu > 0$ with $0 < \mu < |\gamma + p \ln \bar{\alpha}|$ such that $\lim_{t\to\infty} \|z(t, z_0)\| \le \lim_{t\to\infty} \mathrm{H} e^{-\mu(t-t_0)} z_0 = 0$. ■

Remark 1 If the signal $x(t)$ does not be attenuated before entering the model, i.e., $\varpi = 1$, then we have $\left[(I+M)e^{\Lambda\delta}\right]^k z_0 = \left[(I+M)e^{\Lambda\delta}(I+M)\right]^k z_0$. The necessary and sufficient conditions can also be stated as: the eigenvalues of $(I+M)e^{\Lambda\delta}(I+M)$ are strictly inside the unit circle. And the results are the same as [6].

In the following, we characterize the periodic MB-NCS with period T, i.e.,. $A(t+T) = A(t)$, $B(t+T) = B(t)$, $\hat{A}(t+T) = \hat{A}(t)$, $\hat{B}(t+T) = \hat{B}(t)$, and $K(t+T) = K(t)$. Furthermore, the model state is assumed to be updated every τ_k seconds with constants $\zeta = \zeta_k \neq 0$ and $\varpi = \varpi_k$ for all $k \in \mathbb{N}$, i.e., $\hat{x}(\tau_k) = \zeta \hat{x}(\tau_k^-) + \varpi x(\tau_k^-)$. Then system (94.4) can be rewritten as

$$\begin{cases} \dot{z}(t) = \Lambda(t) z(t), & t \neq \tau_k \\ \Delta z(t) = M z(t^-), & t = \tau_k \end{cases} \tag{94.9}$$

where $\Lambda(t)$ is continuous T-periodic matrix bounded for $t \ge t_0 := \tau_0$ and M is a constant matrix.

Theorem 94.2 *Assume* s_i, $i = 1, 2, \ldots, 2n$, *are the eigenvalues of the matrix* S *which is the monodromy matrix of the transformation* $z(t) = \Theta(t)\bar{z}(t)$ *with non-singular and* T*-periodic matrix* $\Theta(t) \in \mathbb{R}^{2n\times 2n}$. *Then the* T*-periodic MB-NCS* (94.1a, 94.1b, 94.1c) *is asymptotically stable if and only if all of its multipliers* s_i, $i = 1, 2, \ldots, 2n$, *satisfy* $|s_i| < 1$.

Proof It follows from [11] that the stability conditions of (94.5) can be determined by the transformed system $\dot{\bar{z}}(t) = \Omega\bar{z}(t)$ with $\Omega = \frac{1}{T}\ln S$. Denoting ω_i, as the eigenvalues of Ω, we have

$$\omega_i = \frac{1}{T}\ln s_i \tag{94.10}$$

and then

$$\mathrm{Re}(\omega_i) = \frac{1}{T}\ln|s_i| \tag{94.11}$$

for $i = 1, 2, \ldots, 2n$. ■

Remark 2 The eigenvalues $s_i, i = 1, 2, \ldots, 2n$, of the matrix S are called the multipliers of system (94.4) and the eigenvalues $\omega_i, i = 1, 2, \ldots, 2n$, of the matrix Ω are called the characteristic exponents. It is important to find the multipliers in order to determine the stability properties of periodic MB-NCS (94.4). First fix a t_0 and choose an arbitrary fundamental matrix $Z(t)$ of system (94.4) and then find the eigenvalues of the matrix $S = \Xi(t_0 + T)\Xi^{-1}(t_0)$.

94.4 Illustrative Example

Consider the plant (94.1a) of periodic MB-NCS with period $T = 2$

$$A(t) = \begin{bmatrix} -1 & \sin(\pi t) \\ 0.5 & -2 \end{bmatrix}, \quad B(t) = \begin{bmatrix} 0.8 \\ 0.1 \end{bmatrix}$$

The 2-periodic plant model (94.1b) is chosen as

$$\hat{A}(t) = \begin{bmatrix} -0.3537 & \cos(\pi t) \\ -0.8562 & -0.4235 \end{bmatrix}, \quad \hat{B}(t) = \begin{bmatrix} 0.5030 \\ 0.7220 \end{bmatrix}$$

Throughout this section, we will use the state feedback controller (94.1c) with $K(t) = [\,-0.9186 \quad -0.3365\,]$, and the 2-periodic update times are $\tau_1 = 0.1$ s, $\tau_2 = 0.7$ s, $\tau_3 = 0.9$ s, $\tau_4 = 1$ s, $\tau_5 = 1.1$ s, $\tau_6 = 1.4$ s, and $\tau_7 = 1.9$ s. In this case $\Lambda(t)$ is given by

$$(t) = \begin{bmatrix} -1.735 & \sin(\pi t) - 0.2692 & 0.7349 & 0.2692 \\ 0.4081 & -2.034 & 0.09186 & 0.03365 \\ -0.9191 & \sin(\pi t) - \cos(\pi t) - 0.09993 & -0.08091 & \cos(\pi t) + 0.09993 \\ 1.928 & -1.367 & -1.428 & -0.6328 \end{bmatrix},$$

and the monodromy matrix S has all its eigenvalues inside the unit circle. The state responses of the periodic MB-NCS (94.1a, 94.1b, 94.1c) with period 2 and the update parameter $\zeta = -0.1$ are plotted in Fig. 94.1. Note that the plant is with the initial conditions of $[\,x(t) \quad \hat{x}(t)\,]^T = [\,1 \quad 1 \quad 1 \quad 1\,]^T$.

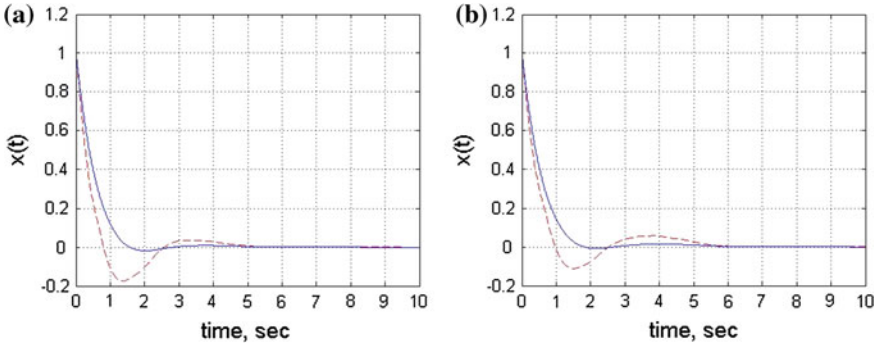

Fig. 94.1 State responses of the periodic MB-NCS (1) with **a** $\varpi = 0.7$; **b** $\varpi = 0.4$

94.5 Conclusion

In this paper, the problems of the stability analysis and model design for the MB-NCS with the transmission attenuation have been investigated. The close relationship between signal attenuation ratio and model design for MB-NCS with admissible update intervals is established also. Furthermore, the stabilizability problem of the T-periodic MB-NCS has been explored successfully. An example with simulation results is illustrated to demonstrate the effectiveness and flexibility of the proposed techniques.

References

1. Zhang, W., Branicky, M. S., & Phillips, S. M. (2001). Stability of networked control systems. *IEEE Control System Magazine, 21*, 84–99.
2. Ishii, H., & Francis, B. (2002). *Limited data rate in control systems with networks*. LNCIS (vol. 275). Berlin: Springer.
3. Montestruque, L. A., & Antsaklis, P. (2004). Stability of model-based networked control systems with time-varying transmission times. *IEEE Transactions on Automatic Control, 49*, 1562–1572.
4. Liu, G., Xia, Y., Chen, J., Rees, D., & Hu, W. (2007). Networked predictive control of systems with random network delays in both forward and feedback channels. *IEEE Transactions on Industry Electron, 54*, 1282–1297.
5. Gao, H. J., Chen, T. W., & Lam, J. (2008). A new delay system approach to network-based control. *Automatica, 44*, 39–52.
6. Ding, B. (2011). Stabilization of linear systems over networks with bounded packet loss and its use in model predictive control. *Automatica, 44*, 2526–2533.
7. Benitez-Perez, H., Benitez-Perez, A., & Ortega-Arjona, J. (2012). Networked control systems design considering scheduling restrictions and local faults. *International Journal of Innovative Computing, Information and Control, 8*, 8515–8526.

8. Arcara, P., Bittanti, S., & Lovera, M. (2000). Periodic control of helicopter rotors for attenuation of vibrations in forward flight. *IEEE Transactions on Control Systems Technology, 8*, 883–894.
9. Brockett, R., & Liberzon, D. (2000). Quantized feedback stabilization of linear systems. *IEEE Transactions on Automation Control, 45*, 1279–1289.
10. Bittanti, S., & Colaneri, P. (2009). *Periodic systems: Filtering and control. Communications and control engineering*. London: Springer.
11. Samoilenko, A. M., & Perestyuk, N. A. (1995). *Impulsive differential equations*. Singapore: World Scientific.

Chapter 95
Evaluating the Performance of the P300-Based Brain Computer Interface for the LEGO Page Turner

S. C. Chen, A. R. See, C. K. Liang and Y. Y. Lee

Abstract The objective of this study is to evaluate a real-time Brain computer interface (BCI) system for a page turner. Electroencephalographic (EEG) signals are simultaneously retrieved using an EEG cap and the LabVIEW^{TM} was used to perform signal pre-processing, feature extraction and execution command. Off-line analysis in the BCI system utilized visual stimulation to induce the individual's visual evoked potential and adopted signal detrend function, independent component analysis and Savitzky-Golay filter method were used to resolve the interference caused by the background noise. Subsequently, EEG features are then extracted and classified to determine the command for the page turner system. The evaluation results from ten volunteers showed a recognition accuracy rate of 93.6 % and average time of around 4.95 s for controlling the page turner robot. The average information transfer rate was 49.10 bits/min. The study has successfully integrated LEGO^{TM} components and a BCI system with high accuracy and good response time.

Keywords Brain computer interface · LEGO^{TM} · Information transfer rate · P300

S. C. Chen (✉) · A. R. See
Department of Electrical Engineering,
Southern Taiwan University of Science and Technology,
Yung Kang District, Tainan City 71005, Taiwan, Republic of China
e-mail: chung@mail.stust.edu.tw

C. K. Liang
Department of Electrical Engineering, National Taitung College, Taitung City 95045, Taiwan, Republic of China

Y. Y. Lee
Department of Graphic Communication Arts, National Taiwan University of Arts, New Taipei City 22058, Taiwan, Republic of China

J. Juang et al. (eds.), *Proceedings of the 2nd International Conference on Intelligent Technologies and Engineering Systems (ICITES2013)*, Lecture Notes in Electrical Engineering 293,
DOI: 10.1007/978-3-319-04573-3_95,

95.1 Introduction

Brain-computer interface (BCI) systems are an important assistive device for the elderly or severely disabled people. The main purpose of BCI is to provide people with diminished capabilities to communicate and control external devices using a method that does not require the brain's normal mode of transmission via peripheral nerves and muscles [1]. The uses of non-invasive methods to measure brain signals and translate it to commands opens a broad range of possibilities. In recent years, advances in physiological measurement devices, signal processing techniques, machine learning and analysis of physiological signals have greatly improved diagnostics and customized applications [2]. Researchers on communication and control can be considered fundamental applications of BCI.

Base from [2], BCIs can be classified as dependent BCI, visual evoked potential (VEP), and independent BCI that includes slow cortical potentials, P300, evoked potentials mu and beta rhythms, and cortical neuronal action potentials. BCI has been widely used in the P300 format. A P300 format of BCI incorporates electroencephalography (EEG) to identify the response gathered from a stimulus where the positive deflection in the EEG right over the parietal cortex occurring around 300 ms after a rare meaningful stimulus is presented [3]. A P300 format of BCI requires no training compared to slow cortical potentials (SCP) or sensorimotor rhythms (SMR), and can enable a quick classification of signals taken from the input [4]. In P300 BCIs different visuo-spatial attention orienting also affected the efficacy of the BCI, with an endogenous (top-down voluntary) orienting of visuo-spatial information was better than an exogenous (bottom-up automatic orienting of visuo-spatial attention [5]. It is also important to note which way is the best to look at comparing the results of P300 BCIs. In one study, it was noted that the best way of comparing P300 BCIs is efficiency due to the fact that efficiency is very versatile and it provides information on the possibility of communication which is often disregarded in many metrics [6].

During the past decade, advances on BCI have developed controls for different applications such as an orthotic hand [7], wheelchairs [8, 9] and living environment adjustments [10]. In the case of the orthotic hand, BCI generates tri-state commands to grasp, open and hold an object by processing the mu wave. Subsequently, autonomous wheelchairs provide more freedom to its users wherein they can control it to travel to a certain destination while avoiding collisions or obstacles. Some were designed to let the users control it autonomously without any preset destinations while a latter study discussed methods on how to control the direction and speed of a simulated and real wheelchair.

In this study, the P300 evoked potential will be used to control the book page turner developed using LEGO bricks. The waveform of a P300 signal has a latency of about 300 ms and is produced through widely used in BCI applications.

95.2 Materials and Methods

In this section, a detailed description on the hardware and software setup of the automated page-turner using BCI is discussed. First, the overall system architecture will be introduced. Second, the BCI protocol including the EEG acquisition, graphical user interface and pattern recognition strategy will be explained. Third, the autonomous book page turner will be shown and finally the integration and implementation protocol will be discussed.

95.2.1 System Architecture

The system can be divided into two core parts namely: (1) Visual evoked potential (VEP) and (2) BCI interface. The system architecture made used of events from an event related potential (ERP) to simultaneously stimulate and acquire EEG signals and afterwards the VEP is analyzed using off-line analysis.

The visual stimuli interface, client side, was first created that includes various stimuli objects and numerous events that are encoded to the NuAmps amplifier (Compumedics) via PrintPort. Afterwards, the EEG signal and stimuli code information will be synchronously retrieved by the NuAmps amplifier and sent to the server side via TCP/IP communications protocol. The data received from the Client Side will then be used for off-line analysis. Second, offline analysis will be performed base from the received data. The BCI is composed of two parts namely: (1) Data acquisition and signal processing and (2) Control device.

95.2.2 Data Acquisition

The NuAmps EEG amplifier by Compumedics was used to measure scalp EEG signals. The user is required to wear an EEG cap to measure the changes in electrical potential through the electrodes. EEG signals are acquired using Ag/AgCl electrodes from the Cz, Pz and vertical electrooculogram (VEOG) with reference electrode placed at channel A2. The impedance of each electrode is kept below 5 kΩ. The EEG signal was sampled at 1000 Hz, and band-pass filtered between 0.1–30 Hz. Data acquisition commences with the generation of stimuli to stimulate the user. Next, different events are encoded and transmitted to the NuAmps™ amplifier while being simultaneously displayed using the Scan 4.3 software. The information gathered is then transferred to a program created using the LabVIEW™ software by National Instruments. Information transfer is made possible by developing a program to access the TCP/IP protocol from the NuAmps™ amplifier and convert the received data packets to make it compatible for real-time analysis in the LabVIEW™ software.

95.2.3 Visual Evoked Potential

95.2.3.1 Pre-processing

The real-time EEG data undergoes pre-processing analysis. In the process of acquiring EEG, there are instances wherein changes in the environment affect the skin impedance. As a result these variations cause the signal baseline to drift. The signal goes through a detrend function and the exponential fit method is used to remove the unwanted offset. Next, unwanted eye movement causes artifacts that contaminate the signal. Previous works have utilized Independent Component Analysis (ICA) as a method to isolate and remove the eye movement signal from the EEG signal. Through the use of the three signal inputs (2 EEG and 1 EOG) ICA was used to produce a clean EEG signal for the succeeding analyses.

95.2.3.2 VEP Algorithm

Depending on the required analysis time, forward or backward isolation is performed on several time segments. After generating several trials, these numerous trials are then averaged to obtain the VEP feature. However, in order to remove the noise generated by using cumulative averaging, the Savitzky-Golay filter is used to smooth the signal and isolate the necessary VEP feature.

Undergoing the different processes mentioned above, the required VEP feature can be acquired but there is the need to reduce the time for feature recognition. To achieve time improvement the mean envelope of the feature is calculated. Finally, the average value of the correlation coefficient is used to analyze the linear relationship of the signals. If the correlation coefficient value is below the set threshold, no control command will be transmitted. However, if the value exceeds the threshold, then a command will be sent to the backend apparatus.

95.2.3.3 Hardware

The Page Turner was created using the LEGO Mindstorms NXT and programming was done using the NI LabVIEW toolkit for LEGO Mindstorms NEXT. The actual device is shown in Fig. 95.1.

95.2.3.4 BCI Performance Evaluation

The performance of the spelling system will be assessed by calculating the information transfer rate (ITR). In this study we will be using selections per minute (SPM) and the time to determine the ITR. These two methods have been widely

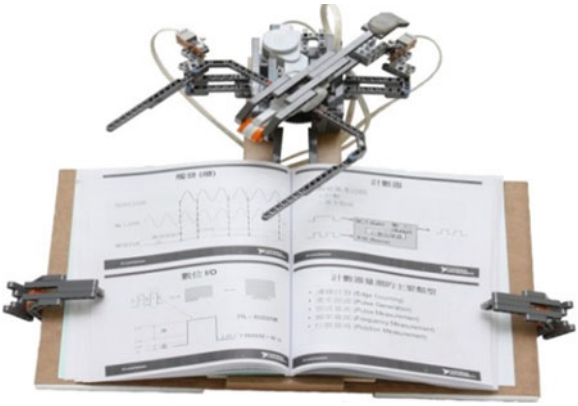

Fig. 95.1 Book page turner

used to quantify the speeds of developed BCI systems [8]. The ITR calculation used in this study is the Wolpaw method based on the formula presented in [11].

$$B_t = \log_2 N + p \log_2 p + (1-p) \log_2 \left[\frac{1-p}{N-1}\right] \tag{95.1}$$

where p is the accuracy of the classification and N is the number of selections. Bt is presented as bits per trial. In this study, number of selections (N) is equivalent to the number of flickering boxes ($N = 2$).

The classification accuracy p is computed by taking the correct selection commands divided by the total number of selections.

ITR is usually calculated in terms of bits/min (bpm) and is calculated using the equation:

$$ITR = \frac{60}{T} \cdot S_N \cdot B_t \tag{95.2}$$

where T is the total time in seconds, S_N the number of selections and Bt is the bit rate.

95.3 Results

The system was tested by 10 volunteers. VEP results from one volunteer are shown in Fig. 95.2. Figure 95.2a demonstrates a left to right selection while Fig. 95.2b exhibits the stimulus reaction of moving from right to left. It can be observed that the peak signal can be observed between the 150–300 ms time interval.

Then initial tests were done by requesting the subjects to select the left or right command. Results from ten volunteers that evaluated the system demonstrated that

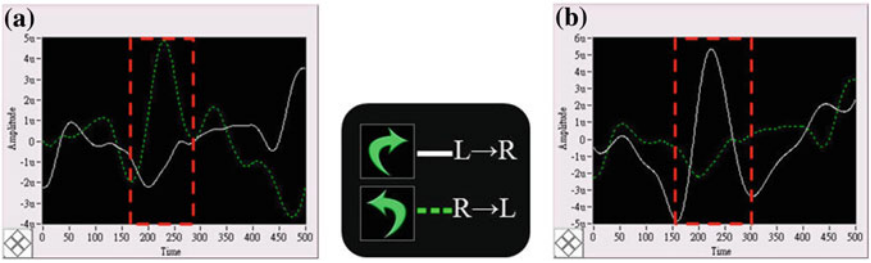

Fig. 95.2 Results of the VEP response for turning **a** left to right and **b** right to left

Table 95.1 Summary of experimental results with each individual's response time and information transfer rate

Subject	Average time per command (s)	Total time (s)	Selections	Accuracy (%)	Bit rate	ITR (bits/min)
1	5.21	130	25	92	3.87	44.62
2	4.87	122	25	96	4.22	51.97
3	4.7	118	25	96	4.22	53.85
4	4.98	125	25	100	4.64	55.95
5	5.05	126	25	84	3.28	38.92
6	4.94	124	25	96	4.22	51.23
7	4.99	125	25	96	4.22	50.72
8	4.79	120	25	92	3.87	48.54
9	5.04	126	25	100	4.64	55.28
10	4.92	123	25	84	3.28	39.95
Average	4.95	123.73	25	93.6	4.05	49.1

the BCI control system showed a recognition accuracy rate of 93.6 % and average time of around 4.95 s for controlling the page turner robot. Subsequently, the ITR for each subject were calculated. The summary of the results is shown in Table 95.1.

95.4 Conclusions

In conclusion, the researchers have successfully evaluated the LEGO Page Turner. The system was able to demonstrate high accuracy and with a moderate response time. The subjects were trained before going into the actual test to achieve the current results. It should be noted that the current method makes use of numerous trials to make a single output. Although the ITR is considered high but the response time still has room for improvement. In the future a more convenient EEG acquisition device could be developed and integrated with an external device that contains the visual stimuli and also the signal processing module will be developed to provide a practical and convenient device for BCI control. An alternative method would be the use of steady state evoked potential (SSVEP) to improve speed.

Acknowledgments We would like to thank National Science Council for funding this project under grant number NSC-100-2632-E-218-001-MY3.

References

1. Wolpaw, J. R., Birbaumer, N., McFarland, D. J., Pfurtscheller, G., & Vaughan, T. M. (2002). Brain-computer interfaces for communication and control. *Clinical Neurophysiology, 113*, 767–791.
2. Cinar, E., & Sahin, F. (2013). New classification techniques for electroencephalogram (EEG) signals and a real-time EEG control of a robot. *Neural Computing and Applications, 22*, 29–39.
3. Townsend, G., Shanahan, J., Ryan, D. B., & Sellers, E. W. (2012). A general P300 brain-computer interface presentation paradigm based on performance guided constraints. *Neuroscience Letters, 531*, 63–68.
4. Kathner, I., Ruf, C. A., Pasqualotto, E., Braun, C., Birbaumer, N., & Halder, S. (2013). A portable auditory P300 brain-computer interface with directional cues. *Clinical Neurophysiology, 124*, 327–338.
5. Marchetti, M., Piccione, F., Silvoni, S., & Priftis, K. (2012). Exogenous and endogenous orienting of visuospatial attention in P300-guided brain computer interfaces: a pilot study on healthy participants. *Clinical Neurophysiology, 123*, 774–779.
6. Quitadamo, L. R., Abbafati, M., Cardarilli, G. C., Mattia, D., Cincotti, F., Babiloni, F., et al. (2012). Evaluation of the performances of different P300 based brain-computer interfaces by means of the efficiency metric. *Journal of Neuroscience Methods, 203*, 361–368.
7. Chen, C. W., Lin, C. C. K., & Ju, M. S. (2009). Hand orthosis controlled using brain-computer interface. *Journal of Medical & Biological Engineering, 29*, 234–241.
8. Muller, S. M. T., Celeste, W. C., Bastos, T. F., & Sarcinelli, M. (2010). Brain-computer Interface Based on Visual Evoked Potentials to Command Autonomous Robotic Wheelchair. *Journal of Medical & Biological Engineering, 30*, 407–415.
9. Jinyi, L., Yuanqing, L., Hongtao, W., Tianyou, Y., Jiahui, P., & Feng, L. (2012). A hybrid brain computer interface to control the direction and speed of a simulated or real wheelchair. *IEEE Transactions on Neural Systems and Rehabilitation Engineering, 20*, 720–729.
10. Carabalona, R., Grossi, F., Tessadri, A., Castiglioni, P., Caracciolo, A., & de Munari, I. (2012). Light on! real world evaluation of a P300-based brain-computer interface (BCI) for environment control in a smart home. *Ergonomics, 55*, 552–563.
11. Volosyak, I. (2011). SSVEP-based Bremen-BCI interface–boosting information transfer rates. *Journal of Neural Engineering, 8*, 036020.

Chapter 96
Tool Control Method Considering Kinematical Constraint in Japanese Calligraphy of a Humanoid Robot

Seiji Sugiyama, Ikuma Oshita and Takahiro Wada

Abstract In this research, a tool control method considering a kinematical constraint of brush for smooth calligraphic specimen is proposed by doing knee bends and by turn back operation of brush of humanoid robots while walking. In our previous research, a system for writing Japanese calligraphy using the whole body motion of a humanoid robot has already been developed. It consists of an instruction system using a virtual haptic interface and a humanoid robot with a brush on its right hand. In the previous method, there is a problem about wrong brush condition. To cope with the difficulty, an upgrade for considering brush characteristics while writing is proposed. Experiments show the smooth writing results for considering the tools' characteristics.

Keywords Humanoid robot hoap-2 · Mobile manipulation

96.1 Introduction

Nowadays, there is a lot of research about humanoid robots [1]. To approach humans, not only basic motion about walking and/or grasping, but also keeping body condition while walking [2] and/or pushing objects while walking [3] are researched. One of advantages of humanoid robots is to adapt to the humans' life environment easily. Adjusting to humans' sizes, robots can use humans' tools [4].

In the research about using tools of robots, Watanabe et al. have achieved cooking salad robots with recognizing tools [5]. Ogura et al. have realized broom sweeping with whole body motions using action [6]. Kujyo et al. have developed tennis swing robots by translating humans' motion skills [7]. In these researches,

S. Sugiyama (✉) · I. Oshita · T. Wada
Department of Human and Computer Intelligence College of Information Science and Engineering, Ritsumeikan University, Shiga 525-8577, Japan
e-mail: seijisan@is.ritsumei.ac.jp

J. Juang et al. (eds.), *Proceedings of the 2nd International Conference on Intelligent Technologies and Engineering Systems (ICITES2013)*, Lecture Notes in Electrical Engineering 293,
DOI: 10.1007/978-3-319-04573-3_96,

the skill translating to the robot such as sampling task skills from various kinds of measurement data on specific tasks is mainly approached. This approach has an advantage not to need to consider tools' characteristics explicitly. However, it is necessary to repeat translating tasks whenever robots and tools change. On the other hand, in order for various robots to be able to use various tools, it is important to describe knowledge to be able to apply various robots by considering characteristics of tools explicitly. Task's knowledge should be described by using tool's knowledge.

In this research, the kinematical knowledge with tools' characteristics is approached. In the case that the instruction data by considering no tools' characteristics is obtained, trajectory planning and control are researched. Using tools with kinematical constraint is our main target. Especially, a method to realize a series of humanoid robot motions in the area more greatly than the movable range of the robot arm is proposed. For example, performance calligraphy using brush is approached and a method to achieve the control using tools' characteristics is proposed.

Sugiura developed the calligraphy by a humanoid robot [8]. However, the robot can write only a few characters because the motion is set in advance and it cannot write while walking. A lot of arm robots for calligraphy can recognize trajectories by using character's image from an instruction camera [9, 10]. Tanaka et al. have constructed calligraphy by instructing the position information with industrial arm robots [11]. Katsuura et al. have developed calligraphy with position and pressure information by using instruction data of arm robots [12]. These researches of arm robots can mainly conduct the control method to realize the brush position and the pressure data that are instruction data. However, no tools' characteristics in the planning and control are considered. Because these robots are fixed at the ground or base structure, there is no concept of mobile manipulation.

A system for writing Japanese calligraphy using the whole body motion of a humanoid robot has already been developed in our previous research [13]. It consists of an instruction system using a virtual haptic interface and a humanoid robot with a brush on its right hand. In the previous method, there is a problem about wrong brush condition. To cope with the difficulty, an upgrade for considering the brush characteristics while writing is proposed in this research. Experiments show the smooth writing result for considering the tools' characteristics.

96.2 System Configuration

Our experimental system consists of a humanoid robot Hoap-2 (Fujitsu Automation Inc., (Fig. 96.1a) with a brush fixed on the right hand using the attachment (Fig. 96.1b), an instruction system using a pen style haptic device PHANToM OMNI and PC monitor (Fig. 96.1c). Trajectory and pressure data of human handwriting is given by this system.

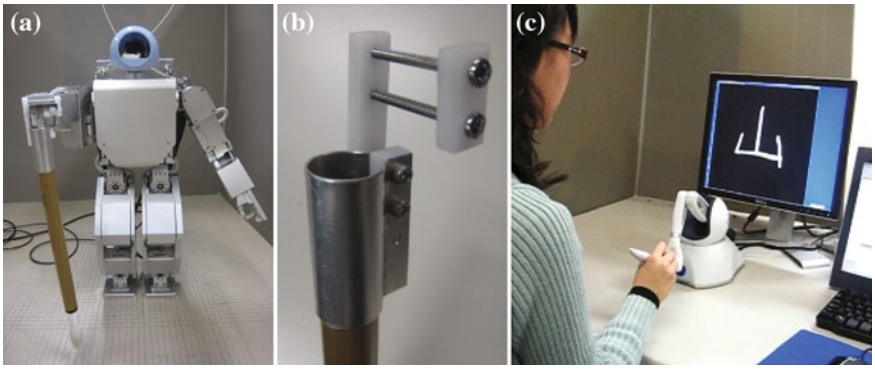

Fig. 96.1 Experimental system

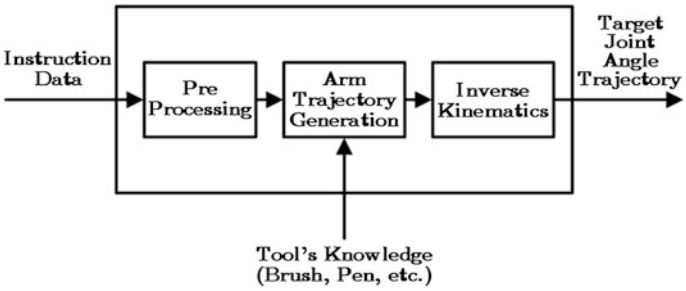

Fig. 96.2 Trajectory generation method

96.3 Brush Control Method Considering Kinematical Constraint

96.3.1 Trajectory Planning

In this research, a control method considering characteristics of tool (brush) is used as shown in Fig. 96.2. Character's shapes in the virtual space of the instruction system are given by using the dotted line called 'PHANToM DATA' as shown in Fig. 96.3. This data is thinned out and becomes simple by using broken line called 'Brush Trajectory'. Each vertex position of the line is named $\boldsymbol{P}_i$. The humanoid robot walks on the dash-dot line called 'Robot Trajectory' only horizontally and vertically.

Because of strong pushing, two problems occur: wrong writing that hair ends are broken brush (Fig. 96.4) and bended brush (Fig. 96.5). They cause different brush height. These problems are the kinematical constraint condition of brush. It is necessary to consider the problems when the trajectory is planned. Describing

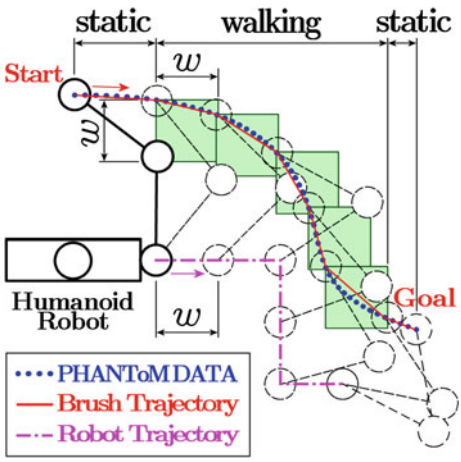

Fig. 96.3 Writing method

Fig. 96.4 Broken brush

Fig. 96.5 Bended brush

tool's knowledge beforehand, even if a brush is changed, robots can use other tools. Using this method, the target joint angle trajectory can be calculated by using the inverse kinematics.

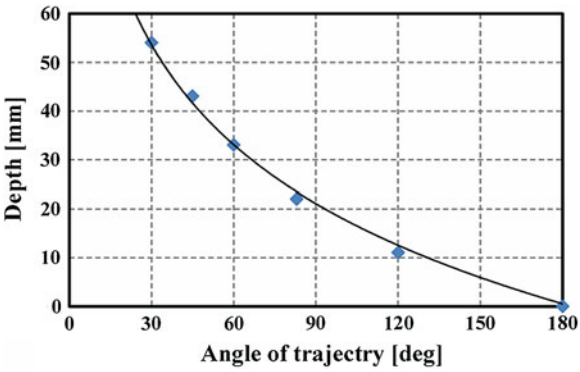

Fig. 96.6 Maximum depth

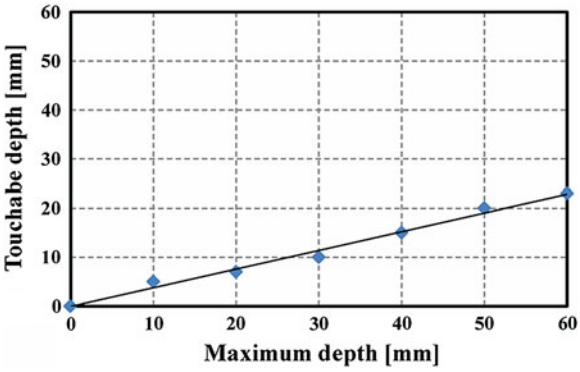

Fig. 96.7 Touchable depth

96.3.2 Brush Characteristics

(1) Maximum Depth: It is impossible to change angle rapidly because the movement of brush makes face of hair ends in the opposite direction. To cope with this difficulty, a static relationship between a writing direction change angle θ_a and a maximum hair ends depth h_a has been investigated experimentally (Fig. 96.6) represented by

$$h_a = -27.7 \log \theta_a + 144. \tag{96.1}$$

Keeping brush depth under this approximate expression, the hair ends does not break.

(2) Touchable Depth: It is impossible to touch paper when bended hair ends occurs because the height of brush changes. To cope with this difficulty, maximum touchable depth h_b is investigated experimentally for contacting paper (Fig. 96.7) represented by

$$h_b = 0.38\ h_c \tag{96.2}$$

where h_c denotes the maximum depth of brush while writing. Keeping brush depth under this approximate expression, the hair ends can touch paper.

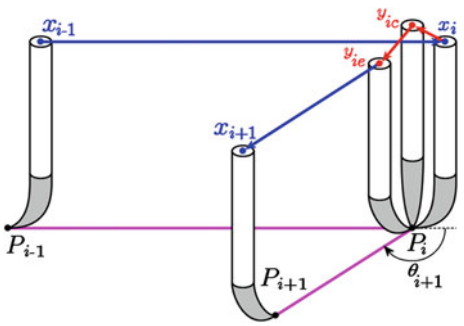

Fig. 96.8 Trajectory planning

96.3.3 *Trajectory Planning Method When the Writing Angle Changes*

The time series data of the robot hand $\mathbf{Z}$ ($\in \mathrm{R}^3$) is represented by

$$\mathbf{Z} = \begin{cases} f^x_{leg}(\Theta_{leg}) + f^y_{arm}(\Theta_{arm}), & \text{if } \omega_x \geq \omega_y \\ f^y_{leg}(\Theta_{leg}) + f^x_{arm}(\Theta_{arm}), & \text{if } \omega_x < \omega_y \end{cases} \tag{96.3}$$

where Θ_{arm} denotes joint angles of all arms, Θ_{leg} denotes joint angles of all foots, ω_x and ω_y denote x and y values of length between $\boldsymbol{P}_i$ and $\boldsymbol{P}_{i+1}$ respectively. In Eq. (96.3), the robot moves horizontally using upper equation and vertically using lower equation.

As shown in Fig. 96.8, the hand trajectory Z from $\boldsymbol{P}_{i-1}$, $\boldsymbol{P}_i$ to $\boldsymbol{P}_{i+1}$ with changing θ_{i+1} is represented by

$$Z = [x_1 \ \ldots \ x_i \ \ y_{ic} \ y_{ie} \ \ x_{i+1} \ \ldots \ x_n] \tag{96.4}$$

where x_i denotes hand trajectory by calculating $\boldsymbol{P}_i$ (top of brush) and represented by

$$x_i = \boldsymbol{P}_i + [\Delta x_i, \Delta y_i, \mathrm{H} - \Delta z_i]^T \tag{96.5}$$

where H denotes the total length of straight hair ends, Δx_i, Δy_i, and Δz_i denote displacements by pushing brush respectively. When the angle change θ_{i+1} is lower the curve shown in Fig. 96.6, robot can write by using only x_i. On the other hand, when it is upper side, it is necessary to change the depth by using Eq. (96.1). In the case of large angle change, using friction to paper, return to the position y_{ic} for reforming the brush condition, after that, move to the position y_{ie} for changing angle and for reforming the brush to next angle, finally move to the position x_{i+1}. y_{ic} and y_{ie} are represented by

$$y_{ic} = \boldsymbol{P}_i + [0, 0, \ H - \Delta z_{ie}]^T \tag{96.6}$$

$$y_{ic} = \boldsymbol{P}_i + [0, 0, \ H - \Delta z_{ie}]^T \tag{96.7}$$

where Δz_{ie} is given by Fig. 96.7.

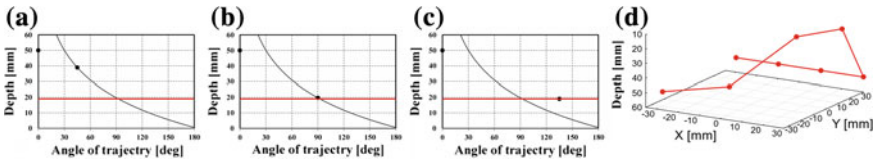

Fig. 96.9 Pressure data with the correction functions in movable range. **a** 45°, **b** 90°, **c** 135°, **d** Brush trajectory

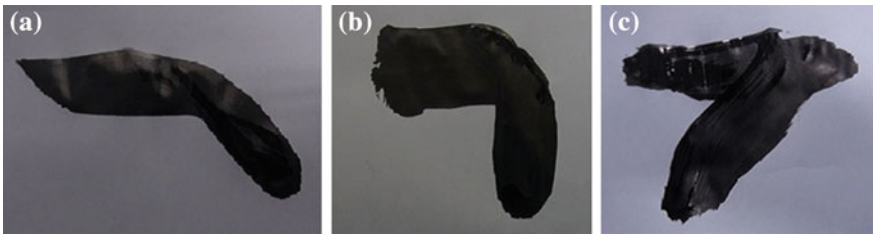

Fig. 96.10 Writing result with the correction functions in movable range. **a** 45°, **b** 90°, **c** 135°

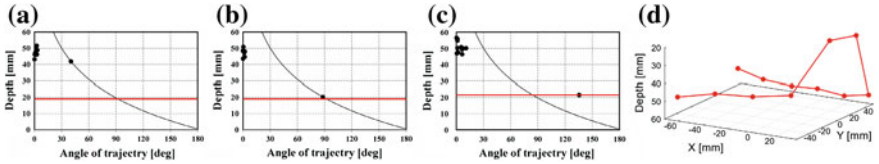

Fig. 96.11 Pressure data with the correction functions while walking. **a** 45°, **b** 90°, **c** 135°, **d** Brush trajectory

96.4 Experimental Results

(1) In the Movable Range: Figure 96.9a–c show the brush pressure data of 45°, 90°, and 135° respectively in the movable range of the arm. It is necessary to modify the writing style at the plotted data on the maximum depth curve. Especially, red horizontal line is the limitation that the brush has to reverse the direction with friction between brush and paper, and use the brush trajectory as shown in Fig. 96.9d. Figure 96.10a–c show the writing results of 45, 90 and 135° respectively in this case. As a result, only the case of 135° has to use the brush trajectory and the reversed motion of brush can be done. Note that the cases of 45° and 90° use only height control.

(2) In the Walking Motion: Figure 96.11a–c show the brush pressure data of 45°, 90°, and 135° respectively while walking. Similarly, Fig. 96.11d shows the brush trajectory. Figures 96.12a–d, 96.13a–d, 96.14a–d show the captured images of the video for writing 45°, 90°, and 135° line while walking.

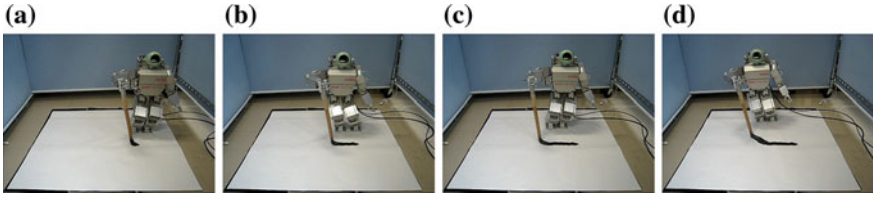

Fig. 96.12 Captured Images of the video for writing 45° line while walking. **a** $t = 7$[s], **b** $t = 45$[s], **c** $t = 83$[s], **d** $t = 122$[s]

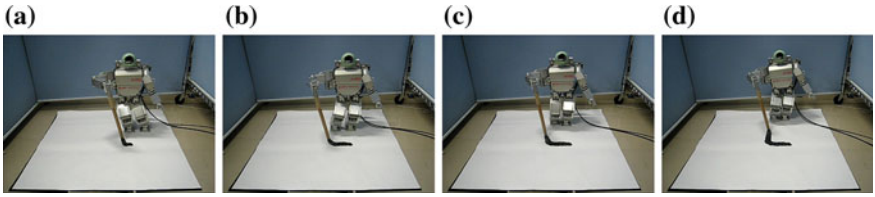

Fig. 96.13 Captured images of the video for writing 90° line while walking. **a** $t = 21$[s], **b** $t = 63$[s], **c** $t = 96$[s], **d** $t = 127$[s]

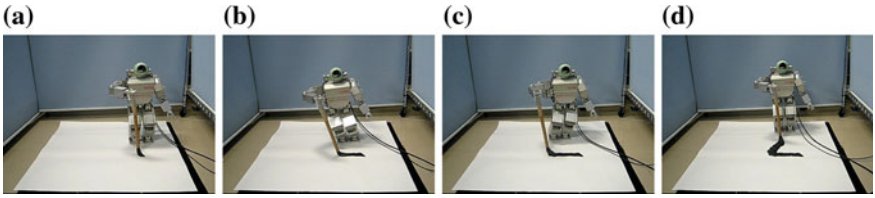

Fig. 96.14 Captured images of the video for writing 135° line while walking. **a** $t = 9$[s], **b** $t = 53$[s], **c** $t = 90$[s], **d** $t = 153$[s]

In 45°, because of small height change, the effectiveness using the correction functions is small. On the other hand, in 90 and 135°, the effectiveness can be found. The reversed brush motion was successful.

96.5 Conclusion

In this research, the control method considering kinematical constraint of brush has been proposed and Japanese calligraphy using whole body motion of a humanoid robot has been realized. Using this control method, smooth brush writing motions that include three angle changes, 45, 90, and 135° could be achieved. Future plan will be conducted to improve the performance.

Acknowledgments The authors would like to thank Ms. Satoko Adachi from Ritsumeikan University, Prof. Masanao Koeda from Osaka Electro-Communication University, and Prof. Tsuneo Yoshikawa from Ritsumeikan University who contributed to the initial design.

References

1. Takanishi, A., et al. (2012). Biped robot technology now. *Robotics Society of Japan*, *30*(4), 1–19 (in Japanese).
2. Yoshida, H., et al. (2000). *Mobile manipulation of humanoid robots-analysis of manipulability and stability in mobile manipulation* (pp. 1924–1929). International Conference on Robotics and Automation.
3. Harada, K., et al. (2004). *Real-time planning of humanoid robot's Gait for force-controlled manipulation* (pp. 616–622). International Conference on Robotics and Automation.
4. Kajita, S. (2005). *Humanoid Robot*. Ohmsha (in Japanese).
5. Watanabe, Y., et al. (2010). *System integration of a lifesized humanoid robot and its application to make a salad with handling general cooking tools* (pp. 2A2–A17). Conference Robotics and Mechatronics (in Japanese).
6. Ogura, T., et al. (2007). *Realization of dynamics simulator embedded robot brain for humanoid robots* (pp. 2175–2180). International Conference on Robotics and Automation.
7. Kunori, H., et al. (2008). *Association of humanoid whole body motion with knowledge of tools* (pp. 2A1–E22). Conference Robotics and Mechatronics (in Japanese).
8. Sugiura, Y. Development of a simulated experience for humanoid robot. http://robot.watch.impress.co.jp/cda/column/2006/07/24/89.html
9. Yao, F. H., et al. (2004). Extracting the trajectory of writing brush in Chinese character calligraphy. *Engineering Application of Artificial Intelligence*, *17*, 631–644.
10. Huebel, N., et al. (2012). *Towards robotic calligraphy*. International Conference on Intelligent Robots and Systems, WedFVT9.5.
11. Tanaka, T., et al. (2003). *Study of sensing methods for sophisticated robot teaching* (pp. 176–177). Proceedings of the Japan Society of Mechanical Engineering (in Japanese).
12. Katsura, S. (2012). Motion copy system. http://www.youtube.com/watch?v=ZeHEsb7XdWM.
13. Sugiyama, S., et al. (2013). Japanese calligraphy using whole body motion of a humanoid robot. *Lecture Notes in Electrical Engineering*, *234*, 345–355.

Chapter 97
Growth Characteristics and Properties of Tin-Doped Indium Oxide Thin Films as a Function of Oxygen Pressure When Prepared by E-beam Evaporation

Hong-Hsin Huang, Yen-Ming Chen and Ming-Chih Huang

Abstract The Indium Tin Oxide (ITO) thin films were prepared by E-beam evaporation at oxygen pressure ranging from 1×10^{-4} to 1×10^{-3} Torr. The structure was analyzed by X-ray diffraction and the grain size was evaluated by Scherrer formula. The resistivity and transmittance were measured by 4-probe method and UV-Visible spectrophotometer, respectively. The crystallinity of ITO films increases with oxygen pressure increasing which also increase the intensity of (440). The grain size of ITO films increased with the oxygen pressure increasing. The resistivity decreased with oxygen pressure increasing, however, the transmittance increased. These results suggested that the deposition parameter of oxygen pressure plays an important role in ITO thin film preparation by E-bean evaporation.

Keywords: ITO thin film · E-beam evaporation · Resistivity · Transmittance

97.1 Introduction

Indium tin oxide (ITO) films are widely used in a variety of applications, including optoelectronic devices, such as organic light emitting devices (OLED), plasma display panels (PDPs), and solar cells, etc. [1], because the ITO films shown high optical transmittance in visible light region and acceptable resistivity when deposited under certain optimized condition. ITO film has been the subject of

H.-H. Huang (✉) · Y.-M. Chen
Department of Electrical Engineering, Cheng Shiu University, Kaohsiung 83347, Taiwan, Republic of China
e-mail: funs@csu.edu.tw

M.-C. Huang
Department of Electrical Engineering, Yu Ta Institute of Technology and Commerce, Ping-Tong county 90942, Taiwan, Republic of China

J. Juang et al. (eds.), *Proceedings of the 2nd International Conference on Intelligent Technologies and Engineering Systems (ICITES2013)*, Lecture Notes in Electrical Engineering 293,
DOI: 10.1007/978-3-319-04573-3_97,

extensive investigations and is generally considered to be an important functional TCO material.

ITO films that exhibit optimum values of conductivity and transparency require an oxygen partial pressure in evaporation process. The ITO's physical properties such as structure, surface morphology, conductivity, etc., which significantly influence OLED performance, are strongly dependent on the specific deposition process and post-treatment [2]. The optical and electrical properties of the ITO films obtained by using electron beam evaporation are reported to be quite sensitive to deposition parameters. Kachouane et al. [3] and park et al. [4] had report the crystallinity and composition of films are affected by the pressure of chamber during deposition. ITO films have been fabricated by DC or RF magnetron sputtering, ion beam sputtering, electron beam evaporation, and pulsed laser deposition.

E-beam evaporation offers two major advantages: (1) a high power density, and hence a wide range of control over evaporation rates, from very low to very high and (2) the source material for evaporation being contained in the water-cooled crucible and its surface area showing a high temperature. Metallurgical reactions between crucible and source materials leading to film contamination are therefore minimized. In this study, the ITO films were deposited by E-beam evaporation and the effect of oxygen pressure was discussed to obtain the optimized deposition parameters for low temperature preparation.

97.2 Experimental

The ITO thin films were prepared by E-beam assisted evaporation on glass substrate as a function of oxygen pressure. The source material was a mixture of 90 % In_2O_3 and 10 % SnO_2. The glass substrate was cleaned by EPA in an ultrasonic cleaner for 15 min. and then DI water was used to move the solvent. And then it was carefully dried by nitrogen gas blowing. For deposition, the substrate was fastened in a curved holder with a working distance of 38 cm and heated to the temperature of 150 °C. A chamber with base pressure of 5×10^{-6} Torr was vacuumed by a diffusion pump. Oxygen gas was introduced into the chamber to adjust the working pressure ranging from 1×10^{-4} to 1×10^{-3} Torr. The deposition rate was monitored by a thickness control system (ULVAC CRTM-8000, Tokyo, Japan) and adjusted by the E-beam power to reach the film thickness of 150 nm.

The structure of ITO thin films deposited on glass substrates was analyzed by X-ray diffraction patterns (SIMENS D5000, Simens, German). The XRD patterns were collected in the 2θ range of 20–65° with 4°/min using a Cu Kα, $\lambda = 1.54056$ Å, radiation operated at 30 kV and 30 mA. The Scherrer formula was used to calculate the grain size, D [5].

$$D = (\lambda \times 0.89)/(B \times \cos\theta) \tag{97.1}$$

where λ is the wave length of x-ray, $\lambda = 1.54056$ Å, B:full width half maximum, θ:diffraction angle.

The transmittance of thin film and glass was measured by UV–VIS spectrophotometer (HP Agilent 8453, Santa Clara, CA, USA) at 350–750 nm. The resistivity of ITO films was measured by 4-probe method with Keithley 236 (Keithley Instruments, Inc., Cleveland, Ohio, USA).

97.3 Results and Discussion

97.3.1 Structure

The structure of the ITO thin films prepared at various oxygen pressures was analyzed by X-ray diffraction as shown in Fig. 97.1 which shows the crystallized ITO thin film could be deposited at various oxygen pressures. The diffraction peaks of (222), (400) and (440) planes were detected, although the (440) plane was not detected at low oxygen pressure. Because the ITO thin film is an oxide ceramic which needs oxygen atom to construct the suitable structure. Lower oxygen pressure is not suitable for crystal formation, thus it was found a sharper peak was detected at oxygen pressure of 1×10^{-3} Torr and the (440) diffraction peak was also detected. Son et al. [6] deposited the ITO thin film on PET substrate with/without oxygen pretreatment, who found the crystalline ITO could be prepared after oxygen pretreatment. They also found the preferred orientation of (222) for non-treated substrate as the result shown in Fig. 97.1. When prepared ITO films at 1×10^{-2} Torr, the prepared ITO film with preferred orientation of (400) was found. In Fig. 97.1, it was found the peak intensity of (400) increases with the oxygen pressure increasing. Park et al. [7] reported that grains are aligned in (222) and (400) direction and changes from (222) to (400) direction with the increasing oxygen flow rate. In Fig. 97.1, the d spacing of (222) planes are about 0.2985 nm which are similar when prepared at various oxygen pressures; however, it is larger than the standard d_0 value, 0.2923 nm. Meng et al. [8] reported the d spacing of (222) planes increased with oxygen flow rate increasing and it reached a maximum value of about 0.2985 nm. It means that a tensile strain was formed in these films.

The grain size of ITO thin film along the (222) direction has been estimated using Scherrer formula and the grain size increased with the increase of oxygen pressure as shown in Fig. 97.2. It means that the higher oxygen pressure is favourable to form bigger grains in the ITO films deposition process.

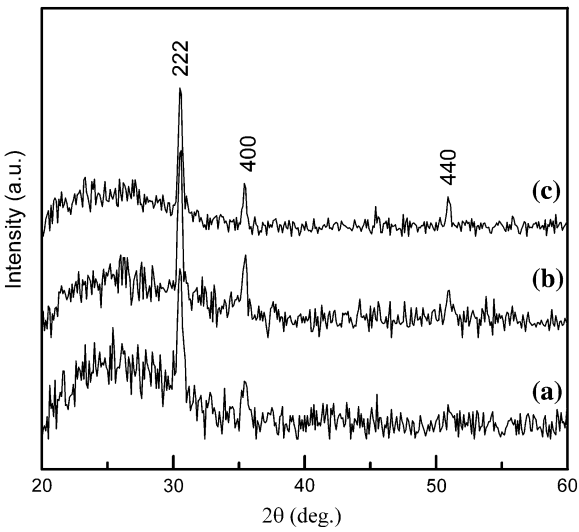

Fig. 97.1 The XRD patterns of ITO thin film prepared at oxygen pressure of **a** 1×10^{-4} Torr, **b** 5×10^{-4} Torr and **c** 1×10^{-3} Torr

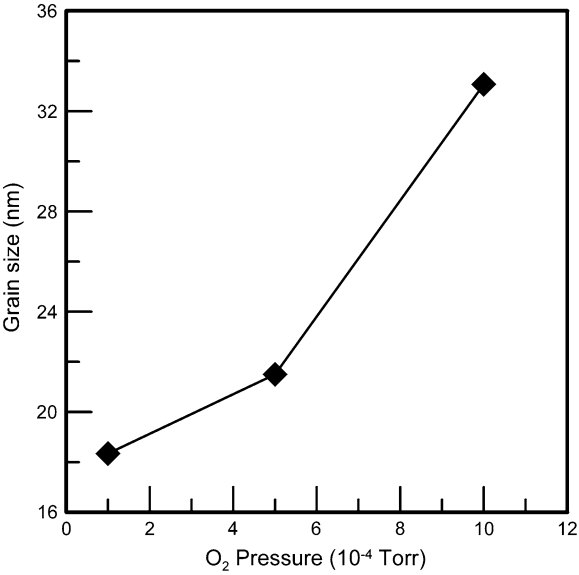

Fig. 97.2 The grain size of ITO thin film prepared at various oxygen pressures

97.3.2 Resistivity and Transmittance

The resistivity of ITO thin films was measured by four probe method and it was plotted as a function of oxygen pressure as shown in Fig. 97.3. The resistivity decreased with the oxygen pressure increasing. It may be caused by more condense morphology (not show here) and larger crystalline grain at higher oxygen

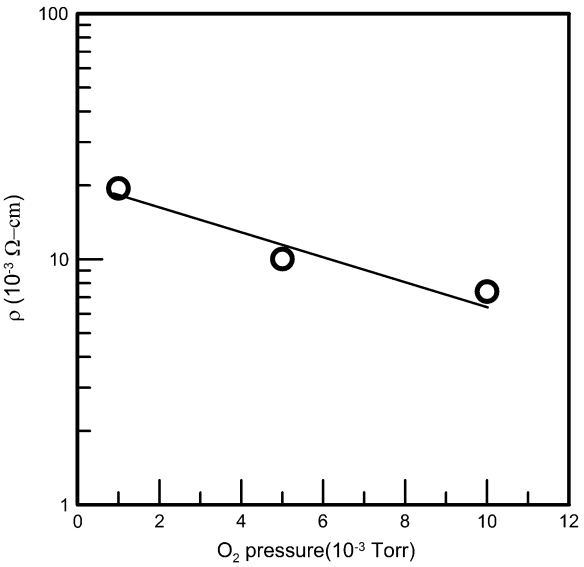

Fig. 97.3 The resistivity of ITO thin film as a function of oxygen pressure

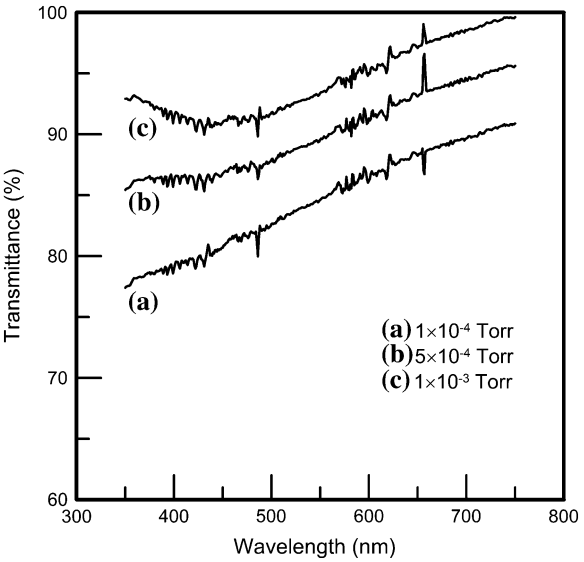

Fig. 97.4 Transmittance of ITO thin film as a function of oxygen pressure

pressure. Meng et al. [8] and Yamaguchi et al. [9] also reported that the resistivity decreased with the oxygen flow rate increasing. Kim et al. [10] prepared the ITO thin film on PET substrate by dc-sputter. They reported the similar trend, where the resistivity of ITO film decreased with oxygen pressure increasing. The influence of oxygen admixture and deposition pressure was investigated by Kim et al. [11] who pointed out the resistivity decreased with oxygen pressure increasing when the oxygen admixture is low which could not change the rf-plasma condition.

The transmittance of ITO films as a function of oxygen pressure was shown in Fig. 97.4. The condense morphology and larger grain size will reduce the reflection of thin film owing to less surface and grain boundary scattering to increase the transmittance. Yamaguchi et al. [9] also reported the similar result for ITO prepared by e-beam evaporation. Young-Soon Kim et al. [11] reported the transmittance increases with the deposition pressure (oxygen pressure) and the transmittance is higher than 80 %. When the deposition pressure (oxygen pressure) is high, i.e. 1×10^{-3} Torr, the transmittance is higher than 90 %.

97.4 Conclusions

The deposition parameter of oxygen pressure plays an important role in ITO thin film preparation by way of E-beam evaporation. The crystallinity of ITO films increases with oxygen pressure increasing. The grain size of ITO films increased with the oxygen pressure increasing. The resistivity decreased with oxygen pressure increasing, however, the transmittance increased. It may be caused by condense morphology and larger grain. These results suggested that the deposition parameter of oxygen pressure plays an important role in ITO thin film preparation.

Acknowledgments This study great thank for Dr. Yuan-Shing Liu who supported the experimental equipment.

References

1. Ahn, J. H., Lee, J.-U., & Kim, T. W. (2007). Impedance characteristics of ITO/Alq_3/Al organic light-emitting diodes depending on temperature. *Current Applied Physics, 7*, 509–512.
2. Granqvist, C. G., & Hultåker, A. (2002). Transparent and conducting ITO films: new developments and applications. *Thin Solid Films, 411*, 1–5.
3. Kachouane, A., Addou, M., Bougrine, E. L., Idrissi, A. B., Messoussi, R., Regragui, M., Bernede, J. C. (2001). Preparation and characterisation of tin-doped indium oxide films. *Materials Chemistry and Physics*, *70*, 285–289.
4. Park, Y.-C., Kim, Y.-S., Seo, H.-K., Ansari, S. G., & Shin, H.-S. (2002). ITO thin films deposited at different oxygen flow rates on Si(100) using the PEMOCVD method. *Surface and Coatings Technology, 161*, 62–69.
5. Cullity, D. (1978). *Elements of X-ray Diffraction* (2nd ed.). MA: Addison-wesley.
6. Son, P. K., Choi, S.-W., & Kim, S. S. (2012). Indium tin oxide exhibiting high polycrystallinity on oxygen plasma-treated polyethylene terephthalate surface. *Nanoscale Research Letters, 7*(118), 1–4.
7. Park, S.-M., Ebihara, K., Ikegami, T., Lee, B.-J., Lim, K.-B., & Shin, P.-K. (2007). Enhanced performance of the OLED with plasma treated ITO and plasma polymerized thiophene buffer layer. *Current Applied Physics, 7*, 474–479.

8. Meng, L.-J., Gao, J., Silva, R. A., & Song, S. (2008). Effect of the oxygen flow on the properties of ITO thin films deposited by ion beam assisted deposition (IBAD). *Thin Solid Films, 516*, 5454–5459.
9. Yamaguchi, M., Ide-Ektessabi, A., Nomura, H., & Yasui, N. (2004). Characteristics of indium tin oxide thin films prepared using electron beam evaporation. *Thin Solid Films, 447–448*, 115–118.
10. Kim, H. H., Cho, M. J., Lim, K. J., Shin, J. H., Park, J. I., & Ahn, J. I. (2002). RF Bias Effect of DC Reactively Sputtered ITO Filmson PET at Room Temperature. In: *proceeding of International Conference on Electrical Engineering*, (pp. 1257–1259). Korea: Jeju Island.
11. Kim, Y.-S., Park, Y.-C., Ansari, S. G., Lee, J.-Y., Lee, B.-S., & Shin, H.-S. (2003). Influence of O_2 admixture and sputtering pressure on the properties of ITO thin films deposited on PET substrate using RF reactive magnetron sputtering. *Surface and Coatings Technology, 173*, 299–308.

Chapter 98
Prepare AFZO Thin Film Based Hydrogen Sensor for Anaerobic Hydrogen Fermentation System

Hung Peng Chang, Hoang Jyh Leu, Xiang-Ling Lin, Chiu Yue Lin and Hong-Hsin Huang

Abstract In this study, aluminum and fluorine-doped zinc oxide (AFZO) thin film was used for hydrogen sensing. A compound of ZnO, ZnF_2 and Al_2O_3 was sintered at 1060 °C as a target and then deposited on glass using a radio frequency (RF) magnetron sputtering. The content of Al_2O_3 in AFZO is essential for the sensing performance improvement of anaerobic hydrogen fermentation system. On-line hydrogen measurement for anaerobic fermentation is an important technology. The on-line hydrogen sensor made of conducting thin film, AFZO, was designed to be used in reducing interferences in gas and liquid phase determination. The aluminum and fluorine-doped thin film has higher electric conductivity and chemical stability than those with the other components. The evaluation of the expected performance of this sensor in each component of anaerobic hydrogen fermentation system was carried out by means of the performance test in ambient air temperature and atmospheric pressure. The sensor performance in liquid phase was investigated by means of amperometry at 0.2 V(vs. Ag/AgCl). This sensor exhibited stable output and fast response when the hydrogen concentration in the gas or liquid phase was changed during anaerobic hydrogen fermentation.

Keywords AFZO · RF magnetron sputtering · On-line · Anaerobic fermentation · Amperometry

H. P. Chang · H. J. Leu (✉) · C. Y. Lin
Green Energy Development Center, Feng Chia University, Taichung 40724, Taiwan, Republic of China
e-mail: hjleu@fcu.edu.tw

H. J. Leu · X.-L. Lin
Department of Fiber and Composite Materials, Feng Chia University, Taichung, Taiwan, Republic of China

H.-H. Huang
Department of Electrical Engineering, Cheng Shiu University, Kaohsiung 83347, Taiwan, Republic of China

J. Juang et al. (eds.), *Proceedings of the 2nd International Conference on Intelligent Technologies and Engineering Systems (ICITES2013)*, Lecture Notes in Electrical Engineering 293,
DOI: 10.1007/978-3-319-04573-3_98,

98.1 Introduction

Hydrogen gas is joining electricity and fossil fuels as a primary energy source, with the superiority of higher energy efficiency, near zero polluting emissions and being renewable. Reliable, cheap, and compact sensors are therefore in high demand to measure H_2 concentration in anaerobic hydrogen fermentation system and to monitor gas leak during H_2 production, storage, transportation and utilization. This is required not only for better control of H_2 involved processes, but for health and safety reasons as well.

Hydrogen is an inflammable gas. Under normal conditions, it is easy to explode [1], if hydrogen concentrations ranging between 4.65 and 74.5 % in air. Hence, the hydrogen detection is an important problem. Sensors can be used simply to identify the presence of hydrogen or to measure its concentration. Quantification of hydrogen concentration is important at the ppm level for the analysis of impurities, at the Lower Flammable Limit (LFL) level of 4 % hydrogen in air for safety applications or at higher concentrations for monitoring and controlling processes. Interaction of hydrogen with the sensing element of a hydrogen detection device can cause changes in temperature, refractive index, electrical properties and mass as well as mechanical changes. A transducer is needed to transform these changes into an electrical signal.

Electrochemical sensors detect changes in charge transport or electrical properties due to electrochemical reactions occurring at a sensing electrode. The earliest electrochemical cells were investigated by Kohlrausch [1] in 1885 and Haber [2, 3] in the early 1900s. The first such cells applied to sensing were Clark electrodes used for oxygen determination [4] and the first electrochemical cell used in hydrogen detection was suggested by LaConti and Maget [5] in the 1970s. The state of the art in electrochemical hydrogen sensing has recently been reviewed by Korotcenkov et al. [6].

Amperometric sensors work at a constant applied voltage and the sensor signal is a diffusion limited current. A review of amperometric gas sensors is given by Stetter and Li [7]. In previous researches [8, 9], the amperometric H_2 sensor has been developed for the in situ determination of hydrogen containing aqueous solutions. Therefore, the sensor is suitable for direct measurements in coloured and turbid solutions and in sediments. Special applications of the sensor are the measurement in deep sea volcanic areas, measurements in the condensate of compost factories and in power stations, but also in the chemical industry to follow chemical reactions.

Aluminum and fluorine-doped zinc oxide (AFZO) thin films have been deposited by many methods such as spray pyrolysis [10], chemical vapor deposition [11], pulsed laser deposition [12], and magnetron sputtering [13]. Among these techniques, magnetron sputtering has attracted great interest because of the inherent ease with which the deposition conditions can be controlled.

Metal oxide hydrogen sensors are typically based on tin oxide. Nevertheless, they have to be operated at elevated temperatures (200–500 °C); and commercially

available sensors usually do not meet detection limits below 1000 ppm of H_2 as they are used to detect hydrogen levels in % range. The need to detect even very low hydrogen concentrations has become increasingly important due to the expanded use of hydrogen as an energy carrier and as a chemical reactant. Thus, new sensitive, fast, and cost-effective hydrogen sensors operated at room temperature became important. Palladium has been proposed as a candidate to realize such sensors. Hydrogen reacts very fast with palladium making palladium hydride with different electrical and physical properties. Hydrogen sensors based on palladium continuous or nanogranular thin films have been reported. On one side, hydrogen sensors show good performance, but on the other side, price of this precious metal is increasing continuously, which makes palladium-free sensors attractive. In here, we report on palladium-free room-temperature hydrogen sensor based on AFZO.

98.2 Experimental Procedure

AFZO powder (Al_2O_3 = 0–4 mol %, ZnF_2 = 1.5 mol %, ZnO 98.5–94.5 mol %) was calcined at 600 °C and sintered at 1060 °C to prepare the ceramic target. Then, it was deposited on glass using a radio frequency (RF) magnetron sputtering. Before the deposition process was started, the base chamber pressure was pumped to less than 5×10^{-6} Torr, and then the deposition pressure was controlled at 5×10^{-3} Torr. In here, the AFZO thin films were deposited at different temperatures from RT to ~200 °C. The optimal condition for this hydrogen sensor is at 100 °C. The structure of FZO thin films was examined by X-ray diffraction (XRD) (PANalytical) analysis in a θ–2θ mode with Cu-Kα radiation (λ = 1.54056 Å). The film morphology was observed by using field emission scanning electron microscopy (FE-SEM) (JEOL, JSM–6700F).

For voltammetric measurements, a three-electrodes cell was used equipped with working, counter, and a reference electrodes [14]. The volume of the analyzed sample was 100 mL, and all measurements were performed at 25 °C using 0.05 mol/L H_2SO_4 solution as supporting electrolyte. All voltammograms were recorded for static solutions. Before each determination, the Pt working electrode was cleaned mechanically, by polishing it on alumina (Merck, 63–200 μm granularity) and electrochemically, by applying a −1.5 V potential pulse for 3 s. For each measurement, the potential was scanned within the range −100 and −1000 mV, with a 50 mV/s scan rate, and the value of the backround current obtained for the 0.05 mol/L H_2SO_4 solution was substracted from the current corresponding to the analyzed solution/sample.

The sensor was characterized by flow injection analysis (FIA) at room temperature. Hydrogen and carbon dioxide were premixed for simulating bio-hydrogen. The mixtures of the gases were supplied through flow controllers to a 500 mL liquid bottle (with 100 mL liquid electrolyte) by a sampler mounted inside. Its electrical response versus time was recorded using a potentiostat with amperometric method.

The liquid samples with mixed bio-gas were injected to the AFZO electrode of flow cell for measurement. A sequence of several gas mixtures of the same volume with increasing concentration of hydrogen was applied to the sensor. The buffer was purged with the nitrogen after each application of the target mixing gas.

98.3 Results and Discussion

In this study, the aluminum and fluorine co-doped ZnO films were maintained at relatively constant level, and the effects of Al_2O_3 in AFZO films were investigated to obtain the best condition for sensing applications in anaerobic hydrogen fermentation system. The detailed compositions of four AFZO thin films were compared in Table 98.1 for further discussion.

In order to realize the surface conditions of AFZO thin films, the FE-SEM was used for film morphology investigation in Fig. 98.1. From the FE-SEM images of FZO and AFZO films, these AFZO films are based on different Al contents, i.e. 0 (as-dep.), 1, 2, and 4 wt%. There are some inhomogeneous surfaces for the FE-SEM images, which are seen at dark and light areas. This denotes that the inhomogeneous surfaces are due to only the surface topography and not to the chemical composition differences within the samples. Under these conditions, any difference in atomic mass within the film would be seen. Moreover, they would not relate to SEM images. Al though we present SEM images only for four samples, the results for other AFZO films are identical. Even for the Al content of 4 wt%, no foreign Al phases are seen.

In Fig. 98.2a, the XRD patterns for FZO and AFZO films were shown for comparison. All the samples are polycrystalline, but the crystallographic quality improves with the increase of Al composition, up to 2 wt%. For the 2 wt%-Al sample, (002) peak dominates. Together with the increase of (002) reflection intensity, the lateral mean grain size decreases as shown in Fig. 98.2b. Based on XRD data, mean grain size was calculated for perpendicular the film surface. From FWHM values for (002) diffraction peaks, the obtained grain size value increases from 22 (for undoped sample) to 25 nm (for 2 wt% of Al), and then it decreases to 20 nm (for 4 wt% of Al). The higher values of grain size indicate more oriented and columnar growth of AZO films for Al content up to $\sim$4 wt%. Therefore, introduction of Al facilitates the growth in c-axis mode, however, for higher Al content, more amorphous-like growth occurs. This corresponds to the increased (002) intensities for 1–2 wt% Al samples.

In Fig. 98.3, several voltammograms, obtained for different hydrogen concentrations, are presented. The peak that appeared at 250 mV (vs. Ag/AgCl) was attributed to hydrogen oxidation. As can be seen from Fig. 98.3, the reduction peak appears at 25 mV (vs. Ag/AgCl). This confirms that electrochemical redox of hydrogen is a reversible process for AFZO thin film electrode. In addition, the reversible peak at -500 mV is due to oxygen redox reactions.

Table 98.1 The composition of four kinds of thin film electrodes

	FZO (wt%)	A_1FZO (wt%)	A_2FZO (wt%)	A_4FZO (wt%)
ZnO	98.5	97.5	96.5	94.5
Al_2O_3	0	1	2	4
ZnF_2	1.5	1.5	1.5	1.5

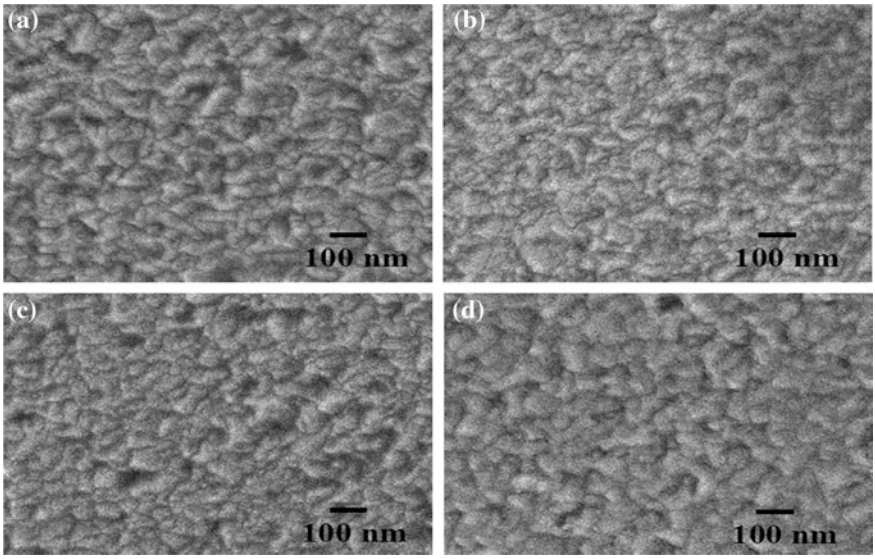

Fig. 98.1 The FE-SEM images of thin film electrodes. **a** FZO, **b** 1 wt% Al_2O_3:FZO, **c** 2 wt% Al_2O_3:FZO and **d** 4wt% Al_2O_3:FZO

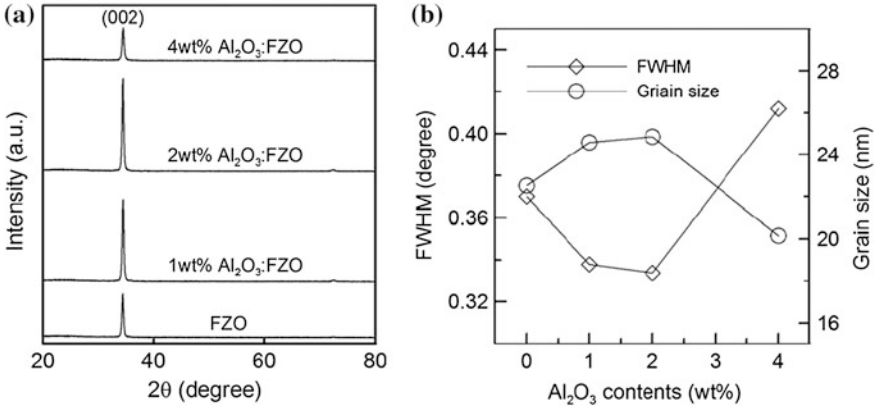

Fig. 98.2 The comparison of **a** X-ray diffraction spectra and **b** FWHM and grain size

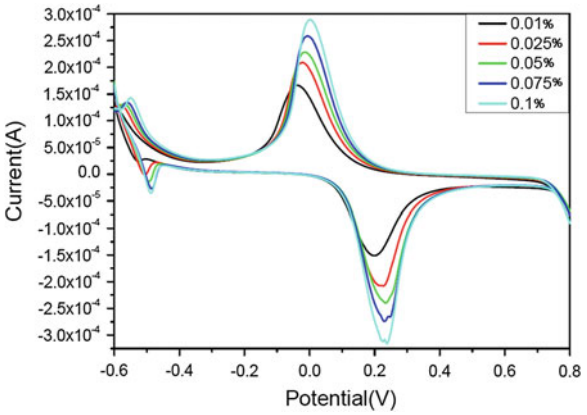

Fig. 98.3 The voltammograms of different hydrogen concentrations between 0.01 and 0.1 % for AFZO electrode in 0.05 mol/L H_2SO_4 solution (50 mV/s scan rate)

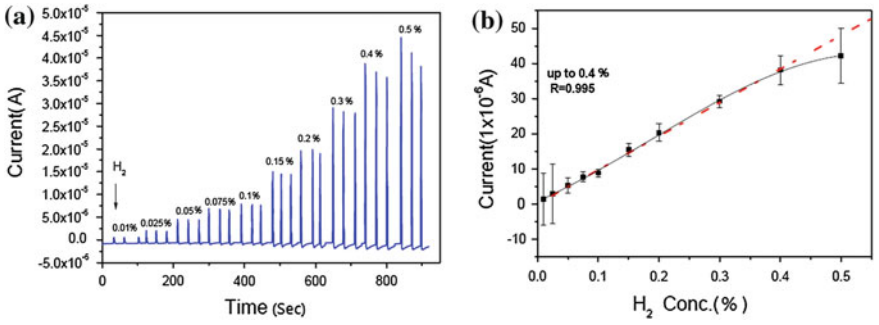

Fig. 98.4 **a** The actual response and **b** the calibration graph of different hydrogen concentrations between 0.01 and 0.1 % for AFZO electrode in 0.05 mol/L H_2SO_4 solution for anaerobic hydrogen fermentation water

The evaluation of the expected performance of this sensor in each component of anaerobic hydrogen fermentation system was carried out by means of the performance test in ambient air temperature and atmospheric pressure. The sensor performance in liquid phase was investigated by means of amperometry at 0.2 V(vs. Ag/AgCl). This sensor exhibited stable output and fast response when the hydrogen concentration in the gas or liquid phase was changed during anaerobic hydrogen fermentation. The actual response and calibration graph in Fig. 98.4 were shown a linear range up to 0.4 % obtained between 0.01 and 0.5 % hydrogen ($r^2 = 0.9995$, $y = 8.91x + 1.0903$). The value calculated for r.s.d. was 3.64 % in FIA ($c = 0.1$ % H_2; $n = 3$,).

98.4 Conclusions

The developed method has proved its accuracy in hydrogen determination in anaerobic hydrogen fermentation water. The highest values for hydrogen were obtained from fermentation water. The detection limit of the method was of 0.03 % (calculated as 3x, the standard deviation of the blank signal), and the limit of quantification was 0.1 % (calculated as 10x, the standard deviation of the blank signal). This hydrogen sensor exhibited stable output and fast response for on-line measurement of bio-hydrogen in gas-liquid separator of anaerobic hydrogen fermentation system.

Acknowledgments We are grateful for the financial support from Feng Chia University (No: 11G27150).

References

1. Kohlrausch, F. (1885). *Wiedemann's Annalen, 262*, 161.
2. Haber, F., & Moser, A. (1905). Das Generatorgas- und das Kohlenelement. *Zeitscrift für Elektrochemie, 11*, 593.
3. Haber, F., & Fleischmann, F. (1906). Uber die Knallgaskette. I. Mitteilung, *Zeitschrift für anorganische und allgemeine Chemie*, *51,* 245.
4. Clark, L. C., Wolf, R., Granger, D., & Tylar, Z. (1953). *Journal of Applied Physiology, 5*, 189.
5. LaConti, A. B., & Maget, H. J. R. (1978). *Journal of the Electrochemical Society, 118*, 506.
6. Korotcenkov, G., Han, S. D., & Stetter, J. R. (2009). *Chemical Reviews, 109*, 1402.
7. Stetter, J. R., & Li, J. (2008). *Chemical Reviews, 108*(2), 352.
8. Weng, Y. C., et al. (2009). *Sensors & Actuators, B: Chemical, 141*, 161.
9. Chao, Y., Yao, S., Buttner, W. J., & Stetter, J. R. (2005). *Sensors & Actuators, B: Chemical, 106*, 784.
10. Ratheesh Kumar, P. M., Sudha Kartha, C. K., Vijayakumar, P., Singh, F., & Avasthi, D. K. (2005). *Materials* Science *and Engineering* B, *117*, 307.
11. Hu, J., & Gordon, R. (1991). *Solar Cells, 30*, 437.
12. Cao, L., Zhu, L., Jiang, J., Zhao, R., Ye, Z. Z., & Zhao, B. H. (2011). *Solar Energy Materials and Solar Cells, 95*, 894.
13. Choi, B. G., Kim, I. H., Kim, D. H., Lee, K. S., Lee, T. S., Cheong, B., et al. (2005). *Journal of the European Ceramic Society, 25*, 2161.
14. Wawrzyniak, J., Ryniecki, A., & Zembrzuski, W. (2005). *Acta Scientiarum Polonorum-Technologia Alimentaria, 42*(2), 5.

Chapter 99
Performance Improvement of the Triple-Band Monopole Plain Antenna by the Grounding Surface Design with the Method of Particle Swarm Optimization

Ming-Chih Huang, Chien-Yuan Liu, Ming-Huei Chen, Sung-Te Lin and Hong-Hsin Huang

Abstract This article presents a research concerning the influence of the grounding surface for a triple-band G-shape monopole plane antenna based on a PSO algorithm. The PSO algorithm utilizes fewer computation and concise program code in comparison with a GA algorithm, and could solve the optimal grounding surface by added with weighting inertia. The design procedure and fabrication steps for an antenna are applied and simulated for triple-band wireless applications. The proposed PSO algorithm provides better precision, faster convergence, and shorter time for solving the global optimal solution.

Keywords PSO · Grounding surface · Triple-band · Micro-strip · Antenna

M.-C. Huang
Department of Electrical Engineering, Yung Ta Institute of Technology and Commerce, Pingtung County, Taiwan, Republic of China

C.-Y. Liu (✉)
Department of Computer Science and Information Engineering, Cheng Shiu University, Kaohsiung, Taiwan, Republic of China
e-mail: cyliu@csu.edu.tw

M.-H. Chen · S.-T. Lin
Department of Electronic Engineering, National Kaohsiung First University of Science and Technology, Kaohsiung, Taiwan, Republic of China

H.-H. Huang
Department of Electrical Engineering, Cheng Shiu University, Kaohsiung, Taiwan, Republic of China

J. Juang et al. (eds.), *Proceedings of the 2nd International Conference on Intelligent Technologies and Engineering Systems (ICITES2013)*, Lecture Notes in Electrical Engineering 293,
DOI: 10.1007/978-3-319-04573-3_99,

99.1 Introduction

Global optimization is critical in research. The problem is usually solved by probabilistic algorithms. Basically, the global searching is classified into two kinds. The first one is nonlinear programming; the second is the probabilistic, e.g. genetic algorithms (GA). GA denotes variables of a problem in form of binary chromosomes. Next, selection, crossover, and mutation of the chromosomes are continuously evolved to adapt to the space. The convergent solution usually is a local optimum. With the assistant of random process, it is able to extend to a global optimum.

Grounding surface design for an antenna is pertained to global optimization problem. The goal of antenna design for the mobile application is focused on modularizing and downsizing. The research of this article adopted the particle swarm optimization (PSO) method to design the grounding surface for a triple-band G-shape antenna. PSO is powerful and has following features:

1. Accurate and fast searching during optimization. It will reduce computing time for solving the problem of complex or compound constraints.
2. No pre-transformation and less parameters. The solution of each particle in PSO is an optimal solution of the design space. Hence, none transformation is needed.
3. Easy to program with parallel. Eventually, only one exchanging is necessary between the optimal solutions of all particles and the global space.

In comparison with GA, the advantage of PSO is easier to implement and without the process of transformation in advance. PSO is popular for the applications of fuzzy control and function optimization, especially for the problems of complex and multi-extreme functions.

99.2 Particle Swarm Optimization Algorithm

99.2.1 Background of the Algorithm

PSO is a population-based searching technique. It is proposed in 1995 by James Kennedy and Russell Eberhart who were inspired by the observation of the foraging social behavior of bird crowd. There are various versions of PSO [1–5]. The research of [6] studied the convergence and parameters selection for solving the searching optimization problems.

The concept of particle population could be deemed as a simple social system. Each entity has its own solution and is named as a particle. Each particle has a fitness value measured from a fitness function. The direction and displacement of a particle is guided by a velocity parameter. Each particle is even distributed in the

solving space and communicates to each other directly or indirectly for gradually moving itself to the optimal position. Therefore, PSO is viewed as an optimized searching method for pursuing the optimal particle in the solving space [7].

In PSO, the moving direction of a particle is affected by the current optimal solution. The pbest denotes the optimal position of the particle up to now. The nbest denotes the optimal position of each neighbor. In the local PSO version, the pbest and nbest are utilized as the basis of the position update for the particle. In contrast, the global version treats all other particles as the neighbors of the particle. The gbest denote the optimal positions of all neighbors, hence, gbest is an instance of nbest.

99.2.2 Procedure of the Algorithm

In the global PSO version, the procedure of the algorithm [8] is listed as below,

Step 1 Initialize all particles with random position and speed for a d-dimension problem space.

Step 2 Calculate the fitness value by a fitness function for each particle.

Step 3 Compare the fitness value of the particle to the pbest of it. Assume that the fitness value is better than the pbest, then, update the pbest with the fitness value and its position.

Step 4 Compare the fitness value of the particle to the gbest of all others. Assume that the fitness value is better than the gbest, then, the gbest is replaced with the fitness value and its position.

Step 5 Adjust the speed and position of all particles according to formulae (99.1), (99.2).

$$V_{id}(t) = V_{id}(t-1) + c_1 * rand() * (P_{id} - X_{id}) + c_2 * rand() * (P_{gd} - X_{id}) \tag{99.1}$$

$$X_{id}(t) = X_{id}(t-1) + V_{id}(t) \tag{99.2}$$

where $V_{id} \in \lceil -V_{max}, V_{max} \rceil$, V_{id} and X_{id} are the speed and the position of the ith particle in d-dimension, respectively. c_1, c_2 are the learning factors and are usually set to 2.0 or 1.49445. P_{id} is the optimal position solution of the particle so far. P_{gd} is the optimal position solution of all neighbors so far. *Rand()* is a uniform random function with a value in [0.0, 1.0].

Step 6 Loop back to step 2 until maximal iterations or the fitness values are achieved.

In the above steps, formula (99.1) calculates new moving speed by using the previous moving speed V_{id}, the optimal position solution so far, and the optimal positions of all neighbors. Then, formula (99.2) updates the particle position.

V_{max} is an important parameter to restrict the speed of a particle. It also affects the searching capability to achieve the target position. If the value is too high, the particle might overshoot over the solution range. On the contrary, the particle would restrict itself in the local optimization. In addition, *h*igher V_{max} would encourage the fully exploration capability. Lower V_{max} would assist the stepwise exploitation capability.

99.3 Simulation and Design of Antenna

Before antenna simulation, we must notice the impedance matching issue. To obtain the maximal power transfer, the impedance of former stage must equally match to that of later stage. For antenna design, the impedance of the feeder line and connectors must match to that of antenna itself. Idea impedance is shown in formula (99.3).

$$\mathrm{Re}[Z_{in}(f)] = 50\ \Omega; \mathrm{Im}[Z_{in}(f)] = 0 \tag{99.3}$$

where Re[Z_{in}(f)] and Im[Z_{in}(f)] is respectively the real part and the image part of the impedance at the resonant frequency of the antenna and feeder line. Since we adopted the approximate model for simulation, in which the electromagnetic field is treated as a closed surface rather than an infinitive free space. Typical impedance of general radio circuit is 50 Ω. Therefore, formula (99.3) is the target of the design.

During antenna design, how many bands and what the requirements about the bandwidth, and the physical copper area of the antenna are the critical specification we must consider. After the specification is defined, we choose the geometric sharp, the feeding type, and the bandwidth of the antenna. Next, the antenna is analyzed through simulation software. Suppose the result of simulation conforms to the specification, the structure of the antenna would be implemented by the layout tools of OrCAD or Protel DxP. Then, the antenna could be fabricated by a PCB prototyping machine. And then, the characteristics of the antenna must be measured. If the result conforms to the specification, the design work is completed. Otherwise, the design process must be repeated for modification until it conforms to the requirement. The design and fabrication flowchart for an antenna is shown in Fig. 99.1.

The simulation diagram of input impedance is depicted by the reflection coefficient diagram. When the reflection value is less than −10 dB, it is deemed as a useful bandwidth. Generally, the wider bandwidth is the better characteristic. Table 99.1 is the specification of the triple-band monopole plain antenna. The operating range for lower band is 2.33–2.56 GHz, 3.1–3.82 GHz for middle band, and 4.84–6.17 GHz for higher band. These ranges conform to the specification of IEEE 802.11 a/b/g/n and WiMAX. Figure 99.2 is the evolution flowchart of the PSO algorithm for the triple-band monopole plain antenna. The antenna

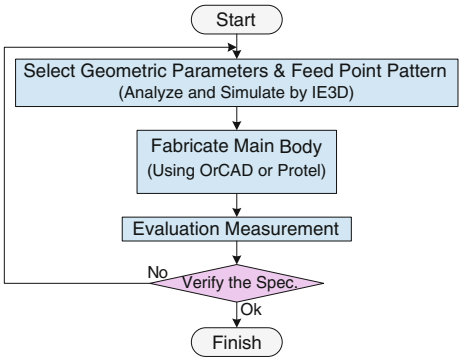

Fig. 99.1 The flowchart of the design and fabrication for an Antenna

Table 99.1 Operating frequencies of WLAN and WiMAX

Wireless systems	Operating frequencies
WLAN	2,400–2,484 MHz, 5,150–5,350 MHz, 5,725–5,875 MHz
WiMAX	2,500–2,690 MHz, 3,300–3,700 MHz, 5,250–5,850 MHz

parameters L_g and W_g are utilized in the flowchart of Fig. 99.2 for the tuning of performance calculation of the PSO algorithm.

A. Initial Population

Ahead of the PSO computation, N chromosomes must be randomly generated. These chromosomes are the initial population. The population size is dependent on the complexity of the solving problem.

B. Specification Design

The parameters L_g and W_g are set up for the optimization. The maximum iteration count is set to 150 and the number of particles is set to 18 for searching the optimal solution. Therefore, the result of the antenna specification is obtained as follows,

$$|S_{11}(f)| < -10\,\text{dB} \quad \text{for} \quad 2.4\,\text{GHz} < f < 2.5\,\text{GHz}, \\ 3.3\,\text{GHz} < f < 3.7\,\text{GHz}, 5.0\,\text{GHz} < f < 6.0\,\text{GHz} \tag{99.4}$$

C. Fitness Evaluation

$$fitness = \sum_{n=1}^{N} (|S_{11}| + 10\Delta f \quad \text{if} \quad |S_{11}| > -10) \qquad 5.0\,\text{GHz} < f < 6.0\,\text{GHz} \tag{99.5}$$

where, Δf is 0.01 GHz frequency interval and N is the number of frequencies.

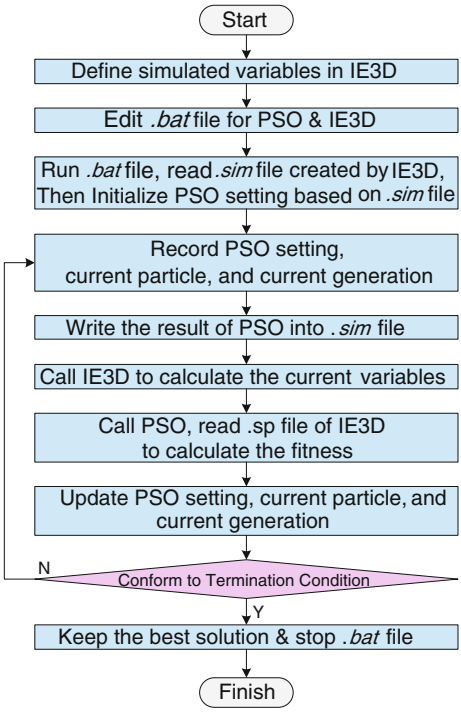

Fig. 99.2 The flowchart of the PSO algorithm for a triple-band monopole plain antenna

99.4 Implementation of the Triple-Band G-Shape Monopole Plain Antenna

The design of traditional dual-band antenna utilizes two resonant circuits to perform the radiation [9–11], e.g. inverted-F [12], dual-U [13], and dual-T [14] monopole antenna. Another design concept applies wider slots [15] or parasitic elements [16] to create multiple resonant modes to realize multi-band and high-bandwidth features for WLAN or WiMAX. Table 99.1 depicts all the operating frequencies. Then, the dimension of grounding surface is added to the PSO. From the result of PSO computation, the optimal antenna dimension could be obtained.

Figure 99.3 illustrates the structure of the triple-band monopole plane antenna. Related parameters of the antenna are listed in Table 99.2. Regarding the antenna, the substrate is made of FR4, the area of the main body is 40×25 mm^2, two paths of radio strips are on the top surface, and the grounding metal is on lower half of the bottom surface. The 50 Ω feeding line is connected to the antenna through a micro strip via a 50 Ω SMA connector for matching the impedances.

The antenna is simulated for its dimensions and current distribution. Figure 99.4a–c illustrate the current distributions of the antenna. Because of longer

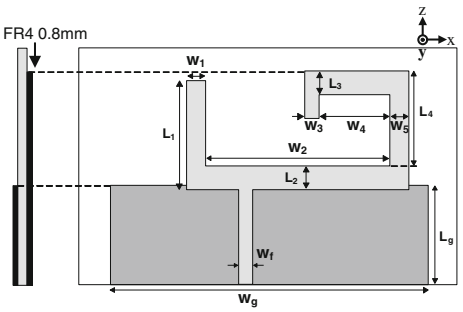

Fig. 99.3 The structure of the triple-band G-shape monopole plain antenna

Table 99.2 The parameters and dimensions of the G-shape antenna

Parameters	Dimensions (mm)	Parameters	Dimensions (mm)
W_g	34	W_4	7.5
L_g	11	W_5	2
W_f	1.5	L_1	12
W_1	2	L_2	2.5
W_2	19.5	L_3	2.5
W_3	1.5	L_4	10

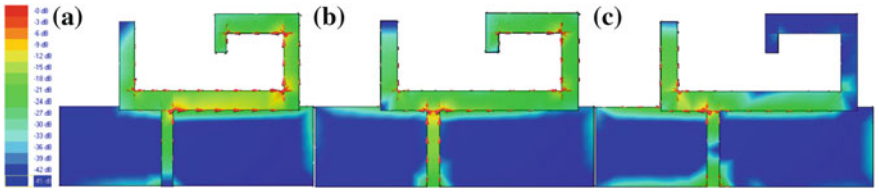

Fig. 99.4 The current distribution diagrams of the G-shape antenna

current loop on the right upper strip, it excites 2.45 GHz mode. On the other side, shorter micro strip on the left upper side excites 5 GHz mode. Then, the grounding metal is coupled to the radio metal with matched impedance under 3.5 and 5.25 GHz.

99.5 Conclusions

The design of a grounding surface affects the performance of a triple-band G-shape monopole plane antenna. The PSO algorithm is proposed for solving the design problem. The PSO algorithm provides concise program code and fewer iteration counts in comparison with a GA algorithm. It also provides higher precision and finer tuning for solving the parameters of the antenna. The designed micro-strip

antenna for triple-band radio communications in the applications of Wi-Fi and WiMAX is simulated and is validates for various operating bands under the matched impedance.

Acknowledgments The authors greatly appreciate to the support of the National Science Council, R.O.C., under the Grant no. NSC 101-2632-E-230-001-NY3.

References

1. Kennedy, J., & Eberhart, R. C. (1995). *Particle swarm optimization*. In Proceedings of IEEE International Conference on Neural Networks (vol. IV, pp. 1942–1948).
2. Shigenori, N., et al. (2003). A hybrid particle swarm optimization for distribution state estimation. *IEEE Transaction on Power Systems, 18*, 60–68.
3. Salman, A., Ahmad, I., & Al-Madani, S. (2002). Particle swarm optimization for task assignment problem. *Microprocessors and Microsystems, 26*, 363–371.
4. Kennedy, J., & Eberhart, R.C. (1997). *A discrete binary version of the particle swarm algorithm*. In Proceedings of IEEE International Conference on Systems, Man, and Cybernetics (pp. 4104–4108).
5. Parsopoulos, K. E., & Vrahatis, M. N. (2002). Recent approaches to global optimization problems through particle swarm optimization. *Natural Computing, 1*, 235–306.
6. Clerc, M., & Kennedy, J. (2002). The particle swarm explosion, stability, and convergence in a multidimensional complex space. *IEEE Transaction on Evolutionary Computation, 6*, 58–73.
7. Hu, X., Shi, Y., & Eberhart, R. C. (2004). *Recent advances in particle swarm*. In Proceedings of IEEE Congress on Evolutionary Computation 2004 (CEC 2004) (pp. 90–97).
8. Eberhart, R. C., & Shi, Y. (2001). *Particle swarm optimization: developments, application and resources*. In Proceedings of the 2001 Congress on Evolutionary Computation, Seoul, South Korea (vol. 1, pp. 81–86).
9. Wu, C. M., Chiu C. N., & Hsu, C. K. (2006). A new non-uniform meandered and fork-type grounded antenna for triple-band WLAN applications. *IEEE Antennas Wireless Propagation Letters, 5*(1), 346–348.
10. Lee, Y., & Seo, Y. M. (2009). Triple-band CPW-fed compact monopole antennas for GSM/PCS/DCS/WCDMA applications. *Electronic Letters, 45*(9), 447–448.
11. Pan, C. Y., et al. (2007). Dual wideband printed monopole antenna for WLAN/WiMAX applications. *IEEE Antennas Propagation Letters, 6*, 149–151.
12. Kuo, Y. L., Cheng, Y. T., & Wong, K. L. (2002). *Printed inverted-F antennas for applications in wireless communication*. In Proceedings of IEEE AP-S International Symposium (vol. 3, pp. 454–457).
13. Chen, I., & Peng, C. M. (2003). Microstrip-fed dual-U-shaped printed monopole antenna for dual-band wireless communication applications. *Electronics Letters*, 39(13), 955–956.
14. Kuo, Y. L., & Wong, K. L. (2003). Printed double-T monopole antenna for 2.4/5.2 GHz dual-band WLAN operations. *IEEE Transaction on Antennas and Propagation, 51*(9), 2187–2192.
15. Jan J. Y., & Su, J. W. (2005). Bandwidth enhancement of a printed wide-slot antenna with a rotated slot. *IEEE Transaction on Antennas and Propagation, 53*(6), 2111–2114.
16. Pan, C. Y., Huang, C. H., & Horng, T. S. (2004). *A novel printed monopole antenna with a square conductor-backed parasitic plane for dual-band WLAN applications*. In Proceedings of IEEE AP-S International Symposium (vol. 1, pp. 261–264).

Chapter 100
Empirical Study of in-Cloud Enterprise Resource Planning System with Access Control Authentication

Bao Rong Chang, Hsiu-Fen Tsai, Ju-Chun Cheng and Yun-Che Tsai

Abstract This paper introduces in-cloud Enterprise Resources Planning (in-cloud ERP) with network security as well as access control authentication using biometrics, where the internal network is totally isolated from external network to enhance in-cloud ERP security Advantages of the cloud system implementation includes significant decrease of hardware cost, centralized monitoring, fast and convenient management, dynamic optimization, highly efficient backup, and excellent performance in operational speed. As a result, in term of operational speed, the proposed approach exclusively outperforms the two well-known benchmark ERP systems, in-house ECC 6.0 and in-cloud ByDesign. Therefore it is good choice to apply this in-cloud ERP system with access control authentication and high network security as information management system in a firm.

Keywords In-cloud enterprise resources planning (in-cloud ERP) · Access control authentication · Biometrics · Intrusion detection · Network security

100.1 Introduction

Hardware, information, and data are the most challenging problems for enterprises, so we can make good use of virtual machine clustering system [1–3] in cloud to solve those problems. This paper introduces in-cloud Enterprise Resources Planning (ERP) [4, 5] in virtualized environment via wired or wireless network

B. R. Chang (✉) · J.-C. Cheng · Y.-C. Tsai
Department of Computer Science and Information Engineering, National University of Kaohsiung, Kaohsiung 81148, Taiwan, Republic of China
e-mail: brchang@nuk.edu.tw

H.-F. Tsai
Department of Marketing Management, Shu Te University, Kaohsiung 82445, Taiwan, Republic of China

J. Juang et al. (eds.), *Proceedings of the 2nd International Conference on Intelligent Technologies and Engineering Systems (ICITES2013)*, Lecture Notes in Electrical Engineering 293,
DOI: 10.1007/978-3-319-04573-3_100,

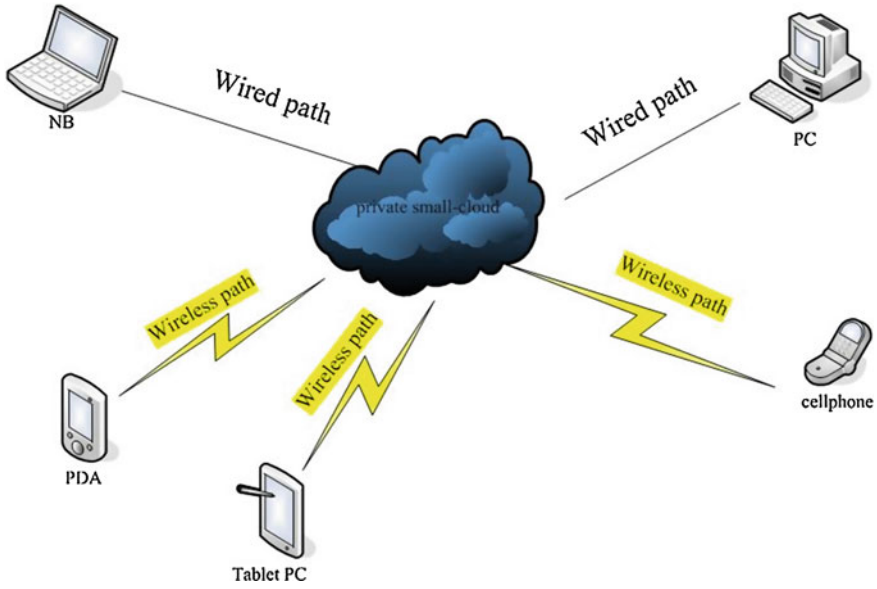

Fig. 100.1 Cloud-Mobile Computing services via wired or wireless network

connected to user devices as shown in Fig. 100.1 and Fig. 100.2, bringing in access control authentication, testing and handling issues on network security [6] in cloud platform. This study makes users connect to ERP in virtual machines via network through PCs, tablets or smart phones. The deployment of a open source ERP application, OpenERP [7], is shown in Fig. 100.3. Any small business adopt this way to attain the virtualized environment in cloud within a firm. Additionally, access control authentication [8, 9] has brought into the virtual machine clustering system in cloud. This function can be utilized in two aspects as follows. One is safe login and logout as well as attendance audit as shown in Fig. 100.4. On the other hand, it can also be applied to identity verification which can ensure all users having the permission to get into make the computing systems secure as shown in Fig. 100.5. Then, detecting potential BotNet [10] and malicious attacks [11] in the network can efficiently increase the network security.

100.2 Cloud Computing-Based ERP System

Virtual machine clustering system in cloud is an integration of virtualization, virtual machines, and virtual services so that it can make existing resources be fully applied, such as VMware ESX/ESXi Server [12], Microsoft Hyper-V R2 [13] or Proxmox Virtual Environment [14]. This system can let users run many operating systems in a single physical computer simultaneously which largely

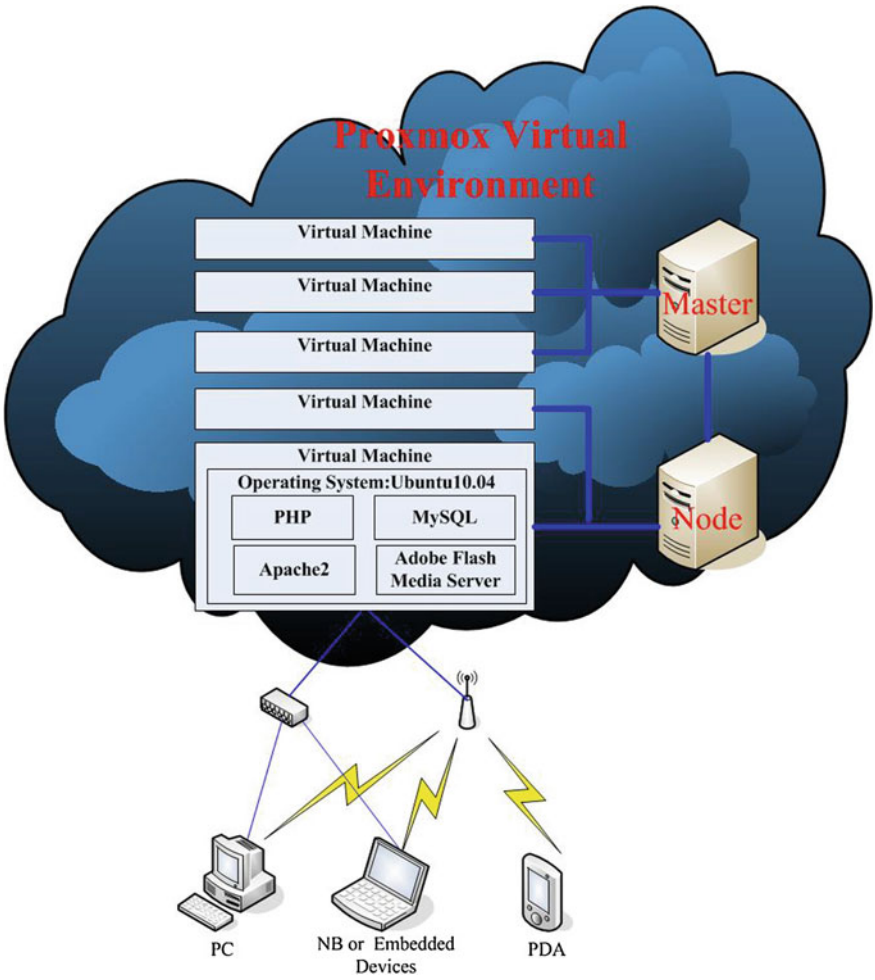

Fig. 100.2 Virtual machine cluster system in cloud (proxmox virtual environment)

decreases the expense of purchasing PCs. Most important of all, it has the following major functions, including virtual machine live migration, virtual storage live migration, distributed resource scheduling, high availability, fault tolerance, backup and disaster recovery, the transfer from physical machines to virtual machines, direct hardware accessing, virtual network switching, and so forth. This study introduces Proxmox Virtual Environment as the cloud computing and service platform with the virtualized environment. The kernel-based virtual machine (KVM) acts as the main core of virtual machine, and it has installed the kernel of Linux-based operating system. OpenERP is adopted in this study as ERP application which provides many solutions for open sources software in the future, having it more expandable, making a great progress on cost deduction.

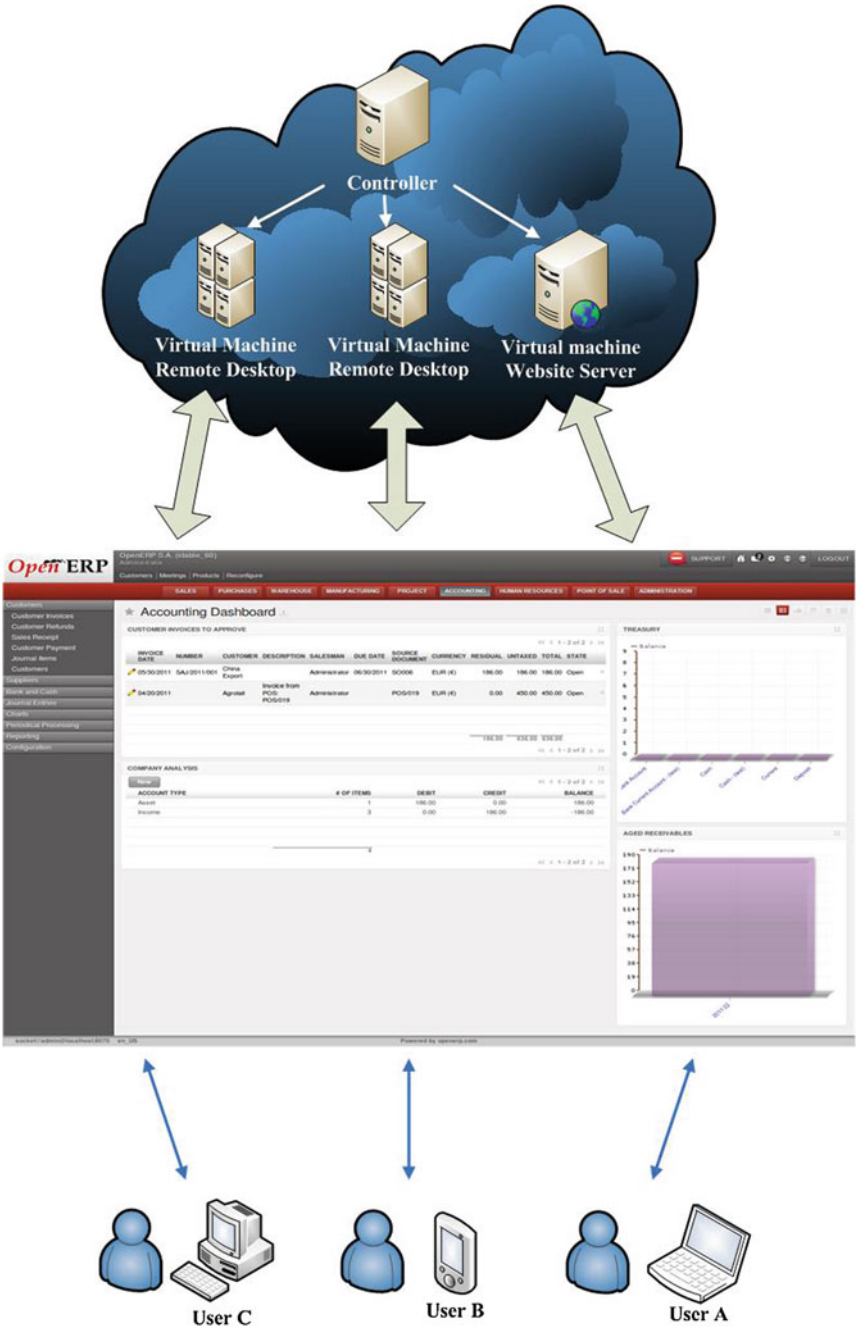

Fig. 100.3 OpenERP deployment. (http://v6.openerp.com/node/910)

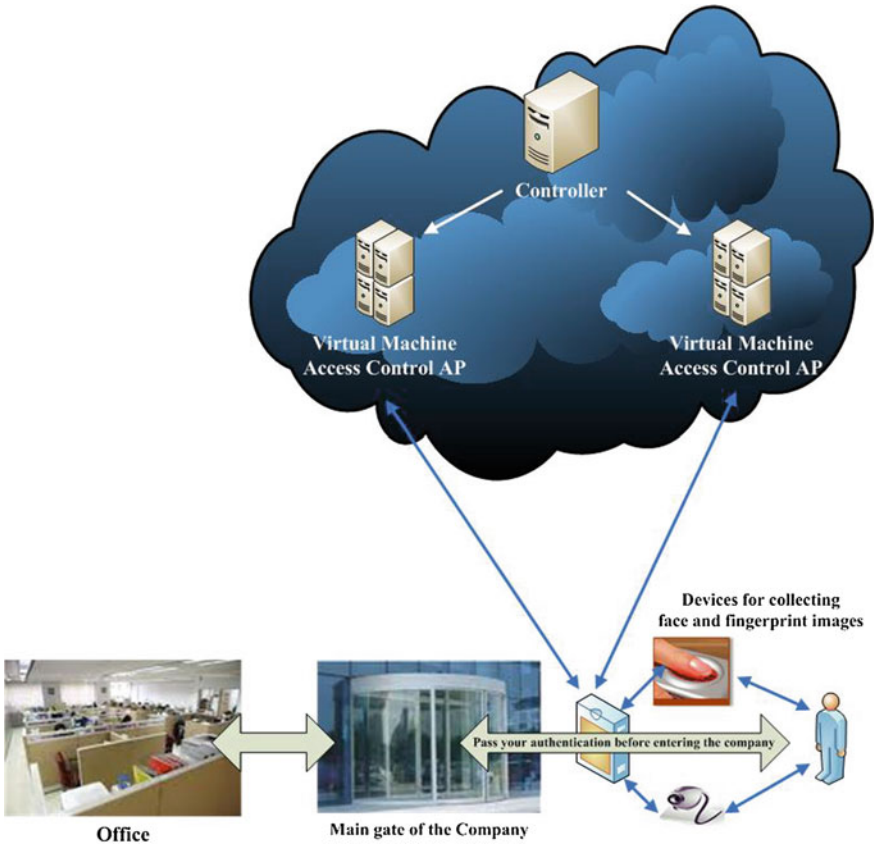

Fig. 100.4 Access control in a firm

100.3 Method

100.3.1 ERP Deployment

The method has been explored in this paper including many aspects as follows:

1. Build Proxmox VE virtual machine clustering server, and manage the virtual machine via WebPages. The webpage of login and management are shown individually as shown in Figs. 100.6 and 100.7.
2. Create a virtual machine and set up its guest operating system in Proxmox VE virtual machine clustering server.
3. Set up OpenERP software package in virtual machine, inclusive of OpenERP AP, PostgreSQL database, and Web interface for end-user. Installation process is shown in Fig. 100.8 and the completion of installation in Fig. 100.9.

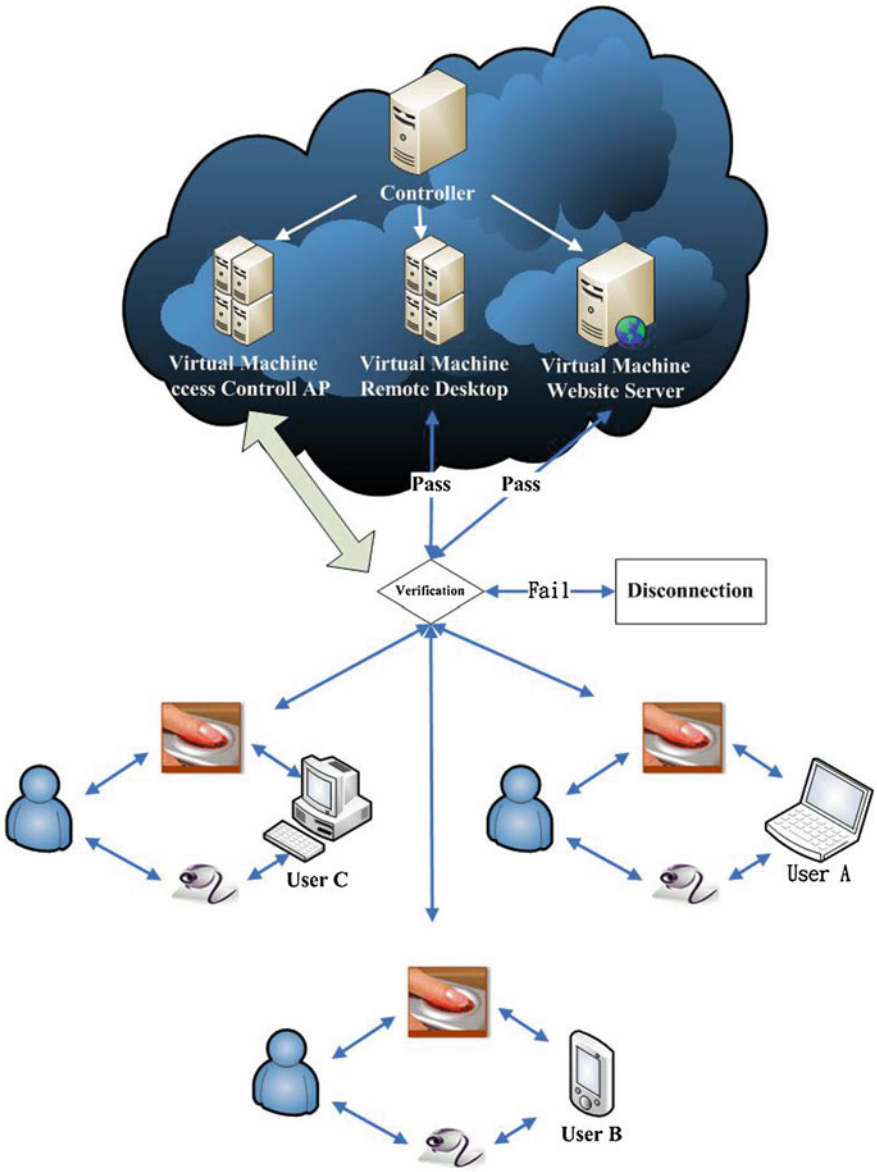

Fig. 100.5 Access control authentication in cloud

4. Key in http://localhost:8096 or http://IP:8096 at browser in virtual machine, pop up into OpenERP login page as shown in Fig. 100.10, and then login to administrator to install the necessary modules resulted in an interface of the user management as shown in Fig. 100.11.

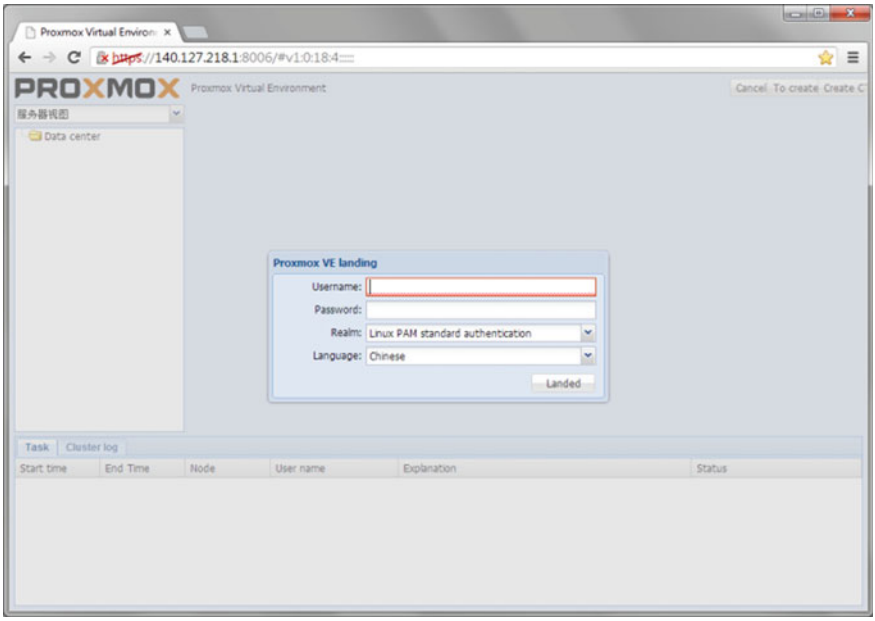

Fig. 100.6 Login to Proxmox VE virtual machine cluster server

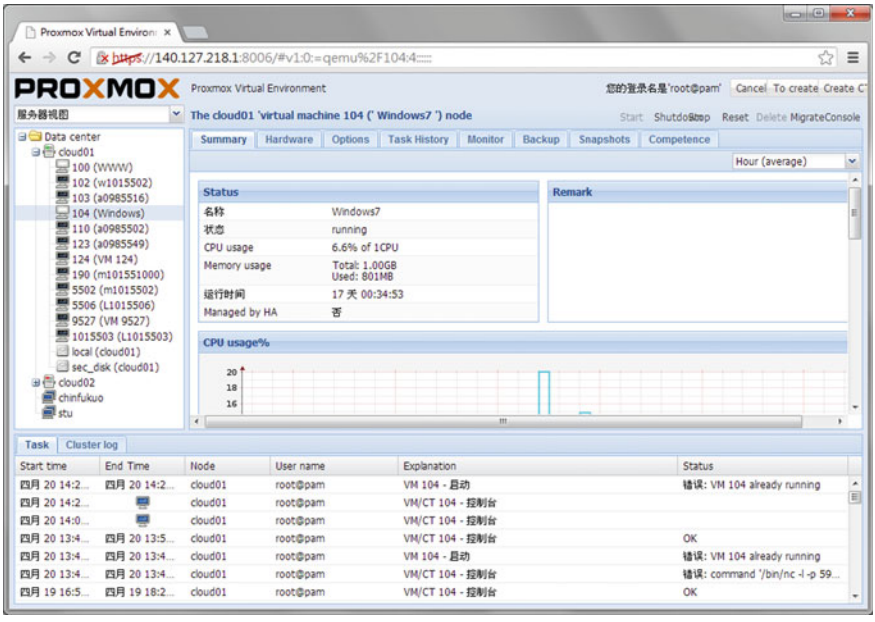

Fig. 100.7 Management web of virtual machine cluster server

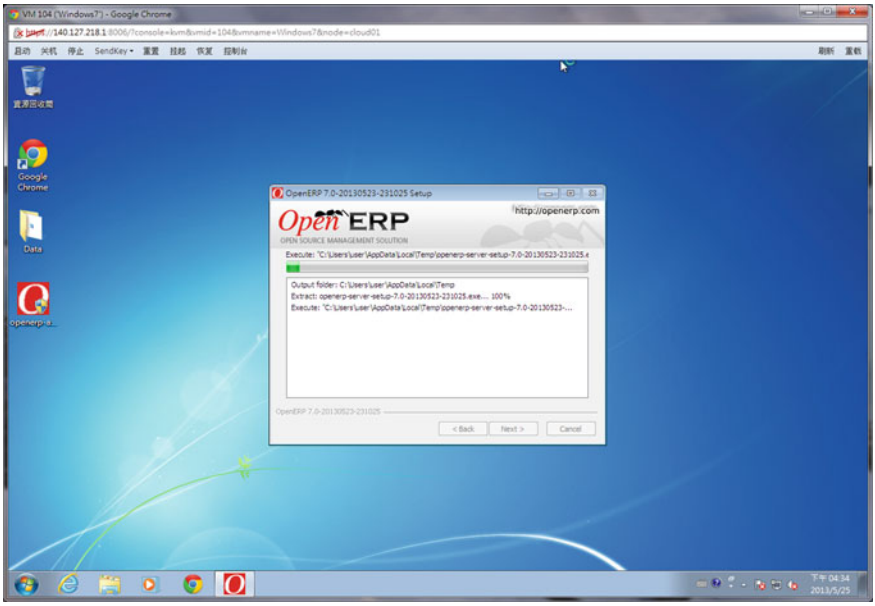

Fig. 100.8 Installation for OpenERP system

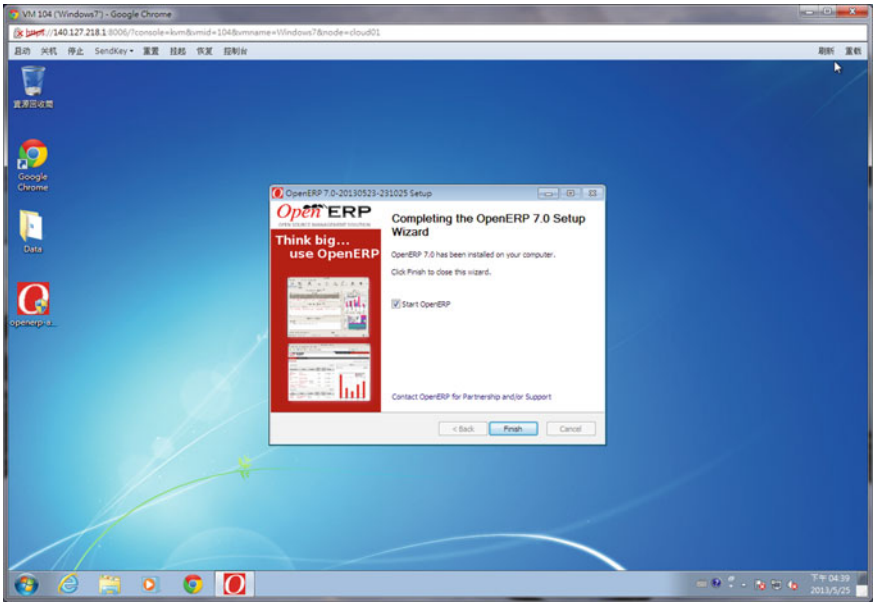

Fig. 100.9 OpenERP Installation success

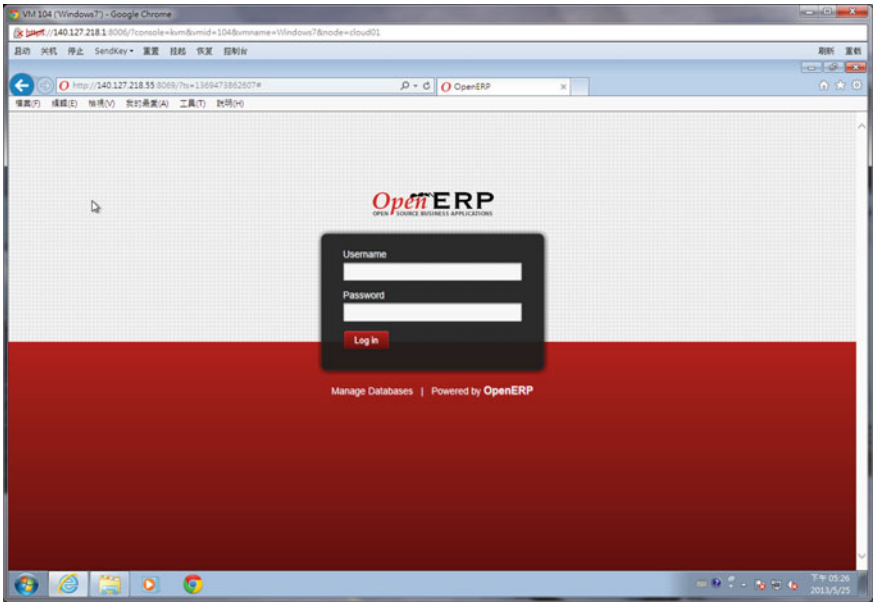

Fig. 100.10 Remote login to OpenERP system

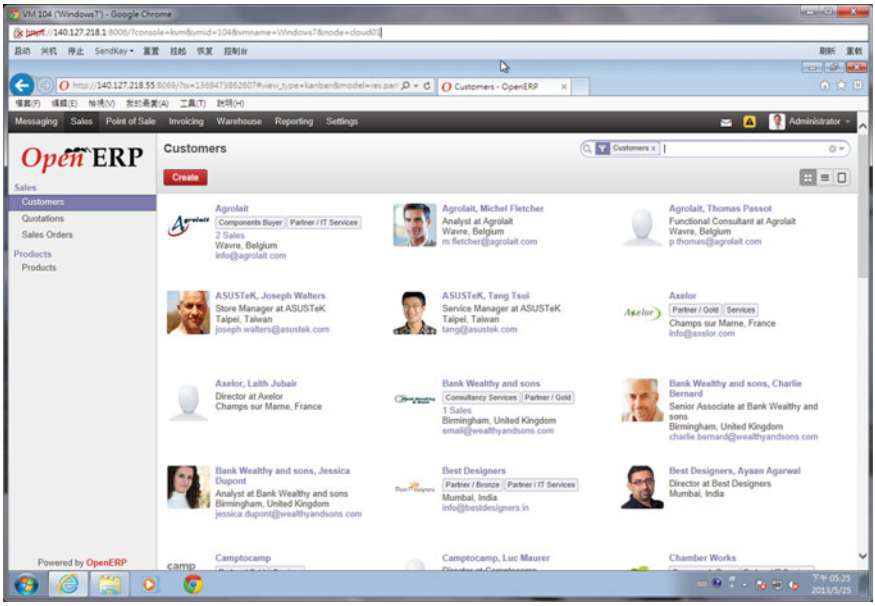

Fig. 100.11 User management in OpenERP

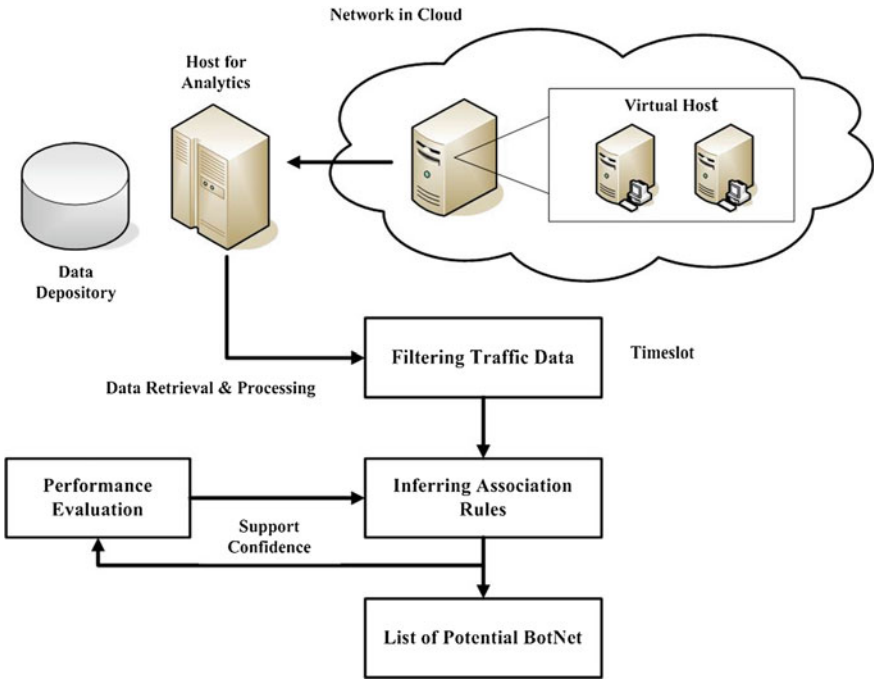

Fig. 100.12 Potential BotNet detection in cloud

5. Set up AP Server for biometric verification [15]. When users log in, it will collect users' biological features with biological capture device in the client end as an evidence of login [16].
6. Collect the records of network traffic flow in the cloud networking based on association rule analysis to establish an automatically identifiable and detectable system to be able to spontaneously distinguish the network traffic flow coming from potential BotNet and normal condition [17] as shown in Fig. 100.12.
7. Introduce the analysis of Multivariate Normal Model and Markov Chain to detect malicious attacks [18] as shown in Fig. 100.13.

100.3.2 Network Security Enhancement

IT only needs to consider the inside and outside of the network configuration and security issues. The use of virtual machines to build firewall and gateway receives multiple benefits, that is, easy management, high scalability and low cost. For example, a virtual machine equipped with pfSense [19] or Zentyal [20] system is all quite easy to manage a network system as shown in Fig. 100.14. If virtual

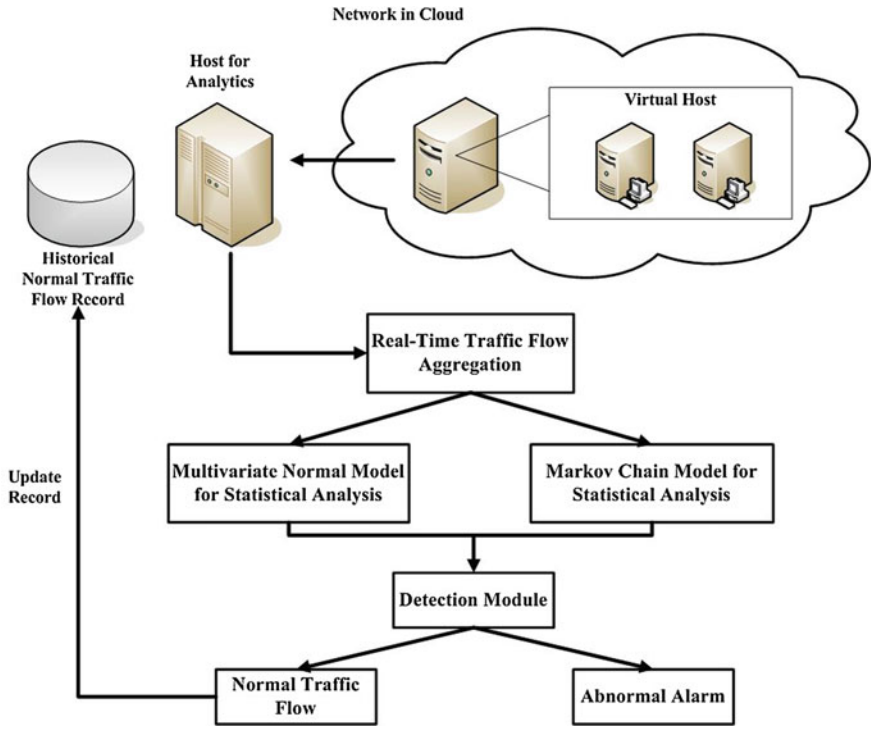

Fig. 100.13 Malicious attacks detection in cloud

Fig. 100.14 Application pfSense establishing firewall and gateway in cloud

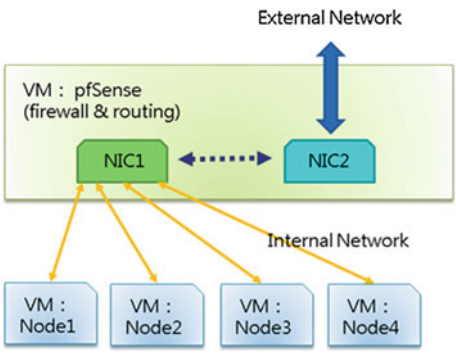

machine management has its own built-in NAT function, IT manager may install an OpenERP [7] into a virtual machine with two network interface cards, one connected to the external network via the bridge mode for internet, whereas the other connected internally via NAT mode for intranet. Without software firewall for protection, the network does not come up with a hardware firewall, apparently leading to less secure environment in which even common network attacks may

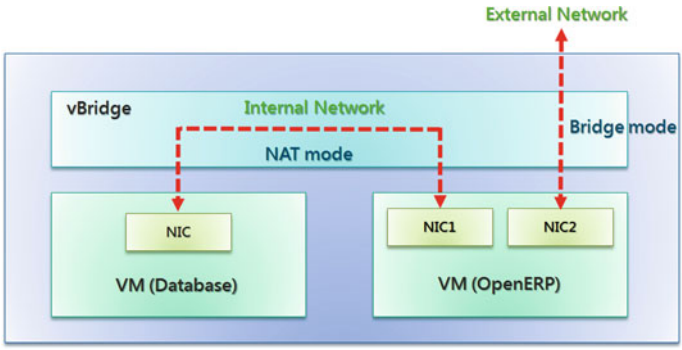

Fig. 100.15 A built-in NAT function in virtualization management establishing network architecture

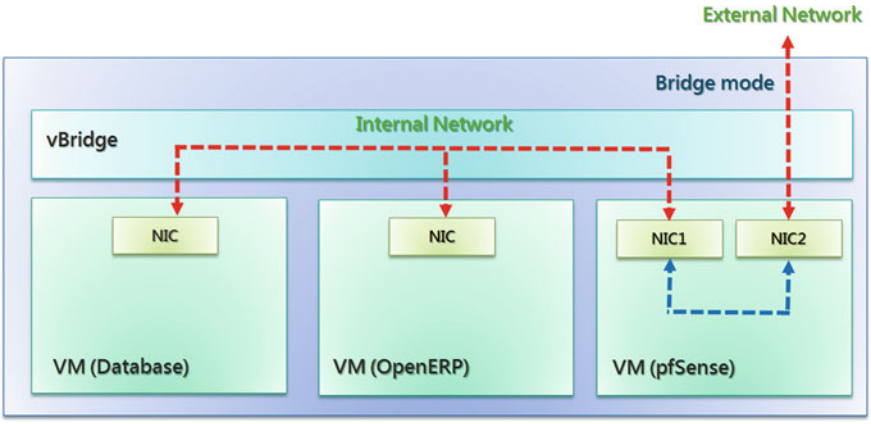

Fig. 100.16 Application pfSense establishing network architecture

also cause system crash as shown in Fig. 100.15. In addition to the scenario mentioned above, IT manager does not consider the use of the built-in NAT function in virtualization management, and in contrast takes alternative scheme into account employing pfSense [19] or Zentyal [20] to build a software firewall server. This way goes through port forwarding service to redirect http port packets to OpenERP. External network can not access the interior one where port forwarding service is not allowed or set. Besides its protection against the common network attacks can also ensure that the user interface gains both the security and stability as shown in Fig. 100.16.

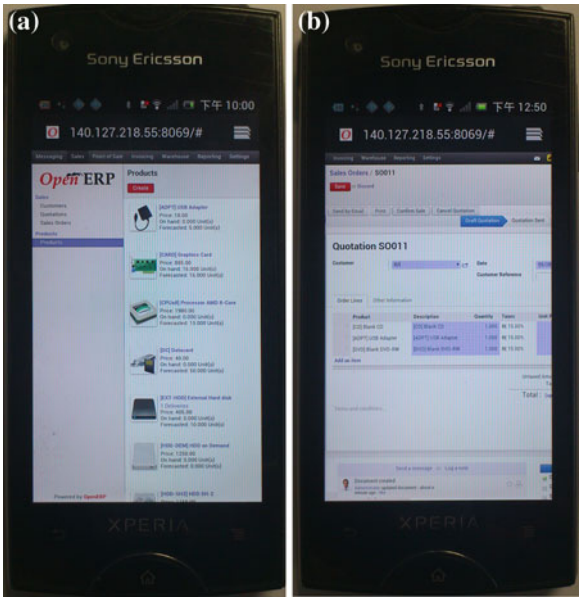

Fig. 100.17 Smart phone login to in-cloud OpenERP system. **a** List of products, **b** Sales order

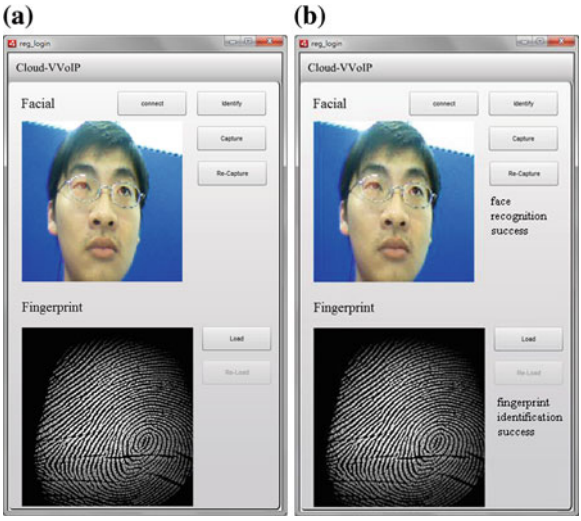

Fig. 100.18 Access control authentication using face and fingerprint identification at smart phone. **a** capture the images, **b** identification

100.4 Experimental Results and Discussion

Users key in http://IP:8096 at browser on an Android smart phone to remote login into ERP system in cloud via 3G/WiFi wireless networking and then begin to test their ERP routines as shown in Fig. 100.17. Access Control Authentication is based on biometric verification: capturing human face and fingerprint at user

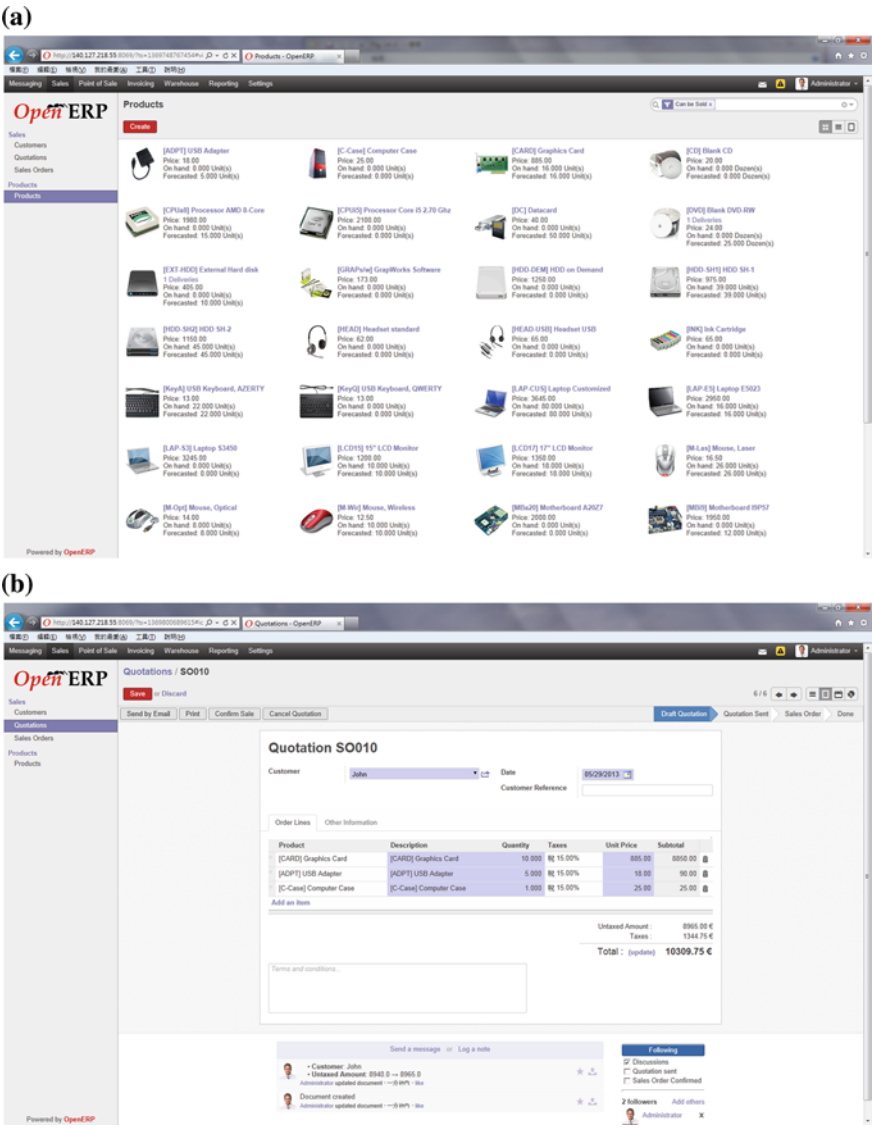

Fig. 100.19 PC login to in-cloud OpenERP system. **a** List of products, **b** Sales order

device, delivering them to the cloud for identification via TCP/IP, and then replying the identification result back to user device. It takes about 2 s for identity verification. The image of verification system is shown in Fig. 100.18. Users key in http://IP:8096 at browser on an personal computer to remote login into ERP system in cloud via 3G/WiFi wireless networking and then begin to test their ERP routines as shown in Fig. 100.19. Apriori algorithm based on association rules has

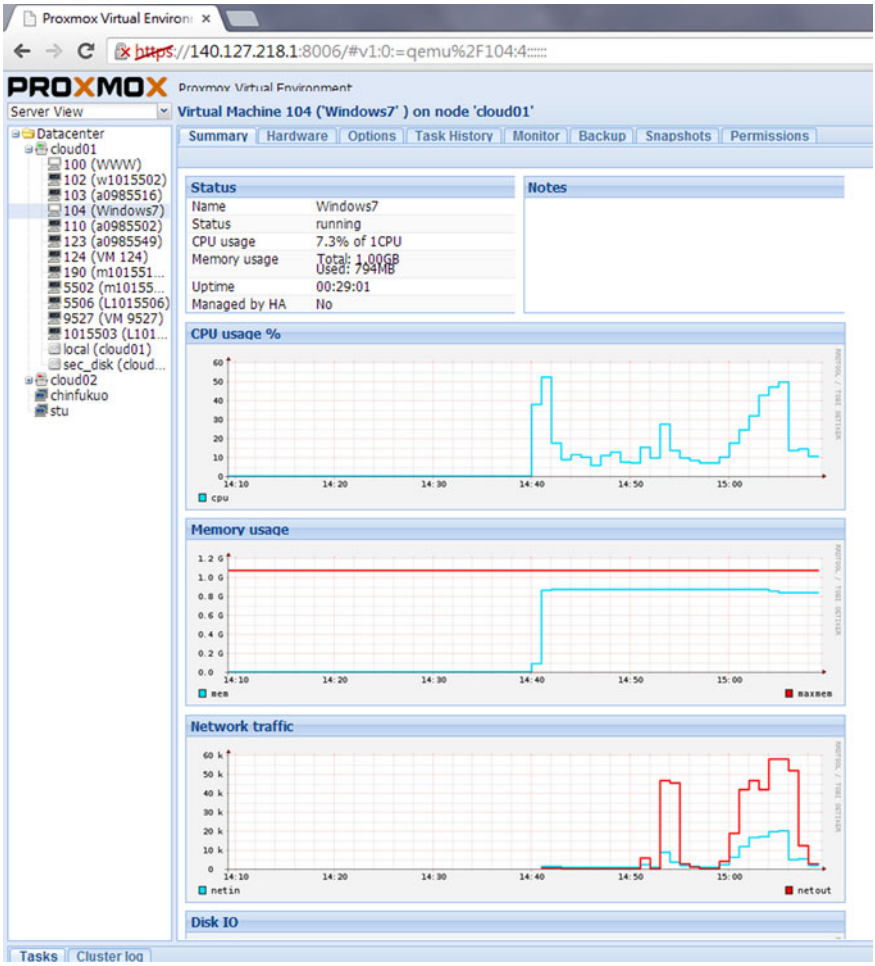

Fig. 100.20 Monitoring the VM workload in Proxmox VE

been executed all the time. As a result, the statistical outcomes derived from Apriori algorithm are fully collected and highlights potential BotNets from multiple period detection. Multivariate Normal Model and Markov Chain is utilized to analyze two above-mentioned situations respectively and then developing a module with the ability of detection and identification is able to combine the two above statistical outcomes.

When there are ten clients connected to a virtual machine (VM) in Proxmox VE, we can collect and organize the VM workload with Proxmox VE management tools at the master site to look at the information about CPU, memory, and bandwidth, depending on the number of simultaneous calls, as shown in Fig. 100.20 and listed in Table 100.1. Two remarkable benchmark ERP platforms,

Table 100.1 VM workload stress test

Option	Quantity
Number of client	10
Bandwidth	20 Kbps
CPU usage	30 % of 1CPU
Memory usage	802 MB

Table 100.2 Performance comparison according to the operational speed (unit: minute; second)

Function	ECC 6.0 (in-house ERP) (min)	Bydesign (in-cloud ERP)	Open ERP (in-cloud ERP)
Create new customer master data	7:10	4:40 min.	3 min.
Create new material master	12:40	10 min.	8:30 min.
Create sales order	5:20	2 min.	1:30 min.
Search function	2:10	5 s.	2 s.

ECC 6.0 [21] and ByDesign [22], are included in a comparative study for ERP performance evaluation where the most concerned measure in term of ERP operational speed is the response time for four operations as listed in Table 100.2.

100.5 Conclusion

According to the overall rating of ERP assessment, the proposed approach to in-cloud OpenERP with network security exclusively outperforms two remarkable benchmark platforms, ECC 6.0 ERP and Bydesign ERP. Therefore it is good choice to apply this in-cloud ERP system with access control authentication and high network security as information management system in a firm because of less expenses, high utilization rate, fast response, user friendliness, high security, and large scalability.

Acknowledgments This work is fully supported by the National Science Council, Taiwan, Republic of China, under grant number: **NSC 100-2221-E-390-011-MY3**.

References

1. Beloglazov, A., & Buyya, R. (2010). Energy efficient allocation of virtual machines in cloud data centers. In 10th IEEE/ACM International Conference on Cluster, Cloud and Grid Computing (pp. 577–578).
2. Laurikainen, R., Laitinen, J., Lehtovuori, P., & Nurminen, J. K. (2012). Improving the efficiency of deploying virtual machines in a cloud environment. In 2012 International Conference on Cloud and Service Computing (pp. 232–239).
3. Sotiriadis, S., Bessis, N., Xhafa, F., & Antonopoulos, N. (2012). Cloud virtual machine scheduling: modelling the cloud virtual machine instantiation. In 2012 Sixth International Conference on Complex, Intelligent and Software Intensive Systems (pp. 233–240).

4. Yang, T. S., Choi, J., Zheng, X., Sun, Y. H., Ouyang, C. S., & Huang, Y. X. (2006). Research of enterprise resource planning in a specific enterprise. In 2006 IEEE International Conference on Systems, Man, and Cybernetics (pp. 418–422).
5. Carvalho, R. A. de, Monnerat, R. M., Sun, Y. H., Ouyang, C. S., & Huang, Y. X. (2008). Development support tools for enterprise resource planning. *IT Professional Magazine, 10*(5), 39–45.
6. Wu, H. Q., Ding, Y., Winer, C., & Yao, L. (2010). Network security for virtual machine in cloud computing. In 2010 5th International Conference on Computer Sciences and Convergence Information Technology (pp. 18–21).
7. OpenERP. (2013). http://v6.openerp.com/
8. Zhao, J. G., Liu, J. C., Fan, J. J., & Di, J. X. (2010). The security research of network access control system. In 2010 First ACIS International Symposium on Cryptography and Network Security, Data Mining and Knowledge Discovery, E-Commerce & Its Applications and Embedded Systems (pp. 283–288).
9. Metz, C. (1999). AAA protocols: Authentication, authorization, and accounting for the Internet. *IEEE Internet Computing, 3*(6), 75–79.
10. Zhang, L.-F., Persaud, A. G., Johnson, A., & Yong, G. (2006). Detection of stepping stone attack under delay and chaff perturbations. In 25th Annual International Performance, Computing, and Communications Conference (pp. 256–266).
11. Yang, H.-Y., Xie, L.-X., & Xie, F. (2008). A new approach to network anomaly attack detection. *Fuzzy Systems and Knowledge Discovery, 4*, 317–321.
12. VMware Virtualization. (2011). http://www.vmware.com/virtualization/
13. Hyper-V Server R2. (2012). http://www.microsoft.com/en-us/server-cloud/hyper-v-server/
14. Proxmox Server Solution GmbH. (2012). http://www.proxmox.com/
15. Wayman, J. L. (2008). Biometrics in identity management systems. *IEEE Security and Privacy, 6*(2), 30–37.
16. Chang, B. R., Huang, C.-F., Tsai, H.-F., & Lin, Z.-Y. (2012). Rapid access control on Ubuntu Cloud computing with facial recognition and fingerprint identification. *Journal of Information Hiding and Multimedia Signal Processing, 3*(2), 176–190.
17. Hsiao, H. W., & Fan, W. C. (2009). Detecting step-stone with network traffic mining approach. In The Fourth International Conference on Innovative Computing, Information and Control (pp. 1176–1179).
18. Hsiao, H. W., Lin, C. S., & Chang, S. Y. (2009). Constructing an ARP attack detection system with SNMP traffic data mining. In The 11th International Conference on Electronic Commerce (pp. 341–345).
19. pfSense. (2013). http://www.pfsense.org/
20. Zentyal. (2013). http://www.zentyal.com/
21. Doedt, M., & Steffen, B. (2011). Requirement-driven evaluation of remote ERP-system solutions: A service-oriented perspective. In 34th IEEE Software Engineering Workshop (pp. 57–66).
22. Elragal, A., & El-Kommos, M. (2012). In-house versus in-cloud ERP systems: A comparative study. *Journal of Enterprise Resource Planning Studies*. DOI: 10.5171/2012.659957

Chapter 101
Stability Analysis of Homogeneous Uncertain Bilinear Systems with Non-Commensurate Time Delays

Ming-Hsun Lin

Abstract The problem of stability analysis for homogeneous uncertain bilinear systems subjected to non-commensurate time delays is considered in this paper. Several delay-dependent and delay-independent criteria are presented to guarantee the asymptotic stability of the overall systems. Furthermore, the decay rate is also estimated.

Keywords Homogeneous bilinear system · Non-commensurate time delays · Uncertainty · Decay rate

101.1 Introduction

It is known that not only engineering areas such as nuclear, thermal, and chemical processes but also physical systems such as biology, socio-economics, and ecology, may be modeled as bilinear systems. During the past decades, the study of bilinear systems has become an active topic of researches. A number of contributions hence have been devoted to the study of stability analysis and controller design for the mentioned systems [1–5, 9, 10]. In practice, due to the information transmission, natural property of system elements, computation of variables, etc., time delay(s) exist(s) in real-life systems. Besides, when modeling a control system, system uncertainty that is occurred as a result of using approximate system model for simplicity, data errors for evaluation, changes in environment conditions, aging, etc., also exist naturally. Therefore, time delay and uncertainty ought to be integrated into the model of bilinear systems. Recently, some works of the research for bilinear systems have investigated the influence of time delay [7, 8].

M.-H. Lin (✉)
General Educational Center, Chung Hwa University of Medical Technology,
Tainan County 717, Taiwan, Republic of China
e-mail: zi6272@yahoo.com.tw

J. Juang et al. (eds.), *Proceedings of the 2nd International Conference on Intelligent Technologies and Engineering Systems (ICITES2013)*, Lecture Notes in Electrical Engineering 293,
DOI: 10.1007/978-3-319-04573-3_101,

Besides, some other works have focused on the problem of stability analysis and/or stabilization control design for bilinear systems subjected to uncertainties [8, 10]. However, it seems the case that non-commensurate time delays exist in bilinear systems has not been treated until now. This paper hence addresses the stability analysis problem for homogeneous bilinear systems with multiple time delays and nonlinear uncertainties. By using differential inequality techniques, several delay-dependent and delay-independent criteria that assure the asymptotic stability of the overall systems are proposed. Furthermore, we also estimate the decay rate. It is shown that the obtained results can be applied to the stability analysis of time-delay systems.

101.2 Main Results

Consider the homogeneous bilinear uncertain time-delay system

$$\dot{x}(t) = \sum_{d=0}^{q} A_d x(t-h_d) + \sum_{i=1}^{m} sat\, u_i(t) \sum_{d=0}^{q} B_{id} x(t-h_d) + \sum_{d=0}^{q} f_d(x(t-h_d),\ t) \tag{101.1}$$

$$x(t) = \Phi(t), \quad t \in [-2h_q,\ 0]$$

where $x(\cdot) \in \mathbb{R}^n$ denotes the state vector, $u_i(\cdot) \in \mathbb{R}$, $i = 1,\ 2,\ \ldots,\ m$, are the inputs, $0 = h_0 < h_1 < h_2 < \ldots < h_q$ represent the known finite delay durations, A A_d B_i, and B_{id} are constant matrices with appropriate dimensions, $\Phi(t)$ is a continuous norm-bounded initial time function, and $f_d(x(t-d),\ t)$ denote nonlinear norm-bounded uncertainties and have the following properties:

$$\|f_d(x(t-h_d),\ t)\| \le \varepsilon_d \|x(t-h_d)\|, \quad d = 0,\ 1,\ 2,\ \ldots,\ q \tag{101.2}$$

where ε and ε_d are positive constants respectively. Define

$$U_i \equiv \max_{t \in [-2h_q,\ \infty)} |u_i(t)|, \quad i = 1,\ 2,\ \ldots,\ m \tag{101.3}$$

$$\rho \equiv \sup_{t \in [-2h_q,\ 0]} \|x(t)\|. \tag{101.4}$$

The matrix A_d is decomposed into $A_d = C_d + D_d$ such that $A_0 + C_d$ is stable or is more stable than A_0. We also assume that $A_0 + C_d$ has the property

$$\|\exp[(A_0 + C_d)t]\| \le k_d \exp(-\eta_d t), \quad d = 1,\ 2,\ \ldots,\ q \tag{101.5}$$

where constants $k_d \ge 1$ and $\eta_d > 0$. Define

$$a_d \equiv \begin{cases} \|A_d\| + \sum_{i=1}^{m} U_i \|B_{id}\| + \varepsilon_d, & d \neq j \\ \|D_j\| + \sum_{i=1}^{m} U_i \|B_{ij}\| + \varepsilon_j, & d = j \end{cases} \qquad d = 1,\ 2,\ \ldots,\ q, \tag{101.6}$$

$$b \equiv \sum_{i=1}^{m} U_i \|B_{i0}\| + \varepsilon_0, \tag{101.7}$$

$$g_j \equiv \|C_j A_0\| + \sum_{i=1}^{m} U_i \|C_j B_{i0}\| + \|C_j\| \varepsilon_0, \tag{101.8}$$

$$c_{jd} \equiv \|C_j A_d\| + \sum_{i=1}^{m} U_i \|C_j B_{id}\| + \|C_j\| \varepsilon_d. \tag{101.9}$$

By using differential inequality technique, we obtain the following results.

Theorem 1 *If $u_i(t)$ are chosen such that any one of the following conditions holds*

$$\eta_j > k_j \left[\sum_{d=1}^{q} a_d + b + h_j (g_j + \sum_{d=1}^{q} c_{jd}) \right], \quad j = 1,\ 2,\ \ldots,\ q, \tag{101.10}$$

where constants a_d, b, g_j, and c_{jd} are defined by (101.6)–(101.9) respectively. Then the bilinear uncertain time-delay system (101.1) is asymptotically stable. Furthermore, the decay rate of the overall system can be estimated as

$$\alpha \equiv \max(\alpha_1,\ \alpha_2,\ \ldots,\ \alpha_q) > 0 \tag{101.11}$$

where positive constant α_j satisfies the following equation:

$$\eta_j - k_j b - \alpha_j = k_j \left[\sum_{d=1}^{q} a_d e^{\alpha_j h_d} + \frac{1}{\alpha_j} (g_j + \sum_{d=1}^{q} c_{jd} e^{\alpha_j h_d})(e^{\alpha_j h_j} - 1) \right], \quad j = 1,\ 2,\ \ldots,\ q, \tag{101.12}$$

Proof The bilinear system (101.1) can be rewritten as

$$\begin{aligned} \dot{x}(t) = {} & (A_0 + C_j) x(t) - C_j \int_{t-h_j}^{t} \dot{x}(\tau) d\tau + D_j x(t-d) + \sum_{d=1, d\neq j}^{q} A_d x(t-h_d) \\ & + \sum_{i=1}^{m} u_i(t) \sum_{d=0}^{q} B_{id} x(t-h_d) + \sum_{d=0}^{q} f_d(x(t-h_d),\ t) \cdot \end{aligned} \tag{101.13}$$

Substitution of (101.1) yields

$$\dot{x}(t) = (A_0 + C_j)x(t) - C_j \int_{t-h_j}^{t} \left\{ \sum_{d=0}^{q} A_d x(\tau - h_d) + \sum_{i=1}^{m} u_i(\tau) \sum_{d=0}^{q} B_{id} x(\tau - h_d) + \sum_{d=0}^{q} f_d(x(\tau - h_d),\ \tau) \right\} d\tau + D_j x(t - h_j) + \sum_{d=1, d\neq j}^{q} A_d x(t - h_d) + \sum_{i=1}^{m} u_i(t) \sum_{d=0}^{q} B_{id} x(t - h_d) + \sum_{d=0}^{q} f_d(x(t - h_d),\ t) \tag{101.14}$$

Then the solution of this system can be expressed as

$$\begin{aligned} x(t) = {} & e^{(A_0+C_j)t}x(0) \\ & + \int_0^t e^{(A_0+C_j)(t-\tau)}[D_j x(\tau - h_j) + \sum_{\substack{d=1 \\ d\neq j}}^{q} A_d x(t - h_d) + \sum_{i=1}^{m} u_i(t) \sum_{d=1}^{q} B_{id} x(t - h_d)]d\tau \\ & + \int_0^t e^{(A_0+C_j)(t-\tau)}[\sum_{i=1}^{m} u_i(\tau) B_{i0} x(\tau) + \sum_{d=0}^{q} f_d(x(\tau - h_d),\ \tau)]d\tau \\ & - C_j \int_0^t \int_{\tau-h_j}^{\tau} e^{(A_0+C_j)(t-\tau)}\{\sum_{d=0}^{q} A_d x(s - h_d) + \sum_{i=1}^{m} u_i(s) \sum_{d=0}^{q} B_{id} x(s - h_d) \\ & + \sum_{d=0}^{q} f_d(x(s - h_d),\ s)\}ds d\tau \end{aligned} \tag{101.15}$$

Taking norm on both sides of (101.15) yields

$$\begin{aligned} \|x(t)\| \le {} & \left\|e^{(A_0+C_j)t}\right\| \|x(0)\| + \int_0^t \left\|e^{(A_0+C_j)(t-\tau)}\right\| \Bigg[\left\|D_j\right\| \|x(\tau - h_j)\| + \sum_{\substack{d=1 \\ d\neq j}}^{q} \|A_d\| \|x(t - h_d)\| \\ & + \sum_{i=1}^{m} |u_i(t)| \sum_{d=1}^{q} \|B_{id}\| \|x(t - h_d)\| \Bigg] d\tau \\ & + \int_0^t \left\|e^{(A_0+C_j)(t-\tau)}\right\| [\sum_{i=1}^{m} |u_i(\tau)| \|B_{i0}\| \|x(\tau)\| \\ & + \|f_0(x(\tau), \tau)\| + \sum_{d=1}^{q} \|f_d(x(\tau - h_d), \tau)\|] d\tau \\ & + \int_0^t \int_{\tau-h_j}^{\tau} \left\|e^{(A_0+C_j)(t-\tau)}\right\| \{ \left\|C_j A_0\right\| \|x(s)\| + \sum_{d=1}^{q} \left\|C_j A_d\right\| \|x(s - h_d)\| \\ & + \sum_{i=1}^{m} |u_i(s)| [\left\|C_j B_{i0}\right\| \|x(s)\| + \sum_{d=1}^{q} \left\|C_j B_{id}\right\| \|x(s - h_d)\|] \\ & + \left\|C_j\right\| (\|f_0(x(s),\ s)\| + \sum_{d=1}^{q} \|f_d(x(s - h_d),\ s)\|)\} ds d\tau \end{aligned} \tag{101.16}$$

where the relations $\|AB\| \le \|A\|\|B\|$ and $\|A+B\| \le \|A\| + \|B\|$ are used. By using (101.2), (101.3), and (101.5), inequality (101.16) becomes

$$\|x(t)\| \le k_j \rho e^{-\eta_j t} + \int_0^t k_j e^{-\eta_j (t-\tau)} \sum_{d=1}^{q} a_d \|x(\tau - h_d)\| d\tau + \int_0^t b k_j e^{-\eta_j (t-\tau)} \|x(\tau)\| d\tau + \int_0^t \int_{\tau - h_j}^{\tau} k_j e^{-\eta_j (t-\tau)} [g_j \|x(s)\| + \sum_{d=1}^{q} c_{jd} \|x(s-h_d)\|] ds d\tau \tag{101.17}$$

where the definitions (101.6 – 101.9) are used. Define a scalar function $v(t)$ as

$$v_j(t) \equiv k_j \rho e^{-\alpha_j t}, \quad t \ge -2h_q \tag{101.18}$$

where ρ is defined by (101.4) and α_j is the unique solution of (101.12). Now, if the condition (101.10) is satisfied, then $v_j(t)$is the solution of the following equation.

$$v_j(t) = k_j \rho e^{-\eta_j t} + \int_0^t k_j e^{-\eta_j (t-\tau)} \sum_{d=1}^{q} a_d v(\tau - h_d) d\tau + \int_0^t b k_j e^{-\eta_j (t-\tau)} v(\tau) d\tau + \int_0^t \int_{\tau - h_j}^{\tau} k e^{-\eta_j (t-\tau)} [g_j v(s) + \sum_{d=1}^{q} c_{jd} v(s-h_d)] ds d\tau. \tag{101.19}$$

Define

$$e_j(t) = \|x(t)\| - v_j(t). \tag{101.20}$$

Then $e_j(t) \le \rho - k_j \rho e^{-\alpha_j t} \le 0$ for $t \in [-2h_q, 0]$. From (101.17), (101.19), and (101.20), we have

$$e_j(t) \le R(t, e_j(\cdot)) \equiv \int_0^t k_j e^{-\eta_j (t-\tau)} \sum_{d=1}^{q} a_d e_j(\tau - h_d) d\tau + \int_0^t b k_j e^{-\eta_j (t-\tau)} e_j(\tau) d\tau + \int_0^t \int_{\tau - h_j}^{\tau} k_j e^{-\eta_j (t-\tau)} [g_j e_j(s) + \sum_{d=1}^{q} c_{jd} e_j(s-h_d)] ds d\tau \ \forall t > 0 \tag{101.21}$$

Now, we shall prove $e_j(t) \le 0$ for all $t > 0$. If this is not true, then let $t_0 > 0$ be the smallest time such that $e_j(t_0) > 0$. However, in light of the definition of $R(t, e_j(\cdot))$, since $e_j(t) \le 0$ for $0 < t < t_0$ we have $R(t_0, e_j(\cdot)) \le 0$. This means that $e_j(t_0) \le 0$. Therefore, this contradiction can infer that $e_j(t) \le 0$ for all $t > 0$ and the transient behavior of the overall system then can be estimated as $\|x(t)\| \le v_j(t) = k_j \rho e^{-\alpha_j t}$, $t \ge 0$. This shows that the condition (101.10) guarantees the asymptotic stability of (101.1). Thus, the proof is completed.

By the well-known fact that $\left\|e^{At}\right\| \le e^{\mu(A)t}$ [6], we then can let $k_j = 1$ and $\eta_j = -\mu(A_0 + C_j)$ in (101.7) and obtain the following results without proof.

Corollary 1 *If inputs $u_i(t)$ can be chosen such that any one of the following conditions is satisfied*

$$\mu(A_0 + C_j) + b + \sum_{d=1}^{q} a_d + h_j\left(g_j + \sum_{d=1}^{q} c_{jd}\right) < 0, \quad j = 1, 2, \ldots, q, \tag{101.22}$$

then the bilinear time-delay system (101.1) is stable with a decay rate $\bar{\alpha} \equiv \max(\alpha_1, \alpha_2, \ldots, \alpha_q) > 0$ where positive constant α_j, $j = 1, 2, \ldots, q$, is the unique solution of the following equation

$$\mu(A_0 + C_j) + b + \alpha_j = -\left[\sum_{d=1}^{q} a_d e^{\alpha_j h_d} + \frac{1}{\alpha_j}\left(g_j + \sum_{d=1}^{q} c_{jd} e^{\alpha_j h_d}\right)\left(e^{\alpha_j h_j} - 1\right)\right]. \tag{101.23}$$

Example 1 Consider the uncertain bilinear time-delay system (101.1) with

$$m = 1, q = 2, \quad h_1 = 0.06, \quad h_2 = 0.08, \quad \varepsilon_0 = 0.2, \ \varepsilon_1 = 0.1, \ \varepsilon_2 = 0.1,$$

$$A_0 = \begin{bmatrix} -2 & 0 & 0 \\ 0 & -2 & 0 \\ 0.2 & -1 & 0.1 \end{bmatrix}, \quad A_1 = \begin{bmatrix} -1 & 0 & 0.1 \\ 0 & -1.5 & 0 \\ -0.1 & 0.5 & -1.5 \end{bmatrix}, \quad A_2 = \begin{bmatrix} -0.1 & 0.05 & 0 \\ 0 & 0 & -0.1 \\ 0 & -0.05 & -0.15 \end{bmatrix},$$

$$B_{10} = \begin{bmatrix} 0.1 & -0.2 & 0 \\ 0.1 & 0 & 0 \\ 0 & 0.1 & -0.1 \end{bmatrix}, \ B_{11} = 0.5\begin{bmatrix} 0.1 & 0 & -0.1 \\ 0 & 0.1 & 0 \\ 0 & -0.1 & 0.2 \end{bmatrix}, \ B_{12} = 0.2\begin{bmatrix} 0.2 & 0 & -0.1 \\ 0 & 0 & 0 \\ 0.2 & 0.1 & 0 \end{bmatrix}$$

Notice that the matrix A is unstable for this case. We choose input $u_1(t) = 1.5\cos 2t$. Then, it is seen that $U_1 = 1.5$. Now, decompose A_1 as

$$A_1 = C_1 + D_1 = \begin{bmatrix} -1 & 0 & 0 \\ 0 & -1.5 & 0 \\ -0.1 & 0.5 & -1.5 \end{bmatrix} + \begin{bmatrix} 0 & 0 & 0.1 \\ 0 & 0 & 0 \\ 0 & 0 & 0 \end{bmatrix}.$$

From Corollary 2, condition (101.22) now is

$$\mu(A_0 + C_1) + b + \sum_{d=1}^{2} a_d + h_1\left(g_1 + \sum_{d=1}^{2} c_{1d}\right) = -0.5056 < 0.$$

Therefore, this bilinear system is stable. Furthermore, by (101.23), the decay rate can be estimated as $\alpha_1 = 0.4602$. If $x(t) = [-2\sin t \quad -0.5(1+t) \quad 2\cos t]^T$ $\forall t \in [-0.06, 0]$, then the transient behavior of this system can be estimated as

$\|x(t)\| \leq 1.5e^{-0.4602t}$. In fact, we can also evaluate the maximal bound of input U_1 by condition (101.22). In this case, it is found that when $U_1 < 2.5357$ the overall system is stable.

101.3 Conclusions

In this paper, the stability analysis problem for homogeneous uncertain bilinear systems with non-commensurate state delays has been addressed. Several delay-dependent and delay-independent conditions that guarantee the stability of overall systems have been proposed. Furthermore, we have also estimated decay rate of overall systems. It is shown that these results can be applied to solve the stability analysis of time-delay systems. We believe that this work is helpful for controller design of uncertain bilinear systems subjected to multiple time delays.

References

1. Bacic, M., Cannon, M., & Kouvaritakis, B. (2003). Constrained control of SISO bilinear system. *IEEE Transactions on Automatic Control, 48*, 1443–1447.
2. Chabour, O., & Vivalda, J. C. (2000). Remark on local and global stabilization of homogeneous bilinear systems. *Systems and Control Letters, 41*, 141–143.
3. Chen, M. S., & Tsao, S. T. (2000). Exponential stabilization of a class of unstable bilinear systems. *IEEE Transactions on Automatic Control, 45*, 989–992.
4. Chen, Y. P., Chang, J. L., & Lai, K. M. (2000). Stability analysis and bang-bang sliding control of a class of single-input bilinear systems. *IEEE Transactions on Automatic Control, 45*, 2150–2154.
5. Chiou, J. S., Kung, F. C., & Li, T. H. S. (2000). Robust stabilization of a class of singular perturbed discrete bilinear systems. *IEEE Transactions on Automatic Control, 45*, 1187–1191.
6. Coppel, W. A. (1965). *Stability and asymptotic behavior of differential equations*. Boston: D. C. Heath.
7. Guojun, J. (2001). Stability of bilinear time-delay systems. *IMA Journal of Mathematical Control and Information, 18*, 53–60.
8. Ho, D. W. C., Lu, G., & Zheng, Y. (2002). Global stabilization for bilinear systems with time delay. *IEEE Proceedings of Control Theory and Application, 149*, 89–94.
9. Jerbi, H. (2001). Global feedback stabilization of new class of bilinear systems. *Systems and Control Letters, 42*, 313–320.
10. Tao, C. W., Wang, W. Y., & Chan, M. L. (2004). Design of sliding mode controllers for bilinear systems with time varying uncertainties. *IEEE Transactions on Systems, Man, and Cybernetics: Part B, 34*, 639–645.

Chapter 102
On the Measurement of Lower Solution Bounds of the Discrete Algebraic Lyapunov Equation

Ming-Hsun Lin

Abstract In this paper, the estimation problem of lower solution bounds for the discrete algebraic Lyapunov equation (the DALE) is addressed. By utilizing linear algebraic techniques, several new lower solution bounds of the DALE are presented. We also propose a numerical algorithm to develop sharper solution bounds. The obtained bounds can give a supplement to those appeared in the literature.

Keywords Discrete algebraic Lyapunov equation · Lower solution bound · Linear algebraic technique

102.1 Introduction

It is known that the Lyapunov equation is widely used in various control systems. Furthermore, solution bounds of the above equation can also treat many control problems that use the Lyapunov equation approach. Gajic and Qureshi [2] explained one motive for studying the solution bounds of the Lyapunov equation: sometimes we are simply interested in the general behavior of the underlying system, and this behavior can be determined by examining certain bounds on the parameters of the solution, rather than the full solution. During the past few decades, research on deriving solution bounds of the continuous and discrete Lyapunov equations has became an attractive research topic, and a number of research approaches have been proposed to this problem [1, 3–6, 8–12, 14–16]. Among those results, them focus on the evaluation for the bounds of single eigenvalues including the extreme ones [3, 4, 6, 7, 11, 14, 15], the trace [4–6, 16], the determinant [3, 4, 6], as well as the bounds of solution matrix [1, 6–11, 15].

M.-H. Lin (✉)
General Educational Center, Chung Hwa University of Medical Technology, Tainan County 717, Taiwan, Republic of China
e-mail: zi6272@yahoo.com.tw

J. Juang et al. (eds.), *Proceedings of the 2nd International Conference on Intelligent Technologies and Engineering Systems (ICITES2013)*, Lecture Notes in Electrical Engineering 293,
DOI: 10.1007/978-3-319-04573-3_102,

In fact, it has been observed that all the aforementioned solution bounds can be defined by matrix bounds. Hence, the matrix bounds are the most general findings. In the literature, matrix bounds of the solution of the DALE have been studied in [6, 9–11, 15]. Many good bounds have been presented. However, it seems that most of these approaches for the matrix bounds contain points of weakness. For example, those results proposed in [9–11] must assume that the matrix Q is positive definite. In many control problems, this matrix may be positive semi-definite. Bounds in [9–11] also have inverse matrices and the computation burden hence may become very heavy when the system dimension becomes large. The matrix A must be normal in one of the bound presented in [11] and must be diagonalizable in [10]. For another bound in [11], an extra Lyapunov equation must be solved. Furthermore, in [9], the lower solution bound has a free matrix and how to choose this matrix such that the obtained bound is the best is still an open problem. To give a supplement to those appeared in the literature is therefore the aim of this paper. A new approach for developing lower matrix bounds of the solution of the DALE then is proposed. In what follows, it is not necessary to assume that Q is positive definite and A is diagonalizable or normal. Several matrix bounds for the DALE (1) are developed by a simple approach. In addition, the presented results do not involve any free variable. Therefore, in comparison with existing literature on the subject, the proposed results are less restrictive and more easily calculated.

102.2 Main Results

Consider the discrete algebraic Lyapunov equation (DALE) which are represented by

$$A^T PA - P = -Q \tag{102.1}$$

where, A, P, $Q \in \mathbb{R}^{n\times n}$, A is a stable matrix, Q denotes a given positive semi-definite matrix, and P is the unique positive semi-definite solution.

The objective of this paper is to find new lower matrix bounds of the solution of the DALE (102.1).

Lemma 1 [13]: Let a real symmetric matrix U be defined as

$$U = M^T N + NM \tag{102.2}$$

where $N \in \mathbb{R}^{n\times n}$ is a given positive semi-definite matrix. Then if and only if the $n \times n$ real matrix $(M^T + M)$ is negative semi-definite then U is negative semi-definite.

Then, by utilizing lemma 1 and some linear algebraic techniques, new upper and lower matrix bounds of the solution of the DALE (102.1) are derived as follows.

Theorem 1. The solution P of the DALE (102.1) has the following bounds.

$$P \geq \frac{-\bar{Q}}{2 + 2\lambda_n[(A-I)^{-T} + (A-I)^{-1}]} \equiv P_{l1} \tag{102.3}$$

and

$$P \geq A^T P_{l1} A + Q \equiv P_{l2} \tag{102.4}$$

where the positive semi-definite matrix $\bar{Q}$ is defined by

$$\bar{Q} \equiv \frac{1}{2}[(A+I)(A-I)^{-1} - I]^T Q[(A+I)(A-I)^{-1} - I]. \tag{102.5}$$

Proof. Because A is stable, it is seen that the matrix $(A-I)$ is nonsingular. Then, the CALE (102.1) can be rewritten as the following continuous-type Lyapunov equation:

$$\begin{aligned} &[(A+I)(A-I)^{-1}]^T P + P[(A+I)(A-I)^{-1}] \\ &= -\frac{1}{2}[(A+I)(A-I)^{-1} - I]^T Q[(A+I)(A-I)^{-1} - I] = -\bar{Q}. \end{aligned} \tag{102.6}$$

It is seen that by using the positive semi-definite matrix R, the DALE (102.1) can be transformed into a continuous-type Lyapunov equation (102.6). Then, by (102.6), we rewrite the DALE (102.1) as

$$\begin{aligned} &[(A+I)(A-I)^{-1}]^T \left[P + \frac{\bar{Q}}{2 + 2\lambda_n[(A-I)^{-T} + (A-I)^{-1}]}\right] \\ &\quad + \left[P + \frac{\bar{Q}}{2 + 2\lambda_n[(A-I)^{-T} + (A-I)^{-1}]}\right](A+I)(A-I)^{-1} \\ &= \bar{Q}\left[\frac{(A+I)(A-I)^{-1}}{2 + 2\lambda_n[(A-I)^{-T} + (A-I)^{-1}]} - \frac{I}{2}\right] \\ &\quad + \left[\frac{[(A+I)(A-I)^{-1}]^T}{2 + 2\lambda_n[(A-I)^{-T} + (A-I)^{-1}]} - \frac{I}{2}\right]\bar{Q} \end{aligned} . \tag{102.7}$$

Since both $\bar{Q}$ and P are positive semi-definite, (102.6) is indeed a Lyapunov equation. This means that $(A+I)(A-I)^{-1}$ is a stable matrix; that is, $\mathrm{Re}\lambda[(A+I)(A-I)^{-1}] < 0$. Then, we have

$$
\begin{aligned}
&2+2\lambda_n[(A-I)^{-T}+(A-I)^{-1}]\\
&=\lambda_n\{I+2(A-I)^{-T}+I+2(A-I)^{-1}]\}\\
&=\lambda_n\{(A-I)^{-T}(A-I)^{T}+2(A-I)^{-T}+(A-I)(A-I)^{-1}+2(A-I)^{-1}\}\\
&=\lambda_n\{[(A+I)(A-I)^{-1}]^{T}+(A+I)(A-I)^{-1}\}\\
&=-\lambda_1\{-(A+I)(A-I)^{-1}-[(A+I)(A-I)^{-1}]^{T}\}\\
&=-2\mu[-(A+I)(A-I)^{-1}]\leq -2\mathrm{Re}\lambda[-(A+I)(A-I)^{-1}]<0.
\end{aligned}
\tag{102.8}
$$

Therefore,

$$
\begin{aligned}
&\frac{(A+I)(A-I)^{-1}}{2+2\lambda_n[(A-I)^{-T}+(A-I)^{-1}]}-\frac{I}{2}+\frac{[(A+I)(A-I)^{-1}]^{T}}{2+2\lambda_n[(A-I)^{-T}+(A-I)^{-1}]}-\frac{I}{2}\\
&=\frac{(A-I)^{-T}(A+I)^{T}+(A+I)(A-I)^{-1}}{2+2\lambda_n[(A-I)^{-T}+(A-I)^{-1}]}-I\\
&\leq\frac{\lambda_n\{[(A+I)(A-I)^{-1}]^{T}+(A+I)(A-I)^{-1}\}I}{2+2\lambda_n[(A-I)^{-T}+(A-I)^{-1}]}-I\\
&=\frac{\{2+2\lambda_n[(A-I)^{-T}+(A-I)^{-1}]\}I}{2+2\lambda_n[(A-I)^{-T}+(A-I)^{-1}]}-I=0.
\end{aligned}
\tag{102.9}
$$

According to Lemma 1, it is seen that the right-hand side of Eq. (102.8) is negative semi-definite. Therefore, Eq. (102.9) is also a continuous Lyapunov equation and its solution is positive semi-definite. That is,

$$
P\geq\frac{-\bar{Q}}{2+2\lambda_n[(A-I)^{-T}+(A-I)^{-1}]}=P_{l1}. \tag{102.10}
$$

Furthermore, the DALE (102.1) can be rewritten as

$$
P=A^{T}PA+Q. \tag{102.11}
$$

Now, substituting P_{l1} into the DALE (102.11) leads to the lower bound (102.4). Thus, the proof is completed.

Remark 1. We find that the sharpness of bounds P_{l1} and P_{l2} can not be compared. However, if $P_{l1}\leq P_{l2}$, the following algorithm is proposed for obtaining tighter lower solution bounds for the DALE (102.1).

Algorithm 1:

Step 1: Set $k = 0$ and $P_l^{(0)} = P_{l1}$.

Step 2: Compute

$$P_l^{(k+1)} = A^T P_l^{(k)} A + Q,\ k = 0,\ 1,\ 2,\ \ldots. \tag{102.12}$$

Then $P_l^{(k+1)}$ are sharper lower bounds of the solution of the DALE (102.1).

Remark 2. Surveying the literature, existing matrix bounds of the solution of the DALE (102.1) are summarized as follows [6, 9–11, 15].

$$P \geq S^{-1}\left(S[Q - M + \eta(A - I)^T(A - I)]S\right)^{1/2} S^{-1} \equiv P_{l3} \tag{102.13}$$

$$P \geq \frac{\lambda_n(Q)}{1 - \sigma_n^2(A)} A^T A + Q \equiv P_{l4} \tag{102.14}$$

$$P \geq \lambda_n(M_n M_n^T) P_1 \equiv P_{l5}, \quad P_1 - A^n P_1 (A^T)^n = I \tag{102.15}$$

$$P \geq \lambda_n(M_n M_n^T)\left[I - (AA^T)^n\right]^{-1} \equiv P_{l6},\ AA^T = A^T A \tag{102.16}$$

$$P \geq \lambda_n(G_{dm}) M_m M_m^T \equiv P_{l7} \tag{102.17}$$

$$P \geq \lambda_n(N^T Q N) N^{-T} R_2 N^{-1} \equiv P_{l8} \tag{102.18}$$

where

$$S \equiv [(A - I)M^{-1}(A - I)^T]^{1/2} \ \text{ with } Q > M \tag{102.19}$$

$$\eta \equiv \frac{\sigma_n^2[(A - I)R]}{2\lambda_1^2[(A - I)M^{-1}(A - I)^T]} + \frac{\sqrt{\sigma_n^4[(A - I)R] + 4\lambda_1^2[(A - I)M^{-1}(A - I)^T]\lambda_n[R(Q - M)R]}}{2\lambda_1^2[(A - I)M^{-1}(A - I)^T]} \tag{102.20}$$

$$M_n \equiv [D,\ A^T D,\ (A^T)^2 D,\ \ldots,\ (A^T)^{n-1} D] \text{ where } Q = DD^T \tag{102.21}$$

$$G_{dm} \equiv \left\{g_{ij}\right\} \in R^{m \times m}, \quad \text{with } g_{ij} \equiv \sum_{k=0}^{\infty} a_i(k) a_j(k), \quad A^k = \sum_{i=0}^{m-1} a_i(k) A^i \tag{102.22}$$

$$R_2 \equiv diag\{1/[1 - |\lambda_i(A)|^2]\} \tag{102.23}$$

$$A = N \Lambda N^{-1}, \quad \Lambda \equiv diag\{\lambda_i(A)\} \tag{102.24}$$

$M_m \equiv [D,\ A^T D,\ (A^T)^2 D,\ \ldots,\ (A^T)^{m-1} D]$ where

$$Q = DD^T \tag{102.25}$$

$$m \equiv \text{the degree of the minimal polynomial of } A. \tag{102.26}$$

From the above conditions, it is seen that most of them contain points of weakness. The matrix Q in [9–11] must be positive definite. In many control problems, this matrix may be positive semi-definite. The matrix A must be normal in (102.16) and must be diagonalizable in (102.18). For bound (102.15), an extra Lyapunov equation must be solved. Furthermore, from (102.22), it is obvious that the computation of constants g_{ij} is very difficult. From the obtained results of this work, it is not necessary to assume that the matrix A is diagonalizable or normal. We also do not assume that the matrix Q is positive definite. It is found the tightness of the obtained results and those appeared in the literature cannot be compared by any mathematical method. However, at least they can give a supplement to each other.

Example 1. Consider the DALE (102.1) with

$$A = \begin{bmatrix} 0.6 & 0.1 \\ 0.1 & 0.8 \end{bmatrix} \text{ and } Q = \begin{bmatrix} 5 & 0 \\ 0 & 8 \end{bmatrix}$$

where matrix A is diagonalizable and normal and Q is positive definite. For this case, the solution matrix of the DALE (102.1) is

$$P = \begin{bmatrix} 8.3982 & 2.0392 \\ 2.0392 & 13.0136 \end{bmatrix}.$$

In this case, we choose $M = \begin{bmatrix} 3 & 0 \\ 0 & 4 \end{bmatrix}$. Then, from the obtained results and (102.13)–(102.18), solution bounds of the DALE (102.1) for this case are shown below.

$$P_{l1} = \begin{bmatrix} 6.9020 & 4.0784 \\ 4.0784 & 10.4314 \end{bmatrix},\ P_{l2} = \begin{bmatrix} 8.0784 & 2.5490 \\ 2.5490 & 12.3137 \end{bmatrix},\ P_{l3} = \begin{bmatrix} 7.5265 & 1.9343 \\ 1.9343 & 11.2136 \end{bmatrix},$$
$$P_{l4} = \begin{bmatrix} 7.4667 & 0.8000 \\ 0.8000 & 10.4667 \end{bmatrix},\ P_{l5} = \begin{bmatrix} 8.0235 & 0.8395 \\ 0.8395 & 8.0235 \end{bmatrix} = P_{l6}, P_{l7} = \begin{bmatrix} 1.7983 & 0.2039 \\ 0.2039 & 2.8569 \end{bmatrix},$$
$$P_{l8} = \begin{bmatrix} 8.2353 & 1.5686 \\ 1.5686 & 8.2353 \end{bmatrix}.$$

For this case, we have $P_{l1} > P_{l2}$, P_{l3}, P_{l4}, P_{l5}, P_{l6}, and P_{l7}. However, the sharpness between P_{l1} and P_{l8} can not be compared. It shows that the obtained results and those appeared in the literature can give a supplement to each other. By using Algorithm 1, we have

$$P_{l2} = \begin{bmatrix} 8.3373 & 2.0392 \\ 2.0392 & 13.0136 \end{bmatrix} > P_{l8} \text{ for } k = 1,$$

Obviously our result P_{l2} now is tighter than the parallel ones in this case. This means that the presented algorithm indeed can work.

102.3 Conclusions

In this paper, lower matrix bounds of the solution for the DALE have been discussed. By using a bilinear transformation, the DALE has been transformed into a continuous Lyapunov equation. Then we have established several lower solution bounds of the DALE by making use of linear algebraic techniques. All proposed bounds are new. According to some satisfaction conditions, respectively, an iterative algorithm has also been developed for obtaining sharper matrix bounds. Finally, we give a numerical example to demonstrate the applicability of the presented schemes.

References

1. Choi, H. H., & Kuc, T. Y. (2002). Lower matrix bounds for the continuous algebraic Riccati and Lyapunov matrix equations. *Automatica, 38*, 1147–1152.
2. Gajic, Z., & Qureshi, M. (1995). *Lyapunov matrix equation in system stability and control*. New York: Academic Press.
3. Hmamed, A. (1991). Discrete Lyapunov equation: Simultaneous eigenvalue lower bounds. *International Journal of Systems and Science, 22*, 1121–1126.
4. Komaroff, N. (1992). Lower bounds for the solution of the discrete algebraic Lyapunov equation. *IEEE Transactions on Automatic Control, 37*, 1017–1018.
5. Komaroff, N., & Shahian, B. (1992). Lower summation bounds for the discrete Riccati and Lyapunov equations. *IEEE Transactions on Automatic Control, 37*, 1078–1080.
6. Lee, C. H. (1996). Upper and lower bounds of the solution for the discrete Lyapunov equation. *IEEE Transactions on Automatic Control, 41*, 1338–1341.
7. Lee, C. H. (1997). New results for the bounds of the solution for the continuous Riccati and Lyapunov equations. *IEEE Transactions on Automatic Control, 42*, 118–123.
8. Lee, C. H., & Chen, C. Y. (2009). Matrix solution bounds of the continuous Lyapunov equation. *Journal of the Franklin Institute, 346*, 741–751.
9. Lee, C. H. (2004). Solution bounds of the continuous and discrete Lyapunov matrix equations. *Journal of Optimization Theory and Appications, 120*(3), 559–578.
10. Lee, C. H., & Kung, F. C. (1997). Upper and lower matrix bounds of the solutions for the continuous and discrete Lyapunov equations. *Journal of the Franklin Institute, 334B*, 539–546.
11. Mori, T., Fukuta, N., & Kuwahara, M. (1985). Eigenvalue bounds for the discrete Lyapunov matrix equation. *IEEE Transactions on Automatic Control, 30*, 925–926.
12. Mori, T., & Kokame, H. (2002). On the solution bounds for three types of Lyapunov matrix equations: continuous, discrete and unified equations. *IEEE Transactions on Automatic Control*, *19*, 1767–1770 (issue: 10).

13. Ostrowski, A., & Schneider, H. (1961). Some theorems on the inertia of general matrices. *Journal of Mathematical Analysis and Applications, 4*, 72–84.
14. Penzl, T. (2000). Eigenvalue decay bounds for solutions of Lyapunov equations: the symmetric case. *Systems & Control Letters*, *40*, 130–144 (issue: 2).
15. Tippett, M. K., & Marchesin, D. (1999). Upper bounds for the solution of the discrete algebraic Lyapunov equation. *Automatica, 35*, 1485–1489.
16. Truhar, N., & Veselic, K. (2007). Bounds on the trace of a solution to the Lyapunov equation with a general stable matrix. *Systems & Control Letters*, *56*, 493–503 (issue: 7-8).

Chapter 103
Upper Bounds Estimation of the Solution of the Discrete Algebraic Lyapunov Equation

Ming-Hsun Lin

Abstract For the solution of the discrete algebraic Lyapunov equation (the DALE), upper matrix bounds are estimated in this paper by utilizing linear algebraic techniques. Several new upper matrix bounds of the solution of the DALE are developed. Finally, a corresponding numerical algorithm is also proposed to obtain sharper bounds. It is shown that the presented results are better than the major ones appeared in the literature.

Keywords Discrete algebraic Lyapunov equation · Upper solution bound · Linear algebraic technique

103.1 Introduction

It is known that the Lyapunov equation approach plays a very important role in analysis and design of control systems. Besides the mentioned equation itself, solution bounds of this equation can also be applied to deal with many control problems. In literature, Gajic and Qureshi [1] have given one motivation for developing the solution bounds of the Lyapunov equation: sometimes we are simply interested in the general behavior of the underlying system, and this behavior can be determined by examining certain bounds on the parameters of the solution, rather than the full solution. Therefore, research on the estimating problem for solution bounds of the continuous and discrete Lyapunov equations has became an attractive topic during the past few decades. A number of research approaches have been proposed to solve the mentioned problem [2–14]. All of those results can be classified into two categories: (i) eigenvalue bounds including

M.-H. Lin (✉)
General Educational Center, Chung Hwa University of Medical Technology, Tainan 717, Taiwan, Republic of China
e-mail: zi6272@yahoo.com.tw

J. Juang et al. (eds.), *Proceedings of the 2nd International Conference on Intelligent Technologies and Engineering Systems (ICITES2013)*, Lecture Notes in Electrical Engineering 293,
DOI: 10.1007/978-3-319-04573-3_103,

the extreme ones [3, 4, 6, 10, 12, 13, 15], the trace [4–6, 14], the determinant [3, 4, 6] and (ii) matrix bounds [2, 6–10, 13, 15]. In fact, it has been observed that all of the former can be defined by the latter. Hence, the matrix bounds of the solution of the Lyapunov equations are the most general findings. In literature, many good matrix bounds of the solution of the continuous and discrete Lyapunov equations have been proposed in [2, 7–9, 15] and [2, 6, 8, 9, 13], respectively. However, for the DALE, it seems that most of the upper matrix bounds contain points of weakness. For example, those results proposed in [8–10] must assume that the matrix Q is positive definite. In many application problems, this matrix is only requested as a positive semi-definite matrix. Bounds in [8–10] also have involved inverse matrices and the computation burden hence may become very heavy when the system dimension becomes large. The matrix A must be normal in one of the previous bounds presented in [10] and must be diagonalizable in that proposed in [9]. For another bound presented in [10], in order to obtain the upper matrix bound, one must solve an extra Lyapunov equation. To improve those weak points and give a supplement to those upper solution bounds of the DALE appeared in the literature is therefore the objective of this paper. A new approach for deriving upper matrix bounds of the solution of the DALE is proposed. Two new upper bounds will be developed. In what follows, the matrix Q is not needed to be positive definite and matrix A can be non-diagonalizable or non-normal. In addition, an Algorithm will be also proposed for measuring tighter solution bounds. Therefore, comparing to the major existing results appeared in the literature, the proposed bounds are less restrictive and more easily to be calculated.

103.2 Main Results

Consider the following discrete algebraic Lyapunov equation (DALE)

$$A^T PA - P = -Q \tag{103.1}$$

where, $A,\ P,\ Q \in \mathbb{R}^{n\times n}$, A represents a stable matrix. For a given positive semi-definite matrix Q, P denotes the unique positive semi-definite solution of (103.1).

The objective of this paper is to find new upper matrix bounds of the solution of the DALE (103.1). Before developing the main results, we review the following useful result.

Lemma 103.1 [16] *Let a real symmetric matrix U be defined as*

$$U = M^T N + NM \tag{103.2}$$

where $N \in \mathbb{R}^{n\times n}$ is a given positive semi-definite matrix. Then the necessary and sufficient condition for U is negative semi-definite is the $n \times n$ real matrix $(M^T + M)$ is negative semi-definite then.

Here, by utilizing the above lemma and linear algebraic techniques, we propose the following new upper matrix bounds of the solution of the DALE (103.1)s.

Theorem 103.1 *If*

$$A^T A < I, \tag{103.3}$$

then the positive semi-definite solution P of the DALE (103.1) has the upper bounds

$$P \le \frac{-\bar{Q}}{2 + 2\lambda_1[(A-I)^{-T} + (A-I)^{-1}]} \equiv P_{u1} \tag{103.4}$$

and

$$P \le A^T P_{u1} A + Q \equiv P_{u2} \tag{103.5}$$

where the positive semi-definite matrix $\bar{Q}$ is defined by

$$\bar{Q} \equiv \frac{1}{2}[(A+I)(A-I)^{-1} - I]^T Q[(A+I)(A-I)^{-1} - I]. \tag{103.6}$$

Proof Because A is stable, it is seen that the matrix $(A - I)$ is nonsingular. Then, the CALE (103.1) can be rewritten as the following continuous-type Lyapunov equation:

$$\begin{aligned} &[(A+I)(A-I)^{-1}]^T P + P[(A+I)(A-I)^{-1}] \\ &= -\frac{1}{2}[(A+I)(A-I)^{-1} - I]^T Q[(A+I)(A-I)^{-1} - I] = -\bar{Q}. \end{aligned} \tag{103.7}$$

From (103.6), we rewrite the DALE (103.1) as

$$\begin{aligned} &[(A+I)(A-I)^{-1}]^T \left[\frac{-\bar{Q}}{2 + 2\lambda_1[(A-I)^{-T} + (A-I)^{-1}]} - P\right] \\ &\quad + \left[\frac{-\bar{Q}}{2 + 2\lambda_1[(A-I)^{-T} + (A-I)^{-1}]} - P\right](A+I)(A-I)^{-1} \\ &= \bar{Q}\left[\frac{-(A+I)(A-I)^{-1}}{2 + 2\lambda_1[(A-I)^{-T} + (A-I)^{-1}]} + \frac{I}{2}\right] \\ &\quad + \left[\frac{-[(A+I)(A-I)^{-1}]^T}{2 + 2\lambda_1[(A-I)^{-T} + (A-I)^{-1}]} + \frac{I}{2}\right]\bar{Q}. \end{aligned} \tag{103.8}$$

It is seen that

$$2 + 2\lambda_1[(A-I)^{-T} + (A-I)^{-1}] = 2\lambda_1[I + (A-I)^{-T} + (A-I)^{-1}]. \tag{103.9}$$

Define a symmetric matrix R as

$$R \equiv (A-I)^{-T} + (A-I)^{-1}. \tag{103.10}$$

If the condition (103.12) is satisfied, then we have

$$A^T A - I = (A-I)^T (A-I) + (A-I) + (A-I)^T = (A-I)^T (R+I)(A-I) < 0. \tag{103.11}$$

Since $(A-I)$ is nonsingular, the above inequality implies

$$1 + \lambda_1[(A-I)^{-T} + (A-I)^{-1}] = \lambda_1[I + (A-I)^{-T} + (A-I)^{-1}] = \lambda_1[R+I] < 0. \tag{103.12}$$

Therefore,

$$\begin{aligned}
&\frac{-(A+I)(A-I)^{-1}}{2 + 2\lambda_1[(A-I)^{-T} + (A-I)^{-1}]} + \frac{I}{2} + \frac{-[(A+I)(A-I)^{-1}]^T}{2 + 2\lambda_1[(A-I)^{-T} + (A-I)^{-1}]} + \frac{I}{2} \\
&= \frac{(A-I)^{-T}(A+I)^T + (A+I)(A-I)^{-1}}{-\{2 + 2\lambda_1[(A-I)^{-T} + (A-I)^{-1}]\}} + I \\
&\le \frac{\lambda_1\{[(A+I)(A-I)^{-1}]^T + (A+I)(A-I)^{-1}\}I}{-\{2 + 2\lambda_1[(A-I)^{-T} + (A-I)^{-1}]\}} + I \\
&= \frac{\{2 + 2\lambda_1[(A-I)^{-T} + (A-I)^{-1}]\}I}{-\{2 + 2\lambda_1[(A-I)^{-T} + (A-I)^{-1}]\}} + I = 0.
\end{aligned} \tag{103.13}$$

In light of Lemma 103.1, inequality (103.20) means (103.16) represents a continuous Lyapunov equation and hence the solution P of the DALE (103.1) satisfies

$$P \le \frac{-\bar{Q}}{2 + 2\lambda_1[(A-I)^{-T} + (A-I)^{-1}]} = P_{u1}. \tag{103.14}$$

Substituting this bound into the DALE (103.11) results in the bound (103.14). Therefore, the proof is completed.

Remark The tightness between P_{u1} and P_{u2} cannot be compared. However, if $P_{u2} \le P_{u1}$, then we have the following algorithm for deriving tighter upper bounds for the solution of the DALE (103.1).

Algorithm 103.1

Step 1: Set $k = 0$ and $P_u^{(0)} = P_{u1}$.

Step 2: Compute

$$P_u^{(k+1)} = A^T P_u^{(k)} A + Q, \; k = 0, \; 1, \; 2, \ldots. \tag{103.15}$$

Then $P_u^{(k+1)}$, $k = 0, \; 1, \; 2, \; \ldots$, are sharper upper solution bounds.

By the inductive method, it is easy to show that $P_u^{(k+1)}$, $k = 0, 1, 2, \ldots$, are sharper solution bounds. The proofs then are omitted.

Comparisons 103.1 Surveying the literature, existing matrix bounds of the solution of the DALE (103.1) are summarized as follows [6, 8–10, 13].

$$P \le \frac{\lambda_1(Q)}{1-\sigma_1^2(A)} A^T A + Q \equiv P_{u3},\ 1-\sigma_1^2(A) > 0 \tag{103.16}$$

$$P \le \lambda_1(M_n M_n^T) P_1 \equiv P_{u4}, \quad P_1 - A^n P_1 (A^T)^n = I \tag{103.17}$$

$$P \le \lambda_1(M_n M_n^T)\left[I - (AA^T)^n\right]^{-1} \equiv P_{u5}, AA^T = A^T A \tag{103.18}$$

$$P \le \lambda_1(G_{dm}) M_m M_m^T \equiv P_{u6} \tag{103.19}$$

$$P \le \lambda_1(N^T Q N) N^{-T} R_2 N^{-1} \equiv P_{u7} \tag{103.20}$$

where

$$M_n \equiv [D,\ A^T D,\ (A^T)^2 D, \ldots,\ (A^T)^{n-1} D] \quad \text{where} \quad Q = DD^T \tag{103.21}$$

$$G_{dm} \equiv \left\{g_{ij}\right\} \in R^{m\times m},\ \text{with}\ g_{ij} \equiv \sum_{k=0}^{\infty} a_i(k) a_j(k), \quad A^k = \sum_{i=0}^{m-1} a_i(k) A^i \tag{103.22}$$

$$R_2 \equiv diag\{1/[1-|\lambda_i(A)|^2]\} \tag{103.23}$$

$$A = N \Lambda N^{-1}, \quad \Lambda \equiv diag\{\lambda_i(A)\} \tag{103.24}$$

$$M_m \equiv [D,\ A^T D,\ (A^T)^2 D, \ldots,\ (A^T)^{m-1} D] \quad \text{where} \quad Q = DD^T \tag{103.25}$$

$$m \equiv \text{the degree of the minimal polynomial of } A. \tag{103.26}$$

In light of the above upper bounds, some points of weakness exist in most of them. In [8–10], the matrix Q must be positive definite. In many application problems, the only request for the matrix Q is that Q is positive semi-definite but not positive definite. n An extra Lyapunov equation must be solved for bound (103.17). Therefore, the computer burdens might become hard. One can also notice that the matrix A must be normal in (103.18) and must be diagonalizable in (103.20). Furthermore, obviously the computation of constants g_{ij} in (103.22) is very difficult. According to the obtained results of this work, it is seen that the assumptions that the matrix A is diagonalizable or normal are not necessary. Furthermore, it is not necessary to assume that the matrix Q is positive definite. Finally, we find that the tightness between the obtained results and those appeared in the literature cannot be compared by any mathematical method. However, at least they can give a supplement to each other.

Example Consider the DALE (103.1). To satisfy all conditions for solution bounds presented in this paper, we choose

$$A = \begin{bmatrix} 0.6 & 0.1 \\ 0.1 & 0.8 \end{bmatrix} \text{ and } Q = \begin{bmatrix} 5 & 0 \\ 0 & 8 \end{bmatrix}$$

where matrix A is diagonalizable and normal and Q is positive definite. For this case, the solution matrix of the DALE (103.1) is

$$P = \begin{bmatrix} 8.3982 & 2.0392 \\ 2.0392 & 13.0136 \end{bmatrix}.$$

Then, from the obtained results and (103.16)–(103.20), upper solution bounds of the DALE (103.1) for this case can be calculated as

$$P_{u1} = \begin{bmatrix} 13.0370 & 7.7037 \\ 7.7037 & 19.7037 \end{bmatrix},$$

$$P_{u2} = \begin{bmatrix} 10.8148 & 4.8148 \\ 4.8148 & 16.1481 \end{bmatrix}, \; P_{u3} = \begin{bmatrix} 10.8039 & 1.8824 \\ 1.8824 & 13.8039 \end{bmatrix},$$

$$P_{u4} = \begin{bmatrix} 13.1938 & 1.3805 \\ 1.3805 & 13.1938 \end{bmatrix} = P_{u5},$$

$$P_{u6} = \begin{bmatrix} 14.3632 & 1.6284 \\ 1.6284 & 22.8128 \end{bmatrix}, \; P_{u7} = \begin{bmatrix} 13.1765 & 2.5098 \\ 2.5098 & 13.1765 \end{bmatrix}.$$

It is seen that bounds P_{u1} and P_{u2} are not very good for this case. However, the sharpness between P_{u1}, P_{u2} and P_{u3}–P_{u7} can not be compared. One can only conclude that the obtained results and those appeared in the literature can give a supplement to each other. However, by using Algorithm 103.1, we have

$$P_{u2} = \begin{bmatrix} 8.4359 & 2.0776 \\ 2.0776 & 13.0527 \end{bmatrix} \text{ for } k = 6.$$

Now the upper bound P_{u2} by using Algorithm 103.1 for $k = 6$ is better than the parallel results P_{u1} and $P_{u3}-\mathrm{P_{u7}}$. This means the proposed algorithm indeed can work.

103.3 Conclusions

In this paper, the estimation problem of the upper matrix bounds of the solution for the DALE has been addressed. It is found that the DALE can be transformed into a continuous Lyapunov equation via utilizing a bilinear transformation. Then, by some linear algebraic techniques, we have developed several upper solution

bounds of the DALE. All proposed bounds are new. An iterative algorithm has been proposed for obtaining sharper matrix bounds. Comparisons between the obtained results and those appeared in the literature have also been made. Finally, we give an illustrative example to demonstrate the applicability of the presented schemes.

References

1. Gajic, Z., Qureshi, M. (1995). *Lyapunov matrix equation in system stability and control*. New York: Academic Press.
2. Choi, H. H., & Kuc, T. Y. (2002). Lower matrix bounds for the continuous algebraic Riccati and Lyapunov matrix equations. *Automatica, 38*, 1147–1152.
3. Hmamed, A. (1991). Discrete Lyapunov equation: Simultaneous eigenvalue lower bounds. *International Journal of Systems and Science, 22*, 1121–1126.
4. Komaroff, N. (1992). Lower bounds for the solution of the discrete algebraic Lyapunov equation. *IEEE Transactions on Automatic Control, 37*, 1017–1018.
5. Komaroff, N., & Shahian, B. (1992). Lower summation bounds for the discrete Riccati and Lyapunov equations. *IEEE Transactions on Automatic Control, 37*, 1078–1080.
6. Lee, C. H. (1996). Upper and lower bounds of the solution for the discrete Lyapunov equation. *IEEE Transactions on Automatic Control, 41*, 1338–1341.
7. Lee, C. H., & Chen, C. Y. (2009). Matrix solution bounds of the continuous Lyapunov equation. *Journal of the Franklin Institute, 346*, 741–751.
8. Lee, C. H. (2004). Solution bounds of the continuous and discrete Lyapunov matrix equations. *Journal of Optimization Theory and Appications, 120*(3), 559–578.
9. Lee, C. H., & Kung, F. C. (1997). Upper and lower matrix bounds of the solutions for the continuous and discrete Lyapunov equations. *Journal of the Franklin Institute, 334B*, 539–546.
10. Mori, T., Fukuta, N., & Kuwahara, M. (1985). Eigenvalue bounds for the discrete Lyapunov matrix equation. *IEEE Transactions on Automatic Control, 30*, 925–926.
11. Mori, T., & Kokame, H. (2002). On the solution bounds for three types of Lyapunov matrix equations: continuous, discrete and unified equations. *IEEE Transactions on Automatic Control, 19*(10), 1767–1770.
12. Penzl, T. (2000). Eigenvalue decay bounds for solutions of Lyapunov equations: the symmetric case. *Systems and Control Letters, 40*(2), 130–144.
13. Tippett, M. K., & Marchesin, D. (1999). Upper bounds for the solution of the discrete algebraic Lyapunov equation. *Automatica, 35*, 1485–1489.
14. Truhar, N., & Veselic, K. (2007). Bounds on the trace of a solution to the Lyapunov equation with a general stable matrix. *Systems and Control Letters, 56*(7–8), 493–503.
15. Lee, C. H. (1997). New results for the bounds of the solution for the continuous Riccati and Lyapunov equations. *IEEE Transactions on Automatic Control, 42*, 118–123.
16. Ostrowski, A., & Schneider, H. (1961). Some theorems on the inertia of general matrices. *Journal of Mathematical Analysis and Applications, 4*, 72–84.

Chapter 104
Automated Stock Trading Algorithm Using Neural Networks

Brett Taylor, Min Kim and Anthony Choi

Abstract One of many applications of artificial neural networks is discovering non-linear patterns in time series data. In this paper, analysis of the efficacy of applying an artificial neural network to the time series data produced by fluctuating stock prices is discussed in more detail. There are few current models that are capable of analyzing stocks but they lack in predicting effectively. Results of this neural network are examined through the generated return on investment. The network used for stock analysis is a four layer, feed-forward artificial neural network. The results of this network reveal that artificial neural networks are capable of performing technical analysis on stock prices. The return on investment ranged anywhere from 0.8 to 5.28 % per month or as extrapolated over a year, as high as 17 %.

Keywords Neural network · Stock market · Trading algorithm · S&P 500 · Autonomous investing

104.1 Introduction

Artificial Neural Networks (ANN's) are artificial intelligence technology that generates successful results in many cases which complex interactions exist between the variables or where no single solution set is available. ANN's, which differ from linear models, can provide modeling in cases where the relationships

B. Taylor · A. Choi (✉)
Department of Electrical and Computer Engineering, Mercer University,
Macon, GA 31207, USA
e-mail: choi_ta@mercer.edu

M. Kim
Department of Government and Sociology, Georgia College and State University,
Milledgeville, GA 31061, USA

J. Juang et al. (eds.), *Proceedings of the 2nd International Conference on Intelligent Technologies and Engineering Systems (ICITES2013)*, Lecture Notes in Electrical Engineering 293,
DOI: 10.1007/978-3-319-04573-3_104,

between data of a problem is either not certain, not linear, or even indefinite [1]. Each artificial neuron, similar to their biological counterpart, talks to one another to complete a defined task thus allowing the neuron to learn. The same is true for a neural network [2, 3]. Neural networks have improved significantly from introduction of the perceptron in 1949. It was in 1986 that the backpropagation discovery proved to be crucial for the revival of ANN's [4]. Until recently, neural network research was limited. Since the invention of personal computers, many new possibilities for the individual have become possible [5]. Many decision support systems owe much to artificial intelligence (AI). The need for AI is growing more due to the capability of forecasting, machine learning for decision-making, and soft computing [6].

Forecasting has been called both an art and a science. It has the ability to recognize patterns through both a logical and an analytical approach. This is used for problems in business, economics and naturally occurring phenomena like the weather [7, 8]. All of these factors have led to ANN's becoming increasingly popular in finance. Also, financial service organizations have been the second largest sponsor of research in ANN's. For this reason, financial topics are a large part of neural network analysis [9].

The stock market is a public market where a large amount of capital is invested and traded all over the world. Many researchers claim that the market is dynamic, nonlinear and complicated in nature [10]. Since 1977, people have been trying to analyze the stock market by price manipulation. If this is successful, then many academic and financial rewards could be realized [11, 12]. Currently, stock traders depend on intelligent trading systems which help them in predicting prices based on various situations. This causes many instantaneous decisions to make a quick return [13].

The stock market is affected by many issues like economic, political, and sentimental factors. These issues interact with one another in a very complex manner [14]. Individual stock prices are constantly fluctuating due to a variety of factors: performance of the company; investor sentiment and speculation; and the movement of the market among many others. Over time, the fluctuations produce time series data sets. Forecasting future price movement based on these data sets is known as technical analysis [15]. Technical analysis ignores some factors that cause stock price movement such as company performance and instead focuses on predicting investor psychology by studying patterns and trends in the time series data [16–18].

The stock market is one of the most popular investments due to its expected profit. As a result, there have been many investigations and research to predict these outcomes. However, qualitative factors, like political or macro-economic effects, make reliable prediction of the stock market extremely hard. One developing possible solution is fuzzy logic, which takes a lot of prior knowledge to complete a solid analysis [19, 20].

Predicting future events from a noisy time series data is commonly done using various forms of statistical models. Typical neural network models are closely related to statistical models and have the capability of pattern recognition. For a

noisy time series prediction, neural networks have delays in embedding previous inputs which are mapped into this prediction. High noise signals are hard to predict and require much tweaking [21].

Empirical results have shown that ANN's outperform linear regression since stocks are so complex, nonlinear, and dynamic. ANN's make very few assumptions as opposed to normality assumptions found in statistical methods. Once an underlying relationship between input variables and outputs are determined, ANN's can determine patterns and predict future events [22]. This is most often done by feed-forward networks with backpropagation. The sliding window over the input sequence in the feed-forward network helps forecasting to have more accurate results [23].

One application of ANN's is pattern recognition in time series data. Past studies have shown that ANNs can successfully perform technical analysis on stock data to predict stock prices, market directions, and/or to produce buy/sell signals [24]. A study by Egeli, Ozturanm and Badur found ANN successful in predicting the direction of market movement with a success rate between 63 and 81 % [25]. In another study, Mahfoud and Mani found that a backpropagation trained neural network aimed at predicting the directional movement of individual stock prices could produce a 13.63 % yearly return on investment with a directional accuracy of 79.2 % [26].

This paper describes an ANN implementation designed to produce an intelligent stock trading strategy. The goal of the strategy is to use 30 days of pervious stock data to predict if the stock's price will increase/decrease more than 3 % at a point 5 days in the future. Using the predictions, an autonomous trading algorithm is created which buys a stock long/short if the stock is predicted to increase/decrease and then automatically sells the stock 5 days from the date of purchase.

104.2 Data Set

The data set was composed of 494 stocks taken from the S&P 500 over the data range of August 1st, 2009 to October 31st, 2011. Six S&P 500 stocks were not used due to incomplete data over the date range. Data used for each stock included the daily high, low, open, close price, and volume. Prices were adjusted in the case of a stock split.

Two additional data points were calculated from the daily closing price: a 5 day and 26 day exponential moving average (EMA). Moving averages are common in technical analysis and used to determine price resistance and price breakouts [27]. The exponential moving averages were calculated using the following equations:

$$EMA(t) = close(t) * k + EMA(t-1) * (1-k) \tag{104.1}$$

$$k = 2/(N+1) \tag{104.2}$$

where t is the current data and N is the length of the EMA in days.

The data set was divided into three groups: a training set, validation set, and test set. Each data set included all 494 stocks. The training set included stock data from August 1st, 2009 to May 31st, 2011. The validation set consisted of stock data from June 1st, 2011 to August 31st, 2011 and the test set consisted of stock data from September 1st, 2011 until October 31st, 2011.

104.3 Network Architecture

The analysis of the data set was done in MATLAB. The back propagation algorithm in MATLAB is used to analyze the data. Backpropagation consists of feeding the data into the input layer, propagating it through the hidden layer and outputting the results to the output layer [28].

A four layer, feed forward artificial neural network was used. The input layer consisted of 210 nodes divided into 7 groups of 30 nodes. The 7 groups are open price, closing price, high price, low price, volume, 5 day EMA and 26 day EMA. The network contained two hidden layers: the first with 40 nodes and the second with 20 nodes. Input and hidden layers utilized a hyperbolic tangent activation function.

The output layer consists of two nodes using log sigmoid activation functions. The first output node was dedicated to predicting a 3 % increase in stock price and the second was dedicated to predicting a 3 % decrease in stock price. For both nodes, the desired output was a 1 if their respective conditions occurred and a 0 otherwise.

Backpropagation was used to train the neural network. The trading algorithm applied a threshold of 0.8 to the networks two outputs. An output above this level triggered a stock purchase; outputs below the threshold were ignored. The trading algorithm automatically sold purchased stocks in 5 days regardless of additional network outputs.

104.4 Initial Results

The initial training of the neural network focused on minimizing the MSE of both the training and validation set. Overtraining, as determined by the point at which the validation MSE begins a consistent increase, occurred at epoch 15. However, if training was stopped at this point, the ability of the network to produce monetary returns was poor. Instead, allowing the network to over train showed improvements in many categories.

To break the network from learning date specific patterns, two steps were taken. The first step was that only every third day of data was used in the testing set. This led to less reinforcement of a pattern only slightly shifted in time. Instead a pattern

found at multiple points in time would gain an edge over a pattern found only once in each stock.

Perhaps more importantly, the entire date range was not used for each stock in the test set. Instead, for the training set one year of consecutive data was chosen at random for each stock. Further testing indicated improved results.

104.5 Training Optimization Algorithm

From the initial results, it was determined MSE minimization is an insufficient criteria for producing an optimally trained neural network. Instead, training should focus on maximizing the potential for the neural network to produce monetary returns. A new training algorithm was developed, with each epoch of the training algorithm with the following steps:

(1) Randomize the order of training set data.
(2) Sequentially train the neural network on the entire training set. Backpropagation was used for weight adjustment, with the error being the difference between the desired network output and the actual output.
(3) Apply the neural network to the validation set to produce predictions. For each predicted buy, calculate the percent gain/loss if the stock was bought at that day's closing price and sold at the closing price 5 days in the future. Calculate the return on investment for the current epoch's percent return.
(4) If the percent return is the largest return so far, save the network.

The training algorithm ran until a larger return had not been found in the past 60 epochs.

104.6 Final Results

The final neural network was trained using the optimization algorithm discussed in the previous section. The network reached optimal training at epoch 44. The MSE of the training and validation set versus epoch number is shown in Fig. 104.1.

Figure 104.2 shows the percent return per investment of the test and validation set as the optimization algorithm was performed. At epoch 44, the validation set produces an overall return on investment of 0.8 %. While the overall return appears low, the Dow Jones Industrial Average was down −5.5 % during this period meaning the network outperformed the market by 6.3 % over this 3 month period.

Applied to the test set, the neural network outperformed the market during September and October 2011. During this period, the network generated a return

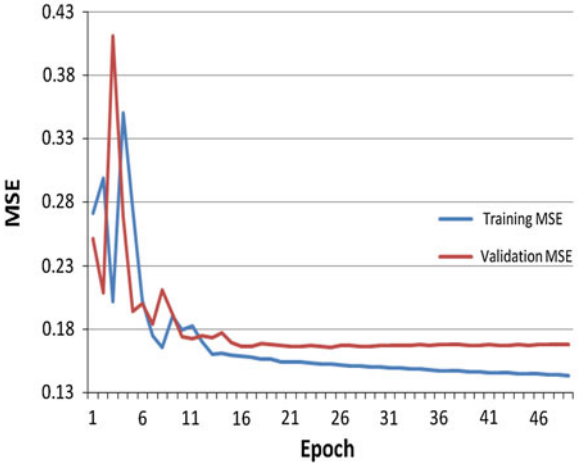

Fig. 104.1 Comparison of training and validation MSE

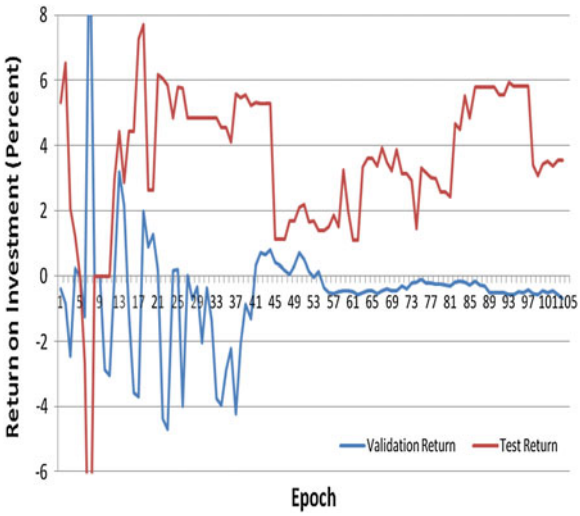

Fig. 104.2 Percent return of the validation and test sets

on investment of 5.28 %. The performance versus the market during this 2 month period was 1.28 %.

Another measure of the neural network performance is the percentage of transactions for which the network predicted the correct direction of price movement. For the validation set, the neural network was correct in 24 of 38 cases for 63.2 % percent correct. For the test set, the neural network was correct in 12 out of 14 cases for 85.7 % percent correct. Figure 104.3 shows the percent correct of the validation and test sets as the network trained.

The results of the network training were best at epoch 25 and epoch 41. At epoch 25, there was a higher return, however, not as many predictions were made.

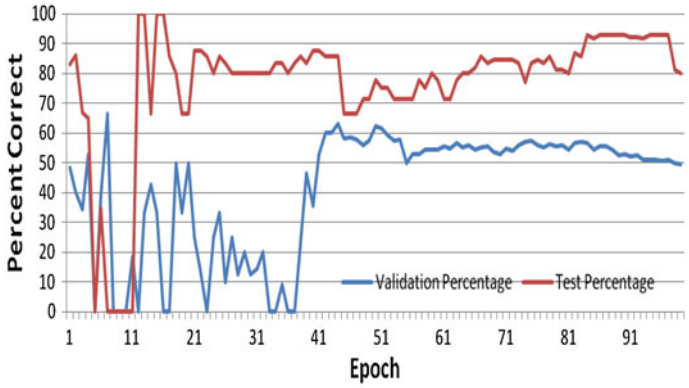

Fig. 104.3 Percent correct of the validation and test sets

The test predictions were at least 80 % when the ANN was predicting a buy. The stocks above the threshold show that the closer that the number is to 1, the stronger the buy signal was from the network. If the number was greater than the threshold, the neural network would predict a buy. When a buy was made, the stock would be purchased and held for 5 days before being sold.

In epoch 41, the return on investment was not as high; however, more predictions of a buy occurred during the month, so this is the better result for the neural network. The stocks above the threshold had a strong enough prediction that the ANN would suggest a buy. There are many more predictions, which results in many more buys per a month. The important part of this is the fact that it is showing that many more buys are predicted as compared to epoch 25. Epoch 25 did, however, return slightly higher yields but with fewer purchases.

The investment opportunities are up to the stockholder. The analysis of these two networks shows great potential for a return on their investment.

104.7 Conclusion

The trading algorithm presented in this paper demonstrated that artificial neural networks are capable of performing technical analysis on individual stocks. The trained ANN predicted the direction of price movement with an average success rate of 74.45 %. This result is within the 63–81 % range given by Egeli, Ozturanm and Badur [25] and slightly below the 79.2 % result produced by Mahfoud and Mani [26].

If the results from the 5 month validation and test period are combined and averaged, the network generated a return of 1.45 % per month or 17.4 % for the year. The combined results outperformed the market by 1.37 % per month or

16.4 % for the year. This return rate slightly exceeds the 13.63 % return on investment found by Mahfoud and Mani [26].

Acknowledgments This research was partially funded NASA. Authors would like to thank Roland Adams for his help with editing.

References

1. Yildirim, I., Ozsahin, S., & Akyuz, K. (2011). Prediction of the financial return of the paper sector with artificial neural networks. *BioResources, 6*(4), 4076–4091.
2. Adya, M., & Collopy, F. (1998). How effective are neural networks at forecasting and prediction? A review and evaluation. *Journal of Forecasting, 17*, 481–495.
3. Vaisla, K., & Bhatt, A. (2010). An analysis of the performance of artificial neural network technique for stock market forecasting. *International Journal on Computer Science and Engineering, 2*(6), 2104–2109.
4. Nygren, K. (2004). *Stock prediction: A neural network approach* (pp. 1–40). Sweden: Royal Institute of Technology.
5. Kutsurelis, J. (1998). *Forecasting financial markets using neural networks: An analysis of methods and accuracy* (pp. 1–68). Monterey: Naval Post Graduate School.
6. Leigh, W., Purvis, R., & Ragusa, J. (2002). Forecasting the NYSE composite index with technical analysis, pattern recognizer, neural network, and genetic algorithm: A case study in romantic decision support. *Decision Support Systems, 32*, 361–377.
7. Gentry, T., Wiliamowski, B., & Weatherford, L. (1995). A comparison of traditional forecasting techniques and neural networks. *Intelligent Engineering Systems through Artificial Neural Networks*, *5*, 765–770.
8. Zhang, G., & Kline, D. (2007). Quarterly time-series forecasting ith neural networks. *IEEE Transactions on Neural Networks, 18*(6), 1800–1814.
9. Kaastra, I., & Boyd, M. (1996). Designing a neural network for forecasting financial and economic time series. *Neurocomputing, 10*, 215–236.
10. Padhiary, P., & Mishra, A. (2011). Development of improved artificial neural network model for stock market prediction. *International Journal of Engineering Science and Technology, 3*(2), 1576–1581.
11. Roodposhi, F., Shams, M., & Kordlouie, H. (2011). Forecasting stock price manipulation in capital market. *World Academy of Science, Engineering and Technology, 80*, 151–161.
12. Gryc, W. (2013). *Neural network predictions of stock price fluctuations* (pp. 1–42). Science.
13. Shah, V. (2007). *Machine learning techniques for stock prediction* (pp. 1–18). New York: Courant Institute of Mathematical Science.
14. Mehrara, M., Moeini, A., Ahrari, M., & Ghafari, A. (2010). Using technical analysis with neural network forecasting stock price index in Tehran stock exchange. *Middle Eastern Finance and Economics, 6*, 50–61.
15. Kirkpatrick, C., & Dahlquist, J. (2006). *Technical analysis: The complete resource for financial market technicians* (pp. 1, 3). Upper Saddle River: Financial Times Press.
16. Investopedia website. (2011). http://www.investopedia.com/articles/trading/02/121602.asp#axzz1gHWeifaP
17. Mizuno, H., Kosaka, M., & Yajima, H. (1998). Application of neural network to technical analysis of stock market prediction. *Studies in Information and Control, 7*(3), 1–14.
18. Schumaker, R., & Chen, H. (2009). A quality stock prediction system based on financial news. *Information Processing and Management, 45*(5), 1–29.

19. Kuo, R., Chen, C., & Hwang, Y. (2001). An intelligent stock trading decision support system through integration of genetic algorithm based fuzzy neural network and artificial neural networks. *Fuzzy Sets and Systems, 118*, 21–45.
20. Tabrizi, H., & Panahian, H. (2000). *Stock price prediction by artificial neural networks: A study of tehran's stock exchange* (pp. 1–17). University of Kashan.
21. Giles, C., Lawrence, S., & Tsoi, A. (2001). Noisy time series prediction using a recurrent neural network and grammatical inference. *Machine Learning, 44*(1), 1–31.
22. Man-Chung, C., Chi-Cheong, W., & Chi-Chung, L. (2000). Financial time series forecasting by neural network using conjugate gradient learning algorithm and multiple linear regression weight initialization. *Computing in Economics and Finance, 2000*(61), 1–6.
23. Frank, R., Davey, N., & Hunt, S. (n.d.). *Time series prediction and neural networks* (pp. 1–12). S.P Hunt Department of Computer Science.
24. Lawrence, R. (1997). *Using neural networks to forecast stock market prices* (pp. 5484–5488). International Joint Conference.
25. Egeli, B., Ozturan, M., & Badur, B. (2011). *Stock market prediction using artificial neural networks* (pp. 116–119). Intelligent Human-Machine Systems and Cybernetics (IHMSC).
26. Mahfound, S., & Mani, G. (1996). Financial forecasting using genetic algorithms. *Applied Artificial Intelligence, 10*(6), 543–566.
27. Stock charts website. (2011). http://stockcharts.com/school/doku.php?id=chart_school:technical_indicators:moving_averages
28. Nazari, J., & Ersoy, O. (1992). *Implementation of back-propagation neural networks with MATLAB* (pp. 1–19). Purdue e-Pubs.

Chapter 105
Properties of Excess Bi_2O_3 0.65 ($K_{0.5}Bi_{0.5}TiO_3$)-0.35 $BaTiO_3$ Ceramics with Separately Calcining Process

W. C. Tzou, Y. C. Ciou, Y. H. Lin, P. S. Cheng and C. F. Yang

Abstract In this study, $K_{0.5}Bi_{0.5}TiO_3$ (KBT) and $BaTiO_3$ (BT3) compositions were calcined separately at 900 and 1100 °C. After calcinition, 0–2 wt% excess Bi_2O_3 was added to form the 0.65KBT + 0.35BT3 + x wt% Bi_2O_3 compositions (x = 0, 1, 2, KBT-BT3-x), then the KBT-BT3-x ceramics were sintered at 1050–1100 °C. The excess Bi_2O_3 was added to compensate for the vaporization of Bi_2O_3 during the sintering process as well as the sintering aid to lower the sintering temperature of the KBT-BT3 ceramics. The effects of excess Bi_2O_3 content and sintering temperature on the properties of the KBT-BT3-x ceramics were investigated by examining the surface morphology, X-ray diffraction (XRD) pattern, and dielectric constant-temperature curve. From the XRD pattern, the differently secondary phases were observed as different sintering temperatures and excess Bi_2O_3 contents were used; From the dielectric constant measurements, the excess Bi_2O_3-doped KBT-BT3 ceramics revealed a larger dielectric constant than the un-doped KBT-BT3 ceramics.

Keywords Calcined separately · Excess Bi_2O_3 · Secondary phases

W. C. Tzou
Department of Electro-Optical Engineering, Southern Taiwan University, Tainan, Taiwan, Republic of China

Y. C. Ciou · C. F. Yang (✉)
Department of Chemical and Materials Engineering, National University of Kaohsiung, Kaohsiung, Taiwan, Republic of China
e-mail: cfyang@nuk.edu.tw

Y. H. Lin · P. S. Cheng
Department of Electronic Engineering National Kaohsiung, University of Applied Sciences, Kaohsiung, Taiwan, Republic of China

J. Juang et al. (eds.), *Proceedings of the 2nd International Conference on Intelligent Technologies and Engineering Systems (ICITES2013)*, Lecture Notes in Electrical Engineering 293,
DOI: 10.1007/978-3-319-04573-3_105,

105.1 Introduction

$Pb(Zr,Ti)O_3$ (PZT) ceramics are widely used for various applications such as filters, oscillators [1], actuators, sensors, and transducers, due to their excellent piezoelectric properties [2]. However, the volatilization of toxic PbO during sintering process causes environmental pollution and an unstability in compositions and electrical properties [3]. Therefore, developing lead-free piezoelectric materials to replace PZT ceramics and lower the level of lead pollution is of considerable interest. $K_{0.5}Bi_{0.5}TiO_3$ (abbreviated as KBT) is a typical of lead-free ferroelectric material, it is a perovskite structure and has a Curie temperature (T_c = 380–385 °C) [4–7] higher than that of $Na_{0.5}Bi_{0.5}TiO_3$ (abbreviated as NBT, T_c = 300 °C) [3, 5–7]. KBT ceramics can be used in ceramic filters [4] and resonators, but it is difficult to fabricate high density KBT ceramics due to the high volatility of the Bi_2O_3 during sintering process [8]. In the past literatures, the electrical characteristics of the NBT ceramics were improved by the addition of other congestions. For example, KBT, $NaNbO_3$, and $BiFeO_3$ modified NBT-based compositions show better piezoelectric properties and ease of poling as compared with the pure NBT ceramics [8–10]. The investigations of the additions to improve the properties of KBT-based ceramics are less reported. Therefore, we tried to improve the characteristics of the KBT ceramics by added some modified compositions with $BaTiO_3$ (BT3) ceramic because BT3 is a typical perovskite structure and lead-free material and also have good piezoelectric and ferroelectric properties. The KBT ceramics can be prepared by a solid-state reaction method, the resulting powders and ceramics usually have many secondary phases [9], and the secondary phases may affect their properties. As we knew, the different calcining processes would influence the properties of the ferroelectric ceramics [10]. Excess Bi_2O_3 content is known to have significant effects on the ferroelectric properties as well as the crystalline structures of Bi_2O_3-based ceramics. For example, the addition of excess Bi_2O_3 would improve the sintering and dielectric properties of $SrBi_2Ta_2O_9$ [11] and $SrBi_4Ti_4O_{15}$ ceramics [12]. The excess Bi_2O_3 content was used as a sintering aid and to compensate for the vaporization of Bi_2O_3 during the sintering process. Therefore, we used a separately calcination method to prepare the KBT and BT3 compositions, and the calcined KBT and BT3 powders were mixed to obtain the $0.65KBT - 0.35BT3 + x$ wt% Bi_2O_3 compositions. We also investigated the effects of excess Bi_2O_3 content on the properties of the KBT-BT3-x ceramics.

105.2 Experimental Process

K_2CO_3, Bi_2O_3, TiO_2, and $BaCO_3$ powders with greater than 99.5 % purity were weighted according to the compositions of KBT and BT3, and the KBT and BT3 powders were ball-milled independently. After the KBT and BT3 powders were

dried and ground, and then KBT and BT3 were calcined at 900 and 1100 °C for 4 h. After being ground, the KBT and BT3 powders were mixed with excess Bi_2O_3 to form the 0.65KBT + 0.35BT3 + x wt% compositions (x = 0, 1, 2, abbreviated as KBT-BT3-0, KBT-BT3-1, KBT-BT3-2). Finally, the mixed powders were ground and uniaxially pressed into pellets of 1 mm in thickness and 12 mm in diameter using a steel die. The pellets were sintered at 1050–1100 °C in air for 2 h. Crystalline structure of the KBT-BT3-x ceramics was investigated by X-ray diffraction (XRD) pattern, and their surface morphology was observed using a scanning electronic microscope (SEM). The KBT-BT3-x ceramics were painted with Ag-Pd paste and sintered at 700 °C for 15 min. Temperature-dependence of dielectric properties were measured with an oscillating amplitude (50 mV) at 1 MHz using an HP4294A impedance analyzer, the measured temperature was changed from 25 to 500 °C in order to find the maximum dielectric constant and Curie temperature (T_c) of the KBT-BT3-x ceramics.

105.3 Results and Discussion

XRD analyses of the KBT-BT3-x ceramics are shown in Fig. 105.1, ABO_3 is the mainly crystalline phase, which is the solid solution of the KBT and BT3 or called $(K_{0.5}Bi_{0.5},Ba)TiO_3$. For 1075–1100 °C-sintered KBT-BT3-0 ceramics, the secondary phases with the diffraction peaks at around 30° and 32.8° are observed. Compared with the results reported by Zhu et al. [4] and JCPD file (NO. 41-0167), the secondary phase is $K_4Ti_3O_8$. Smyth et al. reported that oxygen escapes during the thermal-treated processes, and oxygen vacancies are subsequently generated according to:

$$O_o \rightarrow V_o^{++} + 2e^- + 1/2\ O_2 \tag{105.1}$$

where O_o, V_o^{++}, and e^- denote the oxygen ions at its normal site, oxygen vacancy, and electrons, respectively [13]. If we sinter bismuth-based ceramics in air, the oxygen easily escapes from the Bi_2O_3 to form Bi atoms. The melting points of Bi and Bi_2O_3 are 273 °C and 825 °C, the Bi_2O_3 will volatilize during sintering process, and the following equation occurs and the $K_4Ti_3O_8$ phase reveals in the KBT-BT3-0 ceramics:

$$K_{0.5}Bi_{0.5}TiO_3 \rightarrow K_4Ti_3O_8 + Bi_2O_3 \uparrow \tag{105.2}$$

Although the $K_4Ti_3O_8$ phase is apparently observed in the KBT-BT3-0 ceramic, it is not observed in the KBT-BT3-1 and KBT-BT3-2 ceramics. Those results can prove that the excess Bi_2O_3 content can compensate for the volatilization of Bi_2O_3 during the sintering process, and thus Eq. (105.1) not occurs. This may indicate that the addition of excess Bi_2O_3 have apparent influences on the crystalline structures and then on the lattice constants of the KBT-BT3-x ceramics. Sintered at 1075 and 1100 °C, the full width at half maximum (FWHM) values of the

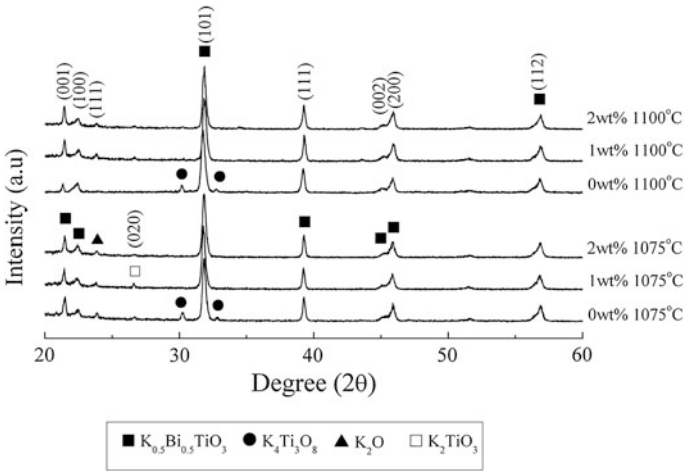

Fig. 105.1 XRD patterns of KBT-BT3-x ceramics as a function of sintering temperature and excess Bi_2O_3 content

KBT-BT3-0 ceramics at the (101) diffraction peak are 0.356 and 0.400, which are larger than those of the KBT-BT3-1 and KBT-BT3-2 ceramics. As excess Bi_2O_3 content increases, a minimum FWHM value of 0.288 can be found in 1075 °C-sintered KBT-BT3-2 ceramics. These results also prove that the excess Bi_2O_3 content can improve the crystallinity of the KBT-BT3-x ceramics, and the optimum excess content in this study is 2 wt%.

Figure 105.2 shows the variations in the lattice constants ***a*** and ***c*** of the KBT-BT3-x ceramics as a function of sintering temperature. The lattice constant ***a*** is almost unchanged as the sintering temperature was raised from 1050 to 1100 °C. This result reveals that the lattice constant ***a*** is not affected by the excess Bi_2O_3 content. The variations in lattice ***c*** are also shown in Fig. 105.2, the lattice constant ***c*** first decreased as the sintering temperature raised from 1050 to 1075 °C, then it increased as sintered at 1100 °C. The decrease of lattice ***c*** in 1075 °C-sintered KBT-BT3-0 and KBT-BT3-1 ceramics is attributed to the Bi_2O_3 evaporating. The secondary phases of $K_4Ti_3O_8$ and K_2TiO_3 are observed in the 1075 °C-sintered KBT-BT3-0 and KBT-BT3-1 ceramics, and the diffraction intensities of the $K_4Ti_3O_8$ and K_2TiO_3 phases are larger than those of the 1100 °C-sintered KBT-BT3-0 and KBT-BT3-1 ceramics. Thus, these secondary phases might be the reason to cause the decrease of lattice ***c*** at 1075 °C. For KBT-BT3-2 ceramics, the lattice ***c*** value was kept at 4.133(A) at the sintering temperatures of 1050–1075 °C and then increased to 4.137(A) at 1100 °C.

Figure 105.3 shows the SEM micrographs of the KBT-BT3-x ceramics, almost no pores existed on the surfaces and a densified structure was observed. Comparing the surface morphologies of the KBT-BT3-x ceramics, the grain sizes were almost unchanged with rising sintering temperature. It suggests that the grain sizes are not dominated by sintering temperature. As the excess Bi_2O_3 content is

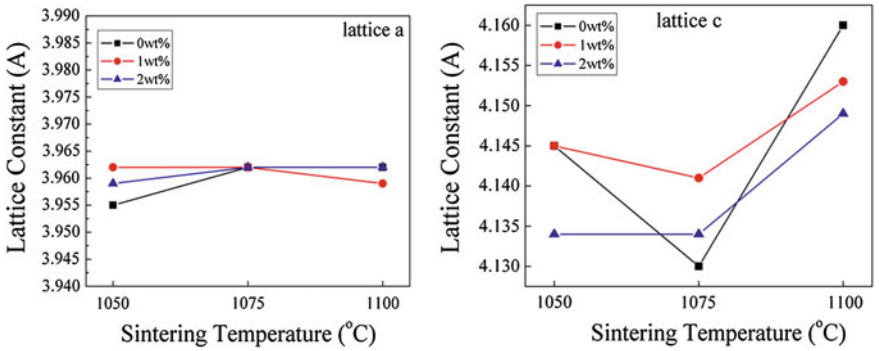

Fig. 105.2 Variations in the lattice constants ***a*** and ***c*** of the KBT-BT3-x ceramics as a function of sintering temperature

increased, the grain size in micrographics is slightly decreased. The ionic radius of Bi^{+3}, K^{+1}, and Ba^{+2} are 0.103, 0.138, and 0.135 nm, respectively. When excess Bi_2O_3 is added, if the Bi_2O_3 (Bi^{+3}) ions are doped into the KBT-BT3 ceramics as an interstitial dopant, the lattice of the KBT-BT3-x ceramics will be changed. However, the 2θ values of the main peaks are almost unchanged as the excess Bi_2O_3 content increases from 1 to 2 wt% (Fig. 105.1). Those results prove that the excess Bi_2O_3 is used to compensate for the vaporization of Bi_2O_3 and the vacancies left by Bi^{+3}. In the KBT-BT3-1 and KBT-BT3-2 ceramics, the excess Bi_2O_3 (or Bi^{+3}) not only compensates for the vaporization of Bi_2O_3 but also is residual at the grain boundary and inhibits grain growth, for that the grain sizes slightly decrease with increasing excess Bi_2O_3 content.

Figure 105.4a shows the dielectric constant-temperature (ε_r–T) curves of the 1075 °C-sintered KBT-BT3-x ceramics. The ε_r–T curves show the ferroelectric characteristics rather than relax or characteristics because as the measured temperature increased, the dielectric constant first increased, reached a maximum at Curie temperature (the temperature to reveal the maximum dielectric constant, Tc), and then decreased. In Fig. 105.4a, the maximum dielectric constant (ε_{max}) obviously increased as excess Bi_2O_3 content increased from 0 to 1 wt% and slightly increased as excess Bi_2O_3 content increased from 1 to 2 wt%. These results prove that 1 wt% excess Bi_2O_3 content is enough to compensate for the vaporization of Bi_2O_3 during the sintering process. Figure 105.4b show the ε_r–T curves of the 1050–1100 °C-sintered KBT-BT3-2 ceramics. From these results, the dielectric constant firstly increased and reached the maximum at 1075 °C, then subsequently decreased at 1100 °C.

Figure 105.5 shows the ε_{max} value of the KBT-BT3-x ceramics as a function of sintering temperature. The ε_{max} value revealed at 1075 °C, independent on excess Bi_2O_3 content. It suggests that the 1100 °C is not the optimum sintering temperature, the optimum excess Bi_2O_3 content and sintering temperature are 2 wt% and

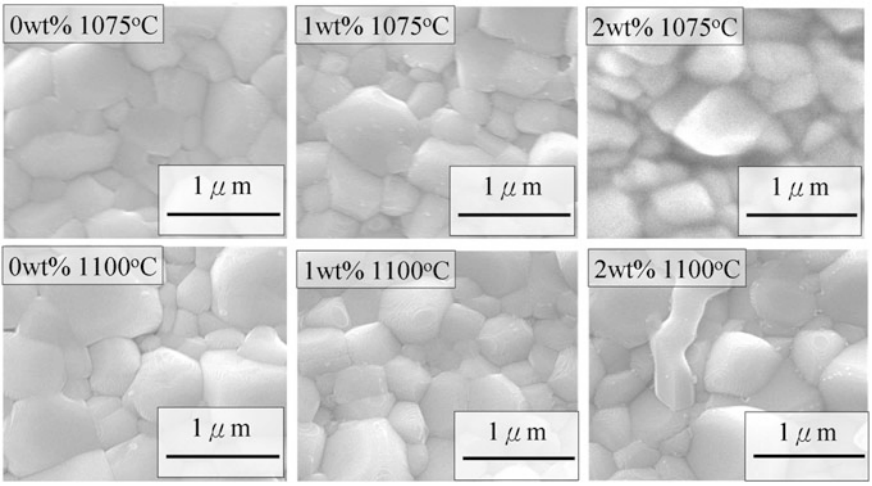

Fig. 105.3 Morphology of the KBT-BT3-x ceramics as a function of sintering temperature

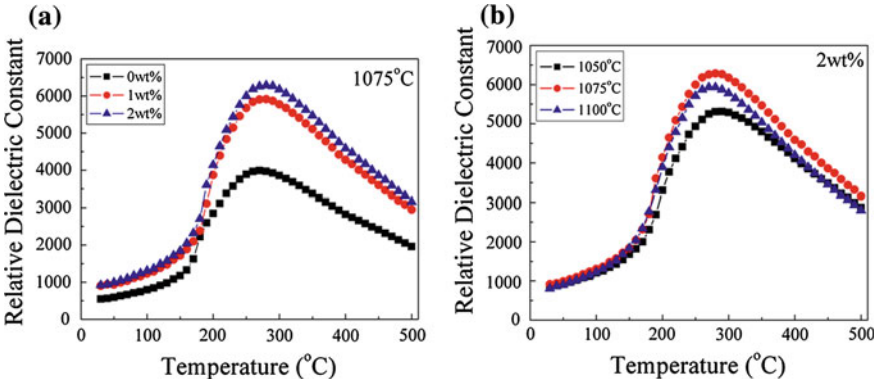

Fig. 105.4 Dielectric constant-temperature curves of (**a**) 1075 °C-sintered KBT-BT3-x ceramics and (**b**) 1050–1100 °C-sintered KBT-BT3-2 ceramics

1075 °C. The Tc value of the KBT-BT3-x ceramics can be predicted by Eq. (105.3):

$$T_C = 0.65 \times 380 + 0.35 \times 120 \tag{105.3}$$

where 380 and 120 °C are the Tc values of the $K_{0.5}Bi_{0.5}TiO_3$ and $BaTiO_3$ ceramics, respectively, and T_C is the predicted Curie temperature of the KBT-BT3-x ceramics. After calculating Eq. (105.3), the predicted Tc value of the KBT-BT3 ceramic is 289 °C. Figure 105.6 shows the Tc values were almost unchanged and close to the predicted Tc value. When the solid-state method is used and

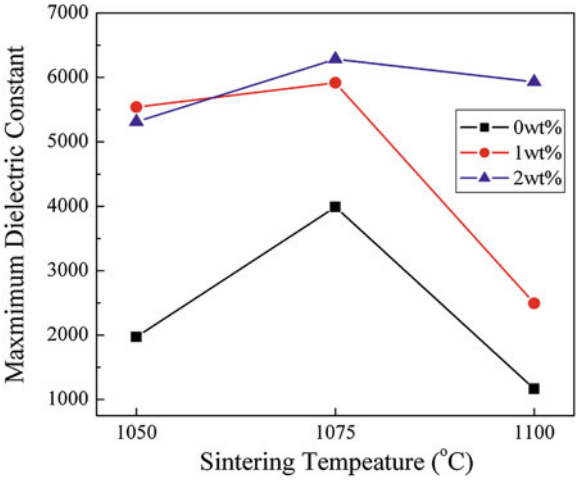

Fig. 105.5 ε_{max} value of KBT-BT3-x ceramics

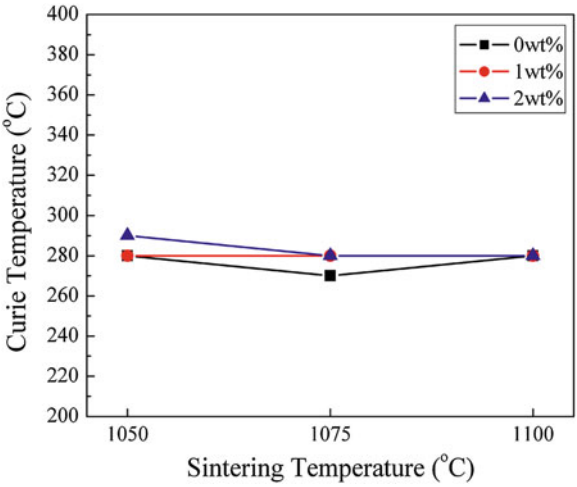

Fig. 105.6 Tc value of KBT-BT3-x ceramics

excess dopant is used, the T_C values of the KBT-BT3-x ceramics will be have a drastically variation, but in this study they have no apparent change. This indicates that the calcined separately is a good method to fabricate KBT-based ceramics.

105.4 Conclusions

In this study, the separately calcined method was well developed to fabricate the KBT-BT3-x ceramics. From the XRD patterns, the secondary $K_4Ti_3O_8$ phase was appeared in KBT-BT3-0, but eliminated as the excess Bi_2O_3 content added, and

the FWHM value reached the minimum value of 0.288 in 1075 °C-sintered KBT-BT3-2 ceramic. The SEM micrographics showed that almost no pores were observed, the KBT-BT3-x ceramics revealed a densified structure, and the grain sizes were almost unchanged with raising sintering temperature and slightly decreased with increasing excess Bi_2O_3 content. Those results suggested that the grain sizes were not dominated by the sintering temperature but dominated by the excess Bi_2O_3 content. The dielectric constant increased with increasing excess Bi_2O_3 content and the maximum value was revealed at 1075 °C-sintered KBT-BT3-2 ceramics.

References

1. Wada, T., Toyoike, K., Imanaka, Y., & Matsuo, Y. (2001). Dielectric and piezoelectric properties of $(A_{0.5}Bi_{0.5})TiO_3$–$ANbO_3$ (A = Na, K) systems. *Japanese Journal of Applied Physics, 40*, 5703–5705.
2. Jaffe, B., Cook, W. R., & Jaffe, H. (1971). *Piezoeelctric Ceramics*. New York: Academic.
3. Li, Y., Chen, W., Xu, Q., Zhou, J., Gu, X., & Fang, S. (2005). Electromechanical and dielectric properties of $Na_{0.5}Bi_{0.5}TiO_3$–$K_{0.5}Bi_{0.5}TiO_3$–$BaTiO_3$ lead free ceramics. *Materials Chemistry and Physics, 94*, 328–332.
4. Zhu, M., Hou, L., Hou, Y., Liu, J., Wang, H., & Yan, H. (2006). Lead-free$(K_{0.5}Bi_{0.5})TiO_3$ powder and ceramics prepared by a sol-gel method. *Materials Chemistry and Physics, 99*, 329–332.
5. Hou, L., Dong, Y., Song, X. M., Zhu, M. K., Wang, H., & Yan, H. (2006). Sol-gel–hydrothermal synthesis and sintering of $K_{0.5}Bi_{0.5}TiO_3$ nanowires. *Materials Research Bulletin, 41*, 1330–1336.
6. Hou, Y. D., Hou, L., Huang, S. Y., Zhu, M. K., Wang, H., & Yan, H. (2006). Comparative study of $K_{0.5}Bi_{0.5}TiO_3$ nanoparticles derived from sol-gel-hydro-thermal and sol-gel routes. *Solid State Communications, 137*, 658–661.
7. Wang, X. X., Tang, X. G., & Chen, H. L. W. (2004). Electromechanical and ferroelectric properties of $(Bi_{1/2}Na_{1/2})TiO_3$-$(Bi_{1/2}K_{1/2})TiO_3$-$BaTiO_3$ lead-free piezoelectric ceramics. *Applied Physics Letters, 85*, 91–93.
8. Buhrer, C. F. (1962). Some properties of bismuth perovskites. *Journal of Chemical Physics, 36*, 798–804.
9. Zaremba, T. (2003). Application of thermal analysis to study of the synthesis of $K_{0.5}Bi_{0.5}Tio_3$ ferroelectric. *Journal of Thermal Analysis and Calorimetry, 74*, 653–658.
10. Yang, C. F., Wu, L., & Wu, T. S. (1992). Influence of calcining temperature to the CuO modified $(Ba_{0.8}Sr_{0.2})(Ti_{0.9}Zr_{0.1})O_3$ ceramics. *Japanese Journal of Applied Physics, 31*, 2170–2176.
11. Wei, Y. F., Kao, C. H., Yang, C. F., Huang, H. H., & Huang, C. J. (2007). The crystal structures and dielectric properties of Bi_2O_3 added $SrBi_2Ta_2O_9$ ceramics. *Materials Letters, 61*, 4643–4646.
12. Wei, Y. F., Yang, C. F., Chen, C. Y., Huang, C. J., & Kao, C. H. (2009). Development of non-stoichiometric SrBi4 + 2xTi4O15 + 3x $(-0.04 \leq x \leq 0.04)$ ceramics. *Advanced Applications of Ceramics, 108*, 102–105.
13. Smyth, D. M., Harmer, M. P., & Peng, P. J. (1989). Defect chemistry of relaxor ferroelectrics and the implications for dielectric degradation. *Journal of the American Ceramic Society, 72*, 2276–2278.

Chapter 106
Use the Grid to Analyze the Influential Factors on Marine Accidents

Chien-Chang Chou, Cheng-Yi Chen, Pei-Chann Chang, Tzu-Min Chang, Kuen-Shiuh Chen, Hua-Zhi Hsu and Kur-Eng Chang

Abstract Based on the collected data including wind, wave, tide and current, this paper uses the grid method to analyze the influential factors on marine accidents in the harbors and waters surrounding Taiwan. Finally, some interesting findings are shown and some useful suggestions are given to the managers of harbors and the decision makers of governmental marine departments. This research results can hope to reduce the risk of the climatic and marine environmental factors, and to increase the navigation safety of ships in the harbors and waters surrounding Taiwan.

Keywords Grid · 3D graphics · Image signal processing · Geographic information system

C.-C. Chou (✉) · K.-S. Chen · H.-Z. Hsu
Department of Shipping Technology, National Kaohsiung Marine University, Kaohsiung, Taiwan, Republic of China
e-mail: ccchou@msil.nkmu.edu.tw

C.-C. Chou
Chou's Science Research Center, Kaohsiung, Taiwan, Republic of China

C.-Y. Chen
Department of Electrical Engineering, Cheng Shiu University, Kaohsiung, Taiwan, Republic of China

P.-C. Chang
Department of Information Management, Yuan Ze University, Taoyuan, Taiwan, Republic of China

T.-M. Chang
Kaohsiung Harbor Marine Survey Co., Ltd, Kaohsiung, Taiwan, Republic of China

K.-E. Chang
Department of Marine Information and Technology, National Kaohsiung Marine University, Kaohsiung, Taiwan, Republic of China

J. Juang et al. (eds.), *Proceedings of the 2nd International Conference on Intelligent Technologies and Engineering Systems (ICITES2013)*, Lecture Notes in Electrical Engineering 293,
DOI: 10.1007/978-3-319-04573-3_106,

106.1 Introduction

Navigation safety is one of important issues in the present marine transportation system. In the past, a lot of researchers obtained the influential factors on navigation safety by using various methodologies, e.g. interview, questionnaire, fuzzy theory, MCDM, AHP and so on. Few identify directly the influential factors on navigation safety by Geographic Information System (GIS). Thus, this paper integrates GIS and Grid method to identify directly the influential factors on navigation safety [1, 3, 4, 6, 8, 10, 14, 16, 19, 21].

Generally, the influential factors on navigation safety include the climatic factor (wind) and marine environmental factors (wave, tide and current). This paper integrates GIS and Grid method to identify directly the relationship between these influential factors and navigation safety. GIS and grid methodologies have been applied widely in many research fields [2, 5, 7, 9, 11–13, 15, 17, 18, 20]. Therefore, GIS and grid methodologies are appropriate approaches for dealing with navigation safety problems.

106.2 Data

The right column of Fig. 106.1 is the map of Taiwan Island. The left column of Fig. 106.1 is the information and the locations of marine accidents in the harbors and waters surrounding Taiwan. The signal "X" in left column of Fig. 106.1 means the location of marine accident. There are three major international ports on the western coast of Taiwan including the ports of Keelung, Taichung and Kaohsiung.

106.2.1 The Port of Keelung

The horizontal axis of Fig. 106.2 is the latitude (N25.324437). The vertical axis of Fig. 106.2 is the longitude (E121.753880). The signal "X" in Fig. 106.2 means the location of marine accident in the water surrounding the port of Keelung.

All marine accidents are separated into 4 areas including northeastern, southeastern, northwestern and southwestern positions. We can see that most of the accidents centralize on the southeastern and northwestern positions (dark colored grids). Few accidents centralize on the northeastern and southwestern positions (light colored grids). The numbers of marine accidents occurred in the southeastern and northwestern positions (dark colored grids) are 244 and 39, respectively. The numbers of marine accidents occurred in the northeastern and southwestern positions (light colored grids) are 28 and 15, respectively.

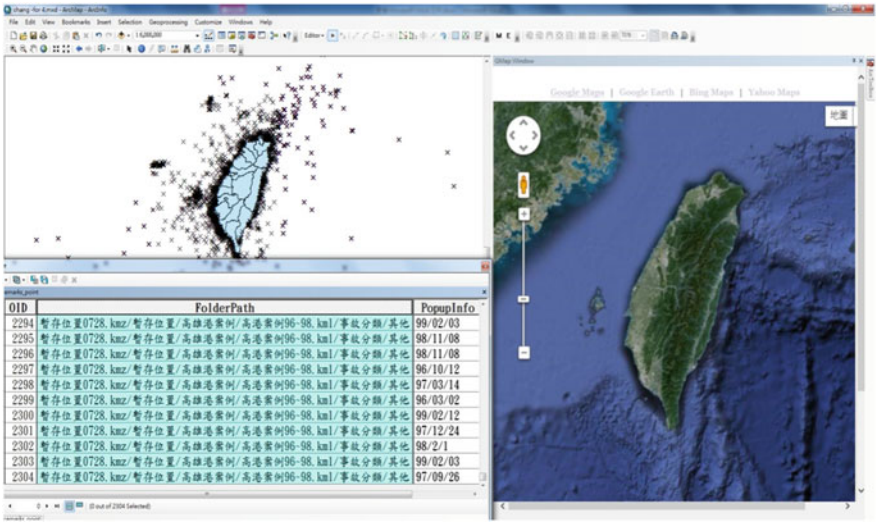

Fig. 106.1 Locations of marine accidents in the harbors and waters surrounding Taiwan

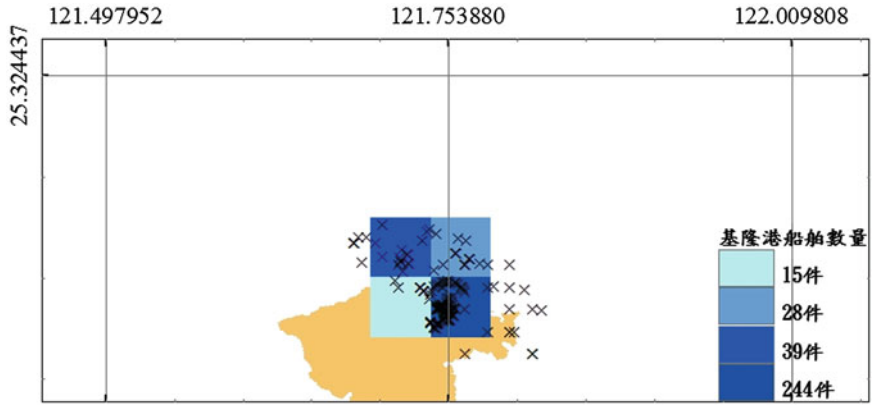

Fig. 106.2 Locations of marine accidents in the water surrounding the port of Keelung

106.2.2 The Port of Taichung

Figure 106.3 is the locations of marine accidents in the water surrounding the port of Taichung. We can see that most of the accidents centralize on the southeastern position (dark colored grids). Few accidents centralize on the northwestern position (light colored grids). The number of marine accidents occurred in the southeastern position (dark colored grids) is 166. The number of marine accidents

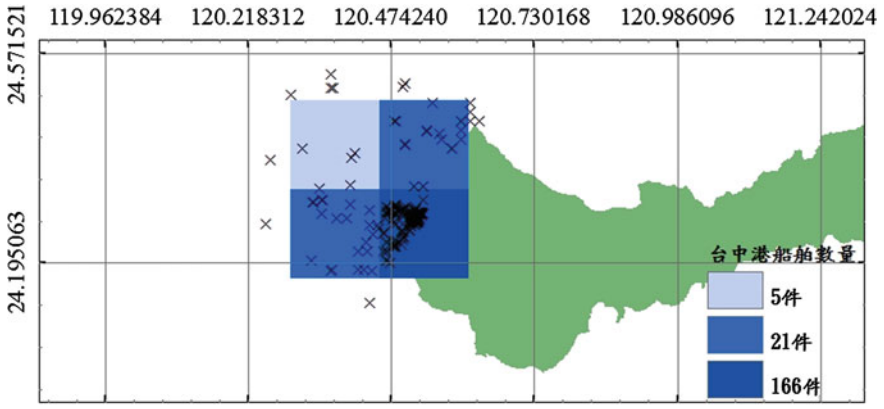

Fig. 106.3 Locations of marine accidents in the water surrounding the port of Taichung

occurred in the northwestern position (light colored grids) is 5. The numbers of marine accidents occurred in the northeastern and southwestern positions are 21.

106.2.3 The Port of Kaohsiung

Figure 106.4 is the locations of marine accidents in the water surrounding the port of Kaohsiung. We can see that most of the accidents centralize on the northwestern and southeastern positions (dark colored grids). Few accidents centralize on the northeastern and southwestern positions (light colored grids). The numbers of marine accidents occurred in the northwestern and southeastern positions (dark colored grids) are 127 and 41, respectively. The numbers of marine accidents occurred in the southwestern and northeastern positions (light colored grids) are 32 and 14, respectively.

106.3 Result Analysis

106.3.1 The Port of Keelung

Figure 106.5 is the gridding of wind, wave, tide and current in the port of Keelung. The first tier from the up is the grid of wind. The second tier is the grid of wave. The third tier is the grid of tide. The last one is the grid of current.

The first tier in Fig. 106.5, the degree of wind is separated into 4 degrees including northeastern, southeastern, northwestern and southwestern positions. The northwestern and southeastern positions (dark colored grids) mean the degree

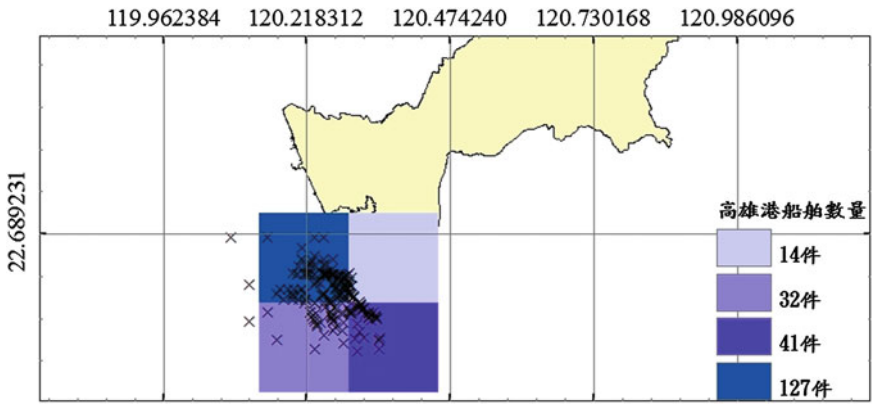

Fig. 106.4 Locations of marine accidents in the water surrounding the port of Kaohsiung

of wind is "very strong" and "strong". The degrees of wind are 6.316666603 and 4.417200089, respectively. The southwestern and northeastern positions (light colored grids) mean the degree of wind is "weak" and "very weak". The degrees of wind are 4.170000076 and 3.480000019, respectively.

106.3.2 The Port of Taichung

Figure 106.6 is the gridding of wind, wave, tide and current in the port of Taichung. The northeastern and northwestern positions (dark colored grids) mean the degree of wind is "very strong" and "strong". The degrees of wind are 14.26333332 and 10.51000023, respectively. The southeastern and southwestern positions (light colored grids) mean the degree of wind is "weak" and "very weak". The degrees of wind are 9.128213882 and 7.224999905, respectively.

106.3.3 The Port of Kaohsiung

Figure 106.7 is the gridding of wind, wave, tide and current in the port of Kaohsiung. The southwestern and northeastern positions (dark colored grids) mean the degree of wind is "very strong" and "strong". The degrees of wind are 3.736666679 and 2.864444494, respectively. The southeastern and northwestern positions (light colored grids) mean the degree of wind is "weak" and "very weak". The degrees of wind are 2.691333294 and 2.191212177, respectively.

Based on the above Figs. 106.2, 106.3, 106.4, 106.5, 106.6, 106.7, we can find (a) the wave and the current are the influential factors on navigation safety in the port of Keelung; (b) the current and the wind are the influential factors on

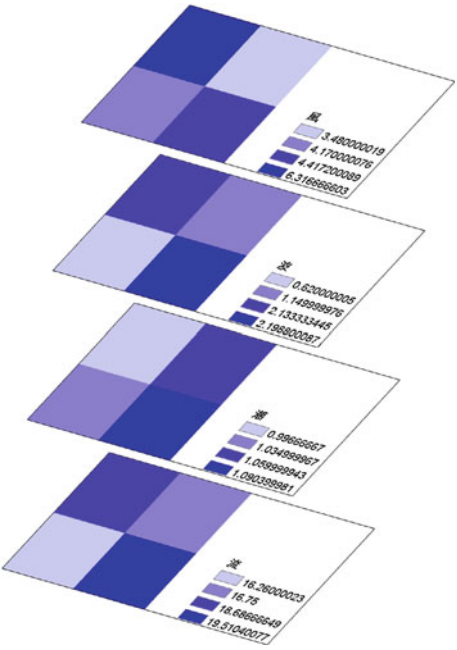

Fig. 106.5 The gridding of wind, wave, tide and current in the port of Keelung

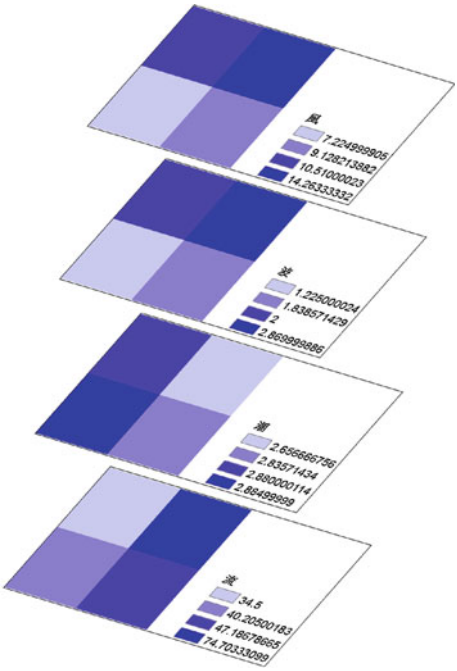

Fig. 106.6 The gridding of wind, wave, tide and current in the port of Taichung

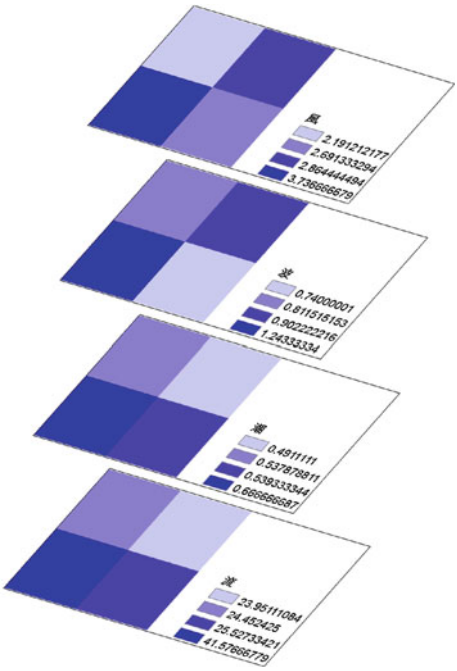

Fig. 106.7 The gridding of wind, wave, tide and current in the port of Kaohsiung

navigation safety in the port of Taichung; (c) the current and the tide are the influential factors on navigation safety in the port of Kaohsiung.

106.4 Conclusions

One of the major advantages of this paper is to integrate GIS and Grid method to study the navigation safety problem. The other is to identify directly the relationship between these influential factors and navigation safety by GIS 3D image.

Acknowledgments This research work was partially supported by the National Science Council of the Republic of China under Grant No. NSC 101-2410-H-022-004.

References

1. Berthelot, K. (2013). A classical ethical problem in ancient philosophy and Rabbinic thought: The case of the shipwrecked. *Harvard Theological Review, 106*(2), 171–199.
2. Cai, Z., Liu, D. M., Gu, X. Q., & Yin, J. M. (2010). Simulation of agricultural climate resources based on GIS in Jiangxi province. *Acta Agriculturae Universitatis Jiangxiensis, 32*(4), 842–846.

3. Ernst, D. R. (2009). Ernst Freund, Felix Frankfurter, and the American Rechtsstaat: A transatlantic shipwreck, 1894–1932. *Studies in American Political Development, 23*(2), 171–188.
4. Gao, C. C. (1996). Meteorology and shipwreck. *Meteorological Monthly, 22*(10), 54–57.
5. Goodchild, M. F., & Janelle, D. G. (2004) *Spatially integrated social science*. New York: Oxford University press.
6. Grocott, D. F. H. (1999). Shipwrecks in the revolutionary and Napoleonic Eras, 1793–1815, causal factors and comments. *Journal of Navigation, 52*(2), 149–162.
7. Guilmoto, C. Z. (2001). Spatial patterns of fertility transition in Indian district. *Population and Development Review, 27*(4), 713–738.
8. Huang, S. J., Xue, Y. B., Shi, L., & Wang, J. F. (2006). An analysis on relationship between the shipwreck of combination vessels and the Gale accident in the Bohai Straits. *Journal of Meteorology and Environment, 22*(3), 30–32.
9. Huang, J.W. (2007) *The research for GIS cell resolution*. Master Thesis, Department of Urban Planning, National Cheng Kung University, Tainan.
10. Huxley, H. H. (1952). Storm and shipwreck in Roman literature. *Greece and Rome, 21*(63), 117–124.
11. Jiang, W. G., Wu, J. J., Gu, L., Liu, X. C., & Li, X. X. (2010). Change monitoring in Wuda coalfield fire area based on remote sensing. *Journal of China Coal Society, 35*(6), 964–968.
12. Kishor, S. (1993). May god give sons to all, gender and child mortality in India. *American Sociological Review, 58*(2), 247–265.
13. Li, S. S., Yan, J. P., & Wan, J. (2012). The spatial-temporal changes of vegetation restoration on Loess plateau in Shaanxi-Gansu-Ningxia region. *Acta Geographica Sinica, 67*(7), 960–970.
14. Liu, X. P. (2001). An analysis on maritime distress over Yantai sea area and preventive measures related. *Meteorological Monthly, 27*(3), 55–57.
15. Liu, Z. J., Yu, X. X., Li, L., & Huang, M. (2011). Vulnerability assessment of eco-environment in Yimeng mountainous area of Shandong province based on SRP conceptual model. *Chinese Journal of Applied Ecology, 22*(8), 2084–2090.
16. Macdonald, D. R. (1999). The shipwrecks of Odysseus and Paul. *New Testament Studies, 45*(1), 88–107.
17. Pagano, M., & Gauvreau, K (2000) *Principles of biostatistics* (2nd ed.). Pacific Grove: Duxbury Thomson Learning.
18. Shen, Z. F., Luo, J. C., Huang, G. Y., & Zhao, Y. F. (2004). Discussion on grid GIS and its application in digital oil fields. *Geography and Geo-information Science, 20*(3), 48–51.
19. Tai, P. T. (2010). Marine perils and rescue in early Japanese colonial Taiwan. *Graduate Institute of Taiwan History Periodical Articles, 61*(3), 191–242.
20. Zhan, S. B., Chen, S. B., Li, Y. H., Cheng, B., & Xuan, Y. H. (2007). Key techniques to development of a raster data-based GIS. *Computer Applications and Software, 24*(3), 18–21.
21. Zhu, T. S., Cao, S. T., Feng, C. C., & Shang, Z. T. (2008). Analysis on the tidewater characteristics of shipwreck. *Journal of Anhui Agricultural Sciences, 36*(35), 15615–15617.

Chapter 107
Effect of Drain FODs on ESD/LU Immunities in the 60-V High-Voltage nLDMOS

Shen-Li Chen, Min-Hua Lee, Yi-Sheng Lai, Chun-Ju Lin, Yu-Ting Huang and Shawn Chang

Abstract Electrostatic discharge (ESD) and latch-up (LU) are the most challenging problems in high-voltage (HV) ICs due to their high power supply voltages. So, an HV LDMOS should be compromised with a high driving capability and high reliability, but it always has obvious conflicts. An MOSFET device fabricated by a multi-finger structure can't completely turn on, which resulting in the ESD capacity per unit length is very low especially for an HV device. Then, the non-uniform turned-on phenomenon in an LDMOS is seriously impacted the ESD reliability. Therefore, a drain-side engineering is investigated in this paper, which is by adding a field-oxide-device (FOD) structure in the drain side. Does it can solve the non-uniform turned-on problem? After a systematic analysis, it is found that by adding FOD structures in the drain-side is favor to ESD capability (I_{t2} value) in the case of high FOD/n^+ ratio as the FOD/N^+ area ratio is larger than 80/100. However, as compared with the original reference DUT, the V_h value is increased about 16.37 $\sim$ 59.87 %, which allows devices more robust in the latch-up (LU) immunity.

Keywords Electrostatic discharge (ESD) · Field oxide device (FOD) · Gate-grounded n-channel MOS (GGnMOS) · Latch-up (LU) · Lateral-diffused MOS (LDMOS) · Trigger voltage (V_{t1}) · Secondary breakdown current (I_{t2})

107.1 Introduction

Recently, many semiconductor companies extend mature from low-voltage (LV) applications, HV power management, green energy or telecommunication module ICs have been focused as the development projects in IC design houses [1–5].

S.-L. Chen (✉) · M.-H. Lee · Y.-S. Lai · C.-J. Lin · Y.-T. Huang · S. Chang
Department of Electronic Engineering, National United University, MiaoLi City 36003, Taiwan, Republic of China
e-mail: jackchen@nuu.edu.tw

J. Juang et al. (eds.), *Proceedings of the 2nd International Conference on Intelligent Technologies and Engineering Systems (ICITES2013)*, Lecture Notes in Electrical Engineering 293,
DOI: 10.1007/978-3-319-04573-3_107,

Generally, the HV MOSFET are fabricated with thick gate oxides and lowly doped source/drain implantations. In order to increase the breakdown voltage, devices are often using some lightly-doped well regions in the drain-side. Meanwhile, ESD protection units used in the HV domains need to be able to withstand a high operating voltage. However, these implant profiles applied for HV applications will dramatically degrade the ESD high current ability of a traditional protection device, such as the gate-grounded n-channel MOS (GGnMOS)-type transistor. Many researches are also focusing on the layout of high-voltage devices [6–8] in order to effectively improve the ESD and LU abilities. Therefore, in this work, we tried to improve effectively ESD and LU ability by modulating the drain layout region with adding FOD structures.

107.2 Layout Design of DUTs

107.2.1 Non-uniform Turned on Issue in MOSTs

In order to effectively discharge the ESD current, the protection circuits on I/O pads are often designed as a multi-finger-type MOST, but the uniformity conduction of finger structure has been concerned as a serious issue for multi-finger structures. The value of secondary breakdown voltage (V_{t2}) is much lower than the value of triggering voltage (V_{t1}) in device performance. As the first-conducting finger was turned-on faster than others, this first conducting finger which would reach the hard-failure situation, but the other fingers did not conduct in time which resulted in device destruction. Therefore, we could conclude that a non-uniform conduction in I/O units would decrease the ESD protection ability of device.

To solve this problem, we intend to add FOD structures on drain-side in an HV-nLDMOS, as shown in Figs. 107.1–107.2. These structures can effectively increase the resistance on drain-side which means increase the parameter R_{on} of an ESD protection device. The larger R_{on} value can make V_{t2} value higher than V_{t1} value possible that solves the non-uniform conduction problem.

107.2.2 Change Parameter b of FODs

At the beginning of this work, the distance between each FOD was varied which means by changing the parameter *b* in Fig. 107.2. The length, width, parameters *a* and *c* of FODs were kept as constant values (FOD = 0.6 μm × 3 μm; *a* = 0.6 μm, *c* = 0.54 μm). As the parameter *b* is a minimum value of 0.6 μm in design rules, the largest number of 14 of FOD columns will be obtained in this area, and then we estimated an appropriate area that can be divisible to reduce column number. After that, the number of columns as 11, and the parameter

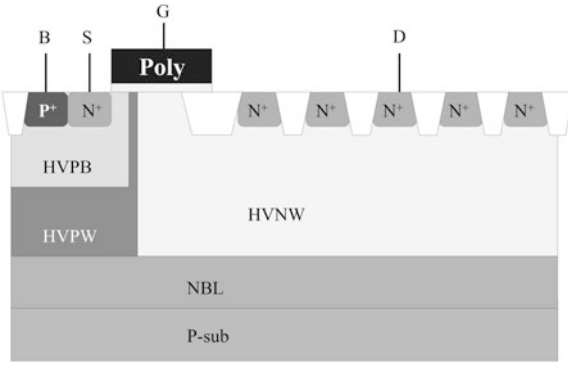

Fig. 107.1 Cross-section view of an HV-nLDMOS as FOD structures added in the drain side

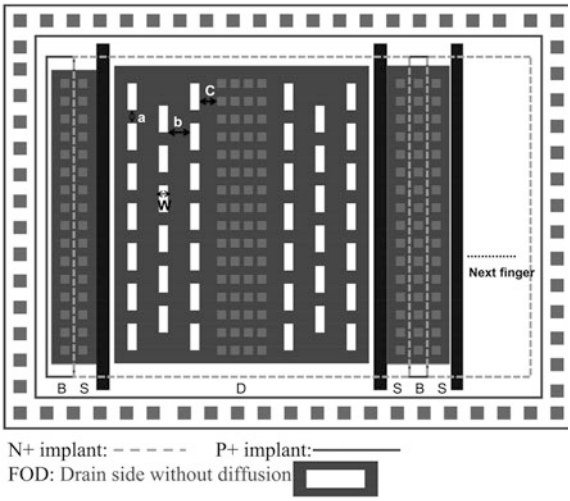

Fig. 107.2 Layout diagram of an HV-nLDMOS as FOD structures added in the drain side

b became 0.9 μm. Then, when the number of FOD columns was reduced as 8, 6, 4 and 2 in sequence, and the corresponding value of parameter *b* are 1.5, 2.4, 3.6 and 7.8 μm, respectively. As changing the parameter *b*, the distance between each column of FOD was also modulated, which would result in the number of FOD columns reduced from 14 to 2. However, the number of FOD in each column was fixed, and then the drain-side resistance would vary from a maximum to a minimum. The minimum value of drain-side resistance was without adding any FOD structure, which was regarded as the reference group (Ref. DUT). So, we defined the reference DUT (Ref. DUT) as none FOD structure on the drain side.

107.2.3 Change Parameter w of FODs

Then, changing the parameter *w* in Fig. 107.2, the width of an FOD structure was varied in this section. The FOD length, parameters *a*, *b* and *c* were kept as constants (the FOD length = 3 μm; *a* = 0.6 μm, *b* = 0.6 μm, *c* = 0.54 μm), and the width *w* of FOD increased from 0.6 μm in the smallest design rule. Then, the number of FOD columns is 14. When the numbers of FOD columns were 14, 11, 8, 6, 4 and 2; the corresponding values of parameter *w* were 0.6, 0.9, 1.5, 2.2, 3.6 and 7.8 μm, respectively. In the case of changing the parameter *w*, the number of FOD columns was reduced from 14 to 2, which meant the drain-side resistance would vary from the smallest to the largest value which was opposite with modulating the parameter *b*. Therefore, we could conclude that by modulating the variable *w* would decrease the number of FOD columns from the maximum value 14 to 2.

With these two methodologies of FOD columns variation, ESD capability of the corresponding structure was observed. All of the entire DUTs were fabricated by a TSMC 0.25 μm 60 V BCD process. The multi-finger structure of an nMOST was used in this work, the channel length (L) is kept to be 2 μm, channel width of each finger (W_f) is 100 μm, finger numbers M = 6, and the total channel width (W_{tot}) is kept a constancy, 600 μm.

107.3 Testing Equipment System

A transmission-line-pulse (TLP) system for experimental testing is controlled by the LabVIEW software. It managed the subsystem electrical machine such as the ESD pulse generator, the high-frequency digital oscilloscope and the digital power electric meter instruments to achieve the automatic measurement. This machine can provide a continuous step-high square wave to device, and short raise time of the continuous square wave can also simulate transient noise of ESD. This HBM-like system has used the short square wave with 100 ns pulse widths and 10 ns rising/falling times to evaluate the voltage and current response of device.

107.4 Measurement Results and Discussion

107.4.1 Change Parameter b of FODs

The test results of snapback I-V curves and TLP data with changing the parameter *b* on FOD structures are shown in Fig. 107.3 and Table 107.1. Here, the total occupied area of FODs with designed parameters *b* and *w* in the drain-side were translated into the FOD/N^+ area ratio. From Table 107.1, we could observe the FOD/n^+ area ratio was within the range of 0 ~ 50/100. With the increasing ratio

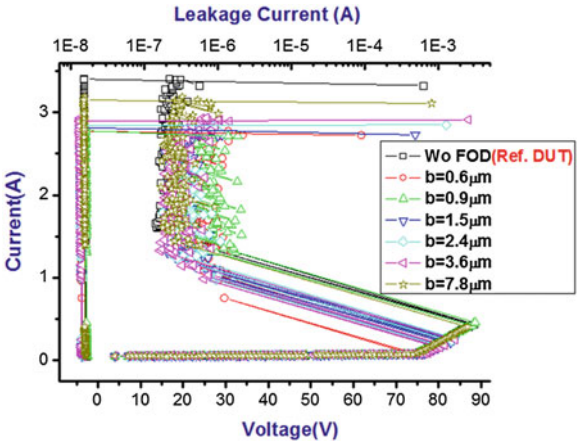

Fig. 107.3 Snapback I-V curves and leakage currents of HV-nLDMOS DUTs with adding FODs in the drain-side (changing the parameter "*b*")

Table 107.1 Snapback key parameters of HV-nLDMOS with adding FOD in the drain-side (changing the parameter "*b*")

Change the variable "b"		The number of FOD columns	V_{t1}(V)	V_h(V)	I_{t2}(A) mean±σ	FOD/N^+ area ratio
	W_0FOD (Ref.DUT)	0	85.692	15.052	3.295 ± 0.295	0
	1. b = 0.6 μm	14	85.125	20.511	2.809 ± 0. 291	44/100
Fixed FOD =	2. b = 0.9 μm	11	85.401	20.759	2.864 ± 0.274	32/100
3 μm * 0.6 μm,	3. b = 1.5 μm	8	83.363	18.422	2.873 ± 0.132	21/100
a = 0.6 μm,	4. b = 2.4 μm	6	84.563	17.516	2.904 ± 0.251	15/100
c = 0.54 μm	5. b = 3.6 μm	4	84.957	19.276	2.943 ± 0.295	10/100
	6. b = 7.8 μm	2	85.002	17.799	3.006 ± 0.268	5/100

of FODs, the I_{t2} value decreased. In this case, we can't achieve how exact FOD structure influence on I_{t2} until next section. From Table 107.1, with adding FOD structures, the V_h value increased obviously because the resistance on the drain-side and series resistance of nLDMOS DUTs were raised. However, it is still hard to increase turned-on resistance (R_{on}) with FOD structures, and that's also one of the reasons why the I_{t2} cannot be effectively increased.

107.4.2 Change the Parameter w of FODs

The next part, the snapback I-V curves and TLP data with changing the parameter *w* were shown in Fig. 107.4 and Table 107.2. When the parameter *w* varied, it made the FOD/N^+ area ratio larger than 50/100 or even more than one. From

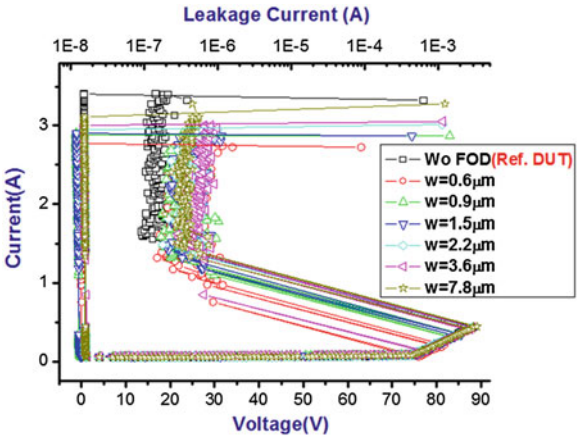

Fig. 107.4 Snapback I-V curves and leakage currents of HV-nLDMOS with adding FOD in the drain-side (changing the parameter "*w*")

Table 107.2 Snapback key parameters of HV-nLDMOS with adding FOD in the drain-side (changing the parameter "*w*")

Change the variable " w"		The number of FOD columns	V_U(V)	V_h(V)	I_{t2}(A) mean ± o	FOD/N^+ area ratio
	W_0FOD(Ref.DUT)	0	85.692	15.052	3.295 ± 0.295	0
	1. FOD = 3 μm*0.6 μm	14	85.125	20.511	2.809 ± 0.291	44/100
Fixed	2. FOD = 3 μm*0.9 μm	11	85.948	21.463	2.808 ± 0.095	57/100
a = 0.6 μm,	3. FOD = 3 μm*1.5 μm	8	86.220	24.063	2.809 ± 0.230	78/100
b = 0.6 μm,	4. FOD = 3 μm*2.2 μm	6	85.985	23.636	2.966 ± 0.177	93/100
c = 0.54 μm	5. FOD = 3 μm*3.6 μm	4	86.208	22.348	3.060 ± 0.277	1 11/100
	6. FOD = 3 μm*7.8 μm	2	87.262	22.537	3.104 ± 0.271	1 33/100

Table 107.2, it could be found that the I_{t2} values were in a low values portion and reached a minimum perigee as the FOD area ratio fell between 44/100 and 78/100. After then as the FOD/N^+ area ratio increased, the I_{t2} value increased as well. From Fig. 107.4, we could also found that the device turned-on resistance by changing the parameter *w* slightly increased as compared with the snapback I-V curves of changing the parameter "*b*".

Furthermore, from Fig. 107.5, we could observe that the V_{t1} (V_h) values indeed increased slightly (obviously) with the FOD/N^+ area ratio which were due to a higher series resistance in the drain side. Then, these DUTs can effectively strengthen the latch-up immunity. In Fig. 107.6, it could be found that the ESD capability decreased with adding FOD structures at the low FOD/N^+ area ratio and appeared with a U-shaped distribution. The minimum value of I_{t2} exists as the FOD/N^+ area ratio fell between 44/100 and 78/100. The I_{t2} value increased as the FOD/N^+ area ratio is larger than 80/100. Possessing a larger turned-on resistance

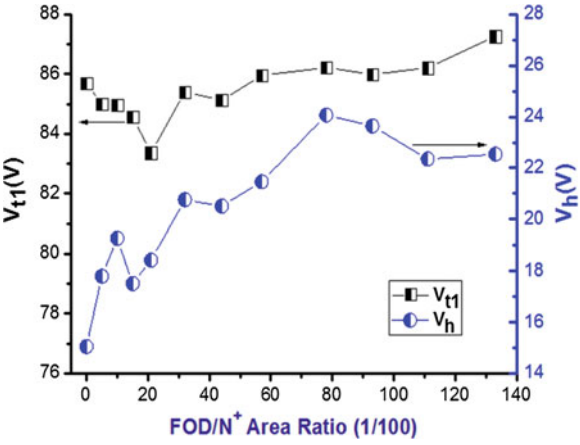

Fig. 107.5 V_{t1} and V_h versus FOD/N^+ area ratio diagrams of HV-nLDMOS DUTs

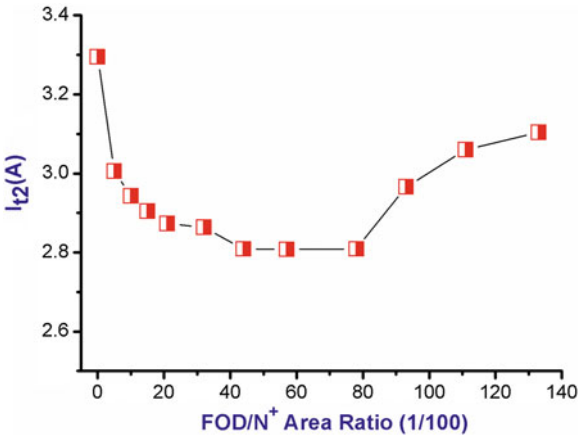

Fig. 107.6 I_{t2} versus FOD/N^+ area ratio diagrams of HV-nLDMOS DUTs

(R_{on}) could be inferred that with a larger FOD/N^+ area ratio which could increase ESD ability by adding FOD in nLDMOS devices.

Therefore, these two different mechanisms parts due to the adding conduction resistance was not large enough to make the V_{t2} value of device greater than V_{t1} which causes the device cannot uniform conduction. The generated heat was accumulated by additional resistance which would result in device burning out. So, those experimental results would inform that the ESD ability of FOD structure was worse in the low FOD/N^+ area ratio. According that, we could increase the FOD/N^+ area ratio in future application in order to make the V_{t2} value of device larger than V_{t1}, and which would result in getting a good ESD ability.

107.5 Conclusion

In this paper, we used a drain-side engineering: by adding FOD structures in the drain-side of the 60-V high voltage nLDMOS devices to solve the non-uniform conducting problem. According to the actual DUTs testing, the I_{t2} of the device would act a U-shaped distribution while the FOD/N^+ area ratio was increased. That is, it has the minimum value of I_{t2} when the FOD/N^+ area ratios were 44/100 to 78/100. Moreover, experimental results show that the I_{t2} values of DUTs would increase as the FOD/N^+ area ratio greater than 80/100. It is worth mentioning that an HV-nLDMOS with the FOD structure in the drain-side can increase the V_h magnitude of the device. Compared with the original reference DUT (without adding any FOD structure); the V_h value has been increased about 16.37 % $\sim$ 59.87 %. Therefore, in the high-voltage applications, we can enlarge the series resistance of drain-side by adding FOD structures to attain high ESD ability and high LU immunity of high-voltage devices.

Acknowledgments In this work, authors would like to thank the National Chip Implementation Center in Taiwan for providing the process information and fabrication platform.

References

1. Tan, Y., Kumar, M., Sin, J. K. O., Cai, J., & Lau, J. (2000). A LDMOS technology compatible with CMOS and passive components for integrated RF power amplifiers. *IEEE Electron Device Letters, 21*, 82–84.
2. Tan, Y., Kumar, M., Sin, J. K. O., & Cai, J. (2001). A SOI LDMOS technology compatible with CMOS, BJT, and passive components for fully-integrated RF power amplifiers. *IEEE Transactions on Electron Devices, 48*, 2428–2433.
3. Gajadharsing, J. R. (2003). Low distortion RF-LDMOS power transistor for wireless communications base station applications. *IEEE MTT-S International Microwave Symposium* (3, pp. 1563–1566).
4. Arnous, M. T., & Boeck, G. (2012). 4 Watt, 45 % bandwidth Si-LDMOS high linearity power amplifier for modern wireless communications systems. *2nd International Conference on Advances in Computational Tools for Engineering Applications* (pp. 110–113).
5. Sagneri, A. D., Anderson, D. I., & Perreault, D. J. (2013). Optimization of integrated transistors for very high frequency dc-dc converters. *IEEE Transactions on Power Electronics, 28*, 3614–3626.
6. Chen, W.-Y., & Ker, M.-D. (2011). Improving safe operating area of nLDMOS array with embedded silicon controlled rectifier for ESD protection in a 24-V BCD process. *IEEE Transactions on Electron Devices, 58*, 2944–2951.
7. Shrivastava, M., & Gossner, H. (2012). A review on the ESD robustness of drain-extended MOS devices. *IEEE Transactions on Device and Materials Reliability, 12*, 615–625.
8. Chen, S.-L., Lee, M.-H., Wu, T.-S., Lai, Y.-S., Lin, C.-J., & Chen, H.-H. (2013). *Source-side layout on LU/ESD reliability in the HV 0.25 um 60 V nLDMOS*. Lecture Notes in Electrical Engineering, pp. 503–511.

Chapter 108
ESD Performance Influence of a 60-V Lateral-Diffused-MOST by the FOD Based (and Dotted-OD) Drain

Shen-Li Chen, Min-Hua Lee, Chun-Ju Lin, Yi-Sheng Lai, Shawn Chang and Yu-Ting Huang

Abstract An lateral-diffused MOS (LDMOS) is often used to as the ESD device in a high-voltage circuit for its low on-resistance benefit. But, it has several serious disadvantages, including the V_h value is not high enough and the device in a multi-finger structure can't completely turn on which resulting in the ESD capability per unit length is very low. So, the non-uniform turned-on phenomenon is seriously impacted the robustness of ESD reliability. Therefore, this paper is based on the drain FOD structure of an nLDMOS, and which will change the OD structure for contacts located in the drain-side. The OD structure will renew as some dotted-ODs layout. Experimental results show that the dotted-OD layout has a higher ESD capability than the FOD structure, and the layout type of dotted-OD will affect the ESD capability of an HV component, where a uniformly distributed type of dotted-OD will have a highest I_{t2} value, the I_{t2} value is increased about 12 % as compared with the traditional LDMOS. The V_h value will increase with the contacts number increasing within the dotted-OD, therefore, this structure can also effectively improve the latch-up (LU) immunity.

Keywords Electrostatic discharge · Field-oxide device · Latch-up · Lateral-diffused MOS · Oxide definition · Secondary breakdown current · Trigger voltage · Turned-on resistance

108.1 Introduction

From the last century, the silicon-based bipolar power transistors and GaAs MESFETs were begun to substitute by high-voltage LDMOS transistors. Recently, the high-voltage (HV) LDMOS devices are widely used in communication

S.-L. Chen (✉) · M.-H. Lee · C.-J. Lin · Y.-S. Lai · S. Chang · Y.-T. Huang
Department of Electronic Engineering, National United University, MiaoLi City 36003, Taiwan, Republic of China
e-mail: jackchen@nuu.edu.tw

J. Juang et al. (eds.), *Proceedings of the 2nd International Conference on Intelligent Technologies and Engineering Systems (ICITES2013)*, Lecture Notes in Electrical Engineering 293,
DOI: 10.1007/978-3-319-04573-3_108,

modules, broadband wireless power amplifier, RF power station, electronic power-switch components, power management ICs, automotive electronics, LED illuminations and LCD drivers [1–3]. The HV devices have become more and more important. However, the operating voltage of an HV device is very high which indeed need better reliability [4, 5]. An LDMOS is still a surface dominated MOSFET structure and most of the LDMOS on-state conduction flows along the silicon surface and high electric field around silicon surface accelerated the impact ionization. Nevertheless, LDMOS transistors are inherently frail with respect to ESD stress and enhancing their ESD robustness has been an on-going target [6, 7].

108.2 Layout Design of DUTs

In this paper, adding the FOD structure in the drain-side of an HV nLDMOS is regarded as basic architecture. Then, changing the contact layout of oxide definition (OD) area in the drain-side makes the OD layout renew as the dotted-OD layout as shown in Figs. 108.1, 108.2, 108.3 and 108.4. As a result, the ESD clamp ability of these new nLDMOS DUTs will be investigated. All test DUTs for this work are fabricated by a TSMC 0.25-μm HV 60-V process. A multi-finger structure of gate-grounded n-channel MOS (GGnMOS) used in this work, the channel length (L) of each finger nLDMOS is kept to be 2-μm, channel width (W_f) of each finger nLDMOS is 100-μm, and total channel width (W_{tot}) is kept a constancy, 600-μm. And, all the stripe number (M) is 6.

Here, the goal of this paper is to adjust the layout manner and location of drain contacts which means adjusting the series resistance and achieving the uniform conducting. Therefore, some layout parameters of an FOD were fixed (column # of FOD is fourteen; FOD length/width = 3-μm × 0.6-μm; a = 0.6-μm, b = 0.6-μm, c = 0.54-μm). The parameter "a" is the spacing between one FOD block and next one FOD block in the same column of FODs; parameter "b" is the distance between the nearest parallel FOD columns; and parameter "c" is the distance between the nearby FOD edge to the drain-contact edge. Then, the dotted-OD contacts number within the central area changed from the minimum one contact (shown in Fig. 108.2), and gradually increased the contacts number within the OD to 2, 4 (shown in Fig. 108.3), 23, 46, and eventually increased to the entire 92 (shown in Fig. 108.4). Meanwhile, as the contacts number increased within the dot OD, the dotted-OD layout will be gradually become the stripe-OD layout and the form of the non-OD layout will distribute in the central zone of drain-side. Moreover, one type of the uniformly distributed dotted-OD layout (shown in Fig. 108.1) designed to investigate the influence of dotted-OD on ESD protection robustness, while the dotted-OD has only one contact.

The layout structure we need that is completely symmetric. Both minimum distances should be suited between a contact to a dotted-OD and a drain-side contact to OD on the vertical direction while channel width is 100-μm. According to the aforementioned description, the maximum number of contacts in a column is

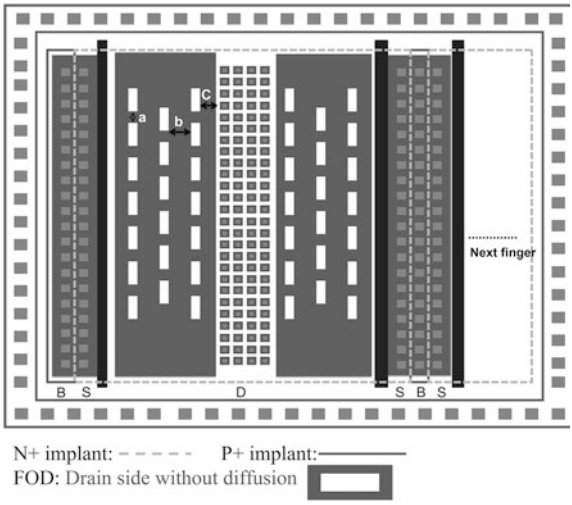

Fig. 108.1 Schematic layout of an HV nLDMOS with adding FOD and dotted-OD structures in the drain-side, where the dotted-OD contains one contact and uniform distributed

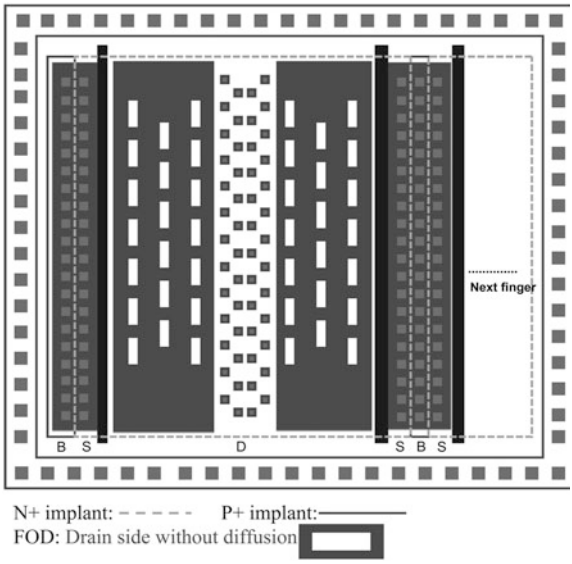

Fig. 108.2 Schematic layout of an HV nLDMOS with adding FOD and dotted-OD structures in the drain-side, where the dotted-OD contains one contact and gap distributed

92 and that is the reason why the maximum number of contacts of dotted-OD is 92. And, the 92 number could be divisible by the contacts which surrounded by dotted-OD, i.e., 1, 2, 4, 23, 46, and 92 contacts. Therefore, these six kinds of contact variation used in this work. In this way, there are two structures taken as for reference DUTs. One is a traditional nLDMOS without adding FOD & dotted-OD, and the other is an nLDMOS only with adding FODs.

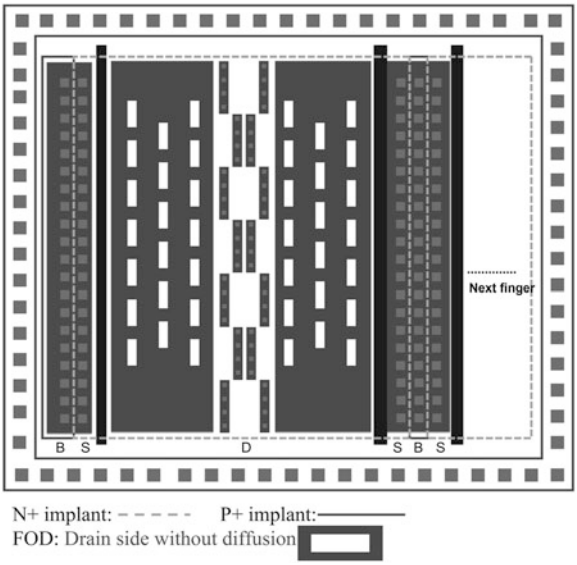

Fig. 108.3 Schematic layout of an HV nLDMOS with adding FOD and dotted-OD structures in the drain-side, where the dotted-OD contains four contacts and gap distributed

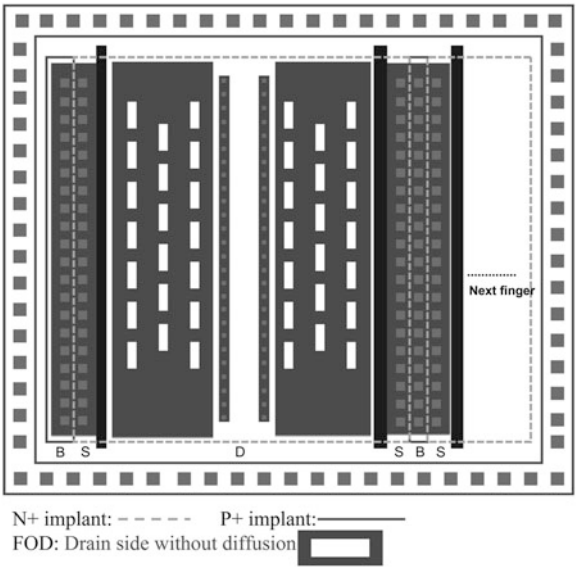

Fig. 108.4 Schematic layout of an HV nLDMOS with adding FOD and dotted-OD structures in the drain-side, where the dotted-OD contains 92 contacts and continuous distributed

108.3 Testing Equipment System

A transmission-line-pulse (TLP) system for experimental testing is controlled by the LabVIEW software, which managed the electronic instrument of subsystem such as the ESD pulse generator, the high-frequency digital oscilloscope and the digital power electric meter instruments, in order to achieve the automatic

measurement. This machine can provide a continuous step-high square wave to a DUT, and shortly raise time of the continuous square wave can also simulate transient noise of an ESD. This HBM-like system has used the short square wave with 100-ns pulse widths and 10-ns rising/falling times to evaluate the voltage and current response of a DUT.

108.4 Measurement Results and Discussion

With adding FOD and dotted-OD on drain-side will be discussed as following: one is the traditional nLDMOS not with any FOD and dotted-OD structures and compared with the only FOD adding or only dotted-OD adding, by changing the layout manner of dotted-OD to study the influence on ESD immunity. Second is changing the number of contacts on dotted-OD structures.

The test results of snapback I–V curves of part one are shown in Fig. 108.5. As only adding the FOD structure in an nLDMOS structure, the resistance of FOD structure is not large enough to cause the I_{t2} value of nLDMOS increased. However, when an nLDMOS device is added the dotted-OD structure, the corresponding I_{t2} value will increase significantly. Then, it shows that a dotted-OD structure is good for ESD current dissipation than an FOD structure, it can make the component with a high ESD current capability. The only adding dotted-OD structure not only has a higher I_{t2} value but also has a higher V_h value than a traditional nLDMOS, so that the dotted-OD structure is worth further developing. However, when a dotted-OD combined with an FOD structure, its I_{t2} value will increase unremarkable, particularly in the discrete layout types have a worse I_{t2} values. The reason for the resistance of an FOD is not large enough to apply at high voltage components, so when adding an FOD structure on a dotted-OD area will weaken the ESD capability. The number of contacts on drain-side of a discrete-type layout is less than of a uniform-type layout, which will result in a current crowding effect, and make the I_{t2} value of components decreased. However, the most important feature of adding an FOD structure is the V_h value obviously increased, it is good for latch-up immunity in the high voltage environment. And, the layout-type distribution of snapback key parameters of V_{t1}, V_h and I_{t2} are shown in Figs. 108.6 and 108.7.

From Fig. 108.8, the second part of contact number modulation in FOD and dotted-OD structures, it can be found that an FOD structure combined with a dotted-OD structure in the drain-side can result in the V_h and I_{t2} values increased. With more contacts number in a stripe OD, it will have a higher V_h value. When the contact number of an OD area is 46, it has the maximum value of V_h. The last DUT of dotted-OD type (dotOD92) is with a different layout of the former groups, it is a long stripe OD (shown in Fig. 108.4). This layout-type makes the drain-side resistance will decrease slightly, which is resulted in the V_h value followed too. In addition, the layout-type distribution of V_{t1} and V_h are shown in Fig. 108.9. In FOD and dotted-OD structures, the distribution aspect of I_{t2} will behave as a bell

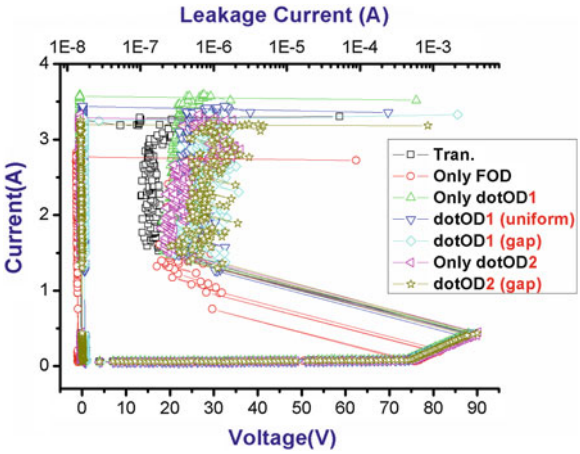

Fig. 108.5 Snapback I–V curves and leakage currents of HV nLDMOS DUTs with adding FOD and dotted-OD structures in the drain-side

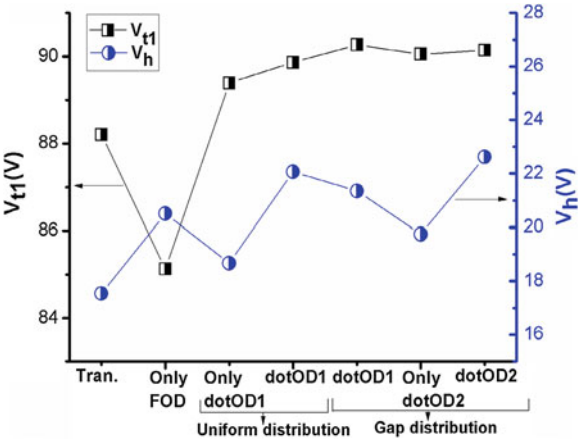

Fig. 108.6 V_{t1} and V_h distributions versus different drain-side engineering

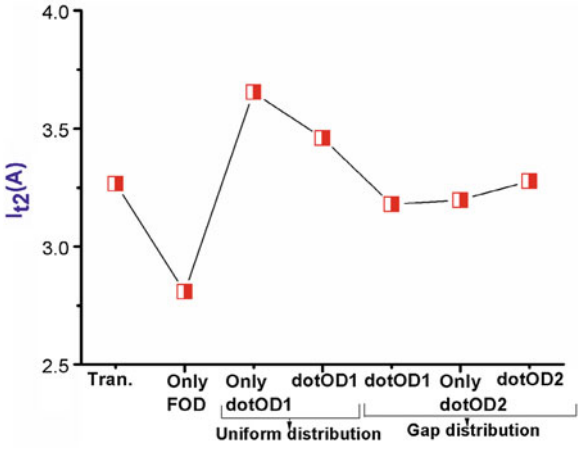

Fig. 108.7 I_{t2} distributions versus different drain-side engineering

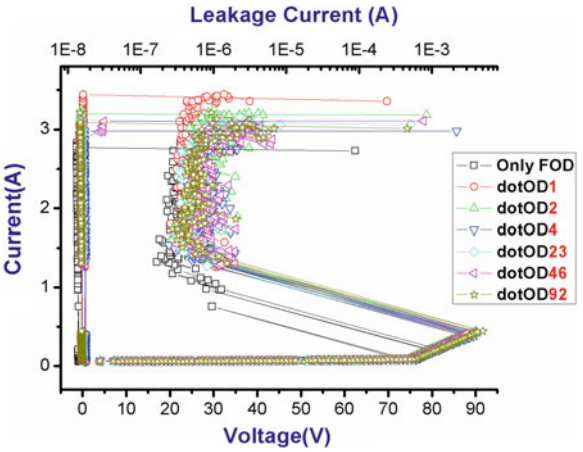

Fig. 108.8 Snapback I–V curves and leakage currents of HV nLDMOS DUTs with adding FOD and dotted-OD structures in the drain-side

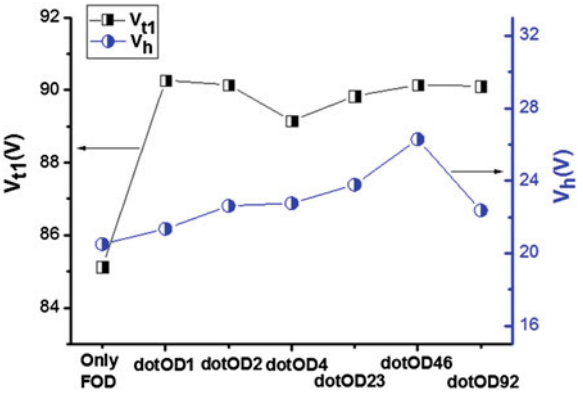

Fig. 108.9 V_{t1} and V_h distributions versus different drain-side engineering

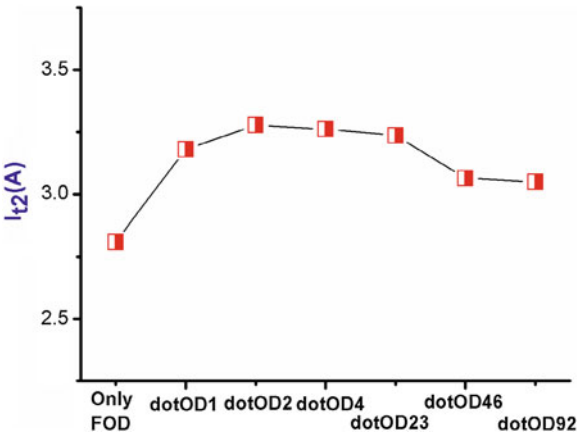

Fig. 108.10 I_{t2} distributions versus different drain-side engineering

shape shown in Fig. 108.10. In the experimental dotOD2 and dotOD4 situations, these DUTs had a higher I_{t2} value. Therefore, a proper design of experimental parameters will be good for component reliability.

108.5 Conclusion

This paper is focused on two crucial subject, one is the comparison of an traditional structure, FOD structure, and dotted-OD structures in the drain-side; the other is FOD structures combined with a dotted-OD structure modulation. After systematic tests, it is found that in high-voltage nLDMOS components, adding an FOD structure in the drain side will cause the I_{t2} value of a DUT decreased, but it will with a higher LU immunity. And, dotted-OD structures in the drain side can improve the I_{t2} value of a DUT; meanwhile, the V_h value will not be sacrificed. So that these two structures combined together should be haven a high ESD capability and high LU immunity. However, although the combination of these two structures have a high V_h value, but the results of I_{t2} compared with a traditional nLDMOS DUT is not increasing so high. Nevertheless, experimental results showed that the I_{t2} value of a uniform-layout type is better than a gap-layout type. In other words, the dotted-OD structure and uniform-layout type should be adopted in the further application.

Acknowledgments In this work, authors would like to thank the National Chip Implementation Center in Taiwan for providing the process information and fabrication platform.

References

1. Zhou, Y., Zhang, W., Wang, L., Xie, H., & Ding, C. (2011). A 230 watts RF LDMOS high power amplifier for WCDMA application. In *IEEE 13th International Conference on Communication Technology* (pp. 298–301).
2. Zhao, L., Wang, L., & Szymanowski, M. (2012). A 20 watt, two-stage, broadband LDMOS power amplifier IC in PQFN8 × 8 package at 2 GHz for wireless applications. In *7th European Microwave Integrated Circuits Conference* (pp. 469–471).
3. Sagneri, A. D., Anderson, D. I., & Perreault, D. J. (2013). Optimization of integrated transistors for very high frequency DC–DC converters. *IEEE Transactions on Power Electronics, 28*, 3614–3626.
4. Salman, A. A., Farbiz, F., Appaswamy, A., Kunz, H., Boselli, G., & Dissegna, M. (2012). Engineering optimal high current characteristics of high voltage DENMOS. In *IEEE International Reliability Physics Symposium* (pp. 3E.1.1–3E.1.6).
5. Qian, Q., Qian, Q., Liu, S., Wan, W., & Sun, W. (2013). Reliability concern on extended E-SOA of SOI power devices with P-sink structures. *IEEE Transactions on Device and Materials Reliability, 13*, 161–166.
6. Cao, Y., Glaser, U., Willemen, J., Frei, S., & Stecher, M. (2010). On the dynamic destruction of LDMOS transistors beyond voltage overshoots in high voltage ESD. In *32nd Electrical Overstress/Electrostatic Discharge Symposium* (pp. 1–10).
7. Chen, S.-L., & Wu, T.-S. (2013). Influence of a deep NBL structure on ESD/latch-up immunities in the power device nLDMOS. *Journal of Advanced Materials Research, 732–733*, 1207–1211.

Chapter 109
Combination of Genetic Algorithm and Hidden Markov Model for EEG-Based Automatic Sleep Staging

Sheng-Fu Liang, Ching-Fa Chen, Jian-Hong Zeng and Shing-Tai Pan

Abstract In this paper, we propose a strategy that combines Genetic Algorithm (GA) and HMM to improve the recognition rate of sleep staging. The GA is used to train a better codebook for HMM. With this method, the accuracy and efficiency of sleep medical diagnosis can be expected to be improved. Moreover, some features used in other research are selected as supporting features. These features are used to train the HMM model and then fed into the trained HMM for recognition. Unlike the existing research on sleep staging by HMM, in which the modeling of HMM is independent of the special properties of the sleep stage transition, the HMM in this study is adjusted to meet these properties. The experimental results show that the proposed method greatly enhances the recognition rate compared with other existing research.

Keywords Sleep staging · Genetic algorithm (GA) · Discrete hidden Markov model (DHMM) · Electroencephalogram (EEG)

S.-F. Liang
Department of Computer Science and Information Engineering,
National Cheng Kung University, Tainan City 701, Taiwan, Republic of China

C.-F. Chen
Department of Electronic Engineering, Kao Yuan University, Kaohsiung 821,
Taiwan, Republic of China

J.-H. Zeng · S.-T. Pan (✉)
Department of Computer Science and Information Engineering,
National University of Kaohsiung, Kaohsiung 811, Taiwan, Republic of China
e-mail: stpan@nuk.edu.tw

J. Juang et al. (eds.), *Proceedings of the 2nd International Conference on Intelligent Technologies and Engineering Systems (ICITES2013)*, Lecture Notes in Electrical Engineering 293,
DOI: 10.1007/978-3-319-04573-3_109,

109.1 Introduction

In human physiology, a good deep sleep (SWS) stage can help with physical recovery; as well, a good rapid eye movement (REM) stage can improve one's learning abilities and memories. However, as age increases, the total length of sleep and time of rapid eye movement (REM) stage will be increasingly shorter. In human pathology, many studies are relating various illnesses to sleep. These include night terrors, nocturnal enuresis, sleepwalking, somniloquy, sleep apnea, and many more. Therefore, it is vital to have a more reliable sleep medical diagnosis. [1, 2].

Sleep staging is traditionally done according to Rechtschaffen and Kales (R&K 1968) rules. In addition to manual sleep staging by doctors and experts, researches have been conducted in recent years on automatic sleep staging for the purpose of staging speed and accuracy. These researches include: application of Artificial Neural Network (ANN) on automatic sleep staging [3], rule-based automatic sleep staging [4], and applications of Hidden Markov Model (HMM) on automatic sleep staging [5, 6].

However, the recognition rate of sleep staging in existing literature is still low. Therefore, other methods should be applied to improve the recognition rate. Since, the HMM allows for the analysis of non-stationary multivariate time series by modeling both the state transition probabilities and the probability of observation of a state. The state estimation in HMM process depends on the preceding state. That is, in the HMM process, the result of the previous state will influence the state recognition result of the next state. This is similar to the process for sleep staging, where must consider the relationship between the previous sleep stage and the next sleep stage. Hence, the HMM is a promising model for sleep staging which possesses the properties of successive stage transition.

All the features used for the training phase or for the testing phase of HMM recognition systems must be quantized based on a trained codebook. It is very important to train the codebook well, since the codebook affect enormously the training of HMM model and hence the recognition rate. Consequently, in this paper, we wish to find a good way to train an optimal codebook to improve the recognition rate. GA solves problems through gene encoding using a set of parameters while simulating the natural evolution process: selection, crossover, and mutation to find an optimal solution. Indeed, GA had been successfully applied to solve the problems in various field. Consequently, GA is used here to train an optimal codebook for HMM.

109.2 Pre-Processing and Features Capture

This section describes the three steps for obtaining and processing sleep data. First, the sleep signals from healthy subjects are recorded. Second, the unwanted signals are filtered out. Then the signal outputs from the filter are transformed to frequency

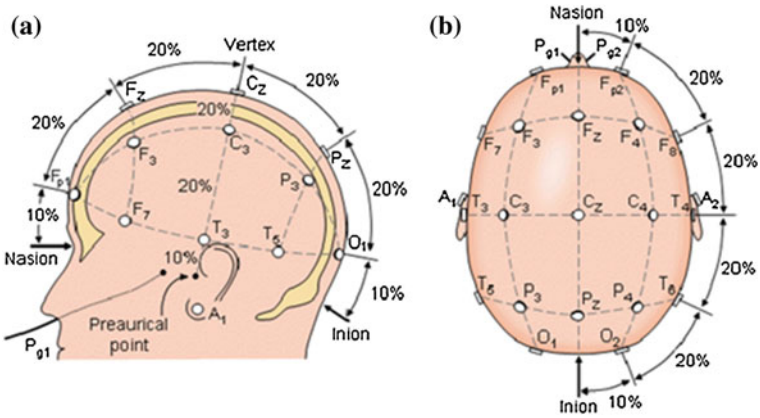

Fig. 109.1 The international 10-20 EEG system of electrodes placement. **a** *left* side view of the head and **b** *bird's eye* view of the head [8]. (A = ear lobe, C = central, Pg = nasopharyngeal, P = parietal, F = frontal, Fp = frontal polar, O = occipital)

domain by FFT. Finally, the desired features will be extracted from sleep signal. These then will be fed into the HMM model for training. The following processing and methods for features calculation are referred to Neural Computing and Brain Computer Interface Lab, NCKU [4].

109.2.1 Recording and Pre-Processing

According to modern standards and minimal requirements for computer-based sleep analysis [7], the recording protocol provides specified channels for these three types of bio-signals: Electroencephalogram (EEG), Electrooculogram (EOG), and chin Electromyogram (EMG). EEG was recorded from several scalp Ag/AgCl electrodes according to the international 10-20 system as shown in Fig. 109.1 [8]. All the scalp electrodes are linked to the earlobes A1 and A2. EOG is recorded as bipolar signals to monitor eye movements during sleep. The two active electrodes are placed on the left outer canthus and right outer canthus. EMG is recorded as bipolar activity of the submental muscle from the chin. The contact impedance between EEG electrodes and skin was calibrated to be less than *5* kΩ by injecting NaCl-conductive gel. Sleep recordings from twenty healthy subjects were analyzed, ranging form nineteen to twenty-seven years in age.

In the pre-processing of the sleep signals, we first use a filter to filter out some unwanted signals to prevent noise interference while extracting features. In EEG and EOG, the filter band is 0.5–30 Hz. In EMG, it is 5–30 Hz. The continuous time signals are segmented on 30 s intervals, which we call it epochs.

109.2.2 Feature Extraction

We select thirteen features which are obtained from those used in the literatures [9–12]. According to R&K rules, we use different protocols for different feature extractions on 30 s intervals as an epoch. The features are listed as follows.

Spectral power: The total spectral power (dB) among the band 0–30 Hz in EEG and EMG, which is used as the features and for the calculation of power ratio.

Power ratio: We calculate the ratio of each frequency band to total power (power (0–30 Hz)). This ratio is set as a feature. The frequency bands are devided as 0–4 Hz(EEG), 4–8 Hz(EEG), 8–13 Hz(EEG), 22–30 Hz(EEG), 0–4 Hz(EOG), these features are used to identify stages Wake, S1, SWS, and REM.

Spectral frequency (SF): The features of median frequency of EEG and median frequency of EMG by Eq. (109.1) are used to identify stage Wake and stage S1.

$$SF = \sum_{i=0}^{30} (fre.(i) * power)/power(0-30) \tag{109.1}$$

EMG energy: The mean of the absolute amplitude of the data points in an epoch of EMG is used to identify stage REM. It is calculate by the following Eq. (109.2):

$$Amp\ M = \frac{1}{N}\sum_{i=1}^{N} |EMG(i)| \tag{109.2}$$

N is the number of sampling points and $EMG(i)$ is the ith sample of EMG.

Alpha ratio (AR): This is used to recognize the stage Wake. The filters with the bands of 8–13 and 22–30 Hz are used to filter the EEG to acquire the necessary signals. Eq. (109.3) is given below to derive the AR:

$$AR = \frac{W_{nA}}{W_{nT}} \tag{109.3}$$

where W_{nA} is the number of windows containing Alpha wave, and W_{nT} is the total number of windows in an epoch.

Spindle ratio (SPR): If the power and frequency of a sudden change is high, then a spindle occurs. This ratio is defined in Eq. (109.4) and is used to detect stage S2.

$$SPR = \frac{W_{nS}}{W_{nT}} \tag{109.4}$$

where W_{nS} is the number of windows which contain spindle.

SWS ratio (SWSR): If the absolute amplitude of the filtered signal in this band 0.5–2 Hz which belongs to the Delta wave is higher than a specified threshold, the window can be classified as stage SWS. The SWSR can be computed as follows:

$$SWSR = \frac{W_{nSWS}}{W_{nT}} \tag{109.5}$$

where W_{nSWS} is the number of windows that are classified as SWS.

109.3 Proposed Strategy for Sleep Staging

In this section, the strategy for sleep staging is proposed. Based on the features introduced in the Sect. 109.2, a codebook is first trained by GA. In the HMM recognition process, there is a HMM model should be trained according to the trained codebook and used for sleep staging. Since the transition of hidden state of HMM is similar to that of the sleep stage, the sleep stages are assigned to be the hidden stages of the HMM. Consequently, for the HMM $\lambda = (A, B, \pi)$ applied on sleep staging, the matrix A means the probability of transition from one sleep stage to another, the matrix B means the probability of the observation from the sleep stage to which the feature vector belongs, the matrix π means the probability of a sleep stage occurs in the initial stage in a sleep sample.

The features of each epoch via vector quantization become the observation and are used to train HMM or estimate the sleep stage by HMM. Since each observation code, which is the feature vector calculated from a 30 s sample of a sleep stage, is used to estimate the sleep stage, the total sleep stages for a sleep sample can then be estimated by testing a sequence of observation codes through HMM. Based on the discussion above, the sleep staging procedure is then summarized as follows.

109.3.1 Procedure of GA-DHMM Sleep Staging

Step 1. Train the codebook by GA.
Step 2. Generate DHMM model by finding $(A.B,\pi)$.
Step 3. A quantized observation code is created from an epoch's feature vector and is quantized using the codebook in Step 1.
Step 4. Perform the Forward Algorithm using $(A.B,\pi)$ in HMM. Recognize the sleep stage with the highest probability at the end of the sleep stage sample.
Step 5. Backtrack using Viterbi Algorithm to deduce the transference of all sleep stages.

Table 109.1 Recognition rates for various sleep stages by the proposed method

	(%)	Wake	S1	S2	SWS	REM
	Wake	**68.83**	3.64	21.36	0	6.17
	S1	21.74	**15.65**	39.07	1.39	22.15
M_{SSRR}:	S2	0.56	1.07	**89.64**	4.76	3.97
88.27 %	SWS	0	0	11.27	**88.73**	0
	REM	0	1.18	5.09	0	**93.73**

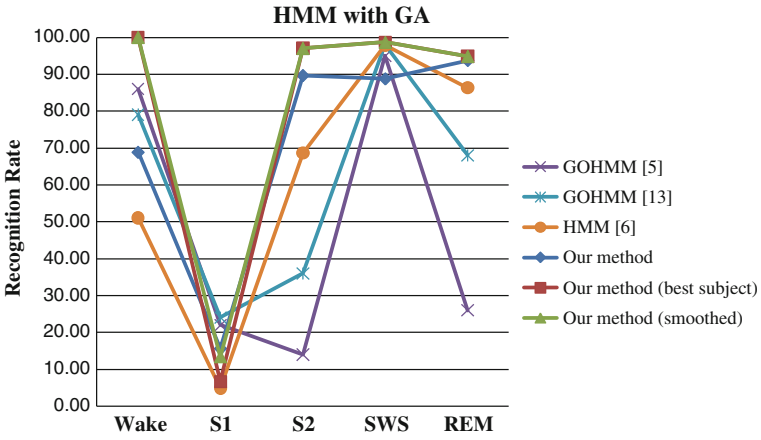

Fig. 109.2 Comparison of the results for each sleep stages with those in the existing research [5, 6, 13]

109.4 Experiment Results

In the experiments, the sleep data from twenty subjects are arranged as ten subjects for training with ten subjects for testing and the cross-validation experiments are adopted here. It is noted that the mean value of the sleep stage recognition rate (M_{SSRR}) for each subject is calculated by the following Eq. (109.6).

$$M_{SSRR} = (\sum_{i=1}^{5} C_i)/E_T \tag{109.6}$$

where C_i is the number of correct recognition for ith stage, E_T is the total epochs. The recognition rates for each sleep stages defined in R&K Rule are listed in Table 109.1. According to this table, the sleep stages S1 get the worst recognition rate. This is due to the least samples for stage S1 between all the stages. However, this result is consistent with that in some researches. Besides, Figs. 109.2 and 109.3 compare the results in this paper to those in some existing papers. It's obvious that the proposed method has got better performance than others method.

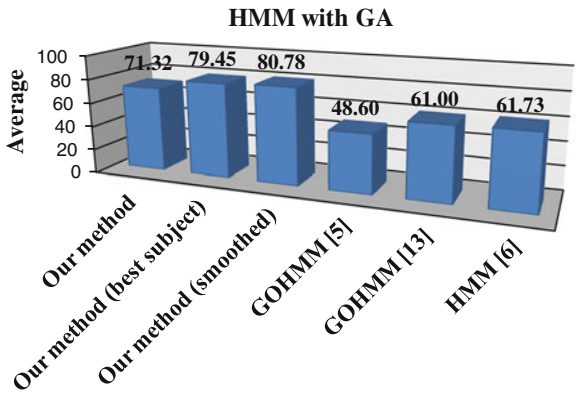

Fig. 109.3 Comparison of average recognition rates with those in the existing research [5, 6, 13]

It is worth to note that, based on the Figs. 109.2 and 109.3, the recognition results after smoothing process is the same as the result without smoothing (the best subject). The reason is that we have put the smoothing process into the HMM model during the training process. Consequently, we can neglect the smoothing process at the end of the recognition process.

References

1. Iber, C., Ancoli-Israel, S., Chesson, A. L., & Quan, S. F. (2007). *The AASM manual for the scoring of sleep and associated events.* Westchester, IL: American Academy of Sleep Medicine.
2. Silber, M. H., Ancoli-Israel, S., Bonnet, M. H., et al. (2007). The visual scoring of sleep in adults. *Journal of Clinical Sleep Medicine, 3*(2), 121–131.
3. Dai, Z. F. (2009). *A sleep staging method based on single channel eeg signal*. Master paper presented at the Department of Mechanical and Electro-Mechanical Engineering, National Sun Yat-sen University, Kaohsiung.
4. Cheng, Y. S. (2009). *A rule-based automatic sleep staging method.* Master paper presented at the Department of Computer Science and Information Engineering, National Cheng Kung University, Tainan.
5. Flexer, A., Dorffner, G., Sykacek, P., & Rezek, I. (2002). An automatic, continuous and probabilistic sleep stager based on a hidden markov model. *Applied Artificial Intelligence, 16*, 199–207.
6. Doroshenkov, L. G., Konyshev, V. A., & Selishchev, S. V. (2007). Classification of human sleep stages based on EEG processing using hidden markov models. *BioMedical Engineering, 41*(1), 25–28.
7. Penzel, T., & Conradt, R. (2000). Computer based sleep recording and analysis. *Sleep Medicine Reviews, 4*, 131–148.
8. Malmivuo, J., & Plonsey, R. (1995). *Principles and applications of bioelectric and biomagnetic fields, bioelectromagnetism*. New York: Oxford University Press.
9. Schaltenbrand, N., Lengelle, R., Toussaint, M., Luthringer, R., Carelli, G., Jacqmin, A., et al. (1996). Sleep stage scoring using the neural network model: Comparison between visual and automatic analysis in normal subjects and patients. *Sleep, 19*(1), 26–35.

10. Kuwahara, H., Higashi, H., Mizuki, Y., Tanaka, S. M. M., & Inanaga, K. (1988). Automatic real-time analysis of human sleep stages by an interval histogram method. *Electroencephalography and Clinical Neurophysiology, 70*(3), 220–229.
11. Duman, F., Erdamar, A., Erogul, O., Telatar, Z., & Yetkin, S. (2009, August). Efficient sleep spindle detection algorithm with decision tree. *Expert Systems with Applications, 36*(6), 9980–9985.
12. Berthomier, C., Prado, J., & Benoit, O. (1999). Automatic sleep EEG analysis using filter banks. *Biomedical Sciences Instrumentation, 35*, 241–246.
13. Flexer, A., Gruber, G., & Dorffner, G. (2005). A reliable probabilistic sleep stager based on a single EEG signal. *Artificial Intelligence in Medicine, 33*, 199–207.

Chapter 110
Modeling and Design of One Real Eight-Phase Traffic Light Control System Using Pure Petri Nets

Yen-Liang Pan, Ben-Yu Liao, Cheng-Chung Yang and Mau-Yi Tian

Abstract With the developing of cities all over the world, the number of vehicle is also growing very fast. Therefore, how to design efficient traffic light controllers to control urban traffic in most cities becomes important. Many peer researchers make their effort in this target. Among them, few use Petri net as the tool to achieve the goal since the Petri net has been to be a powerful modeling tool for various kinds of discrete event systems. However, these algorithms are too complex to be applied in real traffic control. For improving above drawback, this paper tries to use pure Petri nets to design traffic light controllers. Besides, one real crossroad and traffic lights is used as example. Based on the final experimental results, the proposed methodology is practical and useful.

Keywords Modeling · Discrete event System · Traffic light · Petri nets

110.1 Introduction

With the growing number of vehicles, the traffic congestion and transportation delay on urban arterials are increasing. Therefore, it is imperative to improve the safety and efficiency of transportation. One typical traffic light is viewed a signal device positioned at a road intersection or pedestrian crossing to indicate when it is safe to drive, ride or walk, using a universal color code. With the number of vehicles on the world's roads grows sharply, Traffic jam usually occurrences in the

Y.-L. Pan (✉) · B.-Y. Liao · M.-Y. Tian
Department of Avionic Engineering, Air Force Academy, Kaohsiung 82047, Taiwan, Republic of China
e-mail: peterpan960326@gmail.com

C.-C. Yang
Department of Aeronautical and Mechanical Engineering, Air Force Academy, Kaohsiung 82047, Taiwan, Republic of China

J. Juang et al. (eds.), *Proceedings of the 2nd International Conference on Intelligent Technologies and Engineering Systems (ICITES2013)*, Lecture Notes in Electrical Engineering 293,
DOI: 10.1007/978-3-319-04573-3_110,

highway or street in the most cities, especially in the intersections. Therefore, how to design efficient traffic light controllers to control urban traffic in most cities becomes important. Many peer researches make their effort in this target.

Among them, few pioneers choose Petri net [1] as the tool to achieve the goal since Petri nets have been proven to be a powerful modeling tool for various kinds of discrete event systems. Traffic signal control can then be accomplished by using various Petri nets [2–6]. However, these algorithms seem too complex to be applied in real traffic control. For improving above drawback, this paper tries to design traffic light controllers using pure Petri nets. Its advantage is easy to design and practice. One real crossroad and traffic lights is also used as example. According to the experimental results, the scenarios can be accurately identified from our proposed algorithm. More important the proposed Petri net model is deadlock free, exhibits repetitive behavior, and is structurally bounded and live. The rest of this paper is organized as follows. Section 110.2 presents the basic definitions and properties of Petri nets. Section 110.3 then describes and discusses the real traffic light and its control system. Next, Sect. 110.4 presents the modeling results. Conclusions are made in Sect. 110.5.

110.2 Preliminaries of Petri Nets

A PN is a 5-tuple $PN = (P, T, F, W, M_0)$ where P is a finite set of places; T is a finite set of transitions, with $P \cup T \neq \varnothing$ and $P \cap T = \varnothing$; $F \subseteq (P \times T) \cup (T \times P)$ is the set of all directed arcs, W: $(P \times T) \cup (T \times P) \rightarrow N$ is the weight function where $\boldsymbol{N} = \{0, 1, 2, \ldots\}$, and M_0: $P \rightarrow N$ is the initial marking. N is said to be ordinary, denoted as (P, T, F), if $\forall f \in F$, $W(f) = 1$. $N^+(p, t) = W(p, t)$ is the input function that means the multiplicity of a directed arc from p to t if $(p, t) \in F$. $N^-(p, t) = W(t, p)$ is the output function that means the multiplicity of a directed arc from t to p if $(t, p) \in F$. The set of input (resp., output) transitions of a place p is denoted by $\bullet p$ (resp., $p\bullet$). Similarly, the set of input (resp., output) places of a transition t is denoted by $\bullet t$ (resp., $t\bullet$). A PN structure (P, T, F, W) is denoted by N. A PN with a given initial marking is denoted by (N, M_0).

A PN is said to be pure if no place is both input and output places of the same transition. The so-called incidence matrix $[N]$ of a pure Petri nets is defined as $[N] = [N]^- - [N]^+$. A transition t is said to be enabled at marking M, if $\forall p \in \bullet t$, $M(p) \geq W(p, t)$, *or* p is marked with at least $W(p, t)$ tokens, as denoted by $M[t>$. A transition may fire if it is enabled. In an ordinary net, it is enabled if $\forall p \in \bullet t$, $M(p) \geq 1$. Firing t at M gives a new marking M'such that $\forall\ p \in P$, $M'(p) = M(p) - W(p, t) + W(t, p)$. It is denoted as $M[t > M'$. M indicates the number of tokens in each place, which means the current state of the modeled system. When marking M_n can be reached from M_0 by firing a sequence of

Fig. 110.1 A real urban network in Tainan city, Taiwan

transitions σ, this process is denoted by $M\,[\sigma > M_n$ and satisfies the *state equation* $M' = M + [N]\vec{\sigma}$. Here, $\vec{\sigma}$ is a vector of non-negative integers, called *counting vector*, and $\vec{\sigma}(t)$ indicates the algebraic sum of all occurrences of t in σ. The set of all reachable markings for a PN given M_0 is denoted by $R(N, M_0)$.

110.3 Urban Traffic Lights

In this paper, the pure Petri net will be designed to model traffic light control system. Additionally, one real urban traffic network located in Tainan city, Taiwan shown in Fig. 110.1 is used as an example. This is because that it is a very important and crowded crossroad. Furthermore, this urban traffic network consists of the following five signal lights from left to right: a red light (R), a yellow light (Y), a green left-turn arrow (G_L), a green right-turn arrow (G_R), and a green arrow to go straight only (G_S) are shown in Fig. 110.2.

The schematic diagram shown in Fig. 110.3 clearly presents the whole operation system. It describes a traffic light control system with above five traffic signal lights. For convenience, the directions of vehicles heading northward, southward, westward, and eastward are symbolized by the notations s, n, e, and w. In short, G_{Rns} represents a green right-turn arrow in north–south direction, G_{Sns} a green arrow to go straight only in north–south direction, G_{Lns} represents a green left-turn arrow in north–south direction, Y_{ns} represents a yellow light in north–south direction, R_{ns} represents a red light in north–south direction, G_{Rew} represents a green right-turn arrow in east–west direction, G_{Sew} a green arrow to go straight only in east–west direction, G_{Lew} represents a green left-turn arrow in east–west direction, Y_{ew} represents a yellow light in n east–west direction, and R_{ew} represents a red light in east–west direction, respectively.

Fig. 110.2 Five-light bulb signal

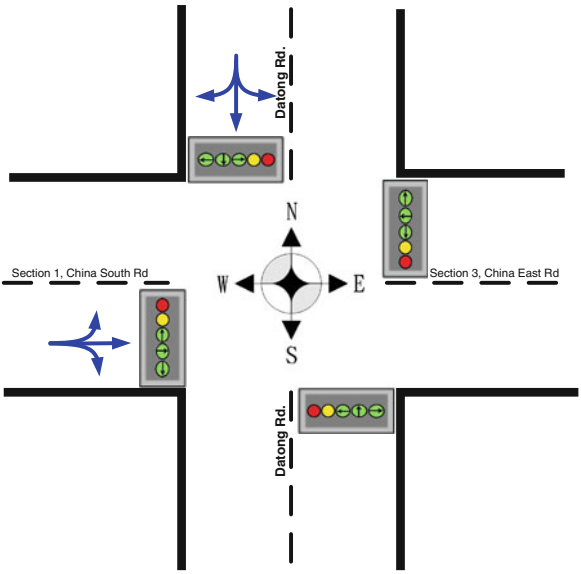

Fig. 110.3 One traffic light control system with five signal lights

Besides, there are total eight phases in this crossroad shown in Table 110.1. The firing sequence is Phase 1, Phase 2, Phase 3, Phase 4, Phase 3, Phase 6, Phase 7, Phase 8, Phase 7, Phase 2, and recycle again. And the reachability graph is shown in Fig. 110.4. Please note that the original phase (i.e. all red lights are turn on simultaneously in initial time) is just appeared in initial phase since two traffic safety rules are needed to consider in real traffic control system as follows: Rule 1: A traffic light control system can then be started if its traffic lights are all set in a red state. Rule 2: No green light is allowed in north–south and east–west directions simultaneously.

110.4 Modeling and Simulation

Based on the previous discussions, this section tries to present and illustrate how to model a crossroad traffic light control system using the pure Petri nets. For tracing easy, we use the popular software HPSHIM [7] to model this traffic light control system and the software INA [8] to analysis our Petri nets model. Figure 110.5 shows the modeling system based on pure Petri nets. Please note that the value of maximum capacity of all places is set to one. Additionally, this model is

Table 110.1 The detailed information of eight phases traffic light control system

Phase	G_{Rns}	G_{Sns}	G_{Lns}	Y_{ns}	R_{ns}	G_{Rew}	G_{Sew}	G_{Lew}	Y_{ew}	R_{ew}
1					◎					◎
2	◎	◎								◎
3				◎						◎
4			◎		◎					◎
6					◎	◎	◎			
7					◎				◎	
8					◎			◎		◎

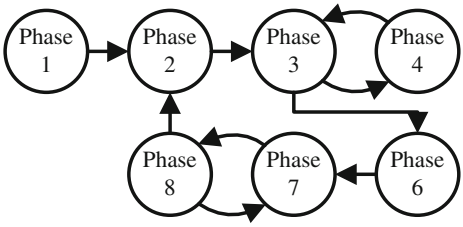

Fig. 110.4 All phases and their changing order

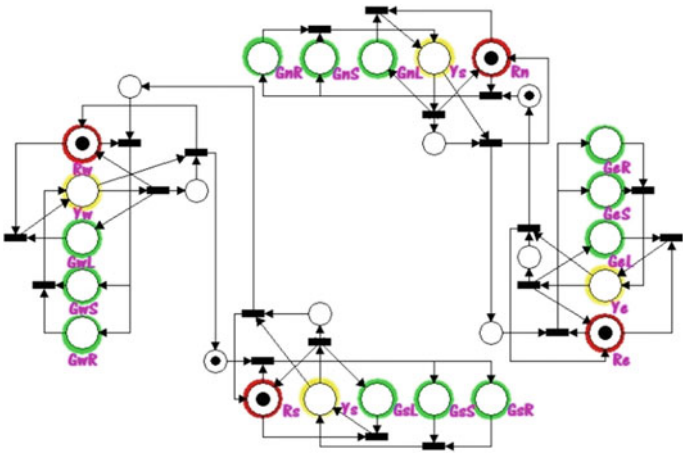

Fig. 110.5 The initial traffic control system modeling by pure Petri nets

symmetric just for easy tracing. Therefore, all phases can then be present according the firing rule of the pure Petri nets. Figure 110.6 shows the all phases modeling by pure Petri nets. According to Figs. 110.6a–h, it is obvious that the firing sequence in Fig. 110.6 is same with the one in Fig. 110.4. In other words,

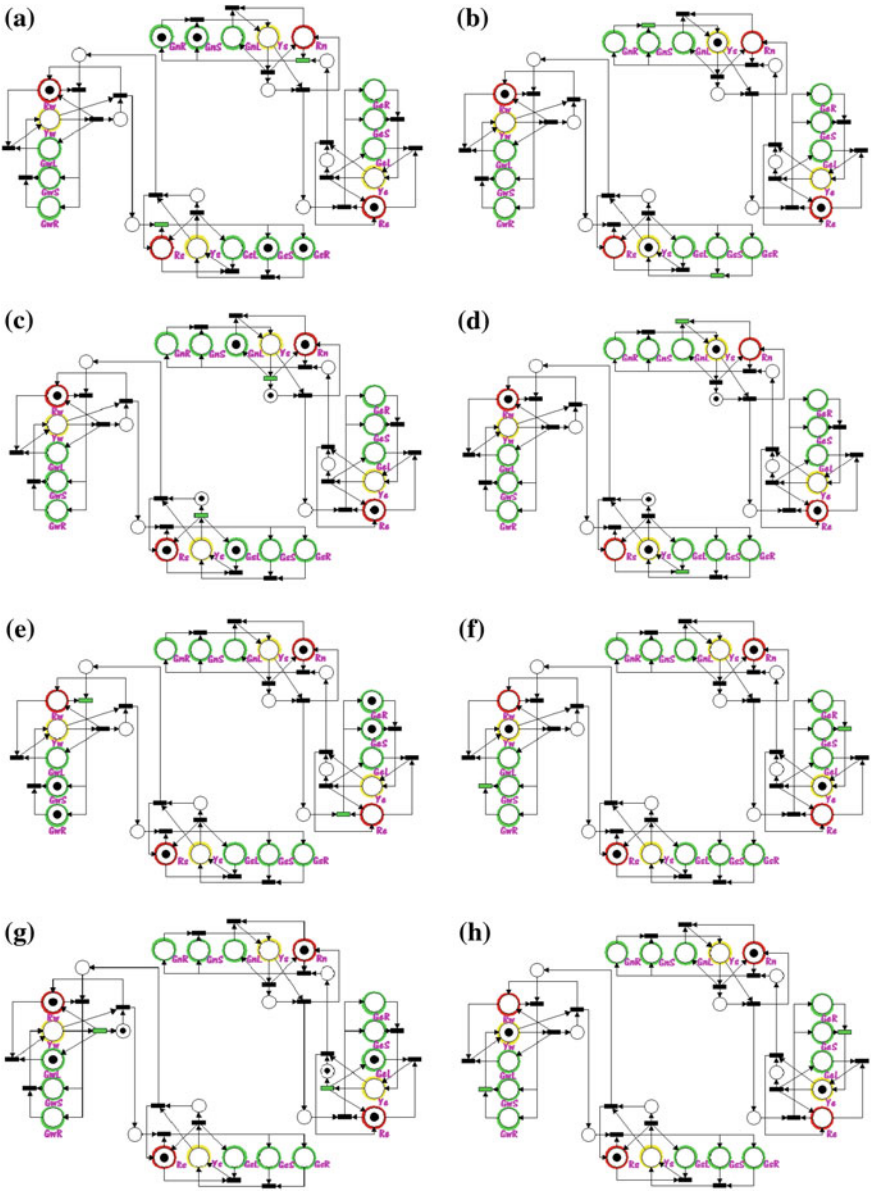

Fig. 110.6 The total firing sequences of the traffic control system

our designed Petri net model can match the eight phases of the real traffic light. Finally, the system is live by using the software INA. It means that our pure Petri net model is correct and practical.

110.5 Conclusions

This paper presents the modeling, analysis, and simulation of one real eight-phase traffic light control system using pure Petri nets. Most important, the proposed method is simpler than all existing literatures and can then be utilized in real traffic light control system. The experimental results also show that the designed Petri net model can match the eight phases of the real traffic light. Please note that the transition time is not under consideration due to paper space limitation. In fact, the duration of every phase also can also be solved once all transitions are set time-variable. The future work will apply the methodology to more complex traffic lights or other discrete event dynamic systems.

References

1. Murata, G. T. (1989). Petri nets: Properties, analysis and applications. *Proceedings of IEEE, 77*, 541–580.
2. Huang, Y. S., Weng, Y. S., & Zhou, M. C. (2010). Critical scenarios and their identification in parallel railroad level crossing traffic control systems. *IEEE Transactions on Intelligent Transportation Systems, 11*, 968–977.
3. Huang, Y. S., & Su, P. J. (2009). Modelling and analysis of traffic light control systems. *IET Control Theory and Applications, 3*, 340–350.
4. Barzegar, B., & Motameni, H. (2011). Simulation of intelligent traffic signal control by coloured petri net. *American Journal of Scientific Research, 23*, 13–21.
5. Ganiyu, R. A., Olabiyisi, S. O., Omidiora, E. O., Okediran, O. O., & Alo, O. O. (2011). Modelling and simulation of A multi-phase traffic light controlled T-type junction using timed coloured petri nets. *The American Journal of Scientific and Industrial Research, 2*, 428–437.
6. Barzegar, S., Davoudpour, M., Meybodi, M. R., Sadeghian, A., & Tirandazian, M. (2010). Traffic signal control with adaptive fuzzy coloured petri net based on learning automata. In *2010 Annual Meeting of the North American Fuzzy Information Processing Society (NAFIPS)* (pp. 1–8).
7. HPSim. Retreived from http://www.winpesim.de/
8. INA. (Integrated Net Analyzer), A Software Tool for Analysis of Petri Nets. Version 2.2, 31.07. (2003). Retrieved from http://www.informatik.hu-berlin.de/~starke/ina.html

Chapter 111
Bidirectional Ant Colony Optimization Algorithm for Cloud Load Balancing

Shin-Hung Li and Jen-Ing G. Hwang

Abstract Cloud computing supplies convenient, on-demand network access to shared computing resources. Although cloud computing has many advantages, some core issues, such as load balancing, need to be resolved. Cloud load balancing provides a mechanism to allocate the appropriate workload for each virtual machine in a cloud computing environment. One of the main characteristics of the cloud computing environment is rapid change; therefore, a good load-balancing method should adapt quickly to environment changes to achieve high performance. This paper proposes a load-balancing method based on the Ant Colony Optimization (ACO) algorithm and describes a simulation using the CloudSim toolkit package. Experimental results show that the proposed method is an effective ACO method for cloud balancing.

Keywords Cloud computing · Load balancing · Ant colony optimization · Pheromones

111.1 Introduction

With the increasing popularity of cloud computing, the cloud faces a major challenge in managing an extremely large number of service requests. In order to maintain the stability of the system and provide good service, an effective load-balancing technique for task scheduling in dynamic cloud environment is required.

S.-H. Li · J.-I. G. Hwang (✉)
Department of Computer Science and Information Engineering, Fu Jen Catholic University, Taipei 24205, Taiwan, Republic of China
e-mail: jihwang@csie.fju.edu.tw

S.-H. Li
e-mail: 400226064@mail.fju.edu.tw

J. Juang et al. (eds.), *Proceedings of the 2nd International Conference on Intelligent Technologies and Engineering Systems (ICITES2013)*, Lecture Notes in Electrical Engineering 293,
DOI: 10.1007/978-3-319-04573-3_111,

Some researchers developed effective algorithms based on the behavior of social animals, because social organisms can effectively adapt to a changing environment. For example, an ant colony can dynamically allocate tasks without a central manager. The Ant Colony Optimization (ACO) algorithm has been used to solve the load-balancing problem in Peer-to-Peer (P2P) environments [1, 2], and in grid computing [3–5]. Recently, ACO has also been applied to the cloud environment [6–8].

In this paper, an improved ACO algorithm is proposed for load balancing in the cloud environment and the CloudSim tool [9, 10], is used to conduct simulations for comparing the effectiveness of different load-balancing strategies.

The rest of the paper is organized as follows: Sect. 111.2 briefly describes the simple ACO algorithm. Section 111.3 discusses the proposed bidirectional ACO algorithm. Section 111.4 shows the experimental results. Finally, Sect. 111.5 presents conclusions.

111.2 Simple Ant Colony Optimization

Ant colony algorithms are computational swarm intelligence methods that were inspired by a number of different behaviors observed in ant colonies. A simple ACO algorithm was proposed by Dorigo et al. [11, 12].

Dorigo et al.'s ACO algorithm was based on the foraging behavior of ants while searching for the shortest path between the ant nest and a food source. Likewise, one can consider the general problem as finding the shortest path between two nodes on a graph. During the shortest-path search, cooperation among the ants is achieved by releasing pheromones to influence the behavior of other ants. How forager ants decide which edge to follow is a probabilistic technique and depends on the pheromone concentrations on different edges. Let τ_{ij} be the pheromone concentration between nodes of i and j in the graph. Initially, the value $\tau_{ij}(0)$ is assigned a random value to indicate the pheromone at time zero, and a number of ants are placed at the starting node. Each ant then creates a path between the starting node and the terminating node by determining the next edge from the current node at every time step (iteration) t. The transition probability $p_{ij}^{k}(t)$ of the kth ant moving from node i to node j at time step t is defined as

$$p_{ij}^{k}(t) = \begin{cases} \dfrac{(\tau_{ij}(t))^{\alpha}}{\sum_{u \in J_k(i)} (\tau_{iu}(t))^{\alpha}} & \text{if} \quad j \in J_k(i) \\ 0 & \text{otherwise} \end{cases}, \tag{111.1}$$

where $J_k(i)$ is the set of feasible nodes linked to node i along the path of the kth ant, and α is a parameter used to intensify the influence of pheromone concentrations. When an ant has traversed a path within the time step t, the ant retraces its path and deposits pheromone on every edge of the path. The concentration of the deposited

pheromone on the edge (i, j) is inversely proportional to the length of the path. That is,

$$\Delta\tau_{ij}^{k}(t) \propto \frac{1}{L^{k}(t)} \tag{111.2}$$

where $\Delta\tau_{ij}^{k}$ is the deposited pheromone, and $L^{k}(t)$ is the length of the path created by the kth ant at time step t. The total pheromone intensity of an edge is then updated using Eq. (111.3).

$$\tau_{ij}(t+1) = (1-\beta_{eva}) \times \tau_{ij}(t) + \sum_{k=1}^{n} \Delta\tau_{ij}^{k}(t) \tag{111.3}$$

where β_{eva} is the pheromone evaporation rate with $\beta_{eva} \in [0, 1]$, and n is the number of ants. The iterations are executed until one of the terminating conditions is true. The solution is the shortest path found among all the paths traversed by the ants.

111.3 The Proposed Algorithm

In this paper, a Bidirectional Load Balancing ACO (BLBACO) algorithm that is inspired by Li et al. [6] and Nishant et al. [7] is proposed. The BLBACO used the Load Balancing ACO (LBACO) [6] characteristics to determine the loading and computing capacity of each virtual machine, and BLBACO also adapted the concept proposed in [7], where the movements of the ants in the system are defined as either a forward movement or a backward movement. Forward movement is the direction of ants moving from the nest to a food source, and backward movement is the direction from the food source to the nest. In the computing cloud, forward movement can be defined as the direction of an under-loaded virtual machine (nest) seeking an over-loaded virtual machine (food), while backward movement is the reversed direction. Once the search is completed, a portion of the tasks that were originally assigned to the over-loaded virtual machine can be reassigned to the under-loaded virtual machine.

The proposed algorithm performs the following procedures:

- Initialize pheromone

At the beginning, an amount of pheromone intensity is initialized at each virtual machine, and each ant is randomly positioned on a virtual machine.

- Select a virtual machine

The probability of the kth ant selecting the jth virtual machine is calculated by the following formula [6]:

$$p_j^k(t) = \begin{cases} \frac{[\tau_j(t)]^{\alpha}[EV_j]^{\beta}[LB_j]^{\gamma}}{\sum_{u \in J_k(i)} [\tau_u(t)]^{\alpha}[EV_u]^{\beta}[LB_u]^{\gamma}} & , if \ \in 1...m \\ 0 & , otherwise \end{cases} \tag{111.4}$$

where $p_j^k(t)$ is the probability of the kth ant selecting the virtual machine j at time step t, $\tau_j(t)$ is the pheromone concentration deposited on the virtual machine j at time step t,EV_j is the computing capacity of the virtual machine j, LB_j is the load balancing factor of the virtual machine j, α, β, and γ are parameters, and m is the total number of virtual machines.

- Update pheromones

Two sets of formulae are used to update pheromones. If all virtual machines are over-loaded or all virtual machines are under-loaded, a one-way update formula is used; otherwise, a set of bidirectional update formula is used. The formulae are described as follows:

Case 1: If all virtual machines are over-loaded state or all virtual machines are under-loaded, a one-way formula is used to update the pheromone intensity:

$$\tau_j(t+1) = (1 - \beta_{eva}) \times \tau_j(t) + \sum_{k=1}^{n} \Delta\tau_j^k(t) \tag{111.5}$$

where $\tau_j(t)$ is the total pheromone intensity of node j at time step t, $\Delta\tau_j^k$ is the pheromone deposited by ant k, and β_{eva} is the pheromone evaporation rate as defined in Eq. (111.3).

Case 2: If the cloud environment contains both over-loaded and under-loaded virtual machines, two pheromone-update formulae are used [7]. The first formula is used when an ant is at an under-loaded node and is searching for an over-loaded node:

$$FP_j(t+1) = (1 - \beta_{eva})FP_j(t) + \sum_{k=1}^{n} \Delta FP_j^k \tag{111.6}$$

where $FP_j(t)$ is the total amount of foraging pheromone at node j at time step t, and ΔFP_j^k is the pheromone deposited by ant k.

The other formula is used when an ant is at an over-loaded node and is returning to the under-loaded node:

$$TP_j(t+1) = (1 - \beta_{eva})TP_j(t) + \sum_{k=1}^{n} \Delta \mathrm{T}P_j^k \tag{111.7}$$

Table 111.1 Number of virtual machines = 50 (fixed)

Iteration	Algorithm	500 tasks Makespan (ms)	300 tasks	100 tasks	50 tasks	25 tasks
1	LBACO	93.86	83.27	60.55	35.17	22.13
	BLBACO	87.77	77.98	54.34	24.48	20.38
30	LBACO	82.11	73.18	52.95	27.34	18.39
	BLBACO	76.09	69.38	45.71	19.11	16.80
70	LBACO	74.62	68.75	48.17	24.24	15.76
	BLBACO	69.78	65.25	42.81	16.02	14.43
100	LBACO	64.0	58.91	39.69	20.15	11.72
	BLBACO	58.10	55.86	36.15	11.32	10.96

Table 111.2 Number of virtual machines = Number of tasks

Iteration	Algorithm	500 tasks Makespan (ms)	300 tasks	100 tasks	50 tasks	25 tasks
1	LBACO	52.64	48.55	48.85	46.44	47.70
	BLBACO	38.62	34.83	35.05	34.84	36.37
30	LBACO	46.58	38.88	43.19	40.74	41.71
	BLBACO	34.18	28.57	30.22	29.08	31.05
70	LBACO	40.01	35.29	37.49	37.44	36.39
	BLBACO	32.25	26.44	27.688	26.33	28.46
100	LBACO	34.75	31.88	31.15	31.64	30.30
	BLBACO	28.028	22.83	23.82	22.59	23.95

where $TP_j(t)$ is the total amount of tracing pheromone of node j at time step t, and ΔTP_j^k is the pheromone deposited by ant k.

111.4 Experimental Results

The proposed BLBACO algorithm was implemented using the Java language and was tested on the CloudSim platform [9, 10]. The LBACO [6] algorithm has outperformed the First-Come-First-Serve (FCFS) algorithm and the basic ACO algorithm. In addition, the approach proposed by Nishant et al. [7] is not suitable for a dynamic environment. Therefore, the proposed BLBACO algorithm compared with LBACO [6]. The experiments used the parameter settings in [6]; that is, the number of ants n is 8, the pheromone evaporation rate β_{eva} is 0.01, and the parameters α, β, and γ in Eq. (111.4) are 3, 2, and 8, respectively.

In the first category of experiments, we fixed the total number of virtual machines to be 50 in each trial, and we varied the number of task requests to be 500, 300, 100, 50, and 25 in different trials. BLBACO and LBACO each executed 5 times for each trial. The makespan averages are shown in Table 111.1.

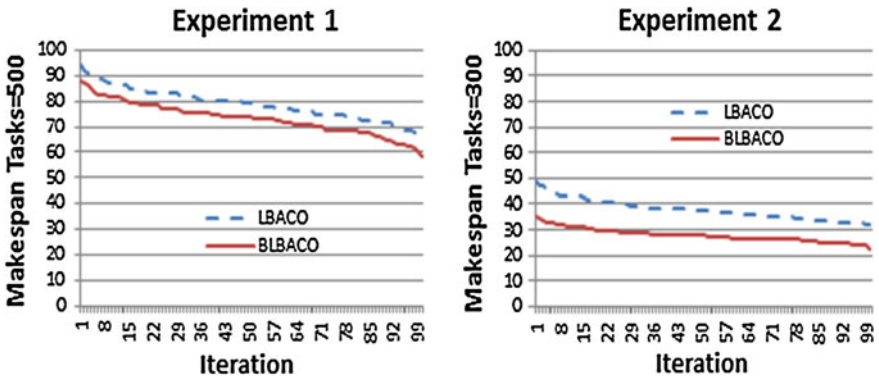

Fig. 111.1 Overall performance of the first experiment category with 500 tasks (*left*) and of the second category experiment with 300 tasks (*right*)

The second category of experiments verified the effectiveness of load-balancing strategies when the cloud environment contains both over-loaded and under-loaded virtual machines. To simplify the experiments, we set an equal number of virtual machines and task requests, and we assumed that the system would contain both under-loaded and over-loaded nodes. The results are listed in Table 111.2. To easily compare the performance of BLBACO with the performance of LBACO, we choose one trial from each category of experiments. The left panel of Fig. 111.1 shows the performance of the first category experiment with 50 virtual machines and 500 task requests, and the right panel shows the performance of the second category experiment with 300 virtual machines and 300 task requests. Based on the experimental results, the performance of BLBACO is better than that of LBACO. This validates the effectiveness of the proposed BLBACO algorithm.

111.5 Conclusions

In this paper, an improved method of cloud load balancing based on the ACO algorithm was proposed. The proposed BLBACO algorithm considers the loading and computing capacity of each virtual machine with bidirectional movement in ACO. The experiments showed that the BLBACO algorithm has better performance compared to LBACO [6]. This indicates that BLBACO can effectively deal with task allocation in a dynamic cloud environment.

References

1. Montresor, A., Meling, H., & Babaoglu, O. (2002). Messor: Load-balancing through a swarm of autonomous agents. In *AP2PC* (pp. 125–137).
2. Michlmayr, E. (2006). Ant algorithms for search in unstructured peer-to-peer networks. In *22th IEEE International Conference on Data Engineering Workshops*. Atlanta, GA, USA.
3. Salehi, M. A., Deldari, H. (2006). Grid load balancing using an echo system of intelligent ants. In *24th IASTED Parallel and Distributed Computing and networks*.
4. Fidanova, S., & Durchova, M. (2006). Ant Algorithm for Grid Scheduling Problem. In I. Lirkov, S. Margenov, & J. Waśniewski (Eds.), *LSSC 2005. LNCS* (Vol. 3743, pp. 405–412). Heidelberg: Springer.
5. Lee, Y. H., Leu, S., & Chang, R. S. (2011). *Improving job scheduling algorithms in a grid environment* (Vol. 27, pp. 991–998). Amsterdam: Future generation computer systems, FGCS.
6. Li, K., Xu, G., Zhao, G., Dong, Y., & Wang, D. (2011). Cloud task scheduling based on load balancing ant colony optimization. In *Conference of ChinaGrid* (pp. 3–9). Liaoning.
7. Nishant, K., Sharma, P., Krishna, V., Gupta, C., Singh, K. P., Nitin, N., & Rastogi, R. (2012). Load balancing of nodes in cloud using ant colony optimization. In *14th International Conference on Conference of Modelling and Simulation*. Cambridge.
8. Kansal, N. J. (2012). Existing load balancing Techniques in cloud computing: A systematic review. *Journal of Information Systems and Communication*.
9. Wickremasinghe, B., Calheiros, R. N., & Buyya, R. (2010). CloudAnalyst: A cloudsim based visual modeller for analysing cloud computing environments and applications. In *24th IEEE International Conference on Advanced Information Networking and Applications* (pp. 446–452). Perth, WA.
10. Buyya, R., Ranjan, R., & Calheiros, R. N (2010) CloudSim: A toolkit for modeling and simulation of cloud computing environments and evaluation of resource provisioning algorithms. In *IEEE International Conference on High Performance Computing* (Vol. 41, pp. 23–50).
11. Dorigo, M., & Di Caro, G. (1999). Ant colony optimization: A new meta-heuristic. In: D. Corne, M. Dorigo, & F. Glover (Eds.), *New ideas in optimization* (pp. 11–32).
12. Dorigo, M., & Stützle, T. (2001). An experimental study of the simple ant colony optimization algorithm. In *WSES International Conference on Evolutionary Computation* (pp. 253–258).

Chapter 112
Autonomous Underwater Vehicle System Implementation in Xingda Harbor

Chin-Yin Chen, Ling-Ji Mu, Ya-Chao Yang and Chao-Ming Yu

Abstract In the recent decades, Autonomous Underwater Vehicles (AUVs) are remarkable machines that revolutionized the process of gathering ocean data. AUV systems have been developed, operated, marketed, produced, sold and utilized in water for various purposes. Accordingly, in this study, the IVER2 AUV which configuration by Taiwan Ocean Research Institute (TORI) and built by OceanServer is discussed. The IVER2 performs routine operations sea surface; all the components are rated to 100 m.

Keywords Autonomous underwater vehicle · Underwater Robot · System integrated

112.1 Introduction

Unknown's environment in which autonomous robots have operated very successfully that has gained much less attention is in the marine cover approximately 70 % of the earth surface. The earth's oceans affect all of earth's inhabitants as they strongly influence the climate and provide much needed resources, e.g., geographical survey, oceanographic mapping, tracking pipes and cables, coastal and offshore structure inspection [1]. Therefore, speedy progress in underwater robotics is steadily supplying scientists for ocean exploration and exploitation. Then much work remains to be done before underwater robots can roam the oceans freely, acquiring scientific data on the temporal and spatial scales that are naturally imposed by the phenomena under study [2]. To meet these goals, underwater robots must be equipped with systems to steer them accurately and reliably in the

C.-Y. Chen · L.-J. Mu · Y.-C. Yang (✉) · C.-M. Yu
Taiwan Ocean Research Institute, National Applied Research Laboratories, Kaohsiung, Taiwan, Republic of China
e-mail: yc_yang@narlabs.org.tw

J. Juang et al. (eds.), *Proceedings of the 2nd International Conference on Intelligent Technologies and Engineering Systems (ICITES2013)*, Lecture Notes in Electrical Engineering 293,
DOI: 10.1007/978-3-319-04573-3_112,

harsh marine. For this reason, there has been considerable interest over the last few years in the development of advanced underwater vehicles. The underwater vehicles world has reached a stage where the remotely operated vehicles (ROVs) industry is very well established with thousands upon thousands of ROVs having been created and deployed since the dawn of this industry. The ability to communicate between the vehicle and the operator is one of the main factors affecting whether a vehicle is to be designed as an ROV or as an autonomous vehicle. Nevertheless, their constraints such as the need for a communications cable and a control platform have limited their capabilities and use [3].

The overcome the deficiencies of ROVs, AUVs have stepped to the forefront of underwater exploration. As AUVs typically operate underwater, the effects of waves and currents on the vehicle motion are greatly reduced, thus, providing the required stability for a suite of sensors on board, such as images sensors. Further mission enhancement could involve AUVs developed with adaptive, cooperative capabilities, long endurance such that the sampling objective can be achieved.

Currently, there are many AUVs being deployed for research purposes, such as JAMSTEC, WHOI, MBARI, FSI and Kongsberg Maritimu were developed for exploring ocean resources and carrying out scientific studies [4]. In past years, Taiwan has been building up facilities and supply for marine industry. In addition to ocean resource, shipbuilding, and offshore engineering, the government has also provided sustained support for the development of underwater technology more than decade. Underwater technology has attracted increasing attention because it is the basis for sustainable development and preservation of our ocean environment. In this study, the IVER2 AUV which configuration by Taiwan Ocean Research Institute (TORI) and built by OceanServer is discussed.

112.2 Components for AUV

The IVER2 Autonomous Underwater Vehicle (AUV) built by the OceanServer. Due to the increasing reliability and availability of AUVs they are now used for a widespread range of applications. It is a small and easily transported, with specifications the exceed those of larger vehicles.

As Fig. 112.1 shown, establishing communication between a notebook and the AUV system is accomplished using WiFi router. The characteristics of those components are discussed as below.

112.2.1 Vehicle Specifications

The overview and specifications of the vehicle for TORI's AUV are shown in Fig. 112.2 and Table 112.1, respectively. This AUV designed using modular design method, which consists of mechanical modular, propulsion modular, vision

Fig. 112.1 Components of TORI's AUV

modular, light modular, sampling modular and sensor modular. The detail characteristics for those components are discussed in some Ref. [3, 4].

112.2.2 Control Console

As Fig. 112.2a shown, to communicate with the Iver2-121 main CPU through the backseat driver CPU, a serial connection must first be created between backseat and main CPU; backseat CPU include Camera CPU and User CPU. The main CPU receives backseat driver commands through a serial port, which permits the user to control the vehicle. Establishing communication between a notebook and Iver2 is accomplished using a portable battery powered Wi-Fi router. The user must connect the operating computer to the Wi-Fi. Through the Wi-Fi connection, user can connect Iver2 AUV using Windows Remote Desktop Connection (WRDC), from notebook, also allows user to easily transfer data as shown in Fig. 112.3.

A. *Mission planning control*

The first step in creating a new mission is opening a geo-referenced map, our used Google earth to create map then could scan in an image of a map to a TIFF file, use the rectify imagery command to enter the coordinates of several points on that image, and then load it into Global Mapper properly overlaid with any other loaded data as shown in Fig. 112.4.

A mission consists of user defined sequence of GPS referenced waypoint that the vehicle follows while collecting specified data using its onboard sensors. For system, creating a mission file requires the use of OceanServer VectorMap (VM) software, a connection to the internet, and Microsoft Windows operating system. Users import maps into VM and add waypoints on top of the map by simply pointing and clicking. A variety of the AUV's operating characteristics and sensor

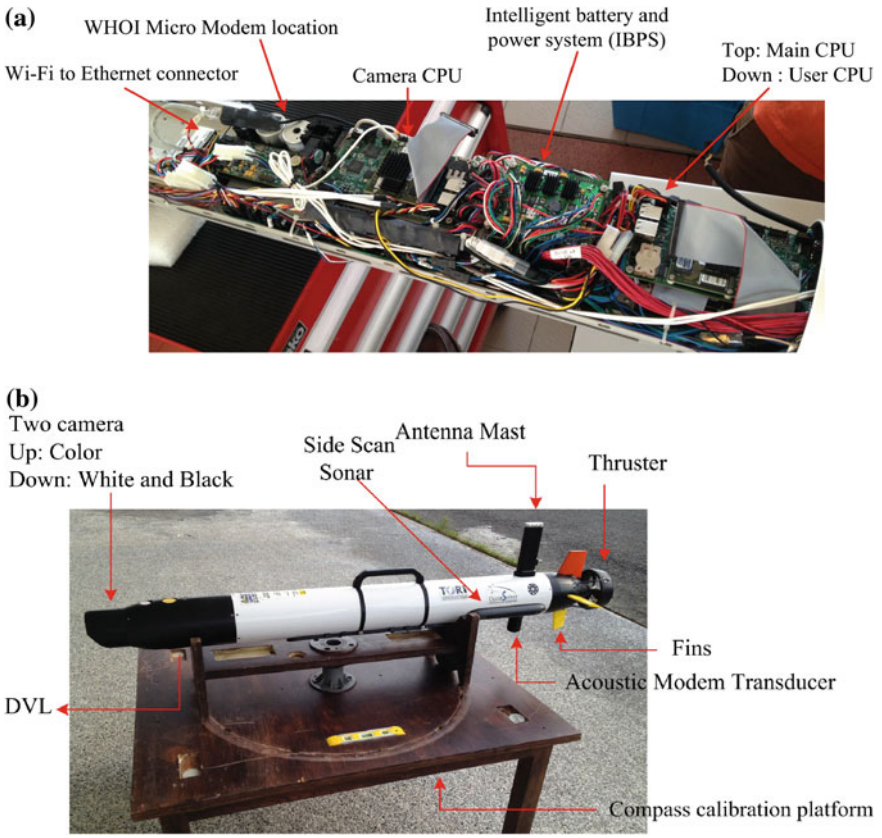

Fig. 112.2 Internal Layout of IVER2. **a** Internal Layout of IVER2. **b** Exterior View of IVER2

Table 112.1 Vehicle specification

Items	Specification
Mechanical characteristic	Size: L 1.4 m, Diameter 0.147 m
	Air weight: 21 kg
Propulsion	DC brushless motor
	4 independent fin control surfaces, yaw, pitch and roll
Navigation and payload	GPS and Compass
	DVL
	Altimeter and Pressured Sensor
	Side Scan
	Camera System
Energy and endurance	24 h@2.5knot
Command and control	802.11n Ethernet Standard
	GPS
	Acoustic Modem
Emergency recovery procedure	Safety Tow Float

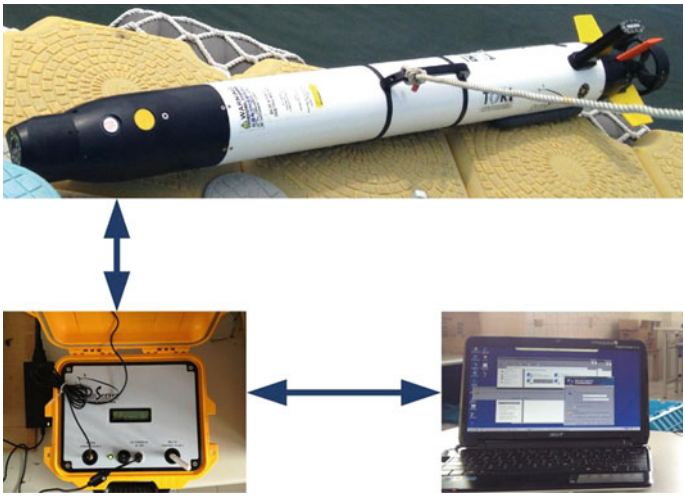

Fig. 112.3 Connecting to the Iver2-121 [3]

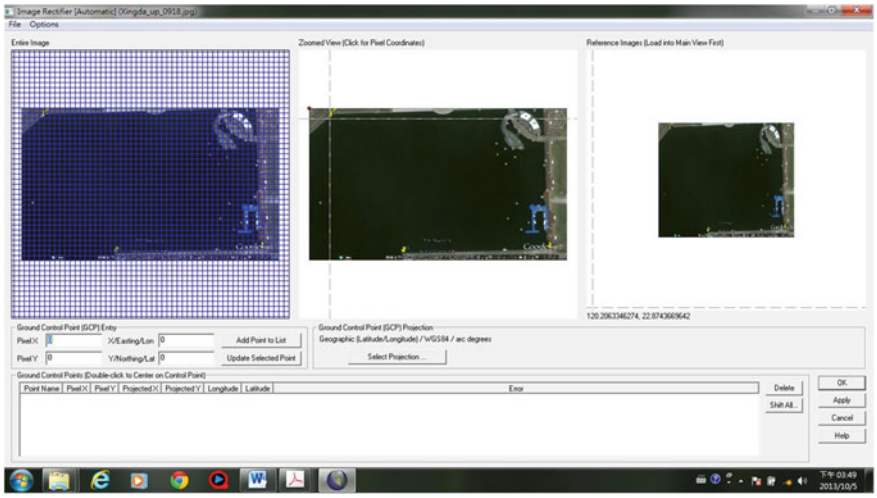

Fig. 112.4 Geo-rectify Imagery

function can be assigned to a waypoint, allowing the AUV to perform the appropriate tasks throughout the course of mission. Figure 112.5 shows VM screen is organized using a paneling concept, where functional panels are placed on each page to build the screen. The VM software displays the width and height of the box, which allows the user to determine the area [5].

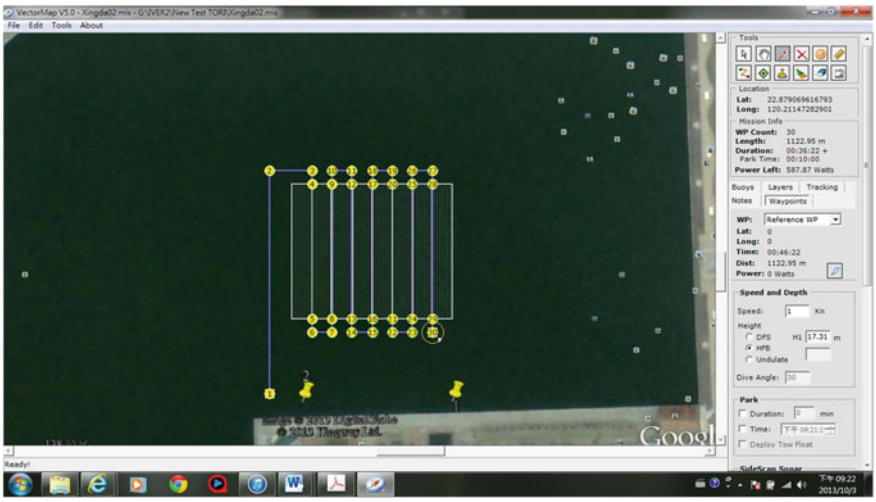

Fig. 112.5 Mission planning and VM screen

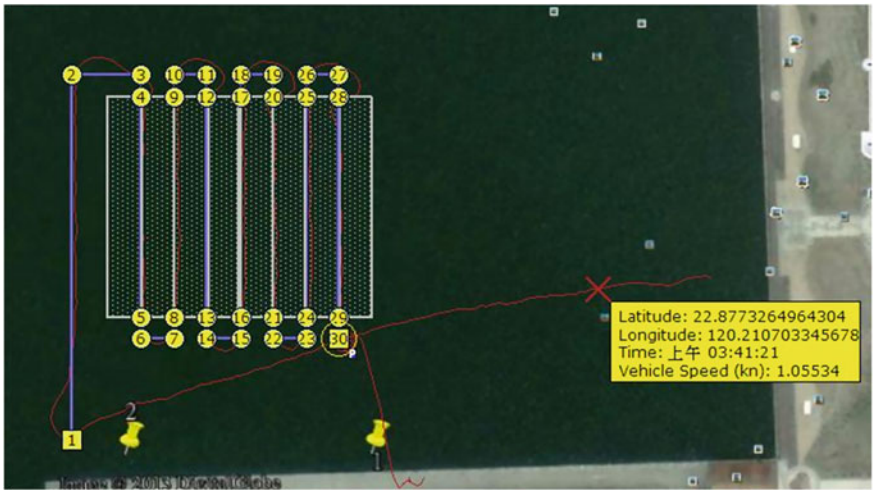

Fig. 112.6 log file in VM software

B. *start mission and log file*

Start the run mission and confirm that the GPS, compass and depth sensor are receiving valid data by verifying that sensors state are green light. When the Iver2 is running a mission, it is continuously logging data that is time and GPS data. Figures 112.6 depict the log data can be overplayed on the mission in VM.

Fig. 112.7 Recovered back in Xingda harbor

112.3 System Implementation in Xingda Harbor

The TORI's AUV system was operated water's surface in Xingda harbor. Once the AUV has entered a park location, it will adjust the motor on/off until it is within the park radius. The AUV recovered back from the boat using the manpower (see the Fig. 112.7). The AUV is propelled by thrusters and fins which it can be autonomous operated in any desired path from the mission command by the underwater vehicle console (UVC) software that resides in the Iver2 and is responsible for running missions (see the Fig. 112.7). The difference sensors are used to carry out Xingda harbor intervention tasks. After the completion of the mission, the Iver2 shall be recovered back to the boat.

112.4 Conclusion

In this paper, the 100 m TORI's AUV Iver2 is presented. For this AUV, it is not only for science observation but also work for offshore engineering. However, in this study, it just describes the environment observation. And furthermore, the main goal of our AUV project is to observe the Xingda harbor underwater environment. And the construction of the underwater software and operate interface infrastructures is to be one of the key point for it.

References

1. Fossen, T. I. (1994). *Guidance and control of ocean vehicles*. Chichester, UK: Wiley.
2. Do, K. D., Jiang, Z. P., & Pan, J. (2002). Underactuated ship global tracking under relaxed conditions. *IEEE Transactions on Automatic Control*, *47*(9), 1529–1536.

3. Petrich, L. J., Stilwell, D. J., Lindner, D. K., Neu, W. L., Abbott, A. L., & Woolsey, C. A. (2009). *Improved guidance, navigation, and control for autonomous underwater vehicles: Theory and experiment*. Blacksburg, VA: Virginia Polytechnic Institute.
4. Gonzalez, L. A. (2004). *Design modeling and control of an autonomous underwater vehicle*. Crawley, WA: The University of Western Australia.
5. Operating Guide: Running a Mission with Iver2, OceanServer Technology, INC.

Chapter 113
Development of Autonomous Master-and-Slave Vehicles with Cruise Technology

Hong-Ming Chen, Ting-En Lee, Juhng-Perng Su and Chong-Qan Liao

Abstract The object of this study is to develop a group of master-and-slave vehicles with the realization of group control and cruise technology. The main feature is to design one large master-vehicle, and two small slave-vehicles. The master vehicle can carry the slave vehicles to perform the security patrol in grouping mode. When executing the security patrol, central monitoring system will command the master vehicle with slave vehicles moving to the corridor of patrolled floor in building. Furthermore, the slave vehicles will be putted down from the master vehicle and autonomously cruise everywhere of patrolled floor. After the cruising of slave vehicles, the master vehicle will carry these slave vehicles to the next place and continue patrolling task. Once multiple vehicles work simultaneously, the efficiency of security patrol will be significantly improved. The experimental results indicate that the designed master-and-slave vehicles have successfully completed the mission of autonomous cruising. Consequently, the proposed development is available in the application of security.

Keywords Master and slave vehicles · Grouping control · Security patrol · Autonomous cruising · Central monitoring system

H.-M. Chen (✉) · C.-Q. Liao
Department of Electronic Engineering, Chienkuo Technology University, Changhua 500, Taiwan, Republic of China
e-mail: steven@ctu.edu.tw

T.-E. Lee
Graduate School of Engineering Science and Technology, National Yunlin University of Science and Technolgy, Yunlin 640, Taiwan, Republic of China

J.-P. Su
Department of Electrical Engineering, National Dong Hwa University, Hualien 974, Taiwan, Republic of China

J. Juang et al. (eds.), *Proceedings of the 2nd International Conference on Intelligent Technologies and Engineering Systems (ICITES2013)*, Lecture Notes in Electrical Engineering 293,
DOI: 10.1007/978-3-319-04573-3_113,

113.1 Introduction

For the consideration of safety and property, the security of houses and buildings is getting popular and important nowadays. In general case, the security equipments are installed in each places of building. According to the sensors with internet, the security company can monitor the environment. However, its passive security has some shortcomings, e.g. sensor breakdown, wrong touch of alarm bell, dead space. That is why security service personnel always busy with some troublesome problems. Accordingly, active security has been investigated for avoiding above problems.

The essence of active security is using moving vehicles or robots instead of built-in equipments. In literature, the robots and vehicles have been maturely developed for various applications. In [1], the robot is applied for loading and unloading cargo at port. In [2], three vehicles have been developed for relieving the victims of a disaster. Specially, one of these vehicles is able to carry others. In [3], controller has been incorporated in the autonomous vehicle design to achieve the path tracking. In [4], an autonomous light truck with laser range finder has been designed for the application of trajectory tracking and exploration. In [5, 6], the image technology has been further applied for vehicles to possess the function navigation and obstacle avoidance.

The main feature of this study is to design one master vehicle and two slave vehicles for demonstrating the autonomous cruising and security patrol in group mode. The central monitoring system will coordinate the master and slave vehicles execute the mission. Consequently, the effectiveness of cruising is expectably improved due to the master and slave vehicles execute at the same time.

113.2 The Design of Master-and-Slave Vehicles

113.2.1 Master Vehicle

Figure 113.1 is the practical photograph of master vehicle. The size of master vehicle is $30 \times 50 \times 20$ cm and which chassis is composed by aluminum extrusion frame. The wheels of master vehicle are driven by four DC motors. The top shell of vehicle is composed of acrylic sheet. A lifting platform as be shown in the right figure of Fig. 113.1 is installed on the rear of vehicle. Therefore, the master vehicle is able to carry two slave vehicles. In addition, the master vehicle possesses the ability of autonomous cruising. When moving to the patrolled position, the master vehicle will puts down the slave vehicles such that the slave vehicles can perform the patrol task.

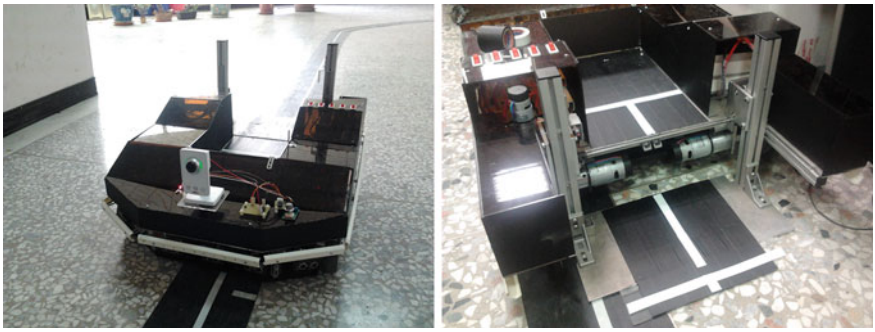

Fig. 113.1 The practical photograph of master vehicle (left figure) and its lifting platform (right figure)

Figure 113.2 is the architecture diagram of control system for master vehicle. The control system is divided into two parts, main control core and secondary control core. The structure of main control core is shown in the right figure of Fig. 113.2, and the control unit is based on the PIC24FJ128 GB106 with 16 bits produced by Microchip. The control unit is utilized to control the sensors, encoder, motor, lifting platform, and obstacle avoidance, and to transfer the data to central monitoring system via Xbee wireless communication module. The secondary control core is based on PIC32MX440F512H with 32 bits produced by Microchip, and which structure is indicated in Fig. 113.3. The secondary control core is utilized to collect data from ultrasound, fire sensor, temperature and humidity sensor, gas sensor, and wireless camera. The sensed data will also be transferred to central monitoring system.

113.2.2 Slave Vehicle

The slave vehicle is a small and track-type vehicle with 10 × 20 × 10 cm. The practical photograph is shown in Fig. 113.4. The front wheels of slave vehicle are driven by two DC motor, and the rear wheels are driven by timing belt. As be depicted in Fig. 113.5, the system structure of slave vehicle is composed of PIC32MX440F512H micro controller, fire sensor, temperature and humidity sensor, trajectory following sensor, ultrasound sensor, gas sensor, and wireless webcam. Accordingly, the immediate image would be transferred to central monitoring system for the real-time surveillance.

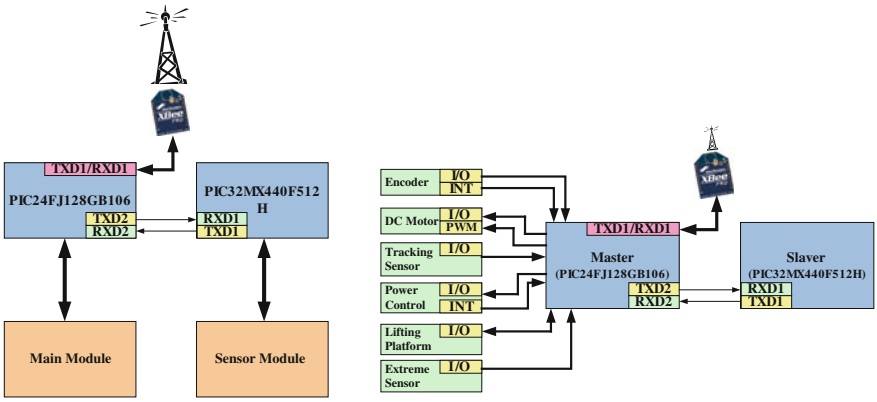

Fig. 113.2 The control system (left figure) and the structure of main control core (right figure) of master vehicle

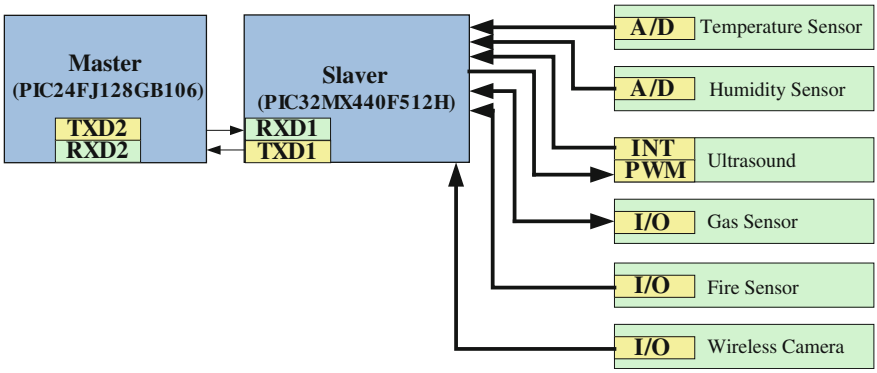

Fig. 113.3 The structure of secondary control core for master vehicle

Fig. 113.4 The practical photograph of slave vehicle

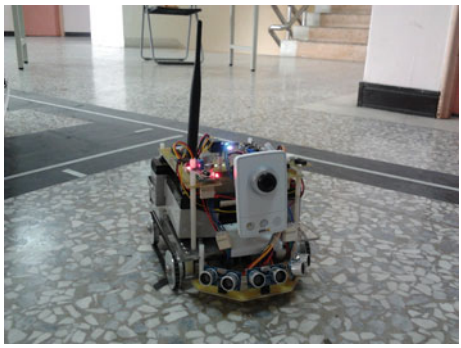

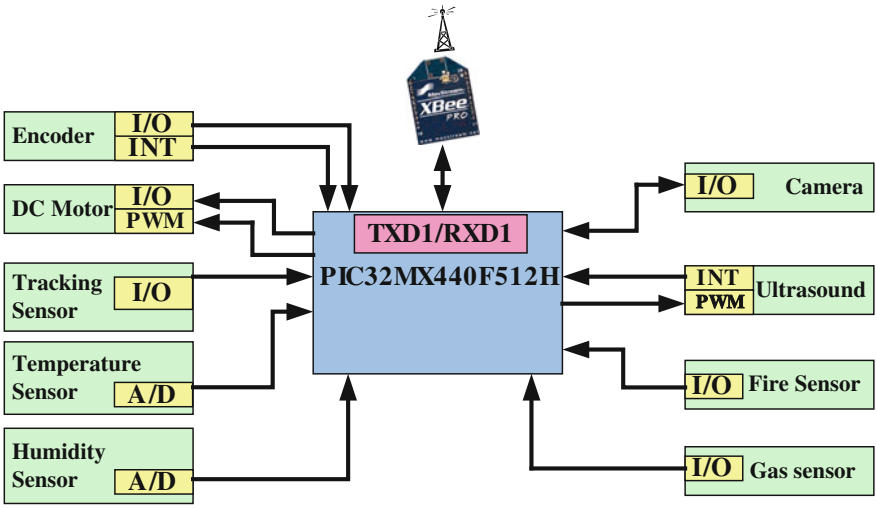

Fig. 113.5 The system structure of slave vehicle

113.3 The Control Interface and Cruse Technology

113.3.1 Control Interface

The human–machine interaction (HMI) of central monitoring system is established by LabVIEW, and the designed control interface is shown in Fig. 113.6. The plan of cruising place used to display the position of master-and-slave vehicles is indicated in the left and top of Fig. 113.6. The information of sensors is shown in the right and top of Fig. 113.6, and the knob and button used to control the motion of vehicles and lifting platform is shown in the bottom of Fig. 113.6.

113.3.2 Cruise Strategy

In this study, the cruise place is designed as one floor of office building. The trajectory for vehicles is made by black and white tapes. As be shown in Fig. 113.7, there are three cruise regions within the blue trajectory. In order to display the position of vehicles in the monitoring system, totally 70 points are utilized for the orientation. Therefore, each point has its identification number to respond the relating position for the surveillance.

For the cruise strategy, the central monitoring system coordinates the master and slave vehicles to execute the security patrol. In general, vehicles are manually controlled by central surveillance. Once the operator commands vehicles to

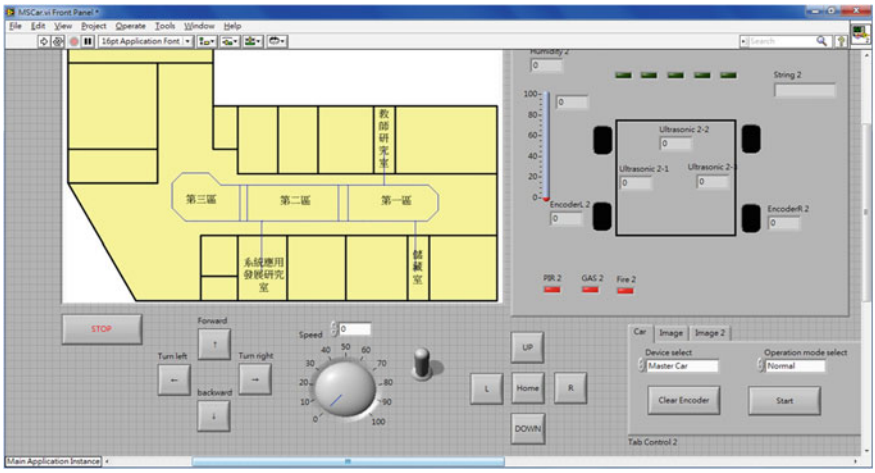

Fig. 113.6 The human–machine intersection of central monitoring system is designed by LabVIW

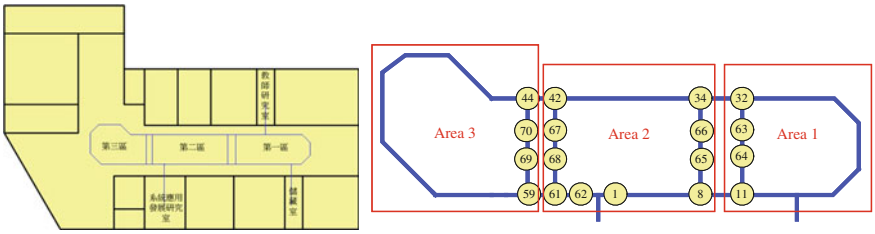

Fig. 113.7 The cruise place and orientation points for the vehicles

Fig. 113.8 The realistic scenes of master and slave vehicles execute the security patrol in area 1 and 2

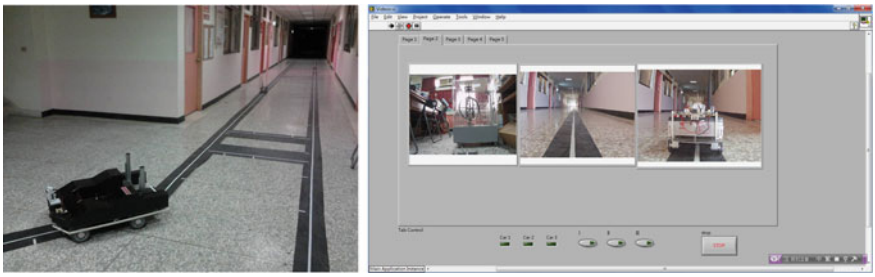

Fig. 113.9 The realistic scene of master vehicle patrols in area 3, and the live video displays the status of vehicles in the human–machine intersection

perform the standard cruise mission, the operation mode will be transferred from active mode to relay mode. Refer to Fig. 113.7, the cruise place is divide into three patrolling areas. Firstly, the master vehicle will move to be nearby the no. 8 point and let first slave vehicle to start patrolling from no.11 point. Therefore, the first slave vehicle will pass no. 11, no. 64, and continue patrolling in area 1. At the same time, master vehicle will move from no. 8 to no. 34, and passing the no. 65 and no. 66. Before moving to no. 42, the second slave vehicle will be assigned to stay in area 2 and be responsible for the patrol. Then, the master vehicle will pass no. 42 and move to patrol area 3. Consequently, the security patrol of business building could be completed by the autonomous master-and-slave vehicles.

113.4 Experimental Results

The experimental results indicated in Figs. 113.8 and 113.9 demonstrate the effectiveness of developed autonomous vehicles. The Fig. 113.8 is the realistic scene of the master vehicle lay down the first and second slave vehicles to patrol the area 1 and area 2, respectively. Moreover, the left figure of Fig. 113.9 shows the master vehicle executing the security patrol in area 3. The live video shown in the right figure of Fig. 113.9 is used to monitor the status of master-and-slave vehicles, and immediately provide the command. These results demonstrate that the autonomous cruising of master-and-slave vehicles could be correctly exercised by the grouping control.

113.5 Conclusions

In the development of autonomous master-and-slave vehicles, we have successfully realized the grouping control by micro chip and design the central monitoring system by LabVIEW. The Xbee module is used for the wireless communication.

Therefore, the immediate image could be transferred back to surveillance station for monitoring the environment. The experimental results also indicate that the master-and-slave vehicles can automatically cruise the assigned place at designated times.

References

1. Park, J. (2008). AGV parking system using artificial visual landmark, in *International Conference on Control, Automation and Systems* (pp. 1579–1582).
2. Yang Y., Xu, G., Wu, X., Feng, H.W., & Xu, Y. (2009). Parent-Child robot system for rescue missions, in *Proceedings of the 2009 IEEE International Conference on Robotics and Biomimetics* (pp. 1427–1432).
3. Sahoo, S., & Shankar, C. S. (2012). Design and implementation of a controller for navigating an autonomous ground vehicle, in *International Conference on Power, Control and Embedded Systems*.
4. Song, H., Kim, J., Jung, E., Lee, J., & Kim, S. (2012). Path-tracking control of a laser guided vehicle using fuzzy inference system, in *International Conference on Control, Automation and Systems*.
5. Taha, Z., Mat-Jizat, J. A., & Ishak, I. (2012). Bar code detection using omnidirectional vision for automated guided vehicle navigation, in *International Conference on Automatic Control and Artificial Intelligence* (pp. 589–592).
6. Takenaga, H., Konishi, M., & Imai, J. (2009). Agent based Rouings of multi mobile robots with vision feedbacks, in *ICROS-SICE International Joint Conference* (pp. 1284–1289).

Chapter 114
The Effect of Hydrogen Plasma Treatment on the Field-Emission Characteristics of Silicon Nanowires

Shih-Fong Lee, Li-Ying Lee and Yung-Ping Chang

Abstract Silicon nanowires (SiNWs) were formed on nickel-coated silicon substrates by a solid–liquid-solid (SLS) growth mechanism. Effect of hydrogen plasma treatment on the field-emission characteristics of the silicon nanowires was investigated. The results show that hydrogen plasma treatment can enhance the field-emission characteristics of the SiNWs showing a decrease in turn-on field as well as an increase in field enhancement factor. It is believed that hydrogen plasma treatment plays an important role in the improvement of field-emission characteristics of silicon emitters.

Keywords Silicon nanowires (SiNWs) · Field-emission · Plasma treatment

114.1 Introduction

Recently, one-dimensional structures, such as nanowires, nanotubes and nanorods, have been intensively investigated due to their excellent unique optical, electronic, mechanical properties, and above all electron emission properties. Much effort has been concentrated on how to fabricate field emission flat panel display using various nanostructures and materials [1–4].

In this work, silicon nanowires (SiNWs) were synthesized with Ni as catalyst through a solid–liquid-solid (SLS) phase growth mechanism on Si substrate in an Ar ambient without any additional silicon source supply [5]. Owing to its high aspect

S.-F. Lee · Y.-P. Chang
Department of Electrical Engineering, Dayeh University, Changhua County 515, Taiwan, Republic of China

L.-Y. Lee (✉)
Department of Electronic Engineering, Chung Chou University of Science and Technology, Changhua County 510, Taiwan, Republic of China
e-mail: ladylee@dragon.ccut.edu.tw

J. Juang et al. (eds.), *Proceedings of the 2nd International Conference on Intelligent Technologies and Engineering Systems (ICITES2013)*, Lecture Notes in Electrical Engineering 293,
DOI: 10.1007/978-3-319-04573-3_114,

ratio, SiNW exhibits a unique quasi-one-dimensional sp^3-bonded crystal structure and a low work function [6, 7]. Similar to carbon nanotubes, it is of interest to investigate the field emission of SiNWs. Nevertheless, a thin oxide layer is always formed on the surface around the SiNWs while the SiNWs are exposed in the air. The silicon oxide thin layer does not assist in the electron transport and field emission.

In an attempt to remove the oxide layer and thus enhance the field emission of SiNWs, the specimen grown with SiNWs was treated with hydrogen (H_2) plasma using a reactive ion etching (RIE) system. In this paper, it is demonstrated that the enhanced field-emission characteristics can be obtained for SiNWs after H_2 plasma treatment. The mechanism behind this improvement is also carefully examined.

114.2 Experiment Details

In this work, SiNWs were synthesized on Si (100) substrate through a solid–liquid-solid (SLS) phase growth mechanism without any additional silicon source supply proposed by Yan and coworkers [5]. In this process, silicon diffuses into Ni particle to form a Si-Ni alloy at elevated temperature. However, on the top surface of the Ni particle, heat is carried away by a steady flow of Ar and the temperature is lowered. Therefore, the solid solubility of Si in Ni is decreased accordingly and a local supersaturation of Si arises near the top surface of Ni particle. To reach equilibrium state, excess Si atoms are expelled from the Ni particle in the form of precipitation. Thus, SiNWs were grown out of the top surface of Ni particle.

The substrates used were n-type Si (100) wafers, which were cleaned ultrasonically in acetone and in ethanol in turn for 10 min each, and then rinsed in deionized water. The cleaned wafer surface was then deposited with a 15 nm thick Ni film using an ultrahigh vacuum thermal evaporator at room temperature. The purpose for this Ni layer is to induce the growth of SiNWs. The thickness of evaporated Ni film was precisely controlled with a thickness monitor.

The synthesis of SiNWs was carried out in a high-temperature tube furnace. The silicon substrate coated with Ni layer was placed in a 4.0×2.5 cm^2 ceramic holder and a 3.5×2.0 cm^2 Si (100) substrate was mounted on top of it. Subsequently, the ceramic holder was placed into a quartz tube furnace for the synthesis of SiNWs and the chamber was pumped down to less than 10^{-3} Torr using a mechanical pump. Argon with the flow rate 500 sccm was introduced into the tube and the temperature was gradually increased with a temperature controller until it reached the target temperature and maintained at that temperature for 10 min. The synthesis temperature and pressure were about 1000 °C and 1 atm, respectively. The growth time was 2 h. The samples were then cooled in Ar flow ambient. The etched sample was first grown for 15 min using the same conditions as for the as-grown sample. After growth phase, these samples were put into an RF plasma etcher to be treated with hydrogen (H_2) plasma for purification. The flow rate of H_2 was set to 30 sccm, RF power was 10 W, and the working pressure was 8–12 m Torr, and the duration of H_2 plasma treatment was varied from 1–6 min.

These specimens were investigated in a Hitachi S-3000 N field-emission scanning electron microscope (FESEM) operated at 15 kV. Energy-dispersive spectrometry (EDS) was used to identify and analyze the chemical composition of the surface. Transmission electron microscopy (TEM, JEOL-2010) was used to characterize the detailed microstructure features of SiNWs. The field-emission measurement was carried out in high vacuum to ensure accurate characterization of the current density versus applied field (*J-E*) relation. Synthesized SiNWs were pasted with silver paste onto a glass substrate coated with conducting indium tin oxide (ITO) and subsequently dried in an oven. The glass substrate together with SiNWs was mounted on a test fixture as the cathode, while an ITO glass substrate was used as the anode with an emission area of -0.007 cm^2. The spacing between the electrodes was adjusted to 50 μm. The vacuum chamber was first pumped down to 10^{-2} Torr with a mechanical pump, and then further pumped down to 10^{-6} Torr with a turbomolecular pump. A Keithley 237 was used to supply the voltage (up to 1000 V) between the electrodes and to measure the emitted current with pA sensitivity, allowing for the accurate characterization of current–voltage (*I–V*) behavior.

114.3 Results and Discussions

Figure 114.1a shows the top-view SEM image of as-grown, untreated SiNWs, while Fig. 114.1b–g are the SEM images of SiNWs after 1–6 min of H_2 plasma treatment. As seen in Fig. 114.1a, after plasma treatment, the top layer of SiNWs conglomerates into cluster, and SiNWs and catalyst originally underneath become exposed. In Fig. 114.1, no change in morphology with plasma treatment time can be clearly seen. This indicates that the changes occur not in the structure of the core at the SiNWs but on the surface only.

The field-emission characteristics of the SiNWs with and without hydrogen plasma treatment are shown in Fig. 114.1. In Fig. 114.1, the field-emission characteristics of SiNWs are obviously enhanced after hydrogen plasma treatment for 5 min. An emitted current density of 3.5 mA/cm^2 at the maximum accessible voltage (with an applied field of 19.5 V/μm) is observed. Furthermore, the specimens with plasma treatment also show a low turn-on field at 6 V/μm, which is defined as the point where the current–voltage curve shows a sharp increase, or simply the field at which the current density is 0.01 mA/cm^2 for convenience. The turn-on field decreases with the increasing plasma treatment time. Specimens treated for 5 min show increased emission current density, the untreated specimen shows low emission current density. Among all specimens, the specimen treated for 5 min exhibits the highest emission current density as well as a low turn-on voltage. These results lead us to conclude that hydrogen plasma treatment under proper conditions can be used to effectively improve the FE characteristics of the SiNWs.

The etching effect of H_2 plasma treatment can be further confirmed with EDS measurements which can be used to identify and analyze chemical elements on the

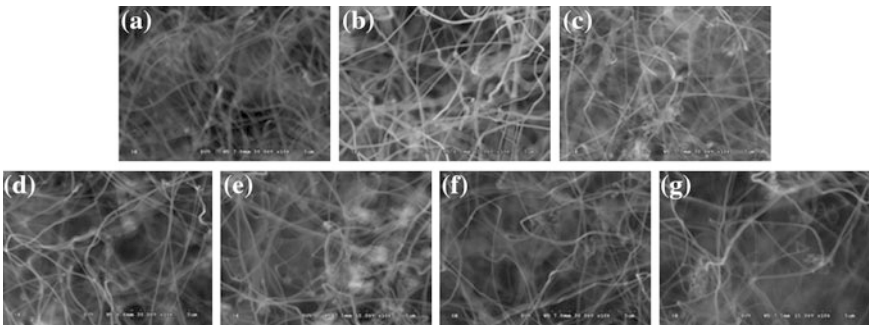

Fig. 114.1 The top-view SEM images of SiNWs for: **a** as-grown, untreated SiNWs, and after: **b** 1, **c** 2, **d** 3, **e** 4, **f** 5, **g** 6 min of H_2 plasma treatment. The magnification factor is 1×10^4

surfaces of SiNWs. Figure 114.2 shows the chemical composition of SiNWs as measured from EDS for as-grown, untreated SiNWs and for SiNWs after 1–6 min of H_2 treatment. Note that the percentage of oxygen was reduced after H_2 plasma treatment. The as-grown, untreated SiNWs have a very high content of oxygen (65.78 % atomic) on their surfaces that is very close to that of insulating silicon dioxide (SiO_2). This indicates that SiNWs are covered with an intrinsic SiO_2 layer. Since only Ar was supplied during growth, these oxygen atoms were originated from the native oxide residing on the silicon substrate and have been proven to be beneficial to the growth of SiNWs [8]. However, electrons in SiNWs have to tunnel through the SiO_2 layer by quantum-mechanically tunneling first before they can be emitted into vacuum. Since the probability for quantum mechanically tunneling is inversely proportional to the exponential of the square of barrier width, it is a very fast decaying function with the barrier width. Hence, this additional obstacle is believed to be the limiting step in the field-emission mechanism for SiNWs and can be used to account for the relatively poor field-emission characteristics of SiNWs. After H_2 plasma treatment, the oxygen content on the surface was decreased continuously with the treatment time and the silicon content was increased continuously with the treatment time accordingly. Obviously, oxygen was removed by hydrogen plasma and the underlying silicon becomes exposed.

Figure 114.3 shows the current density versus applied field (*J*-*E*) characteristics for SiNWs before and after plasma treatment. The emitted current density for the as-grown, untreated SiNWs was 0.125 mA/cm^2. On the other hand, the emitted current densities at the maximum applied field (19 V/μm) are 0.197, 0.290, 0.496, 0.688, 3.54, and 2.50 mA/cm^2 for SiNWs after 1, 2, 3, 4, and 5 min of H_2 plasma treatment, respectively. At the maximum applied field, an increase of more than two orders of magnitude in the emitted current is achieved for the SiNWs after 5 min of H_2 plasma treatment. Based on the results obtained from EDS, the main function of plasma treatment is the etching of SiO_x covering SiNWs. After 2 min of plasma treatment, the oxygen content decreases continuously from 65.78 % for as-grown, untreated SiNWs to 58.03 % for SiNWs after 6 min of plasma treatment.

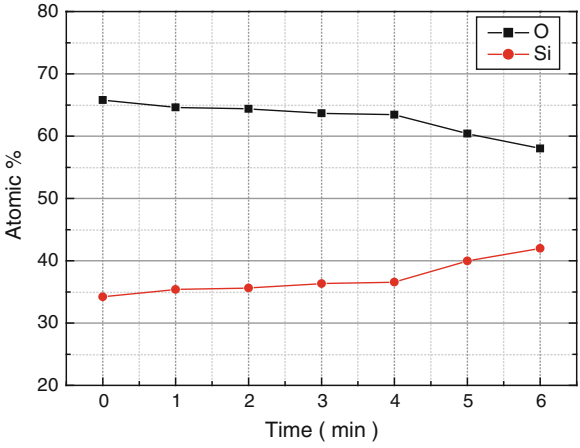

Fig. 114.2 Chemical composition of SiNWs before and after 1–6 min of H_2 plasma treatment

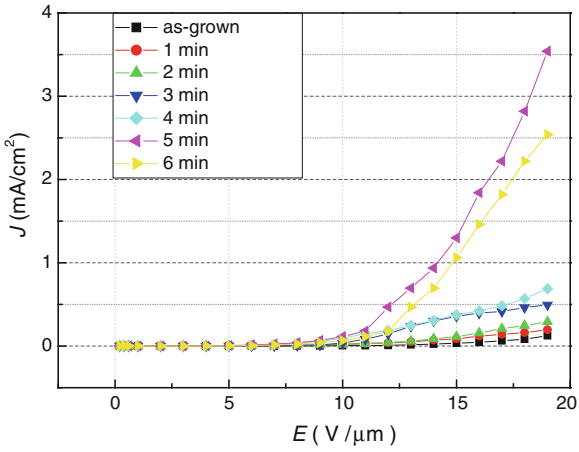

Fig. 114.3 The emitted current density versus applied field (*J-E*) curves for SiNWs before and after H_2 plasma treatment

To further analyze the field-emission characteristics of the SiNWs treated with hydrogen plasma, the equation used to describe the relationships between current density J and the local electric field at the emitter E at high electric fields is given as follows according to Fowler–Nordheim theory [9]:

$$\ln\left(\frac{J}{E^2}\right) = \ln(a^*) - b^*\left(\frac{1}{E}\right)$$

$$a^* = \frac{A\beta^2}{1.1\phi}\exp\left[\frac{1.44\times10^{-7}B}{\phi^{1/2}}\right]$$

$$b^* = \frac{0.95B\phi^{3/2}d}{\beta}$$

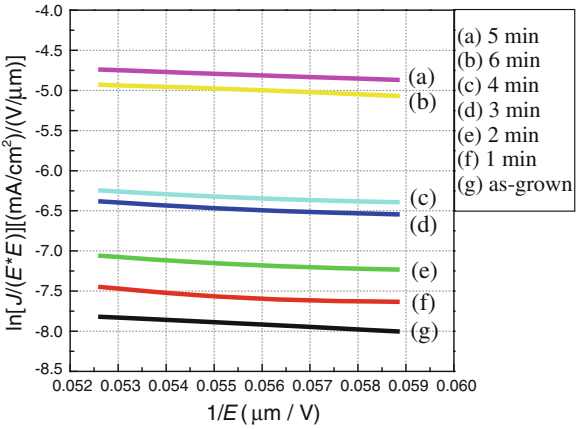

Fig. 114.4 The Fowler–Nordheim plot for SiNWs before and after 1–6 min of H_2 plasma treatment

Table 114.1 The slopes and field enhancement factors β as calculated from the Fowler–Nordheim plot for the SiNWs before and after H_2 plasma treatment

Plasma treatment time (min)	Slope in F–N plot	Field enhancement facor β
as-grown, untreated	30.72	725.4
1	29.55	754.2
2	27.74	803.4
3	25.89	860.8
4	23.66	941.9
5	20.58	1082.9
6	22.29	999.8

where the values for coefficients A and B are $A = 1.54 \times 10^{-6}$, $B = 6.87 \times 10^{7}$, d is the spacing between electrodes, ϕ is the work function of emitter, and β is field enhancement factor.

Thus, the linear relationship between J/E^2 and $1/E$ can be obtained on a semi-logarithmic plot (Fowler–Nordheim plot or F–N plot) for field emission at high fields. Figure 114.4 is the F–N plot for SiNWs before and after 1–6 min of H_2 plasma treatment. The almost linear relationship at high fields is a clear indication that electron emission from SiNWs is obtained.

An even more important cause for the increase of emitted current is the increase in surface roughness caused by the plasma treatment which renders higher field enhancement factor β and more possible emission sites. This is evidenced from the F–N plot for SiNWs before and after H_2 plasma treatment. Table 114.1 shows the slopes and field enhancement factors β as calculated from the F–N plot as shown in Fig. 114.4. As seen in Table 114.1, field enhancement factor β increases from 725.5 for as-grown, untreated SiNWs to 1082.9 for SiNWs after 5 min of H_2 plasma treatment. It is obvious that the emitted current is fully correlated with field enhancement factor β.

114.4 Conclusions

In this study, it is demonstrated that highly condensed nanowire arrays can be readily prepared over a large area by the SLS growth mechanism. The field-emission characteristics of SiNWs can be greatly enhanced by H_2 plasma post-treatment. After H_2 plasma treatment, the field-emission characteristics of SiNWs are greatly enhanced with a lower turn-on electric field and a much larger emitted current. It is found that the increase in field emission is primarily due to the increased field enhancement factor β and the number of possible emission sites caused by the modification by hydrogen plasma treatment.

References

1. Bonard, J. M., Salvetat, J. P., Stöckli, T., de Heer, W. A., Forró, L., & Châtelain, A. (1998). Field emission from single-wall carbon nanotube films. *Applied Physics Letters, 73*, 918.
2. Saito, Y., Tsujimoto, Y., Koshio, A., & Kokai, F. (2007). Field emission patterns from multiwall carbon nanotubes with a cone-shaped tip. *Applied Physics Letters, 90*, 213108.
3. Komoda, T., Sheng, X., & Koshida, N. (1999). Mechanism of efficient and stable surface-emitting cold cathode based on porous polycrystalline silicon films. *Journal of Vacuum Science and Technology B, 17*, 1076.
4. Spindt, C. A., Brodie, I., Humphrey, L., & Westerberg, E. R. (1976). Physical properties of thin-film field emission cathodes with molybdenum cones. *Journal of Applied Physics, 47*, 5248.
5. Yan, H. F., Xing, Y. J., Hang, Q. L., Yu, D. P., Wang, Y. P., Xu, J., et al. (2000). Growth of amorphous silicon nanowires via a solid-liquid-solid mechanism. *Chemical Physics Letters, 323*, 224.
6. Chueh, Y. L., Chou, L. J., Cheng, S. L., He, J. H., Wu, W. W., & Chen, L. J. (2005). Synthesis of taperlike Si nanowires with strong field emission. *Applied Physics Letters, 86*, 133112-1–13112-3.
7. Au, F. C. K., Wong, K. W., Tang, Y. H., Zhang, Y. F., Bello, I., & Lee, S. T. (2003). Electron field emission from silicon nanowires. *Applied Physics Letters, 75*(12), 1700–1702.
8. Wang, N., Tang, Y. H., Zhang, Y. F., Lee, C. S., & Lee, S. T. (1998). Nucleation and growth of Si nanowires from silicon oxide. *Physical Review B, 58*(24), R16024.
9. Fowler, R. H., & Nordheim, L. (1928). Electron emission in intense electric fields. *Proceedings of Royal Society Series A, 119*, 173.

Chapter 115
Enhancement of Field Emission from Silicon Nanowires Treated with Carbon Tetrafluoride Plasma

Shih-Fong Lee, Li-Ying Lee and Yung-Ping Chang

Abstract In this study, a simple method using carbon tetrafluoride (CF_4) plasma to functionalize the surface and to modify the structures of silicon nanowires (SiNWs) grown on silicon substrates is presented. A layer of nickel was evaporated onto a (100) silicon substrate to induce the growth of SiNWs at 1000 °C for 2 h. Oxygen derived from native oxide lying on the silicon substrate was incorporated into SiNWs resulting in silica nanowires. Due to its high resistivity, the emitted currents from SiNWs are much lower than those emitted from carbon nanotubes. After 4 min of CF_4 plasma treatment, a large increase (more than two orders of magnitude) in the emitted current is observed. It is found that conglomeration of SiNWs is found after CF_4 plasma treatment which increases the surface density of emission sites. Furthermore, the SiO_2 layer covering the surface of SiNWs has been removed by CF_4 plasma etching. These two factors combined to obtain the enhanced field-emission characteristics of SiNWs. However, nonvolatile fluorocarbon polymers may form on the sidewall of SiNW after prolonged CF_4 plasma treatment and thus field-emission current is lowered. These results clearly manifest the potential of using SiNWs in field emitter applications.

Keywords Silicon nanowires (SiNWs) · Field-emission · Plasma treatment

S.-F. Lee · Y.-P. Chang
Department of Electrical Engineering, Dayeh University, Changhua County 515, Taiwan, Republic of China

L.-Y. Lee (✉)
Department of Electronic Engineering, Chung Chou University of Science and Technology, Changhua County 510, Taiwan Republic of China
e-mail: ladylee@dragon.ccut.edu.tw

J. Juang et al. (eds.), *Proceedings of the 2nd International Conference on Intelligent Technologies and Engineering Systems (ICITES2013)*, Lecture Notes in Electrical Engineering 293,
DOI: 10.1007/978-3-319-04573-3_115,

115.1 Introduction

Recently, one-dimensional structures, such as nanowires, nanotubes and nanorods, have been intensively investigated due to their excellent unique optical, electronic, mechanical properties, and above all electron emission properties. Much effort has been concentrated on how to fabricate field emission flat panel display using various nanostructures and materials [1, 2]. In the past decade, the research on electron field emission has been mostly focused on the carbon-based materials. Nevertheless, silicon nanowires (SiNWs) are of particular interest to researchers because silicon has been the backbone of electronic devices and the fabrication processes and equipments can be greatly simplified in the future applications of SiNWs.

There are several methods to synthesize silicon nanowires (SiNWs), including the classic metal-catalytic vapor–liquid–solid (MC-VLS) method [1], the solid–liquid-solid (SLS) method [3], the simple thermal evaporation oxide-assisted growth (OAG) method [4], and the solution-grown method [5]. Recently, SiNWs have been grown by combining the OAG method and metal catalysts [6]. In this work, SiNWs were synthesized with Ni as catalyst on Si substrate in an Ar ambient without any additional silicon source supply. The SiNWs have high aspect ratio, adequate for electron field emission. However, because of the low conductivity of the SiNWs, the density of emitted current from SiNWs is about one to two orders of magnitude lower than that from carbon nanotubes (CNTs). Therefore, SiNWs were not considered as a promising candidate for field-emission application.

Various plasma treatments for CNTs using reactive gases (e.g. CF_4) and non-reactive, inert gases (e.g. Ar) have been proven to be an effective post-treatment technique [7]. In this paper, we demonstrate the enhanced field-emission characteristics obtained for the SiNWs after CF_4 plasma treatment. The mechanism behind this improvement is carefully examined and the reason for the degradation after prolonged plasma treatment is also discussed.

115.2 Experiment

In this work, SiNWs were synthesized on n-type Si (100) substrate through a solid–liquid-solid (SLS) phase growth mechanism without any additional silicon source supply proposed by Yan and coworkers [2]. Substrates were cleaned ultrasonically in acetone and in ethanol in turn for 10 min each, and then rinsed in deionized water. The cleaned wafer surface was then deposited with a 15 nm thick Ni film using an ultrahigh vacuum thermal evaporator at room temperature. The purpose for this Ni layer is to induce the growth of SiNWs. The thickness of evaporated Ni film was precisely controlled with a thickness monitor.

The synthesis of SiNWs was carried out in a high-temperature tube furnace. The silicon substrate coated with Ni layer was placed in a 4.0×2.5 cm^2 ceramic

holder and a 3.5 × 2.0 cm^2 Si (100) substrate was mounted on top of it. Subsequently, the ceramic holder was placed into a quartz tube furnace for the synthesis of SiNWs and the chamber was pumped down to less than 10^{-3} Torr using a mechanical pump. Argon with the flow rate 500 sccm was introduced into the tube and the temperature was gradually increased with a temperature controller until it reached the target temperature and maintained at that temperature for 10 min. The synthesis temperature and pressure were about 1000 °C and 1 atm, respectively. The growth time was 2 h. The samples were then cooled in Ar flow ambient. The etched sample was first grown for 15 min using the same conditions as for the as-grown sample. After growth phase, these samples were put into an RF plasma etcher to be treated with carbon tetrafluoride (CF_4) plasma for purification. The flow rate of CF_4 was set to 30 sccm, RF power was 10 W, and the working pressure was 8–12 mTorr, and the duration of CF_4 plasma treatment was varied from 1 to 5 min.

These specimens were investigated in a Hitachi S-3000 N field-emission scanning electron microscope (FESEM) operated at 15 kV. Energy-dispersive spectrometry (EDS) was used to identify and analyze the chemical composition of the surface. Transmission electron microscopy (TEM, JEOL-2010) was used to characterize the detailed microstructure features of SiNWs. The field-emission measurement was carried out in high vacuum to ensure accurate characterization of the current density versus applied field (*J-E*) relation. Synthesized SiNWs were pasted with silver paste onto a glass substrate coated with conducting indium tin oxide (ITO) and subsequently dried in an oven. The glass substrate together with SiNWs was mounted on a test fixture as the cathode, while an ITO glass substrate was used as the anode with an emission area of −0.007 cm^2. The spacing between the electrodes was adjusted to 50 μm. The vacuum chamber was first pumped down to 10^{-2} Torr with a mechanical pump, and then further pumped down to 10^{-6} Torr with a turbomolecular pump. A Keithley 237 was used to supply the voltage (up to 1000 V) between the electrodes and to measure the emitted current with pA sensitivity, allowing for the accurate characterization of current–voltage (*I–V*) behavior. This source-measure unit was fully automated with a computer.

115.3 Results and Discussions

Figure 115.1a shows the SEM image of as-grown, untreated SiNWs, while Fig. 115.1b–f are the SEM images of SiNWs after 1–5 min of CF_4 plasma treatment. As seen in Fig. 115.1a, the silicon substrate was uniformly covered with dense SiNWs that are slender and randomly oriented. The SiNWs have a high aspect ratio (the ratio of the length to the diameter). After plasma treatment, the top layer of SiNWs conglomerates into cluster, and SiNWs and catalyst originally underneath become exposed. The area occupied by SiNWs clusters on the substrate increases with the increasing of CF_4 plasma treatment time. Since CF_4 plasma contains a lot of highly reactive radicals, the SiNWs on the topmost layer

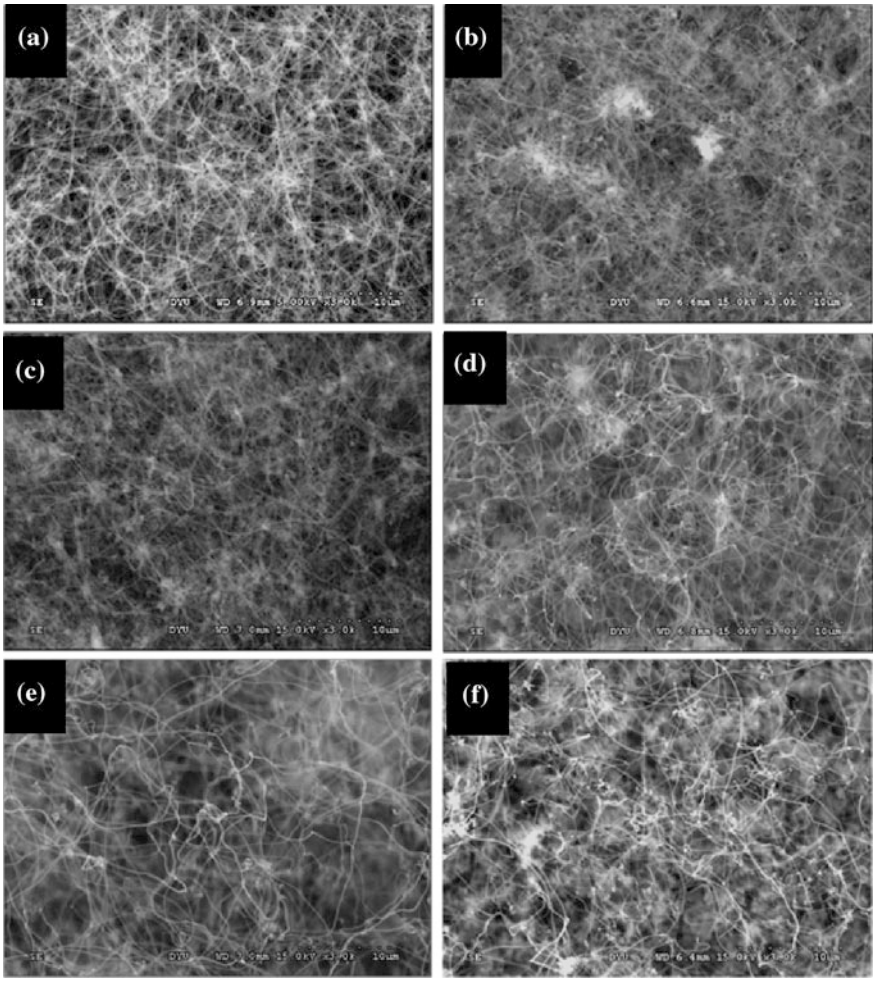

Fig. 115.1 The top-view SEM images of SiNWs: **a** as-grown, untreated SiNWs, and after: **b** 1, **c** 2, **d** 3, **e** 4, **f** 5 min of CF_4 plasma treatment. The magnification factor is 3×10^3

are likely to react with CF_4 plasma. Unsaturated dangling bonds tend to arise on the sidewall and/or at the tips of SiNWs leading to conglomeration and the formation of local cluster of SiNWs through cross-linking.

In a CF_4 plasma, extremely reactive radical species CF_3, CF_2, C, and F will be found in this plasma. Because of the small ion concentration, most of the etching will not be directly due to ions in the plasma. Rather, the constant bombardment of ions incident on the surface creates damage in the form of unsatisfied bonds that are exposed to the reactive radicals. The neutral radicals diffuse to the surface due to the concentration gradient in the plasma. On the surface they quickly react, form volatile products, and are pumped away. Figure 115.2 shows the TEM images of

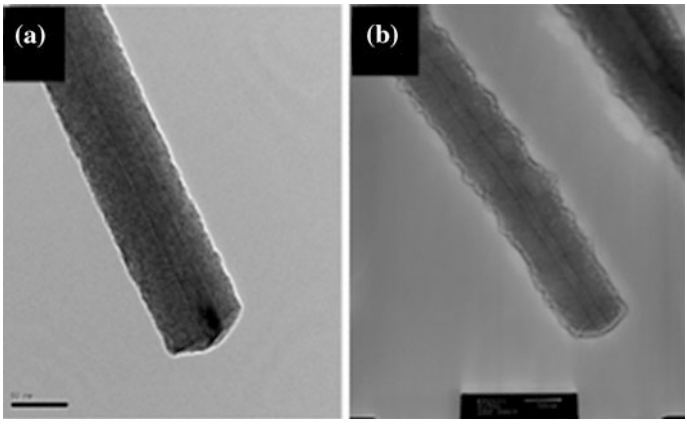

Fig. 115.2 The TEM images of SiNWs: **a** as-grown, untreated SiNWs, and **b** after 2 min of CF_4 plasma treatment

SiNWs before and after CF_4 plasma treatment. In Fig. 115.2a, the side-wall surface of as-grown, untreated SiNWs is smooth with a round tip of low curvature. After 4 min of CF_4 plasma treatment, the surface of SiNW becomes irregular and rough as seen in Fig. 115.2b. Presumably, this is due to etching by fluorine ions in the plasma. Since tips on the surface of SiNWs can induce local field enhancement, they are potential sites for emission.

Figure 115.3 shows the chemical composition of SiNWs as measured from EDS for as-grown, untreated SiNWs and for SiNWs after 1–5 min of CF_4 treatment. After CF_4 plasma treatment, carbon appears and increases with the plasma treatment time presumably due to the silicon carbide (SiC) formed during plasma treatment. It is noted that the percentage was drastically reduced after CF_4 plasma treatment. The as-grown, untreated SiNWs have a very high content of oxygen (65 % atomic) on their surfaces that is very close to that of insulating silicon dioxide (SiO_2). This indicates that SiNWs are covered with an intrinsic SiO_2 layer. Since only Ar was supplied during growth, these oxygen atoms were originated from the native oxide residing on the silicon substrate and have been proven to be beneficial to the growth of SiNWs [8]. However, electrons in SiNWs have to tunnel through the SiO_2 layer by quantum-mechanically tunneling first before they can be emitted into vacuum. Since the probability for quantum mechanically tunneling is inversely proportional to the exponential of the square of barrier width, it is a very fast decaying function with the barrier width. Hence, this additional obstacle is believed to be the limiting step in the field-emission mechanism for SiNWs and can be used to account for the relatively poor field-emission characteristics of SiNWs. The oxygen content on the surface was decreased continuously with the treatment time and the silicon content was increased continuously with the treatment time accordingly. Obviously, oxygen was removed by highly reactive fluorine related groups in the process and the underlying silicon become exposed. The nickel content also increases with the CF_4 plasma treatment time in the first 4 min of

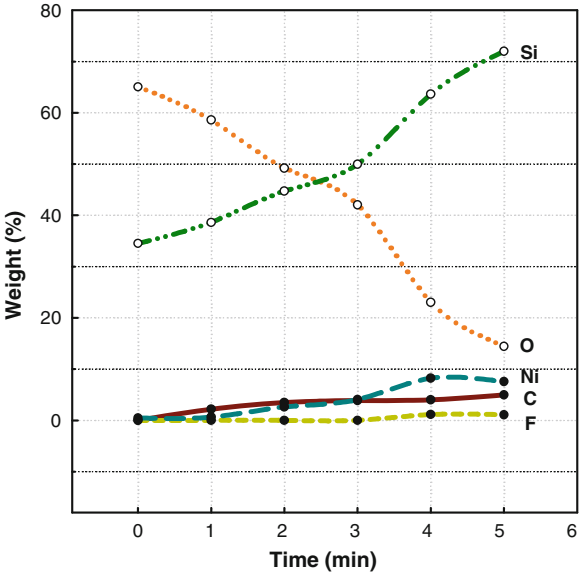

Fig. 115.3 Chemical composition of SiNWs before and after 1–5 min of CF_4 plasma treatment

treatment and decreases slightly afterwards. It seems that the nickel originally enclosed by silicate become exposed in the first 4 min and was removed by the plasma etching since then. Note that fluorine composition is detected after 4 min of CF_4 plasma treatment which is not observed in the first 3 min of treatment. It is an indication that fluorine atoms are chemisorbed to the silicon atoms on the surface and nonvolatile fluorocarbon polymers such as polytetrafluoroethylene $(CF_2)_n$ are formed on the sidewall of SiNW. This process has been reported previously for CF_4 plasma etching [9–11] and is known as polymerization. These fluorocarbon polymers have excellent dielectric properties and are likely to lower the emission current of the SiNWs.

Figure 115.4 shows the current density versus applied field (*J-E*) characteristics for SiNWs before and after plasma treatment. The emitted current density for the as-grown, untreated SiNWs was 0.086 mA/cm^2. On the other hand, the emitted current densities at the maximum applied field were 0.936, 1.06, 7.68, 10.6, and 5.72 mA/cm^2 for SiNWs after 1, 2, 3, 4, and 5 min of CF_4 plasma treatment, respectively. At the maximum applied field, an increase of more than two orders of magnitude in the emitted current is achieved for the SiNWs after 4 min of CF_4 plasma treatment. In the first 3 min of plasma treatment, the main function of plasma treatment is the etching of SiO_x covering SiNWs and the SiNWs begin to conglomerate into cluster thereby increasing the surface density of SiNWs. As the plasma treatment proceeds, the surface of SiNWs become rough and uneven rendering lots of potential emission sites. All these effects are beneficial to the electron emission from SiNWs and the emitted current arrives at its maximum value at around 4 min of CF_4 plasma treatment. However, the fluorocarbon polymers formed after 4 min of CF_4 plasma treatment are electrically insulating in

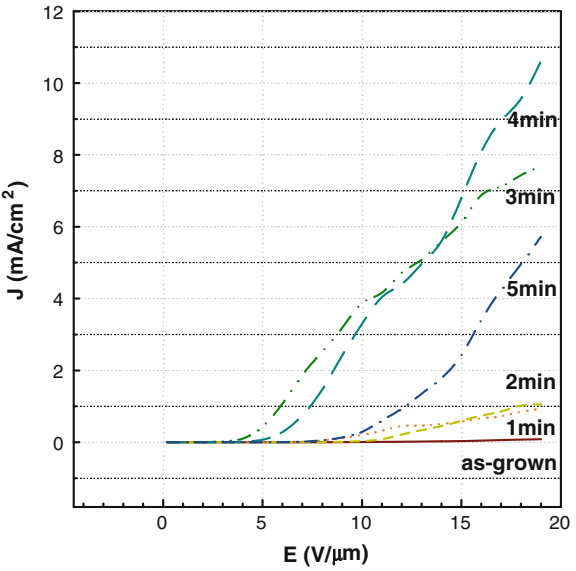

Fig. 115.4 The emitted current density versus applied field (*J-E*) curves for SiNWs before and after CF_4 plasma treatment

nature. Therefore, electrons inside the SiNWs have to tunnel through the fluorocarbon polymer before they can be emitted into vacuum. Thus, the emitted current from SiNWs begins to drop thereafter.

115.4 Conclusions

In this study, it is demonstrated that the field-emission characteristics of SiNWs can be greatly enhanced by CF_4 plasma post-treatment. Several effects of CF_4 plasma treatment can be achieved as follows: First, through plasma treatment, the SiO_2 layer covering the surface of SiNWs can be removed. The removal of insulating SiO_2 makes the electrons inside SiNWs easier to emit. Second, surface morphology of SiNWs can be modified by plasma treatment. The surface densities of SiNWs and potential sites are increased. The change in the field-emission characteristics of SiNWs after plasma treatment can be readily observed. However, prolonged CF_4 plasma treatment results in the formation of nonvolatile insulating fluorocarbon polymers and the emitted current from SiNWs begins to descend.

After CF_4 plasma treatment, the field-emission characteristics of SiNWs are greatly enhanced with a lower turn-on electric field and a much larger emitted current. Furthermore, a current density of 1 mA/cm^2 required basically for flat panel display is obtained at 7.2 V/μm for SiNWs after 4 min of CF_4 plasma treatment. This clearly demonstrates the potential of SiNW as a competitive candidate for flat-panel display application.

References

1. Wagner, R. S., & Ellis, W. C. (1964). Vapor-Liquid-Solid mechanism of single crystal growth. *Applied Physics Letters, 4*(5), 89–90.
2. Yan, H. F., Xing, Y. J., Hang, Q. L., Yu, D. P., Wang, Y. P., Xu, J., et al. (2000). Growth of amorphous silicon nanowires via a solid-liquid-solid mechanism. *Chemical Physics Letters, 323*, 224–228.
3. Pei, L. Z., Tang, Y. H., Chen, Y. W., Guo, C., Zhang, W., & Zhang, Y. (2006). Silicon nanowires grown from silicon monoxide under hydrothermal conditions. *Journal of Crystal Growth, 289*(2), 423–427.
4. Zhang, R. Q., Lifshitz, Y., & Lee, S. T. (2003). Oxide-assisted growth of semiconducting nanowires. *Advanced Materials, 15*, 635–640.
5. Holmes, J. D., Johnston, K. P., Doty, R. C., & Korgel, B. A. (2000). Control of thickness and orientation of solution-grown silicon nanowires. *Science, 287*, 1471–1473.
6. Lee, S. F., Chang, Y. P., & Lee, L. Y. (2009). Plasma treatment effects on surface morphology and field emission characteristics of carbon nanotubes. *Journal of Materials Science: Materials in Electronics, 20*, 851–857.
7. Lee, S. F., Chang, Y. P., & Lee, L. Y. (2008). The effects of annealing Ni catalyst in nitrogen-based gases on the surface morphology and field-emission properties of thermal chemical vapor deposited carbon nanotubes. *New Carbon Materials, 23*, 302–308.
8. Wang, N., Tang, Y. H., Zhang, Y. F., Lee, C. S., & Lee, S. T. (1998). Nucleation and growth of Si nanowires from silicon oxide. *Physical Review B, 58*(24), R16024–R16026.
9. Mogab, C. J., Adams, A. C., & Flamm, D. L. (1978). Plasma etching of Si and SiO_2: The effect of oxygen additions to CF_4 plasmas. *Journal of Applied Physics, 49*, 3796–3803.
10. Coburn, J. W. (1979). In Situ auger electron spectroscopy of Si and SiO_2 surfaces plasma etched in CF_4-H_2 glow discharges. *Journal of Applied Physics, 50*, 5210–5213.
11. d'Agostino, R., Cramarossa, F., Fracassi, F., Desimoni, E., Sabbatini, L., Zambonin, P. G., et al. (1986). Polymer film formation in C_2F_6-H_2 discharges. *Thin Solid Films, 143*, 163–175.

Chapter 116
A Novel Design of Low-Power Double Edge-Triggered Flip-Flop

Chien-Cheng Yu, Kuan-Ting Chen and Jhong-yu Wun

Abstract Flip-flops are known and widely used in VLSI integrated circuit (IC) design. The main advantage of using double edge-triggered flip-flop (DETFF) is that it allows one to maintain a constant throughput while operating at only half the clock frequency. As the increasing usages for flip-flops, the desire to reduce power consumption has led to increased demand for low power consumption flip-flops. This paper compares four previously published DETFFs together with our design for their power consumption. Several HSPICE simulations with different input sequences show that the proposed DETFF reduces power consumption up to 79.5 %, as compared to the existing DETFFs.

Keywords Double edge-triggered flip-flop (DETFF) · Power consumption · Power-delay product (PDP) · Single edge-triggered flip-flop (SETFF)

116.1 Introduction

Flip-flops are one of the most commonly used elements to implement sequential circuits. Among the more popular synchronous digital circuits are edge-triggered flip-flops [1, 2]. Edge-triggered flip-flop circuits may be classified into two types. The first type latches data either on the rising or the falling edge of the clock cycle is so-called single edge-triggered flip-flops (SETFFs). In typical operations, a SETFF receives data when the clock signal is either low (logic 0) or high (logic 1),

C.-C. Yu (✉) · J. Wun
Department of Electronic Engineering, Hsiuping University of Science and Technology, Taichung 41280, Taiwan, Republic of China
e-mail: ccyu@hust.edu.tw

K.-T. Chen
Department of Electrical Engineering, National Chung Hsing University, Taichung 40227, Taiwan, Republic of China

J. Juang et al. (eds.), *Proceedings of the 2nd International Conference on Intelligent Technologies and Engineering Systems (ICITES2013)*, Lecture Notes in Electrical Engineering 293,
DOI: 10.1007/978-3-319-04573-3_116,

stores the data when the clock signal transitions from low to high or vice versa and generates its output during the clock signal's high or low state. The second type of edge-triggered flip-flop operates on both the rising and falling edges of a clock signal. For a given clock signal, these so-called double edge-triggered flip-flops (DETFFs) are faster than SETFFs, and consume about the same power as the SETFFs. The main advantage of using DETFF is that it allows one to maintain a constant throughput while operating at only half the clock frequency.

There are several DETFFs have been proposed [3–15]. Some DETFFs have been presented by Unger [4]. While the flip-flops described in his paper are faster compared with some SETFFs, their complex design has made it undesirable. In [5], Afghahi et al. design is for a dynamic DETFF. The design is not for a static DETFF. The circuits require 20 transistors for a CMOS implementation which does not require an inverted clock. Lu et al. [6] presented a DETFF design which has two loops for maintaining charge levels as a static flip-flop that does not depend on the clock period. This design requires 26 transistors for a CMOS implementation. Gago et al. [7] presented a static DET master–slave flip-flop. The design duplicates a SETFF but shares the clock transistors that are common to both latches. These implementations suffer from a larger clock load at the same level of performance as a SETFF. Blair [8] provided a static DETFF design and a semi-static DETFF design. The static DETFF design is a modified version of Hossain's static design [9].

Though several contributions have been made to the art of DETFFs, a need evidently occurs for a design that still further improves the relative power consumption of DETFFs. The remainder of this paper is organized as follows: Sect. 116.2 presents a brief description of existing DETFFs. The proposed DETFF is described in Sect. 116.3. The simulation results and a comparison between the existing DETFFs and the proposed DETFF in terms of power consumption are discussed in Sect. 116.4. Section 116.5 is a conclusion and summary for the paper.

116.2 Existing Double Edge-Triggered Flip-Flops

Several DETFFs have been described by replicating the latch elements of a SETFF and multiplexing the outputs. Referring to Fig. 116.1, it illustrates the circuit structure of a typical conventional rising edge-triggered flip-flop.

Hossain et al. [9] have provided a static DETFF design which including a 16-transistor CMOS implementation of the static design, arranged in a parallel configuration shown in Fig. 116.2. The design also comprises two latches, each of which has a loop within itself for maintaining charge levels for providing static functionality. The feedback path in each loop includes an inverter and is switched by the clock. The loops are also isolated from each other.

Kuo et al. [10] have proposed two DETFFs, one is based on pass transistors (see Fig. 116.3) and the other is replace two pass transistors of Fig. 116.3 with transmission gates to prevent some spikes and save power (see Fig. 116.4). Figure 116.3

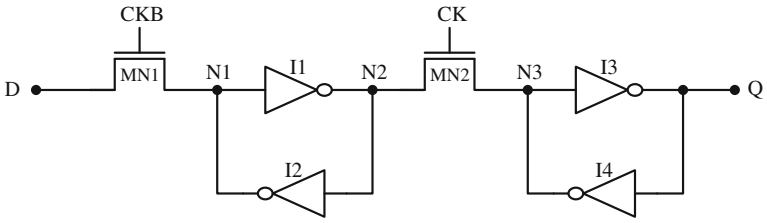

Fig. 116.1 SETFF reported in Ref. [9]

Fig. 116.2 DETFF reported in Ref. [9]

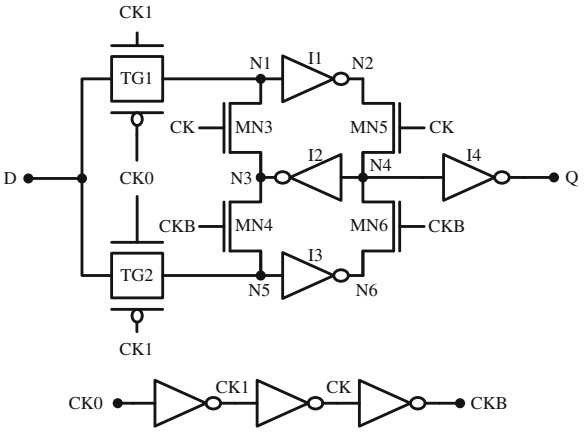

Fig. 116.3 DETFF reported in Ref. [10]

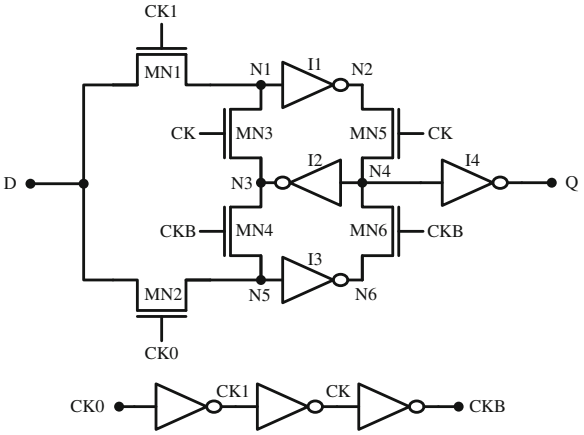

employs six switches and four inverters. The switches MN1, MN3, MN5 and the inverter I1 form the upper loop, and the switches MN2, MN4, MN6 and the inverter I3 form the lower loop. These two loops use same feedback inverter I2 and same output inverter I4. According to this circuit, one of these two loops always samples

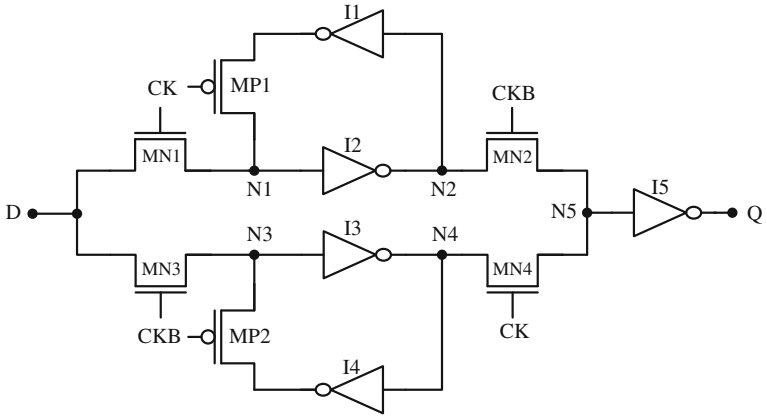

Fig. 116.4 Transmission gate version of Fig. 116.3 [10]

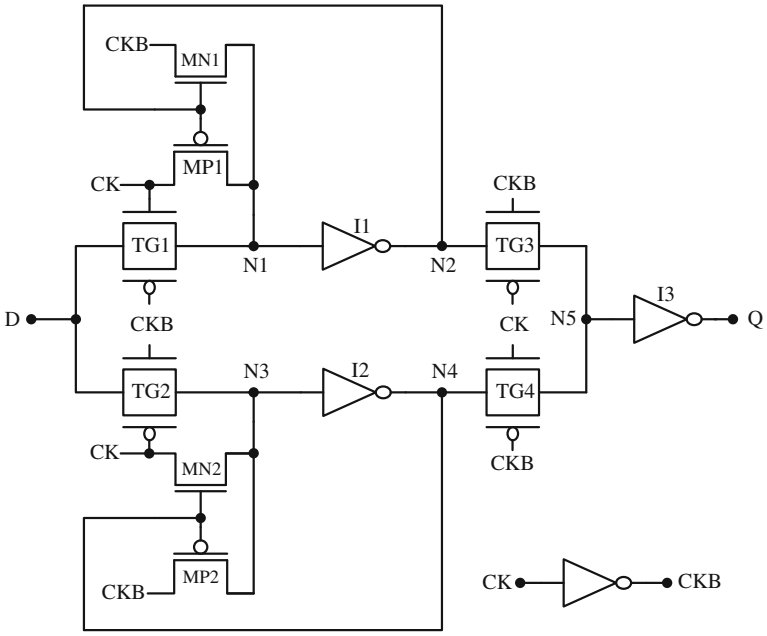

Fig. 116.5 DETFF reported in Ref. [11]

the data and the other loop always holds data. Therefore, only a single feedback loop holds data and the re-design of the DETFF can eliminate one feedback loop and decrease two transistors from the original design.

Pedram et al. [11] have proposed a modified version of Hossain's flip-flop (see Fig. 116.5). The main drawback of this circuit is the use of pass transistors instead

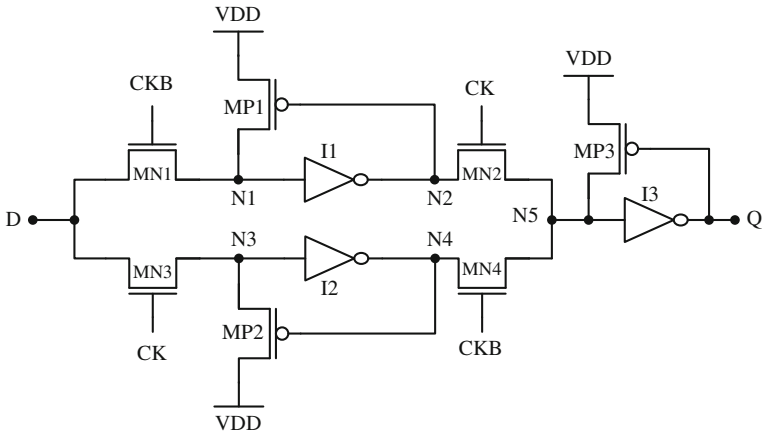

Fig. 116.6 The proposed DETFF

of transmission gates, in order to reduce the total transistor counts. This results in reducing the driving capability of the succeeding stages and causing DC power consumption in the output inverter as explained in [3, 12].

116.3 Proposed Double Edge-Triggered Flip-Flop

The proposed DETFF is illustrated in Fig. 116.6. This design can be thought of as a parallel connection of two latches, one transparent when the clock is high and the other transparent when the clock is low, with a multiplexor selecting the output of the latch that is in hold state. In the upper data path, transistor MP1 provides feedback to pull up storage node N1 substantially to VDD when the signal node N2 is low. Pull-up transistor MP1 ensures that, although a clock signal CKB applied to the gate of MN1 does not reach the voltage VDD, the storage node N1 can still reach VDD. Similarly, in the lower data path, pull-up transistor MP2 provides feedback to pull up node N3 to VDD when the signal node N4 is low. The inclusion of pull-up transistor MP2 ensures that, although the clock signal CK applied to the gate of MN3 does not reach the voltage VDD, the storage node N3 can still reach VDD. Furthermore, to ensure the output node Q can reach VDD when the signal node N5 is high, a charge recovery circuit which consisted of inverter I3 and pull-up transistor MP3 is added.

Moreover, the operation of the proposed DETFF is described as follows: When the clock signal CK is low, for the upper data path, transistors MN1 is ON and MN2 is OFF, respectively. As such, the input signal D is quickly conducted into node N2. If the input signal D is high, node N1 goes to the logic high with the help of pull-up transistor MP1. Node N1 remains high as long as input signal D is at the high level. Meanwhile, for the lower data path, the previously hold data in node N4

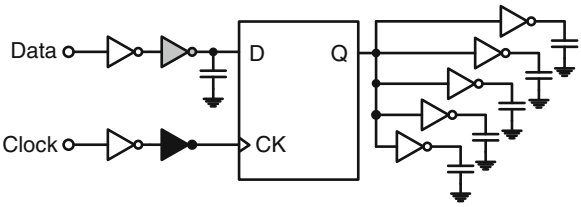

Fig. 116.7 The simulation testbench for flip-flops

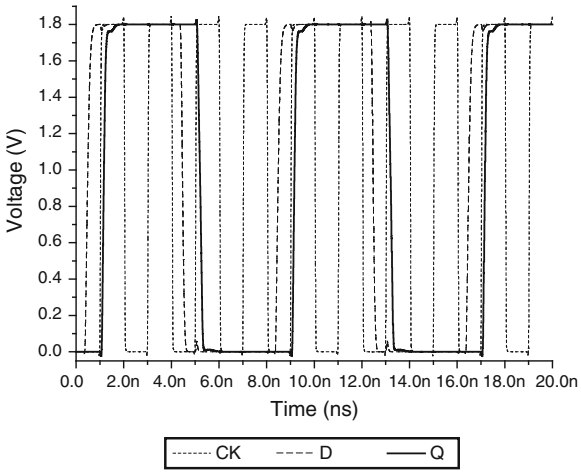

Fig. 116.8 Transient analysis waveforms of this work

is quickly pass to the output node Q with the help of transistor MN4 and inverter I3. On the contrary, when the input signal D is at the high level while the clock signal CK is high, for the lower data path, transistors MN3 is ON and MN4 is OFF, respectively. And the input signal D is then quickly conducted into the node N4 and node N3 goes to the logic high with the help of pull-up transistor MP2. Node N3 remains high as long as input signal D is at the high level. Meanwhile, for the upper data path, the previously hold data in node N2 is quickly pass to the output node Q with the help of transistor MN2 and inverter I3.

116.4 Simulations and Results

In the section, simulations are performed to examine the merit of the proposed DETFF. After a brief description of the testbench, Hspice simulations are performed to examine the performance of the proposed circuit.

Table 116.1 Power consumption of various structures at different data activities

FF	$\alpha = 0$		$\alpha = 0.5$	$\alpha = 1$
	00000000	11111111		
Fig. 116.1	13.76	11.72	42.04	69.23
Fig. 116.2	20.83	17.51	47.46	70.70
Fig. 116.3	25.15	29.81	60.68	85.94
Fig. 116.4	26.55	25.61	56.27	80.56
Fig. 116.5	62.68	28.91	69.76	93.36
this work	12.87	12.66	36.64	57.36

116.4.1 Testbench

The testbench for this paper is illustrated in Fig. 116.7 [3]. The input buffers are used to provide realistic data and clock signals. A fanout of five inverters is used as the nominal load for each DETFF. These inverters, in turn, drive a capacitive load C_L of 25 fF each, to simulate the loading from the previous logic stages, as well as the following stages. The total power consumption is composed of local data power consumption, local clock power consumption and internal power consumption.

116.4.2 Simulation Results and Discussion

In a VLSI circuit, the power saving of using DETFF is strongly dependent on data activity α [3]. This subsection presents the simulation results of the proposed DETFF with the existing DETFFs under different data activities: $\alpha = 0$, $\alpha = 0.5$ and $\alpha = 1$. In the simulations, different flip-flop structures discussed in this paper were designed using a 0.18 um CMOS technology. All simulations are carried out at nominal conditions: VDD = 1.8 V and at room temperature. The clock frequency is kept at 500 MHz. This clock frequency for DETFFs is equivalent to 1 GHz for SETFFs. All the measurements are taken over a 16-cycle data sequence of alternating 1′s and 0′s. The simulated waveform of the proposed DETFF is shown in Fig. 116.8.

Each flip-flop could have input data with different data activities, the power consumption is strongly related to the input data sequence α. Table 116.1 shows the power consumption of various structures at different data activities and indicates the following three cases:

(a) $\alpha = 0.5$, data rate is 500 Mbits/sec
Compared to SETFF, the power consumption of this work is 67.15 % less. Most significantly, compared with other DETFF circuits, the presented circuit can save power consumption in the range between 22.80 and 47.48 %.
(b) $\alpha = 0.5$, data rate is 500 Mbits/sec

For the proposed circuit, the saving power percentage is between 38.21 and 79.47 % for input data sequence 00000000, and between 27.70 and 57.53 % for input data sequence 11111111, respectively.
(c) $\alpha = 1$, data rate is 500 Mbits/sec
For the proposed circuit, the saving power percentage is between 18.87 and 38.56 % for input data sequence 10101010.

116.5 Conclusions

This paper provides a low-power DETFF circuit that offers various advantages. First, the proposed DETFF uses less transistor count than any existing DETFF circuit. Second, the present structure consumes less area compared to the existing DETFF structures. Third, compared with other existing DETFF circuits, the present circuit can save more power consumption. Fourth, the proposed DETFF circuit is well suitable for low power applications. Fifth, the present structure provides a more robust structure with respect to process variations compared to the existing structures.

Acknowledgments The authors deeply acknowledge final support in part from National Science Council, Taiwan, ROC, under contract NSC 102-2622-E-164-002-CC3.

References

1. Weste, N. H. E., & Harris, D. F. (2005). *CMOS VLSI design: A circuits and systems perspective* (3rd ed.). New York: Pearson/Addison-Wesley.
2. Yeo, K. S., Rofail, S. S., & Goh, W. L. (2002). *CMOS/BiCMOS ULSI: Low voltage, low power*. New York: Prentice Hall PTR.
3. Chung, W., Lo, T., & Sachdev, M. (2002). A comparative analysis of low-power low-voltage double-edge-triggered flip-flops. *IEEE Transactions on VLSI Systems, 10*(6), 913–918.
4. Unger, S. H. (1981) Double edge-triggered flip-flops. IEEE Transactions on Computers, *C-30*(6), 447–451.
5. Afghahi, M., & Yuan, J. (1991). Double edge-triggered d-flip-flops for high-speed CMOS circuits. *IEEE Journal of Solid-State Circuits, 26*(8), 1168–1170.
6. Lu, S. L., & Ercegovac, M. (1990). A novel CMOS implementation of double-edge-triggered flip-flops. *IEEE Journal of Solid-State Circuits, 25*, 1008–1010.
7. Gago, A., Escano, R., & Hidalgo, J. A. (1993). Reduced implementation of D-type DET flip-flops. *IEEE Journal of Solid-State Circuits, 28*, 400–442.
8. Blair, G. M. (1997). Low-power double-edge triggered flip-flop. *Electronics Letters, 33*(10), 845–847.
9. Hossain, R., Wronski, L. D., & Albicki, A. (1994). Low power design using double edge triggered flip-flops. *IEEE Transactions on VLSI Systems, 25*, 261–265.
10. Kuo, S. Y., Chiueh, T. D., & Chen, K. H. (1998). Double edge triggered flip-flop, U. S. patent, 5,751,174.

11. Pedram, M., Wu, Q., & Wu, X. (1998). A new design of double edge triggered flip-flops, in *Proceedings of Asian and South Pacific Design Automation Conference (ASP-DAC'98)* (pp. 417–421).
12. Stojanovic, V., & Oklobdzija, V. G. (1999). Comparative analysis of master-slave latches and flip-flops for high-performance and low-power systems. *IEEE Journal of Solid-State Circuits, 34*, 536–548.
13. Chandrakasan, A. P., & Brodersen, R. W. (1995). *Low power digital CMOS design*. Massachusetts: Kluwer Academic Publishers.
14. Sanchez-Sinencio, E., & Andreou, A. G. (1999). *Low-voltage/low-power integrated circuits and systems: Low-voltage mixed-signal circuits*. New York: IEEE Press.
15. Rabaey, J. M., & Pedram, M. (2000). *Low power design methodologies*. Massachusetts: Kluwer Academic Publishers.

Chapter 117
Identification of Flat Panel Glass-Handling Mechanism

Tung-Sheng Zhan, Chih-Cheng Kao and Whei-Min Lin

Abstract The dynamic equations of a flat panel glass-handling robot driven by a permanent magnet synchronous motor (PMSM) are derived by use of Hamilton's principle for the rigid and flexible models. In this paper, we adopt a new modified particle swarm optimization (MPSO) to identify all the parameters of the robot and PMSM simultaneously. This new algorithm is added with a "distance" term in the traditional PSO's fitness function to avoid converging to a local optimum. It is found that the MPSO method can obtain optimal high-quality solutions with high calculation efficiency. In this study, the convergence characteristics of the real-coded genetic algorithm (RGA), PSO and MPSO are compared to demonstrate that the MPSO is superior to the others on identification of the dynamic flexible model.

Keywords LCD glass-handling robot · Modified particle swarm optimization (MPSO) · Permanent magnet synchronous motor (PMSM) · Real-coded genetic algorithm (RGA) · System identification

117.1 Introduction

The flat panel displayers, such as liquid crystal display (LCD) and plasma display panel (PDP), have the merits of small volume, light weight and low power consumption. In order to meet consumers' requirements many LCD manufacturers have made the larger size and thinner film mother glass. The LCD glass-handling

T.-S. Zhan · C.-C. Kao (✉)
Department of Electrical Engineering, Kao-Yuan University,
Kaohsiung 82151, Taiwan, Republic of China
e-mail: t20005@cc.kyu.edu.tw

W.-M. Lin
Department of Electrical Engineering, National Sun Yat-Sen University,
Kaohsiung 804, Taiwan, Republic of China

J. Juang et al. (eds.), *Proceedings of the 2nd International Conference on Intelligent Technologies and Engineering Systems (ICITES2013)*, Lecture Notes in Electrical Engineering 293,
DOI: 10.1007/978-3-319-04573-3_117,

robot is the most fundamental device in transporting the mother glasses among equipment. Therefore, the structure of an LCD glass-handling robot hand should be designed with both high specific payload and stiffness to reduce the unavoidable static deflection of the arm inherently.

In the previous researches [1], not only the dynamic modeling of an LCD glass-handling robot driven by a PMSM was not derived, but also the reports of system identification were not found. In this paper, the rigid and flexible formulations by using Hamilton's principle for the robot system have been expressed by only one and four independent variables, respectively. Furthermore, the dynamic model with four independent variables is reduced to that with only one independent variable under the main assumption that the timing belts are rigid.

This study successfully demonstrates that the dynamic formulation can give a wonderful interpretation of the LCD glass-handling robot in comparison with the experimental results. The angular displacements of the robot arm are measured by a machine vision system of a digital CCD camera while the translational positions of the robot end are obtained by a motion control card. Furthermore, a new identified method using the MPSO is proposed, and it is confirmed that the method can perfectly search the parameters of the LCD glass-handling robot through the comparisons between numerical simulations and experimental results. Moreover, according to these comparisons of identified results and their errors of angular displacements between the rigid and flexible models, it is found that the flexible model presents the better matching with the experimental results.

117.2 Dynamic Equations of the System

In Fig. 117.1, the system [2] consists of one PMSM, two timing belts, three arms and four gears. Here, the machine model of the PMSM is derived in the q-axis as follows:

$$v_q = R_s i_q + \frac{d}{dt}\lambda_q + \omega_s \lambda_d \tag{117.1}$$

where the subscript q represents the parameters in the q-axis, v_q is the stator voltage, R_s is the stator resistance, i_q is the stator current, $\lambda_q = L_q i_q$ is the stator flux linkage, L_q is the inductance, and $\omega_s = p\omega_r$ is the inverter frequency, p is the number of pole pairs, and ω_r is the rotor angular speed.

The dynamic formulations [2] can be expressed by one and four independent variables corresponding to the system is modeled as the rigid and flexible models, respectively. The dynamic model with four independent variables can be reduced to that with only one independent variable under the assumptions that the timing belts, motor shafts, gears and arms are all rigid. For the rigid model, the dynamic equation for the LCD glass-handling robot driven by a PMSM was derived as follows:

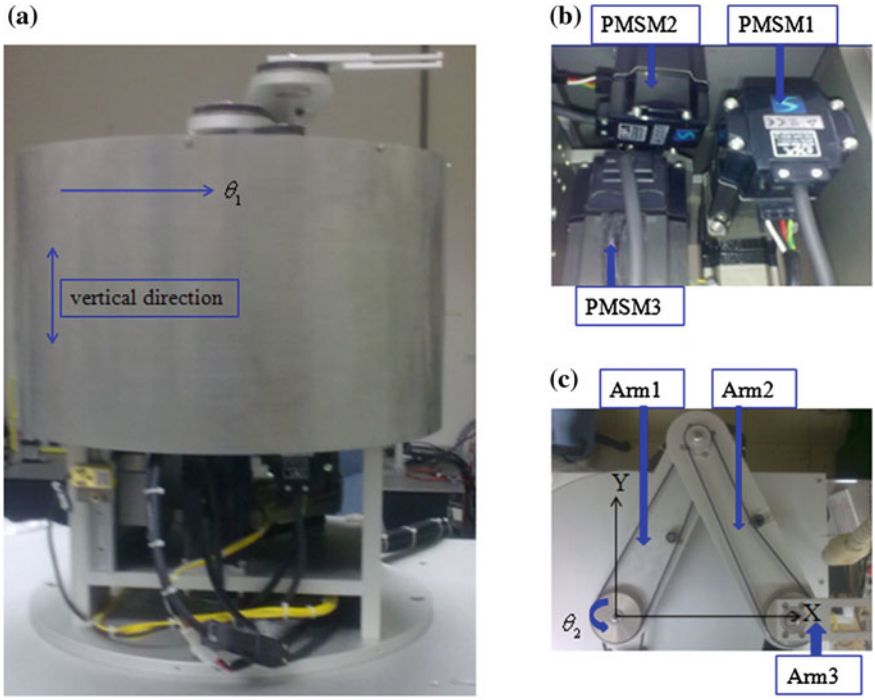

Fig. 117.1 The 3-DOF LCD Glass-handling Robot. **a** Side View, **b** Three PMSM Sets, **c** Top View of Three Arms

$$[J_0 - J_1\cos(n\phi_1) + J_m]\ddot{\phi}_1 + B_m\dot{\phi}_1 + \mu\sin(n\phi_1)\dot{\phi}_1^2 = K_t i_q, \tag{117.2}$$

where the variable ϕ_1 is the angular displacement of Arm 1, and has the properties $\dot{\phi}_1 = \omega_r$; J_0 and J_1 are the moments of inertia of the robots, J_m is the moment of inertia of the rotor, B_m is the damping coefficient of the rotor, μ is the nonlinear damping coefficient, K_t is the motor torque constant and

$$\begin{aligned} J_0 =& I_1 + (n-1)^2 I_2 + (1-2n)^2 I_3 + (n-1)^2 I_4 + 4I_5 + (1-2n)^2 I_6 \\ &+ m_2\left[l_1^2 + (n-1)^2 b^2\right] + m_3\left[l_1^2 + (n-1)^2 l_2^2\right] + m_4 l_1^2 + m_5 l_1^2 \\ &+ m_6\left[l_1^2 + (n-1)^2 l_2^2\right], \\ J_1 =& 2(n-1)[m_2 b + (m_3 + m_6) l_2] l_1, \\ \mu =& n(n-1)[m_2 b + (m_3 + m_6) l_2] l_1. \end{aligned} \tag{117.3}$$

For the flexible model, the four dynamic equations [2] for the LCD glass-handling robot driven by a PMSM were derived as follows:

$$\begin{aligned}
&\{I_1+I_2+I_3+I_4+I_5+I_6+m_2b^2+(m_2+m_3+m_4+m_5+m_6)l_1^2+(m_3+m_6)l_2^2+J_m\\
&+2[m_2b+(m_3+m_6)l_2]l_1\cos\phi_2\}\ddot{\phi}_1\\
&+\{I_2+I_3+I_4+I_6+m_2b^2+(m_3+m_6)l_2^2+[m_2b+(m_3+m_6)l_2]l_1\cos\phi_2\}\ddot{\phi}_2\\
&+I_5\ddot{\phi}_3+(I_3+I_6)\ddot{\phi}_4\\
&+c_1r_1\dot{\phi}_1-\{[m_2b+(m_3+m_6)l_2]l_1\sin\phi_2\}\dot{\phi}_2\left(2\dot{\phi}_1+\dot{\phi}_2\right)+2k_1r_1(r_1\phi_1-r_2\phi_2)=K_ti_q-\tau_{f1},
\end{aligned}\tag{117.4}$$

$$\begin{aligned}
&\left[I_2+I_3+I_4+I_6+m_2b^2+(m_3+m_6)l_2^2+[m_2b+(m_3+m_6)l_2]l_1\cos\phi_2\right]\ddot{\phi}_1\\
&+\left[I_2+I_3+I_4+I_6+m_2b^2+(m_3+m_6)l_2^2\right]\ddot{\phi}_2+(I_3+I_6)\ddot{\phi}_4\\
&+\{[m_2b+(m_3+m_6)l_2]l_1\sin\phi_2\}\dot{\phi}_1^2+2k_1r_2(r_2\phi_2-r_1\phi_1)=-\tau_{f2},
\end{aligned}\tag{117.5}$$

$$I_5\left(\ddot{\phi}_1+\ddot{\phi}_3\right)+2k_2r_2(r_3\phi_3-r_4\phi_4)=-\tau_{f3},\tag{117.6}$$

$$(I_3+I_6)\left(\ddot{\phi}_1+\ddot{\phi}_2+\ddot{\phi}_4\right)+2k_2r_3(r_4\phi_4-r_3\phi_3)=-\tau_{f4},\tag{117.7}$$

where the torques due to damping effect are $\tau_{f_1}=c_1\left(r_1\dot{\phi}_1-r_2\dot{\phi}_2\right)$, $\tau_{f_2}=c_1\left(r_2\dot{\phi}_2-r_1\dot{\phi}_1\right)$, $\tau_{f_3}=c_2\left(r_3\dot{\phi}_3-r_4\dot{\phi}_4\right)$, $\tau_{f_4}=c_2\left(r_4\dot{\phi}_4-r_3\dot{\phi}_3\right)$, c_1 and c_2 are the damping coefficients of timing belts 1 and 2, respectively. The other notations could be seen in nomenclature of Ref. [2].

117.3 Optimal Algorithm

The theoretical origin of Particle Swam Optimization is the predation of flying state of birds in the space is named Particle. Each moving Particle in the space has the adaptive value corresponded to each individual own target function. The PSO has been found to be robust in solving continuous nonlinear optimization problems and can generate high-quality solutions within a shorter calculation time with more stable convergence characteristic than other stochastic methods. The main difference of the proposed modified particle swarm optimization (MPSO) from the PSO is to consider the distance in its fitness function to avoid converging to a local optimum [3]. Figure 117.2 shows the flow chart of the proposed MPSO algorithm.

117.4 Case Study and Discussions

The configured experimental setup of the LCD glass-handling robot driven by a PMSM is shown in Fig. 117.3. The waveform of the applied voltages is generated by NI LABVIEW, which is employed to communicate between the digital and

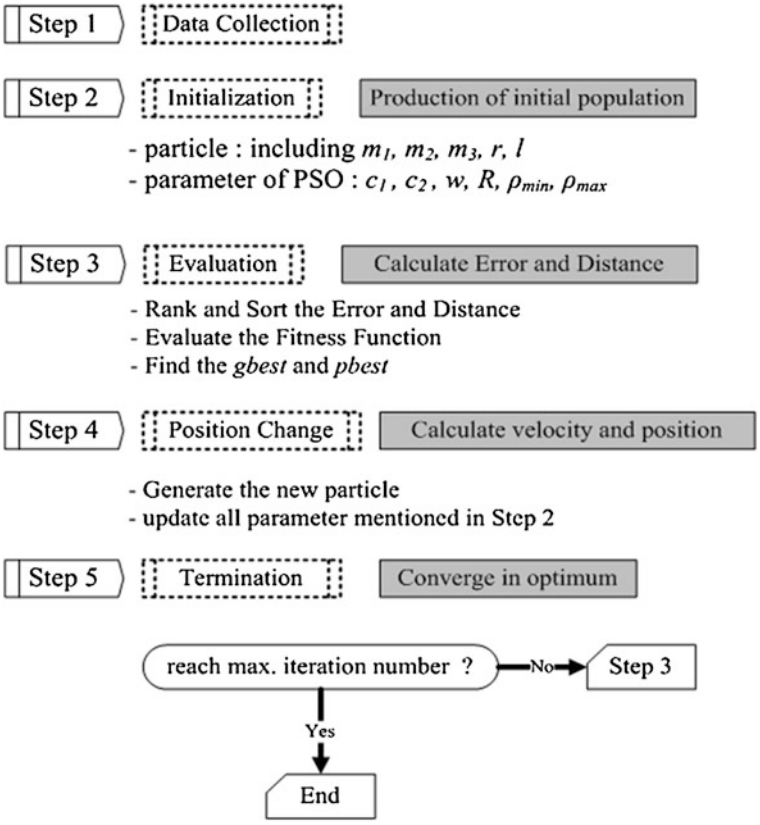

Fig. 117.2 Flow chart of MPSO

analog signals during experimental process. The DA/AD converter (PCI-6052E) with a resolution of 12 bits is used to transform the waveform to the PMSM (MTTSUBISHI HC KFS43 series MR-J2S-40A1, 400 W), which has the specifications as follows: rated output 400 (W), rated torque 1.3 (Nm), rated rotation speed 3000 (rpm) and rated current 2.3 (A). The servo power supplier is implemented by MITSUBISHI MR-J2S-40A1. The image acquisition card is implemented by PCI 1405 and the digital CCD camera is implemented by the SONY SSC-DC393 series. The specifications are shown as follows: imaging device 1/3 type interline transfer, picture elements 752 (horizontal) $\times$ 582 (vertical), Lent mount CS-mount. In order to measure the angular displacements of the rotor, the interface device is implemented by a motion control card NI PCI-7344, which can measure angles with the sampling time $\Delta t = 0.01$ s.

In this paper, the machine vision system of a digital CCD camera is employed to measure the displacements of point m_3 of Arm 3 in the X_1 direction. The sampling time is $\Delta t = 0.25$ s and the time interval is from 0 to 10 s. The machine vision system used in this paper takes a circular red-color pattern pasted upon point m_3 of

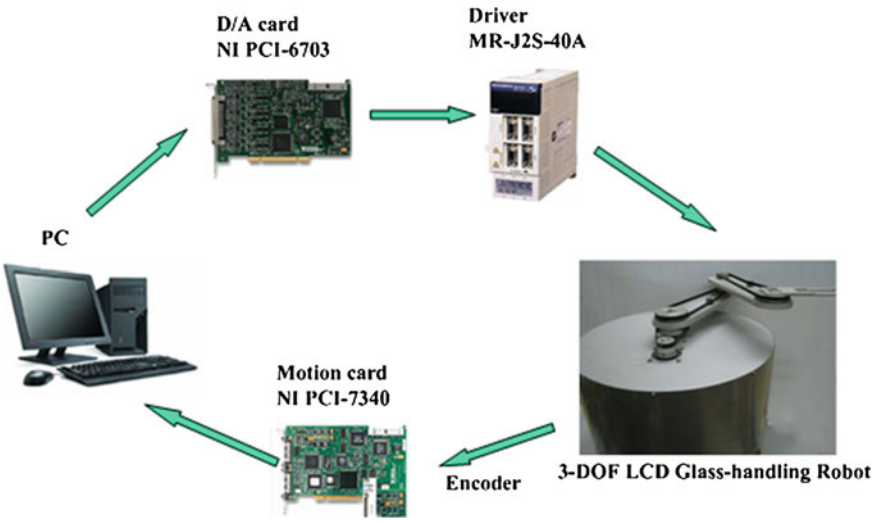

Fig. 117.3 Experimental setup

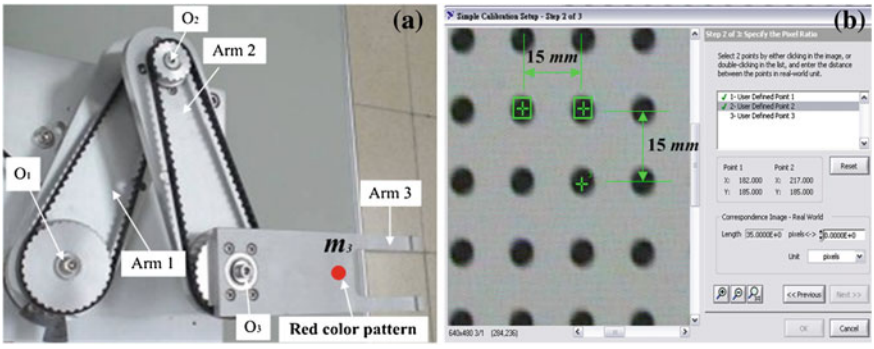

Fig. 117.4 The vision system of flat panel mechanism. **a** The control image frame, **b** The standard calibration grid

Arm 3, and is shown in Fig. 117.4a. Before using the machine vision system, it is very important to have a calibration between one pixel and a real-word unit such as millimeter (mm). Therefore, a standard calibration grid is shown in Fig. 117.4b.

The real distance in the standard calibration grid from one block point center to another one is measured as 15 mm in both the X_1- and Y_1-directions. The calibration result is that one pixel is 0.2 mm in the real world. According to this transformation, the color pattern image coordinate can be transformed into the real-world unit in system identifications. Finally, the color pattern matching algorithm is implemented by using LabVIEW associated with the image acquisition card PCI 1405.

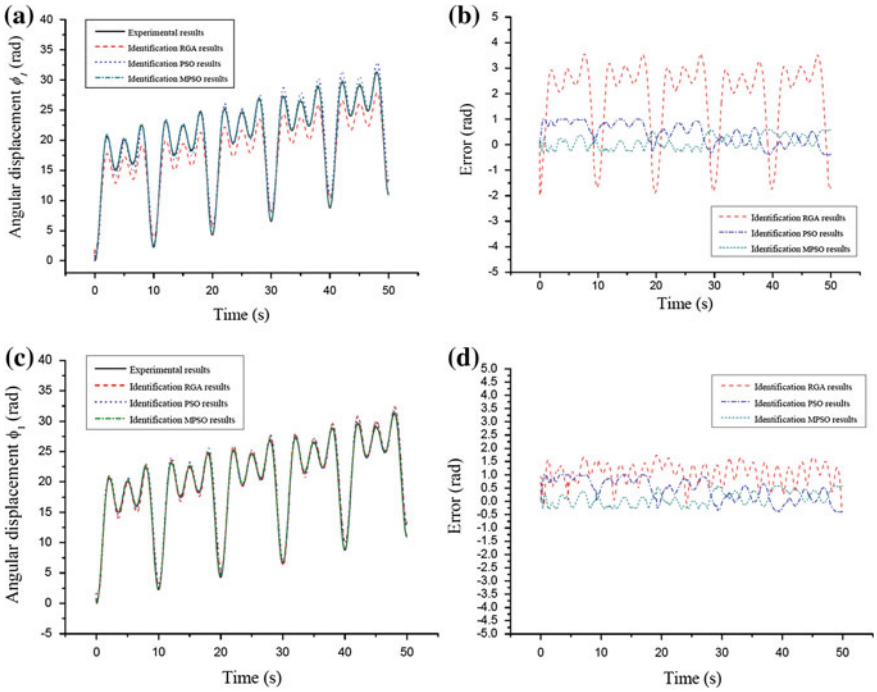

Fig. 117.5 Comparisons between the experimental and identified simulations subject input voltages for the rigid and flexible mode. **a** Angular displacements (*rigid mode*). **b** Angular errors with respect to the experimental results (*rigid mode*). **c** Angular displacements (*flexible mode*). **d** Angular errors with respect to the experimental results (*flexible mode*)

The comparisons between the experimental and identified angular displacements of the robot arm subject to input voltages [2] are shown in Fig. 117.5a–d for the rigid and flexible models. The results clearly show that the PSO and MPSO methods present the better matching than the RGA with the experimental results and converge to one optimum value. It can be found that the identified angular displacements are almost the same as the experimental results with the least angular error for both of rigid and flexible model.

From the comparisons between the experimental results and identified simulations of angular displacements of the robot driven by the PMSM subject to input voltages, and the X_1-directional positions at point m_3 of Arm 3, it is found that the errors of angular displacements of Arm 1 and the translational displacements of Arm 3 are the least for the MPSO method.

References

1. Shin, Y. J., Park, K. T., Ha, J. H., & Shim, S. K. (2008). Performance test of large telescopic ROZBOT for LCD glass handling, in *The IEEE International Conference on Industrial Informatics, Daejeon, Korea*, (pp. 436–441).
2. Fung, R. F., Kung, Y. S., & Wu, G. C. (2010). Dynamic analysis and system identification of an LCD glass-handling robot driven by a PMSM. *Applied Mathematical Modeling, 34*(5), 1360–1381.
3. Lin, W. M., Cheng, F. S., & Tsay, M. T. (2001). Nonconvex economic dispatch by integrated artificial intelligence. *IEEE Transactions on Power Systems, 16*(2), 307–311.

Chapter 118
Single-Port SRAM Cell with Reduced Voltage Supply in Writing Operation

Ming-Chuen Shiau, Chien-Cheng Yu and Kuan-Ting Chen

Abstract As is known in the art, it is relatively difficult to write a logic '1' to the 5-T (five-transistor) static random access memory (SRAM) cell if the SRAM cell currently stores a logic '0'. In this paper, we proposed a 5-T SRAM cell and a cell voltage control circuit coupled to provide power to the SRAM cell. The cell voltage control circuit supplies the SRAM cell with the HV_{DD} supply voltage if the SRAM cell is during a read mode. If the SRAM cell is being written or during a standby mode, the cell voltage control circuit supplies the SRAM cell with the LV_{DD} supply voltage that is less than the HV_{DD} supply voltage. Several HSPICE simulations show that the proposed SRAM cell provides an improvement in SRAM cell topology by providing an efficient solution to the write '1' issue.

Keywords Single-port · SRAM cell · Reduced voltage supply · Writing operation

118.1 Introduction

Digital devices are constantly becoming more pervasive in numerous applications, such as personal computers, consumer electronic devices, and the like. Consequently, the use of digital memories also constantly increases. In a microcomputer, a random access memory (RAM) is used for storing information that is often

M.-C. Shiau
Department of Electrical Engineering, Hsiuping University of Science and Technology, Taichung 41280, Taiwan, Republic of China

C.-C. Yu (✉)
Department of Electronic Engineering, Hsiuping University of Science and Technology, Taichung 41280, Taiwan, Republic of China
e-mail: ccyu@hust.edu.tw

K.-T. Chen
Department of Electrical Engineering, National Chung Hsing University, Taichung 40227, Taiwan, Republic of China

J. Juang et al. (eds.), *Proceedings of the 2nd International Conference on Intelligent Technologies and Engineering Systems (ICITES2013)*, Lecture Notes in Electrical Engineering 293,
DOI: 10.1007/978-3-319-04573-3_118,

altered, if required, while a read-only memory (ROM) is used for storing data which is not changed. [1, 2]. As a result, it is imperative to improve reliability of digital memories so that devices using such memories are likewise reliable. A static-random-access-memory (SRAM) is usually implemented as an array of memory cells organized in rows and columns. Each SRAM cell stores one bit of data and is implemented as a pair of inverters having their inputs and outputs cross-coupled at differential storage nodes. The SRAM cell is stable at one of two possible logic levels.

Many applications for embedded SRAMs require the ability to access the memory array while the integrated circuit is operating in a low power mode [3–9]. The reliability of an SRAM cell depends on many factors. One key factor is the voltage level applied to such a cell. As is known in the art, it is relatively difficult to write a logic '1' to the 5-T SRAM cell if the SRAM cell currently stores a logic '0' [3].

Though several contributions have been made to the art of 5-T SRAM cell, a need evidently occurs for a design that still further improves the problem of writing '1' to the 5-T SRAM cell. The remainder of this paper is organized as follows. Section II presents a brief description of existing SRAM cells. The proposed 5-T SRAM cell is described in Section III. The simulation results and a comparison between the existing SRAM cells and the proposed SRAM cell are discussed in Section IV. Last section is a conclusion and summary for the paper.

118.2 Conventional SRAM Cell

Figure 118.1 illustrates a conventional 6-T (six-transistor) CMOS SRAM cell which includes PMOS pull-up transistors MP1 and MP2, NMOS pull-down transistors MN1 and MN2, and NMOS access transistors MA1 and MA2. The access transistor MA1 is connected between the bit line BL and the node A to provide data access thereto, and the transistor MA2 is connected between the complementary bit line BLB and the node B to similarly provide data access.

In general, SRAM cell is accessed through both of access transistors during read and write operations. Accessing SRAM cell in this manner results in a relatively stable SRAM cell during both read and write operations. The gates of the data access transistors MA1 and MA2 are connected to respective word lines WL; ancillary circuitry including differential-input sense amplifiers are not shown in Fig. 118.1. The access transistors MA1 and MA2 are gated into conduction by an appropriate voltage applied to the respective word lines while a binary '1' is impressed on node A via the bit line BL and a binary '0' is impressed on the complementary bit line BLB. The transistor MN2 conducts to pull the node B toward ground while the node A goes high. The opposite state can be achieved by reversing the signals applied to the bit lines BL and BLB. However, a relatively large layout area is required for the six transistors of SRAM cell. It would therefore be desirable to have an SRAM cell that requires fewer than six transistors, but has the same stability as a 6-T SRAM cell.

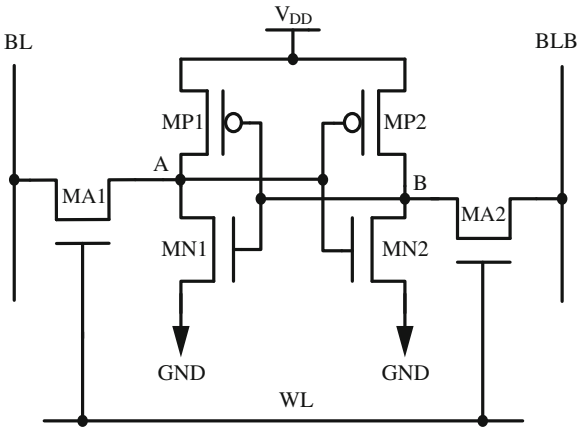

Fig. 118.1 Circuit diagram of conventional 6-T SRAM cell

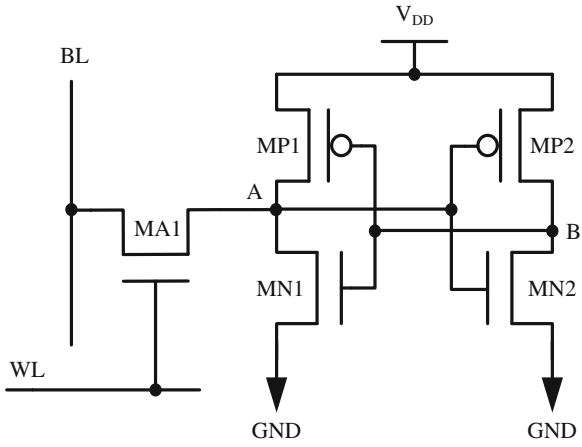

Fig. 118.2 Circuit diagram of conventional 5-T SRAM cell

As shown in Fig. 118.2, the access transistor MA2 and the bit line BLB in Fig. 118.1 have been eliminated to provide a 5-T configuration. To write a logical '1' to SRAM cell, the V_{DD} supply voltage is applied to both bit line BL and word line WL. Under these conditions, NMOS access transistor MA1 is turned on, and a voltage equal to V_{DD}-Vth is applied to node A, where Vth is the threshold voltage of access transistor MA1. To write a logical '0' to SRAM cell, the V_{DD} supply voltage is applied to word line WL, and the V_{SS} supply voltage is applied to bit line BL. Under these conditions, NMOS access transistor MA1 is turned on, and a voltage equal to the V_{SS} supply voltage is applied to node A.

To read SRAM cell, the V_{DD} supply voltage is applied to word line WL, and a read voltage is applied to bit line BL. This read voltage must not be so high as to write a logical 1 to SRAM cell during the read operation. Similarly, this read voltage must not be so low as to write a logical '0' to SRAM cell.

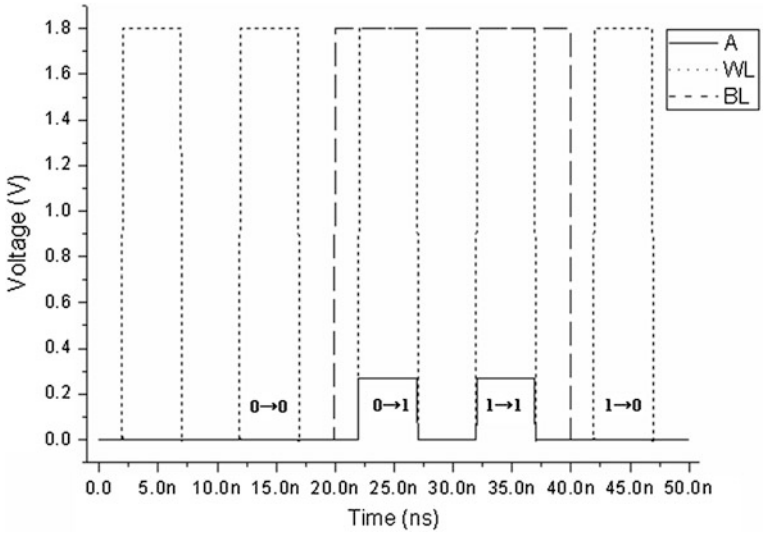

Fig. 118.3 Transient analysis waveforms of writing a data value to the conventional 5-T SRAM cell

Unlike the 6-T cell of Fig. 118.1, the 5-T cell of Fig. 118.2 does not possess symmetry as between writing a binary '1' and a binary '0' to the cell. When effecting a '0' write, the access transistor MA1 is biased into its highly conductive linear mode so that the conductive access transistor MA1 can sink any current that flows through the transistor MP1 and thereby drive the voltage at the node A below the switching threshold of the inverter formed by MP2 and MN2 thus causing the latch to set in the '0' state. Conversely, when writing a '1' to the memory cell, the access transistor MA1 is operating in its highly resistive saturation mode and so the voltage divider formed by the transistor MA1 (in its saturation mode) and the transistor MN1 (in its linear mode) has difficulties driving the voltage at node A high enough to exceed the switching threshold of the inverter formed by transistors MP2 and MN2 to cause the latch to set to the desired '1' state. The simulated waveform of writing a binary '1' and a binary '0' to the 5-T cell is shown in Fig. 118.3.

Various techniques have been developed to address this write '1' problem in 5-T SRAM cells; each technique also generates specific drawbacks when addressing the write '1' problem. However, each of these techniques requires either a more complicated device design, or more complicated operational and clocking schemes, or a combination of each of these solutions. Accordingly, the present technique provides an SRAM system that includes a 5-T SRAM cell and a cell voltage control circuit coupled to provide power to the SRAM cell.

118.3 Proposed SRAM Cell

As shown in Fig. 118.4, the proposed SRAM cell includes a 5-T cell and a voltage control circuit coupled to provide power to the SRAM cell. The 5-T SRAM cell includes an access transistor MA1 and a pair of cross-coupled inverters. The pair of cross-coupled inverters are formed by a pair of pull-up transistors (MP1, MP2) and a pair of pull-down transistors (MN1, MN2) that are stronger than the access transistor.

The cell voltage control circuit, as shown in Fig. 118.5, facilitates such a write operation by supplying the SRAM cell with a LV_{DD} supply voltage (1.0 V) that is less than the HV_{DD} supply voltage (1.8 V) during a write operation. The lower cell voltage weakens the pull-down transistors in the SRAM cell, thereby enabling a logic '1' to be easily written to the SRAM cell. When the SRAM cell is during a read mode, the cell voltage control circuit supplies the SRAM cell with the HV_{DD} supply voltage. When the SRAM cell is during a standby mode, to reduce the power consumption of the SRAM cell, the cell voltage control circuit supplies the SRAM cell with the LV_{DD} supply voltage, thereby resulting in a stable SRAM cell.

As described in more detail below, SRAM cell can be written to store a logic '1' or a logic '0'. As defined herein, SRAM cell stores a logic '1' when node A is held at the HV_{DD} supply voltage, and node B is held at the V_{SS} supply voltage (0 V).

118.3.1 Standby Mode

The standby mode exists when SRAM cell isn't subject to a read condition or a write condition. In the standby mode, word line WL is held at a logic '0'. As a result, access transistor MA1 is turned off, thereby isolating the SRAM cell from bit line BL. Meanwhile, cell voltage control circuit maintains the SRAM cell at the LV_{DD} supply voltage. As a result, cross-coupled inverter pair is powered by the LV_{DD} supply voltage.

118.3.2 Read Mode

In the read mode, data values are read from memory cell. The read mode is described below in connection with the reading of SRAM cell. In the read mode, cell voltage control circuit applies the HV_{DD} supply voltage to the SRAM cell. As a result, SRAM cell maintain its last written data value in a stable manner. Bit line BL is pre-charged to the HV_{DD} supply voltage. To read SRAM cell, the HV_{DD} supply voltage is applied to word line WL, thereby turning on access transistor MA1.

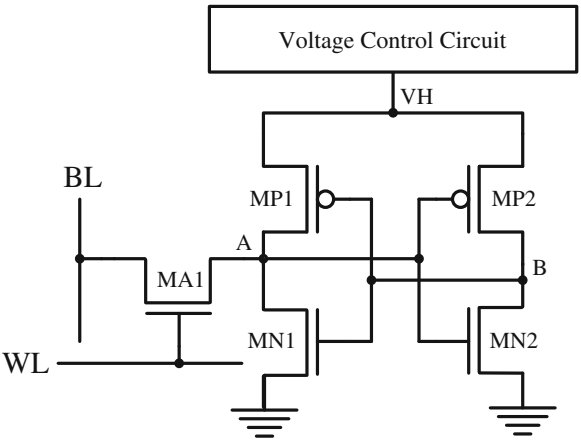

Fig. 118.4 Circuit diagram of the proposed 5-T SRAM cell

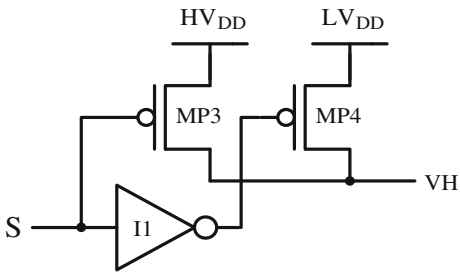

Fig. 118.5 Voltage Control Circuit coupled to the proposed 5-T SRAM cell

If SRAM cell store a logic '1' (i.e., node A is pulled up to the HV_{DD} supply voltage through pull-up transistor MP1), then the voltage on bit line BL remains at the HV_{DD} supply voltage. Conversely, if SRAM cell stores a logic '0' (i.e., node A is pulled down to the V_{SS} supply voltage through pull-down transistor MN1), then the voltage on bit line BL is pulled down to a voltage less than the HV_{DD} supply voltage. A sense amplifier circuit (not shown) coupled to bit line BL senses the voltage on bit line BL to determine the state of the data value stored in SRAM cell.

118.3.3 Write Mode

The write mode is described in connection with a write operation to SRAM cell. In general, a data value is written to SRAM cell by applying the HV_{DD} supply voltage to word line WL, thereby turning on access transistor MA1. A voltage representative of the logic value to be written to SRAM cell is applied to bit line BL. For example, to write a logic '1' to SRAM cell, the HV_{DD} supply voltage is applied to bit line BL. Similarly, to write a logic '0' to SRAM cell, the V_{SS} supply voltage is applied to bit line BL.

It is difficult to write a logic '1' to SRAM cell if SRAM cell currently stores a logic '0'. When SRAM cell stores a logic '0', NMOS pull-down transistor MN1 is turned on, thereby pulling down node A to the V_{SS} supply voltage. While attempting to write a logic '1' to SRAM cell, NMOS pull-down transistor MN1 (which pulls down on node A) contends with access transistor MA1 (which pulls up on node A). However, pull-down transistor MN1 is designed to be stronger than access transistor MA1. In order to write a logic '1' to SRAM cell, pull-down transistor MN1 is therefore made weaker by lowering the voltage on the SRAM cell to a voltage LV_{DD}, which is lower than the HV_{DD} supply voltage.

The lower LV_{DD} voltage on node V_M weakens pull-down transistor MN1 as follows. When SRAM cell stores a logic '0', PMOS pull-up transistor MP2 is turned on, thereby coupling node B to the lower voltage LV_{DD}. Because node B is coupled to the gate of NMOS pull-down transistor MN1, the lower LV_{DD} voltage on node B results in the weakening of NMOS pull-down transistor MN1.

The LV_{DD} voltage is selected to make NMOS pull-down transistor MN1 weaker than access transistor MA1. When pull-down transistor MN1 is sufficiently weakened, node A is pulled up (through access transistor MA1) to a voltage greater than the trigger point of inverter (MP2, MN2). That is, the voltage on node A is allowed to become high enough to flip the state of SRAM cell. After the logic '1' has been written to SRAM cell, cell voltage control circuit raises the voltage on the SRAM cell to the HV_{DD} supply voltage.

It is relatively easy to write a logic '0' to SRAM cell. To write a logic '0' to SRAM cell, word line WL is held at a logic '1' voltage (HV_{DD}), thereby turning on access transistor MA1. Bit line BL is held at a logic '0' voltage, and cell voltage control circuit holds the SRAM cell at a voltage of either HV_{DD} or LV_{DD}. Under these conditions, node A is pulled down to the V_{SS} supply voltage through access transistor MA1, thereby turning on PMOS pull-up transistor MP2. As a result, node B is pulled up to the voltage HV_{DD} or LV_{DD}, thereby turning on NMOS pull-down transistor MN1. In this manner, a logic '0' is stored in SRAM cell.

118.4 Simulations and Results

To evaluate performance, different SRAM cell structures discussed in this paper were designed using a 0.18 um CMOS technology. All simulations are carried out at nominal conditions: $HV_{DD} = 1.8$ V, $LV_{DD} = 1.0$ V and at room temperature. The simulated waveform of writing a data value to the proposed 5-T SRAM cell is shown in Fig. 118.6. It is evident that the proposed SRAM cell provides an efficient solution to the write '1' issue, that is, the proposed 5-T SRAM cell enabling a logic '1' to be easily written to the SRAM cell, as compared to conventional SRAM cells.

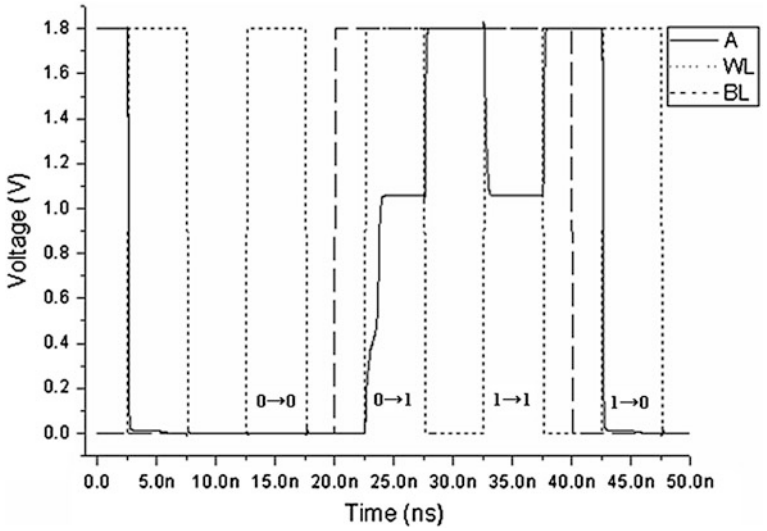

Fig. 118.6 Transient analysis waveforms of writing a data value to the proposed 5-T SRAM cell

118.5 Conclusions

In this paper, we proposed a 5-T SRAM cell and a cell voltage control circuit coupled to provide power to the SRAM cell. The cell voltage control circuit supplies the SRAM cell with the HV_{DD} supply voltage if the SRAM cell is during a read mode. If the SRAM cell is being written or during a standby mode, the cell voltage control circuit supplies the SRAM cell with the LV_{DD} supply voltage that is less than the HV_{DD} supply voltage. Several HSPICE simulations show that the proposed SRAM cell provides an improvement in SRAM cell topology by providing an efficient solution to the write '1' issue.

Acknowledgments The authors deeply acknowledge final support in part from National Science Council, Taiwan, ROC, under contract NSC 102-2622-E-164-002-CC3.

References

1. Itoh, K. (1998). Reviews and prospects of low-power memory circuits. In A. Chandrakasan & R. Brodersen (Eds.), *Low Power CMOS Design* (pp. 313–317). New York: IEEE Press.
2. Taur, Y., & Ning, T. (2002). *Fundamental of modern VLSI devices*. New York: Cambridge University Press.
3. Tran, H. (1996). Demonstration of 5T SRAM and 6T Dual-Port RAM Cell Arrays, in *1996 Symposium on VLSI Circuits Digest of Technical Papers* (pp. 68–69). IEEE Press.
4. Yamaoka, M., Maeda, N., Shinozaki, Y., Shimazaki, Y., Nii, K., Shimada, S., Yanagisawa, K., & Kawahara, T. (2005). Low-power embedded SRAM modules with expanded margins for writing, in *IEEE ISSCC Digest Technical Papers* (pp. 480–481). IEEE Press.

5. Mai, K. W., Mori, T., Amrutur, B. S., Ho, R., Wilburn, B., Horowitz, M. A., et al. (1998). Low-power SRAM design using half-swing pulse-mode techniques. *IEEE Journal of Solid-State Circuits, 33*, 1659–1671.
6. Ohbayashi, S., Yabuuchi, M., Nii, K., Tsukamoto, Y., Imaoka, S., Oda, Y., et al. (2007). A 65-nm SoC embedded 6T-SRAM designed for manufacturability with read and write operation stabilizing circuits. *IEEE Journal of Solid-State Circuits, 42*(4), 820–829.
7. Seevinck, E., List, F. J., & Lohstroh, J. (1987). Static-noise margin analysis of MOS SRAM cells. *IEEE Journal of Solid-State Circuits, 22*(5), 748–754.
8. Ichikawa, T., & Sasaki, M. (1996). A new analytical model of SRAM cell stability in low-voltage operation. *IEEE Transactions on Electron Devices, 43*(1), 54–61.
9. Hobson, R. F. (2007). A new single-ended SRAM cell with write-assist. *IEEE Transactions on VLSI Systems, 15*(2), 173–181.

Chapter 119
Development of an Low Cost Platform for IC Printed Mark Defects Inspection

Hung-Shiang Chuang

Abstract The objective of this research is to develop an low cost automated visual inspection system for IC printed defect marks which consists of two parts: hardware setup and software program based on machine vision technique. The characteristics of the experimental setup is that it is simple and effective to achieve the purpose of defect detection. The core software module is divided into two main parts, namely, image pre-processing and defect detection. The normalized correlation scheme designed to detect the IC printed marks is proposed. Experimental results show that the normalized correlation scheme could help us to decide whether the printed marks are non-defective within a very short period of time.

Keywords Visual inspection system · Normalized correlation scheme · IC printed marks

119.1 Introduction

Integrated Circuits (IC) compressing a large electronic circuit into a very small space are the fundamentals of computer and electronic industry. Due to the rapid growth of IC industry, machine vision based technology has been applied for the automatic defection inspection, e.g., defects inspections of PCB [1], IC printed mark [2], and the defects at BGA solder joints by X-ray imaging [3]. The research [4] presented a new technique can analyze and identify the defects of BGA from X-ray image such as short circuit, small ball and big ball. An automated inspection system can help in reducing the inspection time and increasing the production rate.

H.-S. Chuang (✉)
Department of Electrical Engineering, Kao Yuan University, Lujhu, Kaohsiung 82151, Taiwan, Republic of China
e-mail: t30005@cc.kyu.edu.tw

J. Juang et al. (eds.), *Proceedings of the 2nd International Conference on Intelligent Technologies and Engineering Systems (ICITES2013)*, Lecture Notes in Electrical Engineering 293,
DOI: 10.1007/978-3-319-04573-3_119,

Template matching is regarded as a key procedure in defect detection and it can be thought as a process to find out the discrepancies between a template product which confirms to the design data and the current testing product. The discrepancy provides a cue from which an inspection decision can be made. From this point of view, defect inspection is a pattern matching process and the pattern matching problem can be formulated as follows: Given a source image I and a template image T of size M-by-N, the pattern matching problem is to find the best match of template T and the source image I with minimum distortion or maximum correlation.

The most popular similarity measures for automatic defect detection [5] are the sum of absolute differences (SAD), the sum of squared differences (SSD), and the normalized cross correlation (NCC). However, the normalized cross correlation is the simplest but effective method as a similarity measure, which is invariant to linear brightness and contrast variations, so the NCC measure has been widely used in object recognition and industrial inspection [6]. This paper constructs a simple and efficient image matching system based on normalized cross-correlation, which can efficiently handle image with rotation and translation.

The remainder of the paper is organized as follows. Section 119.2 describes the experimental setup. Section 119.3 introduces the matching algorithm based on the normalized cross-correlation and presents in detail the calculation of similarity measures between two interest points. Section 119.4 presents some experimental results on real images and Sect. 119.5 concludes the paper.

119.2 Experimental Setup

The ICs could be shipped by tray/tube/tape. The packed PLCC or SOP (small outline package) components are usually placed in tubes. There were one inlet tube and two outlet tubes in the developed experimental setup, as shown in Fig. 119.1 where the components were illustrated in Table 119.1. One outlet tube is for non-defective components, and the other outlet tube is for defective components.

During the transfer, the movable stopper mechanism actuated by a pneumatic slide cylinder could permit only one piece of IC chip to freely slide by gravity along the track at a time, as shown in Fig. 119.2. During the inspection process, a IC chip feeder is capable of moving individual parts by gravity from a feed (inlet) tube. Once beneath the CCD device, a frame grabber is triggered to acquire frames from CCD camera. These frames are then interfaced to a PC, which processes corresponding images and determines whether markings on IC chips is qualified.

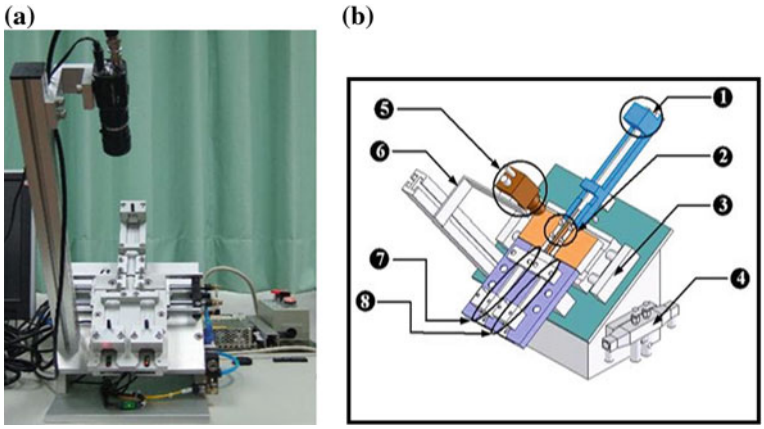

Fig. 119.1 Experimental setup. **a**. Photo. b. Setup layout

Table 119.1 List of major components in the experimental setup

No.	Compents
1	Inlet area
2	Inspection area
3	Slide cylinder
4	5/3 solenoid valves
5	CCD + Lens
6	L-shaped frame
7	Non-defective area
8	Defective area

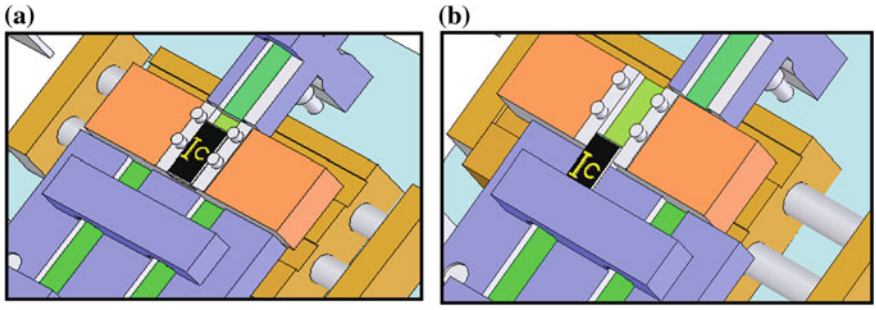

Fig. 119.2 Operation process for the movable stopper actuated by the pneumatic slide cylinder. **a**.Stopper initially stops at the middle position as ICs slide down from the inlet area. **b**.Movable stopper moves to the *left*/*right* limit switch position as ICs pass through the inspection area

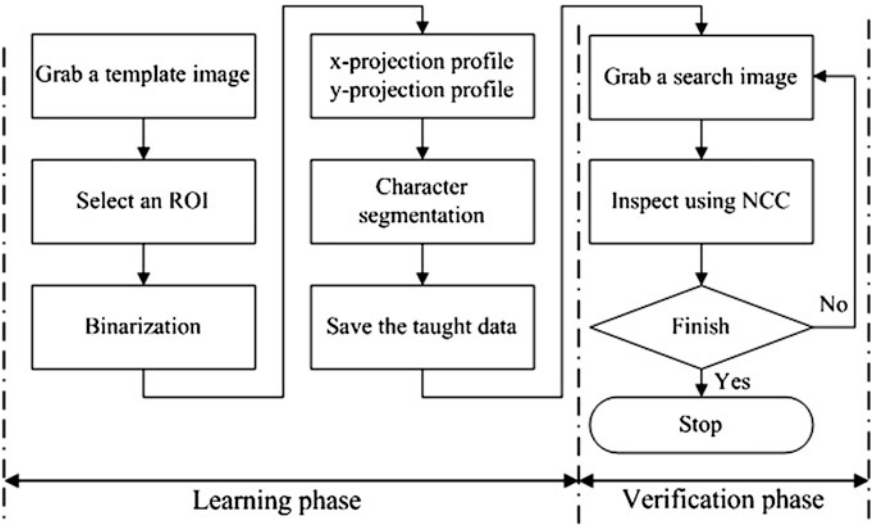

Fig. 119.3 Inspection procedure

119.3 Automatic Optical Inspection

The inspection procedure (Fig. 119.3) comprises two phase: the learning phase and the verification phase. The former includes image acquisition, ROI choice, binarization, projection profiles, and character segregation. The latter mainly determined whether the printed marks on the ICs were defective or non-defective by using the normalized cross-correction (NCC) algorithm.

119.3.1 Learning Phase

Every verification or recognition system needs first to be trained in order to get some information to perform the verification or recognition. Thus, we have developed an interface where we select a reference image that includes the graphical characters to verify. With the help of this interface, we can select and mark all the characters that should be later verified on the production line.

(a) ROI (Region of Interest)
The concept of an ROI is commonly used in many application areas. For IC marking inspection, one usually identifies the area of interest and then calculates some features in the area for character recognition for time-saving. The output of this ROI is the position and gray level of each character. Once these positions have been stored, it is would be easier to find the characters in the image on a different samples during the verification stage in the production line.

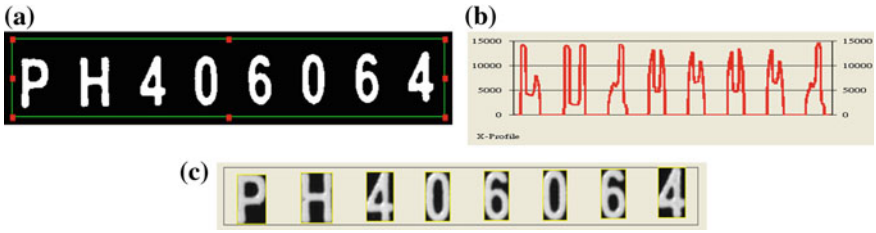

Fig. 119.4 Segmentation using x-profile information. **a**. ROI. **b**. X-projection profile. **c**. Character segmentation

(b) Character Segmentation
Character segmentation is an operation that seeks to decompose an image of a sequence of characters into subimages of individual symbols and it is to enclose each character by a single rectangle or bounding box. Based on the nature of the IC printed marks, the bounding boxes can be identified by using x-projection and y-projection profiles which are realized by summing the gray levels in the ROI with respect to their x/y coordinates respectively.

Figure 119.4a shows the binarized image with an ROI and Fig. 119.4b shows the x-projection profile. The bounding rectangles of segmentation are shown in Fig. 119.4c.

119.3.2 Verification Phase Using Normalized Cross-Correlation Scheme

Normalized cross-correlation (NCC) is a mathematical computation that fulfills an essential role in image processing. For example, it has been used extensively in machine vision for industrial inspection including defect detection in complicated images.

Usually two frames, a target frame and a template frame, are converted to binary images. A normalized cross correlation process is executed. The correlation coefficient shows how much the target frame match the template frame. A perfect fit gives a coefficient of 1.0. Thus the higher the correlation coefficient is, the better they match.

In the correlation-based defect detection applications, the normalized cross correlation used for finding matches of a template image M and a target image I of the same size $m \times n$ is defined as.

$$r = \frac{N\sum IM - \sum I \sum M}{\sqrt{[N\sum I^2 - (\sum I)^2][N\sum M^2 - (\sum M)^2]}} \tag{119.1}$$

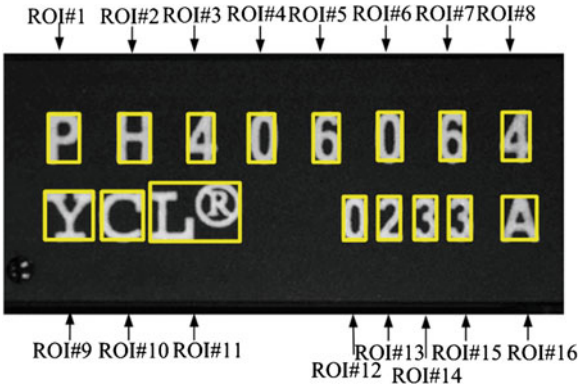

Fig. 119.5 ROI definition for segmented characters

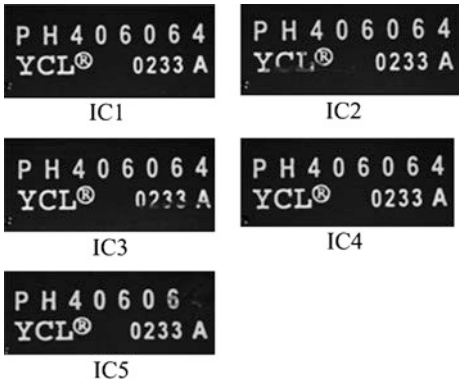

Fig. 119.6 Images of IC1–IC5

$$\text{where } \sum I = \sum_{i=0}^{m}\sum_{j=0}^{n} I(i+u,j+v),\ \sum M = \sum_{i=0}^{m}\sum_{j=0}^{n} M(i,j),$$

$$\sum IM = \sum_{i=0}^{m}\sum_{j=0}^{n} I(i+u,j+v)M(i,j),\ \sum I^2 = \sum_{i=0}^{m}\sum_{j=0}^{n} I^2(i+u,j+v),$$

$$\text{and } \sum M^2 = \sum_{i=0}^{m}\sum_{j=0}^{n} M(i,j).$$

119.4 Experimental Results

The developed algorithm was implemented on SOP ICs in tube. The light source was indoor fluorescent lamps. The camera used in this paper is a Watec 902B 768 × 494-pixel camera with a 30 Hz frame rate.

In on-line tests, recognition speed of inspection system, defined as time between moment at which the target IC drops from the inlet tube and moment at which an inspection result was obtained and target IC drops into the outlet tube,

Table 119.2 Inspection results for IC2–IC4

ROI	#1	#2	#3	#4	#5	#6	#7	#8	#9	#10	#11	#12	#13	#14	#15	#16
IC2	0.982	0.942	0.984	0.956	0.954	0.975	0.968	0.949	0.855	0.**165**	**0.550**	0.927	0.978	0.978	0.956	0.893
IC3	0.987	0.945	0.942	**0.788**	0.912	0.961	**0.799**	**0.441**	0.973	0.976	0.955	0.938	0.908	0.961	0.950	0.923
IC4	0.997	0.983	0.995	0.948	0.998	0.983	0.988	0.996	0.988	0.993	0.982	0.977	0.978	0.973	0.974	0.988
IC5	0.978	0.984	0.957	0.981	0.957	0.979	0.975	0.985	0.945	0.956	0.900	**0.626**	**0.283**	**0.663**	**0.721**	0.859

was determined to be 14.3 s for 10 target ICs (each IC marking comprised 16 segmented characters, as shown in Fig. 119.5).

Moreover, the printed mark ICs in this research are shown in Fig. 119.6 where IC1 is the template IC and IC2–IC5 are the test (target) ICs. Table 119.2 displays the result of the inspection and the values in bold type denote the NCC measure for defective printed marks.

119.5 Conclusions

Accurate, reliable inspection is critical to industrial production. In this paper, we developed an low cost platform for IC printed mark defects inspection. Based on normalized cross-correlation, the proposed system is successfully developed and tested to conduct IC marking inspection (Table 119.2).

Acknowledgments The authors would like to thank B.Z. Liao and C.Y. Chen for their help on experiments.

References

1. Jiang, B. C., Wang, Y. M., & Wang, C. C. (2001). Bootstrap sampling techniques applied to the PCB golden fingers defects classification study. *International Journal of Production Research, 39*(10), 2215–2230.
2. Chang, M. C., & Fuh, C. S. (2001). Fast Search Algorithms for industrial Inspection. *International Journal Pattern Recognition and Artificial Intelligence, 15*(4), 675–690.
3. Sumimoto, T., Maruyama, T., Azuma, Y., Goto, S., Mondou, M., Furukawa, N., & Okada, S. (2003). Development of image analysis for detection of defects of bga by using X-ray images. In: *Instrumentation and Measurement Technology Conference 2003*, Vail, CO, USA, 20–23 May 2003, (pp. 1131–1136).
4. Sa-nguannam, A., Srinonchat, J. (2008). Analysis ball grid array defects by using new image technique. ICSP 2008. In: *Proceedings*, Beijing, China, 26–29 Oct. 2008, (pp. 785–788).
5. Asha, V. (2012). Similarity measures for automatic defect detection on patterned textures. *International Journal of Image Processing and Vision Sciences*, *1*, 18–24.
6. Wei, S. D., & Lai, S. H. (2008). Fast template matching based on normalized cross correlation with adaptive multilevel winner update. *IEEE Transactions on Image Processing, 17*(11), 2227–2235.

Chapter 120
Performance of an In-Vacuum Undulator-2 m Mechanical System in Taiwan Photon Source

Jui-Che Huang, Cheng-Hsing Chang, Jun-Tern Chen, Cheng-Hsiang Chang, Ching-Shiang Hwang, Tsutomu Kohda and Yamato Katsumura

Abstract An advanced undulator technology is critical for highly brilliant synchrotron radiation in a third-generation light source. Tight mechanical specifications are required to obtain a satisfactory magnetic performance and photon energy spectrum. In general, the mechanical deformation and backlash must both be controlled within 10 μm under magnetic force 3600 kgf. This paper describes a mechanical gap-driven system and the deformation of its mechanical frame. The deformation of a magnet support beam can be calculated from the variation of the magnetic field.

Keywords In-vacuum undulator · Gap-driven system · Magnetic force

120.1 Introduction

An undulator is a key device to produce highly brilliant and nano-focusing of hard X-rays (photon energy > 5 keV) in an electron accelerator storage ring. When the electron beam passes through an undulator, wave packets of the synchrotron radiation (SR) are observed. If the interference effect of the wave packets occurs in the entire length of the undulator, the source size is expected to be small and great brilliance can be realized. The quality of a light source is of particular interest in

J.-C. Huang (✉) · C.-H. Chang · J.-T. Chen · C.-H. Chang · C.-S. Hwang
Magnet Group, National Synchrotron Radiation Research Center, 101 Hsin-Ann Rd, Hsinchu, Taiwan
e-mail: huang.juiche@nsrrc.org.tw

T. Kohda
NEOMAX Engineering Co., Ltd, Osaka, Japan

Y. Katsumura
Sumitomo Heavy Industries Finetech Ltd, Okayama, Japan

J. Juang et al. (eds.), *Proceedings of the 2nd International Conference on Intelligent Technologies and Engineering Systems (ICITES2013)*, Lecture Notes in Electrical Engineering 293,
DOI: 10.1007/978-3-319-04573-3_120,

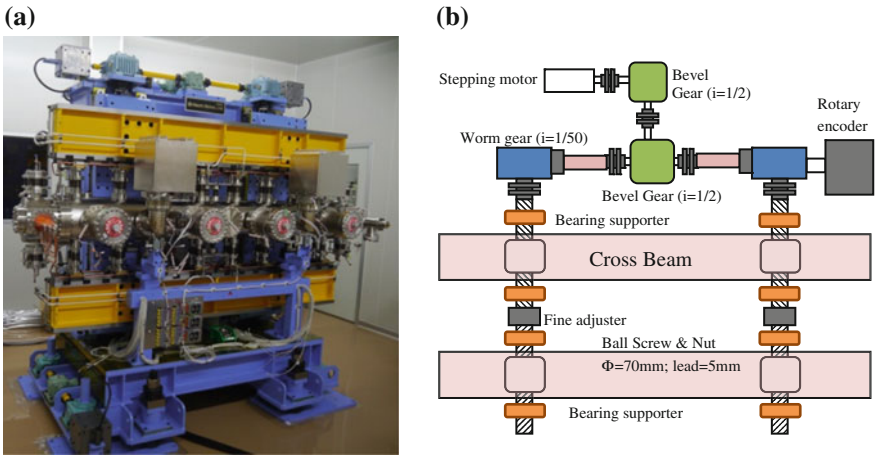

Fig. 120.1 **a** NSRRC in-vacuum undulator. **b** Sketch of the drive system of the undulator

experiments involving an image and a microscope, for which the photon beam must be focused to a small spot of great brightness. In the project phase-I of Taiwan Photon Source (TPS), the plan is to install seven in-vacuum undulators [1]. The gap of the undulator is a main parameter for the strength of the magnetic field and the photon energy of the brilliance can be tuned by control of undualtor gap.

The mechanical system of the TPS undulator (Fig. 120.1a) is designed and constructed by Sumitomo FTEC. A sketch of the mechanical system appears in Fig. 120.1b. A stepping motor controls the undulator gap; a ball screw and nut has great accuracy and no backlash. Two custom-made, highly precise, worm reducers have a small backlash and a self-lock function to ensure that the gap does not alter even at a sudden power outage. A two-piece ball screw connected with a fine adjuster is designed to have the gap change symmetrically from the electron beam center. The length of the ball screw is designed to have an optimized minimum loading; each ball screw is fixed with two bearing supports to provide great rigidity in the axis direction to achieve an accurate control of the gap.

120.1.1 Requirements of Construction of an In-Vacuum Undulator

The TPS in-vacuum undulator-2 m has a magnet of length 2214 mm; the magnetic force in the varied undulator gap was calculated with RADIA [2]. At the minimum gap 3.5 mm, the magnetic attractive force between the upper and lower magnet array attains 3600 kgf. The accuracy requirement of the undulator gap position is within 10 μm. The variation of the undulator gap ranges from 3.5 mm to 50 mm;

Table 120.1 Design parameters of ball screw and stepping motor

	Design value	Design Formula
Ball screw lead (Bsl)	5 mm	From specification
Ball screw rev. speed (Bsrs)	3 rpm	Gap changing speed/(2 × Bsl)
Motor step angle (θs)	0.36°	From specification.
Motor revolution speed (Mrs)	900 rpm	Bsrs × total reduction ratio
Motor operation pulse	10 kHz	Mrs/60 × 360/θs × 1000
Transmission reduction ratio	200	

the minimum rate of gap change must be 30 mm/min to satisfy the requirements of the experimental end station. The stepping motor of the gap-driven system must hence operate at 10 kHz pulse and provide a sufficient torque.

120.1.2 Torque in a Gap-Driven System

An important factor of a driven system is to calculate the load torque, moment of inertia and speed that are converted at the motor output shaft. The load torque and accelerator torque of the NSRRC in-vacuum undulator were carefully evaluated. The design parameters of the stepping motor and ball screw are listed in Table 120.1.

Load Torques of a Driven System. To calculate the load torques, the friction torques must be considered while the gap varies at the maximum load; these friction torques are calculated and presented in Table 120.2.

The load torque can be calculated from the friction torques with the transmission reduction ratio and transmission efficiency. In the current case, the transmission reduction ratio is 200 and the transmission efficiency is 0.45. As a result, the load torque of the undulator driven system is 20.9 kgf cm.

Accelerator Torques of a Driven System. When the driven system begins to move, the accelerator torques are calculated from the moment of inertia or GD_2. GD_2 is generally used in an industrial application with gravitational systems of units; the moment of inertia is a quarter of GD_2.

From Fig. 120.2, the GD_2 to the motor shaft in the undulator gap-driven system is listed in Table 120.3.

The moment of inertia can be calculated from Permissible $GD_2/4$; the total moment of inertia from a driven system is 9.9 kgf cm^2 and the choice of stepping motor (SANYO DENKI, 103H89583-5741) has moment of inertia 25 kgf cm^2. The entire gap-driven system has total moment of inertia 34.9 kgf cm^2. The accelerator torque is calculated with Eq. (120.1):

$$\text{Accelerator torque} = I \times \theta\text{s} \times Ac/g \tag{120.1}$$

in which I denotes total moment of inertia, g gravity coefficient and Ac acceleration of undulator gap change

Table 120.2 Friction torques from the undulator gap-driven system

	Design value	Design formula
Linear guide friction coeff.	0.01	From specification
Linear guide pre-load	1700	From specification
Number of linear guides	16	
Linear guide resistance force	272 kgf	Linear guide friction coeff × pre-load × number of linear guides
Axis load	7472 kgf	Magnetic force + linear guilder resistance force
Ball screw lead angle	0.023 rad	From specification
Ball screw pre-load coeff.	0.33	0.05/sqrt (tan(θs))
Ball screw pre-load	1600 kgf	400 kgf × 4 (number of ball screw)
Ball screw efficiency	0.9	
Ball screw friction torque	1681 kgf mm	Ball screw pre-load × pre-load coeff. × ball screw lead/2π
Ball screw operation torque	13214 kgf mm	Axis load × ball screw lead × 2/2π/ball screw efficiency
Bearing friction coeff.	0.02	From specification
Bearing inner/outer diameter	50/78 mm	Bearing eff. diameter = 1/2 (inner + outer diameter)
Bearing friction torque at shaft	4782 kgf mm	Bearing friction coeff. axis load × Bearing eff. diameter
Total torque	18841 kgf mm	Ball screw friction torque + ball screw operation torque + bearing friction torque

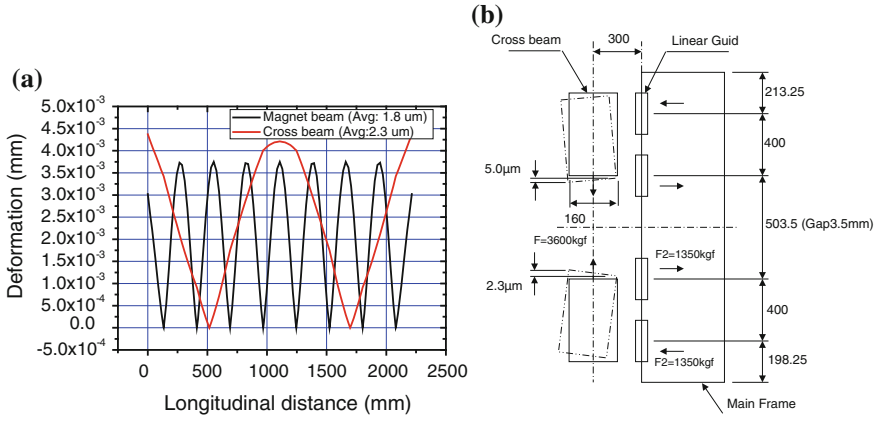

Fig. 120.2 **a** Deformation of the magnet array and cross beam; **b** Deformation of the mechanical frame

The accelerator torque is 4.1 kgf cm, about a quarter of the friction torque. If a safety factor of 2 is considered, the motor must provide 25.0 kgf cm at motor speed pulse 10 kHz. As the ratio of load inertia to motor inertia is 0.45, the present choice of motor can have a satisfactory working efficiency.

Table 120.3 List of GD_2 from an undulator driven system

	GD_2/kgfcm2	Reduction ratio	Permissible GD_2/kgfcm2
Coupling at motor	18.6	$(1/1)^2$	18.60
1st Beveling gear	9.6	$(1/1)^2$	9.60
Coupling at 1st beveling gear	16	$(1/2)^2$	4.00
2nd Beveling gear	9.6	$(1/2)^2$	2.40
Coupling at 2nd beveling gear	16	$(1/4)^2$	1.00
SHAFT × 2	46	$(1/4)^2$	2.90
Worm gear × 2	16	$(1/4)^2$	1.00
Fine adjuster × 2	29.8	$(1/200)^2$	0.001
Coupling at worm gear	160	$(1/200)^2$	0.004
Ball screw × 2	3000	$(1/200)^2$	0.075
Total			39.6

120.2 Deformation of the Mechanical Frame

The minimization of deformation of a magnet array and of its mechanical frame is important to ensure the consistency of magnetic performance throughout all magnetic gaps. At a small undulator gap, a large deformation of magnet array create additional magnetic field kicks and result in a deterioration of the flux density of the photon energy spectrum [3, 4].

IU22 is a linear undulator having only a vertical magnetic field, B_y; an attractive force is uniformly distributed in the vertical direction over the entire magnet supporter beam. A one-dimension beam deformation calculation is therefore used to verify the magnet supporter beam and cross-beam deformation. The magnet support I-beam is made of Aluminum T6061 because its high thermal conductivity property. The result (Fig. 120.2a) shows that the maximum deformation of a magnet array is 3.7 μm at between of two supporters. A maximum 4.3 μm of cross-beam deformation is found at the center of the cross beam. The average deformations of the magnet beam and cross beam are 1.8 μm and 2.3 μm, respectively.

The cross beam deforms in not only the longitudinal direction but also the transverse direction. Under attractive force 3600 kgf, the upper and lower magnet array has 0.03 and 0.01 mrad tilt in the transverse direction (Fig. 120.2b). As a result, the deformation angle is less than the tolerance of the magnet vector angle, 0.04 mrad, and must have no significant effect on the variation of the magnetic field.

Measured deformation of the in-vacuum undulator. The deformation of the magnet array is not directly measurable because it is assembled inside a vacuum chamber. Alternative method is necessary to measure average gap defamation. If a linear undulator has a perfectly distributed magnetic field, the magnetic field is expressible as a function of gap and vertical position, as shown in Eq. (120.2) [5],

$$\mathrm{B(g,y,z)} = \mathrm{B_0 exp}\left(\frac{-\pi g}{\lambda u}\right)\cosh\left(\frac{2\pi y}{\lambda u}\right)\cos\left(\frac{2\pi z}{\lambda u}\right) \tag{120.2}$$

Table 120.4 NSRRC undulator parameters for varied gap

Gap/ mm	Magnetic force/kgf	Magnetic peak field/T	Photon energy 3rd harmonics/ev	d*B*/ *B*/ %	Phase error/ deg	Δ*g*/ μm
3.5	3600	1.55	1.92	0.38	2.1	−2.7
5	1900	1.09	3.32	0.34	2.0	−2.4
6	1335	0.89	4.36	0.25	1.7	−1.8
7	950	0.74	5.40	0.23	1.5	−1.6
9	490	0.53	7.31	0.20	1.5	−1.4
12	195	0.33	9.47	0.20	1.4	−1.4
14	110	0.25	10.29	0.19	1.3	−1.3

in which B_0 is the peak magnetic field, λu is the period length of the undulator, g is the gap of the undulator and y is the height of the undulator.

Field variations result from gap variation, tapering of the magnet array or tilt. The field variation(ΔB/B) from the array tapering and the gap variation are expressed in Eq. 120.3, so that the gap variation can serve to estimate the variation of the field

$$\left(\frac{\Delta B}{B}\right)_{gapvar.} = \frac{-\pi \Delta g}{\lambda u}; \left(\frac{\Delta B}{B}\right)_{taper} = \frac{-\pi \Delta g' z}{\lambda u} \tag{120.3}$$

The variation of the magnetic field, d*B*/*B*, is measured along the longitudinal direction (Table 120.4). If the magnetic force is less than 490 kgf, the field variation is about 2.0 %, which is the existing field variation between the magnet blocks. When the attractive force increases, a magnet supporter beam can be deformed and create gap variations in the longitudinal distance. The variation of the magnetic field is due mainly to the gap variation, but not to a variation in the magnetization vector of the magnet block or the tilt or rotation angle of the magnet supporter beams.

According to the measurements in Table 120.4, the average gap deformation in the longitudinal direction is 2.7 μm. For comparison with the gap variation in Fig. 120.2a, the average deformation in simulation is 4.1 μm. The difference is 1.3 μm, which, with Eq. (120.3), provides a method to measure the gap variation in vacuum. The gap deformation also create the increase of phase error, as a result, the flux density of synchrotron radiation can be reduced compare to the idea case.

120.3 Conclusion

The design and evaluation of an in-vacuum undulator of a driven system and the mechanical deformation are presented in this paper as a guide. The details of load torque and accelerate torque of system are evaluated to achieve high accuracy precision in gap motion. The main conclusions of the work are that

1. The mechanical system with small backlash (less than 10 microns)for NSRRC an in-vacuum undulator is proposed in the paper.
2. The highly precise motion-driven system of an in-vacuum undulator, IU22, is presented, and load torque and accelerator torques are evaluated in details.
3. According to a 1-D calculation, the maximum and average mechanical deformations in the longitudinal direction are 7.9 μm and 4.1 μm, respectively.
4. The variation of the magnetic field can serve to estimate the gap variation of an in vacuum undulator, the average gap variation can be calculated from$\Delta g = (-\lambda u \times \Delta B/B)/\pi$.

References

1. Chang, C. H., Chang, C. H., Huang, J. C., Hwang, C. S., & Yang, J. K. (2009). Progress in Insertion Devices for TPS in Phase I. In *International Particle Accelerator Conference*, San Sebastain, Spain.
2. Chubar, O., Elleaume, P., & Chavanne, J. (1998). A 3D magnetostatic computer code for insertion devices. *Journal of Synchrotron Radiation, 5*, 481–484.
3. Huang, J. C., Hwang, C. S., et al. (2013). Performance of the elliptically polarized undulator in NSRRC. *Journal of Physics Conference Series*, *425*, 032018.
4. Diviacco, B., & Walker, R. (1996). :Recent advances in undualtor performance optimization. Nuclear Instruments and Method in Physics Research A, *368*, 522–532.
5. Tanaka, T., et al. (2009). In situ correction of field errors induced by a temperature gradient in cryogenic undulators. *Physical Review Special Topics Accelerators Beams*, *12*, 120702.

Chapter 121
An Efficient Scanning Approach for Multiple Targets

Cheng-Tiao Hsieh

Abstract Kinect is a popular motion sensor often applied in an intuitive PC games. In recent years, it had been applied to construct a low cost 3D scanner. Kinect scanner is capable of generating a set of point clouds, and its outputs are usually rough and need to be treated by appropriate applications before advanced 3D applications. For this need, this paper proposed a new approach which is capable of building multiple targets from a raw point cloud captured by a Kinect scanner efficiently. The principle of extracting targets is based on Background subtraction and this method had been developed by author in 2013. This paper proposed a segment method which is used to segment a multiple target representation extracted by the previous method. The principle of segment method is based on the clustering algorithm called DBSCAN. By means of this approach, a multiple scanning process can be accomplished.

Keywords Segment · Kinect · Density based clustering algorithm

121.1 Introduction

Kinect is a popular motion sensing device developed by Microsoft. The first commercial Kinect application, Xbox 360 video game, emerged in 2010. Its outstanding performances had grabbed people's attentions, and also encourage people to explore possible Kinect applications as well. In early stage, Kinect applications aimed at creating a natural interaction (NI) environment which allows users to play with PC games intuitively [1]. For instance, Xbox is capable of recognizing human's body to further control PC games. Kinect is the key device to

C.-T. Hsieh (✉)
Department of Industrial Design, Ming Chi University of Technology,
New Taipei City 24301, Taiwan, Republic of China
e-mail: cthsieh@mail.mcut.edu.tw

J. Juang et al. (eds.), *Proceedings of the 2nd International Conference on Intelligent Technologies and Engineering Systems (ICITES2013)*, Lecture Notes in Electrical Engineering 293,
DOI: 10.1007/978-3-319-04573-3_121,

catch human's gestures. Once human's gestures are received by Kinect, a specific software is applied to analyze the gestures and then to meaningfully perform a task. It is the concept of NI process. In recent years, Kinect technology has a big progress in other fields like robot vision, 3D scanning and etc. Especially in 3D scanning field, a low cost 3D scanner based on Kinect technology had been developed successfully [2]. Its price and performances make Kinect very competitive in current 3D scanning market. According to this fact, this paper attempts to propose an approach integrating extracting and segmenting methods together to improve the efficiency of the entire 3D sensing process. However, Kinect based scanner utilizes the concept of structured light to scan objects. Its output usually contains a lot of undesired information. Our approach is capable of scanning multiple objects and removing undesired points within a short time. This technology provides an alternative solution to make a low-cost and efficient 3D scanning process possible.

121.2 Kinect

A completed Kinect is consisting of an infrared range camera, a RGB camera and audio sensors as shown on Fig. 121.1b. Microsoft and AUSU are two main manufacturers of Kinect products. AUSU's first commercial Kinect products, Xtion series, emerged at the market in 2011. Xtion series includes Xtion Pro and Xtion Pro Live as shown on Fig. 121.1.

Xtion Pro Live is similar to Microsoft Kinect which contains full package of Kinect functions, an infrared range camera, a RGB camera and audio sensors. As for Xtion Pro, it only has an infrared range camera used to capture depth information. This range camera technology was developed by PrimeSense and depends on the concept of structured light to capture depth information [3]. Figure 121.2a shows an infrared image with infrared projected pattern and Fig. 121.2b shows a color image displaying depth information. Those images were captured by Xtion Pro with its maximum resolution, 640×480.

Figure 121.2b released the fact that the raw data produced by Kinect usually contains noise and unexpected points. Thus, removing undesired points becomes a requirement of a 3D scanning process. For this need, researchers have developed different algorithms to deal with this event. Most of algorithms are always complicated and not friendly to users. This situation definitely obstructed the development of 3D applications. Based on this drawback, this paper attempted to propose a novel approach to simplify 3D scanning process.

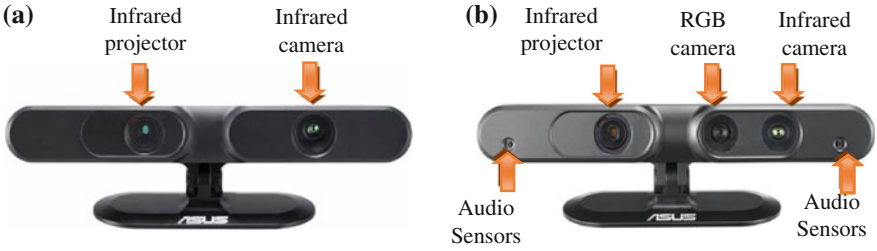

Fig. 121.1 AUSU's Kinect products **a** Xtion Pro **b** Xtion Pro Live

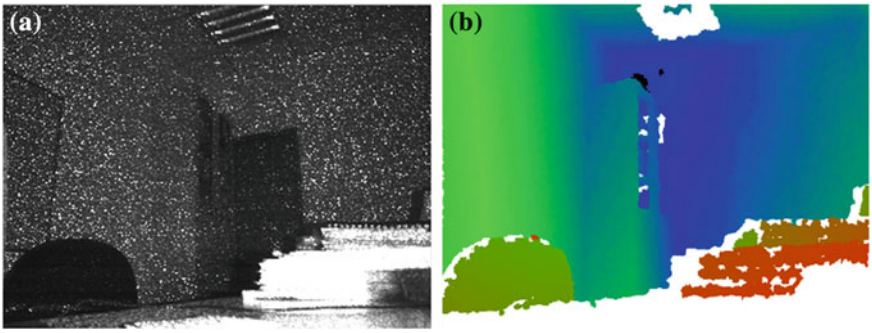

Fig. 121.2 Images captured by Xtion Pro **a** Infrared image and **b** Depth image

121.3 Proposed Approach

All of works in this paper were accomplished by our Kinect-based scanner. Generally, the system of Kinect scanner can be classified into two sub-systems, hardware and software. The hardware sub-system is used to capture surface points from scanned objects. Xtion Pro is the key component to execute the above task. Xtion Pro depends on the concept of structured light to capture depth information, so it inherits all of advantages and disadvantages of structured light scanner. For instance, it can't capture depths from shaded areas as shown on Fig. 121.3b. Figure 121.3a shows that an infrared pattern was projected on scanned targets for dealing a complicated correspondence issue. Depth information was obtained by means of a geometrical triangulation. An appropriate converter was implemented to translate depths to 3D coordinates as Fig. 121.3b.

The tasks of the software sub-system include appropriately performing a scanning procedure and handling output data based on users' desired. For considering an efficient code developing, all of the software was programmed by open sources, i.e. OpenNI, Point Cloud Library (PCL) and VTK. OpenNI is a free SDK for supporting users to develop 3D sensing applications [4]. OpenNI is compatible to both of Microsoft Kinect and Xtion series. PCL is also a free and useful library

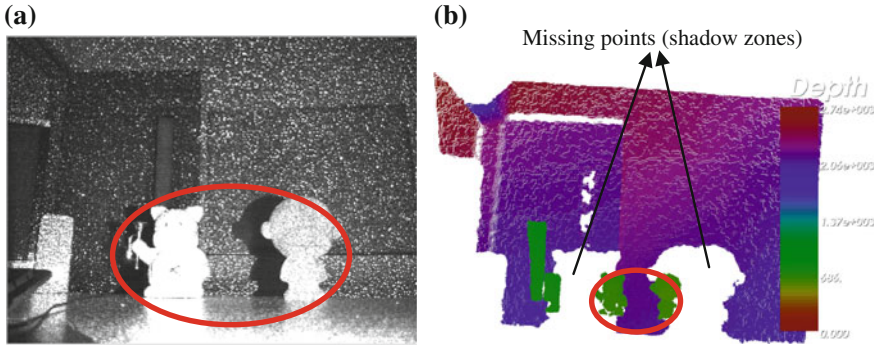

Fig. 121.3 **a** Infrared image for viewing scanning scene, **b** A point cloud data set

for handling 2D/3D image and point cloud [5]. With its assistance, point cloud data set can be handled easily and efficiently. VTK is a free library for computer visualization [6]. This work utilized this library for handling visualization events.

Figure 121.3b illustrates that a raw output of Xtion Pro usually contains a lot of noise and unexpected points. Those undesired points are always difficult to be removed. About this limitation, author had developed an approach to extract a specific target from a raw data [7]. The approach is based on the concept of Background subtraction to extract a target from a raw data. This concept is also applied in this work to extract multiple targets from a raw point cloud. Unfortunately, this approach is not capable of classifying multiple targets separately. All extracted points representing multiple targets were stored in a point cloud representation. According to this, this paper attempted to propose an approach to extract and segment the representation and further to store every target in a dependent representation separately. The proposed approach was summarized as shown on Fig. 121.4. The entire process of our approach can be classified into four steps. Each step is implemented by a specific tool or algorithm. In the end of every step, a specific output is always created.

Scanning multiple targets by a Kinect based scanner is the first step. In this step, our Kinect 3D scanner was used to capture point cloud from scanned objects and its output was saved in a specific format with extension filename xyz. The captured data is a set of point cloud containing noise and undesired points as shown on Fig. 121.3b. The second step is to extract targets from the captured raw data. In this step, Background subtraction was applied to remove undesired points. The extracted result is shown on Fig. 121.5. Unfortunately, all of extracted points were seen as a point cloud representation. This situation is definitely not suitable for advanced computational processes like 3D alignment and reconstruction. For this drawback, an appropriate segment method was proposed to segment the above point cloud into specific number of independent point clouds.

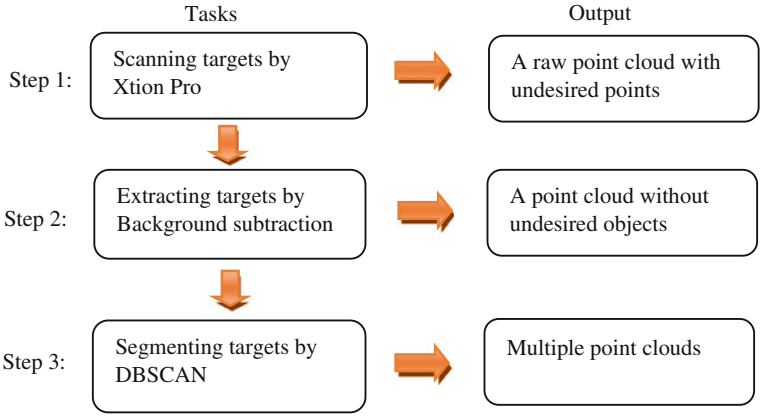

Fig. 121.4 Procedure diagram for illustrating our proposed approach

Fig. 121.5 A point cloud with two targets extracted by background subtraction

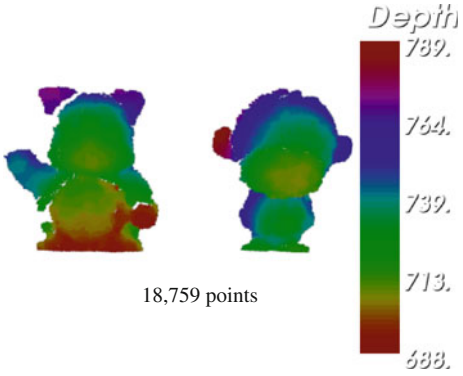

121.4 Segmenting Multiple Targets

This work utilized Background subtraction to extract a point cloud representation of multiple targets from a raw output of Kinect scanner. Background subtraction method can only extract multiple targets from raw data, but it is not capable of separating targets one by one. The goal of this paper attempted to develop an efficient scanning process which is capable of scanning and constructing multiple targets simultaneously. For advanced usage, all of targets must be existed independently. According to this need, this paper utilized the concept of a clustering algorithm to segment a raw point cloud to obtain separated target representations.

The major task of cluster algorithm is to classify data into meaningful groups. Generally, cluster algorithms can be classified into three different types, partition clustering, hierarchical clustering and density based clustering [8]. According to our needs, this paper selected density based clustering algorithm to perform this

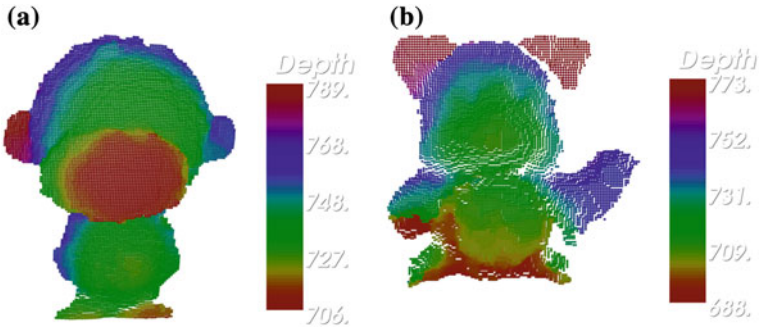

Fig. 121.6 Two independent representations for multiple targets

segment task. DBSCAN is the typical and simple density based clustering algorithm [9]. A density based algorithm utilizes the density property to group data points. The density is specified by the amount of points within a specified radius. Unlike K-means algorithm - a partition clustering algorithm, it can classify data in arbitrary shapes.

DBSCAN usually classifies points into three different point types, i.e. core point, border point and noise point. Core point is a valid point that must contain enough qualified neighbor points to reach the required density. Where, the qualified neighbor point is any point located within a given radius. Border point is the points that don't have enough qualified neighbor points, but it is a neighbor point of a core point. Noise point is not a neighbor point of core points and the amount of its neighbor points is less than the given density. By means of DBSCAN, every point in a multiple target representation will be searched and classified to one of the above point groups. In addition, all of core points may be separated by low density regions. Fig. 121.6 demonstrates two independent target representations that were clustered by DBSCAN.

121.5 Conclusions and Future Work

This paper had demonstrated our approach for extracting and segmenting multiple targets from the raw point cloud captured by our low cost 3D Kinect scanner. By means of this approach, multiple objects can be scanned and their point cloud representations can be constructed appropriately and efficiently. The goal of developing this approach is to build fundamental technologies for supporting Kinect-based applications in 3D scanning field. By means of this approach, a low cost 3D scanning process become possible. We believe it is very helpful to the future development of 3D applications in various fields.

However, our approach for segmenting multiple objects is based on DBSCAN algorithm and the DBSCAN algorithm used in this approach is a two-dimensional

algorithm. Therefore, a couple of make-up requirements are needed during object scanning process. For instance, objects must be located separately with a specific distance and the distance must larger than the radius defined in DBSCAN algorithm. If the distance between two objects are too small, DBSCAN algorithm may fail to cluster the points in two objects appropriately. In addition, objects in the depth images taken by Kinect are not allowed to overlap each other. If two objects are overlap in a depth image, then DBSCAN algorithm may fail to cluster them appropriately. Those limitations will be listed in our future works.

Acknowledgments I would like to thank AUSU company for supporting a free Xtion Pro. With the assistance of Xtion Pro, this work can be accomplished. I also would like to thank people in open source forums and organizations for their kindly programming guidance, especially like OpenNI and VTK forums.

References

1. MicroSoft. (2012). *Human interface guidelines—kinect for windows (*1.5th ed.). MicroSoft.
2. Newcombe, R. A., et al. (2011). *KinectFusion: Real-Time Dense Surface Mapping and Tracking*. In IEEE ISMAR, 2011. Basel, Switzerland: IEEE.
3. Zhang, Z. Y. (2012). Microsoft kinect sensor and its effect. *IEEE Multimedia, 19*(2), 4–10.
4. *OpenNI User Guide*. www.openni.org.
5. Rusu, R. B. (2011). 3D is here: Point Cloud Library (PCL). In *IEEE International Conference on Robotics and Automation (ICRA),* 2011 (pp. 1–4). Shanghai, China: IEEE Xplor.
6. Hansen, C. D., & Johnson, C.R. (2005). *The visualization handbook*. New York: Elsevier Inc.
7. Hsieh, C.-T. (2013). *Extracting target scanned objects from raw scanned data set produced by Kinect-based 3D scanner* in *2013 International Conference on Applied Technology*, Nantou, Taiwan.
8. Tan, P.-N., Steinbach, M., & Kumar, V. (2006). *Introduction to data mining*. Pearson Addison-Wesley.
9. Ester, M., et al. (1996). A density-based algorithm for discovering clusters in large spatial databases with noise. In *Proceedings of the Second International Conference on Knowledge Discovery and Data Mining,* Portland, USA.

Chapter 122
A Power Management Scheme with SDMA for WPANs

Neng-Chung Wang, Chun-Ching Hsu and Chih-Cheng Wen

Abstract In this paper, an SDMA-based power management scheme, called enhanced min-degree searching (EMDS), is proposed for WPANs. EMDS orders the streams among multiple devices to minimize the total wakeup times. In this scheme, every device that can transmit data at the same time is checked using the SDMA. The total wakeup times will be reduced substantially if the majority of the devices can transmit data at the same time. Simulation results show that the performance of the proposed EMDS outperforms that of the existing approaches.

Keywords Piconet · Power management · Space division multiple access · Superframe · WPAN

122.1 Introduction

IEEE 802.15.3 was devised for short-distance wireless connectivity within a wireless personal area network (WPAN). WPANs are used to convey information over short distances among portable devices [1]. IEEE 802.15.3 is based on piconet. The piconet is a wireless ad hoc data communications system that allows a number of devices to communicate with each other in a peer-to-peer mode. Devices comprise the most basic component set of a piconet and a piconet is composed of 255 devices at most. These devices consist of one piconet coordinator (PNC) and the rest. The PNC provides a lot of centralized controlling

N.-C. Wang (✉) · C.-C. Hsu
Department of Computer Science and Information Engineering, National United University, Miao-Li 360, Taiwan, Republic of China
e-mail: ncwang@nuu.edu.tw

C.-C. Wen
Department of Computer Science and Information Engineering, University of Technology, Taichung 413, Taiwan, Republic of China

J. Juang et al. (eds.), *Proceedings of the 2nd International Conference on Intelligent Technologies and Engineering Systems (ICITES2013)*, Lecture Notes in Electrical Engineering 293,
DOI: 10.1007/978-3-319-04573-3_122,

functionalities such as system timing, quality of service (QoS), and power management (PM). If any device of the piconet requires channel time to transmit data, it asks the PNC for isochronous channel time. The PNC will allocate channel time for the device according to the receiving channel time request if the requested channel time is available.

In the MAC of IEEE 802.15.3, the time is divided into multiple superframes [1]. The superframe consists of a beacon, a contention access period (CAP), and a channel time allocation period (CTAP). The beacon is used to set the timing allocations and to communicate management information for the piconet. The beacon consists of the beacon frame as well as any announce commands sent by the PNC. The CAP is used to communicate commands and/or asynchronous data if it is present in the superframe. The CTAP is composed of channel time allocations (CTAs). The CTAs are used for commands, isochronous streams, and asynchronous data connections.

In [2], Guo et al. proposed an intra-superframe power management scheme, called min-degree searching (MDS), for IEEE 802.15.3 WPANs. In this scheme, the intra-superframe PM properly arranges the order of CTAs to minimize the number of total wakeup times.

In this paper, an enhanced min-degree searching (EMDS) scheme is proposed. The proposed EMDS can reduce the number of CTAs required to achieve data transmission among devices. The total wakeup times will be reduced significantly if the majority of all devices can transmit data at the same CTA. In this scheme, the majority of the devices wake up at the first CTA. Some of the devices are not required to wake up again if they need to transmit data in the next CTA. This can notably reduce total wakeup times. Thus, it can increase power-saving efficiency.

The remainder of this paper is organized as follows. Section 122.2 describes the related work. The proposed scheme is presented in Sect. 122.3. Section 122.4 shows the performance evaluation. Section 122.5 draws the conclusions.

122.2 Related Work

122.2.1 Space Division Multiple Access Technology

Space Division Multiple Access (SDMA) is a new technology to optimize performance of current and future mobile communication systems [3, 4]. In mobile communication, it has several advantages which increase the effective communication range, avoid or reduce multipath reflections, and use less radio power. The SDMA technology uses the smart antenna system to achieve the effect of space division. The smart antenna system provides many benefits, such as a wider coverage area, higher spatial reuse, and higher network capacity. The smart antenna system associates multiple antenna elements with a signal processing capability to automatically optimize its radiation and reception pattern in response

to the signal environment. A smart antenna system consists of M antenna elements, whose signals are processed adaptively in order to exploit the spatial dimension of the mobile radio channel. All M elements of the antenna array have to be combined in order to adapt to the current channel.

122.2.2 Min-Degree Searching Scheme

In [2], Guo et al. focused on the intra-superframe PM issue for IEEE 802.15.3 WPANs and proposed a min-degree searching (MDS) scheme. In a piconet, the PNC will allocate the CTAs to every stream if there are many streams among multiple devices. The PNC assigns a CTA for every stream and announces the position and the duration of the CTA in the beacon at the beginning of superframe.

Due to the property of CTAP, each device can know exactly the CTA position in the superframe from the beacon. Hence, every device can go to sleep during the CTAs which are not assigned for its streams. Every device can wake up during the CTAs designated for its streams. Therefore, when a device has multiple streams, it may wake up and sleep for several times if the CTAs/streams are not well ordered. On the other hand, each wakeup and sleeping will consume significant amounts of power [5]. For this reason, the intra-superframe PM properly arranges the order of the CTAs in order to minimize the number of total wakeups times. A sample topology below shows the effect of the order of CTAs on PM.

In [2], it considers a multiple-device, multiple-stream IEEE 802.15.3 WPANs. Note that if there is more than one stream between two devices, it can combine them as a single stream since it is natural to put them at contiguous CTAs within the superframe. In the topology, each device is denoted as a vertex. The MDS scheme adds an edge between two vertices if there is a stream between the two corresponding devices.

An example of power management using MDS is given in Fig. 122.1. In this example, there are six devices: one is PNC and the others are devices. There are multiple streams between these devices. There is an edge between the pair of all devices if the pair of all devices has one stream or more than one stream. The authors arrange the order of edges to allocate corresponding CTAs. Every pair of devices can wake up to transmit data during their CTAs and can sleep when it is not their CTAs.

The basic idea of the MDS scheme is that, each time it selects an edge so that its two associated vertices have the minimum degree. It first needs to get the degrees of vertices and edges. The degree of a vertex is equal to the number of edges incident to the vertex. The degree of an edge is equal to the sum of the degree of two associated vertices. Thus, it can ascertain the degrees of the vertices and the edges, as below.

1. The degree of devices: $\deg(A) = 3$, $\deg(B) = 3$, $\deg(C) = 3$, $\deg(D) = 2$, and $\deg(E) = 1$.

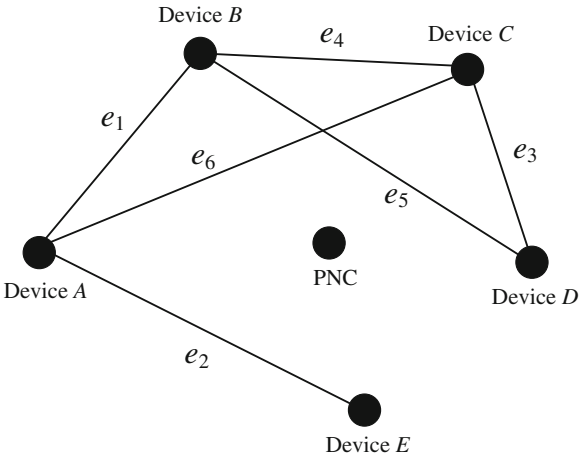

Fig. 122.1 An example of power management

2. The degree of edges: $\deg(e_1) = 6$, $\deg(e_2) = 4$, $\deg(e_3) = 5$, $\deg(e_4) = 6$, $\deg(e_5) = 5$, and $\deg(e_6) = 6$.

It first selects the edge with the minimum degree, it get e_2. It selects an edge from the neighboring edges of e_2 so that the edge is with the minimum degree. It gets the edge order $e_2 \rightarrow e_1$. It selects an edge from the neighboring edges of e_2 and e_1 so that the edge is with the minimum degree. It gets the edge order $e_2 \rightarrow e_1 \rightarrow e_5$. It continues the processing for selecting the edge with the minimum degree. Finally, it gets the edge order $e_2 \rightarrow e_1 \rightarrow e_5 \rightarrow e_3 \rightarrow e_4 \rightarrow e_6$.

For the edge order, device *A* transmits data to device *E* in CTA 1, device *A* transmits data to device *B* in CTA 2, and so on. First, device *A* and device *E* are used in CTA 1, device *A* and device *E* wake up in CTA 1. Then, device *A* and device *B* are used in CTA 2, device *A* still stays awake, it just to awake device *B*. The rest process can be deduced by analogy. Therefore, the number of wakeup times is equal to 2 in CTA 1, the number of wakeup times is equal to 1 in CTA 2, and so on. Therefore, the total number of wakeup is 7. Finally, it can get the order of CTAs.

122.3 Proposed Enhanced Min-Degree Searching Scheme

As an example to illustrate the proposed EMDS scheme, Fig. 122.2 shows a power management scheme using EMDS. There are six devices: one is a PNC and the others are devices *A*, *B*, *C*, *D*, and *E*. In this example, six devices have several demands as regards data transmission and have four sectors. If there are one or more demands for data transmission between two devices, it can use an edge to represent it. Every device divides space into quadrants I, II, III, and IV via four sectors. Every device can transmit and receive signals via different sectors at the

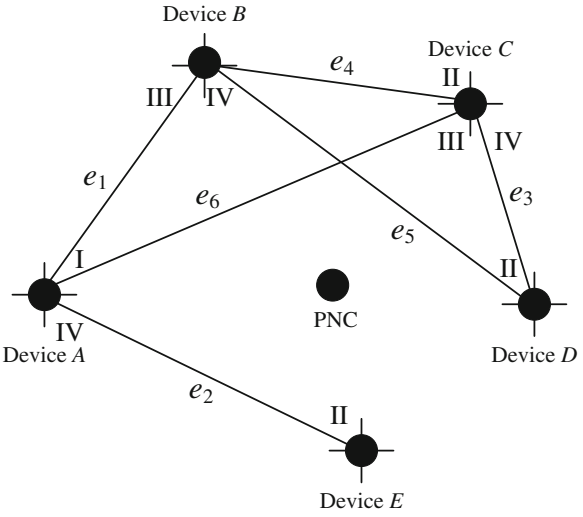

Fig. 122.2 An example of power management based on SDMA technology

same time. Then, it needs to schedule CTAs in the superframe according to the demands. The best schedule can reduce the total wakeup times and make full use of the CTAs to transmit data such that all devices can conserve power and transmit data efficiently.

It checks the edge order depending on whether each device is transmitted within the same quadrant. It also checks whether every device can transmit data at the same time using SDMA technology. For the edge order, device *A* can transmit data to device *E* via the sector of quadrant IV and device *E* can receive data via the sector of quadrant II, device *A* can transmit data to device *B* via the sector of quadrant I, and device *B* can receive data via the sector of quadrant III, and so on. It re-arranges the order of edges to allocate corresponding CTAs within the superframe. Thus, it can get the edge order $\{e_2, e_1, e_5\} \rightarrow \{e_3, e_4, e_6\}$.

For the edge order, devices *A*, *B*, *D*, and *E* transmit data in CTA 1. Devices *A*, *B*, *C*, and *D* transmit data in CTA 2. First, devices *A*, *B*, *D*, and *E* are used in CTA 1, devices *A*, *B*, *D*, and *E* wake up in CTA 1. Then, devices *A*, *B*, *C*, and *D* are used in CTA 2, devices *A*, *B*, and *D* still stay awake, it just to awake device *C*. Therefore, the number of wakeup times is equal to 4 in CTA 1. The number of wakeup times is equal to 1 in CTA 2. Therefore, the total number of wakeups is 5. Finally, it can get the order of CTAs.

122.4 Performance Evaluation

A simulator with C++ was developed to act as a simulation platform to compare the performance of the proposed EMDS with that of standard and MDS. The

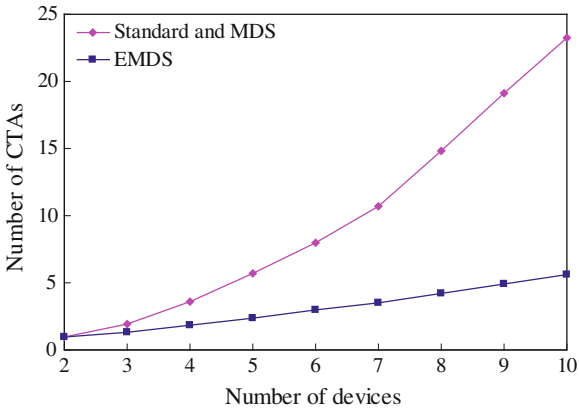

Fig. 122.3 Number of CTAs versus number of devices

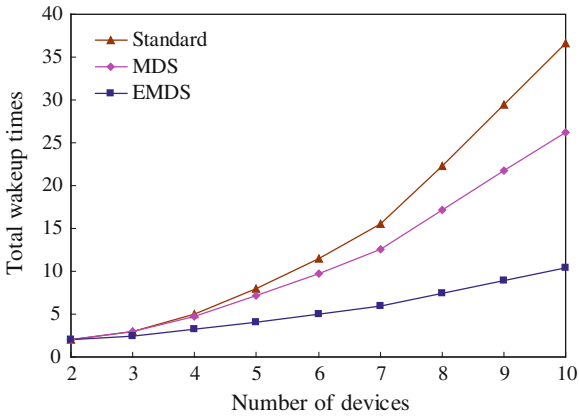

Fig. 122.4 Total wakeup time versus number of devices

simulation modeled a network in a 200 × 200 m area. Several devices and multiple streams were randomly created as a topology.

Figure 122.3 shows the number of CTAs under different numbers of devices. The number of CTAs of EMDS is less than that of standard and MDS. EMDS requires few CTAs to meet the demands of data transmission because multiple pairs of devices are able to transmit data in one CTA. However, standard and MDS need more CTAs to meet similar demands. Figure 122.4 depicts the total wakeup times under different numbers of devices. The total wakeup times of EMDS scheme is smaller than that of standard and MDS. In standard, it randomly allocated the CTAs. So, it needed the maximum number of total wakeup times. In MDS, every device didn't waste redundant wakeup times because the scheme considered the order of CTAs. So, fewer total wakeup times were required than standard. In EMDS, the majority of devices can transmit data at the same time if they do not use the same quadrant to transmit data. In addition, EMDS can save power because of the smaller number of total wakeup times.

122.5 Conclusions

In this paper, an enhanced min-degree searching (EMDS) scheme for 802.15.3 WPANs was proposed. EMDS orders streams among multiple devices such that the total wakeup times can be reduced. Most devices can wake up in the first CTA. If some of their devices continue to transmit data in the next CTA, they won't require being woken up again. Additionally, most devices can transmit data in one CTA by using SDMA technology. Therefore, the total wakeup times and the number of CTAs can be reduced significantly.

Acknowledgments This work was supported by the National Science Council of Republic of China under grants NSC-101-2221-E-239-032 and NSC-102-2221-E-239-020.

References

1. LAN MAN Standards Committee. (2002). "Wireless medium access control (MAC) and physical Layer (PHY) specifications for wireless personal area networks (WPANs)," *IEEE Computer Societ*.
2. Guo, Z., Yao, R., Zhu, W., Wang, X., & Ren, Y. (2005). Intra-superframe power management for IEEE 802.15.3 WPAN. *IEEE Communications Letters, 9*(3), 228–230.
3. Hui, X., & Gao, T. (2010)."random channel allocation scheme for SDMA in a smart antenna systems". In: *Proceedings of the International Conference on Communications and Mobile Computing*, 2, (pp. 130–134).
4. Kountouris, M., & Andrews, J. G. (2012). Downlink SDMA with Limited Feedback in Interference-Limited Wireless Networks. *IEEE Transactions on Wireless Communications, 11*(8), 2730–2741.
5. Li, D., Chou, P., & Bagherzadeh, N. (2002)."Mode selection and mode-dependency modeling for power-aware embedded systems". In: *Proceedings of the 7th Asia and South Pacific and the 15th International Conference on VLSI Design*, (pp. 697–704).

Chapter 123
Identification of Induction Motor System Using Observer/Kalman Filter Identification (OKID) Method

Chien-Hsun Kuo and D.-M. Yang

Abstract This paper introduces system identification of induction motor. System identification or modeling is the process of building mathematical models of dynamical systems based on the available input and output data from the systems. The open-loop system identification called Observer/Kalman Filter System Identification for stable systems without requiring feedback control is addressed here to identify the system.

Keywords Observer/Kalman filter identification (OKID) · System markov parameters · Singular value decomposition (SVD)

123.1 Introduction

The induction machines are widely used in industry due to their reliability, low cost and robustness and hence treated as work horses of industry [1]. But the possibility of faults is unavoidable. Fault identification and diagnosis schemes are intended to provide advanced warnings of incipient faults, so that appropriate maintenance action can be taken at an early stage [2, 3].

System identification deals with the problem of building the mathematical models of dynamical systems according to the input and output data. The criterion of model quality is normally based on how well the models could perform when they attempt to 'fit' the measured data. This technique is important in a diversity of fields such as manufacturing process, communication, economics, and system dynamics and control. For a unknown system, it is mostly required to identify the system model before one can perform the control design.

C.-H. Kuo (✉) · D.-M. Yang
Department of Mechanical and Automation Engineering, Kao Yuan University, Kaohsiung 812, Taiwan, Republic of China
e-mail: t30081@cc.kyu.edu.tw

J. Juang et al. (eds.), *Proceedings of the 2nd International Conference on Intelligent Technologies and Engineering Systems (ICITES2013)*, Lecture Notes in Electrical Engineering 293,
DOI: 10.1007/978-3-319-04573-3_123,

Here, the open-loop system identification (Observer/Kalman Filter Identification, OKID) technique is used to identify the induction motor system. In open-loop system identification, the system is excited directly without adding controller, and the system model is identified from the input and output data. Through the identified system model, one can predict the output via the new input. The predicted output could be compared with the measured one to help prevent the motor faults from developing into a catastrophic machine failure and avoid unnecessary costs and delays caused by the need to carry out unscheduled repairs.

123.2 Observer/Kalman Filter Identification

123.2.1 Kalman Filter

A finite-dimensional, linear, discrete-time, time invariant stochastic system can be expressed as:

$$x_{k+1} = Ax_k + Bu_k + w_k,\ y_k = Cx_k + v_k. \tag{123.1}$$

where $x \in R^{n\times 1}$, $u \in R^{ni\times 1}$, $y \in R^{no\times 1}$ are state, input and output vectors, respectively; [A, B, C] are the state-space system matrices. The sequences of process noise $w \in R^{n\times 1}$ and measurement noise $v \in R^{no\times 1}$ are assumed white, Gaussian, zero mean. The noises w_k and v_k are also assumed uncorrelated with covariance Q and R, respectively.

The technique of Kalman filters can be applied to problems such as optimal estimation, prediction, noise filtering, and stochastic optimal control. From the procedure of the discrete time LQG (Linear Quadratic Gaussian) control [4] and the discrete time Kalman filter [5], it indicates that the steady state Kalman filter gain exists and is used for state estimation in the LQG control. One can write the estimated state with the steady state Kalman filter gain as follows

$$\hat{x}_{k+1} = A\hat{x}_k + Bu_k + AK(y_k - C\hat{x}_k). \tag{123.2}$$

where $\hat{x}$ the estimated state vector.

If one defines the error between the actual output y_k and the estimated output $C\hat{x}_k$ as residual ε_k, one can have

$$\hat{x}_{k+1} = A\hat{x}_k + Bu_k + AK\varepsilon_k,\ y_k = C\hat{x}_k + \varepsilon_k. \tag{123.3}$$

In a Kalman filter sense, Eq. (123.3) is the best description of a stochastic system whose state space model is shown in (123.1). The model using the prediction of (123.3) is called a filter-innovation model [6].

123.2.2 Open-Loop System Identification Algorithm

The difference model, called autoregressive with exogeneous input (ARX), is derived from Kalman filter theories. In Ref. [7], a system is identified through a state observer, which can use a much smaller ARX model order. In Ref [8]. the projection filters which were originally derived for deterministic systems are developed for the identification of linear open-loop stochastic systems. The open-loop observer/Kalman filter identification (OKID) is introduced in the following.

A finite-dimensional, linear, discrete-time, time invariant stochastic system as shown in Eq. (123.3) can also be expressed as

$$\hat{x}_{k+1} = (A - AKC)\hat{x}_k + Bu_k + AKy_k,\ y_k = C\hat{x}_k + \varepsilon_k. \tag{123.4}$$

Then the relation between signal input and output with zero initial condition through Eq. (123.4) could be described as

$$y_k = \sum_{i=1}^{\infty} C\bar{A}^{i-1}AKy_{k-i} + \sum_{i=1}^{\infty} C\bar{A}^{i-1}Bu_{k-i} + \varepsilon_k. \tag{123.5}$$

where $\bar{A} = A - AKC$. Since $\bar{A}$ is asymptotically stable, $\bar{A}^{i-1} \approx 0$ if $i \geq q$ for a sufficient large number q [9]. Thus Eq. (123.5) becomes

$$y_k = \sum_{i=1}^{q} a_i y_{k-i} + \sum_{i=1}^{q} b_i u_{k-i} + \varepsilon_k. \tag{123.6}$$

$$\text{where } a_i = C\bar{A}^{i-1}AK, b_i = C\bar{A}^{i-1}B, i = 1, 2, \ldots, q. \tag{123.7}$$

The model described by Eq. (123.6) is the open-loop ARX model which directly represents the relationship between the signal input and output of the open-loop system. q is the open-loop system ARX model order, and a_i, b_i, the open-loop ARX model parameters, can be estimated through least squares method.

System matrices (A, B, C) and Kalman filter gain K can be realized from the open-loop system Markov parameters and the open-loop Kalman filter Markov parameters, respectively. The open-loop system Markov parameters $Y_s(k) = CA^{k-1}B$, and the open-loop Kalman filter Markov parameters $Y_k(k) = CA^{k-1}AK$, $k = 1, 2, \ldots, q$ can be obtained from the coefficients, a_i, b_i

$$Y_s(k) = b_k + \sum_{i=1}^{k} a_i Y_s(k-i),\ Y_k(k) = a_k + \sum_{i=1}^{k-1} a_i Y_k(k-i). \tag{123.8}$$

where $Y_s(0) = 0$, $Y_k(0) = I$ which is an identity matrix.

123.2.3 Recover System Matrices and Kalman Filter Gain

To recover system matrices, an eigensystem realization method is applied. For the first step, form a Hankel matrix $H(k-1)$ from the open-loop system markov parameters,

$$H(k-1) = \begin{bmatrix} Y_s(k) & Y_s(k+1) & \dots & Y_s(k+\beta-1) \\ Y_s(k+1) & Y_s(k+2) & \dots & Y_s(k+\beta) \\ \dots & \dots & \dots & \dots \\ Y_s(k+\alpha-1) & Y_s(k+\alpha) & \dots & Y_s(k+\alpha+\beta-2) \end{bmatrix}. \quad (123.9)$$

where $Y_s(k)$ is the kth open-loop Markov parameter.

Using singular value decomposition (SVD) [10] of $H(0)$

$$H(0) = U \sum V^T. \quad (123.10)$$

A nth order discrete state space model can be identified as

$$A = \Sigma_n^{-\frac{1}{2}} U_n^T H(1) V_n \Sigma_n^{-\frac{1}{2}},\ B = \Sigma_n^{\frac{1}{2}} V_n^T E_{ni},\ C = E_{no}^T U_n \Sigma_n^{\frac{1}{2}}. \quad (123.11)$$

where Σ_n is the upper left hand $n \times n$ partition of Σ containing the n largest singular values which are in the monotonically non-increasing order along the diagonal. U_n and V_n are the matrices formed by the first n columns of singular vectors associated with the n singular values from U and V, respectively. $E_{ni}^T = [\, I_{ni} \quad 0_{ni} \quad \dots \quad 0_{ni} \,]$, $E_{no}^T = [\, I_{no} \quad 0_{no} \quad \dots \quad 0_{no} \,]$, and n_i the number of inputs, n_o the number of outputs.

Once the open-loop A and C are obtained, one can calculate the open-loop Kalman filter gain from the open-loop Kalman filter Markov parameters and A, C as follows:

$$K = (O^T O)^{-1} O^T \begin{bmatrix} Y_k(1) \\ Y_k(2) \\ \dots \\ Y_k(k) \end{bmatrix}. \quad (123.12)$$

where $O = \left[\, CA \quad CA^2 \quad \cdots \quad CA^k \,\right]^T$.

123.2.4 Computation Steps For OKID

1. Collect a set of experimental input and output data, u and y, from the open-loop system.
2. Estimate the ARX model parameters a_i, b_i from Eqs. (123.6 and 123.7) by choosing suitable ARX model order q.
3. Compute the open-loop system Markov parameters $Y_s(k)$ and Kalman filter Markov parameters $Y_k(k)$ by using Eq. (123.8).

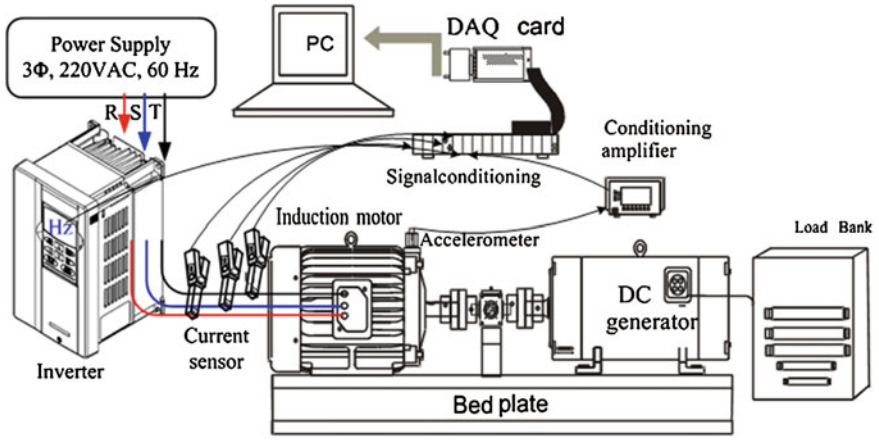

Fig. 123.1 Experimental setup

4. Realize the open-loop system matrices from the open-loop system Markov parameters by using eigensystem realization method, Eqs. (123.9–123.11).
5. Estimate the open-loop Kalman filter gain from the open-loop Kalman filter Markov parameters and the realized system matrices by using Eq. (123.12).

123.3 Experimental Setup

The experimental apparatus used in this study consists of a 3 hp, 1,800 rpm (i.e. $fr = 30$ Hz), 4-pole three phase induction machine driving a 5 kW DC generator via a flexible coupling, as shown in Fig. 123.1. The generator is used to absorb the energy generated by the motor. A piezo-electric accelerometer is mounted on the housing of the induction electrical machine to measure the vibration signal. Three current sensors were used to record the three phase current signals from the inverter. All measured signals were sampled at 6 kHz via a real-time data acquisition device (Type NI 6062E) under the motor no-load condition. The frequency of inverter varies from 1 to 60 Hz.

123.4 Numerical Validation

The inputs consist of three currents into the motor and the output is the vibration signal from the accelerometer. Each data contains 122,880 points. Two sets of input–output data are recorded, one set is implemented for system identification, and the other is used for comparison between the predicted output and the true one. Fig. 123.2 shows new test data (solid) and ARX predicted output (dashed) from

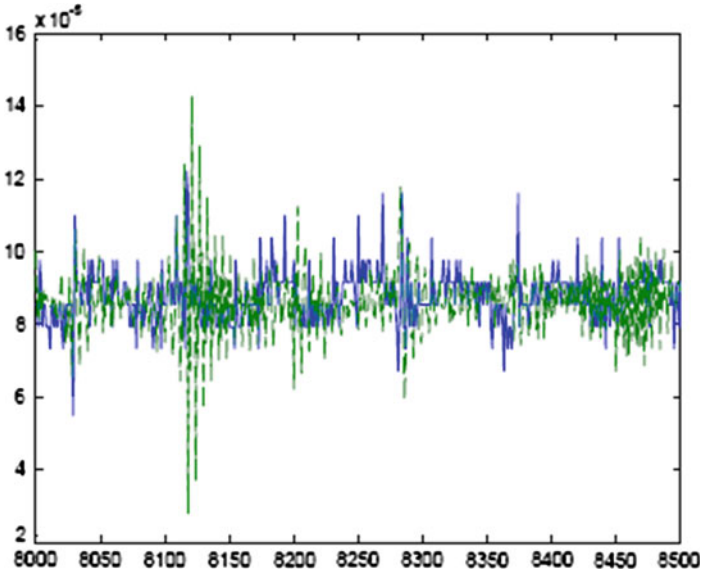

Fig. 123.2 New test data (*solid*) and ARX predicted output (*dashed*) from 8,000 to 8,500 points

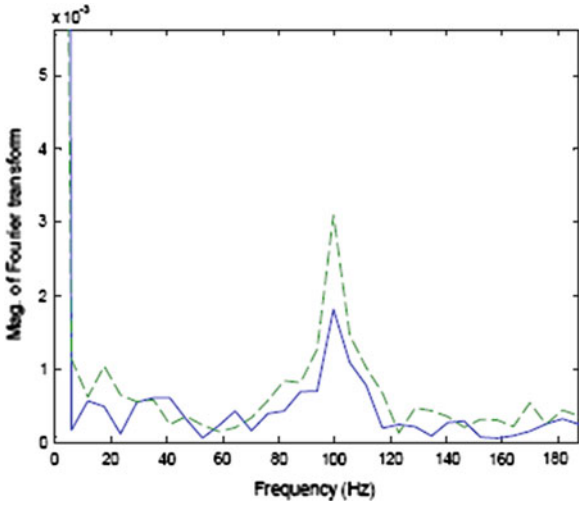

Fig. 123.3 The frequency plot of the real (*solid*) and predicted output (*dashed*) from Fourier Transform

8,000 to 8,500 points. Fig. 123.3 shows the frequency plot of the real (solid) and predicted output (dashed) from Fourier Transform.

123.5 Conclusion

In this paper, the open-loop system identification (Observer/Kalman Filter System Identification, OKID) has been used to identify the induction motor system. The experimental results show that the predicted output is very close to the test data. The effectiveness of the proposed approach is verified.

References

1. Boldea, I., & Nasar, S. A. (2002). *Induction machines handbook*. London: CRC Press.
2. Tavner, P., Ran, L., Penman, J., & Sedding, H. (2008). *Condition monitoring of rotating electrical machines*. London: The Institution of Engineering and Technology.
3. Vachtsevanos, G., Lewis, F. L., Roemer, M., Hess, A., & Wu, B. (2006). *Intelligent fault diagnosis and prognosis for engineering systems*. New York: Wiley.
4. Franklin, G. F., Powell, J. D., & Workman, M. L. (1990). *Digital control of dynamic systems*. London: Addison-Wesley Publishing Company.
5. Gelb, A. (1974). *Applied optimal estimation*. London: The M.I.T. Press.
6. Haykin, S. (1991). *Adaptive filter theory* (2nd ed.). Upper Saddle River, NJ: Prentice-Hall.
7. Phan, M., Horta, L. G., Juang, J.-N., & Longman, R. W. (1993). Linear system identification via an asymptotically stable observer. *Journal of Optimization Theory and Application, 79*(1), 59–86.
8. Chen, C. W., Huang, J.-K., & Juang, J.-N. (1995). Identification of linear stochastic systems through projection filters. *Journal of Guidance, Control and Dynamics, 18*(4), 767–772.
9. Chen, C. W., Juang, J.-N., & Huang, J.-K. (1993). Adaptive linear identification and state estimation. Control and dynamics systems: Advances in theory and applications. In C. T. Leondes (Ed.), *Multidisciplinary engineering systems: Design and optimization techniques and their application* (Vol. 57, pp. 331–368). New York: Academic Press, Inc.
10. Juang, J.-N. (1994). *Applied system identification*. Upper Saddle River, NJ: PRT Prentice-Hall Inc.

Chapter 124
Emerging Scenarios Avoidance Policy for Railroad Level Crossing Traffic Control Systems

Yi-Shun Weng, Yi-Sheng Huang and Bo-Yang Chen

Abstract Timed Petri nets (TPNs) are useful for performance evaluation discrete event systems due to their mathematical formalism. This paper proposes to use TPNs to model parallel railroad level crossing traffic safety control systems. Double-track railroad lines by using TPNs are illustrated. The resulting models allow one to identify and thus avoid critical scenarios in such systems by conditions and events of the model that control the phase of traffic light alternations. Their analysis is performed to demonstrate how the models enforce the phase of traffic transitions by a reachability graph with timed information method. The liveness and reversibility of the proposed model are verified. This helps advance the state-of-the-art in traffic safety related to the intersection of railroads and roadways.

Keywords Timed petri net · Discrete event system · Traffic control system

124.1 Introduction

As the number of vehicles grows sharply, traffic congestion and transportation delay on urban arterials are increasing worldwide; hence it is imperative to improve the safety and efficiency of transportation. Subsequently, several research

This work was supported in part by the National Science Council of Taiwan under Grant NSC 102-2221-E-197-022-MY2.

Y.-S. Weng
Department of Electronic Engineering, Army Academy, Taoyuan 32093, Taiwan, Republic of china

Y.-S. Huang (✉) · B.-Y. Chen
Department of Electrical Engineering, National I-Lan University, I-Lan 260, Taiwan, Republic of china
e-mail: yshuang@niu.edu.tw

J. Juang et al. (eds.), *Proceedings of the 2nd International Conference on Intelligent Technologies and Engineering Systems (ICITES2013)*, Lecture Notes in Electrical Engineering 293,
DOI: 10.1007/978-3-319-04573-3_124,

teams focus their attention on the area of intelligent transportation system (ITS) [1]. Recently, Huang [2] proposed to use STPNs to design an urban traffic light controller that included eight-phase, six-phase and two-phase. Although [2] proposed a solution of the urban traffic light system, it did not consider railroad level crossing control systems. An intersection of a railway and a road on the same level, called *railroad level crossing*, can be found in busy cities.

Here, the vehicles heading are perpendicular to the crossing zone, called direct critical scenario. On the other hand, the vehicles heading are parallel with the crossing zone, called indirect critical scenario. Generally, traffic signals are usually used to manage conflicting requirements for the use of road space—often at road junctions—by allocating the right of way to different sets of mutually compatible traffic movements during distinct time intervals. However, critical scenarios happen when the road traffic light signals cannot be changed according to the train passing automatically. Hence, it is a significant issue to control traffic lights in parallel railroad level crossing control systems.

This paper presents a parallel railroad level crossing traffic control system that has two-phase traffic lights. For convenience, the two-phase lights are modeled with a fixed number of discrete time intervals by TPNs. And also the railroad level crossing system is modeled by TPNs that allows both zero-time-consuming transitions (called immediate ones) and timed one with exponentially distributed random delay. It is interesting that some critical scenarios could happen immediately while a train is approaching the parallel railroad crossing, called crossing zone in this paper. For example, a green traffic light is going on and a train is entering the crossing zone at the same time, resulting in a critical scenario. Therefore, it is an important issue how to evaluate the safety control policy for the parallel railroad level crossing control systems. This work proposes a new way to avoid the critical scenarios from being taken. Then the traffic safety can be guaranteed. In particular, PN toolbox [3] is used to extract the critical scenarios from such system. Reachability analysis is performed to ascertain the liveness, boundedness and reversibility of the developed model.

124.2 Basic of Timed Petri Nets

A Petri net is a particular kind of bipartite directed graphs populated by three types of objects. They are places, transitions, and directed arcs connecting places to transitions and transitions to places [4]. In a PN, it is natural to associate with a place a state which has some duration and to associate with a transition a change of state, this change having no duration. It is then natural to associate the duration of some operation or state with a place, and the time of waiting for an event to the transition to be fired when it occurs. Basically, two models of TPNs can be used; time is associated with the places or with the transitions. Transfers are possible form one to one model to another. In this paper, TPNs are with timings associated with transitions. TPNs allow three types of transitions: (1) immediate one that is

represented by a thin bar and its firing takes no time; (2) random one that is represented by empty bars and its firing takes an exponentially distributed delay; and (3) deterministic one that is represented by empty bars and its firing takes a constant delay. Formally, a TPN can be defined as follows:

TPN = (P, T, I, O, H, M_0).

- $P = \{p_1, p_2, \ldots, p_m\}$ a finite set of places that can be marked with tokens.
- $T = T_{imm} \cup T_{exp} \cup T_{det} = \{t_1, t_2, t \ldots, t_n\}$ a finite set of transitions, partitioned into three disjoint sets, T_{imm}, T_{exp} and T_{det}, representing immediate, exponential, and deterministic ones, respectively. $P \cup T \neq \phi$, and $P \cap T = \phi$.
- I: $P \times T \rightarrow N$ is the input function that defines directed arcs from places to transitions.
- O: $P \times T \rightarrow N$ is the output function that defines directed arcs from transitions to places.
- H $\subseteq$ P $\times$ T a set of inhibitor arcs from p to t.
- M_0: $P \rightarrow N$ is an initial marking.

124.3 Modeling Track Line of Railroad Level Crossing System

An intersection of a railway and a road on the same level is called a railroad level crossing. In [5] deal with a particular phenomenon which may cause collisions at level crossings (LCs), and which corresponds to the accumulation of vehicle waiting queues on the LCs exit zone. However, they emphasize more particularly the phenomenon of a traffic jam in the LC exit zone and goal is to evaluate the collision risk on LCs induced by these circumstances.

Considering the safety of the double-track line railway traffic, two pairs of sensors are needed. The detailed configuration is depicted in Fig. 124.1. The function of the two pairs of sensors is as follows. One pair of sensors (A_1 and A_2) are used to detect the heading southbound trains. The second pair (B_1 and B_2) detect the heading northbound trains. For convenience, sensors A_1, A_2, B_1, and B_2 are set to correspond to transitions t_7, t_{11}, t_{15}, and t_{13}, respectively. Places p_{21}, p_{20} and p_{19} are used to model the barriers, red right, and green light, respectively.

Figure 124.1 shows a double-track railway system that always involves running one track in each direction. The double railroad track system allows the trains running in a direction for each track. To model a double railroad track system, the capacity of p_{17} is assigned two tokens. Figure 124.1 states that the system allows the two different heading trains to pass through the crossing zone concurrently. The inhibited arcs are able to avoid being hit by two trains on the same way.

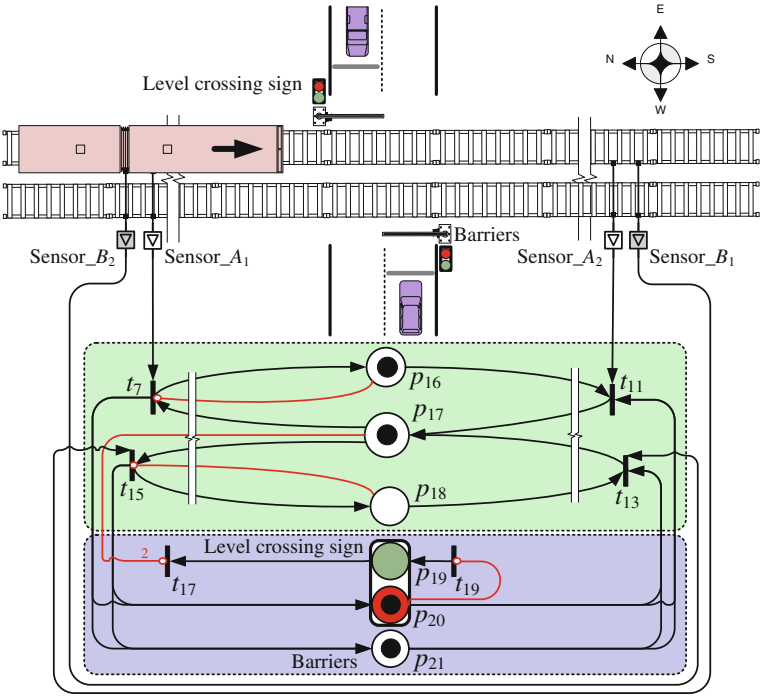

Fig. 124.1 A railroad level crossing model of a double-track line

124.4 Extraction of Emerging Scenarios

Emerging scenarios can happen at a railroad level crossing, especially when a road interacts with a parallel railroad crossing on the same level. To extract them, one has to deal with railroad level crossing control systems carefully. This study focuses on how to prevent a traffic jam on the level crossing-zone from being happened.

124.4.1 Three Indirect Emerging Scenarios

Places R_{we} and R_{ns} are marked: At this moment (i.e. Fig. 124.4), both the red lights are on. It is worthy to notice that the token of p_9 is used to ensure the duration of the traffic lights. Therefore, the traffic safety can be guaranteed while a train is passing through the crossing zone. The reachability graph with the priority information is as shown in Fig. 124.2 indeed proves that the system model is live and reversible. Obviously, $R(M_{0a}) = \{M_{0a}, M_1, M_2, M_3, M_4, M_5, M_{11}, M_{12}, M_{13}\}$. The circle I is normally run after the train passes through the crossing zone. The circle II will go back to the initial one while a train is approaching the crossing zone again.

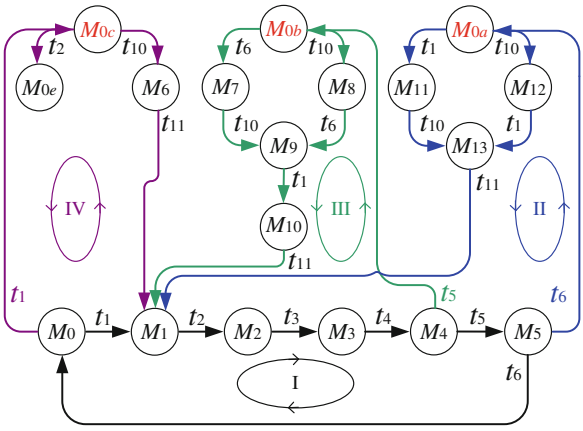

Fig. 124.2 A reachability graph of three indirect emerging scenarios TPN model

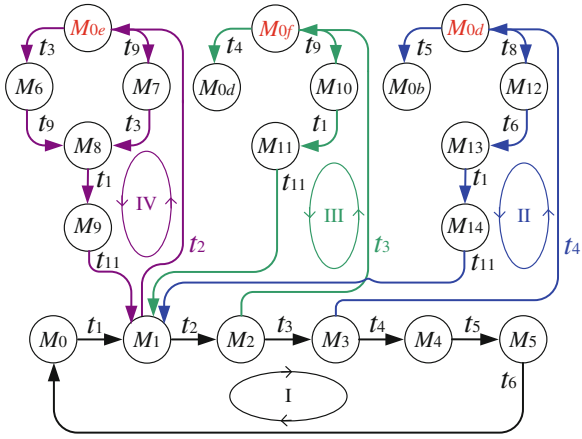

Fig. 124.3 A reachability graph of three direct emerging scenarios TPN model

Places R_{ns} and Y_{we} are marked: At this moment, the yellow light (place Y_{we}) that goes on while a train is entering the crossing zone. In this case, the proposed system model does not seem to do any control work, because the traffic light should be changed to red soon. The reachability graph is circle III in Fig. 124.2. Obviously, $R(M_{0b}) = \{M_{0b}, M_1, M_2, M_3, M_4, M_7, M_8, M_9, M_{10}\}$.

Places R_{we} and G_{ns} are marked: At this moment, the traffic light signals red (place R_{we})/green (place G_{ns}) along the east-westward/south-northward traffic direction. Then a conflict problem happens. As a result, the critical scenario can be avoided by our traffic control system. Case IV (firing t_2) is the same as discussed (Fig. 124.3). Next, direct critical scenarios are discussed, especially, when a green light is on at a crossroad-left traffic light system. At this moment, a train is approaching the crossing zone. Here, the reachability graph shows $R(M_{0c}) = \{M_{0c}, M_{0e}, M_0, M_1, M_2, M_3, M_4, M_5, M_6\}$.

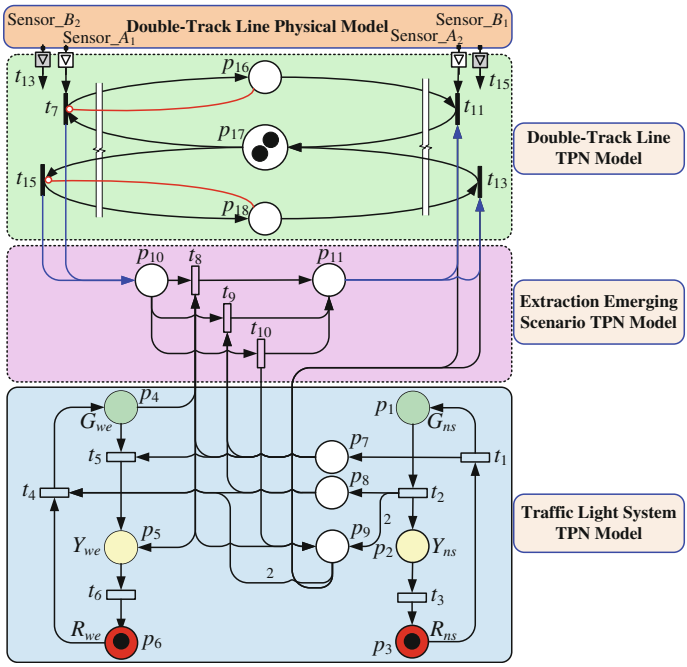

Fig. 124.4 The whole system TPN model of double-track line

124.4.2 Three Direct Emerging Scenarios

Places R_{ns} and G_{we} are marked: Fig. 124.3 shows a direct critical scenario. It states that the green light (i.e. place G_{we}) goes on while a train is entering the crossing zone. It also implies that this case is safe. Its reachability graph is shown in Fig. 124.3 and $R(M_{0d}) = \{M_{0d}, M_{0b}, M_1, M_2, M_3, M_{12}, M_{13}, M_{14}\}$.

Places R_{we} and Y_{ns} are marked: At this moment, the red light (R_{we}) is changing to green (G_{we}) while a train is approaching the crossing zone. It would be a very critical scenario if the traffic lights were not controlled. However, the critical scenario can be avoided by our traffic control system. In this case, $R(M_{0e}) = \{M_{0e}, M_1, M_6, M_7, M_8, M_9\}$ is obtained.

***Places R_{ns} and R_{we} are marked* (*change phase*)**: At this moment, the red light (R_{we}) should be changed to green while a train is entering the crossing zone. As a result, the direct dangerous scenario can be avoided. In this example, the reachability graph shows $R(M_{0f}) = \{M_{0f}, M_{0d}, M_1, M_2, M_{10}, M_{11}\}$.

124.4.3 The Whole System Model for Double-Track Line

A railway system with double-track line is considered. Usually, trains run on the same track when the trains are heading to the same direction. This work constructs a double-track line system model by extending the single-track one. It is obtained as shown in Fig. 124.4. The capacity of places p_9, p_{10} and p_{11} were modified from one to two and change the weight of arcs (i.e. $t_2 \rightarrow p_9$ and $p_9 \rightarrow t_4$) from one to two. In Fig. 124.4, the red light (R_{we}) is changing to green (G_{we}) while a train is approaching the crossing zone. The token of p_9 can be removed if t_9 fires. Once train leaves, the place p_9 is empty. It is worthy to notice that an arc ($p_9 \rightarrow t_9$) is used to describe how to ensure the system operation well while the train is leaving. It states that the system model allows two trains approaching the crossing zone concurrently whatever the heading directions of the trains are.

124.5 Conclusion

This work proposes TPNs models for the parallel railroad level crossing systems. It is worthy to notice that the concept of hybrid systems is used in the proposed models. It is important to point out that the emerging scenarios can be identified accurately from the proposed models. The advantage of approach is that the emerging scenarios in the parallel railroad level crossing system can be avoided by extraction emerging scenario TPN model.

References

1. Kim, W., Liu, Y., & Chang, G. (2012). Advanced traffic management system. *Journal of the Transportation Research Board, 2324*, 91–100.
2. Huang, Y. S., Weng, Y. S., & Zhou, M. (2013). Modular design of Urban traffic light control systems based on synchronized timed Petri nets. *IEEE Transaction on Intelligent Transportation Systems*, *98*, 1–10.
3. Matcovschi, M. H., Mahulea, C., Lefter, C., & Pastravanu, O. (2006). Petri net toolbox in control engineering education. In *Proceedings of IEEE Conference on Computer Aided Control Systems Design.* (pp. 2298–2303). Munich, Germany.
4. Hruz, B., & Zhou, M. (2007). *Modeling and control of discrete event dynamic systems*. London, UK: Springer.
5. Ghazel, M. (2009). Using stochastic Petri nets for level-crossing collision risk assessment. *IEEE Transaction on Intelligent Transport System, 10*, 668–677.

Chapter 125
Integrated Control System Development for a Series Hydraulic Hybrid Vehicle

Tri-Vien Vu, Chih-Keng Chen, Chih-Wei Hung and Trung-Dung Chu

Abstract This paper presents the development and implementation of a PID-based control system for a series hydraulic hybrid propulsion system. At first, a configuration of the system is discussed and modeled in MATLAB/Simulink environment. Then, based on the established model, a two-level control system is developed. Monitoring demands from driver and current states of the system, the top-level controller sends out appropriate demands for the component-level controllers to meet the driver requests under any condition. Performance of the control system is evaluated in different situation of driver demand. The established model provides an efficient tool for control system development. The robustness of the proposed control system allows developing and evaluating the benefit of different power management strategies for the series hydraulic hybrid propulsion system.

Keywords Control system · Series hydraulic hybrid · Simscape · Supervisory control

125.1 Introduction

In all types of hybrid vehicles, the main function of supervisory controller is to coordinate multiple power sources to satisfy the power demand of the driveline with minimum fuel consumption in the most convenient way. In general, control strategies of the hybrid propulsion systems can be classified into three categories included rule-based, semi-optimal, and global optimal. Among of them, the rule-based control strategy is a real-time implementable power management.

T.-V. Vu · C.-K. Chen (✉) · C.-W. Hung · T.-D. Chu
Department of Mechanical and Automation Engineering, Dayeh University, Changhua 51591, Taiwan, Republic of China
e-mail: ckchen@mail.dyu.edu.tw

J. Juang et al. (eds.), *Proceedings of the 2nd International Conference on Intelligent Technologies and Engineering Systems (ICITES2013)*, Lecture Notes in Electrical Engineering 293,
DOI: 10.1007/978-3-319-04573-3_125,

In this kind of control strategy, several rules are utilized to determine the control output according to pre-set conditions. Most papers regarding rule-based control strategy for hydraulic hybrid vehicle used the State-Of-Charge of accumulator as the sole state variable for engine power determination [1–3]. However, these papers have not provided the detail of the control system implementation.

In [4] Matheson and Stecki developed a fuzzy logic controller (FLC) for a parallel hydraulic hybrid vehicle used backward facing model approach. Utilized the power split concept, the FLC decided the best suit operating point of the engine corresponded to the acceleration demand and system states. The established system allowed developing control strategy and estimating fuel consumption. However, the control strategy could not be implemented to the actual system since ADVISOR [5] is a backward facing simulation.

In this work, a physical-based, forward simulation model of a Class II light-duty series hydraulic hybrid vehicle (SHHV) was established utilized components from the Simscape library of MATLAB/Simulink. Based on this model, a control system was developed. A decision-making sub-system (supervisory), which selects activation condition for the engine, was designed using some basic logic blocks. Three individual PID controllers were also utilized to handle the operation of the main components of the proposed system. Performance of the control system was investigated under different input commands.

125.2 System Configuration and Modeling

This paper proposes a configuration of a light-duty hydraulic hybridized truck. Brief layout the system is as shown in Fig. 125.1. In this configuration, diesel engine E was coupled to hydraulic pump P1. P/M unit P2 was connected to the rear wheels through differential DF. High pressure accumulator A1 functions as a secondary power source of the system. Another hydraulic accumulator A2 works as a reservoir in which the fluid was kept at low pressure. This component enables the fluid transfer within the hydraulic components.

Successful modeling of the system is a prerequisite to investigate the benefit of the design and control policy of a new propulsion concept. In this work, the complete model of the proposed system was implemented in Matlab/Simulink environment. The components were selected from the Simscape package. The complete model is as shown in Fig. 125.2. The detail of components selection and parameters setting can be found in [6, 7].

Based on the established model, the Simulink forward looking simulation of the SHHV is developed as shown in Fig. 125.3. The control system was divided into two parts. The top-level part is a supervisor controller and the low-level part is three PID controllers. In essence, the supervisor controller monitors the driver demands and the system state to send out the appropriate commands to the lower controllers. In this scheme, the input from driver consisted of three signals: the desired engine power, the working mode, and the desired vehicle speed.

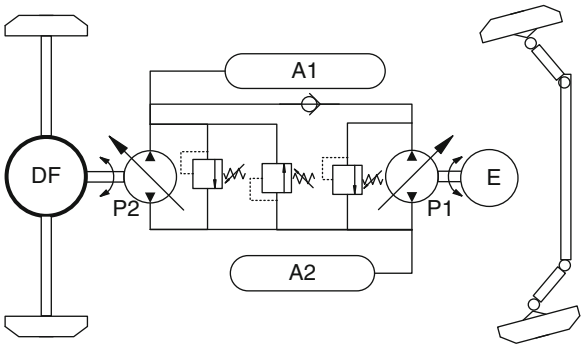

Fig. 125.1 Rear-wheel-drive series hydraulic hybrid configuration

Since the engine is decoupled from the wheels, theoretically, it can operate at any desired operating point. In this scheme, the engine is controlled to operate at desired working power when it is activated and at idle mode when it is deactivated. The desired working power of the engine can be selected heuristically or experimentally. To evaluate the performance of the control system, the working power of the engine and the working mode of the control system were assumed setting by driver manually.

One of the main functions of the supervisor controller is to determine the working mode of the engine, by which different power sources were coordinated. From the power demand, the desired engine speed was interpolated from a 1D-lookup table. Then the desired engine torque was estimated. Based on the selected working mode and the current pressure of the hydraulic system, the control system activated the engine to work in corresponded condition. Five different engine activation conditions are described in Table 125.1. More details about the control strategy development based on the method of engine activation can be found in [8].

Three PID controllers are corresponded for Engine, Pump P1, and Pump/Motor P2 components. The P2 controller was used to generate the desired displacement of P/M P2 to ensure that the vehicle speed is followed the demand one. By controlling the displacement of the pump P1, the load torque of the engine would be changed. Hence, the output torque of the engine could be forced to the desired value. Meanwhile, the engine speed was adjusted to the desired value by controlling the fuel-mass flowed into the combustion chamber of the engine. In this works, the fuel mass was assumed to be handled by controlling the throttle opening position approximately. When the torque and the speed of the engine approached to the desired values, the desired power working of the engine would be satisfied.

The transfer function of a PID controller is given as below.

$$G(s) = K\left(1 + \frac{1}{T_i s} + T_d s\right) \tag{125.1}$$

where K is proportional gain, T_i is integral time, and T_d is derivative time. For more convenient, all output of the PID controllers are normalized, then the control signal for the engine is the throttle opening factor, for the hydraulic pumps are the

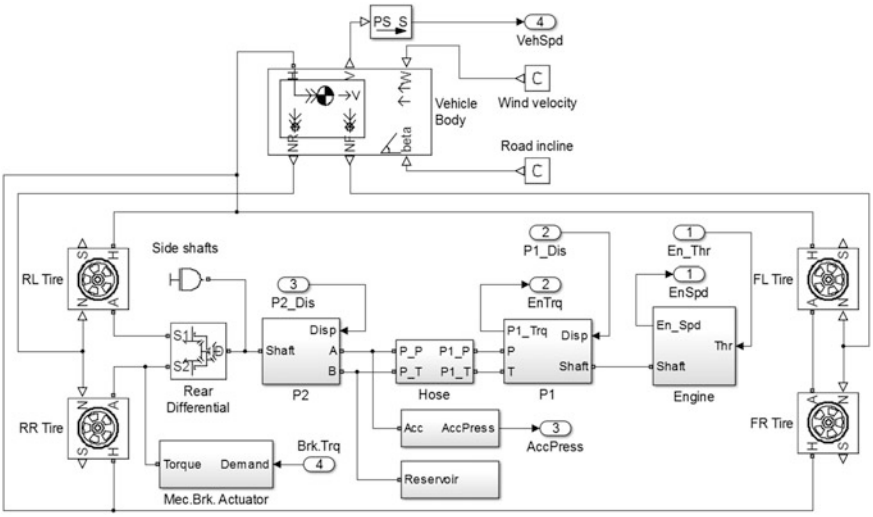

Fig. 125.2 Simulink model of the SHHV

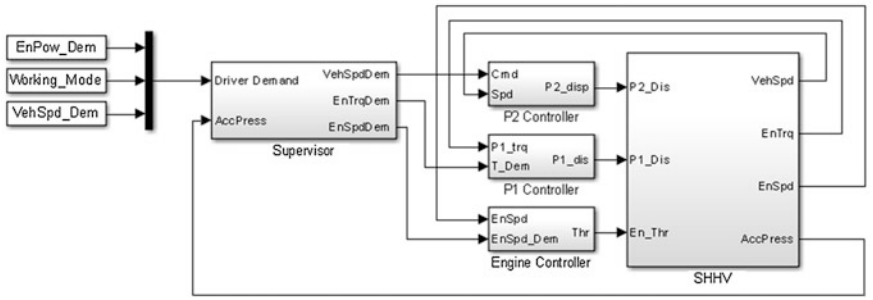

Fig. 125.3 Layout of the SHHV with the control system

Table 125.1 System working mode situation

No.	Engine activate when
1	$V_{dem} > 0; a_{dem} \geq 0; p_L \leq p_{acc} \leq p_H$
2	$p_L \leq p_{acc} \leq p_H$
3	$a_{dem} \geq 0; p_L \leq p_{acc} \leq p_H$
4	$a_{dem} \geq 0$
5	$V_{dem} > 0; a_{dem} \geq 0$

Note V_{dem} and a_{dem} are vehicle demand speed and acceleration respectively; p_L and p_H are the threshold values of the relay block; and p_{acc} is the current pressure of A1

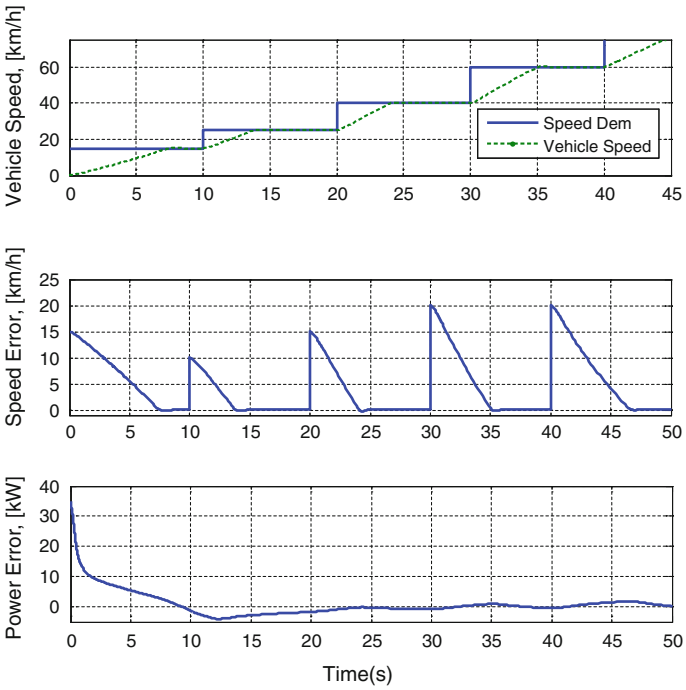

Fig. 125.4 Vehicle speed and engine power error when the vehicle load changed

displacement factor. In a continuous-time system, these factors can be approximate as follow.

$$x(t) = K_p e(t) + K_I \int_0^t e(\tau)d\tau + K_D \frac{de(t)}{dt} \tag{125.2}$$

where *e(t)* is the current error between the set-point and the output, K_p, K_I, K_D are the P, I, D gains, respectively.

125.3 Control System Implementation

To assess the performance of the control system, two simulation cases were carried out. In the first case, the engine was desired to work at the power of 35 kW, the vehicle was demanded to reach the cruising speed of 15 km/h. Then, the cruising speed set to the new value after each 10 s. In the second situation, the driver tried to reach the cruising speed of 50 km/h and the power demand was set to different values: 15, 25, and 45 kW.

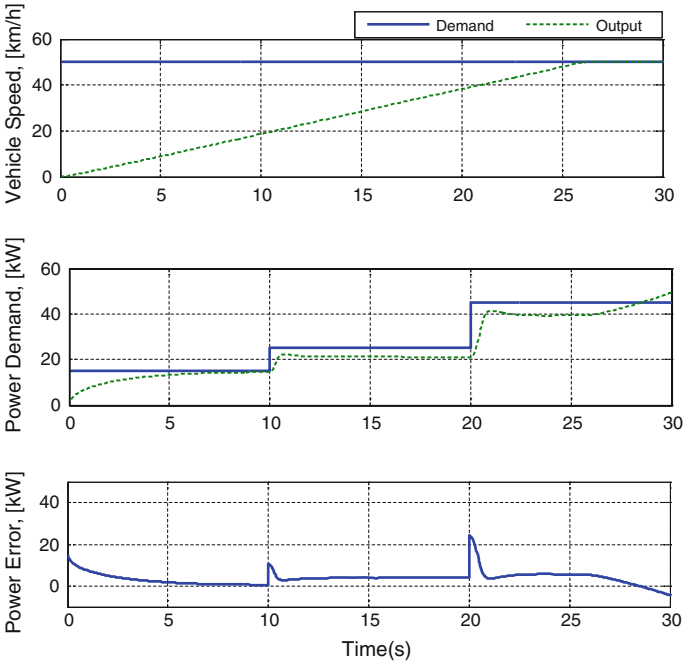

Fig. 125.5 System behaviors in the second situation

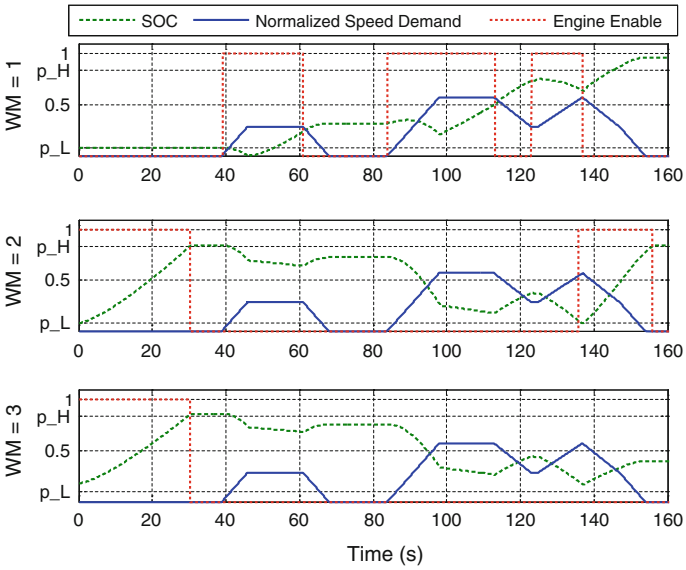

Fig. 125.6 Engine activation state and accumulator pressure under different working modes. *Note WM* Working-mode; *SOC* State-of-charge

The behaviors of the system were as shown in Figs. 125.4 and 125.5 below. The transient of vehicle speed was caused by the limitation of hydraulic pressure and the pump/motor displacement. It can be seen from the lowest part of Fig. 125.5 that the engine operated near the desired power demand. After a short transient time, the error between power demand and engine output power was closed to zero.

In each working mode, the engine was activated under certain condition. In the first working mode, the engine was activated when the vehicle started moving and/or the accumulator pressure was within the thresholds. The engine was deactivated if the brake command occurred. Other two working modes were descripted by Fig. 125.6.

125.4 Conclusion

In this paper, a complete model of SHHV has been established. One supervisor and three individual PID controllers have been implemented and evaluated in different working conditions. The performance of the proposed control system can be improved by using advance parameter tuning techniques. The obtained model and control system provides an efficient tool for fast and effective parameter optimization of series hydraulic hybrid vehicles. The established model also can be used to develop various power management strategies as well as advanced control system.

Acknowledgments This work is supported by the National Science Council under Grant NSC 102-2221-E-212-004.

References

1. Wu, B., Lin, C–. C., Filipi, Z., Peng, H., & Assanis, D. (2004). Optimal power management for a hydraulic hybrid delivery truck. *Vehicle System Dynamics, 42*, 23–40.
2. Kim, Y., & Filipi, Z. (2007). Series Hydraulic Hybrid Propulsion for a Light Truck—Optimizing the Thermostatic Power Management, SAE Technical Paper 2007-24-0080, (2007).
3. Tavares, F., Johri, R., Salvi, A., & Baseley, S. et al. (2011). *Hydraulic hybrid powertrain-in-the-loop integration for analyzing real-world fuel economy and emissions improvements, SAE technical paper* 2011-01-2275.
4. Matheson, P. L., & Stecki, J. S. (2003). *Modeling and simulation of a Fuzzy Logic Controller for a Hydraulic-Hybrid Powertrain for use in Heavy Commercial Vehicles. SAE paper* 2003-01-3275.
5. Markel, T., Brooker, A., Hendricks, T., et al. (2002). Advisor: A systems analysis tool for advanced vehicle modelling. *Journal of Power Sources, 10*(2002), 255–266.
6. Mathworks. SimScape documentation, Retrieved from http://www.mathworks.com/help/phys-mod/simscape

7. Vu, T. V. (2011). Simulation and design of hydraulic hybrid vehicle (Master's thesis, Da-yeh University, 2011).
8. Chen, C. K., Vu, T. V., Hung, C. W., & Wang, C. S. (2013). Control strategies development for a series hydraulic hybrid vehicle based on engine experimental map. *Lecture Notes in Electrical Engineering, 234*, 337–343.

Chapter 126
Adaptive Zero-Phase Filtering Bandwidth of Iterative Learning Control by Particle Swarm Optimization

Yi-Wei Su, Jen-Ai Chao and Yi-Cheng Huang

Abstract This paper utilized the improved particle swarm optimization (IPSO) technique for adjusting the gains of PID controller, Iterative Learning Control (ILC) and the bandwidth of zero-phase Butterworth filter of ILC. The conventional ILC learning process has the potential to excite rich frequency contents and try to learn the error signals. However the learnable and unlearnable error signals should be separated for bettering control process as repetition goes. Producing unlearnable frequencies for error compensation signals should be avoided when the filter bandwidth is not changed at every repetition. Thus the adaptive bandwidth in ILC with the aid of IPSO tuning is proposed here. Simulation results show the controller can cancel the errors as repetition goes. The frequency response of the error signals is verified by the Hilbert Huang Transform (HHT) method. Tracking errors are reduced and validated with application to positioning profile of the Computer Numerical Control (CNC) machine tool and robot arm systems.

Keywords Particle swarm optimization · ILC · Zero phase filter

126.1 Introduction

Conventional PID controllers are widely applied in control systems. Kennedy and Eberhart introduced PSO in 1995 [1]. ILC aims to iteratively reduce the tracking error, over a finite time interval, by incorporating past experience in the actual

Y.-W. Su · Y.-C. Huang (✉)
Department of Mechatronics Engineering, National Changhua University of Education, Changhua 50007, Taiwan, Republic of China
e-mail: ychuang@cc.ncue.edu.tw

J.-A. Chao
Chienkuo Technology University, Changhua 50007, Taiwan, Republic of China

J. Juang et al. (eds.), *Proceedings of the 2nd International Conference on Intelligent Technologies and Engineering Systems (ICITES2013)*, Lecture Notes in Electrical Engineering 293,
DOI: 10.1007/978-3-319-04573-3_126,

control input. Huang and coworkers [2] developed a new approach to signal analysis to avoid generating unphysical results from the Complex Trace formalism. The Complex Trace formalism defines the concepts of instantaneous amplitude, phase, and frequency such that the original signal can be expressed in terms of a Fourier-like expansion based on these concepts. Researchers have used HHT in numerous applications, including fault diagnosis in electrical machines, rolling bearing failure analysis in mechanical engineering, and brain activity signal monitoring in bioengineering [3]. This study utilized the bounded particle space constraints technique of IPSO [4] to improve the velocity updating performance and position updating capability. Error patterns are decomposed using HHT for illustrating the unlearnable error signals that can be reduced at next repetition for bettering control process.

126.1.1 Particle Swarm Optimization

Based on a flock of flying birds, the PSO algorithm simulates the behavior of a swarm as a simplified social system. Since each particle remembers its worst experience, it can explore the search space effectively to identify the most promising solution region. The PSO algorithm is expressed as follows:

$$V_{id}(t) = w \times V_{id}(t-1) + c1 \times \text{Rand}() \times (P_{id} - X_{id}) + c2 \times \text{Rand}() \times \left(P_{gd} - X_{id}\right) \tag{126.1}$$

$$X_{id}(t) = X_{id}(t-1) + V_{id}(t) \tag{126.2}$$

where $V_{id}(t)$ is the current velocity of i particle, $i = 1, \ldots, n$ in which n is the population size; the subscript d is the dimension of the particle; p_{id} is the best previous position of the ith particle; p_{gd} is the best previous position among all the particles in the swarm; and x_{id} is the current position of the ith particle. The constants C_1 and C_2 represent the weighting of the stochastic acceleration terms pulling each particle toward P_{id} and P_{gd} positions. Low values allow particles to roam far from the target regions before being tugged back. On the other hand, high values result in abrupt movement toward, or past, target regions. A parameter called inertia weight w can help balance the global and local search.

126.1.2 Iterative Learning Control

In ILC, the input update utilizes the previous error signal and the learning law is termed P-type ILC. The control algorithm for simplified systems can be represented as:

$$u_{j+1}(kT) = u_j(kT) + \phi Q(z) e_j(kT) \tag{126.3}$$

$$e_j(kT) = y_d(kT) - y_j(kT) \tag{126.4}$$

where $u_{j+1}(kT)$ represents the input at time k and iteration j, $e_j(kT)$ is the difference between the actual output and the desired output at time k and iteration j, and ϕ is the learning gain. P-type ILC is a simple but effective law. The convergence condition for the P-type [5], is

$$\left\|1 - \varphi Q_{zero-phase-filter}(Z) G_{plant}(Z)\right\|_\infty < 1 \tag{126.5}$$

126.1.3 Hilbert-Huang Transform

HHT introduced a new signal analysis technique based on the decomposition of a signal in terms of empirical modes. This method formulates a signal, *X(q)*. The signal contains the process of Intrinsic Mode function (IMF) $c_j(q)$ and the residue R_n of the signal trend. Thus, the signal, *X(q)*, is given by the sum.

$$X(q) = \sum_{j=1}^{n} c_j(q) + R_n \tag{126.6}$$

126.2 Numerical Simulations

To verify proposed method, the first simulated plant (G_1) is a transfer function of a one motion axis of Table CNC [6]. The second one (G_2) is the link of a robot performing a high speed maneuver [7]. The trajectory shape in Fig. 126.1 is close to the real speed or positioning profile. The cycloid in rising height h and accelerated duration from θ to constant height duration β is defined as follows:

$$y = \frac{h}{2\pi}\left[\frac{2\pi t}{\beta} - \sin\frac{2\pi t}{\beta}\right], \text{with} \quad h = 1 \ \text{ and } \ \beta = 5 \tag{126.7}$$

$$G_1(s) = \frac{8.05 \times 10^5 s + 5.233 \times 10^7}{s^4 + 169s^3 + 6.573 \times 10^4 s^2 + 3.421 \times 10^6 s + 5.233 \times 10^7} \tag{126.8}$$

$$G_2(s) = \frac{10780}{(s^3 + 43.8s^2 + 1533s + 10780)} \tag{126.9}$$

Figure 126.2 shows the control block diagram for IPSO-PID-ILC-Filter controller. The comparisons of fixed bandwidth at 30 Hz, stop updating tuning bandwidth at repetition 5 and updating filter bandwidth at every repetition are shown in Table 126.1 for $G_1(s)$ system. Table 126.2 shows the bandwidth variations of the fixed gain, stop updating tuning at repetition 5 and proposed updating

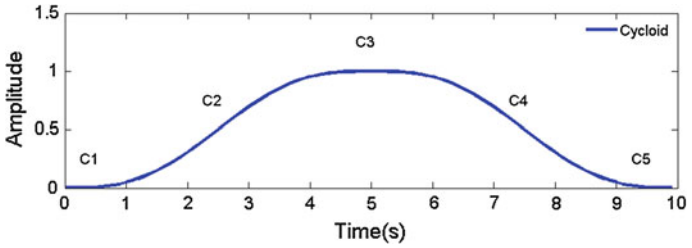

Fig. 126.1 The cycloid curve for numerical simulation

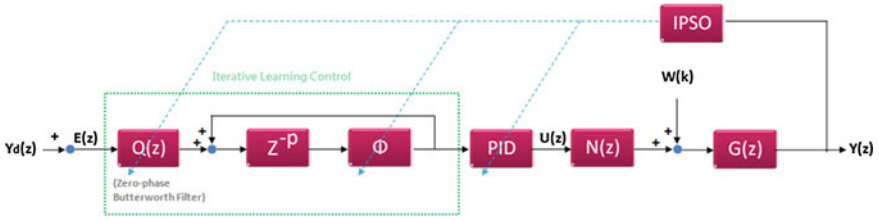

Fig. 126.2 Illustration for the IPSO-PID-ILC-Filter control block diagram

Table 126.1 Simulated RMS performance comparisons of fixed F_C, stop updating tuning bandwidth at repetition 5 and proposed updating filter bandwidth at every repetition

	K_P	K_I	K_D	ϕ	F_C (Hz)	RMS
IPSO-ILC-PID-fixed	0.249	0.130	2.569	0.944	30	3.73×10^{-4}
IPSO-ILC-PID-rep.5	0.525	1.604	3.215	1.035	11.91	3.10×10^{-5}
IPSO-ILC-PID-filter	8.584	1.423	3.238	0.897	30.19	2.92×10^{-5}

Table 126.2 Bandwidth variations of the fixed gain, stop updating tuning at repetition 5 and proposed updating zero-phase filter ILC controllers at every repetition

Command: 3.33 Hz	Rep 1	2	3	4	5	6	7	8	9	10
IPSO-ILC-PID-fixed	30	30	30	30	30	30	30	30	30	30
IPSO-ILC-PID-rep. 5	4.10	6.66	7.83	11.22	11.91	11.91	11.91	11.91	11.91	11.91
IPSO-ILC-PID-filter	1	6.43	12.44	8.36	13.37	10.68	4.02	17.14	18.34	30.19

zero-phase filter ILC. Figure 126.3 plots the RMS errors for $G_1(s)$ and $G_2(s)$ with different frequencies. The IPSO-ILC-PID-filter (the letter w in plot) controller produces less error than the others Tracking error of IPSO-ILC-PID control without filter design reveals the output delay with phase lag error in magnitude. The ILC law tries to excite new signals for every repetition. However, the new exciting signal added to the command in next repetition contains the learnable and un-learnable compensating profile. This command based P-type learning causes

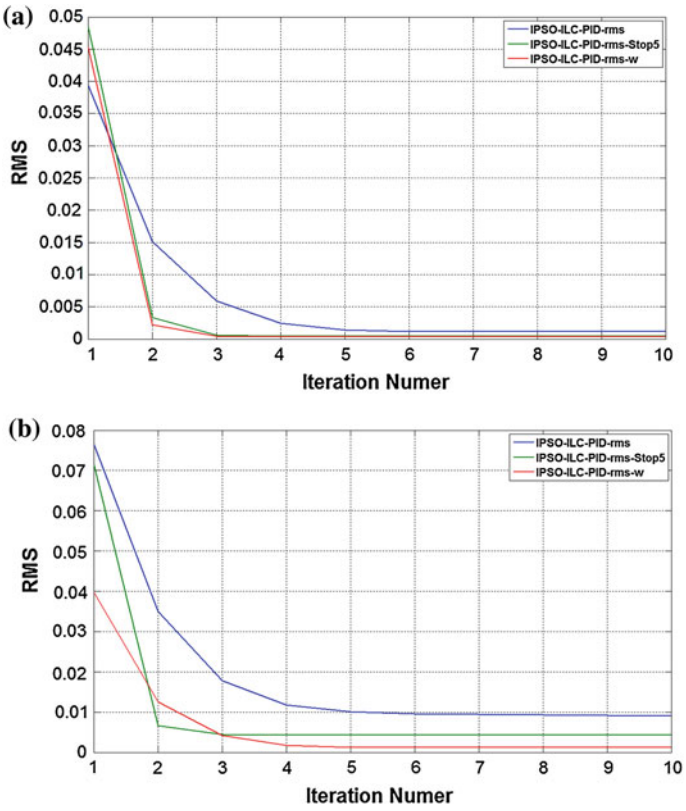

Fig. 126.3 **a** and **b**: The $G_2(s)$ RMS error of three controllers by 3.33 and 6.66 Hz

the updating profile embeds un-learnable signals when the bandwidth filter did not remove it at the last repetition process. Since at sufficient or relative high frequencies, there are some sources to produce errors if the filter bandwidth is not well tuned. Some main errors are in an intermediate frequencies range. Such less dynamic bandwidth adjustment without adaptive tuning renders the learning control converges slowly.

Figure 126.4 illustrates the first IMF time-frequency RMS error response of the $G_2(s)$ system in Fig. 126.3a. The recording tracking errors show the frequency spectrum from the first iteration to the third one. As shown, the frequency amplitude is reduced and suppressed at the high frequency when the adaptive bandwidth tuning mechanism is implemented. As the cut-off bandwidth frequency (F_c) changes from 9.5 to 13.3 Hz and 13.3 to 18.7 Hz, the associated frequency magnitudes are reduced thereafter.

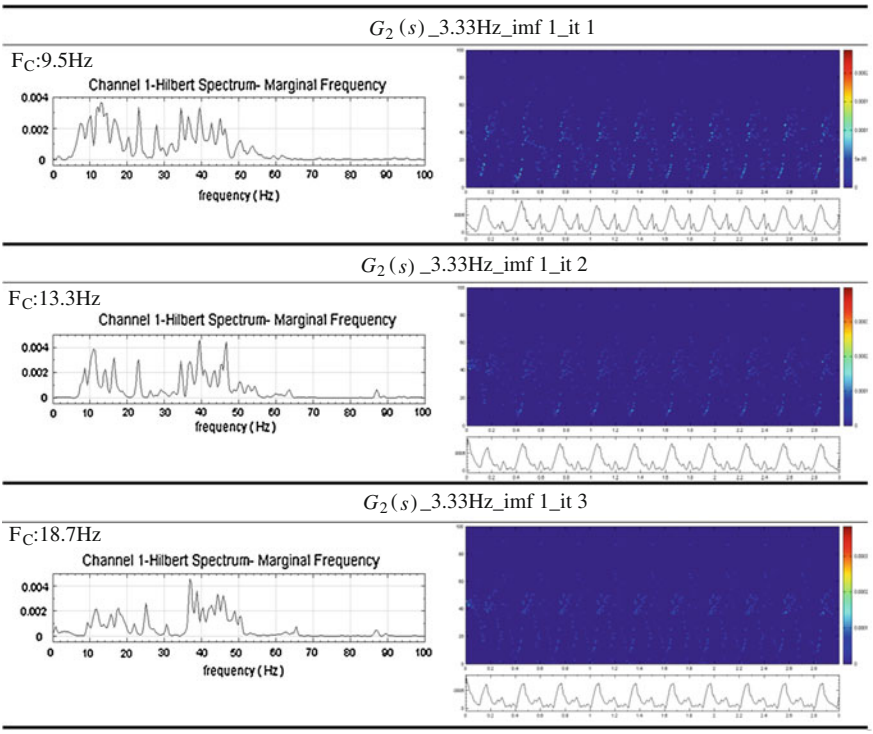

Fig. 126.4 Hilbert-Huang spectrum of the RMS tracking errors of the first IMF by IPSO-ILC-PID-filter controller

126.3 Conclusion

This paper utilized the IPSO technique for adjusting the gains of PID controller, ILC controller and the bandwidth of zero-phase Butterworth Filter. The proposed IPSO-ILC-PID-filter controller shows more bettering tracking control than the conventional IPSO-ILC-PID one. Simulation results show that IPSO-ILC-PID-filter controller will have chance of reducing the high frequencies in the error signals when the filter bandwidth is adaptive tuned at every repetition. The learnable and unlearnable error signals can be separated by each control process. Thus the adaptive bandwidth of a zero phase filter in ILC-PID controller with IPSO tuning characteristic shows potential in this research.

Acknowledgments This work is supported in part by NSC 102-2221-E-018-008.

References

1. Kennedy, J., & Eberhart, R. (1995). Particle swarm optimization. *Proceedings of IEEE International Conference on Neural Networks.* (pp. 1942–1948). Perth, Australia.
2. Huang, N. E., Shen, Z., Long, S. R., Wu, M. C., Shih, H. H., Zheng, Q., et al. (1998). The empirical mode decomposition and the Hilbert spectrum for nonlinear and non-stationary time series analysis. *Proceedings of the Royal Society, 454*, 903–995.
3. Antonino-Daviu, J., Jover Rodriguez, P., Riera-Guasp, M., Arkkio, A., Roger-Folch, J., & Perez, R. B. (2009). Transient detection of eccentricity-related components in induction motors through the Hilbert-Huang transform. *Energy Conversion and Management, 50*(7), 1810–1820.
4. Huang, Y. C., Li, Y. H., & Li, S. T. (2013). Design and experiment of iterative learning controller based on particle swarm optimization approach with new bounded constraints technique. *Journal of Applied Mechanics and Materials, 284–287*, 2233–2237.
5. Wang, D., & Ye, Y. (2005). Design and experiments of anticipatory learning control: Frequency domain approach. *IEEE/ASME Transactions on Mechatronics, 10*(3), 305–313.
6. Tsai, M. S., Yen, C. L., & Ya, H. T. (2011). Development of a novel iterative learning control algorithm using empirical mode decomposition technique. *IEEE International Conference on Mechatronics and Automation* (pp. 1828–1832). China.
7. Elci, H., Longman, R. W., Phan, M. Q., Juang, J.-N., & Ugoletti, R. (2002). Simple learning control made practical by zero-phase filtering: Application to robotics. *IEEE Transactions on Circuit and System I: Fundamental Theory and Applications, 49*, 753–767.

Chapter 127
Combining Event-Related Synchronization and Event-Related Desynchronization with Fuzzy C-Means to Classify Motor Imagery-Induced EEG Signals

Chi-Yuan Lin, Wei-Fan Chiang, Sheng-Chih Yang and Shu-Yi Huang

Abstract Various motor imagery processes produce distinct electroencephalography (EEG). In this study, C3 and C4 electrode were distributed on the scalp surface of a participant to record the event-related potential (left and right hand movement) produced during testing. The event-related synchronization (ERS) and event-related desynchronization (ERD) were analyzed, and energy values of the EEG produced during the event period were calculated and used as event features. Finally, a fuzzy C-means (FCM) classifier was used to classify eigenvalues, grouping the features of left and right hand movement in EEG signals.

Keywords Electroencephalography · BCI · Event-Related synchronization · Event-Related desynchronization · FCM

127.1 Introduction

Brain-computer interfaces (BCIs) facilitate direct communication and message delivery between people and computer interfaces. Because electroencephalography (EEG) reflects basic physiological signals exhibited by biological organisms, this technology can be applied to assist patients that demonstrate limited mobility or be conveniently operated by all users. When a user receives sensory stimulation or thinks, his or her brain activity produces event-related potentials (ERPs).

C.-Y. Lin · W.-F. Chiang (✉) · S.-C. Yang · S.-Y. Huang
Department of Computer Science and Information Engineering, National Chin-Yi University of Technology, Taichung 41170, Taiwan, Republic of China
e-mail: weifan@livemail.tw

J. Juang et al. (eds.), *Proceedings of the 2nd International Conference on Intelligent Technologies and Engineering Systems (ICITES2013)*, Lecture Notes in Electrical Engineering 293,
DOI: 10.1007/978-3-319-04573-3_127,

The features of these EEG signals can be extracted and analyzed, and the results transmitted to an external device to enable control and communication.

When people close their eyes and relax, their Mu rhythm is relatively prominent. However, Beta rhythms are distinct from Mu rhythms. Beta rhythms are changes that occur when preparing for motor action or conducting motor imagery. Mu and Beta rhythms are distributed at 8–12 and 13–30 Hz, respectively [1]. When the brain is concentrated on thinking, the Mu rhythm is suppressed; this is called event-related desynchronization (ERD). One second after the event ends, the Beta rhythm produces gains; this is called event-related synchronization (ERS) [2, 3]. This study explored classifying the features of BCIs by observing changes in the ERD and ERS of Mu and Beta rhythms. Data from a publicly available dataset from the 2003 BCI Competition II were analyzed to evaluate the EEG signals recorded during left and right hand motor imagery.

127.2 Materials

The data used in this study were collected from a publicly available dataset from the 2003 BCI Competition II; the dataset was provided by the Graz University of Technology [4].

The experimental participant was a healthy 25-year-old woman. During the testing period, the participant sat in a chair in a relaxed state. Feedback windows randomly appeared on a computer screen, illustrating figures representing left and right hand movement. Subsequently, the participant followed the prompts to conduct motor imagery. The overall dataset comprised seven experimental runs and 40 trials were conducted per run, yielding 280 items of trial data. All experiments were performed on the same day. To avoid fatiguing the participant and subsequently affecting the quality of the experiment, the participant periodically rested during the testing period. Each test lasted 9 s, and for the first 2 s of the test, the participant was in a relaxed state. At the 2 s mark ($t = 2$ s), the system sounded an audio prompt, notifying the participant that the experiment had begun. Next, a cross "+" symbol appeared on the screen for 1 s, prompting the participant to prepare to conduct motor imagery. At the 3 s mark ($t = 3$ s), the "+" symbol disappeared, changing into an arrow pointing left or right. Based on the direction of the arrow, the participant imagined left or right hand movement. The action continued until the 9 s mark, which indicated the end of the experiment. Figure 127.1 presents the experimental paradigm [4].

Experimental data were obtained using electrode pads distributed on the surface of the scalp. The dataset used C3, Cz, and C4 bipolar EEG channels [anterior (+) and posterior (−)], and the sampling frequency for the EEG signals was 128 Hz. The signals were filtered to between 0.5 and 30 Hz. C3 and C4 electrodes were located on the left and right hemispheres of the brain; Fig. 127.2 shows the electrode positions [4].

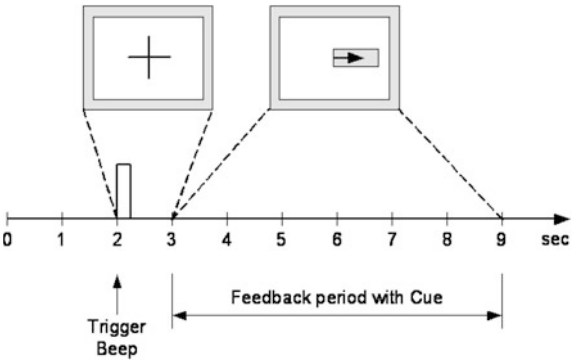

Fig. 127.1 The experimental paradigm of time scheme

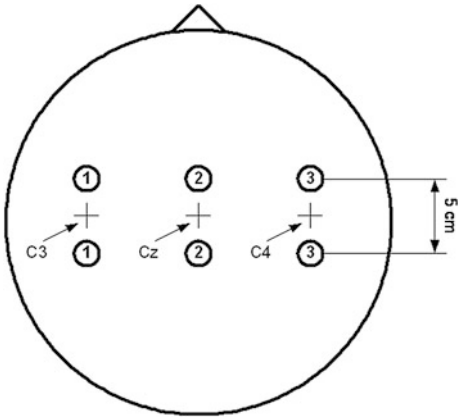

Fig. 127.2 Electrode positions

To prevent the system from influencing the results, the test results were equally and randomly allocated into training and testing samples after the experiment was concluded; this yielded 140 training samples with known classifications and 140 testing samples with unknown classifications.

127.3 Experimental Methods

127.3.1 Feature Extraction

The EEG signals from the data source were observed (Fig. 127.3) and the complete 9 s experiment is presented in waveform diagrams.

From 0 to 2 s (t = 0–2 s), the participant remained in a relaxed state. At the start of Second 3 (t = 3 s), the participant was prompted to conduct motor imagery until the experiment ended at Second 9 (t = 9 s). Figure 127.3 shows that

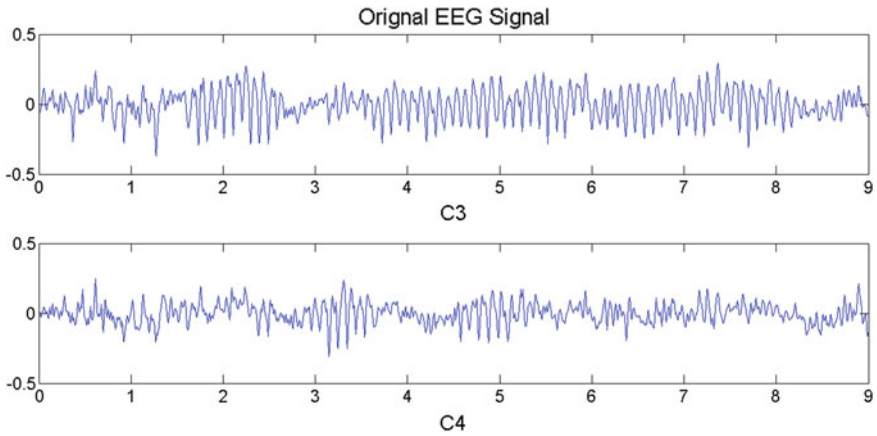

Fig. 127.3 Original EEG signal for left hand

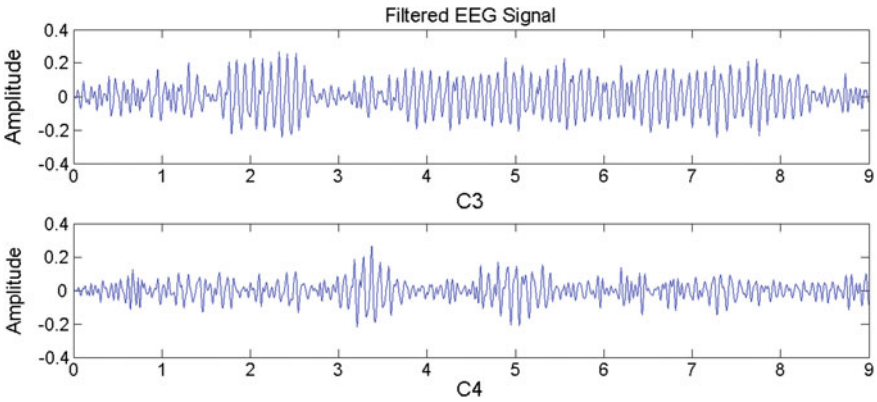

Fig. 127.4 Filtered EEG signal for the left hand

the event features were difficult to observe in unprocessed EEG signals. To clearly observe the motor imagery features of the participant during the test period, the EEG signals must be preprocessed.

A Butterworth filter was used to conduct band-pass filtering of the original EEG signals. The passband frequency was set at 8–30 Hz to retain the Mu and Beta rhythms. Figure 127.4 shows EEG signals at a sampling frequency of 128 Hz after band-pass filtering.

The filtered signals shown in the figures demonstrate that the ERS and ERD features were prominent when the participant conducted motor imagery. In the experiment, the position of the C3 and C4 electrode pads represented the sensorimotor area of the two brain hemispheres. When the participant conducted motor imagery, the Mu rhythm was suppressed; however, the Beta rhythm produced

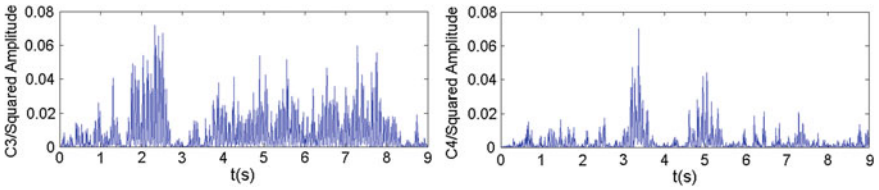

Fig. 127.5 Energy amplitude from imagined left hand movement

gains after the event ended. Furthermore, this phenomenon exhibits contralateral dominance; when the participant imagined left hand movement, ERS appeared in the left sensorimotor area, and ERD appeared in the right left sensorimotor area. Conversely, when the participant imagined right hand movement, ERD appeared in the left sensorimotor area, and ERS appeared in the right sensorimotor area.

This proved that the participant exhibited distinct eigenvalues for the two hand movement tests. Therefore, the signals obtained from the C3 and C4 channels were converted into energy values based on Eqs. (127.1) and (127.2).

$$E_{C3} = \sum_{t} \left| f(t)_{C3} \right|^2 . \tag{127.1}$$

$$E_{C4} = \sum_{t} \left| f(t)_{C4} \right|^2 . \tag{127.2}$$

Figure 127.5 shows that the C3 channel (representing the left sensorimotor area) yielded increased energy amplitudes during the event trigger period (t = 3–9 s), indicating ERS. However, the C4 channel (representing the right sensorimotor area) yielded decreased energy amplitudes, indicating ERD. The right hand movement experiment also yielded expected ERS and ERD results.

Thus, the event eigenvalues can be obtained based on the *i*th test.

$$f^i = \left[mean\left(E^i_{C3}\right), mean\left(E^i_{C4}\right) \right] . \tag{127.3}$$

127.3.2 FCM Classification Algorithm

When a cluster algorithm is used to classify feature samples, the similarities between eigenvalues are compared [5–8]; if the current samples demonstrated similarities, they were classified into the same cluster. After a fuzzy clustering algorithm was used to classify the eigenvalues, the algorithm yielded the membership value of those features. This value was between 0 and 1, and was used to describe the classification membership degree of the eigenvector.

When FCM was used to determine the optimal approximation, it used the smallest objective function as the criterion. The c in Eq. (127.4) represents the

Table 127.1 Classification accuracy rate of the FCM

Time duration (s)	Accuracy rate	Error rate
3–8	0.80714	0.19286
3–7	0.82143	0.17857
3.5–7	0.82857	0.17143
3.5–6.5	0.82143	0.17857
4–8	0.77143	0.22857
4–7	0.79286	0.20714
4–7.5	0.77143	0.22857

class number ($c \geq 2$), the n represents the sample number, and the m represents the fuzzy parameter, where $1 \leq m < \infty$, objective function as following:

$$J_{FCM} = \frac{1}{2}\sum_{j=1}^{c}\sum_{i=1}^{n}\left(u_{ij}\right)^{m}\left\|x_i - w_j\right\|^2 \cdot \tag{127.4}$$

u_{ij} represents the membership degree of data sample, x_i regarding the jth cluster, and w_j represents the cluster center of the jth cluster. Therefore, $\left\|x_i - w_j\right\|^2$ is the Euclidean distance from data sample x^i to cluster center w_j. The steps of the FCM algorithm are listed below [7, 8].

Step 1 Initialize the cluster centroids, fuzzification parameter m, and the value $\varepsilon > 0$. Give a fuzzy c-partition and $t = 1$.
Step 2 Calculate the membership matrix.
Step 3 Update the class centroids.
Step 4 Compute stop criteria Δ. If $\Delta > \varepsilon$, $t = t + 1$ and go to step 2; otherwise stop the process.

127.4 Experimental Results and Conclusions

Favorable feature samples can yield superior classification results. To improve the accuracy level of classifications, the original EEG signals must undergo processing. A Butterworth band-pass filter was used to filter the original EEG signals obtained using the C3 and C4 channels. The Mu and Beta rhythm bandwidth ranges were retained, and the changes in EEG ERS and ERD were observed when the participant conducted motor imagery. Equations were used to obtain the energy values of time segments, and FCM was employed to classify the feature samples. Table 127.1 presents the results of FCM classification.

The results show that ERS and ERD were successfully combined with FCM and can be applied to classify EEG signals. Table 127.1 shows how various time segment selections affected the accuracy rate; the 3.5–7 s time segment yielded a rate of 82.85 % accuracy.

Acknowledgments This work was partly supported by the National Science Council of Taiwan, under grant NSC-99-2221-E-167-024 and NSC-100-2221-E-167-024.

References

1. Sanei, S., & Chambers, J. A. (eds.). (2007). *EEG signal processing* (eds.). UK: Wiley.
2. Luck, S. J. (ed.). (2005). *An introduction to the event-related potential technique*. US: A Bradford Book.
3. Pfurtscheller, G., & Lopes da Silva, F. H. (1999). Event-related EEG/MEG synchronization and desynchronization: Basic principles. *Clinical Neurophysiology, 110*, 1842–1857.
4. Graz Data Sets and Description for the BCI 2003 Competition. http://www.bbci.de/competition/ii/
5. Dunn, J. C. (1974). A fuzzy relative of the ISODATA process and its use in detecting compact well-separated clusters. *Cybernetics and Systems, 3*(3), 32–57.
6. Bezdek, J. C. (1973). *Fuzzy mathematics in pattern classification, Ph.D. dissertation, applied mathematics*. Ithaca: Cornell University.
7. Hsu, W. Y., Lin, C. Y., Chen, Y. F., Hsu, C. Y., & Chen, I. R. (2011). Application of coherence and FCM to finger movement EEG recognition. *1st Conference on Applications of Innovation and Invention* (pp. 409–413).
8. Hsu, W. Y., Lin, C. Y., Kuo, W. F., Michelle Liou, Sun, Y. N., Arthur, C. H. T., et al. (2011). Unsupervised fuzzy C-means clustering for motor imagery EEG recognition. *International Journal of Innovative Computing, Information and Control, 7*(8), 4965–4976.

Chapter 128
Multi-Fault Isolation Combined with Backup Paths and Active Probing on All Optical Networks

Chi-Shih Chao and Szu-Pei Lu

Abstract In this paper, a novel and heterogeneous multi-link failure isolation mechanism is proposed on all-optical networks (AONs). In our study, the concept of fault diagnosis, which is supported by link management protocol (LMP), is introduced for easy implementation on GMPLS networks. Yet, the LMP is incapable on multi-link failure diagnosis; thus, adding the addition of probing path is an efficient strategy for solving its insufficient fault diagnostic capability. In addition, our study notices that the backup path system can provide available information which involves the network status of each backup path. Thus, if the backup path system can be adopted and merged into our mechanism, then the explicit advantage is to reduce the needs of establishing the additional probing paths. Plus, the active probing system is combined with the information, which is provided by the previous backup path system and LMP, for increasing the accuracy of satisfying the *k*-fault diagnostic capability. Consequently, the objectives of high-precision fault localization and cost-effective fault management can be met by our proposed mechanism.

Keywords Multiple link failure · Active probing · Backup/Protection path · *k*-fault diagnostic capability · Shared risk link group

C.-S. Chao (✉)
Department of Communications Engineering, Feng Chia University, Taichung, Taiwan, Republic of China
e-mail: cschao@fcu.edu.tw

S.-P. Lu
Ph.D. Program in Electrical and Communications Engineering, Feng Chia University, Taichung, Taiwan, Republic of China

J. Juang et al. (eds.), *Proceedings of the 2nd International Conference on Intelligent Technologies and Engineering Systems (ICITES2013)*, Lecture Notes in Electrical Engineering 293,
DOI: 10.1007/978-3-319-04573-3_128,

128.1 Introduction

With the emergence of the wavelength-division multiplexing (WDM) and dense wavelength division multiplexing (DWDM) technologies, all-optical networks (AONs) can meet the demands of the explosion of data over Internet. Although AONs are designed to switch and deliver a vast amount of data, they are vulnerable to physical failure such as fiber cuts, optical cross-connect malfunctions and optical amplifier breakdowns [1]. Hence, faults on the optical links or other components can lead to huge data losses. To reduce the effects of such faults, it is critical to develop an efficient and precise fault diagnosis mechanism. Numerous studies have proposed supervising either IP networks or AONs. In general, the failure in these studies fall into two categories: node and link failure.

Natu and Sethi [2] proposed an effective method for diagnosing node failure and deploying monitors. The method is used to localize at most k faulty nodes and also considers the failure of monitor stations. In [3], Zeng et al. implemented an m-cycle scheme, which involves using a heuristic spanning tree to establish the monitoring cycles $\{C_1, C_2, \ldots, C_M\}$ and ensuring that the optical fiber links that form the network are supervised by these monitoring cycles. However, with such design and deployment, it is very possible that different links can have the same alarm code so that ambiguity will be incurred if these links fail simultaneously. For multi-fault diagnosis with m-cycles, a fault inference with healthy information (FIHI) [4] mechanism is proposed in our previous work to facilitate accurate fault localization by establishing an additional probing set and removing redundant alarms using network healthy information. Plus, to achieve cost-effective management, the proposed mechanism also offers a minimal set of monitor stations so that we can use minimal management cost (monitor establishment) to do fault diagnosis.

In these days, AONs have expanded their research horizons to include two new factors in fault diagnosis: SRLG (shared risk link group) and backup paths. Among them, [5, 6] are viewed as being more feasible and applicable in the real world. Zhao et al. [5] proposed a two-stage method in which initial diagnosis results of suspicious faulty links are obtained first and then the real faulty links are further located by the established backup (restoration) paths where the returned establishment messages of backup paths can be used to shrink the size of the suspicious faulty area. Tapolcai et al. [6] proposed a single SRLG failure diagnosis method with the support of backup paths as well as the SRLG-alarm dependency matrix. In this method, predefined backup paths and established lightpaths can serve as probes for isolating one single SRLG fault. In our work, a practical but different way is used to build our fault diagnosis mechanism for AONs. Instead of doing the system from perspectives (or views) of network administrators, the demands of users will mainly direct the design and development of our diagnosis system. We start with, first, identifying the maximum number of faults (e.g., k faults) that AON users want the diagnosis mechanism to isolate at the same time. Then, on the basis of the user demand, a k-fault diagnosis (isolation) mechanism is designed. To meet

the *k*-fault diagnostic capability and make our mechanism feasible in reality, an addition method of active probes is developed for AONs which are equipped with LMP (link management protocol) and backup path establishment. With the aids of established lightpaths/backup paths, engineered additional probes, and LMP, our mechanism gathers much more information for fault diagnosis than any other ones do to achieve *k*-fault diagnostic capability.

In the following sections, the functions of and operating processes for the proposed fault diagnosis mechanism are elaborated. In Sect. 128.2, a LMP solution, which involves using backup paths, is introduced. In Sect. 128. 3, the active probing method is proposed, in which additional probing paths are added for achieving *k*-fault diagnostic capability. Subsequently, the proposed method is analyzed and compared with other methods, and the conclusion and future prospects are outlined.

128.2 Isolating Faults by Using Backup Paths

As stated in [7], LMP is a protocol that can easily implement on Generalized Multi-Protocol Label Switching (GMPLS) networks and also help to precisely isolate single faulty link or span; however, LMP is not applicable for multi-link failure diagnosis on the same lightpath. To solve this problem, the available information provided by any useful systems should be greatly gathered for fault diagnosis. One of these systems, in our mechanism, is the backup path system. For rapid fault recovery (the recovery time is better to below 50 ms), each lightpath on a network must be protected by at least one backup path; thus, the predefined backup paths can serve as probes to provide the information. The other one is the active probing system. It is designed to fetch the network healthy information by sending engineered additional probes periodically. According to these engineered additional probes, the *k*-fault diagnostic capability can be met. In our point of view, combing these two systems is very efficient and useful for fault diagnosis. Therefore, in this section, fault isolation by using backup paths will be elaborated first.

In our mechanism, three typical backup path schemes [8], which are included node disjoint, link disjoint, and braided backup path, with the concept of SRLG are introduced. The concept of SRLG is extremely helpful for shrinking the size of the ambiguous faulty set, which is denoted as suspicious faulty area (*SFA*). Thus, the *SFA* could be small even without any suspicious faulty link if the disjoint backup paths pass through as much the links as possible. For example in Fig. 128.1, it shows a 4 × 4 mesh network comprising two working paths wp_1: (1, 2, 3, 4, 5) and wp_2: (6, 4, 7). Plus, assuming each lightpath has one node disjoint backup path $bp_{1'}$: (1, 9, 10, 11, 12, 13, 5) and $bp_{2'}$: (6, 2, 3, 13, 5, 8, 7). Also, there are two link faults on links (1, 2) and (2, 3) as a failure scenario. As a result from the alarms triggered by the faults, the initial *SFA* will be {link (1, 2), link (2, 3), link (3, 4), link (4, 5)}. Then, in step 1, the fault localization procedures of LMP, on the

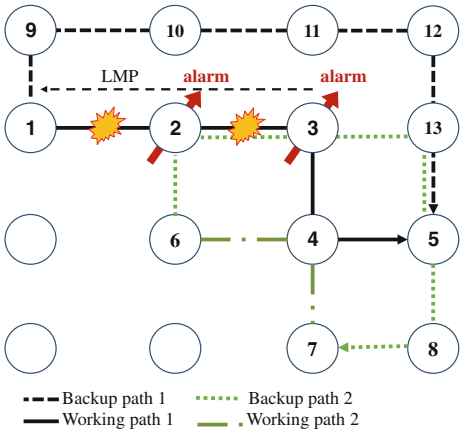

Fig. 128.1 Fault isolation with the aid of node disjoint backup paths

working paths wp_1, send *ChannelStatus* messages, stated in [7], to its upstream nodes, checking the network status of the links when it detect failure (e.g. loss of light). Next, in Step 2, the return messages indicate that link (1, 2) fails; thus, the new *SFA* shrinks to {link (2, 3), link (3, 4), link (4, 5)}. In addition, considering the alarm triggered from the backup path bp_2, link (2, 3) is indicated as failure. Hence, two faults are detected and localized, and suspicious links in the final *SFA* are eliminated in this case. In intuition, if (and only if) the backup paths intersect the links, as much as possible in the *SFA*, then the *SFA* can be shrunk in size. For this reason, the backup path system must be adopted into our fault isolation mechanism.

128.3 Active Probing

As an objective, a fault diagnostic capability is determined on user-demand in our mechanism. It means that the users of AONs can decide which levels of fault diagnosis they want according to their budget on network operation and management. Then, a *k*-fault diagnosis (isolation) mechanism is designed following this objective. To meet the *k*-fault diagnostic capability and make our mechanism feasible in reality, an addition method of active probes is developed for AONs which are equipped with LMP and backup path establishment.

Figure 128.2 shows a part of link-alarm dependency matrix that corresponds with Fig. 128.1. The diagnostic power (*DP*) in the matrix is simply used to indicate the number of disjoint probes for each link. According to this, the managers of AONs can easily know how many additions of probes they need to establish. As an example in Fig. 128.2a, two fiber cuts occur on link (1, 2) and (2, 3) as a multi-fault scenario. Then, link (1, 2) is localized by LMP on the working paths wp_1, and link (2, 3) is also localized because of the alarm of backup path bp_2.

(a)

	wp_1	bp_2	DP
(1, 2)	1		1
(2, 3)	1	1	2*
(3, 4)	1		1
(4, 5)	1		1

*: DP equals to threshold k

(b)

	wp_1	wp_2	bp_2	bp_x	bp_y	DP
(1, 2)	1					1
(2, 3)	1		1			2
(3, 4)	1			1	1	3*
(4, 5)	1					1
(6, 4)		1	1	1		3*
(4, 7)		1			1	2

Fig. 128.2 An example of k diagnotic power. **a** two link faults, **b** three link faults

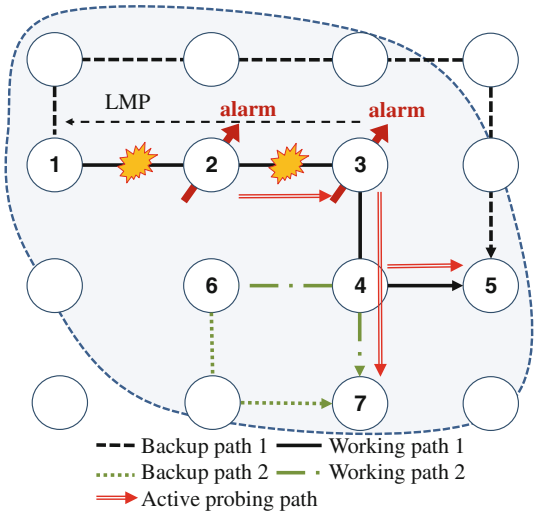

Fig. 128.3 An example of active probing paths establishment

For another example, assume that three fiber cuts occur on link (2, 3), (3, 4), and (6, 4) in Fig. 128.2b. As a result, link (2, 3) and (6, 4) can be localized by LMP on the working path wp_1 and wp_2 respectively. Yet, the system can only be distinguished between link (3, 4) and link (4, 7) if there are two more disjoint backup path bp_x and bp_y which only intersect at the link (3, 4). Thus, in our perspective, the links on the lightpaths, the DP is below the user-demand of k, are all needed to establish additions of probes except the head link on the lightpath which can be always detected by LMP. With this idea of k-fault diagnostic capability, an active probing path (APP) algorithm is proposed.

The procedures of APP is illustrated in Fig. 128.3 which has some modification on Fig. 128.1. In this case, the DP equals to {1, 1, 1, 1}, which corresponds to the links on the Working path 1. It means that there are no backup paths passing

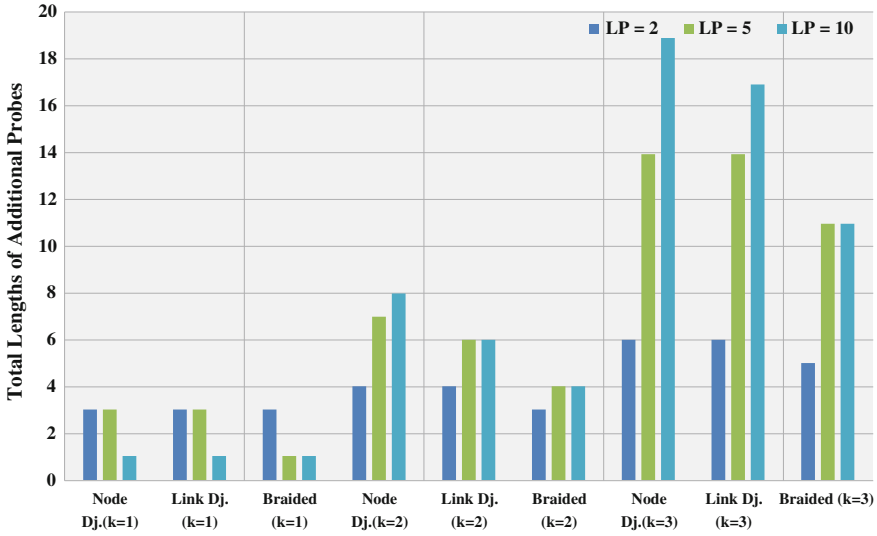

Fig. 128.4 Total lengths of additional probes on different backup methods

through any links on the Working path 1; thus, some probes need to be established on these links which disjoint to the working path wp_1 except the head link on the lightpath. In the first step, a perimeter is extended around Working path 1 at a distance of one hop for limiting the area of searching route. In Step 2, the links on the Working path 2 that *DPs* are less than k and adjacent to the link l_i on the wp_1 are located and stored in the set, $AdjacentLink_{i.}$ Next, the perimeter is extended again by one hop, yet if there are no links adjacent to the links in each $AdjacentLink_i$. Then, the probing paths p_i are established by picking the links from the $AdjacentLink_i$ and the procedures still proceed iteratively until the value of *DP* on each link equals to k. Finally, our mechanism outputs a probing path set for satisfying k-fault diagnostic capability on each link.

In the previous example, the maximal number of additional probing paths should be four on the Working path 1 and 2 because four links are needed to establish additions of probes. Thus, after using our APP procedures, the number of additional probing paths reduces to three in Fig. 128.3, and the total lengths of additional probing paths are still not increased as the optimization which is four links as the total lengths.

128.4 Performance and Conclusions

In Fig. 128.4, the results are evaluated on a 16 * 16 mesh network and showed that more faults occurred at the same time, more lengths of additional probes are needed to establish. In Table 128.1, our methods are establish. In Table 128.1, our

Table 128.1 The summations of m-cycle, FIHI, and our methods

	M-cycle	FIHI	Node Dj. (k = 1)	Link Dj. (k = 1)	Braided (k = 1)	Optimal (k = 1)	Node Dj. (k = 2)	Link Dj. (k = 2)	Braided (k = 2)	Optimal (k = 2)	Node Dj. (k = 3)	Link Dj. (k = 3)	Braided (k = 3)	Optimal (k = 3)
Total lengths of additional probes (LP = 2/5/10)	40/40/40	40/40/40	3/3/1	3/3/1	3/1/1	3/5/6	4/7/8	4/6/6	3/4/4	6/10/14	6/14/19	6/14/17	5/11/11	12/26/34
Fault diagnostic capability	Dynamic	Dynamic	1	1	1	1	2	2	2	2	3	3	3	3
Size of SFA (k = 1)	3.2	2.2	0	0	0	0	0	0	0	0	0	0	0	0
Size of SFA (k = 2)	6	4	0	0	0	0	0	0	0	0	0	0	0	0
Size of SFA (k = 3)	10	6	0	0	0	0	0	0	0	0	0	0	0	0

methods are compared to m-cycle, FIHI, and the optimal solution. Among these methods, the optimal solution is made to use the least lengths of additional probes to achieve k fault diagnostic capability. Yet, our methods are better than optimal according to the aids of backup path and active probe mechanism. Additionally, in the fault diagnostic capability fields, m-cycle and FIHI have uncertain fault diagnostic capability. As a result in the following three fields, with longer lengths of additional probes, m-cycle and FIHI have less fault diagnostic capability due to inaccurate diagnosis. Thus, the average size of *SFAs* with different number of k show that our methods have accurate fault diagnostic capability and cost-efficient probe deployment.

We realize that there are still some practical issues to affect a fault diagnostic mechanism, like node/link combined failure. Thus, we will do further research on this area.

References

1. Ramaswami, R., & Sivarajan, K. N. (2002). *Optical networks: A practical perspective* (2nd ed.). San Francisco: Morgan Kaufmann, pp. 511–565.
2. Natu, N., & Sethi, A. S. (2007). Probe station placement for robust monitoring of networks. *Journal of Network and Systems Management, 16*(4), 351–374.
3. Zeng, H., Huang, C., & Vukovic, A. (2006). A novel fault detection and localization scheme for mesh all-optical networks based on monitoring-cycles. *Photonic Network Communications, 11*(3), 277–286.
4. Chao, C. S., & Lu, S. P. (2012). Toward efficient multi-link failure diagnosis by using monitoring cycle for all-optical mesh networks. *Proceedings of the International Conference on Information Networking* (pp. 228–233).
5. Zhao, Y., Li, X., Li, H., Wang, X., Zhang, J., & Huang, S. (2013). Multi-link faults localization and restoration based on fuzzy fault set for dynamic optical networks. *Optics Express, 21*(2), 1496–1511.
6. Tapolcai, J. (2013). Shared risk link group failure restoration with in-band approximate failure localization. *Optical Switching and Networking, 10*(2), 163–172.
7. Lang, J. (2005, Oct). Link Management Protocol (LMP). IETF RFC 4024.
8. Paradis, L., & Han, Q. (2007). A survey of fault management in wireless sensor networks. *Journal of Network and Systems Management, 15*(2), 171–190.

Chapter 129
A Hybrid Iterative Method Based on MPI and CUDA for Steady-State Solutions of Markov Chains

Yu-Cheng Chou and Wei-Chich Liao

Abstract This paper presents a parallel algorithm that integrates two well-known iterative methods, the Jacobi and Gauss–Seidel methods, for solving steady-state solutions resulting from large Markov chains, using Compute Unified Device Architecture (CUDA) and Message Passing Interface (MPI) paradigms. The parallel algorithm is implemented in CUDA and MPI, and its performance is tested using a system of 1,000 equations for 1,000 unknowns on a GPU workstation and a cluster computer.

Keywords Jacobi method · Gauss–Seidel method · Markov Chain · Parallel computing · Message passing interface · Compute unified device architecture

129.1 Introduction

In this paper, a combination of two classical iterative methods, namely, the Jacobi and Gauss–Seidel methods, for solving linear equation systems resulting from Markov chains, is presented. The Jacobi method is inherently parallel, and the

Y.-C. Chou (✉) · W.-C. Liao
Department of Mechanical Engineering, Chung Yuan Christian University, Zhongli 320, Taoyuan, Taiwan, Republic of China
e-mail: ycchou@cycu.edu.tw

W.-C. Liao
e-mail: g10173014@cycu.edu.tw

Y.-C. Chou
Research and Development Center for Microsystem Reliability, Chung Yuan Christian University, Zhongli 320 Taoyuan, Taiwan, Republic of China

Y.-C. Chou
Center for Biomedical Technology, Chung Yuan Christian University, Zhongli 320, Taoyuan, Taiwan, Republic of China

J. Juang et al. (eds.), *Proceedings of the 2nd International Conference on Intelligent Technologies and Engineering Systems (ICITES2013)*, Lecture Notes in Electrical Engineering 293,
DOI: 10.1007/978-3-319-04573-3_129,

Gauss–Seidel method essentially converges faster than the Jacobi method. In order to take advantages of these two classical methods, a parallel algorithm integrating both methods is presented in this paper. The proposed algorithm's performance is examined, in terms of the computing resources (CPUs or GPUs) and speedup ratio [1], through a linear system of 1,000 equations for 1,000 unknowns. The testing environments include a cluster computer with an MPI (Message Passing Interface) [2, 3] version of the algorithm, and a GPU workstation with a CUDA (Compute Unified Device Architecture) [4] version of the algorithm.

129.2 The Steady-State Solution

While modeling with Markov chains, in a steady state, a linear equation system will be obtained as follows:

$$\mathbf{Q}^{\mathrm{T}}\mathrm{x} = 0, \quad \mathbf{x} \geq 0, \quad \mathbf{x}^{\mathrm{T}}\mathbf{e} = 1. \tag{129.1}$$

In Eq. (129.1), $\mathbf{Q}$ is a square matrix containing transition rates, $\mathbf{x}$ is a vector containing unknown state probabilities to be solved, and $\mathbf{e} = (1, 1, \ldots, 1)^{\mathrm{T}}$. Essentially, three types of methods, including the iterative, decomposition, and direct methods, can be applied to solve a linear system represented by Eq. (129.1). The iterative methods are commonly used for such purposes. In addition, the Jacobi and Gauss–Seidel methods are two classical iterative approaches [5].

129.3 A Hybrid Iterative Parallel Algorithm

In Markov chain problems, the state vector $\mathbf{x}$ can essentially be partitioned into meaningful subsets. Thus, matrix $\mathbf{Q^T}$ can be partitioned respectively, and the unknowns can be solved based on those partitions [6]. As shown below, it is assumed that matrix $\mathbf{Q^T}$ can be divided into K^2 blocks, each of size $\frac{n}{K} \times \frac{n}{K}$. Thus, vector $\mathbf{x}$ can also be divided into K sub-vectors, each of size $\frac{n}{K}$.

$$\begin{bmatrix} \mathbf{Q}_{11}^{\mathbf{T}} & \mathbf{Q}_{12}^{\mathbf{T}} & \cdots & \mathbf{Q}_{1\mathbf{K}}^{\mathbf{T}} \\ \mathbf{Q}_{21}^{\mathbf{T}} & \mathbf{Q}_{22}^{\mathbf{T}} & & \mathbf{Q}_{2\mathbf{K}}^{\mathbf{T}} \\ \vdots & & \ddots & \vdots \\ \mathbf{Q}_{\mathbf{K}1}^{\mathbf{T}} & \mathbf{Q}_{\mathbf{K}2}^{\mathbf{T}} & \cdots & \mathbf{Q}_{\mathbf{KK}}^{\mathbf{T}} \end{bmatrix} \begin{bmatrix} \mathbf{x}_1 \\ \mathbf{x}_2 \\ \vdots \\ \mathbf{x}_{\mathbf{K}} \end{bmatrix} = 0 \tag{129.2}$$

According to the Jacobi method, matrix $\mathbf{Q^T}$ can be decomposed as follows:

$$\mathbf{Q}^{\mathrm{T}} = \mathbf{D} - (\mathbf{L} + \mathbf{U}) \tag{129.3}$$

Fig. 129.1 Dividing matrix **H** among p processes

In Eq. (129.3), **D** is a diagonal matrix, **L** is a strictly lower triangular matrix, and **U** is a strictly upper triangular matrix.

Let

$$\mathbf{H} = \mathbf{D}^{-1}(\mathbf{L} + \mathbf{U}) \tag{129.4}$$

Thus, the *i*th solution vector at the $(n + 1)$th iteration $\mathbf{x}_{\mathbf{i}}^{(\mathbf{n}+1)}$ can be calculated using the *i*th solution vector obtained at the *n*th iteration $\mathbf{x}_{\mathbf{i}}^{(\mathbf{n})}$ as follows:

$$\mathbf{x}_{\mathbf{i}}^{(\mathbf{n}+1)} = \mathbf{H}_{\mathbf{i}} \times \mathbf{x}_{\mathbf{i}}^{(\mathbf{n})} \tag{129.5}$$

Calculations involved in Eq. (129.5) can be performed independently by one processor or one GPU block.

In addition, each processor or GPU block solves for the $\frac{\mathbf{n}}{\mathbf{K}}$ elements of $\mathbf{x}_{\mathbf{i}}^{(\mathbf{n}+1)}$ by adopting the Gauss–Seidel method, as follows:

$$\begin{aligned}\mathbf{x}_{\mathbf{i},\mathbf{j}}^{(\mathbf{n}+1)} = \Big(&\mathbf{H}_{\mathbf{i},1} \times \mathbf{x}_{\mathbf{i},1}^{(\mathbf{n}+1)} + \ldots + \mathbf{H}_{\mathbf{i},\mathbf{j}-1} \times \mathbf{x}_{\mathbf{i},\mathbf{j}-1}^{(\mathbf{n}+1)} \\ &+ \mathbf{H}_{\mathbf{i},\mathbf{j}+1} \times \mathbf{x}_{\mathbf{i},\mathbf{j}+1}^{(\mathbf{n})} + \ldots + \mathbf{H}_{\mathbf{i},\frac{\mathbf{n}}{\mathbf{K}}} \times \mathbf{x}_{\mathbf{i},\frac{\mathbf{n}}{\mathbf{K}}}^{(\mathbf{n})}\Big)\end{aligned} \tag{129.6}$$

In Eq. (129.6), $\mathbf{x}_{\mathbf{i},\mathbf{j}}^{(\mathbf{n}+1)}$ represents the *j*th element of the *i*th solution vector obtained at the $(n + 1)$th iteration by the *i*th processor or the *i*th GPU block.

129.4 Implementations on MPI and CUDA

In this paper, MPICH2 [7–10], an MPI library, is used to implement the hybrid iterative algorithm for a cluster computer environment. In addition, CUDA 5 [11, 12], an NVIDIA CUDA toolkit, is used to implement the algorithm for a CUDA-enabled GPU workstation.

Fig. 129.1 illustrates the method used to divide matrix **H** of size n × n among p different processes. In this paper, a process denotes a processor in a cluster

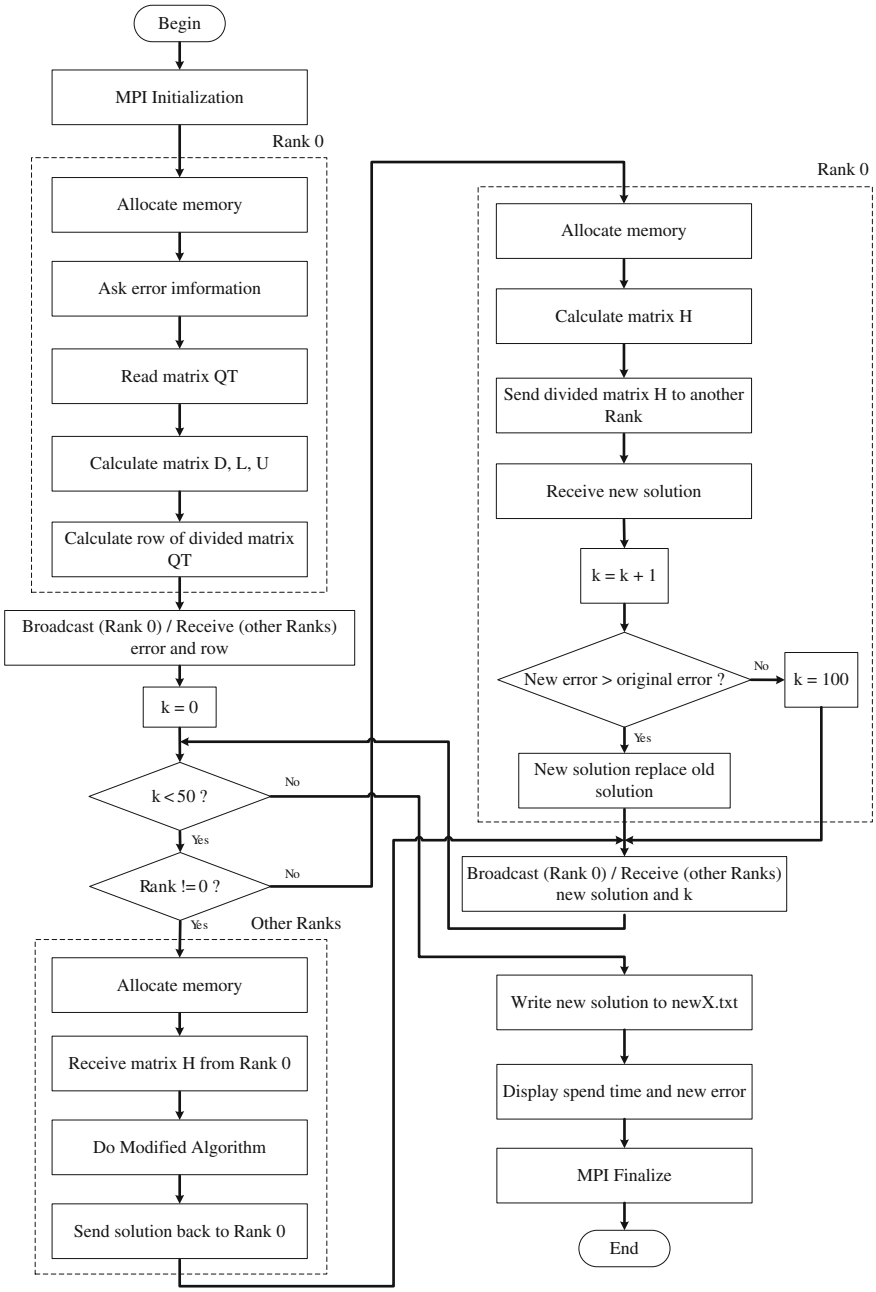

Fig. 129.2 MPI flowchart of the algorithm

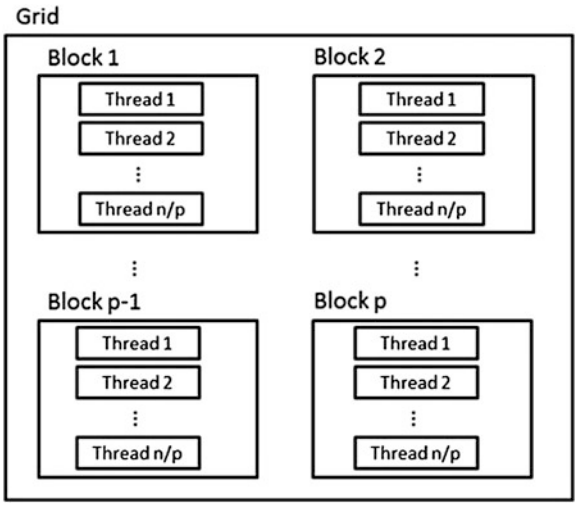

Fig. 129.3 Dividing matrix **H** among p blocks in a CUDA GPU

computer. As shown in Fig. 129.1, matrix **H** is divided into n/p blocks. The hybrid iterative algorithm will be applied to each block to find solution vectors.

The flowchart for the hybrid algorithm's MPI implementation is shown in Fig. 129.2.

Figure 129.3 shows the method used to divide matrix **H** of size n × n among p different blocks in a grid. In a CUDA GPU, a grid consists of multiple blocks, and a block consists of multiple threads. As shown in Fig. 129.3, the calculations are assigned to p blocks. In each block, n/p threads will be invoked to find solution vectors simultaneously.

The flowchart for the hybrid algorithm's CUDA implementation is shown in Fig. 129.4.

129.5 Experimental Results

This section presents experimental results obtained from running the hybrid iterative parallel algorithm to solve a system of equations on a cluster computer and a GPU workstation.

A 26-node cluster computer is used for testing the MPI implementation of the hybrid algorithm. 25 nodes of the cluster computer have identical key specifications, including two CPU cores, 1 GHz frequency of CPU core, and 1.837 GB of memory. The remaining node has two CPU cores, 2.3 GHz frequency of CPU core, and 1.837 GB of memory.

A GPU workstation with a Tesla C2075 board is used for the CUDA implementation of the hybrid algorithm. The key specifications of the Tesla C2017 board includes 448 application-acceleration cores, 1.15 GHz frequency of CUDA

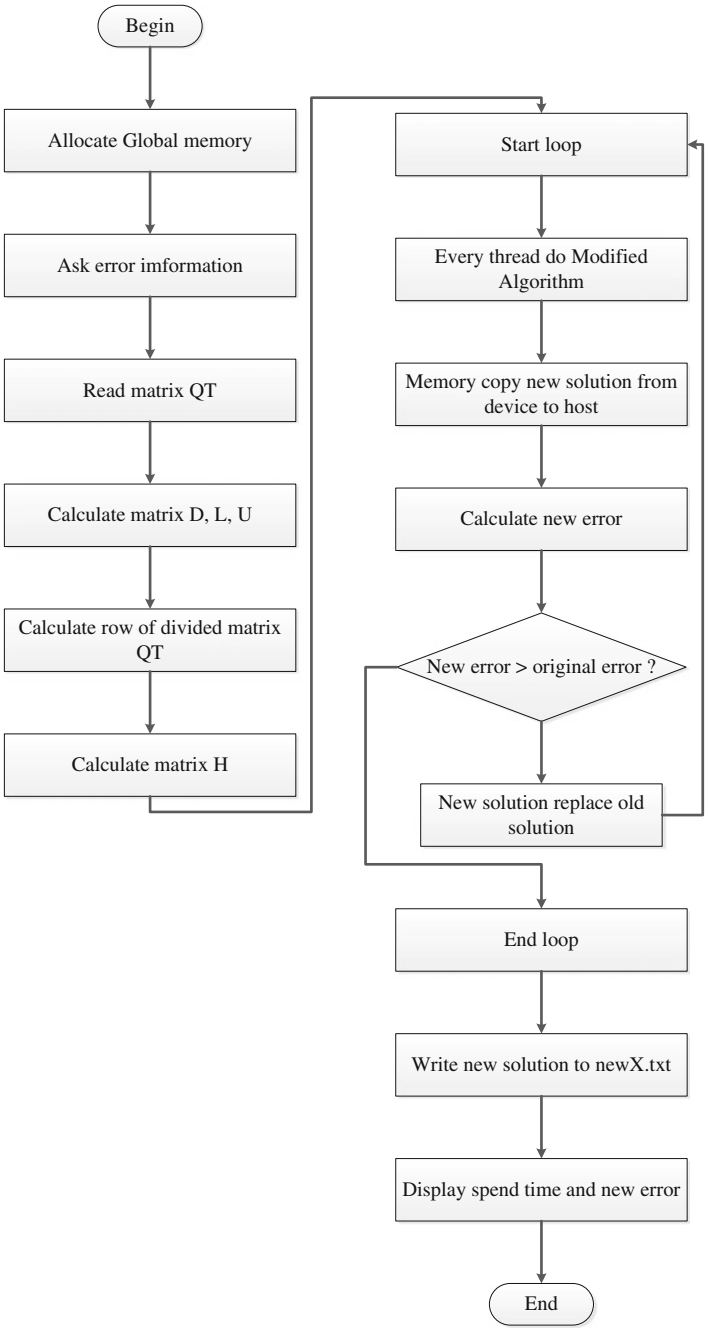

Fig. 129.4 CUDA flowchart of the algorithm

Table 129.1 Experimental results of MPI and CUDA versions of the hybrid iterative algorithm

Implementation	No. of processors/threads	Execution time (s)	Speedup ratio
MPI	1	0.511	1
MPI	25	0.15	3.407
CUDA	1	1.547	1
CUDA	1000	0.007	221

core, 6 GB of dedicated memory, 1.5 GHz of memory speed, and 144 GB/s of memory bandwidth [13].

As shown in Table 129.1, the MPI version of the algorithm has a speedup ratio of 3, when solving solutions with 25 nodes. In addition, the CUDA version of the algorithm achieves a speedup ratio of 221, when solving solutions with 1,000 threads.

129.6 Conclusions

A hybrid iterative parallel algorithm, which integrates two well-known iterative methods, the Jacobi and Gauss–Seidel methods, for solving steady-state solutions resulting from large Markov chains, has been presented in this paper.

The algorithm has been implemented using the MPI and CUDA programming models. The two implementations of the parallel algorithm have been tested using a system of 1000 equations for 1000 unknowns on a cluster computer and a GPU workstation. However, at this moment, the algorithm has not yet achieved its best performance. Therefore, the future work is to improve the performance of the algorithm by optimizing both the MPI program and the CUDA program in terms of memory usage.

Acknowledgments This project is financially supported by the National Science Council of Taiwan under the grants NSC101-2628-E-033-001-MY3 and NSC102-2218-E-033-002-MY2, the Research and Development Center for Microsystem Reliability at Chung Yuan Christian University, and the Center for Biomedical Technology at Chung Yuan Christian University.

References

1. Bylina, J., & Bylina, B. (2008). Merging Jacobi and Gauss–Seidel methods for solving Markov chains on computer clusters. In *Computer Science and Information Technology, 2008. International Multiconference on IMCSIT 2008* (pp. 263–268).
2. Gropp, W. D., Lusk, E. L., & Skjellum, A. (1999). *Using MPI: Portable parallel programming with the message-passing interface* (Vol. 1). MIT Press, Cambridge.
3. Gropp, W. D., Lusk, E. L., & Thakur, R. (1999). *Using MPI-2: Advanced features of the message-passing interface* (Vol. 2). Connecticut: Globe Pequot.
4. NVIDIA. (2013). CUDA Parallel Computing Platform.

5. Stewart, W. J. (1994). *Introduction to the numerical solution of Markov chains* (Vol. 41). Princeton: Princeton University Press.
6. Bylina, J. (2004). A distributed approach to solve large Markov chains. In *Proceedings from EuroNGI Workshop: New Trends in Modeling, Quantitive Methods and Measurements* (pp. 145–154).
7. Argonne National Laboratory. (2013). MPICH: High-Performance Portable MPI.
8. Buntinas, D., Mercier, G., & Gropp, W. (2007). Implementation and evaluation of shared-memory communication and synchronization operations in MPICH2 using the Nemesis communication subsystem. *Parallel Computing, 33*, 634–644.
9. Gropp, W. (2002). MPICH2: A new start for MPI implementations. In *Recent Advances in Parallel Virtual Machine and Message Passing Interface* (pp. 7–7). New York: Springer.
10. Gropp, W., & Thakur, R. (2006). Issues in developing a thread-safe mpi implementation. In *Recent Advances in Parallel Virtual Machine and Message Passing Interface* (pp. 12–21). Heidelberg: Springer.
11. NVIDIA. (2013). The CUDA Toolkit.
12. NVIDIA. (2013). CUDA C Programming Guide.
13. NVIDIA. (2013). Tesla GPU Accelerators for Workstations.

Chapter 130
Analysis and Control of a Wearable Control Valve for Agricultural Supporting System

Feifei Zhao, Tetsuya Akagi and Shujiro Dohta

Abstract Today, the aged workers in agriculture are growing up rapidly in Japan. The development of a human friendly supporting system which can assist the agricultural work is strongly desired. It is needed to have a wearable pressure control system that can control the supporting force. The typical electromagnetic servo valves for pressure control are larger, heavier and more expensive. Therefore, the small-sized quasi-servo valve that consists of two and three-port on/off valves was proposed and tested. The analytical model of the valve was also proposed. The validity of the model was confirmed by comparing the calculated results with the experimental results. In this study, as an analytical design, the control performance with various input duty ratio to compensate the dead zone of the valve was investigated analytically. As a result, the optimal control parameters were obtained.

Keywords Quasi-servo valve · Analytical design · Optimal design

130.1 Introduction

Recently, the average age of Japanese farmers becomes higher by decrease of young farmer because of its low income and hard work. In the case of a grape farmer that can get relatively high income, hard works while bending over prevent to increase the number of farmer. Therefore the development of wearable

F. Zhao (✉)
Tsuyama National College of Technology, Tsuyama, Okayama 708-8025, Japan
e-mail: cho@tsuyama-ct.ac.jp

T. Akagi · S. Dohta
Department of Intelligent Mechanical Engineering, Okayama University of Science, Okayama 700-0005, Japan

J. Juang et al. (eds.), *Proceedings of the 2nd International Conference on Intelligent Technologies and Engineering Systems (ICITES2013)*, Lecture Notes in Electrical Engineering 293,
DOI: 10.1007/978-3-319-04573-3_130,

supporting device which can help their agricultural works such as holding their arm and hip is strongly desired.

In order to control the supporting force, the small-sized and lightweight servo valve with precise pressure control will be required. In our previous study, we proposed and tested a small-sized quasi-servo valve that consists of two on/off type control valves [1]. We also proposed analytical model of the valve and confirmed the validity of the proposed model by comparing the calculated results with the experimental results. The embedded pressure control system using the valve and a micro-computer was also proposed and tested. In the next step, we aim to improve the pressure control performance of the valve. In this paper, we investigate the optical control parameters of the quasi servo valve that is related to the dead zone of the output flow rate.

130.2 Quasi-Servo Valve

130.2.1 Construction

Figure 130.1 shows the schematic diagram of the tested servo valve. The valve consists of two on/off type control valves (Koganei Co.Ltd., G010HE-1) whose both output ports are connected each other. The valve connected with the actuator is a two-port valve. The other is a three-port valve that can change the direction of fluid flow such as a supply or exhaust. The two-port valve is driven by pulse width modulation (PWM) method in order to adjust the valve opening per time. It becomes the quasi fluid resistance. Then, the latter valve is called as "PWM valve", the former is called as "switching valve". The size of the valve is 33 × 19.6 × 10 mm, and the mass is 15.3 g.

130.2.2 Precise Analytical Model of On/Off Valve

Figures 130.2a and b show an inner construction and an analytical model of the three-port type on/off valve, respectively. The valve consists of a solenoid and an armature with a spring. The model of the electric circuit of the solenoid is used as an electric coil and resistance. The valve has an overlap that the valve cannot open and close at the point of a certain displacement (= x_{min}) of the armature. The analytical model of the on/off valve is described as follows. The generated electromagnetic force F_e and The electrical circuit of the solenoid are given by following equations.

$$F_e = K_c i \tag{130.1}$$

$$R_v i + L\frac{di}{dt} = e \tag{130.2}$$

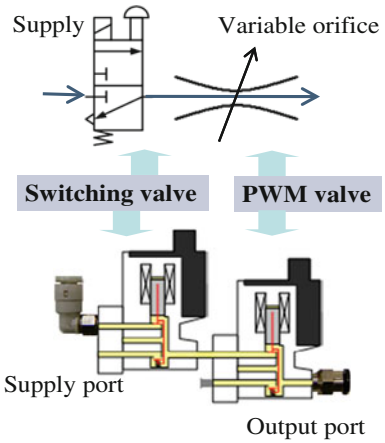

Fig. 130.1 Schematic diagram of quasi-servo valve

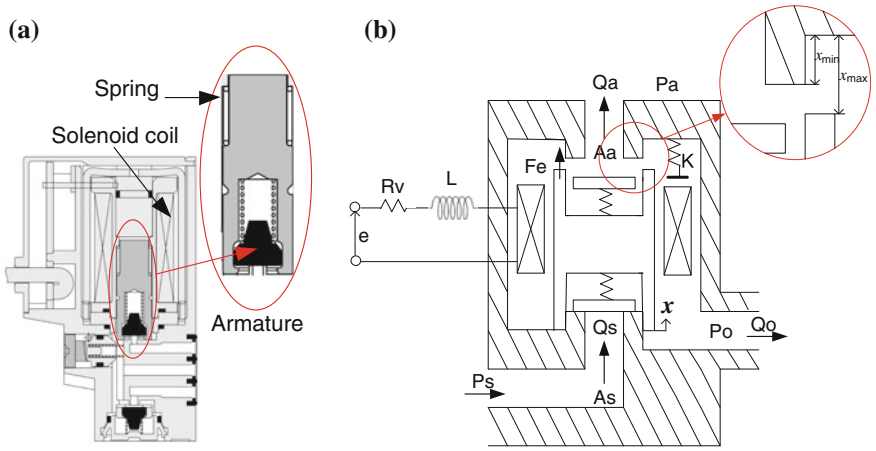

Fig. 130.2 On/off valve in quasi-servo valve. **a** Inner construction. **b** Analytical model of quasi-servo valve

where i, K_c, R_v, e and L are the current, a conversion factor from the current to the force, an electrical resistance, an input voltage to the solenoid and an inductance of the solenoid coil, respectively. The equation of the motion of the armature is given by

$$M\frac{dx^2}{dt^2} + C_v\frac{dx}{dt} + K_v x = F_e \tag{130.3}$$

where M, C_v and K_v are a mass of the armature, damping coefficient and a spring constant, respectively. The sectional area of the valve is changed by the displacement of the armature x. As the sectional area of the supply port A_s and the area of exhaust port A_a starts to change at the point of a certain displacement x_{min} (=0.27 mm) of the armature, both sectional area A_s and A_a are given by Eqs. (130.4a) and (130.4b).

$$A_s = 0,\ A_a = \sqrt{4\pi A_{a0}}(x_{\min} - x)\ (0 \leqq \mathrm{x} < \mathrm{x}_{min}) \tag{130.4a}$$

$$A_s = \sqrt{4\pi A_{s0}}(x - x_{\min}),\ A_a = 0\ (\mathrm{x}_{min} \leqq \mathrm{x} \leqq \mathrm{x}_{max}) \tag{130.4b}$$

From the theory of the nozzle flapper, the maximum value of the sectional area A_a and A_s become A_{a0} and A_{s0}, respectively. The mass flow rate of supply orifice Q_s and the exhaust orifice Q_a are given as follows.

$$Q_s = A_s P_s \sqrt{\frac{2}{RT}} f(z),\ z = \frac{P_o}{P_s} \tag{130.5}$$

$$Q_a = A_a P_o \sqrt{\frac{2}{RT}} f(z),\ z = \frac{P_a}{P_o} \tag{130.6}$$

where R and T mean a gas constant and an absolute temperature, respectively. The function $f(z)$ that expresses the state of flow is given as follows.

$$f(z) = \sqrt{\frac{\kappa}{\kappa - 1}\left(z^{\frac{2}{\kappa}} - z^{\frac{(\kappa+1)}{\kappa}}\right)} \qquad (0.528 < \mathrm{z} \leqq 1) \tag{130.7a}$$

$$f(z) = \sqrt{\frac{\kappa}{\kappa + 1}\left(\frac{2}{\kappa + 1}\right)^{\frac{2}{(\kappa-1)}}} \qquad (0 \leqq \mathrm{z} \leqq 0.528) \tag{130.7b}$$

where κ means a specific heat ratio (=1.4). The output flow rate of the valve that is the flow rate from the output port in the valve is given by

$$Q_o = Q_s - Q_a \tag{130.8}$$

We can predict the output flow rate of the on/off valve by solving the Eqs. (130.1)−(130.8).

130.2.3 Analytical Model and Calculated Result

Figure 130.3 shows the analytical model of the quasi-servo valve connected with a chamber volume. This model includes models of the two-port and the three-port on/off valve mentioned above. Both valves are connected each other through a constant chamber volume V_m. If the pressure change in the chamber volume is

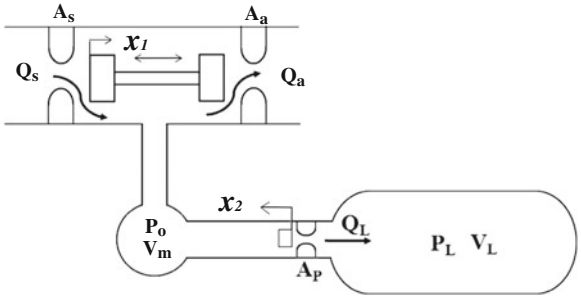

Fig. 130.3 Model of the quasi-servo valve

assumed as an adiabatic change, the following equations about the relation between the pressure P_o and the output flow rate Q_o are given as follows.

$$\frac{dP_o}{dt} = \frac{\kappa RT}{V_m} Q_o \tag{130.9}$$

$$Q_o = Q_s - Q_a - Q_L \tag{130.10}$$

where Q_s is the supply flow rate of the switching valve and it is given by Eq. (130.5). Q_a is the exhaust flow rate of the switching valve from the connected chamber to the load chamber and it is given by Eq. (130.6). As the value of the flow rate Q_L becomes positive or negative (that is a back flow), the flow rate Q_L is given as following equations:

$$Q_L = A_p P_o \sqrt{\frac{2}{RT}} f(z),\ z = \frac{P_L}{P_o} \quad (Po \geqq P_L) \tag{130.11}$$

$$Q_L = -A_p P_L \sqrt{\frac{2}{RT}} f(z),\ z = \frac{P_o}{P_L} \quad (Po < P_L) \tag{130.12}$$

where the sectional area A_p is given as the value calculated by Eqs. (130.4a), (130.4b). The pressure P_L in the volume is given by next equation.

$$\frac{dP_L}{dt} = \frac{\kappa RT}{V_L} Q_L \tag{130.13}$$

By using the equations from (130.1) to (130.13), we can predict the dynamic and static characteristics of the quasi-servo valve.

Figure 130.4 shows the relation between the duty ratio and the mean output flow of the quasi-servo valve. In Fig. 130.4, each colored symbol shows the experimental result using various PWM period. Each colored line shows the calculated results using the proposed model and the identified parameters [2]. From Fig. 130.4, it can be seen that the calculated results using the proposed model

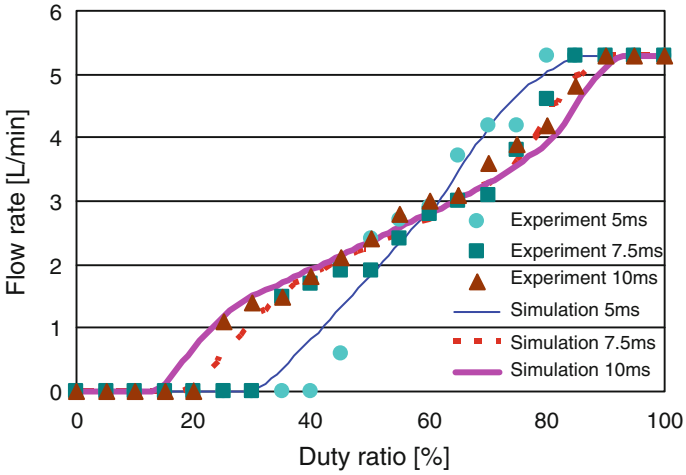

Fig. 130.4 Output flow rate of the valve

agree well with the experimental results. We can conclude that the proposed model and the identified parameters are useful and reliable to estimate the performance of the valve.

130.3 Analytical Design of Pressure Control Using Quasi Servo Valve

130.3.1 Pressure Control System

Figure 130.5 shows the pressure control system using the tested quasi-servo valve in our previous study [3]. The system consists of the quasi-servo valve, a pressure transducer (Matsushita Electronics Co. Ltd., ADP5160) and an embedded controller (Renesas Co. Ltd. H8/3664). The pressure control is done as follows. First, the embedded controller gets the sensor output voltage and the reference voltage through an inner 10 bit A/D converter. In the embedded controller, the difference from the reference voltage is calculated based on following simple P control scheme.

$$u = k_p|e_c| + u_c \tag{130.14}$$

$$\begin{aligned} e_c < 0 \quad & \text{Switchingvalve : turnoff (Exhaust)} \\ e_c = 0 \quad & \text{Switchingvalve : turn off (Exhaust)} \\ e_c > 0 \quad & \text{Switchingvalve : turn on (Supply)} \end{aligned} \tag{130.15}$$

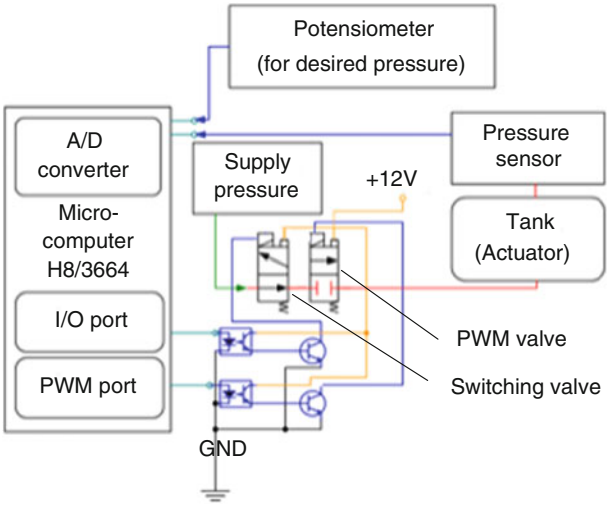

Fig. 130.5 Pressure control system

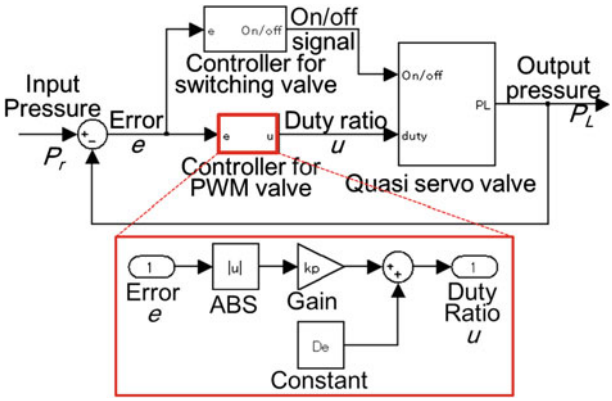

Fig. 130.6 Model of control system

where k_p, e_c, u and u_c mean the proportional gain, the error from the reference pressure, input duty ratio for the PWM control valve and the compensated input duty ratio for initial dead zone of output flow rate, respectively. In addition, the state of switching valve is decided by the positive or negative value of the error e_c in Eq. (130.15).

Figure 130.6 shows the model of the pressure control system using Matlab Simulink.The model of the quasi servo valve given by Eqs. (130.1)–(130.14) is included in the model. The embedded controller in Fig. 130.5 is simulated as an

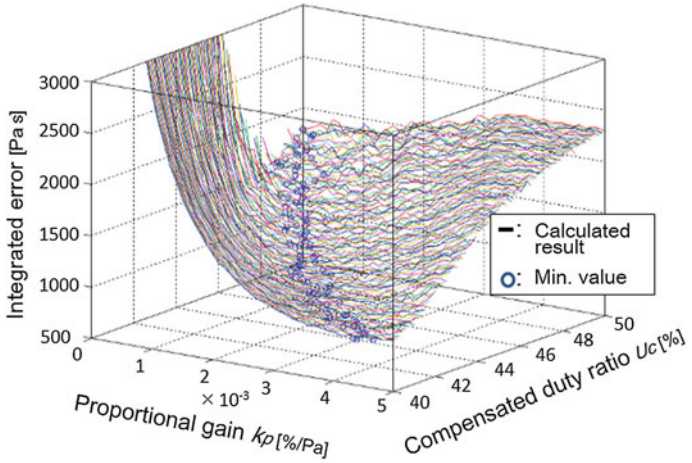

Fig. 130.7 Calculated integrated error of pressure tracking control

analog controller without delay. It is because the sampling period of the embedded controller using integer calculation such as applied control scheme as shown in Eqs. (130.14)–(130.15) is very short, that is less than 1 ms. In addition, the conversion time of the pressure transducer is shorter (less than 1 ms) compared with the dynamics of the valve. The PWM signal generator is also included into the model by using the comparator and chopping wave generator. By using the model, we can estimate the control performance of the valve with various control parameters analytically.

130.3.2 Calculated Results

In order to obtain the better pressure control performance using the valve, not only the optimal proportional gain but also the optimal compensated duty ratio is required. However, huge numbers of combinations of the proportional gain and compensated duty ratio are investigated experimentally is impractical. Therefore, we investigate the control performance of the pressure control using various proportional gains and compensated duty ratios. Figure 130.7 shows the calculated integrated error in the pressure tracking control using the quasi servo valve. In the simulation, the valve was connected to the constant volume of 11.6 cm^3. The sinusoidal desired pressure with the amplitude of 100 kPa, the offset pressure of 250 kPa and frequency of 1 Hz was applied. The integrated error was calculated from absolute pressure error for 1 s from the beginning of the control. The compensated duty ration was changed from 40 to 50 % every 1 %. The

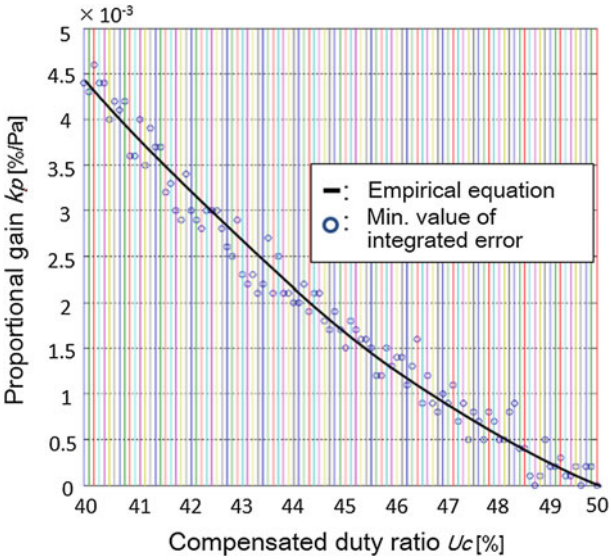

Fig. 130.8 Optimal proportional gain for various compensated duty ratio

calculation was done by using Matlab Simulink based on Runge-Kutta method. In Fig. 130.7, the solid lines show the calculated results of integrated error with various proportional gains and compensated duty ratio. The circles show the minimum value of the integrated error for each compensated duty ratio. From Fig. 130.7, the relation between the optimal proportional gain and compensated duty ratio was obtained as shown in Fig. 130.8. It can be seen that the optimal proportional gain is decreased according to higher compensated duty ratio. From both Figs. 130.7 and 130.8, the integrated pressure error is decreased according to lower compensated duty ratio. As a result, the optimal compensated duty ratio of about 44 % and the optimal proportional gain of about 3.3×10^{-3} %/Pa can be obtained, because the integrated error shows the lowest at this point in Fig. 130.7.

130.4 Conclusions

This study that is aimed to improve the pressure control performance using the quasi servo valve for Agricultural Supporting System can be summarized as follows.

As an estimation of the pressure control performance of the quasi servo valve, the analytical model with pressure controller was proposed and tested by using Matlab. The integrated pressure tracking control error with various control

parameters was also calculated analytically. As a result, the optimal control parameter could be obtained.

As our future work, we aim to estimate the control performance of the real valve with the calculated optimal control performance. In addition, the influence of the connected volume will be also investigated theoretically and experimentally.

References

1. Zhao, F., Akagi, T., & Dohta, S. (2009). Development of small-sized quasi-servo valve for flexible bending actuator. *Proceedings of 2009 CACS International Automatic Control Conference* (pp. 558–562).
2. Aragane, M., Noritsugu, T., Takaiwa, M., & Sasaki, D. (2008). Power assist wear for upper limb driven by sheet-like pneumatic rubber muscle. *Proceedings of the 7th JFPS International Symposium on Fluid Power TOYAMA2008* (pp. 787–792).
3. Moriwake, Y., Akagi, T., Dohta, S., & Zhao, F. (2012). Development of low-cost pressure control type quasi-servo valve using embedded controller. *Journal of Procedia Engineering, 41*, 493–500.

Chapter 131
LEV Suspension System Design and Development

Hsing-Hui Huang, Ming-Jiang Tsai and Hong-Kai Yu

Abstract In this study, the vehicle suspension system design and analysis procedure have been proposed for the Light-weight Electric Vehicles. The objective for the suspension design is quick handling and stably riding performance with LEV system. The contents include the suspension design and mechanical dynamic simulation. In the vehicle quasi-static test simulation, the suspension parameters were compared with new model LEV_2 and the mule car model LEV_1. Through mechanical dynamic simulation, the suspension parameters have been clearly discussed and improved with camber angle change, toe angle change, caster angle change and roll center height change.

Keywords Rigid body motion · Suspension design · K&C test

131.1 Introduction

Vehicles have become indispensable to people's lives, and greatly change people's transportation. It is also expand people's living area, to make life more convenient and efficiency. The vehicle suspension systems design procedure has been proposed for Light-weight Electric Vehicles. The LEV can drive in industrial estate and campus with no license. It can provide a convenient and low energy consumption of transport.

In this paper, the contents including the benchmarking of LEV, systems layout, static load analysis, MBD system building, and mechanical motions. In the analysis of mechanism, some revise of the suspension parameters also find out for improving the performance according to the design procedure.

H.-H. Huang (✉) · M.-J. Tsai · H.-K. Yu
Department of Vehicle Engineering, National Pingtung University of Science and Technology, Pingtung 91201, Taiwan, Republic of China
e-mail: sanlyhuang@mail.npust.edu.tw

J. Juang et al. (eds.), *Proceedings of the 2nd International Conference on Intelligent Technologies and Engineering Systems (ICITES2013)*, Lecture Notes in Electrical Engineering 293,
DOI: 10.1007/978-3-319-04573-3_131,

131.2 Background

In Europe, the LEV can be driven in campus with no license. In other words, it can provide convenience and does not produce exhaust pollution of transportation.

The objective of the LEV are handling and riding performance. By minimize the amount of camber change in the design to reduce uneven wear and reduce energy loss, double A-arm suspension system of front independent suspension system have been selected. The characteristics of this kind of suspension system are with smaller track changes and angle changes than other suspension types. Then the shock absorber actuator friction resistance as well as its control arm can be configured to block the sub-frame generated vibration and noise when traveling, so that double A-arm suspension may have a better steering performance and ride comfort.

K&C testing is one of the methods to validate the design of the chassis. K&C tests are quasi-static test; loads and displacements are applied to a vehicle in very slowly to capture the suspension parameter and force–displacement relationships [1–8].

Evaluate vehicle handling characteristics of the vehicle dynamic behavior is also very important. With the increasingly developed, Computer Aided Engineering (CAE) is available for the vehicle kinematics simulation and the dynamic behavior of the vehicle design evaluation. By simulated vehicle suspension system, the periods for develop a new vehicle can effectively be shorten, but validate the model with experimental results has become an important issue.

131.3 Suspension Design

For the vehicle suspension system design, design requirements and market positioning have to be list first. Then the location of the powertrain and whether power-assisted in steering systems have also been considered in suspension design. Generally, based on different chassis configuration parameters are within the design reference values. The design of vehicle specifications as EC regulations L6 level from the LEV_2, refer to vehicle types of tests have been completed for the mule car, LEV_1. The basic model can be used to design more competitive and were be analyzed and compared.

Refers to EC regulations, L6 level of the technical specifications are laid down as followed and Table 131.1:

1. Max. Weight : under 350 kg
2. Max. Speed : under 45 km/h
3. Body Geometry : L-4000*B-2000*H-2500 (mm).

Table 131.1 Vehicle specifications table

Specifications	Unit	LEV_1	LEV_2
Curb weight	kg	547.9	420
Length	mm	3190	3250
Height	mm	1910	1800
Width	mm	1780	1400
Wheelbase	mm	2600	2600
Turning circle	m	4.74	–
Tires	in.	13	13
F. Suspension	–	Double A-arm	Double A-arm

Table 131.2 System weight evaluation

System evaluation	Weight (kg)	Classification item
Body structure	100	Body structure and joints = 86 kg
		Disassemble roof structure = 14 kg
Powertrain system	70	Motor = 25 kg
		Transmission = 35 kg
		ECU module = 10 kg
Chassis system	130	Suspension system = 100 kg
		Steering system = 15 kg
		Braking system = 15 kg
Exterior and interior	50	Exterior and interior = 50 kg
Total	350	(Not including battery)

EC have a clear specification the body weight for the L6-Level of LEV, its empty weight (without battery) should not exceed 350 kg. Table 131.2 list the evaluate weight for this our design.

In suspension system, the layout of hardpoints through the CAD software is shown in Fig. 131.1. The following processes with double A-arm suspension system [9].

1. Decide dimensions and vehicle bracket (based on customer and market demand).
2. Select tires and wheels specifications.
3. Decide wheel center position (A) and track specifications.
4. Set roll center (B) and the instantaneous center position (C).
5. Calculate the lower ball joint position (D), inclination angle, and scrub radius.
6. Calculate the ball joint position (E), caster angle, and caster moment arm.
7. Based on the use of space, determines the control arm inner position (F), (G).
8. Calculations the Ackerman geometry for determining the knuckle arm position (H).

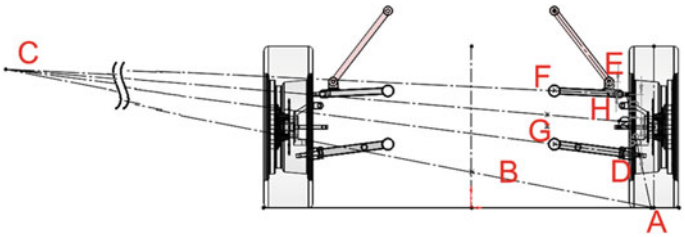

Fig. 131.1 Suspension design with LEV_2

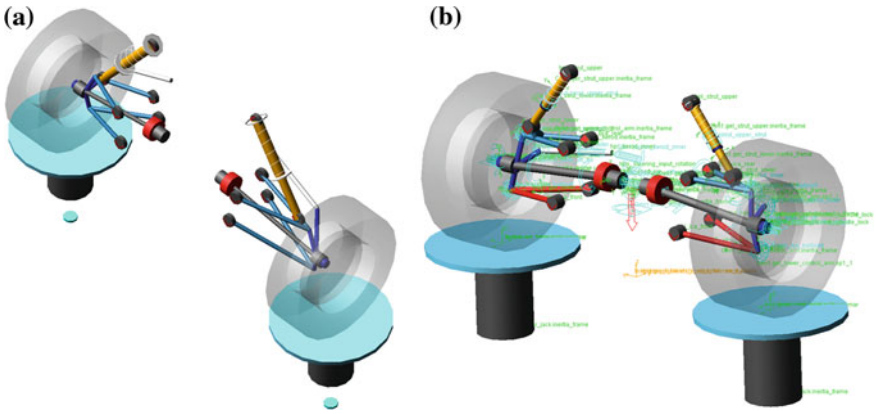

Fig. 131.2 Front suspension model. **a** LEV_1, **b** LEV_2

131.4 Vehicle Model

Using ADAMS simulation software for rigid body motion, as shown in Fig. 131.2, can help designers to conduct various static motion parameters for analyzing and comparing with K&C test platform for model comparison adjustments.

131.5 K&C Testing

The design of the vehicle chassis system based on models of market, consumer and costs, and other factors that determine the various subsystems (such as suspension systems, steering systems and brake systems, etc.). According to the design requirements, the basic design parameters have been set, such as track, wheelbase and roll center height. Confirm the basic suspension parameter, the 1/2 suspension model can be built as shown in Fig. 131.3. The suspension parameters and force–displacement relationships then can be capture by quasi-static analysis.

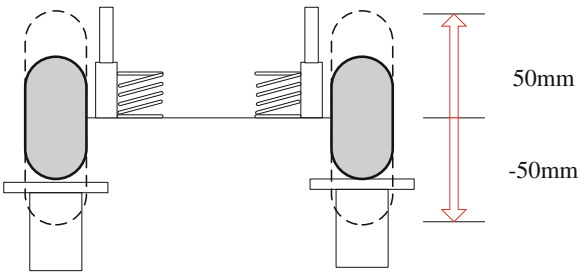

Fig. 131.3 Parallel motion

Table 131.3 Suspension characteristic target in parallel motion

Parameters	Unit	Target		Ideal value			
		Front	Rear	Front		Rear	
				Low	High	Low	High
Toe change	°/mm	0.0043	0.0015	0	0.006	0	0.0074
Camber change	°/mm	0.015	0.0225	0.0075	0.02	0	0.0074
Castor change	°/mm	–	–	Low	High		

Table 131.3 shows the ideal targets of suspension parameter designs according to parallel motion analysis. The parameter change gradient is related to vehicle performance.

131.6 K&C Data Discussion

In kinematic motion, the camber change is too large in the mule car model, LEV_1. So the study model LEV_2 improved these suspension parameters. Double A-arm suspension system, using upper and lower control arms, control tire vertical displacement, lateral displacement and camber changes. In Fig. 131.4, the models of camber change in LEV_2 is about 0.98 to −1.28°; and the LEV_1 is 1.82 to −1.89°. The camber change gradient from −0.0371°/mm in LEV_1 improved to −0.0225°/mm in LEV_2.

In mule car model LEV_1, the toe angle have large changed with different loading. It may induce the tire rolling resistance and noise. In LEV_2, the suspension design tries to improve this situation. The hardpoints of tie rod inner and the tie rod outer are moving with suspension moving path when the wheel vertical movement. As shown in Fig. 131.5, LEV_2 model with the toe angle change ranged is about −0.01 to 0.18°, that is better than LEV_1 model, toe angle change

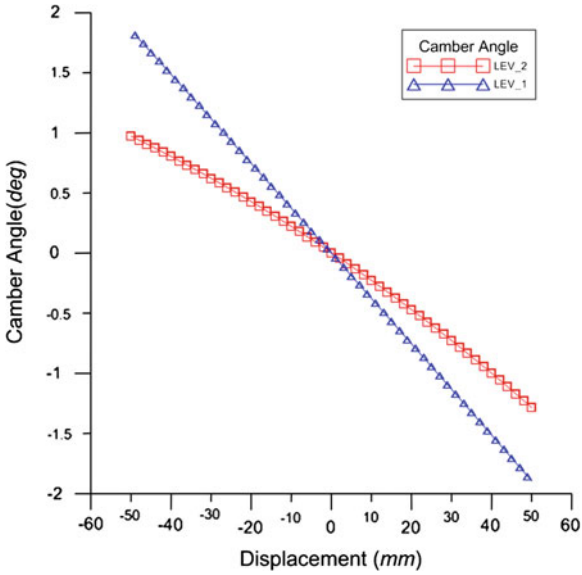

Fig. 131.4 Camber change curve

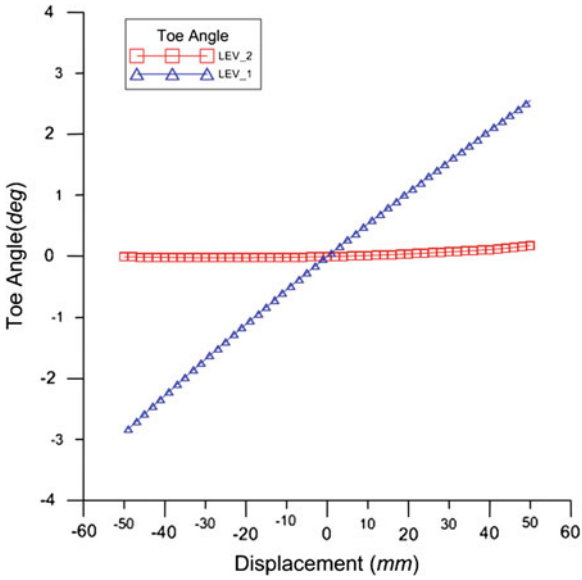

Fig. 131.5 Toe change curve

ranged from −2.83 to 2.56°. Wherein the gradient 0.0538°/mm, improved to 0.0017°/mm.

Caster angle is related to the vehicle performance of straight forward, result in model LEV_1 has not response the cornering precisely and road driving

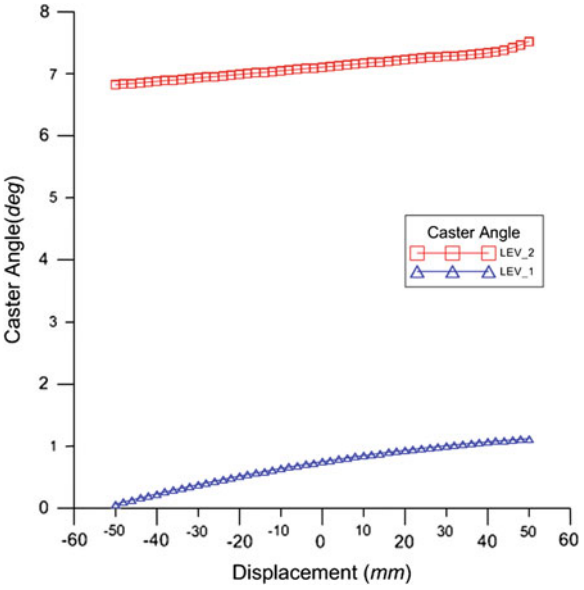

Fig. 131.6 Caster change curve

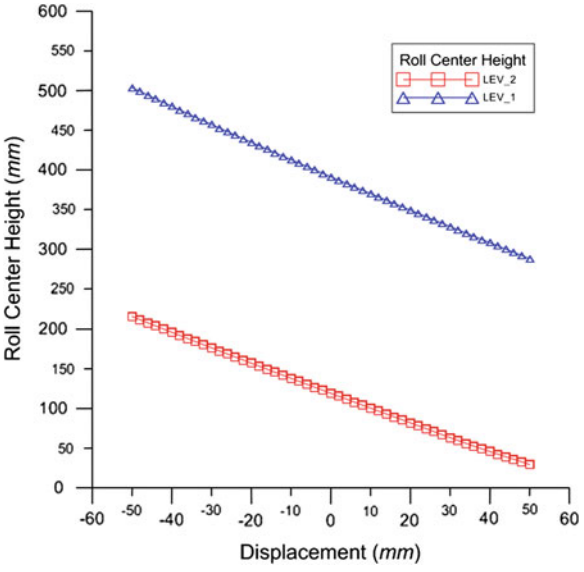

Fig. 131.7 Roll center height change curve

uncertainty problem. Ten the castor setting has been revise then the caster change gradient improved. The analysis result, as shown in Fig. 131.6, the mule car model LEV_1 caster angle change in 0.07–1.12° with wheel vertical displacement. That is why the mule car is in cornering problem. The caster angle of model LEV_2

changes about 6.82–7.52° with wheel vertical displacement. The changes are in the design range which improved vehicle straight stability. The caster changes gradient improves from 0.0106 to 0.0070°/mm.

Roll center height in LEV_1, as shown in Fig. 131.7, the variation range is about 503.85–288.23 mm. This roll center height is more suitable for high chassis of the vehicle models. The model of LEV_2 with lower chassis height should be design with lower roll center height about 216.21–29.59 mm, as shown in Fig. 131.7, which comply with LEV_2 lower center of gravity, reducing the roll moment arising rollover risk.

131.7 Conclusion

The effects of suspension design parameters on chassis have been investigated with rigid body motion analysis. The chassis characteristic have been obtained according to parallel motions. It can improve driving performance and riding comfort with low tires tear. The rigid body motion help engineers to find the problems with mechanical motion interference, and check the efficiency with improvement.

By the design process, the reliability of front suspension can be established for further analysis with steering system. The kinematic and force-torque through the movement then can simulate and confirmed. Finally compose with rear suspension system brake system body and powertrain system conduct with system integration can then achieve the target for full vehicle simulation.

Acknowledgments The authors would like to acknowledge Ministry of Economic Affairs supports of project 102-EC-17-A-16-S1-221.

References

1. Das, S., Ramamurthy, P., & Mahajan, S. K. (2007). Correlation issues for testing and simulation of kinematics and compliance in automotive suspensions. SAE document no. 2007-26-046.
2. Sohn, H. S., Shin, H. W., & Lee, H. W. (1998). The improvement of handling performances through the sensitivity analysis validated by the K&C Test. SAE document no. 980898.
3. Li, M., Changfu, Z., Zhao, P., & Xiangping, J. (2007). Parameters sensitivity analysis and optimization for the performance of vehicle handling. SAE document no. 2007-01-3573.
4. Deakin, A., Shovlin, A., Brooks, P., & Crolla, D. (1998). Design of a single seater racing car suspension system. SAE document no. 983020.
5. Shim, T., & Velusamy, P. C. (2006). Influence of Suspension properties on vehicle roll stability. SAE document no. 2006-01-1950.
6. Burgess, M. J., Fleming, N. P., Wootton, M., & Williams, S. J. (2004). A tool for rapid vehicle suspension design. SAE document no. 2004-01-3543.

7. Franco, J. M. V., & Schaefer, G. (2007). Validation off an SUV model for vehicle dynamics simulation. SAE document no. 2007-01-2655.
8. Rao, P. S., Roccaforte, D., Campbell, R., & Zhou, H. (2002). Developing an ADAMS model of an automobile using test data. SAE document no. 2002-01-1567.
9. Budynas, S. M. (2004). *Essentials of mechanical engineering design*. Singapore: McGraw-Hill.

Chapter 132
Design of Lead–Lag Controller Via Time-Domain Objective Function by Using Cuckoo Search

Huey-Yang Horng

Abstract A large proportion of industrial systems are represented by linear time-invariant transfer functions. The proportional–integral–derivative (PID) controller is one of the most widely used functions. However, the PID controller is susceptible to noise and windup effects. Therefore, the lead–lag controller is a more practical alternative. Traditionally, time-domain or frequency-domain methods have been used to design a lead–lag controller to design specifications. This paper focused on the design of the lead–lag compensator, by optimization of the time-domain objective function. The proposed objective function includes time-domain specifications, including the peak time, maximum overshoot, delay time, setting time and steady state error. In the paper, Cuckoo Search algorithm is chosen to finding the optimal solutions. Cuckoo Search is metaheuristic optimization method recently developed. That is a type of population based algorithm inspired by the behavior of some Cuckoo species in combination with the Lévy flight behavior. Given that the plant is modeled according to a linear time-invariant transfer function, the proposed method designs a lead–lag controller capable of approaching the specifications.

Keywords Lead–lag controller · Cuckoo search · PID controller

132.1 Introduction

Most industrial plant systems can be represented by a linear time-invariant transfer function. Proportional–integral–derivative (PID) controllers are probably the most commonly used controllers in industrial applications. Numerous methods have been proposed for tuning the PID controller parameters [1, 2]. The tuning of the three design parameters, namely, K_P, K_I, and K_D, often relies on experience,

H.-Y. Horng (✉)
Department of Electronic Engineering, I-Shou University, Kaohsiung 84001, Taiwan, Republic of China
e-mail: hyhorng@isu.edu.tw

J. Juang et al. (eds.), *Proceedings of the 2nd International Conference on Intelligent Technologies and Engineering Systems (ICITES2013)*, Lecture Notes in Electrical Engineering 293,
DOI: 10.1007/978-3-319-04573-3_132,

subject-matter knowledge, or a trial and error procedure. The PID controllers are susceptible to high-frequency noise interference and windup (integrator windup) effects. The windup effect causes non-linearity, and directly reduces the performance of the controlled system [3].

Lead–lag controllers provide a more practical alternative. The design of the lead–lag controller has been studied [4–8]. Ou and Lin proposed a method based on Generic Algorithm (GA) and Particle Swarm Optimization (PSO) to design the PID controller, and then compared the results [9]. Cuckoo search algorithm is one of the latest meta-heuristic techniques, developed by Yang and Deb [10, 11].

In this paper, cuckoo search algorithm that uses a time-domain objective function (TDOF) to design the lead–lag controller is proposed. The specifications are peak time, overshoot, delay time, setting time and steady state error. They are directly included in the objective function in cuckoo search. Hence, if the plant is modeled according to a linear time-invariant transfer function, the proposed method can design a lead–lag controller that approaches or meets the time-domain specifications.

132.2 Time-Domain Specifications

It is accepted that in simple, second-order, under-damped systems, the design specification is usually expressed in terms of peak time, percentage overshoot, delay time, setting time, and steady-state error of the step response [1]. For a general system, peak time means the time to reach the first peak.

132.3 Lead–Lag Compensator

The transfer function of a lead–lag (or lag–lead) controller is written as:

$$G_c(s) = K\left(\frac{T_1 s + 1}{\alpha T_1 s + 1}\right) \cdot \left(\frac{T_2 s + 1}{\beta T_2 s + 1}\right), \tag{132.1}$$

where $K > 0,\ \alpha > 1,\ T_1 > 0,\ \beta < 1, T_2 > 0$.

Because the lead–lag controller in Eq. (132.1) now has five unknown parameters, its design is not as straightforward. As a general rule, the phase-lead part of the controller is used primarily to attain a shorter peak time and higher bandwidth, and the phase-lag part is used to provide damping of the system and reduce the steady state error.

132.4 Time-Domain Objective Function

To state the proposed time-domain objective function (TDOF), first define

$$f([x_1, x_2, x_2, x_4, x_5]\,|TDI : lb, ub) = f(\mathbf{x}|TDI : lb, ub)$$

and

$$f(\mathbf{x}|TDI : lb, ub) = \begin{cases} 0, & \text{if } 0 \le lb \le f(\mathbf{x}|TDI) \le ub \\ \frac{f(\mathbf{x}|TDI)-ub}{ub}, & \text{if } f(\mathbf{x}|TDI) > ub \\ \frac{lb-f(\mathbf{x}|TDI)}{lb}, & \text{if } f(\mathbf{x}|TDI) < lb \end{cases} \tag{132.2}$$

where *TDI* is the time-domain indicators, i.e. peak time (T_p), maximum overshoot (M_{os}), delay time (T_d), setting time (T_s) and steady state error (E_{ss}). The result is

$$\begin{aligned} \text{TDOF} = {} & w_1 f\left(\mathbf{x}|T_p : lb, ub\right) + w_2 f(\mathbf{x}|M_{os} : lb, ub) + w_3 f(\mathbf{x}|T_d : lb, ub) \\ & + w_4 f(\mathbf{x}|T_s : lb, ub) + w_4 f(\mathbf{x}|E_{ss} : lb, ub) \end{aligned} \tag{132.3}$$

where $w_1 + w_2 + w_3 + w_4 + w_5 = 1$. In Eq. (132.3), w_i, $(i = 1, 2, \cdots 5)$ represent weights reflecting the relative importance of the corresponding term.

Included in the time-domain objective function are the design specifications expressed as a function of peak time, delay time, maximum overshoot, setting time and steady state error. The lead–lag controller design results in the minimization of the TDOF for all possible parameters. In addition, some tolerances in the time-domain indicators are permissible as in Eq. (132.2).

132.5 Cuckoo Search Algorithm

Cuckoo Search (CS) represents a new optimization metaheuristic algorithm. This algorithm is proposed by Yang and Debin [10, 11]. This algorithm uses a balanced combination of a local random walk and the global explorative random walk, controlled by a parameter p_a. The local random walk can be written as

$$x_i^{t+1} = x_i^t + \alpha s \otimes H(p_a - \varepsilon) \otimes \left(x_j^t - x_k^t\right) \tag{132.4}$$

where x_i^t and x_k^t are two different solutions selected by random permutation. In Eq. (132.4), $H(u)$ is a Heaviside function, ε is a random number drawn from a uniform distribution, and s is the step size. In contrast, the global random walk is carried out using Lévy flights:

$$x_i^{t+1} = x_i^t + \alpha L(s, \lambda) \tag{132.5}$$

where

$$L(s, \lambda) = \frac{\lambda \Gamma(\lambda) \sin(\pi\lambda/2)}{\pi} \cdot \frac{1}{s^{1+\lambda}}, \quad s \ge s_0 \ge 0 \tag{132.6}$$

Here, $\alpha = 0.01$ is the step size scaling factor.

132.6 Design Procedure

The design procedure for calculate the parameters of lead-lag controller can be shown as pseudo code in Fig. 132.1.

```
Initialization
   nests n= 15, MaxGeneration=500,  x = [K,α,T1,β,T2] = (x1,x2,⋯,x5)
   pa=0.25
begin
   Objective function as is in equation (3)
   Generate initial population of n host nests  xi (i = 1,2,⋯,n) , which cause
        closed-loop stable (by using Routh-Hurwitz criterion)
     while (t <MaxGeneration)
        Get a cuckoo randomly /generate a solution by Lévy flights
        and evaluate its fitness Fi
        Choose a nest among n (say, j) randomly
        if (Fi > Fj),
           Replace j by the new solution
        end
        A fraction (pa) of worse nests are abandoned and new ones are built
        Keep the best solutions
        Rank the solutions and find the current best
     end while
   Process results
end
```

Fig. 132.1 Pseudo code of design procedure using cuckoo search

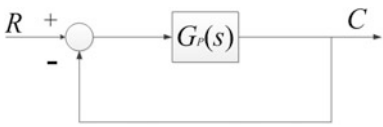

Fig. 132.2 Unity feedback system without controller

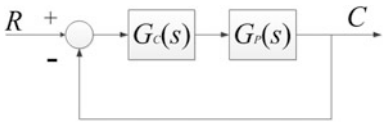

Fig. 132.3 Unity feedback system with controller

132.7 Illustrative Examples

Example 132.1 A unity feedback system as shown in Fig. 132.2 has the following forward transfer function:

$$G_p = \frac{150}{s^2 + 15s + 50}.$$

The closed-loop system is stable. System type = Type 0. The step response of the uncompensated system is shown in Fig. 132.4. Here, the peak time is 0.249 s, the percentage overshoot is 13.3 %, and the steady-state error E_{ss} is equal to 0.273.

As demonstrated, the uncompensated system does not satisfy the design specifications. Therefore, the lead–lag controller is used to improve the transient response as shown in Fig. 132.3.

Suppose the design specifications are given by $0.0990 \le T_p \le 0.1010$, $0.0312 \le T_d \le 0.0318$, $0 \le M_{os} \le 0.0198$, $0 \le E_{ss} \le 0.01$, and $0.0702 \le T_s \le 0.0716$.

In (132.3) the following parameters are set. Let $w_1 = w_2 = w_3 = w_4 = w_5 = 1/5$. $f(\mathbf{x}|T_p : 0.099, 0.101)$, $f(\mathbf{x}|T_d : 0.0312, 0.0318)$, $f(\mathbf{x}|M_{os} : 0.00, 0.0198)$, $f(\mathbf{x}|E_{ss} : 0, 0.01)$, and $f(\mathbf{x}|T_s : 0.090, 0.110)$. If it is allowed that $0.005 \le E_{ss} \le 0.012$, then $29.9697 \le K \le 36.7037$.

When the design procedure using cuckoo search algorithm is completed, $T_p = 0.1002$, $T_d = 0.0285$, $M_{os} = 0.0139$, $T_s = 0.0711$, and $E_{ss} = 0.0098$. The lead–lag controller parameters are $K = 33.5597$, $\alpha = 42.7875$, $T_1 = 0.0826$, $\beta = 0.0405$, and $T_2 = 0.2733$. The TDOF equals 0.0170. The design specifications are closely approximate to the desired results shown in Fig. 132.5.

Example 132.2 A unity feedback system as shown in Fig. 132.2 has the following forward transfer function:

$$G_p(\mathrm{s}) = \frac{160}{s(s^2 + 16s + 60)}.$$

The closed-loop system is stable. The system type is Type 1. The step response of the uncompensated system is shown in Fig. 132.6. Here, the peak time is 1.11 s, the maximum overshoot is 13 %, the setting time is 2.11 s, the steady-state error $E_{ss} = 0.375$.

Assume the design specifications are given by $0.6930 \le T_p \le 0.7070$, $0.2180 \le T_d \le 0.2224$, $0 \le M_{os} \le 0.0198$, $0 \le E_{ss} \le 0.2$, and $0.4916 \le T_s \le 0.5016$.

As demonstrated, the uncompensated system does not satisfy the design specifications. In Eq. (132.3), the following parameters are set:
$w_1 = w_2 = w_3 = w_4 = w_5 = 1/5$. $f(\mathbf{x}|T_p : 0.6930, 0.7070)$, $f(\mathbf{x}|T_d : 0.2180, 0.2224)$, $f(\mathbf{x}|M_{os} : 0.00, 0.0198)$, $f(\mathbf{x}|E_{ss} : 0, 0.2)$, and $f(\mathbf{x}|T_s : 0.4916, 0.5016)$. If it is allowed that $0.008 \le E_{ss} \le 0.22$, then $1.7045 \le K \le 46.8750$.

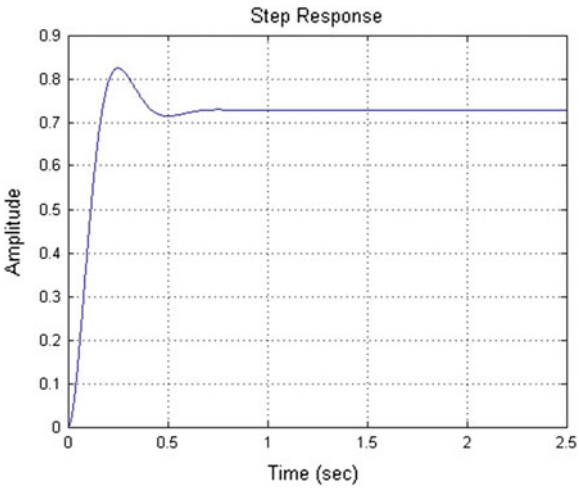

Fig. 132.4 Uncompensated system in Example 132.1

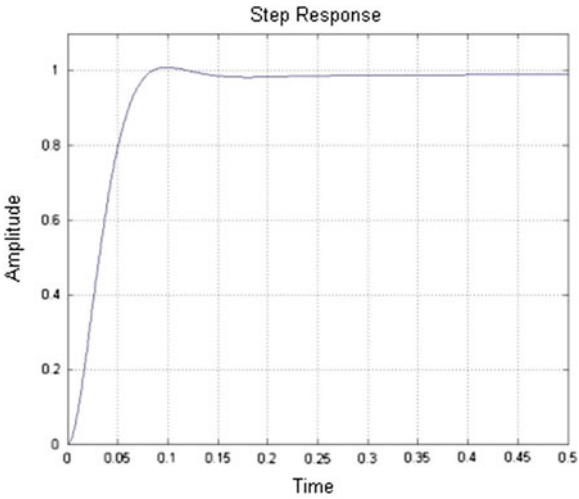

Fig. 132.5 Compensated system in Example 132.1

When the design procedure using cuckoo search algorithm is completed, $T_p = 0.7012$, $T_d = 0.2209$, $M_{os} = 0.0186$, $T_s = 0.4978$, and $E_{ss} = 0.1991$. The lead–lag controller parameters are $K = 1.8834$, $\alpha = 1.3024$, $T_1 = 0.9912$, $\beta = 0.0901$, and $T_2 = 0.2318$. The TDOF equals zero. The design specifications are thus fully met, Fig. 132.7.

Example 132.3 A unity feedback system as shown in Fig. 132.2 has the following forward transfer function:

$$G_p(s) = \frac{700}{(s+2)(s+4)(s+6)}.$$

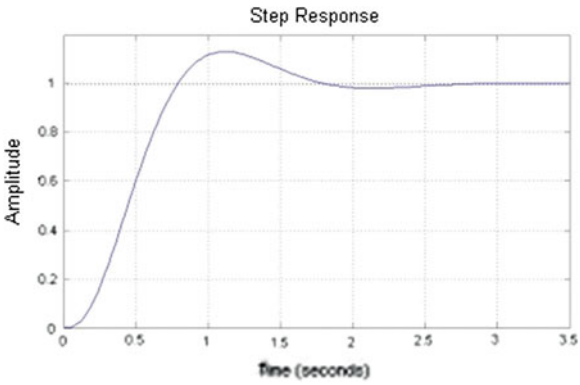

Fig. 132.6 Uncompensated system in Example 132.2

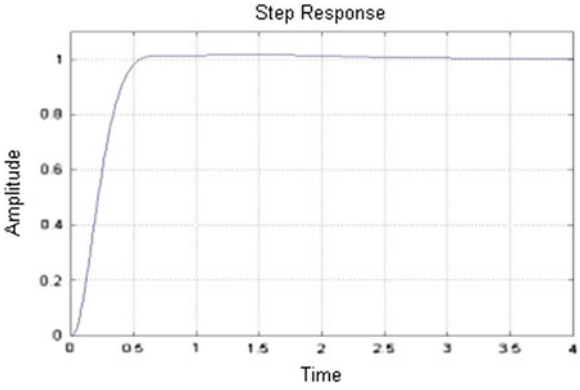

Fig. 132.7 Compensated system in Example 132.2

The system type is Type 0 and the closed-loop system is unstable. The step response of the uncompensated system is shown in Fig. 132.8.

Assume the design specifications are given by:

$0.7425 \leq T_p \leq 0.7575$, $0.2335 \leq T_d \leq 0.2595$, $0 \leq M_{os} \leq 0.0198$, $0 \leq E_{ss} \leq 0.01$, and $0.5265 \leq T_s \leq 0.5373$.

In Eq. (132.3), the following parameters are set: $w_1 = w_2 = w_3 = w_4 = w_5 = 1/5$. $f(\mathbf{x}|T_p : 0.7425, 0.7575)$, $f(\mathbf{x}|T_d : 0.2335, 0.2595)$, $f(\mathbf{x}|M_{os} : 0.00, 0.0198)$, $f(\mathbf{x}|E_{ss} : 0, 0.01)$, and $f(\mathbf{x}|T_s : 0.5265, 0.5373)$.

If it is allowed that $0.09 \leq E_{ss} \leq 0.11$, then $6.1652 \leq K \leq 7.5505$.

When the design procedure using cuckoo search algorithm is finished, $T_p = 0.7287$, $T_d = 0.2517$, $M_{os} = 0.0195$, $T_s = 0.5484$, and $E_{ss} = 0.0095$. The TDOF equals 0.0078, which means the design specifications were not fully met, but they closely approximate to the desired results, Fig. 132.9. The lead–lag controller parameters are $K = 7.1231$, $\alpha = 64.0823$, $T_1 = 0.4320$, $\beta = 0.001$, and $T_2 = 0.4075$.

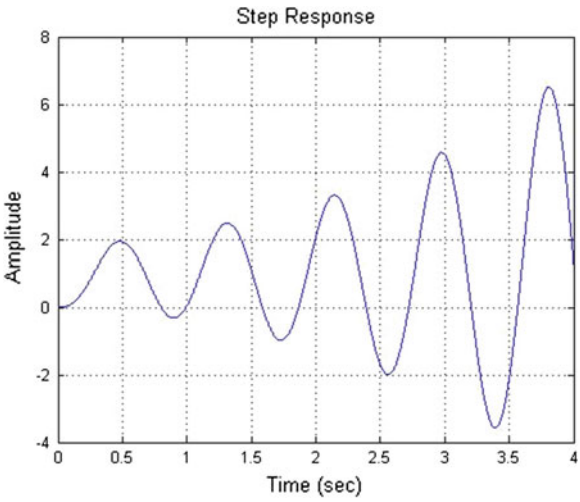

Fig. 132.8 Uncompensated system in Example 132.3

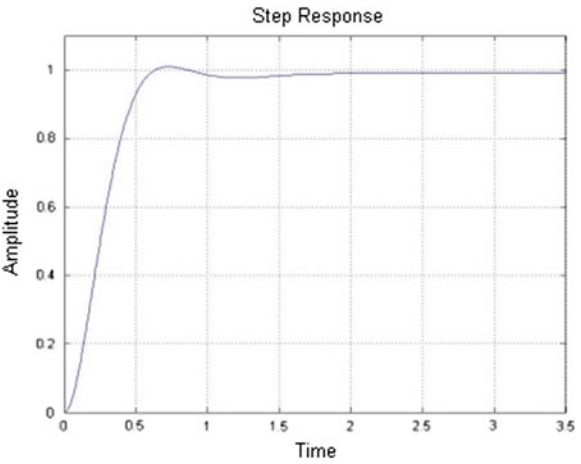

Fig. 132.9 Compensated system in Example 132.3

132.8 Conclusions

A large part of an industrial plant system may be represented by the linear time-invariant transfer function. A simple design procedure using a lead–lag controller to meet or approach the design specification with cuckoo search algorithm has been proposed in this paper. The proposed time-domain objective function is expressed in terms of peak time, maximum overshoot, delay time, setting time and steady state error. Computer simulations support the usefulness of the method.

References

1. Nise, N. S. (2011). *Control systems engineering* (6th ed.). New York: Wiley.
2. Okada1, Y., Yamakawa, Y., Yamazaki, T., & Kurosu, S. (2007, September 17–20). Tuning method of PID controller for desired damping coefficient. In *Proceedings of SICE Anal Conference, Kagawa University, Japan (*pp. 795–799*)*.
3. Aström, K. J., & Murray, R. M. (2008) *Feedback systems: An introduction for scientists and engineers* (3rd ed.). Princeton: Princeton University Press.
4. Yang, J., Chen, C.F., Chen, C. S., & Xu, Y. S. (1991). An approach to automatic tuning of phase-lead and phase-lag compensators. In *Proceedings of the 30th IEEE Conference on Decision and Control, Brighton, England* (Vol. 3 pp. 2944–2945).
5. Dorf, R. C., Jung, S., Dawes, J., & Ng, L. (1995, June). A S-plane analytic technique for lead–lag controller design. In *Proceedings of the American Control Conference Seattle, Washington* (pp. 2227–2228).
6. Tan, N. (2003). Computation of stabilizing lag/lead controller parameters. *Computers and Electrical Engineering, 29*, 835–849.
7. Horng, H. Y., (2012). Lead–lag compensator design based on genetic algorithms. In *Conference on Technologies and Applications of Artificial Intelligence (TAAI)* (pp. 80–85).
8. Horng, H. Y. (2013, February). Lead–lag compensator design based on greedy particle swarm optimization. In *2nd International Symposium on Next-Generation Electronics (ISNE)*.
9. Ou, C., & Lin, W. (2006, June). Comparison between PSO and GA for parameters optimization of PID controller. In *International Conference on Mechatronics and Automation, Luoyang, China* (pp. 2471–2475).
10. Yang, X. S., & Deb, S. (2009, December). Cuckoo search via Lévy flights. In *Proceedings of World Congress on Nature and Biologically Inspired Computing, India* (pp. 210–214). USA: IEEE Publications.
11. Yang, X. S., & Deb, S. (2010). Engineering optimisation by cuckoo search. *International Journal of Mathematical Modelling and Numerical Optimisation*, *1*(4), 330–343.

Chapter 133
Design and Implementation of a Tourism System Using Mobile Augmented Reality and GIS Technologies

Pei-Jung Lin, Chih-Chung Kao, Ka-Hou Lam and I-Chen Tsai

Abstract This study integrated geographic information systems (GIS), location-based services (LBS), mobile augmented reality (MAR), and information related to corporate mobile marketing to create an app for tourists using Android and iPhone systems. The proposed system provides an intuitive information interface capable of augmenting one's experience in the real world with elements of virtual reality, social networking services, and mobile tour guide functions. The goal was to provide tourists with access to information on tourist attractions, local culture, scenery, and shopping. The proposed tourist information system integrates information and communications technology (ICT) with tourism projects promoted by the Tourism Bureau and the Ministry of Economic Affairs as well as mobile marketing provided by 500 local businesses. The integration of a GIS-based computing engine and a corporate management framework ensures the provision of highly accurate mobile marketing information.

Keywords Information and communications technology · Mobile augmented reality · Geographic information systems · Location-based services

133.1 Introduction

This study incorporated information and communications technology (ICT) within a tourist information platform, using location-aware data and connections to social media. Based on the augmented reality (AR) technology of smart mobile devices,

P.-J. Lin (✉)
Department of Computer Science and Information Engineering, Hungkuang University, Taichung 43302, Taiwan, Republic of China
e-mail: pjlin@sunrise.hk.edu.tw

C.-C. Kao · K.-H. Lam · I.-C. Tsai
GEO Informatics Inc., Taichung 407, Taiwan, Republic of China

J. Juang et al. (eds.), *Proceedings of the 2nd International Conference on Intelligent Technologies and Engineering Systems (ICITES2013)*, Lecture Notes in Electrical Engineering 293,
DOI: 10.1007/978-3-319-04573-3_133,

this study integrated geographic information systems (GIS) with cloud computing technology to create a mobile system capable of providing instant access to information on tourist attractions via their cell phones cameras. The proposed system is free from the restrictions of conventional cell phones operating on individual platforms, thereby enabling tourists to access a variety of cross-platform services and AR images to augment real world experiences with the features of virtual reality rendered in 3D. The proposed system provides multimedia information related to tourist attractions as well as electronic maps with a user-friendly interface to help tourists plan sightseeing routes. Links to popular social networking services enable users to use posting and check-in functions to enhance their online "stickiness" user experience. The system also provides information on discounts and promotional offers provided by over 500 local businesses related to a wide range of products and services, thereby enriching the local travel experience for domestic and foreign tourists alike. The ultimate aim was to increase the value of domestic tourist attractions and assist in their transition to new technologically driven platforms, thereby creating a win–win situation for tourists as well as those who serve them.

This study addressed a variety of tourism-related programs instituted by the Tourism Bureau and the Ministry of Economic Affairs in the development of an app designed for use by tourists on smartphones and tablet computers. The app enables users to obtain detailed information on local history, culture, ecology, and shopping, while cooperating businesses can use it for marketing. Location-based services (LBS) facilitate the inclusion of personalized services, in which coupons and promotions are offered for services such as dining, shopping, accommodation, and transportation. The remainder of this paper is organized as follows. Section 133.2 considers previous research into mobile AR and LBS information. Section 133.3 outlines the design of the proposed system, including a POI recommendation function. Section 133.4 presents a number of conclusions.

133.2 Related Work

Taiwan has a solid ICT base and the government is actively involved in a variety of projects and activities aimed at promoting tourism. A key example is the Project Vanguard for Excellence in Tourism, which comprises three major projects: Project Summit, the objective of which is to build top-class spotlights and flagship attractions, Project Keystone, which aims for industry re-building and talent cultivation, and Project Propeller, which exploits existing markets, develops emerging customer bases, and seeks to increase service quality to international standards. Using these strategies, the government hopes to shape Taiwan into a tourist hub in Eastern Asia and an internationally important travel destination. Existing tourism apps developed for front-end mobile device systems make use of quick response codes (QR code) [1, 2] and GPS/LBS applications [3–5] to enable location-based tours, announcements, and sharing functions. Tour services combining local

cultural resources with mobile augmented reality (MAR) [6–9] give tourists immediate access to relevant information. MAR has become a crucial technology in mobile marketing, enabling businesses to develop apps for the promotion of corporate brands and recreational activities [10–12] as well as location-aware advertisements, providing information such as store locations, promotional offers, and mobile coupons.

MAR is the core technology of the system developed in this study, employing the geo-positioning function of smartphones to provide users with travel news and commercial information. Overlapping message boxes are displayed on the images obtained using camera phones [5]. Four key factors related to smart phones have made these applications possible: (a) high-definition screens and powerful processors, (b) accurate GPS functions, (c) sensors, such as e-compasses, gravity sensors, and orientation sensors, and (d) development platforms, such as Junaio or Layar. Juniper Research predicts that the market value of MAR will increase from the current USD 2 million to USD 730 million by 2014. It has also been predicted that the number of MAR app downloads will approach 1.4 billion by 2015. These figures demonstrate the enormous market potential of AR technology. Over the next few years, the diversity of mobile services will make AR applications even more popular and useful. Furthermore, advances in the hardware of mobile devices will lead to increasingly powerful processors and images of greater fidelity, capable of instant face recognition and automatic labeling. Faster network transmission speeds will deliver video and images more quickly, thereby increasing the speed of analysis and recognition. As MAR technology matures, a greater number of commercial agents and advertisers will be able to actualize their creativity and increase consumer participation and interaction in mobile advertising.

133.3 System Design and Implementation

To provide users with accurate GIS and customer relationship management (CRM) mobile marketing information, this study developed a framework integrating a GIS-based computing engine with corporate application management, as shown in Fig. 133.1. (1) The GEO WEB server provides users with the components required to manipulate maps on mobile devices with control over the rendering of landmarks and map layers as well as the display of their content. The function for point of interest (POI) recommendations is also implemented at this level. (2) The enterprise application adopts a service-oriented architecture (SOA) that supports GIS applications for a range of industries and assists in the establishment of spatial information service platforms in accordance with individual needs. (3) The GEO WEB server engine employs the map data functions of GEO WEB API and Google Earth API, to enable the real-time analysis and management of various data structures in GIS data modules.

Users can perform quick searches by aiming the lens of their mobile device at streets or buildings to find local travel information, such as descriptions of

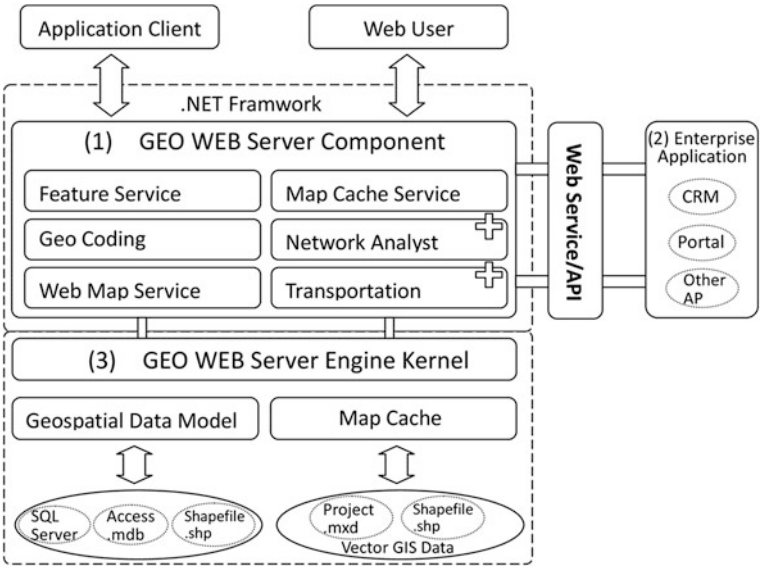

Fig. 133.1 System architecture

attractions, restaurants, shopping facilities, or promotional offers. This study applied MAR technology to present a comprehensive range of POI information on user smartphones or tablet computers for the provision of intuitive tour guide functions. The core technology of MAR was extended through tracking, interaction, and display. GPS and camera functions were combined to enable the identification of one's surroundings as well as tracking functions. For example, when a user directs the lens of their smartphone at a landmark, the system accesses a cloud database using the coordinates given by the GPS receiver to search for buildings with similar features at that location. Once the target has been confirmed, information related to the building is transmitted back to the mobile device and displayed. The proposed system focuses on the location with the user and the orientation of the user's mobile device. The time required to obtain POI information from a cloud database is substantially less than that which would be required to query, transmit, and process large quantities of information through conventional channels.

133.3.1 System Implementation

The framework of the MAR tourist information system was made operable on Android and iPhone systems through the integration of GIS, LBS, AR, and corporate mobile marketing technologies. The proposed system integrates the lens of mobile

Fig. 133.2 System implementation **a** AR display **b** Nearby POI list **c** Map routing display **d** Facebook check-in function

device, GPS, 3G/Wifi networks, and gravity sensors. AR images can be immediately displayed on the screen of the mobile device. In the following section, the primary functions of the system interface are introduced, as shown in Fig. 133.2.

The proposed system displays the image obtained through the camera on the smart device, as shown in Fig. 133.2a. The system also uses message boxes to display POIs with the user located in the center. The POIs are also displayed as white dots in a radar map in the lower right corner of the screen, which changes orientation as the user turns or moves. To provide the user with more interesting POI information, a feature was developed to calculate the distances between the user and the attractions as well as the popularity of the sites that appear. Users can designate the types of attractions in which they are interested, such that POIs in that area are listed in ranked preference. As shown in Fig. 133.2b, the names and addresses of the attractions and their distances from the user enable users to browse and access relevant information quickly. The POI recommendation function is outlined in Sect. 133.3.2. When the user selects a POI, the system presents the address, as shown in Fig. 133.2c, for confirmation of the location. For the sake of effective commercial marketing and customer management, commercial messages and digital coupons from cooperating businesses were also included. Selecting an AR message box links the user to Facebook, whereby the user can share tourist information and check into obtain coupons, as shown in Fig. 133.2d.

133.3.2 POI Recommendation Function

This study developed a POI recommendation function to identify popular POI information according to the current location of the user and the popularity status of the POIs. This function uses a cost function combining a distance factor and popularity status for the recommendation of POIs. The distance factor is defined as follows:

$$d(x,y) = \frac{d_{x,y}}{\max\limits_{z \in \mathbb{S}} d_{x,z}}, \tag{133.1}$$

where $d_{x,y}$ is the distance between the current location of the user, x, and a POI location y; $\max\limits_{z \in \mathbb{S}} d_{x,z}$ is the maximum distance between the user's current location x and all POI locations in set $\mathbb{S}$, including all POIs. This factor is a relative distance value between 0 and 1. The cost function used in the POI recommendation function is defined as follows:

$$f(x,y) = \alpha * d(x,y) + (1-\alpha) * P_y \tag{133.2}$$

where $d(x, y)$ is the distance factor, α is a weight value, and P_y is the popularity status for POI y. The popularity status of POIs can be obtained from social networks. The proposed cost function enables the recommendation of POI information of the greatest relevance to users.

133.4 Conclusions

The objective of this study was to incorporate ICT into the provision of tourism-related services and develop a location-aware tourist information platform with connections to social networking. Technically grounded in the AR of smart mobile devices, the mobile tourist service system integrates GIS positioning data with cloud services, including: (1) a simplified approach to the search for information related to tourist attractions and POIs using the camera lens on mobile devices, (2) a cross-platform design operable on smartphones and tablet computers, (3) AR image interface technology with the integration of real world attractions and the features of virtual reality rendered in 3D, (4) a user-friendly electronic map with route planning function, (5) community service functions to enable the instant sharing of MAR images, (6) analysis and collation of GIS data associated with POIs related to tourism, and (7) mobile access to a cloud database. The proposed system is made available through a mobile tourist-information app using LBS and social networking, representing a breakthrough in smart device tour guide technology. The system also features promotional offers from over 500 businesses, thereby creating a tourist information system with mobile marketing capable of being managed automatically.

Acknowledgments The authors would like to thank the National Science Council of the Republic of China for financially supporting this research under Contract No. NSC 102-2622-E-241-003-CC3.

References

1. Cata, T., Patel, P. S., & Sakaguchi, T. (2013). QR code: A new opportunity for effective mobile marketing. *Journal of Mobile Technologies, Knowledge and Society, 2013*, Article ID 748267. doi: 10.5171/2013.748267
2. Harini, N., & Padmanabhan, T. R. (2013). 2CAuth: A new two factor authentication scheme using QR-code. *International Journal of Engineering and Technology, 5*(2), 1087–1094.
3. Garg, D., & Shukla, A. (2013). GEO ALERT—A location based alarm system using GPS in android. *International Journal of Multidisciplinary in Cryptology and Information Security, 2*(3), 11–14.
4. Abo-Zahhad, M., Ahmed, S. M., & Mourad, M. (2013). Services and applications based on mobile user's location detection and prediction. *International Journal of Communications, Network and System Sciences, 6*, 167–175.
5. Pomberger, G. (2011). Digital graffiti—a framework for implementing location-based systems. *International Journal of Software and Informatics, 5*(1–2), 355–377.
6. Fu, J., Nopasit, C., Paul, G., & Antonio, M. (2011). E-tourism curriculum design: Filling the gap between knowledge demand and supply. In *5th IEEE International Conference on Software, Knowledge Information, Industrial Management and Applications* (*SKIMA 2011*) (pp. 1–8), Benevento, Italy, September 8–11.
7. Grosvenor, C. E., Lott, M. C., & Webber, M. E. (2011). A methodology for analyzing environmental tradeoffs for different travel and information communication technologies (ICT) options. In *IEEE International Symposium on Sustainable Systems and Technology* (*ISSST 2011*), Chicago, USA, May 16–18.
8. Hsu, C. (2011). The feasibility of augmented reality on virtual tourism website. In *International Conference on Ubi-Media Computing* (*U-Media 2011*) (pp. 253–256), Sao Paulo, Brazil, July 3–4.
9. Lim,Y., Park, Y., Heo, J., Yang, J., Kang, M., & Byun, Y. C. (2011). A smart phone application based on AR for Jeju tourism. In *International Conference on Computers, Networks, Systems and Industrial Engineering* (*CNSI 2011*) (pp. 271–272), Jeju Island, South Korea, May 23–25.
10. Schinke, T., Henze, N., & Boll, S. (2010). Visualization of off-screen objects in mobile augmented reality. In *12th International Conference on Human Computer Interaction with Mobile Devices and Services* (*MobileHCI 2010*) (pp. 313–316), September 7–10.
11. Wagner, D., Reitmayr, G., Mulloni, A., Drummond, T., & Schmalstieg, D. (2010). Real-time detection and tracking for augmented reality on mobile phones. *IEEE Transactions on Visualization and Computer Graphics, 16*(3), 355–368.
12. Rangaswamy, N., Challagulla, G., Young, M., & Cutrell, E. (2013). Local pocket internet and global social media bridging the digital gap: Facebook and youth sub-stratum in urban India. In *12th International Conference on Social Implications of Computers in Developing*, Ocho Rios, Jamaica, May 19–20.

Chapter 134
The Novel Measure Method for Ultrasound Transducer with LabVIEW on the High Power

Sheng-Chien Su, Wen-Chung Chang, Chih-Yung Wang and Kai-Hsing Ma

Abstract The objective of this study is the construction of a high power measurement system with NF HS4012 using LabVIEW as the platform of the measurement system for high power transducer. The purpose is to explore high power ultrasound applied to welding and study the size of the ultrasound transducer including its characteristic, energy production and the methods to control energy. The stability and efficiency of the characteristics of the original components and the circuitry of the entire activation system are key points of the investigation for this study.

Keywords LabVIEW · High power transducer · Ultrasound transducer

134.1 Introduction

Laboratory Virtual Instrument Engineering Workbench (LabVIEW) is a graphical programming environment. It can be used for sophisticated measurement and test for high power electrical energy by using intuitive graphical icons program connected to external high power instruments. A 550 W high power electrical energy is generated through a high power converter to drive the ultrasound transducer whose mechanical vibration is applied to vehicle leather by high speed mechanical vibrations [1].

S.-C. Su (✉) · W.-C. Chang · C.-Y. Wang · K.-H. Ma
Department of Electronic Engineering, Southern Taiwan University of Science and Technology, Tainan, Taiwan, Republic of China
e-mail: ct6288@gmail.com

J. Juang et al. (eds.), *Proceedings of the 2nd International Conference on Intelligent Technologies and Engineering Systems (ICITES2013)*, Lecture Notes in Electrical Engineering 293,
DOI: 10.1007/978-3-319-04573-3_134,

134.2 Transducer Equivalent Circuit Model

When we derive the equivalent circuit for the ultrasound transducer, we may draw the frequency versus impedance diagram as shown in Fig. 134.1 with the help of an impedance analyzer. The point of resonant frequency is at the lowest impedance, the point of anti-resonant frequency is at the highest impedance. The characteristic is very important to design circuit generating activation. There are changes which result in the components easily influenced by external pressures. Especially, when the temperature is excessively high, the attenuation of the component results in a change that can be deduced calculation the equivalent impedance characteristic as shown in:

$$Y = \frac{R}{R^2 + X_s^2} + j\left(X_P - \frac{X_S}{R^2 + X_s^2}\right) \tag{134.1}$$

$$Z = \frac{R_S X_P^2}{R_S^2 + (X_P + X_S)^2} + j\left[X_P - \frac{X_P^2 (X_P + X_S)}{R_S^2 + (X_P + X_S)^2}\right] \tag{134.2}$$

At resonant frequency, allowing the highest resonant impedance R_r, this condition is valid when the value of X_S^2 is zero, and the following relationship is obtained:

$$L = \frac{1}{C_1 (2\pi f_r)^2} \tag{134.3}$$

$$R = R_S \tag{134.4}$$

At anti-resonant frequency, the highest impedance value is anti-resonant impedance R_a, when $X_S = -X_P$, then the impedance and angular frequency are represented as:

$$C_1 = \frac{C_b (f_a^2 - f_r^2)}{f_a^2} \tag{134.5}$$

$$C_b = \frac{1}{2\pi f_r \sqrt{R_r R_a}} \tag{134.6}$$

Through the derivation, the resonant frequency f_r, anti-resonant frequency f_a, resonant impedance R_r and series resonant impedance R_a are obtained. Therefore, deriving the values of each component of the equivalent circuit can be further analyzing the changes in the components.

When we research the vibration characteristics of the piezoelectric ceramics, understand the equivalent circuit model for a specific resonant frequency as shown in Fig. 134.2 where Cb denotes piezoelectric ceramics static capacitance, L denotes motional inductance, C1 denotes motional capacitance, and R denotes piezoelectric ceramics resistance loss. In the equivalent circuit model of the

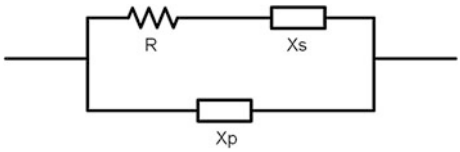

Fig. 134.1 One-port SAW resonator equivalent circuit diagram

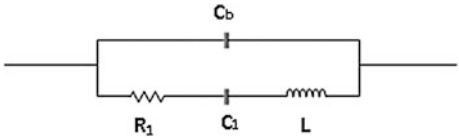

Fig. 134.2 Piezoelectric transducer equivalent circuit model

piezoelectric ceramics, two significant parameter values can be defined for the piezoelectric ceramics: resonant frequency and anti-resonant frequency:

$$f_{resonant} = \frac{1}{2\pi\sqrt{L \cdot C_1}} \tag{134.7}$$

$$f_{anti-resonant} = \frac{1}{2\pi\sqrt{L \cdot \frac{C_1 \cdot C_b}{C_1 + C_b}}} \tag{134.8}$$

Where $f_{resonant}$ denotes resonant frequency, $f_{anti\text{-}resonant}$ denotes anti-resonant frequency. When deriving the equivalent circuit of the transducer, the impedance analyzer may be used to draw the frequency versus impedance diagram and the gain-phase diagram, as shown in Fig. 134.3. From the diagram, it is observed that at the point of resonant frequency is at the lowest impedance, while the point of anti-resonant frequency is at the highest the impedance, the dotted line represents the gain-phase diagram for the piezoelectric ceramics. When the piezoelectric ceramics is operating below the resonant frequency or above the anti-resonant frequency, it becomes capacitive; but when it is operating between the resonant frequency and the anti-resonant frequency, it becomes inductive; and understanding these characteristics is crucial to the design of the activation.

The measuring device is a HP4294A Impedance Analyzer [2], and the frequency scanning range is from 35 to 40 kHz [3]. As shown in Fig. 134.3, the changing impedance of the transducer under different working frequencies, of which the changes between resonant and anti-resonant points are significant. The resonating frequency for the static anti-resonant point measured by the impedance analyzer is 39.725 kHz [3], proving that the results of the entire design is nearing the anti-resonating point, and using the waveform measured by the impedance analyzer [4], the impedance characteristic of the piezoelectric ceramics is physically observed, as well as the positions of the resonant frequency and the anti-resonant frequency, but these characteristics tends to result in unstable frequency drift, hence the need to located a region where the stability is controllable.

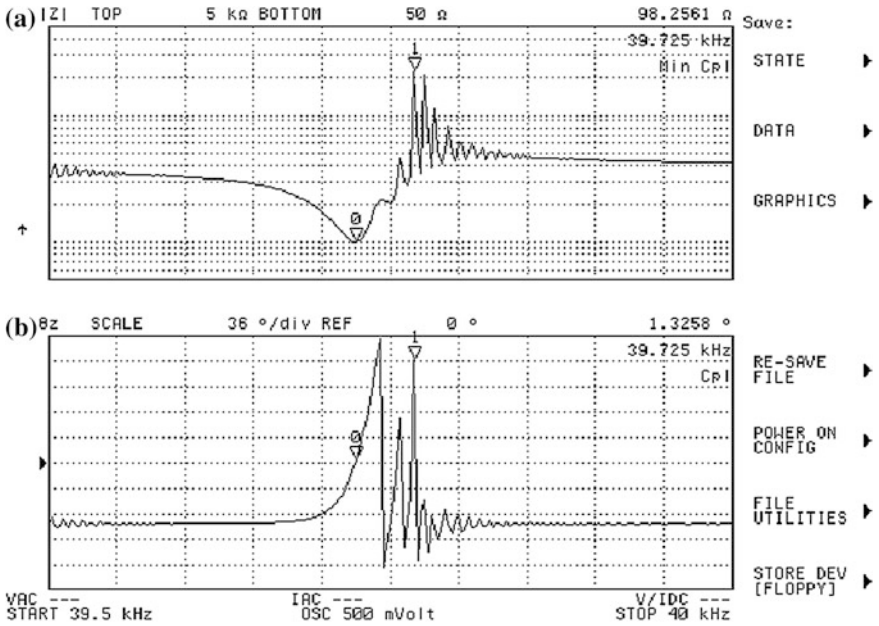

Fig. 134.3 Ultrasound probe physical measurements of characteristics diagram

134.3 High-Power Ultrasonic Transducer Measurement Techniques

Figure 134.4 shows the block diagram of the high power piezoelectric element measurement system that includes the LabVIEW program with a computer, a GBIP Interface card, an arbitrary waveform generator (Agilent 33250A), a oscilloscope (Tektronix TDS3000) and a power amplifier (NF HS4012) [5]. The GBIP Interface card is used to translate the signals between the Waveform Generator and the Oscilloscope. By the man-machine interface command of the LabVIEW program, the Waveform Generator will produce and send a frequency signal to the power amplifier (NF HS4012) enlarge the frequency signal to drive the piezoelectric transducer [6].

We can obtain the piezoelectric feature of transducer using the sweep frequency method in the high power of ultrasound welding system. Typically, this feature is the characteristic impedance of the frequency and phase-frequency characteristics, as Fig. 134.5. It demonstrates that the point B is the resonance point and the point A is the anti-resonance point.

As shown in Fig. 134.6, point A is the piezoelectric characteristic curve of the ultrasound transducer vibrator that is without a housing, the frequency bandwidth of the resonating and the anti-resonating points is approximately 500 Hz, the resonating and anti-resonating resonance levels are high, vibration characteristics

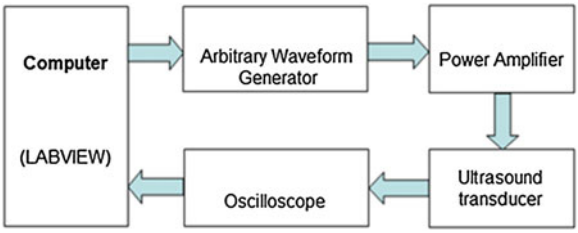

Fig. 134.4 Block diagram of a high power piezoelectric element measurement system

are good. Point B is the piezoelectric characteristic curve of the ultrasound transducer vibrator that is with aluminum-alloy housing, the frequency bandwidth for the resonating and anti-resonating points is approximately 100 Hz, the resonating and anti-resonating resonance levels are low, vibration characteristics becomes small. Point C is the piezoelectric characteristic curve of the ultrasound transducer vibrator that is with titanium-alloyed housing, the frequency bandwidth for the resonating and anti-resonating points is approximately 100 Hz, the resonating and anti-resonating resonance levels are lower, vibration characteristics becomes smaller.

The piezoelectric properties response to heat is extremely sensitive. When a high power ultrasound welding activation system has been working under long periods of time, a lot of heat is generated due to the high speed frictional vibrations, and this phenomenon would cause a drift in the working frequency of the high power ultrasound transducer. Hence, the change in temperature of the high power ultrasound transducer is significant. This study uses this measuring system to further analyze and investigate the properties of the high power ultrasound transducer during temperature changes, and to locate the changes in the characteristic curve and the changes in the working frequency. Typical ultrasound transducer uses a titanium-alloy or aluminum-alloy housing, this study made comparisons between the two working under long periods of time, with the rise in temperature, the overall changes of the characteristics are as shown in the Fig. 134.6. As shown in Fig. 134.7, when the temperature changes are higher for the transducer with an aluminum-alloy housing, changing from 60 to 120°, the overall characteristics curve shows signs of drifting towards the lower left, and at 120°, the resonating and anti-resonating points show signs of attenuation, it is observed that when the temperature reaches a certain level, influencing the efficiency of the vibrations of the ultrasound transducer, and the impedance becomes low while the electrical current becomes high, making it difficult to control the operations of the entire piezoelectric characteristic in a stable region. As shown in Fig. 134.8, when the temperature changes are higher for the transducer with a titanium-alloy housing, changing from 60 to 120°, the overall characteristics curve shows signs of drifting towards the lower left, but since titanium-alloy does not dissipate heat well, at 90° the resonating and anti-resonating points show signs of attenuation, it is observed that when the temperature reaches a certain level, influencing the efficiency of the vibrations of the ultrasound transducer, and the

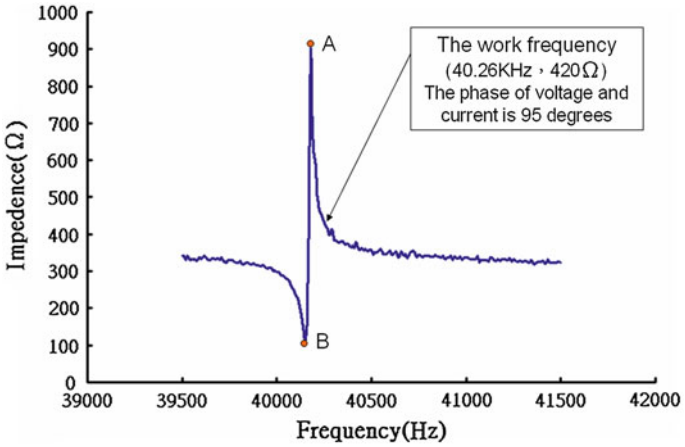

Fig. 134.5 The characteristic impedance of the frequency

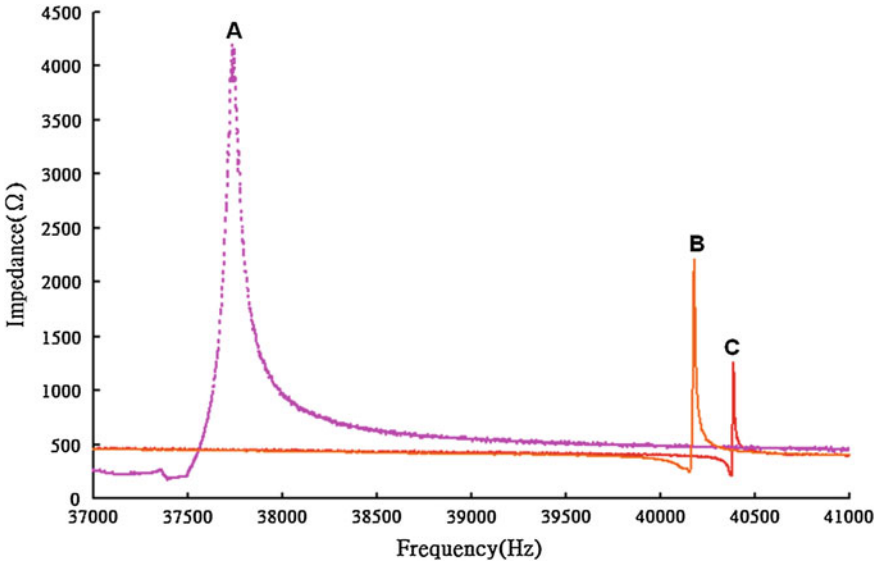

Fig. 134.6 The overall changes of the characteristics in the temperature rise

impedance becomes low while the electrical current becomes high, making it difficult to control the operations of the piezoelectric characteristic in a stable region, while at 120° resonating and anti-resonating points are extremely close, the characteristic curve for the piezoelectric became very poor, possibly not suitable for work continuation, requiring other mechanisms such as air-cooled, water-cooled for the ultrasound transducer to resume to the original piezoelectric characteristic curve.

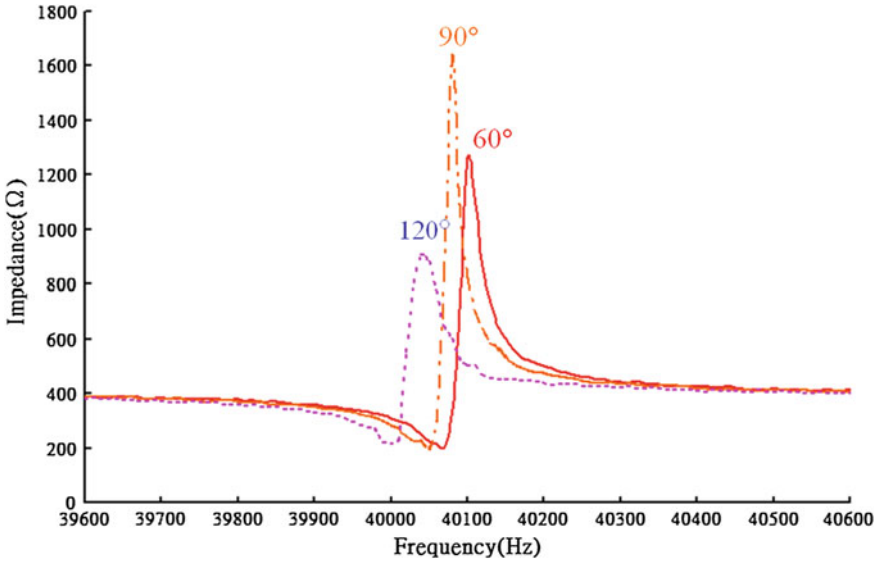

Fig. 134.7 The piezoelectric transducer at works at a high temperature (80 °C)

It was found when the piezoelectric transducer works at a high temperature (120 °C), the impedance characteristic of the piezoelectric transducer will drift to left and down in Fig. 134.7. In other words, as the temperature increases, the working frequency will change and the impedance of the transducer becomes small. The impedance of the transducer becomes small will make the output current become very large immediately. The large output current will raise the output power to burn the mold. Therefore, the ultrasound welding system must adjust continuously the working frequency to keep the output a stable power.

Therefore, on the overall, by comparing the different material characteristics, it was easily discovered that the piezoelectric characteristic for aluminum-alloy are better than that of titanium-alloy. Likewise, temperature characteristics are also better for aluminum-alloy than for titanium-alloy, and comparing Figs. 134.7 and 134.8, when both are at 120°, the piezoelectric characteristic for the aluminum-alloy shows suitability for work, whereas, the piezoelectric characteristic for the titanium-alloy shows that it is not suitable for the continuation of work.

134.4 Results and Discussions

The reaction of piezoelectric property on the heat is very sensitive by the high power measurement system. The high power ultrasound welding drive system for the phenomenon on the long work will make the working frequency of high power ultrasound transducer produces drift. Here, high power ultrasound transducer

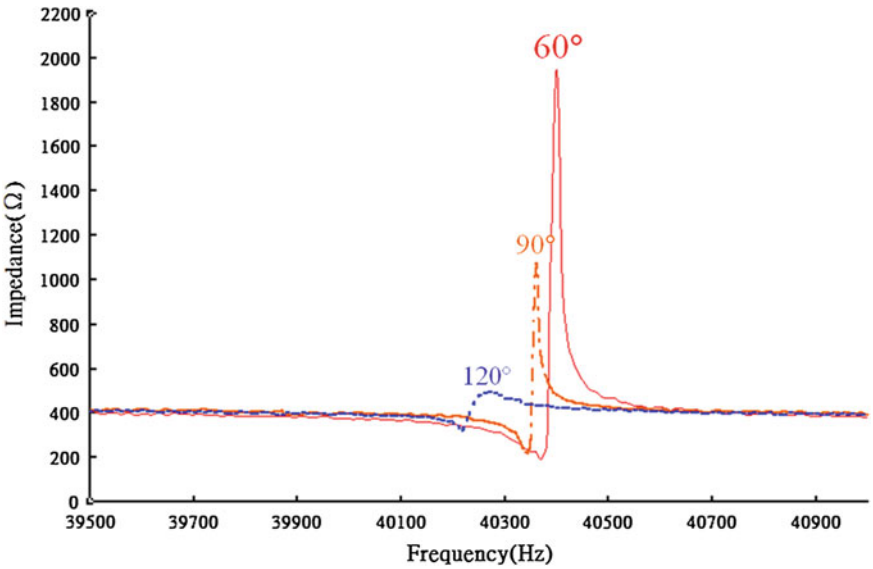

Fig. 134.8 The piezoelectric transducer works a high temperature (80 °C)

temperature change is quite important, so this study used the high power ultrasound transducer temperature measurement system to obtain the impedance change on temperature different conditions. On the material temperature characteristic, aluminum-alloy is better than titanium-alloy by the comparison as such Figs. 134.7 and 134.8. Therefore, ultrasound characteristic changes can be verified to compare the material temperature characteristic of aluminum-alloy and can be found out the change of working frequency by the novel measure method. When the temperature increases to the changes of characteristic on the overall situation, this study can be express in Drift-characteristic to facilitate impedance method design for the high power ultrasound transducer.

134.5 Conclusion

The novel measure method with LabVIEW is can be used in the high power ultrasound. Nowadays, it can be used to identify whether a material is good or bad to implement by determining the stability of the working state on a practical ultrasound welding system. Experimental results prove that the new method can effectively measure the difference on the material base from the changes in the temperature characteristic and working frequency on the ultrasound welding system.

References

1. Uchino, K. (1998). Materials issues in design and performance of piezoelectric actuators: An overview. *Acta Materialia, 46*, 3745–3753.
2. Newnham, R. E. (1997). Molecular mechanisms in smart materials. *MRS Bulletin, 5*, 20–34.
3. Moulson, A. J., & Herbert, J. M. (1990). *Electroceramics*. London: Chapman and Hall.
4. Kazimierczuke, M. K., & Czarkowski, D. (1995). *Resonant power converter*. New York: Wiley.
5. Sokal, N. O., & Sokal, A. D. (1975). Class E-A new class of efficiency tuned single-ended switching power amplifiers. *IEEE Journal of Solid-State Circuits, 3*, 168–176.
6. Ishikawa, J., Mizutani, Y., Suzuki, T., Ikeda, H., & Yoshida, H. (1997). High-frequency drive-power and frequency control for ultrasonic transducer operating at 3 MHz. In *IEEE Industry Applications Conference and Thirty-Second IAS Annual Meeting, 2* (pp. 900–905).

Chapter 135
Study of the Perimeter Deposition Enhanced Cr^{4+} Concentration in Cr^{4+}:YAG Single-Clad Crystal Fiber

Cheng-Nan Tsai, Wei-Chung Ho, Sheng-Lung Huang, Shih-Kun Liu and Yi-Hua Chang

Abstract Cr^{4+}:YAG crystal has been shown an exceptionally successful ultra broad-band amplified spontaneous emission light source that fully cover 1253–1530 nm range (3 dB bandwidth up to 265 nm). Keeping in mind that the amplified spontaneous emission of Cr^{4+}:YAG is proportional to the concentration of Cr^{4+} ions. The Cr^{4+} ions are replenished using an electron-gun to deposit CaO on the source rod circumference under annealing treatment at 1350 °C. The laser-heated pedestal growth method was employed to re-grow the Cr^{4+}:YAG single-clad crystal fiber. The doped concentration of CaO can be in-diffuse and it can serve as charge compensators to enhance the concentration of Cr^{4+} ions. The experimental results indicate that the Cr^{4+} concentration of Cr^{4+}:YAG crystal fiber can be raised by a factor of 196 %.

Keywords Doping · Deposition · Laser heated pedestal growth · Cr^{4+}:YAG · Crystal fiber

C.-N. Tsai (✉) · Y.-H. Chang
Institute of Electronic Engineering, Cheng Shiu University, Kaohsiung 83347, Taiwan, Republic of China
e-mail: chnan@post.csu.edu.tw

W.-C. Ho
Institute of Electronic Engineering, National Kaohsiung University of Apply Science, Kaohsiung 80778, Taiwan, Republic of China

S.-L. Huang
Institute of Photonics and Optoelectronics, National Taiwan University, Taipei 10617, Taiwan, Republic of China

S.-K. Liu
Institute of Photonics and Communication, National Kaohsiung University of Apply Science, Kaohsiung 80778, Taiwan

J. Juang et al. (eds.), *Proceedings of the 2nd International Conference on Intelligent Technologies and Engineering Systems (ICITES2013)*, Lecture Notes in Electrical Engineering 293,
DOI: 10.1007/978-3-319-04573-3_135,

135.1 Introduction

Optical fibers with very broad-band gain have aroused great interest in developing tunable miniature lasers and amplifiers, which can be used in telecommunications with wider gain bandwidth than commercial erbium-doped fiber amplifiers and others reported rare earth (RE)-doped fiber devices. During the past decade, the fast increasing demand of communication capacity results in the emergence of wavelength division multiplexing (WDM) technology. In consequence, it raises the stringent requirement of spectral characteristics of all the optical components used in the optical fiber networking systems. Cr^{4+} doped yttrium aluminum garnet (YAG) has a strong spontaneous emission that can generate near-infrared emission from 1253 to 1530 nm. This broadband emission just covers the low-loss window of low-water-peak optical fiber through out optical communication bands. Such broadband characteristics offer unprecedented one-for-all convenience, flexibility, and simplicity to multi-band component manufacturing as ultra broadband laser source, amplifier, etc. [1–9].

It is well-known that when Cr ions are doped into YAG crystal with a dominant ionic state of +3, Cr^{3+} can substitute for Al^{3+} at the octahedral sites. Selected divalent cations were evaluated for their effectiveness as co-dopant ions in Cr^{4+}:YAG to enhance the Cr^{4+} concentration. The most suitable co-dopants are Ca^{2+} and Mg^{2+}, which divalent ions can serve as efficient charge compensators. It was observed that Ca^{2+} has better efficiency to diffuse into the source rod more efficiently than Mg^{2+} generating fewer defects and stacking faults [10]. The Cr^{4+}:YAG single crystal fiber under oxygen environment at 1500 °C was obtained the highest Cr^{4+} fluorescence efficiency [11]. We adopt the laser heated pedestal growth (LHPG) method to fabricate the Cr^{4+}:YAG crystal fiber. Because of the out-diffusion and evaporation of Cr_2O_3 during LHPG process, the Cr^{4+} concentration decreases substantially, which results in reduced signal gain and amplified spontaneous emission (ASE) power. For this reason, improving the Cr^{4+} charge compensation efficiency is first challenge for ASE power. Sugimoto et al. have been shown that as much as 6 % of Cr ions can exist in a tetravalent coordination state with bulk crystal by Czochralski method [12]. But after diameter-reduction in 70 μm during LHPG method, the ratio of Cr^{4+} to Cr is decreased to less than 1 % [13]. Therefore, enhancement of Cr^{4+} concentration is very important for ASE. However, the Cr^{4+}:YAG crystal fiber in its own repetitive growth process brings with itself one problem: after each re-growth, the concentrations of Cr_2O_3 and Cr^{4+} ions would reduced appreciatively. But the efficiency of the Cr^{4+}:YAG crystal fiber is proportional to the concentration of the Cr^{4+} ions; Hence, using electron gun to deposit CaO on the source rod circumference of the Cr:YAG single crystal fiber followed by re-growth and under oxygen annealing at 1350 °C are crucial for designing highly efficient Cr:YAG single-clad crystal fiber.

In this paper, we demonstrate the enhancement of Cr^{4+} concentration by electron gun deposition of CaO on the source rod circumference of the Cr^{4+}:YAG

Table 135.1 Summary of the dopant concentrations of Cr:YAG single-clad crystal fibers

Sample No.	CaO deposition time(s)	CaO (wt.%)		Cr_2O_3 (wt.%)	
		Core	Clad	Core	Clad
N1	0	0.005	0.013	0.015	0
N2	180	0.012	0.014	0.013	0
A2	180	0.008	0.020	0.011	0.008
N3	210	0.015	0.016	0.018	0
A3	210	0.010	0.020	0.013	0.002

crystal fiber followed by re-growth. The experimental results indicate that the Cr^{4+} concentration of Cr:YAG crystal fiber can be raised above a factor of 50 %.

135.2 Experiment

The source rods were Ca co-doped Cr^{4+}:YAG with 500 × 500 μm in cross section and <111> in crystal orientation. They were first grown at a speed of 24 mm/min with a CO_2 laser power of 6.5 W using the LHPG method in order to obtain 290 μm-diameter crystal fiber. After cutting into 4 cm-long pieces, they were placed in an electron gun chamber with an axially rotated mount for perimeter deposition. CaO was deposited on the source rod followed by re-growth and under oxygen annealing (samples no. denoted A2–A3) at 1350 °C for 4 h or not (samples no. denoted N1–N3), The same LHPG system was used as a heating source and the Cr^{4+}:YAG filled borosilicate capillary tube was codrawn through the hot spot at a growth speed of 4.5 mm/min. The single-clad fiber structure can be produced. The diameters of core and cladding are 40 and 320 μm, respectively.

The composition of the crystal fibers was characterized using an EPMA (JEOL JXA-8900R). A laser scanning confocal microscope was employed for identifying Cr^{4+} ions, which were excited by a 1064 nm Yb^{3+}-doped fiber laser. An objective lens with a numerical aperture of 0.65 was employed to achieve a spatial resolution of about 1 μm. The Cr^{4+} fluorescence intensity was collected by an InGaAs photodiode (Hamamatsu G8370-05).

135.3 Results and Discussions

Table 135.1 shows the estimated perimeter deposition time and dopant concentrations. The total CaO concentration is about linearly proportional to the perimeter deposition time.

Figure 135.1a shows that the line scan of composition of the Cr:YAG single-clad fiber samples. In Fig. 135.1b shows that the major composition of cladding is

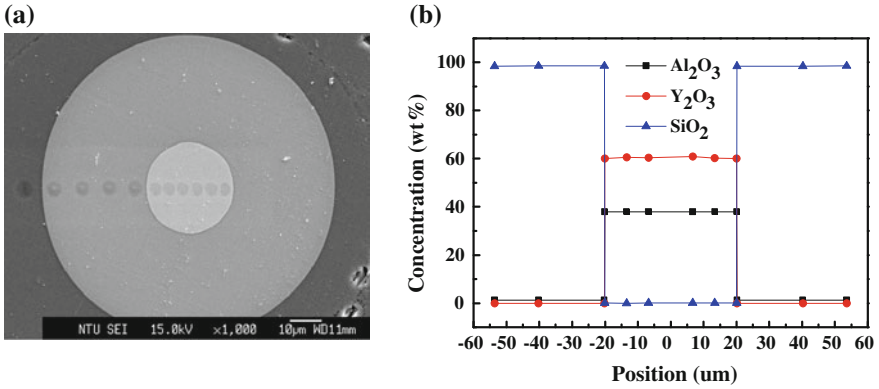

Fig. 135.1 **a** Scanned across the cross section of Cr^{4+}:YAG single-clad crystal fiber, **b** distribution of major concentration by EPMA measured of borosilicate-clad Cr:YAG fiber

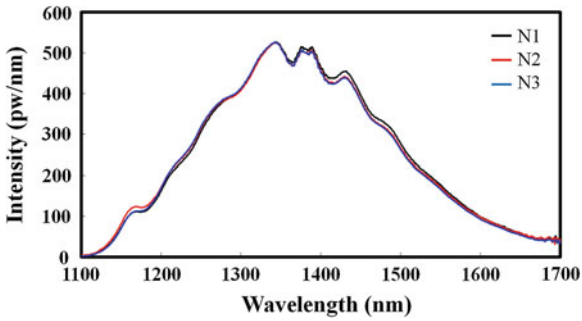

Fig. 135.2 The Cr^{4+} normalized fluorescence spectra of N1, N2 and N3 measured from Cr^{4+}:YAG single-clad crystal fiber

almost SiO_2 (>98.4 %), but the core area is composed of Y_2O_3 and Al_2O_3, whose average concentrations are 60 and 38 wt.%, respectively.

The refractive index of Cr^{4+}:YAG single-clad crystal fiber between core and cladding is 1.820 and 1.474, respectively. The refractive index indicates that Cr^{4+}:YAG crystal fiber and borosilicate capillary tube did not melt into each other while fused by gas torch.

The Cr^{4+} normalized fluorescence spectra of N1, N2 and N3 measured from a 40 μm-core Cr^{4+}:YAG single-clad crystal fiber was shown in Fig. 135.2. The spectra show the representative broadband band emission from 1200 to 1600 nm resulting $^3T_2 \rightarrow {}^3A_2$ transition.

Figure 135.3 shows the measured result of line scanning the cross section of the N1 sample, the Cr^{4+}:YAG single-clad crystal fiber shows a strong fluorescence in the core area.

Figure 135.4 shows that the Cr^{4+} ions are replenished using an electron-gun to deposit CaO on the 290 μm source rod circumference before growth. The LHPG method was employed to re-grow the Cr:YAG single-clad crystal fiber. The doped

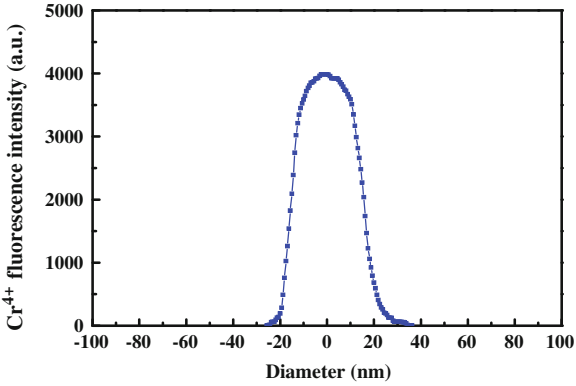

Fig. 135.3 Cr^{4+} fluorescence of Cr^{4+}:YAG single-clad crystal fiber

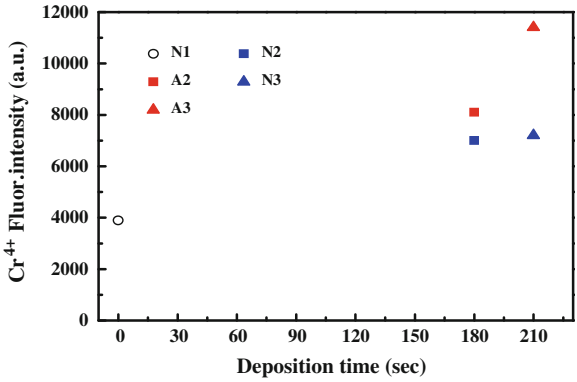

Fig. 135.4 Relation between CaO deposition time and Cr^{4+} fluorescent intensity

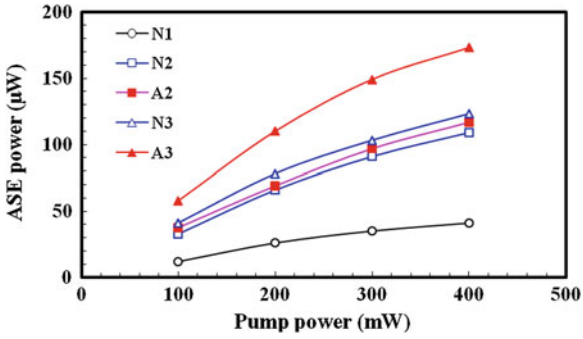

Fig. 135.5 ASE power versus pump power for the Cr:YAG single-clad crystal fiber samples

concentration of CaO can be in-diffuse and it can serve as charge compensators to enhance the concentration of Cr^{4+} ions. The experimental results indicate that the Cr^{4+} concentration of Cr:YAG crystal fiber can be raised by a factor of 196 %.

In this paper, we used the end pumping scheme for the ASE generation. The pumping light was lunched into the core of Cr^{4+}:YAG single-clad crystal fiber

samples. The corresponding fiber length was 3 cm. Figure 135.5 shows that the ASE power of A3 is up to 165 μW for 400 mW pump power. The experiment results indicate that the Cr:YAG single-clad crystal fiber can be used as candidate of an ultra broadband laser material and amplified spontaneous emitter.

135.4 Conclusions

For the ASE, the Cr^{4+}:YAG single-clad crystal fiber must have small core diameter, and long length to have high efficiency. But chromium ions tend to diffuse outward during the LHPG of YAG crystal fiber, in which the average concentration of Cr^{4+} ion decreases significantly after each diameter-reduction step. The Cr^{4+} concentration in the Cr^{4+}:YAG single-clad crystal fiber is effectively enhanced by using electron gun perimeter deposition of CaO. The Cr^{4+} concentration was raised by a factor of 196 % after oxygen annealing at 1350 °C and was produced the Cr^{4+}:YAG single-clad crystal fiber. The ASE power can be achieved 165 μW for 3 cm-length Cr^{4+}:YAG single-clad crystal fiber.

In the future, there are two major points. Firstly, looking forward to enhancing the Cr^{4+} concentration and increasing the fiber length to fabricate the high efficiency Cr^{4+}:YAG single-clad crystal fiber amplifier. Secondly, with the use of the electron gun coating machine, also probes the technical side of Cr:YAG single-clad crystal fiber laser. Both end faces of the Cr^{4+}:YAG single-clad crystal fiber were coated with high-quality optical thin films from TiO_2 and SiO_2 targets, the Cr^{4+}:YAG single-clad crystal fiber combine the output coupler to create a laser cavity in which both the anti-reflectance (AR) effect (for pumping the light source) and the high reflectance (HR) effect (for stimulating the light source) are achieved.

Acknowledgments This work is supported by the National Science Council, Taiwan under grant NSC 101-2221-E-230-012.

References

1. Lai, C. C., Yeh, P., Wang, S. C., Jheng, D. Y., Tsai, C. N., & Huang, S. L. (2012). Strain-dependent fluorescence spectroscopy of nanocrystals and nano-clusters in Cr:YAG crystalline-core fibers and its impact on the lasing behavior. *Journal of Physical Chemistry C, 116*, 26052–26059.
2. Lai, C. C., Ke, C. P., Liu, S. K., Jheng, D. Y., Wang, D. J., Chen, M. Y., et al. (2011). Efficient and low-threshold Cr^{4+}:YAG double-clad crystal fiber laser. *Optics Letters, 36*, 784–786.
3. French, P. M. W., Rizvi, N. H., Taylor, J. R., & Shestakov, A. V. (1993). Continuous-wave mode- locked Cr^{4+}:YAG laser. *Optics Letters, 18*, 39–41.
4. Ishida, Y., & Naganuma, K. (1996). Compact diode-pumped all-solid-state femtosecond Cr^{4+}:YAG laser. *Optics Letters, 21*, 51–53.

5. Pavel, N., Saikawa, J., Kurimura, S., & Taira, T. (2001). High average power diode end-pumped composite Nd:YAG laser passively Q-switched by Cr^{4+}:YAG saturable absorber. *Japanese Journal of Applied Physics, 40*, 1253–1259.
6. Takaichi, K., Lu, J., Murai, T., Uematsu, T., Shirakawa, A., Ueda, K., et al. (2002). Chromium doped $Y_3Al_5O_{12}$ ceramics- a novel saturable absorber for passively self-Q-switched one-micron solid state lasers. *Japanese Journal of Applied Physics, 41*, 96–98.
7. Yagi, H., Yanagitani, T., Yoshida, H., Nakatsuka, M., & Ueda, K. (2006). Highly efficient flashlamp-pumped Cr^{3+} and Nd^{3+} codoped $Y_3Al_5O_{12}$ ceramic laser. *Japanese Journal of Applied Physics, 45*, 133–135.
8. Lo, C. Y., Huang, K. Y., Chen, J. C., Tu, S. Y., & Huang, S. L. (2004). Glass-clad Cr^{4+}:YAG crystal fiber for the generation of superwideband amplified spontaneous emission. *Optics Letters, 29*, 439–441.
9. Lo, C. Y., Huang, K. Y., Chen, J. C., Chuang, C. Y., Lai, C. C., Huang, S. L., et al. (2005). Double-clad Cr^{4+}:YAG crystal fiber amplifier. *Optics Letters, 30*, 129–131.
10. Tsai, C. N., Lin, Y. S., Huang, K. Y., Lin, Y. S., Lai, C. C., & Huang, S. L. (2008). Enhancement of Cr^{4+} concentration in $Y_3Al_5O_{12}$ crystal fiber with pre-growth perimeter deposition. *Japanese Journal of Applied Physics, 47*, 6369–6373.
11. Tsai, C. N., Huang, K. Y., Tsai, H. J., Chen, J. C., Lin, Y. S., Huang, S. L., et al. (2008). Distribution of oxidation states of Cr ions in Ca or Ca/Mg co-doped Cr:$Y_3Al_5O_{12}$ single crystal fibers with nitrogen or oxygen annealing environments. *Journal of Crystal Growth, 310*, 2774–2779.
12. Sugimoto, A., Nobe, Y., & Yamagishi, K. (1994). Crystal growth and optical characterization of Cr, Ca:Y3Al5O12. *Journal of Crystal Growth, 140*, 349–354.
13. Chen, J. C., Lo, C. Y., Huang, K. Y., Kao, F. J., Tu, S. Y., & Huang, S. L. (2005). Fluorescence mapping of oxidation states of Cr ions in YAG crystal fibers. *Journal of Crystal Growth, 274*, 522–529.

Chapter 136
A Robust Steganography Structure Using a Nested Linear Code

Jyun-Jie Wang and Chi-Yuan Lin

Abstract Matrix embedding is a high performance technique for steganography. In the paper, we present one new approaches to matrix embedding based on a convolutional code binary nested embedding scheme. This scheme offers a practical method to realization of embedding algorithm and minimizes the average modified distortion by use of Viterbi quantizer between stego and host object. The novel algorithm performs an embedding procedure through a trellis structure based on generator matrix. Systematic convolutional code and nested structure are adopted to achieve realization of embedding algorithm. In this work, the coding technique proposed is validated as a simple and efficient algorithm.

Keywords Data hiding · Informed coding · Informed embedding · Robustness

136.1 Introduction

In steganography, the cover shall be modified and to obtain the stego. High embedding efficiency is required for a steganographic scheme. Embedding efficiency, which is the average number of embedded bits per embedding change, is a critical subject in steganography, and is involved in an effective steganographic technique referred to as the matrix embedding (ME) codes. In coding theory, an optimal ME code, that is, an ME code that can approach the rate-distortion bound [1],

J.-J. Wang · C.-Y. Lin (✉)
Department of Computer Science and Information Engineering, National Chin-Yi University of Technology, Taichung 411, Taiwan, Republic of China
e-mail: chiyuan@ncut.edu.tw

J.-J. Wang
e-mail: jjwang@ncut.edu.tw

J. Juang et al. (eds.), *Proceedings of the 2nd International Conference on Intelligent Technologies and Engineering Systems (ICITES2013)*, Lecture Notes in Electrical Engineering 293,
DOI: 10.1007/978-3-319-04573-3_136,

is based on an excellent structured code and efficient decoding algorithm that has sufficiently large length, such as LDGM codes [2].

Crandall [3] and Bierbrauer [4] used excellent linear block codes for an ME scheme, which were derived from covering codes that can approach a high embedding efficiency. Galand and Kabatiansky [5] describes several families of covering codes constructed by using the block wise direct sum (BDS) of factorizations. In [5], numbers of the family BDS(6) and BDS(8) lead to highest embedding efficiency, providing a considerable improvement by using nonlinear covering codes. Moreover, Jessica et al. [6] proposed a high embedding efficiency scheme, which was an ME-based embedding technique with large payloads, demonstrated by two types of linear block codes, that is, simple codes and random codes. Fridrich and Soukal [6] resulted in superior steganographic security in a large payload. In addition, [6] used structured simple codes, that is, decoding by using fast Hadamard decoding, to achieve the efficient ME codes and to approach the embedding bound for a large payload. Although [2–6] proposed structured codes for an ME scheme, it was difficult for the embedding efficiency to promote the subject to locate the coset leader in the case of a linear block code with sufficiently large length because of the complexity of the maximum likelihood (ML), that is, optimal decoding, decoding increases as power. Two factors were considered when constructing an embedding scheme: (1) An embedding scheme requires a good structured code, which usually works in sufficiently large length, and (2) The efficient embedding/decoding algorithm is determined on the basis of such structured code, once the first requirement is met. For an extreme case to meet the two criteria, a block code with sufficiently large length decodes by using the maximum likelihood decoding in a conflicting manner. In principle [7, 8, 9], the early work of researchers provides the extreme rate in binning methods when encode the data subject to noisy constraints. However, Costa's theory is only to show that there is an existence of coding scheme that achieve the fundamental bounds. Nonetheless, it provides neither a concrete codes nor computationally efficient algorithms. When a coding scheme is built to reach such limit, two concerns are raised as follows.

The rest of this paper is organized as follows. In Sect. 136.2, we briefly discuss the theory limit of steganography. Section 136.3 describes our major work on proposed nested embedding codes algorithm. In Sect. 136.4, we provide experimental results and constructive discussions. Finally, we state our conclusions in Sect. 136.5.

136.2 The Bound of Nested Binary Linear Codes

For a binary nested embedding scheme, given a binary toggle vector $e_{opt} \in \{0, 1\}^n$, the output of nested embedding scheme form $y = u + e_{opt} + N$, where $u \in \{0, 1\}^n$ is a host signal, and $N \sim Bernoulli(p)$ is a binary channel noise. The scheme of an embedding strategy can be realized by a pair of binary

nested embedding code (C_2, C_1) at a given an optimal embedding rate $R(\delta, p) = h(\delta) - h(p)$. Suppose the toggle vector e_{opt} of embedder must satisfy the constraint $E[w(e_{opt})] \leq n\delta$, where n is the block length and $0 \leq \delta \leq 0.5$. If a good nested binary embedding code (C_1, C_2), where the fine code C_1 is a good p-code and the coarse code C_2 is a good δ-code. A good (n, k_2) δ code has sufficiently large n and $(n - k_2)/n \approx h(\delta)$. Naturally, the expected quantization error by C_2 for each block length n satisfies

$$E[w(e_{opt})] = E[w(u + l')] \approx n\delta, \tag{136.1}$$

Besides, for a good (n, k_1) p-code, the length n of code C_1 is sufficiently large and $k_1/n \approx 1 - h(p)$. The BSC channel is also satisfied by

$$P(\hat{Y} \neq Y) < (1 - h(p)) - k_1/n, \tag{136.2}$$

where Y is a BSC(p) noisy vector and $\hat{Y}$ is the estimation vector. Assuming that code rate of C_1 and C_2 are $h(\delta) = m_2/n$ and $h(p) = m_1/n$, respectively. Further, C_1 can be partitioned into $2^{m_2 - m_1} \approx 2^{n[h(\delta) - h(p)]}$ cosets corresponding to C_2. The optimal embedding rate of nested linear embedding code is given as

$$\begin{aligned} R(\delta, p) &= h(\delta) - h(p) \\ &= (m_2 - m_1)/n, \end{aligned} \tag{136.3}$$

where $h(d) = d \log 2(1/d) + (1 - d) \log (1/(1 - p))$ denotes a binary entropy function. There are two extreme cases describe as follows. As one extreme case, the embedding capacity of the embedder, input constraint $E[w(e_{opt})] \leq n/2$ reduces to the classical capacity $R(1/2, p) = 1 - h(p)$. Another, the embedding capacity, note that $E[w(e_{opt})] \leq n\delta$, is only $R(\delta, 0) = h(\delta)$ but with no channel noise, i.e., $p = 0$. The embedding rate $R(\delta, p)$ of nested binary embedding code $(C_1 p - code, C_2 \delta - code)$ also provide us an optimal average distortion corresponding to C_2 when the channel noise give a Bernoulli symmetric model p as

$$h(\delta) = R(\delta, p) + h(p), \tag{136.4}$$

The δ is given as

$$\begin{aligned} \delta &= h^{-1}(R(\delta, p) + h(p)) \\ &= h^{-1}((m_2 - m_1)/n + h(p)), \end{aligned} \tag{136.5}$$

where $h^{-1}(*)$ is the inverse function of the binary entropy function h. In the end, given a (C_1, C_2) nested binary linear embedding code C with an embedding rate $R(\delta, p)$, there exists a lower bound δ for each bit distortion, with a constraint $0 \leq \delta \leq 1/2$ imposed. For such nested binary linear embedding code C, the embedding efficiency between both the efficiency bound and the maximum likelihood detected algorithms can be related as

$$\frac{R(\delta,p)}{h^{-1}(R(\delta,p)+h(p))} \geq \frac{m_2-m_1}{D_{opt}} \qquad D_{opt} \geq nh^{-1}(R(\delta,p)+h(p)), \tag{136.6}$$

where D_{opt} represents the distortion level estimated in the maximum likelihood detected algorithms.

136.3 Systematic Convolutional Embedding Codes

Given a syndrome s_l of length $N(nR_c)$, it is requested that the sequence $l \in C^1$ of length Nn with the syndrome s_l be found, just as the linear embedding code, Given a code rate $R_m = m'/n'$ of systematic convolutional code, a generator matrix $G(D)$, in connection with time D, is employed to characterize the convolutional code $C(D)$, defined as

$$G_s(D) = [1 \quad g_1(D)\ldots g_{m1}(D)g_{m1+1}(D)\ldots g_{n-1}(D)] \tag{136.7}$$

and

$$H_s(D) = \begin{bmatrix} g_1(D) & 1 & & \\ \vdots & & \ddots & \\ g_{m1}(D) & & & \\ g_{m1+1}(D) & & \ddots & \\ \vdots & & & \\ g_{n-1}(D) & & & 1 \end{bmatrix} = \begin{bmatrix} H_1(D) \\ H_\delta(D) \end{bmatrix}, \tag{136.8}$$

where $H_1(D)$ and $H_\delta(D)$ are a $m_1 \times n$ matrix and a $(m_2 - m_1) \times n$ matrix, respectively. The embedder Λ_2 quantize the arbitrary toggle sequence $x(D)$ to generate the optimal stego sequence $l'(D) \in \Lambda_1$ as

$$\begin{aligned} l'(D) &= (x(D) \mod \Lambda_2) + u(D) \\ &= Q(x(D)) + x(D) + u(D) \\ &= e_{opt}(D) + u(D), \end{aligned} \tag{136.9}$$

where $Q(*)$ represent the Viterbi decoding for Λ_2 trellis structure. For a Bernoulli case, the quantization error by Λ_2 is Bernoulli(δ) distributed and independent. The optimal quantization error $e_{opt}(D)$ by Λ_2 is given as

$$\begin{aligned} e_{opt}(D) &= l'(D) + u(D) \\ &= x(D) \mod \Lambda_2. \end{aligned} \tag{136.10}$$

In the receiver, the extracting procedure can be divided into two steps. The first is to quantize or decode by channel coder Λ_1. The second is to extract the logo

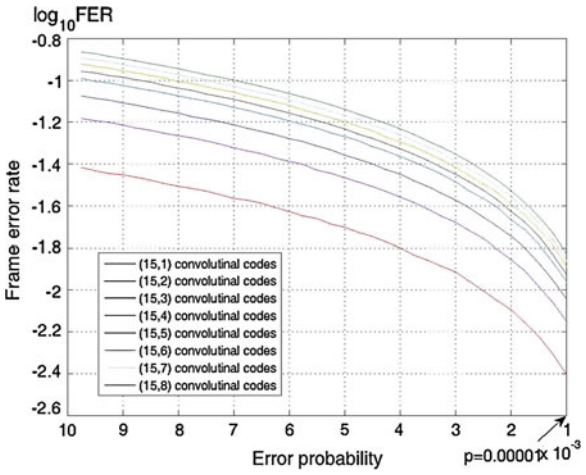

Fig. 136.1 The frame error rate of $(n, 1)$ nested convolutional codes

Table 136.1 The embedding rate of $(n, 1)$ convolutional codes at various error rates p

$R(\delta, p)$	2	3	4	5	6
$p = 0.01$	3.65	3.98	4.12	4.13	4.13
$p = 0.005$	3.97	4.52	4.77	4.96	4.98
$p = 0.002$	4.31	4.98	5.48	5.67	5.74
$p = 5 \times 10^{-4}$	4.43	5.32	5.79	6.21	6.4
$p = 0$	*4.47*	*5.38*	*6.01*	*6.32*	6.73

sequence $s_l(D)$ by $H_2(D)$. Assume that received noisy sequence is $y(D) = l'(D) + n(D)$, where $y(D)$ is a Bernoulli(p) distribution. The syndrome sequence $s_x(D)$ of arbitrary length Nn is then evaluated as

$$\begin{aligned} s_x(D) &= x(D)H_s^T(D) \\ &= (u(D) + l(D))H_s^T(D). \end{aligned} \tag{136.11}$$

Above mentioned sequence $s_l(D)$ and sequence $u(D)$ is given.

136.4 Simulation Results

The experimental results demonstrate three objectives. The first is to address the problem of constructing a $(n, 1)$ convolutional embedding codes for use with ML decoding. The second is to demonstrate simulation results illustrating the frame error rate of the systematic codes are presented in Fig. 136.1 and the average embedding efficiency of the proposed convolutional embedding codes is shown for different code lengths as shown in Table 136.1. Following experiments were conducted on $N = 2000$ code lengths, uniformly logo sequence and cover sequence.

136.5 Concolusions

Proposed in this work is a simple but efficient block codes and convolutional codes binary embedding algorithm. Our construction is based on nested convolutional codes, and is similar to common approaches aiming at nested binning scheme. A conventional ML embedding algorithm turns out infeasible in the case of a large value of $n-m$, while the algorithm presented is enabled to perform binary data embedding, with a fixed complexity, on a long cover sequence, using a Viterbi algorithm, exhibiting a superior efficiency relative to the matrix embedding algorithm. An example of nested binning scheme was introduced by Sect. 136.3. Here, a nested trellis plays the role of a finite complexity construction. A good nested binning scheme can be realized by trellis construction. In the application, the proposed scheme can be practically advantageous to replace the nested linear block code for constructing a nested binning scheme.

Acknowledgments This study is supported in part by the National Science Council of the Republic of China under contract numbers NSC-101-2221-E-167-026 and NSC-102-2221-E-167-001.

References

1. Moulin, P., & Koetter, R. (2005). Data-hiding codes. In *Proceedings of IEEE* (vol. 93, no. 12, pp. 2083–2126). December 2005.
2. Wainwright, M. J. (2007). Sparse graph codes for side information and binning. *IEEE Signal Processing Magazine, 24*(5), 47–57.
3. Crandall, R. (1998). *Some notes on steganography*. Steganography mailing list, available from http://os.inf.tu-dresden.de/westfeld/crandall.pdf
4. Bierbrauer, J. (1998). On Crandall's problem. Available from http://www.ws.binghamton.edu/fridrich/covcodes.pdf
5. Galand, F. & Kabatiansky, G. (2003). Information hiding by coverings. In *Proceedings ITW2003* (pp. 151–154). Paris, France.
6. Fridrich, J., & Soukal, D. (2006). Matrix embedding for large payloads. *IEEE Trans. Information Forensics and Security, 1*, 390–395.
7. Costa, M. H. M. (1993). Writing on dirty paper. *IEEE Transactions on Information Theory*, *29*, 439–441.
8. Miller, M. L., Doërr, G. J., & Cox, I. J. (2004). Applying informed coding and embedding to design a robust high-capacity watermark. *IEEE Transactions on Image Processing*, *13*, (6), 792–807.
9. Cox, I. J., Miller, M. L., & McKellips, A. (1999). Watermarking as communications with side information. *Proceedings of the IEEE*, *87*, 1127–1141.

Chapter 137
Opposition-Based Bare Bone Particle Swarm Optimization

Chang-Huang Chen

Abstract Bare bone particle swarm optimization (BPSO) is a simple approach for solving optimization problem. However, this population-based algorithm also suffers premature problem for some complex problems, especial for high-order dimensional, nonlinear problems. This paper presents a new approach to enhance BPSO's searching capability. The proposed opposition-based bare bone particle swarm optimization (OBPSO) employs opposition learning strategy to extend the exploration capability such that avoiding get stuck on local optimum. A set of six benchmark functions is applied for numerical verification. Experimental results confirm the strength of the proposed approach, based on comparison with PSO and original OBPSO. It is seen that OBPSO outperforms PSO and BPSO both in solution accuracy and convergent rate.

Keywords Bare bone particle swarm · Opposite number · Opposition-based learning · Particle swarm optimization

137.1 Introduction

Population-based optimization, inspired from natural or biological phenomena, dominate current research of intelligent optimization algorithms. For example, genetic algorithm, ant colony, bee algorithm, particle swarm optimization, firefly algorithm, etc. Among them, particle swarm optimization (PSO) is one of the popular algorithms. Spawn from PSO, bare bone particle swarm optimization (BPSO), developed by Kennedy, is a simple optimization algorithm [1]. Due to its simplicity and feature of parameter-free, BPSO has attracts some researchers'

C.-H. Chen (✉)
Department of Electrical Engineering, Tungnan University, New Taipei City 222, Taiwan
e-mail: chchen@mail.tnu.edu.tw

J. Juang et al. (eds.), *Proceedings of the 2nd International Conference on Intelligent Technologies and Engineering Systems (ICITES2013)*, Lecture Notes in Electrical Engineering 293,
DOI: 10.1007/978-3-319-04573-3_137,

attention. Originally, BPSO is formulated as a means of studying the particle distribution of standard PSO. In basic BPSO, velocity term is eliminated, and a Gaussian distribution is used to sampling the problem space based on the information of ever found global best and personal best particle. Despite its simplicity, conventional BPSO is not a particularly good optimizer, i.e., it inevitably tends to converge prematurely in some applications, especially for problems with high dimension and multiple extremes.

Nevertheless, trying to improve BPSO's performance, some modifications have been proposed. For example, Hsieh proposed a modified BPSO by inclusion weight parameter into BPSO [2]. A variant of bare bones particle swarm optimization with jumps has been considered by Krohling and Mendel [3]. In this model, a particle jumps if it has not improved for a given number of iterations. By integrating the concept of global and local model of PSO, Chen also proposed two variants of bare bone particle which outperform BPSO for tested benchmark functions [4, 5]. Combine wavelet mutation to bare bone particle swarm optimizer for image segmentation appeared in [6]. In addition to employ Gaussian distribution function to sampling the problem space, other probability distribution function is also proposed. For example, using double-exponential distribution function is studied by Kennedy [7]. Lévy distributions have been incorporated to traditional BPSO in [8].

Contemporary population-based optimization algorithms rely on some stochastic random sampling mechanism to create new candidate solution from a given population. It frequently encounters the dilemma of exploitation and exploration. Many approaches have been proposed to cure this fault. Opposition-based learning (OBL) strategy is one of the directions. Opposition-based learning was introduced by Tizhoosh [9]. The main idea of OBL is simultaneously exploration a candidate position and its opposite position in the problem domain to achieve a better approximation for current candidate solution. In this paper, after BPSO iteration, OBL is applied to enhance the exploration capability by search the opposite position of each particle with a preset probability.

After this introduction, Sect. 137.2 provides a brief review of BPSO. The concept of Opposition based learning is presented in Sect. 137.3. Section 137.4 gives the proposed algorithm. Experimental results obtained by testing on a suite benchmark function are shown in Sect. 137.5. Finally, a brief conclusion and future direction of study are made in Sect. 137.6.

137.2 Bare Bone Particle Swarm Optimization

BPSO is a population-based iteration optimization algorithm that uses multiple candidate solutions to explore for optimal solution. Let $X = \{x_1, x_2, \ldots, x_m\}$ be the swarm of particles or positions in the problem space, where each particle $x_i = (x_{i1}, x_{i2}, \ldots, x_{in})^T$ represents a candidate solution and, m and n are the number of

particles and number of dimensions of problem in hand, respectively. Meanwhile, let $p_i = (p_{i1}, p_{i2}, \ldots, p_{in})^T$ represents the personal best particle a particle x_i ever found. Further define p_g to represent the global best particles ever found by whole swarm. Specifically, BPSO update the position with a Gaussian distribution of mean equal to $(p_g + p_i)/2$ and standard deviation of $|p_g - p_i|$. In BPSO, to explore for optimal solution at $t + 1$ iteration, a new trial particle is created using the information carried by x_i. In mathematical form, the jth component of the ith trial position of x_i is defined as

$$x_{ij}(t+1) = N(\mu, \sigma) \tag{137.1}$$

where

$$\mu = 0.5(p_{gj} + p_{ij}) \tag{137.2}$$

$$\sigma = \left|p_{gj} - p_{ij}\right| \tag{137.3}$$

where t is counter of iteration. It is clear in (137.2) and (137.3) that μ is the average of the global best and the personal best for dimension j, σ is the difference between global best and personal best particles. Meanwhile, $N(\mu, \sigma)$ is a Gaussian random number with mean of μ and deviation of σ. From (137.1)–(137.3), one can obviously realize that BPSO is a self-adapting algorithm, relying on particles' past experience and information exchange among whole population.

Inspecting Eqs. (137.2) and (137.3), Chen found [10] that if $x_i(t)$ is updated only whenever $x_i(t + 1)$ is better than $x_i(t)$, then current $x_i(t)$ is actually equivalent to the personal best particle p_i. Under this condition, p_i is no longer required. By using a temporary variable x_i', Eqs. (137.1)–(137.3) are modified to

$$x_{ij}' = N(\mu, \sigma) \tag{137.4}$$

with

$$\mu = 0.5(p_{gj} + x_{ij}) \tag{137.5}$$

$$\sigma = \left|p_{gj} - x_{ij}\right| \tag{137.6}$$

BPSO based on Eqs. (137.4)–(137.6) is equivalent to original BPSO with reduced memory consumption. If the performance of x_i' is not better than $x_i(t)$, $x_i(t)$ will not change. So, in Eq. (137.4), t can also be ignored since it will not confuse the operation. The latter version of BPSO will be adopted in this paper.

137.3 Opposition-Based Learning

137.3.1 Definition of Opposite Number

Given a real number $y \in [a, b]$, the opposite number of y, denoted as oy is defined by

$$oy = a + b - y \tag{137.7}$$

This definition can be extended to point in a high dimensional space. Given a point $p = (y_1, y_2, \ldots, y_n)$ in n-dimensional space, where $y_i \in [a_i, b_i]$ and $y_i \in \mathrm{R}$ for $i = 1, 2, \ldots, n$. The opposite point of p, denoted as op, $op = (oy_1, oy_2, \ldots, oy_n)$ where every component oy_i is defined by

$$oy_i = a_i + b_i - y_i \tag{137.8}$$

137.3.2 Definition of Opposition-Based Learning

Given a set of points $\mathrm{P} = \{x_1, x_2, \ldots, x_m\}$ in n-dimensional space where $x_i = (x_{i1}, x_{i2}, \ldots, x_{in})$. Meanwhile, assume $\mathrm{f}(\cdot)$ is the objective function used directly to measure candidate solution's fitness. Suppose minimization problem is to be dealt with at hand. According to the definition of opposite point, $ox_i = (ox_{i1}, ox_{i2}, \ldots, ox_{in})$ is the opposite point of x_i. Now, consider the iterative population-based optimization process with opposition-based learning. If $\mathrm{f}(ox_i) < \mathrm{f}(x_i)$ then point x_i can be replaced by ox_i; otherwise x_i is unchanged. Continue this process until termination condition is met. Hence, the point and its opposite point are simultaneously involved to explore for optimal solution. OBL seems give more chance for explore every corner of the problem space and lead to more chance to achieve better solution.

137.4 The Proposed Approach

The proposed opposition-based bare bone particle swarm optimization, abbreviated as OBPSO, is a two phases searching strategy. First BPSO executes as usual. After all particles searching for the problem space, OBL phase begins with a predefined probability. That means, instead of each particle conducting an opposite search immediately after BPSO phase, a probability $p_r \in (0,1)$, is used to control how often OBL works. Let X denotes the set of particles generated by BPSO phase. In OBL phase, a uniform random number in (0, 1) is first generated and if this value is less than p_r, the opposite points OX of X are created. Then, the best m particles, selected from the union of X and OX, are taken as the candidate solutions for exploration in next iteration. The processes continue until the termination

```
Step  1: Set m, n and mxt; //no.of particles, dimensions and maximum iteration
Step  2: Set pr ; // user defined parameter
Step  3: Initialize X = {x_i} and evaluate each x_i for i=1, 2, …, m;
Step  4: p_g= best of x_i;     t=1;     //t=iteration counter
Step  5: while (t < mxt) do step 6-19
Step  6:   for each particle x_i do steps 7-9        //BPSO phase
Step  7:     create new position x' using Eqs.(137.4)–(137.6) ;
Step  8:     if  f(x') < f(x) then x_i= x';
Step  9:     if  (x′) < f(p_g) then p_g= x′;
Step 10:   end for
Step 11:   t=t+1;
Step 12:   if (rnd(1) < p_r ) and (t < mxt) then       //opposition phase if rnd(1) < p_r
Step 13:     for each particle x_i do  steps 1415   //start of OBL phase
Step 14:       ox_i = opposite position of x_i;
Step 15:       evaluate ox_i ;
Step 16:     end for
Step 16:     P = {x_1, x_2, …, x_m} ∪ {ox_1, ox_2, …, ox_m} ;
Step 17:     X = select best m particles of P; p_g = best of X;
Step 18:     t=t+1;
Step 19:   end if
Step 20: output p_g;       //  p_g=optimal solution
```

Fig. 137.1 Main steps of the proposed algorithm

condition is met. In this paper, termination condition is set as maximum number of iteration. Based on above description, the main steps of the proposed algorithm are outlined in Fig. 137.1 where mxt is the maximum number of iteration, m and n is the number of particles and dimensions, respectively. In Fig. 137.1, rnd(1) is an uniform random number in (0, 1). Note that p_r is a user defined parameter.

137.5 Experimental Verification

The comparisons between the proposed algorithm and original BPSO are presented in this section. Six benchmark functions, listed in Table 137.1, are used to verify the feasibility and capability of the proposed approach. Among this set of functions, f_1−f_3 are unimodal functions while f_4−f_6 are multimodal functions. All function has 30 dimensions. For each of these functions, the goal is to find the solution such that the function value is minimum. In all the experiments, number of particles and maximum number of iterations are set to 30 and 1,000, respectively. For each function, each algorithm will run 50 times and the best as well as the worst solutions among them are recorded. Meanwhile, the average solution and standard deviation among the 50 runs are also calculated for the purpose of comparison.

Table 137.1 Benchmark functions

Function	Range
$f_1(x) = \sum_{i=1}^{n} x_i^2$	$x_i \in (-100, 100)$
$f_2(x) = \sum_{i=1}^{n} \left(100\left(x_{i+1} - x_i^2\right)^2 + (x_i - 1)^2\right)$	$x_i \in (-30, 30)$
$f_3(x) = \sum_{i=1}^{n} \lvert x_i \rvert + \prod_{i=1}^{n} \lvert x_i \rvert$	$x_i \in (-100, 100)$
$f_4(x) = 418.9829 - \sum_{i=1}^{n} \left(x_i \sin\left(\sqrt{\lvert x_i \rvert}\right)\right)$	$x_i \in (-500, 500)$
$f_5(x) = \frac{1}{4000} \sum_{i=1}^{n} x_i^2 - \prod_{i=1}^{n} \cos\left(\frac{x_i}{\sqrt{i}}\right) + 1$	$x_i \in (-600, 600)$
$f_6(x) = -20 \exp\left(-0.2 \sqrt{\frac{1}{n} \sum_{i=1}^{n} x_i^2}\right) - \exp\left(\frac{1}{n} \sum_{i=1}^{n} \cos(2\pi x_i)\right) + 20 + e$	$x_i \in (-32, 32)$

Table 137.2 Numerical results comparison

	Alg.	Mean	Best	Worst	Stdev
f_1	BPSO	7.853e-11	9.872e-13	5.619e-10	1.328e-10
	OBPSO	*5.173e-19*	*1.462e-21*	*7.642e-18*	*1.257e-18*
f_2	BPSO	60.148	6.541	206.682	48.125
	OBPSO	*29.712*	*25.491*	*162.513*	*20.355*
f_3	BPSO	5.158e-8	3.773e-9	4.841e-7	7.251e-8
	OBPSO	*1.481e-16*	*1.151e-17*	*5.303e-16*	*1.390e-16*
f_4	BPSO	2.905e3	1.935e3	4.343e3	466.596
	OBPSO	*2.823e3*	*1.421e3*	*4.442e3*	*764.155*
f_5	BPSO	0.013	2.655e-13	0.220	0.032
	OBPSO	*1.232e-3*	*0.000*	*0.017*	*3.562e-3*
f_6	BPSO	0.185	1.054e-7	2.013	0.513
	OBPSO	*6.409e-11*	*6.743e-12*	*2.628e-10*	*5.109e-11*

137.5.1 Numerical Results

Results for different setting of p_r are conducted. However, only the results obtained by OBPSO for $p_r = 0.5$ are listed in Table 137.2, due to the limitation of paper space. From Table 137.2, one can find that OBPSO outperforms BPSO for these six functions in terms of mean, best and worst solutions. These justify the feasibility and capability of the proposed algorithm.

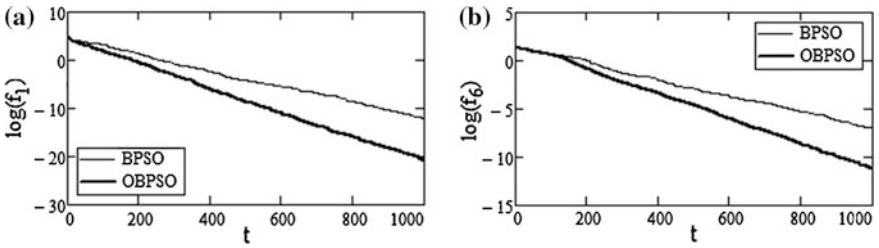

Fig. 137.2 Convergent properties for functions, (**a**) f_1 and (**b**) f_6

137.5.2 Convergent Rate

Since most of the population-based algorithms suffering from long computation time, the convergent characteristics of OBPSO is also investigated in this paper. However, owing to the limitation of paper space, only the convergent rate for f_1 and f_6 are demonstrated in Fig. 137.2. From this figure, one can also find that the convergent speed of OBPSO is much faster than BPSO for these two functions. Actually, from Table 137.2, one can also predict that the convergent property of OBPSO for other functions will be better than BPSO. Note that, for clarity, the vertical axis is in logarithm scale.

137.6 Conclusions

In this paper, an opposition-based bare bone particle swarm optimization, referred to OBPSO, is proposed to improving the performance of the original bare bone particle swarm optimization (BPSO). OBPSO is a two-phase algorithm. At first, BPSO is executed and all particles are evaluated, then OBL phase begins when a probability test is passed. If probability test is fail, particles advance to next iteration according to traditional BPSO. Otherwise, particles generated by BPSO and OBL are sorted and the best m particles are chosen as new candidate solutions for next exploration. Probability test is based on a parameter p_r which is specified by user.

Numerical experiments reveal that OBPSO performs better than BPSO both in solution quality and convergent speed when tested on a suite of benchmark functions containing unimodal and multimodal functions.

Future study will focus on how the parameter p_r affecting the performance of OBPSO and employing OBPSO to real world applications to further verify the effectiveness of the proposed strategy.

References

1. Kennedy, J. (2003). Bare bone particle swarm. In *Proceedings of the IEEE Swarm Intelligence Symposium* (pp. 80–87). IEEE Press.
2. Hsieh, H. I., & Lee, T. S. (2010). A modified algorithm of bare bone particle swarm optimization. *International Journal of Computer Science Issues, 7*(6), 12–17.
3. Krohling, R. A., & Mendel, E. (2009). Bare bones particle swarm optimization with Gaussian or Cauchy jumps. In *Proceedings of 11th Conference on CEC* (pp. 3285–3291).
4. Chen, C. H. (2010). Unified bare bone particle swarm optimization. In *Proceedings of the 3rd International Conference on Power Electronics and Intelligent Transportation Systems* (Vol. 4, pp. 191–195).
5. Chen, C. H. (2011). Bare bone particle swarm optimization with integration of global and local learning strategies. In *International Conference on Machine learning and Cybernetics* (pp. 692–698).
6. Zhang, W., & Zhang, Y.(2010). A novel segmentation algorithm based on bare bones particle swarm optimization and wavelet mutation. In *The Proceedings of the 29th Chinese Control Conference* (pp. 2968–2971).
7. Keendy, J. (2005). Dynamic-probabilistic particle swarms. In *Proceedings of the 2005 Conference on Genetic and Evolutionary Computation, GECCO '05* (pp. 201–207).
8. Richer, T., & Blackwell, T. (2006). The Lévy particle swarm. In *Proceedings of IEEE Congress on Evolutionary Computation* (pp. 3150–3157).
9. Tizhoosh, H. R. (2005). Opposition-based learning: A new scheme for machine intelligence. In *Proceedings of International Conference on Computation Intelligence for Modeling Control and Automation* (Vol. 1, pp. 695–701).
10. Chen, C. H. (2013). A revised bare bone particle swarm optimizer and its variant. In *Accepted by International Conference on Fuzzy Theory and Its Applications*.

Chapter 138
GaN MIS Photodetectors with l,3-bis [2-(2,20-bipyridin-6–yl) -1,3,4-oxadiazol-5-yl]-benzene (Bpy-OXD) Insulators

Chin-Hsiang Chen, Ming-Han Yang and Wei-Chi Lin

Abstract The study reports the fabrication of GaN metal–insulator-semiconductor (MIS) photodetectors (PDs) with a l,3-bis [2-(2,20-bipyridin-6-yl)-1,3, 4-oxadiazol-5-yl]-benzene (Bpy-OXD) insulating layer. With a 5 V applied bias, the dark current and photocurrent of the fabricated GaN MIS PDs with Bpy-OXD insulating layers were 1.5×10^{-9} A and 1.82×10^{-7} A, respectively. It was also found that we can achieve the large photocurrent to dark current contrast ratio from the proposed device with the use of Bpy-OXD layers.

Keywords GaN · MIS · Bpy-OXD · PDs · Organic

138.1 Introduction

In recent years, GaN material has attracted much attention with a large direct band gap and high saturated electron drift velocity. GaN-based light emitting diodes (LED) and laser diodes (LDs) prepared by metalorganic chemical vapor deposition (MOCVD) on sapphire substrate have been successfully commercialized [1, 2]. The superior radiation hardness and high temperature resistance of GaN also make it a suitable material for UV detectors working in extreme conditions. Thus, GaN can also be used for highly sensitive ultraviolet (UV) photodetectors (PDs) [3]. With the high precision, the low power consumption, the high stability, and other characteristics, GaN PDs are important devices that can be used in various commercial and military applications. For example, these devices can be applied in the

C.-H. Chen (✉) · M.-H. Yang · W.-C. Lin
Department of Electronic Engineering, Cheng Shiu University, Kaohsiung, Taiwan, Republic of China
e-mail: chchen@csu.edu.tw

J. Juang et al. (eds.), *Proceedings of the 2nd International Conference on Intelligent Technologies and Engineering Systems (ICITES2013)*, Lecture Notes in Electrical Engineering 293,
DOI: 10.1007/978-3-319-04573-3_138,

civilian areas and the military field, such as flame sensors, solar UV monitoring, air-to-secure communications, missile monitoring, and so on [4]. For PDs applications, various types of GaN-based PDs have been reported [5–7]. Among them, GaN metal–semiconductor-metal (MSM) PDs can be operated with high speed. In order to achieve a high performance MSM PD, it is necessary to reduce dark current, which is originated from carrier leakage occurred at the metal/semiconductor interface. To reduce leakage current, it is possible to insert an insulating layer between metal and the underneath semiconductor [8]. The PDs with this insulating layer was called metal–insulator-semiconductors (MIS) PDs. To achieve this purpose, the l,3-bis [2-(2,20-bipyridin-6-yl)-1,3,4-oxadiazol-5-yl]-benzene (Bpy-OXD) with a wide bandgap and good durability resistance was introduced as an insulating layer between the Schottky contact and a high-quality GaN film in the MSM structure. In this study, we report the fabrication of GaN MIS PDs with the Bpy-OXD layer as an insulating layer of GaN MIS UV PDs. The optical and electrical properties of the fabricated MIS PDs will be also discussed.

138.2 Experiment

The GaN-based MIS photodetectors in this experiment were all epitaxial grown on c-face (0001) sapphire substrates by MOCVD system. Before epitaxial growth, the sapphire substrates were annealed at 1150 °C in H_2 ambient to remove surface contamination. A low temperature GaN nucleation layer was deposited at 550 °C. After the nucleation layer was grown, the temperature was raised to 1060 °C to grow a 2-μm-thick unintentionally doped GaN epitaxial layer. For the growth of undoped GaN layers, trimethylgallium (TMGa) and NH_3 were used as source materials. The MIS PDs were then fabricated. The Bpy-OXD organic insulating layer was deposited on GaN MIS PDs by thermal evaporation at a pressure of 1×10^{-6} Pa in a vacuum chamber. The deposited rate of the Bpy-OXD layer was controlled to be 1 Å/s. The thickness of the organic thin film was approximately 30 nm. Ni/Au (5/5 nm) contact electrodes were subsequently deposited onto the samples. The contacts of the device form two inter-digitated contact electrodes. The fingers of the contact electrodes were 65 μm wide and 1150 μm long with a spacing of 85 μm. The schematic structure of the fabricated GaN MIS PDs with the Bpy-OXD organic insulating layer is shown in Fig. 138.1. An Agilent E5270B semiconductor parameter analyzer was then used to measure dark current–voltage (I–V) characteristics of this GaN MIS detector. The spectral responses were measured by using monochromatic light source 300 W Xe lamp and calibration equipment.

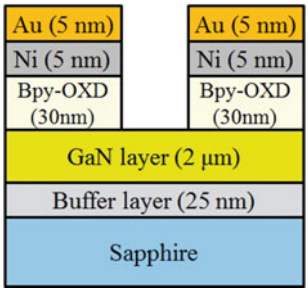

Fig. 138.1 The structure of fabricated GaN MIS PDs with the Bpy-OXD insulator

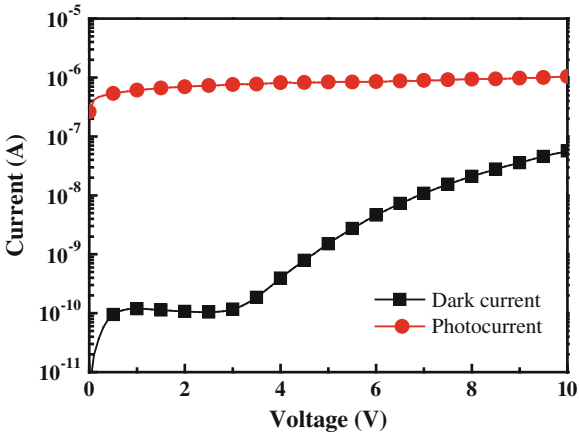

Fig. 138.2 I–V characteristics of the fabricated GaN MIS PDs with the Bpy-OXD layer measured in dark and under illumination

138.3 Results and Discussion

Figure 138.2 shows room temperature current–voltage (I–V) characteristics of the fabricated MIS PDs with the Bpy-OXD layer in dark and under illumination, respectively. With a 5 V applied bias, it was found that leakage current of the fabricated MIS PDs with the Bpy-OXD layer was 1.5×10^{-9} A while the photocurrent can reach around 1.82×10^{-7} A. The smaller leakage current should be attributed to the large Schottky barrier height by using the insertion of this Bpy-OXD layer. As the results, the photo to dark current ratio under a 5 V applied voltage bias is approximate 2 orders of magnitude. This large photo to dark current ratio can contribute to the fact that the semi-insulating properties of Bpy-OXD layer.

The spectral response of the GaN MIS detector with the Bpy-OXD layer was shown in Fig. 138.3. The photoresponses were relatively flat in the short wavelength region when cutoff occurred at approximately 360 nm, which corresponds to the bandgap of GaN. With incident light of 340 nm and an applied bias of 10 V, the measured responsivity was 0.349 A/W for GaN MIS PDs with the Bpy-OXD layer. With the increase in applied bias voltage from 2 to 10 V, it was also found that the measured responsivity of the GaN MIS UV PDs with the Bpy-OXD layer

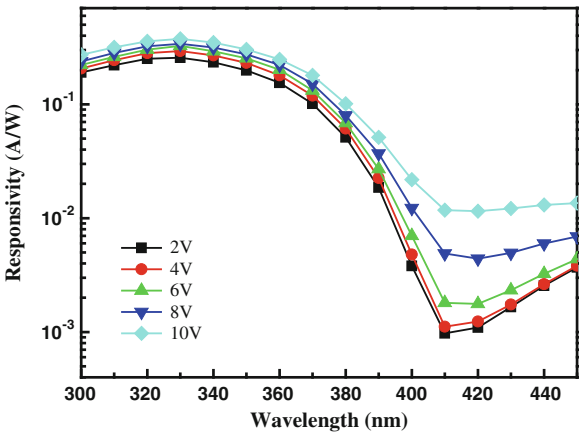

Fig. 138.3 The spectral response of the GaN MIS PDs with Bpy-OXD layers under different applied voltage bias

only increased slightly from 0.256 to 0.376 A/W with incident light of 330 nm. Therefore, we could acquire a reasonably good performance by using the thin Bpy-OXD layer as the insulator of GaN MIS UV PDs. Here, we defined UV to visible rejection ratio as the responsivity measured at 340 nm divided by that at 450 nm. With a 10 V applied bias, it was found that UV to visible rejection ratio was 25.6. This finding indicates a reasonable UV to visible rejection ratio as result of inserting a Bpy-OXD layer into the fabricated PDs.

138.4 Conclusion

GaN MIS PDs with a Bpy-OXD layer were successfully fabricated and characterized. It was found that we can achieve a small dark current and large photocurrent to dark current contrast ratio from the proposed devices with the use of Bpy-OXD layers. With a 5 V applied bias, the dark current and photocurrent of the fabricated GaN MIS PDs with Bpy-OXD insulating layers were 1.5×10^{-9} A and 1.82×10^{-7} A. With incident light of 340 nm and 10 V applied bias, it was found that measured responsivities were 0.34907 A/W for the GaN MIS UV PD with a Bpy-OXD layers. We also achieved large UV to visible rejection ratios from the photodetectors with Bpy-OXD layers.

References

1. Lee, S. Y., Park, K. I., Huh, C., Koo, M., Yoo, H. G., & Kim, S., et al. (2012). Water-resistant flexible GaN LED on a liquid crystal polymer substrate for implantable biomedical applications. *Nano Energy 1*(98), 145–151.
2. Kim, J., Kim, H., & Lee, S. N. (2011). Thermal degradation in InGaN quantum wells in violet and blue GaN-based laser diodes. *Current Applied Physics*, *11*, S167–S170.

3. Souissi, M., Schmerber, G., Derory, A., & Jani, B. E. (2012). Effects of high-temperature annealing on magnetic properties of V-doped GaN thin films grown by MOCVD. *Journal of Magnetism and Magnetic Materials*, *324*, 2539–2542.
4. Müller, A., Konstantinidis, G., Androulidaki, M., Dinescu, A., Stefanescu, A., & Cismaru, A., et al. (2012). Front and backside-illuminated GaN/Si based metal-semiconductor-metal ultraviolet photodetectors manufactured using micromachining and nano-lithographic technologies. *Thin Solid Films 520*, 2158–2161.
5. You, K., Jiang, H., Li, D., Sun, X., Song, H., & Chen, Y., et al. (2012). Shift of responsive peak in GaN-based metal-insulator-semiconductor photodetectors. *Applied Physics Letters*, *100*, 121109.
6. Narita, T., Wakejima, A., & Egawa, T. (2013). Ultraviolet photodetectors using transparent gate AlGaN/GaN high electron mobility transistor on silicon substrate. *Japanese Journal of Applied Physics*, *52*, 01AG06.
7. Li, D., Sun, X., Song, H., Li, Z., Chen, Y., Miao, G., et al. (2011). Influence of threading dislocations on GaN-based metal-semiconductor-metal ultraviolet photodetectors. *Applied Physics Letters, 98*, 011108.
8. Chen, C. H. (2009). Self-organized InGaN nanodots grown by metal–organic chemical vapor deposition system. *Optical Review, 16*, 371.

Chapter 139
Blue Fluorescent Organic Light-Emitting Diodes with Optimized Electron Transportation Layer

Apisit Chittawanij, Sinh-Thanh Nguyen, Lin-Ann Hong, Yu-Sheng Tsai and Fuh-Shyang Juang

Abstract In this research, the optimization of device structures of blue fluorescent organic light emitting diode (OLED) with WBH-301 doped with WBD-701 was fabricated. By adjusting the thickness of each layer in OLED structure as well as total thickness of device, the position of recombination zone was controlled and located in the central region of emitting layer (EML) that significantly increases device efficiency. The device showed the current efficiency of 8.7 cd/A at current density 50 mA/cm^2 and with Commission Internationale de L'Eclairage (CIE) coordinates (x = 0.17, y = 0.34). This efficiency enhancement is important for understanding and further improving high-performance fluorescent OLEDs.

Keywords Organic light-emitting diode (OLED) · Blue fluorescent materials · Fluorescent OLED

139.1 Introduction

Organic light-emitting diodes (OLEDs) has been made to develop OLED displays with high efficiency, long operational lifetime, and high color reproducibility [1]. In particular, extensive research and development have been done for a long time to achieve high-performance blue-emitting OLEDs, because they generally have lower efficiency and shorter lifetime than green- and red-emitting OLEDs due to the higher energy of the excited state of blue emitters. Recently, blue fluorescent OLEDs based on anthracene derivatives have actively been studied because they seem promising to achieve both a high efficiency and a long lifetime [2–7].

A. Chittawanij (✉) · S.-T. Nguyen · L.-A. Hong · Y.-S. Tsai · F.-S. Juang
Institute of Electro-Optical and Materials Science, National Formosa University, Yunlin 632, Taiwan, Republic of China
e-mail: abcd_omo@hotmail.com

J. Juang et al. (eds.), *Proceedings of the 2nd International Conference on Intelligent Technologies and Engineering Systems (ICITES2013)*, Lecture Notes in Electrical Engineering 293,
DOI: 10.1007/978-3-319-04573-3_139,

Generally, fluorescent materials are cheaper and easier to be synthesized but have a 25 % external efficiency limit while phosphorescent materials are more expensive and relatively fewer but possess higher efficiencies due to the harvesting of both singlet and triplet excitons [8–10]. The internal quantum efficiency (IQE) of fluorescent OLEDs is limited to 25 % because only singlet excitons are used for light emission. On the other hand, phosphorescent OLEDs can achieve a 100 % IQE because both the singlet and the triplet excitons can be harvested to produce light. However, phosphorescent materials suffer from instability for practical applications, especially for the blue color [11]. Therefore, further studies on preparation of all fluorescent devices to provide more stable blue OLEDs with excellent performances at high brightness are very important.

139.2 Experiment

The blue fluorescent OLED emitter WBD-701 doped into a host material WBH-301 as emitting layer (EML). The device fabrication, indium tin oxide (ITO)-coated glass substrates were sufficiently cleaned by ultra sonication in acetone, isopropyl alcohol and deionized water before being placed into oven for 10 min to dry out. These substrates are further treated with oxygen plasma prior to use. Ni-100, HTG-1, and Alq_3, serve as hole injection layer (HIL), hole-transporting layer (HTL) and electron transporting layer (ETL), respectively. The HIL is thermally deposited onto ITO substrate, following with HTL, EML, and ETL. Then, the substrate were loaded into a metal vacuum deposition chamber, Liq (0.9 nm) and Al (130 nm) were formed as cathode. The device structures were ITO/Ni-100 (z nm)/HTG-1 (15 nm)/WBH-301: WBD-701 (3 wt%, y nm)/Alq_3 (x nm)/Liq (0.9 nm)/Al (130 nm), as shown in Fig. 139.1. The thermal deposition rates were 0.1 nm/s for organic materials. The active area of the devices was 2.5 mm^2. The current–voltage–luminescence characteristics are measured with a Keithley 2400 source meter. EL spectra and CIE coordinates of the devices are analyzed via a spectrometer (PR650). All measurements are carried out under ambient conditions at room temperature.

139.3 Results and Discussions

In this study, the structure of blue fluorescent OLED device was designed by optimized device structure with suitable thickness of each layer, location of emitting layer (EML) and doping concentration to prevent undesired effects so that it can get high performance. The structure of OLED device was designed with WBH-301: WBD-701 as emitting layer (EML). We focused on respond of current efficiency of devices when thickness of each layer was varied. Four devices (A-1, A-2, A-3, and A-4) were fabricated using the structure of: Ni-100 (75 nm)/HTG-1

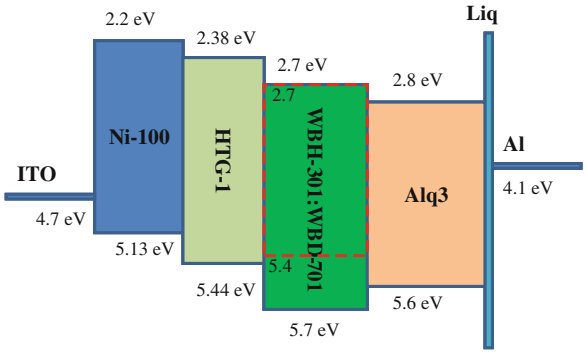

Fig. 139.1 The energy band structure of *blue* OLEDs device

(10 nm)/WBH-301: 3 wt % WBD-701 (40 nm)/Alq_3 (x nm)/LiF (0.9 nm)/Al (130 nm). The thickness of electron transport layer Alq_3 was varied from x = 5, 10, 15, and 20 nm for device A-1, A-2, A-3, and A-4, respectively.

The Current density–Voltage–luminance characteristics of A-1, A-2, A-3, and A-4 can be shown in the Fig. 139.2a. It is obviously that current density was reduced from device A-1 to A-4. When increasing the thickness of ETL, less number of electrons injected to emitting layer. Device A-1, A-2, A-3, and A-4 have driving voltage of 7.2, 8.1, 8.5, and 9.6 V, respectively, at the same current density of 50 mA/cm^2. The luminance characteristic shows in the same trend with current density. It is mean that when the thickness of ETL increased due to the number of electrons move to emitting layer is decreased. At device A-4, there is unbalance of charge carrier inside device result in lower luminance in comparison with device A-3. Device A-3 shows the best performance of 7.6 cd/A at current density of 50 mA/cm^2 as shown in Fig. 139.2b.

To determine the suitable for thickness of EML, three devices (B-1, B-2, and B-3) were fabricated. According to our previous investigations, we have tried to fabricate blue fluorescent OLED with structure of device A-3 [Ni-100 (75 nm)/HTG-1 (10 nm)/WBH-301: 3 wt % WBD-701 (y nm)/Alq_3 (15 nm)/LiF (0.9 nm)/Al (130 nm)] by changing the thickness of EML: y = 45, 50, and 55 nm for device B-1, B-2, and B-3 compared with device A-3. The current density–voltage characteristics of A-3, B-1, B-2, and B-3 can be shown in the Table 139.1. As a result when increasing the thickness from device A-3 to B-3 (8.5–10.6 V), the driving voltage was increased due to total thickness of devices were increased so distance of holes and electrons will be move longer to the recombination zone. The luminance and current efficiency of device B-1 to device B-3 are reduced. The current efficiency of device B-1, B-2, and B-3 are 8.2, 7.93, and 7.4 cd/A at 50 mA/cm^2, respectively. In comparison with device A-3, device B-2 has highest efficiency due to the corresponding total thickness of device. Moreover, by change the thickness of EML, the location of recombination zone shows the negligible difference between three devices.

To further determine the performance of blue fluorescent OLEDs by varying thickness of Ni-100. According to our previous investigations, we have tried to

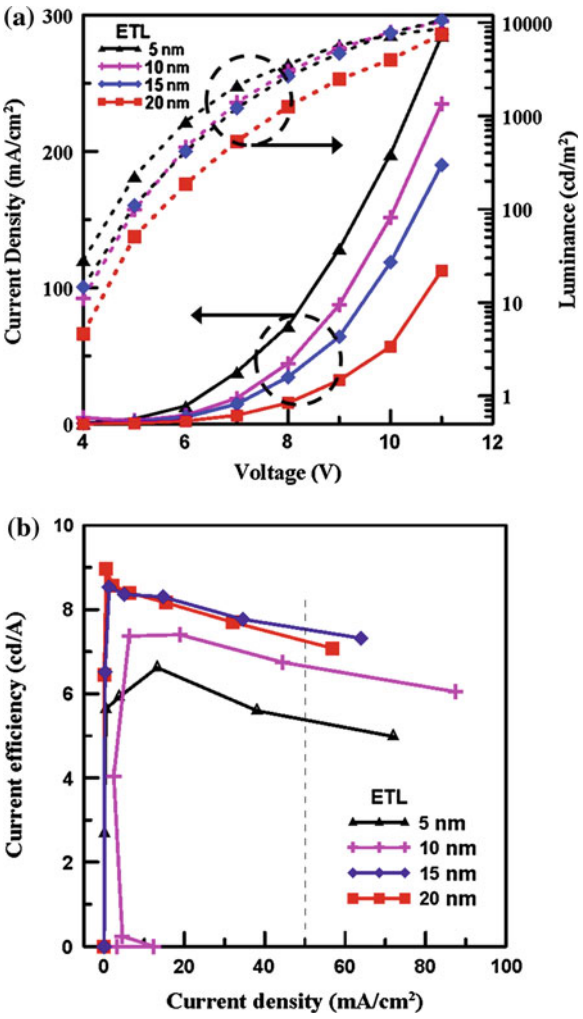

Fig. 139.2 The characteristic of devices with different ETLs thickness, **a** current density–voltage–luminance and **b** current efficiency-current density

fabricate blue fluorescent OLED with structure as device B-1 (75 nm) two devices with 70 and 80 nm of HIL (device C-1 and C-2) are fabricated compared with device B-1. We focused on the relationship of thickness of hole injection layer Ni-100 with total thickness of OLED device. The result showed that the current density of device C-1 and C-2 is higher than device B-1. For those devices, the luminance was the same tended with current density due the hole injection current. The highest luminance of 4,350 cd/m^2 at 50 mA/cm^2 current density is shown in device C-1 as result of balance of hole and electron injected into EML as shown in Fig. 139.3 a.

The current efficiency of device C-1, B-1, and C-2 are 8.7, 8.2, and 7.7 cd/A at 50 mA/cm^2 current density, respectively, as shown in Fig. 139.3a. In comparison

Table 139.1 The composition of the layers and voltage (V), luminance (L) and current efficiency (Yield) characteristics of blue fluorescent OLEDs at 50 mA/cm^2

No	Ni-100 (HIL)	WBH301:WBD701 (EML)	Alq_3 (ETL)	Voltage (v)	Luminance (cd/m2)	Yield (cd/A)	CIE
A-3	75 nm	40 nm	15 nm	8.5	3,700	7.5	0.17:0.32
B-1		45 nm		9.2	4,020	8.2	0.17:0.33
B-2		50 nm		9.4	3,900	7.9	0.17:0.32
B-3		55 nm		10.6	3,650	7.4	0.18:0.34

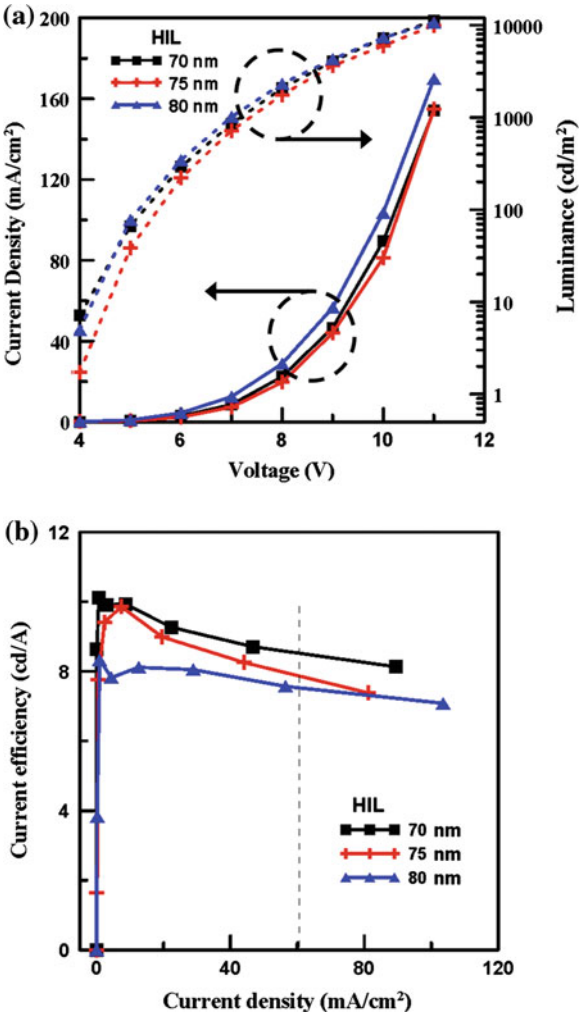

Fig. 139.3 The characteristic of devices with different HILs thickness, **a** current density–voltage–luminance and **b** current efficiency-current density

with device B-1, device C-1 has highest efficiency as well as color CIE (0.17, 0.34). Moreover, by change the thickness of HIL, the location of recombination zone shows the negligible difference between three devices.

139.4 Conclusion

In summary, the device performances of blue fluorescent OLEDs could be improved by using WBH-301 as blue fluorescent host material and WBD-701 as dopant emitter. With an optimized device structure of electron transporting layer, emitting layer, and hole transporting layer. The blue electroluminescent (EL) device achieved an EL efficiency of 8.7 cd/A and luminance of 4,350 cd/m^2 at a current density of 50 mA/cm^2 at saturated blue Commission Internationale de l'Eclairage coordinates of (0.17, 0.34). This efficiency enhancement is important for understanding and further improving high-performance fluorescent OLEDs.

Acknowledgments This work is sponsored by the National Science Council of Taiwan, project no. NSC-99-2221-E-150 -044-MY2, NSC-100-2221-E-150-056 and Science Park University Research Collaboration Program, project 98IB02.

References

1. Hung, L. S., & Chen, C. H. (2002). Recent progress of molecular organic electroluminescent materials and devices. *Materials Science and Engineering Reports, 39*, 143.
2. Shi, J., & Tang, C. W. (2002). Anthracene derivatives for stable blue-emitting organic electroluminescence devices. *Applied Physics Letters, 80*, 3201.
3. Lee, M.-T., Chen, H.-H., Liao, C.-H., Tsai, C.-H., & Chen, C. H. (2004). Stable styrylamine-doped blue organic electroluminescent device based on 2-methyl-9,10-*di*(2-naphthyl)anthracene. *Applied Physics Letters, 85*, 3301.
4. Lee, M.-T., Liao, C.-H., Tsai, C.-H., & Chen, C. H. (2005). Highly Efficient, Deep-Blue Doped Organic Light-Emitting Devices. *Advanced Materials, 17*, 2493.
5. Gao, Z. Q., Mi, B. X., Chen, C. H., Cheah, K. W., Cheng, Y. K., & Wen, W.-S. (2007). High-efficiency deep blue host for organic light-emitting devices. *Applied Physics Letters, 90*, 123506.
6. Kim, S.-K., Yang, B., Ma, Y., Lee, J.-H., & Park, J.-W. (2008). Exceedingly efficient deep-blue electroluminescence from new anthracenes obtained using rational molecular design. *Journal of Materials Chemistry, 18*, 3376.
7. Kim, S.-K., Yang, B., Park, Y.-I., Ma, Y., Lee, J.-Y., Kim, H.-J., et al. (2009). Synthesis and electroluminescent properties of highly efficient anthracene derivatives with bulky side groups. *Organic Electronics, 10*, 822.
8. Zhou, G. J., Wong, W. Y., Suo, S. (2011). *Journal* of *Photochemistry* and *Photobiology C*: *Photochemistry Reviews*, *11*, 133. (C: Photochemistry Reviews)
9. Zhou, G. J., Wong, W. Y., & Yang, X. L. (2011). New design tactics in OLEDs using functionalized 2-phenylpyridine-type cyclometalates of iridium(III) and platinum(II). *Chemistry An Asian Journal, 6*, 1706.

10. Zhou, G. J., Wang, Q., Wang, X. Z., Ho, C. L., Wong, W. Y., Ma, D. G., et al. (2010). Metallophosphors of platinum with distinct main-group elements: a versatile approach towards color tuning and white-light emission with superior efficiency/color quality/brightness trade-offs. *Journal of Materials Chemistry, 20*, 7472.
11. Sun, Y., Giebink, N. C., Kanno, H., Ma, B., Thompson, M. E., & Forrest, S. R. (2006). Management of singlet and triplet excitons for efficient white organic light-emitting devices. *Nature (London), 440*, 908.

Chapter 140
On Reliability Evaluation of Hub-Based Networks

Shin-Guang Chen

Abstract This paper proposes an evaluation method for the reliability of hub-based networks. Such networks are different from the ones evaluated by the traditional methods in two aspects: the number of source/sink nodes is more than one, and the intermediate nodes may be source nodes. The hub-based networks are popular in the modern corporations, and the bottleneck link is a key link in network reliability. However, a detailed study for such networks has not yet been done in the literature. This paper presents the reliability evaluation of such networks. A numerical example is also presented for the explanation of the proposed method.

Keywords Hub-based Network · Stochastic-flow network · Reliability · Minimal Path · Minimal Cut

140.1 Introduction

Network reliability is an important factor on network satisfaction. Many methods have been developed for the evaluation of network reliability. Aggarwal et al. [1] first presented the reliability evaluation method for a binary-state network (no flow happens). Lee [2] used lexicographic ordering and labeling scheme [3] to calculate the system reliability of a binary-state flow network (0 or a positive integer flow). Aggarwal et al. [4] solved such a reliability problem in terms of minimal paths (MPs). Without MPs, Rueger [5] extended to the case that nodes as well as arcs all have a positive-integer capacity and may fail. Considering that each arc has several states/capacities, such a network is called a stochastic-flow network ([6] for perfect node cases; [7] for imperfect node cases). Given the demand d, the system

S.-G. Chen (✉)
Department of Industrial Management, Tungnan University, New Taipei City 222, Taiwan, Republic of China
e-mail: bobchen@mail.tnu.edu.tw

J. Juang et al. (eds.), *Proceedings of the 2nd International Conference on Intelligent Technologies and Engineering Systems (ICITES2013)*, Lecture Notes in Electrical Engineering 293,
DOI: 10.1007/978-3-319-04573-3_140,

reliability is the probability that the maximum flow of the network is not less than d. Normally two terminal networks are evaluated by the above methods where the source/sink nodes and the intermediate nodes are viewed as different nodes. No flow can go through the source/sink nodes. Nonetheless, no flow will be generated from the intermediate nodes. However, the hub-based networks are very different from these features.

The hub-based networks are popular in the modern corporations. Such networks have tree-like topologies, where each node may be connected by some users or other hubs. Therefore, the intermediate nodes may have flows generated and are considered a kind of source nodes. The bottleneck link in a hub-based network is a key link in reliability. A detailed study for such networks has not yet been done in the literature.

This paper proposes a method for the reliability evaluation of hub-based networks in terms of MPs. A path is a set of links whose existence results in the connection of source node and sink node. An MP is a path whose proper subset is not a path. When the network is live, there are several MP vectors with respect to system state d called lower boundary vectors (LBV). Then, the network reliability is the union probability of all these LBVs. The remainder of the work is described as follows: The preliminaries are addressed in Sect. 140.2. The proposed method is presented in Sect. 140.3. Then, a numerical example is explained in Sect. 140.4. Section 140.5 draws the conclusion and discussions of this paper.

140.2 Preliminaries

Let $G = (A, B, M)$ be a stochastic-flow network where $A = \{a_i | 1 \leq i \leq s\}$ is the set of arcs, B is the set of nodes, and $M = (m_1, m_2, \ldots, m_s)$ is a vector with m_i (an integer) being the maximum capacity of b_i. Such a G is assumed to satisfy the following assumptions.

- The capacity of a_i is an integer-valued random variable which takes values from the set $\{0, 1, 2, \ldots, m_i\}$ according to a given distribution.
- The nodes are perfect. That is, they are excluded from the reliability calculation.
- Flow in G satisfies the flow-conservation law [3].
- The states of each arc are statistically independent.

140.2.1 The Hub-Based Network Model

Let $mp_1, mp_2, \ldots, mp_z$ be the MPs. Thus, the network model can be described in terms of two vectors: the capacity vector $X = (x_1, x_2, \ldots, x_s)$ and the flow vector $F = (f_1, f_2, \ldots, f_z)$, where x_i denotes the current capacity of a_i and f_j denotes the current flow on mp_j. Then, such a vector F is feasible iff

$$\sum_{j=1}^{z} \{f_j | a_i \in mp_j\} \leq m_i, \text{ for } i = 1, 2, \ldots, s. \tag{140.1}$$

Constraint (140.1) describes that the total flow through a_i can not exceed the maximum capacity of a_i. We denote such set of F as $U_M = \{F|F \text{ is feasible under } M\}$. Similarly, F is feasible under $X = (x_1, x_2, \ldots, x_s)$ iff

$$\sum_{j=1}^{z} \{f_j | a_i \in mp_j\} \leq x_i, \text{ for } i = 1, 2, \ldots, s. \tag{140.2}$$

For clarity, let $U_X = \{F|F \text{ is feasible under } X\}$. The maximum flow under X is defined as $V(X) = \max \{V(X) = \max\{\sum_{j=1}^{z} \{f_j | F \in U_X\}$.

140.2.2 Reliability Evaluation

Given a demand d, the reliability R_d is the probability that the maximum flow is not less than d, i.e., $R_d = \Pr \{X|V(X) \geq d\}$. To calculate R_d, it is advantageously to find the minimum capacity vector in $\{X|V(X) \geq d\}$. A minimum capacity vector X is said to be a LBV iff (i) $V(X) \geq d$ and (ii) $V(Y) < d$, for any other vector Y such that $Y < X$, in which $Y \leq X$ iff $y_j \leq x_j$, for $j = 1, 2, \ldots, s$ and $Y < X$ iff $Y \leq X$ and $y_j < x_j$, for at least one j. Suppose there are totally w LBVs: $X_1, X_2, \ldots, X_w$, and $E_i = \{X|X \geq X_i\}$, the probability R_d can be equivalently calculated via the well-known inclusion–exclusion principle or the RSDP algorithm [8].

$$\begin{aligned} R_d &= \Pr\{X|V(X) \geq d\} \\ &= \Pr\left(\bigcup_{i=1}^{w} E_i\right) \\ &= \sum_{k=1}^{w} (-1)^{k-1} \sum_{I \subset \{1,2,\ldots,w\}, |I|=k} \Pr\left\{\bigcap_{i \in I} E_i\right\}, \end{aligned} \tag{140.3}$$

where $\Pr\{\bigcap_{i \in I} E_i\} = \prod_{j=1}^{s} \sum_{l=\max\{x_{ij} | \forall i \in I\}}^{m_j} \mu_j(l)$ and μ_j is the given distribution.

140.2.3 Generation of LBVs

At first, we find the flow vector $F \in U_M$ such that the total flow of F equals d. It is defined as in the following equation.

$$\sum_{j=1}^{z} f_j = d. \tag{140.4}$$

Then, let $\mathbf{F} = \{F | F \in U_M$ and satisfies Equation (140.4)$\}$. We show that a LBV X exists if there is a $F \in \mathbf{F}$ by the following lemma.

Lemma 140.1 *Let X be a LBV, then there is a $F \in \mathbf{F}$ such that*

$$x_i = \sum_{j=1}^{z} \{f_j | a_i \in mp_j\} \text{ for } i = 1,\ 2,\ \ldots, s. \tag{140.5}$$

Proof. If X is a LBV, then there is a F such that $F \in U_X$ and $F \in \mathbf{F}$. Suppose there is a k such that $x_k > \sum_{j=1}^{z} \{f_j | a_i \in mp_j\}$. Set $Y = (y_1, y_2, \ldots, y_{(k-1)}, y_k, y_{(k+1)}, \ldots, y_s) = (x_1,\ x_2,\ \ldots,\ x_{(k-1)},\ x_k - 1,\ x_{(k+1)},\ \ldots,\ x_s)$. Hence $Y < X$ and $F \in U_Y$ (since $\sum_{j=1}^{z} \{f_j | a_i \in mp_j\} \le y_i, \forall i$), which indicates that $V(Y) \ge d$ and contradicts to that X is a LBV. □

Given any $F \in \mathbf{F}$, we generate a capacity vector $X_F = (x_1,\ x_2,\ \ldots,\ x_s)$ via Equation (140.5). Then, the set $\Omega = \{X_F \mid F \in \mathbf{F}\}$ is built. Let $\Omega_{min} = \{X | X$ is a minimal vector in $\Omega\}$. Lemma 3.1 indicates that the set Ω includes all LBVs. The following lemma further proves that Ω_{min} is the set of LBVs.

Lemma 140.2 $\Omega_{\min}$ *is the set of LBV*s.

Proof. Firstly, suppose $X \in \Omega_{min}$ (note that $V(X) \ge d$) but it is not a LBV. Then there is a LBV Y such that $Y < X$, which implies $Y \in \Omega$ and thus contradicts to that $X \in \Omega_{min}$. Hence, X is a LBV. Conversely, suppose X is a LBV (note that $X \in \Omega$) but $X \notin \Omega_{min}$ i.e., there is a $Y \in \Omega$ such that $Y < X$. Then, $V(Y) \ge d$ which contradicts to that X is a LBV. Hence, $X \in \Omega_{min}$. □

140.3 The Proposed Method

Given all MPs, the following algorithm searches for all LBVs in G:

Algorithm: Search for all LBVs in G.

Step 1. Find the feasible flow vector $F = (f_1, f_2, \ldots, f_z)$ satisfying both capacity and demand constraints.

i. enumerate f_j for $1 \le j \le z$, $0 \le f_j \le \min\{m_i | a_i \in mp_j\}$ do

ii. if f_j satisfies the following constraints $\sum_{j=1}^{z} \{f_j | a_i \in mp_j\} \le m_i$ and $\sum_{j=1}^{z} f_j = d$, then $\mathbf{F} = \mathbf{F} \cup \{F\}$. end enumerate.

Step 2. Generate the set $\Omega = \{X_F \mid F \in \mathbf{F}\}$.

i. for F in $\mathbf{F}$ do

ii. $x_i = \sum_{j=1}^{z} \{f_j | a_i \in mp_j\}$ for $i = 1, 2, \ldots, s$.

iii. $U_X = U_X \cup \{X_F\}$. //where $X_F = (x_1, x_2, \ldots, x_s)$ may have duplicates.

iv. for X in U_X do//Remove the duplicated vectors.

v. if $X \notin \Omega$, then $\Omega = \Omega \cup \{X\}$. endfor.

Step 3. Find the set $\Omega_{min} = \{X \mid X \text{ is a minimum vector in } \Omega\}$. Let $J = \{j \mid X_j \notin \Omega_{min}\}$.

i. for $i \notin J$ and $1 \le i \le |\Omega|$ do//where $|\Omega|$ denotes the number of elements in Ω.

ii. for $j \notin J$ and $i < j \le |\Omega|$ do

iii. if $X_j \le X_i$, then $J = J \cup \{i\}$ and go to Step 3i.
else if $X_j > X_i$, then $J = J \cup \{j\}$.
endfor.

iv. $\Omega_{min} = \Omega_{min} \cup \{X_i\}$.
endfor.

Step 1 indicates that according to the MPs, the feasible F under Constraint (140.1) and (140.4) is enumerated into set $\mathbf{F}$. Then, the candidate vector set Ω for LBVs can be derived from $\mathbf{F}$ under Eq. (140.5) at Step 2. Finally, the set Ω_{min} of LBVs is filtered by the pair-wise comparisons at Step 3.

140.4 A Numerical Example

Figure 140.1 shows a hub-based network in a famous company. There are 28 MPs found: $mp_1 = \{1, 2, 5, 10, 14\}$, $mp_2 = \{1, 2, 5, 10, 15\}$, $mp_3 = \{2, 5, 10, 14\}$, $mp_4 = \{2, 5, 10, 15\}$, $mp_5 = \{3, 5, 10, 14\}$, $mp_6 = \{3, 5, 10, 15\}$, $mp_7 = \{4, 5, 10, 14\}$, $mp_8 = \{4, 5, 10, 15\}$, $mp_9 = \{5, 10, 14\}$, $mp_{10} = \{5, 10, 15\}$, $mp_{11} = \{6, 8, 10, 14\}$, $mp_{12} = \{6, 8, 10, 15\}$, $mp_{13} = \{7, 8, 10, 14\}$, $mp_{14} = \{7, 8, 10, 15\}$, $mp_{15} = \{8, 10, 14\}$, $mp_{16} = \{8, 10, 15\}$, $mp_{17} = \{9, 10, 14\}$, $mp_{18} = \{9, 10, 15\}$, $mp_{19} = \{10, 14\}$, $mp_{20} = \{10, 15\}$, $mp_{21} = \{11, 10, 14\}$, $mp_{22} = \{11, 10, 15\}$, $mp_{23} = \{12, 11, 10, 14\}$, $mp_{24} = \{12, 11, 10, 15\}$, $mp_{25} = \{13, 11, 10, 14\}$, $mp_{26} = \{13, 11, 10, 15\}$, $mp_{27} = \{14\}$, $mp_{28} = \{15\}$. The demand is 3 GB, and the maximal capacity vector is (1, 2, 1, 1, 3, 1, 1, 3, 1, 3, 3, 1, 1, 3, 3) in 1 GB unit. Table 140.1 gives the historical availability for each arc.

There are 10 LBVs found: $X_1 = \{0, 0, 0, 0, 0, 0, 0, 0, 0, 1, 0, 0, 0, 1, 2\}$, $X_2 = \{0, 0, 0, 0, 0, 0, 0, 0, 0, 1, 0, 0, 0, 2, 1\}$, $X_3 = \{0, 0, 0, 0, 0, 0, 0, 0, 0, 2, 1, 0, 0, 0, 3\}$, $X_4 = \{0, 0, 0, 0, 0, 0, 0, 0, 0, 2, 1, 0, 0, 3, 0\}$, $X_5 = \{0, 0, 0, 0, 0, 0, 0, 0, 1, 2, 0, 0, 0, 0, 3\}$, $X_6 = \{0, 0, 0, 0, 0, 0, 0, 0, 1, 2, 0, 0, 0, 3, 0\}$, $X_7 = \{0, 0, 0, 0, 0, 0, 0, 0, 1, 0, 2, 0, 0, 0, 3\}$, $X_8 = \{0, 0, 0, 0, 0, 0, 0, 1, 0, 2, 0, 0, 0, 3, 0\}$, $X_9 = \{0, 0, 0,$

Table 140.1 The historical availability of each arc

Arcs	Availability (per GB)	Arcs	Availability (per GB)
1	0.91	9	0.92
2	0.88	10	0.91
3	0.92	11	0.93
4	0.90	12	0.93
5	0.88	13	0.88
6	0.87	14	0.87
7	0.93	15	0.89
8	0.89		

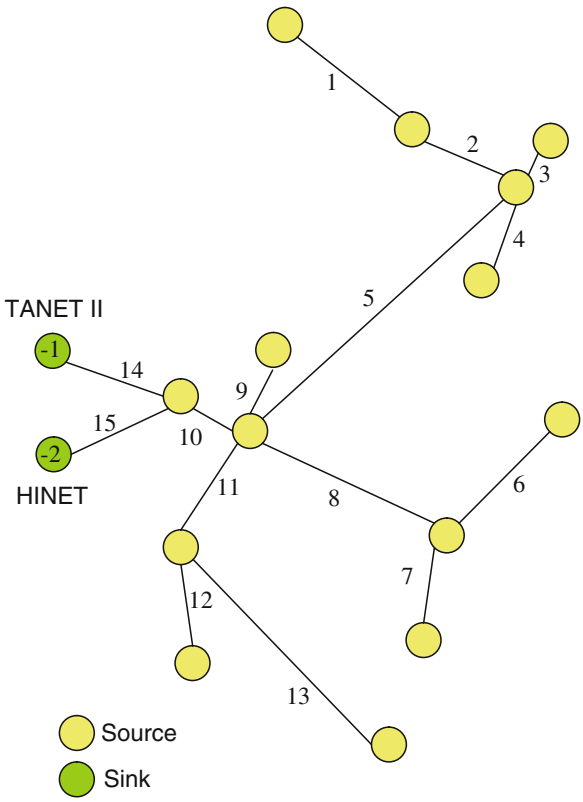

Fig. 140.1 A hub-based network in a famous company

0, 1, 0, 0, 0, 0, 2, 0, 0, 0, 0, 3}, $X_{10} = \{0, 0, 0, 0, 1, 0, 0, 0, 0, 2, 0, 0, 0, 3, 0\}$. Let $E_i = \{X | X \geq X_i\}$. Then, by RSDP, the network reliability

$$R_3 = \Pr\left\{\bigcup_{i=1}^{10} E_i\right\} = 0.996694.$$

140.5 Conclusion

This paper proposes a method to evaluate the reliability of hub-based networks in terms of Minimal Paths (MPs). Traditionally, two-terminal network reliability is deeply investigated. However, the reliability of a hub-based network has not yet been explored. A hub-based network is a computer network with the flows entering from multiple source nodes and exiting by multiple sink nodes, and their intermediate nodes may have flows generated. Such networks have tree-like topologies, where each node may be connected by some users or other hubs. Therefore, the intermediate nodes may have flows generated and are considered a kind of source nodes. The bottleneck link in a hub-based network is a key link in reliability. A detailed study for such networks has not yet been done in the literature.

This paper proposes a method for the reliability evaluation of hub-based networks in terms of MPs. A path is a set of links whose existence results in the connection of source node and sink node. An MP is a path whose proper subset is not a path. When the network is live, there are several MP vectors with respect to system state d called lower boundary vectors (LBV). Then, the network reliability is the union probability of all these LBVs. To demonstrate the proposed method, a numerical example of hub-based network in a famous company is explored. It shows that the proposed method is valuable in practical applications.

Acknowledgments This work was supported in part by the National Science Council, Taiwan, Republic of China, under Grant No. NSC 102-2221-E-236-005.

References

1. Aggarwal, K. K., Gupta, J. S., & Misra, K. B. (1975). A simple method for reliability evaluation of a communication system. *IEEE Transactions on Communications, 23*, 563–565.
2. Lee, S. H. (1980). Reliability evaluation of a flow network. *IEEE Transactions on Reliability, 29*, 24–26.
3. Ford, L. R., & Fulkerson, D. R. (1962). *Flows in networks*. NJ: Princeton University Press.
4. Aggarwal, K. K., Chopra, Y. C., & Bajwa, J. S. (1982). Capacity consideration in reliability analysis of communication systems. *IEEE Transactions on Reliability, 31*, 177–180.
5. Rueger, W. J. (1986). Reliability analysis of networks with capacity-constraints and failures at branches and nodes. *IEEE Transactions on Reliability, 35*, 523–528.
6. Xue, J. (1985). On multistate system analysis. *IEEE Transactions on Reliability, 34*, 329–337.
7. Lin, Y. K. (2001). A simple algorithm for reliability evaluation of a stochastic-flow network with node failure. *Computers and Operations Research, 28*, 1277–1285.
8. Zuo, M. J., Tian, Z., & Huang, H. Z. (2007). An efficient method for reliability evaluation of multistate networks given all minimal path vectors. *IIE Transactions, 39*, 811–817.

Chapter 141
Measurement of Arm and Hand Motion in Performing Activities of Daily Living (ADL) of Healthy and Post-Stroke Subjects—Preliminary Results

Albert Causo, I-Ming Chen and Song Huat Yeo

Abstract This paper presents an ADL measurement system composed of a measurement table, upper limb measurement system that uses IMU sensors, hand measurement system that uses OLE-based sensor (SmartGlove), and a software system that integrates the sensors and record motion data. Some preliminary data are shown, comparing the motion of a healthy subject to a post-stroke patient's motion.

Keywords Activities of daily living · ADL · Arm motion · Hand motion · IMU

141.1 Introduction

Healthcare delivery expansion has never been more important with the increase in number of patients needing post-stroke rehabilitation due to sedentary lifestyle and aging population. Thus, in designing patient rehabilitation programs and building

This is a joint research project with Budapest University of Technology and Economics (Hungary), National Institute of Rehabilitation Medicine (Hungary), and Tan Tock Seng Hospital (Singapore). This work was supported in part by Singapore Millenium Foundation Research Grant and Singapore Food Industries and the Agency for Science, Technology and Research, Singapore, under SERC Grant 092 149 0082.

A. Causo (✉) · I.-M. Chen · S. H. Yeo
Robotics Research Centre, School of Mechanical and Aerospace Engineering, Nanyang Technological University, 50 Nanyang Avenue, Singapore 639789, Singapore
e-mail: acauso@ntu.edu.sg

I.-M. Chen
e-mail: michen@ntu.edu.sg

S. H. Yeo
e-mail: myeosh@ntu.edu.sg

J. Juang et al. (eds.), *Proceedings of the 2nd International Conference on Intelligent Technologies and Engineering Systems (ICITES2013)*, Lecture Notes in Electrical Engineering 293,
DOI: 10.1007/978-3-319-04573-3_141,

robotics rehabilitation systems, accurate measurement of Activities of Daily Living (ADL) is critical [1] since what patient often perceives and what the therapist measures can be different. Chen et al. encourage the development of objective and accurate upper limb motion measurement system since such motions are a good predictor of upper arm recovery [2]. Hsueh et al. point out that having an efficient and valid measure of assessing patient activity is key to patient management and outcome measurement [3].

Engineering research involving ADL include development of measurement systems and rehabilitation robots. Several researchers created systems to measure ADLs in order to track elderly or stroke patients at home [4, 5]. Tanaka has demonstrated the use of robotic suit to aid with ADL-based motion for rehabilitation [6]. Sugar et al. built a robot to aid in repetitive therapy [7], similar to ADL-based therapies. Compared to other post-stroke rehabilitation activities, ADL-based ones may be aided with robotic systems.

This paper discusses preliminary results of measuring ADL motions by healthy subjects and post-stroke patients. The measurement set-up will be described in detail including the five ADL tasks chosen for this project. In Sect. 141.2, the ADL Measurement Table, Upper Limb Motion Measurement System and the ADL Motion Capture Software are presented. The five ADLs are discussed in Sect. 141.3 and the experiments and results are covered in Sect. 141.4.

141.2 Activities of Daily Living Measurement System

141.2.1 ADL Measurement Table

A table and chair have been designed to be able to measure ADL motion consistently across subjects of different heights. Height data of male and female Singaporeans were obtained from the Singapore Ministry of Health. Table markers were used to specify the position of the items used for the ADL, depending on the height of the subject. Three sets of table markers correspond to the different subject groups—blue for tall subjects (heights taller than 169 cm), red for medium (height between 158 to 169 cm), and black for small (height below 158 cm). The table was also designed for left and right-handed people.

A chair positioned at a fixed distance from the table through a platform ensures that the subject's arm would be fully extended when doing the ADL tasks. The thickness of the footrest under the table could also be adjusted accordingly. The chair itself is padded to provide support while at the same time keeps the subject's back straight. Figure 141.1 shows the table and the chair set-up. A vest was designed to minimize compensatory motion of the torso by strapping the patient to the chair back securely.

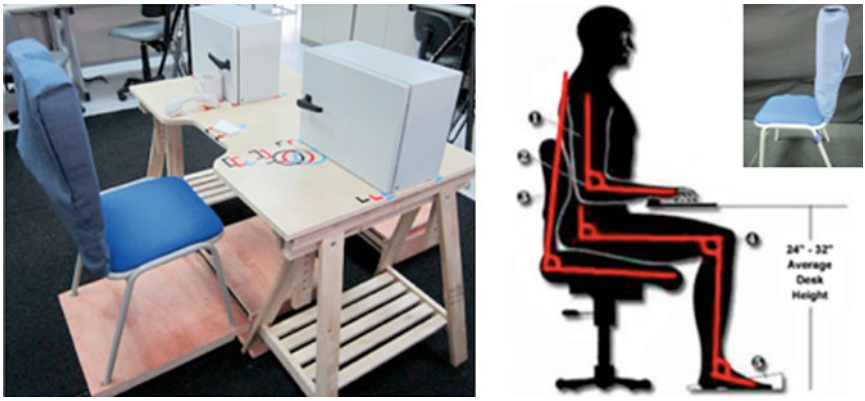

Fig. 141.1 The ADL Table Measurement *left* and the chair *right* designed to make the subject sit upright

141.2.2 Upper Limb Motion Measurement System

To be able to measure arm motion using two inertial measurement units (IMU) sensors, each containing nine sensors inside (3 accelerometers, 3 angular rate gyros and 3 magnetometers), the upper limbs is modeled as a 2-segment compound flexible pole. The IMU sensors provide the orientation (roll, pitch, and yaw) of each sensor unit. The arm posture is described using the orientations of the wrist, forearm, and upper arm. Figure 141.2a shows the arm model with the attached IMUs.

To measure the hand motion, subjects wear a data glove called SmartGlove, which is fitted with Optical Linear Encoder (OLE) sensors. The finger joint angles are measured by converting the linear motion of a strip over the joint to angular data. For more details of the operating principles of the OLE, please refer to Li et al. [8]. The SmartGlove uses ten OLEs to capture the flexion–extension motion of the 10 finger joints based on the multi-point sensing method. The glove measures a total of 15 DOF including the metacarpophalangeal (MCP), proximal interphalangeal (PIP) and distal interphalangeal (DIP) joints. The latter is estimated based on anatomical constraints, assumed to be (2/3) of the measured PIP value.

At the beginning of each measurement session, the IMUs and the SmarGlove have to be calibrated. To calibrate the IMUs, the subjects must stretch out their arms. To calibrate the glove, subjects are asked to make hand gestures such as open palms, fist, or full thumb extension. A special calibration box, which helps in forming 90 degrees at each joint, is used for the MCP and the PIP joints. More details on the upper limb measurement system are available in [9].

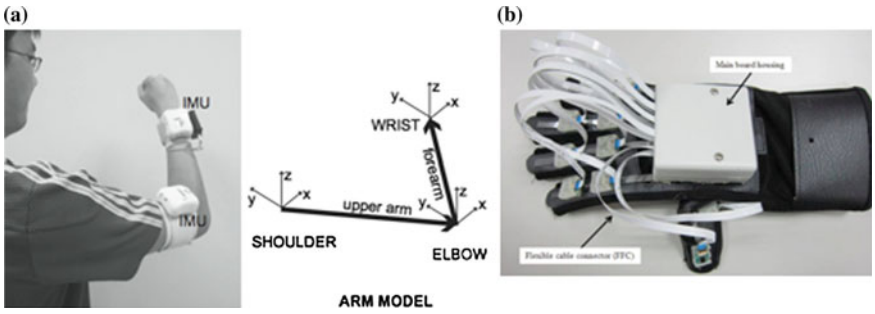

Fig. 141.2 The upper limb with the IMU sensors attached (**a**). The SmartGlove used to measure the hand motion (**b**). The third IMU for measuring wrist motion is attached to the top of the control box

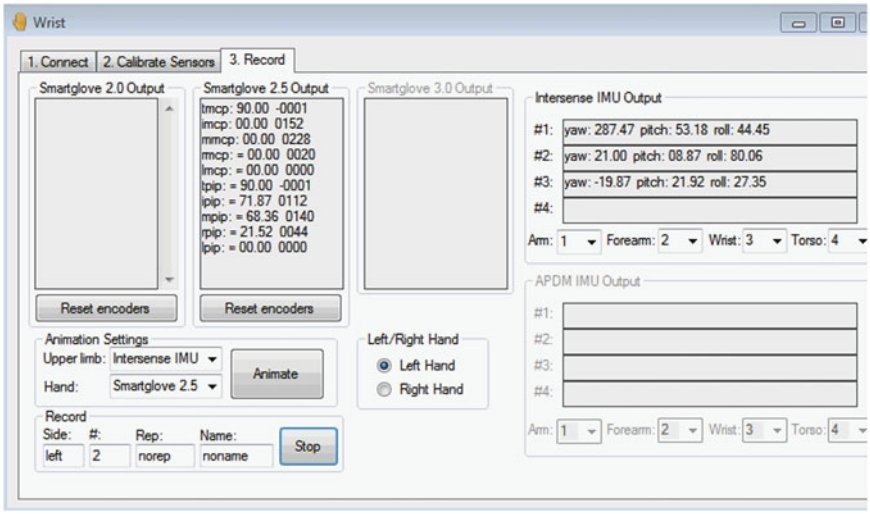

Fig. 141.3 ADL motion capture software shows the three tabs (connect, calibrate and record data)

141.2.3 ADL Motion Capture Software

Integrated software to connect to the sensors, calibrate the sensors, capture data and display data from the experiments was designed. In the first tab (see Fig. 141.3), the software can connect to the IMU via 2.4 GHz radio link while the SmartGlove connects via Bluetooth. In the second tab, the software interface prompts the experimenter to go through the process of sensor calibration. Captured data is shown and recorded in the third tab. The data can be saved in extended

mark-up language (XML) format. The data is saved in this order: time stamp, finger data (subdivided into MCP, PIP and DIP data per finger), upper arm (yaw, pitch, roll), forearm (yaw, pitch, roll), and wrist (yaw, pitch roll), followed by the same set of data uncalibrated.

141.3 Activities of Daily Living and Experiment Process

Five ADLs were measured as advised by the project's medical partners. These ADLs include: picking up a cup, zipping and unzipping a vest, picking up phone, opening and closing a window, and wiping face with a towel. The paraphernalia associated with these ADLs can be seen on the table in Fig. 141.1, which includes a cup with handles, vest (worn by the subjects and attached to the chair), phone, a key box (to represent the window), and a small towel.

Fifteen healthy subjects (8 male, 7 female) from Nanyang Technological University with ages from 21 to 75 years old volunteered for the experiments. Fifteen stroke patients were recruited from Tan Tock Seng Hospital with ages from 40 to 75 years old (8 male, 7 female). Inclusion and exclusion criteria were set for the post-stroke subjects such as the duration of time after onset of stroke, upper limb strength, absence of any upper limb deformity, visual, language and cognitive deficits. Pregnant women, prisoners and legally restricted or incapacitated subjects were excluded. The Institutional Review Boards of Nanyang Technological University and the National Healthcare Group—Domain Specific Review Board (for Tan Tock Seng Hospital experiments) approved the protocols for the research experiments.

Table 141.1 shows the characteristics of the post-stroke patients. Their physical characteristics were measured by therapists and will be used when understanding the quality of motion of the subjects.

Subjects were oriented about the project and their consent was obtained. Subject's height, gender and hand dominance were also recorded. Depending on the height of the subject the footrest, the location of tabletop items, the vest size, and the SmartGlove were adjusted. Afterwards, the subject was then fitted with the IMUs on the arm and the SmartGlove on the hand. Then the subject was asked to sit on the chair and wear the vest, which was secured to the back and legs of the chair. The IMUs on the arm and the SmartGlove were calibrated prior to every use.

After doing the ADL for the dominant side (healthy subjects) or the unaffected side (stroke patients), the non-dominant side (healthy subject) or the affected side (stroke patients) doing ADLs were measured as well.

Figure 141.4 shows the software in action, showing a video of the subject, the actual data being captured, and visualization as data come in.

Table 141.1 Post-stroke subjects with their movement level after stroke

Patient	Gender/ age	Side of stroke	Fugl-Meyer rating	Motricity index (out of 15)	Hand movement scale
1	F/65	Right	21/66	6	3
2	M/54	Left	36/66	10	5
3	F/62	Left	22/66	6	2
4	M/37	Left	24/66	9	2
5	M/50	Right	28/66	9	3
6	M/58	Right	34/66	8	2
7	M/34	Left	35/66	10	3
8	M/31	Right	31/66	10	2
9	F/47	Right	20/66	6	2
10	F/31	Right	30/66	8	3
11	F/30	Right	63/66	12	6
12	F/47	Right	31/66	8	3
13	M/45	Right	23/66	8	2
14	F/53	Right	59/66	12	5
15	F/59	Right	20/66	6	2

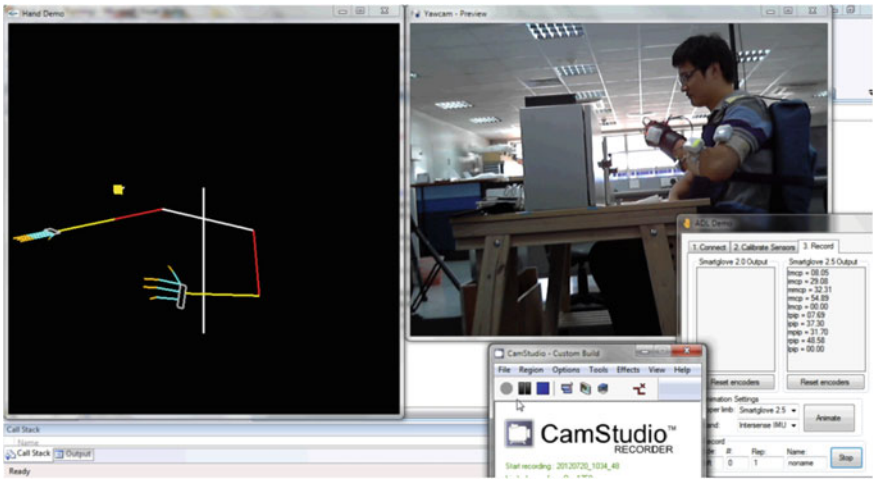

Fig. 141.4 Shows the measurement system in action. The *left box* visualizes the data as it is captured. The *right box* shows the video of the experiments

141.4 Results and Discussion

Figures 141.5 and 141.6 show representative data from a healthy subject and a stroke patient, respectively. Both graphs show the right side, which for the patient is the affected side. The two subjects show big differences in doing the Picking Up A Cup ADL. For example, the stroke patient has a big range of motion for the

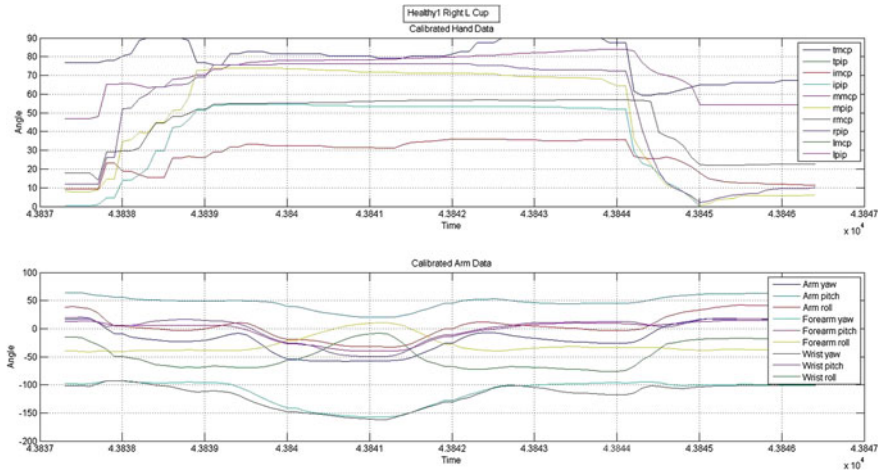

Fig. 141.5 Right side measurement of a healthy subject while doing picking up a cup ADL. The *upper* graph is for the hand, the *lower* for the arm

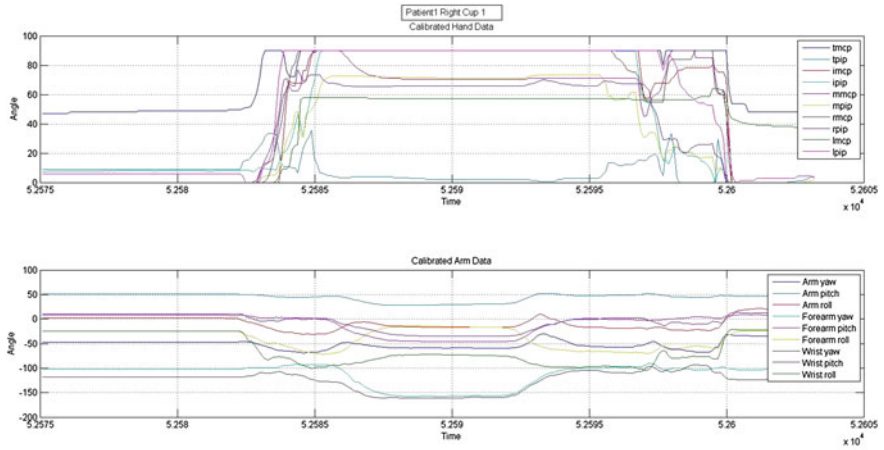

Fig. 141.6 Right side measurement of a post-stroke patient while doing picking up a cup ADL. The *upper* graph is for the hand, the *lower* for the arm

upper arm yaw (Around 300°), while the healthy subject has a range of motion not exceeding 100° for any upper limb orientation parameter. The stroke subject also takes almost three times as long to finish the task ($\sim$20 s) than the healthy subject ($\sim$7 s).

This study is just an initial step towards the completion of a robotic rehabilitation system. What has been accomplished in this paper is the quantification and

accurate capture of complete upper limb motion (from proximal to distal) while doing rehabilitation related activity (i.e., the ADLs). Future work involves the processing and analysis to obtain Range of Motion, Task Completion Time, Motion Linearity, Peak Velocity, and Jerk Score Movement.

References

1. Sager, M. A., Dunham, N. C., Schwantes, A., Mecum, L., Halverson, K., & Harlowe, D. (1992). Measurement of activities of daily living in hospitalized elderly: a comparison of self-report and performance-based methods. *Journal of the American Geriatrics Society, 40*(5), 457–462.
2. Chen, S. Y., & Winstein, C. J. (2009). A systematic review of voluntary arm recovery in hemiparetic stroke: critical predictors for meaningful outcomes using the international classification of functioning, disability, and health. *Journal of Neurolic Physical Therapy, 33*(1), 2–13.
3. Hsueh, I. P., Chen, J. H., Wang, C. H., Hou W. H., & Hsieh, C. l. (2013). Development of a computerized adaptive test for assessing activities of daily living in outpatients with stroke. *Journal of Physical Therapy*, *93*(5), 681–693, doi: 10.2522/?ptj.20120173
4. Hong, X. (2008). HomeADL for adaptive ADL monitoring within smart homes. *Proceedings of 30th Annual International Conference of IEEE Engineering in Medicine and Biology Society*, August 2008, pp. 3324–3327.
5. Bang, S. L. Toward real time detection of the basic living activity in home using a wearable sensor and smart home sensors. *Proceedings of 30th Annual International Conference of IEEE Engineering in Medicine and Biology Society,* (EMBS 2008), August 2008, pp. 5200–5203.
6. Tanaka, E. (2012). Gait and ADL rehabilitation using a whole body motion support type mobile suit evaluated by cerebral activity. *Proceedings of IEEE International Conference on Systems, Man, and Cybernetics* (*SMC*), October 2012, pp. 3286–3291.
7. Sugar, T.G., Jiping, H., Koeneman, E. J., Koeneman, J. B., Herman, R., Huang, H. et al. (2007), Design and control of RUPERT: A device for robotic upper extremity repetitive therapy. *IEEE Transactions on Neural Systems and Rehabilitation Engineering*, *15*(3), 336–346.
8. Li, K., Chen, I. M., & Yeo S. H. (2010). Design and validation of a multi-finger sensing device based on optical linear encoder. *IEEE International Conference on Robotics and Automation*, pp. 3629–3634.
9. Ding, Z. Q., Luo, Z. Q., Causo, A., Chen, I. M., Yue, K. X., Yeo, S. H., et al. (2011). Inertia sensor-based guidance system for upperlimb posture correction. *Journal of Medical Engineering and Physics, 35*(2), 269–276.

Chapter 142
Application of TRIZ and Universal Design in the Innovation Design of the Building Descending Structure

Kuo-Yi Li

Abstract The goal of the present research is to design a new building descending structure which can solve the problems of the darkness in fire scenes and the vertical support of the fixing frame. The research method uses the contradiction matrix of TRIZ to find out the parameters which are to be improved and prevented from deteriorating and then uses seven principles of the universal design to design a building descending structure providing a night vision and general vertical supporting function. The principle thereof is to use the fluorescent strips for assisting escapers in finding out the descending device quickly and completing the escaping action under the illumination of LED lights. A bottom of the vertical support has a U-shaped contact, which is applied to various surrounding walls. It belongs to the humanized fire-fighting and escaping equipment.

Keywords TRIZ · Universal design · Descending structure

142.1 Introduction

Generally, a large amount of heavy smoke attendant on fire scenes not only comprises combustion products, such as carbon granules, residues, and ashes but also contains a large amount of toxic gases, such as hydrogen cyanide (HCN), hydrogen sulfide (H_2S), and carbon monoxide (CO) which makes a great harm to human beings [1]. In the fire scene filled with heavy smoke and high temperature, an efficient escaping method can save lives. The descending and escaping equipment is an efficient refuge and escape method, especially the descending apparatus set in every floor has a great effect on escaping in the scene where the

K.-Y. Li (✉)
Department of Industrial Engineering and Management, National Chin-Yi University of Technology, Taichung, Taiwan, Republic of China
e-mail: kyli@ncut.edu.tw

J. Juang et al. (eds.), *Proceedings of the 2nd International Conference on Intelligent Technologies and Engineering Systems (ICITES2013)*, Lecture Notes in Electrical Engineering 293,
DOI: 10.1007/978-3-319-04573-3_142,

fire blocks the exit of the escaping ladder [2, 3]. Therefore, the present research utilizes an innovation solution of TRIZ and a universal design to design a building descending structure containing a night vision and general vertical supporting function to solve the darkness in the fire scenes and the safety and the vertical support problem of the fixing frame, thereby increasing the refuge and escape efficient of the descending apparatus.

142.2 Methodology

TRIZ, a theory of Inventive Problem Solving, was invented by Genrich Althshuller used to be an examiner in Russian marine patent office. He picked up forty thousands patents from two hundred thousands patents as the patents disclosing preferable innovation methods and found that every innovative patent was designed to solve an innovative issue, including the demand conflict and the contradiction problem [4]. TRIZ is composed of many inventive tools, such as Contradiction Matrix, 40 Inventive Principles, Substance-Field Analysis, 76 Standard Solution, Rules of Evolution, and Algorithm of Inventive Pro [5].

TRIZ divides the contradiction into a physical contradiction and a technical contradiction. The technique contradiction functions in a system when one parameter is improved and the other parameter is set to be deteriorated, such as power output in contradiction to the oil consumption. The physical contradiction functions when the same parameter has two opposite characteristics, such as cold and hot. The technical contradiction utilizes the 39 engineering parameters and the 40 inventive principles to solve problems. The physical contradiction utilizes a separation principle to solve problems [6]. The technique contradiction is a conflict between two parameters. The conflict shows a possibility by a two-dimensional matrix performed by 39×39 engineering parameters. The longitudinal axis represents the parameter which is to be improved, and the transverse axis represents the parameter which is to be deteriorated. The matrix element is a suggestive innovation rule for this situation and therefore 40 principles are divided [6–9].

The universal design was claimed by Professor Ron Mac in America in 1985. He thought that the product design should consider all elements without being restricted to specific objects while taking the object into consideration. It is a kind of design method possible to obviate the differences of ages and abilities when the product and environmental designs are executed and to allow the product to be suitable for most people [10]. The universal design mostly executes the product design according to seven principles, including (1) equitable use, (2) flexibility in use, (3) simple and intuitive use, (4) perceptible information, (5) tolerance for error, (6) low physical effort, and (7) size and space for approach and use. By these seven principles, the product can be suitable for most people.

142.2.1 Measure 1: Problem of the Darkness in Fire Scenes and the Solution

In the real fire scene, not only the high temperature but the heavy smoke renders people unable to determine where they are. However, it cannot take too much time to finish the illumination job as the escaping time in the fire scene is very precious. Accordingly, in the contradiction matrix of TRIZ, the parameter to be improved is defined as NO.18 "Brightness", namely the light per unit area, and the parameter prevented from deteriorating is defined as NO.9 "Speed", namely the executing time or required time. The contradiction matrix obtains 3 inventive principles, including (1) NO.10 "Preliminary action" which functions by adhering fluorescent strips to the escape fixing frame of the descending apparatus in advance and conducting escapers to find out the escaping device quickly in the dark fire scene. The solar LED light can have its battery greatly charged by receiving solar energy in advance for providing a good illumination immediately when there is a fire; (2) NO.13 "Other way around" which executes opposite actions or makes objects reversed. It does not fit in this measure; and (3) NO.19 "Periodic action" which functions by using a periodic action to replace a continuous action. It does not fit in this measure.

When the seven principles of the universal design are used to analyze the problem of the darkness in fire scenes, this problem needs to be overcome for all escapers, regardless of ages and objects. Therefore, it meets the equitable use. In the fire scene, since the time is precious, the escaping equipment must be simple and easy to use. Therefore, it meets the simple and intuitive use. The escapers in the fire scene may be elders, infirm people, woman, and children who have smaller efforts, so the escaping equipment must be operated by using small efforts. Therefore, it meets the low physical effort. By these contents of the three principles, including the equitable use, the simple and intuitive use, and the low physical effort, the design of florescent strips and the solar LED light can solve this problem.

142.2.2 Measure 2: Safety Problem of the Fixing Frame of the Descending Apparatus and the Solution

When escapers use the descending apparatus to descend, the fixing frame of the descending apparatus bears a very large effort and moment of force, and the structure of the ground cement of the building is decreased due to the earthquake shock and aging materials. Therefore, the safety of the escapers is affected. In the contradiction matrix of TRIZ, the parameter to be improved is defined as NO.14 "Strength", namely the degree of resisting responsive powers. The parameter prevented from deteriorating is defined as NO.35 "Adaptability", namely the property of bearing environmental variations. The contradiction matrix obtains 3

inventive principles, including (1) NO.15 "Dynamism" which makes characteristic of objects or an outer environment adjustable in order to obtain the best performance in the operation. It does not fit in this measure; (2) NO.3 "Local quality" which increases the vertical and the horizontal support units to enhance the structure strength, wherein the bottom of the vertical support unit has a U-shaped contact suitable for various shapes of surrounding walls; and (3) NO.32 "Optical changes" which changes the colors and transparent degree of the object or peripheral affairs. It does not fit in this measure.

When the seven principles of the universal design are used to analyze the safety of the fixing frame of the descending apparatus, certain strength must be provided when men, women, elders, and children use the escaping equipment to ensure the descending safety. Therefore, it meets the equitable use. It is very easy to install and operate the fixing frame of the descending apparatus. Therefore, it meets the simple and intuitive use. By the principles, including the equitable use and the simple and intuitive use, the design of vertical and horizontal support units can reinforce the strength of the structure and ensure the safety of the escapers.

142.2.3 Measure 3: Problem of the Vertical Support of the Fixing Frame of the Descending Apparatus and the Solution

When the cantilever of the fixing frame of the descending apparatus is used, a vertical force is imparted onto the surrounding wall. If the contact end is planar, a direct fasten is sufficient. If the contact end is irregular, a U-shaped fixing means is adopted to provide a stable support. Therefore, in the contradiction matrix of TRIZ, the parameter to be improved is defined as NO.12 "Shape", namely an outer contour. The parameter prevented from deteriorating is defined as NO.35 "Adaptability", namely the property of bearing environmental variations. The contradiction matrix obtains 3 inventive principles, including (1) NO.1 "Segmentation" which uses a U-shaped contact end that is installed on various surrounding walls and fixed by a toggle clamping mechanism for providing a preferable clamping performance; (2) NO.15 "Dynamism" which makes characteristic of objects or an outer environment adjustable in order to obtain the best performance in the operation. It does not fit in this measure; and (3) NO.29 "Pneumatics or hydraulics" which uses the gas or liquid to replace the fixing component of an object. It does not fit in this measure.

When the seven principles of the universal design are used to analyze the problem of the vertical support of the fixing frame of the descending apparatus, the U-shaped end can stably abut on various surrounding walls, such as cement walls, brick walls, wood walls, rail walls, irregular walls, and windows, thereby meeting the flexibility in use.

142.3 Product Design

To solve the darkness in fire scenes, the safety problem of the fixing frame, and the problem of the vertical support, the inventor designs a building descending providing a night version and general vertical supporting function according to the aforementioned inventive principles derived from the analysis of the contradiction matrix. According to the above three measures, an inventor software is utilized to convert the possible inventive principles into a solid structure, which is described as follows.

142.3.1 Structure and Function of the Product

The present invention comprises fluorescent strips, a solar LED light, a vertical support unit, a horizontal support unit, a U-shaped contact end, and a toggle clamping unit. When there is a fire causing the dark fire scene, the fluorescent strips assist escapers in finding out the escaping equipment of the descending apparatus quickly, and the LED light helps a swift installation of the fixing frame of the descending apparatus for completing the escaping action within a golden time. With regard to the device of the general vertical supporting function, the U-shaped contact end or other shapes of the contact end can be efficiently installed on cement walls, rail walls, wood walls, brick walls, or windows, thereby reinforcing the structure strength of installing the fixing frame. Herein, the structure and components of the present invention is described by the perspective view and the operation view in different angles. Figure 142.1 shows an entire configuration. Figure 142.2 shows a vertical installation on an irregular wall. Figure 142.3 shows an escaping and descending situation under the instruction of fluorescent strips and the LED light. Figure 142.4 shows a vertical installation on a cement wall, an irregular wall and a rail wall.

142.3.2 Features of the Product

The present invention is a building descending structure providing a night vision and general vertical supporting function. The features are:

(1) Fixing frame with a good strength and safety: By the horizontal support unit and the vertical support unit, the fixing frame of the descending apparatus forms a rigid body with a good strength to prevent escapers from falling down.
(2) Do not influence the appearance of the building: The vertical support unit can be taken out of the wall surface and stored in the box. Alternatively, the vertical support unit can be rotated to a horizontal location. Therefore, it does not affect the appearance of the building.

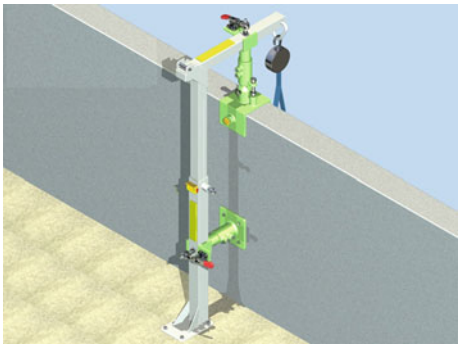

Fig. 142.1 Entire configuration

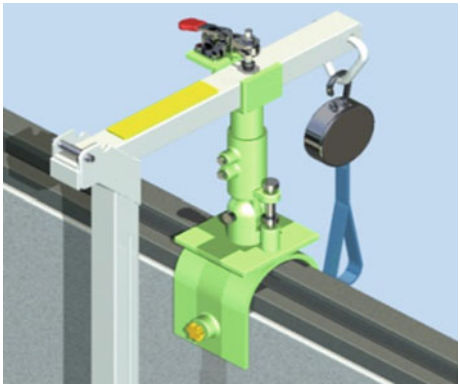

Fig. 142.2 Install on an irregular wall vertically

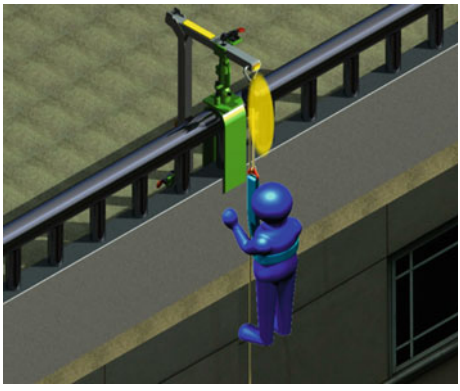

Fig. 142.3 Escaping under fluorescent strips

(3) Fluorescent strips leads escaper to the location of the descending apparatus: When there is a fire, escapers are conducted by the fluorescent strips to find out the fixing frame of the descending apparatus quickly. Therefore, they can escape within a golden time.

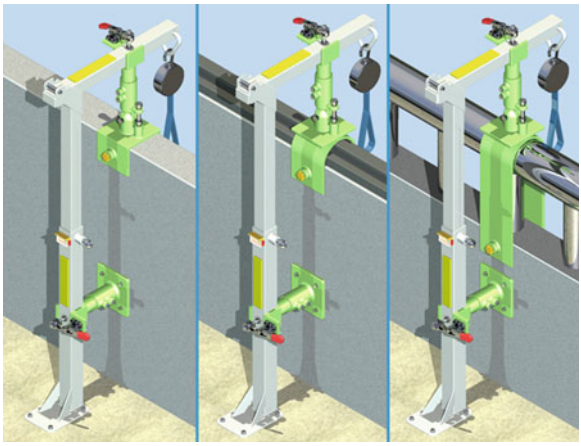

Fig. 142.4 Install on a cement wall, an irregular wall, and a rail wall vertically

(4) LED light assists people in completing the operation of the fixing frame: By the LED light, escapers can quickly complete the installation of the fixing frame to escape and descend.
(5) Broad application in various walls: The vertical support unit of the present invention uses the U-shaped contact according to different shapes of wall surfaces, whereby it can be widely installed on all surrounding walls.

142.4 Conclusion

The innovation of the present invention utilizes the contradiction matrix of TRIZ to analyze the product function, develops a model product according to the inventive principles which are found out, inspects by using seven principles of the universal design, and uses an inventor software to convert the possible inventive principles into a solid structure. The present invention is a building descending structure providing a night vision and general vertical supporting function. The nigh version device is to solve the darkness in fire scenes. The general vertical support unit applies the present invention in all kinds of walls. When there is a fire, the fluorescent strips assist escapers in finding out the descending apparatus quickly, and the LED light helps a quick installation of the escape equipment to complete the escaping action. With regard to the general vertical supporting function, the U-shaped contact design can be efficiently installed on cement walls, rail walls, wood walls, brick walls, or windows, thereby reinforcing the strength of the installation structure of the fixing frame and allowing the fixing frame to form a rigid body with a good strength. Practically, the vertical support unit can be detached when the fixing frame is not used, or the vertical support unit can be placed at a horizontal location relative to the wall. Therefore, the appearance of the

building is not affected. Considering the entire configuration, the present invention is conducive to a clean appearance and has a simple structure, an easy operation, a quick installation, a safety and reliability property, a night version function, and a broad application in various walls.

References

1. Black, W. Z. (2010). COSMO—Software for designing smoke control systems in high-rise buildings. *Fire Safety Journal, 45*(6), 337–348.
2. Zhang, G., Lee, A. H., Lee, H. C., & Clinton, M. (2006). Fire safety among the elderly in Western Australia. *Fire Safety Journal, 41*(1), 57–61.
3. Li, K. Y. (2004). Analysis of the mechanical property-safety management of descending apparatus of schools. *Journal of Industrial Safety and Technology, 51*, 24–30.
4. Kuo, T. Y., & Lin, C. C. (2010). Application of TRIZ in an innovation design of small fishing nets. *Industrial Design, 38*(1), 92–95.
5. Teng, C. J., & Yeh, G. C. (2011). Application of TRIZ in analyzing wrapping devices. *Science and Engineering Technique, 7*(3), 35–51.
6. Sung, M. H. (2009). *Systematized innovation theory and application of TRIZ*. Taipei: Tin-Miao Book Publishing Company.
7. Zhou, Y. C. (2010). Contradiction theory and application of TRIZ. *Science and Management, 3*, 15–18.
8. Althshuller, G. (1998), *TRIZ Keys to technical innovation*. Technical Innovation Center, pp. 15–21.
9. Bukhman, I. (2012), *TRIZ technology for innovation*. Watertown: TRIZ Solutions LLC.
10. Ho, X. C. (2007). Theory and method of the universal design. *Packaging Engineering, 28*(7), 119–121.

Chapter 143
Application of TRIZ in the Innovation Design of the Dry-Powdered Fire Extinguisher Training Device

Kuo-Yi Li

Abstract The goal of the present research is to design a new training device for dry-powdered fire extinguishers which can solve the environmental contamination caused by the training operation of dry-powdered fire extinguishers. The research method uses the contradiction matrix of TRIZ to find out the parameters which are to be improved and prevented from deteriorating and designs a dry-powdered fire extinguisher training device with the functions of wind-directional adjustment and environmental protection. The principle thereof is to change the traditional training method adopting an open tray extinguishing means into an extinguishing train conducted in a half-closed space. When the dry powder is shot at the flame, a gas cap sensor will activate a gas discharging device to filter and recycle the powder for reusing. It belongs to the superior fire-fighting equipment with the functions of environmental protection and safety.

Keywords TRIZ · Dry-powdered fire extinguisher · Training device

143.1 Introduction

The components of dry-powdered extinguishers include sodium bicarbonate ($NaHCO_3$), potassium bicarbonate ($KHCO_3$), and ammonium biphosphate ($NH_4H_2PO_4$). When the sodium bicarbonate is dissolved in the water, the solution is weakly alkaline and the PH value is less than 8.6. The main harm is that it irritates the respiratory system, skin, and eyes [1]. However, when the extinguishing training is conducted in a high-concentrated residential district, such as apartments or outdoors, the sprayed sodium bicarbonate powder from the fire

K.-Y. Li (✉)
Department of Industrial Engineering and Management, National Chin-Yi University of Technology, Taichung, Taiwan. Republic of China
e-mail: kyli@ncut.edu.tw

J. Juang et al. (eds.), *Proceedings of the 2nd International Conference on Intelligent Technologies and Engineering Systems (ICITES2013)*, Lecture Notes in Electrical Engineering 293,
DOI: 10.1007/978-3-319-04573-3_143,

extinguisher adversely pollutes the nearby houses, flowers, plants, and trees and causes damages to people's health and the environment [2]. Therefore, the present research utilizes an innovation solution of TRIZ to design a dry-powdered fire extinguisher training device which solves problems of the environmental contamination, the safety problem of igniting, the problem of training places, and the wind-directional influence and promotes the training efficiency of the dry-powdered fire extinguishers.

143.2 Methodology

TRIZ, a theory of Inventive Problem Solving, was invented by Genrich Althshuller used to be an examiner in Russian marine patent office. He picked up forty thousands patents from two hundred thousands patents as the patents disclosing preferable innovation methods and found that every innovative patent was designed to solve an innovative issue, including the demand conflict and the contradiction problem [3, 4]. TRIZ is composed of many inventive tools, such as Contradiction Matrix, 40 Inventive Principles, Substance-Field Analysis, 76 Standard Solution, Rules of Evolution, and Algorithm of Inventive Pro [5].

TRIZ divides the contradiction into a physical contradiction and a technical contradiction. The technique contradiction functions in a system when one parameter is improved and the other parameter is set to be deteriorated, such as power output in contradiction to the oil consumption. The physical contradiction functions when the same parameter has two opposite characteristics, such as cold and hot. The technical contradiction utilizes the 39 engineering parameters and the 40 inventive principles to solve problems. The physical contradiction utilizes a separation principle to solve problems. [3, 6]. The technique contradiction is a conflict between two parameters. The conflict shows a possibility by a two-dimensional matrix performed by 39 $\times$ 39 engineering parameters. The longitudinal axis represents the parameter which is to be improved, and the transverse axis represents the parameter which is to be deteriorated. The matrix element is a suggestive innovation rule for this situation and therefore 40 principles are divided [6–9].

143.2.1 Measure 1: Problem of the Contamination of the Dry Powder and the Solution

The extinguishing training of dry-powdered fire extinguishers is to experience the extinguishing skills, so the dry powder must be sprayed out to extinguish flames. Such operation inevitably pollutes the environment. Accordingly, in the contradiction matrix of TRIZ, the parameter to be improved is defined as NO.27

"Reliability", namely to predict functions obtained by the operation, and the parameter prevented from deteriorating is defined as NO.31 "Harmful side effects", namely the harmful effects generated in the operation to decrease the efficiency. The contradiction matrix obtains 4 inventive principles, including (1) NO.35 "Parameter change" which functions by changing an open extinguishing mode which is executed by putting oil trays at an open space for extinguishing into an extinguishing training conducted in a half-closed space, thereby reducing the environmental contamination caused by the dry powder; (2) NO.2 "Extraction" which makes the dry powder sprayed at the flame extracted and sucked into a collecting box by using an exhauster; (3) NO.40 "Composite material" which uses the composite material to replace the homogeneous material. It does not fit in this measure; and (4) NO.26 "Copying" which uses the simple or cheap duplicate products to replace expensive objects. It does not fit in this measure.

143.2.2 Measure 2: Problem of Ignitions of Flames Burning Trainers and the Solution

The traditional dry-powdered training method is executed by making the trainer carry a flambeau and ignite the gasoline in the oil tray. This method is simple and efficient but has the risk of burning the trainer if he or she is careless. Accordingly, in the contradiction matrix of TRIZ, the parameter to be improved is defined as NO.27 "Reliability", namely to predict functions obtained by the operation, and the parameter prevented from deteriorating is defined as NO.17 "Temperature", namely the state of an overall thermal variation. The contradiction matrix obtains 3 inventive principles, including (1) NO.3 "Local quality" which functions by using an electronic ignition to replace the flambeau ignition, thereby the igniting operation is reliable and does not burn the trainer; (2) NO.35 "Parameter change" which uses an electronic igniting gun to catch fire and allows the flame to ignite the gasoline in the oil tray by merely pressing the switch; and (3) NO.10 "Preliminary action" which completes all of the actions in advance. It does not fit in this measure.

143.2.3 Measure 3: Problem that the Training of Dry-Powdered Fire Extinguishers Needs a Larger Place and the Solution

The fire extinguishing training of dry-powdered extinguishers needs to be conducted in a large and vacant space, which provides an enough space to allow the powder dust to distribute without harming the health of nearby people's lungs or to prevent the flame in the oil tray from burning the trainees. Accordingly, in the

contradiction matrix of TRIZ, the parameter to be improved is defined as NO.6 "Area of non-moving object", namely the area of the fixing member, and the parameter prevented from deteriorating is defined as NO.30 "Harmful factors acting on object", namely the exterior harmful effects in itself. The contradiction matrix obtains 4 inventive principles, including (1) NO.27 "Cheap disposable" which uses cheap objects to replace expensive objects. It does not fit in this measure; (2) NO.2 "Extraction" which only takes out the required components or properties. It does not fit in this measure; (3) NO.39 "Inert environment" which uses the inert environment to replace the normal environment. It does not fit in this measure; and (4) NO.35 "Parameter change" which reduces a training place which is a small space having an area of 4.5 m in length, 1.5 m in width, and 2 m in height and comprising two handcarts with 1.5 m in length and 1 m in width and a telescoping sleeve which can extended to 2.5 m in length.

143.2.4 Measure 4: Problem of Extinguishing by a Wind-Directional Adjustment and the Solution

During the extinguishing training of dry-powdered fire extinguishers, trainees need to adjust the extinguishing location to extinguish the flame if the wind direction changes, whereby they can learn the correct extinguishing skill. Accordingly, in the contradiction matrix of TRIZ, the parameter to be improved is defined as NO.35 "Adaptability", namely the property of bearing environmental variations, and the parameter prevented from deteriorating is defined as NO.30 "Harmful factors acting on object", namely the exterior harmful effects in itself. The contradiction matrix obtains 4 inventive principles, including (1) NO.35 "Parameter change" which functions by using a blower to adjust the wind direction and simulate different wind flows in the nature, thereby rendering trainees able to learn the correct extinguishing skills; (2) NO.11 "Beforehand cushioning" which completes all of the actions in advance. It does not fit in this measure; (3) NO.32 "Optical changes" which changes the colors of objects. It does not fit in this measure; and (4) NO.31 "Porous materials" which renders the object porous. It does not fit in this measure.

143.3 Product Design

In view of the urbanizing development, it is not easy to find out a vacant space enough for extinguishing training. However, the fire-fighting article stipulates that every institution needs to conduct the extinguishing training periodically every year to make sure that employees can use dry-powdered fire extinguishers correctly and that the training operation cannot pollute the environment. Therefore,

the inventor designs a dry-powdered fire extinguisher training device providing a wind-directional adjustment and environmental protection function according to the aforementioned inventive principles derived from the analysis of the contradiction matrix. According to the above four measures, an inventor software is utilized to convert the possible inventive principles into a solid structure, which is described as follows.

143.3.1 Structure and Function of the Product

To attain a traditional extinguishing training method of dry-powdered fire extinguishers, firefighters conduct trainees to use dry-powdered fire extinguishers to shoot at flames of burning oil trays in an open space. The training operation would cause a serious environmental contamination as shown in Figs. 143.1 and 143.2. The present invention executes the extinguishing training in a half-closed space and utilizes an electronic igniting device to ignite gasoline in the oil tray. The powder dust generated by extinguishing is stored in a dry powder collecting box via a sucking device, and a wind-directional adjusting device is applied to simulate the blowing of wind, thereby experiencing the extinguishing skills in different wind directions.

The present invention comprises a body and a separable gas cap. The body includes an oil tray, an igniting device, a dry powder exhausting device, and a dry powder collecting box. The separable gas cap includes a fixing frame, a telescoping sleeve, a sensor, and an adjustable telescoping stem. Herein, the structure and components of the present invention is described by the perspective view and the operation view in different angles. Figure 143.3 is the inner structure of the body, including the oil tray, the exhausting device, and the wind-directional adjusting device. Figure 143.4 is the outer structure of the body, including the oil tray replacing door and the ring-shaped latch. When there is a large amount of dry powder accumulated in the oil tray, people should open the oil tray replacing door for a standby. Figure 143.5 shows the fixing frame of the separable gas cap needs to align with the body, whereby the ring-shaped latch can be fastened and fixed. The sensor inside the fixing frame of the gas cap must be aware in the operation, and the emitter and the receiver should be adjusted to a testing status. Figure 143.6 is an operation situation of the dry-powdered fire extinguisher training device.

143.3.2 Installation and Operation of the Product

The main components of the present invention comprise a body, an oil tray, a dry powder collecting box, an electronic igniting device, a fixing frame, a telescoping sleeve, handcarts, and a sensor. The function, the correct installation, and the detachment of every component should be aware in the operation to obtain the

Fig. 143.1 Pollution (1) of dry-powder

Fig. 143.2 Pollution (2) of dry-powder

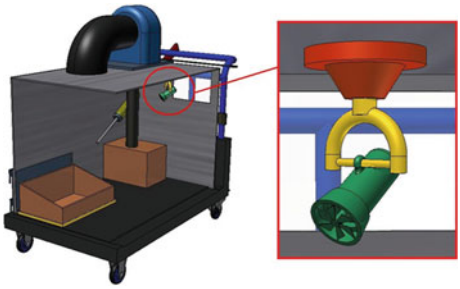

Fig. 143.3 The interior structure of the body

functions of the present invention successfully. Herein, the installation and operation of the extinguishing training device is described.

(1) Fix the body of the extinguisher training device: The operator seeks for a training place with 4.5 m in length and 1.5 m in width, pushes the device from a storing place toward the training place, fixes the body, and pours adequate water and oil into the oil tray.

Fig. 143.4 The exterior structure of the body

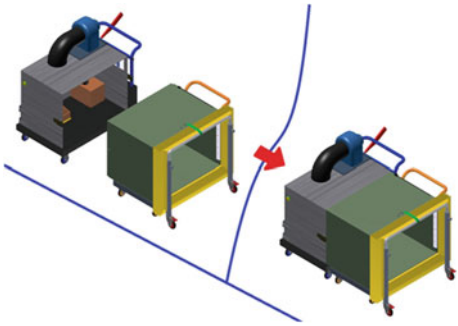

Fig. 143.5 The combination of this invention

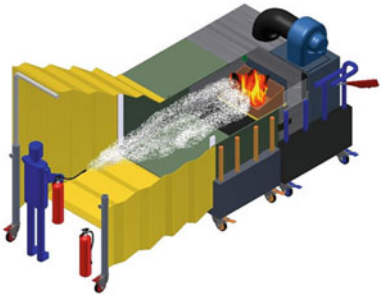

Fig. 143.6 The operation of this invention

(2) Extend and fix the telescoping sleeve of the separable gas cap: Extend the telescoping sleeve to the place appropriate 2.5 m in length, raise the adjustable telescoping stem on the telescoping sleeve up to 2 m, and fix it by the screw.
(3) The operator ignites and extinguishes the fire: Use the electronic igniting device to ignite the gasoline in the oil tray. The operator carries the dry-powdered extinguisher to shoot the dry powder at the oil tray and extinguish the fire. When the dry powder passes the sensor of the fixing frame of the

separable gas cap, the dry powder exhausting device is actuated to suck the dry powder into the powder collecting box.

(4) Descend and push the telescoping sleeve of the separable gas cap toward the fixing frame for tidying: After the extinguishing training, the telescoping sleeve of the separable gas cap is descended and pushed toward the fixing frame for a collection.

143.4 Conclusion

The innovation of the present invention utilizes the contradiction matrix of TRIZ to analyze the product function, develops a model product according to the inventive principles which are found out, and uses an inventor software to convert the possible inventive principles into a solid structure. In the operation of the present invention, the body and the separable gas cap are connected, and the telescoping sleeve is extended and fixed, thereby forming a half-closed extinguishing space with 4.5 m in length, 1.5 m in width, and 2 m in height. The present invention occupies a small space, which is very suitable for the urbanization. The extinguishing trainees use the electronic igniting device to burn the gasoline in the oil tray and shoot the dry powder at the oil tray for extinguishing. The entire operation only takes about 30 s to complete a cycle and meets a convenient and practical function. The use of the wind-directional adjusting device can simulate the blowing of wind, which attains an experience of feeling the high temperature in fire scenes and learning extinguishing skills in different wind directions. Furthermore, the dry powder can be recycled and reused, so the present invention is an extinguishing training equipment meeting the green need. Specifically, the present invention includes features of preventing the dry-powdered contamination, recycling and reusing the dry powder, saving the space, and attaining the safety and efficiency.

References

1. Wikipedia: Sodium Bicarbonate. (2011). http://zh.wikipedia.org/wiki/%E7%A2%B3%E9%85%B8%E6%B0%AB%E9%88%89.
2. Zhang, G., Lee, A. H., Lee, H. C., & Clinton, M. (2006). Fire safety among the elderly in Western Australia. *Fire Safety Journal, 41*(1), 57–61.
3. Liu, T. L., & She, T. C. (2009). Application of systematized innovation process-take office chairs as an example. *Vanung Commercial Journal, 14*, 259–276.
4. Kuo, T. Y., & Lin, C. C. (2010). Application of TRIZ in an innovation design of small fishing nets. *Industrial Design, 38*(1), 92–95.
5. Teng, C. J., & Yeh, G. C. (2011). Application of TRIZ in analyzing wrapping devices. *Science and Engineering Technique, 7*(3), 35–51.

6. Sung, M. H. (2009). *Systematized innovation theory and application of TRIZ*. Taipei: Tin-Miao Book Publishing Company.
7. Zhou, Y. C. (2010). Contradiction theory and application of TRIZ. *Science and Management, 3*, 15–18.
8. Althshuller, G. (1998). *TRIZ keys to technical innovation*. Technical Innovation Center, pp. 15–21.
9. Bukhman, I. (2012). *TRIZ Technology for Innovation*. Watertown: TRIZ Solutions LLC.

Chapter 144
Harmonic Reduction Solution by Applying On-Line Trained Adaptive Neural Controller for Shunt Active Filter

Nguyen Thi-Hoai Nam, Chun-Tang Chao, Chi-Jo Wang and Cheng-Ting Hsu

Abstract This paper proposes an intelligent control method for shunt active power filter to compensate the harmonic distortion in three phase power systems. For electric power systems, harmonics contamination generated by the nonlinear nature of the load is a serious and harmful problem. Shunt active filter (AF) has been employed to mitigate line current harmonics. In the presented system, Fuzzy Logic Controller (FLC) is first designed to implement the AF. Then the initial training data with two inputs, the error and derivate of the error, and one output signal from FLC can be obtained. Finally, a Neural Network (NN) with on-line training features is designed by using S-function in Simulink to achieve better performance. Simulation results show the effectiveness of the proposed active power filter system which improves the power quality, reduces the current harmonics and obtains better transient and steady-state responses.

Keywords Active filter · Harmonics reduction · Neural network · On-line training

144.1 Introduction

In recent years, with the rapid economic development, all kinds of nonlinear loads based on power electronic devices (diode and thyristor rectifiers, electronic starters and arc furnaces, etc.) have been used in power systems and induced the appearance of dangerous phenomenon of harmonic currents flow in the electrical feeder networks, producing distortions in the current and voltage waveforms.

N. T.-H. Nam · C.-T. Chao (✉) · C.-J. Wang · C.-T. Hsu
Department of Electrical Engineering, Southern Taiwan University of Science and Technology, Tainan, Taiwan, Republic of China
e-mail: tang@mail.stust.edu.tw

J. Juang et al. (eds.), *Proceedings of the 2nd International Conference on Intelligent Technologies and Engineering Systems (ICITES2013)*, Lecture Notes in Electrical Engineering 293,
DOI: 10.1007/978-3-319-04573-3_144,

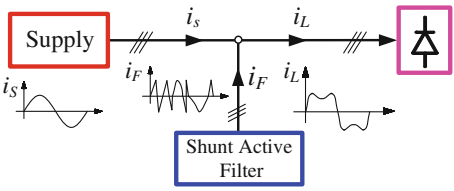

Fig. 144.1 Power system with nonlinear load and shunt AF

As a result, harmful consequences occur: equipment overheating, malfunction of solid state material, interferences with telecommunication systems, etc. The quality of powersupply is seriously reduced, so power quality distortion has become a serious problem in electrical power systems due to the increase of nonlinear loads drawing non-sinusoidal currents. Nowadays, Shunt active filter (AF) have been widely used for harmonic mitigation as well as reactive power compensation, load balancing, voltage regulation, and voltage flicker compensation [1, 2]. Neural Network (NN) based control methodologies have emerged in recent years as effective means of solving nonlinear control problems [3–5]. The proposed design is based on the control model that uses on-line trained adaptive NN controller to control the AF for reducing the harmonics of the electrical power systems. It does not exceed the thresholds fixed by the IEEE 519 standards [6]. Research results have been simulated and verified in the Matlab/Simulink software environment.

144.2 Mathematical Model of Shunt Active Filter

AF is a power electronics device based on the use of power electronics inverters. The Shunt Active Power Filter is connected in a common point connection between the source of power system and the load system. The AF will prevent the source of the polluting currents circulating in the power system lines, as shown in Fig. 144.1 [7].

Suppose that i_L, i_F, i_S are receiver absorbed current, desired power supply current and the current AF must provide, respectively. Then we have the relationship among them in formula given by:

$$i_F = i_L - i_S \tag{144.1}$$

If we let

$$i_L = i_f + i_H \tag{144.2}$$

where i_f is the fundamental component of load current, also the desired power supply current i_S, and i_H is the harmonic current generated in load branch. From Eqs. (144.1) and (144.2), we obtain Eq. (144.3)

$$i_F = i_H \tag{144.3}$$

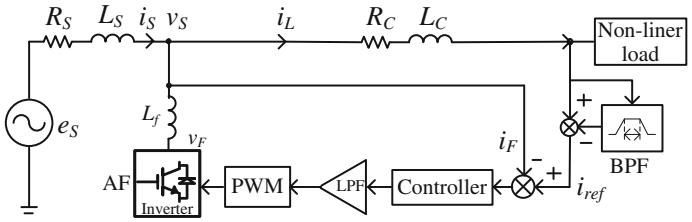

Fig. 144.2 The active filter control structure

Eq. (144.3) indicates that shunt active power filter is intended to generate exactly the same harmonics contained in the polluting current i_L but with opposite phase.

144.3 Control System Design

144.3.1 Control Structure of Active Filter

To control AF to produce current tracking with the load current harmonic, the control structure as shown in Fig. 144.2 is used [7, 8], where BPF is a band pass filter, LPF is a low pass filter, and PWM is pulse width modulation. In this paper, we apply the method of notch filter which consists of two identical band-pass filters in series. The fundamental frequency is set to 50 Hz. The transfer functions of the BPF and LPF are given by Eq. (144.4).

$$H_{BPF}(s) = \frac{K_{BPF}.B.S}{s^2 + B.s + \omega_c^2}; H_{LPF}(s) = \frac{K_{LPF}}{\tau s + 1} \tag{144.4}$$

144.3.2 On-Line Trained Adaptive Neural Controller Design

In the paper, the proposed on-line trained adaptive neural controller is designed to control the AF for harmonic mitigation as well as reactive power compensation for three phase power system, as shown in Fig. 144.3, where i_{ref} is the harmonic current generated in power system and it is also the reference signal for the controller to track. The output current of the AF (i_F) is expected to have the same harmonic current value contained in the polluting current but with opposite phase. Both signals are compared to generate error (e) as the input of on-line trained adaptive neural controller. The output of on-line trained adaptive neural controller u_N, which passes through LPF, is compared with carrier signal (v_s), and the

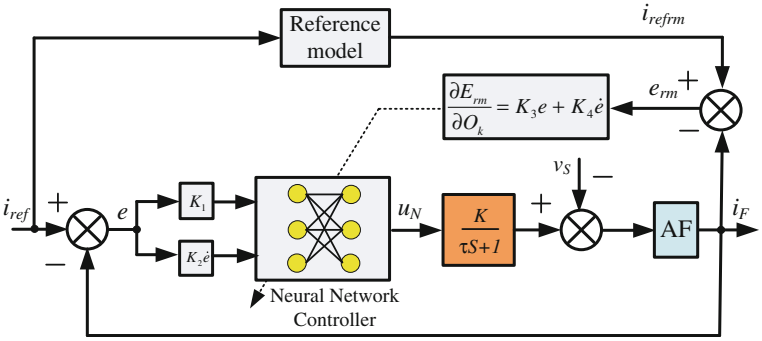

Fig. 144.3 On-line trained adaptive NN controller diagram

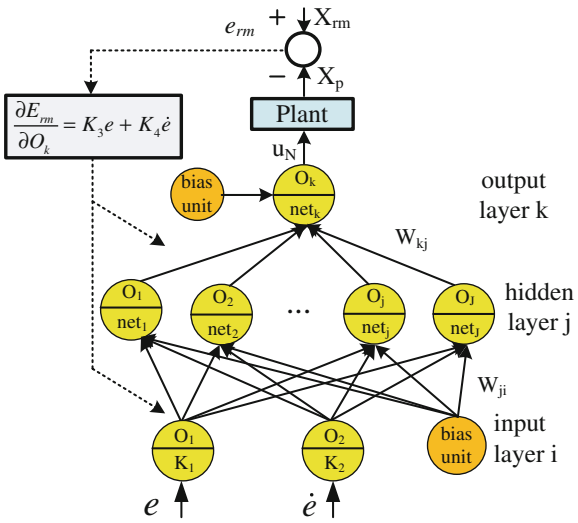

Fig. 144.4 Schematic diagram of the proposed NN controller

resulting signal is used to switch 6 IGBTs of AF filter. The three-layer NN structure shown in Fig. 144.4 is adopted to implement the proposed NN controller.

The net input to a node j in the hidden layer is calculated according to the following equation.

$$net_j = \sum \left(W_{ji} \cdot O_i\right) + \theta_j \tag{144.5}$$

The output of node j is

$$O_j = f\left(net_j\right) = \tanh\left(\beta \cdot net_j\right) \tag{144.6}$$

where O_j represents the output of units in the hidden layers, net_j is the summed input to the units in the hidden layers, W_{ji} are the connective weight between input

layers and hidden layers, $\beta > 0$ is a constant, and f denotes the activation function, which is a hyperbolic tangent activation function

$$f(net_j) = \frac{2}{1 + e^{-\beta \cdot net_j}} - 1; \quad (-1 < f(net_j) < 1) \tag{144.7}$$

The net input to a node k in the output layer is

$$net_k = \sum (W_{kj} \cdot O_j) + \theta_k \quad j = 1, 2, \ldots J, \quad k = 1, 2, \ldots K \tag{144.8}$$

The corresponding output of neural network is

$$O_k = f(net_k) = \tanh(\beta \cdot net_k) \tag{144.9}$$

The energy function E is defined as

$$E_N = \frac{1}{2}(X_{rmN} - X_{pN})^2 = \frac{1}{2} e_N^2 \tag{144.10}$$

where X_{rmN} and X_{pN} represents the outputs of the reference model and the plant at the Nth iteration. The back-propagation algorithm is used to update the weights in the NN [9].

It should be claimed that before implementing the on-line trained adaptive NN in Fig. 144.3, a PD-like Fuzzy Logic Controller (FLC) has been designed to control the AF. The performance comparison can be found in the following section.

144.4 Simulation Results

Simulation results with methodologies of on-line trained adaptive NN controller is implemented by Matlab/Simulink, as shown in Fig. 144.5, for electrical power system with AF. Table 144.1 summarizes the simulation parameters. The training result of desired output and practical output is shown in Fig. 144.6 indicating that the practical output almost tracks the desired output with the error converging to 0 (Figs. 144.7).

The system simulation results applying on-line trained adaptive NN controller are shown in Figs. 144.8–144.10. The THD value drops to 1.03 %.

Figure 144.11 shows how AF current tracks the reference signal i_{ref} with on-line learning NN controller. In the first 0.01 s, the output of controller has not tracked its reference signal successfully, but after 0.01 s these two signals almost coincide. Once again, it indicates the active operation of AF that helps to eliminate the harmonics in power system. Moreover, consider that the motor runs in different conditions: heavy load, medium load, and light load, the respective fundamental currents are 700, 470, and 280 A. Table 144.2 reports the THD values in each case.

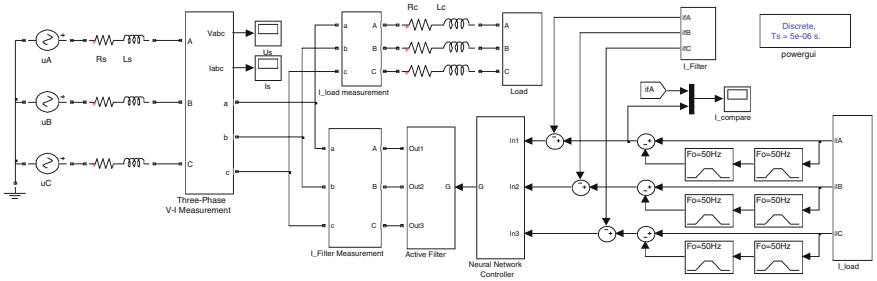

Fig. 144.5 The simulation model of electrical power system with AF

Table 144.1 Simulation parameters of electrical power system

Parameter	Value
Supply's voltage $e_s$and frequency f_s	220 V, 50 Hz
Line's inductance $L_s$and resistance R_s	0.03 mH, 0.1 Ω
Impedance upstream of the rectifier $L_c$andR_c	0.07 mH, 0.3 Ω
Inductance L_{DC}, capacitor C_{DC}, resistance R_{DC}	0.3 mH, 470 μF, 0.45 Ω
Active filter input DC supply: capacitor C, E,r	3.46×10^{-3} F, 600 V, $5x10^{-4}$ Ω
Active filter output impedance L_f	1.2 mH
if_{iref}'s calculating, band-pass filter: damping factor ξ	0.707
LPF corrector: gain K, time constant τ	1, 5 e^{-6} s
Carrier signal's peak amplitude & frequency	10, 10 kHz

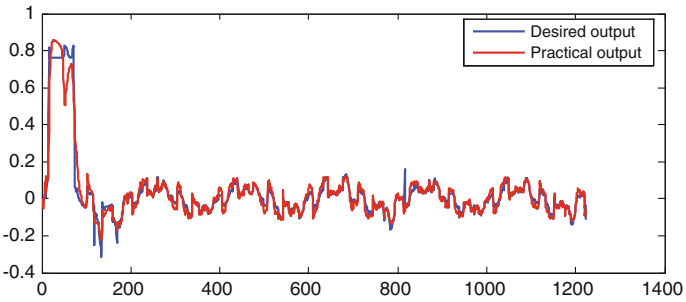

Fig. 144.6 Desired output and practical output

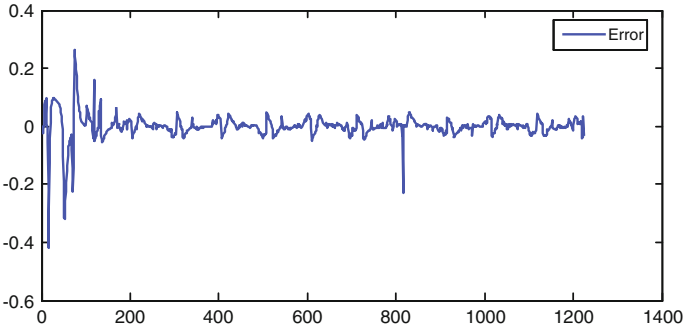

Fig. 144.7 Error after training

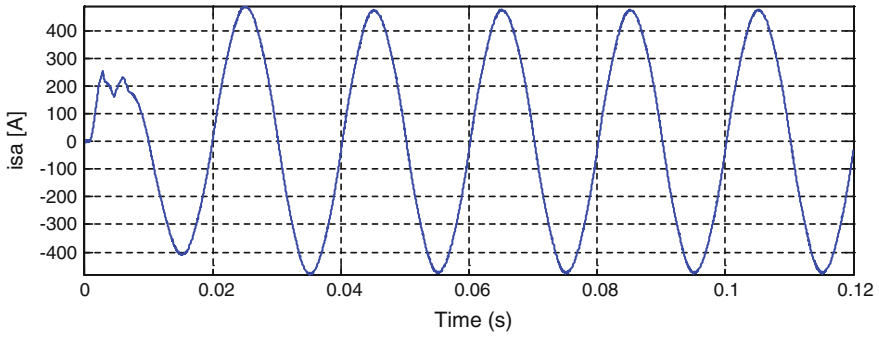

Fig. 144.8 Supply current i_{sa} with NN

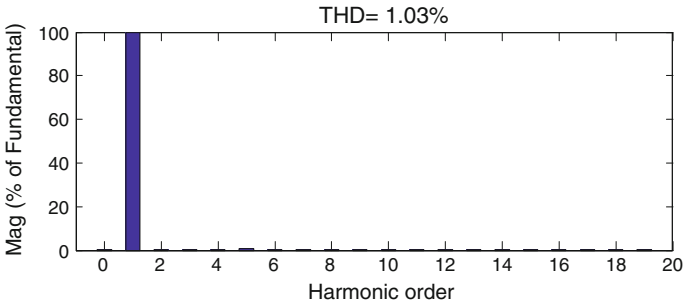

Fig. 144.9 Harmonic spectrum of i_{sa} with NN

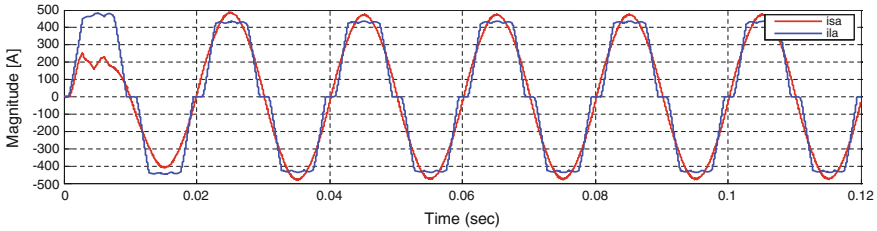

Fig. 144.10 Currents i_{sa} and i_{la} applying AF with on-line trained adaptive NN controller

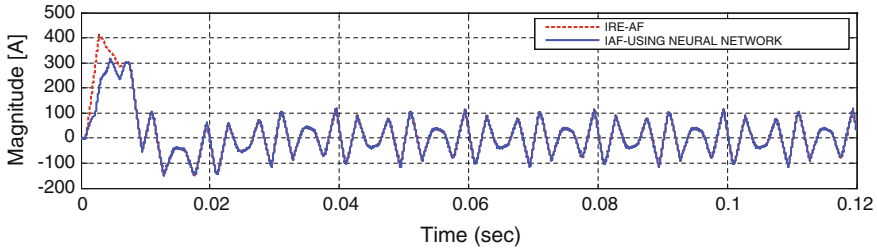

Fig. 144.11 AF current and its reference with on-line trained adaptive NN controller

Table 144.2 Total harmonic distortion (THD) (%) in different running conditions of load

Controller	Load		
	Heavy load: $R_{dc} = 0.07$	Medium load: $R_{dc} = 0.45$	Light load: $R_{dc} = 1.2$
Without active filter	THD = 3.46	THD = 12.54	THD = 20.33
With AF using FLC	THD = 0.49	THD = 1.04	THD = 3.23
With AF using NN controller	THD = 0.45	THD = 1.03	THD = 2.44

144.5 Conclusion

In this paper, the NN controller for AF is developed to reduce the harmonic current for nonlinear loads in electric power systems. It shows that with AF and on-line trained adaptive NN controller design, the system achieves abetter response under different running conditions of load. The simulations results also show that Shunt AF achieves good dynamic and steady-state responses. Furthermore, the THD value doesn't exceed 5 %, conforming to the IEEE 519 standards.

References

1. Elmitwally, A., Abdelkader, S., & Elkateb, M. (2000). Performance evaluation of fuzzy controlled three and four wire shunt active power conditioners. *IEEE Power Engineering Society Winter Meeting*, *3*, 1650–1655.
2. Yongjing, W., & Min, Z. (2005). Parallel type harmonic suppressor with an active filter and a lc filter connected in series. *Marine Electric and Electronic Technology*, *4*, 14–16.
3. Padma, S., Rajaram, M., Lakshmipathi, R., & Madhubalan, S. (2011). Neural network controller for static synchronous series compensator (SSSC) in transient stability analysis. In *Power Electronics (IICPE)* (pp. 1–6).
4. Nitin, G., Singh, S. P., & Dubey, S. P. (2010). Neural network based shunt active filter for harmonic and reactive power compensation under non-ideal mains voltage. In *IEEE (ICIEA)* (pp. 370–375).
5. Chen, S. C., Jyh, L. Y., Sum, N. V., & Mao, S. M. (2013). A Novel Fuzzy Neural Network Controller for Maglev System with Controlled-PM Electromagnets. *Intelligent Technologies and Engineering Systems, 234*, 551–561.
6. Khalid, S., & Dwivedi, B. (2011). Power quality issues, problems, standards and their effects in industry with corrective means. *International Journal of Advances in Engineering and Technology, 1*, 1–11.
7. Hocine, B., & Hind, D. (2005). Shunt active filter controlled by fuzzy logic. *Engineering Sciences, 2005*(18), 231–247.
8. Karuppanan, P., & Mahapatra, K. K. (2012). PI and fuzzy logic controllers for shunt active power filter-a report. *ISA Transactions, 51*, 667–671.
9. Michael, N. (2005). *Artificial intelligence: A guide to intelligent systems* (2nd ed.). England: Pearson Education.

Chapter 145
Terminate Fiber Optic Connector Using the Hand Polishing Method

Michael Phi Nguyen and Jeng-Nan Juang

Abstract Hand polishing technique is one of many different methods to terminate fiber optic connectors. Although there are now machines or fast fit connectors used to terminate connectors, hand polishing method with the use of a hot melt is known for its reliability as it involves a personal touch, time and patients. This journal outlines the process to make ready a fiber optic cable and to terminate a FC connector. This process can be used to terminate any other connectors as the procedure is the same; however, the components may differ from one connector to another. The procedure is well written to refresh those individuals that have experience with termination within the in-door and out-door plant. In addition, the process is written to introduce those individuals new to fiber optics with a short introduction to fiber optics and terminologies used in the industry.

Keywords Fiber optics · Connector · Cladding · Core · Termination · Hot melt

145.1 Introduction

Fiber Optic cables come in many different shape, size, length, and connector types. Most fiber optic patch cord is uniquely built for its application. The reasons for its variability are quite similar to the vast purpose of conductors that ranges from small to large diameter. For example, 22 AWG copper duplex wires are popularly used for home theater purposes. Meanwhile, large diameter $4/\phi$ aluminum triplex conductors are used for distributing power to residential homes. Comparably, fiber optic patch cords are simply a transmission medium with the end goal of transmitting light e from one end of a connector to the other. This is just like any metal

M. P. Nguyen (✉) · J.-N. Juang
Department of Electrical and Computer Engineering, Mercer University,
Macon, GA 31207, USA
e-mail: mpn21msstate@gmail.com

J. Juang et al. (eds.), *Proceedings of the 2nd International Conference on Intelligent Technologies and Engineering Systems (ICITES2013)*, Lecture Notes in Electrical Engineering 293,
DOI: 10.1007/978-3-319-04573-3_145,

conducting medium transmitting electrons. Although both materials share the same purpose, the science and method to terminate the two cables are completely different. It is very easy for any individual that are newly exposed to fiber optics to cross reference terminology, topologies and even associate analogies that are communicated in the metal conducting environment. Therefore, this journal refers to common metal conducting terminologies because of its common knowledge within the Electrical Engineering community.

145.2 Industry Standards

It is very common to be exposed to abbreviated names, short hand symbols and unusual designator within the fiber optic work environment. This is similar to how an oscilloscope has evolved to the term O-scope; $1/\phi$ notation is referred to as 1-AWG within the power distribution industry; Hot-Leg is referred to as the positive black conductor within a residential configuration; and 1:4 is referred to as one to four SWR (standing wave ratio) within the RF community. It is very important to understand and communicate to other fiber optic experts with the same common terminology as most companies and vendors communicate in the same fashion.

For example fiber optic modes are designated by its wavelength. Wavelength such as 1310 (thirteen-ten) and 1550 (fifteen-fifty) are widely used to describe a single mode system. Likewise, 850 (eight-fifty) and 1300 (thirteen/thirteen hundred) are referred to as systems that are multimode. Although these wavelengths are measured in nanometer, the units are usually dropped and are not mentioned because of its commonality within the industry. Similarly, there are different type of connectors such as LC, FC, ST, and SC. Each type of connector is specified by its geometric end shape, type of polish, and its associated core and cladding size. For example a FC connector can be ordered from the manufacture in the following core and cladding sizes: SM-9/125, and MM-50/150, MM-62.5/125, MM-50/125. Although the size of the core and cladding are in μm (micron), these dimensions are understood in the industry; therefore, its units are again not usually spoken or mentioned. Moreover, FC (Frank Charley) connectors can also be purchased in many different types of polishing such as PC (Physical Contact), and UPC (Ultra Polish Contact). Likewise, FC are sold with different end faces such as APC (Angled physical contact), Pre-Radius and Flat.

145.3 The Components

Even though it is important to understand certain specifications necessary to make a purchase of a connector from vendors, it is equally important to identify each component associated with a cable and connector. As shown below in Fig. 145.1, a typical fiber optic cable consists of a core, cladding, coating, buffer, and jacket.

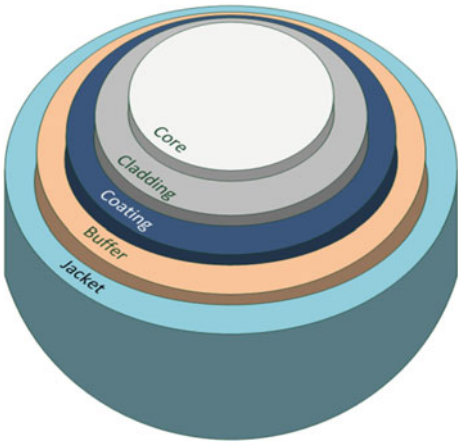

Fig. 145.1 Fiber optic components

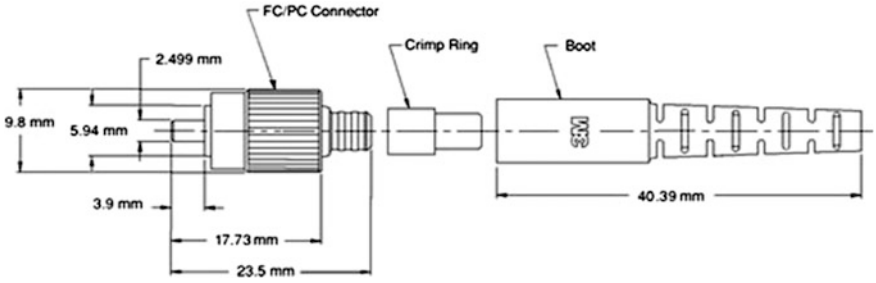

Fig. 145.2 3 M FC/PC multi mode connector [2]

Although a strength member such as Kevlar fibers or metal cores are not shown in the figure, it is usually sandwich between the buffer and jacket. In addition, FC connector consists of a Body Assembly (FC/PC Connector), crimp ring, and boot. Figure 145.2 displays a multimode FC connector, which identifies each component. Moreover, the dimension for a connector is extremely important with terminating connectors. As shown below in Fig. 145.3, the connector is completely assembled with the Body Assembly being approximately 13 mm long while the entire length of the connector is approximately 50 mm. Furthermore, it is important to note that boot can be purchase in a short or long configuration. Beside the length of the boot it is important to take note of the diameter of the boot as it will determine the jacket size fitting of the cable.

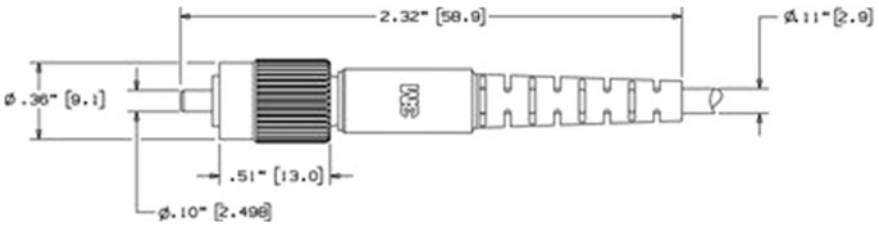

Fig. 145.3 3 M FC/PC single mode connector [2]

Table 145.1 Necessary materials required

Material description	Vendor/Item number
Fiber optic connector FC/PC	3 M/8203
Fiber optic cable 2.0 mm SM	FIS/S09-SX01-CNPY20
Cable strippers miller	FIS/W0-1224D
Adhesive epoxy—EPO-TEK	FIS/353ND
Plastic stick	West system/WSY-804-60
Syringe 0.9 mm needle	FIS/501473-3IRC100
Carbide scribe	FIS/F19773
Heat over curing stand	FIS/9451S
Work mat	FIS/F1-0024
Polishing glass plate	FIS/F1-9111A
Rubber polishing pad 70 shore hardness	FIS/PP-575
Microscope 200x	FIS/F1-VS200F2.5
Microscope 400x	FIS/F1-VS400F2.5
Microscope with 1.25 adapter (F1-MA1.25)	FIS/F1-MA1.25
Polishing pucks 1.25 mm	FIS/F16925FC
Mixing plastic cup (1 oz)	Science lab
Permanent marker	Minor material
Deionized water	Science lab/NC-3064
Polishing films (30, 6, 3, 1, 0.5) and final polishing film	FIS/3 M assortment of polishing films
Kevlar shears	FIS/F1-KS1
Isopropyl alcohol	FIS/F1-000728
Crimp tool	FIS/31227
Low lint tissues	FIS/34-155

145.4 Building Materials

The materials used throughout this procedure can be purchase from any vendor; however, the majority of the materials used to develop this procedure are purchased from FIS, Fiber Instrument Sales, INC. Table 145.1 given below has a description of all materials used in this procedure along with its associated item number from FIS and other vendors [2].

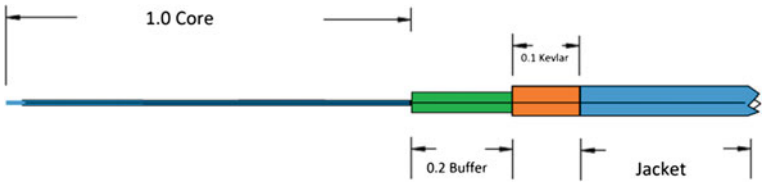

Fig. 145.4 Cable preparation

145.5 Make Ready Fiber Optic Cable

It is good practice and important to maintain a safety mind set while keeping an organized and clean work station. Wear eye protection and remind cautious as shrapnel of fiber optics glass are easily camouflage to any surface and could easily cause splinters and permanent damage to skin or eye. Be sure to set aside all materials including a strip of masking tape to collect all the debris. Start by using a permanent marker; mark the jacket of the pigtail 1.3″ from the end. Starting at the mark, strip and remove the 2.0 mm jacket using the Cable Strippers. Once the jacket is stripped the buffer along with the Kevlar should be exposed. Again using a permanent marker, measure and make a mark on the Kevlar 0.1″ from the stripped jacket. In the same way, measure and make a mark on the Buffer 0.2″ from the stripped jacket using a permanent marker. Afterward, trim the Kevlar on the mark using Kevlar Shears. Starting at the mark, strip and remove the buffer/coating using the Cable Strippers. Shortly, apply Alcohol on the tissue then remove any excessive coating off the Fiber. Inspect the fiber, buffer, Kevlar, and jacket. Clean the entire incision once more with a new Alcohol wet tissue. The incision made on the fiber optic cable should be similar to Fig. 145.4.

145.6 Install Cable into Body Assembly

Set aside the fiber cable then add the two part epoxy into a mixing cup according to the instructions per the adhesive instruction. After the epoxy is added into the cup, mix the two parts using a mixing stick. Afterward, set aside the mixed epoxy then attach the springe needle into its adaptor. Then pull the plunger top from the syringe, and add the mixed epoxy into the barrel of the syringe using the mixing stick. Then attach the plunger top into the barrel of the syringe and continue to add pressure until a bead of epoxy is visible to the end of the needle. Immediately, apply alcohol on the tissue then wipe and clean the bead off at the end of the needle. Set aside the syringe, then insert the boot with the larger diameter facing the incision then move the boot away from the incision. Likewise, insert the crimp ring with the larger diameter facing the incision then move the crimp ring near the boot. Set aside the fiber optic pigtail as the epoxy is ready to be filled in the body

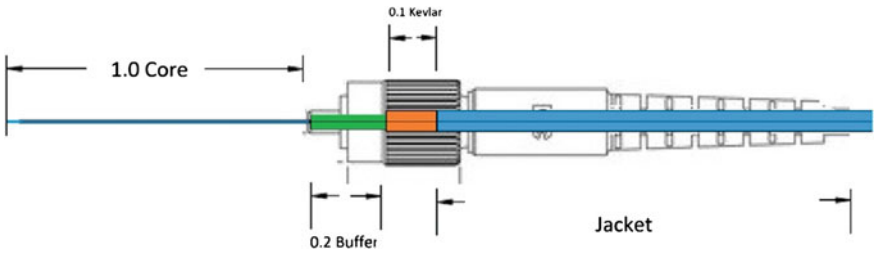

Fig. 145.5 Fiber inserted in body assembly

of the connector. While holding the fiber optic connector body, fill one drop of epoxy into the rear of the body assembly cavity until a bead of epoxy appears on top of the ferrule. Immediately, wet the fiber optic pigtail incision with the epoxy starting from the mark on the jacket until the end of the pigtail. Be sure to wet the fiber, buffer Kevlar and jacket with a thin coat of epoxy. Afterward, insert the wet fiber into the rear body assembly until it bottoms out inside the cavity of the fiber optic body. Immediately inspect the rear of the body to ensure that there is no excessive epoxy spilling out from the body. Then clean the excessive epoxy using a wet alcohol tissue only if there is excessive epoxy. Also, if the rear of the body assembly looks dry add a small bead of epoxy on the terminus tip and at the body assembly. It is important to note that excessive epoxy at the rear of the body assembly will cause stiffness at the rear termination.

The epoxy must go through its curing process to successfully seal the fiber to its connector. Begin this process by curing the connector in the heat oven according to the adhesive instruction. It is important to make sure that the cable is in a straight position with very minimum slack on the end. After the epoxy is completely cured, use a scribe to gently scribe the fiber at the adhesive bead. Afterward, grip the fiber optic connector using an index finger and thumb with the glass pointing upward. With the other hand, grasp the fiber that is pre-scribe with thumb and index finger. Pull the pre-scribe fiber directly upward to remove the excessive fiber away from the ferrule. Shortly after, pull the crimp toward the body assembly then crimp the ring using the FC slot on the crimp tool. Finally slide the boot upward to cover the crimp. The fiber cable should resemble the Fig. 145.5 with a detached core.

145.7 Polish Fiber Optical End Face

It is important to keep in mind that the ferrule and core is extremely fragile; therefore, using deionized or drinking water as lubricant throughout each polishing set is recommended. Likewise, it is good practice to apply minimum downward pressure while polishing to avoid the potential of cracking the optical fiber ferrule. Be sure to clean the end face with precision wipes and isopropyl alcohol after each polishing set. Start by air polishing the fiber using a 30 μm grit polishing film.

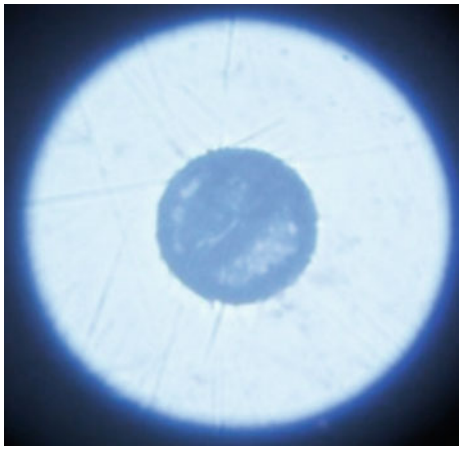

Fig. 145.6 200x cloudy ferrule

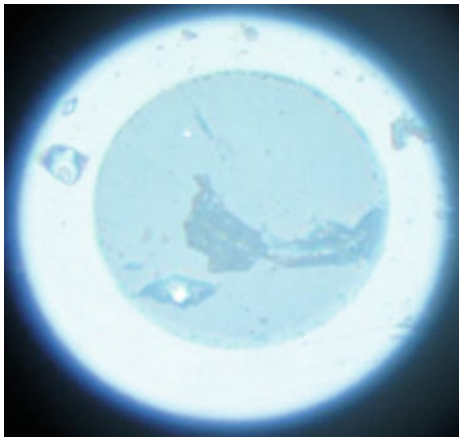

Fig. 145.7 200x scratched surface

Afterwards, setup the polishing station by placing the work mat on the polishing station, then placing the glass polishing plate on the work mat. Afterwards, place the rubber pad on top of the glass polishing plate. Be sure to set aside the polishing films, microscopes, and polishing pucks. Add 3 oz of water on the top of the rubber pad then place the 6 μm grit polishing film on the rubber pad. The water will act as an adhesive to hold the polishing film in place while polishing. Afterwards, add 3 oz of deionized water on top of the 6 μm grit polishing film. Then place the polishing puck on top of the wet polishing film. Next, insert the fiber optic body inside the center hole of the polishing puck. The connector is now ready for polishing, be sure to grip the fiber optic pin and center stem of the polishing puck with an index finger and thumb. Wet polish the terminus tip in Fig. 145.8 motions with very minimum downward pressure until the entire

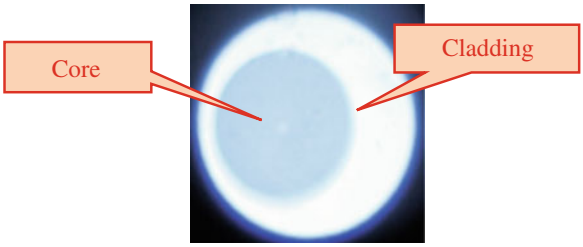

Fig. 145.8 400x final polished

adhesive bead is removed. Be very cautious as applying too much downward pressure while wet polishing can cause the ferrule to crack. Repeat each wet polishing successive step with a finer diamond film grade starting with 3.0–1.0 then 0.5 μm film. Finalize this procedure by dry polishing with a final polishing film. Then verify the polishing quality with a fiber optic microscope. No scratches or chips should be visible within the optical fiber core. Figure 145.6 shown below may resemble the earlier stage of polishing. More polishing is needed as the cladding is very dark and cloudy. Figure 145.7 shown below may resemble a ferrule that has been polished or scribed incorrectly. If this occurs, repeat the process and continue to polish with more dense film to remove the scratches. Figure 145.8 shown below resembles a well-polished ferrule. The cladding along with core is well lite and defined.

145.8 Conclusion

After the ferrule is well polished, repeat the same process to terminate the other pig tail end of the patch cord. Once the patch cord is terminated at both ends, be sure to test the cable by plugging the connectors into a network switch. Verify that the network has well to great signal rates normal to the vendor's specifications. Signal loss can be improved by removing the connector from the switch and re-polishing the connector. Likewise, fiber optic cables can be tested for insertion and return loss. This can be tested using a light source along with a power meter.

On the whole, terminating fiber optic connectors may seem over whelming and many mistakes will occur in the beginning. However, this hand polishing method will eventually become better each time. The hand polishing method with the use of a hot melt is very popular in the fiber optic industry. There are many companies that offer courses to train individuals on this method. The courses offered are recommended; however, this type of training is extremely expensive.

Acknowledgments The author would like to thank Rusty Blair and Floyd Harrison for the opportunity to receive training in fiber optics. In addition, the author would like to thank Derrek Anderson and Bruce DeLorme for becoming involve in the process and reviewing this journal.

References

1. Palais, J. C. (2005). *Fiber optic communications*. Upper Saddle River: Pearson Education Inc.
2. 3 M FC/APC Connector. http://solutions.3m.com/wps/portal/3M/en_US/NA_Communication_Technologies/Home/Products/?N=7569749+4294853052&rt=rud
3. FIS, Fiber Instrument Sales, INC. http://www.fiberinstrumentsales.com/
4. Mixing Sticks. http://www.jamestowndistributors.com/userportal/show_product.do?pid=2433
5. Deionized Water. http://www.sciencecompany.com/deionized-water-1-gal-p16280c670.aspx
6. BTS. http://www.btstraining.com/
7. FOA, FiberOpticAssoication Saftey. http://www.thefoa.org/tech/safety.htm
8. Mixing Cup. http://www.myamericanmedical.com/products/non-sterile-graduated-plastic-medicine-cups.html?gclid=CJL6x4Kto7oCFUPl7AodbywADg

Chapter 146
Operating Energy Harvesting Array at Higher Vibration Modes

Yuejuan Li, Marvin H. Cheng and Cheng-Yi Chen

Abstract Harvesting energy from vibration sources in different environments has become important as the price of energy keeps on increasing. To collect power generated by vibration source more efficiently, this paper introduces an operating scheme that maximize the amount of collectable in higher modes of the energy harvesting devices. Furthermore, energy harvesting array proposed to collect power from various frequency bands makes the harvesting technique more feasible for regular electronic devices.

Keywords Energy harvesting · Piezoelectric cantilever · Vibration modes

146.1 Introduction

Due to the arising price of energy since the past decade, many researchers have started to investigate various sustainable sources that can continuously generate power. Among the new sustainable energy sources, solar and wind energy have been widely adopted in industrial applications and daily residential area. However, these two major renewable energy sources are greatly limited by climate conditions. In particular, they cannot be used in specific areas, such mineral tunnels and underground environment, where typically energy sources are not available. To compensate the drawback, energy harvesters using piezoelectric component can be an excellent alternative in such kind of environments. With its high power density

Y. Li · M. H. Cheng (✉)
Department of Mechanical and Aerospace Engineering, West Virginia University, Morgantown, WV 26506, USA
e-mail: marvin.cheng@mail.wvu.edu

C.-Y. Chen
Department of Electrical Engineering, Cheng Shiu University, Kaohsiung 83347, Taiwan, Republic of China

J. Juang et al. (eds.), *Proceedings of the 2nd International Conference on Intelligent Technologies and Engineering Systems (ICITES2013)*, Lecture Notes in Electrical Engineering 293,
DOI: 10.1007/978-3-319-04573-3_146,

and insensitivity to climate conditions, energy harvesting devices have been studied intensively in the past decade.

To increase the amount of generated power, the operational status and optimized processing circuits of major types of piezoelectric material, including piezoceramic (PZT), polyvinylidene fluride (PVDF), and macro-fiber composite (MFC), have been well investigated for different environmental scenarios [1]. The major disadvantage of piezoelectric energy harvesting devices is that a single device can only generate tiny amount of power which can barely be used for general purposes. To maximize the amount of collectable power, the harvesters are usually operated at their resonant frequencies for greater vibration amplitudes. However, among all harvesting scenarios, most of the harvesting components are operated at their first modes. In the recent studies, Li et al. [2, 3] have demonstrated that the amount of collected power can be at least six times greater while operating them at their second modes. Thus, self-support circuits used for machine monitoring or low-power lighting can be possibly implemented if a constant vibration source can be identified.

This paper investigates the potential of operating energy harvesting devices at their higher mode. To maximize the amount of harvestable energy, a modulus approach of harvesting array that integrates multiple piezoelectric components was designed fabricated. An operating procedure of such an energy harvesting array is also discussed for the most efficient harvesting.

146.2 Model of Piezoelectric Cantilever Beam

To identify adequate vibration frequencies for piezoelectric devices, it is necessary to derive a model that can estimate the vibration modes and their corresponding frequencies. In the past, Bernoulli–Euler beam theory [4] was used to estimate the resonant frequencies of continuous cantilever beam. However, the discrete model derived by Li and Cheng [2] has provided a means to estimate the frequencies at different modes. Thus, the operating frequencies of cantilever beams can be tuned to fit the environmental vibration source for maximal harvestable power.

The frequency estimation based on the discrete model assumes that the cantilever is uniform and homogeneous beam. The total length of the cantilever is l and the total mass of the cantilever is m. The beam is separated into n segments with equal length. Each segment has its mass located at the center of individual segment. Figure 146.1 illustrates the configuration of a 4-segment cantilever beam. The 4-segment separation yields four concentrations of mass. The length of each segment is $l/4$ with a mass of $m/4$. These concentrations are located at station 1, 2, 3 and 4. Station 5 is a special station without mass concentration, which is the root of the cantilever beam. To model a discrete cantilever, the equation of motion can be written as

$$\mathbf{m}\ddot{\mathbf{x}} + \mathbf{k}\mathbf{x} = \{0\}, \tag{146.1}$$

where **m** is the mass matrix of the stations, **x** is the motion of the cantilever beam at different locations, and **k** is the stiffness matrix. Substitute the harmonic function displacement **x** with harmonic functions $\mathbf{x} = \mathbf{A}\sin(\omega t + \phi)$, and then multiply (146.1) with an inverse matrix $\mathbf{a} = \mathbf{k}^{-1}$, the equation can be represented as

$$-\omega^2 \cdot \mathbf{a} \cdot \mathbf{m} \cdot \mathbf{A} + \mathbf{I} \cdot \mathbf{A} = \{0\}. \tag{146.2}$$

Replace λ with $1/\omega^2$, the following equation can be obtained

$$(\mathbf{a} \cdot \mathbf{m} - \lambda \mathbf{I}) \cdot \mathbf{A} = \{0\}. \tag{146.3}$$

Thus, the characteristic determinant of $\mathbf{a}\cdot\mathbf{m} - \lambda\mathbf{I}$ becomes

$$\left| \begin{bmatrix} a_{11} & a_{12} & a_{13} & \cdots \\ a_{21} & a_{22} & \cdot & \cdots \\ a_{31} & \cdot & \cdot & \cdots \\ \cdot & \cdot & \cdot & \cdots \end{bmatrix} \begin{bmatrix} m_{11} & m_{12} & m_{13} & \cdots \\ m_{21} & m_{22} & \cdot & \cdots \\ m_{31} & \cdot & \cdot & \cdots \\ \cdot & \cdot & \cdot & \cdots \end{bmatrix} - \lambda \begin{bmatrix} 1 & 0 & 0 & \cdots \\ 0 & 1 & 0 & \cdots \\ 0 & 0 & 1 & \cdots \\ \cdot & \cdot & \cdot & \cdots \end{bmatrix} \right| = 0, \tag{146.4}$$

The resonant frequency of the nth mode can then be determined by the eigenvalue λ_n. The coefficients of flexibility matrix can be obtained by placing a unit load at each station with area moment method. Notice that the two length l_1 and l_2 are different, where l_1 is the distance between two neighboring stations and l_2 is the distance between the tip of the beam and the neighboring mass. To calculate the corresponding coefficients of a_{ij}, several assumptions are made. They are (1) the cantilever beam is uniform and evenly divided into n segments and the length of each segment is l/n; (2) the mass of each segment is located at its center; and (3) the distance l_1 between two adjacent mass centers is l/n and the distance l_2 between the tip of the cantilever beam and the mass centers at both ends is $l_1/2$. Larger n can provide better accuracy. With this setup, the coefficients of the flexibility matrix can be calculated by

$$a_{ij} = \begin{cases} \frac{1}{2EI}[(n-j)l_1 + l_2]^2 \times \left\{\frac{2}{3}[(n-j)l_1 + l_2] + (j-i)l_1\right\}, & \text{if } i \le j \\ \frac{1}{6EI}\left\{(i-j)l_1 \times [(n-i)l_1 + l_2]^2 + 2[(n-j)l_1 + l_2] \times [(n-i)l_1 + l_2]^2\right\}, & \text{if } i > j \end{cases}, \tag{146.5}$$

where E is the modulus of elasticity and I is the area moment of inertia about the neutral axis. With this setup, the coefficient a_{11} of the 4-segment cantilever beam, which represents the unit area moment between station 1 and its root (station 5) divided by EI, is

$$a_{11} = \frac{1}{2}(3l_1 + l_2)^2 \times \frac{2}{3}(3l_1 + l_2)\frac{1}{EI} = \frac{343}{1536}\frac{l^3}{EI}. \tag{146.6}$$

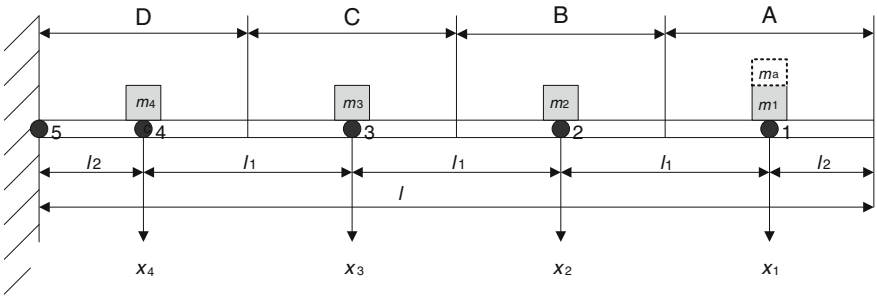

Fig. 146.1 Uniform cantilever with lumped mass and applied force

Thus, the resonant frequencies of each mode can be derived by deriving all the coefficients of a_{ij}. If a proof mass needs to be attached at specific locations to adjust frequency at different modes, the mass matrix can be modified accordingly to obtain the corresponding resonant frequencies.

146.3 Experimental Setup

To verify the frequency estimation of the proposed model, two unimorph PVDF piezoelectric devices were used to verify the calculated results. In the experimental setup, the power generated by piezoelectric cantilever beam is rectified by a full-bridge rectifier and then stored through a charging circuit to a solid-state battery. The properties of the two piezoelectric components are listed in Table 146.1. To verify the calculated results with actual responses of the cantilever beams, a swept waveform from 1 to 200 Hz with 800 mV_{pp} amplitude was generated from a signal generator within a 30 s period. The swept waveform was sent to the amplifier of the shaker and converted to mechanical outputs. The output voltage and current generated by the piezoelectric components were measured by a data acquisition device, PCI-6024E, manufactured by National Instrument. The collected data was then processed by MATLAB.

As to the harvesting array, a modulus approach is adopted to integrate multiple piezoelectric components. Each module includes eight piezoelectric components. Figure 146.2 illustrates a fabricated harvesting module. These components are connected in parallel to eliminate the power loss due to phase difference among individual components. The output voltage generated by individual modules is connected to a capacitor. As the voltage level of capacitor is raised to a preset threshold, a solid-state battery is then charged through the capacitor.

Table 146.1 Physical properties of adopted piezoelectric cantilever beam

	DT2-028 K
Length (mm)	72
Effective length (mm)	70
Width (mm)	16
Thickness (μm)	230
Density (kg/m^3)	1450
Mass (g)	0.39
Equivalent elasticity (GPa)	4.2

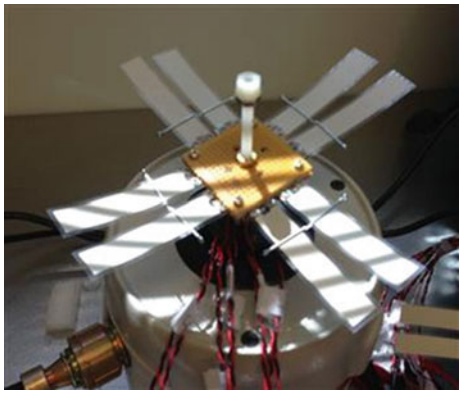

Fig. 146.2 Configuration of a module that includes eight piezoelectric components used for energy harvesting

146.4 Performance of Energy Harvesting

146.4.1 Single Piezoelectric Unit

To evaluate the amount of energy generated by mechanical vibration, a piezoelectric component (DTK-028 K) was operated at its first and second mode. A 0.6 g proof mass was attached at specific locations to adjust the resonant frequencies for maximal amount of power that can be generated.

With the mathematical model proposed in the previous section, the resonant frequency of the first mode without any proof mass attached is 12.9 Hz and it is 81 Hz for the second mode. While operating a single piezoelectric component (DT2-028 K) at these two frequencies, the generated powers are 1.6 and 28.5 μW, separately. It is clear that the piezoelectric component can generate much greater power at its second mode. The only drawback is that the excitation frequency cannot always at the resonant frequencies. Thus, the model proposed in the previous section can be used to adapt the operational frequencies of the piezoelectric component to the environmental vibration source. Figure 146.3 illustrates the frequency variation with a 0.6 g proof mass. The resonant frequency of the second mode can be adjusted between 43 and 81 Hz.

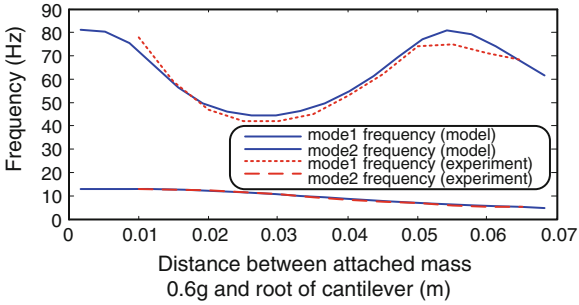

Fig. 146.3 Variation of frequency of piezoelectric component

To verify the incremental amount of harvested energy, the resonant frequency is adjusted to 45 and 52 Hz. Without attached mass, the energy generated by a single cantilever beam is 1.6 μW at 13 Hz, 0.7 μW at 45 Hz, and 0.3 μW at 52 Hz. If the 0.6 g proof mass is attached at 30 mm away from the root, the resonant frequency of its second mode becomes 45 Hz, and the harvested energy at this frequency becomes 18.1 μW. If the proof mass is attached at 40 mm away from the root, the resonant frequency of its second mode becomes 52 Hz, and the harvested energy at this frequency becomes 13.6 μW. In either case, the harvestable amount of power can be increased dramatically. Therefore, instead of operating a piezoelectric component at its first mode, it is suggested to adjust the component to be operated at its second mode with an attached mass.

146.4.2 Piezoelectric Device Array

It is clear that single piezoelectric component can only generate limited amount of power. In order to increase the harvestable energy, eight components are integrated as a module. Thus, the collecting process can be much more efficient with multiple modules. One important issue needs to be considered is that the phases of individual components may not be the same. Connecting all components in series can possibly reduce the output power instead of increasing it due to the phase inconsistence. In the configuration shown in Fig. 146.2, the eight components are connects in parallel after rectifying output voltage. Individual modules do not charge the adopted solid-state battery directly. Instead, the charging process is controlled by a microcontroller unit. Figure 146.4 demonstrates the schematic diagram of the charging mechanism.

The major consideration of the mechanism is that the adopted solid-state battery can be damaged if the charging voltage is higher than its tolerable limit. To ensure the output voltage of harvesting module is within the limited range, a charging capacitor is used for each module to prevent noise with high voltage peaks. To compensate between charging efficiency and effective charging range, the range of output voltage is set to be 4.1 $\sim$ 4.3 V for current setup. The charging sequence

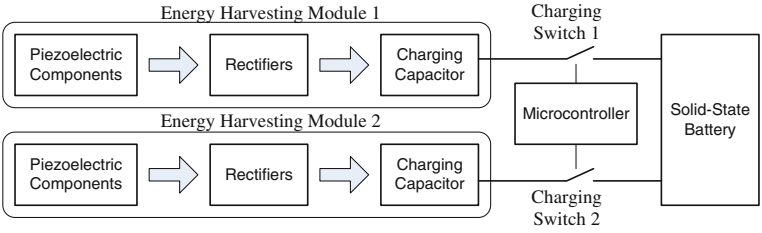

Fig. 146.4 Configuration of charging sequence of the energy harvesting mechanism

of the energy harvesting array is controlled by a microcontroller unit. As the output voltage of individual module is lower than 4.1 V, the charging switch is toggled to another module.

To charge the capacitor from 4.1 to 4.3 V, the required charging duration is ~30 s. If the solid-state battery is discharged to 3.9 V, the required charging time is ~115 min to get it full charged to 4.4 V if a single module is used. If two modules are used, the charging period can be reduced to one half, which is ~57 min.

146.5 Conclusions

This paper proposes a feasible operating scheme that effectively harvests environmental vibration energy to a usable amount. With the operating scheme, various self-powered applications can be further investigated. In the future, our research will be focused on the implementation of those applications, such as bridge monitoring and lighting in mineral environment.

References

1. Anton, S. R., & Sodano, H. A. (2007). A review of power harvesting using piezoelectric materials (2003–2006). *Smart Materials and Structures, 16*, R1–R21.
2. Li, Y. J., Cheng, M. H., & Bakhoum, E. G. (2013). Operation of energy harvesting devices in different vibration modes. In: *Energytech, 2013*, (pp. 1–6).The conference in Cleveland, OH.
3. Li, Y., Cheng M. H. & Bakhoum, E. (2012). Circuit development of piezoelectric energy harvesting device for recharging solid-state batteries. In *the Proceedings of the ASME 2012 International Mechanical Engineering Congress and Exposition (IMECE)*, IMECE2013-88103, Houston TX.
4. Vierck, R. K. (1979). *Vibration Analysis* (2nd ed.). New York: Harper and Row.

Chapter 147
A Loop Partitioning Method by Implementation of Gaussian Elimination

Chien-Chih Chang

Abstract Extracting parallelism from nested loop with Unimodular Matrix Transformation gains the benefits of efficiency, flexibility and easy coding in realization of auto-restructuring compiler. With unimodular matrix transformation, the partitioning matrix dominates the number of independent parallel sets and the complexity of this transformation. In this paper, we propose a fast method to derive the required partitioning matrix for the loop parallelization. This method can quickly and easily derive the partitioning matrix on the basis of data dependence Distance Matrix and Modified Gauss Elimination. Examples show the complexity of computational time is close to $1/2 \times (n \times m)$ in most cases and the partitioning numbers are still kept in optimal values as those proposed by previous research works. Finally, we emphasize that this method is more efficient in deeper nested loop especially for loop depth $n \geq 4$.

Keywords Unimodular matrix transformation · Data dependence distance matrix · Gauss elimination

147.1 Introduction

The main objective of loop transformation tried to run sequential nested loop parallelism in parallel processing system. One of the solutions is running the original loop in reordering to exploit the inherent parallelism. In 1974, Lamport [4] proposed the hyperplane approach to exploit parallelism according to the time transformation. The approach tried to execute the loop body concurrently for all the points lying along a plane. How to determine the proper hyperplane is

C.-C. Chang (✉)
Department of Electrical Engineering, Cheng Shiu University, Kaohsiung 83347, Taiwan, Republic of China
e-mail: chang968@ms13.hinet.net

J. Juang et al. (eds.), *Proceedings of the 2nd International Conference on Intelligent Technologies and Engineering Systems (ICITES2013)*, Lecture Notes in Electrical Engineering 293,
DOI: 10.1007/978-3-319-04573-3_147,

important. While for a nested loop with a good few of depths and data dependencies, the derivation of the hyperplane (or wavefront) will be interminable.

Unimodular matrix transformation is an alternative choice that treats the wavefront in terms of matrix transformations of the index vector of the original nested loop [2]. Extracting parallelism from nested loop with unimodular matrix transformation has the benefits of efficiency, flexibility and easy coding in realization of auto restructuring compiler.

Early for Minimum Distance, Peir [5] proposed that a linear combination iteration points can be partitioned as an independent execution set xi. The xi can be expressed as the vector form $X_i = X_{i,0} + A \times D_c$, where each row of D_c is a distance vector of original loop. Peir treated the partitioning matrix as an integer problem which is NP-complete and all the dependence vectors must be linearly independent. Wolf and Monica [8] derived the transformation matrix by transforming it into a fully permutable loop. They unified the combinations of loop interchange, skewing and reversal as unimodular transformation to derive the transformation matrix. D'Hollander [3] improved the Minimum Distance method via a partitioning algorithm and labeled the partition for scheduling. Those methods have certain contributions in deriving the partitioning matrix. However, there exist weak points in results of those appeared in the literature. For example, in [1, 7], the derivation of partitioning matrix must solve inequalities. It is inconvenience. In [6], the same derivation consumed a large of time for deeper nested-loop especially for $n \geq 4$.

In this paper, we proposed a more efficient method to derive the partitioning matrix. The method derived the partitioning matrix on the basis of Data Dependence Distance Matrix and Modified Gauss Elimination. This method can realize easily the auto-compiler than previous works and overcome the drawbacks in deriving the partitioning matrix of deeper nested-loop. Examples show the method getting the partitioning matrix less than $1/2 \times (n \times m)$ time complexity in most cases and the partitioning numbers are still kept in optimal values as those in previous works. Finally we emphasize that this method is very efficient in deeper nested-loop for loop depth $n \geq 4$.

147.2 Background and Definitions

A nested loop is parallelizable if only if the loop is lexicographically positive.

Peir [7] proposed that an independent execution set of nested loop L can be obtained from $x_i = x_{i,0} + K \times D^c$, where $x_{i,0}$ are set of initial points, and *K* is partitioning matrix, with $D^t = K \times D^c$ it's transferred the original dependence vector matrix into an upper triangular matrix D^t, then with D^t to partition loop into certain independent execution set. The derivation of partitioning matrix *K* in algorithms is viewed as an integer programming and NP-complete.

Banerjee [2] proposed a matrix-based theory in transformations of double loop. In this method a derivation of unimodular transformation matrix of double loop had been discussed. The paper studies well of the properties of the unimodular transformation. The disadvantage was that the derivation of the matrix must be determined by manual labor, and was determined difficultly while loop depth exceeded tree. Latterly, In 1992 D'Hollander [3] proposed a partitioning and labeling algorithm with unimodular transformation. An algorithm finded unimodular U, V such that the transferred dependence matrix $D^t = UDV$. The method saved the solving inequalities in derivation the partitioning matrix. But it become complexity while the distance matrix growing, the computation time is bounded by $O(n^2(m + n)(1 + 5\log_2 \Gamma)$.

147.3 The Properties of Unimodular Matrix

In this section, rulers and definitions of the unimodular matrix are desribed. Then, we obtain the partitioning matrix by those properties.

Definition 1 After the following operations, a unimodular matrix still is a unimodular:

(1) exchange any two row or column of the matrix
(2) multiply a row or a column by -1
(3) multiply a row (column) by an integer factor and add with another row(column)

Definition 2 The transformed loop bounded calculated from shift data dependence matrix D^s andD^t, where D^scan be obtained from following steps [5]:

For i=1 to n
  For j=i+1 to n
  {IF($d^t_{i,j} > 0$ then f=$\lfloor d^t_{i,j}/d^t_{j,j} \rfloor$
    $D_i = D_i - f \times D_j$
  Else f=$\lceil -d^t_{i,j}/d^t_{j,j} \rceil$
    $D_i = D_i + f \times D_j$}

Definition 3 The data dependence matrix of a outer-parallel nested loop has following form:

$$a_{i,j} = 0, i > j, a_{i,j} \in D^t$$

Definition 4 The numbers of partition of a nested loop is equivalent to [5]

$$N = \prod_{i=1}^{n} a_{i,i}, a_{i,i} \in D^t$$

For example, a transformed loop's data dependence matrix is $\begin{bmatrix} 2 & 1 & -3 \\ 0 & 3 & 4 \\ 0 & 0 & 5 \end{bmatrix}$ and the nested-loop can be partitioning into $2 \times 3 \times 5 = 30$ parallel subsets. With D^t and D^s the original loop can be transformed as follows [5]:

DOALL $ip_1 = 1, d^t_{1,1}$
DOALL $ip_2 = 1, d^t_{2,2}$
DOALL $ip_3 = 1, d^t_{3,3}$
:
DOALL $ip_n = 1, d^t_{n,n}$
DO $i_1 = ip_1, U_1, 1$

$$DOi_2 = \left(ip_2 + (i_1 - ip_1)/d^t_{1,1} \times d^s_{1,2}\right) \text{ MOD } d^t_{2,2}), U_2,\ d^t_{2,2}$$

$$DOi_3 = ((ip_3 + (i_1 - ip_1)d^t_{1,1} \times d^{\ s}_{1,3} + (i_2 - ip_2)/(d^t_{2,2} \times d^s_{2,3}\ )$$

$$\text{MOD } d^t_{3,3}\ ),\ U_3,\ d^t_{3,3}$$

$$\text{DO } i_K = (i_{Pk} + \sum_{k=1}^{i-1} (i_k - i_{pk})/(d^t_{kk} \times d^s_{ki}) \text{MOD } d^t_{ii}, u_{ii}, d^t_{ii}$$

ENDDO i_k
:
ENDDO i_{p1}

147.4 Algorithms of the Method

For loop parallelization, one must derive the partitioning matrix T and transfer the sequential nested-loop's Dependence Matrix into the diagnosis matrix $D^t = T \times D$.

In algorithms, we first get the Data Dependence Matrix D and then combined it with the identity matrix I as an argument matrix [D|I]. Without loosing generality, we assume a dependence matrix $D_{n \times m}$ with dimensions $m \geq n$ in order to simplify the algorithms. When $m \leq n$, *D* can be extended with (n–m) zero vectors because a zero-vector not affect the parallelism. The method of derivation the partitioning matrix can briefly described as below:

In Fig. 147.1a, there specified iteration (a) have data dependence with iteration (b), (c) and the distance vector are {(4, 3) (2, 1)} individually. Our method firstly select (2, 1) as b-vector. Secondly deriving the partitioning matrix, after transformation the relations of the iteration show in (b) and the distance vector become {(0, 1) (2, 1)}. From Fig. 147.1b, we can easily observed that iteration a' c' can be

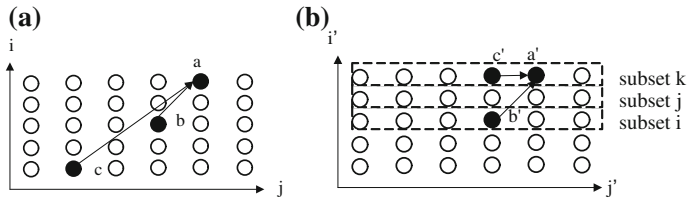

Fig. 147.1 Iteration space of transformation. **a** Before transformation, **b** After transformation

partitioned into the same subset k while iteration b' in another subset *i*. Clearly subset j and k can be running in parallel. The algorithms are specified below:

Algorithms part I : initial the data dependence matrix

1. Set $D = [a_{i,j}]_{n\times n}$. For $a_{i,j}$ i is the ith data dependence set in loop body and j is the jth data dependence relative to loop level.
2. Set $k = n$

```
for i = 1 to n
    if a_{i,j} ∈ p-vector then change row[i] with row[k]
      k = k-1
```

this process find the p-vector and sink it in the bottom.

Step 2 put the p-vector into the bottom row of the matrix

Part II : Reduction the D to D^t and derive T

Part II : Reduction the D to D^t and derive T

1. Let $I_{n\times n}$ is identity matrix, se $i_0 = 1, j_0 = 1$.
2. Let $A_{n\times n} \leftarrow D_{n\times n}$. Construct the Argument matrix [A| I]

For i= i_0 to n do

IF (a_{ii}>$a_{i+1,\ j}$ Λ $a_{i+1,\ j}$ ≠0) then change [row i] with [row i+1]

This processing find the b-vector and put it into the top of the matrix

4. For i= i_0 to n

$p_i = \lfloor a_{i,j} / a_{i,j} \rfloor$

[row i+1]←[row i+1]−p_i×[row i]

IF($a_{i+1,j} = 0 \wedge a_{i+1,j+1} < 0$) then reverse [row i+1]

5. For i= i_0 to n

IF $a_{i+1,j}$ ≠0 then goto step 3

6. i=i_0+1, j=j_0+1 goto step 3 until i=n

7. $D^t = A$, T=$I_{n\times n}$

Example: a deeper nested-loop's data dependencies matrix implemented of our algorithm that can obtain the partitioning matrix D^t

$$D = \begin{bmatrix} 1 & -2 & -4 & 2 \\ 2 & 4 & -2 & -2 \\ 3 & 0 & -4 & 2 \\ 0 & 2 & 2 & 2 \end{bmatrix} \quad I = \begin{bmatrix} 1 & 0 & 0 & 0 \\ 0 & 1 & 0 & 0 \\ 0 & 0 & 1 & 0 \\ 0 & 0 & 0 & 1 \end{bmatrix}$$

1. $$\begin{bmatrix} 1 & -2 & -4 & 2 \\ 2 & 4 & -2 & -2 \\ 3 & 0 & -4 & 2 \\ 0 & 2 & 2 & 2 \end{bmatrix} \begin{bmatrix} 1 & 0 & 0 & 0 \\ 0 & 1 & 0 & 0 \\ 0 & 0 & 1 & 0 \\ 0 & 0 & 0 & 1 \end{bmatrix}$$

2. $$\begin{bmatrix} 1 & -2 & -4 & 2 \\ 0 & 8 & 6 & -6 \\ 0 & 6 & 8 & -4 \\ 0 & 2 & 0 & 2 \end{bmatrix} \begin{bmatrix} 1 & 0 & 0 & 0 \\ -2 & 1 & 0 & 0 \\ -3 & 0 & 1 & 0 \\ 0 & 0 & 0 & 1 \end{bmatrix}$$

3. $$\begin{bmatrix} 1 & -2 & -4 & 2 \\ 0 & 2 & 0 & 2 \\ 0 & 6 & 8 & -4 \\ 0 & 8 & 6 & -6 \end{bmatrix} \begin{bmatrix} 1 & 0 & 0 & 0 \\ 0 & 0 & 0 & 1 \\ -3 & 0 & 1 & 0 \\ -2 & 1 & 0 & 0 \end{bmatrix}$$

4. $$\begin{bmatrix} 1 & -2 & -4 & 2 \\ 0 & 2 & 0 & 2 \\ 0 & 0 & 8 & -10 \\ 0 & 0 & 6 & -14 \end{bmatrix} \begin{bmatrix} 1 & 0 & 0 & 0 \\ 0 & 0 & 0 & 1 \\ -3 & 0 & 1 & -3 \\ -2 & 1 & 0 & -4 \end{bmatrix}$$

5. $$\begin{bmatrix} 1 & -2 & -4 & 2 \\ 0 & 2 & 0 & 2 \\ 0 & 0 & 6 & -14 \\ 0 & 0 & 8 & -10 \end{bmatrix} \begin{bmatrix} 1 & 0 & 0 & 0 \\ 0 & 0 & 0 & 1 \\ -2 & 1 & 0 & -4 \\ -3 & 0 & 1 & -3 \end{bmatrix}$$

6. $$\begin{bmatrix} 1 & -2 & -4 & 2 \\ 0 & 2 & 0 & 2 \\ 0 & 0 & 6 & -14 \\ 0 & 0 & 2 & 4 \end{bmatrix} \begin{bmatrix} 1 & 0 & 0 & 0 \\ 0 & 0 & 0 & 1 \\ -2 & 1 & 0 & -4 \\ -1 & -1 & 1 & 1 \end{bmatrix}$$

7. $$\begin{bmatrix} 1 & -2 & -4 & 2 \\ 0 & 2 & 0 & 2 \\ 0 & 0 & 2 & 4 \\ 0 & 0 & 6 & -14 \end{bmatrix} \begin{bmatrix} 1 & 0 & 0 & 0 \\ 0 & 0 & 0 & 1 \\ -1 & -1 & 1 & 1 \\ -2 & 1 & 0 & -4 \end{bmatrix}$$

8. $$\begin{bmatrix} 1 & -2 & -4 & 2 \\ 0 & 2 & 0 & 2 \\ 0 & 0 & 2 & 4 \\ 0 & 0 & 0 & -26 \end{bmatrix} \begin{bmatrix} 1 & 0 & 0 & 0 \\ 0 & 0 & 0 & 0 \\ -1 & -1 & 1 & 1 \\ 1 & 4 & -3 & -7 \end{bmatrix}$$

9. $$\begin{bmatrix} 1 & -2 & -4 & 2 \\ 0 & 2 & 0 & 2 \\ 0 & 0 & 2 & 4 \\ 0 & 0 & 0 & 26 \end{bmatrix} \begin{bmatrix} 1 & 0 & 0 & 0 \\ 0 & 0 & 0 & 0 \\ -1 & -1 & 1 & 1 \\ -1 & -4 & 3 & 7 \end{bmatrix}$$

$$D^t = \begin{bmatrix} 1 & -2 & -4 & 2 \\ 0 & 2 & 0 & 2 \\ 0 & 0 & 2 & 4 \\ 0 & 0 & 0 & 26 \end{bmatrix} \quad T = \begin{bmatrix} 1 & 0 & 0 & 0 \\ 0 & 0 & 0 & 0 \\ -1 & -1 & 1 & 1 \\ -1 & -4 & 3 & 7 \end{bmatrix}$$

The parallel partitioning sets $N = 1 \times 2 \times 2 \times 26 = 104$. The computational steps $= 9$.

147.5 Conclusions

In this paper, we propose a fast method to obtain the partitioning matrix for unimodular transformation. According to the mentioned method, the partitioning matrix on the basis of Data Dependence Distance Matrix and Modified Gauss Elimination is derived. Examples show the computational time complexity is close to $1/2 \times (n \times m)$ in most cases. However, it is $O(n2(m + n)(1 + 5\log 2\Gamma)$ in [3] and is a NP-Complete problem in [5]. This method also has the following advantages: (1) easy realization for auto-parallelization restructuring compiler and (2) more efficiency for deeper nested-loop with loop depth $n \geq 4$. Therefore, the result method improves drawbacks of those methods in the literatures

References

1. Banerjee, U., Chen, S. C., Kuck, D., & Towle, R. (1979). Time and parallel processor bounds for fortran-like loops. *IEEE Transactions on Computers, C-28*, 660–670.
2. Banerjee, U. (1990). Unimodular transformations of double loops, *Proceedings of the Third Workshop on Languages and Compilers for Parallel Computing, Irvine, California*, August 1–3, 1990.
3. D'Hollander, E. H. (1991). Partitioning and labeling of loops by unimodular transformations. *IEEE Transactions on Parallel and Distributed Systems, 3*(4), 465–476.
4. Lamport, L. (1974). The parallel execution of DO loops. *Communications of the ACM, 17*, 83–93.
5. Peir, J. K., & Cytron, R. (1989). Minimum distance: A method for partitioning recurrences for multiprocessors. *IEEE Transactions on Computer, 38*, 1203–1211.
6. Sheu, J.-P., & Tai, T.-H. (1991). Partitioning and mapping nested loops on multiprocessor systems. *IEEE Transactions on Parallel and Distributed Systems, 2*(4), 430–439.
7. Wolf, M. E., & Lam, M. S. (1991). A loop transformation theory and an algorithm to maximize parallelism. *IEEE Transactions on Parallel and Distributed Systems, 2*(4), 452–471.
8. Wolfe, M. J. (1986). Loop skewing : The wavefront method revisited. *International Journal of Parallel Programming, 15*, 279–293.

Chapter 148
Implementation and Experimental Study of Medical Ward Air Conditioning System Control

Chih-Neng Hsu, Hong-Yue Chen, Ming-Te Chao and Chun-Yu Wu

Abstract This paper focuses on the design, implementation, and micro dusty experimental and analysis of the medical ward air conditioning system control. The original air conditioning cycle design airflow rate must not only be maintained, but also the same amount of supply air and return air. It is mainly directed toward the environmental quality of the air conditioning renovation, including micro dusty, temperature, humidity, indoor differential pressure, and air speed impact experimental analysis. Hospitals need long-term air conditioning operation to maintain cleanliness indoor with temperature and humidity control. As a result, the hospital will have a heavy electricity loading. Therefore, the medical ward must reduce the air conditioning cycle times to reach a comfortable indoor environment with constant temperature and humidity, using an individual air conditioning control and inverter control motor system. This process will add to automatic fan valve maintenance temperature, humidity, micro dusty in ISO 14644-1 standard class 10,000 and indoor air quality improvement. Moreover, this process will reduce air conditioning loading and improve good environmental quality.

Keywords Air conditioning system · Ventilation · Environmental quality

148.1 Introduction

Hospital indoor ventilation circulation and air quality can use air conditioning to keep good environmental. In general, hospital air conditioning must consider the patient's condition and shall be divided into positive pressure ward (for example, surgery and burns ward) and negative pressure ward (for example, TB or SARS

C.-N. Hsu (✉) · H.-Y. Chen · M.-T. Chao · C.-Y. Wu
Department of Refrigeration, Air Conditioning and Energy Engineering, National Chin-Yi University of Technology, Taichung City 41170, Taiwan, Republic of China
e-mail: cnhsu@ncut.edu.tw

J. Juang et al. (eds.), *Proceedings of the 2nd International Conference on Intelligent Technologies and Engineering Systems (ICITES2013)*, Lecture Notes in Electrical Engineering 293,
DOI: 10.1007/978-3-319-04573-3_148,

patients). In addition, medical staff, patient protection, mobile route, location of the supply air and return air, and moving lines shall be also considered as path lines. This process will reduce the air conditioning pipe line design, load consumption, and maintain excellent indoor air quality, as well as micro dusty, the amount of bacteria, temperature and humidity, ventilation circulation, air velocity, positive and negative pressure, CO_2, CO, and physical factor control.

Mai et al. [1] aims to study the relations between subjective indoor air quality, in particular, the effect of dampness, type of building, concentration of CO_2, CO, O_2, and total hydrocarbon, as well as air humidity. Huang et al. [2] have suggested that teaching hospital shall periodically monitor the air for microorganisms. Sun [3] analyzed some problems including insufficient fresh air volume, simple air conditioning mode, backward management, and incomplete operation maintenance rules, and provided corresponding countermeasures. Kavgic et al. [4] focused on the analysis of thermal comfort and indoor air quality in a mechanically ventilated theatre.

Kwon et al. [5] investigated the initial velocity distribution of exhaled air from coughing and speaking. Chen et al. [6] presented the air conditioning system of fresh air plus dry cooling conditioning fan coil units. Wang et al. [7] measured the energy savings of air conditioning systems for hospitals. Jiang et al. [8] presented the methods for improving indoor air quality of the newly decorated residential building in Hangzhou. Sekhar et al. [9] studied the thermal comfort and indoor air quality (IAQ) characteristics of naturally/mechanically ventilated (NMV) and air conditioned (AC) bedrooms in a hot and humid climate. Liang et al. [10] presented an air conditioning system design case of an infectious hospital, where the pressure design is based on dynamic isolation theory. They are also provided application of some new scientific achievements, and discuss some design experiences of isolation ward. The current paper aims are investigated the design, implementation, as well as experimental measurement and analysis of the medical ward air conditioning system control.

148.2 Ward Area and Floor Plan

The original ward floor area is 458 m^2, in which the original medical ward area is 22.684 m^2, as shown in Figs. 148.1 and 148.2. The wards operate for 24 h, including the treatment area, the operating room, nursing station, spa room, and ICU wards. The original medical ward does not have a buffer area set up in the past. The ward positive pressure is not established when the nursing staff enter and leave the ward. Thus, the ward will be redesigned, with additional buffer, automatic doors, and interlock measures to maintain a positive pressure in the medical ward and meet the micro dusty particle ISO standard class 10,000.

After the medical ward is redesigned, the ward area is 55.273 m^2, but the supply air (SA) and return air (RA) quantity remained unchanged, as shown in Figs. 148.3 and 148.4. The redesigned medical ward temperature and relative

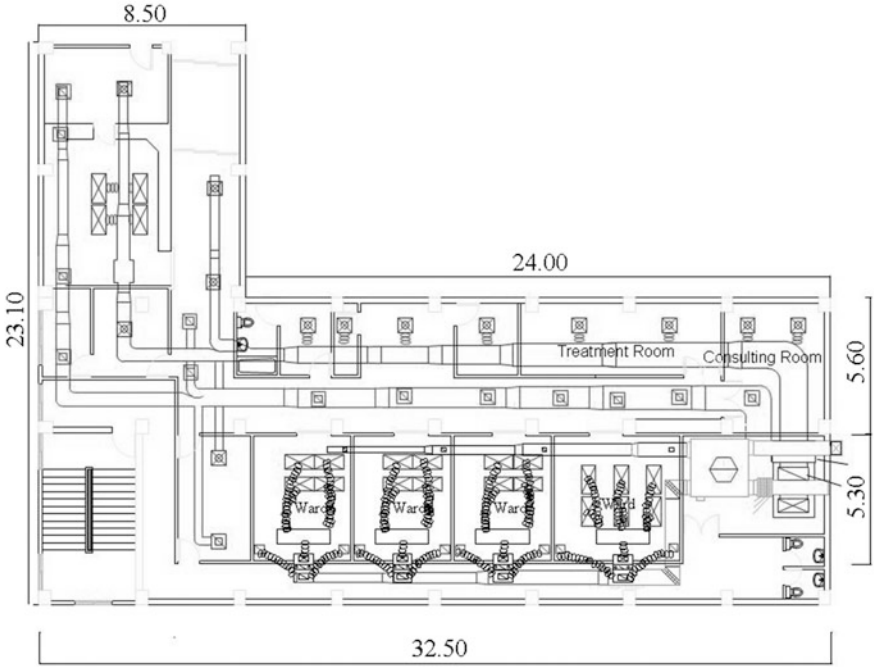

Fig. 148.1 Original medical ward area for severe degree burn injuries ward (unit: m)

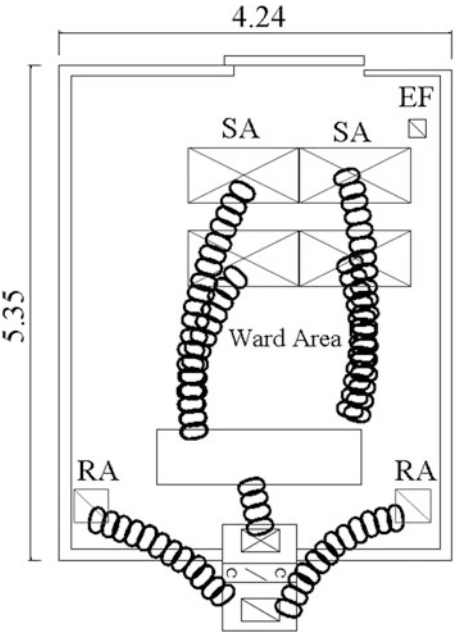

Fig. 148.2 Original medical ward area for severe degree burn injuries ward air conditioning system design model (unit: m)

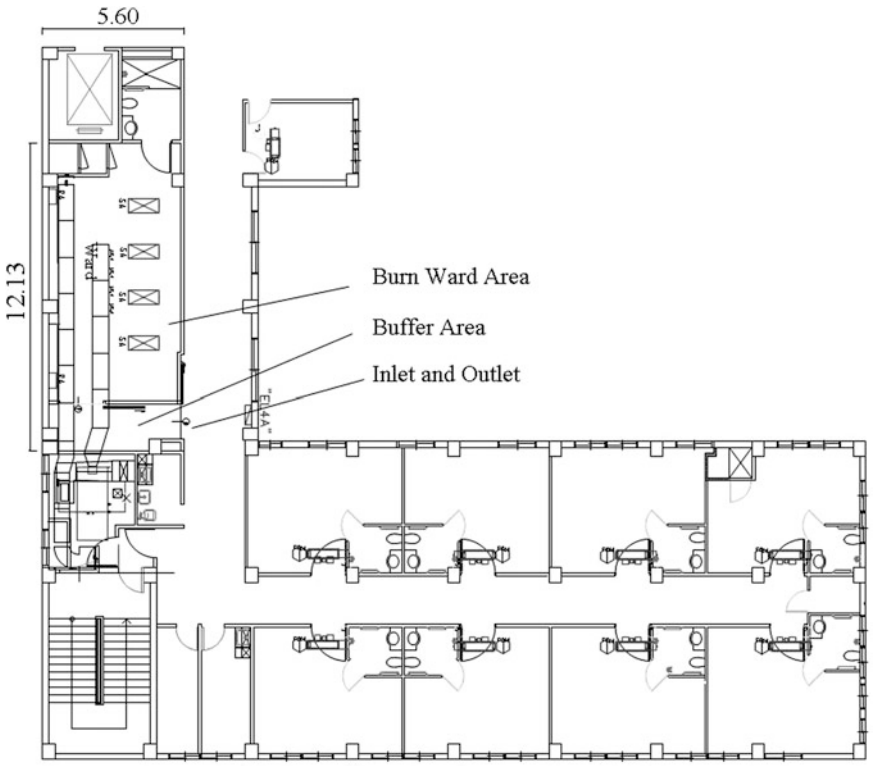

Fig. 148.3 Redesigned medical ward area for mild degree burn injuries ward (unit: m)

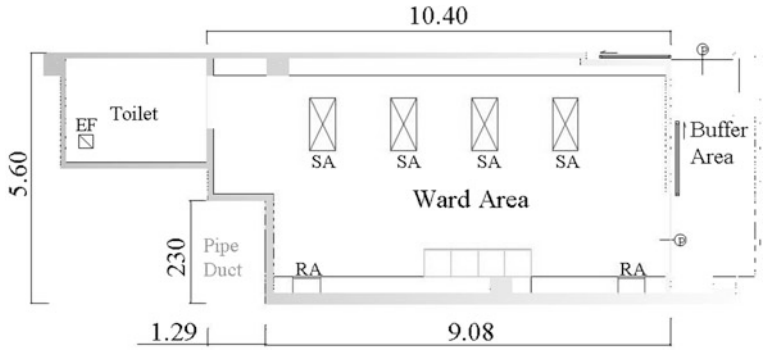

Fig. 148.4 Redesiged medical ward area for mild degree burn injuries ward air conditioning system design model (unit: m)

Fig. 148.5 Ward internal renovation

Fig. 148.6 Light steel frame and pipe design

humidity shall be controlled at 23 °C ± 2 °C and 55 % ± 5 % RH. The micro dusty must meet the ISO 14644-1 standard class 10,000. The positive pressure of the medical ward area is higher than 8 Pa, and the buffer area is higher than 2 Pa, meeting the redesign value.

148.3 Design and Implementation of Medical Ward Air Conditioning System

The design and implementation of the regional hospital medical ward air conditioning system by the construction alteration plans is shown in Fig. 148.5. Figure 148.6 shows the light steel frame compartment and pipe design guideline. Figure 148.7 shows the windmill and air duct device. Figure 148.8 shows the double PID controller and control display panel construction with device construction build. All of the construction operation procedures must be in accordance with the design graphic of the Refrigeration and Air Conditioning Industries Governance Act, Indoor Air Quality Act, and Fire Services Act of the government.

Fig. 148.7 Windmill and air duct device

Fig. 148.8 Double PID controller and control display panel

Fig. 148.9 Micro dusty counter

148.4 Measurement

148.4.1 Micro Dusty Counter

This paper will be used as a basis for measuring the equipment and specification, including micro dusty counter, as shown in Figs. 148.9 and 148.10, and Table 148.1.

Fig. 148.10 Micro dusty counter setup, calibration, and measurement

Table 148.1 Micro dusty counter specification

Model	Met one/3313
Voltage/frequency	100–240 V, 50/60 Hz
Measurement range	6 channels (0.3, 0.5, 1, 3, 5, 10 μm)
Capture flow rate	1 CFM
Data storage sample	2,000 samples
Calculation efficiency	50 % for 0.30 micron and 1 ft^3/min
Maximum number of display	9,999,999

The multi-function ventilation testing instruments (TSI/9565-P) are shown in Fig. 148.12 and Table 148.3.

148.4.2 Micro Dusty Measurement Procedure

1. Testing for the As-Built.
2. The ward micro dusty particles must meet the design specification.
3. Test items must be completed, including the relative indoor positive pressure, air velocity, temperature, and humidity.
4. Measurement position shall be at 1 m from the floor level.
5. The average particle concentration at each of the particle measuring locations falls below the class limit. When the total number of locations sampled is less than 10, the calculated 95 % UCL of the particle concentration is below the class limit, as shown in Table 148.2. The minimum number of sampling locations $= \sqrt{A}$, where A is the area of the floor in m^2, as shown in Fig. 148.11.

Table 148.2 Distribution for the 95 % UCL

Number of locations (L)	2	3	4	5	6	7	8	9	>9*
95 % UCL factor	6.31	2.92	2.35	2.13	2.02	1.94	1.90	1.86	N/A

The 95 % UCL = M + (UCL factor × SE)

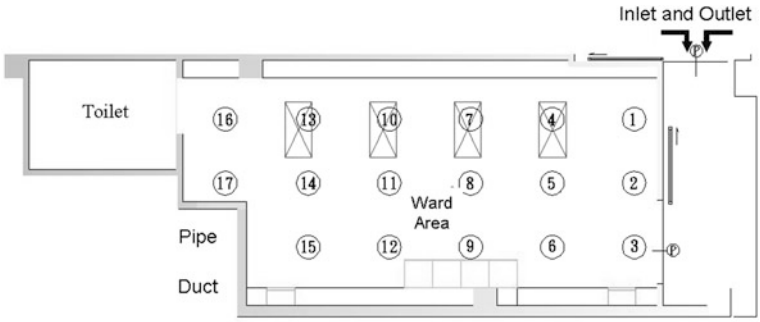

Fig. 148.11 Micro dusty sampling position

6. The Medical Ward Micro dusty Particle Design Level

0.5 μm Micro-dustry particle/on air	
English	ISO
10,000/ft^3 (Class 10,000)	352,000/m^3 (Class 7)

A particle counter with a sampling rate of 28.3 L/min, i.e., 1 ft/min is used; however, the ISO 14644-1 requires a minimum sample time of 1 min.

148.4.3 Indoor Positive Pressure, Temperature, Relative Humidity, and Velocity Measurement

1. Indoor positive testing: According to the NEBB regulations, neighborhood pressure is usually 10 ± 2.5 Pa; hence, the plan and design of the ward area shall be above 8 Pa and former chamber buffer shall be higher than 2 Pa.
2. Temperature and relative humidity testing: Temperature and humidity measurement location, number and record forms for owners cognitive.
3. Velocity: The measured distance supply air and return air is 5 cm to 7.5 cm. Design allowable value is 0.5 m/s. Thus, the balance and control of the volume and velocity of air conditioning system tests must be re-adjusted if the velocity testing results exceeded the design value.

Fig. 148.12 Multi-function ventilation testing instrument (TSI/9565-P)

Table 148.3 Multi-function ventilation testing instrument (TSI/9565-P) specification

Model	TSI/9565-P
Static/differential pressure	−15 to +15 in H_2O (−28 to +28 mmHg); −3735 to +3735 Pa), Accuracy : ±1 % of reading ±0.005 in H_2O (±0.01 mm Hg, ±1 Pa), Resolution : 0.001 in H_2O (0.1 Pa, 0.01 mm Hg)
Velocity	0–50 m/s, Accuracy: ±0.015 m/s, Resolution: 0.01 m/s
Temperature	−10 to 60 °C, Accuracy: ±0.3 °C, Resolution: 0.1 %RH
Relative humidity	5–95 % RH, Accuracy: ±3 % RH, Resolution: 0.1 % RH
Time constant (s)	1, 5, 10, 20, 30

4. Measurement instrument and specification are shown in Fig. 148.12 and Table 148.3.

148.5 Results and Discussion

After the design and engineering implementation of the medical ward, all of the micro dusty particles measurement data results met the ISO 14644-1 standard class 10,000, as shown in Fig. 148.13.

The indoor positive pressure measurement result is 58.7 Pa with meet the medical ward area to the front chamber buffer area must be greater than the design value of 8 Pa. The front chamber buffer area to the hospital aisle area measurement result is 8.5 Pa, higher than 2 Pa, thereby meeting the design value.

Temperature and relative humidity measurement results are consistent with the 23 °C ± 2 °C and 55 % ± 5 % of the design value, as shown in Fig. 148.14.

All of the HEPA supply air velocity measurement results are between 0.35 m/s and 0.4 m/s, in good agreement with the design value under 0.50 m/s. The return

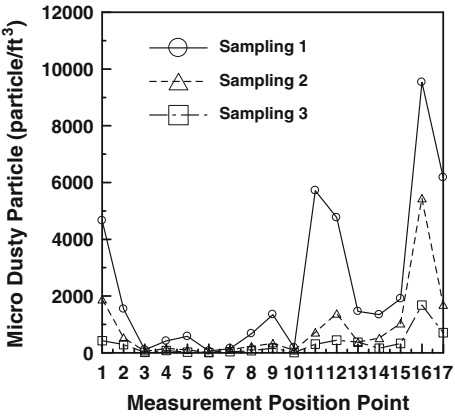

Fig. 148.13 Micro dusty particle sampling results

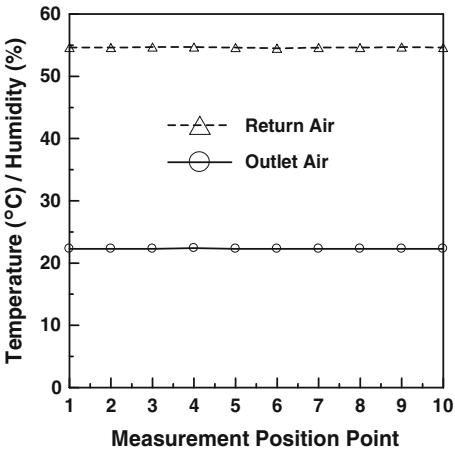

Fig. 148.14 Temperature and relative humidity measurement results

air velocity measurement results are also between 1.45 m/sec and 1.7 m/sec, and do not exceed 2.0 m/s, as shown in Fig. 148.15.

The medical ward can be accommodate up to 10 people, and the CO_2 concentration is close to 850 ppm and 600 ppm when the air conditioning ventilation system is fixed 190 CFM and 462 CFM, respectively, as shown in Fig. 148.16.

148.6 Conclusions

This article has been successfully completed measurement and analysis of the medical ward micro dusty, temperature and relative humidity, ventilation circulation, air velocity, positive and negative pressures, environmental quality through redesigning and constructing the ward.

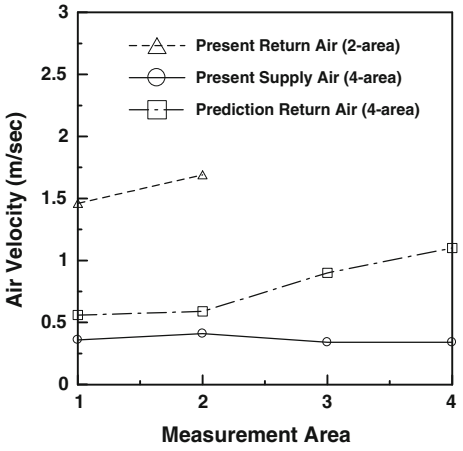

Fig. 148.15 Supply air (*SA*) and return air (*RA*) velocity measurement results

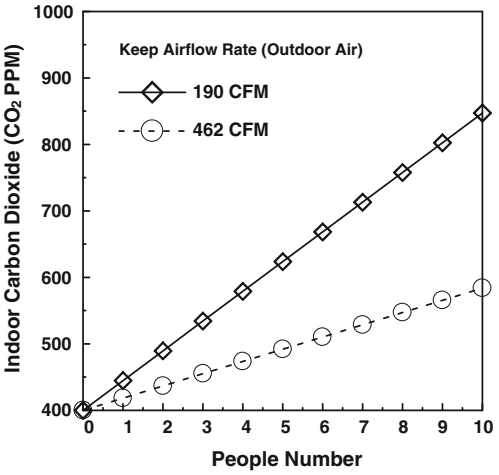

Fig. 148.16 Accumulated up to the people number versus CO_2 concentration results

The measurement and analysis results shows that all of the positions of micro dusty particles size are less than the 0.5 μm, in good agreement meet with the ISO 14644-1 standard class 10,000.

The medical ward temperature is between 22.3 °C and 22.4 °C, and meets design standard of 23 °C ± 2 °C. Relative humidity is between 54.5 and 54.7 % also met the design standard at 55 % ± 5 % RH.

The air velocity is between 0.34 and 0.41 m/s also met the standard under 0.5 m/s for ISO14644-1 standard. The return air velocity do not exceed 2.0 m/s, but between 1.46 and 1.69 m/s.

Future work, we will suggest (1) the ward can do the fluid flow analysis of computational fluid dynamics (CFD), (2) measurement and analysis of long-term monitoring the ward indoor air quality.

Acknowledgments The authors would like to thank the Engineering Division of the National Science Council (NSC) and the BING KUN CONSTRUCTION Co., Ltd. of the Republic of China, Taiwan, for financially supporting this research under contract number NSC 102-2622-E-167-022-CC3 and NCUT12TER002.

References

1. Mai, F. D., Tsai, C. F., Hsu, Y. W., & Chen, W. K. (2005). The detection of hospital indoor air quality. *Instruments Today, 27*, 73–80.
2. Huang, L. L., Mao, I. F., Chen, M. L., & Huang, C. T. (2006). The microorganisms of indoor air in a teaching hospital. *Taiwan Journal of Public Health, 25*, 315–322.
3. Sun, L. (2006). Common problems and their countermeasures in air conditioning systems for hospitals. *HV & AC Journal for China, 36*, 118–120.
4. Kavgic, M., Mumovic, D., Stevanovic, Z., & Young, A. (2008). Analysis of thermal comfort and indoor air quality in a mechanically ventilated theatre a cooling. *Energy and Buildings, 40*, 1334–1343.
5. Kwon, S. B., Park, J. Y., Jang, J. Y., Cho, Y. G., Park, D. S., Kim, C. G., et al. (2012). Study on the initial velocity distribution of exhaled air from coughing and speaking. *Chemosphere, 87*, 1260–1264.
6. Chen, Z., Zhong, C., & Ding, L. (2006). Design of ventilating and air conditioning system for teaching complex of a hospital in Guangzhou. *HV & AC Journal for China, 39*, 30–32.
7. Wang, J. B., Tu, G. B., Guang, J. J., & Pan, B. B. (2006). Measures on energy saving of air conditioning system for hospitals. *Gas and Heat, 26*, 1–210.
8. Jiang, P., Sheng, J. P., & Lu, Y. (2011). The methods of improving indoor air quality. *Energy Procedia, 11*, 2594–2599.
9. Sekhar, S. C., & Goh, S. E. (2011). Thermal comfort and IAQ characteristics of naturally/mechanically ventilated and air-conditioned bedrooms in a hot and humid climate. *Building and Environment, 46*, 1905–1916.
10. Liang, L., & Liu, H. (2007). Air conditioning and ventilation system design for negative Pressure isolation wards. *HV & AC Journal for China, 37*, 89–93.

Chapter 149
Improvement of Angular CCT Uniformity in Multi-Chip White LED with Silica–Phosphor Mixture

Nguyen Doan Quoc Anh and Hsiao-Yi Lee

Abstract In this paper, the impact of SiO_2 (silica) concentration on angular CCT uniformity of a multi-chip white LED (MCW-LED) is presented. Here, the silica particles are mixed with the phosphor particles to enhance the scattering. It is suggested that the silica–phosphor layer with 10 % weight of SiO_2 can improve the uniformity of CCT due to enough scattering property in the layer. The simulation results show that the CCT deviation can reduce from 2,211 to 1,719 K for the MCW-LED working averagely at CCT 7,700 K.

Keywords Multi-chip white light LEDs · Silica · Quartz · Color uniformity

149.1 Introduction

In general, angular CCT uniformity (ACU) and luminous flux are the main purposes in white light LEDs [1, 2]. There are several studies which have been proposed to improve the ACU of LEDs by optimizing the state of the phosphor or the optical structure of phosphor-converted white light LEDs. It was shown that the spatial color uniformity in white LEDs is analyzed by five packaging methods [3]. It was testified that the location of phosphor material in the silicone lens significantly affects the color performance. Sommer et al. demonstrated that the refractive indexes of the silicone matrix and the phosphor particle as well as the distinct phosphor particle sizes strongly affect on the radiant flux of phosphor-converted high power white light-emitting diodes [4]. Liu et al. analyzed the factors affecting color distribution of white light LEDs [5]. Moreover, the effects

N. D. Quoc Anh · H.-Y. Lee (✉)
Department of Electrical Engineering, ICITES, National Kaohsiung University of Applied Sciences, Kaohsiung 80778, Taiwan, Republic of China
e-mail: leehy@mail.ee.kuas.edu.tw

J. Juang et al. (eds.), *Proceedings of the 2nd International Conference on Intelligent Technologies and Engineering Systems (ICITES2013)*, Lecture Notes in Electrical Engineering 293,
DOI: 10.1007/978-3-319-04573-3_149,

of phosphor materials and packaging structures on the angular CCT uniformity in phosphor-in-cup LED packages are also studied by Shuai et al. [6].

The light encounters phosphor particles in its propagation path and scatters many times before escaping from phosphor silicone layer (PSL). During the multi-scattering process, the blue light is weakened because of the absorption of phosphors, but the converted yellow light will be increased for each scattering. Therefore, the final ACU of white LEDs significantly depends on the scattering effects of PSL. It means that white light uniformity shows more advantages as the scattering of PSL is enhanced [2].

In this work, the SiO_2 particles are added in the PSL making the conformal silica–phosphor layer in a MCW-LED package. It is testified that the participation of the SiO_2 particles can dominate the light scattering process in the phosphor layer. The LED packaging light distribution can be independent of its wavelength. Through the simulation results, the appropriate concentration of SiO_2—is proposed for the novel layer. Therefore, the uniform spatial color distribution of the package can be accomplished.

149.2 Methods of Study

Based on Monte Carlo ray-tracing method, the silica–phosphor structure of a MC-WLED is simulated by using LightTools 8.0.0 software. In the structure, a thin PSL, with the fixed thickness is 0.08 mm. The SJ1 and SJ2 silicone lenses cover 9 LED chips and are adhesive to the board as shown in Fig. 149.1a. The refractive index of SJ1 and SJ2 are 1.41 and 1.53 respectively. The radius of SJ1 is 6 mm while the height of SJ2 is 2 mm. Each LED chip, with a square base of 1.14 mm, and a height of 0.15 mm, is bound on the center of board. The radiant flux of each blue chip is 1.16 W at wavelength 453 nm.

The silica–phosphor structure, which is used in the study, is the addition of the silica particles to the conformal PSL as shown in Fig. 149.1b. The refractive index of phosphor particles and silicone matrix are kept constant at 1.83 and 1.5 respectively, as same as actual material. The silica and phosphor particles have average radius of 1 and 7.25 μm, respectively.

The chemical component of silicon dioxide, also known as silica, is an oxide of silicon with the chemical formula SiO_2 which has some constitutions such as melanophlogite, tridymite, quartz, and so on [7]. Quartz is widely used in many industries due to its high thermal and chemical stability and abundance [8]. The refractive index and the density of the quartz particles are set to 1.54 and 2.65 g/cm^3 respectively, while the silicone matrix and phosphor material are remained as origin. In this study, the quartz particles and the phosphor particles are mixed together with the silicone glue uniformly and coated on the surfaces of the LED chips.

To better understand the scattering of the SiO_2 and phosphor particles in the novel PSL, the angular Mie-scattering diagram is computed according to Mie

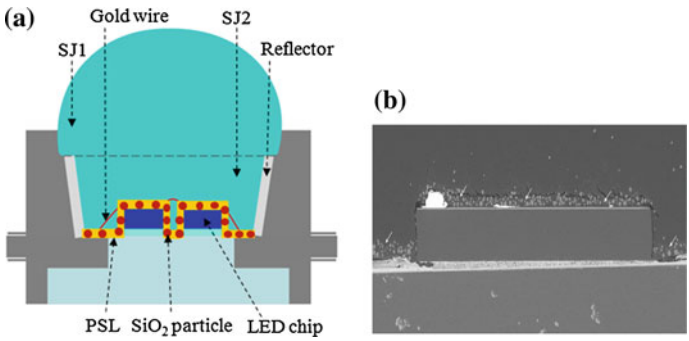

Fig. 149.1 **a** Schematic illustration of optical structure of the actual MCW-LED and **b** SEM images of cross section of PLS structure

theory [2]. The angular scattering amplitudes, S_1 and S_2 can be calculated by the following equations:

$$S_1 = \sum_{n=1}^{\infty} \frac{2n+1}{n(n+1)} [a_n(x,m)\pi_n(\cos\theta) + b_n(x,m)\tau_n(\cos\theta)] \tag{149.1}$$

$$S_2 = \sum_{n=1}^{\infty} \frac{2n+1}{n(n+1)} [a_n(x,m)\tau_n(\cos\theta) + b_n(x,m)\pi_n(\cos\theta)] \tag{149.2}$$

where $\pi_n(\cos\theta)$ and $\tau_n(\cos\theta)$ are expressed in terms of the Legendre polynomials

$$\pi_n(\cos\theta) = \frac{P_n^{(1)}(\cos\theta)}{\sin\theta} \tag{149.3}$$

$$\tau_n(\cos\theta) = \frac{dP_n^{(1)}(\cos\theta)}{d\theta} \tag{149.4}$$

The expansion coefficients a_n and b_n are defined as

$$a_n(x,m) = \frac{\psi_n'(mx)\psi_n(x) - m\psi_n(mx)\psi_n'(x)}{\psi_n'(mx)\xi_n(x) - m\psi_n(mx)\xi_n'(x)} \tag{149.5}$$

$$b_n(x,m) = \frac{m\psi_n'(mx)\psi_n(x) - \psi_n(mx)\psi_n'(x)}{m\psi_n'(mx)\xi_n(x) - \psi_n(mx)\xi_n'(x)} \tag{149.6}$$

where $x = 2\pi\alpha/\lambda$ is the particle size parameter, α is the spherical particle radius, λ is the relative scattering wavelength, m is the refractive index of a particle relative, $\psi_n(x)$ and $\xi_n(x)$ are the Riccati–Bessel functions. In Mie theory, both the silica and phosphor particle are assumed to be spherical. To compute the Mie-scattering, two dominant wavelengths are traced. The first one is 453 nm corresponding to the

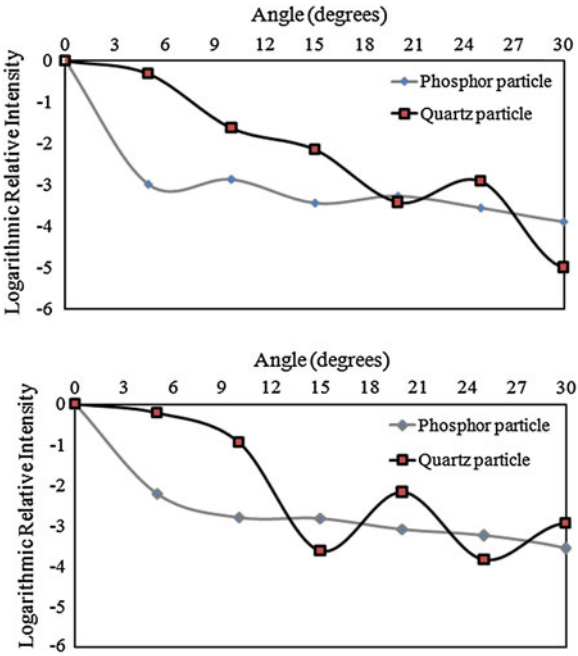

Fig. 149.2 Angular Mie-scattering diagram of the SiO_2 particle and of the phosphor particle for 453 nm (*top*) and 555 nm (*bottom*)

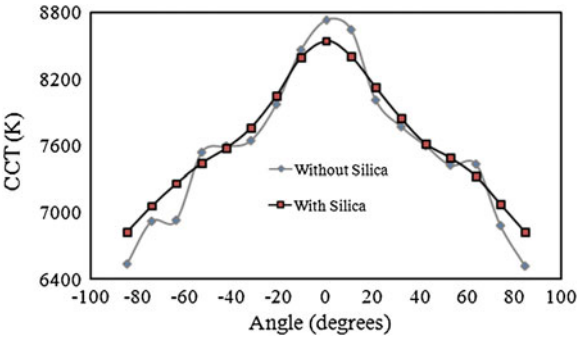

Fig. 149.3 The spatial CCT distributions corresponding with 10 % weight of SiO_2 and without it

blue light which is the emission peaks of the LED chips. The other is 555 nm representing the yellow light which is the emission peaks of the phosphor. Figure 149.2 presents the difference between the scattering intensity distributions of the SiO_2 particle and that of the phosphor particle. According to the results, the spatial CCT distribution of the MCW-LED package may also reconfigure and perform better when SiO_2 particles are added in the phosphor layer.

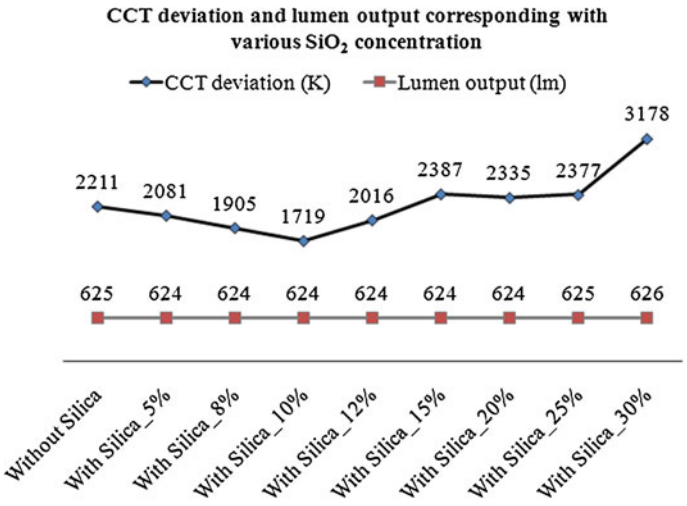

Fig. 149.4 CCT deviation and lumen output of the MCW-LED package for different weight of SiO_2

149.3 Results and Discussions

In the section, the effect of the SiO_2 concentration on angular CCT uniformity and lumen output of the silica–phosphor layer in the MCW-LED package is analyzed. CCT deviation is calculated by the subtraction of maximum CCT by minimum CCT. Angular CCT uniformity is characterized by CCT deviation. The phosphor and silica concentration are changed to control the CCT of the MCW-LED at 7,700 K. It also means that the weight percentage of them is varied. As the weight percentage of the SiO_2 increases from 5 % to 30 %, the phosphor needs to be reduced from 29.79 to 25.15 % for keeping the CCT. The total percentage of weight of the novel PSL is the sum of three types of component, including the silicone matrix and the phosphor particles as well as the SiO_2 particles. Through the analysis, it can be concluded that it has the big influence on the spatial color distribution. When the weight of SiO_2 is changed, the total effect of the scattering for phosphor layer is also changed at the same time.

Referring to the results in Fig. 149.3, it can be found that the spatial color distribution of the silica–phosphor structure is flatter than the rest. This is due to the appropriate scattering of SiO_2 in the novel structure. Thus, the blue light has more probabilities to propagate along the LED chip surfaces. As the additional 10 % weight of SiO_2, CCT deviation can decrease from 2,211 K to 1,719 K.

Figure 149.4 shows that the CCT deviation and lumen output corresponding with different weight of SiO_2 are ranged from 0 to 30 % continuously. It can be found that the general tendency of the lowest CCT deviation occurs at 10 % SiO_2. As a result, the lumen output seems not to be influenced by the SiO_2 concentration. Therefore, with the structure, the 7,700 K MCW-LED with better CCT uniformity can be accomplished.

149.4 Conclusions

Based on Monte Carlo and Mie-scattering simulation tools, the impact of SiO_2 particles on spatial color distribution of the MCW-LED is testified. The SiO_2 particles are mixed in the phosphor layer to enhance the scattering. As the increased scattering events, it means that the scattered light, especially the blue light, has more probabilities to propagate along the horizontal direction of the chip surfaces. The simulation results show that the silica–phosphor mixture has big influence on the color uniformity as maintaining the lumen output. The conformal silica–phosphor layer with 10 % SiO_2 can improve the CCT deviation to 1,719 K from 2,211 K, which is important to obtain white light quality for the package. Moreover, the paper also provides the important technical parameters of SiO_2 particles for enhancing ACU of various structures such as in-cup phosphor, remote phosphor. In the future work, the silica–phosphor structure can be further optimized for the SiO_2 particles size.

References

1. Zheng, H., Luo, X. B., Hu, R., Cao, B., Fu, X., Wang, Y. M., et al. (2012). Conformal phosphor coating using capillary microchannel for controlling color deviation of phosphor-converted white light-emitting diodes. *Optics Express, 20*, 5092–5098.
2. Liu, S., & Luo, X. B. (2011). *LED packaging for lighting applications: Design, manufacturing and testing*. Beijing: Chemical Industry Press and Wiley.
3. Liu, Z. Y., Liu, S., Wang, K., & Luo, X. B. (2008). Optical analysis of color distribution in white LEDs with various packaging methods. *IEEE Photonics Technology Letters, 20*(24), 2027–2029.
4. Sommer, C., Reil, F., Krenn, J. R., Hartmann, P., Pachler, P., Hoschopf, H., et al. (2011). The impact of light scattering on the radiant flux of phosphor-converted high power white light-emitting diodes. *The Journal of Lightwave Technology, 29*(15), 2285–2291.
5. Liu, Z. Y., Liu, S., Wang, K., & Luo, X. B. (2008). Analysis of factors affecting color distribution of white LEDs. In *2008 International Conference on Electronic Packaging Technology & High Density Packaging* (Vols. 1 and 2, pp. 386–393).
6. Shuai, Y., He, Y. Z., Tran, N. T., & Shi, F. G. (2011). Angular CCT uniformity of phosphor converted white LEDs: Effects of phosphor materials and packaging structures. *IEEE Photonics Technology Letters, 23*(3), 137–139.
7. Wikipedia, Silicon dioxide. (2013). Retrieved form http://en.wikipedia.org/wiki/Silicon_dioxide
8. Wikipedia, Quartz. (2013). Retrieved from http://en.wikipedia.org/wiki/Quartz

Chapter 150
An Innovative Miniature UHF RFID Tag Antenna Applied for Metal Surface

Tsung-Fu Chien, Chun-Chieh Wang and Chih-Kuang Wu

Abstract This paper proposes a novel miniature RFID tag antenna used in metal surface structure for UHF radio frequency identification systems. The antenna is designed in the FR4 substrate with size of $18 \times 18 \times 1.6$ mm^3. Antenna structure includes two metal trimmed radiators where two short-circuit connected to metal ground plane designed for reducing the interference of the metal surface and two symmetrical zigzag strips to reduce the size of the antenna. Four L-shaped strips and two cutting triangles are added to adjustment conjugate impedance. The antenna 10 dB impedance bandwidth, from 793 to 979 MHz, is suitable for UHF RFID applications.

Keywords RFID · UHF dipole antenna · Metallic surface

150.1 Introduction

The radio frequency identification technology is consisted for three parts. It is including the tag, the reader and information management. Particularity of the radio frequency identification technology is not restricted by space, using radio waves to a fast object tracking and data exchange. The tag is a very important element in this process because it is a path and power for the passive tag chip operation. The tag system is consisted for a chip and an antenna. The maximum read distance will be obtained when antenna is designed with complex impedance

T.-F. Chien (✉) · C.-C. Wang · C.-K. Wu
Department of Electrical Engineering, Southern Taiwan University of Science and Technology, Tainan, Taiwan, Republic of China
e-mail: jeng12@mail.stust.edu.tw

T.-F. Chien · C.-C. Wang · C.-K. Wu
RFID Research Center, Chang Jung Christian University, Tainan, Taiwan, Republic of China

J. Juang et al. (eds.), *Proceedings of the 2nd International Conference on Intelligent Technologies and Engineering Systems (ICITES2013)*, Lecture Notes in Electrical Engineering 293,
DOI: 10.1007/978-3-319-04573-3_150,

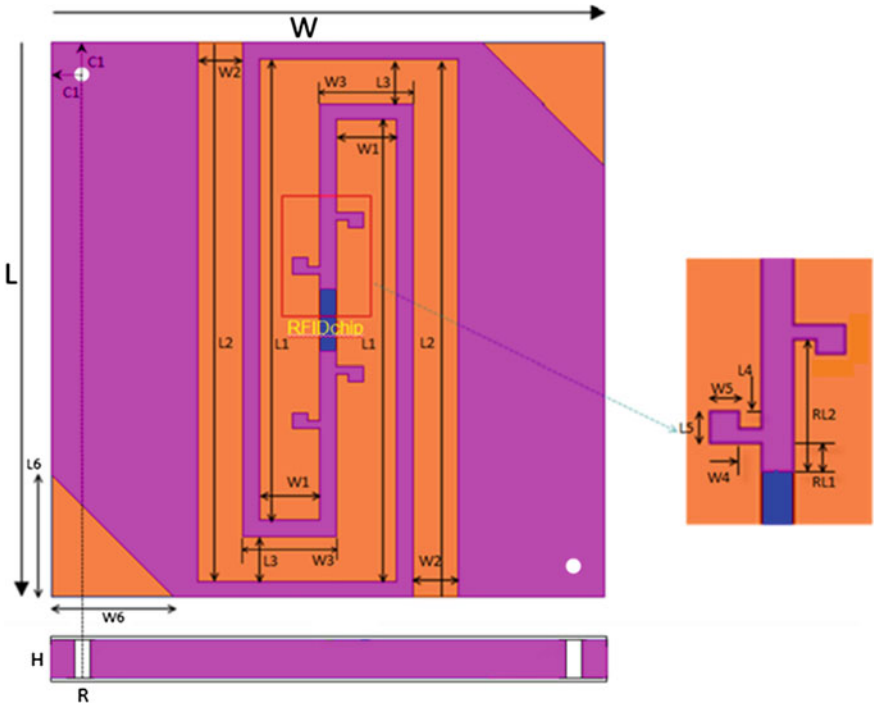

Fig. 150.1 Structure of the proposed antenna

conjugate matching [1]. However, as the tag is attached to the metal body, its transmission distance will be significantly weakened [2, 3]. To overcome this interference problem, achieving a successful application of RFID technology in metal industry relies heavily on the design of tag antenna. Many metal tags have been proposed, such as microstrip patch antenna [4, 5], a planar inverted-F antenna (PIFA) [6] and loop type feed line connected to the ground plate [7], to be used on metallic surfaces. In this paper, an innovative miniature RFID antenna effectively mounted on metal objects is proposed.

The antenna with two symmetrical road line to minimize the antenna size, four L-shaped strips and two triangle shape cutting added to adjustment impedance, and two short-circuit connected between radiator metal and ground plane.

150.2 Antenna Design and Results

The antenna is produced on an FR4 substrate with a thickness of 1.6 mm and a permittivity of 4.4. Size of the antenna is $18 \times 18 \times 1.6$ mm^3 for the use of the metal surface shown in Fig. 150.1 includes two transmitting sheet metal and two

Table 150.1 Parameters of the antenna structure

W	18 mm	W5	0.5 mm	L3	2 mm	RL1	0.5 mm
W1	2 mm	W6	4 mm	L4	0.25 mm	RL2	2.5 mm
W2	1.5 mm	L	18 mm	L5	0.5 mm	H	1.6 mm
W3	4.25 mm	L1	15.5 mm	L6	4 mm	R	0.25 mm
W4	0.5 mm	L2	17.5 mm	C1	1 mm		

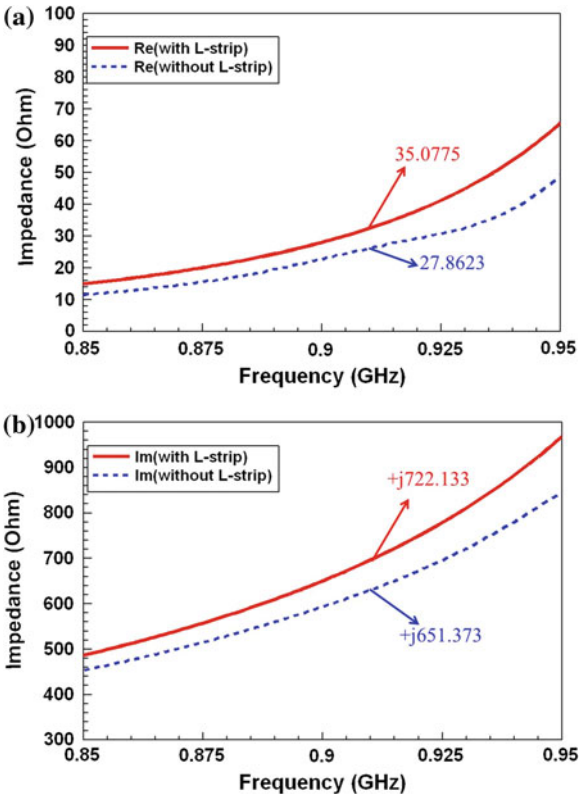

Fig. 150.2 Simulated impedance of the proposed antenna with and without L-shaped strips at 915 MHz **a** Real part impedance **b** Image part impedance

symmetrical road line to reduce the size of the antenna and the parameters of this proposed are show in Table 150.1. Two short circuits connected to sheet metal and ground plane. Four L-shaped strips and two cutting triangles are added to adjustment impedance. The proposed antenna is designed for a PHILIPS RFID chip (SL3 ICS10) with input impedance of 35 + j725 Ω at 915 MHz. The size of the L-shaped strips and cutting triangles will be appropriately adjusted to match the complex conjugate impedance of 35 + j725 Ω. Impedance matching can be adjusted by the two missing triangles and L-shaped strips as shown in Fig. 150.2.

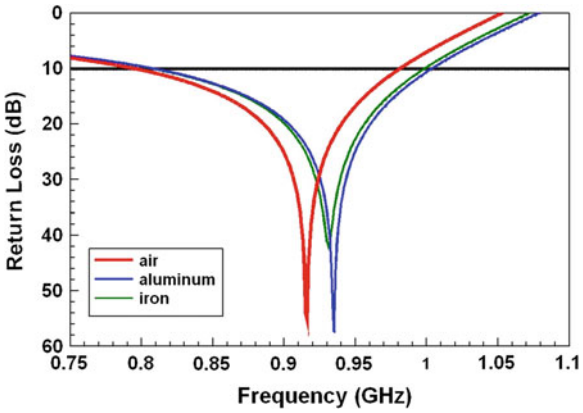

Fig. 150.3 The antenna's bands as mounted in different metal surface

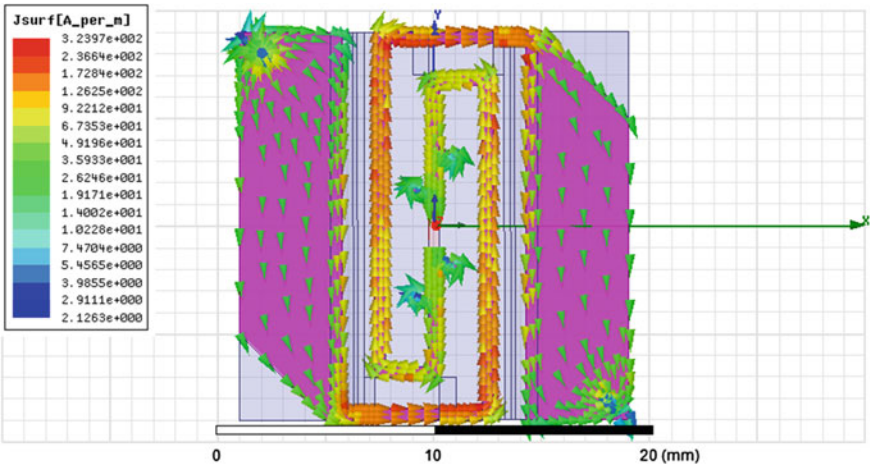

Fig. 150.4 Simulated current distributions at 915 MHz frequencies

The antenna's bands in different mounted metal environments and the simulated return losses of the proposed antenna are shown in Fig. 150.3. The simulated results of this paper are obtained through high frequency simulation software (HFSS). The simulated result based on 10 dB return loss (793–979 MHz) could covers different UHF RFID applications.

The surface current distributions of the proposed antenna at the resonant frequencies (915 MHz) are plotted in Fig. 150.4. From Fig. 150.4, the surface current distributions are concentrated on the two symmetrical zigzag strips.

150.3 Conclusions

In this paper, a novel miniature RFID tag antenna mounted in metal surface for UHF radio frequency identification systems is proposed. It is found that four L-shaped strips metal plate and two triangle shape cutting could change the antenna impedance effectively. The miniaturized antenna with measured impedance bandwidth, from 793 to 979 MHz, it covers different UHF RFID bands. Therefore, it is suitable for UHF RFID applications in different UHF RFID bands. The proposed UHF RFID Antenna can be used for vehicles management application due to its high immunity from metallic objects. Besides, the antenna is suitable to be mounted on human skin for personnel indentify system in the hospital as its low the frequency offset on the human skin. Therefore, In the future, as the RFID chip is more advanced, it will be adopted in medical care, electronic traffic control (ETC), and merchandise control the fields to further significantly reduce labor costs and provide more convenient life for people.

References

1. Monti, G., Catarinucci, L., & Tarricone, L. (2010). Broad-band dipole for RFID applications. *Progress in Electromagnetics Research C, 12*, 163–172.
2. Foster, P., Burberry, R. (1999). Antenna problems in RFID systems. *In: IEE* Colloquium on RFID Technology (pp. 31–35).
3. Dobkin, D. & Weigand, S. (2005). Environmental effects on RFID tag antennas. *IEEE MTT-S International Microwave Symposium Digest* (pp. 135–138).
4. Park, Y., Lee, S., Kang, J., & Chung, Y. C. (2007). Various UHF RFID tag for metallic object. In *IEEE Antennas and Propagation Society International Symposium* (pp. 2285–2288), Hawaii, USA.
5. Ukkonen, L., Schaffrath, M., Engels, D. W., Syd̈anheimo, L., & Kivikoski, M. (2006). Operability of folded microstrip patch-type tag antenna in the UHF RFID bands within 865–928 MHz. *IEEE Antennas and Wireless Propagation Letters, 5*(1), 414–417.
6. Hirvonen, M., Pursula, P., Jaakkola, K., & Laukkanen, K. (2004). Planar inverted-F antenna for radio frequency identification. *Electronic Letters, 40*(14), 848–850.
7. Ng, M. L., Leong, K. S., & Cole, P. H. (2006). A small passive UHF RFID tag for metallic item identification. *International Technical Conference on Circuits/Systems, Computers and Communications* (pp. 10–13), Chiang Mai, Thailand, July 2006.

Chapter 151
Performance of Joint Linear Transceiver Design with BER-Minimized Block Delay for Detection

Chun-Hsien Wu and Cheng-Yu Tsai

Abstract This paper builds an algorithm of determining the BER-minimized block delay for the joint linear transceiver design with intrablock ZF equalization. Simulations demonstrate that the proposed optimized ZF transceiver design with BER-minimized block delay for detection can yield an improved BER performance, compared with the previous design. Moreover, simulation results show that a sub-optimum MMSE transceiver design with the proposed BER-minimized block delay can be devised to perform almost as well as the optimum MMSE transceiver design.

Keywords Block delay detection · ZF · Precoder · Oblique projection

151.1 Introduction

Modern wireless communication systems employ the block-by-block transmission technique to migrate the inter-symbol interference (ISI) [1]. Exploiting fully channel state information (CSI) to jointly optimize the transmitter and receiver of a block transmission system is shown to achieve the best system performance [2]. When the added redundancy is insufficient, i.e., the inter-block interference (IBI) may exist, recent studies of [3–5] provide the optimum linear transceiver design based on the oblique projection framework. Particularly, [3] shows the merit of designing an optimum precoder against a certain delay block for detection, while [4] builds an algorithm for determining the optimum block delay under intrablock minimum mean-squared-error (MMSE) equalization criterion. However, the optimum block delay is not investigated in [4] for the criterion with intrablock zero-forcing (ZF)

C.-H. Wu (✉) · C.-Y. Tsai
Department of Photonics and Communication Engineering, Asia University, Taichung 41354, Taiwan, Republic of China
e-mail: chwu@asia.edu.tw

J. Juang et al. (eds.), *Proceedings of the 2nd International Conference on Intelligent Technologies and Engineering Systems (ICITES2013)*, Lecture Notes in Electrical Engineering 293,
DOI: 10.1007/978-3-319-04573-3_151,

equalization. Consequently, this paper builds the optimum block delay for intrablock zero-forcing (ZF) criterion and shows (via simulations) the above optimum block delay can be used for providing a sub-optimum MMSE transceiver design of [4].

Note that unless particularly specified, the notation of symbols in [3] and [4] are adopted herein.

151.2 Proposed Algorithm of Determining Optimum Block Delay

This section builds the signal model for a transceiver based on the results of [3] and [4], and then, formulates the design problem of pursuing the optimum block delay for detection so that the average bit-error-rate (BER) of the transceiver with intrablock ZF equalization is minimized, subject to the transmission power constraint.

151.2.1 Signal Model

In the transmitter of a block transmission system, $\mathbf{s}(n)$ denotes the nth block of M zero-mean uncorrelated data symbols, and $\mathbf{F}$ denotes the $M \times M$ block-based precoder. In the receiver, $\bar{\mathbf{y}}_{Q(n)} = vec([\mathbf{y}(n-Q+1), \ldots, \mathbf{y}(n)])$ denotes the nth stacked Q successive blocks of P received symbols $\mathbf{y}(n)$. Similarly, $\bar{\mathbf{v}}_{Q(n)}$ denotes the nth stacked Q successive blocks $\mathbf{v}(n)$ of P zero-mean complex additive white Gaussian noise (AWGN) samples. Let $\mathscr{H}$ represent an $QP \times (QM + K)$ effective full column channel matrix that combines the Lth-order FIR channel effect and the redundancy-generating matrix, where the parameter K depends highly on the redundancy form of cyclic-prefix (CP) or trailing-zeros (TZ) (see detail derivations in [3–5]). Then, for the delay block s(n–d), where d is an integer and represents the system block delay ($d \geq 0$), $\bar{\mathbf{y}}_{Q(n)}$ can be formulated as

$$\bar{\mathbf{y}}_{Q(n)} = \mathcal{H}_d \mathbf{F}\mathbf{s}(n-d) + \tilde{\mathcal{H}}_d \tilde{\mathbf{z}}_d(n) + \bar{\mathbf{v}}_{Q(n)} \tag{151.1}$$

where for a given d $\mathcal{H}_d$ is the right $(d+1)$th block of M columns of $\mathscr{H}$ and $\tilde{\mathcal{H}}_d$ is the remaining matrix after deleting $\mathcal{H}_d$ from $\mathscr{H}$; $\tilde{\mathbf{z}}_d(n)$ is the remaining vector after deleting $\mathbf{F}\mathbf{s}(n-d)$ from the precoded symbols in $\bar{\mathbf{y}}_Q(n)$. For $\mathbf{s}(n-d)$ of (151.1), $\mathcal{H}_d$ models the effective intrablock ISI effects within $\mathbf{s}(n-d)$, and $\mathcal{H}_d$ models the IBI effects from $\tilde{\mathbf{z}}_d(n)$.

According to the results of [3] and [4] with a modified oblique projection framework, a $M \times QP$ matrix $\mathbf{W}_d$ for a certain d can be devised to suppress the IBI effects for $\mathbf{s}(n-d)$ of (151.1). The implementation of $\mathbf{W}_d$ is given by

$$\mathbf{W}_d = \mathbf{G}\mathbf{S}_e\mathbf{E}_{\mathbf{U}_d\mathbf{B}_d}(\tilde{\mathbf{M}}_d)^H_{Q(P-M)-K}, \tag{151.2}$$

where $\mathbf{G}$ denotes a $M \times M$ block-based equalizer, S_e extracts the lower M rows of the matrix, projected by $\mathbf{E}_{\mathbf{U}_d\mathbf{B}_d}$, an oblique projection constructed with $\mathbf{U}_d$ and $\mathscr{B}_d$, and $\mathbf{M}_d$ is an unitary matrix (see details in [3, 4]). Hence, applying $\mathbf{W}_d$ of (151.2) to $\bar{\mathbf{y}}_Q(n)$ of (151.1) yields the nth equalized block of symbols $\hat{\mathbf{s}}(n)$, and is given by

$$\hat{\mathbf{s}}(n) = \mathbf{G}\mathbf{U}_d\mathbf{F}\mathbf{s}(n-d) + \mathbf{G}\mathbf{v}_d(n), \tag{151.3}$$

where $\mathbf{U}_d = \mathbf{S}_e\mathbf{U}_d$ is the lower $M \times M$ block of $\mathbf{U}_d$, and $\mathbf{v}_d(n) = \mathbf{S}_e\mathbf{E}_{\mathbf{U}_d\mathbf{B}_d}(\tilde{\mathbf{M}}_d)^H_{Q(P-M)-K}\bar{\mathbf{v}}_Q(n)$ is the $M \times 1$ oblique-projected noise vector with a positive-definite covariance matrix [3, 4]. From (151.3), resulting block-based equalizer $\mathbf{G}$ is independently applied for the effective intrablock ISI (caused by$\mathbf{U}_d$) equalization for $\mathbf{s}(n-d)$; meanwhile, the IBI effects of (151.1) is completely eliminated by the implementation of $\mathbf{W}_d$ with $\mathbf{E}_{\mathbf{U}_d\mathbf{B}_d}$ and $(\tilde{\mathbf{M}}_d)^H_{Q(P-M)-K}$. Based on the above results, the block-by-block disjoint detection, relying on (151.3), is adopted in the following design problem.

151.2.2 Design Problem Formulation

Let $\mathbf{e}_d(n) = \hat{\mathbf{s}}(n) - \mathbf{s}(n-d)$ denote the error between the equalized block of the detector input $\hat{\mathbf{s}}(n)$ and the delay block $\mathbf{s}(n-d)$. Assume that the average normalized power of each data symbol is 1 and the variance of each noise sample is σ_v^2. Furthermore, the data symbols and noise samples are assumed statistically uncorrelated. By substituting (151.3) into $\mathbf{e}_d(n)$, and applying the intrablock ZF equalization criterion, i.e., $\mathbf{G}\mathbf{U}_d\mathbf{F} = \mathbf{I}_M$, where $\mathbf{I}_M$ is the identity matrix of dimension M, the covariance matrix of the error $\mathbf{e}_d(n)$, defined as $\mathrm{R}_{ed} = E[\mathbf{e}_d(n)\mathbf{e}_d^H(n)]$ is given by

$$\mathbf{R}_{ed}(\mathrm{ZF}) = \mathbf{G}\mathbf{R}_{vd}\mathbf{G}^H \tag{151.4}$$

where $\mathbf{R}_{vd} = E[\mathbf{v}_d(n)\mathbf{v}_d^H(n)]$ is the $M \times M$ covariance matrix of the oblique-projected noise $\mathbf{v}_d(n)$ of (151.3).

For an N-ary QAM constellation (assuming that a Gray mapping from bits to symbols is used), the average BER for intrablock ZF equalization criterion (under block-by-block disjoint detection, as described above) is approximately given by [5]

$$\bar{P}_{ae(\mathrm{ZF})} \cong \frac{\alpha}{M}\sum_{i=0}^{M-1} erfc\left(\sqrt{\beta^{-1}[\mathbf{R}_{ed(\mathrm{ZF})}]_{ii}^{-1}}\right) \tag{151.5}$$

where $\alpha = 2(1 - 1/\sqrt{N})/\log_2 N$, and $\beta = 2(N-1)/3$ are constants for a given N, $erfc(\zeta) := (2/\sqrt{\pi})\int_\zeta^\infty e^{-x^2}dx$ and the $[\mathrm{R}_{ed(\mathrm{ZF})}]_{ii}$ represents the ith diagonal element

of $\mathrm{R}_{ed(\mathrm{ZF})}$ of (151.4) for $0 \le i \le M-1$. When $[\mathrm{R}_{ed(\mathrm{ZF})}]_{ii}$ in (151.5) is reasonably small, $\bar{P}_{ae(\mathrm{ZF})}$ is a convex function of $[\mathrm{R}_{ed(\mathrm{ZF})}]_{ii}$ [5]. Consequently, the proposed optimum d and $\mathbf{F}$ are devised to minimize (and simultaneously achieve) the lower bound of $\bar{P}_{ae(\mathrm{ZF})}$ of (151.5), subject to a bound P_T on the average transmission power, given by $\mathrm{tr}(\mathbf{F}\mathbf{F}^H)$, where $\mathrm{tr}(\cdot)$ stands for the trace of a matrix. Moreover, by using the facts that the lower bound of $\bar{P}_{ae(\mathrm{ZF})}$ is achieved if and only if the diagonal elements of $\mathrm{R}_{ed(\mathrm{ZF})}$ are equal, and that minimizing the lower bound of $\bar{P}_{ae(\mathrm{ZF})}$ involves minimizing the $\mathrm{tr}(\mathrm{R}_{ed(\mathrm{ZF})})$, the design problem of our target is

$$\begin{aligned} &\min_{\mathbf{F},d} \mathrm{tr}(\mathrm{R}_{ed(\mathrm{ZF})}) \text{ subject to, } \mathrm{tr}(\mathbf{F}\mathbf{F}^H) \le P_T, \\ &\text{and } \mathrm{R}_{ed(\mathrm{ZF})} \text{ being an equal-diagonal matrix.} \end{aligned} \tag{151.6}$$

Section 151.2.3 provides the optimum designs of d and $\mathbf{F}$ for the problem of (151.6).

151.2.3 BER-Minimized Block Delay for Intrablock ZF Equalization

The following Theorem 1 is established to the optimum d of (151.6).

Theorem 1 *Let* $\mathscr{H} = \mathbf{K}\boldsymbol{\Delta}\boldsymbol{\Gamma}$ *be the singularvalue-decomposition (SVD) [6] of* $\mathscr{H}$ *with* $\boldsymbol{\Delta} = [\bar{\Delta}, \mathbf{O}_{(QM+K)\times[Q(P-M)-K]}]^T$, *where* $\bar{\Delta}$ *is a positive-diagonal square matrix of dimension* $(QM+K)$; $\mathbf{K}$ *and* $\boldsymbol{\Gamma}$ *are unitary matrices of dimension* QP *and* $(QM+K)$, *respectively. For intrablock ZF equalization criterion the optimum BER-minimized block delay of the design problem of* (151.6) *is given by*

$$d_{\mathrm{BER-min}}^{\mathrm{ZF}} = \arg \min_{0 \le d \le du-1} \left(\sum_{i=0}^{M-1} [\boldsymbol{\Gamma}_d]_i^H \bar{\Delta}^{-2} [\boldsymbol{\Gamma}_d]_i \right), \tag{151.7}$$

where $d_u = \lfloor (QM+K)/M \rfloor$ *with* $\lfloor \rfloor$ *being floor-integer, and* $\boldsymbol{\Gamma}_d$ *denotes the* $(d+1)$th *block of* M *columns of* $\boldsymbol{\Gamma}$; $[\mathbf{A}]_i$ *denotes the* ith *column of matrix* $\mathbf{A}$.

Proof The proof resembles the derivations in Theorems in [4] and [7].

Once the BER-minimized block delay of (151.7) is obtained, the optimum $\mathbf{W}_d$ of (151.2) and the signal model of (151.3) can be constructed according to $d_{\mathrm{BER-min}}^{\mathrm{ZF}}$. Consequently, the associated optimum $\mathbf{F}$ and $\mathbf{G}$ for detecting the BER-minimized block of symbols can be obtained by substituting the $d_{\mathrm{BER-min}}^{\mathrm{ZF}}$ into the design problem of (151.6) and applying the results of [5].

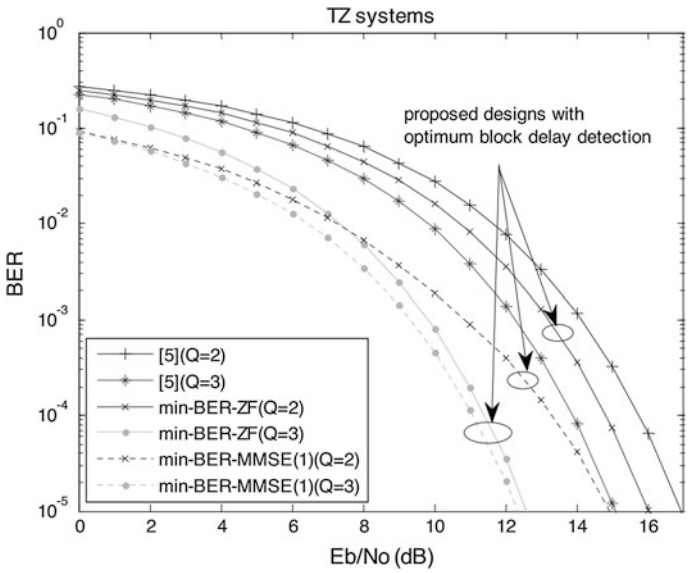

Fig. 151.1 Average BER performance for 200 randomly generated channels

151.3 Computer Simulations

In this section, simulations, in terms of BER, are conducted to verify the optimum designs in Sect. 151.2 under existing IBI cases. The systems with $(P, M, L) = (18, 16, 6)$, redundancy in the form of TZ, and 4-ary QAM modulation were considered through randomly generated FIR channels, each is of a unit-2 norm. The BER curves of the proposed designs, denoted by min-BER-ZF, were theoretically calculated based on (151.5). Moreover, the BER performances of our previous proposed designs with intrablock MMSE equalization of [4], denoted by min-BER-MMSE (151.1), were sketched for comparison. For insight into the effect of different block delay, the BER curves for the designs of min-BER-MMSE (151.2) and min-BER-MMSE (151.3) (i.e., the MMSE designs in [4] that use the block delays with $r_d = M$ and the proposed $d^{\mathrm{ZF}}_{\mathrm{BER-min}}$ of (151.7), respectively) are also illustrated.

Figure 151.1 shows that our min-BER-ZF and min-BER-MMSE (151.1) designs could improve BER performance of the min-BER design in [5]. The min-BER-MMSE (151.1) design outperformed our min-BER-ZF design near 1.8 dB at a BER of around 10^{-4} for $Q = 2$. Similar results exhibited as Q was increased from 2 to 3. As illustrated in Fig. 151.1, the proposed min-BER-MMSE (151.1) design achieved the best performance throughout the E_b/N_0 range for $Q = 2$ and $Q = 3$, respectively. Additionally, the BER curve of our min-BER-MMSE design approached that of our min-BER-ZF design as E_b/N_0 was increased for $Q = 2$ and $Q = 3$, respectively. This finding does not clearly exhibit in previous works,

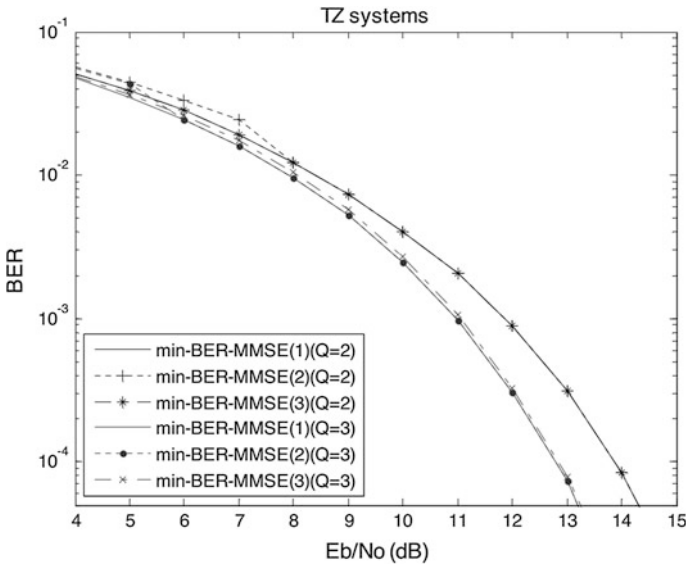

Fig. 151.2 Comparison of the various MMSE designs for one randomly generated channel

especially the cases of existing IBI. Figure 151.2 captured BER curves of the above MMSE designs for one channel realization of Fig. 151.1. According to Fig. 151.2, the min-BER-MMSE (151.2) and the min-BER-MMSE (151.1) designs achieved almost identical BER performance in moderate-to-high E_b/N_0 range for $Q = 2$ and $Q = 3$, respectively, despite the fact that the min-BER-MMSE (151.2) design failed to perform as well as the other two MMSE designs in low E_b/N_0 range. In contrast, the BER curve of min-BER-MMSE (151.3) was tightly close to that of min-BER-MMSE (151.1) throughout the E_b/N_0 range for =2 and =3, respectively, within 0.1 dB at a given BER.

151.4 Conclusions

In this paper, for intrablock ZF equalization criterion the algorithm has been built in Theorem 1 for directly calculating the BER-minimized block delay once the CSI is obtained. Since the optimum block delay of Theorem 1 is calculated without transmission power constraint, it can be used for a sub-optimum MMSE transceiver design that exhibits almost as well as the optimum one, as shown in simulations. Applying the proposed transceiver design to power-limited cooperative communication networks presents a potential research direction.

Acknowledgments The authors would like to thank National Science Council (NSC) of R. O. C., Taiwan, for partly financially supporting this research under Contracts No. NSC 100-2221-E-468-015, 101-2221-E-468-002, and 102-2221-E-468-002.

References

1. Kaleh, G. K. (1995). Channel equalization for block transmission system. *IEEE Journal on Selected Areas in Communications, 13*, 110–121.
2. Scaglione, A., Giannakis, G. B., & Barbarossa, S. (1999). Redundant filterbank precoders and equalizers—Part I: Unification and optimal designs. *IEEE Transactions on Signal Processing, 47*, 1988–2006.
3. Wu, C. H. (2011). The precoder design for intrablock MMSE equalization and block delay detection with a modified oblique projection framework. *IEICE Transactions on Fundamentals*, *E94-A*(2), 829–832.
4. Wu, C. H. (2012). Algorithm of determining BER-minimized block delay for joint linear transceiver design with CSI. *IEICE Transactions on Fundamentals*, *E95-A*(3), 657–660.
5. Wu, C. H., & Chern, S. J. (2007). Minimum BER block-based precoder design for zero-forcing equalization: An oblique projection framework. *IEEE Transactions on Signal Processing, 55*(12), 5630–5642.
6. Golub, G. H., & Loan, C. F. V. (1989). *Matrix computations* (2nd ed.). Baltimore, MD: John Hopkins University Press.
7. Wu, C. H. (2013). On the study of a novel decision feedback equalizer with block delay detection for joint transceiver optimization. *IEICE Transactions on Communications*, *E96-B*(3), 737–748.

Chapter 152
Modeling and Characterization of the Thermal Behavior of SiGe-HBTs

Shu-Hui Liao

Abstract In this paper, an accurate characterization method of the thermal impedance of silicon on insulator (SOI) technology silicon–germanium (SiGe) heterojunction bipolar transistors (HBTs) is proposed. The impact of electrical behavior and self-heating effects based on physical simulation and electrical characterization were analyzed in several different areas. Various aspects of the optimization of device performances are described. All the results of investigation are used for designing and optimizing Si/SiGe HBTs on SOI devices performance.

Keywords Self-heating effects · Silicon-on-insulator · SiGe HBTs

152.1 Introduction

SiGe is a significant enabling technology for the realization of integrated circuits used in high performance optical networks and radio frequency applications. The fabrication of SiGe base bipolar transistors on silicon-on-insulator (SOI) substrates offers several benefits that are important for high speed circuit performance. SiGe BiCMOS with SOI technology is one of the preferable platforms for wireless and communication application. It is widely used for low-power, high-speed and large-dynamic range RF application such as 3G wireless and fiber-based circuits design. Many research results have demonstrated that a SiGe based bipolar transistor on thin-film SOI substrate can offer a higher base–collector breakdown voltage (BV_{CEO}), higher Early voltage (V_A), and a better BV_{CEO}-f_T trade-off [1–4]. However, these advantages usually come with self-heating due to the low thermal conductance of the buried oxide where the heat generated at the base/collector

S.-H. Liao (✉)
Department of Electronic Engineering, Chung Chou University of Science and Technology, Changhua 51003, Taiwan, Republic of China
e-mail: liao@dragon.ccut.edu.tw

J. Juang et al. (eds.), *Proceedings of the 2nd International Conference on Intelligent Technologies and Engineering Systems (ICITES2013)*, Lecture Notes in Electrical Engineering 293,
DOI: 10.1007/978-3-319-04573-3_152,

junction must be conducted away from the active device area or else the device will be operated at some higher temperature that would reach a special circumstance on its performance as well as reliability.

In this work, SiGe base bipolar transistors on thin-film SOI substrates are considered. Two-dimensional numerical simulation of heat transfer was verified by the semiconductor device simulator DESSIS-ISE [5] to investigate the severe thermal effects and thus thermal instability problem resulting from the poor thermal conductivity of the buried oxide layer.

152.2 Device Characteristics and Simulation Methods

The schematically illustrated structure of the npn SiGe base bipolar transistors on thin-film SOI substrates discussed in this work is shown in Fig. 152.1. Four main variables, including the buried oxide thickness T_{OX}, the width of the emitter W_E, the silicon thickness T_{Si}, and the distance from n^+ reach-through to the intrinsic SiGe base L_{col}, were identified with the potential effect on the device performance of the SiGe base bipolar transistors on thin-film SOI substrates. These four variables were studied within the overall device design of an SOI bipolar transistor structure because this is one of the designs that has been shown to give better high quality device performance. Uniform doping concentrations 1×10^{20}, 1×10^{18}, 1×10^{17}, and 1×10^{15} cm^{-3} were used in the emitter, the base, the collector, and the substrate of the device, respectively. Moreover, the doping concentrations of p^+-extrinsic base region, n^+-reach-through region and n^+ -sub-collector region are all allowed of 1×10^{20} cm^{-3}.

All the simulations in this work are made by a two-dimensional electrical device simulator DESSIS-ISE. The system of differential equations comes from solving the Boltzmann transport equation. Drift–diffusion model is for isothermal simulations with stationary transport in low power density devices with long active regions. Thermodynamic model extends the drift–diffusion approach to account for electro-thermal effects under the assumption that the charge carriers are in thermal equilibrium with the lattice. Thermodynamic model is taken into account for self-heating effects in high power-density with long active regions. The drift diffusion approximation and thermodynamic approximation models were used for solving the carrier continuity and Poisson's equation. The simulator allows for simultaneous solution of the Poisson's equation, the continuity equation for electrons and holes, and the heat flow equation.

Thermal resistance is a mathematical concept analogous to the electrical resistance. Several methods have been proposed and employed to characterize the thermal resistance R_{Th}. Some of these studies have focused on measurement-based extractions, while others have focused on measurement and modeling of the devices [6–10]. Thermal resistance is the junction temperature $T_{junction}$ rise relative to the ambient temperature due to certain power dissipation inside a transistor.

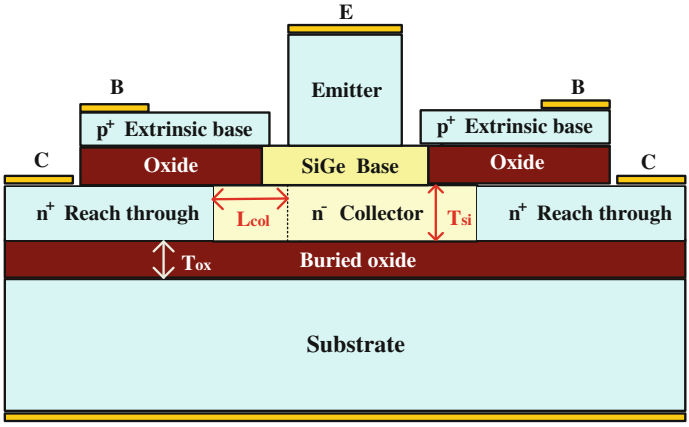

Fig. 152.1 Schematic cross-section of a SiGe base bipolar transistor on thin-film SOI substrate

$$T_{junction} = T_{ambient} + R_{Th} \times P_{diss} \tag{152.1}$$

where R_{Th} is the thermal resistance and P_{diss} the power dissipation inside a transistor.

DESSIS-ISE simulation software was used to compute the temperature distribution from the given power. A program was used to average the temperature distribution over the area of base–collector junction. Finally, the thermal resistance was obtained by Eq. (152.1). As a consequence, the self-heating characteristics of the SiGe base bipolar transistors on thin-film SOI substrates can be achieved.

152.3 Modeling Results and Discussion

Figure 152.2 give the display of two dimension temperature distributions of SiGe base bipolar transistors on thin-film SOI. Figure 152.3 shows a plot of the simulated lattice temperature evolution for the device as a function of device depth on the same structure. This performance evolution is then explained by the increased self-heating of the SiGe base bipolar transistor on SOI substrate which presents much higher temperature where the buried oxide serves as an effective blockade of the heat generated from the device itself, thus increases the thermal resistance.

The impact of self-heating effects in SiGe base bipolar transistors on SOI substrates can be analyzed in several different areas. Figure 152.4 gives the effect of emitter width on the variation of thermal resistance for a fixed buried oxide thickness of 0.1 μm. It was found that the thermal resistance was reduced by ~37.89 % when the emitter width was increased by a factor of 5. As the effective emitter width needs to be small enough to minimize collector current crowding effects, too much wider emitter width is forbidden. The self-heating effect as a

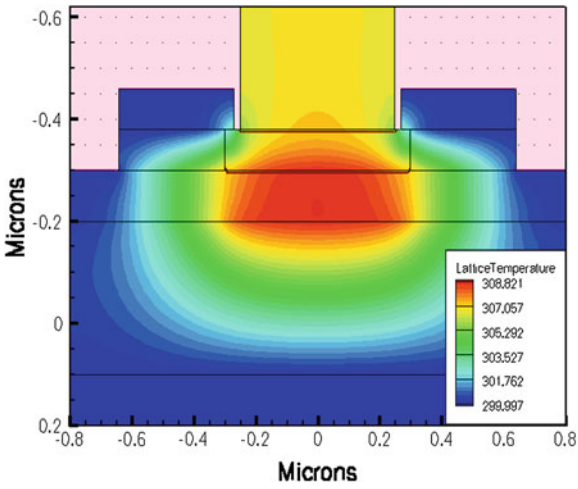

Fig. 152.2 Two-dimensional temperature profile of a *SiGe base bipolar transistor* on thin-film SOI substrate. The buried oxide thickness is 0.30 μm and the distance from n^+ reach-through to the edge of the intrinsic base L_{col} is 0.05 μm

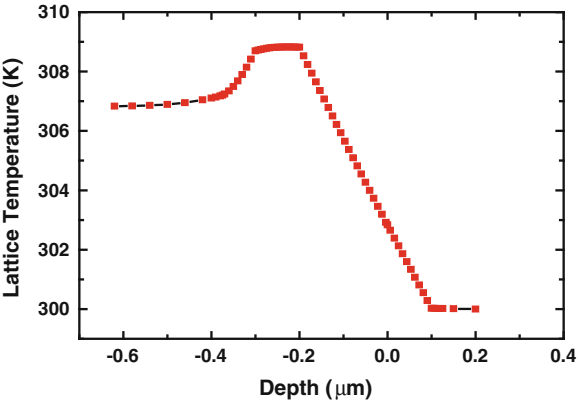

Fig. 152.3 Simulated lattice temperature of SiGe base bipolar transistor on thin-film SOI substrate as a function of device depth. The buried oxide thickness is 0.30 μm and the distance from n^+ reach-through to the SiGe base L_{col} is 0.05 μm. Moreover, cut is taken through the *center* of emitter

function of the silicon thickness is shown in Fig. 152.5. It was found that the thermal resistance decreases with the increase of silicon thickness. Finally, the effect on the plot of the distance of L_{col} was investigated. Figure 152.6 shows the characteristics of L_{col} and thermal resistances with different buried oxide thickness values of 0.05, 0.10, 0.15, and 0.30 μm, respectively. It was found that the tendency of different buried oxide thickness toward the same trend. However, as the n^+-reach-through region plays an important role in the performance of the device, the distance from the n^+-reach-through region to the SiGe base region must be minimized to avoid RF performance losses due to transiting time or series resistance effects [11]. This proves that enabling a short distance of L_{col} is necessary and there is a trade-off in L_{col}.

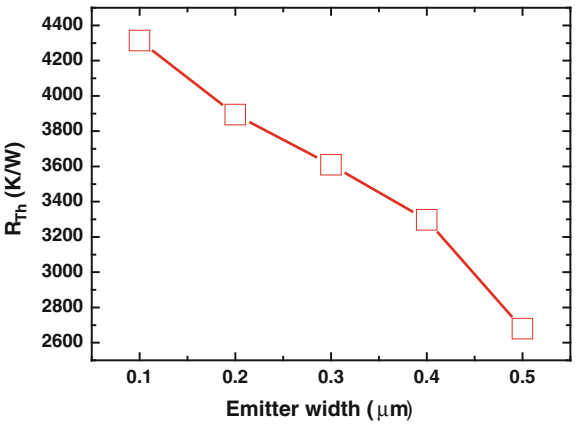

Fig. 152.4 The effect of emitter width to the variation of thermal resistance for a fixed buried oxide thickness of 0.1 μm. It was found that the thermal resistance is reduced by ∼37.89 % when the emitter width is increased by a factor of 5

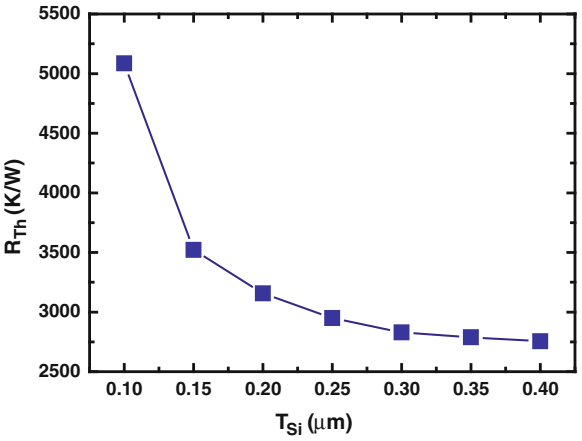

Fig. 152.5 Thermal resistance R_{Th} as a function of silicon thickness T_{Si}. R_{Th} of the transistor degrades when T_{Si} increases

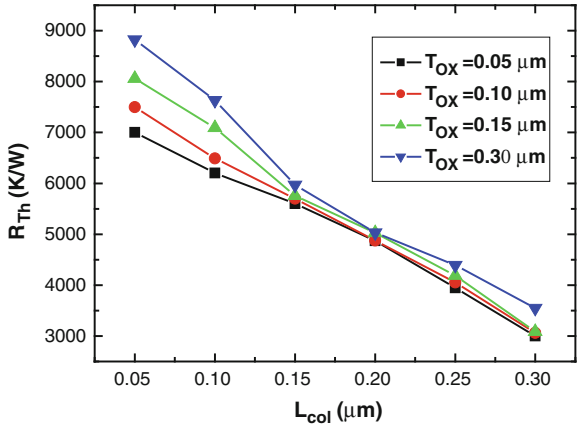

Fig. 152.6 The characteristics of L_{col} and thermal resistance R_{Th} for different buried oxide thickness, respectively

152.4 Conclusions

A comprehensive analysis of the self-heating effect of the single-finger SiGe base bipolar transistor on thin-film SOI substrate has been characterized. The key factors and interactions affecting the thermal resistance were evaluated in detail. The simulated results have shown that the buried oxide thickness is of benefit to optimize and better understand the performance of the device. In addition, the enhancement of silicon thickness can degrade the thermal resistance and thus needs to be carefully considered in the device design. As the effective emitter width must be small enough to minimize collector current crowding effects, too wider emitter width is forbidden. As a consequence, the results of this work can be suggested as an effective means for optimizing the thermal design of bipolar transistors fabricated in SOI technology.

References

1. Cai, J., Ajmera, A., Ouyang, C., Oldiges, P., Steigerwalt, M., Stein, K., et al. (2002). Fully-depleted-collector polysilicon-emitter SiGe-base vertical bipolar transistor on SOI. In *2002 Symposium on VLSI Technology, Digest of Technical Papers* (pp. 172–173).
2. Avenier, G., Schwartzmann, T., Chevalier, P., Vandelle, B., Rubaldo, L., Dutartre, D., et al. (2005). A self-aligned vertical HBT for thin SOI SiGe BiCMOS. In *Proceedings of IEEE BCTM* (pp. 128–131).
3. Chantre, A., Avenier, G., Chevalier, P., Vandelle, B., Saguin, F., Maneux, C., et al. (2006). SiGe HBT design for CMOS compatible SOI. In *Proceedings of ISTDM* (pp. 268–269).
4. Chevalier, P., Barbalat, B., Rubaldo, L., Vandelle, B., Dutartre, D., Bouillon, P., et al. (2005). 300 GHz f_{max} self-aligned SiGeC HBT optimized towards CMOS compatibility. In *Proceedings of IEEE BCTM* (pp. 120–123).
5. DESSIS-ISE (2004). ISE-TCAD Release 10.0, User's Manual, Zurich.
6. Ganci, P. R., Hajjir, J. -J. J., Humphrise, C. T. P., Lapham, J., & Buss, D. (1992). Self-heating in high-performance bipolar transistors on SOI substrates. In *IEDM Technical Digest* (pp. 417–420).
7. Mastrapasqua, M., Palestri, P., Pacelli, A., Celler, G. K., Frei, M. R., Smith, P. R., et al. (2002). Minimizing thermal resistance and collector-to-substrate capacitance in SiGe BiCMOS on SOI. *IEEE Transactions on Electron Device Letters, 23*, 145–147.
8. Vanhoucke, T., Boots, H. M. J., & Van Noot, W. D. (2004). Revised method for extraction of the thermal resistance applied to bulk and SOI SiGe HBTs. *IEEE Electron Device Letters, 25*, 150–152.
9. Li, H., Ma, Z., Ma, P., & Racancelli, M. (2007). Thermal resistance of SiGe HBTs at high power densities. *Semiconductor Science and Technology, 22*, S68–S71.
10. Nigrin, S., Armstrong, G. A., & Kranti, A. (2007). Optimisation of trench isolated bipolar transistors on SOI substrates by 3D electro-thermal simulations. *Solid-State Electronics, 51*, 1221–1228.
11. Chantre, A., Avenier, G., Boissonnet, L., Borot, G., Bouillon, P., Brossard, F., et al. (2006). Prospects for complementary SiGeC BiCMOS on thin-film SOI. *ECS Transactions, 3,* 355–363.

Chapter 153
Design of Maximum Efficiency Two-Axis Sun Tracking System for Universal PV Panels

Yoko Amano

Abstract The solar energy extracted from photovoltaic (PV) panels depends on solar insolation, as a general rule, the PV panel is always being normal to the incident radiation, however, the best incident angle to obtain the maximum solar energy is various, since protective sheets of PV panels use different materials by manufactures. In this paper, design of Maximum Efficient Two-Axis (META) sun tracking system for universal PV panels is firstly proposed. The META sun tracking system can move any PV panel to follow the sun trajectories and keep the best incident angle, so that solar energy efficiency can be substantially improved. In this work, an automatic two-axis sun tracking system has been designed using photo sensors and a current sensor on a mechanical structure with two DC motors for adjusting the tilt and azimuth angle of the PV panel. The maximum hourly electrical power of the META sun tracking system has been evaluated and compared traditional sunflower type sun tracker.

Keywords Maximum solar energy · Sun tracking system · Photovoltaic power generation · Multiple sensor system

153.1 Introduction

The increasing energy dependence, limited sources of the fossil fuels, their increasing prices, and the negative environmental impacts force mankind to improve the utilization of the available renewable energy sources. Solar energy is rapidly advancing as an important means of renewable energy resource in many

Y. Amano (✉)
Department of Electrical and Electronics Engineering, Graduate School of Electrical and Electronics Engineering, College of Engineering, Nihon University, Koriyama 963-8642, Japan
e-mail: amano@ee.ce.nihon-u.ac.jp

J. Juang et al. (eds.), *Proceedings of the 2nd International Conference on Intelligent Technologies and Engineering Systems (ICITES2013)*, Lecture Notes in Electrical Engineering 293,
DOI: 10.1007/978-3-319-04573-3_153,

applications like thermal energy storage systems and electric power generation systems. Such systems use collectors in the form of optical reflectors or photovoltaic (PV) modules to collect the solar energy. The average solar energy intercepted by a fixed PV during the whole day, is less than maximum attainable. This is due to the static placement of the PV which limits their area of exposure to direct solar radiation. More energy can be extracted in a day, if the PV is installed on a tracker with an actuator that follows the sun. The automatic two-axis sun tracking systems with open-loop or closed-loop are presented in [1–4], and confirmed efficiency than the fixed PV. But, these sun tracking systems are only like sunflowers, and can not up more efficiency. It could not compensate for disturbances and has low accuracy.

This paper proposes the design and construction for Maximum Efficiency Two-Axis (META) sun tracking system with photo sensors and a current sensor, a closed loop mechanism overcomes the issues related to cloudy or rainy weather conditions.

In the present work, a two-axis solar tracking system has been designed and built using sensors and two DC motors, a maximum efficiency sun tracking control has been implemented. The performance of the META sun tracking system has been evaluated for important parameters like solar energy received by the PV panel, hourly maximum output powers have been compared with sunflower type sun tracker and improvements have been justified through the experimental result analysis.

153.2 Description of the Proposed Sun Tracking System

The complete configuration of the META sun tracking system is illustrated in Fig. 153.1. An arrangement for placing the photo-sensor module has been made in a plane parallel with the PV panel. Two DC motors that are a tilt DC motor and an azimuth DC motor with gears are used to obtain required torque, and electrical driver circuits to move the DC motors for changing the PV panel's position. A note PC including the sun tracking control algorithm connects with the two-axis sun tracking equipment by a USB-I/O device.

153.2.1 Mechanical Constitutions of META Sun Tracking

A mechanical constitution of the META sun tracking is presented in Fig. 153.2, where β is a tilt angle, while α is an azimuth angle of the PV panel. The upper part changes the tilt angle β into the direction of north–south, while the lower part changes the azimuth angle α into the direction of east–west.

The torque required to modify both the angles is generated by the tilt DC motor and the azimuth DC motor supplied from 12 V battery. The gear ratio of the tilt

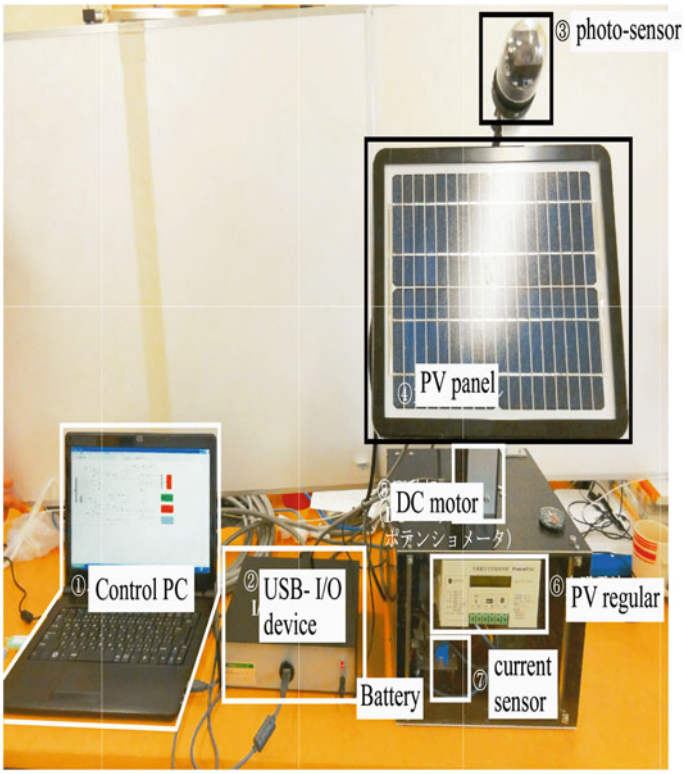

Fig. 153.1 Configuration of the proposed sun tracking system

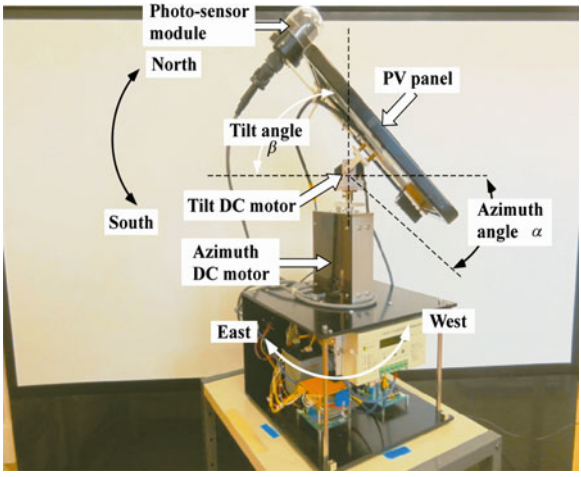

Fig. 153.2 Mechanical constitution of the META sun tracking

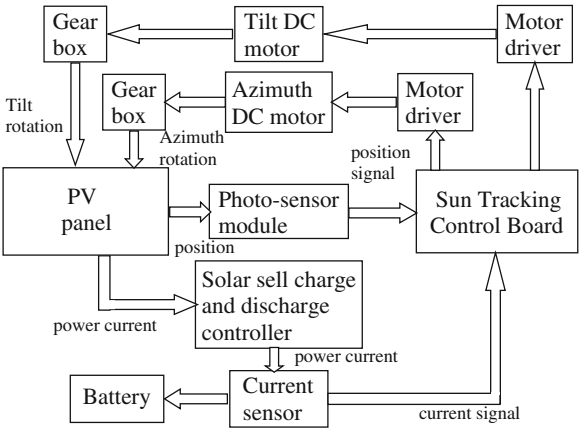

Fig. 153.3 Schematic block diagram of the proposed sun tracking system

DC motor gearbox shown in Fig. 153.3 for shifting the tilt angle β is 12:40:25, while the gear ratio for shifting the azimuth angle α is 12:50:35.

The PV panel with the total mass of 1.8 kg, the rated maximum power of 10 W, the rated open voltage of 21.7 V, the rated short current of 0.64 A.

153.2.2 META Sun Tracking System Process

The META sun tracking system accommodates both degrees of freedom; azimuth and tilt, schematic block diagram of the META sun tracking system is shown in Fig. 153.3. The photo-sensor module with four photo sensors is used and thus is implemented in both degree of freedom. If one of photo sensors gets more light intensity than the pair other, note the voltage difference will receive as an analog signal at an Analog–Digital Converter (ADC) channel of the sun tracking control board. The sun tracking control analyzes this date and generates a drive digital signal to actuate the relative motor to move the photo-sensor module as a position where equal light is being illuminated in the pair of the photo sensor. So that, the drive digital signal from the sun tracking control is for azimuth as well as the tilt tracking and the motor rotation in either clockwise or anti-clockwise direction depending on the shadow by the photo-sensor module due to rectangular metal sheet.

When all the four photo sensors are equally illuminated by the sun, then the analog voltage signals received on the ADC channel will have equal values and the sun tracking control will not generate any drive digital signal to actuate the DC motors.

On the other hand, Metal-Oxide Silicon Field-Effect Transmitter (MOSFET) has been used as DC motor driver to amplify the current level of the movement of the DC motor with the gearbox and to achieve the desired speed of the DC motors.

If the four photo sensors are equally illuminated by the sunshine, a current sensor measures a powerful current from the PV panel through a solar sell charge and discharge controller that protects the solar cells in the PV panel. In order to get the maximum power current from the current sensor, the tilt DC motor moves by north and south 5°, and by 0.1° is changed to get the maximum current. Then the azimuth DC motor by east and west 5°, and by 0.1° changes until the maximum current have already once obtained, the all two DC motors stop in this position of the PV panel.

153.2.3 Flow Chart of Sun Tracking Control

The currently implement algorithm of the Maximum Power Point Tracking (MPPT) is shown in Fig. 153.4, this algorithm is described as *hill-climbing*. It is based on the measurement of the light intensity from the PV panel by the photo sensors, for two different of the east part and the west part set-point voltages Ve (t) and Vw (t), respectively.

If the Ve (t) > Vw (t) at the level (A) shown in Fig. 153.4, the PV panel is moved to east by the azimuth DC motor. On the other way, the Ve (t) > Vw (t) is not at the level (B), the PV panel is turned to west direction.

When Ve (t) = Vw (t) is brought at the level (C), it comes the next process that the PV panel is moved by the tilt DC motor on the same way.

The aforementioned activeness is done at "photo sensor worked" shown in Fig. 153.4. Now, at the level (D), the power current from the PV panel measured by the current sense to get the current i_{max}, and the tilt DC motor moves by north and south to obtain the maximum power current i_T from the PV panel. If $i_T > i_{max}$ is confirmed, setting $i_{max} = i_T$ at the level (E), and the azimuth DC motor moves by east and west to get the maximum power current from the PV panel. When $i_A > i_{max}$ is checked, and setting $i_{max} = i_A$ at the level (F), and holding the position of the PV panel according to MPPT algorithm.

153.2.4 Experimental Simulink Model

The experimental Simulink model of the META sun tracking control system for an actual machine test is shown in Fig. 153.5. The voltages from the azimuth photo sensors are compared in a block of the azimuth photo sensors, and are checked as $V_n\ (t) = V_s\ (t)$, according to the flow chart shown in Fig. 153.4, the azimuth DC motor moves by north–south until voltages $V_n\ (t) = V_s\ (t)$. In the same way, another block of the tilt photo sensors drives the tilt DC motor to getting voltages $V_e\ (t) = V_w\ (t)$.

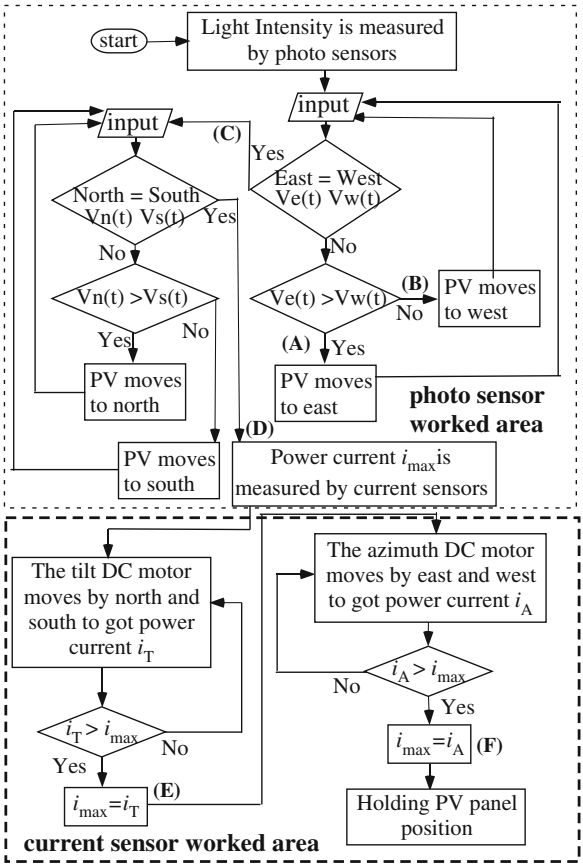

Fig. 153.4 Flow chart of the META sun tracking control to MPPT algorithm

For obtaining maximum solar energy, the block of the current sensor one more time moves the two DC motors to set the PV panel as the best incident angle. The ADC and the USB-I/O of Fig. 153.5 joint the actual machine shown in Fig. 153.2.

153.3 Experimental Results

In order to verify the performance of the META sun tracking system, the experimental setup is shown in Fig. 153.6, the illumination by turning on an adjustable lamp corresponds to three irradiance that are 8, 12 and 16 W/m^2.

Figure 153.7 shows generated power from the PV panel under the three irradiance using the META sun tracking system shown in right column graphs, and the sunflower type sun tracker shown in lift column graphs. The generated power to the META sun tracking system has got up about 50 % than the sunflower type sun tracker.

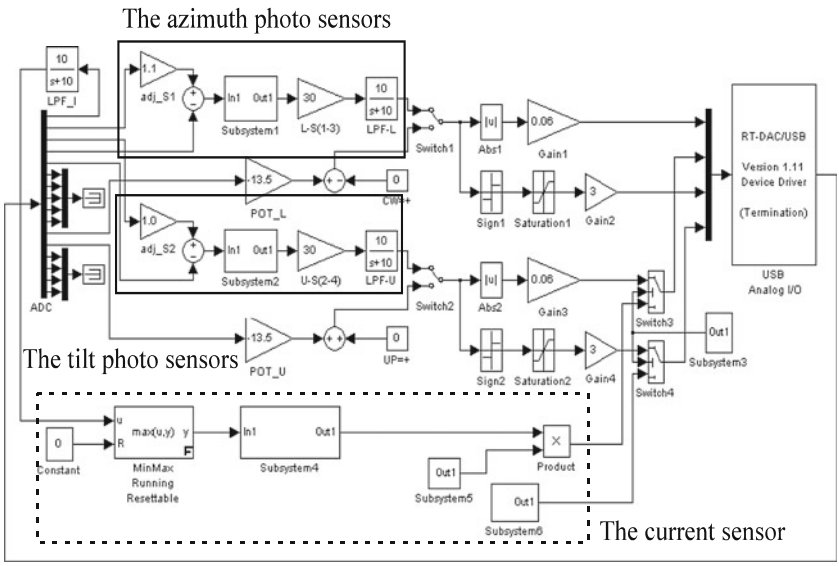

Fig. 153.5 Experimental Simulink model of the proposed sun tracking control

Fig. 153.6 Experimental setup

The control process with the flow chart shown by Fig. 153.4 is presented in Fig. 153.8. Firstly, the photo sensors measure sunlight intensity from 0 to 10 s to reach the level (D) shown in Fig. 153.3. Secondly, the current sensor finds the maximum power current from 10 to 20 s until getting the a stable maximum power

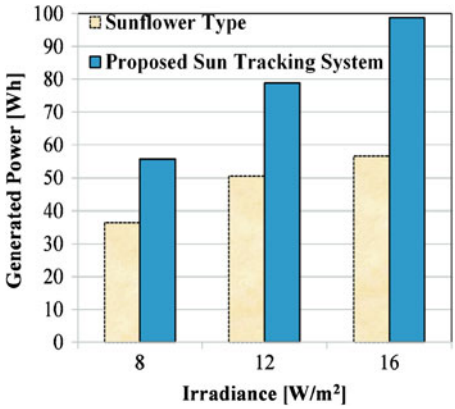

Fig. 153.7 Comparison of generated power with two type sun tracking

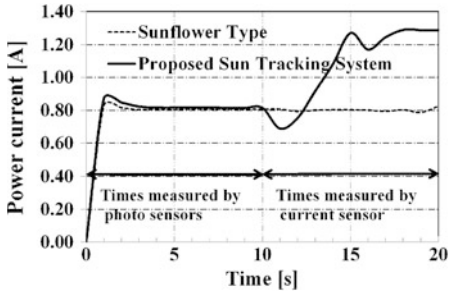

Fig. 153.8 Generated Power compared sunflower type with proposed sun tracking system

current. Since the tilt DC motor has moved about east–west and the azimuth DC motor have moved about north–south. From 10 to 13 s the measured power current is fall than sunflower type, but, from 13 to 20 s the maximum power current is measured about 50 % than the sunflower type sun tracker.

153.4 Conclusion

This paper proposes the new META sun tracking system for obtaining the maximum generated power from the universal PV panel, the maximum hourly electrical power of the META sun tracking system has been evaluated and compared traditional sunflower type sun tracker. In future, the utility of the META sun tracking system is confirmed by a large-capacity PV panel.

References

1. Vital, D., & Ricci, R. (2013) Design, testing and simulation of hybrid wind-solar energy systems, Doctoral School on Engineering Sciences.
2. Fei, X., & Guoxian Z. (2011) Simulation and analysis of computer control tracking system based on solar germaetric for fresnal lenses concentration photoviltics. In *Proceedings of IEEE Computer Society*.
3. Durgadevi, A., Arulselvi, S., & Natarajan, S. P. (2011) study and implementation of maximum power point tracking (MPPT) algorithm for photovoltaic systems. In *Proceedings of International Conference on Electrical Energy Systems*.
4. Vladimir, V. R., Simone, B., & Giorgio, S. (2009) Low-computer MPPT technique exploiting the PV model MPP locus characterization. IEEE on ISA Transactions.

Chapter 154
Current–Voltage Numerical Simulation of Organic Light Emitting Diodes with Dual-Layer Structures

Teh-Chao Liao, Hsueh-Tao Chou, Jeng-Hauh Yang, Yu-Sheng Tsai, Lin-Ann Hong and Chia-Hsiu Chang

Abstract The use of numerical simulation method to study the current–voltage (I–V) of organic light emitting diode (OLED) has always been an effective method to upgrade the luminous efficiency of OLED. As the I–V theoretical simulation equations are based on injected carrier passing through Schottky barrier, and considering that carrier capturing defect and carrier mobility rate might be generated within the inner organic layer of Pool–Frenkel model, the study had made a comparison between the I–V theoretical model with a double-layer device and the experimental data, and proposed the best parameters for the theoretical model after careful adjustment and comparison to establish an optimal simulated numerical model with a double-layer OLED current–voltage. Finally, a study was made on the carrier capturing defect and mobility rate affected by electric field and temperature.

T.-C. Liao (✉)
Department of Electro-Optics Engineering, National Formosa University, Yunlin 63201, Huwei, Taiwan, Republic of China
e-mail: techao@nfu.edu.tw

T.-C. Liao
Graduate School of Engineering Science and Technology,
National Yunlin University of Science and Technology, Yunlin 64002, Douliou, Taiwan, Republic of China

H.-T. Chou
Graduate School of Electronic Engineering,
National Yunlin University of Science and Technology, Yunlin 64002, Douliou, Taiwan, Republic of China

J.-H. Yang · Y.-S. Tsai · L.-A. Hong · C.-H. Chang
Institute of Electro-Optical and Materials Science, National Formosa University, Yunlin, Huwei 63201, Taiwan, Republic of China

J. Juang et al. (eds.), *Proceedings of the 2nd International Conference on Intelligent Technologies and Engineering Systems (ICITES2013)*, Lecture Notes in Electrical Engineering 293,
DOI: 10.1007/978-3-319-04573-3_154,

154.1 Introduction

To upgrade the luminous efficiency of OLED has always been the pursuing goal [1] for researchers. Currently, the development approach of OLED towards a multi-layer structure is a complex system [2]. Therefore, to establish the single- and double-layer organic light emitting devices through a theoretical simulation method with current–voltage characteristic-related simulation parameters is a feasible way to simplify [3] the development of OLED structures at lowest production costs.

The current–voltage characteristics of OLED are the key factors affecting the luminous efficiency of devices. Among them are metal electrodes, the size of energy gap, the injected carrier and the conduction mechanism of carrier. The carrier of organic light emitting devices (electrons and electron holes) will encounter charge injection problem on the interface between electrode and organic layer. The charge injection theory can be classified as thermal activation and tunneling effect, etc. [4–6]. When the charge has overcome the interfacial energy barrier and flown through the organic layer, it is known as charge spreading, its theory of which includes Ohmic's Law [7–9] space charge limited current (SCLC) [10] and injection charge limited current (ICLC) [11], etc. The study has found that the injection charge limited can only exist at low electric field range; and J-V characteristics can only be explained in high electric field range through equations quoted by simulated SCLC after considering that their electric densities would be affected by changes in defective charge density parameters and carrier mobility rate; as well as their electric densities would be affected by changes in carrier mobility rate and Poole–Frenkel effects.

A single-layer Alq_3 electron, single-layer NPB hole only, and double-layer NPB/Alq_3 light emitting devices were made by this study to compare with J-V characteristic curves and the simulated equations of light emitting devices. However, the parameter values had to be fine-tuned in order to find out the best simulated parameter values.

154.2 J-V Equations

The J-V behavior where carrier is being injected from metal to the organic layer has been studied by many scholars [10]. When the transmission of carrier is restricted by organic layer, it is known as Space Charge Limited Current (SCLC). The famous Mott-Gurney square law is shown as follow.

$$J_{SCLC} = \frac{9}{8}\mu\varepsilon\frac{V^2}{L^3} \tag{154.1}$$

Considering that the carrier would be captured due to the existing defects found in material, and the natural defects of heterogeneous or non-crystallize structure of

material, it is mandatory to consider the defective charge density (n_t) [5, 12] from charge density (n_f).

$$\theta = \frac{n_f}{n_f + n_t} = \frac{N_C}{N_t}\exp\left(-\frac{q\varphi_B}{kT}\right) \tag{154.2}$$

N_c Referred to as the effective density of energy state of conduction band
N_t Referred to as the electrons captured by defects.

The equation is then changed into [4]:

$$J_{SCLC} = \frac{9}{8}\mu\varepsilon\theta\frac{V^2}{L^3} \tag{154.3}$$

Following a change in external electric field, the traditional SCLC model is unable to fully explain the experimental data as a higher voltage will generate a higher experimental current density than the theoretical results obtained. In 1970, Pai et al. [13] detected that the carrier mobility rate was equivalent to electric field correlation function using TOF (time-of-flight) method under a high electric field condition. To enable the theoretical model to fully explain the carrier transmission condition under both low electric field and high electric field conditions, and taking Poole–Frenkel model and temperature factors into account, the mathematical equations of carrier mobility rate under a high electric field condition following the temperature and electric field changes are as follows.

$$\mu(E,T) = \mu_0\exp\left(-\frac{\Delta}{kT}\right)\exp\left[B\left(\frac{1}{kT_0} - \frac{1}{kT_0}\right)\sqrt{E}\right] \tag{154.4}$$

B Referred to as constants
μ_0 Referred to as the carrier mobility rate under zero electric field condition
Δ Referred to as the activation energy

$$\gamma = B\left(\frac{1}{k_aT} - \frac{1}{k_aT_0}\right) \tag{154.5}$$

γ Referred to as the Poole–Frenkel parameter.

Considering that the carrier mobility rate and current density will vary following a change in high electric field and temperature, we get the following equation after bringing (154.4) into (154.3).

$$J_{SCLC} = \frac{9}{8}\mu_0\varepsilon\theta\frac{V^2}{L^3}\exp\left(-\frac{\Delta}{kT}\right)\exp\left[B\left(\frac{1}{k_aT} - \frac{1}{k_aT_0}\right)\sqrt{\frac{V}{L}}\right] \tag{154.6}$$

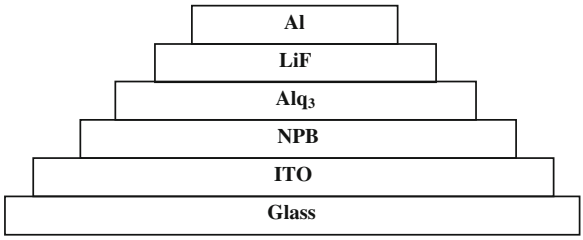

Fig. 154.1 The structural diagram of double-layer device energy band and the cross-sectional structure of the device

This is a quoted equation adopted by this study to simulate SCLC after considering that a change in defective charge density and carrier mobility rate would affect its current density.

154.3 Experiment

The material NPB (N,N'-dipheny1-N,N'-(2-napthy1)-4,4'-diamine) was used as the electron hole transmission material, Alq_3 [Tris (8-quinolinolato) aluminum] as the electron transmission material, LiF (lithium fluoride) as the electron injection material, and Al (aluminum) as the cathode material by the study. After ensuring that the vacuum chamber pressure had reached up to $\sim 10^{-5}$ torr, the electron hole transmission layer or electron injection layer, light emitting layer (or light emitting layer plus electron hole restricted layer), and electron transmission layer or electron injection layer were vapor deposited, respectively in sequence at a speed of 0.02–2.0 Å/s. The double-layer NPB/Alq_3 light emitting structure is shown in Fig. 154.1.

154.4 Results and Discussion

The SCLC theory was used by this thesis to simulate and study the current–voltage characteristics of OLED. Initially, the parameters of NPB and Alq_3 single-layer organic layer were extracted (the experimental data and theoretical calculations were compared and adjusted; and after adjusting some of the parameters, they were found to be able to allow the simulated values to get close to experimental values). The parameters used are shown in Table 154.1.

Then, SCLC theory was used to study the current–voltage characteristics of a double-layer NPB/Alq_3 OLED as shown in Fig. 154.1. With regard to the double-layer device simulation, the thickness of NPB material was fixed at 30 nm; and Alq_3 material, 60 nm. The simulation results of J-V characteristics are shown Fig. 154.2. The S1–S4 curve values were larger than experimental values (EXP). After adjusting the NPB material as $\Delta = 0.45$, the characteristic curve had

Table 154.1 The parameters used by NPB and Alq_3 in SCLC theoretical model

Mate.\Para.	ε_r	μ_0	Δ	θ	B
Alq_3	3	0.127	0.33	0.38	22.65×10^{-24}
NPB	2	54.7206	0.43	0.88	22.65×10^{-24}

(Δ: activation energy, θ: trapped charge density, B: field and temperature dependent mobility constant)

@NPB(30nm)-Alq_3(60nm)-LiF(0.8nm)-Al(150nm)

Para.\Curve	S1	S2	S3	S4	S5
Δ1	0.33	0.31	0.35	0.33	0.33
Δ2	0.43	0.43	0.43	0.41	0.45
θ1	0.88	0.88	0.88	0.88	0.88
θ2	0.38	0.38	0.38	0.38	0.38
B1	22.65	22.65	22.65	22.65	22.65
B2	34	34	34	34	34

@ A change in activation energy

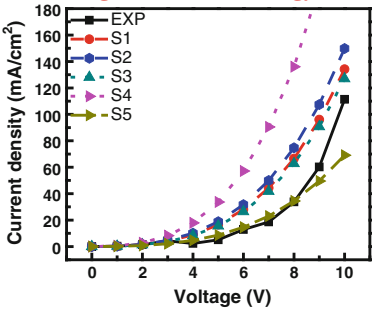

Fig. 154.2 The J-V characteristic *curves* of double-layer NPB (30 nm)/Alq3(60 nm) OLED

dropped to S5. When voltage was lower than 8 V in particularly, the simulated characteristic curve was very close to experimental value and such result was much similar to ohmic characteristics [14]. When voltage was higher than 8 V, the current appeared to be J-V^m and m > 2. This indicated that voltage would affect the activation energy, and the charge mobility rate would increase more obviously following an increase in electric field [15], causing the gradient of current–voltage characteristic curve to increase rapidly. When the NPB material was lowered as $\Delta = 0.41$, the current increased significantly as shown in curve S4. As the Alq_3 electron hole current that flew in from NPB took up the majority of total current, it would trapped the parameter θ of Alq_3 simulation values. When $\theta_2 = 0.38$ and NPB $\theta_1 = 0.88$, it indicated that the trapping states at NPB interface was more apparent, and so its values were much higher [14, 16].

Fig. 154.3. Showing the comparison of experimental data and simulation curves of double-layer NPB(45 nm)/Alq_3(60 nm) OLED. When the thickness of NPB had increased, an adjustment was made as $\Delta = 0.28$ to meet with the experimental values.

Fig. 154.4. Showing the comparison of experimental data and simulation curves related to temperature of double-layer NPB(45 nm)/Alq_3(55 nm) OLED. The experimental curves from temperatures 300–360 K, 330 K and 360 K appeared to be $J \propto V^m$, and among them, m > 2. The result showed that the higher the temperature, the greater would be m [17]. At temperature 360 K, the

@NPB(45nm)-Alq_3(60nm)-LiF(0.8nm)-Al(150nm)

Para.\Curve	S1	S6	S7
Δ1	0.33	0.28	0.28
Δ2	0.43	0.43	0.43
Θ1	0.88	0.88	0.88
Θ2	0.38	0.38	0.38
B1	22.65	22.65	20.65
B2	34	34	34

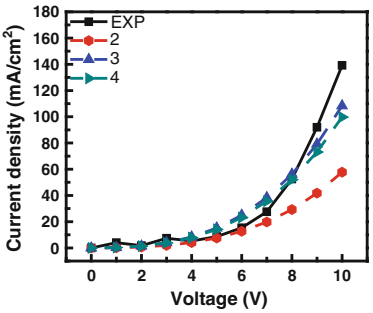

Fig. 154.3 The J-V characteristic *curves* of double-layer NPB (45 nm)/Alq3(60 nm) OLED

@NPB(45nm)-Alq_3(55nm)-LiF(0.8nm)-Al(150nm)

Para.\Curve	S-300k	S-330k	S-360k
Δ1	0.34	0.34	0.34
Δ2	0.43	0.43	0.43
Θ1	0.2	0.2	0.2
Θ2	0.8	0.8	0.8
B1	22.65	22.65	22.65
B2	34	34	34

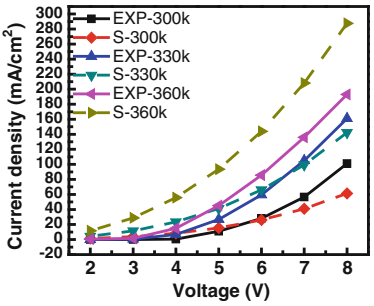

Fig. 154.4 The J-V characteristic *curves* of double-layer NPB (45 nm)/Alq3(55 nm) OLED under different environmental temperatures

simulation values were much larger than experimental values. The reason was that the predicted mobility rate of theoretical simulation was much greater than experimental results as affected by temperature factor (density and strength). Hence, the activation energy values had to be adjusted as $\Delta_2 = 0.44$–0.45.

154.5 Conclusions

The parameters Δ and θ in SCLC theoretical model were respectively adjusted to simulate the current–voltage characteristics of double-layer NPB/Alq_3 OLED. The simulated results were much easier to meet with experimental data under a low voltage range. The simulation results under 8 V were found to meet with experimental values. When the thickness of NPB had increased, it was necessary to adjust Δ to allow the simulated results to meet with experimental values. This

explains that the θ value will possibly change following an increase in the thickness of NPB (as the defects will affect the current parameters) and decrease the error. Under a high voltage condition when the carrier mobility rate was greater than low voltage, it would cause a large variance between simulation results and experimental values. But this also explains that we can simulate the current–voltage characteristics of OLED through simple adjustment of three parameters. As we are able to find out the best simulation values under different thicknesses and different environmental temperatures, the study serves as an important and valuable reference in future development of OLED.

Acknowledgments We would like to thank the National Science Council Republic of China, projects NSC-102-2221-E-150-066-MY2, for financial support.

References

1. Reineke, S.,Lindner, F., Schwartz, G., Seidler, N.,Walzer, K., Lussem, B., & Leo, K. (2009). White organic light-emitting diodes with flourescent tube efficiency. *Nature 459*, 234.
2. Juang, F.-S., Hong, L.-A., Wang, S.-H., Tsai, Y.-S., Yun Chi1, M.-H., Shieh2, H.-P., J.-S., Hsu. (2011) *Japanese Journal of Applied Physics 50* 04DK04.
3. Jang, S.E., Yook, K.S., Lee,J.Y. (2010). High power efficiency in simplified two layer blue phosphorescent organic light-emitting diodes. *Organic Electronics 11* 1154–1157.
4. Jeng-Hauh, Y. (2012). Study on carriers transport electrical characteristics in organic light-emitting diode. (pp. 9–12).
5. Sze, S. M. (1981). *Physics of semiconductor devices*. New York: Wiley.
6. Rhoderick, E. H., & Williams, R. H. (1988). *Metal-semiconductor-contacts*. Oxford: Clarendon.
7. Dongge, M., Hummelgen, I. A., Hu, B., & Karasz, F. E. (1999). *Applied Physics Letters, 86*, 3181.
8. He, Y., & Kanicki, J. (2000). *Applied Physics Letters, 76*, 661.
9. Ma, D., Hummelgen, I. A., Jing, X., Hong, Z., Wang, L., Zhao, X., et al. (2000). *Journal of Applied Physics, 87*, 312.
10. Lamberrt, M. A., & Mark, P. (1970). *Current Injection in Solids*. NewYork: Academic.
11. Lee, S. G., & Hattori, R. (2009). "Derivation of current-voltage equation for OLED using device simulation". In: *International Meeting on Information Display.*
12. Murgatroyd, P. N. (1970). Theory of space-charge-limited current enhanced by Frenkel effect. *Journal of Physics. D. Applied Physics, 3*, 151–156.
13. Pai, D. M. (1970). *J. Chem. Phys, 52*, 2285.
14. Yang, Jie, & Shen, Jun. (1999). *Journal of Applied Physics, 85*, 2699.
15. Staudigel, J., Stossel, M., Steuber, F., & Simmerer, J. (1999). *Applied Physics Letters, 75*, 217.
16. Cvikl, B. (2008). *Journal of Applied Physics, 104*, 113721.
17. Chu T-Y. Songa_, O-K., (2007). *Applied Physics Letter 91*, 073508.

Chapter 155
Comments on How a New Engineering Field Develops: A Case Study from Iterative Learning and Repetitive Control

Richard W. Longman, Khawla A. Alnajjar and Xiaoqiang Ji

Abstract Iterative learning control and repetitive control try to converge to zero tracking error in the real world while performing a repetitive task. They use the error from the previous run or period to adjust the command in the current run or period. Because they want zero error, they push to the limit all of the analysis tools of control theory. The development of the field has required an intricate interplay between theoretical developments, computer simulations, and experiments. Reviewing this interplay, it is clear that each of these approaches in isolation repeatedly come up with wrong conclusions, or wrong directions for research. Advancement of the field required an interplay between each of the approaches. The paper describes this interplay, and suggests that this is an important case study of what is generally required for new fields of engineering to develop to have a practical impact.

Keywords Iterative learning control · ILC · Repetitive control

155.1 Introduction

Iterative learning control (ILC) and repetitive control (RC) are two relatively new fields within control theory. ILC started developing fast in 1984 motivated by industrial robots doing repetitive operations. Feedback control systems do not do what you command them to do. The command determines a forcing function in a differential equation, and the associated particular solution is what the control

R. W. Longman (✉) · X. Ji
Department of Mechanical Engineering, Columbia University, New york, NY 10027, USA
e-mail: RWL4@columbia.edu

K. A. Alnajjar
Department of Electrical Engineering and Computer Engineering, Wireless Research Center, University of Canterbury, 8140 Christchurch, New Zealand

J. Juang et al. (eds.), *Proceedings of the 2nd International Conference on Intelligent Technologies and Engineering Systems (ICITES2013)*, Lecture Notes in Electrical Engineering 293,
DOI: 10.1007/978-3-319-04573-3_155,

system does. When repeatedly performing the same operation, ILC records the error and the command each run, and based on the error, modifies the command in the next run. The aim is to converge to zero tracking error. This can produce higher precision in manufacturing resulting in improved product quality, and can also allow higher speed operation resulting in increased productivity. In ILC the control system returns to the same starting position before each new run. RC is similar to ILC, but applies to control systems that perform a periodic command and/or are subject to a periodic disturbance of known period. In this case, the error in the previous period is recorded and used to modify the command in the current period, modifying the command in real time. References [1–3] give good overall information about the field. References [4, 5] present the author's approaches to designing ILC and RC.

The first author has been in this field since 1984, and this paper highlights some of the unexpected twists and turns his thinking took as he developed research results. Consider three different approaches to engineering problems.

(1) *Theoretician*: Someone whose attention is on the mathematics and producing mathematical results and proofs.
(2) *Simulator*: Someone who emphasizes computer simulation as a convenient and easy way to predict the behavior of the real world. Some fields require considerable sophistication in developing computer code for this purpose.
(3) *Experimentalist*: Some engineers love to work in the laboratory, put together hardware, and just find ways to make things work the way then intend.

The twists and turns relate to how these three approaches interrelate. Examples are given that show how each approach can lead one in the wrong direction, each can set research directions that sound good, but are actually misguided, or produce conclusions that are wrong. Often people strongly emphasize one of these approaches. The message of the paper is that in order to make the most progress in the most effective research directions needed to advance a field, one must combine all approaches. This same message was presented in quite different forms in [6, 7].

155.2 Iterative Learning Control

We consider the simplest form of ILC, one which seems very intuitive. Let $u_j(k)$ be the command to a digital control system at time step k in iteration or run j. And let the desired output be $y^*(k)$ for time steps from 1 to p. Then the simplest ILC updates the command in the next run as

$$\begin{aligned} u_{j+1}(k) &= u_j(k) + \phi e_j(k+1) \\ e_j(k) &= y^*(k) - y_j(k) \end{aligned} \tag{155.1}$$

where $e_j(k)$ is error. In words, if the output was two units too low in the last run at a certain time, increase the command by two units in the next run, or more generally by learning gain ϕ times two units. We assume that there is a one time-step delay going through the digital system, so we look at the error one step ahead. Write the system in modern control form as

$$x_j(k+1) = Ax_j(k) + Bu_j(k) \quad y_j(k+1) = Cx(k+1) \tag{155.2}$$

one way to compute the error is to imitate what the control system does. In the $j = 0$ iteration, apply a command equal to the desired output in Eq. (155.2). Observe the output, compute the error, and then update the command from Eq. (155.1) and apply to the system. Call this Method 1. Method 2 mathematically derives the update of the error vector $\underline{e}_j$ for all time steps in a run to satisfy

$$\underline{e}_{j+1} = (I - \phi P)\underline{e}_j = \begin{bmatrix} 1 - CB\phi & 0 & \cdots \\ -CAB\phi & 1 - CB\phi & \cdots \\ \vdots & \vdots & \ddots \end{bmatrix} \underline{e}_j \tag{155.3}$$

ILC is easiest analyzed using a matrix formulation, while RC is easiest analyzed using z-transforms and higher order difference equations. Both fields push the limits of the abilities of standard control methods to analyze the stability and performance behavior. And this leads to many interesting research issues.

155.3 Misconceptions by One Approach Corrected by Another Approach

As commented above, the message to be conveyed is that too much emphasis on one of the three approaches can easily make a researcher spend time addressing research issues that seem the logical direction to go from the given approach, but are found to be misguided when viewed by other approaches. Hence, progress in a field depends on an interplay between approaches. This is illustrated here by a series of examples.

Misconception 1

Theoretician: The Theoretician in developing the concept of ILC, thinks that the best possible ILC is one that converges to zero tracking error for the largest possible class of systems. Then one can turn on the ILC, go get a cup of coffee, and come back to find that the control system now is tracking the desired trajectory perfectly. Mathematical development for Eq. (155.3) says that the simplest ILC law (155.1) converges to zero error if the diagonal elements of the matrix are less than unity in magnitude, and this is very easy to satisfy. And it produces stability independent of the dynamics of the system represented in the A matrix. A very powerful result. Further research in this same direction allows him to prove that for nearly all nonlinear systems it also converges to zero error. He publishes results, and as usual

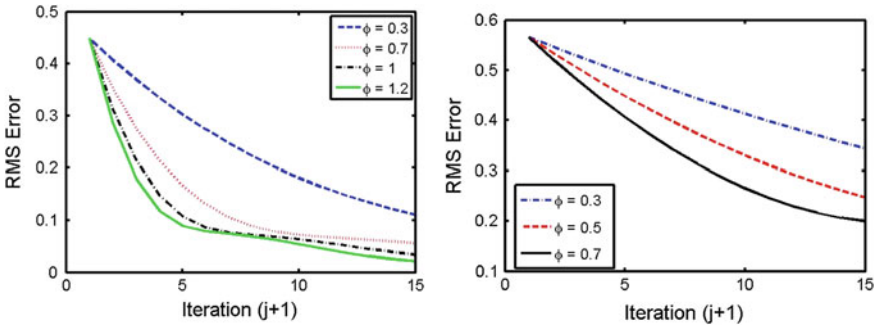

Fig. 155.1 Reduction in Root Mean Square (RMS) error as a function of iterations, *left* plot for transfer function $1/(s+1)$ and *right* for $2/[(s+1)(s+2)]$ fed by zero order hold at 20 Hz sample rate, and desired trajectory $y^*(t) = 0.5[1 - \cos(\pi t)]$

he has a section giving numerical results for simple problems, to show it all works. He even studies the effect of adjusting the learning gain ϕ. See (Fig. 155.1).

Experimentalist: The experimentalist runs experiments on a robot. After 15 iterations the $400,000 robot is making so much noise that one cannot continue for fear of damaging the hardware.

Simulator: The simulator uses a simple model of the robot, and runs iterations to see what would have happened if the experimentalist could have continued the iterations. The RMS of the tracking error reaches exponential overflow. This does not look like guaranteed convergence to zero error. He then simplifies the problem by shortening the trajectory and using slower sample rate, and finds the theoretician was right, it does converge to zero error. In the left of Fig. 155.2 the RMS error at iteration 3×10^5 is 3.657×10^{-47}. But the maximum error reaches 10^{51}. It does converge but there is a bad transient that makes his result useless in the world.

Misconception 2

Theoretician: Anyone who knows anything about control theory will tell you that the first necessity in designing a control system is to have an asymptotically stable system. The theoretician says, "I need asymptotic stability of my ILC or RC system." The behavior in Fig. 155.2 is not technically unstable, but it is for practical purposes. The behavior of the corresponding RC problem is in fact unstable.

Experimentalist: During the first 7 iterations in the experiment on the robot reported above, the RMS error decrease by a factor of 50 and then the error started to grow as it does in the simplified problem in Fig. 155.2. A factor of 50 is a very big improvement in tracking accuracy. So now the result in Fig. 155.2 is not useless at all, just turn off the iterations when the error goes through a minimum. Further theoretical study establishes that this is nearly a universal phenomenon in ILC. Figure 155.2 applies to a simplified situation, but a detailed look at the beginning of the plot shows an improvement of RMS error by a factor a bit less than 10 in the first 7 or 8 iterations.

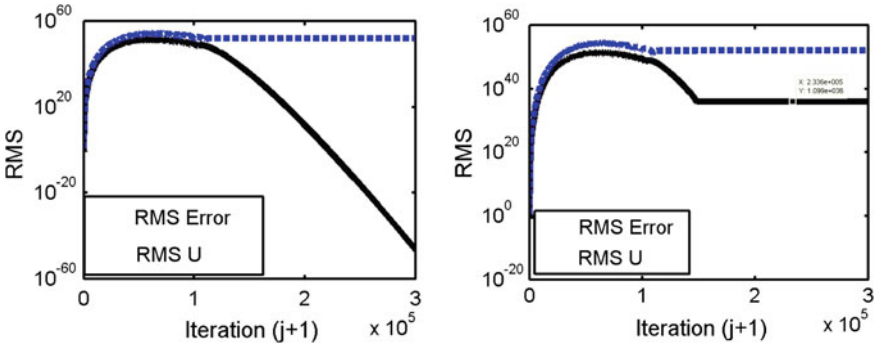

Fig. 155.2 RMS error in radians and RMS of the control input for a third order system, 100 Hz sample rate, 1 s trajectory, $[a/(s+a)][\omega_n^2/(s^2+2\zeta\omega_n s+\omega_n^2)]$, $a=8.8, \omega_n=37, \zeta=0.5$, $y^*(t)=\sin(2\pi t)$. *Left:* method 1, *right:* method 2. Solid line RMS error, dashed line RMS command

Misconception 3

Experimentalist: Some experimentalists like to play with hardware, trying different things until they get something to work. RC experiments run at Xerox Corporation aimed to eliminate periodic velocity errors in a belt drive produced by imprecise machining and mounting of gears and timing belt. It did not take many iterations for the RMS error to drop to a noise level, and then the experimentalist ran 1,000 iterations. The experimentalist was convinced by this, that he had succeeded in making a well behaved RC system with substantially improved velocity output. He concluded the RC system was stable.

Theoretician: The theoretician complains he knows the system is unstable from the mathematics. Try again. It was not easy to try again, since data storage reached limits in buffers. The experimentalist finds that there is an instability that starts to be observed after 2,500 periods. The theoretician was right.

Experimentalist: "I don't care what you say, I will make a better filter and try again." Then he runs 10,000 iterations with no evidence of instability.

Theoretician: The theoretician initially thinks he just needs to run longer. But then he wonders if it could be stable. Some thinking says that maybe the update each iteration, that is supposed to accumulate to produce instability, might be so small that maybe it is beyond the last digit in the analog to digital converters, and hence cannot accumulate to produce instability. Analysis of the situation shows that this is true. Unstable in theory, but stable in practice—until the model was improved. And with this result a new way to design stable RC was developed.

Misconception 4

Theoretician: The theoretician says, of course we want the ILC law or RC law to converge to zero tracking error.

Experimentalist: In RC experiments on the same velocity control system at Xerox Corporation, a particularly good RC design caused the hardware to make

considerable noise. Errors were being corrected very far above the bandwidth of the feedback control system, requiring commands 11 times as large as the error to be corrected. Clearly, the very accurate RC control was wearing out the hardware with big control commands. Conclusion, one should not always aim for zero error, and one needs to create RC design methods that cut off the learning above some chosen frequency.

Misconception 5

Theoretician: The theoretician develops a more sophisticated control law, for example by replacing the ϕ in Eq. (155.1) by P^T (see Eq. (155.3)) and now the RMS of the tracking error decays monotonically to zero instead of going to 10^{51} radians on its way to zero. However, he notes that the control action required for zero error must satisfy an equation that involves P^{-1}. This inverse is guaranteed to exist, but the largest singular value of the inverse is estimated as 10^{53}. The convergence to zero error is guaranteed, so the control action must grow to reach such values.

Experimentalist: The experimentalist applies this ILC law, and he sees no difficulty. The error reduces substantially. So ridiculous error growth in theory, but in the real world everything behaves well.

Theoretician: The theoretician now needs to explain the results. The part of the control action that needs to grow to such large numbers, grows so slowly that it is never seen in applications. In fact, it might not be able to grow because the update is again beyond the last digit in the analog to digital converters.

Misconception 6

Simulator: The simulator, does computer simulations with the expectation that he/she is showing what the real world will do if an experiment were run. Can we trust the simulations? The answer can be no. (1) The simulations were wrong in the velocity control system because no one thought that the quantization level in the analog to digital converter might be important and stabilizing. (2) The RMS error computation for Fig. 155.2 can be computed by method 1 or method 2 below Eq. (155.2). The second method on the left of Fig. 155.2 shows convergence to zero error. The first method on the right plot in Fig. 155.2 shows says it does not converge. Both methods are mathematically identical, but give different results in simulations. (3) The theoretician may aim to design ILC or RC to be as robust to model inaccuracy as possible as a main objective, but the experimentalist notes that the most robust ILC laws have worse final error level in hardware. All simulations converge to a final error level. But this final error level is determined by numerical noise in the simulations and has nothing to do with the final error level one would observe in the world. The simulator has no way to deal with this without having a model of the irreproducibility level of the hardware.

References

1. Ahn, H.-S., Chen, Y., & Moore, K. L. (2007). Iterative learning control: Brief survey and categorization. *IEEE Transactions on Systems, Man, and Cybernetics, Part-C, 37*, 1099–1122.
2. Moore, K., & Xu, J.-X. (Eds.). (2000). Special issue on iterative learning control. *International Journal of Control*, *73*(10).
3. Bien, Z., & Xu, J.-X. (Eds.). (1998). *Iterative Learning Control: Analysis, Design Integration and Applications*. Boston: Kluwer Academic Publishers.
4. Longman, R. W. (2000). Iterative learning control and repetitive control for engineering practice. *International Journal of Control, 73*(10), 930–954.
5. Longman, R. W. (2010). On the theory and design of linear repetitive control systems. *European Journal of Control, 16*(5), 447–496.
6. Longman, R. W. (2003). On the interaction between theory, experiments, and simulation in developing practical learning control algorithms. *International Journal of Applied Mathematics and Computer Science, 13*(1), 101–111.
7. Longman, R. L. (2012). Learning from theory, simulations, and experiments: A case study from iterative learning control. In N. M. Seel (Ed.), *Encyclopedia of the Sciences of Learning*. New York: Springer Publications.

Chapter 156
Innovation and Entrepreneurship Education in Engineering

R. Radharamanan and Jeng-Nan Juang

Abstract In this paper, project based innovation and entrepreneurship education activities developed and implemented at Mercer University School of Engineering (MUSE) are highlighted and how MUSE promotes entrepreneurial mindset among engineering students is presented and discussed in term of curriculum development and extracurricular activities. The course sequence developed and implemented integrates elements of entrepreneurship with engineering; develops an entrepreneurial mindset in engineering students; fosters innovation and creativity in engineering disciplines; helps the students to develop business plans for the entrepreneurial design projects and compete in the annual business plan competition, and promotes new ventures creation. Selected creative student design projects are presented, analyzed, and discussed.

Keywords Innovation · Entrepreneurship · Engineering education

156.1 Introduction

The field of entrepreneurship has been defined as the "study of the sources of opportunities; the process of discovery, evaluation, and exploitation of opportunities" [1]. The entrepreneur has been described as "an innovator or developer who recognizes and seizes opportunities, converts these opportunities into workable and/or marketable ideas" [2]. The importance of entrepreneurship education has been emphasized in business schools and recently in some of the engineering schools. There is a growing need to enhance the entrepreneurship education in universities and colleges due to globalization and emerging international competitions [3].

R. Radharamanan (✉) · J.-N. Juang
School of Engineering, Mercer University Macon, GA 31207, USA
e-mail: radharaman_r@mercer.edu

J. Juang et al. (eds.), *Proceedings of the 2nd International Conference on Intelligent Technologies and Engineering Systems (ICITES2013)*, Lecture Notes in Electrical Engineering 293,
DOI: 10.1007/978-3-319-04573-3_156,

The educational system at the university level at present is not capable of developing students' motivation, competences and skills concerning innovation and entrepreneurship. Instead, entrepreneurship education requires learning methods, pedagogical processes and framework for education, which universities at the moment have not mastered. Such changes, however, involve parallel transformations of didactics, pedagogy and university context [4]. Design for manufacture and assembly and concurrent engineering concepts have been addressed in technology ventures and engineering entrepreneurship education [5]. Creation of academic ventures and business incubation has received increased attention lately [6].

With the changing role of universities, the role of academics has also changed. From being more likely to have the role of advisors, facilitating the transfer of knowledge to the new venture, they are today more likely to be members of the entrepreneurial team, thus playing a greater role in identifying and developing the entrepreneurial opportunities, acquiring resources, and organizing the venture.

Entrepreneurial education must include skill building courses in negotiation, leadership, new product development, creative thinking and exposure to new technological innovation. Technology must be embraced within the classrooms. Solomon et al. [7] conducted one of the most comprehensive empirical analyses on entrepreneurship education. In their view of entrepreneurship pedagogy, they stated, "A core objective of entrepreneurship education is that it differentiates from typical business education. Clearly, for entrepreneurship education to embrace the 21st century, professors must become more competent in the use of academic technology and also expand their pedagogies to include new and innovative approaches to the teaching of entrepreneurship".

Since 2006 KEEN (Kern Entrepreneurship Education Network) schools are preparing more entrepreneurial engineers in the United States [8]. There are more than 20 KEEN schools that share the same vision to instill entrepreneurial mindset into engineering undergraduates. MUSE, one of the KEEN schools, has recently established the Mercer Center for Innovation and Entrepreneurship (MCIE) to promote entrepreneurship education at Mercer campus and collaborate with other KEEN schools in the areas of common interest that include but not limited to: low cost rapid prototyping, smart product design, assistive technologies, alternate energy technologies, and integration of engineering and general education.

156.2 Mercer Entrepreneurship Education (MEEEP) and MCIE

The purpose of Mercer University's School of Engineering is to educate a student who is prepared to be practicing engineer, one who can responsibly contribute to a global society that is becoming ever more dependent on technology. While the focus of the engineering school is to educate engineers, its graduates may enter many fields of graduate studies, especially those requiring the disciplined problem

Table 156.1 Courses taken by semester

Sophomore-1	Sophomore-2	Junior-1	Junior-2	Senior-1	Senior-2
			EGR480	EGR487	EGR488
			MGT427	EGR482	EGR483
	(ECN150)	MKT361			
		MGT363			

1 fall semester, *2* spring semester

solving methods developed in the undergraduate curriculum. The engineering graduates have entered professional graduate programs in medicine, law, and business, as well as graduate engineering programs. There are about 450 undergraduate and 180 graduate students at Mercer School of Engineering. The ABET accredited undergraduate program has biomedical, computer, electrical, environmental, industrial, and mechanical engineering specializations. There are 28 engineering faculty engaged in teaching undergraduate and graduate programs.

The entrepreneurship certificate program was established through Kern Family Foundation Grants in 2007. This program is open to all engineering students at MUSE. Students who complete the course requirements will receive a Certificate of Achievement in Engineering Entrepreneurship. Table 156.1 shows the courses taken by semester to complete the certificate program in entrepreneurship: ECN150: Principles of Microeconomics; MKT361: Principles of Marketing; MGT363: Principles of Management; MGT427: Entrepreneurship; EGR480: Introduction to Senior Design; EGR482: Engineering Innovation and Creativity; EGR487: Engineering Design Exhibit I; EGR483: Entrepreneurship in Engineering Design; and EGR488: Engineering Design Exhibit II. The catalog description of the entrepreneurship certificate program courses are also found in Mercer University Catalog [9].

In addition to the certificate program courses, course modules on creativity, invention, innovation, and entrepreneurship have been developed and taught in the following freshman through senior level courses: EGR107: Introduction to Engineering Design; MAE205: Visualization and Graphics; EGR245: Electrical Engineering Fundamentals; ISE370: Manufacturing Processes; MAE305L: Manufacturing Practices Lab; ISE425: Computer Assisted Manufacturing Systems and Lab; ISE429: Robotics; BME412: Biomechanics; and BME413: Advanced Biomechanics. The MEEEP courses and course modules developed and offered across the curriculum from freshman through senior year helps to instill entrepreneurial mindset to students graduating from MUSE.

Since 2007, all engineering students took one or more courses and/or modules listed in the entrepreneurship certificate program; 30 entrepreneurial senior design projects were funded; 120 or more students participated in the business plan/entrepreneurial senior design project competitions; one of the projects received national and state recognition; ten projects received regional/Mercer awards; more than 45 papers were presented in regional, national, and international conferences by faculty and students; students and faculty applied for five provisional patents and two utility patents; students and faculty are in the process of forming at least

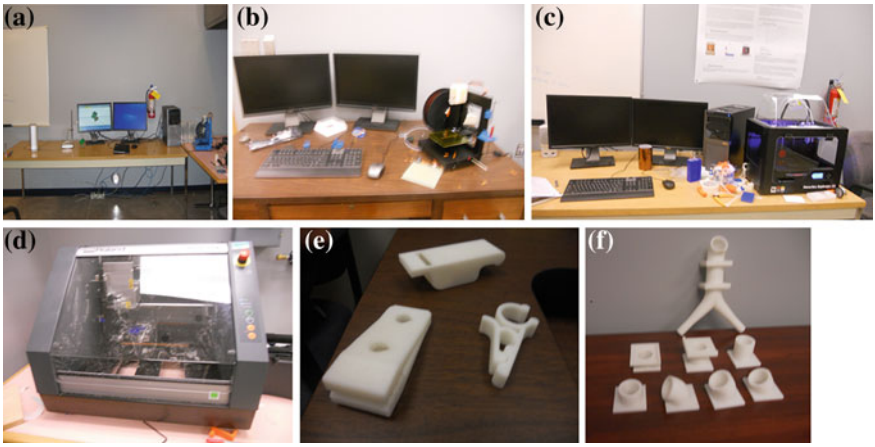

Fig. 156.1 **a** 3D scanning/printing facility; **b** 3D UP printer; **c** 3D MakerBot replicator; **d** CNC mill; **e** sample parts printed; and **f** samples for testing

two startup companies focusing on low cost electromechanical and biomedical devices; and more than 30 students are working as intrapreneurs in major industries/corporations in Georgia and neighboring states.

In 2010, Mercer's Academic Initiatives Monetary Fund (AIM Fund) has approved the creation of the "Mercer Center for Innovation and Entrepreneurship" at MUSE, to enhance the activities of MEEEP across Mercer campus. The center is operating since August 2010. The MCIE focuses on cross-disciplinary educational programs (teaching, collaboration, and learning) as well as research and scholarly activities among Mercer faculty and students. This unique center initially involves the School of Engineering, School of Medicine, School of Law, School of Business and Economics, and College of Liberal Arts. Possible future participation is envisioned from other colleges and schools such as College of Nursing, College of Pharmacy and Health Sciences, School of Theology, and School of Music. The MCIE provides an interdisciplinary collaboration that is necessary for submitting competitive extramural funding proposals. It serves as a platform for diverse scholarly activities, curricular and co-curricular enhancements.

A low cost 3-D scanning/printing facility, Fig. 156.1a, has been added to the MCIE to enhance innovation and creativity aspects among engineering students as well as to instill entrepreneurial mindset that includes making prototypes of their design products as well as learning to commercialize the products they made. During the fall semester (2011) more than 50 seniors, juniors, freshman, and honors students were trained to scan 3D objects as well as design and print 3D parts/products in the new facility. During the spring and fall semesters of 2012 and 2013 more than 100 students/academic year were trained in this facility that include honors students/projects, senior design projects, class projects and special projects. Two more 3-D printers and a CNC Mill (Fig. 156.1b, c, and d respectively) have been added to the facility to meet the growing needs for the rapid

prototyping and 3-D printing of Mercer engineering students to successfully complete their innovative open ended design projects. Samples printed using the 3D UP printer is shown in Fig. 156.1e and f.

156.3 Mercer Entrepreneurship Student Club

Mercer Entrepreneurship Student Club (MESC) started in 2007, as part of MEEEP to promote students activities on innovation and entrepreneurship across Mercer campus. More than 60 engineering students through MESC are actively engaged in: recruiting students to the entrepreneurship program; participating in the entrepreneurship certificate program; taking entrepreneurship related courses; participating in entrepreneurial senior design projects, listening to successful entrepreneurs through invited speakers and seminar; developing business plans and competing in the design and business plan competitions; helping to organize KEEN regional conferences and Mercer innovation chase competitions; promoting activities during national entrepreneurship week; raising funds to participate and present technical papers on their senior design and business plans through "Cookout" lunches and dinners and selling T-shirts that were designed and made by entrepreneurship club students; presenting technical papers in the regional, national and international conferences such as ASEE, IEMS, ICMES, and NCIIA; participating in KEEN regional conferences and KEEN related competitions; and actively participating in the activities of MCIE.

156.4 Entrepreneurial Design Projects

MCIE has funded several entrepreneurial design projects in the areas of Biomedical, Computer, Electrical, Environmental, Industrial/Manufacturing, and Mechanical Engineering. Only selected creative student design project(s)/course module(s) in manufacturing involving CAD/CAM, Rapid Prototyping and Robotics are briefly presented and discussed below:

156.4.1 Retrofitting of Tabletop CNC Lathe (Senior Design Project)

This project [10] describes the infusion of new technology and the resulting extended useful life of a 20 year old computer numerical controlled (CNC) tabletop lathe. Key to the success of the project was the ability to have a low cost, high performance real-time controller that was compatible with the existing

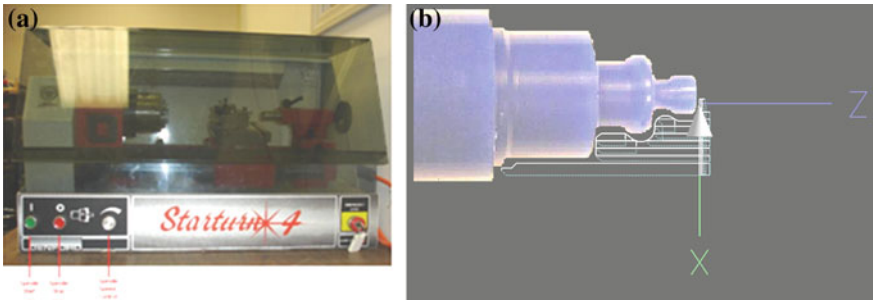

Fig. 156.2 Tabletop CNC lathe: **a** retrofitted and functional; **b** artifact made

electrical components of the lathe. The Enhanced Machine Controller (EMC) Project software installed on a personal computer running a Linux Operating System was the basis of the new controller design. Artifacts were created using G-codes from existing models. The retrofitted lathe is currently being used in the Intelligent Manufacturing Systems Lab at Mercer University for teaching computer aided manufacturing and providing hands-on experience to students taking manufacturing courses (Fig. 156.2).

156.4.2 Prototyping with the MakerBot Cupcake (Senior Design Project)

The MakerBot Cupcake [11] CNC machine that uses additive manufacturing technology to create objects made of Acrylonitrile Butadiene Styrene (ABS) was assembled and made operational. It converts a 3D model to a usable physical object. Alterations such as reducing idler wheel thickness, using a higher grade material for the insulation between the heater barrel and the rest of the extruder, and fabricating a removable heat source were made to the machine to ease maintenance and improve reliability.

The MakerBot consists of a wooden frame, a build platform with X and Y pulleys for movement, and a Z platform on which the extruder sits. The extruder, and the X, Y, and Z stepper motors all have a circuit board which is connected to the Cupcake's motherboard (Fig. 156.3). Cupcake uses additive technology to form 3-D parts, which is ideal for prototyping and manufacturing a small number of parts. Additive technology allows the capability to print interior structures.

The following steps were taken to achieve successful operation of MakerBot:

- Downloading software
- Testing motors independently for vibration and backlash

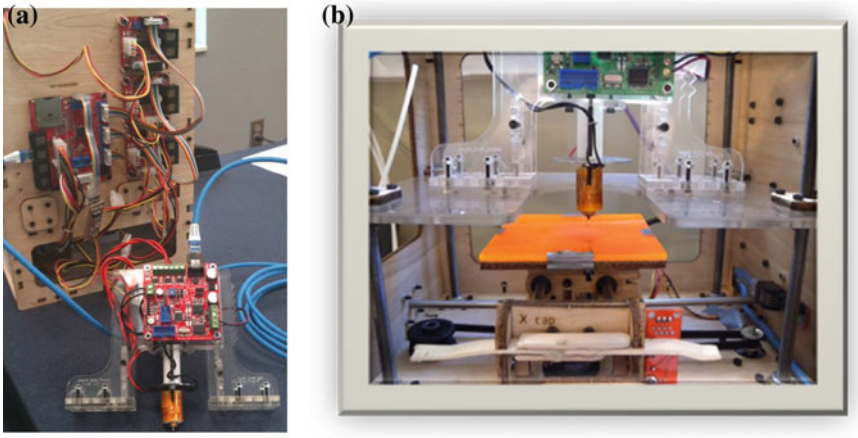

Fig. 156.3 MakerBot: **a** circuit board details and **b** assembly

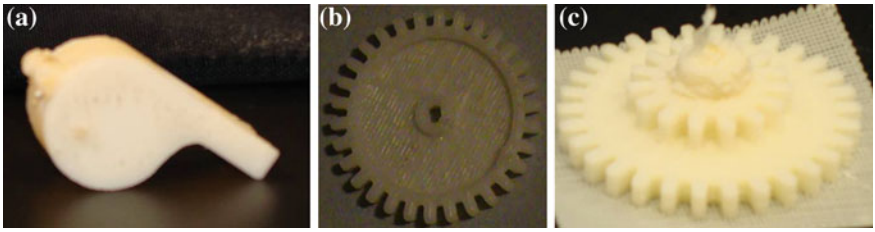

Fig. 156.4 Printed parts: **a** whistle; **b** single gear and **c** double gear

- Testing extruder for idler wheel and heater barrel
- Printing: misprints or successful prints.

Using the MakerBot, a whistle was successfully printed as shown in Fig. 156.4a. The interior ball did not come free from the bottom wall, and it is possible that this is a complication of the nozzle being too close to the Z platform at the start of the build, or an error in the G-codes. The whistle is a good example to print because of its interior features. The whistle is hollow with an interior ball, which cannot be achieved using a traditional milling machine.

Single and double gears were printed that have a hollow honeycomb interior, which reduces use of unnecessary ABS filament. This can be seen in the interior of the gear. Both the single and double gears were printed and are shown in Fig. 156.4b and c respectively.

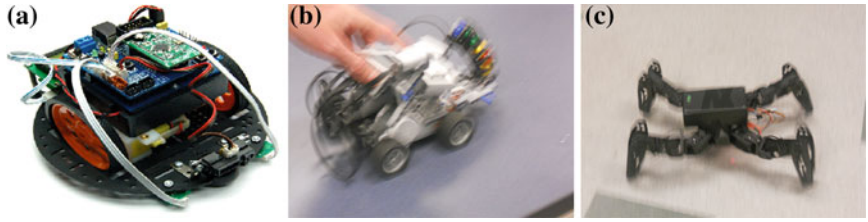

Fig. 156.5 **a** Autonomous POP BOT built and tested; **b** Lego robot; **c** Quadruped robot

156.4.3 Autonomous Robot Competition (ISE429 Robotics: Course Module)

The POP BOT [12], a complete robot kit, was chosen as the robot platform for the competition. The kit comes with everything needed to construct an autonomous robot. This includes motors, wheels, chassis material, LCD display, and several sensors. The sensors included in the kit were two touch sensors, two infrared reflector boards, and an infrared range finder. In addition, the kit includes a piezo speaker, two line LCD display, servo motor with head mount, two DC motors, main board with USB interface, USB connector cable, program disk, wiring, wheels, platform, construction parts, four batteries, and a companion manual. The robot is propelled by two 5 V motors. The robot comes with multiple sensors for different applications of the robot. The sensors chosen for the competition were the infrared sensors. The kit has one infrared sensor which was complimented by additional sensors to provide movement in multiple directions. The robot used controlled movements to avoid obstacles and continue forward progress. The robot was coded to make simple direction changes using the motors to move and avoid obstacles.

Student teams constructed autonomous robots to compete in two different contests. The first contest places the robots in an arena and challenges them to avoid obstacles and other robots. The robot must operate without human control and for a specified length of time. The second test places the robot in a hallway and challenges the robot to traverse the hallway from one end to the other while avoiding obstacles placed in its path. The robot must also operate without human control for the length of the challenge.

To complete these challenges, the robot must be outfitted with sensors to detect obstacles. These sensors are triggered by external stimuli and converted to signals sent to the arduino [12]. The signals from the sensors are interpreted and used to program the behavior of the robot. One of the POP BOT built and tested by a student team for the competition is shown in Fig. 156.5a.

Upon completion of the robot build, it was tested with regards to the competitions it would be participating in. The robot demonstrated capable performance in the obstacle avoidance. The infrared sensors were able to detect objects up to 32 cm away. Small changes in motor speed and direction proved to be effective in

directing the robot to avoid obstacles when detected. The robot performed well in the course traversal but could be improved by introducing course correction in the coding. Another improvement would be the use of fuzzy logic to control the speed of the motors. Other robots built and tested by student teams include but not limited to Lego robot, Fig. 156.5b, and Quadruped robot, Fig. 156.5c.

Student teams of all the projects discussed in this section participated in the annual design project competitions held at MUSE. These projects results were presented in the ASEE, KEEN, NCIIA, IEMS, and ICMES conferences and published in the conference proceedings.

156.5 Results and Conclusions

The entrepreneurship courses and modules developed and implemented help to instill entrepreneurial mindset among engineering students and graduates. Extra-curricular activities such as business plan competitions, Mercer innovation chase competitions, participation in conferences, and invited speakers/seminars promote innovation and creativity among students. The entrepreneurship certificate program established in 2007 is expanding and achieved a number of milestones: both undergraduate and graduate students are attracted to the entrepreneurship related courses; a number of entrepreneurial senior design projects were funded and the student teams participated in the "Business Plan Competitions" as well as presented their design projects in regional, national, and international conferences. Some of the design projects received regional and national recognitions/awards during the period 2007–2013.

Acknowledgments The authors wish to express their sincere thanks to Kern Family Foundation for the initial grant during 2007–2009 and the expansion grant during 2009–2011 to promote invention, innovation, and entrepreneurship in engineering education at MUSE.

References

1. Shane, S., & Venkataraman, S. (2000). The Promise of entrepreneurship as a field of research. *Academy of Management Review, 25*(1), 217–226.
2. Kuratko, D. (1995). *Entrepreneurship in international encyclopedia of business and management*. London: International Thomson Press.
3. Hisrich R. D., Peters, M. P., & Shepherd, D. A. (2008). *Entrepreneurship* (7th ed.). New York: McGraw-Hill.
4. Blenker, P., Dreisler, P., Faergemann, H. M., & Kjeldsen, J. (2008). A framework for developing entrepreneurship education in a university context. *International Journal of Entrepreneurship and Small Business, 5*(1), 45–63.
5. Anderson, D. M. (2008). *Design for manufacturability and concurrent engineering*. California: CIM Press.

6. Timmons, J. A., & Spinelli, S. (2009). *New venture creation: Entrepreneurship for the 21st Century* (8th ed.). New York: McGraw-Hill.
7. Solomon, G. T., Duffy, S., & Tarabishy, A. (2002). The state of entrepreneurship education in the United States. A nationwide survey and analysis. *International Journal of Entrepreneurship Education, 1*(1), 65–86.
8. Kriewall, T. J., & Mekemson, K. (2010). Instilling the entrepreneurial mindset into engineering undergraduates. *Journal of Engineering Entrepreneurship, 1*(1), 5–19.
9. Mercer Engineering Entrepreneurship Education Program. (2012). Mercer University Catalog, Macon Campus, Academic year 2012–2013, 316–317.
10. Amato, D., Laree, A., Abroad, R., & Duan, T. (2007). *CNC lathe project critical design review*. Macon, GA: School of Engineering, Mercer University.
11. Dawson, S. N., Coonce, A. M., & Cox, L. J. (2010). Recycling system for the cupcake 3D printer. In *Critical design review*. Macon: School of Engineering, Mercer University.
12. The Arduino Compatible POP-BOT Mobile Robot Kit. (2012, April 16). Activity Manual Version 1.0 Standard, Innovative Experiment Co. Ltd.